

Versatile Trityl Radicals: Improving Applications via Tailored Synthesis

DISSERTATION

zur
Erlangung des Doktorgrades (Dr. rer. nat.)
der
Mathematisch-Naturwissenschaftlichen Fakultät
der
Rheinischen Friedrich-Wilhelms-Universität Bonn

vorgelegt von
Maurizio-Nicolas Fleck
aus Bonn

Bonn, 2021

Angefertigt mit Genehmigung der Mathematisch-Naturwissenschaftlichen Fakultät der
Rheinischen Friedrich-Wilhelms-Universität Bonn

1. Gutachter	Prof. Dr. Olav Schiemann
2. Gutachter	Prof. Dr. Snorri Sigurdsson
Tag der Promotion	11.12.2021
Erscheinungsjahr	2021

Table of Contents

Abstract	III
Zusammenfassung	V
Acknowledgements	VIII
1. Introduction	
1.1. Stable Radicals	
1.1.1 Triarylmethyl Radicals	
1.1.1.1 Properties	1
1.1.1.2 Synthesis	7
1.1.2 Nitroxides	
1.1.2.1 Properties	19
1.1.2.2 Synthesis	20
1.1.3 Other Stable Radicals	23
1.2 Applications of Stable Radicals	25
1.2.1 Exploiting the Reactivity of Stable Radicals	25
1.2.2 Magnetic Materials: Interaction of Spin Centers	27
1.2.3 Spin Labelling EPR	
1.2.3.1 Spin Labelling: A Valuable Tool in Structural Biology	30
1.2.3.2 Spin Labelling: Bioconjugation Chemistry	31
1.2.3.3 Spin Labels: Paramagnetic Tags for Biomolecules	34
1.2.3.4 In-Cell EPR	36
1.2.3.5 Model Compounds: EPR-based Distance Measurements	38
1.2.4 Functional EPR-Spectroscopy	40
1.2.5 Dynamic Nuclear Polarization	41
1.3 EPR Spectroscopy	
1.3.1 The Spin System	42
1.3.2 Characterization of Stable Radicals via cw-EPR Spectroscopy	46
1.3.3 Distance Measurements via Pulsed EPR	48
2. Aim of the Work	
2.1 Trityl Radicals	51
2.2 Model Compounds Containing Fe ³⁺ -Centers	53
3. Results and Discussion	
3.1 Trityl Radicals	
3.1.1 Odorless Access to <i>tert</i> -Butylarylsulfides via Pd-catalyzed C-S Cross-Coupling	54
3.1.2 Synthesis and Crystal Structure of a Silylated Trityl Alcohol	55
3.1.3 C-C Cross-Coupling Reactions of Trityl Radicals	56
3.1.4 Trityl-Porphyrin Conjugates: Exchange Coupling in Photogenerated Multi-Spin Systems	57
3.1.5 SLIM: A Bioresistant and Short-Linked Trityl Spin Label	59
3.1.6 OxSLIM: Synthesis and Evaluation of a Highly Hydrophilic Trityl Spin Label	60

3.2. Iron(III) Model Compounds for EPR-based Distance Measurements	
3.2.1 Synthesis and Characterization of Iron(III)-nitroxide Model Compounds.....	61
3.2.2 EPR Based Distance Measurements Involving Fe(III)-Centers	62
4. Summary and Outlook.....	64
5. References	
5.1 Abbreviations	66
5.2 Literature.....	67
6. Appendix	76
[A0] Curriculum Vitae	78
[A1] Improved, Odorless Access to Benzo[1,2-d;4,5-d']-bis[1,3]dithioles and Tert-butyl Arylsulfides via C-S Cross Coupling	81
[A2] Tris[2,2,6,6-tetramethyl-8-(trimethylsilyl)benzo-[1,2-d;4,5-d']bis(1,3-dithiol) -4-yl]methanol diethyl ether monosolvate	123
[A3] C–C Cross-Coupling Reactions of Trityl Radicals: Spin Density Delocalization, Exchange Coupling, and a Spin Label	141
[A4] Excitation Energy Transfer and Exchange-Mediated Quartet State Formation in Porphyrin-Trityl Systems.....	221
[A5] SLIM: A Short-Linked, Highly Redox-Stable Trityl Label for High-Sensitivity In-Cell EPR Distance Measurements	255
[A6] Ox-SLIM: Synthesis of and Site-Specific Labelling with a Highly Hydrophilic Trityl Spin Label	311
[A7] Synthesis of μ_2 -Oxo-Bridged Iron(III) Tetraphenylporphyrin–Spacer– Nitroxide Dimers and their Structural and Dynamics Characterization by using EPR and MD Simulations.....	387
[A8] Pulsed EPR Dipolar Spectroscopy on Spin Pairs with one Highly Anisotropic Spin Center: The Low-Spin Fe ^{III} Case	465
[A9] Pulsed EPR Dipolar Spectroscopy under the Breakdown of the High-Field Approximation: The High-Spin Iron(III) Case	515

Abstract

Though organic radicals are generally considered as highly reactive species, this paradigm was disproved already in 1900 by *M. Gomberg* discovering the triphenylmethyl radical. Nowadays, numerous stable radicals are known and, likewise, a plethora of their applications have been developed. The unique properties of sulfur-rich trityl radicals (TAM-radicals) i.e., long relaxation times, high stability, and narrow EPR-linewidths, facilitated their widespread use for MRI-imaging, *in-vivo* oximetry, dynamic nuclear polarization (DNP), and as spin labels for EPR-based distance measurements. Despite the tremendous progress at the application site, the synthetic chemistry of these stable radicals did not evolve equally.

Therefore, it was the aim of this PhD-thesis to 1) broaden the scope of functionalization options, and 2) to apply these to develop TAM-radicals with improved properties tailored to the desired applications. Accordingly, a major part of this thesis was dedicated to the synthesis of spin labels suitable for *in-cell* experiments and benchmarking their performance with known species. In view of their beneficial EPR properties, the incorporation of TAM-radicals into prospective paramagnetic materials was studied as well. Though the focus of the presented work lies on synthetic chemistry, the motivation was drawn from improving the application perspectives of TAM-radicals.

Starting with the synthesis of the TAM-scaffold, tetrakis(*tert*-butylthio)benzene is a common precursor for all TAM-radicals. Its synthesis regularly involves the excessive use of highly malodorous *tert*-butyl thiol and low yields are associated with the harsh S_NAr -chemistry employed. Utilizing thiourea as a sulfur source, an odorless two-step process to obtain tetrakis(*tert*-butylthio)benzene in a high yield via a Pd-catalyzed C-S cross-coupling was developed in course of this thesis.

In appreciation of the versatility of C-C cross-coupling reactions, their performance on TAM-radicals was explored to enable more diverse functionalizations. For that, an iodination procedure was developed and subsequently, *Suzuki-Miyaura* coupling was used to construct π -conjugated TAM-radical arrays, including a trityl biradical, and a trityl-porphyrin system. The latter was then altered by insertion of different metal-ions and subjected to studies on the formation of multispin systems upon photoexcitation. These studies carried out in collaboration with other researchers targeted the development of materials for spintronics consisting of TAM-radicals. Moreover, *Sonogashira-Hagihara* couplings were examined, whereby a competitive, yet unexpected, carbothiolation was encountered. However, restraining this side reaction through rational reagent choice ultimately allowed to isolate an ethynyl-substituted trityl radical, which holds implications for the development of spin labels.

Considering trityl spin labels in general, representatives known prior to this work suffer from major drawbacks: 1) Based on esters and amides of the so-called *Finland trityl*, the linkage to the bioconjugation group is unnecessary long, 2) their hydrophobic nature leads to undesired

and non-specific interactions with biomolecules and themselves, and 3) their resistance towards intracellular reductants needs to be improved. Using a mild *Mitsunobu/Retro-Diels-Alder* sequence, a **short-linked maleimide** trityl spin label, given the acronym SLIM, was developed, bearing a simple methylene group as an appreciably short linker. Additionally, the installed imidomethylene-unit affects the reduction potential in an advantageous manner, such that SLIM exhibits an outstanding *in cell* resistance. This allowed to carry out highly sensitive EPR-based distance measurements within intact oocytes of the African clawed frog (*X. laevis*), performed in close cooperation with other group members. Further research aimed at an increased hydrophilicity of trityl spin labels. In this course, the hydroxylated Ox-SLIM was developed, combining the beneficial properties of SLIM with a high hydrophilicity to circumvent undesired aggregation with biomolecules. During the synthesis of Ox-SLIM, the construction of (hydrophilic) trityl scaffolds was revisited and procedures were carefully optimized. Taking advantage of its excellent performance, Ox-SLIM allowed to carry out EPR-based distance measurements down to protein concentrations as low as 45 nM, setting a new benchmark in that area.

Furthermore, this thesis deals with the synthesis of model compounds for EPR-based distance measurements involving Fe³⁺-centers. In anticipation of carrying out such measurements on biomolecules, model compounds with a well-defined geometric arrangement between an Fe³⁺-center and a spin-label were required to develop and validate the respective methodology. Hence, iron(III)-nitroxide and -trityl model compounds were synthesized and thoroughly characterized. It was found that these species dimerize via μ_2 -oxo-bridged iron-centers and the dynamics of these supramolecular entities was characterized by EPR-based distance measurements as well as MD-simulations as part of an in-house collaborative study. Ultimately, these model systems were utilized by others in the group to develop a proper methodology for EPR-based distance measurements towards *low*- and *high*-spin Fe³⁺-centers.

Zusammenfassung

Obgleich organische Radikale zumeist als hochreaktive Spezies angesehen werden, wurde dieses Paradigma bereits 1900 durch *M. Gomberg* mit der Entdeckung des Triphenylmethylradikals widerlegt. So sind heutzutage zahlreiche stabile Radikale mitsamt vielfältigster Anwendungsmöglichkeiten bekannt. Die einzigartigen Eigenschaften schwefelreicher Tritylradikale (sog. „TAM-Radikale“), insbesondere deren lange Relaxationszeiten, hohe Stabilitäten, sowie schmale EPR-Linienbreiten, forcierten deren weite Anwendung im Rahmen der Magnetresonanztomographie, *in-vivo* Oximetrie, dynamischen Kernpolarisation, sowie als Spinlabel für EPR-basierte Abstandsmessungen. Trotz des bemerkenswerten Fortschritts im Hinblick auf der Seite möglicher Anwendungen entwickelte sich die synthetische Chemie dieser Radikale nur zögerlich.

Zusammenfassend sind die Ziele dieser Dissertation daher wie folgt zu definieren: 1) Neue Methoden zur Funktionalisierung von Tritylradikalen sollen entwickelt und 2) genutzt werden, um TAM-Radikale besser auf die beabsichtigte Anwendung anzupassen. Ein Fokus der gegenständlichen Arbeit liegt diesbezüglich auf der Synthese neuer Trityl Spinlabel für Abstandsmessungen in intrazellulärer Umgebung und deren Vergleich mit bekannten Spezies. Ferner wurde auch die Konstruktion paramagnetischer Materialien bestehend aus TAM-Radikalen untersucht, motiviert durch deren vorteilhaften spektroskopischen Eigenschaften. Zwar liegt der praktische Fokus der gegenständlichen Arbeit auf der Synthese und Funktionalisierung, jedoch zielt jedes Teilprojekt stets auf die Verbesserung des Anwendungspotentials von TAM-Radikalen ab.

Eine gemeinsame Vorstufe aller TAM-Radikale ist das 1,2,4,5-Tetrakis(*tert*-butylthio)benzol, dessen Darstellung üblicherweise über eine harsche S_NAr -Reaktion unter Einsatz des übelriechenden *tert*-Butylthiols verläuft. Um dies zu umgehen, wurde eine zweistufige, praktisch geruchsfreie, Synthesesequenz entwickelt, um Tetrakis(*tert*-butylthio)benzol in hohen Ausbeuten erhalten zu können. Hierbei fungiert Thioharnstoff als Schwefelquelle und die C-S Bindung wird im Rahmen einer palladiumkatalysierten Kreuzkupplung geknüpft.

Im Hinblick auf das o.g. Ziel 1) und die Vielfältigkeit palladiumkatalysierter C-C Kreuzkupplungsreaktionen wurde deren Anwendbarkeit auf TAM-Radikale untersucht. Hierzu wurden zunächst iodierte TAM-Radikale synthetisiert, welche sodann im Rahmen einer *Suzuki-Miyaura* Kupplung zu π -konjugierten Radikalsystemen, u.a. einem Tritylbiradikal und einem Tritylporphyrin, umgesetzt wurden. Letztere wurden durch Metallierung derivatisiert und Untersuchungen zur Bildung höherer Spinzustände nach Laseranregung unterzogen. Diese in Kollaboration mit anderen Wissenschaftlern durchgeführte Studie beleuchtete die Eignung von TAM-Radikalen als Bausteine von magnetischen Materialien für Spintronics.

Ferner wurden *Sonogashira-Hagihara* Kupplungen untersucht, wobei unerwartet eine konkurrierende Carbothiolierung beobachtet wurde. Dennoch konnte durch entsprechende Wahl der Reaktionsbedingungen und Reagenzien ein alkynyl-substituiertes Tritylradikal synthetisiert werden, welches grundsätzlich Anwendungspotenzial als Spinlabel besitzt.

In der bisherigen Literatur bekannte Trityl Spinlabel weisen signifikante Nachteile auf, da 1) die Anknüpfung der Funktion zur Biokonjugation über lange Alkylester/amide vollbracht wird, 2) die Lipophilie des Tritylgerüsts zu unspezifischen Wechselwirkungen mit Biomolekülen führt und 3) die Widerstandsfähigkeit gegenüber zellulären Reduktionsmitteln noch verbesserungswürdig scheint.

Mittels einer milden *Mitsunobu/Retro-Diels-Alder* Sequenz konnte das Spinlabel SLIM (engl. „short-linked maleimide“) synthetisiert werden. Hier ist ein Maleimid zur Biokonjugation über eine benzyliche Imidomethylen-Gruppe an das Arylgerüst des Tritylradikals angebunden, sodass eine äußerst kurze Verknüpfung erreicht wird. Gleichzeitig wird hierdurch das Reduktionspotential des Radikals vorteilhaft verschoben, sodass eine besonders hohe Reduktionsstabilität resultiert. Dies erlaubte schließlich in Zusammenarbeit mit anderen Mitgliedern der Arbeitsgruppe, EPR-basierte Abstandsmessungen in intakten Eizellen des afrikanischen Klauenfrosches *X. laevis* durchzuführen. Weitere Untersuchungen hatten sodann auf die Entwicklung eines hydrophileren Tritylspinlabels zum Ziel, woraus das Spinlabel Ox-SLIM resultierte. Durch eine Hydroxylierung der äußeren Substituenten weist Ox-SLIM die vorteilhaften Eigenschaften von SLIM auf, aggregiert jedoch nicht in ungewollter Weise mit Biomolekülen. Unter Ausnutzung seiner hervorragenden Performance konnten mit Ox-SLIM erstmals EPR-basierte Abstandsmessungen bei Proteinkonzentrationen von nur 45 nM durchgeführt werden.

Ein weiterer Teil dieser Dissertation beschreibt die Synthese und Charakterisierung von Modellverbindungen für EPR-basierte Abstandsmessungen zu Eisen(III)-zentren. Um die entsprechende Methodik zu entwickeln und zu validieren, wurden Modellsysteme mit einem definierten Eisen-Radikal-Abstand benötigt. Daher wurden ein geeignetes Eisen(III)-Nitroxid und -Trityl System synthetisiert und gründlich charakterisiert. Es stellte sich heraus, dass diese Systeme supramolekulare Dimere über μ_2 -oxo-verbrückte Eisen-Zentren bilden, deren Dynamik mithilfe von EPR-basierten Abstandsmessungen und MD-Simulationen in einer kollaborativen Studie innerhalb des Instituts beschrieben werden konnte. Schlussendlich wurden die Modellsysteme in hinreichender Menge synthetisiert und von anderen Mitgliedern der Arbeitsgruppe verwendet, um eine Methodik für Abstandsmessungen zu *low*- und *high*-Spin Eisen(III)-Zentren zu entwickeln.

Acknowledgements

First and foremost, my appreciation goes to Prof. Dr. Olav Schiemann, acting as a demanding, yet even more supportive, supervisor of this thesis. During numerous fruitful discussions, he provided guidance through the jungle of science, but also allowed myself to pursue own research ideas. I learned that patience is a crucial virtue of a good scientist, who should always aim to surpass oneself instead of only benchmarking with others. Beyond that, he eagerly promoted me to the first Fast Track PhD-student at the faculty of natural sciences and joined me to take all administrative hurdles on the way. I am truly grateful for this ongoing support over the past four years, which goes way beyond the supervision of this PhD-thesis.

Moreover, I want to acknowledge the commitment of Prof. Dr. Snorri Sigurdsson as the second reviewer of this thesis. Further, my thank goes to Prof. Dr. Arne Lützen, the lectures of whom triggered my fascination for organic chemistry already at an age of 15, for joining the doctoral committee. Additionally, I also appreciate that Prof. Dr. Oliver Gruss became part of the doctoral committee.

As science is not a matter of lone warriors, I want to acknowledge the enthusiastic supporters of the work presented in this thesis. Especially, M.Sc. Caspar Heubach, performing all biochemical experiments, M.Sc. Tobias Hett, conducting numerous EPR-measurements, and Dr. Dinar Abdullin, supporting any EPR-issue, shall be mentioned here. Nonetheless, the outstanding working atmosphere created by all current and former group members, including M.Sc. Martin Peter, M.Sc. Maria Vicino, M.Sc. Christine Wübben, (Dr. in spe) Jaques Jassoy, M.Sc. Kevin Kopp, and B.Sc. Jonas Brode, is gratefully acknowledged. Furthermore, the analytical core facilities (NMR, MS, HPLC) of the chemistry department deserve my gratitude for their reliable and high-quality work.

Moreover, I want to thank my family for the rigorous support during my entire academic track. Especially my grandfather Ulrich Fleck motivated me to pursue my goals and triggered my fascination for natural sciences, though he was educated as a lawyer.

Last, but certainly not least, I want to express my outmost gratitude to Caroline for being a supportive and understanding partner in life 😊.

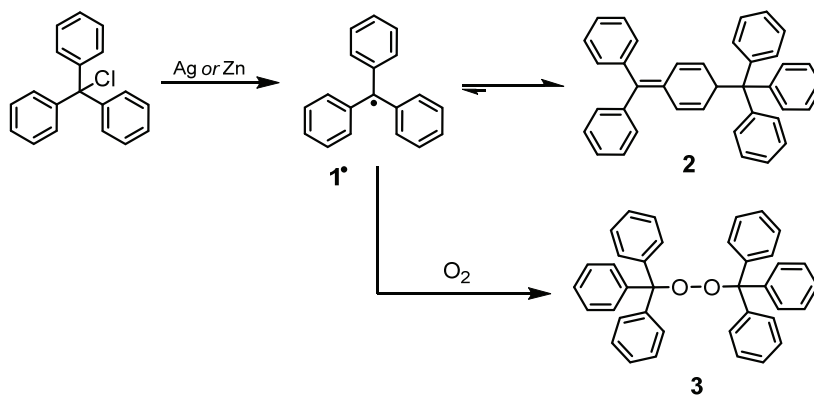
1. Introduction

1.1. Stable Radicals

1.1.1 Triarylmethyl Radicals

1.1.1.1 Properties

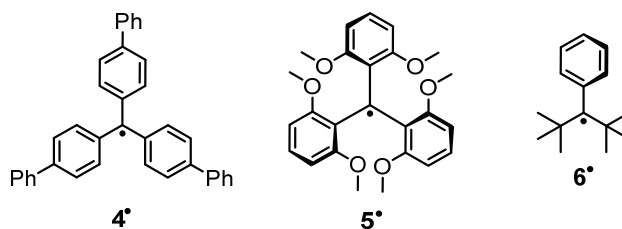
Regularly, radicals are considered as unstable and highly reactive species that occur predominantly as intermediates of chemical transformations. However, this paradigm was disproved already in 1900 by *Moses Gomberg* at the University of Michigan, who coincidentally discovered the triphenylmethyl radical **1**[•] while exploring synthetic access to tetraphenyl methane. Though he was not aware of the exact electronic structure of **1**[•], later referred to as the *Gomberg radical*, he concluded the existence of a trivalent carbon from his meticulous experimental data. Soon after, he published these paradigm-shifting results both in German and English^[1,2] stating “[...] *experimental evidence [...] forces me to the conclusion that we have to deal here with a free radical [...]*”. As shown in Scheme 1, radical **1**[•] recombines to its head-to-tail dimer **2**, whereby the equilibrium is clearly in favor of the dimer, though increasing homolytic dissociation is observed with rising temperature.^[3] Upon contact to oxygen, the head-to-head peroxide **3** forms as a crystalline solid. Attempts to isolate **1**[•] as a solid led exclusively to **2**, so that the existence of the trivalent radical species **1**[•] was doubted within the scientific community of that time. However, in 1910, the German chemist *Wilhelm J. Schlenk* reported the isolation of **4**[•] (Scheme 2) as a dark violet solid which hardly undergoes dimerization in solution,^[4] so that the existence of trivalent species such as **1**[•] was ultimately proven. Beyond question, the emergence of carbon-centered radicals after *Gomberg*'s initial studies was one of the most striking disruptions in chemistry during the early 20th century and triggered a rethinking of valence bond theory. However, it should be noted that although *Gomberg* was nominated for the Nobel prize several times, it was never granted to him despite the tremendous influence of his discovery.^[5]



Scheme 1: Formation of the triphenylmethyl radical **1**[•] and its reactivity.

Obviously, the rationale for the stability of **1**[•] and its analogs was of question. Already in his initial publication,^[1] *Gomberg* recognized the relevance of steric factors that contribute to the

kinetic stability of triphenylmethyl radicals. Soon after, the importance of resonance stabilization was pointed out by the pioneering work of *Linus Pauling* and *George W. Wheland*^[6] and extensive delocalization of the unpaired electron was observed later via electron paramagnetic resonance (EPR) spectroscopy.^[7] Such delocalization of spin density leads to a decrease of the kinetic stability, since the well accessible outer carbon atoms experience radical-type reactivity, as indicated by the formation of **2**. For all triphenylmethyl radicals, the radical-bearing p_z -orbital at the central carbon overlaps to a certain extent with the aromatic π -orbitals of the adjacent phenyl substituents, leading to delocalization of spin density. Vice versa, tilted geometries achieved by 2,6-disubstitution as in **5**[•] restrain the delocalization of the radical center and thereby increase the kinetic stability so far, that crystals suitable for X-ray diffraction could be obtained.^[8] By analogy, the high stability of the tertiary benzyl radical **6**[•] can be rationalized: The two bulky *tert*-butyl substituents force the phenyl plane to adapt a twisted conformation preventing spin delocalization.^[9]



Scheme 2: Structure of radicals **4**[•], **5**[•], and **6**[•].

At this point, it is important to differentiate between stable and persistent radicals.^[10] Following earlier suggestions by *Ingold* and *Griller*,^[11] the IUPAC^[12] recommends the term *persistent* for radicals with lifetime of at least a few minutes in inert solvents. The radicals presented so far are *persistent* in that sense, rendering characterization possible, but decomposition especially upon contact to atmospheric oxygen and moisture occurs. Such a kinetic instability renders extensive storage under ambient conditions impossible and curtails the utility of these early triphenylmethyl radicals with respect to applications as presented later in this thesis.

Therefore, radicals that are *stable* in a sense that handling and storage becomes viable, were sought for. In line with the previous considerations, extensive substitution of the aryl rings adjacent to the radical center served this purpose leading to perhalogenated triphenylmethyl radicals such as **7**[•]. The sterical congestion imposed by the *ortho* chlorine atoms in **7**[•] leads to a tilting of the three phenyl planes resulting in an overall propeller-like structure of the radical, as evident from the crystal structure^[13] depicted in Figure 1.

ⁱ International Union for Pure and Applied Chemistry

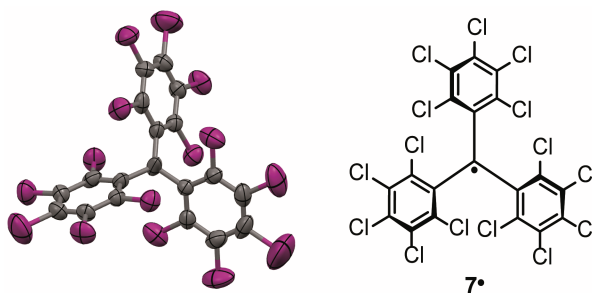
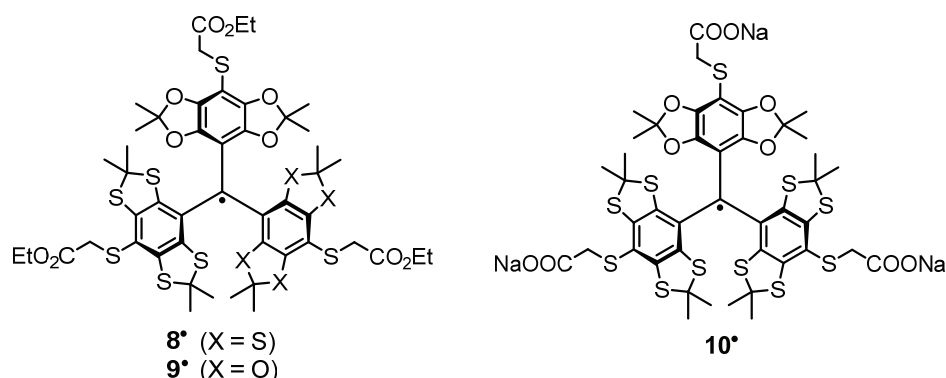


Figure 1: Crystal (left) and Lewis (right) structure of perchlorinated trityl radical **7•** with ellipsoids drawn at 50 % probability level.

Consequently, perchlorinated triphenylmethyl radicals as well as the preceding triphenylmethanes exhibit helical chirality and chiral resolution was achieved via HPLC. Racemization of the enantiomers occurs with a barrier of $\Delta G^\ddagger = 80.4 \text{ kJ mol}^{-1}$ for the tetraphenylmethane **7-H** and 96.0 kJ mol^{-1} for a radical derived from **7•**.^[14] At room temperature, racemization of the latter proceeded with a half-life time of $t_{1/2} < 15 \text{ min}$.^[14] Moreover, functionalization of perchlorinated triphenylmethyl radicals through the aromatic *para*-positionsⁱⁱ was performed extensively and the stability of these radicals is remarkable,^[15,16] as they appear inert to various conditions including concentrated H_2SO_4 and HNO_3 as well as temperatures up to $300 \text{ }^\circ\text{C}$.

This outstanding persistence facilitated their utilization for functional materials, examples for which are provided in section 1.2.2. Besides halogenation, substitution with sulfur and oxygen, incorporated into (thio)ketal moieties, does also lead to significant stabilization of triphenylmethyl radicals, with examples **8•** - **10•** shown in Scheme 3.

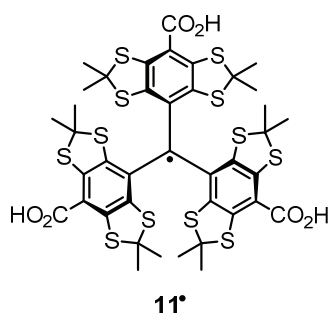
These compounds were extensively studied in the 1990s by *Nycomed* searching for EPR imaging (section 1.2.4) probes.^[17–19] In general, the solution stability increased upon replacing ketals for thioketals, and the free carboxylates appeared less stable than the corresponding esters.



Scheme 3: Structure of trityl radicals **8•** - **10•**.

ⁱⁱ The indicator *para* is relative to the central carbon atom.

Correspondingly, **8•** and **9•** exhibit half-life times of 2700 h, and 100 h respectively, measured in non-degassed acetonitrile. At the same time, a half-life time of 60 h was observed for **10•** in non-degassed aqueous solution.^[18]



Scheme 4: Structure of “Finland Trityl” radical **11•**, a TAM-radical.

These observations led to the development of the so-called Finland Trityl **11•** (Scheme 4), a water soluble tetrathiatriarylmethyl radical (TAM-radical)ⁱⁱⁱ, the synthesis of which was disclosed within the academic community in 2002.^[20]

Its high stability alongside the option to carry out proper functionalization via esterification and amidation (see section 1.3.3) made the use for various applications viable, as described in chapter 1.3.

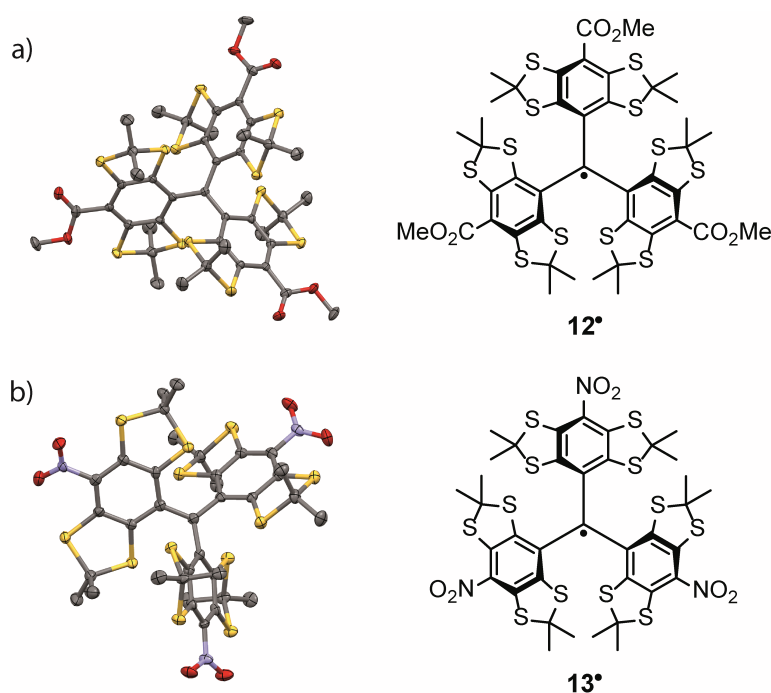


Figure 2: Crystal (left) and Lewis (right) structures of TAM-radicals (a) **12•** and (b) **13•**, hydrogen atoms were omitted for the sake of clarity and ellipsoids are drawn at 50 % probability level.

ⁱⁱⁱ A clear focus of this thesis lies on trityl radicals of the TAM-type. Hence, the term trityl radicals will be used synonymously to TAM radicals, except stated otherwise.

As already discussed for the perchlorinated trityl radicals (*vide supra*), steric congestion triggers TAM-radicals to adapt an almost C_3 -symmetric propeller-like structure. Therein, the three aryl planes are twisted, adapting dihedral angles between 72° (**12 \bullet**)^[21] and 75.6° (**13 \bullet**)^[22] according to the crystal structures shown in Figure 2.

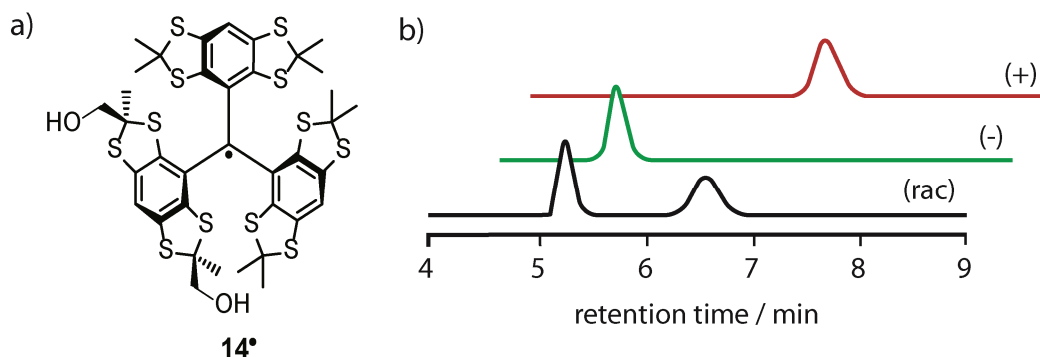
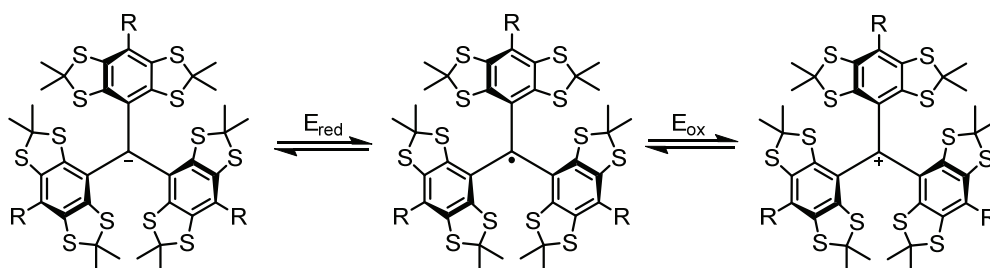


Figure 3: a) Structure of trityl radical **14 \bullet** . b) Chiral HPLC traces for racemic **14 \bullet** (black) and both enantiomers (green and red) after heating to 58°C for 5h. Adapted with permission from Y. Li et al., *J. Org. Chem.* 2019, 84, 11774 – 11782. ©2019 to the American Chemical Society.

Concomitantly, helical chirality is generated and enantiopure samples of TAM-radicals were obtained via preparative chiral HPLC.^[23] The configurational stability of the enantiomers exceeded that of perchlorinated trityl radicals, as a racemization half-life time of 343 h was observed for the ethyl ester derivative of **13**. Molecular propellers completely inert to racemization were obtained through installation of peripheral hydroxyl groups, as demonstrated for **14 \bullet** (Figure 3a).^[24]

As shown in Figure 3b, resolution of (*rac*)-**14 \bullet** allowed the isolation of both enantiomers via preparative chiral HPLC. Even after heating to 58°C in CDCl_3 for 5h, no evidence for racemization was visible in the corresponding HPLC traces (Figure 3b).

Though conjugation of the aromatic π -orbitals with the radical-containing p_z -orbital at the central carbon atom is reduced by the twisted arrangement of the aryl planes, spin density is extensively delocalized into the skeleton of TAM-radicals. While 70 % of the spin density is localized at the central carbon atom, approximately 10 % is spread into each aryl substituent.^[25] Furthermore, TAM-radicals are redox active as depicted in Scheme 5: they can undergo reversible reduction to trityl anions or, vice versa, oxidation to tritylium cations.



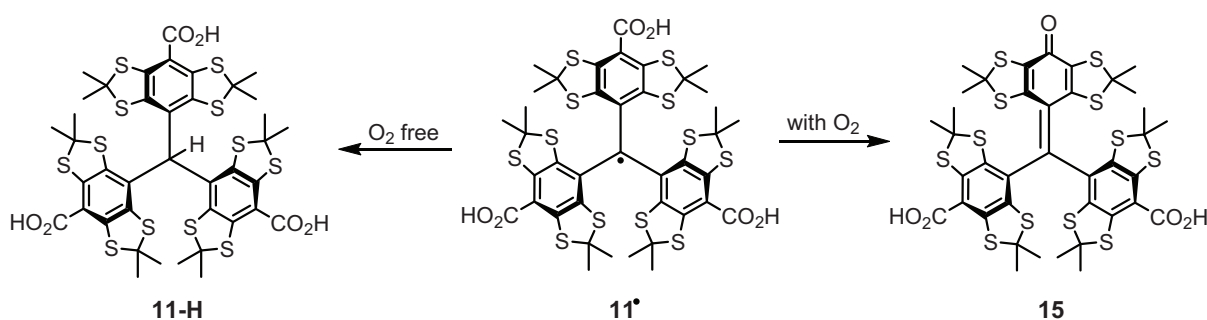
Scheme 5: Redox processes applicable to TAM-radicals.

Table 1: Redox potentials of various TAM-radicals determined by cyclic voltammetry

Entry	Substituent -X	E _{red} [mV]*	E _{ox} [mV]*	Ref.
1	-CO ₂ H (11 [•])	- 642 - 642	+ 434 + 456	[26] [27]
2	-CO ₂ CH ₂ CO ₂ H	- 309	+ 733	[27]
3	-CO ₂ (CH ₂) ₃ N(CH ₃) ₃ ⁺ Br ⁻	- 261	-	[28]
4	-CO ₂ (CH ₂) ₃ SO ₃ ⁻ Na ⁺	- 356	-	[28]
5	-CO ₂ NHCO ₂ H	- 459	+ 643	[27]
6	-poly-arginine (amide)	- 475	+ 666	[26]
7	-tripeptide (amide)**	- 429	+ 648	[29]

All redox potentials were measured at room temperature in aqueous phosphate buffer at a pH of 7.4. *Electrode potentials are reported vs. an Ag/AgCl reference electrode and were recalculated where required. **peptide chain: arginine-glycine-aspartate.

The corresponding redox potentials are strongly dependent on the aromatic substitution pattern as described in Table 1, which displays the redox potential for various TAM-radicals determined by cyclic voltammetry in aqueous phosphate buffer at pH 7.4. Being thermodynamic properties, the redox potentials are immediately dependent on the stabilization of the species resulting from oxidation or reduction of the radical. Electron withdrawing groups (EWGs) support the delocalization of negative charge density and thereby stabilize carbanions, while electron donating groups (EDGs) stabilize carbenium ions. In line with this, EWGs such as esters (Table 1, entries 2-4) or amides (Table 1, entries 5-7) make trityl radicals more susceptible to one-electron reduction. However, carboxylates^{iv} act as EDGs due to their inherent negative charge, meaning that the thermodynamic barrier for reduction is increased (Table 1, entry 1). The exact opposite trend was observed for the oxidation potentials (Table 1), so that the redox potentials of trityl radicals can be adjusted into the desired direction by suitable aromatic substitution.



Scheme 6: Metabolism of TAM-radicals in rat liver microsomes.^[31] Incubations were performed at 37 °C and a radical concentration of 100 μM in 0.1 M phosphate buffer containing 1 mM NADPH.

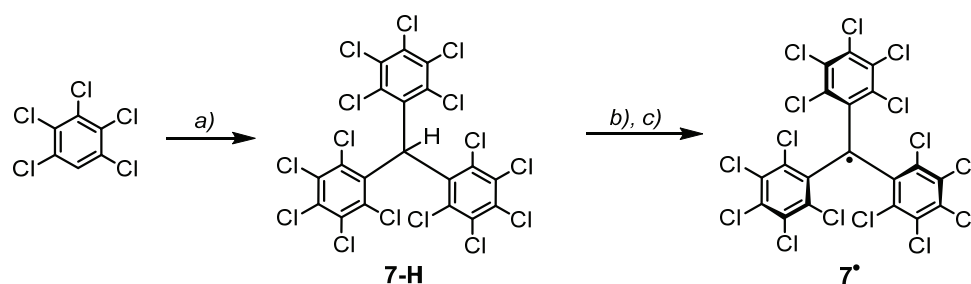
In view of their widespread application to biological systems (*vide infra*, sections 1.2.3 and 1.2.4), the fate of TAM-radicals after *in vivo* application was studied as well. For *Finland Trityl* **11**[•], both aerobic and an anaerobic metabolism pathways were identified

^{iv} It should be noted that carboxylic acids are regularly deprotonated at the pH value of 7.4, so that the carboxylate dominates the equilibrium in the present case.

(Scheme 6).^[28,30,31] In the former case, an oxidative decarboxylation yielding a quinone (**15**) was observed, while reductive processes gave the corresponding tetraphenylmethane (**11-H**) under anaerobic conditions. Proven by a systematic study carried out in rat liver microsomes, both processes are catalyzed enzymatically.^[31] Moreover, a recent study revealed that an oxidative decarboxylation of **11•** yielding **15** can also be triggered by UV-light in the presence of atmospheric oxygen.^[32]

In a nutshell, perchlorinated trityl radicals exhibit an outstanding stability towards oxidative conditions and high temperatures. However, they are quite susceptible towards light-induced degradation and suffer from lacking resistance to cellular environments^[33], what restrained their use for most biological applications. By contrast, TAM-radicals exhibit a high resistance towards (biological) reductants.^[34] Thus, they occur as a viable platform to design stable radicals suitable for applications in the biological context, e.g., as spin labels (cf. 1.2.3.3).

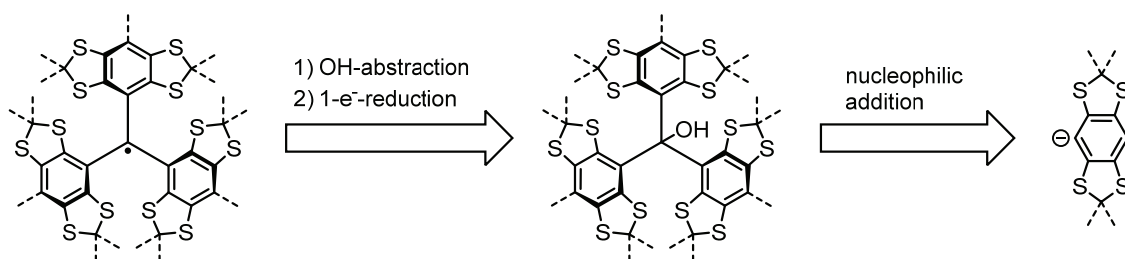
1.1.1.2 Synthesis



Scheme 7: Synthesis of perchlorinated triphenylmethyl radical **7•**.^[35,36] a) AlCl_3 , CHCl_3 , $160\text{ }^\circ\text{C}$, 2.5 h, 80 %. b) KOH , 18-crown-6, CH_2Cl_2 , r.t., 20 h. 90 %. c) *p*-chloranil, CH_2Cl_2 , r.t., 4 h, 98 %.

Exploiting their redox activity (Scheme 5), trityl-type radicals are generally obtained either by oxidation of a trityl anion, or reduction of a tritylium cation.

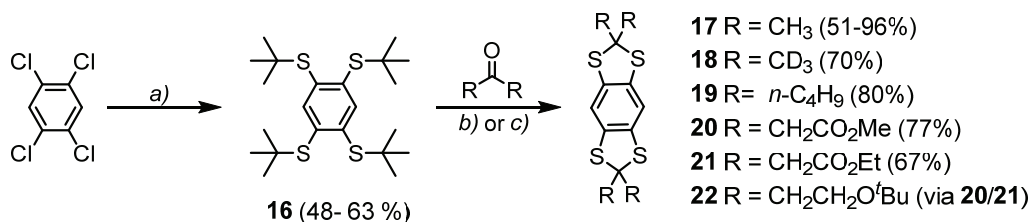
Pursuing the first approach, synthetic access to perchlorinated trityl radicals is gained via a *Friedel-Crafts* type condensation of polychlorinated benzene with chloroform yielding triphenylmethane **7-H**.^[36] Deprotonation to **7** with e.g. $\text{KOH}/18\text{-crown-6}$ ^[35] or $n\text{-Bu}_4\text{NOH}$ ^[37] and subsequent treatment of the resulting triphenylmethyl anion with a weak oxidant such as I_2 ^[35] or *p*-chloranil^[37] provides the corresponding radical.



Scheme 8: Retrosynthesis of TAM-radicals. For the sake of clarity, possible substitution is indicated by dashed lines.

By contrast, TAM radicals are commonly obtained from tritylium cations generated *in situ* from a trityl alcohol under acidic conditions (Scheme 8). The latter can be assembled by nucleophilic addition of a 2,2,6,6-tetrasubstituted benzo[1,2d;4,5d']bis[1,3]dithiol-4-yl synthon to a suitable C₁ or ketone building block.

Compared to perchlorinated trityl radicals, TAM-radicals are a rather young member in the group of stable radicals and interest into these arose in the early 2000s. Accordingly, their synthetic chemistry is a still evolving field and this chapter aims to provide a comprehensive summary of important strategies and current developments in the context of this thesis.



Scheme 9: Synthesis of benzo[1,2d;4,5d']bis[1,3]dithiol building blocks. a) sodium *tert*-butyl thiolate, DMF, 150°C, 2h. b) HBF₄-Et₂O, toluene, reflux, 16h. c) BF₃-Et₂O, CHCl₃, reflux, 16h. Isolated yields in parentheses.

The required benzo[1,2d;4,5d']bis[1,3]dithiols are thioketals and can thus be obtained from the corresponding ketone and 1,2,4,5-benzenetetrathiol.^[38] However, the synthesis of 1,2,4,5-benzenetetrathiol appears cumbersome and the compound is prone to oxidative degradation,^[39] so that 1,2,4,5-tetrakis(*tert*-butylthio)benzene **16** was introduced by *Reddy* et al.^[20] as a convenient surrogate. It was obtained by reaction of sodium *tert*-butyl thiolate with commercially available 1,2,4,5-tetrachlorobenzene as shown in Scheme 9. An alternative procedure by *Hintz* et al.^[40] using NaH for deprotonation of *tert*-butylthiol provided **16** in a yield of 48%. It should be noted that the S_NAr reaction to **16** requires an excess of *tert*-butylthiolate releasing the volatile thiol (bp. 62 °C) during the work-up, which exhibits a typical mercaptane odor with an extremely low threshold of < 0.33 ppb.^[41]

Especially for large-scale preparations, this might lead to a harassment of the environment through (usually) unfiltered fume-hood exhausts. This issue was addressed in literature by thermal inactivation^[42] of all vapors or purging them through a KMnO₄ solution.^[40] It should be noted that the aforementioned S_NAr reaction does more likely occur with 1,2,4,5-tetrafluorobenzene, exploiting the stronger polarization of the C_{sp2}-F bond.^[39] However, the ready commercial availability of 1,2,4,5-tetrachlorobenzene facilitated its use for the above mentioned transformation.

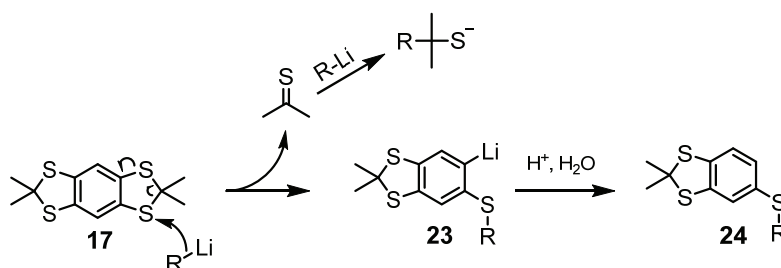
Both under *Lewis*- and *Brønsted* acidic conditions, the *tert*-butyl thioethers can be cleaved by elimination of 2-butene and the corresponding thioketals are formed with various ketones through short intermediacy of the free arylthiol.

As shown in Scheme 9, symmetric benzo[1,2d;4,5d']bis[1,3]dithiols **17-21** were obtained by reaction of **16** with acetone,^[20,43] 5-nonanone,^[44] and dimethyl-1,3-acetonedicarboxylate^[45] as

well as its ethyl derivative^[46] under catalysis of $\text{BF}_3\text{-Et}_2\text{O}$ or $\text{HBF}_4\text{-Et}_2\text{O}$. In principal, also deuterated compounds such as **18** can be obtained using deuterated ketones.^[47] However, enolization of the ketone under the reaction conditions leads to significant D/H-exchange and a final deuteration degree of 86%.^[48] Also asymmetric ketones have been employed for formation of the corresponding benzo[1,2d;4,5d']bis[1,3]dithiols, as e.g. for the synthesis of **14**.^[49]

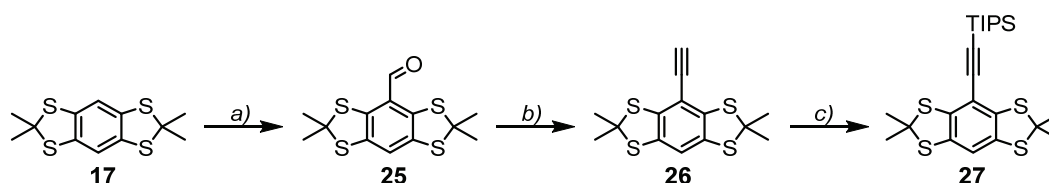
Apart from that, follow-up chemistry at this stage is viable, e.g. for the synthesis of **22** from **20** or **21**.^[45,50] Even though the functionalization of the trityl skeleton has been predominantly carried out on the trityl alcohol stage, the assembly of trityl alcohols from already functionalized building blocks has been described recently.^[40]

The functionalized benzo[1,2d;4,5d']-bis[1,3]dithiols required for that purpose are most commonly obtained by deprotonation with a strong base and addition of a proper electrophile.



Scheme 10: Mechanism for the competitive thioketal cleavage proposed by *Hintz et al.* R = alkyl.

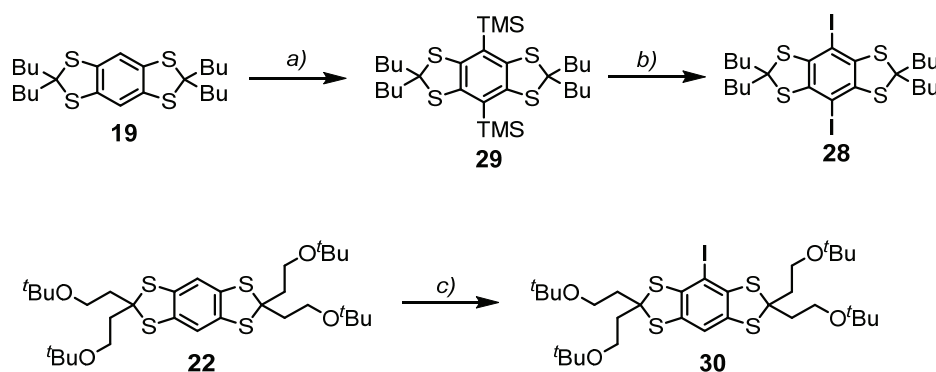
However, a competitive nucleophilic thioketal cleavage, diminishing the yield of the desired synthon, was found recently by *Hintz et al.*^[40] According to the proposed mechanism of this side-reaction (Scheme 10), a nucleophilic attack of the alkyl lithium base to the thioketal leads to formation of an *ortho*-lithiated thioether (**23**), which undergoes proto-demetalation yielding a trithiobenzene (**24**) after an aqueous work-up. Going from **17** to **24**, a thione is eliminated, which quenches an additional equivalent of the lithium alkyl. Interestingly, *Hintz et al.*^[40] did not report any thioketal cleavage using CH_3Li at 25°C in THF for 100 min to deprotonate **17**.



Scheme 11: Synthesis of ethynyl-functionalized benzo[1,2d;4,5d']bis[1,3]dithiols. a) 1. CH_3Li , THF, r.t., 100 min. 2. N-formylpiperidine, r.t., 16h, 78 %. b) *Bestmann-Ohira-reagent*, Cs_2CO_3 , THF, MeOH, r.t., 17 h, 62 %. c) 1. LDA, THF, 0°C , 5 min. 2. TIPS-Cl, r.t., 20 h, 95 %.

Accordingly, **25** was obtained from **17** in a *Bouveault*-type reaction and a subsequent *Bestmann-Ohira*-reaction afforded alkyne **26**, which was then TIPS-protected giving **27** as shown in Scheme 11.^[40]

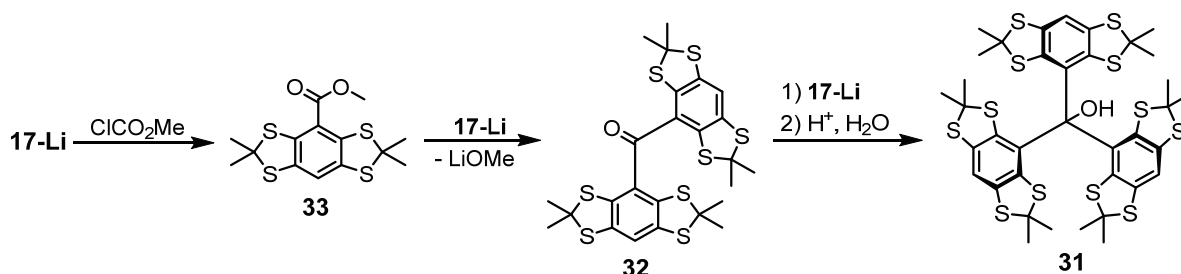
The occurrence of thioketal cleavage can also be circumvented using non-nucleophilic bases such as lithium 2,2,6,6-tetramethylpiperide (LiTMP). The reduced basicity of LiTMP ($pK_a = 35$),^[51] compared to alkyl lithium bases, impedes quantitative deprotonation. However, it does not react with electrophiles as, e.g., TMS-Cl, due to its low nucleophilicity,^[52] so that the deprotonation and electrophilic quenching via an equilibrium becomes sufficient.



Scheme 12: Functionalization of benzo[1,2d;4,5d']bis[1,3]dithiols upon deprotonation with non-nucleophilic LiTMP in equilibrium. a) 1. LiTMP, THF, -78 °C, 30 min. 2. TMS-Cl, -78 °C to r.t., 16 h. b) ICl, CH₂Cl₂, 0 °C, 2 h, 80 % over two steps. c) 1. LiTMP, THF, -78 °C, 2 h. 2. I₂, to r.t., 16 h, 75 %.

Using this approach (Scheme 12), 4,8-diiodo-2,2,6,6-tetrabutylbenzo[1,2d;4,5d']bis[1,3]dithiol **28** was obtained from **22** through intermediacy of the corresponding bis(trimethylsilyl)-derivative **29** and allowed for the synthesis of conjugated polymers via *Sonogashira-Hagihara* coupling.^[44] By analogy, direct (mono)iodination of **22** was feasible by deprotonation with LiTMP and addition of iodine, yielding **30**.^[45]

The key step enroute to trityl radicals (Scheme 13) is the generation of the benzo[1,2d;4,5d']bis[1,3]dithiol-4-yl synthon and its nucleophilic addition to assemble a trityl alcohol. The former is usually achieved by deprotonation of the benzo[1,2d;4,5d']bis[1,3]dithiol with strong lithium alkyl bases giving e.g., **17-Li**. Subsequently, triarylmethanols are formed through nucleophilic attack of the intermediately formed aryl lithium to various carbonyl compounds.



Scheme 13: Mechanism for the formation of triarylmethanol **31** by reaction of lithiated **17** (**17-Li**) with methyl chloroformate.

Since the occurrence of thioketal cleavage (*vide supra*) was discovered just recently, rather harsh lithiation conditions were employed to **17** in the earlier literature using *n*-butyl lithium

at room temperature for 2h^[20,47] to 16h,^[53] or even at 35 °C for 2h^[54]. Subsequently, trityl alcohols are obtained by reaction of the aryl nucleophiles with various C₁ building blocks, such as dimethyl carbonate,^[40] diethyl carbonate,^[55] or methyl chloroformate.^[20,47,48,53,54] Within the literature, the yields for trityl alcohol **31** vary within a range of 39 %^[54] to 86 %, ^[40] presumably due to issues with the aforementioned thioketal cleavage, and the yield was shown to increase by slow addition of the carbonyl compound via a syringe-pump.^[53] As depicted in Scheme 13, the formation of trityl alcohol **31** using e.g., methyl chloroformate, proceeds via the intermediacy of diarylketone **32** and methyl benzoate **33**. Consequently, **31** was also synthesized from previously isolated ketone **32** in yields up 96%, based on the latter.^[43] The ketone itself was obtained either by altered stoichiometry in the reaction of **17-Li** with methyl chloroformate^[43] or recently by reaction of **17-Li** with methyl formate and subsequent *Dess-Martin-oxidation* of the resulting diarylmethanol.^[40]

Moreover, issues with thioketal cleavage can be circumvented by generating the required aryllithium species via lithium-halogen exchange, as recently demonstrated for **30** by *Poncelet et al.*^[45]

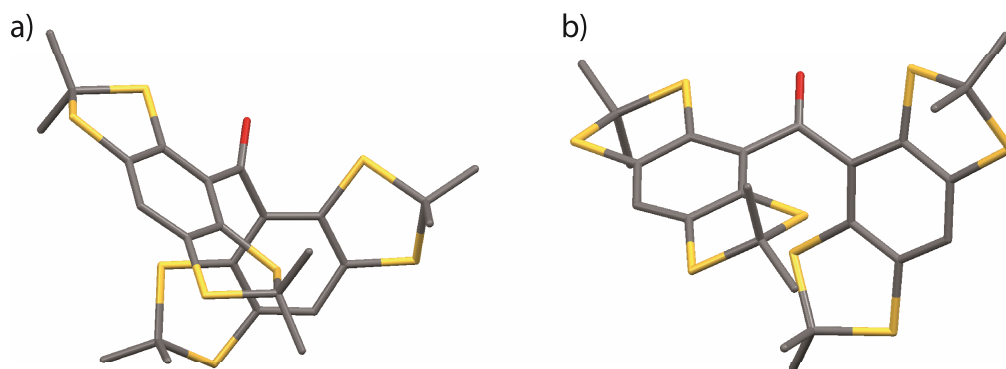
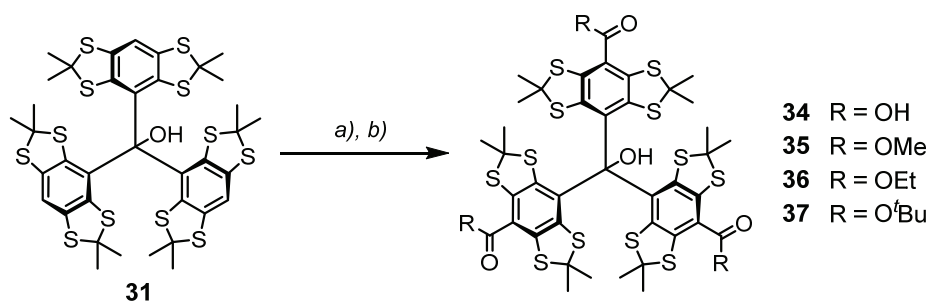


Figure 4: DFT (PBE, def2-TZVP, D3BJ) structure of ketone **32**. a) from a sideview and b) viewed alongside the *Bürgi-Dunitz* trajectory. Hydrogen atoms were omitted for the sake of clarity. Calculations were performed by the author using the *Orca*^[56,57] software package in anticipation of this thesis.

It should also be noted, that the nucleophilic addition step leading to the triarylmethanol is also cumbersome with respect to steric factors. First, *Bürgi-Dunitz-trajectory*, a nucleophile usually approaches on, appears rather crowded by the bulky thioketal moieties. Additionally, the propeller-like structure of the resulting trityl alcohol requires extensive structural reorganization during the formation of the triarylmethyl scaffold (Figure 4).

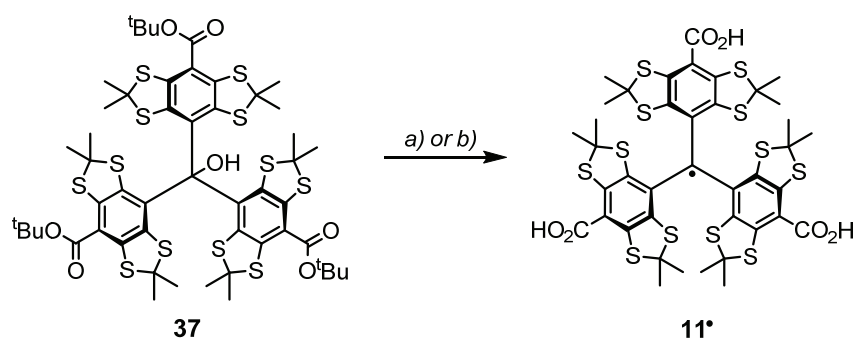
Tailoring trityl radicals for certain applications requires proper functionalizations, e.g., with a bioconjugation group for spin labels (cf. section 1.2.3). Most commonly, this is achieved by carboxylation at the trityl alcohol stage, where subsequent esterification or amidation allows for introduction of the desired functional groups. For this, trityl alcohol **31** presents a valuable platform and carboxylation is carried out by deprotonation with an excess of alkyl lithium bases and trapping of the resulting anion by suitable carbonyl electrophiles as shown in Scheme 14.



Scheme 14: Carboxylation of trityl alcohol **31**. a) e.g. 10 equiv. *n*-BuLi, TMEDA, 2 – 16 h. b) CO₂ for **34**, (OMe)₂CO for **35**, (OEt)₂CO for **36**, Boc₂O for **37**.

Common conditions for the initial threefold deprotonation include the use of 10 eq. *n*-butyl lithium/TMEDA,^[40,47,55,58,59] but *tert*-butyl lithium^[20] has also been employed for this purpose. The applied reactions times for this deprotonation step vary from 30 min (*tert*-butyl lithium, TMEDA, benzene)^[20] to 18 h (*n*-butyl lithium, TMEDA, Et₂O),^[53] though systematic experiments of *Hintz et al.* proved that reaction times > 2.5 h lead to decomposition of the compounds, when applying the latter conditions.^[40] Interestingly, no indication for the cleavage of thioketals within the assembled triarylmethyl scaffold were found, even with *tert*-butyl lithium.^[40] More diverse is the nature of carbonyl compounds utilized in the second step as well as the yields of threefold-functionalized trityl alcohols. Using solid CO₂,^[55] *Rogozhnikova et al.* obtained the tricarboxylic acid **34** in a yield of 62 %, *Jasoy et al.* reported a similar yield of 64 % for the use of gaseous CO₂.^[53] Other authors used dimethylcarbonate affording **35**,^[60] or diethylcarbonate to obtain **36** in yields of 48 % – 52 %,^[47,59] respectively. The corresponding *tert*-butyl ester **37** was accessible through the use of Boc₂O in yields varying between 39% and 85%.^[47,53] An enhanced reactivity of Boc₂O after activation with DMAP was reported and used for further functionalization of substituted trityl alcohols by *Hintz et al.*^[40] In all these reactions, side products arise from non-exhaustive carboxylation, which are regularly separable by column chromatography. The tremendous variation in yields using Boc₂O might be explained, as the reagent is hygroscopic and tends to decompose during storage, so that protic impurities result.

After the carboxylation step, the radical center is installed and further functionalization can be carried out at the radical stage. The radical itself is obtained by abstraction of hydroxide from the trityl alcohol with Me₃SiBr,^[61] a *Lewis* acid such as BF₃,^[62] or strong *Brønsted* acids such as CF₃COOH^[24] or CF₃SO₃H^[63] and subsequent reduction of the intermediate tritylium cation with tin(II). Beyond that, trityl radicals were also obtained through disproportionation of tritylium cations under aerobic conditions generated by treating trityl alcohols with CF₃COOH.^[53,55] While *tert*-butyl esters are cleaved under these acidic conditions^[53] as shown for the synthesis of the Finland trityl **11•** in Scheme 15, other alkyl esters require hydrolysis with alkali hydroxides to obtain the carboxylic acid suitable for further functionalization,^[43] regularly by amidation or esterification.



Scheme 15: Synthesis of the *Finland trityl* **11•**. a) CF₃COOH, O₂, r.t., 16 h or b) 1) CF₃COOH, CH₂Cl₂, r.t., 2 h, 2) SnCl₂, THF, r.t., 15 min.

Activation of the carboxyl group prior to reaction with a suitable amine or alcohol was performed by a large variety of typical reagents, as summarized in Table 2.

Table 2: Activation reagents employed for the synthesis of trityl radicals consisting of esters and amides.

Entry	Activation reagent/method	Ref.
1	oxalyl chloride	[29,64,65]
2	thionyl chloride	[55]
3	<i>Mukaiyama</i> esterification ^[66]	[53,58,67,68]
4	BOP/HOBt	[25,69–74]
5	HBTU/DMAP	[48]
6	BOP-Cl	[75]
7	EDC/DMAP	[76]
8	CDI	[77]
9	pentafluorophenyl ester	[26]

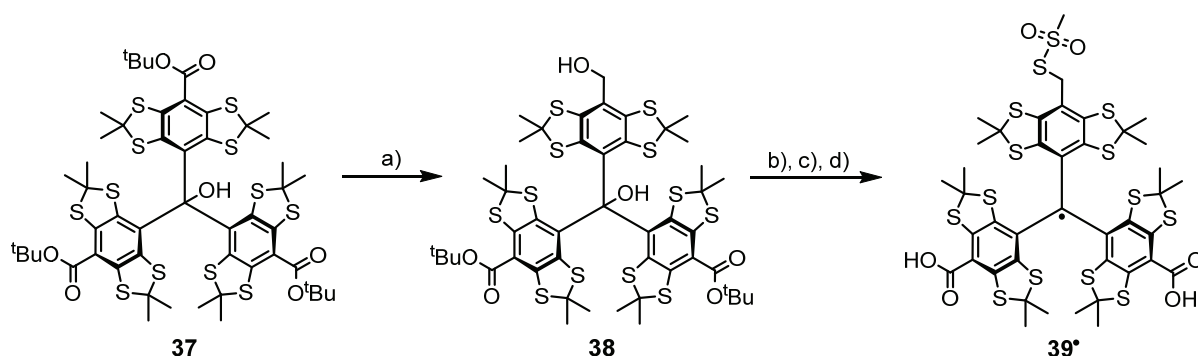
BOP: benzotriazol-1-yloxytris(dimethylamino)phosphonium hexafluoro-phosphate; HOBt: hydroxybenzotriazole; HBTU: hexafluorophosphate benzotriazole tetramethyl uronium; BOP-Cl: Bis(2-oxo-3-oxazolidinyl)phosphinic chloride; EDC: 1-ethyl-3-(3-dimethylaminopropyl)carbodiimid; CDI: carbonyldiimidazol.

Generating the corresponding acyl chloride by treatment with oxalyl chloride (Table 2, entry 1) and subsequent reaction with an amine allowed *Liu et al.*^[64] to build-up dendritic trityl radicals and this type of activation was also used by *Gajan et al.*^[65] as well as *Driesschaert et al.*^[29] Alternatively, the acyl chloride was also obtained by treatment with thionyl chloride (Table 2, entry 2).^[55] An alkynyl-function allowing click-chemistry was introduced by reaction of the radical sodium carboxylate with propargyl tosylate.^[78] Various trityl spin labels (cf. section 1.2.3.3) were obtained by esterification of **11•** employing the *Mukaiyama* esterification^[53,58] (CMPI, DMAP, Et₃N)^[66] and these conditions proved suitable also for more complex substrates (Table 2, entry 3).^[67]

Most employed by number of publications was the carboxyl activation using BOP/HOBt (Table 2, entry 4),^[25,69–74] e.g., for the synthesis of of amide-based trityl spin labels and, very similar, BOP-Cl (Table 2, entry 6)^[75] as well as the combination HBTU/DMAP (Table 2, entry 5)^[48] were also used for amide coupling. A *Steglich-type* amide coupling (Table 2, entry 7) was used by *Song et al.*^[76] employing a combination of EDC and DMAP. Finally, also the *Staab-reagent* (CDI) was used by *Kuzhelev et al.* (Table 2, entry 8),^[77] and *Driesschaert et*

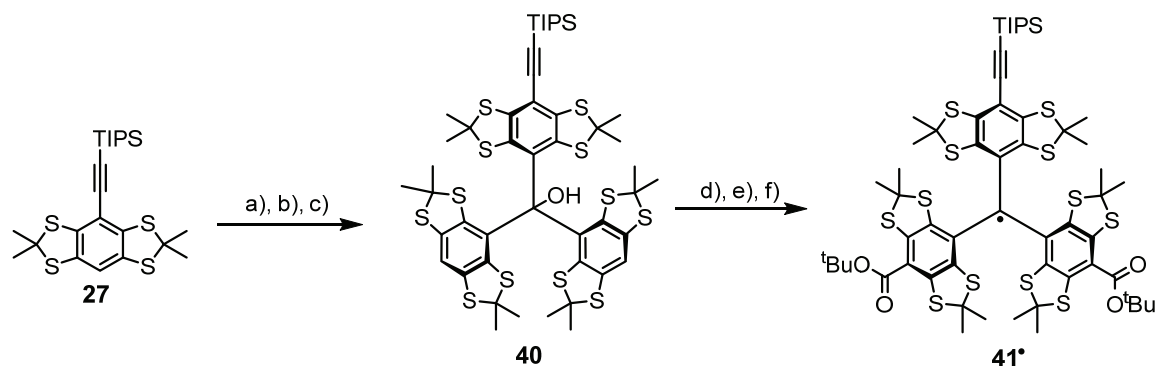
al.^[26] prepared pentafluorophenyl esters for carboxyl activation (Table 2, entry 9). Finally, the reaction of cesium carboxylates with alkyl bromides was also employed for the synthesis of variously esterified trityl radicals.^[79]

Though *Jassoy et al.*^[53] stated that the use of BOP/HOBt (Table 2, entry 4) or classical *Steglich* conditions did not succeed for the formation of esters from **11**[•], no other peculiarities concerning the use of certain coupling reagents have been reported. Rather, the explicit choice of an activation method seems to depend on the preference of the respective scientists. Though esterification and amidation of **11**[•] and its derivatives is the most common practice to obtain functionalized trityl radicals within the literature, several other approaches have been reported.



Scheme 16: Synthesis of the methanethiosulfonate **39**[•], used for discriminative detection of biothiols. a) LiAlH_4 , THF, r.t., 2h, 50 %. b) $\text{CH}_3\text{SO}_2\text{Cl}$, $i\text{-Pr}_2\text{NEt}$, CH_2Cl_2 , r.t., 16 h. c) $\text{CH}_3\text{SO}_2\text{SNa}$, DMF, r.t., 16 h, 48 % over two steps. d) 1. $\text{BF}_3\text{-Et}_2\text{O}$, CH_2Cl_2 , r.t., 30 min. 2. SnCl_2 , THF, r.t., 10 min, 50 %.

As shown in Scheme 16, statistical carbonyl reduction of with LiAlH_4 afforded benzyl alcohol **38**. Treatment with mesyl chloride afforded the corresponding benzyl chloride^v and an $\text{S}_{\text{N}}1$ -reaction with sodium methanethiosulfonate was employed to form the benzylic C-S bond.^[80] After radical generation by subsequent addition of $\text{BF}_3\text{-Et}_2\text{O}$ and SnCl_2 , trityl radical **39**[•] was obtained and used to distinguish various biothiols by the cw-EPR signature of their disulfides formed with **39**[•].^[80]



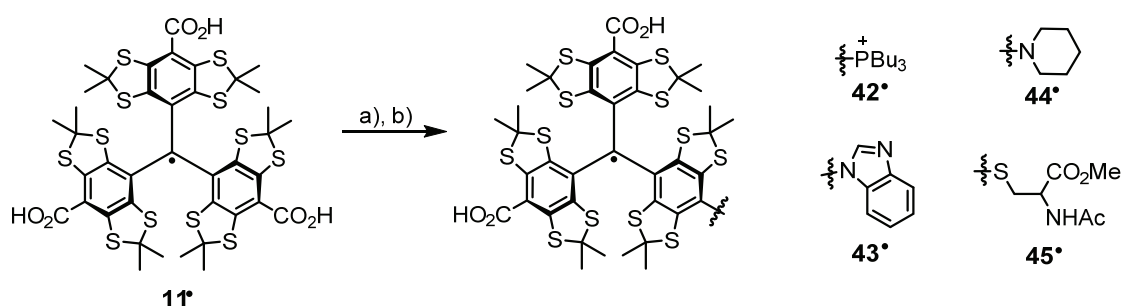
Scheme 17: Synthesis of ethynyl-substituted trityl radicals through early stage functionalization. a) MeLi , THF, r.t., 100 min. b) exchange for Et_2O . c) **32**, 30 °C, 7d, 72 % over three steps. d) 1. $n\text{-BuLi}$, TMEDA, $n\text{-hexane}$, r.t., 15 min. 2. Boc_2O , DMAP, Et_2O , r.t., 4 h, 31 %. e) CF_3COOH , r.t., 60 min. f) SnCl_2 , r.t., 50 min, 56 % over two steps.

^v Though formation of a benzyl mesylate might be expected, the benzyl chloride was identified via MS.

The approaches presented beforehand are all based on the functionalization of an already assembled trityl platform, commonly starting from **31**.

A rationale for this is given by the rather harsh lithiation conditions employed throughout the literature enroute to the trityl alcohol scaffold (*vide supra*), which are not necessarily compatible with an early stage functionalization. Until now, except from results presented in section 3.1.6, the only example for such an early stage functionalization was provided recently by Hintz et al^[40] (Scheme 17), reporting the nucleophilic addition of lithiated **27** to ketone **32** affording asymmetric trityl alcohol **40**. Subsequent carboxylation and functional group manipulations allowed isolating the TIPS-ethynyl-substituted trityl radical **41**[•], however, isolation of the free (deprotected) alkyne was not reported. While the lithiation of **27** was performed in THF with methyl lithium to restrain cleavage of the thioketals, the solvent was exchanged for Et₂O for the nucleophilic addition to increase the stability of the aryl lithium intermediate.^[40]

An intrinsic drawback of the transformations summarized in Table 2 is their statistical nature if applied to **11**[•] as a platform, especially in the case of spin labels, where monofunctionalized radicals are desired. The use of prefunctionalized aryl synthons as described in Scheme 17 circumvents this issue, however, the chosen functionalization needs to be compatible with the lithiation conditions, or protected in a proper way.

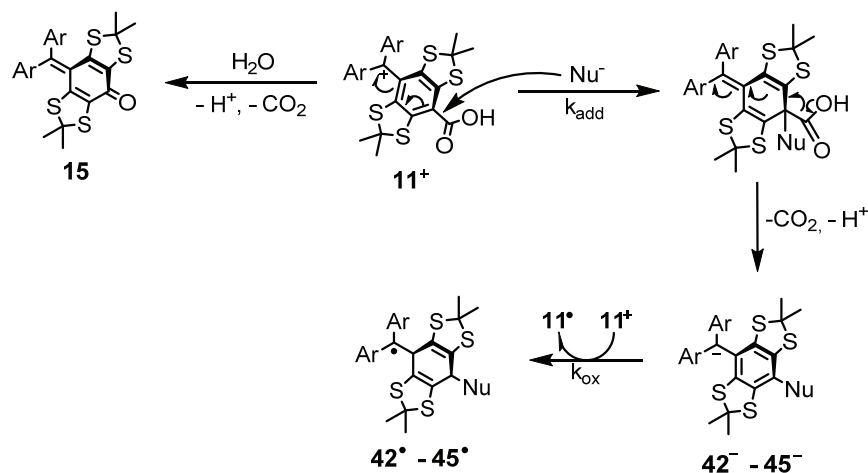


Scheme 18: Nucleophilic quenching of *in-situ* generated tritylium cations. a) K₂IrCl₆, H₂O, r.t., 1 min . b) 50 eq. P(n-Bu)₃ for **42**[•] (46 %), 50 eq. benzoimidazole for **43**[•] (43 %), 50 eq. cyclohexylamine for **44**[•] (38 %), 50 eq. N-acetylcystein methyl ester and 50 eq. NaOH for **45**[•] (42 %).

Another completely different approach yields monofunctionalized trityl radicals by nucleophilic quenching of tritylium cations. The steric congestion present at the central carbon does not only stabilize such cations, but also impedes nucleophilic attacks at this position, which therefore, take place at the readily accessible *para*-positions. Generating **11**⁺ by oxidation of **11**[•] with iridium(VI) and treatment with various nucleophiles *in situ* afforded the monofunctionalized trityl radicals **42**[•] - **45**[•] as shown in Scheme 18.^[81]

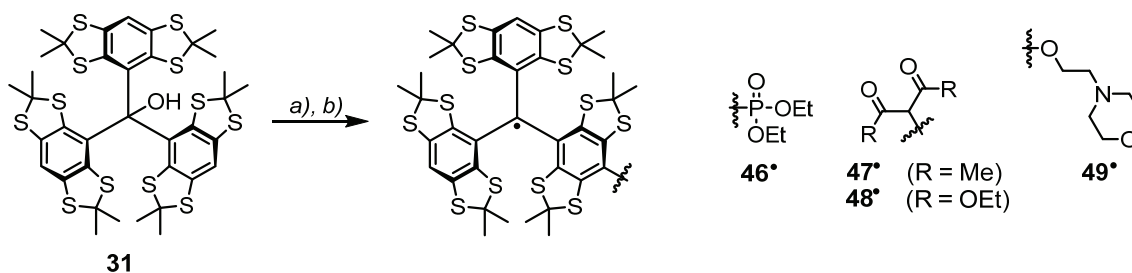
Overall, this reaction is a decarboxylative *ipso*-substitution and allowed to form C-P, C-N, and C-S bonds. Though these transformations provide access to monofunctionalized trityl radicals without the need for a statistical step, the yield of these transformations is intrinsically limited to 50 % according to the mechanism proposed in Scheme 19. A nucleophilic attack to the *para*-position of **11**⁺ is anticipated, followed by the elimination of

CO₂ and H⁺ from the resulting quinoid intermediate, resulting in trityl anions **42⁻** – **45⁻**. The latter are destabilized by the electron donating nature of the heteroatomic substituents and consequently oxidized by **11⁺**, affording **42[•]**–**45[•]**. As the reactions were carried out in aqueous media, quinone **15** arose as a side product from the nucleophilic action of water.



Scheme 19: Mechanism for the transformation shown in Scheme 18.

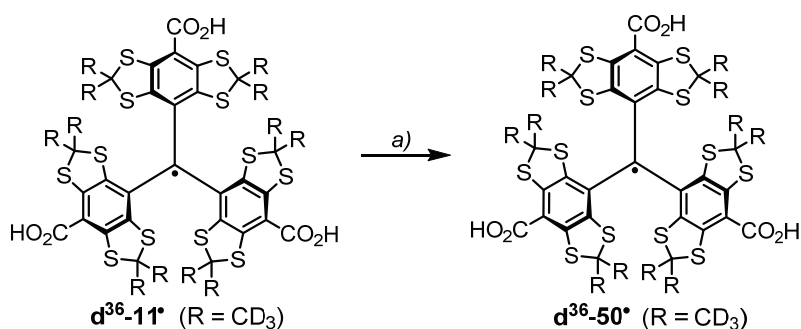
The aforementioned work was extended by *Tormyshev et al.*^[55,82] using a tritylium triflate generated from trityl alcohol **31** as shown in Scheme 20.



Scheme 20: Nucleophilic quenching of tritylium cations generated from a trityl alcohol. a) CF₃SO₃H, CH₂Cl₂. b) PO(OEt)₂Cl for **46[•]** (56 %), acetyl acetone, NaH for **47[•]** (56 %), ethyl malonate, NaH for **48[•]** (54 %), and N-(2-hydroxyethyl)-morpholin for **49[•]** (12 %).

Instead of a second equivalent of tritylium cation, the oxidation of the intermediate anions can also proceed with oxygen^[27], so that yields might exceed 50 %, provided the nucleophilic addition step (k_{add} , Scheme 19) is faster than the oxidation step (k_{ox} , Scheme 19). Accordingly, radicals **46[•]** – **49[•]** were isolated in yields of 12 – 56 %. While the addition of P-nucleophiles and C-nucleophiles derived from CH-acidic 1,3-dicarbonyls was feasible, it should be noted that the addition of O-nucleophiles did not succeed well, as yields dropped significantly for **49[•]**.

Recently, *Sanzhaeva et al.* reported on the synthesis of a sulfonated trityl radical^[83] (Scheme 21). For this, a deuterated version of **11[•]** was treated with Na₂SO₃ and K₂Cr₂O₇ under basic conditions, affording the trifold sulfonated trityl radicals **d³⁶-50[•]**. It was anticipated that the reaction proceeds through a radical recombination between **d³⁶-11[•]** and SO_{3[•]} formed *in situ*.^[83]

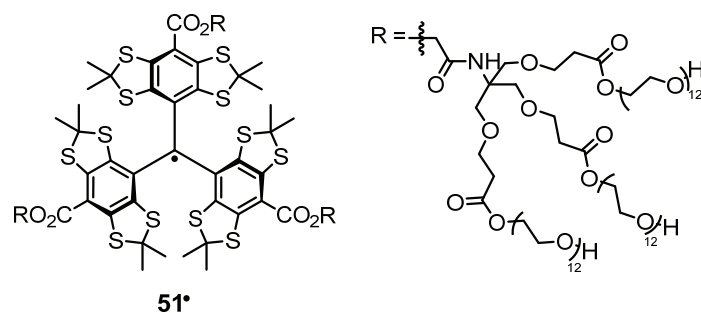


Scheme 21: Synthesis of a sulfonated trityl radical via substitutive decarboxylation. a) NaOH, Na₂SO₃, K₂Cr₂O₇, r.t., 30 min, 95 %.

Most of the techniques trityl radicals are utilized for, aim to study biomolecules or biological samples in aqueous media, rendering their water solubility crucial.

Carboxylate-substituents as used in **11**[•] and derivatives thereof may provide sufficient solubility, however, the resulting radicals are rather amphiphilic with non-polar methyl groups dominating their surface. As a result, self-aggregation of **11**[•] mediated by hydrophobic effects occurs already at micromolar concentrations and spontaneous self-assembly of spherical nanoparticles is observed above 15 mM in aqueous solution.^[84]

Non-covalent interactions as such also lead to formation of aggregates with proteins, a particular problem encountered within spin-labelling studies.^[58,85,86] For instance, almost quantitative binding of Finland trityl **11**[•] to bovine serum albumin (BSA), presumably through *Sudlow site I*, was reported at concentrations above 60 μM.^[87] Upon such non-covalent binding to proteins, the peak-to-peak amplitude of the cw-EPR signal of trityl radicals decreases^{vi} and this behavior was implemented as a convenient measure for the aggregation tendency of trityl radicals through non-specific interactions with proteins.^[50,76,87] Facing these issues with “classical” trityl radicals derived from Finland trityl **11**[•], several approaches aiming at an increased hydrophilicity of trityl radicals were developed.



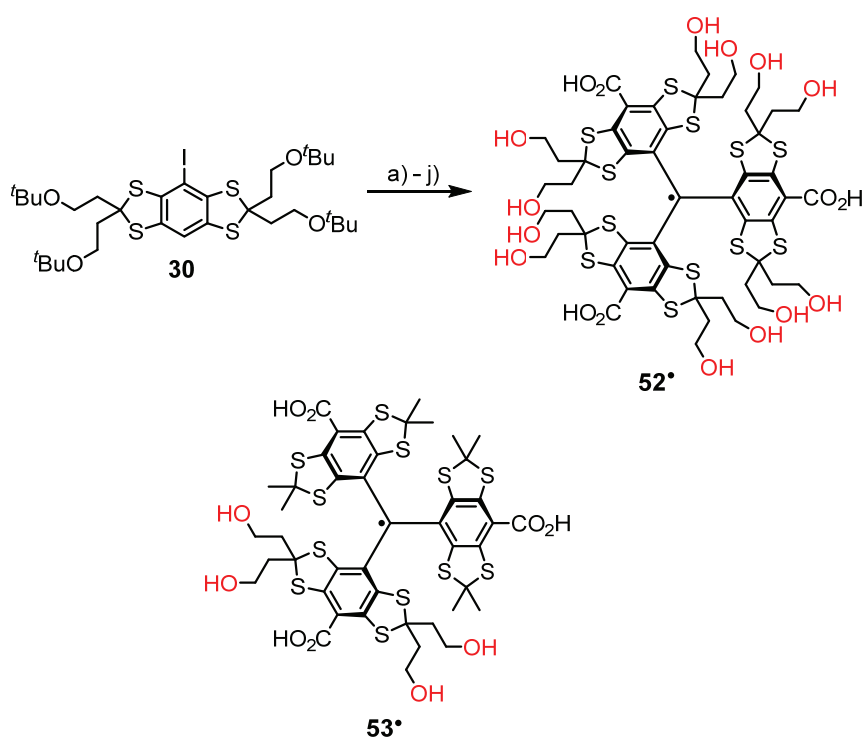
Scheme 22: A PEGylated trityl radical studied for *in-vivo* oxymetry.

The most convenient one among these is the conjugation of **11**[•] to highly polar tags. Using PEGs for this purpose (Scheme 22), **51**[•]^[76,88] was obtained via esterification, which did not

^{vi} The immobilization upon binding leads to a broadening of the EPR-linewidth, so that the peak-to-peak amplitude is decreased.

show any aggregation with BSA on the one hand and an increased *in-vivo* stability due to the steric shielding on the other hand.^[76,88]

Also conjugation to other hydrophilic entities such as dextrans^[89] and oligopeptides^[29] was reported in literature, but the molecular size of these rather large conjugates reduced tissue perfusion and inhibited an application for functional EPR-spectroscopy (section 1.2.4) beyond initial studies.^[45] Also in terms of spin labelling (section 1.2.3), such large radical conjugates are undesirable, as interfering interactions with proteins might occur. Following the interest into smaller, but still hydrophilic trityl radicals, hydroxyl groups were introduced at the thioketal units (Scheme 23).



Scheme 23: Synthesis of the hydrophilic trityl radical **52[•]** (top) and structure of the less hydroxylated trityl radical **53[•]** (bottom). a) *sec*-BuLi, n-hexane, -78 °C, 45 min. b) CO(OEt)₂, r.t., 16 h, 80 % over two steps. c) *sec*-BuLi, TMEDA, -30 °C, 2 h. d) CO₂ (gas), 30 min. e) CH₃I, Na₂CO₃, DMF, 50 °C, 1h, 60 % over three steps. f) HCO₂H, 45 °C, 90 min. g) CF₃SO₃H, CH₃CN, 0 °C, 30 min. h) SnCl₂, THF, r.t., 30 min.

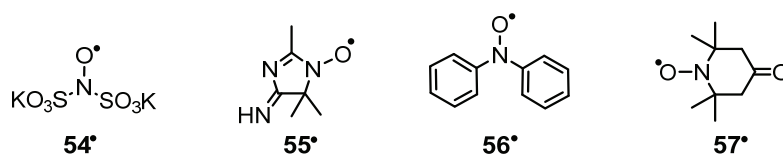
The most prominent representative of such radicals is Ox063 **52[•]**, which occurred early on in patent literature.^[46] However, its synthesis remained elusive^[50] until a proper protocol was published by *Poncelet et al.* recently (Scheme 23).^[45] For **52[•]**, difficulties from a synthetic perspective are imposed by the tremendous steric congestion triggered by the twelve 2-hydroxyethyl substituents (cf. Figure 4). Therefore, less hydroxylated and thus more conveniently accessible surrogates such as **53[•]** were developed.^[50]

In total, many studies tackled the functionalization of trityl radicals. Around the millennium turn, the focus of the scientific community shifted from perchlorinated trityl radicals, suitable for material applications, to TAM-radicals bearing a great application potential in biological contexts. However, the true chemical diversity for TAM radicals is still rather limited, as a

clear bias to esters and amides of **11**[•], or **52**[•] more recently, is evident. Though the nucleophilic quenching of tritylium cations (Schemes 18 – 20) mark an enticing exception from this statement, such functionalization approaches have not been pushed beyond a proof-of-concept, yet. The same holds for the synthesis of asymmetric trityl alcohols without a statistical step (Scheme 17): Though the principle synthetic pathway has been paved, its transfer to a trityl radical with immediate application was lacking. Additionally, side reaction such as the nucleophilic thioketal cleavage competing deprotonation (Scheme 10) were examined just quite recently, such that issues with reproducibility of earlier studies can be rationalized. A reason for this might be that most of the research targeting TAM-radicals has been carried out by groups rather interested into the functionalized radical than the chemistry behind it. However, the rising number of studies tackling the synthesis of TAM-radicals themselves underlines the current interest into the synthetic chemistry of these interesting molecules.

1.1.2 Nitroxides

1.1.2.1 Properties



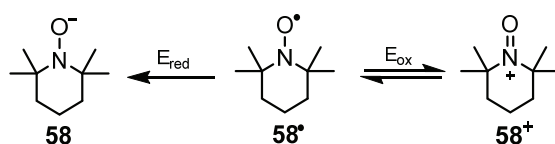
Scheme 24: Important landmarks in nitroxide synthesis.

Aminoxyradicals, commonly referred to as nitroxides, are N,N-disubstituted N-O[•] radicals with a long history (Scheme 24). The first inorganic nitroxide, Fremy's salt **54**[•], was described already in 1845. The first organic nitroxide, porphyrexide **55**[•], was reported almost concomitantly with the *Gomberg radical* in 1901 by *Schwerin*,^[90] but its radical character was identified only later by *Holden* via EPR-spectroscopy.^[91] In 1914, *Wieland* reported the synthesis of diphenylnitroxide **56**[•] and concluded the presence of a radical entity from the unique reactivity of the compound.^[92] An important further landmark was established by the introduction of 4-oxo-TEMPO **57**[•], as its skeleton is easily assembled from acetone^[93] making stable nitroxide radicals available to a wide scientific community.

Until today, nitroxides attract broad attention in the scientific community and more than 8200 papers^{vii} dealing with their synthesis, properties, and applications have been published so far. Though the radical center is typically drawn located at the oxygen atom (Scheme 24), the free electron is delocalized over the three electron N-O[•] bond. Depending on the substituents of the nitrogen atom, spin densities of $\rho_N = 0.2 - 0.5$ on the nitrogen and $\rho_O = 0.35 - 0.55$ on the oxygen atom were observed, while the remaining spin density spreads into the backbone.^[94] Consequently, an N-O[•] bond length of 1.25 – 1.30 Å results, midway

^{vii} Google Scholar search for scientific papers containing “nitroxide” in the title as of 10.02.2021.

between the length of an N-OH single bond ($d_{\text{NO}} \approx 1.43 \text{ \AA}$) and an N=O double bond ($d_{\text{NO}} \approx 1.20 \text{ \AA}$).^[10] With respect to stability, tertiary alkyl substituents at the nitrogen atom are most beneficial, such that these derivatives are encountered the most. Nitroxides featuring secondary or primary alkyl substituents are prone to intermolecular disproportionation yielding the corresponding hydroxylamine and nitronium.^[95] Moreover, the formation of diamagnetic head-to-head dimers was observed for e.g. diethylnitroxide, while *tert*-alkyl nitroxides exhibit no dimerization tendency.^[96]

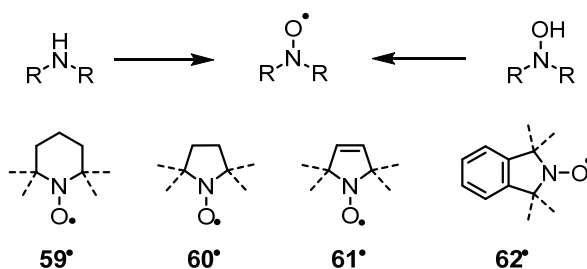


Scheme 25: Redox activity of nitroxide radical **58•**.

Nitroxides are redox-active as oxidation to nitronium cations or reduction to hydroxylamide anions is feasible, where the latter one is considered irreversible, if carried out electrochemically.^[94]

As exemplarily shown for the TEMPO radical **58•** in Scheme 25, reversible oxidation to **58+** proceeds at an electrode potential of +0.68 V against an Ag/AgCl-electrode,^[97] while for the irreversible reduction to **58-**, the redox potential is strongly pH-dependent, measuring for instance – 0.02 V against an Ag/AgCl^{viii} electrode under neutral conditions.^[98] Compared to trityl radicals (cf. Table 1), the reduction of nitroxides is thermodynamically easier, while the oxidation proceeds at slightly higher potentials.

1.1.2.2 Synthesis



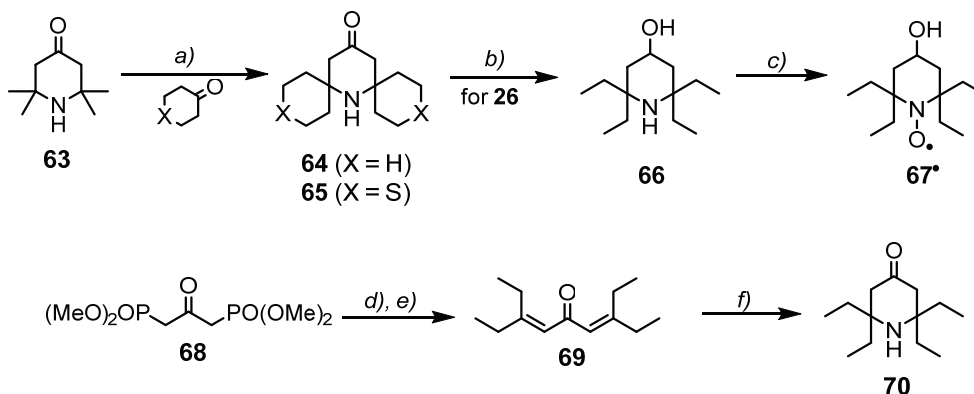
Scheme 26: General, oxidative, synthesis of nitroxide radicals (top) and platforms to construct stable nitroxide radicals (bottom). Generally, α -substitution as indicated by dashed bonds is employed to increase the kinetic stability further.

As shown in Scheme 26, nitroxides are obtained in an oxidative fashion either from secondary amines or hydroxylamines. Most common conditions for the oxidation of amines include the use of hydrogen peroxide in combination with catalytic tungstate or molybdate,^[99] but also organic peroxy acids such as *m*-chloroperbenzoic acid (mCPBA) were

^{viii} Electrode potentials were given against standard calomel electrode in the reference and were recalculated for the sake of comparability.

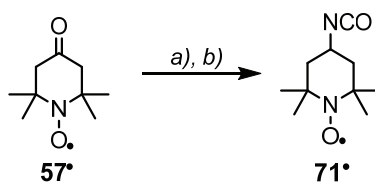
frequently employed.^[100] By contrast, milder oxidants such as e.g. $K_3[Fe(CN)_6]$,^[101] PbO_2 ,^[102] $NaIO_4$,^[103] or MnO_2 ^[104] sufficed for the synthesis of nitroxides from hydroxylamines.

Generally, cyclic nitroxides are more stable than their acyclic analogs.^[10] Hence, several heterocyclic platforms (**59[•]**-**62[•]**, cf. Scheme 26) were used to create stable nitroxide radicals. Enroute to nitroxide radicals, secondary amines are the most important precursors and consequently, syntheses of piperidine-based nitroxides (Scheme 27) start from 2,2,6,6-tetraethylpiperidin-4-on **63**, which is commercially available or easily prepared by condensation of acetone with ammonia.^[93]



Scheme 27: Assembly of bis(spirocyclohexyl) and tetraethyl-piperidines as precursors of nitroxides. a) NH_4Cl , DMSO, 5 h, 16 % for **25**, 30 % for **26**. b) Raney Ni, EtOH, 60 °C, 72 h, 63 %. c) mCPBA, CH_2Cl_2 , r.t., 3 h, 65 %. d) 1) LDA, THF, 0 °C, 30 min, 2) n-BuLi, -35 °C, 1 h, 3) 3-pentanone, r.t., 16 h. e) 3-pentanone, CsOH, C_6H_6 , H_2O , 80 °C, 18 h, 31 % over two steps. f) NH_4OH , sealed tube, 105 °C, 20 h, 40 %.

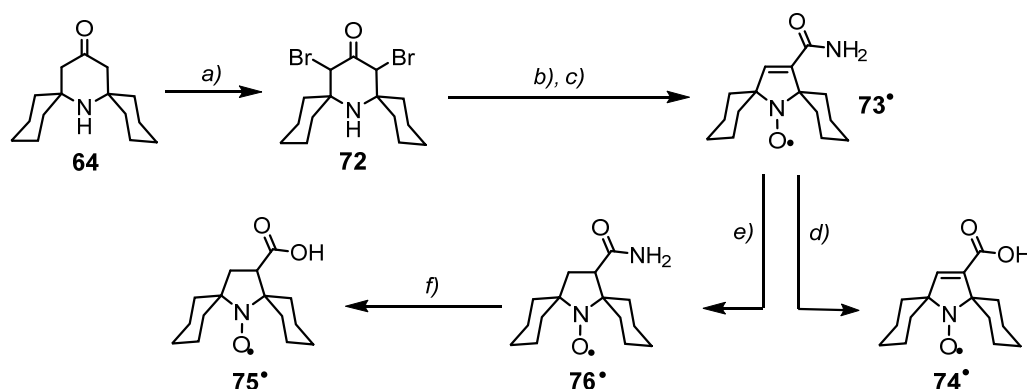
Subsequently, α -spiro centers can be constructed through an exchange reaction with a cyclic ketone under catalysis of NH_4Cl .^[105] Supported by experiments with ^{15}N -labelled NH_4Cl , the reaction runs via a crossed aldol condensation of **63** with the cyclic ketone and subsequent *aza-Michael* addition of ammonia,^[105] giving α -spirocyclohexyl piperidines such as **64** and **65**. While the corresponding nitroxide can be obtained immediately from the former, reductive cleavage of **65** with *Raney nickel* provides tetraethyl piperidine **66** and finally tetraethyl-nitroxide **67[•]** after oxidation with mCPBA.^[106] Alternatively, a twofold *Horner-Wadsworth-Emmons* reaction of phosphonate **68** with 3-pentanone gave ketone **69**, from which tetraethyl piperidine **70**, a direct precursor of **57[•]**, was obtained by an *aza-Michael* cyclization with aqueous ammonia.^[107]



Scheme 28: Exemplary functionalization of piperidine-type nitroxides. a) NH_4OAc , $NaBH_3CN$, MeOH, r.t., 48 h, 75 %. b) diphosgene, $(PhCH_2)_3N$, PhMe, r.t., 2 h, 64 %.

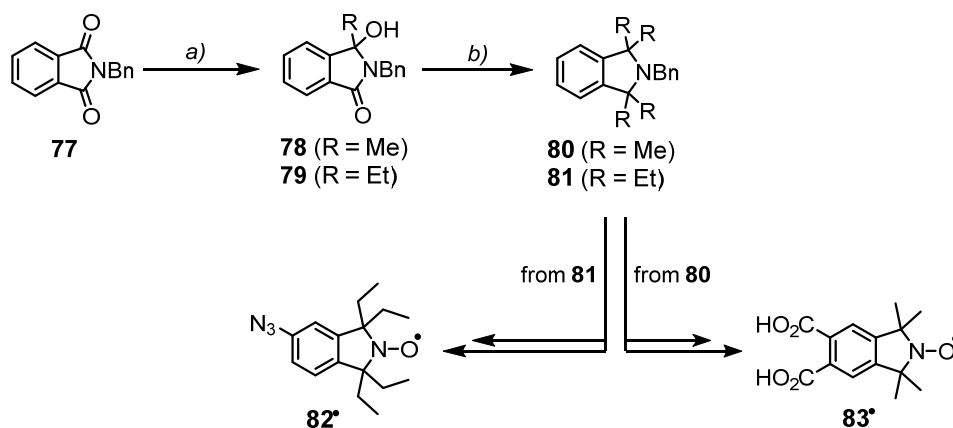
Moreover, the stability of the radical center allows for proper functionalization at the 4-position as outlined in Scheme 28. Reductive amination of **57[•]** with sodium

cyanoborohydride^[108] and subsequent reaction with diphosgene afforded isocyanate **71**[•],^[109] which was capable of conjugation to amino-functionalized RNA in the sense of spin labelling.^[110]



Scheme 29: Synthesis of 5-membered cyclic nitroxides via a *Favorskii-rearrangement*. a) Br_2 , AcOH, r.t., 16 h, 70 %. b) NH_4OH , 1,4-dioxane, 40 °C, 30 min, 50 %. c) Na_2WO_4 , Na_2EDTA , H_2O_2 , MeOH/ H_2O , r.t., 30 days, 69 %. d) NaOH, EtOH/ H_2O , 165 °C (microwave), 25 min, 80 %. e) NaBH_4 , LiCl, THF, 65 °C, 30 min; then 34 °, 65 °C, 7 days, 89 %. f) KOH, EtOH/ H_2O , sealed tube, 120 °C, 48 h, 75 %.

The cheap commercial availability of **63** rendered the synthesis of pyrrolin and pyrrolidin-nitroxides via ring-contraction reactions feasible. As shown in Scheme 29,^[111] a *Favorskii-rearrangement* of ketone **72** with concomitant elimination of HBr, followed by oxidation with H_2O_2 made pyrrolin nitroxide **73**[•] available. Subsequent amide hydrolysis afforded **74**[•], that allows further functionalization via its carboxylic acid entity. The corresponding pyrrolidin derivative **75**[•] was obtained by conjugate addition of hydride using LiBH_4 and hydrolysis of intermediate **76**[•].



Scheme 30: Synthesis of isoindolin nitroxides via exhaustive *Grignard* alkylation. a) MeMgI, PhMe, r.t., 1 h, 95 % for **39**; EtMgI, PhMe, r.t., 2 h, 93 % for **40**. b) MeMgI, PhMe, 120 °C, 72 h, 53 % for **41**, EtMgI, PhMe, 120 °C, 72 h, 51 % for **42**. For **82**[•] and **83**[•], each five steps from **80**, **81** respectively, are required.

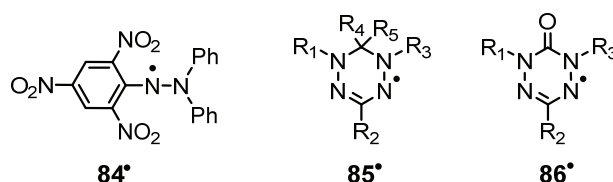
Obviously, a different strategy is required for isoindoline nitroxides, which regularly starts from N-benzylphthalimide **77** as shown in Scheme 30. An exhaustive *Grignard*-type alkylation^[112,113] via the intermediacy of hydroxyamides **78** and **79** afforded isoindolines **80** and **81**.^[112] It should be noted that a direct alkylation of **77** is possible, but increased yields were obtained employing the aforementioned two-step procedure.^[112]

Further functionalization profits from the ease of aromatic substitution and exemplarily, azide **82**[•] is obtained from **80**,^[113] or water soluble **83**[•] from **81**, respectively.^[114]

Through tailored synthesis of nitroxide radicals, the essentials of which were presented beforehand, a plethora of applications was enabled. Given their long history, a wide chemical diversity including various platforms and functionalization has been implemented during numerous studies within the past decades.

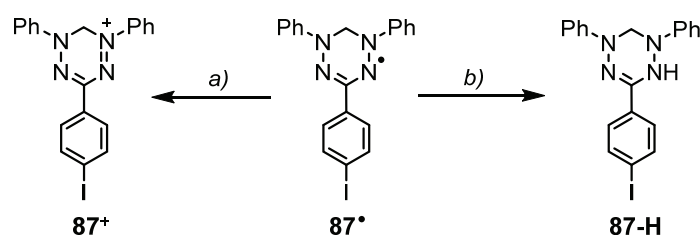
1.1.3 Other Stable Radicals

Triphenylmethyl-based radicals (section 1.1.1) and nitroxides (section 1.1.2) constitute the most important classes of stable radicals with respect to their wide applicability. Nonetheless, other species exist as well, which deserve a concise presentation in the following.



Scheme 31: Examples for nitrogen centered stable radicals. R_n = alkyl, (hetero)aryl, or H.

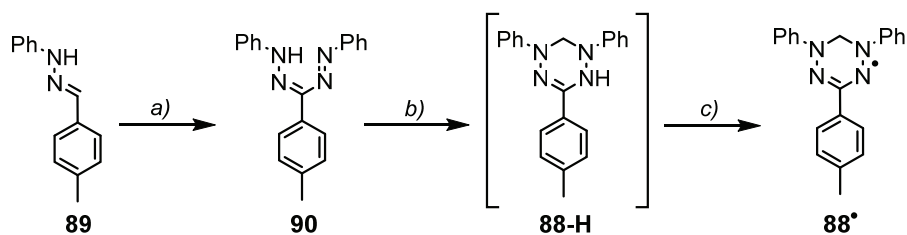
Shown in Scheme 31, N,N-diphenyl-N'-picrylhydrazyl (DPPH) **84**[•] is a notable example discovered by *Goldschmidt* already in 1920.^[115] While the application of such hydrazyl radicals is exclusively related to **84**[•], incorporation of the structural motif into conjugated cyclic compounds led to the development of *Kuhn-type* verdazyl radicals **85**[•]^[116] and soon after *oxo-verdazyls* **86**[•].^[117]



Scheme 32: Redox chemistry applied to a verdazyl radical. a) NOBF₄, CH₂Cl₂, r.t., 1 min, 85 % of **87-BF₄**. b) ascorbic acid, CH₂Cl₂/MeOH, r.t., 10 min, 32 %.

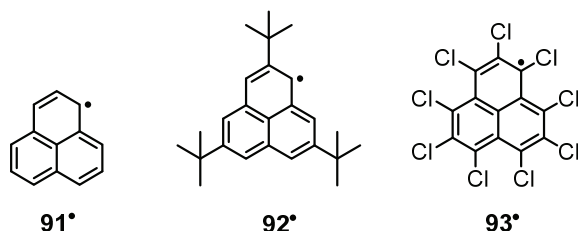
Also verdazyl radicals are redox-active as shown exemplarily for **87**[•] (Scheme 32). Both the product of oxidation, **87**⁺BF₄⁻, and reduction, **87-H**, were isolated and crystal structures were obtained.^[118]

As shown for verdazyl **88**[•], synthetic access can be obtained from hydrazones such as **89** (Scheme 33), which gives formazane **90** upon treatment with phenyldiazonium chloride.^[119] The following condensation with formaldehyde provides *leuco-verdazyl* **88-H**, which is readily oxidized to radical **88**[•] by atmospheric oxygen.^[119]



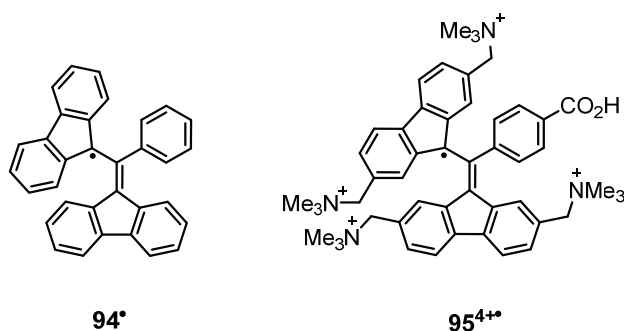
Scheme 33: Synthesis of verdazyl radicals from hydrazones. a) $\text{PhN}_2^+\text{Cl}^-$, Bu_4NBr , Na_2CO_3 , $\text{CH}_2\text{Cl}_2/\text{H}_2\text{O}$, 5°C , 45 min, 48 %. b) CH_2O , DMF, NaOH, r.t., 2 h. c) O_2 , 27 % over two steps.

A further interesting instance of stable radicals is given by phenalenyls (Scheme 34), which can be viewed as open-shell excerpts from graphene.^[120] Though the parent compound **91*** is stable enough to prove spin-delocalization via EPR-spectroscopy,^[121] it is prone to dimerization and decomposition upon contact to oxygen.^[122] Synthetic efforts to stabilize phenalenyl radicals were governed by peripheral substitution and notable results include 2,5,8-tri-*tert*-butylphenalenyl **92***^[123] and perchlorophenalenyl **93***^[124].



Scheme 34: Structure of representative phenalenyl radicals.

Reported by *Koelsch* in 1957^{ix}, α,γ -bis(diphenylene)- β -phenylallyl (BDPA) radicals (Scheme 35) derived from **94*** build up another notable class of stable radicals.^[125] Despite their generally limited persistence, especially in solution,^[126] extensive chemical substitution recently allowed to endow BDPA radical **95*** with both water-solubility and remarkable persistence.^[127]

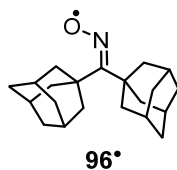


Scheme 35: Structure of representative BDPA radicals.

Though distinct examples of persistent radicals belonging to other classes than those presented so far exist, their overall stability is comparably low. While the unpaired electron of

^{ix} Though the paper was published in 1957, the work had been submitted to the same journal already in 1932, but was rejected as the reviewers doubted the radical character of the compounds.

all radicals presented in this chapter is located in a π -orbital, adamantyl-substituted iminoxyl **96•** shown in Scheme 39 is an example for a stable σ -radical worth noting.^[128]



Scheme 36: A stable iminoxyl- σ -radical.

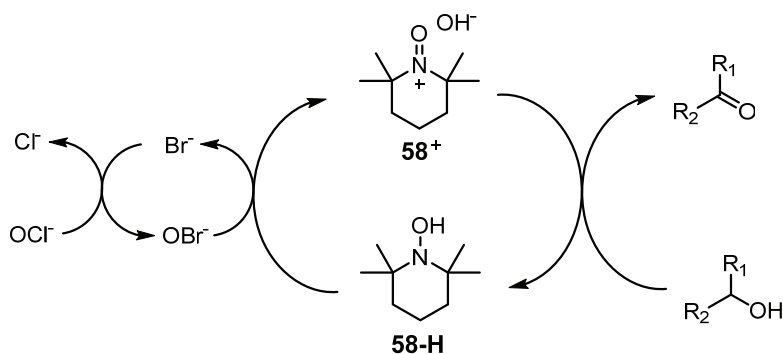
Further compound classes with the capability to form stable/persistent radicals are described in a comprehensive book publication by Hicks^[10].

1.2 Applications of Stable Radicals

As outlined in the preceding chapter, numerous radical compounds are stable enough to be handled and stored without any special precaution. Though paramagnetic organic molecules are already interesting for the sake of their own, a plethora of applications for stable radicals has emerged ranging from synthesis (section 1.2.1) via material science (section 1.2.2) to structural biology (section 1.2.3).

Each of these applications relies on the availability of tailored radicals in terms of functionalization, stability, and/or spectroscopic properties. The following subsections will therefore address the most important applications with respect to a) desired properties of the radical species and b) suitable molecular entities, building up on the previous chapter. Owing to their widespread utilization, an inevitable focus lies on nitroxide and triphenylmethyl radicals.

1.2.1 Exploiting the Reactivity of Stable Radicals



Scheme 37: Mechanism of TEMPO-catalyzed alcohol oxidation. R₁ = alkyl, R₂ = alkyl, H.

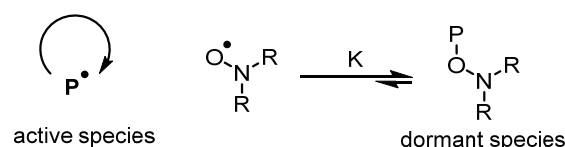
Stable radicals offer not only perspectives with respect to applications exploiting their paramagnetic nature (*vide infra*). The unique nature of the radical center can also be exploited targeting its (remaining) reactivity, which has been done extensively for nitroxide radicals. Compared to triphenylmethyl radicals, their low molecular weight as well as

synthetic access from well affordable precursors facilitated their use as valuable reagents in organic synthesis.

As outlined in section 1.1.2, nitroxides are redox-active and were consequently employed for oxidative transformations in catalytic fashion, the foremost of which is the oxidation of alcohols. Here, the use of catalytic amounts of 2,2,6,6-tetramethylpiperidinoxyl (TEMPO, **58**•), combined with bromide as a co-catalyst allows the efficient oxidation of alcohols with NaOCl as the stoichiometric oxidant.^[129] In this reaction (Scheme 37), the nitroxide (**58**•) is oxidized to an intermediate oxoammonium ion **58**⁺, which in turn serves as the oxidant for the alcohol under formation of the respective hydroxylamine **58-H**. The reoxidation of the latter one by hypochlorite profits from the addition of bromide enabling the intermediacy of hypobromite.^[130] The catalytic use of TEMPO is environmentally benign, especially compared to other oxidation methods utilizing e.g. Cr(VI) or reagents with a low atom economy alike the *Swern-oxidation* or the *Dess-Martin oxidation*. Apart from hypochlorite, also other stoichiometric oxidants were employed including iodine^[131] or oxone (KHSO₅).^[132] More recently, catalytic Fe(NO₃)₃ alongside TEMPO enabled the oxidation of alcohols at room-temperature with the use of stoichiometric O₂.^[133] Though the commercial availability of TEMPO renders it most abundant for oxidations as such, derivatives with enhanced reactivity, as e.g. azaadamantane-N-oxyl radicals,^[134] exist as well.

Moreover, oxidative transformations beyond simple alcohol oxidations were mediated by the nitroxide radical TEMPO. These include α -chlorination of carbonyl compounds,^[135] nitration of olefins,^[136] and more recently also gold-catalyzed cyclizations^[137] as well as olefin borylations.^[138]

Furthermore, the reactivity of radical centers can be exploited for polymerization processes. Typical radical chain polymerizations yield products with broad molecular weight distributions, i.e., a high dispersity. This observation is owed to radical recombination and chain-termination reactions that interfere with the linear growth of polymer chains. By contrast, these side reactions are lacking for anionic polymerizations, so that the dispersity of the products approaches unity. However, anionic polymerizations generally require rigorous exclusion of protic impurities, e.g., water from the reaction mixture, especially if *Grignard reagents* or lithium organyls are used as initiators. However, the use of stable radicals allows for combining the economic efficiency of radical polymerization with the aim for ideal dispersity. Such processes are known as controlled living radical polymerization and proceed through a general mechanism depicted in Scheme 38.^[139]

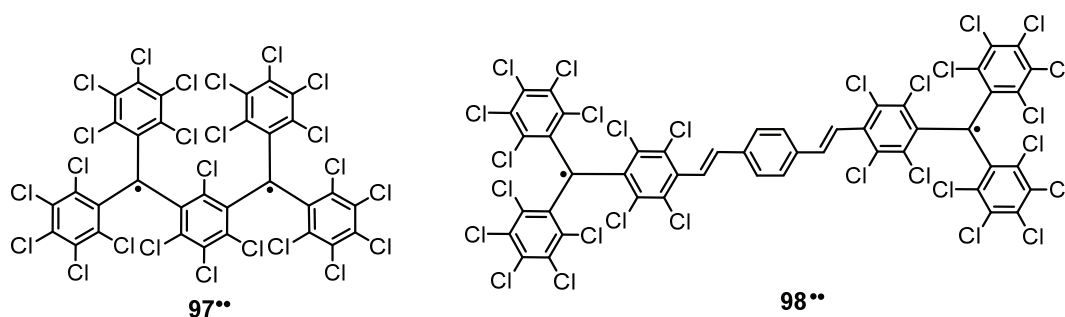


Scheme 38: General mechanism of the nitroxide-mediated polymerization.

The reaction of a radical initiator with the monomer results in formation of an intermediate radical \mathbf{P}^\bullet , which is the active species within the polymerization. Concealing this radical entity through reaction with a stable radical yields a dormant adduct, e.g. an alkoxyamine when using nitroxides. Both species are in equilibrium favoring the dormant adduct with $K = 2.1 \cdot 10^{-11}$ M for the exemplary case of styrene and TEMPO.^[140] While chain termination reactions are absent, chain recombination is efficiently suppressed by the low, though constant, concentration of active chain carriers (i.e. radical centers). Additionally, the *persistent radical effect* restrains chain recombination further: The thermodynamic stability of nitroxides renders their recombination disfavored, leading to an increase in their concentration upon chain recombination. The resulting excess of nitroxide facilitates the formation of the dormant alkoxyamine species providing good control over the polymerization process. Beyond the combination of nitroxides with a classical radical initiator, also alkoxyamines forming both latter ones in situ can be applied.^[139] Such nitroxide-mediated polymerizations are particularly useful for the well-controlled synthesis of block-copolymers.^[141]

1.2.2 Magnetic Materials: Interaction of Spin Centers

The aforementioned applications of stable radicals, predominantly nitroxides, were based on their unique reactivity in the sense of organic synthesis. However, also the paramagnetic nature of nitroxides and trityl radicals opens up numerous application perspectives. This does not only account for monoradical compounds, but also for magnetic materials consisting of more than one radical center. The magnetic properties of such compounds are governed by the interaction between the spin centers, as determined by the electron-electron interaction terms. Among these, the exchange coupling J , a description of which is reserved to chapter 1.3 for the sake of conciseness, determines the macroscopic magnetic properties. The extent of exchange coupling correlates with the overlap of the singly occupied molecular orbitals (SOMOs) of both radical centers. A ferromagnetic coupling ($J > 0$) can only result for an orthogonal set of SOMOs, while a non-zero overlap integral will lead to non-degenerated SOMOs and consequently an antiferromagnetic coupling.

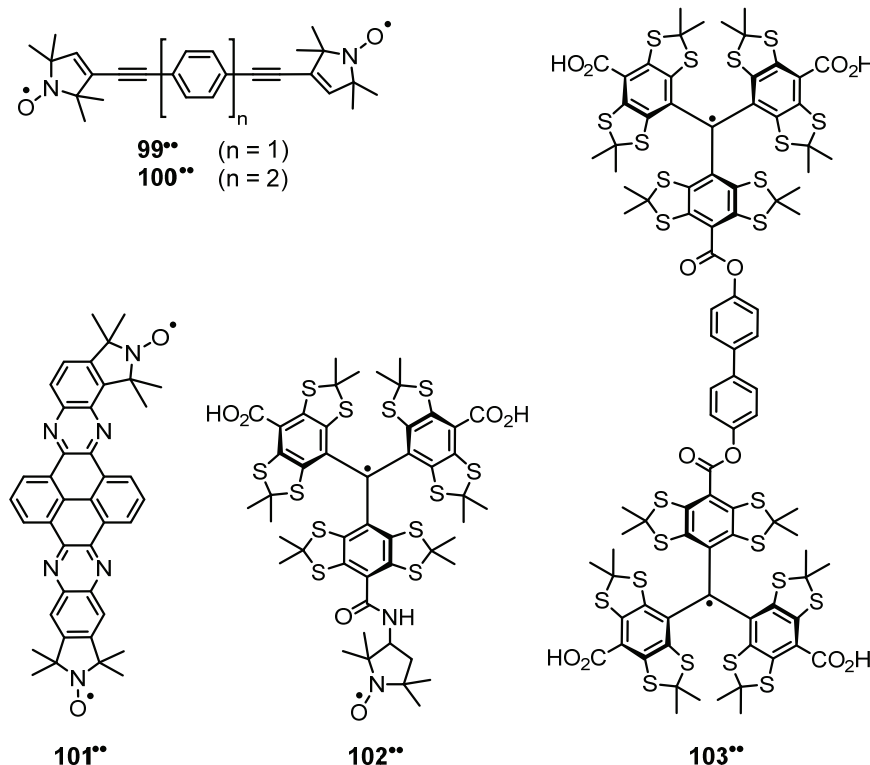


Scheme 39: Exchange coupled perchlorinated triarylmethyl biradicals.

Moreover, π -conjugation in the spacer bridging both radical centers will increase the magnitude of the exchange coupling, which will, vice versa, decrease with the interspin distance.

For the design of molecular magnets, strong exchange coupling is most desirable and the influences of structural features on J have been studied extensively in the group of Veciana. It was found that ferromagnetic coupling is mediated by 1,3-phenylene spacers and accordingly, **97^{••}** (Scheme 39) features an exchange coupling constant of $J > + 200 \text{ cm}^{-1}$.^[142] Other spacers, such as alkynes,^[143] or 1,4-phenylene units as in **98^{••}** give rise to strong, yet antiferromagnetic coupling with $J = - 15 \text{ cm}^{-1}$ in the case of **98^{••}**.

With respect to the magnitude of J it should be noted that 1 cm^{-1} equals 30 GHz, such that the exchange coupling in the above mentioned examples exceeds the Zeeman splitting lying in the range of 9.5 GHz for conventional X-Band EPR-spectroscopy.



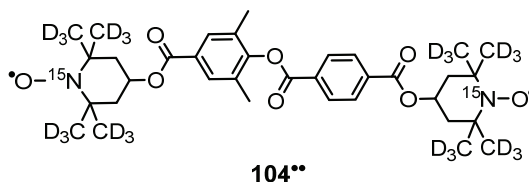
Scheme 40: Structure of nitroxide and TAM-based biradicals exhibiting exchange coupled spins.

Since the spin density of nitroxides is hardly delocalized into their backbone, nitroxide biradicals **99^{••}** and **100^{••}** (Scheme 40) exhibit a small exchange coupling constant of 73 MHz and 11 MHz, respectively, though the bridging unit is fully conjugated.^[144] Analogous considerations apply to **101^{••}**, which shows a small, but notably ferromagnetic, exchange interaction of 3.2 MHz.^[145]

By contrast, spin density is extensively delocalized into the skeleton of TAM-radicals. Accordingly, a rather large exchange coupling constant of 3360 MHz (0.112 cm^{-1}) was observed for the mixed biradical **102^{••}**, even though the amide-based linkage breaks π -conjugation.^[72]

The same holds for TAM-biradical **103^{••}**, where an exchange coupling constant of 75 MHz was observed despite lacking π -conjugation and the rather long interspin distance of 2.27 nm.^[67,146]

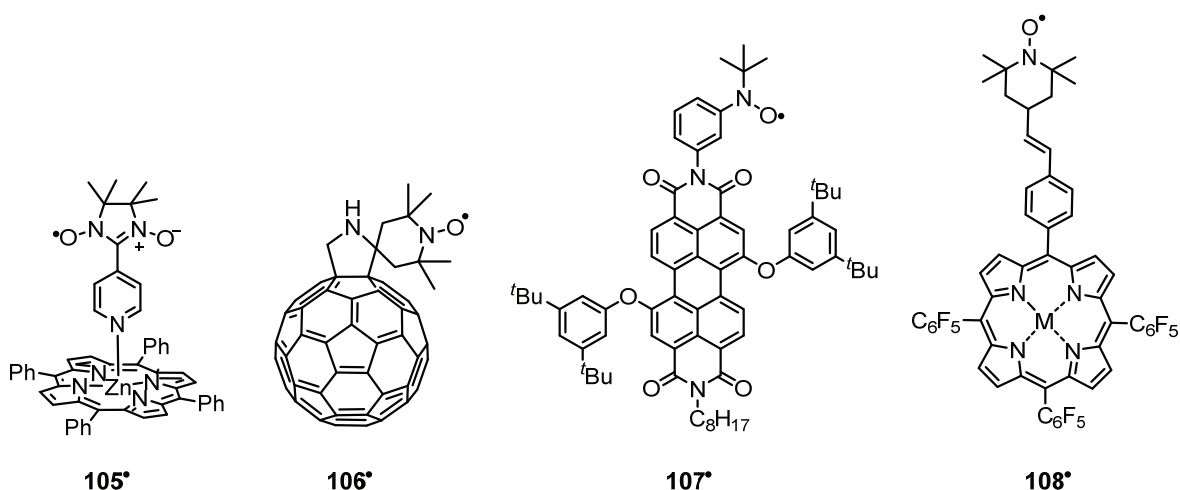
One prospective application of multiradical systems is the construction of qubits for quantum computing (QC) and quantum information processing (QIP).



Scheme 41: A nitroxide biradical used for quantum gate operations.

The first report of a quantum gate operation on an electron system was shown with nitroxide biradical **104^{••}** (Scheme 41). It exhibits an exchange coupling constant of $J = -0.14$ MHz, which is small enough to address each spin individually.^[147] In this particular case, ¹⁵N-labelling of the nitroxide entities was used to reduce the EPR-linewidth and deuteration of the adjacent methyl groups prolonged phase-coherence times. Notably, a distinction between both chemically identical radical centers was possible, since the twisting in the *p*-phenyl-linker renders the *g*-tensors of both nitroxides non-collinear.^[147]

Moreover, radical-chromophore systems are of great interest for the construction of electron spin qubits. These allow for the generation of well-defined spin states with a high polarization, i.e., population difference in terms of the *Boltzmann distribution*, upon photoexcitation. The interaction of the transient (i.e., photogenerated) spin center with the stable radical is also determined by exchange coupling and hence, the formation of transient higher spin states such as quartets can occur.



Scheme 42: Radical chromophore systems. M = 2H, Zn.

The first example of such a radical-chromophore system (Scheme 42) was provided with **105[•]**, a zinc porphyrin axially coordinated by a nitronyl nitroxide.^[148] Soon after, the formation of a quartet state was observed upon photoexcitation of fullerene-linked nitroxide

106•.^[149] Accordingly, a quintet was observed in time-resolved EPR (TREPR) after photoexcitation of a fullerene-bisnitroxide.^[150] Studies with a *tert*-butylphenyl nitroxide linked to a perylene diimide (PDI) chromophore (**107•**) revealed a ferromagnetic exchange interaction between the photogenerated chromophore triplet and the stable radical doublet.^[151] A very recent report on nitroxide-porphyrins **108•** disclosed a dependency of the exchange interaction on the central metal of the porphyrin moiety.^[152] While the photogenerated triplet state of the free-base (M = 2H) porphyrin exhibited only a weak exchange coupling to the nitroxide radical, the formation of a quartet state governed by strong exchange coupling was observed for the corresponding zinc derivative.^[152]

1.2.3 Spin Labelling EPR

1.2.3.1 Spin Labelling: A Valuable Tool in Structural Biology

The close structure-function relationship of proteins and oligonucleotides evoked the keen interest of the scientific community into structure elucidation of these biomacromolecular entities. Among the methods employed for this purpose, X-ray crystallography has been used for the vast majority (88.5 %) of the > 169,000 structures currently deposited in the PDB^x. Though this method provides atomic resolution, the structure is determined in the artificial environment of a crystal lattice. Here, packing effects might lead to structural artefacts, so that the resulting structure is not necessarily identical to the one encountered in the native cellular environment. Additionally, growing the required crystals is not trivial for biomacromolecules compared to e.g., inorganic salts and their high water content renders such crystals fragile. By contrast, NMR-spectroscopy enables to study biomolecules in solution with atomic resolution. Though well-developed NMR experiments are highly versatile in the toolbox of structural biologists^{xi}, their performance suffers from size limitations. Beyond 25 kDa, the complexity of spectra increases tremendously,^[153] rendering NMR-spectroscopy cumbersome for larger biomolecules. Recent advances addressed this issue^[154] and in selected cases proteins up to 670 kDa in size were subjected to NMR studies.^[155] However, studying such large systems makes isotopic labelling inevitable, which is on the one hand expensive and on the other hand not possible within every expression system.^[154]

Awarded with the Nobel Prize in Chemistry 2017, cryo-electron microscopy (cryo-EM) is an emerging technique^{xii} for structural studies on biomolecules.^[156] While resolution limitations

^x Protein Data Bank, an open access database for 3D structures of biomacromolecules consisting of currently >169,000 entries (as of 15.10.2020; www.rcsb.org).

^{xi} Approximately 7.7 % of the structures deposited in the PDB have been solved by NMR (15.10.2020).

^{xii} Approximately 3.6 % of the structures deposited in the PDB have been solved by cryo-EM (15.10.2020).

impeded the widespread use initially, recent developments allowed to approach atomic resolution with a current limit around 2 \AA .^[157]

Beyond coping with difficulties implied by the size of biomacromolecular systems, other approaches aim at the reduction of complexity by focusing on crucial structural parameters rather than the entire structure at atomic resolution. In that sense, the distance dependence of *Förster resonance energy transfer* (FRET) can be exploited to gain distance constraints, provided that suitable fluorescence labels are used.^[158] However, their large size can lead to interference with the protein structure, reducing the significance of the resulting distance information.^[159,160]

As paramagnetic centers are naturally rare in biomolecules, the size limitations of e.g., NMR-spectroscopy can be circumvented using EPR-spectroscopy. Additionally, this technique does not require the use of single crystals, such that studies can be carried out under more native conditions compared to X-ray crystallography.

The required paramagnetic centers can be either naturally occurring (metal) cofactors or artificially introduced radicals, referred to as spin labels. The latter serve as capable reporters for the microenvironment encountered at the respective labelling site. Thus, the local mobility of the spin label can be extracted from EPR-measurements, which provides insights into the dynamics of the peptide backbone.^[161,162] Also information on solvent accessibility and local polarity can be obtained through this methodology.^[161,162]

Even more interesting, also spatial information in the sense of distance constraints can be obtained via EPR spectroscopy, provided that at least two paramagnetic centers are presents within the biomolecular system.

For the sake of conciseness at this point, the technical details of EPR-based distance measurements are summarized in chapter 1.3.

1.2.3.2 Spin Labelling: Bioconjugation Chemistry

EPR-based distance measurements as described above emerged as a powerful tool for structural studies on proteins^[53,58,163–173] and oligonucleotides^[113,174–183]. Even the precise localization of metal ions via EPR-based trilateration has been demonstrated.^[184,185]

However, at least two paramagnetic centers are needed in a system to be suitable for subsection to this methodology. The generally diamagnetic nature of proteins thus requires either the use of intrinsic paramagnetic (metal) cofactors (e.g., Fe^{3+} , Mn^{2+} , Cu^{2+})^[165] or the introduction of artificial spin centers through spin labels. Following the latter approach, several strategies for their site-directed introduction exist and the key for such an experiment to succeed is both a high site-selectivity and a high efficiency of the spin labelling process, during which the spin label is linked to the biomolecules. This linkage is most commonly of covalent nature, however, also non-covalent labelling strategies, e.g. through coordination of

metal ions,^[186] or intercalation into DNA duplexes^[187] has been reported. For proteins, spin labelling is carried out predominantly in a postsynthetic fashion, however, genetic encoding of spin-labelled amino acids has been reported.^[188] After expression of the respective protein, the outstanding nucleophilicity^[189] and low natural abundance^[190] of cysteines is frequently exploited for spin labelling.

Table 3: Postsynthetic spin-labelling reactions leading for covalent labelling of proteins

Entry	Label type	Tabelling via	Target	Linkage	Ref.*
1	methanethiosulfonate	S _N -reaction	cysteine	disulfide	[166,167,169,171,173,184,192]
2	dithiopyridine	S _N -reaction	cysteine	disulfide	[70]
3	iodoacetamide	S _N -reaction	cysteine	thioether	[170,193,194]
4	substituted pyridine**	S _N Ar-reaction	cysteine	thioether	[195,196]
5	maleimide	<i>Michael</i> -addition	cysteine	thioether	[58,86,194,197–199]
6	alkene	thiol-ene-reaction	cysteine	thioether	[53]
7	azide	CuAAC click reaction	UAA**	triazole	[198,200]
8	ethynyl	CuAAC click reaction	UAA**	triazole	[126,140]
9	1,2,4,5-tetrazin	<i>Diels-Alder</i> -reaction	UAA**	pyridazine	[201]
10	hydroxylamine	ketoxime formation	UAA**	ketoxime	[202,203]

*The references provided here are not exhaustive. **This type of labelling reaction has only been reported for gadolinium-based spin labels consisting of pyridine-units as part of the ligand backbone. ***UAA = unnatural amino acid, as e.g. 4-azidophenylalanin (entry 8), or e.g. 4-acetylphenylalanin (entry 10).

In S_N-type reactions, disulfides are obtained upon spin labelling with methanethiosulfonates (Table 3, entry 1) or dithiopyridines (Table 3, entry 2), likewise, thioethers with iodoacetamides (Table 3, entry 3). Further, electron-deficient pyridine units enabled labelling via a S_NAr-reaction with -NO₂ or -SO₂Ph as leaving groups (Table 3, entry 4). Moreover, maleimides allow labelling via *Michael addition* (Table 3, entry 5) of cysteine residues yielding thioethers, which are also obtained in a thiol-ene reaction^[191] (Table 3, entry 6) using alkenes.

If suitable cysteines do not occur in the wild-type of the respective protein, site-directed mutagenesis allows for their introduction, while surplus cysteines can be removed vice versa. Carrying out labelling this way, the knock-out of cysteines crucial for the biological activity needs to be excluded with suitable experiments. Beyond cysteines, also unnatural amino acids can serve as targets for spin labelling of proteins. Accordingly, the intrinsic selectivity of the biorthogonal CuAAC click reaction^[204] facilitated its use with azido- or ethynyl-substituted spin labels targeting the respective coupling partners, which are introduced to the protein via unnatural amino acids (Table 3, entries 7, 8). Moreover, a 1,2,4,5-tetrazin-based spin label was recently conjugated to a protein via a *Diels-Alder-cycloaddition* with an unnatural amino acid featuring a cyclooctyne-moiety (Table 3, entry 9). Additionally, conjugation of hydroxylamino-nitroxides to 4-acetylphenylalanin via formation of an O-alkylketoxime (Table 3, entry 10) allowed for selective spin labelling. It should be noted that approaches targeting other amino acids, such as tyrosine, have been reported,^[205] but lack

widespread application beyond the proof-of-concept yet.

Frequently, the aim of EPR-based distance measurements is to observe structural changes of proteins e.g., upon binding of a substrate. Within such studies, the capability to distinguish between the *apo* and *holo* conformation of the protein is required, and hence a strategic selection of the labelling sites is crucial. For this purpose, open-source computational tools such as *mtsslWizard*^[206] or *MMM*^[207] have been developed within the scientific community. These programs permit *in silico* labelling of the protein based on an input structure and predict the expected distance distributions.

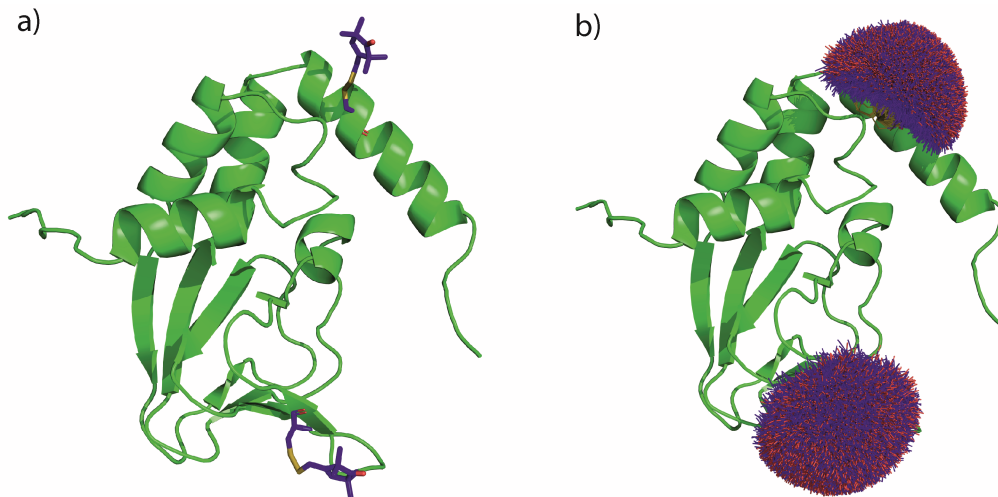


Figure 5: Cyclic Nucleotide Binding Domain (CNBD) of the K₁ potassium channel of *Mesorhizobium Loti*. The structure of the wild-type (PDB-ID: 2KXL) was solved by NMR-spectroscopy^[208]. (a) Using the *mtsslWizard* software implemented to PyMOL, glutamic acid 289 and isoleucine 340 were replaced by cysteines and labelled with nitroxide spin label **109•** *in silico*. Only one explicit rotamer is shown. (b) Instead of a single rotamer (a), the entire “conformer cloud” is shown, which the distance distribution can be estimated from.

The latter results from flexibility of the linker between the protein and the spin label. This leads to a rich ensemble of label conformations as shown in Figure 5b, rather than one distinct interspin distance as anticipated from Figure 5a. Notably, recent advances for the application of force fields for the optimization of large (biomolecular) structures^[209] allowed to simulated distance distributions also with MD-based algorithms, providing an increased accuracy compared to the aforementioned accessible-volume approach implemented into e.g. *mtsslWizard* or *MMM*.^[210]

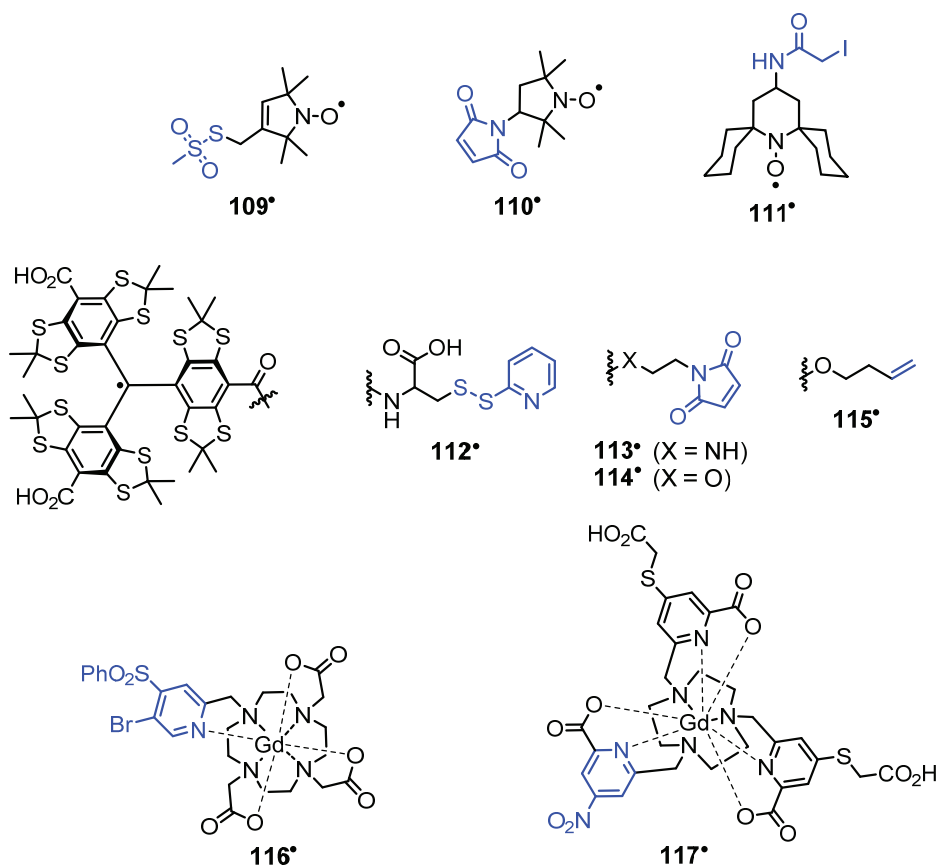
As noted above, spin labelling EPR is also a powerful tool targeting oligonucleotides.^[113,174–183] Spin labelling of DNA and RNA has been reviewed^[211] and as the synthesis of RNA and DNA is regularly carried out *in vitro*, presynthetic labelling strategies are more important for oligonucleotides than for proteins.

Generally, the nucleotide base, the sugar, and the phosphodiester backbone are all suitable labelling sites.^[211] Moreover, also approaches for non-covalent spin labelling of both DNA^[187] and RNA^[212] have been developed. Concerning spin labelling, however, this thesis is focused

on the development of improved spin labels for proteins and accordingly, a comprehensive presentation of techniques applicable to oligonucleotides cannot be provided at this point. Generally, the nucleotide base, the sugar, and the phosphodiester backbone are all suitable labelling sites.^[211] Concerning spin labelling, however, this thesis is focused on the development of improved spin labels for proteins and accordingly, a comprehensive presentation of techniques applicable to oligonucleotides cannot be provided at this point.

1.2.3.3 Spin Labels: Paramagnetic Tags for Biomolecules

After establishing a suitable labelling methodology (*vide supra*), the next key issue to the success of EPR-based distance measurements is the proper choice of the spin label itself. For that, a plethora of labels has been proposed in literature and the majority of these can be classified as nitroxides, TAM-radicals, or gadolinium complexes with examples shown in Scheme 43.



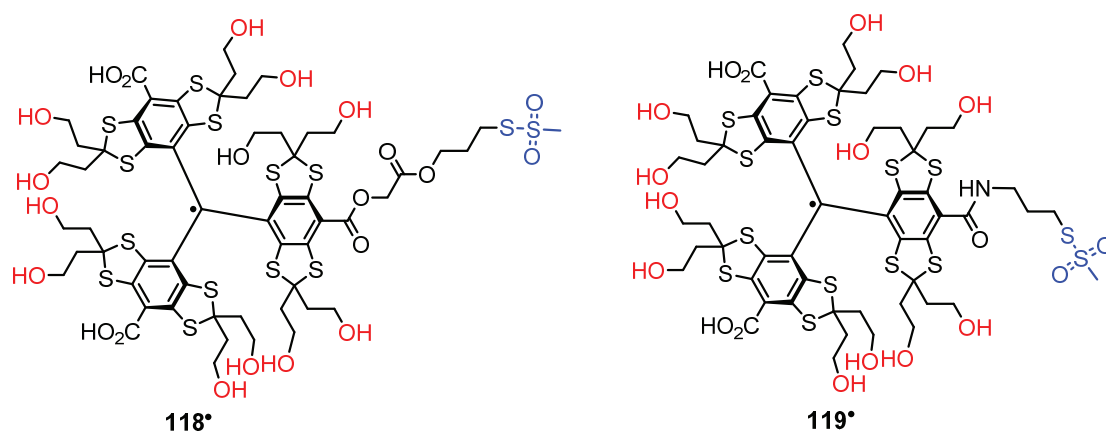
Scheme 43: Structure of several spin labels among nitroxides (top row), TAM-radicals (middle row), and gadolinium complexes (bottom row). For the sake of clarity, the bioconjugation group is highlighted in blue.

The nitroxides MTSL **109***^[166,167,169,171,173,184,192] and maleimido-PROXYL **110***,^[213–216] which are both nowadays available from commercial suppliers, are the most used spin labels across numerous studies, thus serving as a benchmark for the development of new labels. Generally, EPR-based distance measurements are carried out at cryogenic temperatures to encounter

sufficient T_M -relaxation times, which decrease with rising temperature. Aiming for measurements at ambient temperatures aroused the interest into spin labels with increased transversal relaxation times. In accordance, spirocyclohexyl nitroxide spin label **111** \bullet was prepared and allowed to measure distances up to 3.2 nm at 295 K with a protein sample immobilized in a glassy trehalose matrix.^[217] Nonetheless, a more recent study revealed that the substitution pattern adjacent to the NO-group has only a negligible influence on the T_M -relaxation times at room temperature and T_M -values around 700 ns were obtained for variously substituted nitroxides.^[218] However, the transversal relaxation rates at cryogenic temperatures may vary significantly among variously substituted nitroxides.^[218,219]

Apart from nitroxides, TAM-type trityl radicals (section 1.1.1) received rising attention as spin labels, especially with respect to their relaxation properties, exhibiting T_M values in the range of 10 μ s at 300 K.^[77] Spin labels of that type are typically amides (e.g., **112** \bullet , **113** \bullet)^[70,86] or esters (e.g., **114** \bullet , **115** \bullet)^[53,58,85] of the *Finland Trityl* **11** \bullet , among which **112** \bullet paved the way for distance measurements on proteins at physiological temperatures.^[220]

Later, other TAM-radical based spin labels were also used to perform EPR-based distance measurements at room temperature, both on proteins^[70] and DNA.^[222] Beyond trityl-trityl distance measurements, trityl-nitroxide distances were accessible at room temperature utilizing RIDME,^[223] and trityl/nitroxide-copper distances exploiting distance-dependent T_1 -relaxation enhancement,^[224,225] respectively. Moreover, the narrow EPR-spectra of trityl radicals yields large signal-to-noise ratios for distance measurements via DQC-EPR^[58,73,146] and the spin state of $s = 1/2$ renders data analysis simple.^[25]



Scheme 44: Highly hydrophilic spin labels **118** \bullet and **119** \bullet . For the sake of clarity, hydroxyl groups were highlighted in red and bioconjugation groups (methanethiosulfonates) in blue.

However, an inherent drawback of trityl spin labels based on the hydrophobic core of **11** \bullet is their propensity to aggregate with proteins in an unspecific fashion. This implies unspecific, yet undesirable, labelling which reduces the significance of the resulting distance information. Thus, the recent availability of **52** \bullet facilitated its use as a platform to construct the hydrophilic spin trityl labels **118** \bullet and **119** \bullet (Scheme 44), which do not suffer from aggregation with proteins.

Another important class of spin labels are gadolinium complexes such as for instance **116**[•]^[226] and **117**[•]^[196] which found wide application for EPR-based distance measurements.^[172,173] The lacking radical character of these labels implies a high chemical stability, however, their spin state of $s = 7/2$ imposes challenges for data analysis and working at high microwave frequencies (W-band) is regularly required.^[165,227] The transversal relaxation rate of gadolinium spin labels is strongly dependent on the nature of the chelating ligand and can exceed that of trityl radicals at cryogenic temperatures,^[228] but measurements at ambient temperatures are not feasible.

Furthermore, photogenerated triplet states of porphyrins^[229] or fullerenes^[230] have been proposed as spin labels, but these techniques have not been employed beyond a proof-of-concept yet.

1.2.3.4 In-Cell EPR

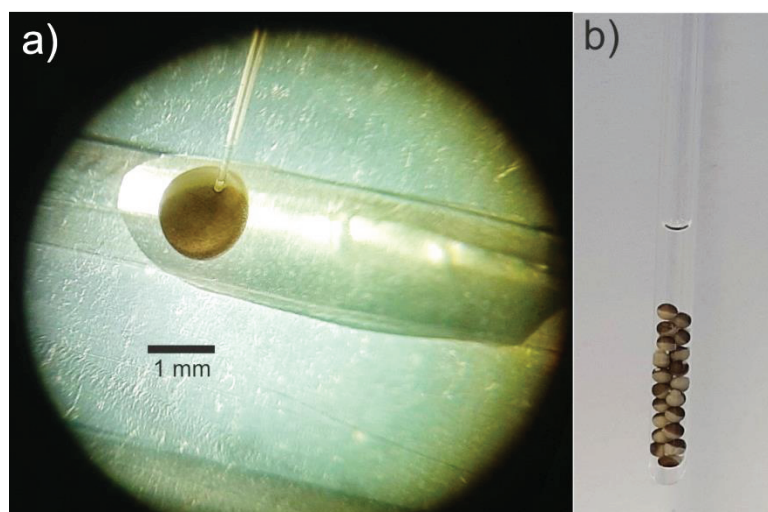


Figure 6: a) Microinjection into an oocyte of *X. laevis* viewed through an optical microscope. b) Oocytes filled into an EPR glass tube after injection. Pictures were made by the author with a Samsung Galaxy A50 smartphone camera.

Proteins and nucleic acids are vivid actors on the cellular stage, which differs remarkably from common *in vitro* conditions (i.e., aqueous buffers) by effects such as molecular crowding.^[231,232] Therefore, it is of great interest to study these biomolecules in their native environment by performing EPR-based distance measurements within intact cells. However, the reducing conditions encountered in the cytosol challenge the chemical stability of spin labels. To probe for the latter, sodium ascorbate has been used frequently as a surrogate to mimic cellular reductants,^[34,58,199,233] but lysates of HEK^{xiii}-cells,^[233] HeLa^{xiv}-cells,^[179] *Escherichia Coli* bacteria,^[233] and *Xenopus laevis* oocytes^[34,199] served this purpose as well. For practical reasons, oocytes of the African clawed frog *Xenopus laevis* are frequently employed for *in-cell* EPR experiments, as their large size allows for microinjection of spin-

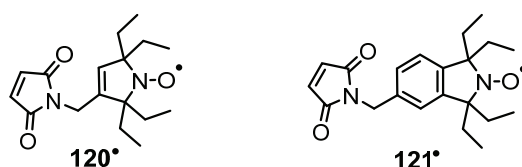
^{xiii} Human Embryonic Kidney cells

^{xiv} Cells of a human cervical carcinoma, first isolated in 1951 from the patient **Henrietta Lacks**.

labelled protein constructs (Figure 6a).^[234] Subsequent transfer of the cells into EPR tubes, as shown in Figure 6b, does then allow to perform distance measurements.

Moreover, electroporation can be used to transfer labelled protein constructs into smaller cells, such as *Escherichia Coli* bacteria.^[228]

Tetramethylnitroxides such as **109•** and **110•** suffer from reduction within minutes if exposed to aqueous ascorbate or cytosolic extracts^[34] and hence give only poor signal quality within *in-cell* experiments.^[235] By contrast, sterically shielded nitroxide spin labels (Scheme 45) such as **120•**^[199] and **121•**^[233] exhibited an increased stability towards bioreduction and intracellular distance measurements have been performed with the former.



Scheme 45: Sterically shielded nitroxide spin labels with increased reduction stability.

Notably, TAM-radicals provide an excellent platform for the design of spin labels suitable for *in-cell* experiments owing to their high stability towards bioreduction.^[34,58] In consequence, labels **114•**^[228] and **115•**^[53] were recently used for *in-cell* EPR based distance measurements on proteins.

Obviously, gadolinium spin labels (e.g., **116•** and **117•**) do not suffer from bioreduction and were hence successfully used for *in-cell* EPR experiments.^[195,226,236] However, the central Gd³⁺-ion might be exchanged for other metal ions present in the cell.^[236] The high relevance of *in-cell* EPR studies was underlined very recently by *Collauto* et al. showing a conformational change of RNA duplexes upon switching from *in-vitro* conditions into oocytes of *X. laevis*.^[237] As described in section 3.1.5, recent advances targeting trityl spin labels for *in-cell* experiments as part of this thesis enabled to detect such a phenomenon for a protein as well. It should be noted that an exact comparison of different literature data assessing the reduction stability of various spin labels is hardly possible, as the composition and individual activity of the utilized cell-lysates is not necessarily equal. However, as a rule of thumb, current trityl spin labels perform at least on par with sterically shielded nitroxides regarding intracellular stability, persisting for hours under cytosolic conditions. Finally, the low spin concentrations encountered for *in-cell* experiments render the use of trityl radicals generally advantageous due to the high signal-to-noise ratios obtained (c.f. section 1.3.3).

1.2.3.5 Model Compounds: EPR-based distance measurements

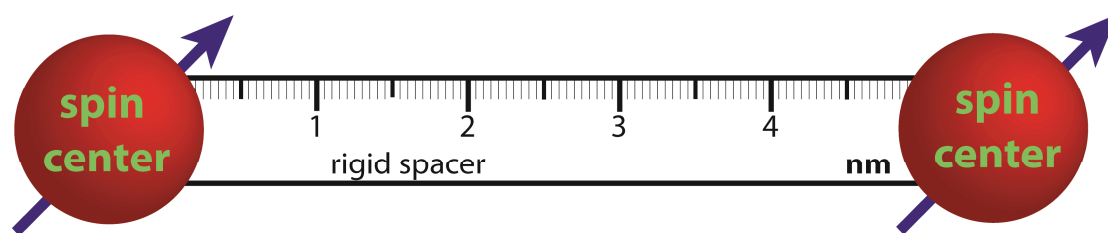
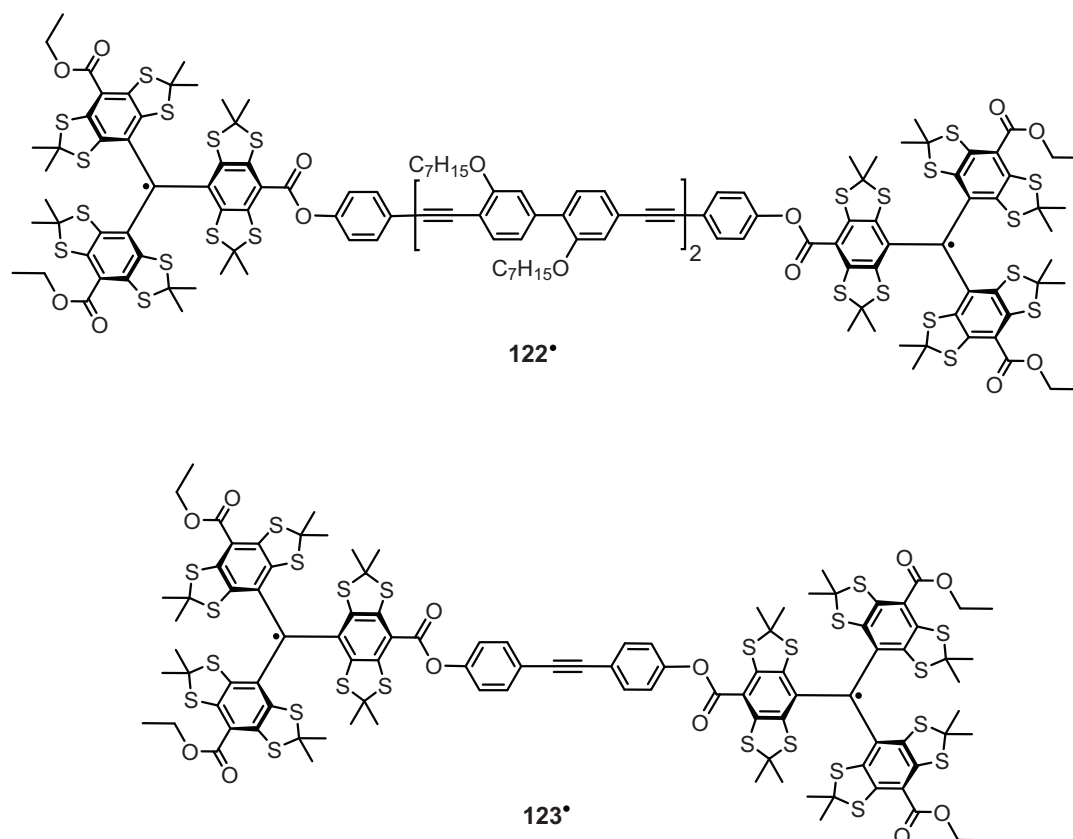


Figure 7: Schematic arrangement of a model compound for EPR-based distance measurements.

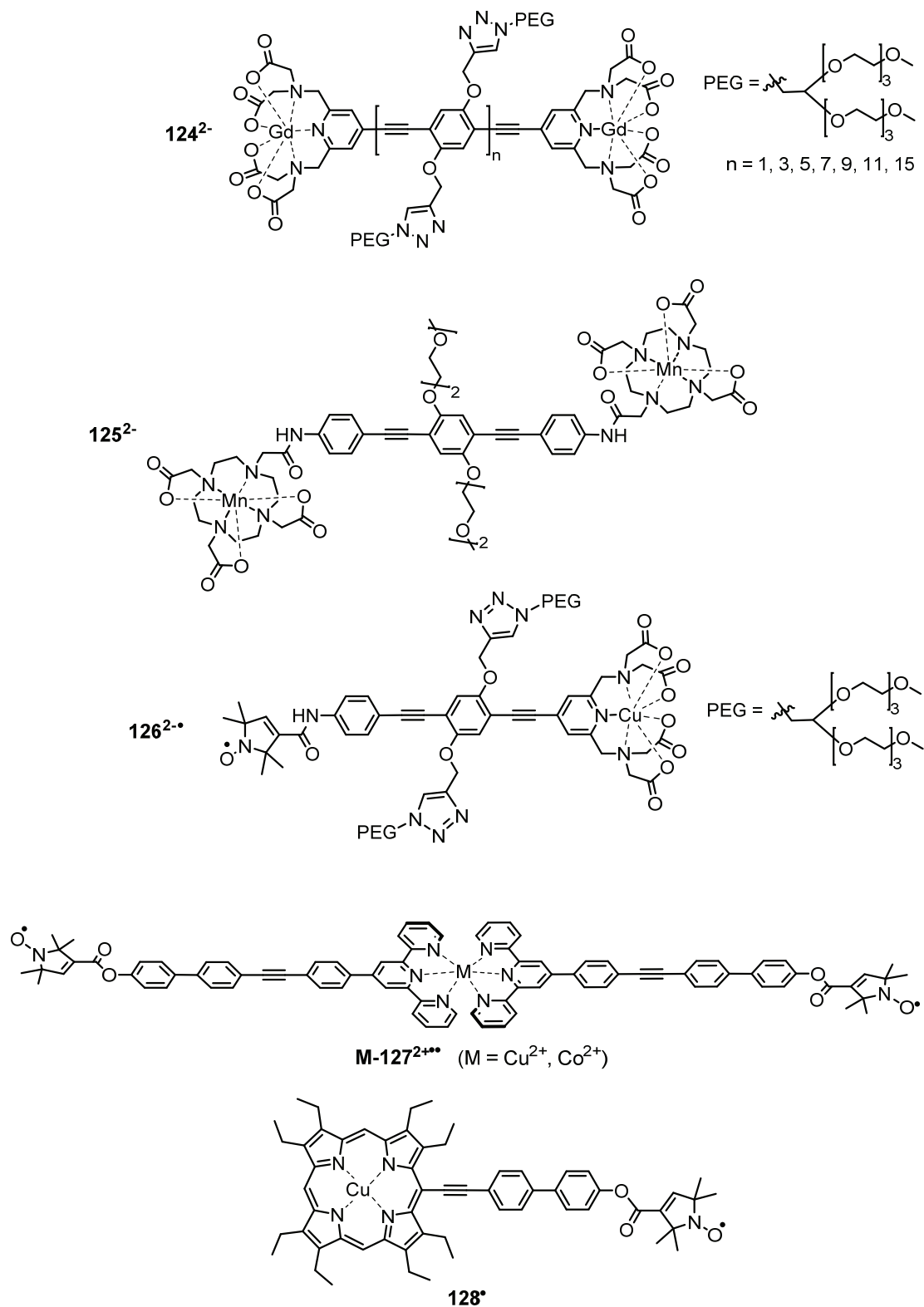
In parallel to application of EPR-based distance measurements to immediate biological questions, model compounds were used extensively to validate and explore the methodology, especially when using novel spin labels. Such a model compound arranges a two spin centers in a fixed and well-defined distance through a rigid spacer. As trityl radicals entered the regime of spin labels quite late compared to nitroxide radicals, the interest into model compounds consisting the former arouse. This holds especially with respect to the application of single frequency techniques, which are highly beneficial in terms of the signal-to-noise ration if applied to trityl radicals.



Scheme 46: Selected trityl biradicals used as model compounds for EPR-based distance measurements.

Accordingly, compounds **99•** - **103•** were studied to elucidate the influence of exchange coupling on EPR-based distance measurements.^[145,238] Additionally, compounds **122•** and **123•** (Scheme 46) were used to validate the methodology for EPR-based distance measurements involving trityl radicals^[25,73,239] and more recently, **103•** and multiradical

derivatives thereof were used to compare the performance of various pulsed EPR-based distance measurements on trityl radicals.^[146] Beyond artificially introduced spin centers, also intrinsic paramagnetic metal cofactors can be utilized to perform EPR-based distance measurements (section 1.3.3).



Scheme 47: Structure of selected model systems for EPR-based distance measurements involving metal centers. For the sake of clarity, the counterions of the charged metal complexes were omitted.

These occur natively both in proteins^[240] and nucleic acids.^[241] Accordingly, distance measurements involving paramagnetic Fe³⁺, Cu²⁺, Gd³⁺, and Mn²⁺-centers have been conducted,^[165] and even spin labels consisting of the latter three have found application.^[172,173,186,242,243]

However, several challenges come along with applying pulsed-dipolar spectroscopy to metal centers, as large *g*-anisotropies trigger very broad EPR-spectra and relaxation times are much shorter than for organic radicals.^[165] This fostered the interest into model systems to validate the methodology of metal-involving EPR-based distance measurements. To avoid exchange coupling effects that might interfere with the EPR-based distance measurements on the one hand, a minimum distance of ≈ 2 nm should be kept between the spin centers. On the other hand, too long distances render the distance measurement rather cumbersome, so that a distance between 2 – 5 nm appears desirable, though entire sets of molecular rulers have been described as well.^[244]

The structure of selected model compounds involving metal centers is shown in Scheme 47, including both metal-metal and metal-radical systems. Commonly, the spacer is built from acetylene- and/or phenylene-units, which ensure molecular rigidity, so that narrow distance distributions result. For systems that are tailored to be used in aqueous media, polar side-chains promoting the solubility of the final model system can be installed by additional aromatic functionalization (cf. **124²⁻**,^[244] **125²⁻**,^[245] and **126^{2•}**,^[246]). The metal-binding site of such water-soluble systems is regularly built from carboxylate-based ligands such as PyMTA (**124²⁻** and **126^{2•}**) or DOTA (**125²⁻**), which form highly stable complexes with di- and trivalent metal cations. Moving to organic solvents, different ligand systems were employed, such as terpyridines^[247] (**M-127^{2+••}**^[248,249]) or porphyrins (**128[•]**^[250]). For **M-127^{2+••}**, the cation-induced self-assembly of two nitroxide-bearing terpyridine ligands was exploited to construct model compounds with Cu²⁺^[249] and Co²⁺^[248] ions, which were subsequently used for EPR-based distance measurements. Moreover, porphyrins provide a suitable platform for model compounds, as they form stable complexes with many metals, allow for chemical modification, and mimic the ligand sphere of cofactors such as *heme* quite well.

1.2.4 Functional EPR-Spectroscopy

While spin labelling EPR allows for elucidation of microscopic structural information, other EPR-based techniques utilize stable radicals to gain information about rather macroscopic properties of biological systems.

An enticing feature of trityl radicals is the dependence of their EPR-linewidth on local oxygen concentrations in the sample.

In accordance, trityl radicals serving as oxygen probes were developed and allowed for EPR-based oximetry.^[50,251–253] Combined with EPR-based magnetic resonance imaging (MRI), this

method provides spatial information about local oxygen concentrations *in vivo*.^[83,254] An important application of this method is the detection of local hypoxia in tumors.^[255]

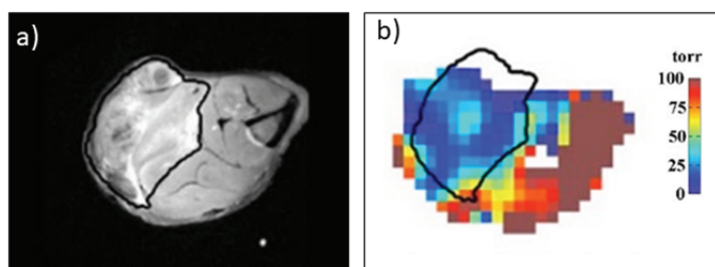


Figure 8: T₂-weighted conventional ¹H-MRI image (a) showing an intramuscular carcinoma in the leg of a rabbit, encircled in black. (b) EPR-based oximetry allowed for selective detection of the tumor tissue by observing tumor hypoxia. The local oxygen partial pressures are color-coded referring to the scale on the right edge of the picture. Adapted with permission from *Med. Phys.* 2010, 37, 2553 – 2559. Copyright ©2010 to the American Association of Physicists in Medicine.

In one example provided by *Epel et al.*,^[254] an intramuscular carcinoma of a rabbit is clearly evident from conventional ¹H-MRI images due to the distinct nature of the tumor tissue as shown in Figure 8a. Interestingly, tumor hypoxia was detectable by oximetry based on spatially resolved cw-EPR after injection of a suitable trityl radical into the femoral artery (Figure 8b).

It should be noted that nitroxides have also been employed for in-vivo oximetry, though spatial resolution was lacking.^[256] However, the narrow single-line EPR spectra of trityl radicals render them superior for this purpose.^[257] Apart from that, nitroxides were applied as MRI contrast agents^[258] and recent studies aimed to improve their sensitivity as oxygen probes by isotopic labelling.^[259]

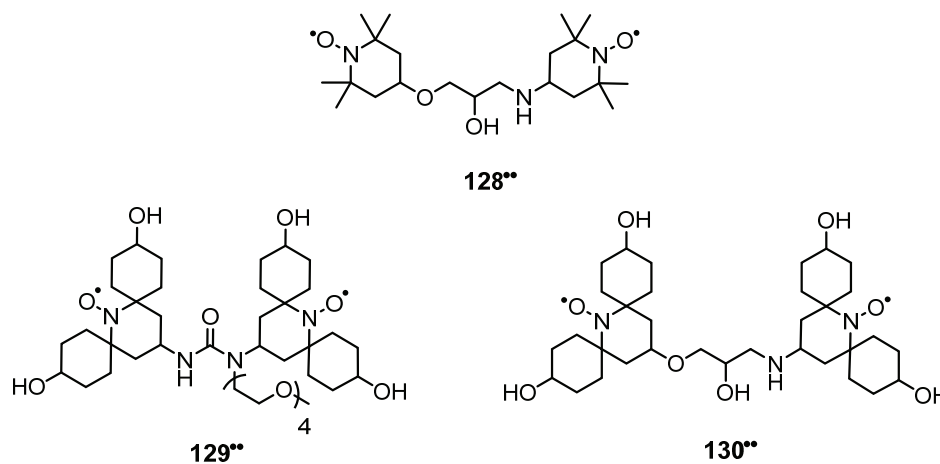
Moreover, both nitroxides^[260–262] and trityl radicals^[61,263] allowed to probe for pH-values in microenvironments via EPR. Beyond that, viscosity measurements were enabled by a recently introduced ¹³C-labelled derivative of **11•**, the spectral shape of which appeared highly sensitive towards molecular tumbling rates.^[264] Furthermore, the discriminative detection of biothiols was feasible using a trityl-based methanethiosulfonate thiol trap **39•**, yielding different EPR spectra for various biothiols as e.g., cysteine or glutathione.^[80]

1.2.5 Dynamic Nuclear Polarization

Another application field of stable radicals is dynamic nuclear polarization (DNP)^[265,266]. The sensitivity of NMR-spectroscopy suffers from a small population difference (polarization), while the larger *Zeeman-splitting* encountered for EPR comes along with an enhanced sensitivity. The principle of DNP is to transfer the strong electronic spin polarization to the nuclear spins, resulting in significant sensitivity improvements. Nitroxides^[267] have been used extensively for this technique and tailored biradicals of these became common polarizing agents for cross-effect DNP, which is performed in the solid state.^[268–273] The efficiency of DNP is characterized by the enhancement factor ϵ , describing the increase in

NMR signal intensity upon using the polarizing agent. Here, the biradicals TOTAPOL **128**^{••}[268] ($\epsilon = 42$), AMUPol **129**^{••}[272] ($\epsilon = 222$), and the recently introduced cyolyTOTAPOL **130**^{••}[273] ($\epsilon = 164$) are representative examples for highly-efficient polarizing agents (Scheme 48). The aforementioned enhancement factors were determined for a ^{13}C -MAS-NMR on proline at 110 K.[273]

However, also pure trityl radicals were found well-suited for DNP experiments[274,275] and signal-to-noise ratios were enhanced by factors up to 10,000[276] using the Finland trityl **11**[•] in liquid-state NMR experiments on ^{13}C -urea.



Scheme 48: Nitroxide biradicals, which were developed for cross-effect DNP.

1.3 EPR Spectroscopy

1.3.1 The Spin System

A property unique to radicals is the presence of an unpaired electron rendering these compounds paramagnetic. This allows their subjection to electronic paramagnetic resonance spectroscopy (EPR), a concise introduction to which is provided in the following.

The pioneering work of *Stern* and *Gerlach* in 1922 provided the first experimental evidence for the quantization of the intrinsic angular momentum of electrons,[277] which is since referred to as the electron spin \vec{s} :

$$|\vec{s}| = \hbar\sqrt{S(S+1)} \quad (1)$$

Here, $S = 1/2$ is the spin quantum number of the electron and \hbar the reduced *Planck constant*. The components of the spin vector \vec{s} along the principal axes are complementary observables and hence, only one component can be determined alongside the vector length $|\vec{s}|$ (*Heisenberg uncertainty principle*). Generally, the component of \vec{s} in the z -direction of the laboratory coordinate system is chosen and determined by:

$$s_z = m_s \hbar \quad (2)$$

Here, m_s is the magnetic quantum number, which can adopt values of $+1/2$ and $-1/2$. In possession of both charge and angular momentum, the electron exhibits a magnetic moment $\vec{\mu}_e$:

$$\vec{\mu}_e = -g_e \frac{e}{2m_e} \vec{S} \quad (3)$$

While e is the elementary charge and m_e the mass of the electron, g_e refers to the g -factor (*Landé factor*). The latter relates the magnetic moment to the angular momentum equaling $g_e \approx 2.0023$ for the free electron and is known with outstanding precision into the ppt-regime.^[278] While organic radicals exhibit g -values around $g \approx 2$, spin-orbit coupling can lead to tremendous deviations for paramagnetic species based on transition metals. The projection of the magnetic moment along the z -direction results from Equations 2 and 3 as:

$$\mu_{e,z} = -g_e \mu_B m_s; \quad \mu_B = \frac{e\hbar}{2m_e} \quad (4)$$

Here, μ_B is the so-called *Bohr magneton*. Consequently, the energy related to the magnetic moment positioned in the external magnetic field B_0 applied along the z -direction can be described as:

$$E = \vec{\mu}_e \cdot \vec{B}_0 \Rightarrow E_z = -\mu_{e,z} B_0 = g_e \mu_B m_s B_0 \quad (5)$$

With respect to the quantization imposed by the possible values of m_s , two distinct energy levels exist and transitions between those can be triggered by electromagnetic radiation, provided its energy amounts to the energy difference between both levels:

$$h\nu = \Delta E = g_e \mu_B B_0 \quad (6)$$

Here, ν is the frequency of the respective electromagnetic radiation and Equation 6 is referred to as the *resonance condition*, while the energy splitting itself is referred to as the *Zeeman-splitting*. This implies that electromagnetic radiation suitable in frequency (Equation 6) will be absorbed by a paramagnetic sample positioned in an external magnetic field, laying the foundation of Electron Paramagnetic Resonance (EPR) spectroscopy. Indeed, the first EPR experiments were conducted by *Zavoisky* in 1944 on samples of manganese chloride^[279]. The absorption intensity scales with the population difference between both levels, which can be described through the *Boltzmann distribution* as given in Equation 7.

$$\frac{N_{m_s=+\frac{1}{2}}}{N_{m_s=-\frac{1}{2}}} = e^{-\frac{\Delta E}{k_B T}} = e^{-\frac{g_e \mu_B B_0}{k_B T}} \quad (7)$$

In a macroscopic picture, this population difference induces a net magnetization along the z -axis, the magnetic component of the electromagnetic radiation can interact with. As this population difference (i.e. the *Zeeman-splitting*) increases with the magnitude of B_0 , measurements at higher magnetic fields come along with increased sensitivity. Since the magnetic moment induced by electrons exceeds that of protons^{xv}, larger population

^{xv} The magnitude of μ depends on the charge-to-mass ratio of the particle (Equation 2). Since protons are about a factor of 1800 heavier than electrons, their intrinsic magnetic moment is lower.

differences coming along with enhanced sensitivity are encountered for EPR-spectroscopy in comparison to NMR-spectroscopy.

Moreover, interactions of the electron spin with its environment occur and affect the appearance of EPR spectra beyond the g-value. A concise representation of these effects is given with the *Spin Hamiltonian*, a simplified^{xvi} expression of which is provided in Equation 8:

$$\hat{H}_s = \sum_i \frac{g_i \mu_B B_0}{\hbar} \hat{S}_i - \sum_k \frac{g_k \mu_B B_0}{\hbar} I_k + \sum_i \sum_k \hat{S}_i A_{ik} \hat{I}_k + \sum_i \sum_{j \neq i} \hat{S}_i D \hat{S}_j + \sum_i \sum_{j \neq i} -2J \hat{S}_i \hat{S}_j$$

$$\hat{H}_s = \hat{H}_{EZ} - \hat{H}_{NZ} + \hat{H}_{hyp} + \hat{H}_{dip} + \hat{H}_{ex}$$

$$\begin{aligned} \hat{H}_{EZ} &= \text{electronic Zeeman splitting} & \hat{H}_{dip} &= \text{dipolar coupling} \\ \hat{H}_{NZ} &= \text{nuclear Zeeman splitting} & \hat{H}_{ex} &= \text{exchange coupling} \\ \hat{H}_{hyp} &= \text{hyperfine splitting} \end{aligned} \quad (8)$$

Interactions with nuclear spins (I_K), called *hyperfine coupling*, lead to splitting of signals determined by the hyperfine coupling constant A . The multiplicity of a signal affected by hyperfine coupling to N nuclei with a nuclear spin of I is determined by $M = 2N \cdot I_k + 1$.

With more than one paramagnetic center in place, also interactions between the electron spins arise. These can occur either through space, determined by the *dipolar coupling* constant D , or through bonds and direct overlap of the electronic wave functions, determined by the *exchange coupling* constant J .

Considering the latter contribution, a system of two coupled electron spins neglecting dipolar and electron-nuclear interactions can be described by Equation 9^{xvii}:

$$\hat{H}_s = \sum_{i=1}^2 \frac{g_i \mu_B B_0}{\hbar} \hat{S}_i + -2J \hat{S}_1 \hat{S}_2 \quad (9)$$

In consequence, four eigenvalues of the aforementioned Hamiltonian arise (Equation 10), assuming that the g-values of both interacting spins are identical.

$$\begin{aligned} E_1 &= +\frac{3}{2}J \\ E_2 &= -\frac{1}{2}J + g\mu_B B_0 & E_3 &= -\frac{1}{2}J - g\mu_B B_0 & E_4 &= -\frac{1}{2}J \end{aligned} \quad (10)$$

In total, both a singlet and a triplet state, separated by $2J$ in absence of an external magnetic field B_0 , result as depicted in Figure 9.

^{xvi} Zero-field-splitting effects and terms accounting for the nuclear spin regime have been omitted for the sake of conciseness.

^{xvii} Using an exchange term of $H_{ex} = -2JS_1S_2$ is most common in chemistry. However, some textbooks from a physicist perspective use $H_{ex} = +JS_1S_2$ or $H_{ex} = -JS_1S_2$ instead. Therefore, numeric values of J are only comparable in the context of the same formalism. Throughout this thesis, the formalism of equation 9 is used and literature values were recalculated accordingly, if required.

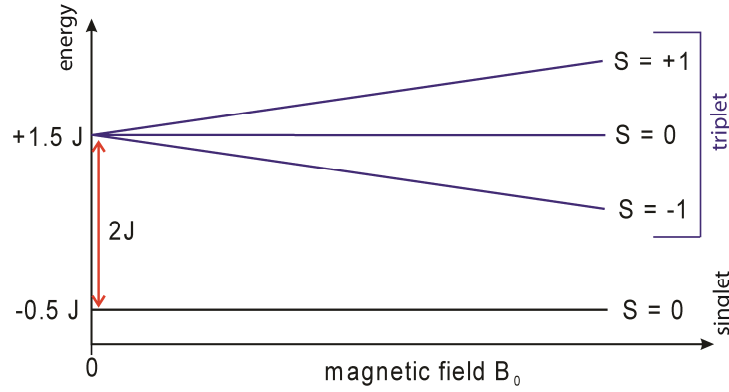


Figure 9: Schematic energy profile for a system of two antiferromagnetically ($J < 0$) coupled electron spins.

With respect to the sign of J , two distinct cases are encountered: For $J < 0$, the singlet appears as the ground state and the coupling is antiferromagnetic (cf. Figure 9), while the triplet is the ground state of a system with ferromagnetic coupling identified by $J > 0$, vice versa. Exploiting the macroscopic magnetization generated by population of the triplet level, J can be elucidated measuring the temperature dependency of the magnetic susceptibility χ using the *Bleaney-Bowers equation* (Equation 11):^[280]

$$\chi = \frac{Ng^2\mu_B^2}{k_B T} \frac{2e^{\frac{2J}{k_B T}}}{1+3e^{\frac{2J}{k_B T}}} \quad (11)$$

Also the intensity of the half-field EPR transition ($\Delta m_s = \pm 2$) can be used instead of the magnetic susceptibility, as its intensity is immediately related to the population of the triplet state.^[281] However, to be accessible via these methods, the magnitude of J needs to be in the range of $k_B T$ at reasonable temperatures^{xviii}, meaning $J > 1 \text{ cm}^{-1}$.

The validity of the expressions above relies on the assumption of a strong exchange coupling, meaning that the magnitude of J is large compared to other terms of the Spin Hamiltonian (Equation 8). Therefore, the applicability of the strong coupling regime depends on the individual spin system and a general range of J cannot be defined.

The dipolar coupling operator for two interacting spins with the same g -value and a dipolar coupling much smaller than the *Zeeman* interaction is given by Equation 12:

$$\hat{H}_{dip} = \frac{g^2\mu_B^2}{r^3} \hat{S}_{z,1}\hat{S}_{z,2}(1 - 3\cos^2\theta) = D \hat{S}_{z,1}\hat{S}_{z,2}(1 - 3\cos^2\theta) \quad (12)$$

Here, r is the interspin distance, θ the angle between the distance vector and the direction of the magnetic field B_0 , and D refers to the dipolar coupling constant. According to Equation 12, a dipolar coupling frequency of $\nu_{\perp} = D$ results for an orientation of $\theta = 90^\circ$, while $\nu_{\parallel} = -2D$ results for $\theta = 0^\circ$ (cf. Figure 10).

Hence, the dipolar coupling tensor is traceless, so that effects of such coupling can only be observed for sufficiently immobilized systems, classically in frozen solution or for powdered samples. Since θ is distributed isotropically within such a non-crystalline sample, the solid-

^{xviii} Using liquid helium for cooling, temperatures in the regime of 3-4 K can be approached.

state spectra of a dipolar coupled spin system are governed by the so-called *Pake* pattern, from which the dipolar coupling constant D can be read off immediately (cf. Figure 10).

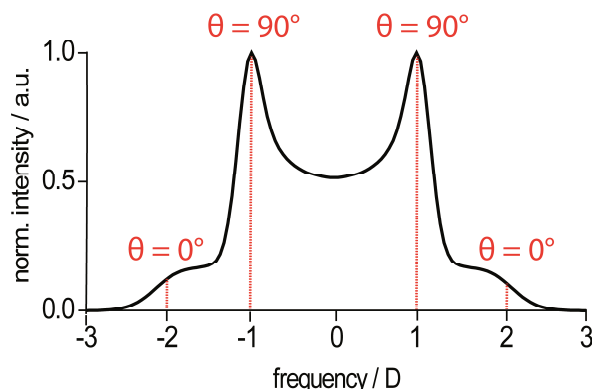


Figure 10: Pake pattern arising from dipolar coupling. A Gaussian distance distribution was implemented to simulate the shown Pake pattern. For the sake of clarity, the Pake-pattern shown here appears in the frequency domain. A recorded cw-EPR spectrum will appear differently (1st derivative), also depending on the spectral character of the radical species.

1.3.2 Characterization of Radicals via cw-EPR Spectroscopy

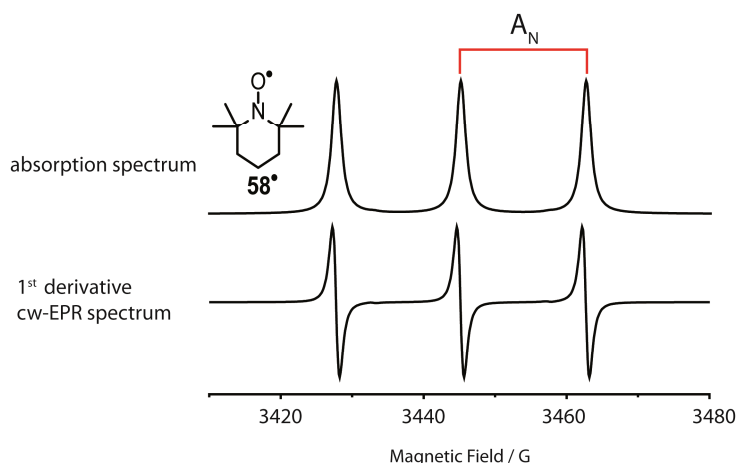


Figure 11: Exemplary first derivative X band cw-EPR spectrum (bottom) and the corresponding absorbance spectrum (top) of the nitroxide TEMPO **58•** recorded at room temperature. The splitting caused by the isotropic hyperfine coupling to the nitrogen atom (A_N) is indicated in red.

The most common method to record EPR spectra is the continuous wave (cw-EPR) experiment. Here, microwave radiation with constant frequency is applied and the external magnetic field is swept until the resonance condition (Equation 6) is fulfilled. To enhance the sensitivity of the measurement further, an additional magnetic field, modulated with a high frequency (kHz), is applied. This corresponds to the setup of a lock-in amplifier, allowing to cancel out noise efficiently. However, this technique provides the EPR spectrum as its first derivative instead of a classical absorbance spectrum (Figure 11). Due to the hyperfine coupling to one nitrogen atom, the exemplary cw-EPR spectrum of **58•** given in Figure 11 exhibits a triplet structure characteristic for nitroxides.

The cheap availability of electromagnets renders X-band cw-EPR spectroscopy most common, which requires a microwave frequency of ca. 9.6 GHz to fulfil the resonance condition at a magnetic field of 340 mT (3400 G) for a spin system possessing a g-factor of 2, which holds true for most organic radicals. However, superconducting magnets allow to carry out measurements at higher frequencies and EPR-setups operating with up to 263 GHz are nowadays commercially available. Using synchrotron radiation, even EPR-setups operating in THz-regime have been realized.^[282]

To elucidate parameters such as g-values or hyperfine coupling constants from cw-EPR spectra, it is common practice to fit these with proper software such as *EasySpin*.^[283] In general, any interaction leading to a splitting (e.g. hyperfine coupling) that exceeds the linewidth can be studied by cw-EPR. Thus, cw-EPR is a valuable tool to characterize organic radicals, also from the viewpoint of a synthetic chemist.

First of all, an EPR signal of any kind proves the presence of a radical species and quantitative measurements allow to judge about its quantity. Secondly, hyperfine couplings provide information about nuclei in vicinity to the electron spin and the substitution pattern of the radical, since the spin density is regularly not located exclusively on a single atom.

Thus far, cw-EPR-spectra as the example shown in Figure 11 were discussed for the isotropic case, as regularly encountered for samples in the liquid state. Here, molecular tumbling appears fast on the EPR-timescale and eventual anisotropic contributions vanish due to the rotational averaging.^{xix} However, the g-value is tensor in general (Equation 13), and its anisotropic nature can be observed for immobilized samples, e.g. in frozen-solution or upon binding to a large, slow-rotating biomolecules.

$$g = \begin{pmatrix} g_{xx} & & \\ & g_{yy} & \\ & & g_{zz} \end{pmatrix} \text{ with } g_{iso} = \frac{1}{3}(g_{xx} + g_{yy} + g_{zz}) \quad (13)$$

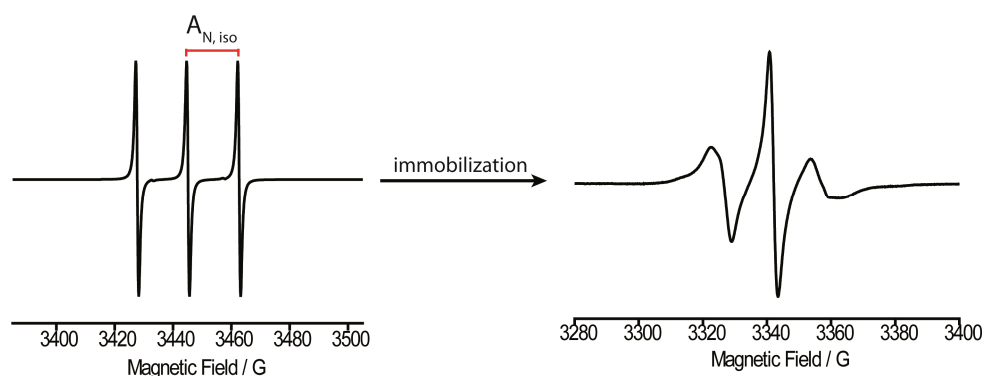


Figure 12: X-Band cw-EPR spectra (298 K) of the nitroxide spin label MTSL **109**^{*} in aqueous solution (left) and attached to both cysteins of the protein YopO₈₉₋₇₂₉ C219A V599C N624C. The data has been taken from *Molecules* 2019, 24, 2735 and was provided with permission for reprint by the authors.

^{xix} This condition might not necessarily be fulfilled for large supramolecular aggregates.

Figure 12 illustrates the effect of immobilization for a nitroxide spin label (**109**[•]). In liquid solution at room-temperature, the isotropic case is encountered yielding a spectrum analogous to the one shown in Figure 11 above. Upon binding to a protein, the spin label gets immobilized and anisotropic contributions of both the g -tensor and the hyperfine-tensor lead to a distortion of the cw-EPR spectrum, which can be exploited to judge about the mobility of the label in a quantitative manner. Information on the local mobility of the spin label can also be utilized in terms of structural biology.

For TAM-radicals, the g -anisotropy is less pronounced and diagnostic hyperfine splittings are lacking for typical spin labels based on **11**[•]. However, ¹³C-labelling of the central carbon of **11**[•] allowed to use the anisotropy of the hyperfine splitting for determination of local viscosities.^[264]

Moreover, the presence of dipolar coupling can affect the appearance of cw-EPR spectra of immobilized samples^{xx}, such that a Pake pattern (cf. Figure 10) is imposed to the signal. Thus, interspin distances can be determined from cw-EPR measurements as long as the effects of dipolar coupling are not hidden beyond the linewidth. For nitroxide, this methodology is viable till an upper limit of 1.5 – 1.7 nm,^[284] while trityl radicals allow to determine interspin distances up to 2.4 nm via cw-EPR,^[25] due to their smaller linewidth.

1.3.3 Distance Measurements via Pulsed EPR

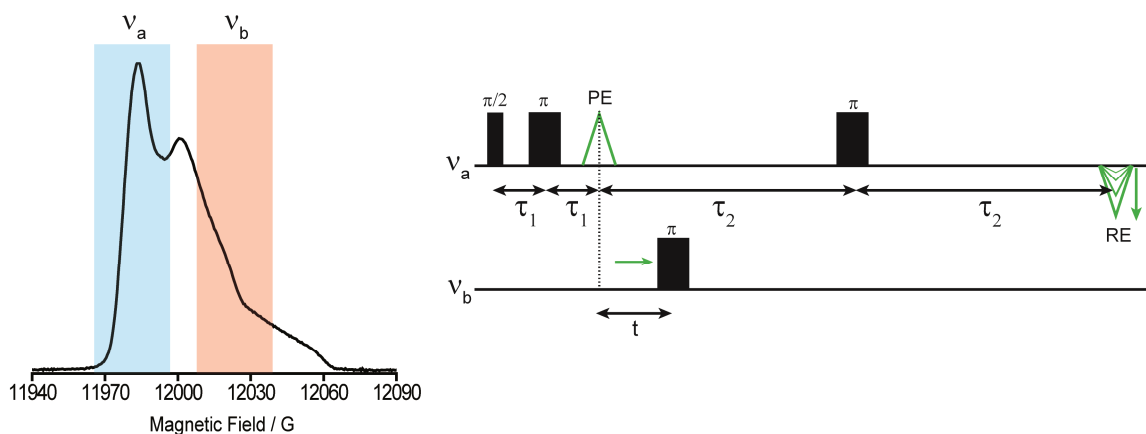


Figure 13: Q-Band EPR-spectrum (field-sweep, absorption spectrum) of the protein YopO₈₉₋₇₂₉ C219A V599C N624C, doubly labelled with MTSL **109**[•] (left). The widths and spectral positions of the microwave pulses applied during the PELDOR-sequence (right) are schematically indicated. PE = primary echo, RE = refocused echo. Note, that the spectral position of both pulses might be slightly shifted in a real experimental setup.

Since the magnitude of D falls below the cw-EPR-linewidth for larger interspin distances, pulsed EPR techniques are used to elucidate the dipolar coupling in these cases. By means of these, distances up to 8 nm are generally accessible,^[163,285] though certain cases allowed to measure distances up to 16 nm.^[286]

^{xx} The dipolar coupling tensor is traceless. Hence, effects of dipolar coupling vanish out for the isotropic case.

The most frequently used method for this purpose is the **pulsed electron electron double resonance (PELDOR)** experiment,^[287] the pulse-sequence of which is depicted in Figure 13. The first two pulses applied to spin A form a *Hahn-echo sequence*, resulting in the primary echo. During the following interval τ_2 , a 180° pulse is applied to spin B. As both spins interact, characterized by the dipolar coupling frequency D , the manipulation of spin B affects the *Lamor frequency* of spin A and accordingly, its precession frequency is shifted during the first τ_2 -interval.

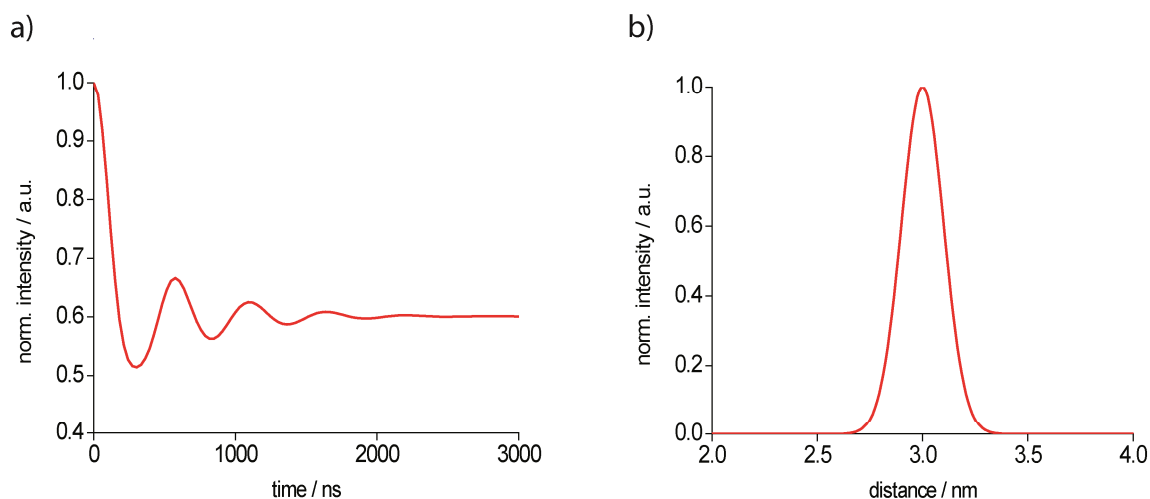


Figure 14: a) Simulated time trace as it would be obtained from a pulsed EPR experiment for the Gaussian distance distribution shown in b).

Subsequent precession with the new *Lamor frequency* during the remaining τ_2 -interval results in a phase shift of spin A, affecting the intensity of the refocused echo obtained later. Measuring its intensity against the position of the π -pulse on spin B, the echo intensity is modulated with the dipolar coupling frequency, resulting in a time trace as shown in Figure 14a.

This time trace is modulated with a superposition of all dipolar coupling frequencies present. For all aforementioned experiments, a time trace such as the one shown in Figure 9b is obtained. In principle, a *Fourier* transformation of the time trace would give the *Pake* pattern (Figure 10), the mean interspin distance can be calculated from.

However, the presence of multiple distances leads to a superposition of modulation frequencies within the time trace, so that a clear modulation is not necessarily visible anymore due to destructive interference. To circumvent this issue, methodologies to extract the distance distribution immediately from the time trace, such as *Tikhonov regularization*, exist as well^[288] and their application emerged to a standard in the field. Those methodologies are implemented in common software packages, e.g., *DeerAnalysis*, which enable to analyze the obtained data.^[289]

It should be noted that each microwave pulse features a certain bandwidth related to its length and only spins appearing in parts of the spectrum lying within this bandwidth are

affected by the pulse. In the exemplary case of PELDOR (Figure 13), the shape of the EPR-spectrum needs to be narrow enough to be coverable by microwave pulses, but still broad enough to avoid significant overlap of the pulses at ν_A and ν_B , respectively. For instance, the first condition is regularly not fulfilled for systems consisting of a metal center, which exhibit generally rather broad EPR spectra. In such a case, the RIDME sequence^[290] (Figure 15a) can be applied.^[291]

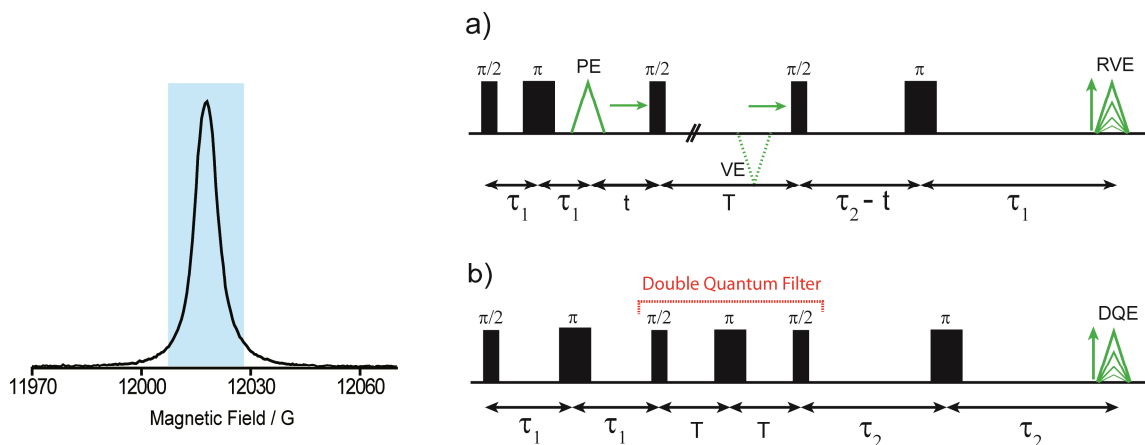


Figure 15: Q-Band EPR-spectrum (field-sweep, absorption spectrum) of the protein YopO₈₉₋₇₂₉ C219A V599C N624C, doubly labelled with a trityl radical (left). The width of a microwave pulse applied during the single-frequency experiments RIDME (a) and DQC (b) is schematically indicated in blue, revealing that almost the entire trityl-spectrum is coverable by a microwave-pulse. PE = primary echo, VE = virtual echo, RVE = refocused virtual echo, DQC = double-quantum echo. Together with an extensive phase cycling, the double-quantum filter subsequence highlighted in (b) ensures, that only double-quantum transitions containing the dipolar interaction contribute to the DQE.

Here, the manipulating π -pulse applied to spin B in PELDOR is replaced by a time interval T , during which the second spin is statistically expected to flip by longitudinal relaxation processes (*vide infra*). On the other hand, very narrow EPR spectra obtained for e.g., TAM-radicals, render PELDOR disfavored with respect to excessive pulse overlap, lowering the sensitivity of the measurement. By contrast, single frequency techniques such as RIDME, DQC^[292] (Figure 15b), or SIFTER^[293] profit from such narrow EPR spectra^[146] and enable highly sensitive measurements, since the entire EPR spectrum is coverable by the bandwidth of the microwave pulses (cf. Figure 15).

Moreover, electron spin relaxation becomes an important issue considering pulsed EPR experiments. Generally, two types of relaxation are distinguished. The magnetization along the z -axis is affected by longitudinal relaxation, determined by T_1 described in Equation 15:

$$M_z = M_{z,eq} (1 - e^{-\frac{t}{T_1}}) \quad (15)$$

As the longitudinal magnetization resembles the population difference of the *Zeeman* levels, this type of relaxation is energetically driven. In other words, the spin system returns to thermal equilibrium as given by the *Boltzmann distribution* (Equation 7) by longitudinal relaxation with T_1 . Applying a pulse sequences several times in a row, the signal intensity can suffer from saturation effects, so that T_1 determines the possible repetition frequency (i.e. *shot repetition time*) of the respective measurement.

But also the magnetization in the xy -plane decays exponentially by entropically driven spontaneous alterations of the *Lamor frequency* of individual spins, described by the relaxation time T_2 . Additionally, local field inhomogeneities trigger varying *Lamor frequencies* among the individual spins and contribute to a dephasing of the spins in the xy -plane described by T_{2i} . Both contributions can hardly be disentangled experimentally and thus, the so-called phase memory time T_M is defined according to Equation 16:

$$M_{xy} = M_{xy,0} e^{-\frac{t}{T_M}} \text{ with } \frac{1}{T_M} = \frac{1}{T_2} + \frac{1}{T_{2i}} \quad (16)$$

The magnitude of T_M determines the time window in which a time trace (Figure 14a) can be recorded. The longer the distances of interest are, the longer is the modulation period resembled in the time trace, such that the precise determination of longer distances require a longer time trace and thus sufficient T_M times.

2. Aim of the Work

2.1 Trityl Radicals

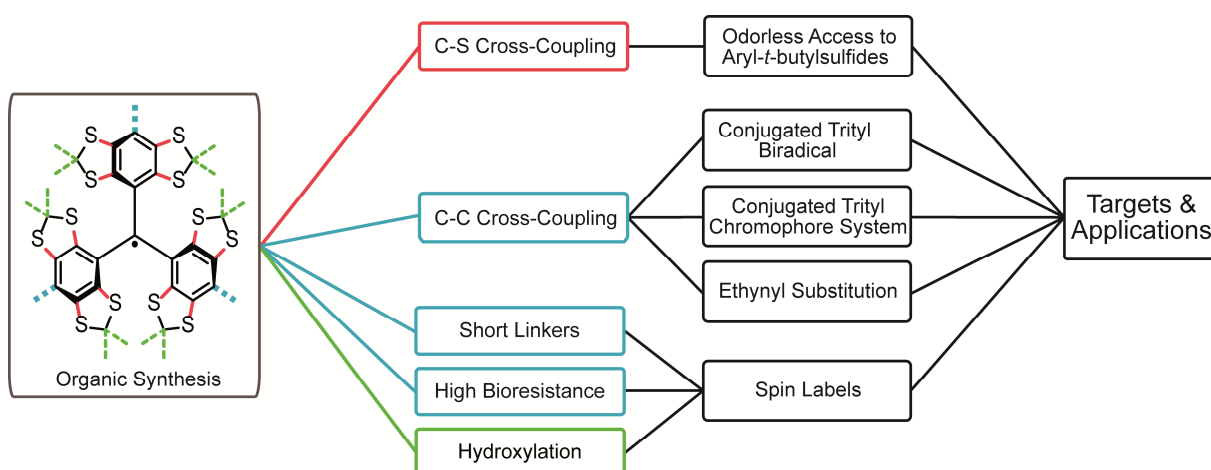


Figure 16: Aims of the work in the context of trityl radicals summarized in a mindmap. The color of the boxes on the left side correspond to the respective site of chemical modification as indicated in the structure for a generic trityl radical.

As noted beforehand, the limited synthetic methodology targeting the functionalization of TAM-radicals misfits the wide application perspective clearly. Therefore, the aim of this thesis is to expand the chemical diversity of such trityl radicals. By advancing their synthesis, current limitations regarding their application, are addressed. As shown in Figure 16, the anticipated work is located between organic synthesis and the (physicochemical) application perspectives of the resulting compounds. Though the focus lies on the synthetic site, the possible advancements on the application site will be explored as well – at least on the level of a proof-of-concept. Hence, the work will not be limited to synthesis exclusively, as EPR-spectroscopic or biology-related data will be acquired as well.

As the bias to esters and amides of **11**[•] is apparent within the literature, the first goal is to develop an alternative, yet more versatile, option for functionalization. In that respect, palladium catalyzed C-C cross-coupling reactions shall be taken into account. Awarded with the Nobel Prize in 2010, these transformations appear well-established and allow for a large chemical diversity of products.^[294] Additionally, they provide access to π -conjugated scaffolds, which are of high interest for applications in the context of magnetic materials (section 1.2.2). In pursuit of this idea, a halogenated trityl radical and alcohol are sought for, serving as a platform to conduct C-C cross-coupling chemistry. Beyond studying the demands and peculiarities of these transformations on trityl radicals and alcohols, target molecules will be synthesized employing the developed methodology. With respect to prospective spin labels, these targets will include an ethynyl-functionalized TAM-radical giving rise to bioconjugation via click-chemistry. As for material applications, a conjugated biradical as well as a chromophore-radical conjugate will be of interest, which will allow to assess the effect of π -conjugation on spin exchange coupling.

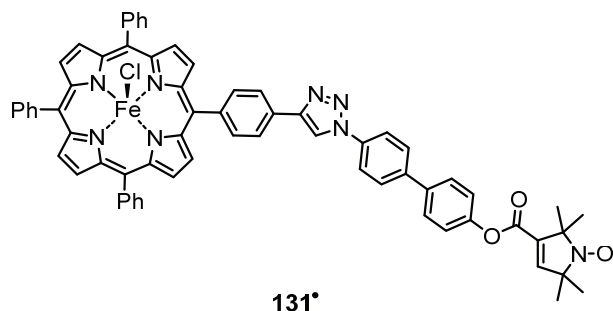
Moreover, the use of ester- and amide-based linkages to construct spin labels implies the generation of unnecessarily long linkers to the biomolecules. As outlined beforehand, a major drawback of such spin labels are the resulting undesirably broad distance distributions. Additionally, esters and amides are electron-withdrawing groups (EWGs), which stabilize a trityl anion resulting from bioreduction, clearly evident from the redox potentials presented in Table 1. Hence, another aim of this work is the development of improved spin labels to cope with these issues. Since the bioconjugation to cysteines via maleimides proved to be selective and reliable (cf. **110**[•], **113**[•], **114**[•]), the first target will be a maleimide-based trityl spin label with a simple benzylic methylene group serving as a short linker. Concomitantly, such a methylene unit would not act as an EWG, so that an improved bioresistance is expected from such a molecular architecture.

In the next step, another intrinsic disadvantage of spin labels based on the platform of **11**[•] will be addressed, which is their propensity to aggregate with biomolecules in a non-specific fashion through hydrophobic interactions. Taking advantage of the aforementioned efforts targeting a short-linked, maleimide-based trityl spin label, the synthetic strategy will be transferred to a hydroxylated trityl platform, such as **52**[•]. This will lead to a highly hydrophilic trityl spin label, which is expected not to aggregate with proteins.

Beyond the focus on targets, also the accessibility of trityl radicals in general shall be improved. A key precursor for all kind of TAM-radicals is 1,2,4,5-tetrakis-(*tert*-butylthio)benzene **16**, which is regularly obtained by S_NAr chemistry from 1,2,4,5-tetrachlorobenzene. This chemistry does not only require harsh conditions giving a rather low yield, but also the excessive use of *tert*-butylthiol, a highly malodorous compound, which can hardly be handled in a typical academic laboratory without special precautions. Therefore, another goal of this work is to find an alternative, preferably odorless, access to

the important intermediate **16**. For this, the use of palladium catalyzed *Migita*-like C-S cross-coupling^[295] is anticipated, with the thiolate nucleophile generated in-situ from a suitable surrogate.

2.2 Model Compounds Containing Fe³⁺-Centers



Scheme 49: Structure of model compound **131[•]**.

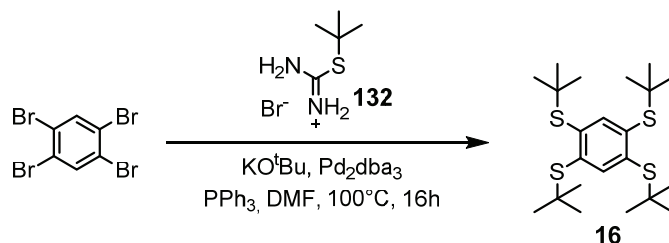
In addition to the focus on trityl radicals, also certain model systems will be of interest for this thesis. While distance measurements involving metals such as Cu²⁺, Mn²⁺, and Gd³⁺ are carried out routinely, application of this methodology to Fe³⁺ is challenging. This is not only due to the high *g*-anisotropy, but also due to short relaxation times, especially in the case of *high-spin* iron(III). Therefore, model systems containing an Fe³⁺-center bridged to a nitroxide and a trityl radical shall be synthesized and characterized. The defined geometric arrangement between the Fe³⁺-center and the stable radical will allow for thorough validation of the EPR-methodology to measure the distances between them. Focus will also lie on the adjustment of the spin states, i.e., switching between *low*- and *high-spin* Fe³⁺. Taking advantage of preceding work,^[296] **131[•]** will be synthesized. Here, a porphyrin is used as the ligand system to accommodate the iron(III)-center, while a rigid biphenyl spacer attached via click-chemistry allows to connect the stable radical, a nitroxide in the case of **131[•]**, to the system. Beyond a thorough characterization of **131[•]**, the synthesis of an analogous compound with the nitroxide exchanged for a trityl radical will be of interest.

3. Results and Discussion

3.1 Trityl Radicals

3.1.1 Odorless Access to *tert*-Butylarylsulfides via Pd-catalyzed C-S Cross-Coupling

The results of this project have been published in *Molecules* prior to submission of this thesis. The original article alongside the Supporting Information is provided in Appendix A1.



Scheme 50: Synthesis of **16** via Pd-catalyzed C-S cross-coupling.

Benzo[1,2-d;4,5-d']bis[1,3]dithioles are integral building blocks for trityl radicals as presented in section 1.3.1 and beyond that also of interest for the construction of fluorescent dyes^[297] and conjugated polymers.^[44] As shown in Scheme 9, access to these thioketals is commonly achieved via 1,2,4,5-tetrakis(*tert*-butylthio)-benzene **16** serving as a convenient surrogate for the highly air-sensitive 1,2,4,5-benzenetetrathiol. However, the regular synthesis of **16** involves harsh conditions, excessive use of extremely malodorous *tert*-butylthiol, and ultimately gives rather low yields (cf. section 1.1.1.2).

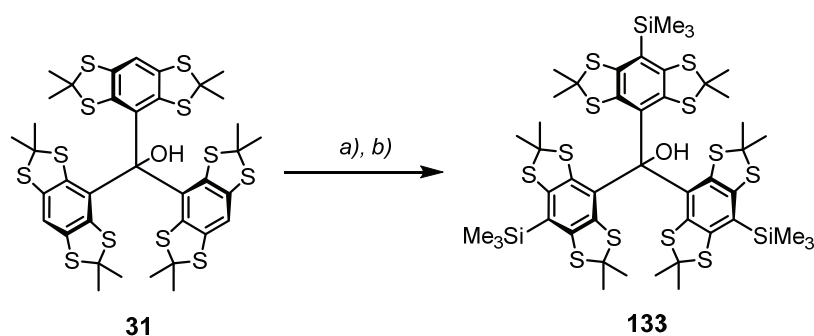
Taking advantage of palladium catalyzed carbon-heteroatom cross-coupling reactions,^[298] a *Migita*-type^[295] C-S coupling reaction was considered as a needed alternative to replace the cumbersome S_NAr-chemistry used beforehand. To circumvent the usage of neat *tert*-butylthiol, the required thiol was generated *in situ* from a previously synthesized *tert*-butyl isothiuronium salt **132**. These salts, easily available from thiourea and the respective alkyl bromide, are known to hydrolyze in aqueous media to give the corresponding thiol. This concept has been employed for the “odorless” synthesis of *tert*-butylarylsulfides of electron-poor heterocycles by S_NAr-reactions.^[299,300] Though a previous study exploited the in-situ formation of alkylthiols from alkyl bromides and thiourea via isothiuronium salts for C-S cross-coupling reactions in aqueous media,^[301] yields stalled for tertiary substrates, presumably due to competitive elimination reactions. Following a very early report on the formation of thiolates upon treatment of isothiuronium salts with bases in non-aqueous media,^[302] the suitability as thiol surrogates within the synthesis of **16** via a C-S cross-coupling process was studied in this project.

For an initial assessment of reactivity, 4-bromoanisole was used as a model-substrate to obtain the corresponding *tert*-butylthioether by treatment with *tert*-butyl isothiuronium bromide and KO^tBu in DMF in the presence of a Pd⁰-catalyst. Various phosphine ligands were screened and notably, simple PPh₃ enabled a quantitative conversion under the chosen conditions. Though rather bulky monophosphine ligands^[303,304] including XPhos,^[301] or

bidentate ligands such as XantPhos^[305] performed well in previous work focusing on primary alkylthiols, these exhibited inferior reactivity in the present case involving a tertiary thiolate. Additionally, milder bases such as K_3PO_4 , Cs_2CO_3 , or K_2CO_3 led to lower yields compared to KO^tBu . More interestingly, the addition of 18-crown-6 depleted the reactivity entirely in the case of K_2CO_3 and K_3PO_4 . This led to the assumption, that the rate-determining step is the nucleophilic displacement of bromide by the *tert*-butylthiolate at the intermediately occurring Pd^{II} -center. Accordingly, bulky phosphine ligands hamper this step explaining the low conversion rates observed with these. Moreover, this step is expected to be accelerated by the low solubility of resulting KBr in DMF, which is adversely influenced by the addition of the crown-ether. Ultimately, a procedure for the synthesis of **16** from 1,2,4,5-tetrabromobenzene was developed using the results obtained for the model reaction with 4-bromoanisole. The transformation is odorless and gives yields of 88 % of **16** on a 10 g scale, while the product is isolated by simple filtration (Scheme 50).

3.1.2 Synthesis and Crystal Structure of a Silylated Trityl Alcohol

The results of this project have been published in *Acta Crystallographica E* prior to submission of this thesis. The original article alongside the Supporting Information is provided in Appendix A2.



Scheme 51: Synthesis of silylated trityl alcohol **31**. a) $n\text{-BuLi}$, TMEDA, Et_2O , r.t., 2h. b) Me_3SiCl , r.t., 16 h, 67 % over two steps.

Trityl alcohol **133** was obtained by silylation of **31**, as shown in Scheme 51. Since the β -effect of silicon can be exploited for further electrophilic functionalization, **133** is an important precursor for the synthesis of e.g. halogenated trityl alcohols (cf. section 3.1.3). Single crystals of $\mathbf{133}\cdot\text{Et}_2\text{O}$ were obtained by slow evaporation of an etheric solution and subjected to X-ray diffraction yielding the crystal structure shown in Figure 17. Notably, the structure deviates from the expected C_3 -symmetry as the dihedral angles between the three aryl-planes are inequivalent ($\pm 73.7^\circ$, $\pm 73.7^\circ$, $\pm 70.2^\circ$). Given the bond angles of 112.2° , 113.5° , and 114.0° at the central carbon atom, its geometric arrangement appears rather trigonal planar than tetrahedral. These observations can be attributed to the presence of the hydroxyl-group

imposing additional steric congestion to the already crowded structure of **133**·Et₂O, leading to the aforementioned distortion.

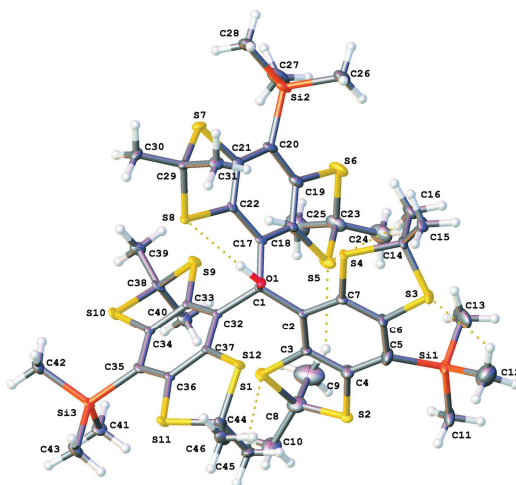
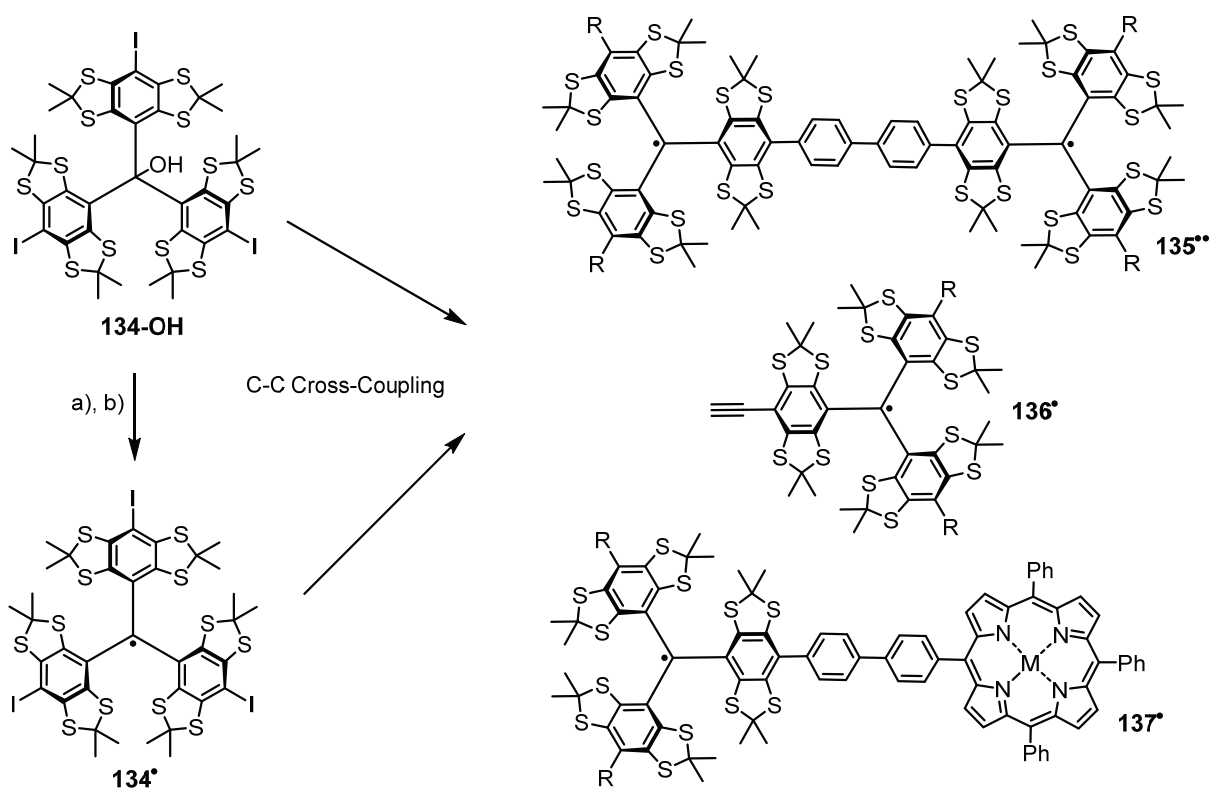


Figure 17: Crystal structure of **133**·Et₂O. Solvent molecules (Et₂O) were omitted for the sake of clarity, hydrogen bonds are indicated by dashed yellow lines. Only one of the enantiomers is shown, the racemic compound crystallizes in space group $P\bar{1}$. Ellipsoids are drawn at a probability level of 50 %.

3.1.3 C-C Cross-Coupling Reactions of Trityl Radicals



Scheme 52: Synthesis of π -conjugated trityl radical systems via palladium catalyzed C-C Cross Coupling reactions. a) BF₃·Et₂O, CH₂Cl₂, r.t., 1h. b) SnCl₂, THF, r.t., 15 min, 92 % over two steps. R = 4-CO₂Me-Ph, M = 2H or Zn.

The results of this project have been published in *The Journal of Organic Chemistry* prior to submission of this thesis. The original article alongside the Supporting Information is provided in Appendix A3.

Seeking for functionalization methods beyond carboxylation (cf. chapter 2.1), trityl alcohol **134-OH**, obtained from **133** by *ipso*-iododesilylation, was introduced to enable palladium catalyzed C-C cross coupling reactions of trityl radicals (Scheme 52). Subsequently, **134•** was accessed from **134-OH** and the performance of *Suzuki-Miyaura* and *Sonogashira-Hagihara* reactions was examined both on the trityl alcohol (e.g., **134-OH**) and the radical (e.g., **134•**) stage. While the *Suzuki-Miyaura* couplings performed well, a competitive carbothiolation^[306] involving an insertion of alkyne into the trityl backbone was observed for *Sonogashira-Hagihara* coupling reactions. However, this side reaction could be restrained using bulky alkynes and proper conditions. Ultimately, the C-C-cross coupling methodology was utilized to obtain the π -conjugated entities **135••** - **137•**. Compared to the similar biradical **103••**, **135••** features an exchange coupling constant increased by a factor of ≈ 1100 , owing to the extended π -conjugation. Exploiting a *Sonogashira-Hagihara* coupling with TIPS-acetylene, followed by deprotection, ethynyl trityl radical **136•** was obtained. The short-linked alkyne moiety renders **136•** interesting for the use as a spin label with unnatural amino acids (UAAs). Finally, a trityl-porphyrin (**137•**) conjugate was synthesized. Here, the insertion of metals into the porphyrin ligand allows to control the physicochemical properties of this trityl-chromophore conjugate (cf. section 3.1.4). Enroute to **135••** - **137•**, valuable building blocks were obtained and characterized, which allow for synthesis of π -conjugated trityl radical arrays in a modular fashion. Notably, due to spin-orbit coupling, the *g*-values of the obtained trityl radicals increased with the degree of iodination, giving rise to future studies on *g*-engineered radical systems.

3.1.4 Trityl-Porphyrin Conjugates: Exchange Coupling in Photogenerated Multi-Spin Systems

The results of this project have been published in *Chemistry – A European Journal* prior to submission of this thesis. The original article alongside the Supporting Information is provided in Appendix A4.

Covalently linked chromophore-radical systems allow for photogeneration of organic multi-spin systems, the properties of which are governed by exchange-coupling of the stable radical doublet to the photogenerated spin state of the organic dye. The high versatility of such systems facilitated a widespread application ranging from spin catalysis^[307] to information technology.^[308] The rational design of such radical-chromophore systems requires several considerations. First, efficient synthetic access to both the chromophore and the stable radical unit with proper functionalization is required. Since the chemistry of nitroxides and porphyrins is well-developed, most systems were based on these two entities. By contrast to

the former, trityl radicals of the TAM-type allow for construction of π -conjugated arrays such as **137[•]**, the excited state dynamics of which was studied in this project.

As shown in Figure 18, initial photoexcitation of the chromophore, a (metallo)porphyrin in the case of **137[•]**, yields an excited singlet chromophore ($^1C-^2R$). Mediated by the exchange coupling to the stable radical doublet, a triplet state chromophore ($^3C-^2R$) can be generated via enhanced intersystem crossing (EISC) and higher spin states such as a quartet are accessible from this intermediate state as well.

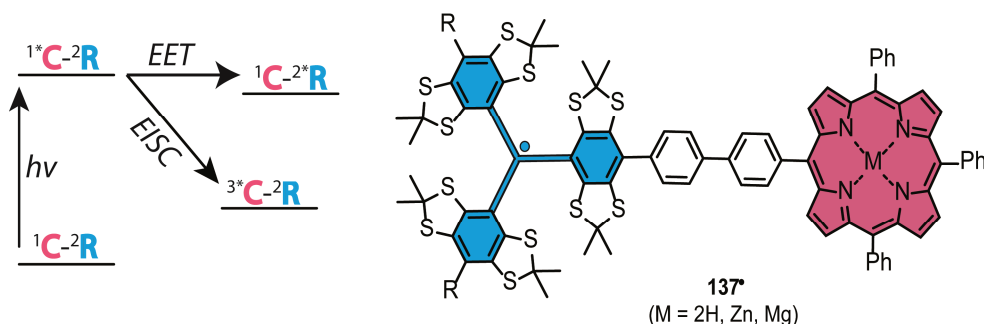
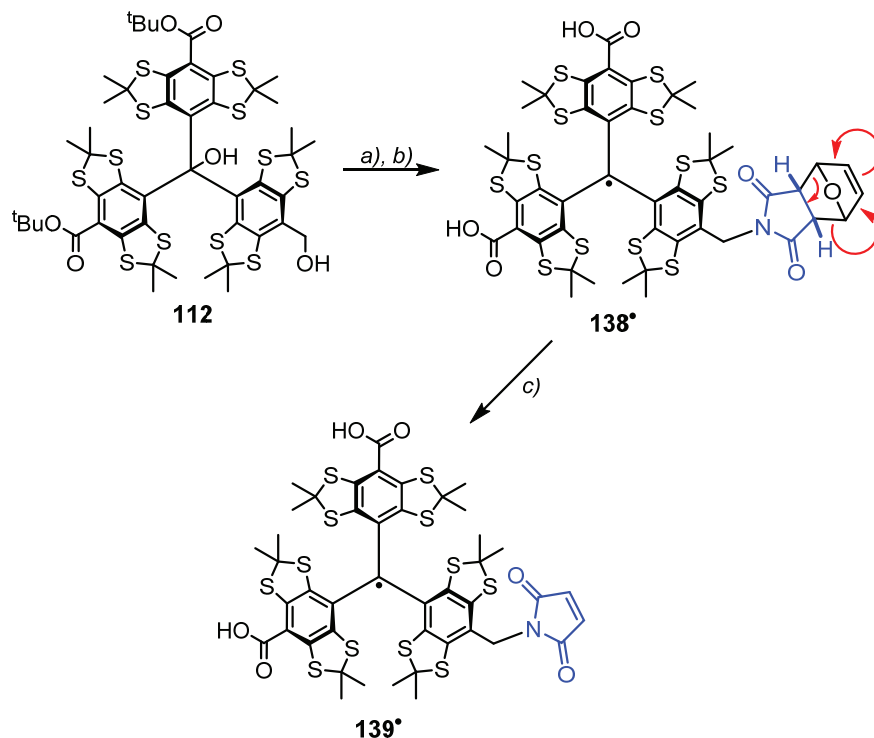


Figure 18: Chromophore-Trityl systems as models to study the effect of exchange-coupling in photogenerated multi-spin systems. R = 4-CO₂Me-Ph.

Using **137[•]**, the spin dynamics upon photoexcitation was studied by means of femtosecond transient absorption spectroscopy (fs-TA) and time-resolved EPR (TREPR). Indeed, the sensitivity of cw-EPR was sufficient to detect the formation of a quartet state after photoexcitation of **137[•]** and a quantum yield of $\approx 5\%$ was assigned to this process. Beyond this EISC-based pathway, excitation energy transfer (EET) was observed with a quantum yield of $\approx 95\%$. Here, the energetic accessibility of an excited state of the radical doublet triggers *Förster-type* energy transfer diminishing the triplet yield. Though metalation of the porphyrin entity allows to alter the triplet polarization pattern, analogous results were obtained for the free-base, magnesium-, and zinc-derivative of **137[•]**. Moreover, these compounds feature an increased propensity for oxidative degradation compared to simple doublet trityl radicals. Altogether, this project provided a proof-of-concept that TAM-type trityl radicals are suitable building blocks for chromophore-radical systems and provides an understanding of the applicable spin-dynamics. However, the low EISC-rate is a major drawback of compounds as **137[•]**, so that future studies might address this issue by altering the chromophore unit.

3.1.5 SLIM: A Bioresistant and Short-Linked Trityl Spin Label

The results of this project have been published in *Angewandte Chemie* and *Angewandte Chemie – International Edition* prior to submission of this thesis. The original article alongside the Supporting Information is provided in Appendix A5.



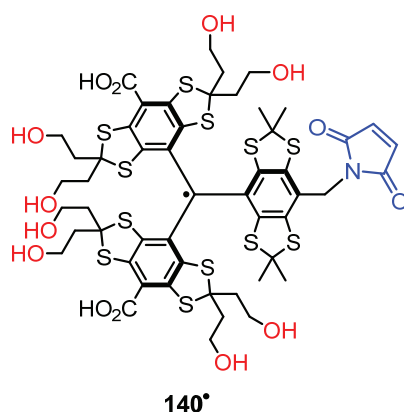
Scheme 53: Synthesis of the SLIM spin label **139*** through a mild *Mitsunobu/Retro-Diels-Alder* sequence. a) *endo*-4,7-epoxy-3,3a,7,7a-tetrahydro-2H-isoindoli-1,3-dione, Ph_3P , DEAD, THF, 0°C , 30 min, 70 %. b) 1) CF_3COOH , CH_2Cl_2 , r.t., 2h; 2) SnCl_2 , THF, 20 min, 95 %. c) CH_3CN , 60°C , 24 h.

As outlined in chapter 2.1, the construction of trityl spin labels from esters/amides of the Finland Trityl **11*** comes along with long linkers resulting in broad, yet insignificant, distance distributions, an issue addressed in this project. For that, a maleimide concealed as the *Diels-Alder* adduct with furane was attached to the benzylic position of a trityl alcohol via a *Mitsunobu*-reaction. After radical generation and concomitant cleavage of the *tert*-butyl esters, trityl radical **138*** was obtained. The thermal lability of its *endo*-tetrahydroisoindolindion-unit allowed unmasking the maleimide moiety through a *Retro-Diels-Alder* fragmentation at 60°C giving **139*** (Scheme 53). Notably, the benzylic imidomethylene-substituent of the resulting short-linked maleimide (“SLIM”) spin-label **139*** does not act as an EWG. Accordingly, the reduction potential of **139*** is lowered by 46 mV compared to **11***, endowing it with an outstanding resistance to cellular reductants. Exploiting the selective Michael-addition of cystein-residues to the maleimide biolinker, a doubly-labelled mutant of Yersinia Outer Protein O (YopO), crucial for the pathogenicity of *Yersinia* bacteria, was synthesized with a labelling efficiency exceeding 94 %. Subsequently, EPR-based distance measurements were performed both *in-vitro* and *in-cell*, after microinjection of the labelled protein construct into oocytes of *Xenopus laevis*. The resulting

data revealed a conformational change of the protein upon entering the cytosol. This underlines the importance of conducting structural studies on biomolecules under the most native conditions, meaning within intact cells. Given its reduction resistance, the novel spin label SLIM (**139**[•]) allows for such measurements to be carried out with high sensitivity.

3.1.6 OxSLIM: Synthesis and Evaluation of a Highly Hydrophilic Trityl Spin Label

The results of this project have been published in *Chemistry – A European Journal* prior to submission of this thesis. The original article alongside the Supporting Information is provided in Appendix A6.



Scheme 54: Structure of Ox-SLIM **140**[•], a highly hydrophilic trityl spin label.

Another major drawback of conventional trityl spin labels was their propensity to aggregate with biomolecules through hydrophobic interactions, giving rise to unspecific labelling (cf. section 1.2.3.4). Even though the hydrophilic trityl radicals **118**[•] and **119**[•] were used successfully as spin labels, their design is rather conservative, bearing a long ester/amide-based linker. Taking advantage of previous results (cf. section 3.1.5), a hydroxylated trityl spin label with a **short-linked maleimide**, given the acronym Ox-SLIM (**140**[•]), was introduced in this project.

Synthetically, **140**[•] was approached in a modular fashion utilizing an improved *Mitsunobu/Retro-Diels-Alder* sequence. The hydroxyl-groups were initially protected as *tert*-butyl ethers and later as formate esters, to enable mild hydrolysis without endangering the concealed maleimide in the final steps of the synthesis. In analogy to **139**[•] (SLIM), Ox-SLIM **140**[•] exhibits a high bioresistancy. However, by contrast, it does not suffer from unspecific aggregation with proteins. Nonetheless, highly efficient spin labelling via cysteines was viable as proven for *Yersinia* Outer Protein O (YopO) and EPR-based distance measurements on this mutant were consistent with the results obtained with other spin labels beforehand (section 3.1.5).

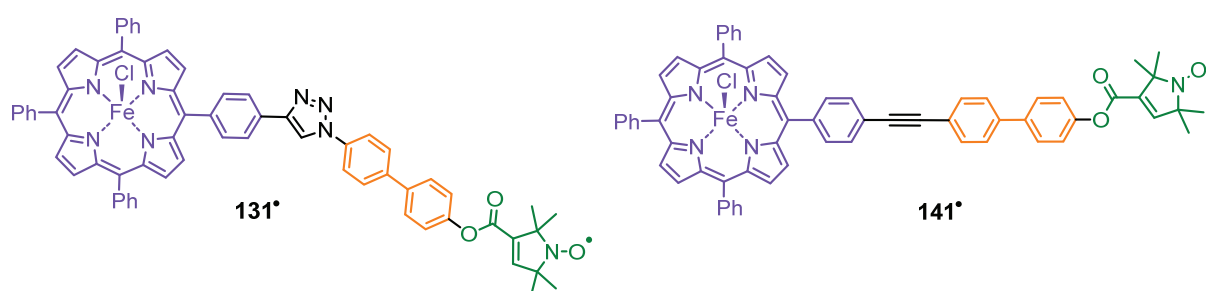
Ultimately, the advantageous T_M -relaxation behavior of **140**[•] was exploited to conduct ultra-sensitive EPR-based distance measurements with protein concentrations as low as 45 nM, setting up a new benchmark.

In summary, **140**[•] unites the recent advances regarding trityl spin labels in a single molecule, rendering it highly promising for future studies beyond the proof-of-concept provided here.

3.2. Iron(III) Model Compounds for EPR-based distance measurements

3.2.1 Synthesis and Characterization of Iron(III)-nitroxide Model Compounds

The results of this project have been published in *Chemistry – A European Journal* prior to submission of this thesis. The original article alongside the Supporting Information is provided in Appendix A7.



Scheme 55: Structures of iron(III)-spacer-nitroxide model compounds **131**[•] and **141**[•]. For the sake of clarity, the porphyrin unit is highlighted in purple, the biphenyl spacer in orange, and the nitroxide unit in green.

As described in section 2.2, proper model compounds were required to advance EPR-based distance measurements involving iron(III)-centers. While previous studies targeted the synthesis of **131**[•]^[296] and **141**[•],^[309] the samples obtained from these were partly impure and distance measurements were not viable. Therefore, this project aimed at the synthesis of sufficient quantities of **131**[•] and **141**^{•xxi} for thorough characterization and their following subsection to EPR-based distance measurements. Both systems (cf. Scheme 55) are constructed from a tetraphenylporphyrin building block, which a biphenyl linker with an adjacent nitroxide is attached to. While **141**[•] features a linear ethynyl connection between the porphyrin and the bridge, **131**[•] appears angled with a triazole bridging the biphenyl and the porphyrin. A peculiarity of iron(III)-porphyrins, which had not been considered initially,^[296,309] is their capability to form μ_2 -oxo bridged supramolecular complexes,^[310–312] illustrated in Figure 19.

Despite their size, such a μ_2 -oxo dimerization was also observed for **131**[•] and **141**[•], and a quantitative conversion to the desired species was achieved by acid- or base-treatment (cf. Figure 19), proven by MALDI(+)-MS. The color change upon dimerization allowed for their detection via UV-Vis spectroscopy.^[313]

Additionally, a strong antiferromagnetic exchange interaction between the iron(III)-centers within the dimer renders them EPR-silent,^[312] an issue the failure of the initial RIDME-

^{xxi} The synthesis of **135**[•] was performed by Dr. Christoph Klein in the group of Prof. Dr. Arne Lützen at the University of Bonn. Both are coauthors of the respective publication.

experiments^[296,309] was attributed to. However, the presence of a nitroxide radical in each monomeric unit enabled to perform nitroxide-nitroxide distance measurements using the PELDOR-technique. As shown in Figure 18b, the twisting of the porphyrin planes in the μ_2 -oxo dimers results in various torsion angles α and thus a multitude of internitroxide-distances. Combining distance information obtained via PELDOR with MD simulations, the molecular dynamics of **(131[•])₂O** and **(141[•])₂O** in frozen solution could be investigated. It was found that α is not distributed equally between 0° and 180° , as two distinct twisting ranges (30° - 60° and 125° - 145°) are encountered, between which a scissor-like motion is assumed. Metaphorically speaking, the μ_2 -oxo dimers **(131[•])₂O** and **(141[•])₂O** resemble a step motor. Ultimately, the thorough characterization of **131[•]** and **141[•]** during this project had immediate implications for subsequent studies on iron-nitroxide/trityl distance measurements (cf. section 3.2.2).

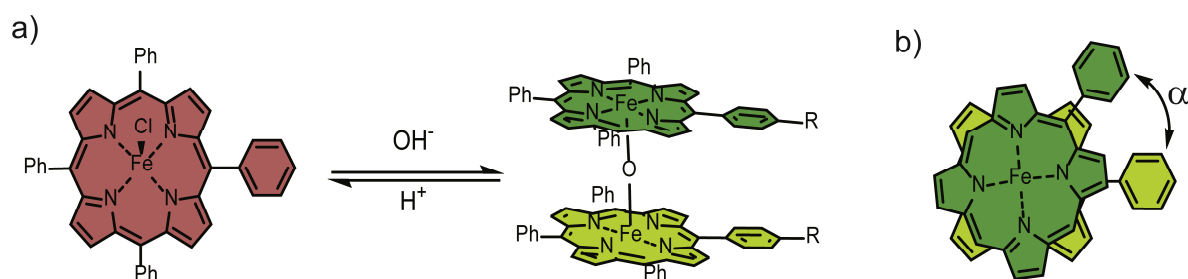
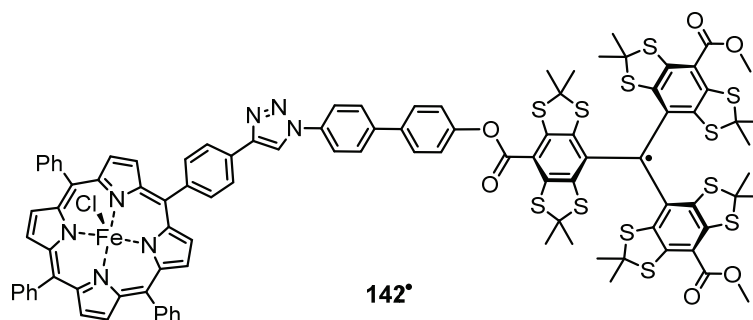


Figure 19: a) μ_2 -oxo dimerization of iron(III)-porphyrins. b) top-view of the μ_2 -oxo complex with indication of the twisting angle α between the porphyrin planes. The color-code was chosen according to the appearance of the compounds in solution.

3.2.2 EPR Based Distance Measurements Involving Fe(III)-Centers

The results of this project have been published in *Chemistry – A European Journal* prior to submission of this thesis. The original articles alongside their Supporting Information are provided in Appendices A8 and A9.



Scheme 56: An iron(III)-spacer-trityl model compound.

Taking advantage of the aforementioned results presented in section 3.2.1, pure and “monomeric” samples of **131[•]** and **141[•]** could be prepared. The aim of this project was then,

to establish a methodology for EPR-based distance measurements to iron(III)-spin centers, both for the *high*- and the *low*-spin case.

Coordinated by chloride, the iron center in **131**[•] and **141**[•] occurs in its *high*-spin configuration. A high *g*-anisotropy and fast electron spin relaxation coming along with this presented a crucial challenge for EPR-based distance measurements. While cryogenic temperatures (3.8 K) enabled to cope with the former issue, the zero-field-splitting (ZFS) of the *high-spin* iron center required a proper theoretical description. In brief, the dipolar coupling frequency becomes additionally dependent from the angle of the effective *g*-tensor of the iron atom and the distance vector to the nitroxide, called ζ .^{xxii} Including these findings into the data analysis, precise distance measurements between a nitroxide radical and a high-spin iron(III)-center in **131**[•], **141**[•], and a spin-labelled myoglobin construct became viable.^{xxiii} Moreover, distance measurements involving *low-spin* iron(III)-centers were explored and in the course of these studies, compound **142**[•], a trityl analog of **131**[•] was synthesized (Scheme 56). By addition of a π -accepting ligand, in this case imidazole, the iron(III)-center in **131**[•], **141**[•], and **142**[•] could be switched into its low-spin configuration. Adapting the achievements made for the *high-spin* case previously, highly precise distance measurements between nitroxide/trityl radicals and low-spin iron(III)-centers were enabled.

^{xxii} This does only apply assuming an effective axial *g*-tensor of the iron(III)-center, meaning $g'_{xx} = g'_{yy}$, which holds true in the present case.

^{xxiii} It should be noted that the data concerning compound **131**[•] has been excluded from the corresponding publication (Appendix A9) for the sake of conciseness.

4. Summary and Outlook

Through the work related to this thesis, several advances regarding the synthesis and development of trityl radicals have been achieved.

The synthesis of **16** via the C-S cross-coupling process described in section 3.1.1 provided a needed alternative to the conventional route via S_NAr chemistry. This accounts especially with respect to the lacking commercial availability of **16** in sufficient quantities. The fact that benzo[1,2d;4,5d']bis[1,3]dithiols are not exclusively used as building blocks for trityl radicals, but also for fluorescent dyes^[314] or polymers^[315], highlights the value of this synthetic access additionally.

With the implementation of C-C cross coupling reactions (section 3.1.3), conjugated systems consisting of TAM-radicals could be obtained for the first time. Beyond the introduction of building blocks for a modular synthesis of such systems, also a terminal acetylene-function was immediately attached to a TAM-radical. However, the free alkyne **136**[•] appeared quite unstable towards atmospheric conditions, which might explain, why a concurrently published study^[316] did not report on the isolation of such a compound. Another finding was that g-values of the trityl radicals can be controlled via the extent of iodination. This provides the future capability to synthesize g-engineered trityl multiradicals for prospective studies regarding quantum information processing.

Further, the use of the developed cross-coupling methodology allowed to construct trityl-porphyrin systems, which were subsequently studied with respect to the formation of multi-spin systems after photoexcitation (section 3.1.4). Though a quartet state could be observed by cw-EPR, the low quantum yield for its formation presents a crucial drawback. Therefore, alternative systems might be synthesized in future studies. This could include the use of perylendiimide (PDI)-based chromophores, since these exhibit a) lower intrinsic ISC-rates and b) have the potential to cope with the issue of excited energy transfer.

The two novel spin labels **139**[•] (SLIM) and Ox-SLIM **140**[•] presented in sections 3.1.5 and 3.1.6 display major advances compared to previous trityl spin labels. Their reduction resistance is outstanding, their short linkers give rise to narrow distance distributions, and in the case of **140**[•], non-specific interactions with proteins could be restrained efficiently. From a synthetic perspective, the applied *Mitsunobu/Retro-Diels-Alder* sequence allowed for an elegant introduction of the maleimide moiety. Moreover, the synthetic studies carried out to obtain **140**[•] contributed to a general improvement of the synthesis of hydrophilic trityl radicals, as many useful building blocks were obtained on the way. These will be useful in future studies aiming at the synthesis of hydrophilic trityl radicals for applications beyond spin labelling. However, it should be noted that the synthetic effort to obtain **140**[•] was rather high, though a spin label with excellent performance resulted. A very recent report^[83] introduced the sulfonated **d³⁶-50**[•], which showed significantly less non-specific aggregation to bovine serum albumin (BSA) than **11**[•]. These findings might be exploited in future studies

to obtain spin labels derived from **50**. Despite the success of maleimides for bioconjugation via cysteines, covalent unspecific labelling was encountered to a marginal extent during the studies on Yersinia Outer Protein YopO. This can likely be attributed to the minor reactivity of maleimides towards lysines,^[317] 38 of which are present in the studied YopO mutant. Therefore, other bioconjugation groups, such as iodoacetamides, might be used to construct short-linked trityl spin labels.

Concerning the iron(III)-model compounds presented in chapter 3.2, EPR-based distance measurements involving both *low*- and *high-spin* iron(III)-centers were enabled. These results highlight how research in the field of spectroscopy can profit from inclusion of organic synthesis in an interdisciplinary manner.

5. References

5.1 Abbreviations

μ_B	Bohr magneton ($\mu_B = 9.274 \cdot 10^{-24} \text{ J T}^{-1}$)
BDPA	α,γ -bis(diphenyl)- β -phenylallyl
BOP	benzotriazol-1-yloxytris(dimethylamino)phosphonium hexafluorophosphate
BOP-Cl	bis(2-oxo-3-oxazolidinyl)phosphinic chloride
CDI	carbonyldiimidazol
cryo-EM	cryogenic electron microscopy
cw-EPR	continuous wave electron paramagnetic resonance
DNP	dynamic nuclear polarization
DPPH	N,N-diphenyl-N'-picrylhydrazide
DQC	double quantum coherence
e	elementary charge ($e = 1.602 \cdot 10^{-19} \text{ C}$)
EDC	1-ethyl-3-(3-dimethylaminopropyl)carbodiimid
EDG	electron donating group
EISC	enhanced intersystem crossing
EPR	electron paramagnetic resonance
EWG	electron withdrawing group
FRET	Förster resonance energy transfer
g_e	g-factor of the free electron ($g_e = 2.002319304\dots$)
\hbar	reduced Planck constant ($\hbar = 1.054 \cdot 10^{-19} \text{ J s}$)
HBTU	hexafluorophosphate benzotriazole tetramethyl uronium
HEK-cells	human embryonal kidney cells
HOBT	hydroxybenzotriazole
HPLC	high performance liquid chromatography
ISC	intersystem crossing
J	exchange coupling constant
k _B	Boltzmann constant ($k_B = 1.38 \cdot 10^{-23} \text{ J K}^{-1}$)
MAS	magic angle spinning
mCPBA	3-chloroperoxybenzoic acid
m_e	electron mass ($m_e = 9.109 \cdot 10^{-31} \text{ kg}$)
m_s	magnetic quantum number
MS	mass spectrometry
NMR	nuclear magnetic resonance
PDB	Protein Data Bank (accessible via www.rcsb.org)
PDI	perylene diimide
PEG	polyethylenglycol
PELDOR	pulsed electron electron double resonance
QC	quantum computing

5. References

QIP	quantum information processing
SLIM	short-linked maleimide
SOMO	singly occupied molecular orbital
T	temperature
t	time
TAM-radical	tetrathiotriarylmethyl radical
TEMPO	2,2,6,6-tetramethylpiperidinoxyl
TIPS	triisopropylsilyl
TMP	2,2,6,6-tetramethylpiperidine
TREPR	time-resolved electron paramagnetic resonance
χ	magnetic susceptibility

5.2 Literature

- (1) Gomberg, M., *J. Am. Chem. Soc.* **1900**, *22*, 757–771.
- (2) Gomberg, M., *Ber. Dtsch. Chem. Ges.* **1900**, *33*, 3150–3163.
- (3) Colle, T. H.; Glaspie, P. S.; Lewis, E. S., *J. Org. Chem.* **1978**, *43*, 2722–2725.
- (4) Schlenk, W.; Weickel, T.; Herzenstein, A., *Liebigs Ann. Chem.* **1910**, *372*, 1–20.
- (5) Tidwell, T. T., *Angew. Chem. Int. Ed.* **2001**, *40*, 331–337.
- (6) Pauling, L.; Wheland, G. W., *J. Chem. Phys.* **1933**, *1*, 362–374.
- (7) Maki, A. H.; Allendoerfer, R. D.; Danner, J. C.; Keys, R. T., *J. Am. Chem. Soc.* **1968**, *90*, 4225–4231.
- (8) Kahr, B.; Jackson, J. E.; Ward, D. L.; Jang, S. H.; Blount, J. F., *Acta Cryst. B* **1992**, *48*, 324–329.
- (9) Schreiner, K.; Berndt, A., *Angew. Chem. Int. Ed.* **1974**, *13*, 144–145.
- (10) Hicks, R. G., *Stable Radicals*; Wiley-VCH Verlag GmbH: Weinheim, **2010**.
- (11) Griller, D.; Ingold, K. U., *Acc. Chem. Res.* **1976**, *9*, 13–19.
- (12) IUPAC, *Compend. Chem. Terminol.* **2019**, <https://doi.org/10.1351/goldbook>.
- (13) Guasch, J.; Fontrodona, X.; Ratera, I.; Rovira, C.; Veciana, J., *Acta Cryst. C* **2013**, *69*, 255–257.
- (14) Veciana, J.; Crespo, M. I., *Angew. Chem. Int. Ed.* **1991**, *30*, 74–76.
- (15) Ballester, M.; Riera, J.; Castañer, J.; Badía, C.; Monsó, J. M., *J. Am. Chem. Soc.* **1971**, *93*, 2215–2225.
- (16) Ballester, M.; Castañer, J.; Riera, J.; Ibáñez, A.; Pujadas, J., *J. Org. Chem.* **1982**, *47*, 259–264.
- (17) Andersson, S.; Radner, F.; Rydbeck, A.; Wistrand, L. G., Patent *US5530140*, **1996**.
- (18) Andersson, S.; Radner, F.; Rydbeck, A.; Servin, R.; Wistrand, L. G., Patent *US5728370*, **1998**.
- (19) Jorgensen, M.; Gundersen, L.; Andersson, S.; Almen, T.; Wistrand, L. G.; Wikstroem, H.; Golman, K.; Servin, R.; Michelsen, P., Patent *WO1991/012024*, **1991**.
- (20) Reddy, T. J.; Iwama, T.; Halpern, H. J.; Rawal, V. H., *J. Org. Chem.* **2002**, *67*, 4635–4639.
- (21) Decroos, C.; Prangé, T.; Mansuy, D.; Boucher, J.-L.; Li, Y., *Chem. Commun.* **2011**, *47*, 4805–4807.
- (22) Liu, Y.; Villamena, F. A.; Sun, J.; Xu, Y.; Dhimitruka, I.; Zweier, J. L., *J. Org. Chem.* **2008**, *73*, 1490–1497.
- (23) Driesschaert, B.; Robiette, R.; Lucaccioni, F.; Gallez, B.; Marchand-Brynaert, J., *Chem. Commun.* **2011**, *47*, 4793–4795.
- (24) Li, Y.; Zhai, W.; Liao, Y.; Nie, J.; Han, G.; Song, Y.; Li, S.; Hou, J.; Liu, Y., *J. Org. Chem.* **2019**, *84*, 11774–11782.
- (25) Kunjir, N. C.; Reginsson, G. W.; Schiemann, O.; Sigurdsson, S. T., *Phys. Chem. Chem. Phys.* **2013**, *15*, 19673–19685.
- (26) Driesschaert, B.; Bobko, A. A.; Eubank, T. D.; Samouilov, A.; Khramtsov, V. V.; Zweier, J. L., *Bioorganic Med. Chem. Lett.* **2016**, *26*, 1742–1744.
- (27) Tan, X.; Chen, L.; Song, Y.; Rockenbauer, A.; Villamena, F. A.; Zweier, J. L.; Liu, Y., *Chem. Res. Toxicol.* **2017**, *30*, 1664–1672.

5. References

- (28) Decroos, C.; Bolland, V.; Boucher, J. L.; Bertho, G.; Xu-Li, Y.; Mansuy, D., *Chem. Res. Toxicol.* **2013**, *26*, 1561–1569.
- (29) Driesschaert, B.; Leveque, P.; Gallez, B.; Marchand-Brynaert, J., *Tetrahedron Lett.* **2013**, *54*, 5924–5926.
- (30) Serda, M.; Wu, Y.-K.; Barth, E. D.; Halpern, H. J.; Rawal, V. H., *Chem. Res. Toxicol.* **2016**, *29*, 2153–2156.
- (31) Decroos, C.; Li, Y.; Bertho, G.; Frapart, Y.; Mansuy, D.; Boucher, J.-L., *Chem. Res. Toxicol.* **2009**, *22*, 1342–1350.
- (32) Kuzhelev, A. A.; Tormyshev, V. M.; Plyusnin, V. F.; Rogozhnikova, O. Y.; Edeleva, M. V.; Veber, S. L.; Bagryanskaya, E. G., *Phys. Chem. Chem. Phys.* **2020**, *22*, 1019–1026.
- (33) Elewa, M.; Maltar-Strmečki, N.; Said, M. M.; El Shihawy, H. A.; El-Sadek, M.; Frank, J.; Drescher, S.; Drescher, M.; Mäder, K.; Hinderberger, D.; Imming, P., *Phys. Chem. Chem. Phys.* **2017**, *19*, 6688–6697.
- (34) Jagtap, A. P.; Krstic, I.; Kunjir, N. C.; Hänsel, R.; Prisner, T. F.; Sigurdsson, S. T., *Free Radic. Res.* **2015**, *49*, 78–85.
- (35) Veciana, J.; Riera, J.; Castañer, J.; Ferrer, N., *J. Organomet. Chem.* **1985**, *297*, 131–141.
- (36) Ballester, M.; Riera, J.; Castañer, J.; Rovira, C.; Armet, O., *Synthesis* **1986**, *1986*, 64–66.
- (37) Veciana, J.; Carilla, J.; Miravittles, C.; Molins, E., *J. Chem. Soc. Chem. Commun.* **1987**, 812–814.
- (38) Joergensen, M.; Rise, F.; Andersson, S.; Almen, T.; Aabye, A.; Wistrand, L. G. Wikstroem, H. .; Golman, K.; Servin, R., Patent *WO1991/012024*, **1991**.
- (39) Dirk, C. W.; Cox, S. D.; Wellman, D. E.; Wudl, F., *J. Org. Chem.* **1985**, *50*, 2395–2397.
- (40) Hintz, H.; Vanas, A.; Klose, D.; Jeschke, G.; Godt, A., *J. Org. Chem.* **2019**, *84*, 3304–3320.
- (41) Davos, M.; Patte, F.; Rouault, J.; Lafort, P.; Van Gemert, L., *Standardized Human Olfactory Thresholds*; Oxford University Press, **1990**.
- (42) Müller, D.; Adelsberger, K.; Imming, P., *Synth. Commun.* **2013**, *43*, 1447–1454.
- (43) Dhimitruka, I.; Velayutham, M.; Bobko, A. A.; Khramtsov, V. V.; Villamena, F. A.; Hadad, C. M.; Zweier, J. L., *Bioorganic Med. Chem. Lett.* **2007**, *17*, 6801–6805.
- (44) Dane, E. L.; King, S. B.; Swager, T. M., *J. Am. Chem. Soc.* **2010**, *132*, 7758–7768.
- (45) Poncelet, M.; Huffman, J. L.; Khramtsov, V. V.; Dhimitruka, I.; Driesschaert, B., *RSC Adv.* **2019**, *9*, 35073–35076.
- (46) Thaning, M., Patent *WO1998/39277*, 1998.
- (47) Frank, J.; Elewa, M.; M. Said, M.; El Shihawy, H. A.; El-Sadek, M.; Müller, D.; Meister, A.; Hause, G.; Drescher, S.; Metz, H.; Imming, P.; Mäder, K., *J. Org. Chem.* **2015**, *80*, 6754–6766.
- (48) Dhimitruka, I.; Grigorieva, O.; Zweier, J. L.; Khramtsov, V. V., *Bioorg. Med. Chem. Lett.* **2010**, *20*, 3946–3949.
- (49) Li, Y.; Zhai, W.; Liao, Y.; Nie, J.; Han, G.; Song, Y.; Li, S.; Hou, J.; Liu, Y., *J. Org. Chem.* **2019**, *84*, 11774–11782.
- (50) Qu, Y.; Li, Y.; Tan, X.; Zhai, W.; Han, G.; Hou, J.; Liu, G.; Song, Y.; Liu, Y., *Chem. Eur. J.* **2019**, *25*, 7888–7895.
- (51) Campbell, M.; Snieckus, V.; Baxter, E. W., *Encyclopedia of Reagents for Organic Synthesis*; John Wiley & Sons, Ltd, **2008**.
- (52) Krizan, T. D.; Martin, J. C., *J. Am. Chem. Soc.* **1983**, *105*, 6155–6157.
- (53) Jassoy, J. J.; Berndhäuser, A.; Duthie, F.; Kühn, S. P.; Hagelueken, G.; Schiemann, O., *Angew. Chem. Int. Ed.* **2017**, *56*, 177–181.
- (54) Xia, S.; Villamena, F. A.; Hadad, C. M.; Kuppusamy, P.; Li, Y.; Zhu, H.; Zweier, J. L., *J. Org. Chem.* **2006**, *71*, 7268–7279.
- (55) Rogozhnikova, O. Y.; Vasiliev, V. G.; Troitskaya, T. I.; Trukhin, D. V.; Mikhalina, T. V.; Halpern, H. J.; Tormyshev, V. M., *Eur. J. Org. Chem.* **2013**, *2013*, 3347–3355.
- (56) Neese, F., *WIREs Comput. Mol. Sci.* **2012**, *2*, 73–78.
- (57) Neese, F., *WIREs Comput. Mol. Sci.* **2018**, *8*, 4–9.
- (58) Jassoy, J. J.; Heubach, C. A.; Hett, T.; Bernhard, F.; Haege, F. R.; Hagelueken, G.; Schiemann, O., *Molecules* **2019**, *24*, 2735.
- (59) Driesschaert, B.; Leveque, P.; Gallez, B.; Marchand-Brynaert, J., *Eur. J. Org. Chem.* **2014**, *2014*, 8077–8084.
- (60) Edeleva, M. V.; Marque, S. R. A.; Rogozhnikova, O. Y.; Tormyshev, V. M.; Troitskaya, T. I.; Bagryanskaya, E. G., *J. Polym. Sci. A*, **2018**, *56*, 2656–2664.
- (61) Driesschaert, B.; Marchand, V.; Levêque, P.; Gallez, B.; Marchand-Brynaert, J., *Chem. Commun.* **2012**, *48*, 4049–4051.
- (62) Driesschaert, B.; Charlier, N.; Gallez, B.; Marchand-Brynaert, J., *Bioorg. Med. Chem. Lett.* **2008**, *18*, 4291–4293.

5. References

- (63) Trukhin, D. V.; Rogozhnikova, O. Y.; Troitskaya, T.; Vasiliev, V. G.; Bowman, M. K.; Tormyshev, V. M.; Troitskaya, T. I.; Vasiliev, V. G.; Bowman, M. K.; Tormyshev, V. M., *Synlett* **2015**, *27*, 893–899.
- (64) Liu, Y.; Villamena, F. A.; Zweier, J. L., *Chem. Commun.* **2008**, 4336–4338.
- (65) Gajan, D.; Bornet, A.; Vuichoud, B.; Milani, J.; Melzi, R.; Van Kalker, H. A.; Veyre, L.; Thieuleux, C.; Conley, M. P.; Grüning, W. R.; Schwarzwälder, M.; Lesage, A.; Copéret, C.; Bodenhausen, G.; Emsley, L.; Jannin, S.; Swager, T. M., *Proc. Natl. Acad. Sci. USA* **2014**, *111*, 14693–14697.
- (66) Mukaiyama, T., *Angew. Chem. Int. Ed.* **1979**, *18*, 707–721.
- (67) Jassoy, J. J.; Meyer, A.; Spicher, S.; Wübben, C.; Schiemann, O., *Molecules* **2018**, *23*, 682.
- (68) Abdullin, D.; Matsuoka, H.; Yulikov, M.; Fleck, N.; Klein, C.; Spicher, S.; Hagelueken, G.; Grimme, S.; Lützen, A.; Schiemann, O., *Chem. Eur. J.* **2019**, *25*, 8820–8828.
- (69) Liu, Y.; Villamena, F. A.; Song, Y.; Sun, J.; Rockenbauer, A.; Zweier, J. L., *J. Org. Chem.* **2010**, *75*, 7796–7802.
- (70) Yang, Z.; Liu, Y.; Borbat, P.; Zweier, J. L.; Freed, J. H.; Hubbell, W. L., *J. Am. Chem. Soc.* **2012**, *134*, 9950–9952.
- (71) Liu, Y.; Song, Y.; Rockenbauer, A.; Sun, J.; Hemann, C.; Villamena, F. A.; Zweier, J. L., *J. Org. Chem.* **2011**, *76*, 3853–3860.
- (72) Liu, Y.; Villamena, F. A.; Rockenbauer, A.; Song, Y.; Zweier, J. L., *J. Am. Chem. Soc.* **2013**, *135*, 2350–2356.
- (73) Reginsson, G. W.; Kunjir, N. C.; Sigurdsson, S. T.; Schiemann, O., *Chem. Eur. J.* **2012**, *18*, 13580–13584.
- (74) Zhai, W.; Feng, Y.; Liu, H.; Rockenbauer, A.; Mance, D.; Li, S.; Song, Y.; Baldus, M.; Liu, Y., *Chem. Sci.* **2018**, *9*, 4381–4391.
- (75) Trukhin, D. V.; Rogozhnikova, O. Y.; Troitskaya, T. I.; Kuzhelev, A. A.; Amosov, E. V.; Halpern, H. J.; Koval', V. V.; Tormyshev, V. M., *Russ. J. Org. Chem.* **2019**, *55*, 296–301.
- (76) Song, Y.; Liu, Y.; Hemann, C.; Villamena, F. A.; Zweier, J. L., *J. Org. Chem.* **2013**, *78*, 1371–1376.
- (77) Kuzhelev, A. A.; Trukhin, D. V.; Krumkacheva, O. A.; Strizhakov, R. K.; Rogozhnikova, O. Y.; Troitskaya, T. I.; Fedin, M. V.; Tormyshev, V. M.; Bagryanskaya, E. G., *J. Phys. Chem. B* **2015**, *119*, 13630–13640.
- (78) Driesschaert, B.; Khramtsov, V. V., Patent WO2019/018655, **2019**.
- (79) Decroos, C.; Bolland, V.; Boucher, J. L.; Bertho, G.; Xu-Li, Y.; Mansuy, D., *Chem. Res. Toxicol.* **2013**, *26*, 1561–1569.
- (80) Tan, X.; Ji, K.; Wang, X.; Yao, R.; Han, G.; Villamena, F. A.; Zweier, J. L.; Song, Y.; Rockenbauer, A.; Liu, Y., *Angew. Chem. Int. Ed.* **2020**, *59*, 928–934.
- (81) Decroos, C.; Prange, T. P.; Mansuy, D.; Boucher, J.-L.; Li, Y., *Chem. Commun.* **2011**, *47*, 4805–4807.
- (82) Tormyshev, V. M.; Rogozhnikova, O. Y.; Bowman, M. K.; Trukhin, D. V.; Troitskaya, T. I.; Vasiliev, V. G.; Shundrin, L. A.; Halpern, H. J., *Eur. J. Org. Chem.* **2014**, *2014*, 371–380.
- (83) Sanzhaeva, U.; Poncelet, M.; Tseytlin, O.; Tseytlin, M.; Gencheva, M.; Eubank, T. D.; Khramtsov, V. V.; Driesschaert, B., *J. Org. Chem.* **2020**, *85*, 10388–10398.
- (84) Marin-Montesinos, I.; Paniagua, J. C.; Peman, A.; Vilaseca, M.; Luis, F.; Van Doorslaer, S.; Pons, M., *Phys. Chem. Chem. Phys.* **2016**, *18*, 3151–3158.
- (85) Joseph, B.; Tormyshev, V. M.; Rogozhnikova, O. Y.; Akhmetzyanov, D.; Bagryanskaya, E. G.; Prisner, T. F., *Angew. Chem. Int. Ed.* **2016**, *55*, 11538–11542.
- (86) Giannoulis, A.; Yang, Y.; Gong, Y.-J.; Tan, X.; Feintuch, A.; Carmieli, R.; Bahrenberg, T.; Liu, Y.; Su, X.-C.; Goldfarb, D., *Phys. Chem. Chem. Phys.* **2019**, *21*, 10217–10227.
- (87) Song, Y.; Liu, Y.; Liu, W.; Villamena, F. A.; Zweier, J. L., *RSC Adv.* **2014**, *4*, 47649–47656.
- (88) Liu, W.; Nie, J.; Tan, X.; Liu, H.; Yu, N.; Han, G.; Zhu, Y.; Villamena, F. A.; Song, Y.; Zweier, J. L.; Liu, Y., *J. Org. Chem.* **2017**, *82*, 588–596.
- (89) Poncelet, M.; Driesschaert, B.; Tseytlin, O.; Tseytlin, M.; Eubank, T. D.; Khramtsov, V. V., *Bioorg. Med. Chem. Lett.* **2019**, *29*, 1756–1760.
- (90) Piloty, O.; Schwerin, B. G., *Ber. Dtsch. Chem. Ges.* **1901**, *34*, 1870–1887.
- (91) Holden, A. N.; Yager, W. A.; Merritt, F. R., *J. Chem. Phys.* **1951**, *19*, 1319.
- (92) Wieland, H.; Offenbächer, M., *Ber. der Dtsch. Chem. Ges.* **1914**, *47*, 2111–2115.
- (93) Wu, A.; Yang, W.; Pan, X., *Synth. Commun.* **1996**, *26*, 3565–3569.
- (94) Tebben, L.; Studer, A., *Angew. Chem. Int. Ed.* **2011**, *50*, 5034–5068.
- (95) Nilsen, A.; Braslau, R., *J. Polym. Sci. A* **2006**, *44*, 697–717.
- (96) Adamic, K.; Bowman, D. F.; Gillan, T.; Ingold, K. U., *J. Am. Chem. Soc.* **1971**, *93*, 902–908.
- (97) Suga, T.; Pu, Y.-J.; Oyaizu, K.; Nishide, H., *Bull. Chem. Soc. Jpn.* **2004**, *77*, 2203–2204.

5. References

- (98) Kato, Y.; Shimizu, Y.; Yijing, L.; Unoura, K.; Utsumi, H.; Ogata, T., *Electrochim. Acta* **1995**, *40*, 2799–2802.
- (99) Studer, A.; Vogler, T., *Sci. Synth.* **2009**, *40b*, 845.
- (100) Rychnovsky, S. D.; Beauchamp, T.; Vaidyanathan, R.; Kwan, T., *J. Org. Chem.* **1998**, *63*, 6363–6374.
- (101) Alewood, P. F.; Hussein, S. A.; Jenkins, T. C.; Perkins, M. J.; Sharma, A. H.; Siew, N. P. Y.; Ward, P., *J. Chem. Soc. Perkin Trans. 1* **1978**, 1066–1076.
- (102) Field, L. M.; Lahti, P. M.; Palacio, F.; Paduan-Filho, A., *J. Am. Chem. Soc.* **2003**, *125*, 10110–10118.
- (103) Shultz, D. A.; Vostrikova, K. E.; Bodnar, S. H.; Koo, H. J.; Whangbo, M. H.; Kirk, M. L.; Depperman, E. C.; Kampf, J. W., *J. Am. Chem. Soc.* **2003**, *125*, 1607–1617.
- (104) Reznikov, V. A.; Volodarsky, L. B., *Tetrahedron* **1993**, *49*, 10669–10692.
- (105) Sakai, K.; Yamada, K. ichi; Yamasaki, T.; Kinoshita, Y.; Mito, F.; Utsumi, H., *Tetrahedron* **2010**, *66*, 2311–2315.
- (106) Paletta, J. T.; Pink, M.; Foley, B.; Rajca, S.; Rajca, A., *Org. Lett.* **2012**, *14*, 5322–5325.
- (107) Wetter, C.; Gierlich, J.; Knoop, C. A.; Müller, C.; Schulte, T.; Studer, A., *Chem. Eur. J.* **2004**, *10*, 1156–1166.
- (108) Gölz, J. P.; Bockelmann, S.; Mayer, K.; Steinhoff, H.-J.; Wieczorek, H.; Huss, M.; Klare, J. P.; Menche, D., *ChemMedChem* **2016**, *11*, 420–428.
- (109) Dulog, L.; Lutz, S., *Liebigs Ann. Chem.* **1991**, *1991*, 971–972.
- (110) Edwards, T. E.; Okonogi, T. M.; Robinson, B. H.; Sigurdsson, S. T., *J. Am. Chem. Soc.* **2001**, *123*, 1527–1528.
- (111) Kirilyuk, I. A.; Polienko, Y. F.; Krumkacheva, O. A.; Strizhakov, R. K.; Gatilov, Y. V.; Grigor'ev, I. A.; Bagryanskaya, E. G., *J. Org. Chem.* **2012**, *77*, 8016–8027.
- (112) Jayawardena, V. C.; Fairfull-Smith, K. E.; Bottle, S. E., *Aust. J. Chem.* **2013**, *66*, 619.
- (113) Haugland, M. M.; El-Sagheer, A. H.; Porter, R. J.; Peña, J.; Brown, T.; Anderson, E. A.; Lovett, J. E., *J. Am. Chem. Soc.* **2016**, *138*, 9069–9072.
- (114) Fairfull-Smith, K. E.; Brackmann, F.; Bottle, S. E., *Eur. J. Org. Chem.* **2009**, *2009*, 1902–1915.
- (115) Goldschmidt, S.; Renn, K., *Ber. Dtsch. Chem. Ges.* **1922**, *55*, 628–643.
- (116) Kuhn, R.; Trischmann, H., *Angew. Chem. Int. Ed.* **1963**, *2*, 155–155.
- (117) Neugebauer, F. A.; Fischer, H., *Angew. Chem. Int. Ed.* **1980**, *19*, 724–725.
- (118) Jobelius, H.; Wagner, N.; Schnakenburg, G.; Meyer, A., *Molecules* **2018**, *23*, 1758.
- (119) Berry, D. E.; Hicks, R. G.; Gilroy, J. B., *J. Chem. Educ.* **2009**, *86*, 76–79.
- (120) Novoselov, K. S.; Geim, A. K.; Morozov, S. V.; Jiang, D.; Zhang, Y.; Dubonos, S. V.; Grigorieva, I. V.; Firsov, A. A., *Science*, **2004**, *306*, 666–669.
- (121) Hass, C.; Kirste, B.; Kurreck, H.; Schlömp, G., *J. Am. Chem. Soc.* **1983**, *105*, 7375–7383.
- (122) Beer, L.; Mandal, S. K.; Reed, R. W.; Oakley, R. T.; Tham, F. S.; Donnadieu, B.; Haddon, R. C., *Cryst. Growth Des.* **2007**, *7*, 802–809.
- (123) Goto, K.; Kubo, T.; Yamamoto, K.; Nakasuji, K.; Sato, K.; Shiomi, D.; Takui, T.; Kubota, M.; Kobayashi, T.; Yakusi, K.; Ouyang, J., *J. Am. Chem. Soc.* **1999**, *121*, 1619–1620.
- (124) Haddon, R. C.; Chichester, S. V.; Stein, S. M.; Marshall, J. H.; Mujsce, A. M., *J. Org. Chem.* **1987**, *52*, 711–712.
- (125) Koelsch, C. F., *J. Am. Chem. Soc.* **1957**, *79*, 4439–4441.
- (126) Mandal, S.; Sigurdsson, S. T., *Chem. Eur. J.* **2020**, *26*, 7486–7491.
- (127) Mandal, S.; Sigurdsson, S. T., *Chem. Commun.* **2020**, *56*, 13121–13124.
- (128) Lindsay, D.; Horswill, E. C.; Davidson, D. W.; Ingold, K. U., *Can. J. Chem.* **1974**, *52*, 3554–3556.
- (129) de Nooy, A. E.; Besemer, A. C.; van Bekkum, H., *Synthesis*, **1996**, *10*, 1153–1176.
- (130) Sheldon, R. A.; Arends, I. W. C. E.; Brink, G. J. Ten; Dijkman, A., *Acc. Chem. Res.* **2002**, *35*, 774–781.
- (131) Miller, R. A.; Hoerrner, R. S., *Org. Lett.* **2003**, *5*, 285–287.
- (132) Bolm, C.; Magnus, A. S.; Hildebrand, J. P., *Org. Lett.* **2000**, *2*, 1173–1175.
- (133) Jiang, X.; Zhang, J.; Ma, S., *J. Am. Chem. Soc.* **2016**, *138*, 8344–8347.
- (134) Shibuya, M.; Tomizawa, M.; Suzuki, I.; Iwabuchi, Y., *J. Am. Chem. Soc.* **2006**, *128*, 8412–8413.
- (135) Jing, Y.; Daniliuc, C. G.; Studer, A., *Org. Lett.* **2014**, *16*, 4932–4935.
- (136) Naveen, T.; Maity, S.; Sharma, U.; Maiti, D., *J. Org. Chem.* **2013**, *78*, 5949–5954.
- (137) An, H.; Mai, S.; Xuan, Q.; Zhou, Y.; Song, Q., *J. Org. Chem.* **2019**, *84*, 401–408.
- (138) Lu, W.; Shen, Z., *Org. Lett.* **2019**, *21*, 142–146.
- (139) Sciannamea, V.; Jérôme, R.; Detrembleur, C., *Chem. Rev.* **2008**, *108*, 1104–1126.
- (140) Fukuda, T.; Terauchi, T.; Goto, A.; Ohno, K.; Tsujii, Y.; Miyamoto, T.; Kobatake, S.; Yamada, B., *Macromolecules* **1996**, *29*, 6393–6398.

5. References

- (141) Jennings, J.; He, G.; Howdle, S. M.; Zetterlund, P. B., *Chem. Soc. Rev.* **2016**, *45*, 5055–5084.
- (142) Veciana, J.; Rovira, C.; Ventosa, N.; Crespo, M. I.; Palacio, F., *J. Am. Chem. Soc.* **1993**, *115*, 57–64.
- (143) Wu, S.; Li, M.; Phan, H.; Wang, D.; Heng, T. S.; Ding, J.; Lu, Z.; Wu, J., *Angew. Chem. Int. Ed.* **2018**, *57*, 8007.
- (144) Weber, A.; Schiemann, O.; Bode, B.; Prisner, T. F., *J. Magn. Reson.* **2002**, *157*, 277–285.
- (145) Margraf, D.; Cekan, P.; Prisner, T. F.; Sigurdsson, S. T.; Schiemann, O., *Phys. Chem. Chem. Phys.* **2009**, *11*, 6708–6714.
- (146) Meyer, A.; Jassoy, J. J.; Spicher, S.; Berndhäuser, A.; Schiemann, O., *Phys. Chem. Chem. Phys.* **2018**, *20*, 13858–13869.
- (147) Nakazawa, S.; Nishida, S.; Ise, T.; Yoshino, T.; Mori, N.; Rahimi, R. D.; Sato, K.; Morita, Y.; Toyota, K.; Shiomi, D.; Kitagawa, M.; Hara, H.; Carl, P.; Hçfer, P.; Takui, T., *Angew. Chem. Int. Ed.* **2012**, *51*, 9860–9864.
- (148) Ishii, K.; Fujisawa, J. I.; Ohba, Y.; Yamauchi, S., *J. Am. Chem. Soc.* **1996**, *118*, 13079–13080.
- (149) Mizuochi, N.; Ohba, Y.; Yamauchi, S., *J. Phys. Chem. A* **1997**, *101*, 5966–5968.
- (150) Conti, F.; Corvaja, C.; Toffoletti, A.; Mizuochi, N.; Ohba, Y.; Yamauchi, S.; Maggini, M., *J. Phys. Chem. A* **2000**, *104*, 4962–4967.
- (151) Giacobbe, E. M.; Mi, Q.; Colvin, M. T.; Cohen, B.; Ramanan, C.; Scott, A. M.; Yeganeh, S.; Marks, T. J.; Ratner, M. A.; Wasielewski, M. R., *J. Am. Chem. Soc.* **2009**, *131*, 3700–3712.
- (152) Grzegorzec, N.; Mao, H.; Michel, P.; Junge, M. J.; Lorenzo, E. R.; Young, R. M.; Krzyaniak, M. D.; Wasielewski, M. R.; Chernick, E. T., *J. Phys. Chem. A* **2020**, *124*, 6168–6176.
- (153) Frueh, D. P.; Goodrich, A. C.; Mishra, S. H.; Nichols, S. R., *Current Opinion in Structural Biology*, Elsevier, **2013**, pp 734–739.
- (154) Rößler, P.; Mathieu, D.; Gossert, A. D., *Angew. Chemie Int. Ed.* **2020**, *59*, 19329–19337.
- (155) Sprangers, R.; Kay, L. E., *Nature* **2007**, *445*, 618–622.
- (156) Callaway, E., *Nature* **2020**, *578*, 201.
- (157) Vonck, J.; Mills, D. J., *Current Opinion in Structural Biology*, Elsevier, **2017**, pp 48–54.
- (158) Piston, D. W.; Kremers, G. J., *Trends Biochem. Sci.* **2007**, *32*, 407–414.
- (159) Peter, M. F.; Gebhardt, C.; Mächtel, R.; Glaenger, J.; Thomas, G. H.; Cordes, T.; Hagelueken, G., *bioRxiv* **2020**, <https://doi.org/10.1101/2020.11.23.394080>.
- (160) Bordenave, T.; Helle, M.; Beau, F.; Georgiadis, D.; Tepshi, L.; Bernes, M.; Ye, Y.; Levenez, L.; Poquet, E.; Nozach, H.; Razavian, M.; Toczek, J.; Stura, E. A.; Dive, V.; Sadeghi, M. M.; Devel, L., *Bioconjug. Chem.* **2016**, *27*, 2407–2417.
- (161) Klare, J. P.; Steinhoff, H. J., *Photosynth. Res.* **2009**, *102*, 377–390.
- (162) Klare, J. P., *Biol. Chem.* **2013**, *394*, 1281–1300.
- (163) Schiemann, O.; Prisner, T. F., *Q. Rev. Biophys.* **2007**, *40*, 1–53.
- (164) Abdullin, D.; Florin, N.; Hagelueken, G.; Schiemann, O., *Angew. Chem. Int. Ed.* **2015**, *54*, 1827–1831.
- (165) Abdullin, D.; Schiemann, O., *ChemPlusChem* **2020**, *85*, 353–372.
- (166) Park, S.-Y.; Borbat, P. P.; Gonzalez-Bonet, G.; Bhatnagar, J.; Pollard, A. M.; Freed, J. H.; Bilwes, A. M.; Crane, B. R., *Nat. Struct. Mol. Biol.* **2006**, *13*, 400–407.
- (167) Banham, J. E.; Timmel, C. R.; Abbott, R. J. M.; Lea, S. M.; Jeschke, G., *Angew. Chem Int. Ed.* **2006**, *45*, 1058–1061.
- (168) Denysekov, V. P.; Prisner, T. F.; Stubbe, J.; Bennati, M., *Proc. Natl. Acad. Sci. USA* **2006**, *103*, 13386–13390.
- (169) Pilotas, C.; Ward, R.; Branigan, E.; Rasmussen, A.; Hagelueken, G.; Huang, H.; Black, S. S.; Booth, I. R.; Schiemann, O.; Naismith, J. H., *Proc. Natl. Acad. Sci. USA* **2012**, *109*, E2675–E2682.
- (170) Herget, M.; Baldauf, C.; Schölz, C.; Parcej, D.; Wiesmüller, K.-H.; Tampé, R.; Abele, R.; Bordignon, E., *Proc. Natl. Acad. Sci. USA* **2011**, *108*, 1349–1354.
- (171) Glaenger, J.; Peter, M. F.; Thomas, G. H.; Hagelueken, G., *Biophys. J.* **2017**, *112*, 109–120.
- (172) Abdelkader, E. H.; Feintuch, A.; Yao, X.; Adams, L. A.; Aurelio, L.; Graham, B.; Goldfarb, D.; Otting, G., *Chem. Commun.* **2015**, *51*, 15898–15901.
- (173) Matalon, E.; Huber, T.; Hagelueken, G.; Graham, B.; Frydman, V.; Feintuch, A.; Otting, G.; Goldfarb, D., *Angew. Chem. Int. Ed.* **2013**, *52*, 11831–11834.
- (174) Marko, A.; Denysekov, V.; Margraf, D.; Cekan, P.; Schiemann, O.; Sigurdsson, S. T.; Prisner, T. F., *J. Am. Chem. Soc.* **2011**, *133*, 13375–13379.
- (175) Hardwick, J. S.; Haugland, M. M.; El-Sagheer, A. H.; Ptchelkine, D.; Beierlein, F. R.; Lane, A. N.; Brown, T.; Lovett, J. E.; Anderson, E. A., *Nucleic Acids Res.* **2020**, *48*, 2830–2840.
- (176) Schiemann, O.; Cekan, P.; Margraf, D.; Prisner, T. F.; Sigurdsson, S. T., *Angew. Chem.* **2009**, *121*, 3342–3345.

5. References

- (177) Stelzl, L. S.; Erlenbach, N.; Heinz, M.; Prisner, T. F.; Hummer, G., *J. Am. Chem. Soc.* **2017**, *139*, 11674–11677.
- (178) Krstić, I.; Frolow, O.; Sezer, D.; Endeward, B.; Weigand, J. E.; Suess, B.; Engels, J. W.; Prisner, T. F., *J. Am. Chem. Soc.* **2010**, *132*, 1454–1455.
- (179) Wuebben, C.; Blume, S.; Abdullin, D.; Brajtenbach, D.; Haege, F.; Kath-Schorr, S.; Schiemann, O., *Molecules* **2019**, *24*, 4482.
- (180) Kerzhner, M.; Matsuoka, H.; Wuebben, C.; Famulok, M.; Schiemann, O., *Biochemistry* **2018**, *57*, 2923–2931.
- (181) Domnick, C.; Eggert, F.; Wuebben, C.; Bornewasser, L.; Hagelueken, G.; Schiemann, O.; Kath-Schorr, S., *Angew. Chem. Int. Ed.* **2020**, *59*, 7891–7896.
- (182) Wuebben, C.; Vicino, M. F.; Mueller, M.; Schiemann, O., *Nucleic Acids Res.* **2020**, *48*, 10518–10526.
- (183) Duss, O.; Michel, E.; Yulikov, M.; Schubert, M.; Jeschke, G.; Allain, F. H. T., *Nature* **2014**, *509*, 588–592.
- (184) Abdullin, D.; Florin, N.; Hagelueken, G.; Schiemann, O., *Angew. Chem. Int. Ed.* **2015**, *54*, 1827–1831.
- (185) Abdullin, D.; Schiemann, O., *Dalt. Trans.* **2021**, *50*, 808–815.
- (186) Wort, J. L.; Ackermann, K.; Giannoulis, A.; Stewart, A. J.; Norman, D. G.; Bode, B. E., *Angew. Chem. Int. Ed.* **2019**, *58*, 11681–11685.
- (187) Juliusson, H. Y.; Sigurdsson, S. T., *ChemBioChem* **2020**, *21*, 2635–2642.
- (188) Schmidt, M. J.; Borbas, J.; Drescher, M.; Summerer, D., *J. Am. Chem. Soc.* **2014**, *136*, 1238–1241.
- (189) Brotzel, F.; Mayr, H., *Org. Biomol. Chem.* **2007**, *5*, 3814–3820.
- (190) Moura, A.; Savageau, M. A.; Alves, R., *PLoS One* **2013**, *8*, e77319.
- (191) Li, Q. F.; Yang, Y.; Maleckis, A.; Otting, G.; Su, X. C., *Chem. Commun.* **2012**, *48*, 2704–2706.
- (192) Berliner, L. J.; Grunwald, J.; Hankovszky, H. O.; Hideg, K., *Anal. Biochem.* **1982**, *119*, 450–455.
- (193) Wawrzynow, A.; Collins, J. H.; Coan, C., *Biochemistry* **1993**, *32*, 10803–10811.
- (194) Bleicken, S.; Assafa, T. E.; Zhang, H.; Elsner, C.; Ritsch, I.; Pink, M.; Rajca, S.; Jeschke, G.; Rajca, A.; Bordignon, E., *ChemistryOpen* **2019**, *8*, 1057–1065.
- (195) Yang, Y.; Yang, F.; Gong, Y.-J.; Chen, J.-L.; Goldfarb, D.; Su, X.-C., *Angew. Chem. Int. Ed.* **2017**, *56*, 2914–2918.
- (196) Shah, A.; Roux, A.; Starck, M.; Mosely, J. A.; Stevens, M.; Norman, D. G.; Hunter, R. I.; El Mkami, H.; Smith, G. M.; Parker, D.; Lovett, J. E., *Inorg. Chem.* **2019**, *58*, 3015–3025.
- (197) Perussi, J. R.; Tinto, M. H.; Nascimento, O. R.; Tabak, M., *Anal. Biochem.* **1988**, *173*, 289–295.
- (198) Braun, T. S.; Widder, P.; Osswald, U.; Groß, L.; Williams, L.; Schmidt, M.; Helmle, I.; Summerer, D.; Drescher, M., *ChemBioChem* **2020**, *21*, 958–962.
- (199) Karthikeyan, G.; Bonucci, A.; Casano, G.; Gerbaud, G.; Abel, S.; Thomé, V.; Kodjabachian, L.; Magalon, A.; Guigliarelli, B.; Belle, V.; Ouari, O.; Mileo, E., *Angew. Chem. Int. Ed.* **2018**, *57*, 1366–1370.
- (200) Widder, P.; Berner, F.; Summerer, D.; Drescher, M., *ACS Chem. Biol.* **2019**, *14*, 839–844.
- (201) Kugele, A.; Silkenath, B.; Langer, J.; Wittmann, V.; Drescher, M., *ChemBioChem* **2019**, *20*, 2479–2484.
- (202) Fleissner, M. R.; Brustad, E. M.; Kálai, T.; Altenbach, C.; Cascio, D.; Peters, F. B.; Hideg, K.; Schultz, P. G.; Hubbell, W. L., *Proc. Natl. Acad. Sci. USA* **2009**, *106*, 21637–21642.
- (203) Hahn, A.; Reschke, S.; Leimkühler, S.; Risse, T., *J. Phys. Chem. B* **2014**, *118*, 7077–7084.
- (204) Kolb, H. C.; Finn, M. G.; Sharpless, K. B., *Angew. Chem. Int. Ed.* **2001**, *40*, 2004–2021.
- (205) Mileo, E.; Etienne, E.; Martinho, M.; Lebrun, R.; Roubaud, V.; Tordo, P.; Gontero, B.; Guigliarelli, B.; Marque, S. R. A.; Belle, V., *Bioconjug. Chem.* **2013**, *24*, 1110–1117.
- (206) Hagelueken, G.; Ward, R.; Naismith, J. H.; Schiemann, O., *Appl. Magn. Reson.* **2012**, *42*, 377–391.
- (207) Jeschke, G., *Protein Sci.* **2018**, *27*, 76–85.
- (208) Schünke, S.; Stoldt, M.; Lechera, J.; Kaupp, U. B.; Willbold, D., *Proc. Natl. Acad. Sci. USA* **2011**, *108*, 6121–6126.
- (209) Spicher, S.; Grimme, S., *Angew. Chem. Int. Ed.* **2020**, *59*, 15665–15673.
- (210) Spicher, S.; Abdullin, D.; Grimme, S.; Schiemann, O., *Phys. Chem. Chem. Phys.* **2020**, *22*, 24282–24290.
- (211) Shelke, S. A.; Sigurdsson, S. T., *Eur. J. Org. Chem.* **2012**, *2012*, 2291–2301.
- (212) Saha, S.; Hetzke, T.; Prisner, T. F.; Sigurdsson, S. T., *Chem. Commun.* **2018**, *54*, 11749–11752.
- (213) Duxbury, C. L.; Legge, R. L.; Paliyath, G.; Barber, R. F.; Thompson, J. E., *Phytochemistry* **1991**, *30*, 63–68.

5. References

- (214) Pavićević, A.; Luo, J.; Popović-Bijelić, A.; Mojović, M., *Eur. Biophys. J.* **2017**, *46*, 773–787.
- (215) Galazzo, L.; Maso, L.; De Rosa, E.; Bortolus, M.; Doni, D.; Acquasaliente, L.; Filippis, V. De; Costantini, P.; Carbonera, D., *Sci. Rep.* **2017**, *7*, 1–14.
- (216) Griffith, O. H.; McConnell, H. M., *Proc. Natl. Acad. Sci. USA* **1966**, *55*, 8–11.
- (217) Meyer, V.; Swanson, M. A.; Clouston, L. J.; Boratyński, P. J.; Stein, R. A.; McHaourab, H. S.; Rajca, A.; Eaton, S. S.; Eaton, G. R., *Biophys. J.* **2015**, *108*, 1213–1219.
- (218) Kuzhelev, A. A.; Strizhakov, R. K.; Krumkacheva, O. A.; Polienko, Y. F.; Morozov, D. A.; Shevelev, G. Y.; Pyshnyi, D. V.; Kirilyuk, I. A.; Fedin, M. V.; Bagryanskaya, E. G., *J. Magn. Reson.* **2016**, *266*, 1–7.
- (219) Rajca, A.; Kathirvelu, V.; Roy, S. K.; Pink, M.; Rajca, S.; Sarkar, S.; Eaton, S. S.; Eaton, G. R., *Chem. Eur. J.* **2010**, *16*, 5778–5782.
- (220) Krumkacheva, O.; Bagryanskaya, E., *J. Magn. Reson.* **2017**, *280*, 117–126.
- (221) Tormyshev, V. M.; Chubarov, A. S.; Krumkacheva, O. A.; Trukhin, D. V.; Rogozhnikova, O. Y.; Spitsyna, A. S.; Kuzhelev, A. A.; Koval, V. V.; Fedin, M. V.; Godovikova, T. S.; Bowman, M. K.; Bagryanskaya, E. G., *Chem. Eur. J.* **2020**, *26*, 2705–2712.
- (222) Shevelev, G. Y.; Krumkacheva, O. A.; Lomzov, A. A.; Kuzhelev, A. A.; Rogozhnikova, O. Y.; Trukhin, D. V.; Troitskaya, T. I.; Tormyshev, V. M.; Fedin, M. V.; Pyshnyi, D. V.; Bagryanskaya, E. G., *J. Am. Chem. Soc.* **2014**, *136*, 9874–9877.
- (223) Kuzhelev, A. A.; Krumkacheva, O. A.; Shevelev, G. Y.; Yulikov, M.; Fedin, M. V.; Bagryanskaya, E. G., *Phys. Chem. Chem. Phys.* **2018**, *20*, 10224–10230.
- (224) Yang, Z.; Jiménez-Osés, G.; López, C. J.; Bridges, M. D.; Houk, K. N.; Hubbell, W. L., *J. Am. Chem. Soc.* **2014**, *136*, 15356–15365.
- (225) Yang, Z.; Bridges, M. D.; López, C. J.; Rogozhnikova, O. Y.; Trukhin, D. V.; Brooks, E. K.; Tormyshev, V.; Halpern, H. J.; Hubbell, W. L., *J. Magn. Reson.* **2016**, *269*, 50–54.
- (226) Yang, Y.; Yang, F.; Gong, Y.-J.; Bahrenberg, T.; Feintuch, A.; Su, X.-C.; Goldfarb, D., *J. Phys. Chem. Lett.* **2018**, *9*, 6119–6123.
- (227) Goldfarb, D., *Phys. Chem. Chem. Phys.* **2014**, *16*, 9685–9699.
- (228) Yang, Y.; Pan, B. Bin; Tan, X.; Yang, F.; Liu, Y.; Su, X. C.; Goldfarb, D., *J. Phys. Chem. Lett.* **2020**, *11*, 1141–1147.
- (229) Di Valentin, M.; Albertini, M.; Zurlo, E.; Gobbo, M.; Carbonera, D., *J. Am. Chem. Soc.* **2014**, *136*, 6582–6585.
- (230) Krumkacheva, O. A.; Timofeev, I. O.; Politanskaya, L. V.; Polienko, Y. F.; Tretyakov, E. V.; Rogozhnikova, O. Y.; Trukhin, D. V.; Tormyshev, V. M.; Chubarov, A. S.; Bagryanskaya, E. G.; Fedin, M. V., *Angew. Chem. Int. Ed.* **2019**, *58*, 13271–13275.
- (231) Wang, Y.; Sarkar, M.; Smith, A. E.; Krois, A. S.; Pielak, G. J., *J. Am. Chem. Soc.* **2012**, *134*, 16614–16618.
- (232) Rivas, G.; Minton, A. P., *Trends in Biochemical Sciences*. Elsevier, **2016**, pp 970–981.
- (233) Braun, T. S.; Widder, P.; Osswald, U.; Groß, L.; Williams, L.; Schmidt, M.; Helmle, I.; Summerer, D.; Drescher, M., *ChemBioChem* **2020**, *21*, 958–962.
- (234) John, L.; Drescher, M., *Bioprotocol* **2018**, *8*, e2798.
- (235) Igarashi, R.; Sakai, T.; Hara, H.; Tenno, T.; Tanaka, T.; Tochio, H.; Shirakawa, M., *J. Am. Chem. Soc.* **2010**, *132*, 8228–8229.
- (236) Qi, M.; Groß, A.; Jeschke, G.; Godt, A.; Drescher, M., *J. Am. Chem. Soc.* **2014**, *136*, 15366–15378.
- (237) Collauto, A.; Bülow, S.; Gophane, D. B.; Saha, S.; Stelzl, L. S.; Hummer, G.; Sigurdsson, S. T.; Prisner, T. F., *Angew. Chem. Int. Ed.* **2020**, *59*, 23025–23029.
- (238) Weber, A.; Schiemann, O.; Bode, B.; Prisner, T. F., *J. Magn. Reson.* **2002**, *157*, 277–285.
- (239) Akhmetzyanov, D.; Schöps, P.; Marko, A.; Kunjir, N. C.; Sigurdsson, S. T.; Prisner, T. F., *Phys. Chem. Chem. Phys.* **2015**, *17*, 24446–24451.
- (240) Messerschmidt, A., *Handbook of Metalloproteins*; John Wiley & Sons, Ltd: Chichester, 2011.
- (241) Hud, N. V., *Nucleic Acid - Metal Ion Interactions*; Royal Society of Chemistry, **2009**.
- (242) Wu, Z.; Feintuch, A.; Collauto, A.; Adams, L. A.; Aurelio, L.; Graham, B.; Otting, G.; Goldfarb, D., *J. Phys. Chem. Lett.* **2017**, *8*, 5277–5282.
- (243) Merz, G. E.; Borbat, P. P.; Muok, A. R.; Srivastava, M.; Bunck, D. N.; Freed, J. H.; Crane, B. R., *J. Phys. Chem. B* **2018**, *122*, 9443–9451.
- (244) Qi, M.; Hülsmann, M.; Godt, A., *J. Org. Chem.* **2016**, *81*, 2549–2571.
- (245) Akhmetzyanov, D.; Ching, H. Y. V.; Denysenkov, V.; Demay-Drouhard, P.; Bertrand, H. C.; Tabares, L. C.; Policar, C.; Prisner, T. F.; Un, S., *Phys. Chem. Chem. Phys.* **2016**, *18*, 30857–30866.
- (246) Ritsch, I.; Hintz, H.; Jeschke, G.; Godt, A.; Yulikov, M., *Phys. Chem. Chem. Phys.* **2019**, *21*, 9810–9830.
- (247) Narr, E.; Godt, A.; Jeschke, G., *Angew. Chem. Int. Ed.* **2002**, *41*, 3907–3910.

5. References

- (248) Giannoulis, A.; Ackermann, K.; Spindler, P. E.; Higgins, C.; Cordes, D. B.; Slawin, A. M. Z.; Prisner, T. F.; Bode, B. E., *Phys. Chem. Chem. Phys.* **2018**, *20*, 11196–11205.
- (249) Meyer, A.; Abdullin, D.; Schnakenburg, G.; Schiemann, O., *Phys. Chem. Chem. Phys.* **2016**, *18*, 9262–9271.
- (250) Bode, B. E.; Plackmeyer, J.; Prisner, T. F.; Schiemann, O., *J. Phys. Chem. A* **2008**, *112*, 5064–5073.
- (251) Bobko, A. A.; Dhimitruka, I.; Eubank, T. D.; Marsh, C. B.; Zweier, J. L.; Khramtsov, V. V., *Free Radic. Biol. Med.* **2009**, *47*, 654–658.
- (252) Liu, Y.; Villamena, F. A.; Sun, J.; Wang, T. yao; Zweier, J. L., *Free Radic. Biol. Med.* **2009**, *46*, 876–883.
- (253) Wang, X.; Peng, C.; He, K.; Ji, K.; Tan, X.; Han, G.; Liu, Y.; Liu, Y.; Song, Y., *Analyst* **2020**, *145*, 4964–4971.
- (254) Epel, B.; Haney, C. R.; Hleihel, D.; Wardrip, C., *Med. Phys.* **2010**, *37*, 2553–2559.
- (255) Muz, B.; de la Puente, P.; Azab, F.; Azab, A. K., *Hypoxia* **2015**, *3*, 83.
- (256) Liu, K. J.; Grinstaff, M. W.; Jiang, J.; Suslick, K. S.; Swartz, H. M.; Wang, W., *Biophys. J.* **1994**, *67*, 896–901.
- (257) Ardenkjær-Larsen, J. H.; Laursen, I.; Leunbach, I.; Ehnholm, G.; Wistrand, L. G.; Petersson, J. S.; Golman, K., *J. Magn. Reson.* **1998**, *133*, 1–12.
- (258) Wang, X.; Emoto, M.; Miyake, Y.; Itto, K.; Xu, S.; Fujii, H.; Hirata, H.; Arimoto, H., *Bioorg. Med. Chem. Lett.* **2016**, *26*, 4947–4949.
- (259) Weaver, J.; Burks, S. R.; Liu, K. J.; Kao, J. P. Y.; Rosen, G. M., *J. Magn. Reson.* **2016**, *271*, 68–74.
- (260) Bobko, A. A.; Eubank, T. D.; Voorhees, J. L.; Efimova, O. V.; Kirilyuk, I. A.; Petryakov, S.; Trofimov, D. G.; Marsh, C. B.; Zweier, J. L.; Grigor'Ev, I. A.; Samouilov, A.; Khramtsov, V. V., *Magn. Reson. Med.* **2012**, *67*, 1827–1836.
- (261) Kirilyuk, I. A.; Bobko, A. A.; Khramtsov, V. V.; Grigor'ev, I. A., *Org. Biomol. Chem.* **2005**, *3*, 1269–1274.
- (262) Samouilov, A.; Efimova, O. V.; Bobko, A. A.; Sun, Z.; Petryakov, S.; Eubank, T. D.; Trofimov, D. G.; Kirilyuk, I. A.; Grigor'Ev, I. A.; Takahashi, W.; Zweier, J. L.; Khramtsov, V. V., *Anal. Chem.* **2014**, *86*, 1045–1052.
- (263) Bobko, A. A.; Dhimitruka, I.; Zweier, J. L.; Khramtsov, V. V., *J. Am. Chem. Soc.* **2007**, *129*, 7240–7241.
- (264) Poncelet, M.; Driesschaert, B., *Angew. Chem. Int. Ed.* **2020**, *59*, 16451–16454.
- (265) Abragam, A.; Goldmann, M., *Rep. Prog. Phys.* **1978**, *41*, 395–467.
- (266) Swager, T. M.; Temkin, R. J.; Herzfeld, J.; Griffin, R. G., *Acc. Chem. Res.* **2013**, *46*, 1933–1941.
- (267) Levien, M.; Hiller, M.; Tkach, I.; Bennati, M.; Orlando, T., *J. Phys. Chem. Lett.* **2020**, *11*, 1629–1635.
- (268) Song, C.; Hu, K. N.; Joo, C. G.; Swager, T. M.; Griffin, R. G., *J. Am. Chem. Soc.* **2006**, *128*, 11385–11390.
- (269) Mentink-Vigier, F., *Phys. Chem. Chem. Phys.* **2020**, *22*, 3643–3652.
- (270) Kubicki, D. J.; Casano, G.; Schwarzwälder, M.; Abel, S.; Sauvée, C.; Ganesan, K.; Yulikov, M.; Rossini, A. J.; Jeschke, G.; Copéret, C.; Lesage, A.; Tordo, P.; Ouari, O.; Emsley, L., *Chem. Sci.* **2016**, *7*, 550–558.
- (271) Zagdoun, A.; Casano, G.; Ouari, O.; Schwarzwälder, M.; Rossini, A. J.; Aussenac, F.; Yulikov, M.; Jeschke, G.; Copéret, C.; Lesage, A.; Tordo, P.; Emsley, L., *J. Am. Chem. Soc.* **2013**, *135*, 12790–12797.
- (272) Sauvée, C.; Rosay, M.; Casano, G.; Aussenac, F.; Weber, R. T.; Ouari, O.; Tordo, P., *Angew. Chem. Int. Ed.* **2013**, *52*, 10858–10861.
- (273) Geiger, M.-A.; Jagtap, A. P.; Kaushik, M.; Sun, H.; Stöppler, D.; Sigurdsson, S. T.; Corzilius, B.; Oschkinat, H., *Chem. Eur. J.* **2018**, *24*, 13485–13494.
- (274) Jähnig, F.; Kwiatkowski, G.; Däpp, A.; Hunkeler, A.; Meier, B. H.; Kozerke, S.; Ernst, M., *Phys. Chem. Chem. Phys.* **2017**, *19*, 19196–19204.
- (275) Mathies, G.; Caporini, M. A.; Michaelis, V. K.; Liu, Y.; Hu, K. N.; Mance, D.; Zweier, J. L.; Rosay, M.; Baldus, M.; Griffin, R. G., *Angew. Chem. Int. Ed.* **2015**, *54*, 11770–11774.
- (276) Ardenkjær-Larsen, J. H.; Fridlund, B.; Gram, A.; Hansson, G.; Hansson, L.; Lerche, M. H.; Servin, R.; Thaning, M.; Golman, K., *Proc. Natl. Acad. Sci. USA* **2003**, *100*, 10158–10163.
- (277) Gerlach, W.; Stern, O., *Z. Phys.* **1922**, *9*, 349–352.
- (278) Odom, B.; Hanneke, D.; D'urso, B.; Gabrielse, G., *Phys. Rev. Lett.* **2006**, *97*, 030801.
- (279) Salikhov, K. M.; Zavoiskaya, N. E., *Resonance* **2015**, *20*, 963–968.
- (280) O'Connor, C. J., *Prog. Inorg. Chem.* **1972**, *29*, 203–283.
- (281) Bencini, A.; Gatteschi, D., *EPR of Exchange Coupled Systems*; Springer Verlag, **1990**.

5. References

- (282) Holldack, K.; Schnegg, A., *J. Large-Scale Res. Facil.* **2016**, 2, A51.
- (283) Stoll, S.; Schweiger, A., *J. Magn. Reson.* **2006**, 178, 42–55.
- (284) Banham, J. E.; Baker, C. M.; Ceola, S.; Day, I. J.; Grant, G. H.; Groenen, E. J. J.; Rodgers, C. T.; Jeschke, G.; Timmel, C. R., *J. Magn. Reson.* **2008**, 191, 202–218.
- (285) Reginsson, G. W.; Schiemann, O., *Biochem. Soc. Trans.* **2011**, 39, 128–139.
- (286) Schmidt, T.; Wälti, M. A.; Baber, J. L.; Hustedt, E. J.; Clore, G. M., *Angew. Chem. Int. Ed.* **2016**, 55, 15905–15909.
- (287) Pannier, M.; Veit, S.; Godt, A.; Jeschke, G.; Spiess, H. W., *J. Magn. Reson.* **2000**, 142, 331–340.
- (288) Edwards, T. H.; Stoll, S., *J. Magn. Reson.* **2018**, 288, 58–68.
- (289) Jeschke, G.; Chechik, V.; Ionita, P.; Godt, A.; Zimmermann, H.; Banham, J.; Timmel, C.; Hilger, D.; Jung, H., *Appl. Magn. Reson.* **2006**, 30, 473–498.
- (290) Milikisyants, S.; Scarpelli, F.; Finiguerra, M. G.; Ubbink, M.; Huber, M., *J. Magn. Reson.* **2009**, 201, 48–56.
- (291) Abdullin, D.; Duthie, F.; Meyer, A.; Müller, E. S.; Hagelueken, G.; Schiemann, O., *J. Phys. Chem. B* **2015**, 119, 13539–13542.
- (292) Saxena, S.; Freed, J. H., *Chem. Phys. Lett.* **1996**, 251, 102–110.
- (293) Jeschke, G.; Pannier, M.; Godt, A.; Spiess, H. W., *Chem. Phys. Lett.* **2000**, 331, 243–252.
- (294) Colacot, T. J.; Matthey, J., *Platin. Met. Rev.* **2011**, 55, 84–90.
- (295) Migita, T.; Shimizu, T.; Asami, Y.; Shiobara, J.; Kato, Y.; Kosugi, M., *Bull. Chem. Soc. Jpn.* **1980**, 53, 1385–1389.
- (296) Fleck, N., Bachelor Thesis, University of Bonn, **2016**.
- (297) Wessig, P.; Freyse, D.; Schuster, D.; Kelling, A., *Eur. J. Org. Chem.* **2020**, 2020, 1732–1744.
- (298) Hartwig, J. F., *Acc. Chem. Res.* **1998**, 31, 852–860.
- (299) Masquelin, T.; Delgado, Y.; Baumlé, V., *Tetrahedron Lett.* **1998**, 39, 5725–5726.
- (300) Russell Bowman, W.; Burchell, C. J.; Kili, P.; Slawin, A. M. Z.; Wormald, P.; Woollins, J. D., *Chem. Eur. J.* **2006**, 12, 6366–6381.
- (301) Wang, L.; Zhou, W.-Y.; Chen, S.-C.; He, M.-Y.; Chen, Q., *Adv. Synth. Catal.* **2012**, 354, 839–845.
- (302) Luzzio, F. A., *Synth. Commun.* **1984**, 14, 209–214.
- (303) Fernández-Rodríguez, M. A.; Shen, Q.; Hartwig, J. F., *J. Am. Chem. Soc.* **2006**, 128, 2180–2181.
- (304) Xu, J.; Liu, R. Y.; Yeung, C. S.; Buchwald, S. L., *ACS Catal.* **2019**, 9, 6461–6466.
- (305) Itoh, T.; Mase, T., *Org. Lett.* **2004**, 6, 4587–4590.
- (306) Iovine, V.; Cruciani, F.; Picini, F.; Varrone, M.; Rossi, E., *ChemistrySelect* **2016**, 1, 5201–5205.
- (307) Buchachenko, A. L.; Berdinsky, V. L., *Chem. Rev.* **2002**, 102, 603–612.
- (308) Teki, Y., *Chem. Eur. J.* **2020**, 26, 980–996.
- (309) Klein, C., PhD-Thesis, University of Bonn, **2018**.
- (310) Fleischer, E. B.; Srivastava, T. S., *J. Am. Chem. Soc.* **1969**, 91, 2403–2405.
- (311) Fleischer, E. B.; Palmer, J. M.; Srivastava, T. S.; Chatterjee, A., *J. Am. Chem. Soc.* **1971**, 93, 3162–3167.
- (312) Murray, K. S., *Coord. Chem. Rev.* **1974**, 12, 1–35.
- (313) Ghosh, S. K.; Patra, R.; Rath, S. P., *Inorg. Chim. Acta* **2010**, 363, 2791–2799.
- (314) Wessig, P.; Freyse, D.; Schuster, D.; Kelling, A., *Eur. J. Org. Chem.* **2020**, 2020, 1732–1744.
- (315) Dane, E. L.; King, S. B.; Swager, T. M., *J. Am. Chem. Soc.* **2010**, 132, 7758–7768.
- (316) Hintz, H.; Vanas, A.; Klose, D.; Jeschke, G.; Godt, A., *J. Org. Chem.* **2019**, 84, 3304–3320.
- (317) Renault, K.; Fredy, J. W.; Renard, P. Y.; Sabot, C., *Bioconjug. Chem.* **2018**, 29, 2497–2513.

6. Appendix

The results presented in this thesis have already been published peer-reviewed scientific journals. In the following, the original articles alongside the respective supporting information are reprinted.

These reprints appear in their original format including the page numbers related to the journals. For the sake of clarity, the page numbers related to this thesis have been added as well.

List of Appendices

- [A0] Curriculum Vitae
- [A1] Improved, Odorless Access to Benzo[1,2-d;4,5-d']-bis[1,3]dithioles and Tert-butyl Arylsulfides via C-S Cross Coupling
- [A2] Tris[2,2,6,6-tetramethyl-8-(trimethylsilyl)benzo-[1,2-d;4,5-d']bis(1,3-dithiol)-4-yl]methanol diethyl ether monosolvate
- [A3] C-C Cross-Coupling Reactions of Trityl Radicals: Spin Density Delocalization, Exchange Coupling, and a Spin Label
- [A4] Excitation Energy Transfer and Exchange-Mediated Quartet State Formation in Porphyrin-Trityl Systems
- [A5] SLIM: A Short-Linked, Highly Redox-Stable Trityl Label for High-Sensitivity In-Cell EPR Distance Measurements
- [A6] Ox-SLIM: Synthesis of and Site-Specific Labelling with a Highly Hydrophilic Trityl Spin Label
- [A7] Synthesis of μ_2 -Oxo-Bridged Iron(III) Tetraphenylporphyrin–Spacer–Nitroxide Dimers and their Structural and Dynamics Characterization by using EPR and MD Simulations
- [A8] Pulsed EPR Dipolar Spectroscopy on Spin Pairs with one Highly Anisotropic Spin Center: The Low-Spin FeIII Case
- [A9] Pulsed EPR Dipolar Spectroscopy under the Breakdown of the High-Field Approximation: The High-Spin Iron(III) Case

Curriculum Vitae

.

..

Education

University of Bonn 01/2017 – 0*/2021

Fast-Track PhD in Chemistry , Physical Organic Chemistry

- M.Sc. modules (60 credit points) i.a. in Industrial Chemistry, Structural Biology, and Spectroscopy

- Design and Synthesis of stable trityl radicals for bioconjugation and material applications

University of Bonn 10/2013 - 10/2016

Bachelor of Science in Chemistry

- Cumulative grade average 1.3 (with honors) on a scale of 1.0 to 5.0

- Tutor for thermodynamics (2 semesters)

Amos-Comenius-Gymnasium, Bonn

A-Levels (“Abitur”) (1.5, scale 1.0 to 6.0)

06/2013

University studies in chemistry alongside school (15 ECTS with exams)

10/2011 – 07/2012

Employments

BASF SE, Ludwigshafen, Germany 02/2020 - 04/2020

Research Intern, Homogenous Catalysis

Awards

German national youth science contest (“Jugend forscht”) 05/2011

- 1st-Place nationwide in category chemistry (1st of 1856)

Society of German Chemists (GDCh e.V.)

02/2017

- Award for an excellent Bachelor degree

Voluntary Commitment

German national youth science contest (*Jugend forscht*) since 2018

- Jury member (chemistry), regional contest

Maltese paramedic training center, Bonn, Germany

since 2018

- Lecturer for pharmacology in paramedic courses

German Red Cross

since 2017

- Paramedic apprenticeship (520 h training, 2017 - 2019)

- Engagement in emergency medical service and disaster response unit

Scientific Publications:

1. N. Fleck, G. Schnakenburg, A. C. Filippou, O. Schiemann*, *Acta Cryst. E* **2018**, 74, 539 – 543.
<https://doi.org/10.1107/S2056989018004516>
2. D. Abdullin[§], N. Fleck[§], C. Klein, P. Brehm, S. Spicher, A. Lützen, S. Grimme, O. Schiemann*, *Chem. Eur. J.* **2019**, 25, 2586 – 2596.
<https://doi.org/10.1002/chem.201805016>
3. N. Fleck, T. Hett, J. Brode, S. Richert, A. Meyer, O. Schiemann*, *J. Org. Chem.* **2019**, 84, 3293 – 3303.
<https://doi.org/10.1021/acs.joc.8b03229>
4. D. Abdullin, H. Matsuoka, M. Yulikov, N. Fleck, C. Klein, S. Spicher, G. Hagelueken, S. Grimme, A. Lützen, O. Schiemann*, *Chem. Eur. J.* **2019**, 25, 8820 - 8828.
<https://doi.org/10.1002/chem.201900977>
5. D. Abdullin, P. Brehm, N. Fleck, S. Spicher, S. Grimme, O. Schiemann*, *Chem. Eur. J.* **2019**, 25, 14388 – 14398.
<https://doi.org/10.1002/chem.201902908>
6. N. Fleck, C. Heubach, T. Hett, P. Bawol, H. Baltruschat, O. Schiemann*, *Angew. Chem. Int. Ed.* **2020**, 59, 9767-9772. <https://doi.org/10.1002/anie.202004452>
N. Fleck, C. Heubach, T. Hett, P. Bawol, H. Baltruschat, O. Schiemann*, *Angew. Chem.* **2020**, 132, 9854 – 9859.
7. O. Nolden[§], N. Fleck[§], E. Lorenzo, M. R. Wasielewski, O. Schiemann, P. Gilch, S. Richert*, *Chem. Eur. J.* **2020**, 27, 2683 – 2691.
<https://doi.org/10.1002/chem.202002805>
8. K. Kopp, O. Schiemann, N. Fleck*, *Molecules* **2020**, 25, 3666.
<https://www.mdpi.com/1420-3049/25/16/3666>
9. N. Fleck, C. Heubach, T. Hett, S. Spicher, S. Grimme, O. Schiemann*, *Chem. Eur. J.* **2021**, 27, 5292 – 5297.
<https://doi.org/10.1002/chem.202100013>

[§]equal contribution; *corresponding author.

[A1]: Improved, Odorless Access to Benzo[1,2-d;4,5-d']-bis[1,3]dithioles and *Tert*-butyl Arylsulfides via C-S Cross Coupling

Reprinted with permission from

Kevin Kopp, Olav Schiemann, Nico Fleck*, *Molecules* **2020**, *25*, 3666.

Published with Open Access by MDPI (Basel, CH) under CC-BY license, ©**2020** to the authors.

Contributions:

- Conceptualization of the work
- Experimental Design
- Compound Characterization (in part)
- Writing of the manuscript

Article

Improved, Odorless Access to Benzo[1,2-d;4,5-d']-bis[1,3]dithioles and *Tert*-butyl Arylsulfides via C-S Cross Coupling

Kevin Kopp, Olav Schiemann  and Nico Fleck *

Institute of Physical and Theoretical Chemistry, Rheinische Friedrich-Wilhelms-University Bonn, Wegelerstr. 12, 53115 Bonn, Germany; kopp@pc.uni-bonn.de (K.K.); schiemann@pc.uni-bonn.de (O.S.)

* Correspondence: fleck@pc.uni-bonn.de

Academic Editor: Antal Csámpai

Received: 24 July 2020; Accepted: 11 August 2020; Published: 12 August 2020



Abstract: Benzo[1,2-d;4,5-d']bis[1,3]dithioles are important building blocks within a range of functional materials such as fluorescent dyes, conjugated polymers, and stable trityl radicals. Access to these is usually gained via *tert*-butyl aryl sulfides, the synthesis of which requires the use of highly malodorous *tert*-butyl thiol and relies on S_NAr -chemistry requiring harsh reaction conditions, while giving low yields. In the present work, *S-tert*-butyl isothiuronium bromide is successfully applied as an odorless surrogate for *tert*-butyl thiol. The C-S bond formation is carried out under palladium catalysis with the thiolate formed in situ resulting in high yields of *tert*-butyl aryl sulfides. The subsequent formation of benzo[1,2-d;4,5-d']bis[1,3]dithioles is here achieved with scandium(III)triflate, a less harmful reagent than the usually used Lewis acids, e.g., boron trifluoride or tetrafluoroboric acid. This enables a convenient and environmentally more compliant access to high yields of benzo[1,2-d;4,5-d']bis[1,3]dithioles.

Keywords: palladium catalysis; trityl radicals; thioketal; thioether; isothiuronium bromide

1. Introduction

Benzo[1,2-d;4,5-d']bis[1,3]dithioles **1** (Figure 1) have emerged as important building blocks for a range of functional materials. For example benzo[1,2-d;4,5-d']bis[1,3]dithiole-based fluorescent dyes (“S4 DBD dyes” **2**) exhibit large Stokes shifts making them promising candidates for super-resolution microscopy such as stimulated emission depletion (STED) microscopy [1,2]. Moreover, conjugated polymers **3** consisting of such building blocks show fluorescence response upon oxidation rendering these materials interesting for oxidant sensing [3]. Another widespread application lies in the synthesis of triarylmethyl radicals **4** (“TAM-radicals” **4**), a class of highly stable radicals employed in site-directed spin labeling of biomolecules for electron paramagnetic resonance (EPR)-based structure determination in vitro [5–7], at room temperature [5,6] and within cells [8–10]. Furthermore, such triaryl methyl (TAM)-radicals are used as sensors for local oxygen concentrations within EPR-imaging [11,12], as pH-probes [13], viscosimetry [14], and as polarizing agents for dynamic nuclear polarization (DNP) [15,16]. Additionally, TAM radicals incorporating benzo[1,2-d;4,5-d']bis[1,3]dithiol moieties were recently taken into account for the design of magnetic materials and information transfer [17,18]. The synthesis of all of the thioketals shown in Figure 1 regularly involves 1,2,4,5-tetrakis(*tert*-butylthio)benzene **5** as the starting material [4], since the 1,2,4,5-tetrathio benzene required for ketal formation easily undergoes oxidative degradation rendering its isolation cumbersome [19]. Precursor **5** is usually synthesized from 1,2,4,5-tetrachlorobenzene [4,20] via S_NAr -type reactions, which not only require harsh conditions, but also the use of excessive *tert*-butyl thiolate, generated from the free thiol and sodium [4] or sodium hydride [20] in situ.

Tert-butylthiol however, is a quite volatile (Bp. 64 °C) and highly malodorous compound with an extremely low odor threshold of 0.33 ppb [21]. Considering the accompanied formation of H₂ entraining free thiol into the gas-phase and the elevated temperatures of the reaction, the problematic nature of this synthetic step becomes apparent. In order to avoid harassment of the environment during this reaction, several strategies have been proposed in the literature, such as washing the gas-stream with KMnO₄ [20] or thermal inactivation of the fume hood exhaust [22]. While the gas inlet can get clogged resulting in dangerous overpressures within the former approach, the latter one appears costly and requires a redesign of the fume hood exhaust system. This makes the synthesis of benzo[1,2-d;4,5-d']bis[1,3]dithioles **1** rather unfit for e.g., academic laboratories. Additionally, precursor **5** is not commercially available in reasonable quantities, making a more convenient approach to aryl-*tert*-butyl thioether such as **5** highly desirable.

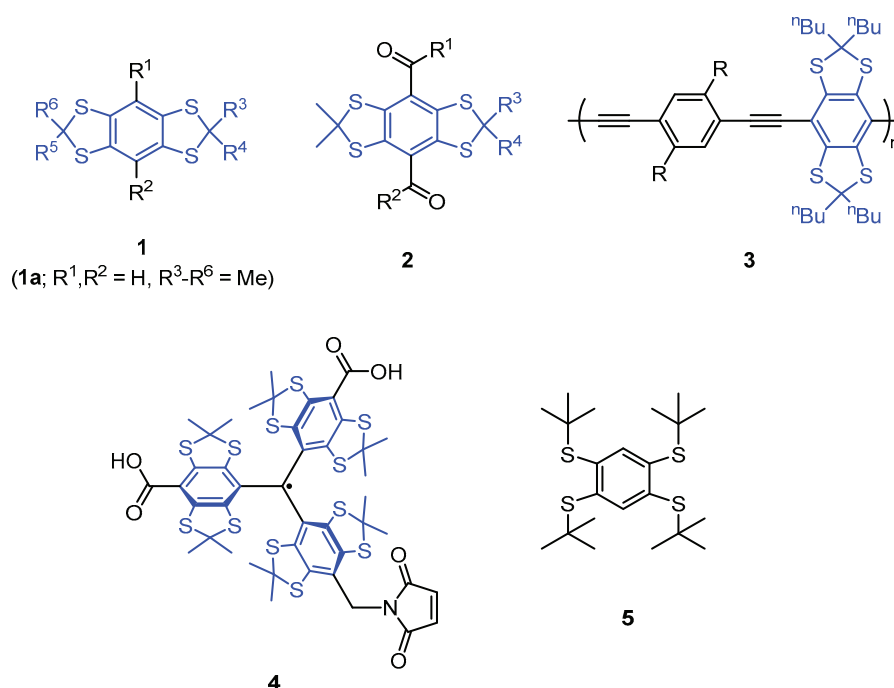


Figure 1. Lewis structures of benzo[1,2-d;4,5-d']bis[1,3]dithioles **1**, “S₄-DBD” dyes **2**, thioketal containing conjugated polymers **3**, spin label **4**[•] and 1,2,4,5-tetrakis(*tert*-butylthio)benzene **5**. For the sake of clarity, the benzo[1,2-d;4,5-d']bis[1,3]dithiole motif is highlighted in blue.

Considering the accomplishments in catalytic carbon-heteroatom-bond formation in form of Pd-catalyzed cross-coupling reactions [23], a similar approach would be desirable for the task here. There is a plethora of examples for catalytic C-S-bond formations [24–29], which hold some advantages as e.g., milder reaction conditions and better conversions as compared to classical S_NAr-type reactions. However, such an approach should avoid the use of free thiols altogether. Although C-S cross-coupling reactions using appropriate thiol surrogates are known, these usually need to be synthesized from the corresponding thiols, such as alkyl thioacetates [30]. Another possibility has been described by Wang et al. [31] in form of a one-pot synthesis, in which the necessary thiolate nucleophile was generated in situ using an alkyl bromide and thiourea as the sulfur source. Nonetheless, the yields for tertiary substrates stalled due to a competing elimination pathway.

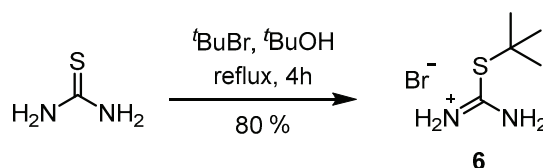
In the present study, the olfactory hazard and lack of conversion was circumvented by synthesis of *S-tert*-butyl isothiuronium bromide from thiourea and *tert*-butyl bromide and its use as thiolate source in a subsequent cross-coupling reaction. Since the isothiuronium salt is completely odorless and the thiolate appears only in situ, the described process enables odorless access to benzo[1,2-d;4,5-d']bis[1,3]dithioles and this with improved yields. It should be noted, that *S-tert*-butyl

isothiuronium bromide has already been applied as a thiolate source for the functionalization of electron-poor heterocycles via nucleophilic substitution reactions [32,33]. Furthermore, a smoother conversion of **5** to the thioketal 2,2,6,6-tetramethyl- benzo[1,2-d;4,5-d']bis[1,3]dithiole **1a** by use of catalytic amounts of Sc(OTf)₃ was possible, which in comparison to previous protocols avoids the use of large amounts of hazardous Lewis acids like HBF₄ and BF₃.

2. Results and Discussion

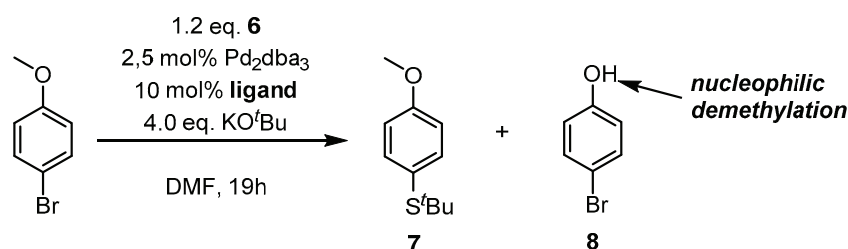
Although it is well-known that S-alkyl isothiuronium salts form alkylthiols upon treatment with aqueous hydroxide [34], their behavior towards bases in nonaqueous media has been studied only rarely. An early report of Luzzio et al. [35] described the formation of thiolates from S-alkyl isothiuronium halides treated with NaH or NaOEt in refluxing THF or EtOH, respectively. Based on this, the capability of S-*tert*-butyl isothiuronium halides to form the corresponding thiolate exploitable for in-situ C-S cross coupling was assumed.

Though S-*tert*-butyl isothiuronium halides were occasionally described in older literature [36], the procedures applied for their synthesis utilized gaseous hydrogen halides rendering them inconvenient and dangerous. In contrast, S-*n*-alkyl isothiuronium halides are easily prepared by reaction of the corresponding alkyl halide with thiourea in refluxing ethanol [34,37], but the competing elimination dominates the reactivity of tertiary alkyl halides inhibiting the formation of the desired S-*tert*-butyl isothiuronium salt. Accordingly, the reaction of thiourea with *tert*-butyl bromide in refluxing ethanol yielded pure S-ethyl isothiuronium bromide (Figure S3). This issue was circumvented by replacing EtOH for *t*-BuOH, so that the only electrophile in the reaction mixture was the *tert*-butyl group. Consequently, pure S-*tert*-butyl isothiuronium bromide **6** was obtained in a yield of 80% after recrystallization on a 10 g scale as shown in Scheme 1.



Scheme 1. Synthesis of S-*tert*-butyl isothiuronium bromide.

With convenient access to the S-*tert*-butylisothiuronium salt **6** at hand, the performance of Pd-catalyzed C-S cross coupling of aryl bromides with *tert*-butyl thiolate generated in situ from **6** was examined. Aryl bromides were chosen as appropriate substrates, since cross-coupling reactions generally proceed worse with aryl chlorides and the aryl iodides are more expensive and commercially harder to come by. Inspired by an early publication by Migita et al. [25] an initial catalyst loading of 5 mol% of Pd catalyst with 10 mol% of phosphine ligand was chosen. We used the very common Pd₂(dba)₃ (2.5 mol%) as a Pd(0)-source, as dibenzylideneacetone is easily displaced by other ligands simplifying adjustments to the reaction conditions with regard to different phosphine ligands. Additionally, potassium *tert*-butoxide was used as a strong base for activation of the thiolate. Seeking for optimal conditions, 4-bromoanisole was subjected to C-S cross coupling tests using various conditions as shown in Scheme 2. 4-Bromoanisole was chosen, since no S_NAr background-reactivity was expected and the analysis of the reaction mixtures is easily possible via ¹H-NMR. In order to gain sufficient reactivity, an initial temperature/ligand screening was performed giving the results shown in Table 1.



Scheme 2. General reaction Scheme for the screening of optimal conversion of 4-bromoanisole.

Table 1. Screening of various phosphine ligands for C-S cross coupling to 7.

No.	T [°C]	Ligand	Conversion * [%]	7 * [%]	8 * [%]	Selectivity to 7 [%]
1	50	Ph ₃ P	23	14	9	59
2	50	XPhos	7	0	7	0
3	50	XantPhos	0	0	0	0
4	80	Ph ₃ P	100	100	0	100
5	80	dppf	69	34	35	49
6	80	XantPhos	38	2	36	4.8
7	80	XPhos	43	0	43	0
8	80	BrettPhos	45	0	45	0
9	80	SPhos	62	0	62	0
10	80	ⁿ Bu ₃ P	78	61	17	78
11	80	none	59	0	59	0
12 **	80	none	72	0	72	0
13 **	80	SPhos	65	0	65	0

* ratios estimated from ¹H-NMR of the crude reaction mixtures, signal assignment according to independently prepared samples of 7 and 8 (SI). ** without Pd₂dba₃.

As evident from entries 1–3 (Table 1), low to no conversion of the substrate occurs at 50 °C. For cases where cross-coupling reactivity towards 7 was low, a competitive nucleophilic O-demethylation yielding 8 was observed. However, increasing the temperature to 80 °C gives quantitative conversion to the desired product 7 using Ph₃P as a ligand (entry 4, Table 1). All other ligands show considerably less conversion at this temperature, decreasing in the order Ph₃P > ⁿBu₃P > dppf >> Xantphos > XPhos/SPhos/BettPhos. Considering the steric demand of these ligands, the nucleophilic displacement of bromide by the thiolate anion in the catalytic cycle seems to be challenging. As for low reaction temperatures, the competitive O-demethylation (entries 5–10, Table 1) also for rather inactive catalysts [38]. As expected, no S_NAr background reaction was observed (Table 1, entries 11–13) and Pd₂dba₃ did not show any catalytic activity without phosphine ligands (Table 1, entry 11). Having established the combination Pd₂dba₃/Ph₃P as a suitable catalyst system, the choice of base and solvent were assessed (Table 2).

Table 2. Screening of bases and solvent.

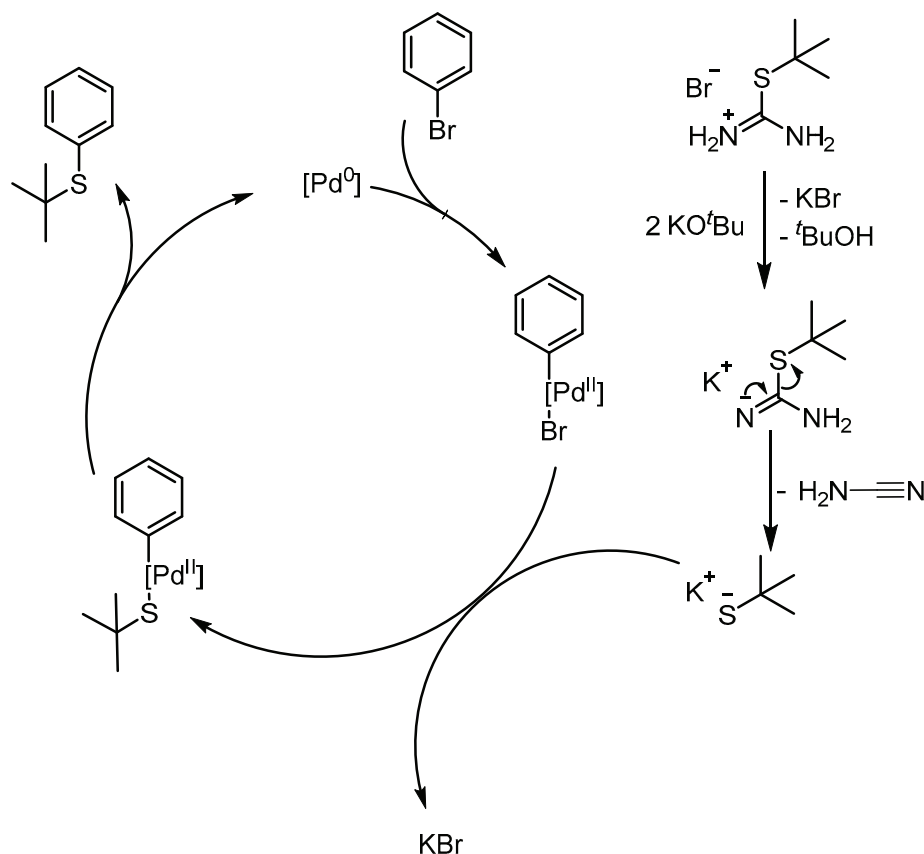
No.	Base	Solvent	Conversion * [%]	7 * [%]	8 * [%]	Selectivity to 7 [%]
1	KO ^t Bu	DMF	100	100	0	100
2	KO ^t Bu	<i>n</i> BuOH	61	61	0	100
3	Cs ₂ CO ₃	DMF	19	19	0	100
4	K ₂ CO ₃	DMF	42	42	0	100
5 **	K ₂ CO ₃	DMF	0	0	0	0
6	K ₃ PO ₄	DMF	43	43	0	100
7 **	K ₃ PO ₄	DMF	12	12	0	100
8	KO ^t Bu ***	DMF	22	22	0	100

All reactions were carried out at 80 °C with 1.2 eq. 6, 10 mol% Ph₃P, 2.5 mol% Pd₂dba₃, and 4.0 eq. of base. * ratios estimated from ¹H-NMR of the crude reaction mixture, signal assignment according to independently prepared samples of 7 and 8. ** 10% mol% 18-crown-6 added. *** 2.4 eq. used.

While the transformation of 4-bromoanisole to 7 smoothly proceeds in DMF, the yield was diminished to 61% upon using *n*-butanol (Table 2, entry 1). As *n*-butanol is already a much less

appropriate solvent for the formation of **7**, DMF was kept as the solvent and further screening of other bases was carried out in the latter. The use of milder bases such as Cs_2CO_3 , K_2CO_3 , or K_3PO_4 resulted in lower yields (Table 2, entries 2–6). Also, using reduced amounts of KO^tBu (Table 2, entry 7) dramatically reduces the yield. Interestingly, the yields were also significantly reduced by addition of 10 mol% 18-crown-6 to the reaction mixtures (Table 2, entries 4, 6).

Thus, the use of KO^tBu , DMF and simple Ph_3P enabled quantitative conversion of 4-bromoanisole to thioether **7**, while the reactivity with other ligands was significantly lower. At higher temperature, the cross-coupling reaction dominates and runs likely through a typical $\text{Pd}^0/\text{Pd}^{\text{II}}$ catalytic cycle (Scheme 3).



Scheme 3. Assumed mechanism for the formation of *tert*-butyl thioethers from isothiuronium salts.

Considering the mechanism proposed in Scheme 3, thiolate formation is assumed to already occur at low temperature. This assumption is supported by the *O*-demethylation already occurring at $50\text{ }^\circ\text{C}$ (Table 1, entries 1–3), which requires the presence of the thiolate anion. However, the nucleophilic displacement of bromide with the sterically demanding *tert*-butyl thiolate appears challenging, compared to the oxidative addition into the $\text{C}_{\text{sp}^2}\text{-Br}$ bond, especially since the displacement is known to run through an associative pathway at the Pd^{II} -center [39]. Thus, the substitution of bromide by the thiolate is suspected to be the rate-determining step in the catalytic cycle. This is further encouraged by the observation that the reaction readily proceeds in DMF, whereas the yield is heavily diminished in *n*-butanol. As the solubility of KBr in DMF is low [40], precipitation of the latter facilitates the nucleophilic displacement. The addition of a crown ether, however, increases both the solubility of KBr and the nucleophilicity of bromide, hampering this step and thereby the entire reaction.

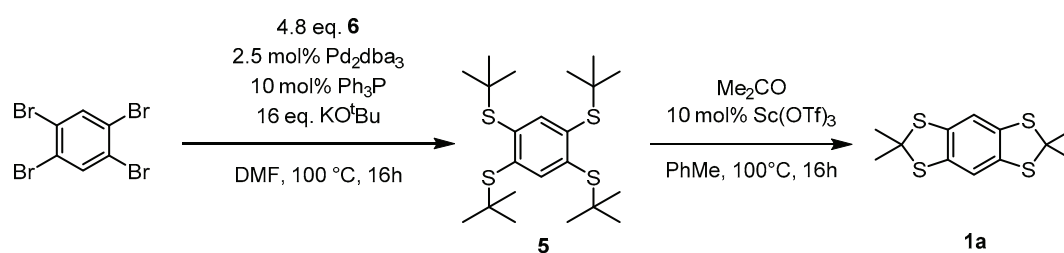
With regard to the monodentate ligands no reactivity was observed when using biarylphosphines (XPhos, SPhos, BrettPhos; Table 1, entries 2, 7–9), despite their successful application for C-S cross coupling reactions in general [24]. The order of reactivity for the formation of **7** decreases in the

order $\text{Ph}_3\text{P} > {}^n\text{Bu}_3\text{P} > \text{XPhos/BrettPhos/SPhos}$, while the respective cone angles increase in the reverse order Ph_3P (131.4°) $< {}^n\text{Bu}_3\text{P}$ (152.2°) $< \text{SPhos}$ (201.9°) $< \text{XPhos}$ (209.8°) [41]. This observation can be rationalized through the associative displacement of bromide for thiolate being the rate-determining step. The steric congestion imposed by ligands with a large cone angle restrains the attack of the sterically demanding *tert*-butyl thiolate even further. In contrast and although performing considerably worse than Ph_3P and ${}^n\text{Bu}_3\text{P}$, the bidentate ligands dppf and XantPhos gave conversion to the desired product, with dppf performing about a factor 18 better than XantPhos. Though the exact coordination mode within the catalytic cycle is not known, the lower bite angle [42] (99°) of dppf is assumed to impose less steric congestion compared to XantPhos (108°), thereby facilitating the nucleophilic displacement step. Interestingly, XantPhos has been reported to catalyze C-S cross-coupling [26], however here only a very low reactivity was observed (Table 1, entries 3,6). Most of the recent studies on C-S cross-coupling with thiol surrogates focused on primary alkyl thiols, thus neglecting the influence of sterically demanding nucleophiles. Interestingly, the O-demethylation dominated especially with ligands, that render the nucleophilic displacement on the Pd^{II} -center disfavored for steric reasons (vide infra). As the latter one is believed to be rate-determining, the cross-coupling is slowed down in these cases, so that educt reacts predominantly through the O-demethylation pathway.

Considering the aforementioned transformation of 4-bromoanisole so 7, Park et al. [30] used a $\text{Pd}(\text{dba})_2/\text{dppf}$ catalyst system and obtained a yield of 87% using *S-tert*-butylthioacetate as sulfur source, however with an increased temperature of 110°C . Exploiting the in situ formation of thiolates from *tert*-butyl bromide and thiourea, Wang et al. [31] obtained *S-tert*-butylthiobenzene (yield 76%) and 4-nitro-*S-tert*-butylthiobenzene (yield 77%) from the respective aryl bromides using a $\text{Pd}_2\text{dba}_3/\text{XPhos}$ catalyst system and yields were significantly higher for primary alkyl substrates.

To probe for a more general substrate applicability, 1,4-diiodobenzene, 4-bromonitrobenzene, 4-chloroanisole, and 4-fluoroanisole were subjected to the desired transformation as shown in Table 3. For 1,4-diiodobenzene, quantitative conversion to the desired 1,4-bis(*tert*-butylthio)benzene was observed (conditions Table 1, entry 4) even at lower reaction temperature (50°C). Though the nucleophilic displacement step (Scheme 3) is assumed to be rate determining for aryl bromides, the easier oxidative addition into the C-I bond seems to facilitate the desired transformation here. With 4-nitrobromobenzene, full conversion to the *tert*-butyl thioether was observed already at 25°C (Table 3, entry 3). However, the same result was obtained without Pd-catalyst (Table 3, entry 4), which suggests that reaction proceeds in this case via an $\text{S}_{\text{N}}\text{Ar}$ -mechanism. This raises the question, whether the aforementioned result of Wang et al. relied on a true palladium catalyzed C-S cross coupling reaction or also on an $\text{S}_{\text{N}}\text{Ar}$ -reaction. In contrast, 4-chloroanisole (Table 3, entries 5,6) and 4-fluoroanisole (Table 3, entries 7,8) do yield no conversion to 7 regardless of type of catalyst. Instead O-demethylation occurs (Figures S36 and S37). Since Ph_3P -ligated palladium species lack the capability of activating $\text{C}_{\text{ar}}\text{-Cl}$ and $\text{C}_{\text{ar}}\text{-F}$ bonds [29,39], both educts cannot enter the catalytic cycle presented in Scheme 3. In addition, 4-fluoro- and 4-chloroanisole do also not show any $\text{S}_{\text{N}}\text{Ar}$ -chemistry under the conditions used. Such a reaction maybe achieved with thiolate nucleophiles, e.g., by coordination to an electron withdrawing metal fragment [43], substitution by EWGs [44], or elevated temperatures [45].

With proper reaction conditions at hand, 1,2,4,5-tetrabromobenzene was used as a substrate to obtain the desired 1,2,4,5-tetrakis(*tert*-butylthio)benzene 5 as shown in Scheme 4.



Scheme 4. Synthesis of 2,2,6,6-Tetramethylbenzo[1,2-d:4,5-d']bis[1,3]dithiole 1a.

Table 3. Screening of further substrates.

No.	Substrate	Catalyst	T [°C]	Yield * [%]
1 *	1,4-diiodobenzene	Ph ₃ P/Pd ₂ dba ₃	80	100
2 *	1,4-diiodobenzene	Ph ₃ P/Pd ₂ dba ₃	50	100
3	4-nitrobromobenzene	Ph ₃ P/Pd ₂ dba ₃	25	100
4	4-nitrobromobenzene	none	25	100
5 **	4-chloroanisole	Ph ₃ P/Pd ₂ dba ₃	80	0
6 **	4-chloroanisole	none	80	0
7 **	4-fluoroanisole	Ph ₃ P/Pd ₂ dba ₃	80	0
8 **	4-fluoroanisole	none	80	0

All reactions were carried out in dry DMF for 19 h with 1.2 eq. **6**, 10 mol% Ph₃P, 2.5 mol% Pd₂dba₃, and 4.0 eq. of KO^tBu unless stated otherwise. Yields were determined from ¹H-NMR spectra of the crude reaction mixtures. * stoichiometry was adapted to a twofold substitution accordingly. ** extensive O-demethylation was observed as outlined in the Supporting Information.

Here, the applicability of this transformation was further increased by reducing the catalyst load to 1.25 mol% Pd per coupling site and the desired product **5** was obtained in a yield of 88% on a 10 g scale after simple washing with methanol. This exceeds the literature yields varying between 48% [20] and 71% [46] significantly, while using the same isolation method. It should however be noted, that the transformation of 1,2,4,5-tetrabromobenzene to **5** proceeds with quantitative conversion (see Figure S6), proofed by quantitative ¹H-NMR with mesitylene as internal standard.

The subsequent transformation to the thioketals is regularly carried out using an excess of BF₃ or HBF₄ [20,46], both reagents appear toxic and dangerous in handling. By contrast, thioetal **1a** could also be obtained in a yield of 83% on a 1 g scale by using catalytic amounts of Sc(OTf)₃. Though yields of 96% were obtained with HBF₄, and 78% with BF₃ respectively [10], scandium(III)triflate appears undeniably as the safer and environmentally more benign reagent in this case.

3. Experimental

3.1. General

Commercially available chemicals were used without further purification, dry solvents were purchased in sealed containers over molecular sieves. All reactions involving air and water sensitive substrates were carried out under argon atmosphere using standard Schlenk techniques. Solvents were degassed by simple purging of the respective dry solvents with argon gas for 30 minutes. Observation of the reactions via thin layer chromatography was performed on aluminum silica plates with F254-fluorescence indicator obtained from Merck, the spots were visualized using 254 nm UV-light. Column chromatography was conducted using silica gel (60 Å pore size, 40–63 µm particle size) purchased from Merck. Solvents were removed under reduced pressure by a rotary evaporator.

3.2. Synthetic Procedures

S-tert-butyl isothiuronium bromide 6: Thiourea (4.08 g, 53.6 mmol) was dissolved in *tert*-butanol (35 mL) and heated to reflux. Then *tert*-butyl bromide (9.76 g, 71.2 mmol, 1.32 eq.) was added and the mixture was stirred for 4 h under reflux. Completion of the reaction was determined by the absence of thiourea monitored by TLC (acetone/cyclohexane 10:1). The reaction mixture was then poured into cyclohexane whereupon a white solid precipitated, which was subsequently filtered off, washed with cold acetone and dried in high vacuum to afford the title compound as a white crystalline solid (9.16 g, 43.0 mmol, 80.2%). ¹H-NMR (400 MHz, 298 K, DMSO-*d*₆, δ in ppm): 1.49 (s, 9H), 9.15 (s, 4H). ¹³C-NMR (100 MHz, 298 K, DMSO-*d*₆, δ in ppm): 30.9, 51.0, 166.0. HRMS (ESI+, *m/z*, [M – Br]⁺): calc. for C₅H₁₃N₂S, 133.0794; found 133.0794.

4-Methoxy-*tert*-butylthiobenzene 7: 4-Bromoanisole (1.00 g, 5.34 mmol), *tert*-butyl isothiuronium bromide (1.37 g, 6.43 mmol, 1.20 eq.), tris(dibenzylideneacetone)dipalladium(0) (0.12 g, 0.13 mmol, 2.5 mol%), triphenylphosphine (0.142 g, 0.54 mmol, 10 mol%) and potassium *tert*-butoxide (2.40 mg,

21.4 mmol, 4.00 eq.) were dissolved in dry and degassed DMF (40 mL) under argon atmosphere. The mixture was stirred for 19 h at 80 °C. Afterwards, the reaction was quenched with water (100 mL) and extracted with DCM (3 × 30 mL). The unified organic phases were repeatedly washed with 2M-HCl-solution (3 × 50 mL) and dried over MgSO₄. The solvents were removed under reduced pressure and the crude product was subjected to column chromatography on silica eluting with cyclohexane/ethyl acetate 100:1 (*v/v*) affording 648 mg (62%, 3.31 mmol) of a faint yellow oil after drying in oil pump vacuum.

Since a distillation was not suitable with such a small amount, high vacuum was used to remove residual solvents from the product. However, this diminished the yield owing to the volatile nature of the title compound. However, we gave the isolation of most pure material priority, since it was employed as reference in the following NMR-experiments. ¹H-NMR (400 MHz, 298 K, CDCl₃, δ in ppm): 1.26 (s, 9H), 3.81 (s, 3H), 6.83–6.88 (m, 2H), 7.41–7.47 (m, 2H). ¹³C-NMR (100 MHz, 298 K, CDCl₃, δ in ppm): 30.9, 45.6, 55.4, 114.1, 123.7, 139.0, 160.3. MS (EI+, *m/z*, [M]⁺): calc. for C₁₁H₁₆OS, 196.0922; found 196.0917.

1,2,4,5-Tetrakis(*tert*-butylthio)benzene 5: 1,2,4,5-Tetrabromobenzene (10.0 g, 25.4 mmol), *S-tert*-butyl isothiuronium bromide (26.0 g, 122 mmol, 4.80 eq.), potassium *tert*-butoxide (45.6 g, 406 mmol, 16.0 eq.), tris(dibenzylideneacetone)dipalladium(0) (0.582 g, 0.63 mmol, 2.5 mol%) and triphenylphosphine (0.666 g, 2.54 mmol, 10 mol%) are placed in a Schlenk tube under argon atmosphere and are subsequently dissolved in dry DMF (200 mL). The mixture is then stirred for 16 h at 100 °C.

After completion of the reaction the mixture is quenched with water (200 mL) and extracted with DCM (3 × 50 mL). The organic phase is then separated, washed a few times with 2M hydrochloric acid and dried over MgSO₄. The solvent is removed under reduced pressure and the crude product is washed with methanol. The product is obtained as an off white solid (9.63 g, 22.4 mmol, 88%). ¹H-NMR (400 MHz, 298 K, CDCl₃, δ in ppm): 1.36 (s, 36H), 7.94 (s, 2H). ¹³C-NMR (100 MHz, 298 K, CDCl₃, δ in ppm): 31.5, 48.3, 139.5, 144.9. MS (EI+, *m/z*, [M]⁺): calc. for C₂₂H₃₈S₄, 430.1856; found 430.1855.

For measuring the conversion via quantitative ¹H-NMR, mesitylene was used as an internal standard. The above mentioned reaction was carried out using 100.7 mg 1,2,4,5-Tetrabromobenzene (255.8 μmol) with analogous stoichiometry as above and 32.2 μL mesitylene (27.9 mg, 232.5 μmol, 0.909 eq.) were added. The work-up was carried out as described and solvents were only removed with a vacuum above 600 mbar to avoid evaporation of mesitylene. The conversion was estimated to 99.6 ± 4 % based on two independent samples and integration of the ¹H-NMR spectrum (Figure S6). The error of app. 4 % accounts for weighting uncertainty and variance between both samples.

2,2,6,6-Tetramethylbenzo[1,2-d:4,5-d']bis[1,3]dithiole 1a: 1,2,4,5-Tetrakis(*tert*-butylthio)benzene (1.00 g, 2.32 mmol), scandium triflate (0.114 g, 0.23 mmol, 10 mol%), and acetone (1.72 mL, 1.34 g, 23.2 mmol, 10.0 eq.) were dissolved in 10 mL dry toluene and heated to 100 °C under argon for 16 h. After reaching room temperature, 10 mL 0.5 M HCl was added to the reaction mixture and the organic phase was separated off. After washing the aqueous phase was 10 mL diethyl ether, the unified organic phases were dried over MgSO₄ and solvents were removed under reduced pressure. The title compound was obtained as a pure white solid in a yield of 0.546 g (82%, 1.90 mmol). ¹H-NMR (400 MHz, 298 K, CDCl₃, δ in ppm): 1.88 (s, 12H), 7.02 (s, 2H). ¹³C-NMR (XY MHz, 298 K, CDCl₃, δ in ppm): 31.4, 65.9, 116.9, 135.9. MS (ESI+, *m/z*, [M]⁺): calc. for C₁₂H₁₄S₄, 285.9978; found 285.9971.

General procedure for condition screening with 4-bromoanisole. 4-Bromoanisole (100 mg, 0.535 mmol), *tert*-butyl isothiuronium bromide (137mg, 0.641 mmol, 1.2 eq.), tris(dibenzylideneacetone)dipalladium(0) (2.5 mol%), phosphine ligand (10 mol%) and base (4.0 eq.) were dissolved in dry and degassed DMF (4 mL) under argon atmosphere. The mixture was stirred for 19 h at the given temperature. Afterwards, the reaction was quenched with water (10 mL) and extracted with DCM (3 × 3 mL). The unified organic phases were repeatedly washed with 2M-HCl-solution (3 × 5 mL) and dried over MgSO₄. The solvents were removed under reduced pressure regularly giving an oil containing rests of DMF. Due to the volatile nature of the products, drying of the resulting oil in high vacuum was not performed.

The analysis of the crude products was performed by $^1\text{H-NMR}$ in CDCl_3 and independently prepared samples of 4-bromoanisole, 4-bromophenol, and 4-methoxy-*tert*-butylthiobenzene (*vide infra*) were used as external reference as shown in Figure S15. It should be noted, that the chemical shifts appeared sensitive to traces of DMF remaining in the crude products, so that the reference spectra were recorded in CDCl_3 containing 1% DMF.

General procedure for screening with other substrates. The respective educt (100 mg), *S-tert*-butylisothiuronium bromide (1.20 eq.), tris(dibenzylideneacetone)dipalladium(0) (2.5 mol%), triphenyl phosphine (10 mol%), and potassium *tert*-butanolate (4.0 eq.) were placed in a Schlenk tube and dissolved in 4 mL dry DMF. The reactions were stirred at the indicated reaction temperature and afterwards quenched by addition of 10 mL water and extracted with DCM (3×3 mL). The unified organic phases were repeatedly washed with 2M-HCl-solution (3×5 mL) and dried over MgSO_4 . The solvents were removed under reduced pressure regularly giving an oil containing rests of DMF. Due to the volatile nature of the products, drying of the resulting oil in high vacuum was not performed.

4. Conclusions

In this work, odorless *S-tert*-butylisothiuronium bromide is exploited as a surrogate for *tert*-butyl thiol for C-S cross coupling reactions yielding *tert*-butyl aryl thioethers. Interestingly, the ligand performance dropped with increasing steric congestions, though sterically demanding ligands are known to accelerate the often rate-determining reductive elimination. Therefore, the nucleophilic displacement step is assumed to be rate-determining in the present case. Accordingly, simple Ph_3P yields quantitative conversions, while more sophisticated ligands, including those of the biarylphosphine type, failed to provide sufficient reactivity. While the reaction conditions can be tuned even milder with aryl iodides, the presented procedure cannot be expanded to chloro- and fluoroarenes. With activated nitroarenes, however, thioetherification already occurs at room temperature but via an $\text{S}_{\text{N}}\text{Ar}$ reaction instead of a catalytic cross-coupling process. Based on this, efficient access to benzo[1,2-*d*;4,5-*d'*]bis[1,3]dithioles via C-S cross coupling of 1,2,4,5-tetrabromobenzene is established, outperforming the previous route via $\text{S}_{\text{N}}\text{Ar}$ -reactions. Additionally, the ease of thioketal formation was enhanced by using catalytic amounts of $\text{Sc}(\text{OTf})_3$ instead of stoichiometric amounts of less effective and hazardous Lewis-acids.

Supplementary Materials: The following are available online. NMR-spectra and mass spectrometric data can be found in the Supporting Information.

Author Contributions: Conceptualization, N.F. and O.S.; methodology, N.F.; investigation, K.K.; resources, O.S.; writing—original draft preparation, all authors; writing—review and editing, all authors; project administration, N.F.; funding acquisition, O.S. All authors have read and agreed to the published version of the manuscript.

Funding: This research received no external funding.

Conflicts of Interest: The authors declare no conflict of interest.

References

1. Wessig, P.; Freyse, D.; Schuster, D.; Kelling, A. Fluorescent Dyes with Large Stokes Shifts Based on Benzo[1,2-*d*:4,5-*d'*]Bis[1,3]Dithiole (“S4-DBD Dyes”). *Eur. J. Org. Chem.* **2020**, *2020*, 1732–1744. [[CrossRef](#)]
2. Hell, S.W.; Wichmann, J. Breaking the Diffraction Resolution Limit by Stimulated Emission: Stimulated-Emission-Depletion Fluorescence Microscopy. *Opt. Lett.* **1994**, *19*, 780. [[CrossRef](#)] [[PubMed](#)]
3. Dane, E.L.; King, S.B.; Swager, T.M. Conjugated Polymers That Respond to Oxidation with Increased Emission. *J. Am. Chem. Soc.* **2010**, *132*, 7758–7768. [[CrossRef](#)]
4. Reddy, T.J.; Iwama, T.; Halpern, H.J.; Rawal, V.H. General Synthesis of Persistent Trityl Radicals for EPR Imaging of Biological Systems. *J. Org. Chem.* **2002**, *67*, 4635–4639. [[CrossRef](#)] [[PubMed](#)]
5. Yang, Z.; Liu, Y.; Borbat, P.; Zweier, J.L.; Freed, J.H.; Hubbell, W.L. Pulsed ESR Dipolar Spectroscopy for Distance Measurements in Immobilized Spin Labeled Proteins in Liquid Solution. *J. Am. Chem. Soc.* **2012**, *134*, 9950–9952. [[CrossRef](#)] [[PubMed](#)]

6. Shevelev, G.Y.; Krumkacheva, O.A.; Lomzov, A.A.; Kuzhelev, A.A.; Rogozhnikova, O.Y.; Trukhin, D.V.; Troitskaya, T.I.; Tormyshev, V.M.; Fedin, M.V.; Pyshnyi, D.V.; et al. Physiological-Temperature Distance Measurement in Nucleic Acid Using Triarylmethyl-Based Spin Labels and Pulsed Dipolar EPR Spectroscopy. *J. Am. Chem. Soc.* **2014**, *136*, 9874–9877. [[CrossRef](#)]
7. Jassoy, J.J.; Heubach, C.A.; Hett, T.; Bernhard, F.; Haege, F.R.; Hagelueken, G.; Schiemann, O. Site Selective and Efficient Spin Labeling of Proteins with a Maleimide-Functionalized Trityl Radical for Pulsed Dipolar EPR Spectroscopy. *Molecules* **2019**, *24*, 2735. [[CrossRef](#)]
8. Yang, Y.; Pan, B.B.; Tan, X.; Yang, F.; Liu, Y.; Su, X.C.; Goldfarb, D. In-Cell Trityl-Trityl Distance Measurements on Proteins. *J. Phys. Chem. Lett.* **2020**, *11*, 1141–1147. [[CrossRef](#)]
9. Fleck, N.; Heubach, C.A.; Hett, T.; Haege, F.R.; Bawol, P.P.; Baltruschat, H.; Schiemann, O. SLIM: A Short-Linked, Highly Redox-Stable Trityl Label for High-Sensitivity In-Cell EPR Distance Measurements. *Angew. Chem. Int. Ed.* **2020**, *59*, 9767–9772. [[CrossRef](#)]
10. Jassoy, J.J.; Berndhäuser, A.; Duthie, F.; Kühn, S.P.; Hagelueken, G.; Schiemann, O. Versatile Trityl Spin Labels for Nanometer Distance Measurements on Biomolecules In Vitro and within Cells. *Angew. Chem. Int. Ed.* **2017**, *56*, 177–181. [[CrossRef](#)]
11. Epel, B.; Haney, C.R.; Hleihel, D.; Wardrip, C. Electron Paramagnetic Resonance Oxygen Imaging of a Rabbit Tumor Using Localized Spin Probe Delivery. *Med. Phys.* **2010**, *37*, 2553–2559. [[CrossRef](#)] [[PubMed](#)]
12. Bobko, A.A.; Dhimitruka, I.; Zweier, J.L.; Khramtsov, V.V. Trityl Radicals as Persistent Dual Function pH and Oxygen Probes for in Vivo Electron Paramagnetic Resonance Spectroscopy and Imaging: Concept and Experiment. *J. Am. Chem. Soc.* **2007**, *129*, 7240–7241. [[CrossRef](#)] [[PubMed](#)]
13. Bobko, A.A.; Dhimitruka, I.; Komarov, D.A.; Khramtsov, V.V. Dual-Function pH and Oxygen Phosphonated Trityl Probe. *Anal. Chem.* **2012**, *84*, 6054–6060. [[CrossRef](#)] [[PubMed](#)]
14. Poncelet, M.; Driesschaert, B. A ¹³C-labelled Triarylmethyl Radical as an EPR Spin Probe Highly Sensitive to Molecular Tumbling. *Angew. Chem. Int. Ed.* **2020**. accepted article. [[CrossRef](#)]
15. Mathies, G.; Caporini, M.A.; Michaelis, V.K.; Liu, Y.; Hu, K.N.; Mance, D.; Zweier, J.L.; Rosay, M.; Baldus, M.; Griffin, R.G. Efficient Dynamic Nuclear Polarization at 800 MHz/527 GHz with Trityl-Nitroxide Biradicals. *Angew. Chem. Int. Ed.* **2015**, *54*, 11770–11774. [[CrossRef](#)]
16. Ardenkjær-Larsen, J.H.; Fridlund, B.; Gram, A.; Hansson, G.; Hansson, L.; Lerche, M.H.; Servin, R.; Thaning, M.; Golman, K. Increase in Signal-to-Noise Ratio of >10,000 Times in Liquid-State NMR. *PNAS* **2003**, *100*, 10158–10163. [[CrossRef](#)]
17. Fleck, N.; Hett, T.; Brode, J.; Meyer, A.; Richert, S.; Schiemann, O. C–C Cross-Coupling Reactions of Trityl Radicals: Spin Density Delocalization, Exchange Coupling, and a Spin Label. *J. Org. Chem.* **2019**, *84*, 3293–3303. [[CrossRef](#)]
18. Nolden, O.; Fleck, N.; Lorenzo, E.R.; Wasielewski, M.R.; Schiemann, O.; Gilch, P.; Richert, S. Excitation energy transfer and exchange-mediated quartet state formation in porphyrin-trityl systems. *Chem. Eur. J.* **2020**. accepted article. [[CrossRef](#)]
19. Dirk, C.W.; Cox, S.D.; Wellman, D.E.; Wudl, F. Isolation and Purification of Benzene-1,2,4,5-Tetrathiol. *J. Org. Chem.* **1985**, *50*, 2395–2397. [[CrossRef](#)]
20. Hintz, H.; Vanas, A.; Klose, D.; Jeschke, G.; Godt, A. Trityl Radicals with a Combination of the Orthogonal Functional Groups Ethyne and Carboxyl: Synthesis without a Statistical Step and EPR Characterization. *J. Org. Chem.* **2019**, *84*, 3304–3320. [[CrossRef](#)]
21. Devos, M.; Patte, F.; Rouault, J.; Laffort, P.; Van Gemert, L.J. *Human Olfactory Thresholds*; Oxford University Press: Oxford, UK, 1990.
22. Müller, D.; Adelsberger, K.; Imming, P. Organic Preparations with Molar Amounts of Volatile Malodorous Thiols. *Synth. Commun.* **2013**, *43*, 1447–1454. [[CrossRef](#)]
23. Hartwig, J.F. Carbon–Heteroatom Bond-Forming Reductive Eliminations of Amines, Ethers, and Sulfides. *Acc. Chem. Res.* **1998**, *31*, 852–860. [[CrossRef](#)]
24. Xu, J.; Liu, R.Y.; Yeung, C.S.; Buchwald, S.L. Monophosphine Ligands Promote Pd-Catalyzed C–S Cross-Coupling Reactions at Room Temperature with Soluble Bases. *ACS Catal.* **2019**, *9*, 6461–6466. [[CrossRef](#)]
25. Migita, T.; Shimizu, T.; Asami, Y.; Shiobara, J.; Kato, Y.; Kosugi, M. The Palladium Catalyzed Nucleophilic Substitution of Aryl Halides by Thiolate Anions. *Bull. Chem. Soc. Jpn.* **1980**, *53*, 1385–1389. [[CrossRef](#)]

26. Itoh, T.; Mase, T. A General Palladium-Catalyzed Coupling of Aryl Bromides/Triflates and Thiols. *Org. Lett.* **2004**, *6*, 4587–4590. [[CrossRef](#)]
27. Fernández-Rodríguez, M.A.; Shen, Q.; Hartwig, J.F. A General and Long-Lived Catalyst for the Palladium-Catalyzed Coupling of Aryl Halides with Thiols. *J. Am. Chem. Soc.* **2006**, *128*, 2180–2181. [[CrossRef](#)]
28. Fernández-Rodríguez, M.A.; Hartwig, J.F. A General, Efficient, and Functional-Group-Tolerant Catalyst System for the Palladium-Catalyzed Thioetherification of Aryl Bromides and Iodides. *J. Org. Chem.* **2009**, *74*, 1663–1672. [[CrossRef](#)]
29. Murata, M.; Buchwald, S.L. A General and Efficient Method for the Palladium-Catalyzed Cross-Coupling of Thiols and Secondary Phosphines. *Tetrahedron* **2004**, *60*, 7397–7403. [[CrossRef](#)]
30. Park, N.; Park, K.; Jang, M.; Lee, S. One-Pot Synthesis of Symmetrical and Unsymmetrical Aryl Sulfides by Pd-Catalyzed Couplings of Aryl Halides and Thioacetates. *J. Org. Chem.* **2011**, *76*, 4371–4378. [[CrossRef](#)]
31. Wang, L.; Zhou, W.-Y.; Chen, S.-C.; He, M.-Y.; Chen, Q. A Highly Efficient Palladium-Catalyzed One-Pot Synthesis of Unsymmetrical Aryl Alkyl Thioethers under Mild Conditions in Water. *Adv. Synth. Catal.* **2012**, *354*, 839–845. [[CrossRef](#)]
32. Bowman, R.W.; Burchell, C.J.; Kilian, P.; Slawin, A.M.Z.; Wormald, P.; Woollins, J.D. Investigations on Organo-Sulfur-Nitrogen Rings and the Thiocyanogen Polymer, (SCN)_x. *Chem. Eur. J.* **2006**, *12*, 6366–6381. [[CrossRef](#)] [[PubMed](#)]
33. Masquelin, T.; Delgado, Y.; Baumlé, V. A facile preparation of a combinatorial library of 2, 6-disubstituted triazines. *Tet. Lett.* **1998**, *39*, 5725–5726. [[CrossRef](#)]
34. Urquhart, G.; Gates, J.; Connor, R. n-Dodecyl (lauryl) mercaptane. *Org. Synth.* **1941**, *21*, 36. [[CrossRef](#)]
35. Luzzio, F.A. Decomposition of S-Alkylisothiuronium Salts Under Anhydrous Conditions - Application to a Facile Preparation of Nonsymmetrical Dialkyl Sulfides. *Synth. Commun.* **1984**, *14*, 209–214. [[CrossRef](#)]
36. Sprague, J.M.; Johnson, T.B. The Preparation of Alkyl Sulfonyl Chlorides from Isothioureas. *J. Am. Chem. Soc.* **1937**, *59*, 1837–1840. [[CrossRef](#)]
37. Stevens, H.P. IX—Thiocarbamide Hydrochloride. *J. Chem. Soc. Trans.* **1902**, *81*, 79–81. [[CrossRef](#)]
38. Feutrill, G.; Mirrington, R. Reactions with Thioethoxide Ion in Dimethylformamide. Selective Demethylation of Aryl Methyl Ethers. *Aust. J. Chem.* **1972**, *25*, 1719. [[CrossRef](#)]
39. Hartwig, J.F. *Organotransition Metal. Chemistry. From Bonding to Catalysis*; University Science Books: Mill Valley, CA, USA, 2010.
40. Labban, A.K.S.; Marcus, Y. The Solubility and Solvation of Salts in Mixed Nonaqueous Solvents. 1. Potassium Halides in Mixed Aprotic Solvents. *J. Solution Chem.* **1991**, *20*, 221–232. [[CrossRef](#)]
41. Niemeyer, Z.L.; Milo, A.; Hickey, D.P.; Sigman, M.S. Parameterization of Phosphine Ligands Reveals Mechanistic Pathways and Predicts Reaction Outcomes. *Nat. Chem.* **2016**, *8*, 610–617. [[CrossRef](#)]
42. Birkholz, M.N.; Freixa, Z.; Van Leeuwen, P. Bite Angle Effects of Diphosphines in C–C and C–X Bond Forming Cross Coupling Reactions. *Chem. Soc. Rev.* **2009**, *38*, 1099–1118. [[CrossRef](#)]
43. Dickens, M.J.; Gilday, J.P.; Mowlem, T.J.; Wddowson, D.A. Transition metal mediated thiation of aromatic rings. *Tetrahedron* **1991**, *47*, 8621–8634. [[CrossRef](#)]
44. Masato, Y.; Sakauchi, N.; Sato, A. Iminopyridine Derivates and Use Thereof. Patent WO 2009131245, 29 October 2009.
45. Xuelei, Y.; Zhulun, W.; Athena, S.; Cardozo, M.; DeGraffenreid, M.; Di, Y.; Fan, P.; He, X.; Jaen, J.C.; Labelle, M.; et al. The synthesis and SAR of novel diarylsulfone 11β-HSD1 inhibitors. *Bioorg. Med. Chem. Lett.* **2010**, *20*, 7071–7075. [[CrossRef](#)]
46. Rogozhnikova, O.Y.; Vasiliev, V.G.; Troitskaya, T.I.; Trukhin, D.V.; Mikhulina, T.V.; Halpern, H.J.; Tormyshev, V.M. Generation of Trityl Radicals by Nucleophilic Quenching of Tris(2,3,5,6-Tetrathiaaryl)-methyl Cations and Practical and Convenient Large-Scale Synthesis of Persistent Tris(4-Carboxy-2,3,5,6-Tetrathiaaryl)Methyl Radical. *Eur. J. Org. Chem.* **2013**, *2013*, 3347–3355. [[CrossRef](#)] [[PubMed](#)]

Sample Availability: Samples of the compounds are not available from the authors.



© 2020 by the authors. Licensee MDPI, Basel, Switzerland. This article is an open access article distributed under the terms and conditions of the Creative Commons Attribution (CC BY) license (<http://creativecommons.org/licenses/by/4.0/>).

SUPPORTING INFORMATION

Improved odorless access to benzo[1,2-d;4,5-d']bis[1,3]dithioles and *tert*-butyl arylsulfides via C-S cross coupling

Kevin Kopp, Olav Schiemann, Nico Fleck*

Institute of Physical and Theoretical Chemistry, University of Bonn, Wegelerstr. 12, 53115 Bonn, Germany.

*E-Mail: *fleck@pc.uni-bonn.de*

Table of Contents

1. Analytical data of products.....	3
1.1 NMR spectroscopy	3
1.2 Mass spectrometry.....	8
2. Condition screening.....	12
2.2 ¹ H-NMR data.....	14
3 Literature	27

1. Analytical data of products

1.1 NMR spectroscopy

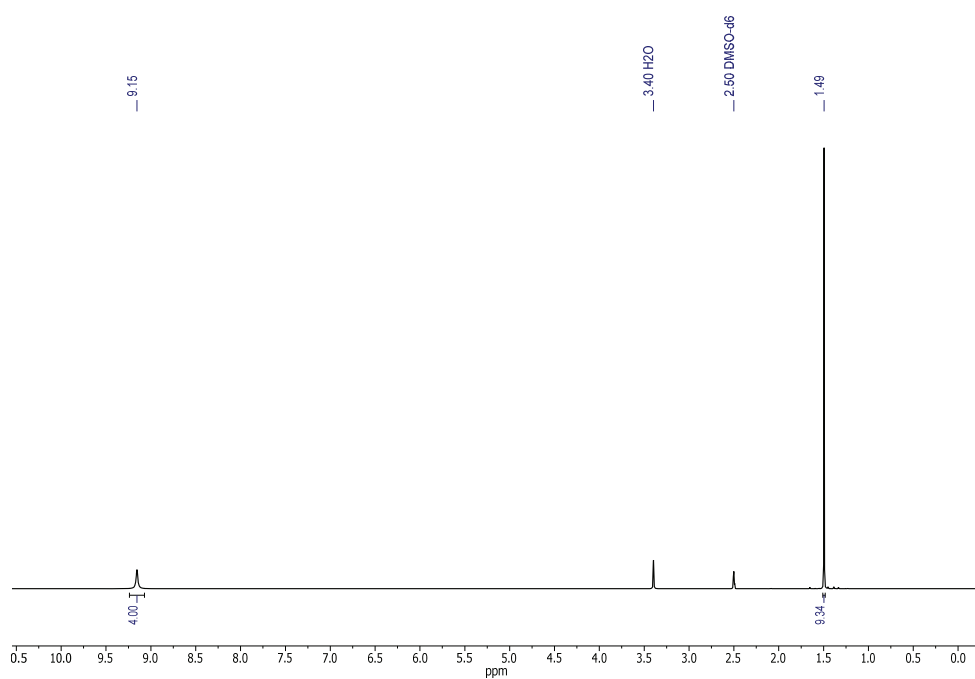


Figure S1. ¹H-NMR (400 MHz, 298 K, DMSO-d₆) spectrum of *S*-*tert*-butyl isothiuronium bromide **6**.

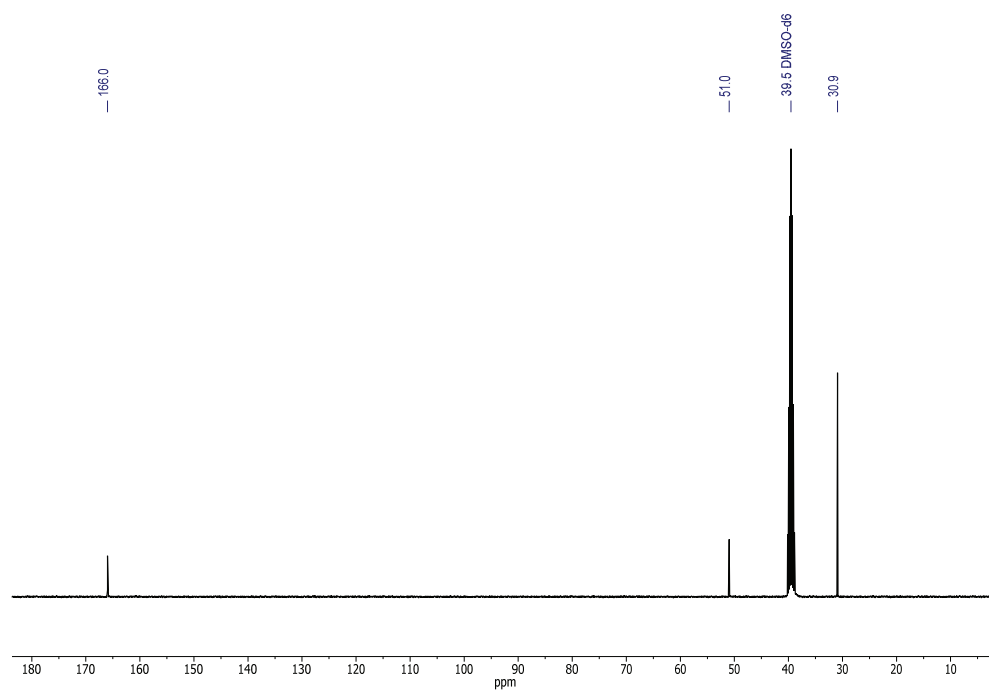


Figure S2. ¹³C-NMR (100 MHz, 298 K, DMSO-d₆) of *S*-*tert*-butyl isothiuronium bromide **6**.

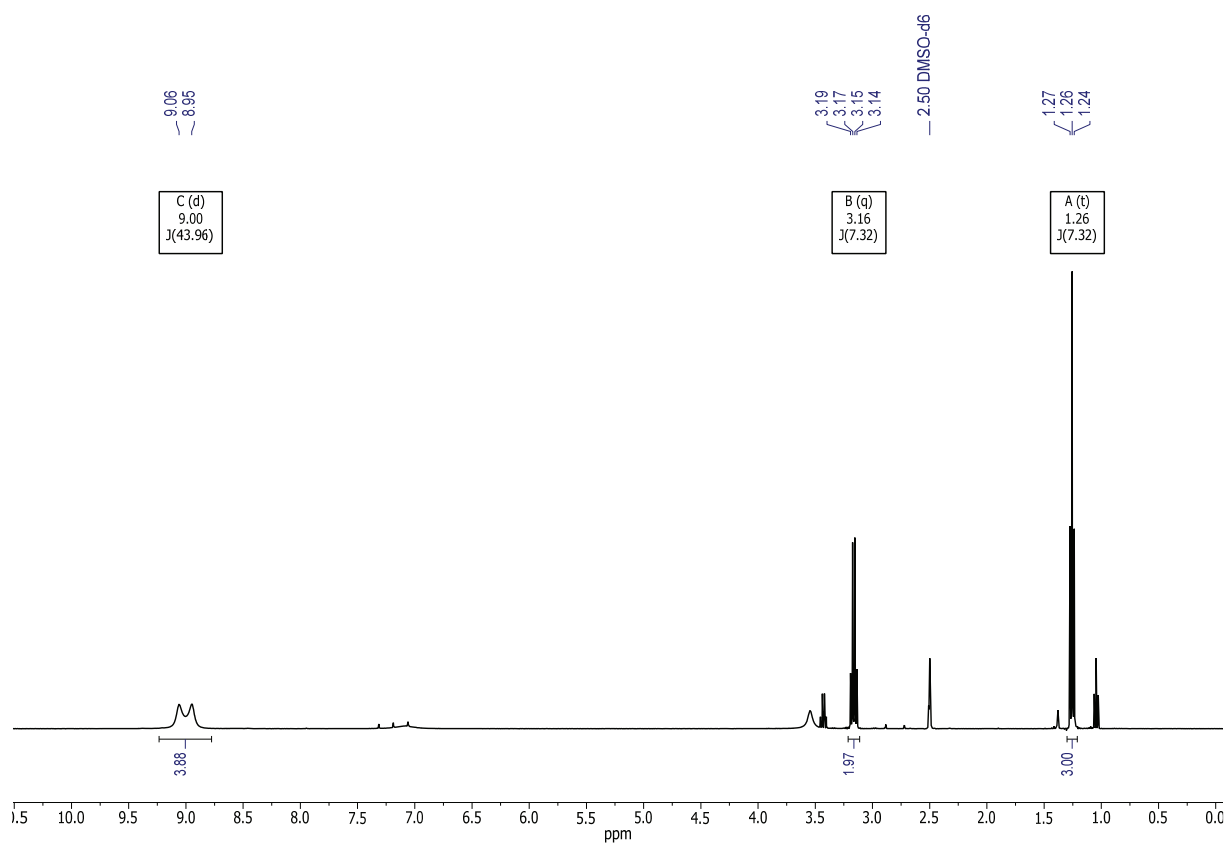


Figure S3. $^1\text{H-NMR}$ (400 MHz, 298 K, DMSO- d_6) of reaction 2.1 when using EtOH as solvent.

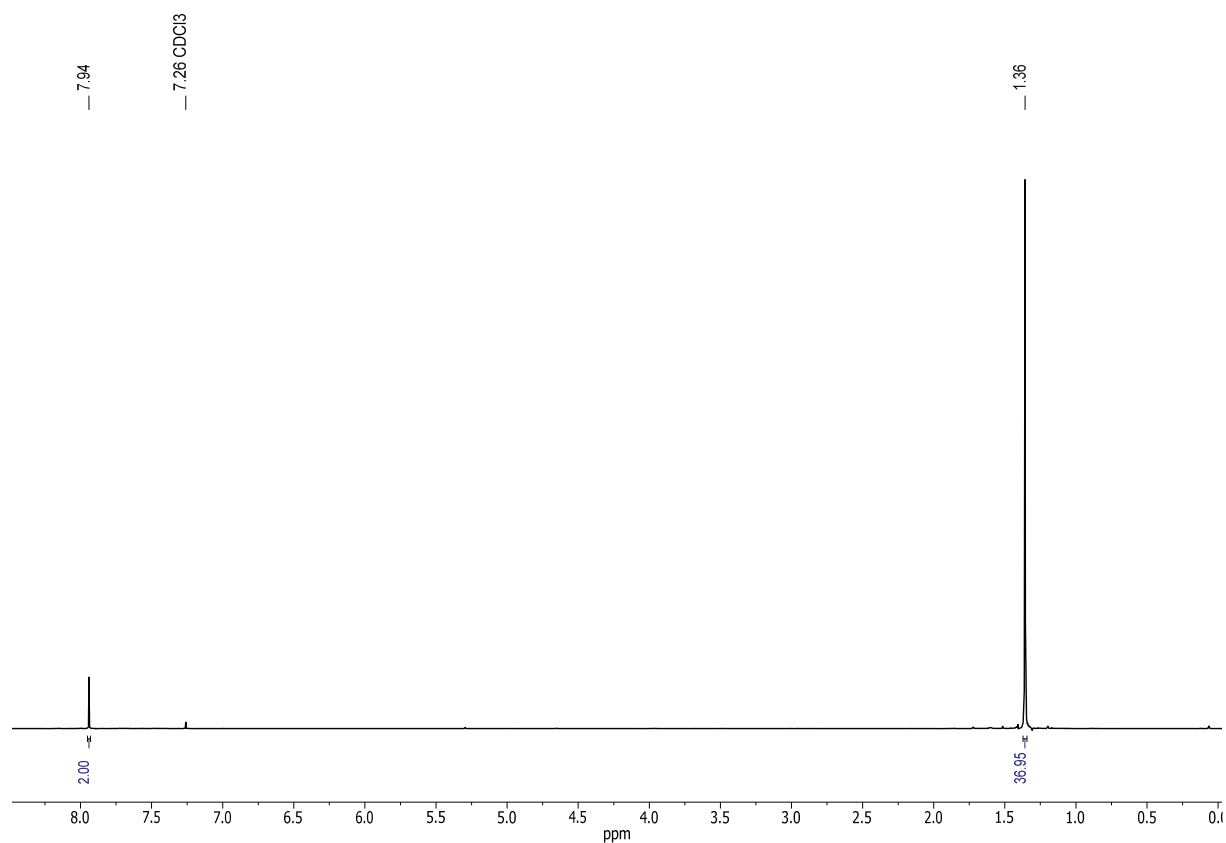


Figure S4. $^1\text{H-NMR}$ (400 MHz, 298 K, CDCl_3) of 1,2,4,5-Tetrakis(*tert*-butylthio)benzene **5**.

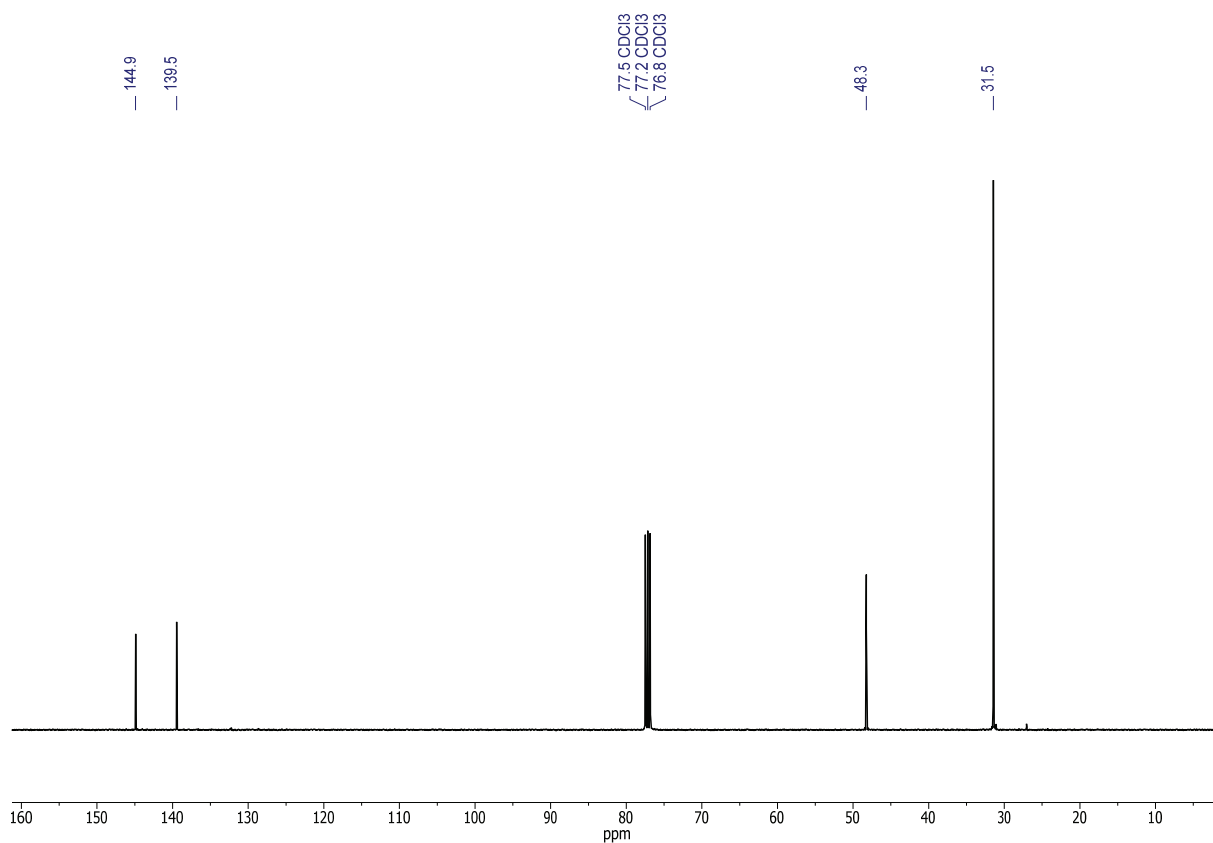


Figure S5. ¹³C-NMR (100 MHz, 298 K, CDCl₃) of 1,2,4,5-Tetrakis(*tert*-butylthio)benzene **5**.

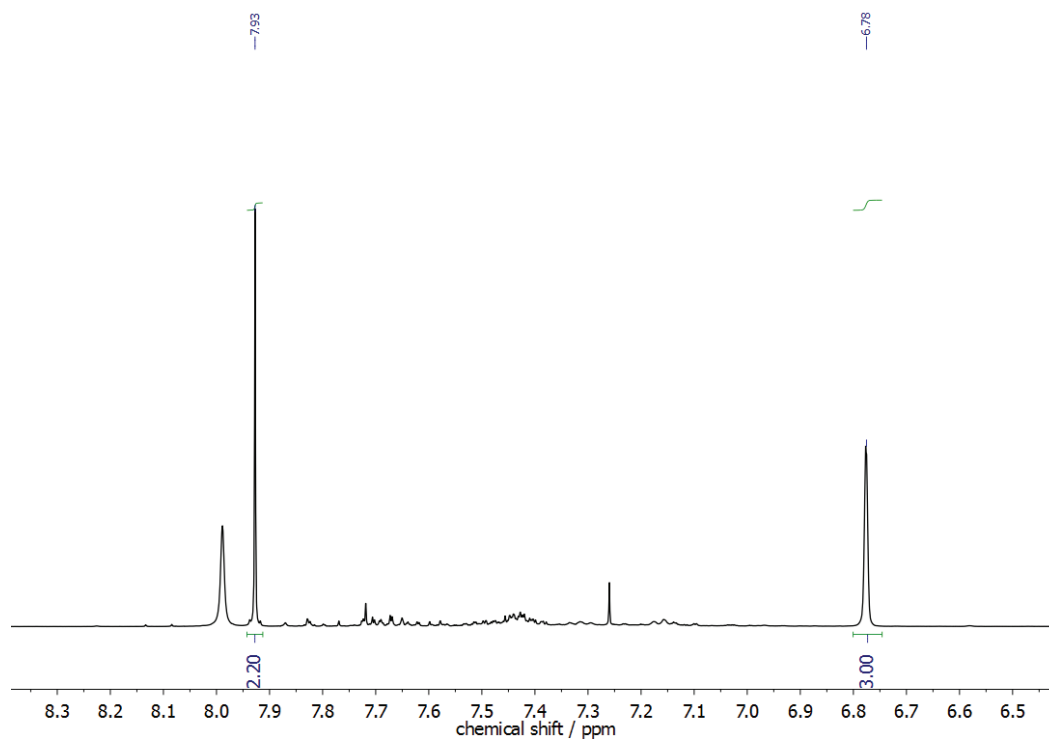


Figure S6. ¹H-NMR (400 MHz, 298 K, CDCl₃) of the reaction mixture converting 1,2,4,5-tetrabromobenzene to **5** containing mesitylene as an internal standard.

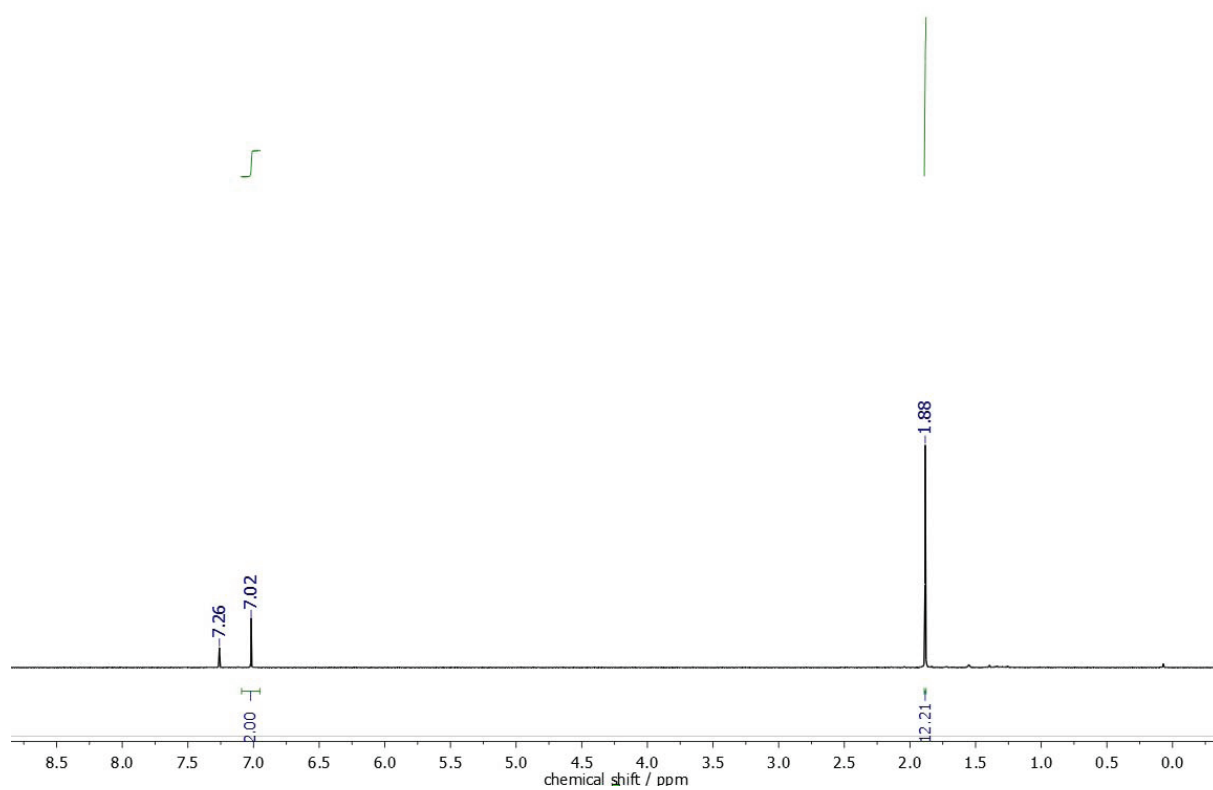


Figure S7. $^1\text{H-NMR}$ (400 MHz, 298 K, CDCl_3) of **1a**.

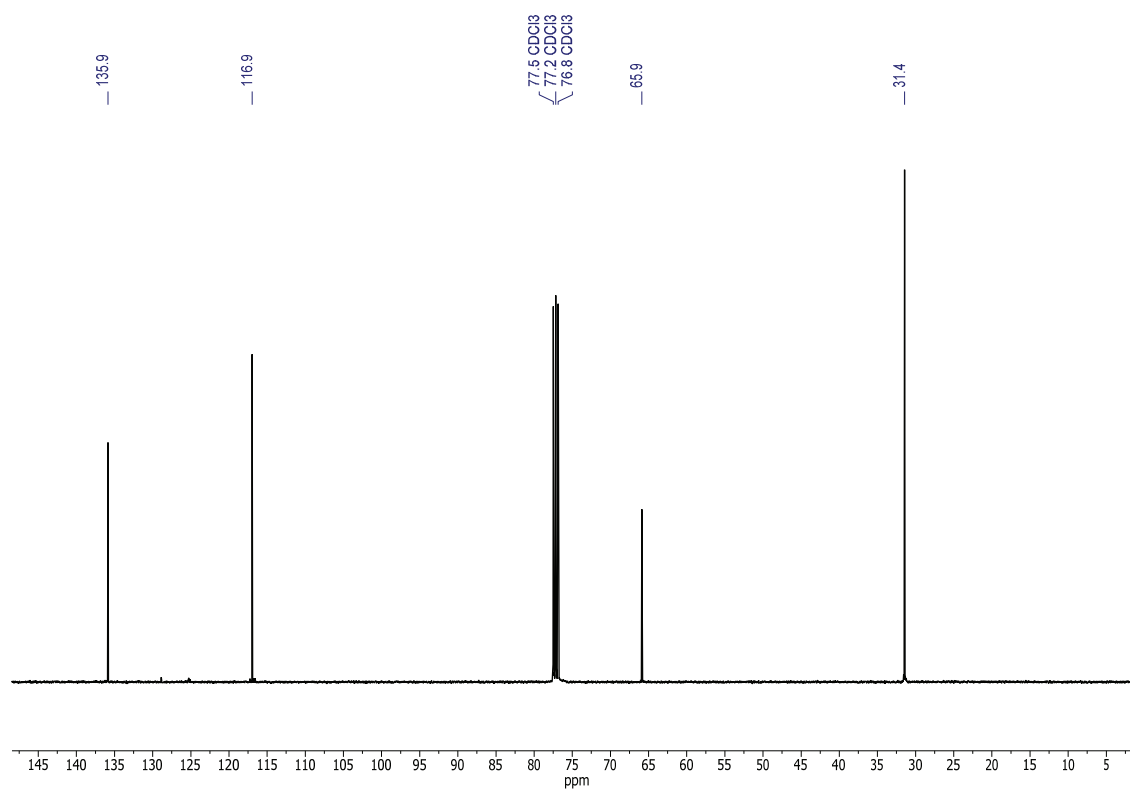


Figure S8. $^{13}\text{C-NMR}$ (100 MHz, 298 K, CDCl_3) of **1a**.

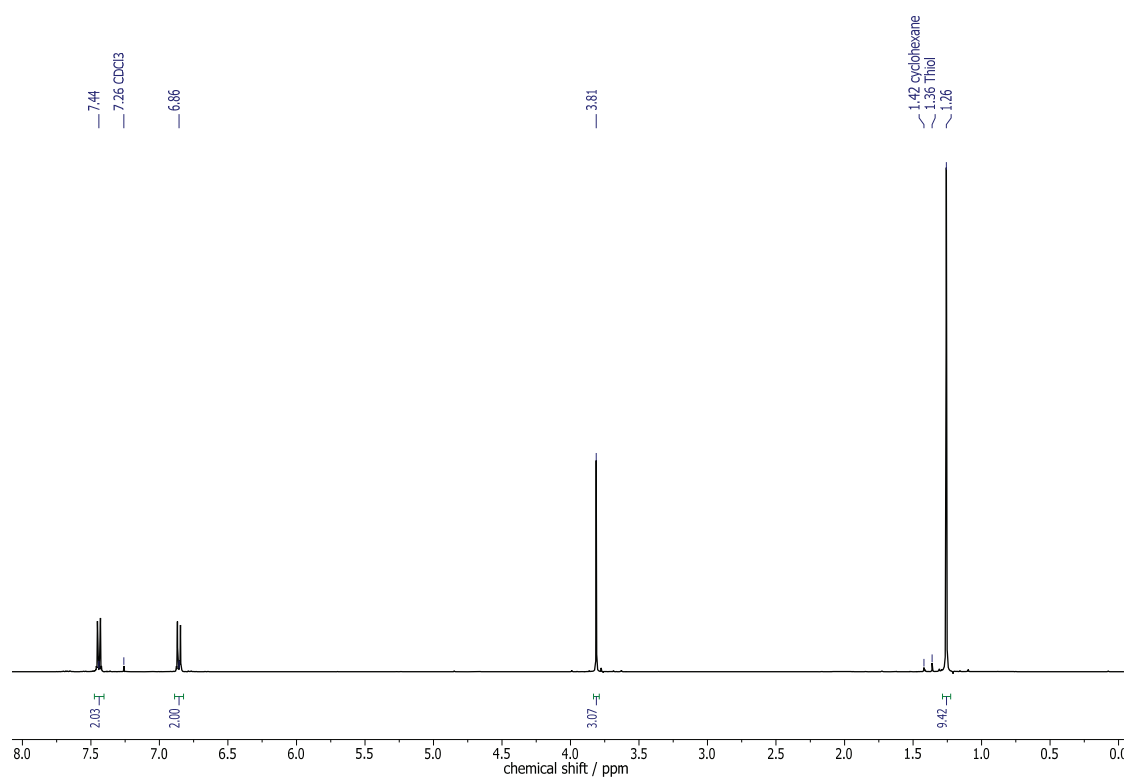


Figure S9. ¹H-NMR (400 MHz, 298 K, CDCl₃) of 4-methoxy-*tert*-butylthiobenzene **7**.

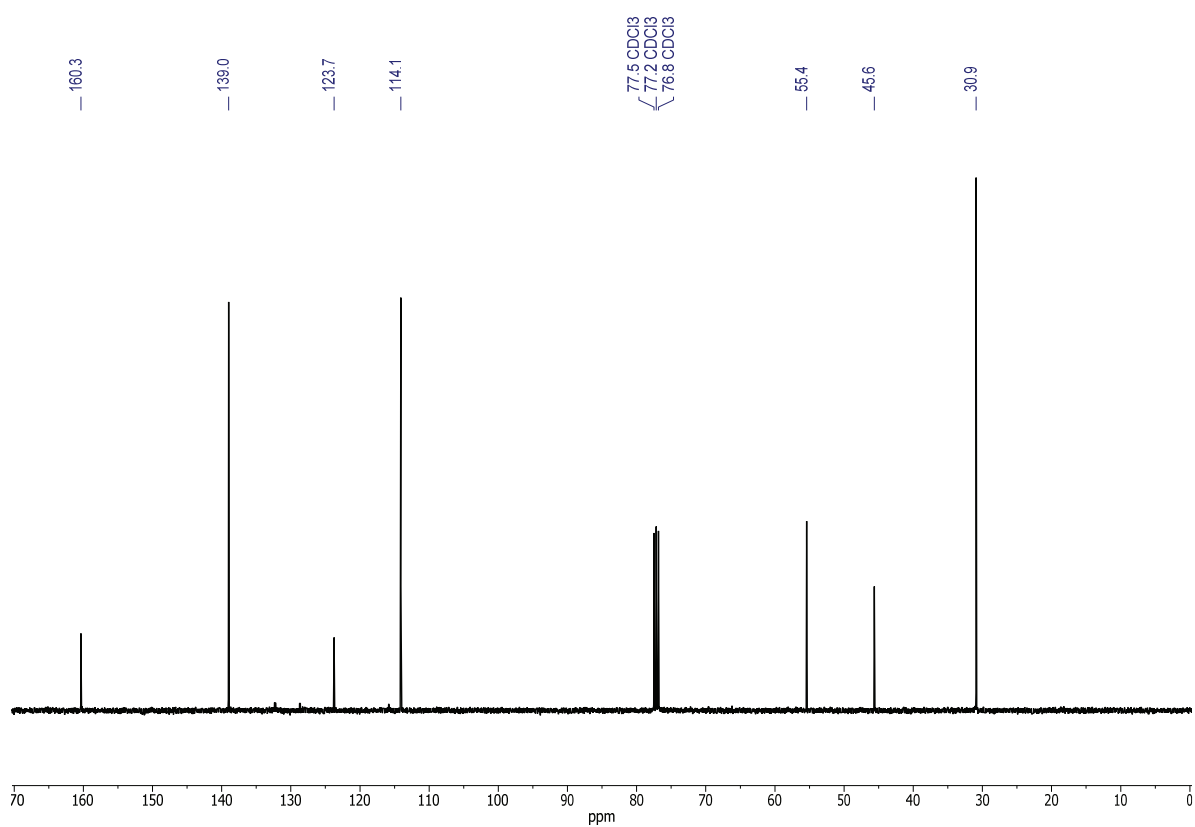


Figure S10. ¹³C-NMR of 4-methoxy-*tert*-butylthiobenzene **7**.

1.2 Mass spectrometry

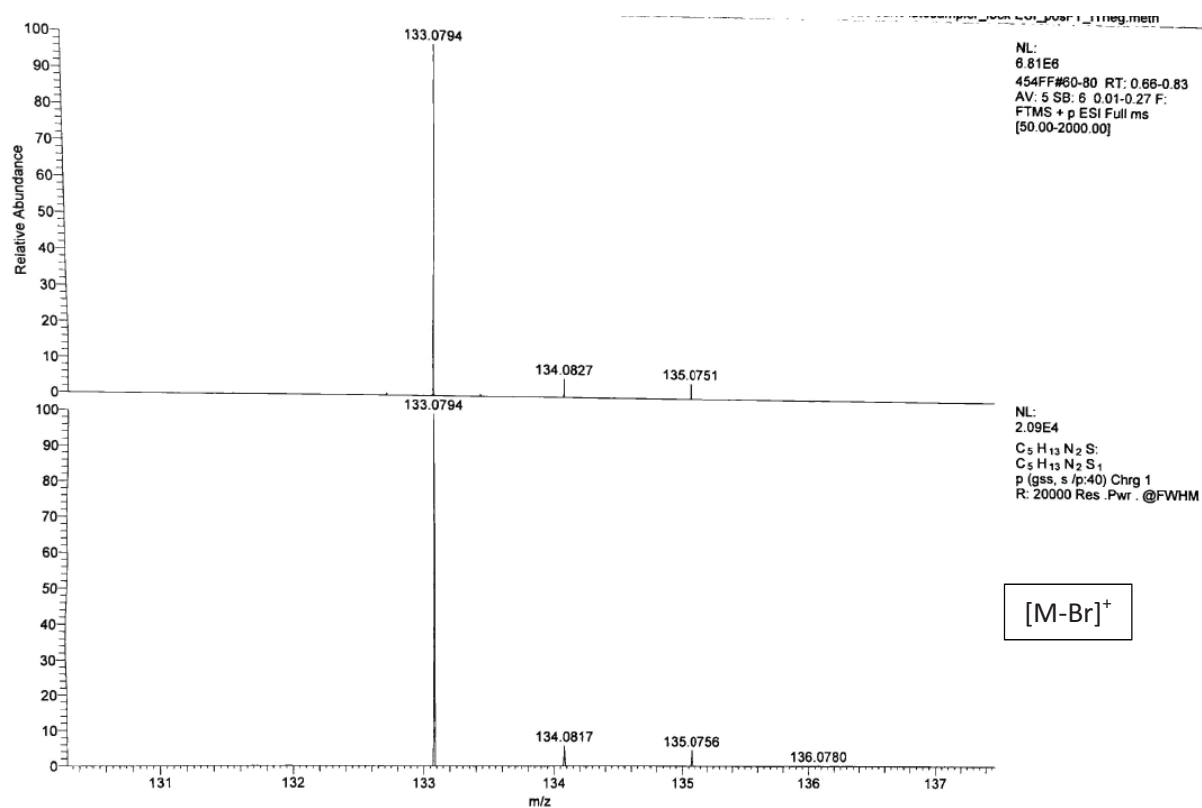
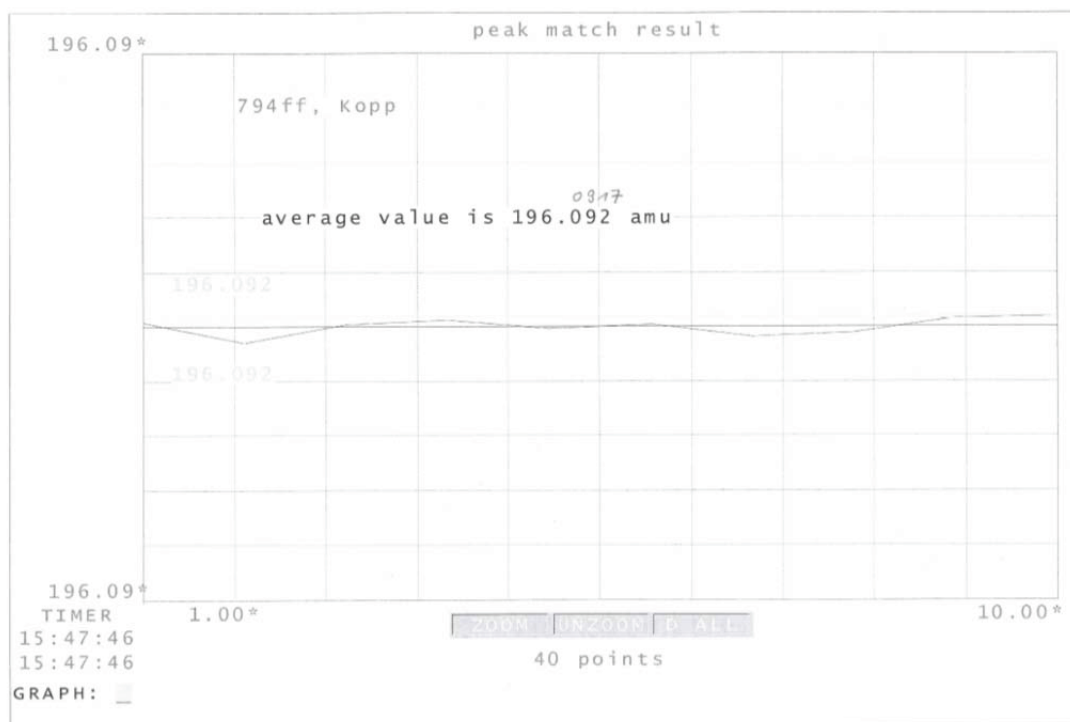
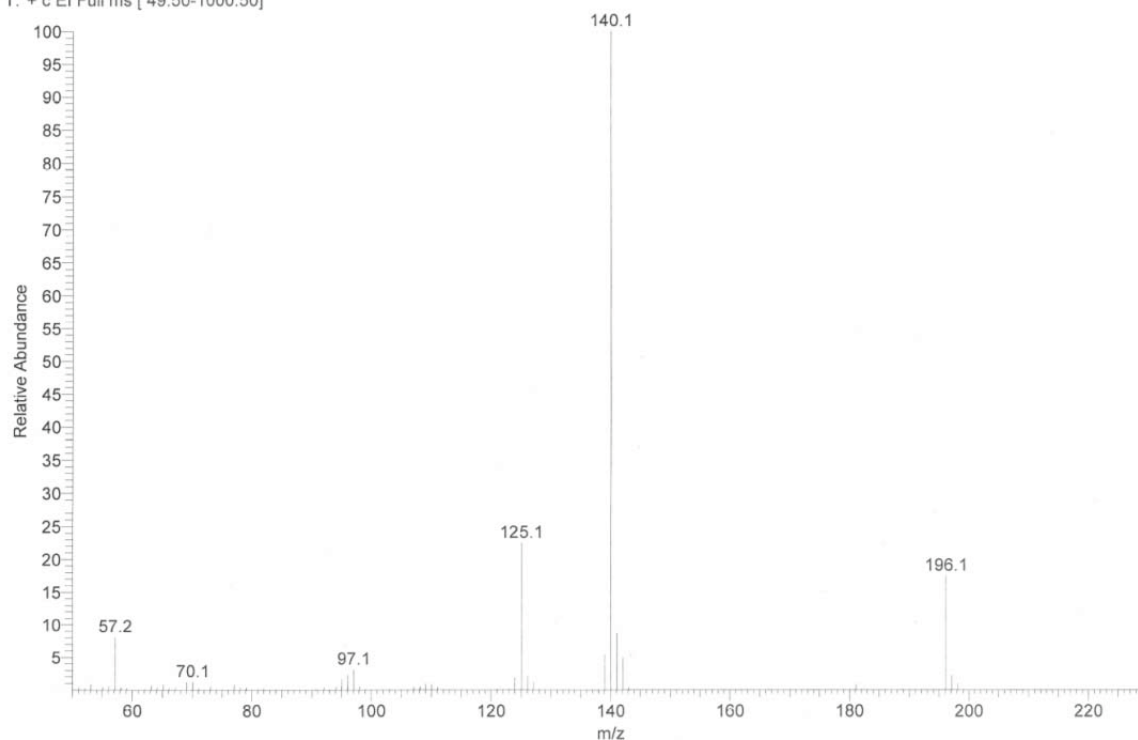


Figure S11. ESI(+)-MS (top) of S-*tert*-butyl isothiuronium bromide **6** and calculated isotope pattern (bottom).

794ff #8 RT: 0.52 AV: 1 NL: 9.31E6
T: + c EI Full ms [49.50-1000.50]



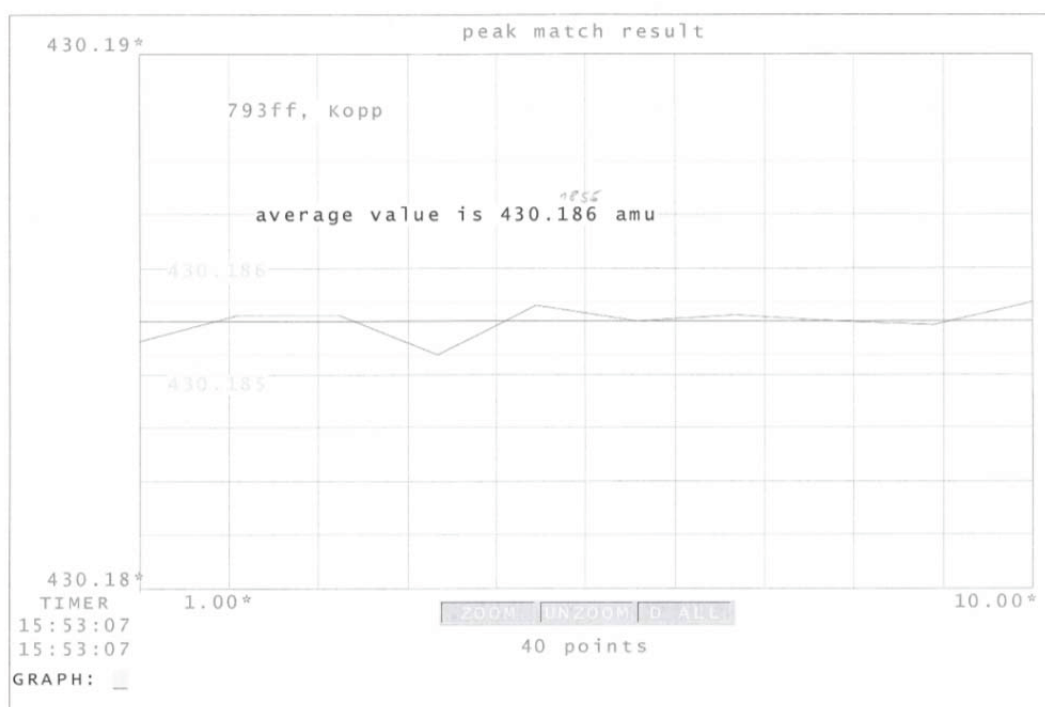
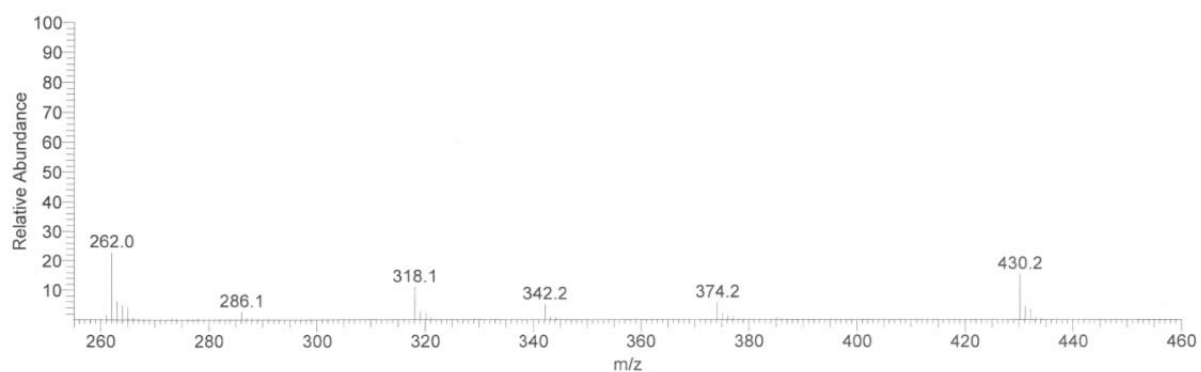
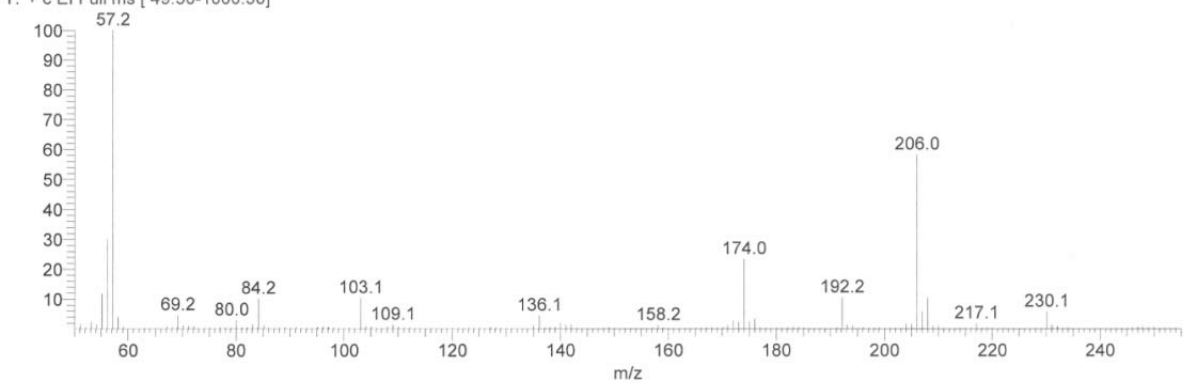
7/14/2020 3:48:10 PM

THERMO-PC

MAT 95 XP

Figure S12. EI(+)-MS (top) of 4-methoxy-*tert*-butylthiobenzene **7** and average value of exact mass (bottom).

793ff #16 RT: 1.11 AV: 1 NL: 3.20E7
T: + c EI Full ms [49.50-1000.50]



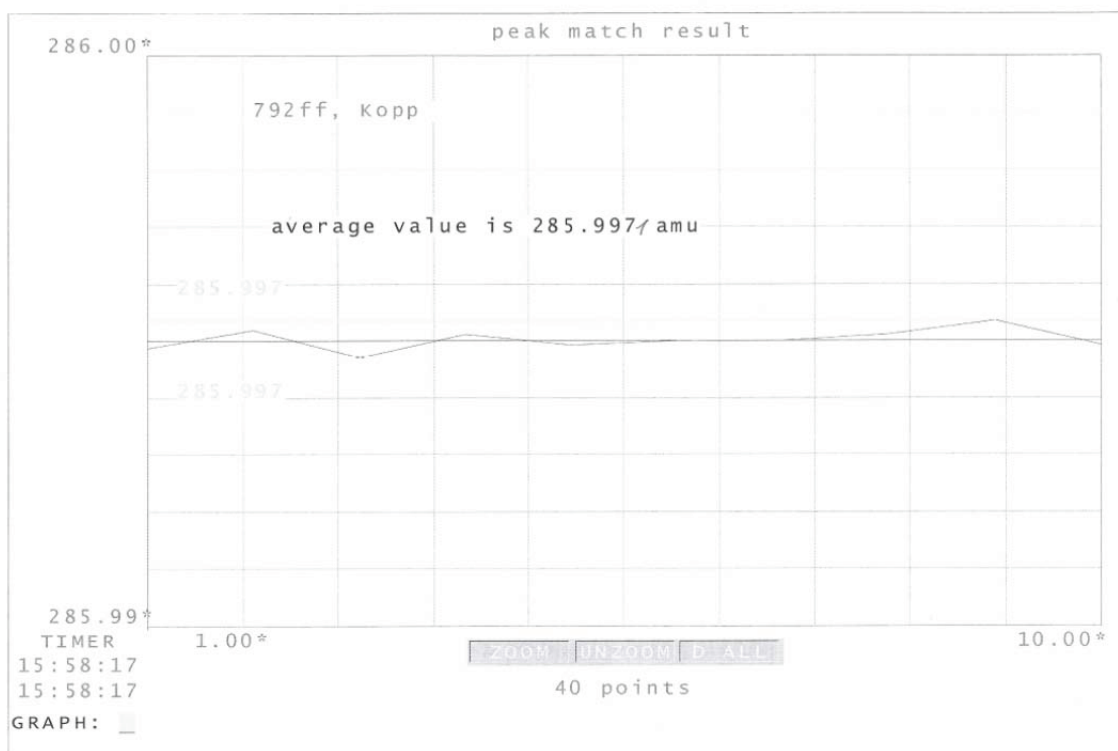
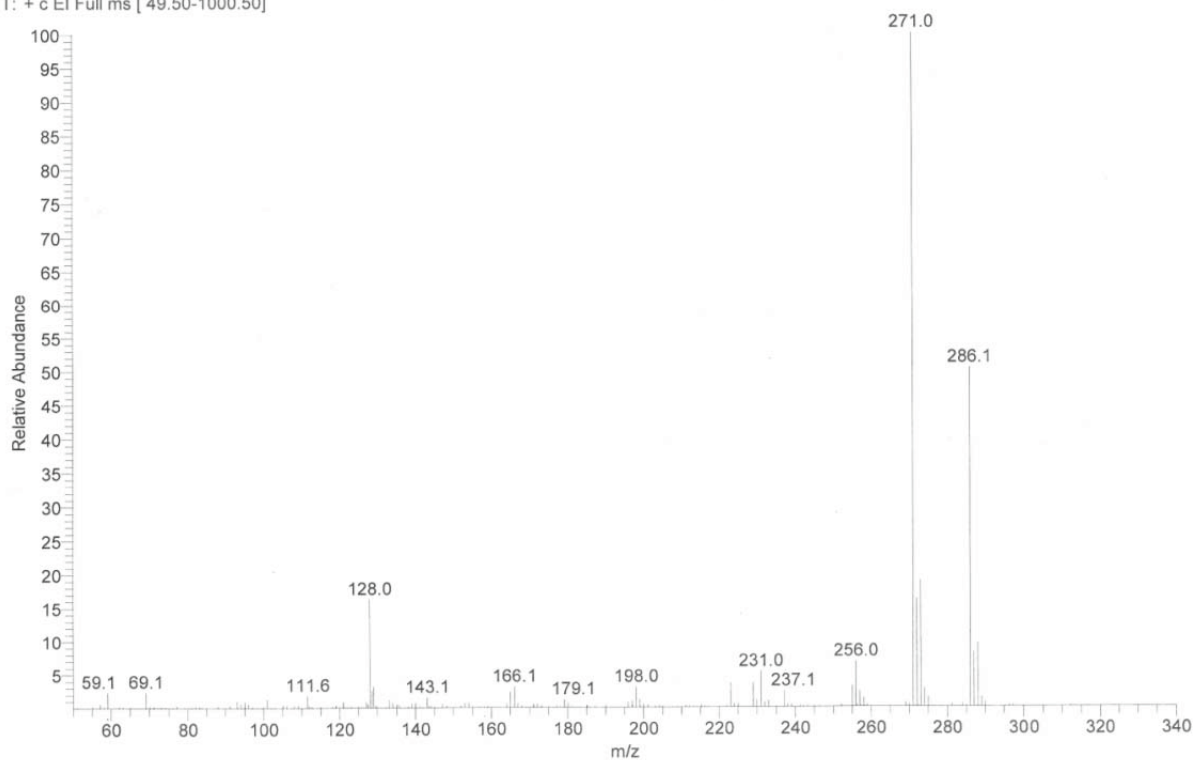
7/14/2020 3:53:28 PM

THERMO-PC

MAT 95 XP

Figure S13. EI(+)-MS (top) of 1,2,4,5-tetrakis(*tert*-butylthio)benzene **5** and average value of exact mass (bottom).

792ff #9 RT: 0.63 AV: 1 NL: 2.61E6
T: + c EI Full ms [49.50-1000.50]



7/14/2020 3:58:34 PM

THERMO-PC

MAT 95 XP

Figure S14. EI(+)-MS (top) of **1a** and average value of exact mass (bottom).

2. Condition screening

Screening of conditions with other substrates

The analysis of the reaction mixtures was carried out via $^1\text{H-NMR}$, products were identified via comparison of literature values for 1,4-bis(*tert*-butylthio)benzene⁴, 4-chlorophenol⁵, 4-fluorophenol⁶, and 4-(*tert*-butylthio)nitrobenzene⁷.

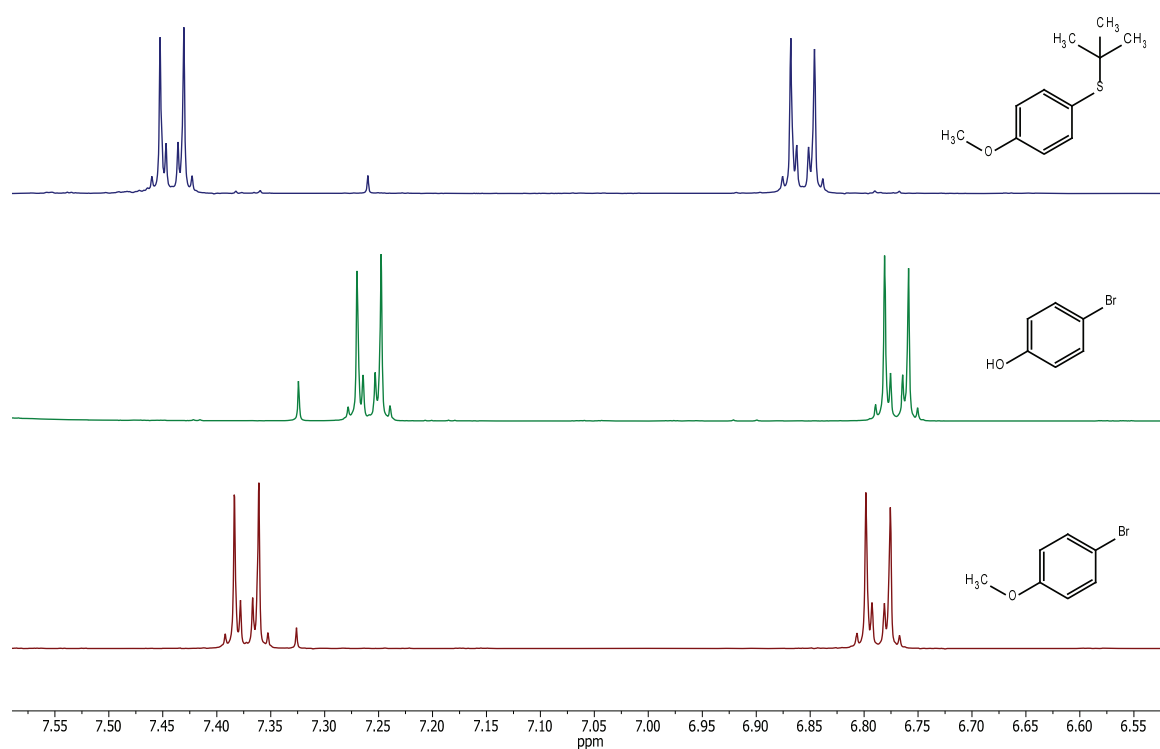


Figure S15. Reference spectra of 4-bromoanisole (bottom), 4-bromophenol (middle) and 4-methoxy-*tert*-butylthiobenzene (top).

Table S1. Reaction conditions.

Reaction No.	Temperature [°C]	ligand	base	Solvent
1	50	Ph ₃ P	KO ^t Bu	DMF
2	50	XPhos	KO ^t Bu	DMF
3	50	Xantphos	KO ^t Bu	DMF

4	80	Ph ₃ P	KO ^t Bu	DMF
5	80	XPhos	KO ^t Bu	DMF
6	80	Xantphos	KO ^t Bu	DMF
7	80	dppf	KO ^t Bu	DMF
8	80	SPhos	KO ^t Bu	DMF
9	80	BrettPhos	KO ^t Bu	DMF
10	80	ⁿ Bu ₃ P	KO ^t Bu	DMF
11	80	none	KO ^t Bu	DMF
12 [*]	80	none	KO ^t Bu	DMF
13 [*]	80	SPhos	KO ^t Bu	DMF
14	80	Ph ₃ P	KO ^t Bu	ⁿ BuOH
15	80	Ph ₃ P	K ₂ CO ₃	DMF
16	80	Ph ₃ P	Cs ₂ CO ₃	DMF
17	80	Ph ₃ P	K ₃ PO ₄	DMF
18 ^{**}	80	Ph ₃ P	KO ^t Bu	DMF
19 ^{***}	80	Ph ₃ P	K ₂ CO ₃	DMF
20 ^{***}	80	Ph ₃ P	K ₃ PO ₄	DMF

* without Pd₂dba₃. ** reduced amounts of base to 2.4 eq. *** addition of 10mol% of 18-C-6.

2.2 $^1\text{H-NMR}$ data

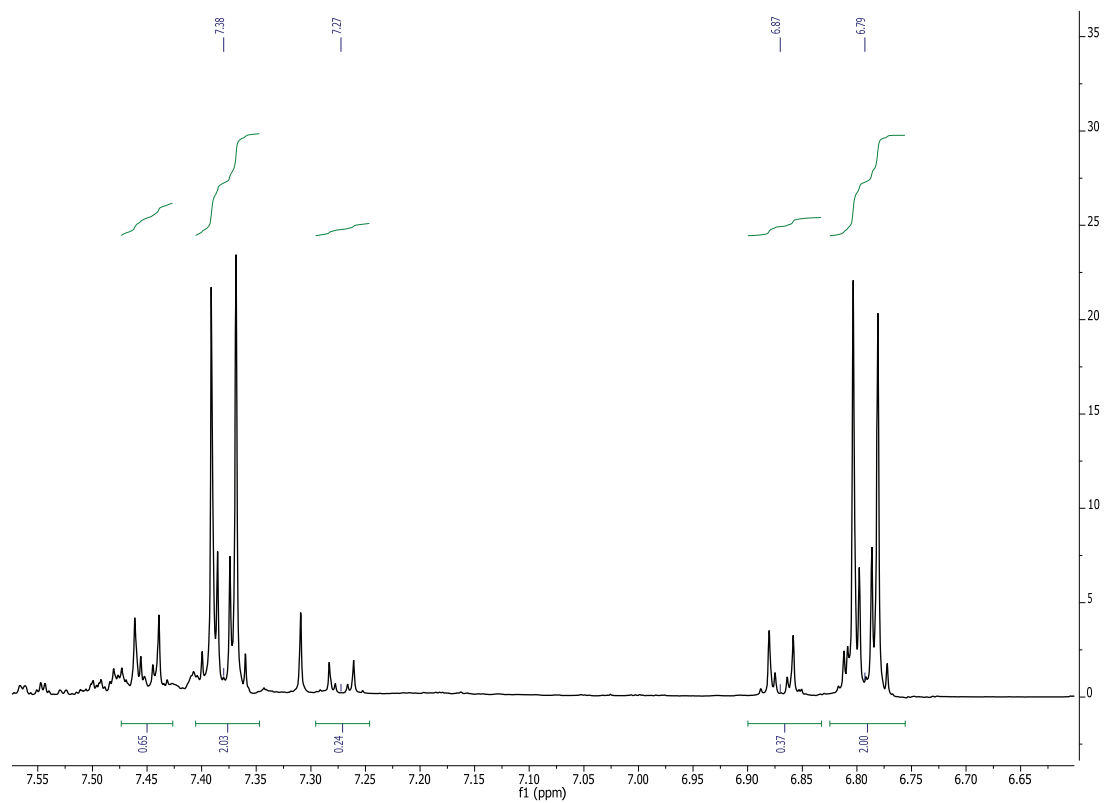


Figure S16. $^1\text{H-NMR}$ (400 MHz, 298 K, CDCl_3) of reaction 1.

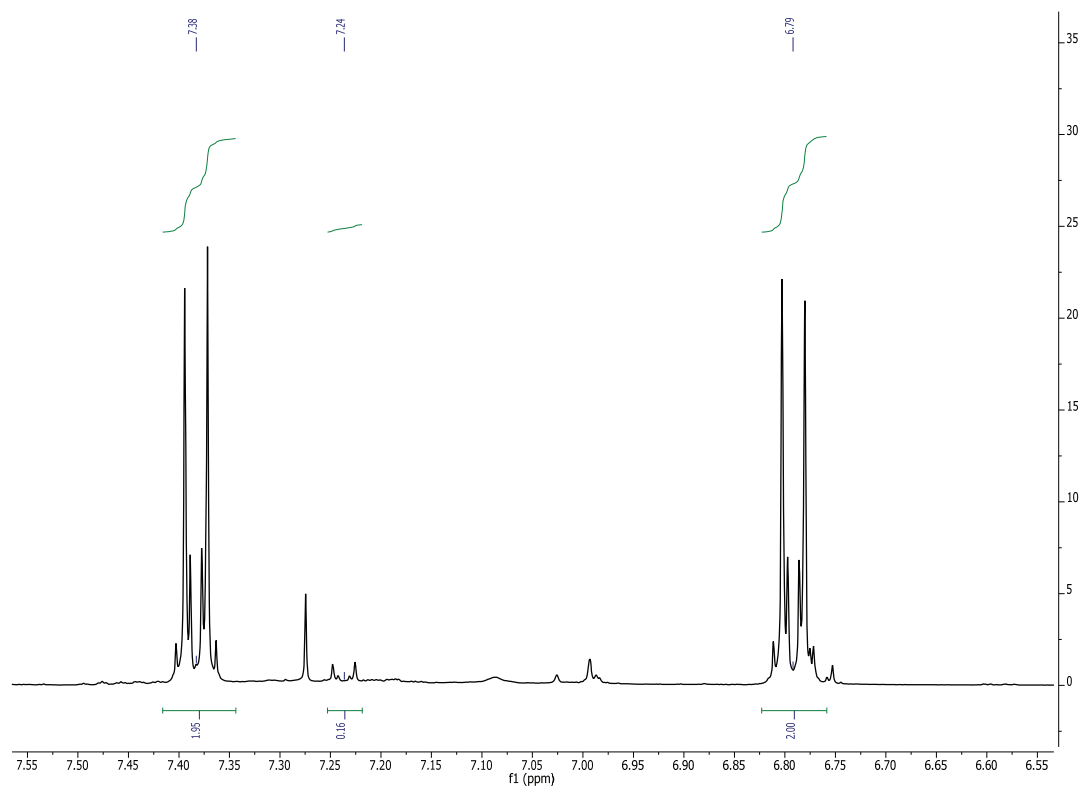


Figure S17. $^1\text{H-NMR}$ (400 MHz, 298 K, CDCl_3) of Reaction 2.

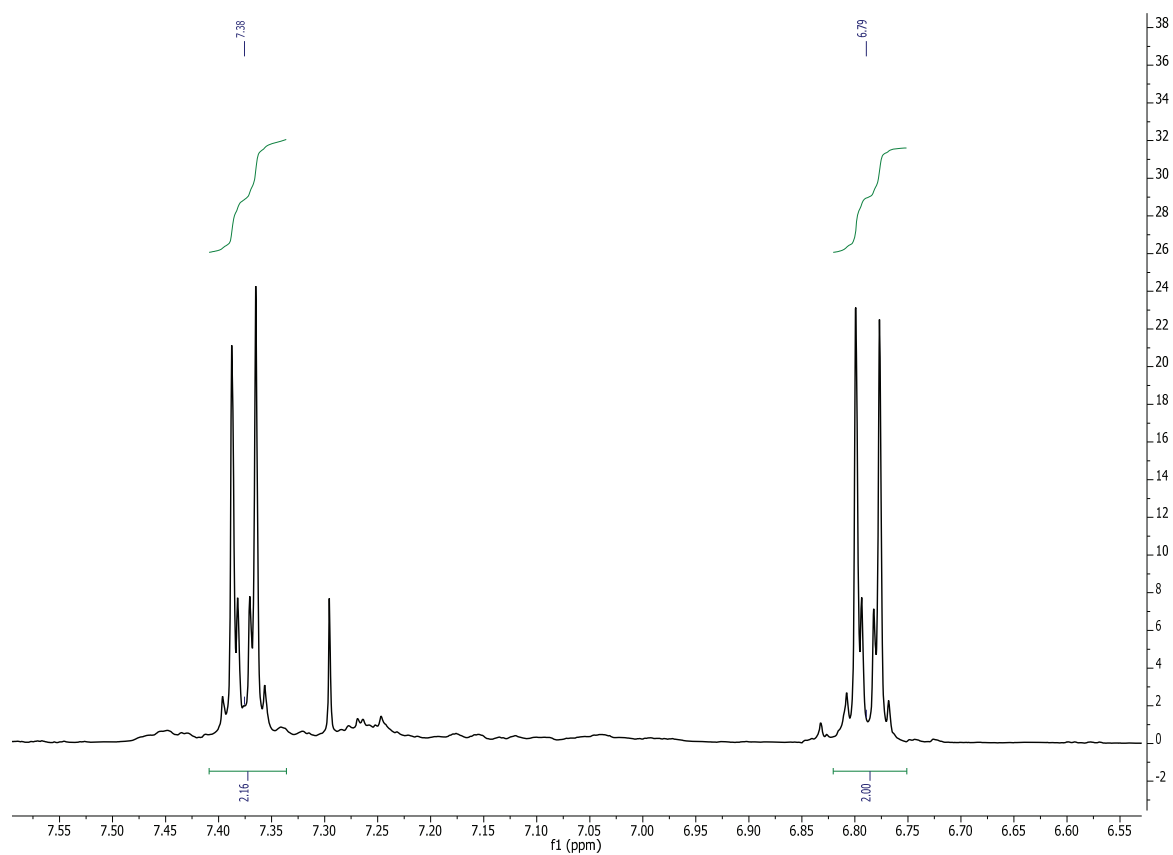


Figure S18. $^1\text{H-NMR}$ (400 MHz, 298 K, CDCl_3) of reaction 3.

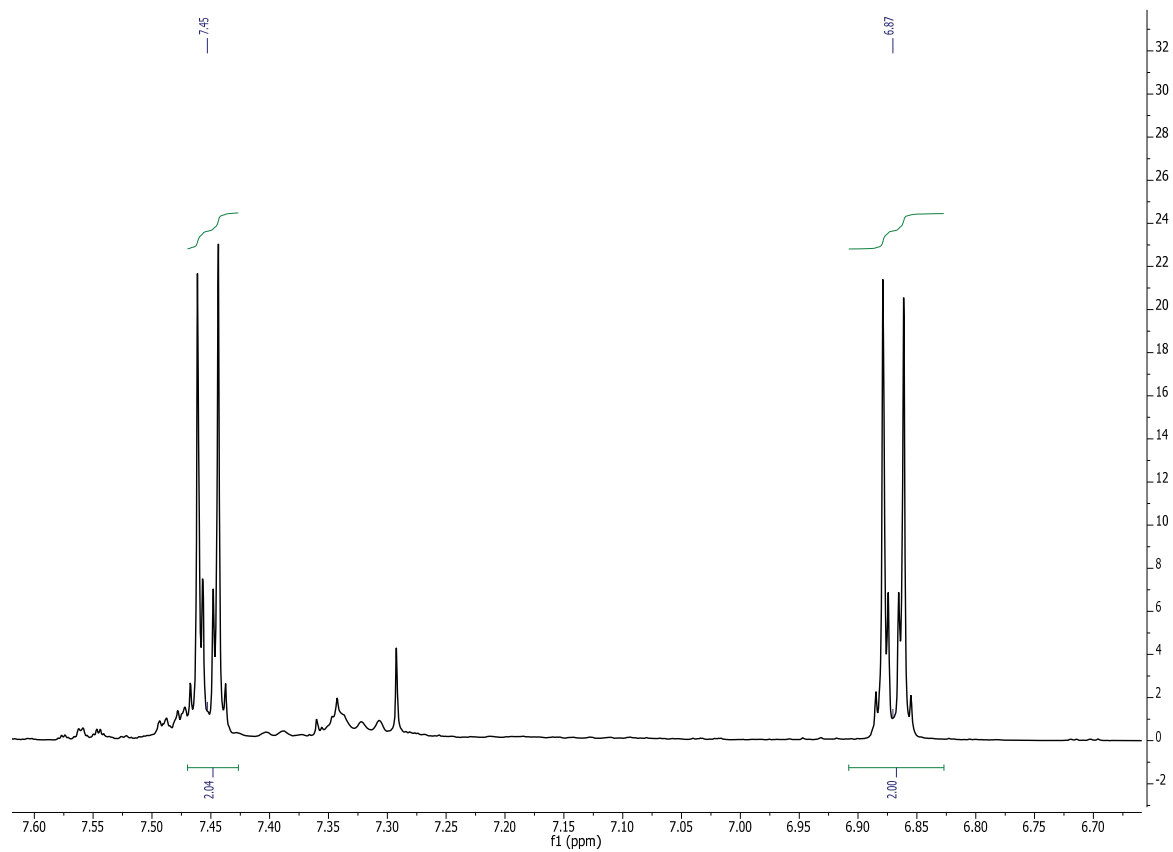


Figure S19. $^1\text{H-NMR}$ (500 MHz, 298 K, CDCl_3) of reaction 4.

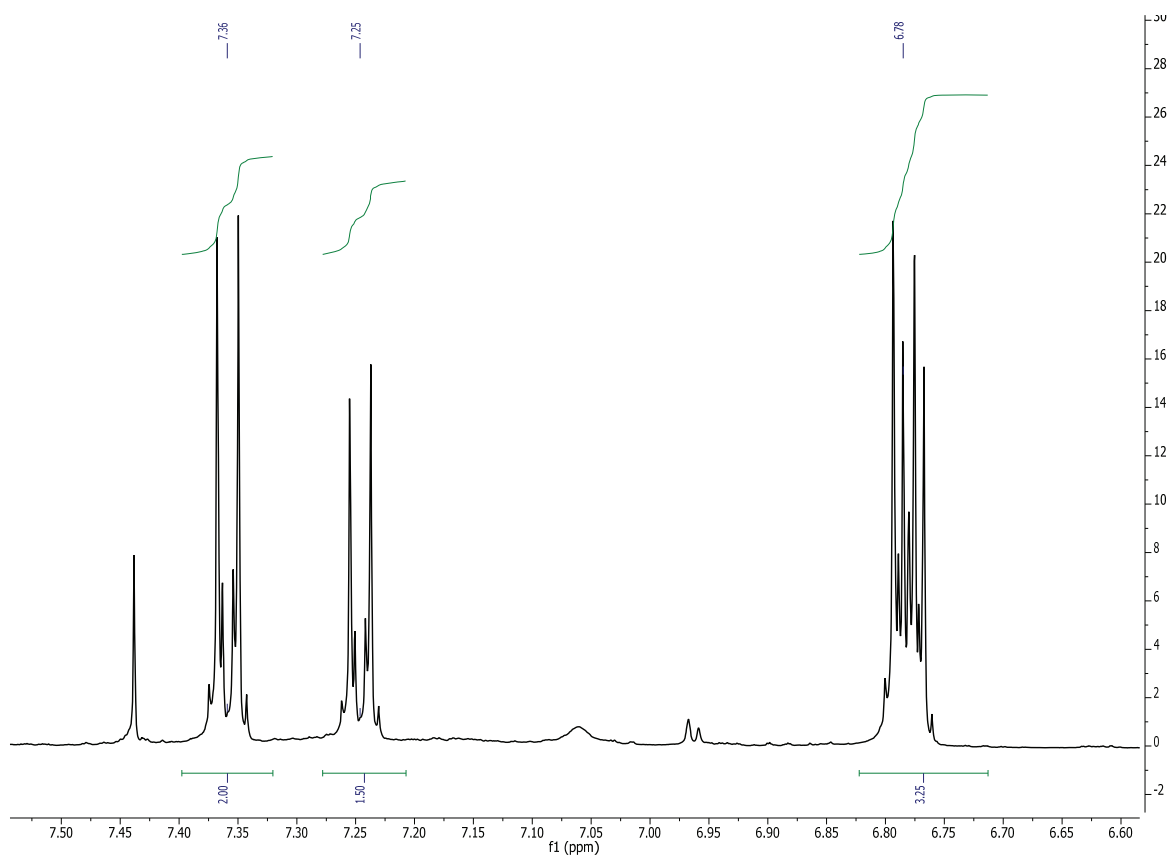


Figure S20. $^1\text{H-NMR}$ (500 MHz, 298 K, CDCl_3) of reaction 5.

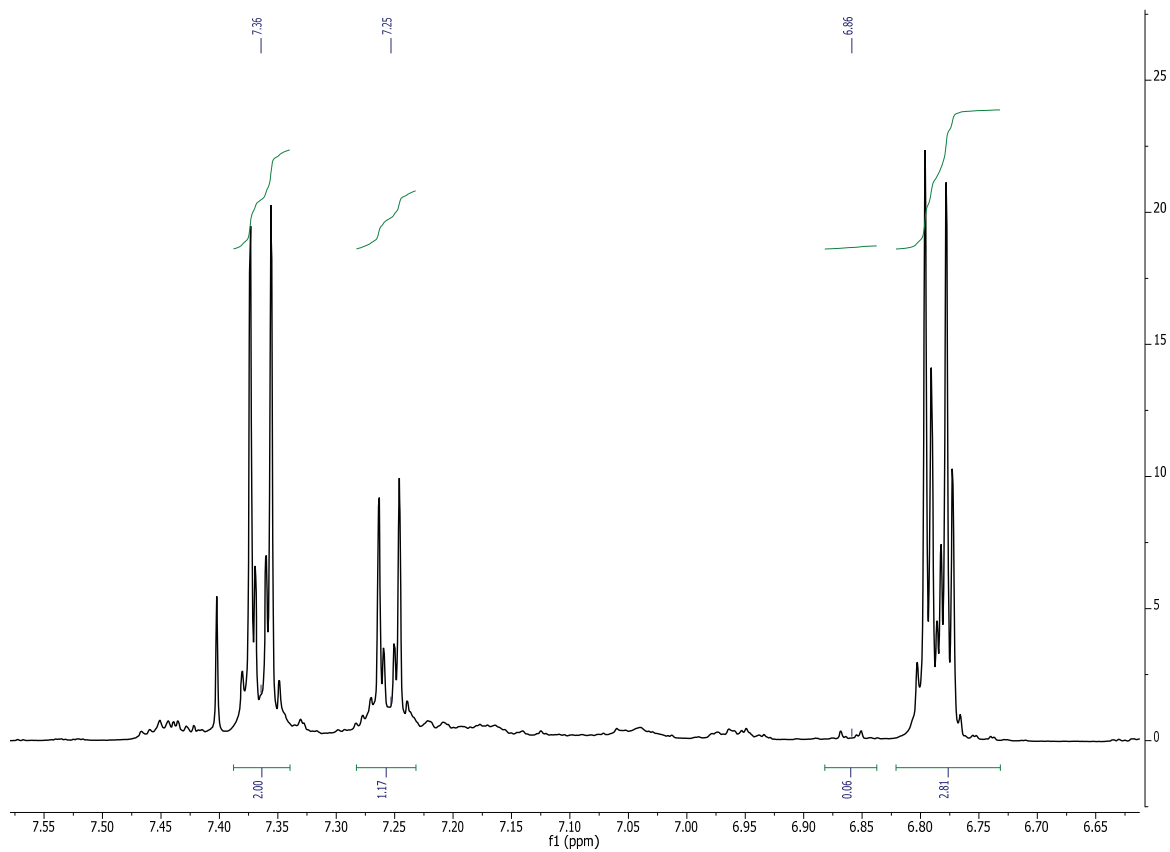


Figure S21. $^1\text{H-NMR}$ (500 MHz, 298 K, CDCl_3) of reaction 6.

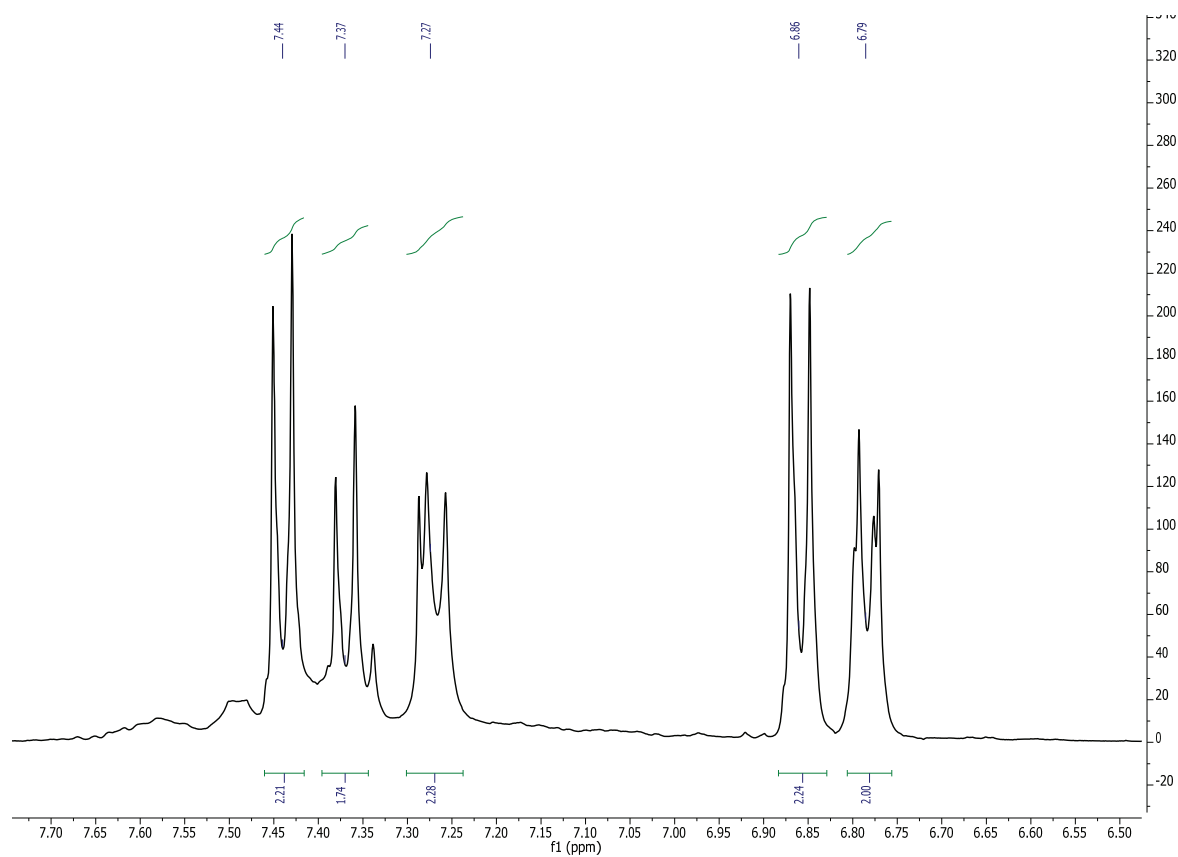


Figure S22. $^1\text{H-NMR}$ (400 MHz, 298 K, CDCl_3) of reaction 7.

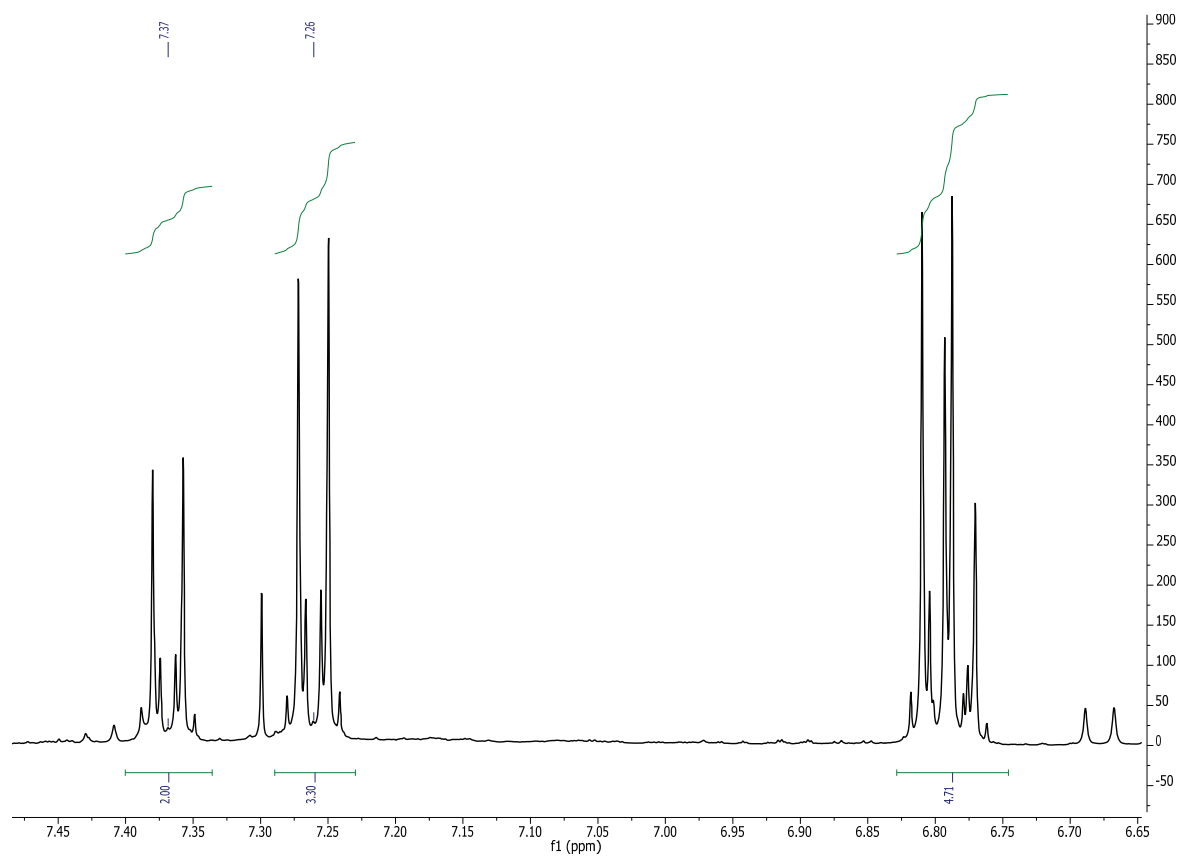


Figure S23. $^1\text{H-NMR}$ (400 MHz, 298 K, CDCl_3) of reaction 8.

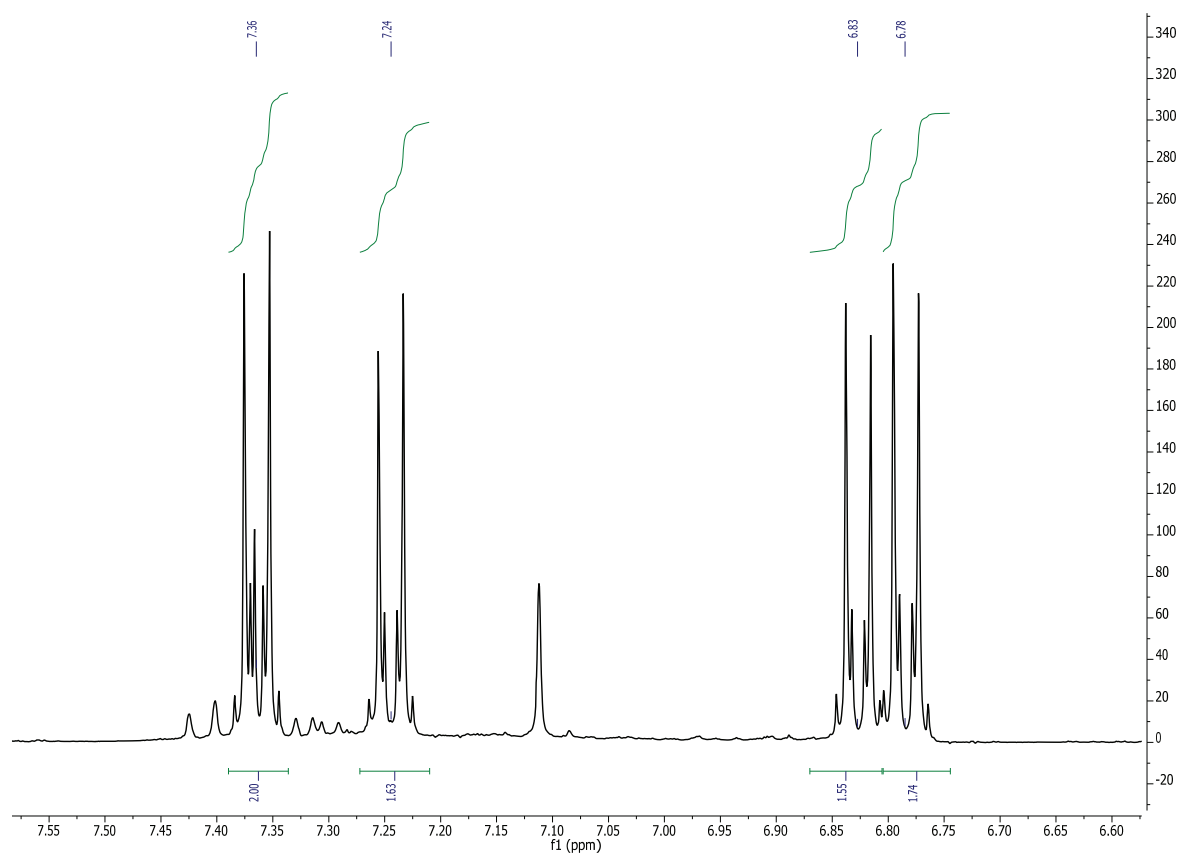


Figure S24. $^1\text{H-NMR}$ (400 MHz, 298 K, CDCl_3) of reaction 9.

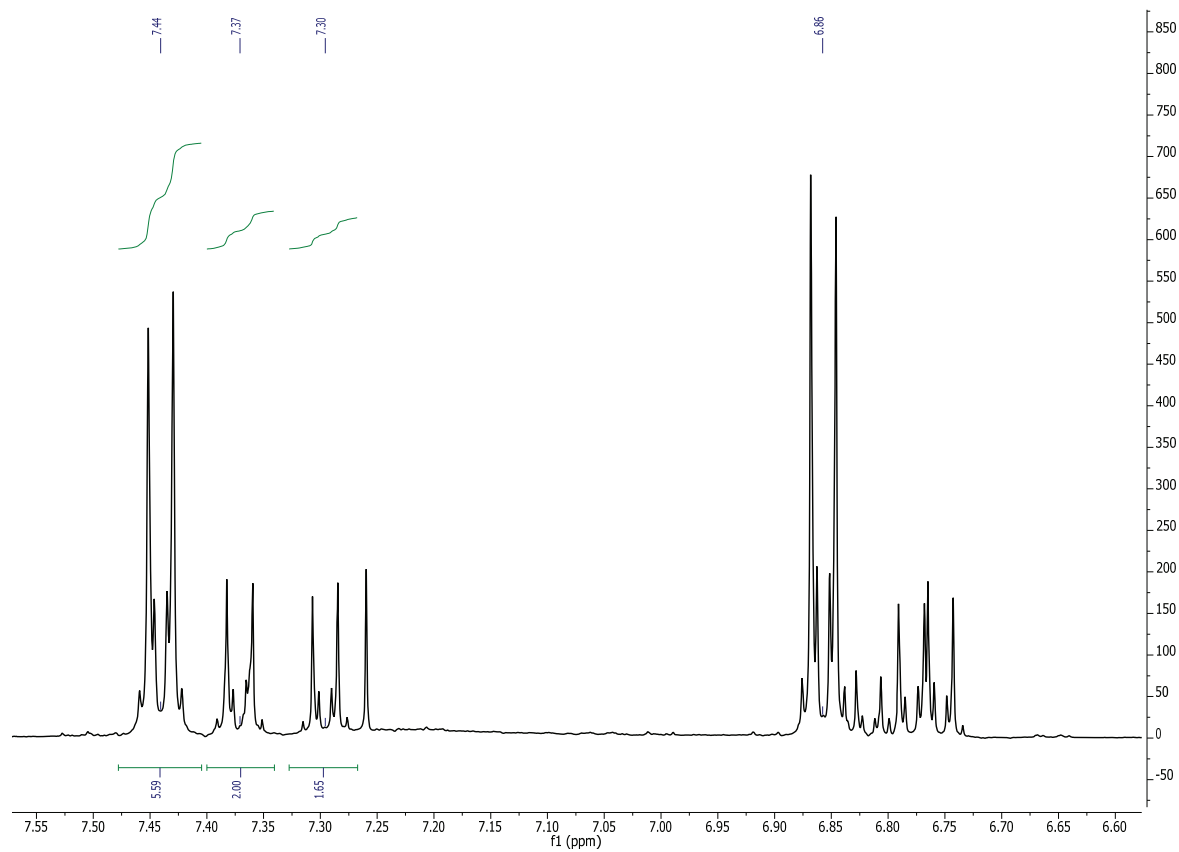


Figure S25. $^1\text{H-NMR}$ (400 MHz, 298 K, CDCl_3) of reaction 10.

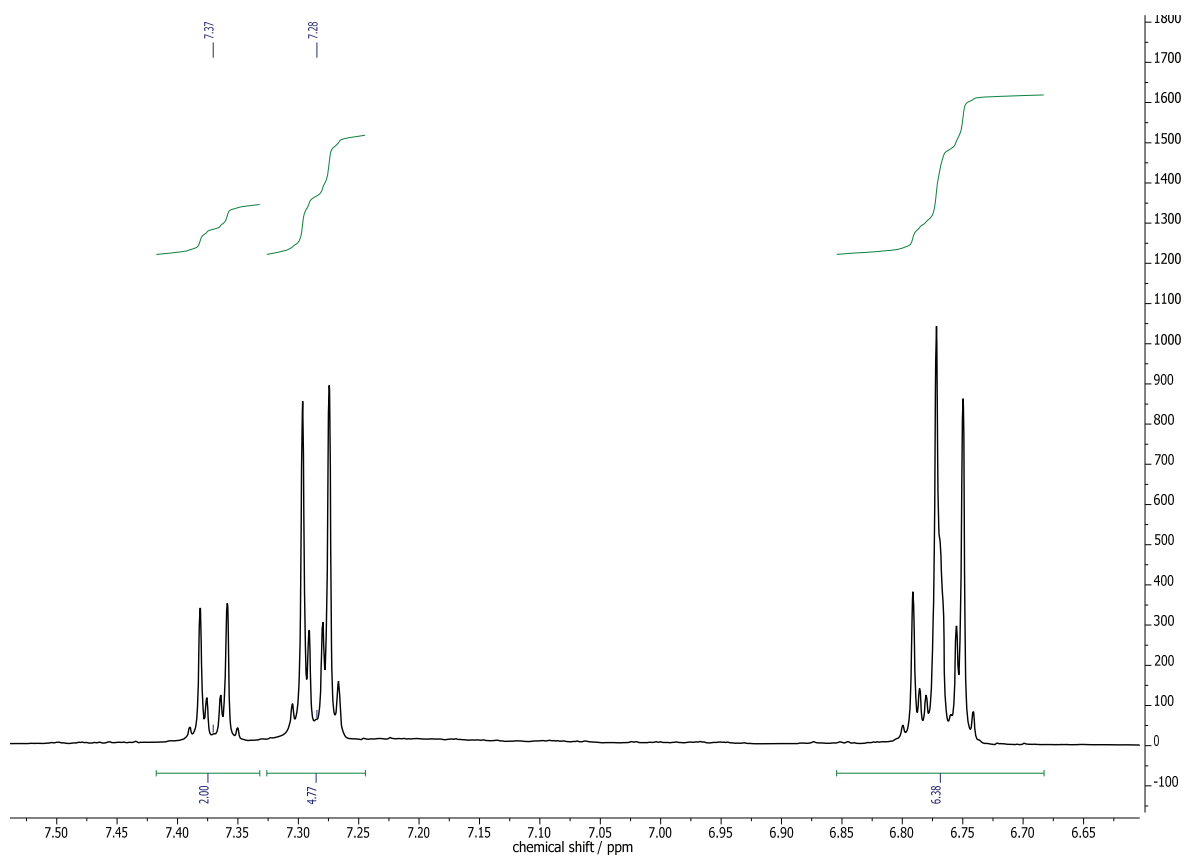


Figure S26. $^1\text{H-NMR}$ (400 MHz, 298 K, CDCl_3) of reaction 11.

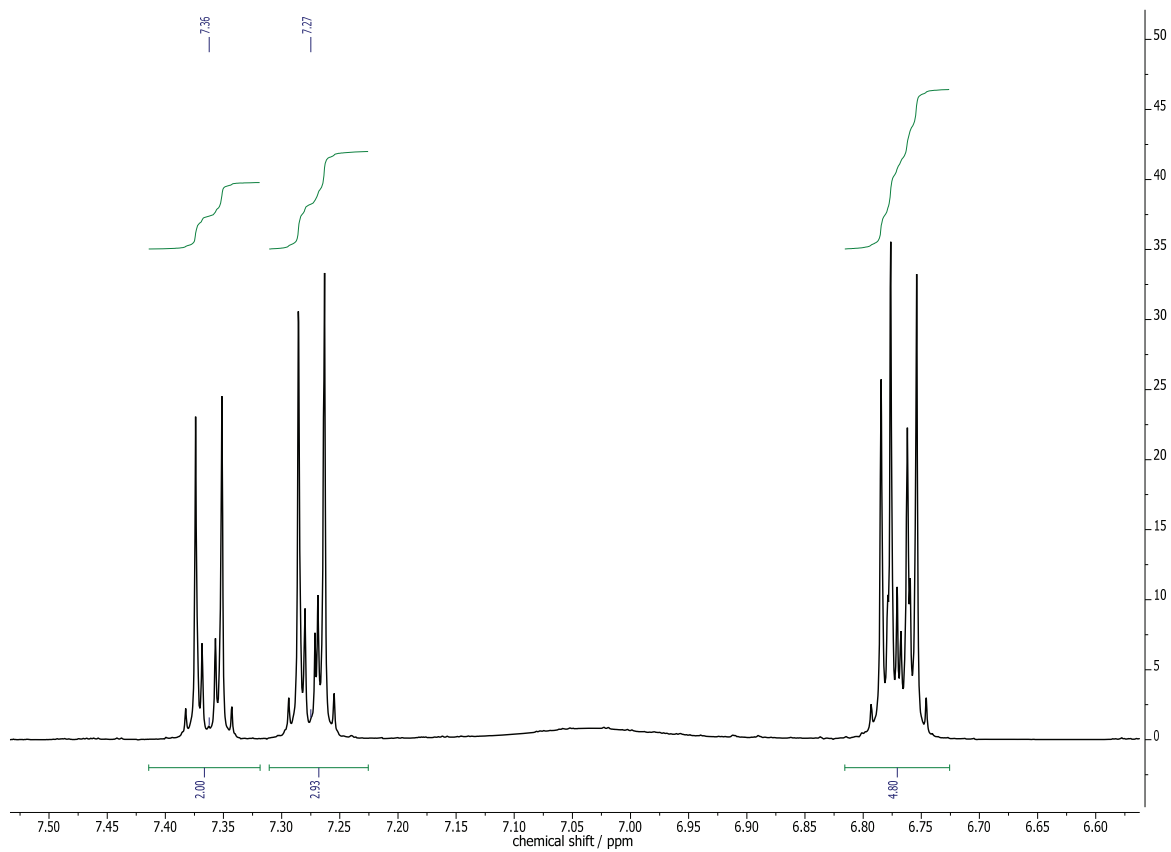


Figure S27. $^1\text{H-NMR}$ (400 MHz, 298 K, CDCl_3) of reaction 12.

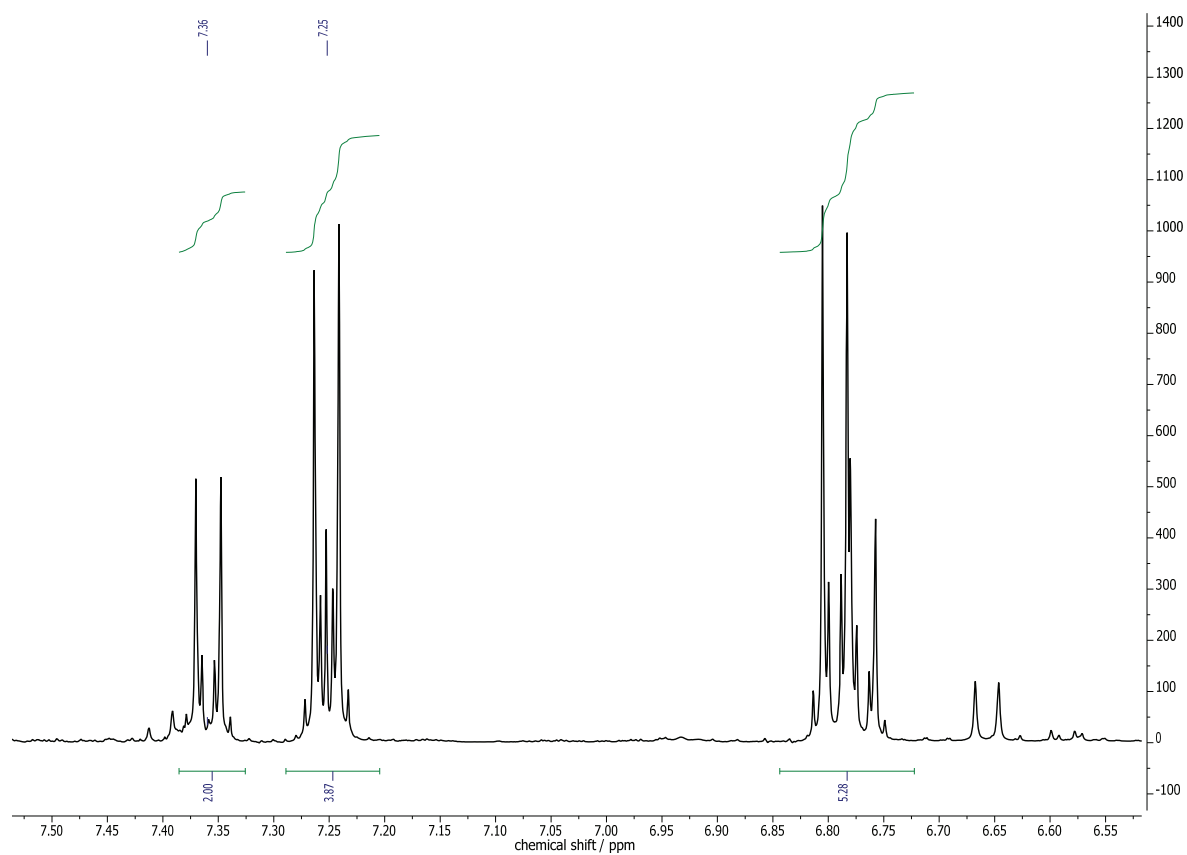


Figure S28. $^1\text{H-NMR}$ (400 MHz, 298 K, CDCl_3) of reaction 13.

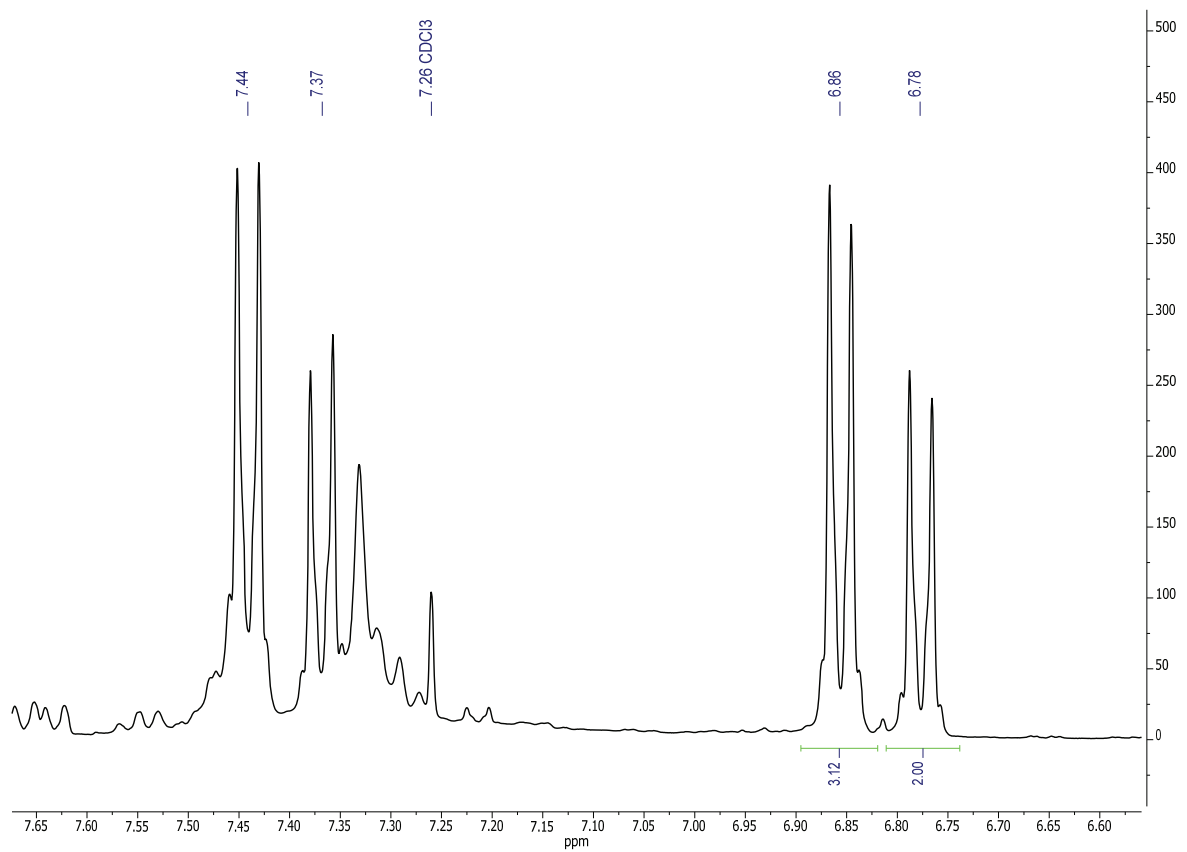


Figure S29. $^1\text{H-NMR}$ (400 MHz, 298 K, CDCl_3) of reaction 14.

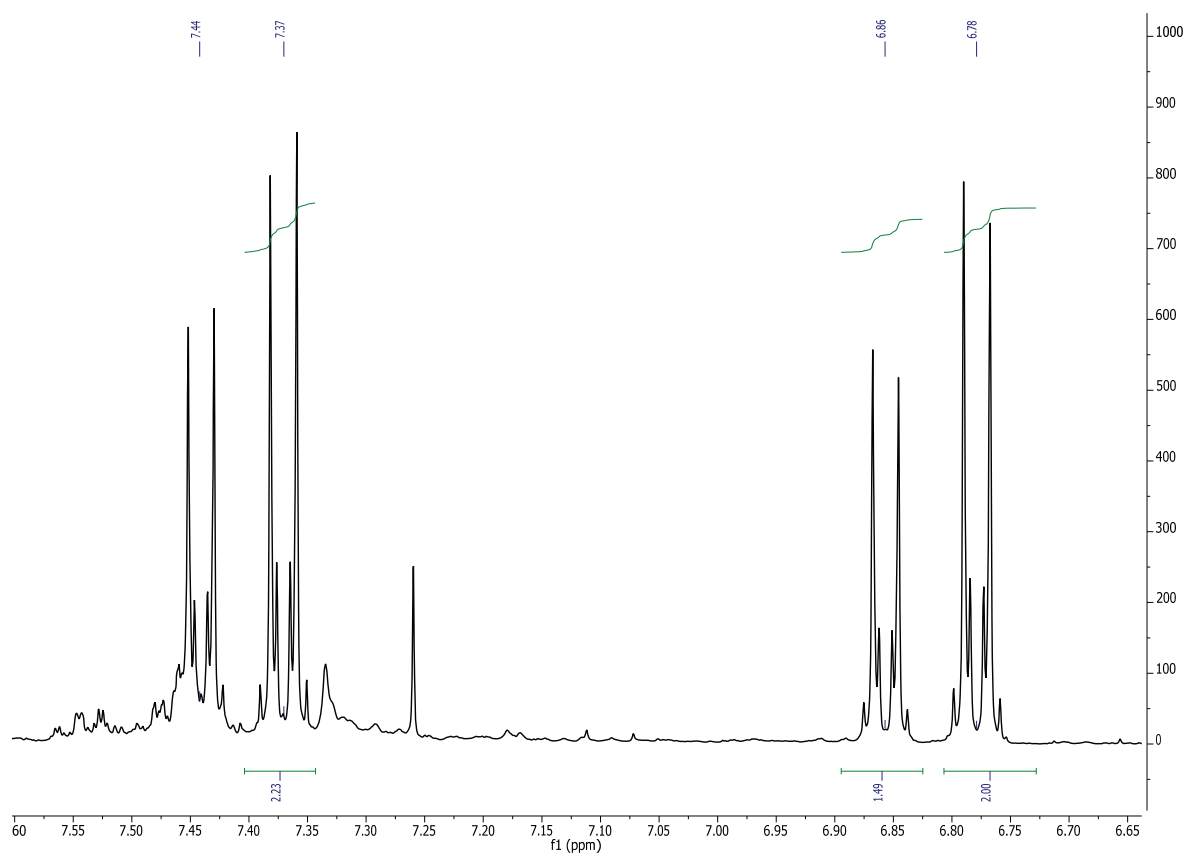


Figure S30 $^1\text{H-NMR}$ (400 MHz, 298 K, CDCl_3) of reaction 15.

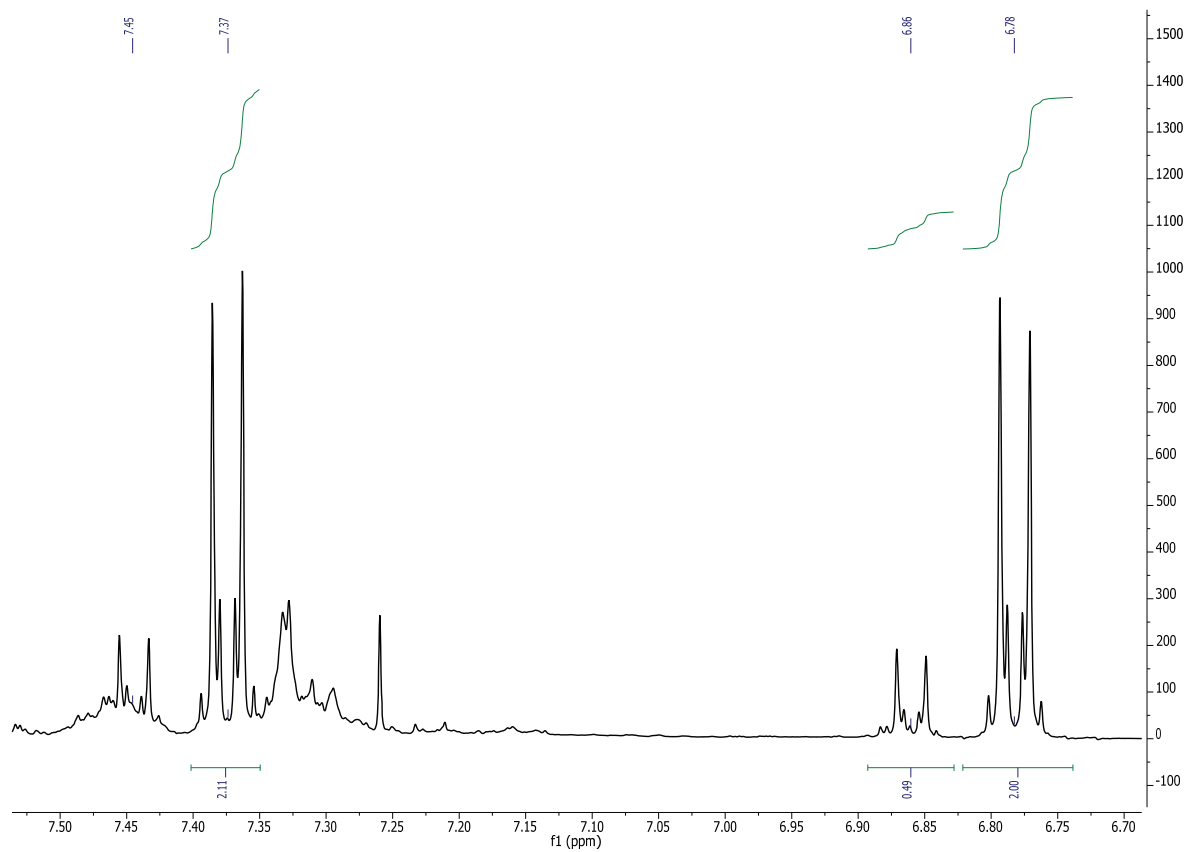


Figure S31. $^1\text{H-NMR}$ (400 MHz, 298 K, CDCl_3) of reaction 16.

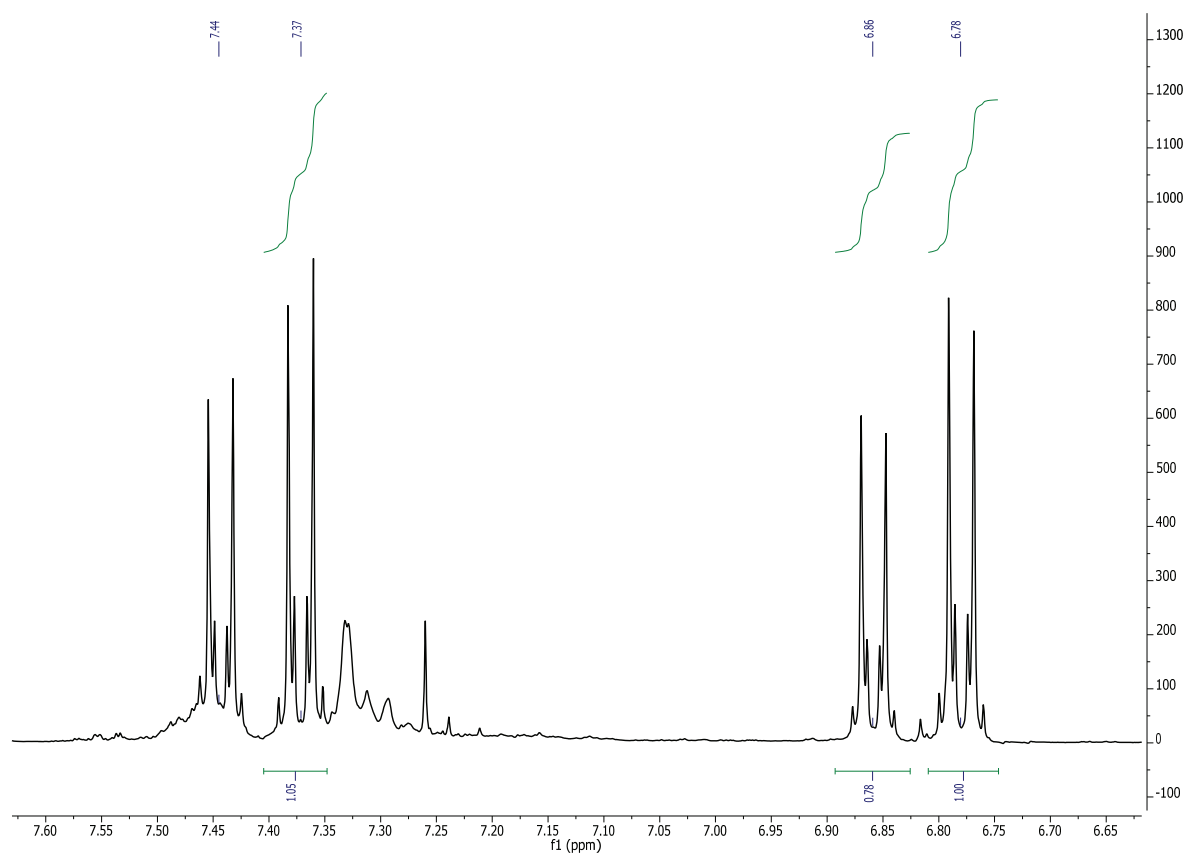


Figure S32. $^1\text{H-NMR}$ (400 MHz, 298 K, CDCl_3) of reaction 17.

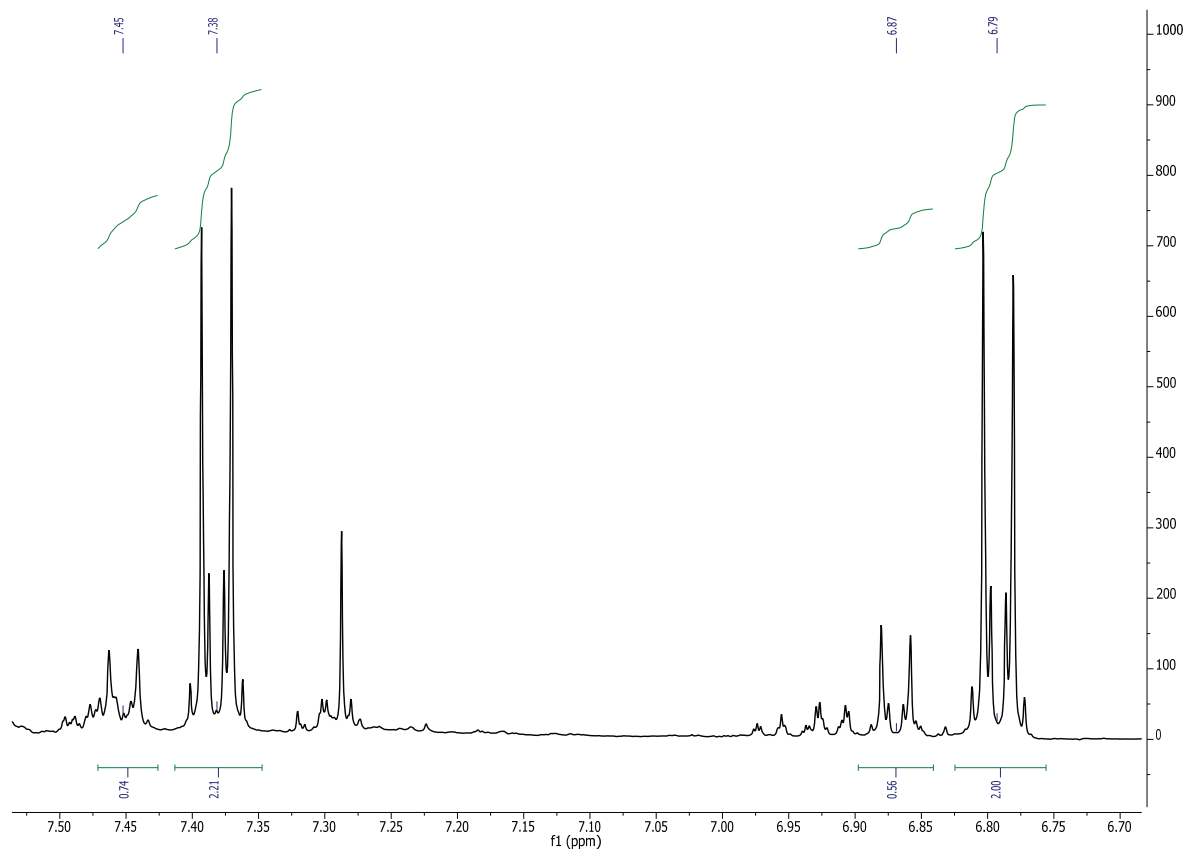


Figure S33. $^1\text{H-NMR}$ (400 MHz, 298 K, CDCl_3) of reaction 18.

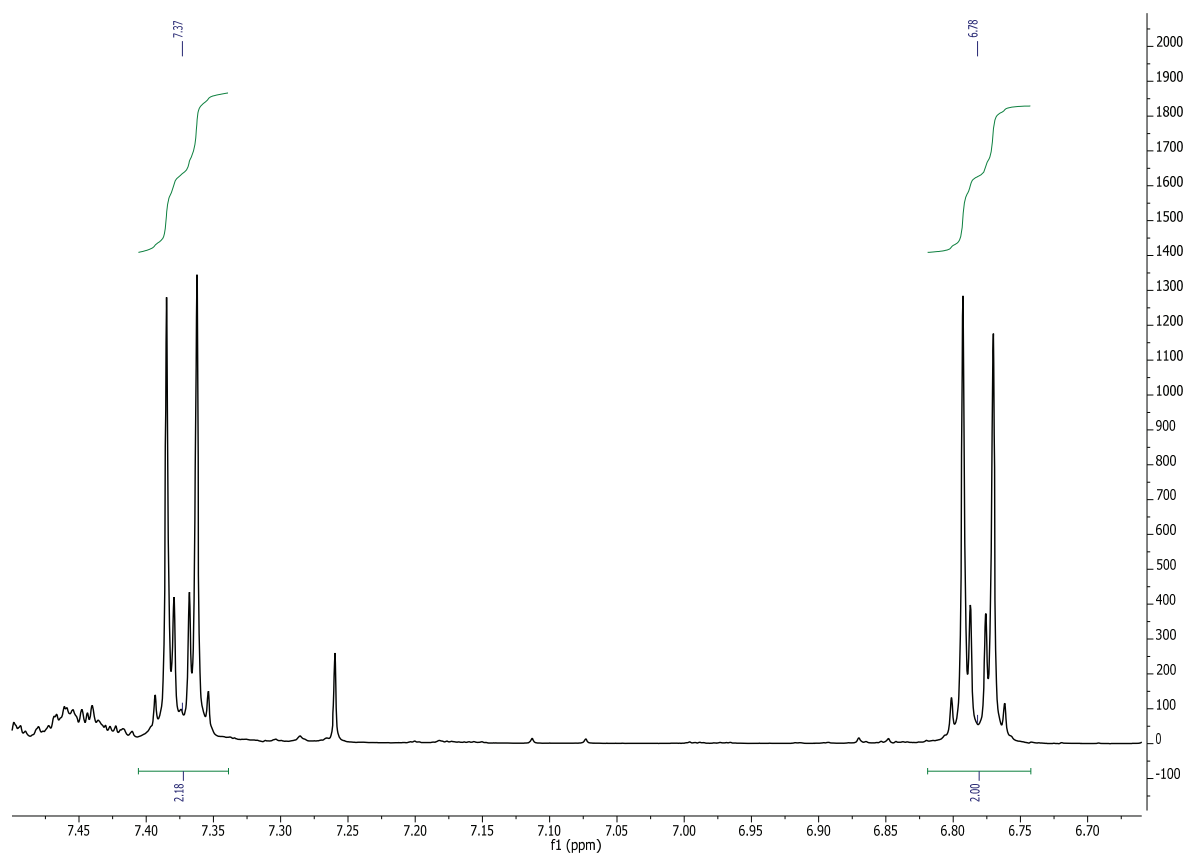


Figure S34. $^1\text{H-NMR}$ (400 MHz, 298 K, CDCl_3) of reaction 19.

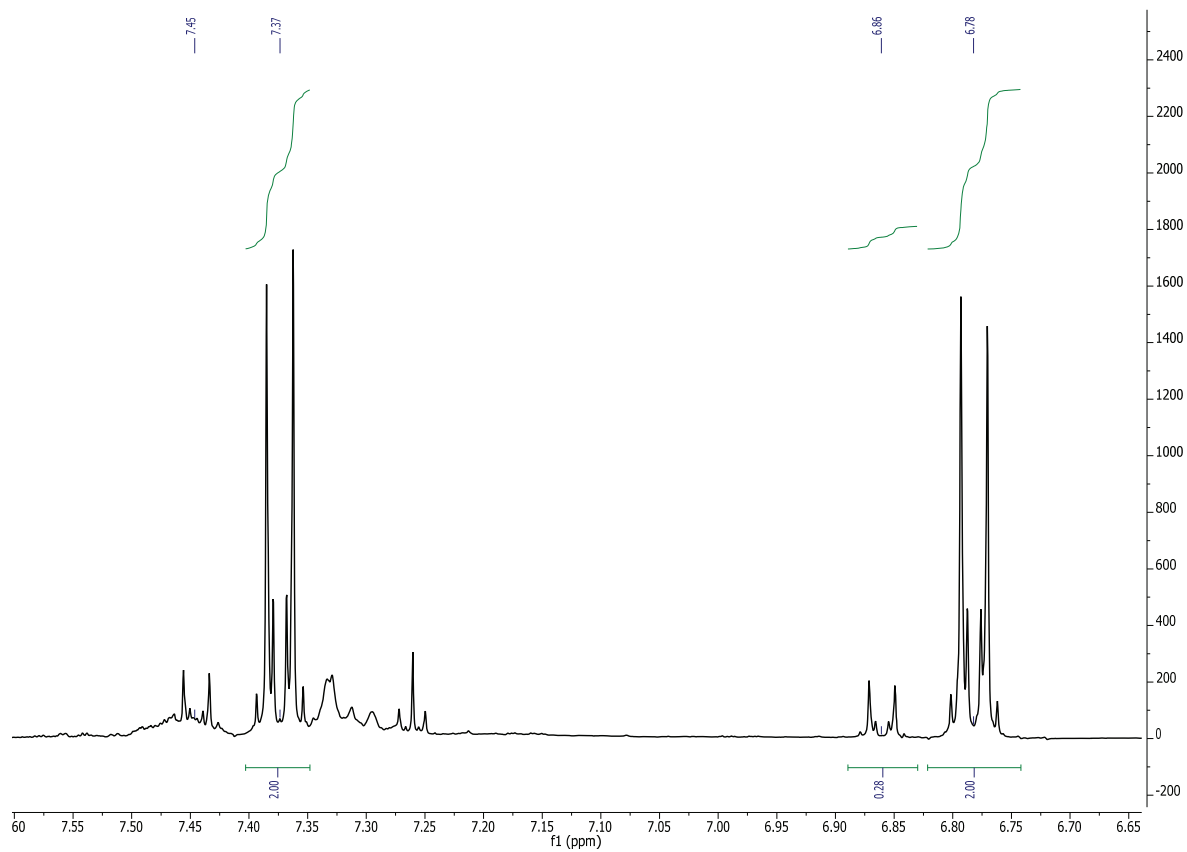


Figure S35. $^1\text{H-NMR}$ (400 MHz, 298 K, CDCl_3) of reaction 20.

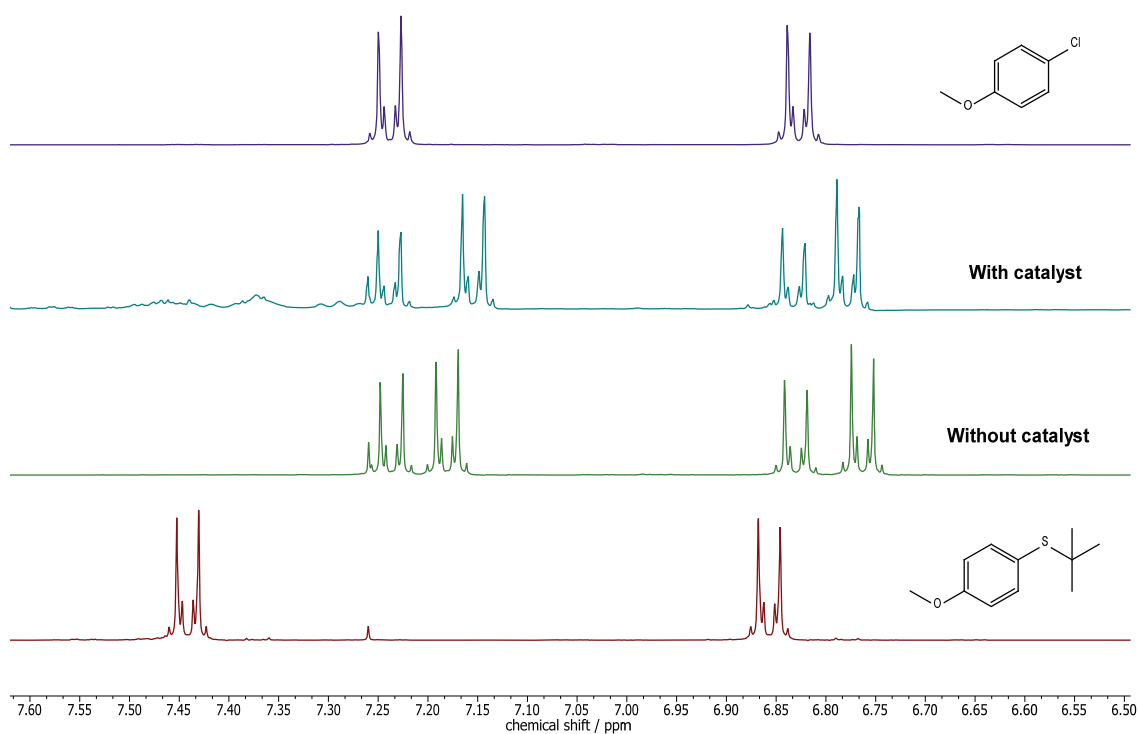


Figure S36. $^1\text{H-NMR}$ (400 MHz, 298 K, CDCl_3) of the reactions with 4-chloroanisole.

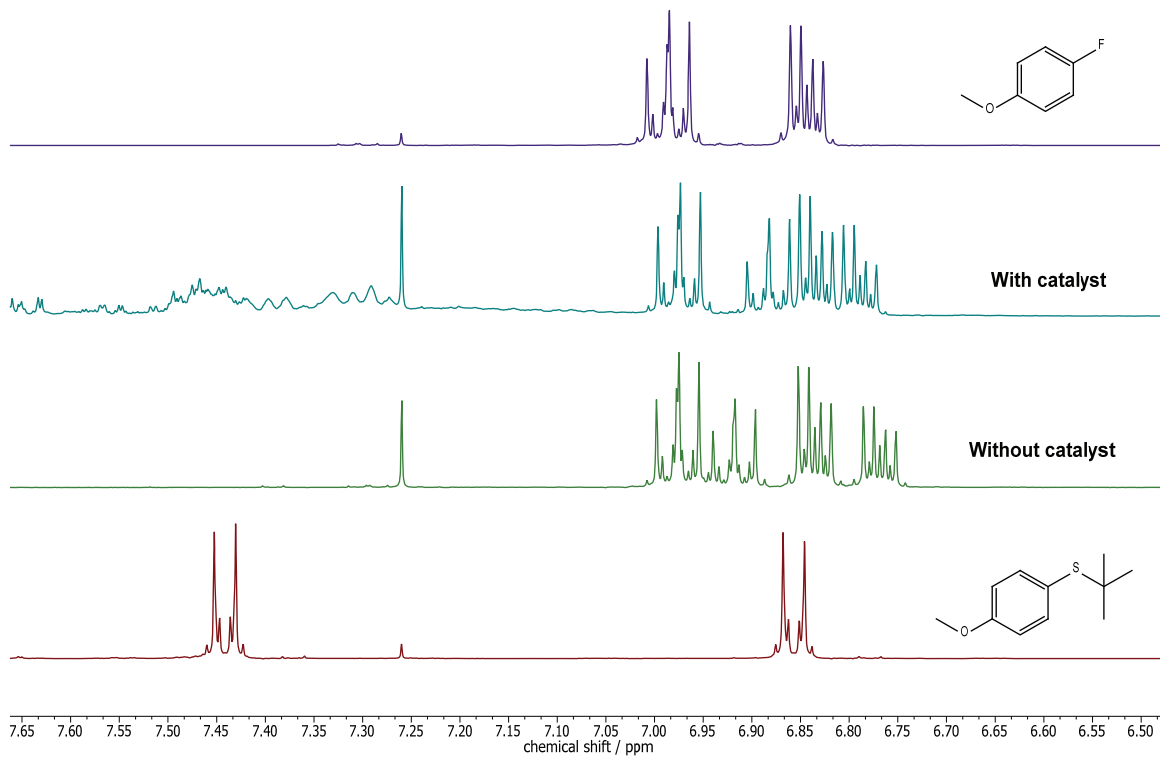


Figure S37. $^1\text{H-NMR}$ (400 MHz, 298 K, CDCl_3) of the reactions with 4-fluoroanisole.

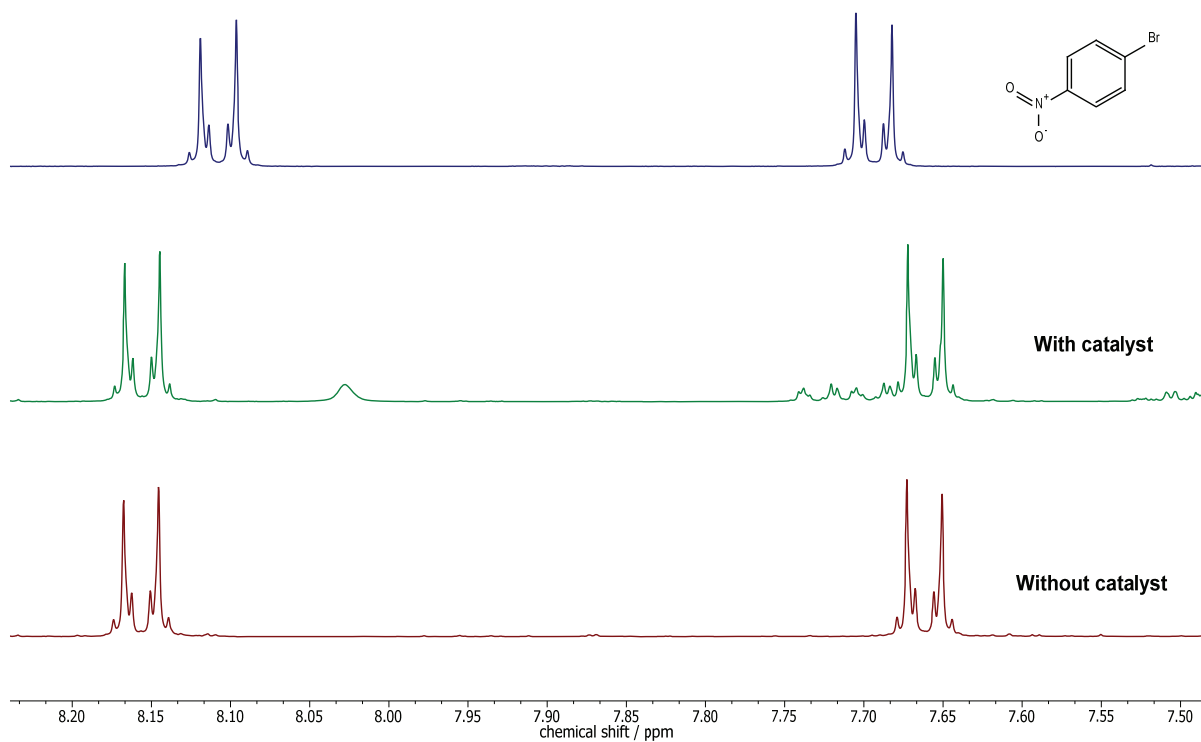


Figure S38. $^1\text{H-NMR}$ (400 MHz, 298 K, CDCl_3) of the reactions with 4-nitrobromobenzene

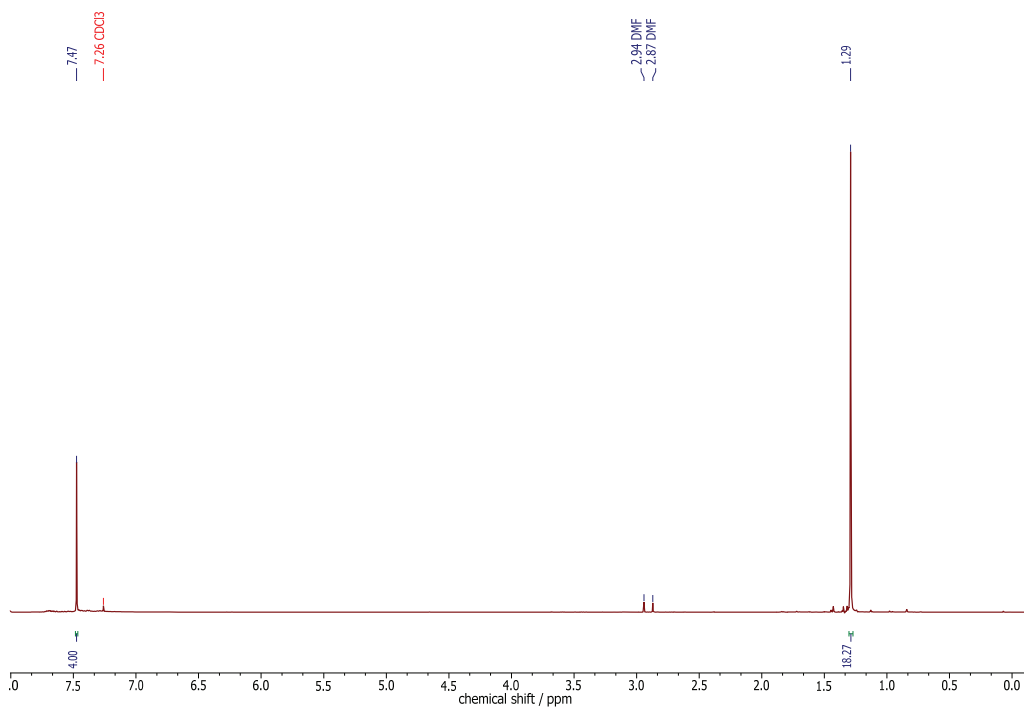


Figure S39. $^1\text{H-NMR}$ (400 MHz, 298 K, CDCl_3) of the reaction with 1,4-diiodobenzene at 50 °C.

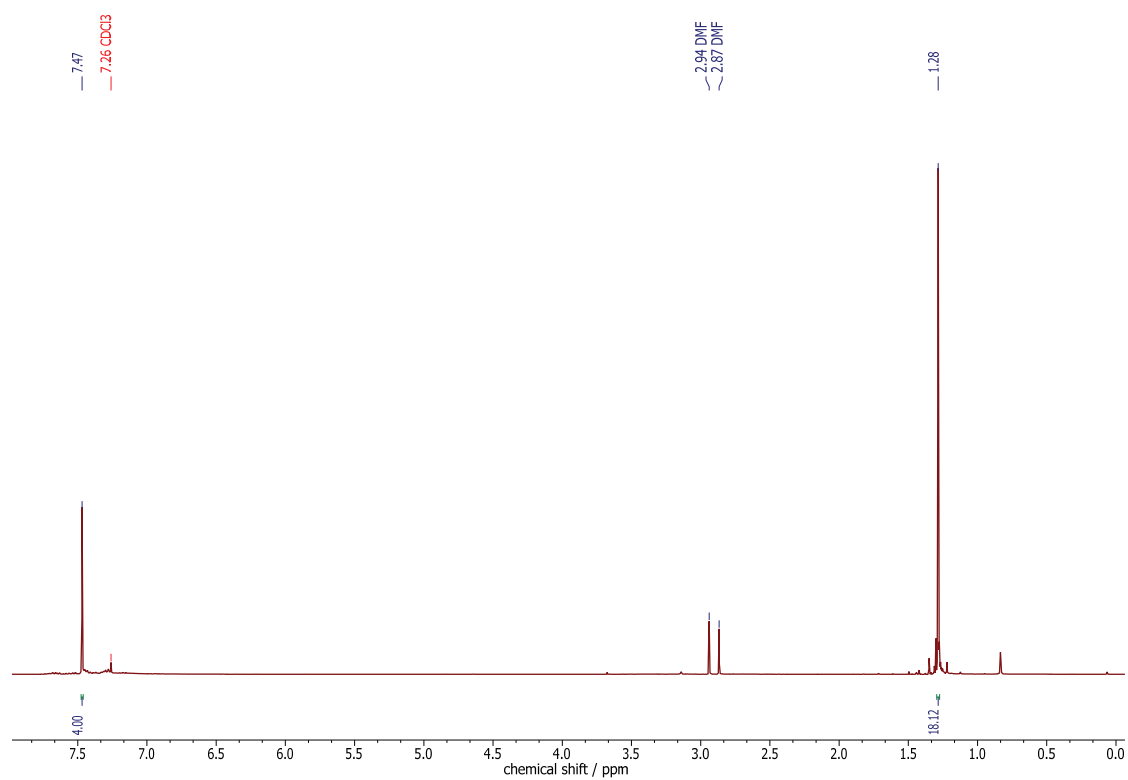


Figure S40. ¹H-NMR (400 MHz, 298 K, CDCl₃) of the reaction with 1,4-diiodobenzene at 80 °C.

3 Literature

- (1) Fulmer, G. R.; Miller, A. J. M.; Sherden, N. H.; Gottlieb, H. E.; Nudelman, A.; Stoltz, B. M.; Bercaw, J. E.; Goldberg, K. I.; Gan, R.; Apiezon, H. NMR Chemical Shifts of Trace Impurities : Common Laboratory Solvents , Organics , and Gases in Deuterated Solvents Relevant to the Organometallic Chemist. *Organometallics* **2010**, *29*, 2176–2179.
- (2) Wang, L.; Zhou, W.-Y.; Chen, S.-C.; He, M.-Y.; Chen, Q. A Highly Efficient Palladium-Catalyzed One-Pot Synthesis of Unsymmetrical Aryl Alkyl Thioethers under Mild Conditions in Water. *Adv. Synth. Catal.* **2012**, *354*, 839–845.
- (3) Reddy, T. J.; Iwama, T.; Halpern, H. J.; Rawal, V. H. General Synthesis of Persistent Trityl Radicals for EPR Imaging of Biological Systems. *J. Org. Chem.* **2002**, 4635–4639.
- (4) Cogolli, P.; Testafari, L.; Tingoli, M.; Tiecco, M.; *J. Org. Chem.* **1979**, *44*, 2636 – 2642.
- (5) Bovonsombat, P.; Ali, Rameez; K., Chiraphorn; L., Juthamard; P., Kawin; Aphimanchindakul, S.; Pungcharoenpong, N.; Timsuea, N.; Arunrat, A.; Punpongjareorn, N.; *Tetrahedron* **2010**, *66*, 6928 – 6935.
- (6) Furuya, T.; Kaiser, H.; Ritter, T.; *Angew. Chem. Int. Ed.* **2008**, *47*, 5993 – 5996.
- (7) Wang, L.; Zhou, W.-Y.; Chen, S.-C.; He, M.-Y.; Chen, Q. A Highly Efficient Palladium-Catalyzed One-Pot Synthesis of Unsymmetrical Aryl Alkyl Thioethers under Mild Conditions in Water. *Adv. Synth. Catal.* **2012**, *354*, 839–845.

[A2]:Tris[2,2,6,6-tetramethyl-8-(trimethylsilyl)benzo-[1,2-d;4,5-d']bis(1,3-dithiol)-4-yl]methanol diethyl ether monosolvate

Reprinted with permission from

Nico Fleck, Gregor Schnakenburg, Alexander C. Filippou, Olav Schiemann*, *Acta Cryst. E* **2018**, 74, 539 – 542.

Published with Open Access by IUCr (Chester, GB) under CC-BY license, ©2020 to the authors.

Contributions:

- Experimental work
 - Organic synthesis incl. compound characterization
- Writing of the manuscript



Tris[2,2,6,6-tetramethyl-8-(trimethylsilyl)benzo[1,2-*d*];4,5-*d'*]bis(1,3-dithiol)-4-yl]methanol diethyl ether monosolvate

Nico Fleck,^a Gregor Schnakenburg,^b Alexander C. Filippou^b and Olav Schiemann^{a*}

Received 23 January 2018
Accepted 17 March 2018

^aUniversity of Bonn, Institute of Physical and Theoretical Chemistry, Wegelerstrasse 12, 53115 Bonn, Germany, and
^bUniversity of Bonn, Institute of Inorganic Chemistry, Gerhard-Domagk-Strasse 1, 53121 Bonn, Germany.
*Correspondence e-mail: schiemann@pc.uni-bonn.de

Edited by G. S. Nichol, University of Edinburgh, Scotland

Keywords: crystal structure; triarylmethanol; trityl radical; EPR; spin label.

CCDC reference: 1829596

Supporting information: this article has supporting information at journals.iucr.org/e

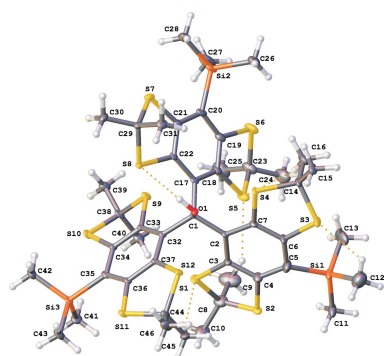
The title compound, a triarylmethanol, C₄₆H₆₄OS₁₂Si₃ **1**, was synthesized *via* lithiation of tris-2,2,6,6-tetramethylbenzo[1,2-*d*];4,5-*d'*]bis[1,3]dithiol-4-yl-methanol, **2**, and electrophilic quenching with trimethylsilyl chloride. The current crystal structure reveals information about the reactivity of this compound and compares well with the structure reported for the unsubstituted parent compound **2** [Driesschaert *et al.* (2012). *Eur. J. Org. Chem.* **33**, 6517–6525]. The title compound **1** forms molecular propellers and crystallizes in $P\bar{1}$, featuring an unusually long Si–C_{ar} bond of 1.910 (3) Å. Moreover, the geometry at the central quaternary carbon is rather trigonal-pyramidal than tetrahedral due to vast intramolecular stress. One trimethylsilyl group is disordered over two positions in a 0.504 (4):0.496 (4) ratio and one S atom is disordered over two positions in a 0.509 (7):0.491 (7) ratio. The contribution of disordered diethyl ether solvent molecule(s) was removed using the *PLATON SQUEEZE* (Spek, 2015) solvent masking procedure. These solvent molecules are not considered in the given chemical formula and other crystal data.

1. Chemical context

The reported triarylmethanol **1** is the direct precursor of the corresponding triarylmethyl radical. Such tetrathiarlylmethyl radicals, also called trityl radicals, can be used as spin labels for EPR-based distance measurements (Reginsson *et al.*, 2012; Kunjir *et al.*, 2013) and have recently been employed for structure determination in proteins (Jasoy *et al.*, 2017; Yang *et al.*, 2012) as well as nucleic acids (Shevelev *et al.*, 2015). They are also used for dynamic nuclear polarization experiments (Jähnig *et al.*, 2017). Trityl radicals feature a very narrow linewidth in EPR spectra, slow spin–spin relaxation at room temperature and show line-broadening depending on the oxygen concentration in their surroundings. The latter property also makes them suitable as oxygen probes (Frank *et al.*, 2015). However, most of the trityl radicals reported in the literature feature carboxylic acid derivatives as substituents in the *para*-position. The title compound **1** is a promising precursor for differently *para*-substituted trityl alcohols and their corresponding radicals.

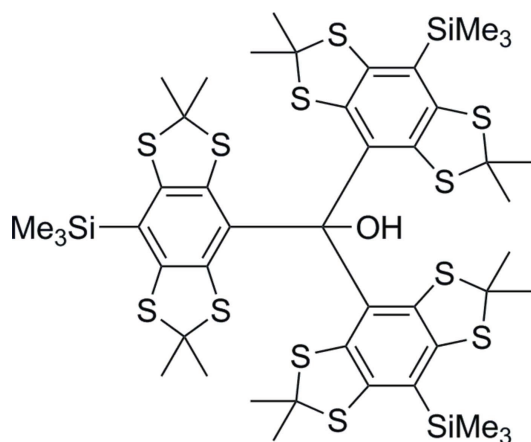
2. Structural commentary

Compound **1** crystallizes (in space group $P\bar{1}$ with the unit cell containing two molecules) from diethyl ether as a racemic mixture with respect to the propeller-like conformation of the



OPEN ACCESS

aryl building blocks. The unit cell consists of one *P*- and one *M*-configured molecule, as shown in Fig. 1.



The structure of the title compound deviates from C_3 symmetry, since the dihedral angles between the aryl planes are not equivalent (± 73.7 , ± 73.7 , $\pm 70.2^\circ$). Moreover, the structure of **1** exhibits a Si–C_{ar} bond length of 1.909 (3) Å to 1.945 (4) Å, whereas a bond length X₃Si–C_{ar} of 1.863 (14) Å is typically expected (Allen *et al.*, 1987). This elongation of the Si–C_{ar} bond may be due to the steric stress at the *para*-

Table 1
Hydrogen-bond geometry (Å, °).

<i>D</i> –H... <i>A</i>	<i>D</i> –H	H... <i>A</i>	<i>D</i> ... <i>A</i>	<i>D</i> –H... <i>A</i>
O1–H1...S8	0.84	2.32	3.031 (2)	142
C9–H9C...S5	0.98	3.05	3.926 (5)	150
C12–H12A...S3	0.98	2.51	3.184 (16)	126
C13–H13B...S6 ⁱ	0.98	2.85	3.734 (10)	150
C15–H15B...S11 ⁱⁱ	0.98	3.00	3.866 (4)	148
C16–H16C...S5	0.98	3.00	3.912 (4)	155
C26–H26C...S6	0.98	2.68	3.364 (5)	127
C31–H31A...S12 ⁱⁱ	0.98	2.81	3.435 (3)	123
C41–H41A...S10	0.98	2.87	3.508 (5)	123
C42–H42C...S10	0.98	2.60	3.291 (3)	128
C45–H45C...S1	0.98	2.96	3.867 (4)	155

Symmetry codes: (i) $-x + 2, -y + 2, -z + 2$; (ii) $-x + 2, -y + 2, -z + 1$.

positions caused by vicinal sulfur atoms. Additionally, the bond angles between the tetrathiarlyl substituents at C1 are 112.2 (2), 113.5 (2) and 114.0 (2)°, exceeding the tetrahedral angle of 109.5°. Therefore, regarding its geometry, C1 is situated between a tetrahedral and a trigonal–planar environment with a deviation of 0.409 (4) Å from the plane through atoms C2, C17 and C32. This coincides with the experimental observation that the title compound forms the corresponding carbocation with low effort, meaning its structure is already similar to the transition state according to Hammond's postulate. However, the C1–O1 bond length of 1.439 (3) Å

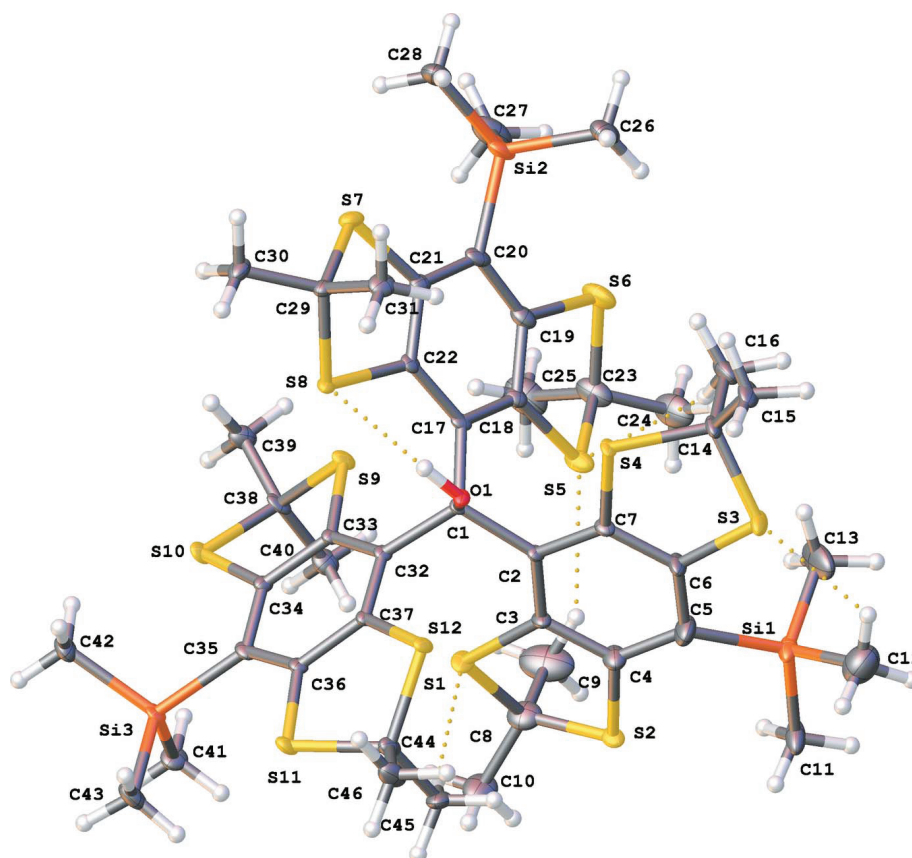


Figure 1
Crystal structure of the title compound, **1**. Displacement ellipsoids are at the 50% probability level. Only the major disorder component is shown.

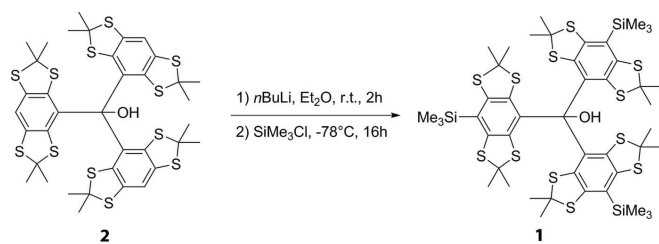


Figure 2
Synthesis of the title compound **1**.

fits the value expected for tertiary alcohols, which is 1.440 (12) Å (Allen *et al.*, 1987) and does not show any elongation. Regarding the envelope-configured 1,3-dithianes, C—S—C angles between 94.4 (2) and 96.1 (2)° and C—C—S—C torsion angles in 1,3-dithianes between 18.7 and 26.9° are observed, with the methylene groups pointing either above or below the aromatic ring plane although without regularity. This is also observed within the crystal structure of the unsubstituted trityl alcohol **2** (Fig. 2).

The molecular structure of compound **1** features an O1—H1···S8 hydrogen bond with a donor to acceptor atom distance of 3.031 (2) Å, which falls into the regime of a moderately strong hydrogen bond according to Jeffrey (1997). In addition, the H1···S8 distance of 2.32 Å is significantly shorter than 2.90 Å, the sum of the van der Waals radii (Bondi, 1964). The remaining five intramolecular hydrogen bonds listed in Table 1 belong into the category of weak electrostatic hydrogen bonds, with the shortest having a donor–acceptor atom distance of 3.435 (3) Å and the longest a donor–acceptor distance of 3.926 (5) Å. Other contacts between the molecules were not observed.

3. Supramolecular features

In the crystal, a number of C—H···S interactions occur (Table 1).

4. Database survey

The Cambridge Structural Database (CSD, Version 5.38; Groom *et al.*, 2016) contained two structures of *para*-substituted trityl radicals [ESECUB (Decroos *et al.*, 2011) and TIXCEJ (Liu *et al.*, 2008)] and one structure determination for compound **2** (REGBUG; Driesschaert *et al.*, 2012). As found here for compound **1**, the reported structure of **2** also deviates from C_3 symmetry, with dihedral angles for the aryl planes of ± 75.3 , ± 70.7 , $\pm 69.9^\circ$. However, in contrast to the crystal structure reported here, Driesschaert *et al.* (2012) do not report on any hydrogen bonding within the structure of **2** but the C—H···S distances are very similar than those in Table 1.

5. Synthesis and crystallization

Tris-(2,2,6,6-tetramethylbenzo[1,2-*d*;4,5-*d*]bis[1,3]dithiol-4-yl)methanol **2** was obtained following the procedure of Jassoy

et al. (2017). The synthesis of the title compound **1** was reported in the literature (Karlson *et al.*, 2014). However, the procedure was changed slightly, resulting in a more convenient work-up and increased yield.

Tris-(2,2,6,6-tetramethylbenzo[1,2-*d*;4,5-*d*]bis[1,3]dithiol-4-yl)methanol **2** (4.00 g, 4.52 mmol) was dissolved in 200 mL of dry diethyl ether under argon. Dry tetramethylethylenediamine (6.80 mL, 5.24 g, 45.1 mmol, 10 eq.) was added and the solution was cooled to 273 K. Subsequently, *n*-butyl lithium (2.5 M in hexanes, 18.08 mL, 45.2 mmol, 10 eq.) was added dropwise. The reaction mixture was allowed to warm up to room temperature while stirring for 3 h. Afterwards, the reaction mixture was cooled down to 195 K and trimethylsilyl chloride (6.30 mL, 5.40 g, 49.7 mmol, 11.0 eq.) was added dropwise. Then, the cooling bath was removed and the mixture was stirred for 16 h at room temperature. The reaction was then quenched with 10 mL 1 M NaOH and the organic solvents were removed under reduced pressure. The dark-greenish residue was taken up in methylene chloride (200 mL) and washed with water (200 mL) twice. The organic phase was separated and dried over sodium sulfate. After removal of the solvents under reduced pressure, the crude product was purified by washing with acetone. For that, the residue was suspended in acetone (50 mL) and treated with ultrasound for 3 min. Then, the mixture was centrifuged at 3200 g (Eppendorf Centrifuge 5810 R) for 5 min, whereupon a colorless solid separated. This procedure was repeated with the precipitated solid three times, until the supernatant was clear and almost colorless. The pure product was obtained as a colorless solid after drying the precipitate under vacuum with a yield of 3.32 g (3.01 mmol, 67%). The pure product was then crystallized in the following way: compound **1** was dissolved in diethyl ether, the clear solution placed in an open tube at 278 K and the solvent was slowly evaporated over three days. This yielded light-yellow plates of **1** suitable for X-ray diffraction.

^1H NMR (500 MHz, CD_2Cl_2 , 298 K, δ in ppm): 6.50 (*s*, 1H), 1.77 (*s*, 18H), 1.65 (*s*, 9H), 1.61 (*s*, 9H), 0.46 (*s*, 27H). ^{13}C NMR (126 MHz, CD_2Cl_2 , 298 K, δ in ppm): 144.92, 144.53, 140.83, 138.79, 133.56, 130.66, 85.11, 62.13, 61.86, 34.92, 32.24, 29.33, 27.20, 2.66. The assignment of NMR signals for trityl alcohols has been discussed by Tormyshev *et al.* (2012). ESI(+) (*m/z*): 1100.089 [M] $^+$, 1123.078 [$M + \text{Na}$] $^+$. HRMS–ESI(+): 1100.0908 (calculated for $\text{C}_{46}\text{H}_{64}\text{OS}_{12}\text{Si}_3$: 1100.0908). Elemental analysis [%]: C 49.33, H 5.77, S 33.95 (calculated for $\text{C}_{46}\text{H}_{64}\text{OS}_{12}\text{Si}_3$: C 50.14, H 5.85, S 34.91).

6. Refinement

Crystal data, data collection and structure refinement details are summarized in Table 2. H atoms were positioned geometrically and refined using a riding model as idealized hydroxy and methyl groups (SHELXL AFIX codes 147 and 137), thus including free rotation around the respective C—O and C—C bonds. $U_{\text{iso}}(\text{H})$ was set to 1.5 times $U_{\text{eq}}(\text{C}, \text{O})$. At a first attempt, a diethyl ether solvent molecule was modeled over three partially occupied positions summing up to one molecule. This model still contained a residual of approximately

Table 2
Experimental details.

Crystal data	
Chemical formula	C ₄₆ H ₆₄ OS ₁₂ Si ₃
<i>M</i> _r	1101.96
Crystal system, space group	Triclinic, <i>P</i> $\bar{1}$
Temperature (K)	100
<i>a</i> , <i>b</i> , <i>c</i> (Å)	14.9964 (4), 15.1070 (4), 16.0026 (4)
α , β , γ (°)	91.6815 (13), 117.6083 (11), 99.1383 (12)
<i>V</i> (Å ³)	3149.79 (15)
<i>Z</i>	2
Radiation type	Cu <i>K</i> α
μ (mm ⁻¹)	4.64
Crystal size (mm)	0.34 × 0.18 × 0.04
Data collection	
Diffraction	Bruker D8-Venture
Absorption correction	Multi-scan (SADABS; Bruker, 2015)
<i>T</i> _{min} , <i>T</i> _{max}	0.252, 0.754
No. of measured, independent and observed [<i>I</i> > 2 σ (<i>I</i>)] reflections	74526, 11369, 9723
<i>R</i> _{int}	0.091
(sin θ / λ) _{max} (Å ⁻¹)	0.600
Refinement	
<i>R</i> [<i>F</i> ² > 2 σ (<i>F</i> ²)], <i>wR</i> (<i>F</i> ²), <i>S</i>	0.064, 0.183, 1.03
No. of reflections	11369
No. of parameters	632
No. of restraints	214
H-atom treatment	H-atom parameters constrained
$\Delta\rho_{\text{max}}$, $\Delta\rho_{\text{min}}$ (e Å ⁻³)	0.89, -1.34

Computer programs: SMART and SAINT (Bruker, 2015), SHELXS (Sheldrick, 2008), SHELXL2014/7 (Sheldrick, 2015) and OLEX2 (Dolomanov *et al.*, 2009).

two electrons, which could not be further incorporated into an appropriate model of a fourth orientation of the ether. Therefore, we decided to use the PLATON SQUEEZE (Spek, 2015) solvent masking procedure as implemented in OLEX2 (Dolomanov *et al.*, 2009). The calculated solvent void in the unit cell has a volume of 580 Å³ and 127 e have been recovered. The previous model of the refined parts of the diethyl ether molecules without the use of solvent masking is added as a part of a SHELXL res file to the refine_special_details section of the CIF file. The C5-bonded trimethylsilyl group shows a half-to-half disorder over two positions slightly above and below the plane of the respective phenyl ring. This disorder could be resolved by individual refinement of the respective parts with occupancy factors linked together via a free variable [occupancy ratio 0.504 (4):0.496 (4)]. Additionally two Si–C distance restraints to 1.80 (1) Å were applied for two Si–C bonds, and some *U*_{iso} and *U*_{anis} restraints were used. Atom S2 is disordered over two positions in a 0.509 (7):0.491 (7) ratio. The two disordered S atoms were

treated with SIMU/ISOR restraints; the bond lengths to neighbouring atoms C4 and C8 were subjected to a SADI restraint.

Funding information

Funding for this research was provided by: Deutsche Forschungsgemeinschaft (grant No. CRC813, project A6 to O. Schiemann).

References

- Allen, F. H., Kennard, O., Watson, D. G., Brammer, L., Orpen, A. G. & Taylor, R. (1987). *J. Chem. Soc. Perkin Trans. 2*, pp. S1.
- Bondi, A. (1964). *J. Phys. Chem.* **68**, 441–451.
- Bruker (2015). SADABS, SMART and SAINT. Bruker AXS Inc., Madison, Wisconsin, USA.
- Decroos, C., Prangé, T., Mansuy, D., Boucher, J. & Li, Y. (2011). *Chem. Commun.* **47**, 4805–4807.
- Dolomanov, O. V., Bourhis, L. J., Gildea, R. J., Howard, J. A. K. & Puschmann, H. (2009). *J. Appl. Cryst.* **42**, 339–341.
- Driesschaert, B., Robiette, R., Le Duff, C., Collard, L., Robeyns, K., Gallez, B. & Marchand-Brynaert, J. (2012). *Eur. J. Org. Chem.* **33**, 6517–6525.
- Frank, J., Elewa, M., Said, M., El Shihawy, H. A., El-Sadek, M., Müller, D., Meister, A., Hause, G., Drescher, S., Metz, H., Imming, P. & Mäder, K. (2015). *J. Org. Chem.* **80**, 6754–6766.
- Groom, C. R., Bruno, I. J., Lightfoot, M. P. & Ward, S. C. (2016). *Acta Cryst. B* **72**, 171–179.
- Jähnig, F., Kwiatkowski, G., Däpp, A., Hunkeler, A., Meier, B. H., Kozerke, S. & Ernst, M. (2017). *Phys. Chem. Chem. Phys.* **19**, 19196–19204.
- Jassoy, J. J., Berndhäuser, A., Duthie, F., Kühn, S. P., Hagelueken, G. & Schiemann, O. (2017). *Angew. Chem. Int. Ed.* **56**, 177–181.
- Jeffrey, G. A. (1997). *An Introduction to Hydrogen Bonding*. New York: Oxford University Press.
- Karlon, M., Napolitano, R., Visigalli, M., Lerche, M. H., Jensen, P. & Tedoldi, F. (2014). *Triarylmethyl radicals*, Patent WO2014009240.
- Kunjir, N. C., Reginsson, G. W., Schiemann, O. & Sigurdsson, S. T. (2013). *Phys. Chem. Chem. Phys.* **15**, 19673–19685.
- Liu, Y., Villamena, J., Sun, Y., Xu, I., Dhimitruka, I. & Zweier, J. (2008). *J. Org. Chem.* **73**, 1490–1497.
- Reginsson, G. W., Kunjir, N. C., Sigurdsson, S. T. & Schiemann, O. (2012). *Chem. Eur. J.* **18**, 13580–13584.
- Sheldrick, G. M. (2008). *Acta Cryst. A* **64**, 112–122.
- Sheldrick, G. M. (2015). *Acta Cryst. C* **71**, 3–8.
- Shevelev, G. Y., Krumkacheva, O., Lomzov, A. A., Kuzhelev, A., Trukhin, D. V., Rogozhnikova, O. Y., Tormyshev, V. M., Pysnyi, D. V., Fedin, M. V. & Bagryanskaya, E. G. (2015). *J. Phys. Chem. B*, **119**, 13641–13648.
- Spek, A. L. (2015). *Acta Cryst. C* **71**, 9–18.
- Tormyshev, V. M., Genae, A. M., Sal'nikov, G. E., Rogozhnikova, O. Y., Troitskaya, T. I., Trukhin, D. V., Mamatyuk, V. I., Fadeev, D. S. & Halpern, H. J. (2012). *Eur. J. Org. Chem.* **2012**, 623–629.
- Yang, Z., Liu, Y., Borbat, P., Zweier, J. L., Freed, J. H. & Hubbell, W. L. (2012). *J. Am. Chem. Soc.* **134**, 9950–9952.

supporting information

Acta Cryst. (2018). E74, 539-542 [https://doi.org/10.1107/S2056989018004516]

Tris[2,2,6,6-tetramethyl-8-(trimethylsilyl)benzo[1,2-*d*;4,5-*d'*]bis(1,3-dithiol)-4-yl]methanol diethyl ether monosolvate

Nico Fleck, Gregor Schnakenburg, Alexander C. Filippou and Olav Schiemann

Computing details

Data collection: *SMART* (Bruker, 2015); cell refinement: *SAINT* (Bruker, 2015); data reduction: *SAINT* (Bruker, 2015); program(s) used to solve structure: *SHELXS* (Sheldrick, 2008); program(s) used to refine structure: *SHELXL2014/7* (Sheldrick, 2015); molecular graphics: *OLEX2* (Dolomanov *et al.*, 2009); software used to prepare material for publication: *OLEX2* (Dolomanov *et al.*, 2009).

Tris[2,2,6,6-tetramethyl-8-(trimethylsilyl)benzo[1,2-*d*;4,5-*d'*]bis(1,3-dithiol)-4-yl]methanol diethyl ether monosolvate

Crystal data

$C_{46}H_{64}OS_{12}Si_3$	$Z = 2$
$M_r = 1101.96$	$F(000) = 1164$
Triclinic, $P\bar{1}$	$D_x = 1.162 \text{ Mg m}^{-3}$
$a = 14.9964 (4) \text{ \AA}$	Cu $K\alpha$ radiation, $\lambda = 1.54178 \text{ \AA}$
$b = 15.1070 (4) \text{ \AA}$	Cell parameters from 9511 reflections
$c = 16.0026 (4) \text{ \AA}$	$\theta = 3.0\text{--}72.3^\circ$
$\alpha = 91.6815 (13)^\circ$	$\mu = 4.64 \text{ mm}^{-1}$
$\beta = 117.6083 (11)^\circ$	$T = 100 \text{ K}$
$\gamma = 99.1383 (12)^\circ$	Plate, clear yellowish blue
$V = 3149.79 (15) \text{ \AA}^3$	$0.34 \times 0.18 \times 0.04 \text{ mm}$

Data collection

Bruker D8-Venture diffractometer	$T_{\min} = 0.252$, $T_{\max} = 0.754$
Radiation source: microfocus sealed X-ray tube, Incoatec $I_{\mu}s$	74526 measured reflections
Mirror optics monochromator	11369 independent reflections
Detector resolution: 7.9 pixels mm^{-1} fine slicing ω and φ scans	9723 reflections with $I > 2\sigma(I)$
Absorption correction: multi-scan (SADABS; Bruker, 2015)	$R_{\text{int}} = 0.091$
	$\theta_{\max} = 67.7^\circ$, $\theta_{\min} = 3.0^\circ$
	$h = -18 \rightarrow 17$
	$k = -18 \rightarrow 18$
	$l = -19 \rightarrow 19$

Refinement

Refinement on F^2	214 restraints
Least-squares matrix: full	Primary atom site location: structure-invariant direct methods
$R[F^2 > 2\sigma(F^2)] = 0.064$	Hydrogen site location: inferred from neighbouring sites
$wR(F^2) = 0.183$	H-atom parameters constrained
$S = 1.03$	
11369 reflections	
632 parameters	

$$w = 1/[\sigma^2(F_o^2) + (0.1335P)^2 + 2.6751P]$$

$$\text{where } P = (F_o^2 + 2F_c^2)/3$$

$$(\Delta/\sigma)_{\max} = 0.001$$

$$\Delta\rho_{\max} = 0.89 \text{ e } \text{\AA}^{-3}$$

$$\Delta\rho_{\min} = -1.34 \text{ e } \text{\AA}^{-3}$$

Extinction correction: *SHELXL2014/7*

(Sheldrick 2015),

$$F_c^* = kFc[1 + 0.001xFc^2\lambda^3/\sin(2\theta)]^{-1/4}$$

Extinction coefficient: 0.0018 (2)

Special details

Geometry. All esds (except the esd in the dihedral angle between two l.s. planes) are estimated using the full covariance matrix. The cell esds are taken into account individually in the estimation of esds in distances, angles and torsion angles; correlations between esds in cell parameters are only used when they are defined by crystal symmetry. An approximate (isotropic) treatment of cell esds is used for estimating esds involving l.s. planes.

Refinement. H atoms were positioned geometrically and refined using a riding model as idealised hydroxy- and methyl groups (AFIX codes 147 and 137), thus including free rotation around the respective C-O and C-C bonds. The $U_{\text{iso}}(\text{H})$ was set to 1.5 times $U_{\text{eq}}(\text{C/O})$. At a first attempt a diethyl ether solvent molecule was modeled over three partially occupied positions summing up to one molecule. This model contained still Q-peaks of approx. 2 electrons, which could no be further incorporated into an appropriate model of a forth orientation of the ether. Therefore, we decided to use the solvent masking procedure - as implemented in Olex2 (Dolomanov *et al.*, 2009)). The previous model of the refined parts of diethyl ether molecules is added as a part of a Shelx-RES-file to this section. The C5-bonded trimethylsilyl group shows a half-to-half disorder over two positions slightly above and below the plane of the respective phenyl ring. This disorder could be resolved by individual refinement of the respective parts with occupancy factors linked together via a free variable. Additionally two Si-C distance restraints to 180 (1) pm has been applied for two Si-C bonds, and some U_{iso} and U_{aniso} restraints were used.

PART OF THE RES-FILE FOR THE DISORDERED DIETHYL ETHER MOLECULE INCLUDING Q-PEAKS: >>>
 DFIX 1.48 0.01 O2 C49 O2S C49S DFIX 2.4 0.01 O2 C50 O2 C47 O2S C50S O2S C47S DFIX 1.48 0.01 O2 C48 O2S
 C48S DFIX 2.4 0.01 O2 C47 O2S C47S DFIX 1.54 0.01 C50 C49 C48 C47 C50S C49S C48S C47S DFIX 1.54 0.01
 C50T C49T DFIX 1.54 0.01 C47T C48T DFIX 1.48 0.01 C48T O2T DFIX 1.48 0.01 O2T C49T DFIX 2.48 0.01 C48T
 C49T DFIX 2.48 0.01 C47T O2T DFIX 2.48 0.01 O2T C50T SIMU 0.01 0.02 2 O2T > C50T SIMU 0.01 0.02 2 O2S >
 C50S SIMU 0.01 0.02 2 O2 > C50 RIGU 0.01 0.01 O2 > C50S RIGU 0.01 0.01 O2 > C50T ISOR 0.02 0.04 C50S C47T
 C47S C48S O2S C49S C50T C49T O2T C48T C47 C48 O2 = C49 C50 ISOR 0.01 0.02 C50S C47T ISOR 0.005 0.01
 C47T C50S ISOR 0.001 0.002 C50S ISOR 0.005 0.01 C48 C47T ISOR 0.005 0.01 C50 SUMP 1 0.001 1 3 1 4 1 5
 FVAR 0.13459 0.50735 0.24003 0.3846 0.3772 PART 1 O2 O 0.79116 0.65541 0.99956 31.00000 0.06543 0.04975
 0.04965 = -0.00072 0.04561 0.00256 C47 C 0.68695 0.76136 0.91836 31.00000 0.03672 0.06954 0.04613 = -0.00159
 0.02800 0.00548 AFIX 33 H47A H 0.62092 0.77987 0.89833 31.00000 -1.50000 H47B H 0.74274 0.81100 0.95993
 31.00000 -1.50000 H47C H 0.69454 0.74611 0.86234 31.00000 -1.50000 AFIX 0 C48 C 0.69114 0.67801 0.97272
 31.00000 0.04645 0.04377 0.04303 = 0.00343 0.02874 -0.00366 AFIX 23 H48A H 0.68391 0.69227 1.02980 31.00000
 -1.20000 H48B H 0.63544 0.62702 0.93166 31.00000 -1.20000 AFIX 0 C49 C 0.81142 0.57840 1.05476 31.00000
 0.07746 0.04791 0.05614 = 0.00453 0.03660 -0.00465 AFIX 23 H49A H 0.76026 0.52318 1.01798 31.00000 -1.20000
 H49B H 0.80914 0.59064 1.11479 31.00000 -1.20000 AFIX 0 C50 C 0.92022 0.56745 1.07495 31.00000 0.07775
 0.03830 0.02915 = 0.00545 0.03727 0.02086 AFIX 33 H50A H 0.93907 0.51666 1.11200 31.00000 -1.50000 H50B H
 0.92097 0.55586 1.01472 31.00000 -1.50000 H50C H 0.96954 0.62290 1.11092 31.00000 -1.50000 AFIX 0 PART 0
 PART 2 O2S O 0.80496 0.41812 0.83113 51.00000 0.04242 0.01173 0.02512 = 0.00026 0.02239 0.00148 C47S C
 0.63092 0.43229 0.78311 51.00000 0.05496 0.02781 0.10646 = 0.00791 0.05577 0.02148 AFIX 33 H47D H 0.55907
 0.40093 0.74948 51.00000 -1.50000 H47E H 0.64970 0.45113 0.84923 51.00000 -1.50000 H47F H 0.63991 0.48557
 0.75225 51.00000 -1.50000 AFIX 0 C48S C 0.69956 0.36881 0.78057 51.00000 0.04342 0.01560 0.04336 = 0.00295

0.02662 0.01208 AFIX 23 H48C H 0.69101 0.31461 0.81144 51.00000 -1.20000 H48D H 0.68117 0.34919 0.71407
 51.00000 -1.20000 AFIX 0 C49S C 0.87446 0.36079 0.83049 51.00000 0.03885 0.00950 0.01506 = 0.00470 0.01092
 -0.00216 AFIX 23 H49C H 0.85738 0.34134 0.76431 51.00000 -1.20000 H49D H 0.86760 0.30627 0.86155 51.00000
 -1.20000 AFIX 0 C50S C 0.98333 0.41458 0.88367 51.00000 0.02572 0.02320 0.01865 = 0.00666 0.01154 0.00333
 AFIX 33 H50D H 1.03110 0.37707 0.88395 51.00000 -1.50000 H50E H 0.98952 0.46819 0.85226 51.00000 -1.50000
 H50F H 0.99971 0.43324 0.94917 51.00000 -1.50000 AFIX 0 PART 0 PART 3 O2T O 0.68349 0.55785 0.87942
 41.00000 0.08189 0.06899 0.08683 = 0.01661 0.05060 0.01595 C47T C 0.69930 0.70010 0.96924 41.00000 0.03297
 0.06769 0.07028 = -0.01037 0.03848 -0.00697 AFIX 33 H47G H 0.73596 0.73543 1.03204 41.00000 -1.50000 H47H H
 0.71121 0.73487 0.92339 41.00000 -1.50000 H47I H 0.62566 0.68654 0.94920 41.00000 -1.50000 AFIX 0 C48T C
 0.73819 0.61238 0.97402 41.00000 0.06026 0.06820 0.08184 = 0.01147 0.04640 -0.00876 AFIX 23 H48E H 0.81276
 0.62594 0.99507 41.00000 -1.20000 H48F H 0.72706 0.57752 1.02093 41.00000 -1.20000 AFIX 0 C49T C 0.72052
 0.47357 0.87752 41.00000 0.08416 0.05573 0.09867 = 0.03191 0.04896 0.01075 AFIX 23 H49E H 0.72175 0.44039
 0.93037 41.00000 -1.20000 H49F H 0.79146 0.48813 0.88675 41.00000 -1.20000 AFIX 0 C50T C 0.65152 0.41355
 0.78303 41.00000 0.10387 0.04811 0.11528 = 0.03104 0.06179 0.01396 AFIX 33 H50G H 0.67780 0.35804 0.78363
 41.00000 -1.50000 H50H H 0.58152 0.39827 0.77432 41.00000 -1.50000 H50I H 0.65115 0.44596 0.73075 41.00000
 -1.50000 AFIX 0 PART 0 Q1 Q 0.87840 0.64330 1.06050 11.00000 0.05000 2.190 Q2 Q 0.94500 0.37550 0.85740
 11.00000 0.05000 1.270 <<<<

Fractional atomic coordinates and isotropic or equivalent isotropic displacement parameters (\AA^2)

	<i>x</i>	<i>y</i>	<i>z</i>	$U_{\text{iso}}^*/U_{\text{eq}}$	Occ. (<1)
S1	0.69743 (6)	0.71217 (5)	0.52986 (6)	0.01790 (19)	
S2S	0.5696 (2)	0.81471 (17)	0.5664 (3)	0.0154 (5)	0.509 (7)
S3	0.89076 (6)	1.11185 (6)	0.72696 (6)	0.0236 (2)	
S4	1.00639 (5)	1.02542 (5)	0.65703 (5)	0.01273 (18)	
S5	0.93657 (6)	0.81063 (6)	0.77883 (5)	0.0213 (2)	
S6	1.13719 (7)	0.82128 (7)	0.93714 (6)	0.0282 (2)	
S7	1.30244 (6)	0.79203 (5)	0.69151 (6)	0.01820 (19)	
S8	1.10059 (5)	0.77389 (5)	0.53140 (5)	0.01330 (18)	
S9	0.95695 (6)	0.61647 (5)	0.61759 (5)	0.01480 (19)	
S10	0.84595 (6)	0.47280 (5)	0.46182 (5)	0.01626 (19)	
S11	0.65178 (6)	0.71730 (5)	0.21722 (5)	0.01615 (19)	
S12	0.77538 (5)	0.86504 (5)	0.36777 (5)	0.01236 (18)	
Si1	0.69340 (15)	0.99991 (13)	0.74868 (15)	0.0252 (7)	0.504 (4)
Si1S	0.63902 (16)	1.02339 (14)	0.67283 (16)	0.0270 (7)	0.496 (4)
Si2	1.34975 (7)	0.82358 (6)	0.92788 (6)	0.0223 (2)	
Si3	0.66839 (6)	0.49178 (6)	0.24913 (6)	0.0150 (2)	
O1	0.95362 (15)	0.89480 (13)	0.52132 (14)	0.0102 (4)	
H1	0.9979	0.8807	0.5080	0.015*	
C1	0.9234 (2)	0.82424 (19)	0.5669 (2)	0.0106 (4)	
C2	0.8534 (2)	0.86769 (19)	0.5959 (2)	0.0107 (5)	
C3	0.7569 (2)	0.8247 (2)	0.5815 (2)	0.0145 (6)	
C4	0.7001 (3)	0.8704 (2)	0.6112 (3)	0.0233 (7)	
C5	0.7365 (3)	0.9575 (3)	0.6598 (3)	0.0323 (9)	
C6	0.8325 (3)	0.9997 (2)	0.6714 (2)	0.0213 (7)	

C7	0.8895 (2)	0.9575 (2)	0.6391 (2)	0.0124 (6)	
C8	0.6076 (3)	0.6992 (3)	0.5781 (3)	0.0299 (8)	
C9	0.6567 (4)	0.6697 (4)	0.6763 (4)	0.0552 (12)	
H9A	0.6771	0.6117	0.6730	0.083*	
H9B	0.6075	0.6631	0.7010	0.083*	
H9C	0.7174	0.7151	0.7185	0.083*	
C10	0.5117 (3)	0.6320 (3)	0.5099 (3)	0.0356 (9)	
H10A	0.4805	0.6545	0.4478	0.053*	
H10B	0.4627	0.6242	0.5348	0.053*	
H10C	0.5300	0.5738	0.5029	0.053*	
C11	0.5648 (8)	0.9405 (7)	0.7318 (8)	0.035 (3)	0.504 (4)
H11A	0.5128	0.9394	0.6656	0.053*	0.504 (4)
H11B	0.5462	0.9727	0.7736	0.053*	0.504 (4)
H11C	0.5686	0.8785	0.7474	0.053*	0.504 (4)
C11S	0.6114 (11)	0.9658 (9)	0.7616 (9)	0.048 (3)	0.496 (4)
H11D	0.5878	0.9009	0.7404	0.072*	0.496 (4)
H11E	0.5580	0.9903	0.7681	0.072*	0.496 (4)
H11F	0.6740	0.9758	0.8230	0.072*	0.496 (4)
C12	0.6858 (10)	1.1186 (6)	0.7389 (9)	0.050 (3)	0.504 (4)
H12A	0.7547	1.1546	0.7612	0.075*	0.504 (4)
H12B	0.6563	1.1385	0.7778	0.075*	0.504 (4)
H12C	0.6422	1.1264	0.6724	0.075*	0.504 (4)
C12S	0.6782 (9)	1.1423 (8)	0.7090 (8)	0.042 (3)	0.496 (4)
H12D	0.7322	1.1536	0.7753	0.063*	0.496 (4)
H12E	0.6193	1.1674	0.7028	0.063*	0.496 (4)
H12F	0.7045	1.1712	0.6687	0.063*	0.496 (4)
C13	0.7901 (7)	0.9908 (8)	0.8727 (6)	0.053 (3)	0.504 (4)
H13A	0.7800	0.9283	0.8865	0.080*	0.504 (4)
H13B	0.7819	1.0307	0.9170	0.080*	0.504 (4)
H13C	0.8592	1.0086	0.8798	0.080*	0.504 (4)
C13S	0.5219 (5)	1.0181 (6)	0.5587 (5)	0.037 (2)	0.496 (4)
H13D	0.5409	1.0336	0.5093	0.056*	0.496 (4)
H13E	0.4820	1.0609	0.5647	0.056*	0.496 (4)
H13F	0.4806	0.9568	0.5414	0.056*	0.496 (4)
C14	1.0211 (3)	1.1019 (2)	0.7552 (2)	0.0200 (7)	
C15	1.0781 (3)	1.1956 (2)	0.7551 (3)	0.0259 (8)	
H15A	1.0451	1.2145	0.6914	0.039*	
H15B	1.1496	1.1931	0.7732	0.039*	
H15C	1.0761	1.2390	0.8006	0.039*	
C16	1.0746 (3)	1.0643 (3)	0.8492 (2)	0.0279 (8)	
H16A	1.0820	1.1065	0.9007	0.042*	
H16B	1.1425	1.0560	0.8603	0.042*	
H16C	1.0337	1.0060	0.8472	0.042*	
C17	1.0223 (2)	0.80852 (19)	0.6547 (2)	0.0122 (5)	
C18	1.0354 (2)	0.8110 (2)	0.7474 (2)	0.0145 (6)	
C19	1.1330 (3)	0.8122 (2)	0.8245 (2)	0.0189 (7)	
C20	1.2209 (2)	0.8106 (2)	0.8155 (2)	0.0180 (7)	
C21	1.2046 (2)	0.8029 (2)	0.7213 (2)	0.0142 (6)	

C22	1.1077 (2)	0.79875 (19)	0.6436 (2)	0.0125 (6)
C23	1.0042 (3)	0.7670 (3)	0.8926 (2)	0.0288 (8)
C24	0.9651 (3)	0.7987 (3)	0.9588 (3)	0.0409 (11)
H24A	0.9763	0.8648	0.9660	0.061*
H24B	1.0023	0.7780	1.0210	0.061*
H24C	0.8916	0.7738	0.9318	0.061*
C25	0.9910 (4)	0.6646 (3)	0.8790 (3)	0.0429 (11)
H25A	0.9186	0.6370	0.8552	0.064*
H25B	1.0326	0.6434	0.9399	0.064*
H25C	1.0133	0.6475	0.8331	0.064*
C26	1.3716 (3)	0.9374 (3)	0.9911 (3)	0.0285 (8)
H26A	1.3768	0.9841	0.9515	0.043*
H26B	1.4354	0.9466	1.0514	0.043*
H26C	1.3140	0.9412	1.0034	0.043*
C27	1.3473 (4)	0.7314 (3)	1.0037 (3)	0.0403 (11)
H27A	1.2910	0.6809	0.9650	0.060*
H27B	1.3371	0.7548	1.0558	0.060*
H27C	1.4126	0.7104	1.0300	0.060*
C28	1.4621 (3)	0.8195 (3)	0.9072 (3)	0.0347 (9)
H28A	1.4504	0.7620	0.8702	0.052*
H28B	1.5243	0.8248	0.9684	0.052*
H28C	1.4704	0.8695	0.8721	0.052*
C29	1.2354 (2)	0.8224 (2)	0.5714 (2)	0.0154 (6)
C30	1.2719 (3)	0.7776 (2)	0.5092 (3)	0.0228 (7)
H30A	1.3445	0.8029	0.5313	0.034*
H30B	1.2314	0.7886	0.4432	0.034*
H30C	1.2631	0.7124	0.5132	0.034*
C31	1.2502 (3)	0.9242 (2)	0.5710 (3)	0.0214 (7)
H31A	1.2271	0.9503	0.6126	0.032*
H31B	1.2100	0.9385	0.5061	0.032*
H31C	1.3230	0.9495	0.5939	0.032*
C32	0.8655 (2)	0.74079 (19)	0.4918 (2)	0.0109 (4)
C33	0.8767 (2)	0.6516 (2)	0.5076 (2)	0.0115 (4)
C34	0.8192 (2)	0.5809 (2)	0.4325 (2)	0.0120 (5)
C35	0.7463 (2)	0.5947 (2)	0.3412 (2)	0.0141 (6)
C36	0.7371 (2)	0.6845 (2)	0.3271 (2)	0.0119 (5)
C37	0.7959 (2)	0.7566 (2)	0.3995 (2)	0.0111 (4)
C38	0.8890 (2)	0.4986 (2)	0.5879 (2)	0.0166 (7)
C39	0.9658 (3)	0.4392 (2)	0.6430 (2)	0.0203 (7)
H39A	1.0200	0.4457	0.6244	0.030*
H39B	0.9303	0.3760	0.6285	0.030*
H39C	0.9961	0.4578	0.7112	0.030*
C40	0.7995 (3)	0.4882 (2)	0.6093 (2)	0.0215 (7)
H40A	0.8251	0.5054	0.6772	0.032*
H40B	0.7631	0.4251	0.5921	0.032*
H40C	0.7524	0.5272	0.5724	0.032*
C41	0.5858 (3)	0.4220 (2)	0.2915 (3)	0.0235 (7)
H41A	0.6292	0.4044	0.3540	0.035*

H41B	0.5462	0.3677	0.2463	0.035*	
H41C	0.5386	0.4573	0.2965	0.035*	
C42	0.7586 (3)	0.4307 (2)	0.2315 (2)	0.0222 (7)	
H42A	0.7983	0.4708	0.2084	0.033*	
H42B	0.7194	0.3773	0.1848	0.033*	
H42C	0.8054	0.4118	0.2920	0.033*	
C43	0.5797 (3)	0.5163 (2)	0.1276 (2)	0.0269 (8)	
H43A	0.5279	0.5466	0.1304	0.040*	
H43B	0.5458	0.4596	0.0851	0.040*	
H43C	0.6189	0.5555	0.1034	0.040*	
C44	0.6490 (2)	0.8268 (2)	0.2665 (2)	0.0177 (7)	
C45	0.5651 (3)	0.8175 (3)	0.2959 (3)	0.0254 (8)	
H45A	0.4984	0.7943	0.2403	0.038*	
H45B	0.5647	0.8766	0.3224	0.038*	
H45C	0.5782	0.7754	0.3439	0.038*	
C46	0.6336 (3)	0.8933 (2)	0.1934 (2)	0.0250 (8)	
H46A	0.6883	0.8972	0.1756	0.038*	
H46B	0.6356	0.9530	0.2206	0.038*	
H46C	0.5670	0.8726	0.1369	0.038*	
S2	0.5825 (2)	0.80229 (18)	0.5960 (3)	0.0152 (5)	0.491 (7)

Atomic displacement parameters (\AA^2)

	U^{11}	U^{22}	U^{33}	U^{12}	U^{13}	U^{23}
S1	0.0118 (4)	0.0104 (4)	0.0299 (4)	-0.0058 (3)	0.0113 (3)	-0.0037 (3)
S2S	0.0108 (6)	0.0183 (7)	0.0175 (8)	-0.0042 (5)	0.0095 (6)	-0.0011 (6)
S3	0.0157 (4)	0.0176 (4)	0.0356 (4)	-0.0051 (3)	0.0142 (3)	-0.0159 (3)
S4	0.0086 (3)	0.0088 (3)	0.0184 (4)	-0.0047 (3)	0.0069 (3)	-0.0069 (3)
S5	0.0151 (4)	0.0295 (5)	0.0164 (4)	-0.0050 (3)	0.0080 (3)	-0.0001 (3)
S6	0.0222 (5)	0.0387 (5)	0.0134 (4)	-0.0039 (4)	0.0032 (3)	-0.0009 (3)
S7	0.0081 (3)	0.0157 (4)	0.0254 (4)	0.0018 (3)	0.0038 (3)	-0.0004 (3)
S8	0.0071 (3)	0.0111 (4)	0.0178 (4)	-0.0021 (3)	0.0043 (3)	-0.0056 (3)
S9	0.0125 (4)	0.0075 (3)	0.0162 (3)	-0.0028 (3)	0.0017 (3)	-0.0010 (3)
S10	0.0159 (4)	0.0058 (4)	0.0190 (4)	-0.0024 (3)	0.0033 (3)	-0.0034 (3)
S11	0.0121 (4)	0.0112 (4)	0.0154 (4)	-0.0008 (3)	-0.0003 (3)	-0.0036 (3)
S12	0.0080 (3)	0.0065 (3)	0.0163 (4)	-0.0018 (3)	0.0018 (3)	-0.0026 (3)
Si1	0.0163 (10)	0.0207 (11)	0.0404 (14)	-0.0054 (8)	0.0189 (10)	-0.0148 (8)
Si1S	0.0232 (12)	0.0224 (11)	0.0444 (15)	0.0027 (8)	0.0246 (11)	-0.0049 (9)
Si2	0.0154 (5)	0.0156 (5)	0.0202 (5)	0.0001 (3)	-0.0033 (4)	-0.0038 (3)
Si3	0.0111 (4)	0.0091 (4)	0.0173 (4)	-0.0048 (3)	0.0032 (3)	-0.0061 (3)
O1	0.0076 (8)	0.0078 (8)	0.0149 (8)	-0.0022 (7)	0.0065 (7)	-0.0021 (7)
C1	0.0079 (7)	0.0064 (7)	0.0148 (7)	-0.0021 (6)	0.0043 (6)	-0.0016 (6)
C2	0.0079 (9)	0.0072 (9)	0.0144 (9)	-0.0016 (8)	0.0043 (8)	-0.0020 (8)
C3	0.0073 (14)	0.0165 (16)	0.0173 (15)	-0.0024 (12)	0.0058 (12)	-0.0052 (12)
C4	0.0159 (13)	0.0236 (14)	0.0304 (14)	-0.0040 (11)	0.0139 (11)	-0.0077 (11)
C5	0.0251 (15)	0.0315 (16)	0.0441 (16)	0.0016 (12)	0.0218 (13)	-0.0136 (12)
C6	0.0137 (16)	0.0179 (17)	0.0291 (18)	-0.0061 (13)	0.0112 (14)	-0.0142 (13)
C7	0.0087 (12)	0.0122 (12)	0.0143 (12)	-0.0032 (10)	0.0057 (10)	-0.0014 (10)

C8	0.0224 (13)	0.0324 (14)	0.0371 (14)	-0.0026 (11)	0.0183 (11)	0.0054 (11)
C9	0.0381 (19)	0.072 (2)	0.052 (2)	-0.0080 (18)	0.0231 (17)	0.0236 (18)
C10	0.0232 (16)	0.0264 (17)	0.0545 (19)	-0.0067 (14)	0.0204 (15)	-0.0026 (15)
C11	0.031 (6)	0.029 (5)	0.052 (7)	-0.010 (4)	0.031 (5)	-0.022 (4)
C11S	0.056 (9)	0.056 (8)	0.048 (7)	-0.002 (6)	0.043 (7)	-0.006 (6)
C12	0.047 (4)	0.051 (5)	0.059 (4)	0.017 (3)	0.029 (3)	0.004 (3)
C12S	0.040 (4)	0.051 (4)	0.049 (4)	0.023 (3)	0.027 (3)	0.004 (3)
C13	0.040 (5)	0.083 (8)	0.034 (5)	-0.009 (5)	0.024 (4)	-0.027 (5)
C13S	0.027 (4)	0.027 (4)	0.064 (6)	0.015 (3)	0.024 (4)	0.009 (4)
C14	0.0133 (16)	0.0178 (17)	0.0255 (17)	-0.0057 (13)	0.0100 (14)	-0.0141 (13)
C15	0.0188 (16)	0.0171 (16)	0.0373 (18)	-0.0083 (13)	0.0144 (14)	-0.0158 (13)
C16	0.0200 (18)	0.035 (2)	0.0206 (17)	-0.0062 (15)	0.0075 (15)	-0.0136 (15)
C17	0.0095 (9)	0.0066 (9)	0.0152 (9)	-0.0028 (7)	0.0028 (7)	-0.0013 (7)
C18	0.0121 (12)	0.0114 (12)	0.0161 (12)	-0.0030 (10)	0.0052 (10)	-0.0019 (10)
C19	0.0173 (16)	0.0148 (16)	0.0173 (15)	-0.0035 (13)	0.0045 (13)	-0.0015 (12)
C20	0.0127 (15)	0.0094 (15)	0.0206 (16)	-0.0024 (12)	0.0001 (13)	-0.0020 (12)
C21	0.0106 (12)	0.0087 (12)	0.0191 (12)	-0.0012 (10)	0.0047 (10)	-0.0013 (10)
C22	0.0112 (12)	0.0068 (12)	0.0151 (12)	-0.0029 (10)	0.0044 (10)	-0.0027 (9)
C23	0.027 (2)	0.036 (2)	0.0178 (17)	-0.0071 (16)	0.0092 (15)	0.0050 (15)
C24	0.035 (2)	0.063 (3)	0.0242 (19)	-0.004 (2)	0.0181 (18)	0.0033 (18)
C25	0.051 (3)	0.039 (3)	0.031 (2)	-0.008 (2)	0.018 (2)	0.0089 (18)
C26	0.0201 (18)	0.0244 (19)	0.0277 (18)	-0.0022 (15)	0.0029 (15)	-0.0068 (14)
C27	0.041 (2)	0.025 (2)	0.030 (2)	0.0001 (18)	-0.0026 (18)	0.0044 (16)
C28	0.0200 (17)	0.039 (2)	0.0280 (18)	0.0076 (15)	-0.0027 (14)	-0.0098 (15)
C29	0.0084 (12)	0.0133 (13)	0.0215 (13)	-0.0003 (10)	0.0057 (10)	-0.0026 (10)
C30	0.0139 (16)	0.0190 (17)	0.0358 (19)	0.0009 (13)	0.0132 (15)	-0.0058 (14)
C31	0.0152 (16)	0.0127 (16)	0.0319 (18)	-0.0037 (13)	0.0096 (14)	-0.0009 (13)
C32	0.0071 (7)	0.0073 (7)	0.0153 (7)	-0.0024 (6)	0.0042 (6)	-0.0020 (6)
C33	0.0070 (8)	0.0079 (9)	0.0163 (8)	-0.0017 (7)	0.0039 (7)	-0.0021 (7)
C34	0.0077 (10)	0.0078 (10)	0.0175 (10)	-0.0011 (8)	0.0044 (8)	-0.0016 (8)
C35	0.0089 (14)	0.0123 (15)	0.0175 (15)	-0.0050 (12)	0.0057 (12)	-0.0034 (12)
C36	0.0071 (10)	0.0096 (10)	0.0154 (10)	-0.0022 (8)	0.0037 (8)	-0.0021 (8)
C37	0.0066 (8)	0.0081 (9)	0.0159 (8)	-0.0016 (7)	0.0042 (7)	-0.0027 (7)
C38	0.0148 (16)	0.0083 (14)	0.0163 (15)	-0.0054 (12)	0.0015 (13)	-0.0032 (11)
C39	0.0189 (17)	0.0125 (16)	0.0234 (16)	0.0011 (13)	0.0054 (14)	0.0037 (12)
C40	0.0221 (18)	0.0134 (16)	0.0249 (17)	-0.0038 (13)	0.0103 (14)	-0.0002 (13)
C41	0.0149 (17)	0.0154 (17)	0.0346 (19)	-0.0054 (13)	0.0101 (15)	-0.0048 (14)
C42	0.0212 (17)	0.0158 (17)	0.0239 (17)	-0.0035 (13)	0.0086 (14)	-0.0075 (13)
C43	0.0258 (19)	0.0184 (18)	0.0204 (17)	-0.0023 (14)	0.0002 (15)	-0.0063 (13)
C44	0.0139 (16)	0.0103 (15)	0.0210 (16)	0.0011 (12)	0.0022 (13)	-0.0031 (12)
C45	0.0091 (15)	0.0265 (19)	0.0325 (19)	0.0022 (14)	0.0042 (14)	-0.0083 (15)
C46	0.0234 (18)	0.0144 (17)	0.0249 (18)	0.0062 (14)	0.0005 (15)	0.0006 (13)
S2	0.0110 (6)	0.0170 (7)	0.0170 (9)	-0.0038 (5)	0.0084 (6)	-0.0010 (6)

Geometric parameters (Å, °)

S1—C3	1.767 (3)	C13—H13C	0.9800
S1—C8	1.827 (4)	C13S—H13D	0.9800

S2S—C4	1.786 (4)	C13S—H13E	0.9800
S2S—C8	1.908 (5)	C13S—H13F	0.9800
S3—C6	1.774 (3)	C14—C15	1.533 (5)
S3—C14	1.823 (3)	C14—C16	1.519 (5)
S4—C7	1.776 (3)	C15—H15A	0.9800
S4—C14	1.828 (3)	C15—H15B	0.9800
S5—C18	1.771 (3)	C15—H15C	0.9800
S5—C23	1.829 (4)	C16—H16A	0.9800
S6—C19	1.775 (3)	C16—H16B	0.9800
S6—C23	1.813 (4)	C16—H16C	0.9800
S7—C21	1.768 (3)	C17—C18	1.401 (4)
S7—C29	1.823 (3)	C17—C22	1.401 (4)
S8—C22	1.773 (3)	C18—C19	1.407 (5)
S8—C29	1.827 (3)	C19—C20	1.396 (5)
S9—C33	1.766 (3)	C20—C21	1.409 (5)
S9—C38	1.832 (3)	C21—C22	1.397 (4)
S10—C34	1.768 (3)	C23—C24	1.527 (6)
S10—C38	1.819 (3)	C23—C25	1.524 (6)
S11—C36	1.773 (3)	C24—H24A	0.9800
S11—C44	1.827 (3)	C24—H24B	0.9800
S12—C37	1.761 (3)	C24—H24C	0.9800
S12—C44	1.817 (3)	C25—H25A	0.9800
Si1—C5	1.945 (4)	C25—H25B	0.9800
Si1—C11	1.884 (10)	C25—H25C	0.9800
Si1—C12	1.821 (8)	C26—H26A	0.9800
Si1—C13	1.863 (10)	C26—H26B	0.9800
Si1S—C5	1.976 (4)	C26—H26C	0.9800
Si1S—C11S	1.857 (11)	C27—H27A	0.9800
Si1S—C12S	1.788 (12)	C27—H27B	0.9800
Si1S—C13S	1.844 (7)	C27—H27C	0.9800
Si2—C20	1.909 (3)	C28—H28A	0.9800
Si2—C26	1.871 (4)	C28—H28B	0.9800
Si2—C27	1.881 (4)	C28—H28C	0.9800
Si2—C28	1.871 (4)	C29—C30	1.526 (4)
Si3—C35	1.910 (3)	C29—C31	1.519 (4)
Si3—C41	1.875 (4)	C30—H30A	0.9800
Si3—C42	1.871 (4)	C30—H30B	0.9800
Si3—C43	1.868 (4)	C30—H30C	0.9800
O1—H1	0.8400	C31—H31A	0.9800
O1—C1	1.439 (3)	C31—H31B	0.9800
C1—C2	1.550 (4)	C31—H31C	0.9800
C1—C17	1.559 (4)	C32—C33	1.401 (4)
C1—C32	1.544 (4)	C32—C37	1.413 (4)
C2—C3	1.397 (4)	C33—C34	1.414 (4)
C2—C7	1.407 (4)	C34—C35	1.408 (4)
C3—C4	1.404 (5)	C35—C36	1.400 (4)
C4—C5	1.397 (5)	C36—C37	1.407 (4)
C4—S2	1.799 (4)	C38—C39	1.530 (4)

C5—C6	1.404 (5)	C38—C40	1.518 (5)
C6—C7	1.400 (5)	C39—H39A	0.9800
C8—C9	1.511 (6)	C39—H39B	0.9800
C8—C10	1.520 (5)	C39—H39C	0.9800
C8—S2	1.705 (5)	C40—H40A	0.9800
C9—H9A	0.9800	C40—H40B	0.9800
C9—H9B	0.9800	C40—H40C	0.9800
C9—H9C	0.9800	C41—H41A	0.9800
C10—H10A	0.9800	C41—H41B	0.9800
C10—H10B	0.9800	C41—H41C	0.9800
C10—H10C	0.9800	C42—H42A	0.9800
C11—H11A	0.9800	C42—H42B	0.9800
C11—H11B	0.9800	C42—H42C	0.9800
C11—H11C	0.9800	C43—H43A	0.9800
C11S—H11D	0.9800	C43—H43B	0.9800
C11S—H11E	0.9800	C43—H43C	0.9800
C11S—H11F	0.9800	C44—C45	1.523 (5)
C12—H12A	0.9800	C44—C46	1.525 (5)
C12—H12B	0.9800	C45—H45A	0.9800
C12—H12C	0.9800	C45—H45B	0.9800
C12S—H12D	0.9800	C45—H45C	0.9800
C12S—H12E	0.9800	C46—H46A	0.9800
C12S—H12F	0.9800	C46—H46B	0.9800
C13—H13A	0.9800	C46—H46C	0.9800
C13—H13B	0.9800		
C3—S1—C8	96.06 (16)	C17—C18—S5	125.4 (2)
C4—S2S—C8	91.3 (2)	C17—C18—C19	120.0 (3)
C6—S3—C14	96.06 (15)	C19—C18—S5	114.6 (2)
C7—S4—C14	95.31 (14)	C18—C19—S6	114.1 (3)
C18—S5—C23	95.05 (16)	C20—C19—S6	121.8 (2)
C19—S6—C23	94.64 (16)	C20—C19—C18	124.0 (3)
C21—S7—C29	95.61 (14)	C19—C20—Si2	118.8 (2)
C22—S8—C29	94.48 (14)	C19—C20—C21	114.8 (3)
C33—S9—C38	95.63 (14)	C21—C20—Si2	126.4 (3)
C34—S10—C38	95.11 (14)	C20—C21—S7	123.1 (2)
C36—S11—C44	95.94 (14)	C22—C21—S7	114.8 (2)
C37—S12—C44	95.72 (14)	C22—C21—C20	122.1 (3)
C11—Si1—C5	116.3 (3)	C17—C22—S8	123.2 (2)
C12—Si1—C5	109.0 (5)	C21—C22—S8	114.7 (2)
C12—Si1—C11	106.2 (6)	C21—C22—C17	122.0 (3)
C12—Si1—C13	107.7 (6)	S6—C23—S5	104.15 (18)
C13—Si1—C5	110.1 (3)	C24—C23—S5	108.2 (3)
C13—Si1—C11	107.2 (5)	C24—C23—S6	109.3 (3)
C11S—Si1S—C5	103.6 (5)	C25—C23—S5	111.0 (3)
C12S—Si1S—C5	118.5 (4)	C25—C23—S6	111.2 (3)
C12S—Si1S—C11S	109.7 (6)	C25—C23—C24	112.6 (3)
C12S—Si1S—C13S	101.5 (5)	C23—C24—H24A	109.5

C13S—Si1S—C5	111.8 (3)	C23—C24—H24B	109.5
C13S—Si1S—C11S	112.0 (5)	C23—C24—H24C	109.5
C26—Si2—C20	105.85 (16)	H24A—C24—H24B	109.5
C26—Si2—C27	111.40 (19)	H24A—C24—H24C	109.5
C26—Si2—C28	107.75 (18)	H24B—C24—H24C	109.5
C27—Si2—C20	110.87 (17)	C23—C25—H25A	109.5
C28—Si2—C20	115.02 (16)	C23—C25—H25B	109.5
C28—Si2—C27	106.0 (2)	C23—C25—H25C	109.5
C41—Si3—C35	107.76 (14)	H25A—C25—H25B	109.5
C42—Si3—C35	108.79 (14)	H25A—C25—H25C	109.5
C42—Si3—C41	114.03 (16)	H25B—C25—H25C	109.5
C43—Si3—C35	115.80 (15)	Si2—C26—H26A	109.5
C43—Si3—C41	106.23 (17)	Si2—C26—H26B	109.5
C43—Si3—C42	104.41 (17)	Si2—C26—H26C	109.5
C1—O1—H1	109.5	H26A—C26—H26B	109.5
O1—C1—C2	101.3 (2)	H26A—C26—H26C	109.5
O1—C1—C17	107.7 (2)	H26B—C26—H26C	109.5
O1—C1—C32	107.1 (2)	Si2—C27—H27A	109.5
C2—C1—C17	112.2 (2)	Si2—C27—H27B	109.5
C32—C1—C2	113.5 (2)	Si2—C27—H27C	109.5
C32—C1—C17	114.0 (2)	H27A—C27—H27B	109.5
C3—C2—C1	125.0 (3)	H27A—C27—H27C	109.5
C3—C2—C7	117.6 (3)	H27B—C27—H27C	109.5
C7—C2—C1	117.4 (3)	Si2—C28—H28A	109.5
C2—C3—S1	125.3 (2)	Si2—C28—H28B	109.5
C2—C3—C4	120.3 (3)	Si2—C28—H28C	109.5
C4—C3—S1	114.5 (2)	H28A—C28—H28B	109.5
C3—C4—S2S	114.0 (3)	H28A—C28—H28C	109.5
C3—C4—S2	114.4 (3)	H28B—C28—H28C	109.5
C5—C4—S2S	121.9 (3)	S7—C29—S8	104.30 (16)
C5—C4—C3	123.5 (3)	C30—C29—S7	108.9 (2)
C5—C4—S2	121.6 (3)	C30—C29—S8	109.5 (2)
C4—C5—Si1	123.0 (3)	C31—C29—S7	111.3 (2)
C4—C5—Si1S	119.0 (3)	C31—C29—S8	110.3 (2)
C4—C5—C6	114.9 (3)	C31—C29—C30	112.2 (3)
C6—C5—Si1	117.6 (3)	C29—C30—H30A	109.5
C6—C5—Si1S	123.6 (3)	C29—C30—H30B	109.5
C5—C6—S3	122.3 (3)	C29—C30—H30C	109.5
C7—C6—S3	114.6 (2)	H30A—C30—H30B	109.5
C7—C6—C5	123.1 (3)	H30A—C30—H30C	109.5
C2—C7—S4	124.3 (2)	H30B—C30—H30C	109.5
C6—C7—S4	115.3 (2)	C29—C31—H31A	109.5
C6—C7—C2	120.5 (3)	C29—C31—H31B	109.5
S1—C8—S2S	101.3 (2)	C29—C31—H31C	109.5
C9—C8—S1	110.6 (3)	H31A—C31—H31B	109.5
C9—C8—S2S	117.7 (4)	H31A—C31—H31C	109.5
C9—C8—C10	111.8 (4)	H31B—C31—H31C	109.5
C9—C8—S2	104.0 (4)	C33—C32—C1	125.4 (3)

C10—C8—S1	108.5 (3)	C33—C32—C37	117.8 (3)
C10—C8—S2S	106.1 (3)	C37—C32—C1	116.8 (3)
C10—C8—S2	112.7 (3)	C32—C33—S9	125.3 (2)
S2—C8—S1	109.2 (2)	C32—C33—C34	119.9 (3)
C8—C9—H9A	109.5	C34—C33—S9	114.7 (2)
C8—C9—H9B	109.5	C33—C34—S10	114.7 (2)
C8—C9—H9C	109.5	C35—C34—S10	122.1 (2)
H9A—C9—H9B	109.5	C35—C34—C33	123.2 (3)
H9A—C9—H9C	109.5	C34—C35—Si3	118.5 (2)
H9B—C9—H9C	109.5	C36—C35—Si3	125.8 (2)
C8—C10—H10A	109.5	C36—C35—C34	115.7 (3)
C8—C10—H10B	109.5	C35—C36—S11	123.3 (2)
C8—C10—H10C	109.5	C35—C36—C37	122.4 (3)
H10A—C10—H10B	109.5	C37—C36—S11	114.4 (2)
H10A—C10—H10C	109.5	C32—C37—S12	123.2 (2)
H10B—C10—H10C	109.5	C36—C37—S12	115.9 (2)
Si1—C11—H11A	109.5	C36—C37—C32	120.9 (3)
Si1—C11—H11B	109.5	S10—C38—S9	104.94 (16)
Si1—C11—H11C	109.5	C39—C38—S9	108.5 (2)
H11A—C11—H11B	109.5	C39—C38—S10	108.7 (2)
H11A—C11—H11C	109.5	C40—C38—S9	110.3 (2)
H11B—C11—H11C	109.5	C40—C38—S10	111.6 (2)
Si1S—C11S—H11D	109.5	C40—C38—C39	112.4 (3)
Si1S—C11S—H11E	109.5	C38—C39—H39A	109.5
Si1S—C11S—H11F	109.5	C38—C39—H39B	109.5
H11D—C11S—H11E	109.5	C38—C39—H39C	109.5
H11D—C11S—H11F	109.5	H39A—C39—H39B	109.5
H11E—C11S—H11F	109.5	H39A—C39—H39C	109.5
Si1—C12—H12A	109.5	H39B—C39—H39C	109.5
Si1—C12—H12B	109.5	C38—C40—H40A	109.5
Si1—C12—H12C	109.5	C38—C40—H40B	109.5
H12A—C12—H12B	109.5	C38—C40—H40C	109.5
H12A—C12—H12C	109.5	H40A—C40—H40B	109.5
H12B—C12—H12C	109.5	H40A—C40—H40C	109.5
Si1S—C12S—H12D	109.5	H40B—C40—H40C	109.5
Si1S—C12S—H12E	109.5	Si3—C41—H41A	109.5
Si1S—C12S—H12F	109.5	Si3—C41—H41B	109.5
H12D—C12S—H12E	109.5	Si3—C41—H41C	109.5
H12D—C12S—H12F	109.5	H41A—C41—H41B	109.5
H12E—C12S—H12F	109.5	H41A—C41—H41C	109.5
Si1—C13—H13A	109.5	H41B—C41—H41C	109.5
Si1—C13—H13B	109.5	Si3—C42—H42A	109.5
Si1—C13—H13C	109.5	Si3—C42—H42B	109.5
H13A—C13—H13B	109.5	Si3—C42—H42C	109.5
H13A—C13—H13C	109.5	H42A—C42—H42B	109.5
H13B—C13—H13C	109.5	H42A—C42—H42C	109.5
Si1S—C13S—H13D	109.5	H42B—C42—H42C	109.5
Si1S—C13S—H13E	109.5	Si3—C43—H43A	109.5

Si1S—C13S—H13F	109.5	Si3—C43—H43B	109.5
H13D—C13S—H13E	109.5	Si3—C43—H43C	109.5
H13D—C13S—H13F	109.5	H43A—C43—H43B	109.5
H13E—C13S—H13F	109.5	H43A—C43—H43C	109.5
S3—C14—S4	105.04 (16)	H43B—C43—H43C	109.5
C15—C14—S3	107.6 (2)	S12—C44—S11	105.83 (16)
C15—C14—S4	109.3 (2)	C45—C44—S11	110.4 (2)
C16—C14—S3	111.4 (2)	C45—C44—S12	111.5 (2)
C16—C14—S4	110.9 (2)	C45—C44—C46	111.7 (3)
C16—C14—C15	112.2 (3)	C46—C44—S11	109.1 (2)
C14—C15—H15A	109.5	C46—C44—S12	108.1 (2)
C14—C15—H15B	109.5	C44—C45—H45A	109.5
C14—C15—H15C	109.5	C44—C45—H45B	109.5
H15A—C15—H15B	109.5	C44—C45—H45C	109.5
H15A—C15—H15C	109.5	H45A—C45—H45B	109.5
H15B—C15—H15C	109.5	H45A—C45—H45C	109.5
C14—C16—H16A	109.5	H45B—C45—H45C	109.5
C14—C16—H16B	109.5	C44—C46—H46A	109.5
C14—C16—H16C	109.5	C44—C46—H46B	109.5
H16A—C16—H16B	109.5	C44—C46—H46C	109.5
H16A—C16—H16C	109.5	H46A—C46—H46B	109.5
H16B—C16—H16C	109.5	H46A—C46—H46C	109.5
C18—C17—C1	124.2 (3)	H46B—C46—H46C	109.5
C22—C17—C1	119.0 (3)	C8—S2—C4	97.9 (2)
C22—C17—C18	116.6 (3)		

Hydrogen-bond geometry (Å, °)

<i>D</i> —H... <i>A</i>	<i>D</i> —H	H... <i>A</i>	<i>D</i> ... <i>A</i>	<i>D</i> —H... <i>A</i>
O1—H1...S8	0.84	2.32	3.031 (2)	142
C9—H9C...S5	0.98	3.05	3.926 (5)	150
C12—H12A...S3	0.98	2.51	3.184 (16)	126
C13—H13B...S6 ⁱ	0.98	2.85	3.734 (10)	150
C15—H15B...S11 ⁱⁱ	0.98	3.00	3.866 (4)	148
C16—H16C...S5	0.98	3.00	3.912 (4)	155
C26—H26C...S6	0.98	2.68	3.364 (5)	127
C31—H31A...S12 ⁱⁱ	0.98	2.81	3.435 (3)	123
C41—H41A...S10	0.98	2.87	3.508 (5)	123
C42—H42C...S10	0.98	2.60	3.291 (3)	128
C45—H45C...S1	0.98	2.96	3.867 (4)	155

Symmetry codes: (i) $-x+2, -y+2, -z+2$; (ii) $-x+2, -y+2, -z+1$.

[A3]: C–C Cross-Coupling Reactions of Trityl Radicals: Spin Density Delocalization, Exchange Coupling, and a Spin Label

Reprinted with permission from

Nico Fleck, Tobias Hett, Jonas Brode, Andreas Meyer, Sabine Richert, Olav Schiemann*,
J. Org. Chem. **2019**, *84*, 3293 - 3303.

Published by ACS Publications (Washington, USA), ©**2019** to the American Chemical Society.

Contributions:

- Experimental Work:
 - Organic synthesis incl. compound characterization
 - cw-EPR spectroscopy
- Writing of the manuscript

C–C Cross-Coupling Reactions of Trityl Radicals: Spin Density Delocalization, Exchange Coupling, and a Spin Label

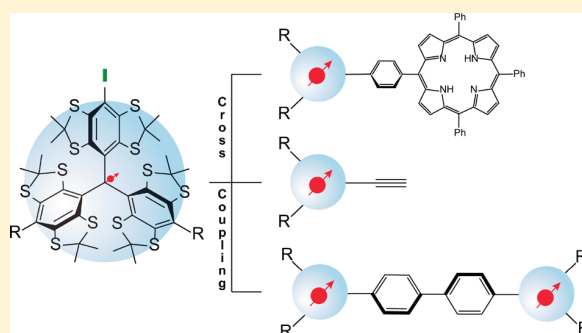
Nico Fleck,[†] Tobias Hett,[†] Jonas Brode,[†] Andreas Meyer,^{†,§} Sabine Richert,[‡] and Olav Schiemann^{*,†,§}

[†]Institute of Physical and Theoretical Chemistry, Rheinische Friedrich-Wilhelms-University Bonn, Wegelerstr. 12, 53115 Bonn, Germany

[‡]Institute of Physical Chemistry, University of Freiburg, Albertstraße 21, 79104 Freiburg, Germany

S Supporting Information

ABSTRACT: Organic radicals are usually highly reactive and short-lived species. In contrast, tetrathiatriarylmethyl radicals, the so-called trityl- or TAM-radicals, are stable and do survive over longer times even under in-cell conditions. In addition, they show strong EPR signals, have long phase memory times at room temperature, and are reporters on local oxygen and proton concentrations. These properties facilitated their use for magnetic resonance imaging, dynamic nuclear polarization, and spin-labeling EPR under in-cell conditions. Thus, synthetic approaches are required for functionalization of TAM radicals tailored to the desired application. However, most TAM derivatives reported in the literature are based on esterification of the Finland trityl, which is prone to hydrolysis. Here, we report on an approach in which TAM is site-selective iodinated and subsequently C–C cross-coupled to various building blocks in a modular approach. This yields conjugated trityl compounds such as a trityl attached to a porphyrin, an alkinyl functionalized trityl radical, and a strongly exchange-coupled trityl biradical. This synthesis approach thus has implications not only for magnetic resonance spectroscopy but also for the design of molecular magnets or quantum computing devices.



INTRODUCTION

Commonly, organic radicals are associated with low stability and short lifetimes as they are highly reactive open-shell species. Even though this accounts for the majority of organic radicals, this paradigm was disproved by Gomberg already in 1900 by the discovery of the triphenylmethyl radical.¹ Nowadays, numerous stable organic radicals such as carbon-centered phenalenyls² and triarylmethyls (trityls)^{3,4} as well as nitrogen-centered ones like verdazyls^{5,6} or nitroxides⁷ are well-known. Techniques like magnetic resonance imaging (MRI),^{8–10} dynamic nuclear polarization (DNP),^{11,12} and spin labeling electron paramagnetic resonance (EPR) spectroscopy^{13–15} have been established as powerful tools in the life sciences, which all depend on the availability of such persistent radicals. Even though nitroxides have been the reliable flagship radicals for these techniques for decades,¹⁶ trityl radicals have emerged as promising alternatives¹⁷ for the following reasons: (1) Trityl radicals derived from the Finland trityl **1**[•] (Figure 1)¹⁸ are considerably more persistent than the Gomberg radical.¹⁹ For example, trityl derivatives such as the commercially available Oxo63²⁰ are used to map local oxygen distributions in vivo with MRI.²¹ (2) Using trityl radicals, large enhancement factors were achieved in DNP,^{22,23} including dissolution DNP experiments.²⁴ (3) The long lifetime of trityl radicals under *in-cell* conditions,²⁵ the long phase memory time T_m ,²⁶ and the narrow EPR line width²⁷ make them promising

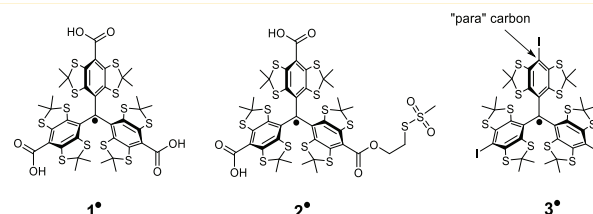


Figure 1. Structure of the Finland trityl radical **1**[•], a spin label **2**[•] derived from it, and the iodinated trityl radical **3**[•].

candidates for single-frequency EPR distance measurements^{28–30} within cells²⁵ and at ambient temperature.³¹ In particular, the two latter advantages are important for structural biology studies because they enable measurements under truly biological conditions. Compared to nitroxides, trityl radicals can be more or less stable, depending on the type of nitroxide and trityl and the solution conditions used.^{32–34} The larger size of the trityl labels as compared to nitroxides and the wider spin density distribution do not impose a broader distance distribution,^{29,30} nor do trityl labels per se induce observable structural changes, probably because the

Received: December 20, 2018

Published: February 28, 2019

labels have been attached to the biomolecular surface so far.^{25,31}

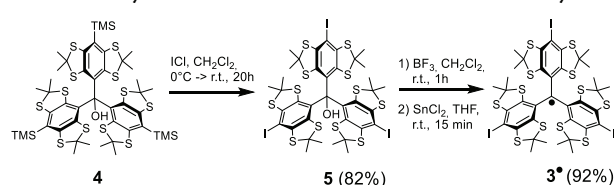
Despite these applications, the reproducible and efficient synthesis of trityl radicals remains challenging, as recent reports show.³⁵ In addition, the functionalization strategies for trityl radicals are limited. They do involve the nucleophilic quenching of the tritylium cation with various C-, P-, and N-nucleophiles, leading to a monofunctionalization at the para position marked in Figure 1.^{36,37} Also, thiol-substituents have been attached to the para positions, and their S_N2 reactivity has been used in the synthesis of, for example, dendrimeric oxygen probes.³⁸ However, the majority of functionalizations are based on the esterification of **1**[•], leading to molecules such as **2**[•].²⁵ Accordingly, the functionalization is predominantly carried out by reaction with an alcohol or amine carrying further desired functional groups.^{39–42} Because the resulting ester linkages are rather nonrigid and can be hydrolyzed under harsh labeling conditions,⁴³ it is desirable to develop new functionalization strategies for trityl spin labels. Furthermore, the properties of trityl groups make them also interesting candidates for magnetic or electronic materials and quantum computing.⁴⁴ Also for these fields, new synthesis approaches are needed that increase the chemical stability and geometric rigidity of the linker groups as well as the electronic conjugation between the spin centers.

In the present work, the site-selective iodine functionalization of trityl radicals in the para position is reported. This iodine derivative **3**[•] (Figure 1) is then used in C–C cross-coupling reactions of the Suzuki–Miyaura and Sonogashira–Hagihara type. To emphasize the broad scope of this method, we demonstrate the synthesis and characterization of four model compounds with properties that make them interesting for spin labeling, for quantum computing, and as molecular magnets.

RESULTS AND DISCUSSION

Synthesis. Iodination. In order to enable the application of C–C cross-coupling strategies, the idea was to derivatize trityl radicals with halogen atoms in the para positions, preferably with iodine, because of its high reactivity in this type of reactions. Instead of the target compound **3**[•], one could also envision to prepare, for example, the boronic acid derivative; however, **3**[•] enables a broader scope of different C–C coupling schemes. The synthesis (Scheme 1) of **3**[•] starts from the

Scheme 1. Synthesis of the Iodine Functionalized Trityl **3[•]**



^aYields are given in parentheses.

closed-shell trityl alcohol **4**, which was prepared according to the literature.^{25,45} The iodine substituent was then introduced by an *ipso*-iododesilylation with iodine monochloride obtaining trityl alcohol **5** as a gray-greenish powder in a yield of 82% on a 5 g scale. The conversion of alcohol **5** into radical **3**[•] was achieved by abstraction of the central OH-group with BF₃ and reduction of the resulting tritylium cation with SnCl₂. The

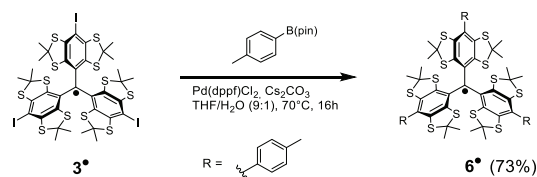
target molecule **3**[•] is obtained as a deep green powder in a yield of 92% on a 500 mg scale. Proceeding via the silyl-derivative **4** was required as direct approaches for iodination of the unsubstituted trityl alcohol failed.

In the successful reaction sequence depicted in Scheme 1, the radical was generated in the last step of the synthesis, which is more convenient, because it enables NMR monitoring until the last step. Crystallization attempts of the trityl radical derivatives were not successful. However, single crystals of alcohol **5** suitable for X-ray diffraction were obtained by slow evaporation of a diethyl ether solution. The obtained crystal structure (Figure S1, CCDC 1867300) is very similar to the structure of its unsubstituted precursor⁴⁶ with respect to the geometric arrangement of the aryl planes showing the typical propeller shaped conformation with dihedral angles of ±68.9°, ±74.4°, and ±81.9° between them. Thus, the molecule is not C₃-symmetric in the solid state. However, this distortion averages out in solution on the NMR time scale, so that the NMR spectra show a C₃-symmetric spectrum (see Figures S48 and S49). Because of the helical structure of the trityl alcohol, the methyl groups become diastereotopic, resulting in four resonances each in the ¹H and ¹³C NMR. The C_{ar}–I bond length of 2.086 Å compares well to typical literature values.⁴⁷ Moreover, the structure features a moderate hydrogen bond of the OH-hydrogen to a thioacetal sulfur with a length of *d*(H⋯A) = 2.343(5) Å. Although halogen bonding has been studied⁴⁸ for tris(4-iodophenyl)methanol,⁴⁹ no evidence for this was observed in the crystal structure of **5**, presumably for steric reasons.

C–C Cross-Coupling. The iodine substitution at the aryl ring enables C–C cross-coupling via reactions of the Sonogashira–Hagihara and the Suzuki–Miyaura type, which were both examined on the closed-shell alcohol **5** and the radical compound **3**[•]. Both coupling reactions have a wide scope and do not require the use of organometallic reagents as, for example, for Negishi or Kumada coupling reactions. This was important, because the reaction of **3**[•] with, for example, *n*-BuLi led to unselective alkyl-coupling.⁵⁰

Suzuki–Miyaura Coupling. In an exemplary reaction, trityl radical **3**[•] was reacted with 6 equiv of *p*-tolylboronic acid (Scheme 2), smoothly forming the coupling product **6**[•] with a

Scheme 2. Suzuki–Miyaura Coupling Reaction with Trityl **3[•]**

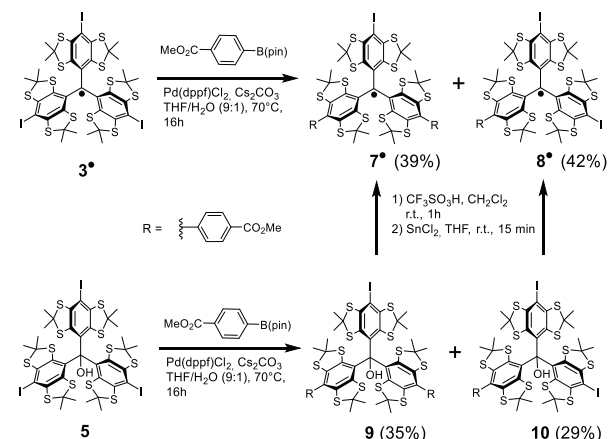


^aYields are given in parentheses.

yield of 73%. However, it would be useful to be able to perform the C–C cross-coupling reaction in such a way that either only one or two aryl groups are attached in the first step, leaving either two or one iodine positions for further functionalizations. This is for example important for designing trityl spin labels with only one biocompatible group. However, performing the Suzuki coupling in a statistical way using only two equivalents of *p*-tolylboronic acid led to a product mixture, which could not be separated by chromatography. Instead, the

statistical coupling of **3*** with two equivalents of the more polar 4-methoxycarbonylphenylboronic acid pinacol ester (**Scheme 3**) enabled the separation of the coupling products by column

Scheme 3. Statistical Suzuki–Miyaura Reaction of **3* and **6*****



^aYields are given in parentheses.

chromatography on silica, providing the mono- and bis-coupled products **7*** and **8*** in yields of 39% and 42%, respectively.

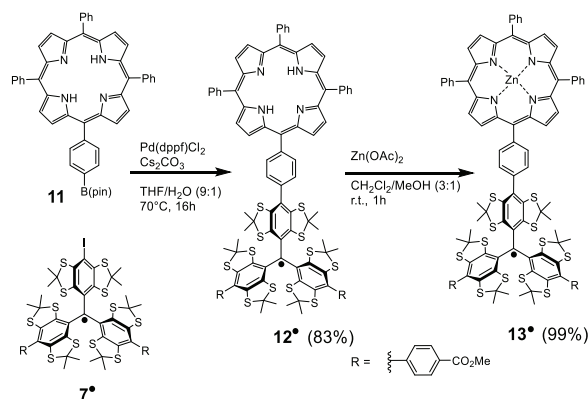
The analogous reaction with the closed shell trityl alcohol **5** led to coupling products **9** and **10** with yields of 35% and 29%. Protonation of these with $\text{CF}_3\text{SO}_3\text{H}$ in dichloromethane and subsequent reduction with SnCl_2 provided **7*** and **8*** in yields of 86% and 88%, respectively. The use of a Bronsted acid instead of BF_3 was indicated in order to prevent side reactions from the methyl esters.

In both ways, the (mono)functionalization of trityl radicals is feasible in a rather modular approach through subsequent coupling reactions. Regarding the reaction conditions, the solvent mixture $\text{THF}/\text{H}_2\text{O}$ provided sufficient solubility of the trityl species. With respect to the type of catalyst, $\text{Pd}(\text{dppf})\text{Cl}_2$ proved to be superior over $\text{Pd}(\text{OAc})_2/\text{P}(t\text{-Bu})_3$ (only partial coupling products for **6***; see the [Supporting Information, p S17](#)) or $\text{Pd}(\text{Ph}_3\text{P})_2\text{Cl}_2$ (no reaction for **6***). Cesium carbonate is well-soluble in organic solvents and therefore the base of choice for Suzuki coupling reactions.⁵¹

Conjugated Porphyrin–Trityl Model Compound. Having achieved the monofunctionalization, the aim was to attach further groups via C–C cross-coupling that enable different applications. In this line, compounds **12*** and **13*** are model compounds for the study of exchange-mediated spin polarization transfer from the excited porphyrin to the trityl, which holds promise for applications in the field of molecular spintronics.^{52,53} The slow spin relaxation of the trityl might be particularly suitable for the storage of spin information. In addition, the order (low to high field) of absorptive (*a*) and emissive (*e*) transitions in the triplet state EPR spectrum of the porphyrin is reversed in **12*** (eaaaaa) compared to the otherwise identical compound **13*** (aaaaee).^{54,55} The influence of this initial triplet state spin polarization pattern on spin-information transfer can thus be explored.⁵⁶

Compounds **12*** and **13*** were synthesized according to **Scheme 4** by using **7*** as the trityl building block and coupling this via a Suzuki–Miyaura reaction with porphyrin borolan **11**.⁵⁷ After purification by column-chromatography, pure **12***

Scheme 4. Synthesis of **12* and **13*****



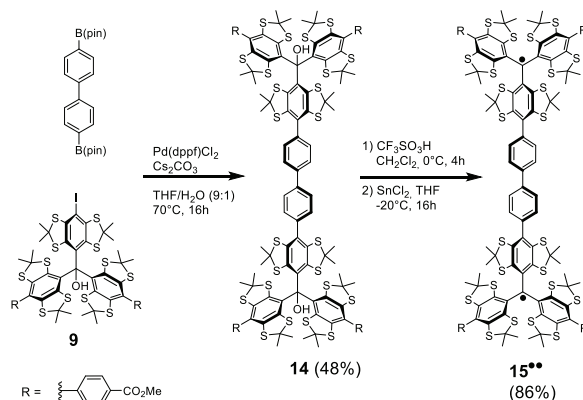
^aYields in parentheses.

was obtained in a yield of 83% as a brown-purple solid. In the following step, a zinc(II) ion was incorporated into the porphyrin, yielding **13*** quantitatively as a dark reddish solid.

Conjugated Trityl Biradical. Earlier attempts to synthesize trityl containing biradicals led to only very weakly exchange-coupled compounds,^{42,58} which may be due to the use of π -conjugation breaking groups for linking the trityls to the molecular bridges. In contrast, the C–C cross-coupling approach presented here enables the connection via conjugated groups. Compound **15**** seemed to be a suitable test system because it enables a direct comparison with related nitroxide⁵⁹ and trityl⁵⁸ systems.

A Suzuki–Miyaura coupling of trityl alcohol **9** with 4,4'-bis(4,4,5,5-tetramethyl-1,3,2-dioxaborolan-2-yl)biphenyl (**Scheme 5**) gave **14** in a yield of 48%. The following

Scheme 5. Synthesis of Biradical **15****



^aYields are given in parentheses.

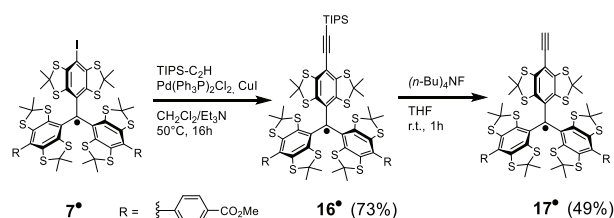
conversion to biradical **15**** was carried out by treatment with $\text{CF}_3\text{SO}_3\text{H}$ and reduction of the resulting cation with SnCl_2 in a yield of 86%. It was also possible to obtain **15**** by a Suzuki–Miyaura coupling of **7*** with 4,4'-bis(4,4,5,5-tetramethyl-1,3,2-dioxaborolan-2-yl)-biphenyl. However, during column chromatography, **15**** was oxidized to the corresponding trityl alcohols and sulfoxides, presumably because of exposure to air (see the [Supporting Information, p S18](#)).

Such an increased sensitivity of exchange-coupled trityl biradicals toward oxygen during chromatography was also

reported by Jassoy et al.⁵⁸ Therefore, the coupling and column chromatography steps were carried out at the alcohol stage. Earlier reports aiming at building conjugated systems with perchlorinated trityl radicals (PTM-radicals) used Horner–Wadsworth–Emmons reactions,^{60,61} which are less versatile than the Suzuki–Miyaura reaction employed here.

Sonogashira–Hagihara Coupling. Ethynyl-substituted stable radicals can be used for spin labeling via *click reaction* with unnatural amino acids containing azides.⁶² The Sonogashira–Hagihara coupling reaction is a versatile tool for introducing such terminal alkynes. Current approaches to synthesize ethynyl-substituted trityl radicals use the esterification of **1**^{•25} with propargyl alcohols. However, as ester groups are rather nonrigid and prone to hydrolysis, it is desired to attach an ethynyl group directly to the para-position of a trityl radical. As an example of such a building block, a Sonogashira–Hagihara coupling of **7**[•] was performed with triisopropylsilyl acetylene in CH₂Cl₂/Et₃N catalyzed by Pd(Ph₃P)₂Cl₂ (Scheme 6). The

Scheme 6. Synthesis of **17**^{•a}



^aYields are given in parentheses.

corresponding coupling product **16**[•] was isolated with a yield of 73%. After removal of the TIPS-protection group with *n*Bu₄NF, the ethynyl-trityl radical **17**[•] was obtained with a yield of 49%. Using less bulky acetylene building blocks such as trimethylsilyl acetylene or 2-methyl-3-buten-2-ol and common solvents such as THF led to unwanted side reactions. It is presumed that a competitive carbathiolation⁶³ by insertion of the alkyne into a C–S bond of the cyclic thioacetals takes place. A detailed survey with discussion and additional experimental data is enclosed in the Supporting Information on pages S20–S41. For PTM-radicals, Sonogashira–Hagihara coupling was demonstrated very recently, where obviously no side reactions as in the present case occurred.⁶⁴ However, it was shown that spin labels based on PTM-radicals are reduced under in-cell conditions.⁶⁵

Magnetic Resonance Spectroscopy. All paramagnetic compounds in this study were characterized by continuous wave (cw) X-band EPR. They all show an EPR spectrum characteristic for trityl radicals (see the Supporting Information, pp S11–S15). Figure 2a shows the room-temperature spectrum of **7**[•] as an example and Figure 2b that of **17**[•], in which an additional $A_{\text{iso}}(^1\text{H})$ hyperfine-coupling constant of 3.7 MHz from the ethynyl hydrogen atom could be resolved. The ¹³C-hyperfine interactions observed are all similar to the values determined for **1**[•] and its derivatives⁶⁶ and are reported in Table S2 together with the *g*-values and line widths. In general, the line widths of the trityl radicals presented here are slightly larger than the corresponding values reported for **1**[•].⁶⁶ This is attributed to unresolved hydrogen hyperfine interactions from the aryl substituents and/or the quadrupole moment of iodine. The latter is supported by the line width of **16**[•] being significantly smaller than that of its precursor **7**[•]. Additionally,

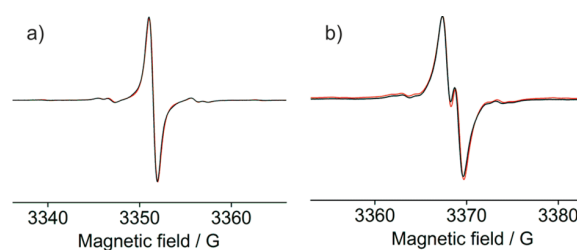


Figure 2. Continuous wave X-band EPR spectra ($T = 298\text{ K}$, $c = 50\ \mu\text{M}$ in toluene) of (a) **6**[•] and (b) **17**[•]. The experimental spectrum is plotted as black solid lines, and the simulation is overlaid as a red line.

the g_{iso} -value of trityl increases linearly with the number of iodine substituents in the para positions from 2.0032 (**7**[•] no iodine atom) to 2.0051 (**3**[•] three iodine atoms), as shown in Figure 3. This is related to spin–orbit coupling, the magnitude

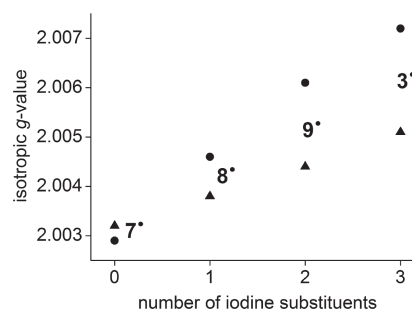


Figure 3. Experimental (\blacktriangle) g_{iso} -values of iodine containing trityl radicals compared to the calculated values from DFT (\bullet).

of which increases with the atomic number of the involved elements.⁶⁷ In the case of aromatic compounds, the shift in g_{iso} (Δg) upon replacing n equivalent hydrogen atoms by n heavy atoms (e.g., iodine) can be approximated by⁶⁸ $\Delta g \approx \sum_i \lambda_i \rho_i$ ($i = 1$ to n). Here, λ_i is the spin–orbit coupling constant and ρ_i is the Hückel spin density on the heavy atom. The same trend was observed for the g -values calculated by DFT (PBE, def2-SVP), but the spin density on the iodine substituents seems to be slightly overestimated (Figure 3).

The hyperfine interactions with hydrogen atoms of the porphyrin ring in **12**[•] and **13**[•] are not resolved in the cw X-band EPR spectra but can be inferred from ¹H NMR spectra. The ¹H NMR spectra of **12**[•] and its diamagnetic analogous trityl alcohol **12-OH** are shown in Figure 4. Both the signals of the bridging phenyl ring (signal 2, Figure 4) and the signals of the aryl groups of the trityl core (signal 3, Figure 4) are broadened beyond visibility in the spectrum of **12**[•] because of paramagnetic broadening. In contrast, the signals from the pyrrol hydrogen atoms (signal 4, Figure 4) are still present, but they are shifted. The signal marked with an asterisk in Figure 4 exhibits the strongest paramagnetic shift (δ_{para}) and is attributed to the two pyrrol hydrogen atoms in closest proximity to the bridging phenyl ring as they feature the largest spin density according to DFT calculations (Figure S3). Using eq 1, an $A(^1\text{H})$ hyperfine coupling constant of 4 mG can be estimated for these atoms:⁶⁹

$$A(^1\text{H}) = \frac{(\delta - \delta_{\text{dia}}) \cdot T}{1.16 \times 10^2 \cdot g_{\text{iso}}} = 4\text{ mG} = 11.2\text{ kHz} \quad (1)$$

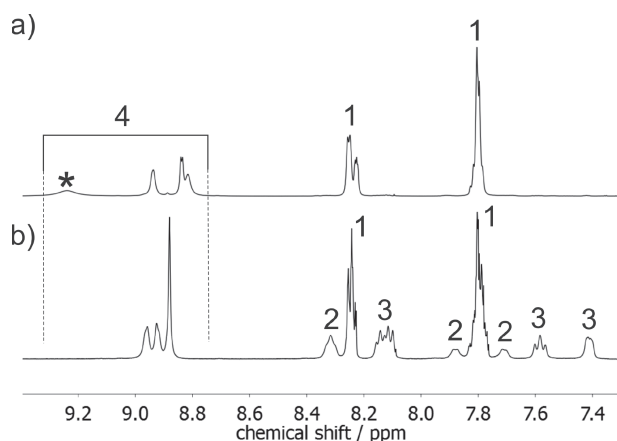


Figure 4. ^1H NMR spectra of (a) 12^\bullet and (b) 12-OH at 298 K in CD_2Cl_2 . Signal 1, H_{ph} (porphyrin); signal 2, H_{ph} (bridge); signal 3, H_{ph} (trityl); signal 4, H_{pyrrol} (porphyrin).

Here, $\delta = 9.28$ ppm was extracted from the spectrum of 13^\bullet (Figure 4a), $\delta_{\text{dia}} = 8.96$ ppm was taken from the spectrum of 12-OH (Figure 4b), and g_{iso} was determined to be 2.0032 from the cw X-band EPR spectrum at $T = 298$ K.

The coupling constant of 4 mG indicates that spin density is distributed into the porphyrin core, which is a key condition to study the interaction of a photoexcited porphyrin spin triplet with the trityl spin doublet. The three terminal phenyl groups of the tetraphenylporphyrin (signal 1, Figure 4) are not affected.

Exchange Coupling in 15^\bullet . Figure 5 shows the room-temperature liquid state cw X-band EPR spectrum of 15^\bullet . The

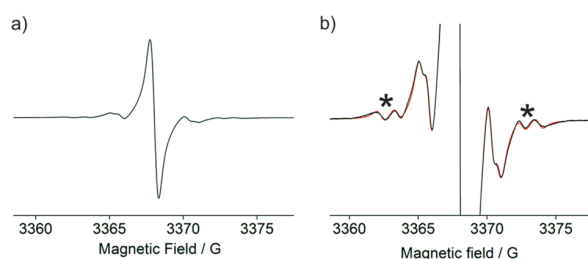


Figure 5. Experimental (black) and simulated (red) cw X-band EPR spectrum of $16^\bullet\bullet$ at 298 K: (a) full signal range and (b) focused on the ^{13}C -satellites.

intense central line is due to trityl centers carrying no ^{13}C atom. The much less intense lines at lower and higher field of the central line are due to molecules carrying one ^{13}C atom in the *ipso* ($A_{\text{iso}} = 32$ MHz) or *ortho* ($A_{\text{iso}} = 25$ MHz) positions. The corresponding ^{13}C hyperfine splitting is halved as compared to the monotrityl radical because of strong exchange coupling.⁷⁰ The four lines of even weaker intensity and marked by asterisks belong to the *ipso* or *ortho* ^{13}C coupling in monotrityl impurities (7%) serving here as an internal standard and highlighting that this coupling is indeed halved in 15^\bullet .

Taking J -coupling into account, the shift of the ^{13}C -hyperfine satellites was simulated using a home-written *EasySpin*⁷¹ script. This yielded a lower limit of 550 MHz for J (Figures 5b and S6). To further investigate the magnetic exchange coupling, measurements in frozen solution were conducted (Figure 6). At cryogenic temperatures between 3.8

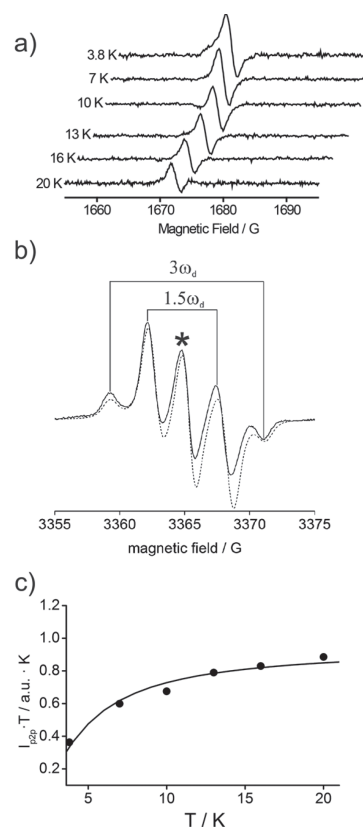


Figure 6. (a) Stacked plot of the half-field spectra of $15^\bullet\bullet$. (b) cw X-band EPR spectrum of $15^\bullet\bullet$ at 100 K in $\text{CH}_2\text{Cl}_2/\text{MeOH}$ (2:1). The Pake pattern is indicated by $1.5\omega_d$ and $3\omega_d$. The asterisk indicates the double quantum transition, and the fit is overlaid as a dashed line. (c) Plot of the intensity of the half-field signal I_{p2p} times T versus T (●, experimental data; solid line is the best fit with $J = -2.8$ cm^{-1}).

and 20 K, the $\Delta m_S = \pm 2$ transition within the triplet state of $15^\bullet\bullet$ could be observed (Figure 6a). As can be seen from the stack-plot, the peak-to-peak intensity of the half-field signal drops with increasing temperature. Plotting the peak-to-peak intensity I_{p2p} multiplied by the temperature T against T and using the Bleaney–Bowers type equation given in eq 2⁷² permit extracting the value of the exchange coupling constant J via least-squares fitting (Figure 6c).

$$I_{p2p}T = C \left(\frac{1}{3 + \exp(-2J/k_B T)} \right) \quad (2)$$

Here, $C = 3.8 \pm 0.1$ K is a spectrometer constant and k_B refers to the Boltzmann constant. The best fit to the experimental data revealed an antiferromagnetic coupling within $15^\bullet\bullet$ of $J = -2.8 \pm 0.2$ cm^{-1} (see Figure S7) according to the convention of $H_{\text{ex}} = -2JS_A S_B$. This value corresponds well to the result of $J = -4.4$ cm^{-1} obtained from a broken-symmetry DFT (PBE, def2-SVP) calculation. The cw X-band EPR spectrum of $15^\bullet\bullet$ in the main-field region at 100 K is provided in Figure 6b. This spectrum is a superposition of a dipolar Pake pattern and a double quantum transition,⁷³ where both show a markedly different saturation behavior (see Figure S8). From the Pake pattern a dipolar coupling constant D of 11 MHz can be read off. Using eq 3 for the strong coupling regime, a distance r of 16.7 Å between both spins can be calculated.^{74,75}

$$D_{\text{strong}} = 1.5 \cdot 52.01 \text{ MHz} \frac{\text{Nm}^3}{r^3} \quad (3)$$

The spectrum was simulated with *EasySpin* by adding a second signal accounting for the 2-photon-transition to the Pake pattern.

This spin–spin distance could be confirmed nicely via a pulsed EPR experiment called Double Quantum Coherence (DQC) experiment⁷⁶ (Figure 7), yielding a distance

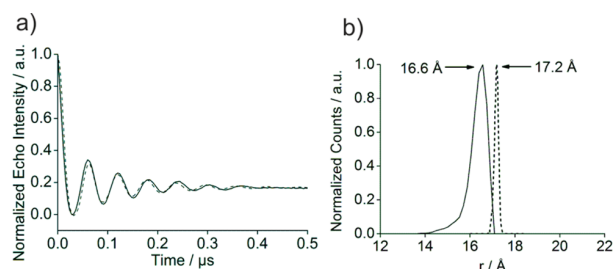


Figure 7. DQC data of **15^{••}**. (a) The background-corrected DQC time trace and (b) the corresponding distance distribution. The experimental distance distribution was corrected by a factor of $\sqrt[3]{1.5}$ in order to account for the strong coupling regime. The distribution expected from MD is overlaid as a dashed line.

distribution peaking at 16.6 Å. From the DFT-derived structure of **15^{••}**, a distance of 18.7 Å between the central carbons can be estimated, which leads to a distance difference between experiment and theory that is on the far side of the error. However, taking spin density delocalization into account⁷⁷ (see the Supporting Information, pages S5 and S6) reduces the theoretical spin–spin distance to 17.2 Å, well within the error of the experiment and theory. Because of the large size of J , a disentanglement of a distribution in J (ΔJ) from the distribution in r (Δr) was not attempted.

Comparison. Figure 8 shows four different types of biradicals with comparable interspin distances or radical

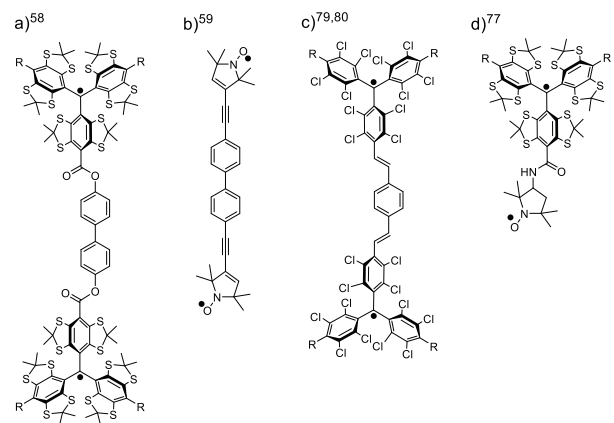


Figure 8. Literature-known biradicals for comparison.

centers as in **15^{••}**. Compared to **15^{••}**, the esterified trityl biradical⁵⁸ (Figure 8a) and the conjugated bis-nitroxide⁵⁹ (Figure 8b) show a roughly 3 orders of magnitude smaller exchange coupling. Also mixed trityl-nitroxide biradicals display much smaller J -values: for the example here, only 0.112 cm^{-1} at a much shorter interspin distance of 10.6 Å

(Figure 8d).⁷⁸ Perchlorinated trityl radicals (PTM-radicals)^{79,80} do show exchange coupling in the same order of magnitude, with the one in Figure 8c exhibiting a J of 15 cm^{-1} . Thus, the example of **15^{••}** shows that conjugated trityl radicals of the thioaryl-type can feature strong J -coupling in the same order of magnitude as the PTM radicals.

CONCLUSION

In this study, the synthesis of an iodine-substituted trityl radical was shown and its reactivity in Pd-catalyzed C–C cross-coupling reactions was examined. Whereas Suzuki–Miyaura type reactions perform well, an unexpected side reaction was encountered for Sonogashira–Hagihara type reactions. However, both coupling reactions provide an efficient tool to chemists aiming at building novel structures with trityl radicals. Exemplarily, we attached an ethynyl function directly to a trityl radical enabling click-chemistry for, for example, spin labeling of biomolecules. Second, a conjugated trityl biradical with a strong antiferromagnetic exchange coupling of $J = -2.8 \text{ cm}^{-1}$ is described. Exploiting the ease of the coupling reactions further, two trityl-porphyrin conjugates are presented. These enable the study of exchange-mediated spin-polarization transfer between photoexcited chromophore triplet states and trityl radicals. All these examples show that a large diversity of structures involving conjugated trityl radical centers becomes accessible through the presented C–C coupling reactions.

EXPERIMENTAL SECTION

General Procedures. Where indicated, solvents were degassed by applying three freeze–pump–thaw cycles. Thin-layer chromatography was conducted using 250 μm F₂₅₄ silica plates provided by Merck, and spots were visualized with UV light at 254 nm. For column chromatography, silica gel (60 Å pore size, 40–63 μm particle size) purchased from Merck was used. Medium pressure liquid chromatography (MPLC) was performed with a Sepacore X10 system by Büchi (Essen, Germany) using Büchi FlashPure cartridges. Solvents were generally removed under reduced pressure by a rotary evaporator, and products were further dried in an oil-pump vacuum at 10^{-3} mbar.

Nuclear Magnetic Resonance Spectroscopy. NMR spectra were recorded on Avance I 300, Avance I 400, Avance III HD 500, or Avance III HD 700 spectrometers from Bruker BioSpin, Rheinstetten, Germany. Chemical shifts are reported referenced to hydrogen residual peaks of the NMR solvent.⁸¹

Because of the helical chirality of trityl alcohols, a nonsymmetric C₁-structure is expected for **7[•]**, **8[•]**, **9**, and **10**. Accordingly, the NMR spectra of **9** and **10** exhibit a distinct resonance for each methyl group at the thioacetals. As the phenyl rings are twisted against each other, their aromatic protons become diastereotopic, leading to four resonances for **9** resolved at 700 MHz and eight resonances for **10**, which however coincide into multiplets even at 700 MHz.

Mass Spectrometry. ESI(+) and APCI-spectra were measured using an OrbitrapXL instrument from Thermo Fisher Scientific, Berlin, Germany. MALDI(+)-spectra were recorded in a Bruker Daltonics autoflex TOF/TOF time-of-flight spectrometer (Bruker, Rheinstetten, Germany) using DCTB as matrix.

EPR Spectroscopy. X-Band cw-EPR spectra were recorded on a Bruker EMX Micro cw X-Band EPR spectrometer (Bruker BioSpin GmbH, Rheinstetten, Germany) using a standard 4119HS resonator. The external magnetic field was modulated with a frequency of 100 kHz and an amplitude of 0.1 G. The microwave power was adjusted to 0.6054 mW, and all measurements were conducted with a time constant of 10.24 ms. The half-field signal for the trityl biradical was measured using a ER4122SHQE resonator with a modulation amplitude of 2.0 G and a microwave power of 54.45 mW. A detailed description of the instrumentation and proceeding for the DQC

experiment can be found on in the [Supporting Information, pages S7 and S8](#).

Elemental Analysis. Elemental analysis was conducted on a VarioEL analyzer (Elementar Analysensysteme, Langensfeld, Germany). Elemental analysis of trityl compounds suffers from inaccuracy because of their high sulfur content, which effects the calibration of the instrument.

Computational Methods. For the calculation of *g*-values and spin densities, the structures were preoptimized with GFN-xTB⁸² and further refined with DFT using the PBE functional and a def2-SVP basis set with D3BJ dispersion correction as implemented in ORCA.^{83,84} Both spin densities and *g*-values were obtained from the ORCA output files. MD simulations for 298.15 K were carried out using GFN-xTB with a time step of 4 fs.

Syntheses. *Tris(8-iodo-2,2,6,6-tetramethylbenzo-[1,2-d;4,5-d']-bis-[1,3]dithiol-4-yl)-methanol, Trityl Alcohol 5.* *Tris(8-(trimethylsilyl)-2,2,6,6-tetramethylbenzo-[1,2-d;4,5-d']-bis-[1,3]dithiol-4-yl)-methanol* (5.00 g, 4.55 mmol) was dissolved in 350 mL of dry dichloromethane, and the solution was cooled to 0 °C. Then, iodine monochloride (3.30 g, 1.06 mL, 20.4 mmol, 4.50 equiv) was added to the reaction mixture via a syringe. Iodine monochloride has a mp of approximately 288 °C; therefore, it should be melted in a water bath prior to addition and transferred with a prewarmed syringe. After the mixture was stirred at room temperature overnight, the reaction was quenched by addition of 150 mL of 5% sodium thiosulfate solution and the phases were separated. The dark greenish organic phase was dried over magnesium sulfate, and the solvent was removed under reduced pressure yielding a dark green residue. The crude product was purified by washing with *N,N*-dimethylformamide followed by acetone. For that, the residue was suspended in dimethylformamide (35 mL) and sonicated for 10 min. Then, the mixture was centrifuged at 3200g (Eppendorf Centrifuge 5810 R) for 5 min, whereupon a greyish solid separated. The dark supernatant was discarded, and the procedure was repeated with the precipitated solid three times. Finally, the precipitant was washed with 30 mL of acetone following the procedure above obtaining a greyish/greenish solid with a yield of 4.73 g (3.74 mmol, 82%). Crystals suitable for X-ray diffraction were grown by slow evaporation of a solution of the title compound in Et₂O at 3 °C over 1 week. ¹H NMR (500 MHz, CD₂Cl₂, 298 K, δ): 6.20 (s, 1H), 1.85 (s, 9H), 1.82 (s, 9H), 1.77 (s, 9H), 1.68 (s, 9H). ¹³C{¹H}-NMR (126 MHz, CD₂Cl₂, 298 K, δ): 144.4, 143.7, 136.3, 135.0, 130.9, 85.0, 83.5, 61.4, 60.8, 35.2, 32.2, 29.0, 27.2. HRMS (ESI+) *m/z*: [M]⁺ calcd for C₃₇H₃₇I₃OS₁₂, 1261.6621; found, 1261.6636. Elemental analysis [%]: Anal. Calcd for C₃₇H₃₇I₃OS₁₂: C, 35.18; H, 2.95; S, 30.46. Found: C, 35.33; H, 3.09; S, 29.42.

Tris(8-(4-methylphenyl)-2,2,6,6-tetramethylbenzo-[1,2-d;4,5-d']-bis-[1,3]dithiol-4-yl)-methyl Radical, Trityl Radical 6[•]. Trityl radical 3[•] (135 mg, 108 μmol), 4-methylphenylboronic acid (89 mg, 651 μmol, 6.0 equiv), cesium carbonate (210 mg, 651 μmol, 6.0 equiv) and Pd(dppf)Cl₂ (5 mg, 5 mol %) were dissolved in a deoxygenated mixture of THF and water (10:1) under argon. The reaction mixture was heated to 70 °C for 16 h and allowed to cool to room temperature. Then, the solvents were removed under reduced pressure. The residue was extracted with dichloromethane, and the organic phase was washed with 0.1 M Na₂EDTA and dried over magnesium sulfate. After removal of the solvents under reduced pressure, the crude product was purified by column chromatography on silica eluting with cyclohexane/ethyl acetate 2:1. Yield: 91 mg (73%). HRMS (APCI) *m/z*: [M]⁺ calcd for C₅₈H₅₇S₁₂, 1137.1103; found, 1137.1100.

Tris(8-(4-methylphenyl)-2,2,6,6-tetramethylbenzo-[1,2-d;4,5-d']-bis-[1,3]dithiol-4-yl)-methanol; Trityl Alcohol 6-OH. (150 mg, 0.119 mmol), *p*-methylphenylboronic acid (97 mg, 0.714 mmol, 6.0 equiv), cesium carbonate (230 mg, 0.714 mmol, 6.0 equiv), and Pd(dppf)Cl₂ were placed in a Schlenk flask under argon atmosphere. Then, 20 mL of degassed THF/H₂O (10:1, v/v) was added and the reaction mixture was stirred at 70 °C for 16 h. Afterward, 0.1 M Na₂EDTA solution was added (50 mL), and the aqueous phase was extracted three times with 30 mL of dichloromethane. The unified organic phases were dried over magnesium sulfate, and the solvents were

removed under reduced pressure. The product was isolated as a gray/greenish solid after column chromatography on silica eluting with cyclohexane/ethyl acetate 2:1 (v/v). Yield: 104 mg (76%). ¹H NMR (500 MHz, CD₂Cl₂, 298 K, δ): 7.33 (d, 2H, ³J_{H,H} = 8 Hz), 7.27 (d, 2H, ³J_{H,H} = 8 Hz), 7.24 (d, 2H, ³J_{H,H} = 7.4 Hz), 7.15 (d, 2H, ³J_{H,H} = 7.4 Hz), 6.54 (s, 1H), 2.41 (s, 3H), 1.87 (s, 9H), 1.78 (s, 9H), 1.72 (s, 9H), 1.65 (s, 9H). ¹³C{¹H}-NMR (126 MHz, CD₂Cl₂, 298 K, δ): 140.1, 139.3, 139.1, 138.9, 138.8, 138.6, 133.6, 131.4, 129.8, 129.6, 128.9, 63.3, 62.7, 54.4, 54.2, 54.0, 53.8, 53.6, 35.5, 32.7, 29.7, 27.8, 21.7. HRMS (APCI) *m/z*: [M]⁺ calcd for C₅₈H₅₈OS₁₂, 1154.1133; found, 1154.1133.

{(8-(4-Carboxylphenyl)-2,2,6,6-tetramethylbenzo-[1,2-d;4,5-d']-bis-[1,3]dithiol-4-yl)-bis(8-iodo-2,2,6,6-tetramethylbenzo-[1,2-d;4,5-d']-bis-[1,3]dithiol-4-yl))-methyl Radical Methyl Ester and {Bis(8-(4-carboxylphenyl)-2,2,6,6-tetramethylbenzo-[1,2-d;4,5-d']-bis-[1,3]dithiol-4-yl)-(8-iodo-2,2,6,6-tetramethylbenzo-[1,2-d;4,5-d']-bis-[1,3]dithiol-4-yl))-methyl Radical Dimethyl Ester; Trityl Radicals 7[•] and 8[•]. Trityl radical 3[•] (133 mg, 107 μmol), 4-methoxycarbonylphenylboronic acid pinacol ester (56 mg, 214 μmol, 2.0 equiv), cesium carbonate (69 mg, 214 μmol, 2.0 equiv), and Pd(dppf)Cl₂ (4 mg, 5.3 μmol, 5 mol %) were dissolved in a deoxygenated mixture of THF and water (20 mL, 10:1) under argon. The reaction mixture was heated to 70 °C for 16 h and allowed to cool to room temperature. Then, the solvents were removed under reduced pressure. The residue was extracted with dichloromethane, and the organic phase was washed with 0.1 M Na₂EDTA and dried over magnesium sulfate. After removal of the solvents under reduced pressure, the crude product was purified by column chromatography on silica eluting with a gradient of cyclohexane/ethyl acetate 9:1 to 2:1.

Trityl radical 8[•] yield: 56 mg, 42%. HRMS (APCI) *m/z*: [M]⁺ calcd for C₅₃H₅₀IO₄S₁₂, 1260.9397; found, 1260.9418. Trityl radical 9[•] yield: 52 mg, 39%. HRMS (ESI+) *m/z*: [M]⁺ calcd for C₄₅H₄₃I₂O₂S₁₂, 1252.7995; found, 1258.8099.

{(8-(4-Carboxylphenyl)-2,2,6,6-tetramethylbenzo-[1,2-d;4,5-d']-bis-[1,3]dithiol-4-yl)-bis(8-iodo-2,2,6,6-tetramethylbenzo-[1,2-d;4,5-d']-bis-[1,3]dithiol-4-yl))-methanol Methyl Ester and {Bis(8-(4-carboxylphenyl)-2,2,6,6-tetramethylbenzo-[1,2-d;4,5-d']-bis-[1,3]dithiol-4-yl)-(8-iodo-2,2,6,6-tetramethylbenzo-[1,2-d;4,5-d']-bis-[1,3]dithiol-4-yl))-methanol Dimethyl Ester; Trityl Alcohols 9 and 10. Trityl alcohol 5 (840 mg, 665 μmol), 4-methoxycarbonylphenylboronic acid pinacol ester (327 mg, 1.33 mmol, 2.00 equiv), cesium carbonate (432 mg, 1.33 mmol, 2.00 equiv), and Pd(dppf)Cl₂ (24.3 mg, 33 μmol, 5 mol %) were dissolved in 80 mL of degassed THF/H₂O (9:1, v/v). The reaction mixture was refluxed for 16 h under argon; afterward, the solvents were removed under reduced pressure. The residue was taken up in 100 mL of dichloromethane and washed with water and brine. The organic phase was then dried over MgSO₄, and solvents were removed under reduced pressure yielding a greenish crude product. Trityl alcohols 9 and 10 were obtained from MPLC-purification (80 g of SiO₂, CH₂Cl₂/cyclohexane 7:3 (0 → 5 min), CH₂Cl₂/cyclohexane 9:1 (5 → 8 min), CH₂Cl₂/cyclohexane 1:0 (8 → 25 min)).

Analytical data for 9. ¹H NMR (700 MHz, CD₂Cl₂, 298 K, δ): 1.64 (s, 3H), 1.66 (s, 3H), 1.71 (s, 3H), 1.71 (s, 3H), 1.72 (s, 3H), 1.76 (s, 3H), 1.78 (s, 3H), 1.81 (s, 3H), 1.83 (s, 3H), 1.85 (s, 3H), 1.86 (s, 3H), 1.91 (s, 3H), 3.92 (s, 3H), 3.92 (s, 3H), 6.43 (s, 1H), 7.33–7.37 (m, 2H), 7.50–7.53 (m, 2H), 8.05–8.12 (m, 4H). ¹³C{¹H}-NMR (176 MHz, CD₂Cl₂, 298 K, δ): 27.80, 27.81, 27.82, 29.3, 29.7, 29.8, 32.47, 32.48, 32.49, 33.3, 35.5, 35.6, 35.8, 52.7, 61.1, 61.7, 63.2, 63.5, 63.86, 63.94, 84.4, 85.5, 129.3, 130.30, 130.33, 130.84, 130.86, 131.41, 131.43, 132.1, 132.66, 132.74, 136.1, 136.7, 138.40, 138.44, 138.83, 138.87, 138.95, 138.98, 140.3, 140.4, 144.2, 144.9, 145.86, 145.90, 166.9, 166.9. HRMS (ESI+) *m/z*: [M]⁺ calcd for C₅₃H₅₁IO₃S₁₂, 1277.9424; found, 1277.9447.

Analytical data for 10. ¹H NMR (700 MHz, CD₂Cl₂, 298 K, δ): 1.63 (s, 3H), 1.69 (s, 6H), 1.71 (s, 3H), 1.75 (s, 3H), 1.79 (s, 6H), 1.81 (s, 3H), 1.83 (s, 3H), 1.84 (s, 3H), 1.87 (s, 3H), 1.89 (s, 3H), 3.92 (s, 3H), 6.31 (s, 1H), 7.34 (d, 1H, ³J_{H,H} = 7.9 Hz), 7.50 (d, 1H, ³J_{H,H} = 7.9 Hz), 8.06 (d, 1H, ³J_{H,H} = 7.9 Hz), 8.10 (d, 1H, ³J_{H,H} = 7.9 Hz). ¹³C{¹H}-NMR (176 MHz, CD₂Cl₂, 298 K, δ): 27.79, 27.82,

27.83, 29.4, 29.6, 29.9, 32.2, 33.0, 33.1, 35.5, 35.7, 35.9, 52.7, 61.1, 61.4, 61.79, 61.81, 63.4, 64.0, 84.2, 85.5, 85.6, 125.6, 129.3, 130.27, 130.29, 130.9, 131.2, 131.8, 132.7, 135.8, 135.9, 136.8, 137.0, 138.5, 138.6, 139.0, 140.3, 144.2, 144.3, 144.9, 145.0, 145.8, 166.9. HRMS (ESI+) m/z : $[M]^+$ calcd for $C_{45}H_{44}I_2O_3S_{12}$, 1269.8023; found, 1269.8042.

General Procedure for Generation of Trityl Radicals from Trityl Alcohols. Method A. The trityl alcohol (45 μ mol) was dissolved in 5 mL of dry dichloromethane, and boron trifluoride diethyl ether complex (50 mg, 45 μ L, 0.352 mmol, 7.80 equiv) was added at 0 °C. The reaction mixture was stirred at room temperature for 90 min. Then, tin(II)-chloride (15 mg, 80 μ mol, 1.76 equiv, dissolved in 1 mL of dry THF) was added; the reaction mixture was stirred for additional 20 min and then quenched by addition of 50 mL of water. The organic phase was extracted with dichloromethane twice, after drying over magnesium sulfate; the solvents were removed under reduced pressure, and the radical was obtained as a dark green powder.

Method B. The trityl alcohol (45 μ mol) was dissolved in 5 mL of dry dichloromethane, and trifluoromethanesulfonic acid (8.8 mg, 5.2 μ L, 58 μ mol, 1.30 equiv) was added at 0 °C. The reaction mixture was stirred at room temperature for 1 h. Then, tin(II)-chloride (15 mg, 80 μ mol, 1.76 equiv, dissolved in 1 mL of dry THF) was added; the reaction mixture was stirred further for 15 min and then quenched by addition of 50 mL of water. The organic phase was extracted with dichloromethane twice. After drying over magnesium sulfate, the solvents were removed under reduced pressure; the radical was obtained as a dark green powder.

Tris(8-iodo-2,2,6,6-tetramethylbenzo-[1,2-d;4,5-d']-bis-[1,3]-dithiol-4-yl)-methyl radical, trityl radical **3***, method A. Yield: 41 mg (90%), dark green solid. HRMS (ESI+) m/z : $[M]^+$ calcd for $C_{37}H_{36}I_3S_{12}$, 1244.6600; found, 1244.6609.

Trityl radical **6***, method A. Yield: 43 mg (84%), dark green solid. HRMS (ESI+) m/z : $[M]^+$ calcd for $C_{58}H_{57}S_{12}$, 1137.1103; found, 1137.1100.

Trityl radical **7***, method B. Yield: 49 mg (86%), dark green solid.

Trityl radical **8***, method B. Yield: 50 mg (88%), dark green solid.

Bis(8-(4-carboxylphenyl)-2,2,6,6-tetramethylbenzo-[1,2-d;4,5-d']-bis-[1,3]dithiol-4-yl)-(8-(5,10,15,20-tetraphenylporphyrin-5-(4-phenyl)-yl)-2,2,6,6-tetramethylbenzo-[1,2-d;4,5-d']-bis-[1,3]dithiol-4-yl))-methyl Radical Dimethyl Ester, Trityl Porphyrin **12*.** Trityl radical **8*** (22 mg, 17.5 μ mol), porphyrin **11** (17.5 μ mol, 1.00 equiv), cesium carbonate (6 mg, 18.5 μ mol, 1.05 equiv), and Pd(dppf)Cl₂ (1 mg, 1.3 μ mol, 7.5 mol %) were dissolved in 10 mL of degassed THF/H₂O (9:1, v/v). The reaction mixture was stirred at 70 °C for 8 h under TLC control (SiO₂, CH₂Cl₂) until the trityl spot (R_f = 0.85) disappeared. After the mixture reached room temperature, the solvents were evaporated in high vacuum. The residue was taken up in 10 mL of dichloromethane and washed with water (20 mL). The organic phase was separated and dried over Na₂SO₄, and the solvents were removed under reduced pressure. Column chromatography on silica eluting with dichloromethane yielded 25 mg (83%) of pure product. ¹H NMR (700 MHz, CD₂Cl₂, 298 K, δ): -2.78 (s, 2H), 1.57 (bs, $\Delta_{1/2}$ = 245 Hz), 3.45 (bs, $\nu_{1/2}$ = 750 Hz), 4.49 bs, $\nu_{1/2}$ = 100 Hz), 7.81–7.87 (m, 9H), 8.24–8.31 (m, 6H), 8.83–8.89 (m, 4H), 8.98 (s, 2H), 9.28 (bs, $\nu_{1/2}$ = 53 Hz). HRMS (ESI+) m/z : $[M]^+$ calcd for $C_{97}H_{79}N_4O_4S_{12}$, 1747.2744; found, 1747.2748.

Bis(8-(4-carboxylphenyl)-2,2,6,6-tetramethylbenzo-[1,2-d;4,5-d']-bis-[1,3]dithiol-4-yl)-(8-(5,10,15,20-tetraphenylporphyrin-5-(4-phenyl)-yl)-2,2,6,6-tetramethylbenzo-[1,2-d;4,5-d']-bis-[1,3]dithiol-4-yl))-methanol Dimethyl Ester, Trityl Porphyrin **12-OH.** Trityl alcohol **9** (11 mg, 8.6 μ mol), porphyrin **11** (6 mg, 8.6 μ mol, 1.00 equiv), cesium carbonate (3 mg, 9 μ mol, 1.05 equiv), and Pd(dppf)Cl₂ (1 mg, 1.3 μ mol, 15 mol %) were dissolved in 10 mL of degassed THF/H₂O (9:1, v/v). The reaction mixture was stirred at 70 °C for 8 h under TLC control (SiO₂, CH₂Cl₂) until the trityl spot (R_f = 0.82) disappeared. After the mixture reached room temperature, the solvents were evaporated in high vacuum. The residue was taken up in 10 mL of dichloromethane and washed with water (20 mL). The organic phase was separated and dried over Na₂SO₄, and the

solvents were removed under reduced pressure. Column chromatography on silica eluting with dichloromethane yielded 12 mg (80%) of pure product. ¹H NMR (700 MHz, CD₂Cl₂, 298 K, δ): -2.78 (s, 2H), 1.71 (s, 3H), 1.74 (s, 3H), 1.80 (s, 6H), 1.82 (s, 3H), 1.84 (s, 3H), 1.84 (s, 3H), 1.91 (s, 3H), 1.92 (s, 3H), 1.96 (s, 3H), 1.97 (s, 3H), 2.03 (s, 3H), 3.93 (s, 3H), 3.94 (s, 3H), 6.64 (s, 1H), 7.39–7.43 (m, 2H), 7.55–7.61 (m, 2H), 7.69–7.72 (m, 1H), 7.76–7.83 (m, 9H), 7.86–7.90 (m, 2H), 8.09–8.16 (m, 4H), 8.22–8.27 (m, 6H), 8.29–8.33 (m, 2H), 8.88 (s, 4H), 8.92 (s, 2H), 8.96 (s, 4H). ¹³C{¹H}-NMR (176 MHz, CD₂Cl₂, 298 K, δ): 166.4, 145.5, 145.4, 142.2, 142.03, 142.02, 140.5, 140.0, 139.8, 139.7, 139.1, 138.70, 138.69, 138.63, 138.4, 138.3, 138.2, 137.8, 137.75, 134.6, 134.5, 133.0, 132.13, 132.10, 131.30, 131.25, 131.0, 130.26, 129.8, 128.8, 127.8, 127.0, 126.74, 126.73, 120.37, 120.32, 119.5, 84.0, 63.21, 63.19, 63.10, 62.64, 62.63, 62.5, 52.1, 35.2, 35.1, 35.0, 32.4, 32.3, 32.1, 29.5, 29.1, 29.0, 27.5, 27.3, 27.2, 26.9. HRMS (ESI+) m/z : $[M]^+$ calcd for $C_{97}H_{81}N_4O_5S_{12}$, 1767.2865; found, 1767.2877.

Bis(8-(4-carboxylphenyl)-2,2,6,6-tetramethylbenzo-[1,2-d;4,5-d']-bis-[1,3]dithiol-4-yl)-(8-(zinc(II)-5,10,15,20-tetraphenylporphyrin-5-(4-phenyl)-yl)-2,2,6,6-tetramethylbenzo-[1,2-d;4,5-d']-bis-[1,3]dithiol-4-yl))-methyl Radical Dimethyl Ester, Trityl Porphyrin **13*.** Trityl porphyrin **12*** (15 mg, 8.6 μ mol) was dissolved in 3 mL of dichloromethane, and zinc acetate dihydrate (8 mg, 38.7 μ mol, 4.5 equiv) dissolved in 1 mL of methanol was added. The reaction mixture was stirred for 2 h at room temperature and then poured onto 20 mL of water. Extraction with 20 mL of dichloromethane and removal of the solvents under reduced pressure led to a crude product, which was purified by column chromatography on silica eluting with dichloromethane. Compound **13*** was obtained in a yield of 15 mg (96%) as a dark reddish solid. ¹H NMR (400 MHz, CD₂Cl₂, 298 K, δ): 1.57 (bs, $\Delta_{1/2}$ = 260 Hz), 4.49 bs, $\Delta_{1/2}$ = 100 Hz), 7.76–7.83 (m, 9H), 8.20–8.28 (m, 6H), 8.89–8.95 (m, 4H), 9.00 (d, ³J_{H,H} = 4.8 Hz, 2H), 9.34 (bs, $\Delta_{1/2}$ = 53 Hz). HRMS (ESI+) m/z : $[M]^+$ calcd for $C_{97}H_{77}N_4O_4S_{12}Zn$, 1811.1879; found, 1811.1908.

4,4'-Bis[*Bis*(8-(4-carboxylphenyl)-2,2,6,6-tetramethylbenzo-[1,2-d;4,5-d']-bis-[1,3]dithiol-4-yl)-(8-yl)-2,2,6,6-tetramethylbenzo-[1,2-d;4,5-d']-bis-[1,3]dithiol-4-yl))-methanol]-biphenyl Tetramethyl Ester, Trityl Alcohol **14.** Trityl alcohol **9** (40 mg, 31.3 μ mol, 2.00 equiv), 4,4'-bis(4,4,5,5-tetramethyl-1,3,2-dioxaborolan-2-yl)-biphenyl (6.3 mg, 15.7 μ mol, 1.00 equiv), cesium carbonate (10.0 mg, 31.3 μ mol, 2.00 equiv), and Pd(dppf)Cl₂ (2 mg, 2.6 μ mol, 8.3 mol %) were solved in 10 mL of THF/H₂O (9:1, v/v) previously degassed by three freeze–pump–thaw cycles. The reaction mixture was heated to 70 °C under argon for 16 h. Then, the solvents were removed under reduced pressure and the residue was taken up in 30 mL of degassed dichloromethane and washed with 20 mL of degassed water. The organic phase was separated and dried over MgSO₄; after removal of the solvents, a pale-yellow solid was obtained in a yield of 37 mg (48%). ¹H NMR (700 MHz, CD₂Cl₂, 298 K, δ): 1.68 (s, 6H), 1.69 (s, 6H), 1.70 (s, 6H), 1.75 (s, 6H), 1.75 (s, 6H), 1.77 (s, 6H), 1.80 (s, 6H), 1.81 (s, 6H), 1.83 (s, 6H), 1.88 (s, 6H), 1.91 (s, 12H), 3.93 (s, 12H), 6.57 (s, 2H), 7.36–7.41 (m, 6H), 7.55 (d, ³J_{H,H} = 7.8 Hz, 4H), 7.58 (d, ³J_{H,H} = 7.5 Hz, 2H), 7.72–7.79 (m, 4H), 8.08 (d, ³J_{H,H} = 7.9 Hz, 4H), 8.12 (d, ³J_{H,H} = 7.9 Hz, 4H). ¹³C{¹H}-NMR (176 MHz, CD₂Cl₂, 298 K, δ): 26.9, 22.2, 27.27, 27.28, 28.9, 29.0, 29.1, 29.2, 29.3, 29.40, 29.43, 29.45, 31.79, 31.80, 31.9, 32.3, 32.4, 33.8, 34.9, 39.7, 35.01, 35.03, 52.1, 62.3, 62.6, 63.0, 63.1, 63.14, 63.15, 83.9, 127.1, 128.78, 128.79, 128.9, 129.1, 129.7, 130.2, 130.9, 131.1, 131.2, 132.05, 132.10, 132.6, 137.68, 137.72, 137.99, 138.00, 138.25, 138.27, 138.28, 138.64, 128.68, 138.77, 139.6, 139.8, 139.9, 140.4, 140.5, 145.39, 145.41, 166.4. HRMS (ESI+) m/z : $[M]^+$ calcd for $C_{118}H_{110}O_{10}S_{24}$, 2456.1400; found, 2456.1560.

4,4'-Bis[*Bis*(8-(4-carboxylphenyl)-2,2,6,6-tetramethylbenzo-[1,2-d;4,5-d']-bis-[1,3]dithiol-4-yl)-(8-yl)-2,2,6,6-tetramethylbenzo-[1,2-d;4,5-d']-bis-[1,3]dithiol-4-yl))-methyl radical]-biphenyl Tetramethyl Ester, Trityl Biradical **15**.** Trityl alcohol **14** (20 mg, 8.16 μ mol) was dissolved in 5 mL of dry dichloromethane, and trifluoromethanesulfonic acid (3 μ L, 16.3 μ mol, 2.00 equiv) was added at 0 °C, whereupon the color of the reaction mixture turned to a dirty dark green. After 4 h at 0 °C, tin(II)-chloride (3 mg, 13.9 μ mol, 1.7 equiv, dissolved in 1 mL of dry THF) was added; the color of the reaction

mixture then turned to a clear dark green, and the mixture was stirred for an additional 16 h at room temperature. Subsequently, the solvents were removed in high vacuum, and degassed water (10 mL) and degassed dichloromethane (10 mL) were added under argon. The dark green organic phase was separated, and all solvents were removed in high vacuum (10^{-3} mbar) until a dark green solid was obtained in a yield of 17 mg (86%). HRMS (ESI+) m/z : $[M]^+$ calcd for $C_{118}H_{110}O_{10}S_{24}$, 2420.1336; found, 2420.1335.

{Bis(8-(4-carboxylphenyl)-2,2,6,6-tetramethylbenzo-[1,2-d;4,5-d']-bis-[1,3]dithiol-4-yl)-(8-(2-trimethylsilylethynyl)-2,2,6,6-tetramethylbenzo-[1,2-d;4,5-d']-bis-[1,3]dithiol-4-yl))-methyl Radical Dimethyl Ester, Trityl Radical 16⁺}. Trityl radical 7⁺ (77 mg, 61 μ mol), copper(I)-iodide (1 mg, 10 mol %), and Pd(Ph₃P)₂Cl₂ (2 mg, 5 mol %) were dissolved in 25 mL of degassed CH₂Cl₂/Et₃N (1:1, v/v), and TIPS-acetylene (41 μ L, 33 mg, 183 μ mol, 3.00 equiv) was added under argon. The reaction mixture was stirred at 50 °C for 16 h; then the solvents were removed in high vacuum. The residue was taken up in 20 mL of dichloromethane and washed with water and brine. The organic phase was separated and dried over MgSO₄, and solvents were removed under reduced pressure. The crude product was purified by column chromatography on silica eluting with cyclohexane/ethyl acetate (2:1) affording 59 mg (73%) of a deep green solid. HRMS (ESI+) m/z : $[M]^+$ calcd for $C_{55}H_{51}O_4S_{12}$, 1315.177; found, 1315.179.

*{Bis(8-(4-carboxylphenyl)-2,2,6,6-tetramethylbenzo-[1,2-d;4,5-d']-bis-[1,3]dithiol-4-yl)-(8-ethynyl-2,2,6,6-tetramethylbenzo-[1,2-d;4,5-d']-bis-[1,3]dithiol-4-yl))-methyl Radical Dimethyl Ester, Trityl Radical 17⁺}. Trityl radical 16⁺ (30 mg, 22.8 μ mol) was dissolved in 2 mL of dry THF, and tetra-*n*-butyl ammonium fluoride (68 μ L 1 M in THF, 68 μ mol, 3.00 equiv) was added under argon, whereupon the mixture turned turquoise. The reaction mixture was stirred at room temperature for 3 h; then the solvents were removed in high vacuum. The residue was taken up in 20 mL of dichloromethane and washed with water and brine; the organic phase then became ochre. The organic phase was separated and dried over MgSO₄, and solvents were removed under reduced pressure. The crude product was purified by column chromatography on silica eluting with dichloromethane, affording 13 mg (49%) of a deep green solid. HRMS (ESI+) m/z : $[M]^+$ calcd for $C_{64}H_{71}O_4S_{12}Si$, 1315.1765; found, 1315.1766.*

■ ASSOCIATED CONTENT

📄 Supporting Information

The Supporting Information is available free of charge on the ACS Publications website at DOI: 10.1021/acs.joc.8b03229.

X-ray crystallography data; computational details; pulsed/cw EPR data and spectra; reaction details; discussion of the Sonogashira coupling reactions; NMR spectra; mass spectra; MPLC data (PDF)
Structural information for trityl alcohol 5 (CIF)

■ AUTHOR INFORMATION

Corresponding Author

*E-mail: schiemann@pc.uni-bonn.de

ORCID

Olav Schiemann: 0000-0001-6346-9779

Present Address

[§]A.M.: Max Planck Institute for Biophysical Chemistry, Am Fassberg 11, 37077 Göttingen, Germany.

Notes

The authors declare no competing financial interest.

■ ACKNOWLEDGMENTS

Funding of the Deutsche Forschungsgemeinschaft via the SPP1601 is gratefully acknowledged. The authors thank B.Sc. Leonard Maurer and Prof. Dr. Stefan Grimme, Mulliken Center for Theoretical Chemistry at the University of Bonn,

for providing the latest version of the GFN-xTB program and practical advice. The authors also thank Dr. Gregor Schnakenburg, Institute for Inorganic Chemistry at the University of Bonn, for conducting the X-ray diffractometry and the Deutsche Forschungsgemeinschaft (DFG) for funding the diffractometer.

■ REFERENCES

- (1) Gomberg, M. An Instance of Trivalent Carbon: Triphenyl Methyl. *J. Am. Chem. Soc.* **1900**, *22*, 757–771.
- (2) Hicks, R. G. *Stable Radicals*; Wiley-VCH Verlag GmbH: Weinheim, 2010.
- (3) Veciana, J.; Carilla, J.; Miravittles, C.; Molins, E. Free Radicals as Clathrate Hosts: Crystal and Molecular Structure of 1: 1 Perchlorotriphenylmethyl Radical - Benzene. *J. Chem. Soc., Chem. Commun.* **1987**, 812–814.
- (4) Teruel, L.; Viadel, L.; Carilla, J.; Fajari, L.; et al. A New Constituent of Organic Magnetic Materials. *J. Org. Chem.* **1996**, *61*, 6063–6066.
- (5) Kuhn, R.; Trischmann, H. Surprisingly Stable Nitrogenous Free Radical. *Angew. Chem., Int. Ed. Engl.* **1963**, *2*, 155.
- (6) Schnakenburg, G.; Meyer, A. Syntheses, Spectroscopy, and Crystal Structures of 3-(4-Bromophenyl)-1,5-Diphenylformazan and the 3-(4-Bromophenyl)-1,5-Diphenylverdazyl Radical and the Crystal Structure of the by Product 5-Anilino-3-(4-Bromophenyl)-1-Phenyl-1H-1,2,4-Triazole. *Acta Cryst. E* **2018**, *74*, 292–297.
- (7) Likhtenshtein, G. I.; Yamauchi, J.; Nakatsuiji, S. *Nitroxides: Applications in Chemistry, Biomedicine, and Material Science*; Wiley-VCH Verlag GmbH: Weinheim, 2008.
- (8) Williams, B. B.; Halpern, H. J. In *Vivo EPR Imaging. In Biomedical EPR, Part A: Free Radicals, Metals, Medicine, and Physiology*; Eaton, S. R., Eaton, G. R., Berliner, L. J., Eds.; Springer US: Boston, MA, 2005; pp 283–319.
- (9) Wang, X.; Emoto, M.; Miyake, Y.; Itto, K.; Xu, S.; Fujii, H.; Hirata, H.; Arimoto, H. Novel blood-brain barrier-permeable spin probe for in vivo electron paramagnetic resonance imaging. *Bioorg. Med. Chem. Lett.* **2016**, *26*, 4947–4949.
- (10) Epel, B.; Haney, C. R.; Hleihel, D.; Wardrip, C.; et al. Electron Paramagnetic Resonance Oxygen Imaging of a Rabbit Tumor Using Localized Spin Probe Delivery. *Med. Phys.* **2010**, *37*, 2553–2559.
- (11) Ni, Q. Z.; Daviso, E.; Can, T. V.; Markhasin, E.; Jawla, S. K.; Swager, T. M.; Temkin, R. J.; Herzfeld, J.; Griffin, R. G. High Frequency Dynamic Nuclear Polarization. *Acc. Chem. Res.* **2013**, *46*, 1933–1941.
- (12) Abragam, A.; Goldman, M. Principles of Dynamic Nuclear Polarisation. *Rep. Prog. Phys.* **1978**, *41*, 395–467.
- (13) Reginsson, G. W.; Schiemann, O. Studying Biomolecular Complexes with Pulsed Electron-Electron Double Resonance Spectroscopy. *Biochem. Soc. Trans.* **2011**, *39*, 128–139.
- (14) Schiemann, O.; Fritscher, J.; Kisseleva, N.; Sigurdsson, S. T.; Prisner, T. F. Structural Investigation of a High-Affinity Mn(II) Binding Site in the Hammerhead Ribozyme by EPR Spectroscopy and DFT Calculations. Effects of Neomycin B on Metal-Ion Binding. *ChemBioChem* **2003**, *4*, 1057–1065.
- (15) Klare, J. P.; Steinhoff, H. J. Spin Labeling EPR. *Photosynth. Res.* **2009**, *102*, 377–390.
- (16) Berliner, L. J.; Grunwald, J.; Hankovszky, H. O.; Hideg, K. A Novel Reversible Thiol-Specific Spin Label: Papain Active Site Labeling and Inhibition. *Anal. Biochem.* **1982**, *119*, 450–455.
- (17) Tidwell, T. Triarylmethyl and Related Radicals. In *Stable Radicals*; Wiley-Blackwell, 2010; pp 1–31.
- (18) Andersson, S.; Rydbeck, A.; Mahno, R. S. US Patent 5728370, 1999.
- (19) Reddy, T. J.; Iwama, T.; Halpern, H. J.; Rawal, V. H. General Synthesis of Persistent Trityl Radicals for EPR Imaging of Biological Systems. *J. Org. Chem.* **2002**, *67*, 4635–4639.
- (20) Günther, U. WO Patent 2012/062975 A1, 2012.

- (21) Bobko, A. A.; Dhimitruka, I.; Zweier, J. L.; Khramtsov, V. V. Trityl Radicals as Persistent Dual Function pH and Oxygen Probes for in Vivo Electron Paramagnetic Resonance Spectroscopy and Imaging: Concept and Experiment. *J. Am. Chem. Soc.* **2007**, *129*, 7240–7241.
- (22) Mathies, G.; Caporini, M. A.; Michaelis, V. K.; Liu, Y.; Hu, K. N.; Mance, D.; Zweier, J. L.; Rosay, M.; Baldus, M.; Griffin, R. G. Efficient Dynamic Nuclear Polarization at 800 MHz/527 GHz with Trityl-Nitroxide Biradicals. *Angew. Chem., Int. Ed.* **2015**, *54*, 11770–11774.
- (23) Mathies, G.; Jain, S.; Reese, M.; Griffin, R. G. Pulsed Dynamic Nuclear Polarization with Trityl Radicals. *J. Phys. Chem. Lett.* **2016**, *7*, 111–116.
- (24) Jähnig, F.; Kwiatkowski, G.; Däpp, A.; Hunkeler, A.; Meier, B. H.; Kozerke, S.; Ernst, M. Dissolution DNP Using Trityl Radicals at 7 T Field. *Phys. Chem. Chem. Phys.* **2017**, *19*, 19196–19204.
- (25) Jassoy, J. J.; Berndhäuser, A.; Duthie, F.; Kühn, S. P.; Hagelueken, G.; Schiemann, O. Versatile Trityl Spin Labels for Nanometer Distance Measurements on Biomolecules In Vitro and within Cells. *Angew. Chem., Int. Ed.* **2017**, *56*, 177–181.
- (26) Owenius, R.; Eaton, G. R.; Eaton, S. S. Frequency (250 MHz to 9.2 GHz) and Viscosity Dependence of Electron Spin Relaxation of Triarylmethyl Radicals at Room Temperature. *J. Magn. Reson.* **2005**, *172*, 168–175.
- (27) Bowman, M. K.; Mailer, C.; Halpern, H. J. The Solution Conformation of Triarylmethyl Radicals. *J. Magn. Reson.* **2005**, *172*, 254–267.
- (28) Meyer, A.; Jassoy, J. J.; Spicher, S.; Berndhäuser, A.; Schiemann, O. Performance of PELDOR, RIDME, SIFTER, and DQC in Measuring Distances in Trityl Based Bi- and Triradicals: Exchange Coupling, Pseudosecular Coupling and Multi-Spin Effect. *Phys. Chem. Chem. Phys.* **2018**, *20*, 13858–13869.
- (29) Kunjir, N. C.; Reginsson, G. W.; Schiemann, O.; Sigurdsson, S. T. Measurements of Short Distances between Trityl Spin Labels with CW EPR, DQC and PELDOR. *Phys. Chem. Chem. Phys.* **2013**, *15*, 19673–19685.
- (30) Reginsson, G. W.; Kunjir, N. C.; Sigurdsson, S. T.; Schiemann, O. Trityl Radicals: Spin Labels for Nanometer-Distance Measurements. *Chem. - Eur. J.* **2012**, *18*, 13580–13584.
- (31) Shevelev, G. Y.; Krumkacheva, O. A.; Lomzov, A. A.; Kuzhelev, A. A.; Rogozhnikova, O. Y.; Trukhin, D. V.; Troitskaya, T. I.; Tormyshev, V. M.; Fedin, M. V.; Pyshnyi, D. V.; et al. Physiological-Temperature Distance Measurement in Nucleic Acid Using Triarylmethyl-Based Spin Labels and Pulsed Dipolar EPR Spectroscopy. *J. Am. Chem. Soc.* **2014**, *136*, 9874–9877.
- (32) Azarkh, M.; Okle, O.; Eyring, P.; Dietrich, D. R.; Drescher, M. Evaluation of spin labels for in-cell EPR by analysis of nitroxide reduction in cell extract of *Xenopus laevis* oocytes. *J. Magn. Reson.* **2011**, *212*, 450–454.
- (33) Jagtap, A. P.; Krstic, I.; Kunjir, N. C.; Hänsel, R.; Prisner, T. F.; Sigurdsson, S. T. Sterically shielded spin labels for in-cell EPR spectroscopy: Analysis of stability in reducing environment. *Free Radical Res.* **2015**, *49*, 78–85.
- (34) Karthikeyan, G.; Bonucci, A.; Casano, G.; Gerbaud, G.; Abel, V. T.; Kodjabachian, L.; Magalon, A.; Guigliarelli, B.; Belle, V.; Ouari, O.; Mileo, E. A Bioresistant Nitroxide Spin Label for In-Cell EPR Spectroscopy: In Vitro and In Oocyte Protein Structural Dynamics Studies. *Angew. Chem., Int. Ed.* **2018**, *57*, 1366–1370.
- (35) Rogozhnikova, O. Y.; Vasiliev, V. G.; Troitskaya, T. I.; Trukhin, D. V.; Mikhulina, T. V.; Halpern, H. J.; Tormyshev, V. M. Generation of Trityl Radicals by Nucleophilic Quenching of tris(2,3,5,6-Tetraiaaryl)methyl Cations and Practical and Convenient Large-Scale Synthesis of Persistent tris(4-Carboxy-2,3,5,6-Tetraiaaryl)methyl Radical. *Eur. J. Org. Chem.* **2013**, *2013*, 3347–3355.
- (36) Tormyshev, V. M.; Rogozhnikova, O. Y.; Bowman, M. K.; Trukhin, D. V.; Troitskaya, T. I.; Vasiliev, V. G.; Shundrin, L. A.; Halpern, H. J. Preparation of Diversely Substituted Triarylmethyl Radicals by the Quenching of tris(2,3,5,6-Tetraiaaryl)methyl Cations with C-, N-, P-, and S-Nucleophiles. *Eur. J. Org. Chem.* **2014**, *2014*, 371–380.
- (37) Decroos, C.; Prange, T.; Mansuy, D.; Boucher, J.; Li, Y. Unprecedented ipso aromatic nucleophilic substitution upon oxidative decarboxylation of tris(p-carboxytetraiaaryl)methyl (TAM) radicals: a new access to diversely substituted TAM radicals. *Chem. Commun.* **2011**, *47*, 4805–4807.
- (38) Tan, X.; Tao, S.; Liu, W.; Rockenbauer, A.; Villamena, F. A.; Zweier, J. L.; Song, Y.; Liu, Y. Synthesis and Characterization of the Perthiatriarylmethyl Radical and Its Dendritic Derivatives with High Sensitivity and Selectivity to Superoxide Radical. *Chem. - Eur. J.* **2018**, *24*, 6958–6967.
- (39) Trukhin, D. V.; Rogozhnikova, O. Y.; Troitskaya, T. I.; Vasiliev, V. G.; Bowman, M. K.; Tormyshev, V. M. Facile and High-Yielding Synthesis of TAM Biradicals and Monofunctional TAM Radicals. *Synlett* **2016**, *27*, 893–899.
- (40) Akhmetzyanov, D.; Schöps, P.; Marko, A.; Kunjir, N. C.; Sigurdsson, S. T.; Prisner, T. F. Pulsed EPR Dipolar Spectroscopy at Q- and G-Band on a Trityl Biradical. *Phys. Chem. Chem. Phys.* **2015**, *17*, 24446–24451.
- (41) Shevelev, G. Y.; Krumkacheva, O. A.; Lomzov, A. A.; Kuzhelev, A. A.; Trukhin, D. V.; Rogozhnikova, O. Y.; Tormyshev, V. M.; Pyshnyi, D. V.; Fedin, M. V.; Bagryanskaya, E. G. Triarylmethyl Labels: Toward Improving the Accuracy of EPR Nanoscale Distance Measurements in DNAs. *J. Phys. Chem. B* **2015**, *119*, 13641–13648.
- (42) (a) Liu, Y.; Song, Y.; Rockenbauer, A.; Sun, J.; Hemann, C.; Villamena, F. A.; Zweier, J. L. Synthesis of Trityl Radical-Conjugated Disulfide Biradicals for Measurement of Thiol Concentration. *J. Org. Chem.* **2011**, *76*, 3853–3860. (b) Liu, Y.; Villamena, F. A.; Song, Y.; Sun, J.; Rockenbauer, A.; Zweier, J. L. Synthesis of ¹⁴N- and ¹⁵N-Labeled Trityl-Nitroxide Biradicals with Strong Spin-Spin Interaction and Improved Sensitivity to Redox Status and Oxygen. *J. Org. Chem.* **2010**, *75*, 7796–7802.
- (43) Yang, Z.; Bridges, M. D.; Lopez, C. J.; Rogozhnikova, O. Y.; Trukhin, D. V.; Brooks, E. K.; Tormyshev, V.; Halpern, H. J.; Hubbell, W. L. A triarylmethyl spin label for long-range distance measurement at physiological temperatures using T₁ relaxation enhancement. *J. Magn. Reson.* **2016**, *269*, 50–54.
- (44) Cage, B.; McNeely, H.; Russek, S. E.; Halpern, H. J. Thermomagnetic Properties of the Finland Trityl Radical. *J. Appl. Phys.* **2009**, *105*, 043905.
- (45) Fleck, N.; Schnakenburg, G.; Filippou, C.; Schiemann, O. Tris[2,2,6,6-Tetramethyl-8-(Trimethylsilyl)benzo-[1,2-d;4,5-d]bis-(1,3-Dithiol)-4-yl]methanol Diethyl Ether Monosolvate. *Acta Cryst. E* **2018**, *74*, 539–542.
- (46) Driesschaert, B.; Robiette, R.; Le Duff, C. S.; Collard, L.; Robeyns, K.; Gallez, B.; Marchand-Brynaert, J. Cofigurationally Stable Tris(tetraiaaryl)methyl Molecular Propellers. *Eur. J. Org. Chem.* **2012**, *33*, 6517–6525.
- (47) Allen, F. H.; Kennard, O.; Watson, D. G.; Brammer, L.; Orpen, A. G.; Taylor, R. Tables of bond length determined by X-ray and neutron diffraction. Part 1. Bond lengths in organic compounds. *J. Chem. Soc., Perkin Trans. 2* **1987**, S1–S19.
- (48) Shishkin, O. V. Evaluation of True Energy of Halogen Bonding in the Crystals of Halogen Derivatives of Trityl Alcohol. *Chem. Phys. Lett.* **2008**, *458*, 96–100.
- (49) Urzua, J.; Torneiro, M. Divergent Synthesis of Porous Tetraphenylmethane Dendrimers. *J. Org. Chem.* **2017**, *82*, 13231–13238.
- (50) 3[•] reacted with *n*-BuLi under Formation of Alkyl-Coupling Products and not I/H-exchange products (see the [Supporting Information](#), p S17).
- (51) Littke, A. F.; Fu, G. C. A Convenient and General Method for Pd-Catalyzed Suzuki Cross-Couplings of Aryl Chlorides and Arylboronic Acids. *Angew. Chem., Int. Ed.* **1998**, *37*, 3387–3388.
- (52) Yamauchi, S. Recent Developments in Studies of Electronic Excited States by Means of Electron Paramagnetic Resonance Spectroscopy. *Bull. Chem. Soc. Jpn.* **2004**, *77*, 1255–1268.
- (53) Giacobbe, E. M.; Mi, Q.; Colvin, M. T.; Cohen, B.; Ramanan, C.; Scott, A. M.; Yeganeh, S.; Marks, T. J.; Ratner, M. A.; Wasielewski, M. R. Ultrafast Intersystem Crossing and Spin Dynamics of Linked to

a Nitroxide Radical at Fixed Distances. *J. Am. Chem. Soc.* **2009**, *131*, 3700–3712.

(54) Clarke, R. H.; Connors, R. E.; Schaafsma, T. J.; Kleibeuker, J. F.; Platenkamp, R. J. The Triplet State of Chlorophylls. *J. Am. Chem. Soc.* **1976**, *98*, 3674–3677.

(55) Van Dorp, W. G.; Schoemaker, W. H.; Soma, M.; Van der Waals, J. H. The lowest triplet state of free base porphyrin. *Mol. Phys.* **1975**, *30*, 1701–1721.

(56) Ishii, K.; Ishizaki, T.; Kobayashi, N. Experimental Evidence of a Selection Rule of Intersystem Crossing to the Excited Quartet States: Metallophthalocyanines Coordinated by 4-Amino-TEMPO. *J. Phys. Chem. A* **1999**, *103*, 6060–6062.

(57) Mani, T.; Niedzwiedzki, D. M.; Vinogradov, S. A. Generation of Phosphorescent Triplet States via Photoinduced Electron Transfer: Energy and Electron Transfer Dynamics in Pt Porphyrin – Rhodamine B Dyads. *J. Phys. Chem. A* **2012**, *116*, 3598–3610.

(58) Jassoy, J. J.; Meyer, A.; Spicher, S.; Wübben, C.; Schiemann, O. Synthesis of Nanometer Sized Bis- and Tris-Trityl Model Compounds with Different Extent of Spin – Spin Coupling. *Molecules* **2018**, *23*, 682.

(59) Weber, A.; Schiemann, O.; Bode, B.; Prisner, T. F. PELDOR at S- and X-Band Frequencies and the Separation of Exchange Coupling from Dipolar Coupling. *J. Magn. Reson.* **2002**, *157*, 277–285.

(60) Souto, M.; Bendixen, D.; Jensen, M.; Diez-Cabanes, V.; Cornil, J.; Jeppesen, J. O.; Ratera, I.; Rovira, C.; Veciana, J. Synthesis and Characterization of Ethylenedithio-MPTTF-PTM Radical Dyad as a Potential Neutral Radical Conductor. *Molecules* **2016**, *2*, 46–56.

(61) Elsner, O.; Ratera, I.; Rovira, C.; Veciana, J. Ferrocene as a Ferromagnetic Coupler. Synthesis and Characterization of a Ferrocene Bridged Polychlorotriphenylmethyl Diradical. *J. Organomet. Chem.* **2001**, *639*, 251–257.

(62) Kucher, S.; Korneev, S.; Tyagi, S.; Apfelbaum, R.; Grohmann, D.; Lemke, E. A.; Klare, J. P.; Steinhoff, H. J.; Klose, D. Orthogonal Spin Labeling Using Click Chemistry for in Vitro and in Vivo Applications. *J. Magn. Reson.* **2017**, *275*, 38–45.

(63) Iovine, V.; Cruciani, F.; Picini, F.; Varrone, M.; Rossi, E.; et al. Competitive Carbothiolation and Sonogashira Cross-Coupling in the Reaction of Trimethylsilylacetylene with Arylthioacetates. *ChemistrySelect* **2016**, *1*, 5201–5205.

(64) Wu, S.; Li, M.; Phan, H.; Wang, D.; Heng, T. S.; Ding, J.; Lu, Z.; Wu, J. Toward Two-Dimensional π -Conjugated Covalent Organic Radical Frameworks. *Angew. Chem., Int. Ed.* **2018**, *57*, 8007–8011.

(65) Elewa, M.; Maltar-Strmecki, N.; Said, M.; El Shihawy, H.; El-Sadek, M.; Frank, J.; Drescher, S.; Drescher, M.; Mäder, K.; Hinderberger, D.; Imming, P. Synthesis and EPR-spectroscopic characterization of the perchlorotriarylmethyl tricarboxylic acid radical (PTMTC) and its ^{13}C labelled analogue (^{13}C -PTMTC). *Phys. Chem. Chem. Phys.* **2017**, *19*, 6688–6697.

(66) Kuzhelev, A. A.; Tormyshev, V. M.; Rogozhnikova, O. Y.; Trukhin, D. V.; Troitskaya, T. I.; Strizhakov, R. K.; Krumkacheva, O. A.; Fedin, M. V.; Bagryanskaya, E. G. Triarylmethyl Radicals: An EPR Study of ^{13}C Hyperfine Coupling Constants. *Z. Phys. Chem.* **2017**, *231*, 777–794.

(67) Martin, W. C. Table of Spin-Orbit Energies for p-Electrons in Neutral Atomic (core) n p Configurations. *J. Res. Natl. Bur. Stand., Sect. A* **1971**, *75A*, 109–111.

(68) Sinclair, J.; Kivelson, D. Electron Spin Resonance of Substituted Triphenylmethyl Radicals. *J. Am. Chem. Soc.* **1968**, *90*, 5074–5080.

(69) Bertine, I.; Luchinat, C.; Parigi, G.; Ravera, E. *NMR of Paramagnetic Molecules*, 2nd ed.; Elsevier B.V., 2017.

(70) Goldfarb, D.; Stoll, S. *EPR Spectroscopy*, 1st ed.; Wiley, 2018.

(71) Stoll, S.; Schweiger, A. EasySpin, a comprehensive software package for spectral simulation and analysis in EPR. *J. Magn. Reson.* **2006**, *178*, 42–45.

(72) (a) Bencini, A.; Gatteschi, D. *EPR of Exchange Coupled Systems*, 1st ed.; Springer: Heidelberg, 1990. (b) Abrabam, A.; Bleaney, B. *Electron Paramagnetic Resonance of Transition Ions*, 1st ed.; Oxford University Press, 1970.

(73) Fritscher, J.; Beyer, M.; Schiemann, O. Synthesis, Crystal Structure and Magnetic Properties of a Novel Nitroxide Biradical. Theoretical Investigation of the Exchange Mechanisms. *Chem. Phys. Lett.* **2002**, *364*, 393–401.

(74) Jeschke, G. Determination of the Nanostructure of Polymer Materials by Electron Paramagnetic Resonance Spectroscopy. *Macromol. Rapid Commun.* **2002**, *23*, 227–246.

(75) Margraf, D.; Cekan, P.; Prisner, T. F.; Sigurdsson, S. T.; Schiemann, O. Ferro- and Antiferromagnetic Exchange Coupling Constants in PELDOR Spectra. *Phys. Chem. Chem. Phys.* **2009**, *11*, 6708–6714.

(76) Saxena, S.; Freed, J. H. Theory of Double Quantum Two-Dimensional Electron Spin Resonance with Application to Distance Measurements. Theory of Double Quantum Two-Dimensional Electron Spin Resonance with Application to Distance Measurements. *J. Chem. Phys.* **1997**, *107*, 1317–1340.

(77) Riplinger, C.; Kao, J. P. Y.; Rosen, G. M.; Kathirvelu, V.; Eaton, G. R.; Eaton, S. S.; Kutateladze, A.; Neese, F. Interaction of Radical Pairs Through-Bond and Through-Space: Scope and Limitations of the Point - Dipole Approximation in Electron Paramagnetic Resonance Spectroscopy. *J. Am. Chem. Soc.* **2009**, *131*, 10092–10106.

(78) Liu, Y.; Villamena, F. A.; Rockenbauer, A.; Song, Y.; Zweier, J. L. Structural Factors Controlling the Spin – Spin Exchange Coupling. *J. Am. Chem. Soc.* **2013**, *135*, 2350–2356.

(79) Ballester, M.; Riera, J.; Castañer, J.; Badía, C.; Monsó, J. M. Inert Carbon Free Radicals. Perchlorodiphenylmethyl and Perchlorotriphenylmethyl Radical Series. *J. Am. Chem. Soc.* **1971**, *93*, 2215–2225.

(80) Bonvoisin, J.; Launay, J.-P.; Rovira, C.; Veciana, J. Purely Organic Mixed-Valence Molecules with Nanometric Dimensions Showing Long-Range Electron Transfer. Synthesis, and Optical and EPR Studies of a Radical Anion Derived from a Bis(triarylmethyl)-Diradical. *Angew. Chem., Int. Ed. Engl.* **1994**, *33*, 2106–2109.

(81) Fulmer, G. R.; Miller, A. J. M.; Sherden, N. H.; Gottlieb, H. E.; Nudelman, A.; Stoltz, B. M.; Bercaw, J. E.; Goldberg, K. I. NMR Chemical Shifts of Trace Impurities: Common Laboratory Solvents, Organics, and Gases in Deuterated Solvents Relevant to the Organometallic Chemist. *Organometallics* **2010**, *29*, 2176–2179.

(82) Grimme, S.; Bannwarth, C.; Shushkov, P. A Robust and Accurate Tight-Binding Quantum Chemical Method for Structures, Vibrational Frequencies, and Noncovalent Interactions of Large Molecular Systems Parametrized for all spd-Block Elements ($Z = 1-86$). *J. Chem. Theory Comput.* **2017**, *13*, 1989–2009.

(83) Neese, F. The ORCA Program System. *WIREs Comput. Mol. Sci.* **2012**, *2*, 73–78.

(84) Neese, F. Software Update: The ORCA Program System, Version 4.0. *WIREs Comput. Mol. Sci.* **2018**, *8*, e1327.

Supporting Information

C-C Cross Coupling reactions of Trityl Radicals: Spin Density Delocalization, Exchange Coupling and a Spin Label

Nico Fleck¹, Tobias Hett¹, Jonas Brode¹, Andreas Meyer^{1,2}, Sabine Richert³, Olav Schiemann^{1,*}

¹Institute of Physical and Theoretical Chemistry, Rheinische Friedrich-Wilhelms-University Bonn, Wegelerstr. 12, 53115 Bonn, Germany

² Current address: Max Planck Institute for Biophysical Chemistry, Am Fassberg 11, 37077 Göttingen, Germany

³Institute of Physical Chemistry, University of Freiburg, Albertstraße 21, 79104 Freiburg, Germany

Table of contents

1. Crystallographic Data	S4
2. Computational results.....	S6
2.1 Inclusion of spin density distribution in 16 ^{••} for distance calculation	S6
3. Pulsed EPR.....	S8
4. cw EPR spectroscopy	S10
4.1 cw-EPR spectroscopy on 15 ^{••} in the liquid state.....	S10
4.2 cw-EPR spectroscopy on 15 ^{••} in the frozen state.....	S11
4.3 cw-EPR spectra of new compounds	S12
5. Reaction of 3 [•] with n-butyl lithium.....	S17
6. Catalysts for Suzuki-Coupling	S18
7. Oxygen sensitivity of 15 ^{••}	S19
8. Sonogashira reactions	S21
8.1 General procedure for <i>Sonogashira-Hagihara</i> reactions.....	S21
8.2 General remarks	S21
8.3 Reaction with TIPS-acetylene	S24
8.4 Reaction with trimethylsilylacetylene.....	S33
8.5 Reaction with 2-Methyl-3-butyn-2-ol	S34
9. NMR spectra of new compounds	S43
9.1 Trityl alcohol 5.....	S43
9.2 Trityl alcohol 6-OH	S44
9.3 Trityl alcohol 9.....	S45
9.4 Trityl alcohol 10.....	S46
9.5 Trityl alcohol 14.....	S47
9.6 Trityl porphyrin 12-OH.....	S49
10. High-Resolution Mass Spectra	S51
11. MALDI(+) and ESI(+) mass spectra of trityl radicals	S59
12. Medium pressure liquid chromatography	S63
13. References	S66

1. Crystallographic Data

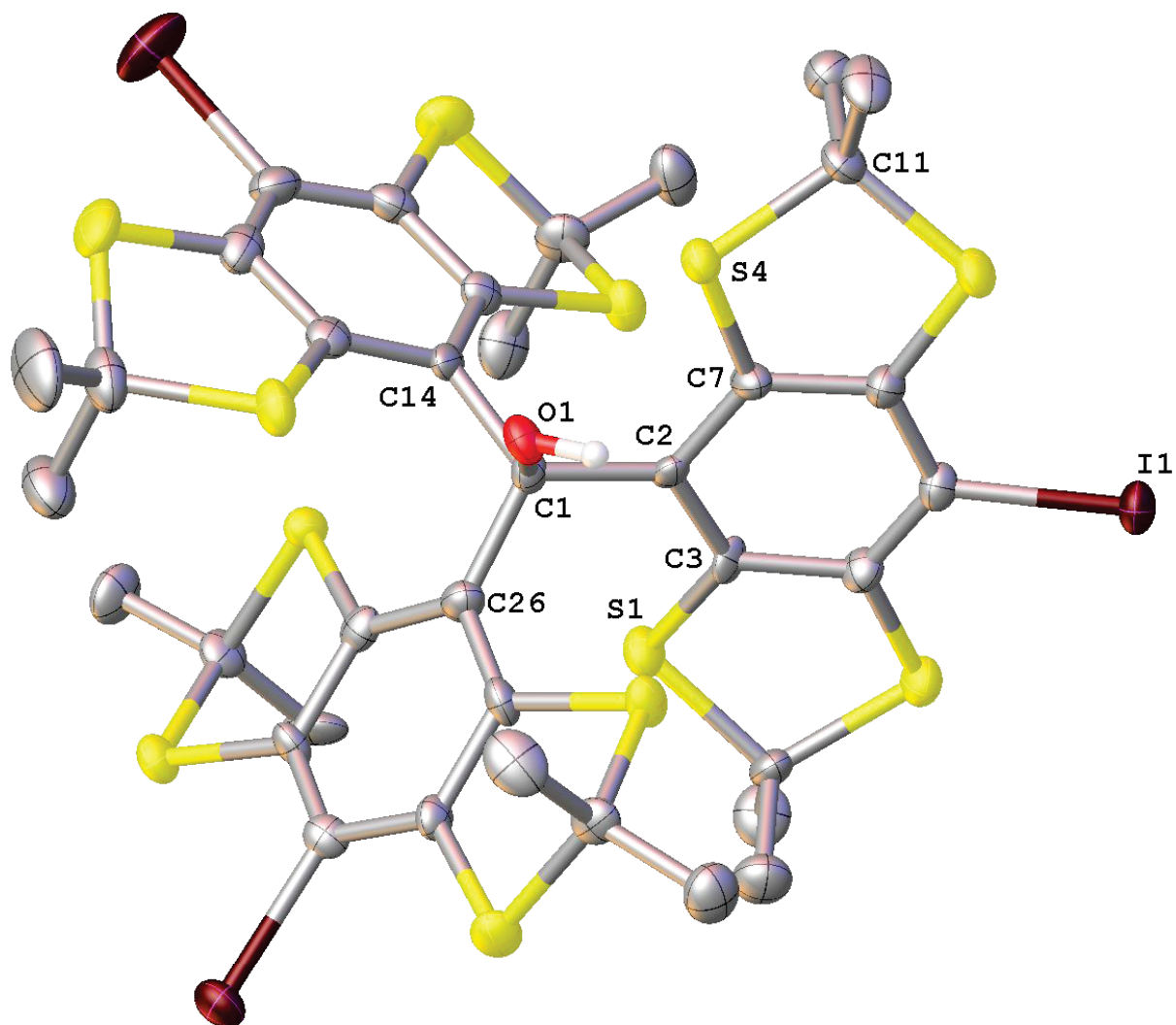


Figure S1: Crystal structure of trityl alcohol 5. The ellipsoid contour was set to 30% probability level.

The CIF-file containing all structural information can be obtained online as additional Supporting Information.

Crystallographic data for **5**

Crystal Habitus	clear greenish yellow plate
Device Type	Bruker X8-KappaApexII
Empirical formula	C ₄₁ H ₄₇ I ₃ O ₂ S ₁₂
Moiety formula	C ₃₇ H ₃₇ I ₃ OS ₁₂ , C ₄ H ₁₀ O
Formula weight	1337.20
Temperature/K	100
Crystal system	orthorhombic
Space group	Pca2 ₁
a/Å	26.4750(8)
b/Å	10.6566(3)
c/Å	18.4500(6)
α/°	90
β/°	90
γ/°	90
Volume/Å³	5205.4(3)
Z	4
ρ_{calc} / g/cm³	1.706
μ/mm⁻¹	2.316
F(000)	2640.0
Crystal size/mm³	0.2 × 0.09 × 0.04
Absorption correction	empirical
T_{min}; T_{max}	0.3729; 0.7460
Radiation	MoKα (λ = 0.71073)
2θ range for data collection/°	4.674 to 55.996°
Completeness to theta	0.998
Index ranges	-34 ≤ h ≤ 26, -14 ≤ k ≤ 13, -24 ≤ l ≤ 24
Reflections collected	87159
Independent reflections	12545 [R _{int} = 0.1364, R _{sigma} = 0.0917]
Data/restraints/parameters	12545/1/538
Goodness-of-fit on F²	1.027
Final R indexes [I ≥ 2σ (I)]	R ₁ = 0.0653, wR ₂ = 0.1403
Final R indexes [all data]	R ₁ = 0.0789, wR ₂ = 0.1497
Largest diff. peak/hole / e Å⁻³	1.89/-1.32
Flack parameter	0.068(19)

2. Computational results

2.1 Inclusion of spin density distribution in 16^{**} for distance calculation

The dipolar coupling constant considering the delocalization of spin density can be described by an extended point-dipole approach¹:

$$D = \frac{\mu_0 g^2 \beta_e^2}{4\pi\hbar} \sum_{a=1}^i \sum_{b=i+1}^N \frac{1}{r_{ab}^3} \rho_a \rho_b \quad (eq. S1)$$

Here, g equals the trityl g -factor of 2.0032, β_e is the Bohr magneton, and \hbar the reduced Planck constant. r_{ab} indicates the distance between two atoms bearing the spin densities ρ_a and ρ_b . From this dipolar coupling constant, the effective interspin distance r_{eff} can be determined as:

$$r_{eff} = \sqrt[3]{\frac{\mu_0 g^2 \beta_e^2}{4\pi\hbar} \frac{1}{D}} \quad (eq. S2)$$

Figure S2 shows the distribution of spin density within 15^{**} schematically. Whereas the central carbon atom of the trityl core exhibit each about 30 % of the spin density, approximately 5 % is delocalized in each phenyl ring (purple) and 0.5 % into each phenyl ring (blue). Note that the spin density on the hydrogen atoms was neglected as only 0.07 % of the spin density was localized on all 108 hydrogen atoms together. The percentage values refer to the entire spin density of 2 electrons. Since the spin density in the phenyl rings decays rapidly with the distance from the central carbon (first phenyl ring: 5 %, second phenyl ring 0.5 %), it was assumed that spin A is not delocalized across the dashed line in Figure S2 and vice versa. By this, only distances across the dashed line contribute to the dipolar coupling constant between spin A and spin B. This yields an effective interspin distance of 1.75 nm for the optimized structure of 15^{**} , which is in a stretched conformation. Thus, any bending of the structure shortens the distance between the two trityl centers and therefore also the effective interspin distance. In order to account for this, a molecular dynamics (MD) simulation was performed, which was then convoluted with the spin density distribution in order to obtain a distribution of the effective interspin distances. The MD simulation was carried out using the *GFN-xTB*² program with a simulation time of 250 ps, a time step of 4 fs and a temperature of 298 K. The DFT-optimized structure was used as an input. Then, a home-written *MATLAB* script was used to calculate the effective interspin distance for each frame of the MD simulation based on the procedure described above. The distance distribution was then obtained as a histogram of these effective interspin distances yielding the plot in Figure 7b in the main text.

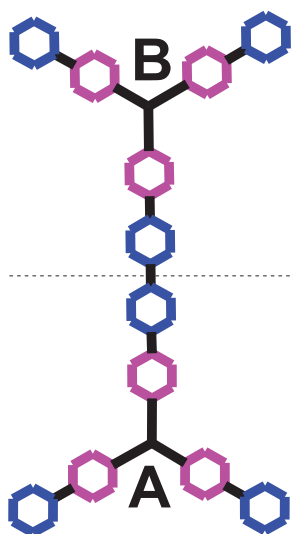


Figure S2: Schematic representation of the spin density distribution in $15^{\bullet\bullet}$. The central carbon atoms of the trityl core exhibit each a spin density of 0.58, the phenyl rings in purple of app. 0.10 and the phenyl rings in blue of app. 0.01.

2.2 Spin density distribution in 12^{\bullet}

The Mulliken spin density populations in 12^{\bullet} were obtained from DFT calculations (PBE, def2-SVP). As shown by the $^1\text{H-NMR}$ spectrum in the main text (Figure 4), one signal in the pyrrolic region is strongly shifted compared to the other ones. The spin densities for the hydrogen atoms, which occur in the $^1\text{H-NMR}$ of 12^{\bullet} are provided below in figure S3. Since H_{p1} features the largest spin density among the pyrrolic hydrogens, it was therefore assigned to the most-shifted signal in the NMR-spectrum (Figure 4, main text). The signals, which do not encounter a paramagnetic shift in the $^1\text{H-NMR}$ also do not hold spin density according to the DFT calculations.

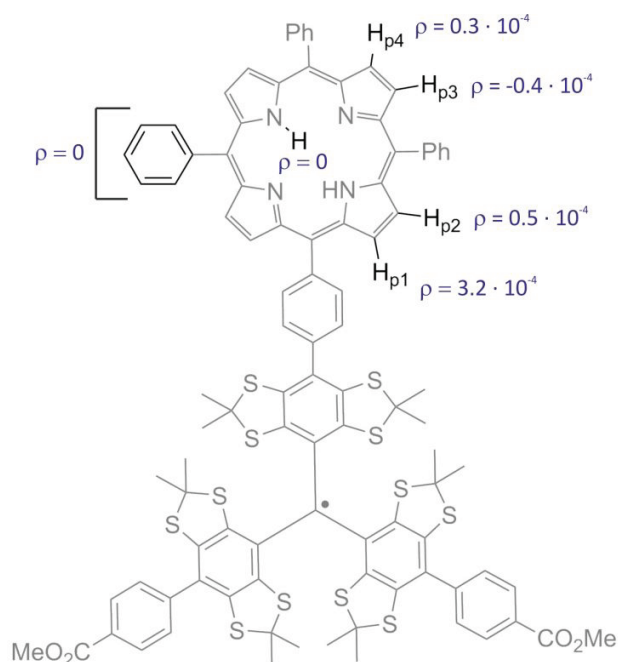


Figure S3: Spin density distribution within 12^{\bullet} according to DFT.

3. Pulsed EPR

Pulsed EPR measurements were conducted on a Bruker (Bruker BioSpin GmbH, Rheinstetten, Germany) ELEXSYS E580 EPR spectrometer equipped with a CF935 helium gas-flow cryostat (Oxford Instruments, Abington, United Kingdom) and an Oxford Instruments ITC 502 temperature controller. An ER 5106QT-II resonator was used at Q-Band frequencies in combination with a 150 W TWT-amplifier (model: 187 Ka) from Applied Systems Engineering, Texas, USA. All data was acquired using quadrature detection.

Before setting up the DQC experiment, an echo-detected field sweep based on the Hahn echo sequence was conducted. Herein, the $\pi/2$ and π pulse lengths were set to 12 ns and 24 ns, respectively. The phase of the microwave was adjusted for subsequent experiments already at the stage of Hahn echo optimization. Care was taken that the full signal intensity was detected in the real channel, whereas signal contributions of the imaginary channel were minimized. By means of the echo-detected field sweep, the resonance field of the trityl signal was determined.

For the DQC-measurement, a 6-pulse sequence³ was used in conjunction with a 64-step phase cycling in order to filter out single-quantum coherences. All pulse lengths, interpulse delay times and further relevant parameters are given in table S1.

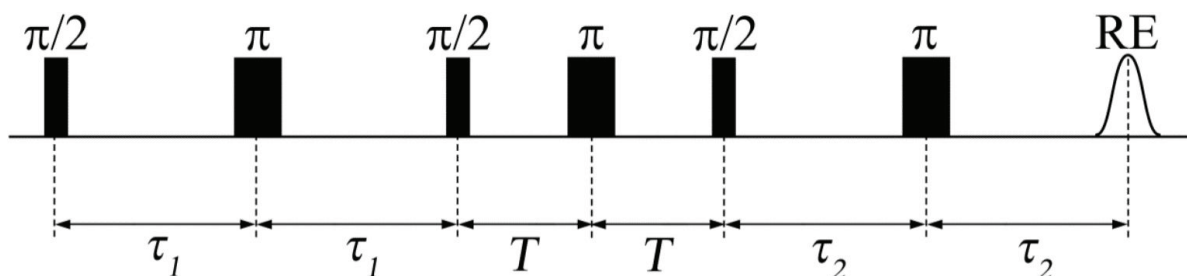


Figure S4: Applied DQC pulse sequence.

Table S1: DQC parameters.

Quantity	Value
$\pi/2$ -Pulse	12 ns
π -Pulse	24 ns
τ_1, τ_2	350 ns
T	50 ns
SRT	3 ms

Data analysis was performed using the *MATLAB* toolkit *DeerAnalysis*^{4,5}. The time trace was pre-processed by applying a background correction. Applying Fast Fourier Transformation as implemented in the *DeerAnalysis* software to the background-corrected time trace yields the Pake pattern shown in Figure S5.

Due to the fast oscillation with a period of 60 ns, a time increment of 4 ns was used for the DQC-experiment. However, *DeerAnalysis 2018* imposes a lower limit of 8 ns as time increment, so that half of the points are discarded prior to analysis, leading to insufficient fits of the time trace. Upon request, the program was modified by its author, *Gunnar Jeschke*, so that time steps of 4 ns could also be handled. Applying a regularization parameter $\alpha = 0.794$ yields the corresponding distance distribution. The regularization parameter was chosen from the L-curve shown in Figure S2 according to the GCV-criterion as implemented in *DeerAnalysis*.

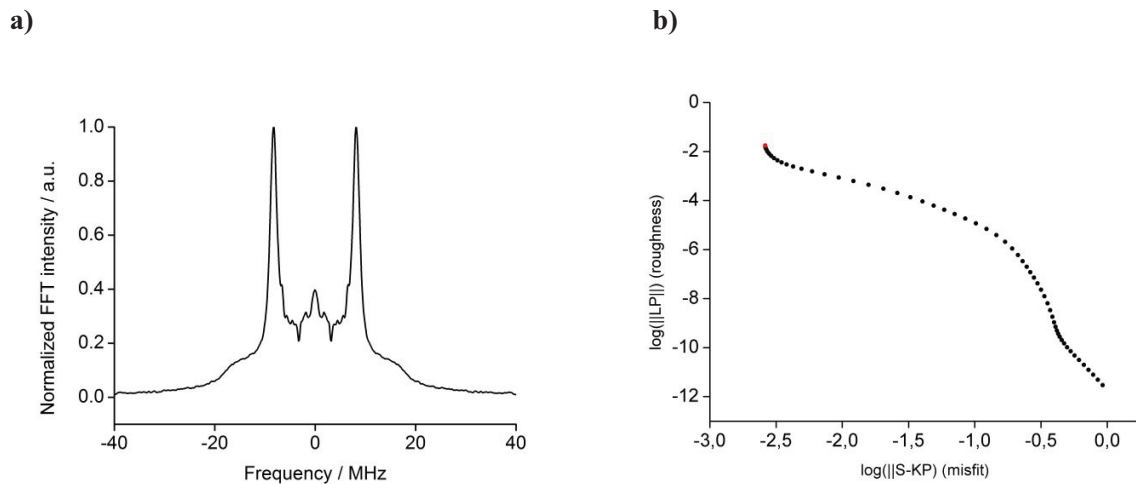


Figure S5: a) Pake pattern obtained from the Fourier Transformation of the DQC time trace. b) L-Curve of the Tikhonov-regularization. The regularization parameter chosen for data analysis is marked in red.

4. cw EPR spectroscopy

4.1 cw-EPR spectroscopy on $15^{\bullet\bullet}$ in the liquid state

The cw X-band EPR spectrum of $15^{\bullet\bullet}$ was simulated with *EasySpin*⁶ in combination with a home-written *MATLAB* script. The position of the ^{13}C -hyperfine satellites is sensitive to an increasing J up to 550 MHz. While spectra simulated with lower J -values can be distinguished, higher J values do not change the shape of the spectrum further, as the strong coupling regime is accessed as shown in fig. S6.

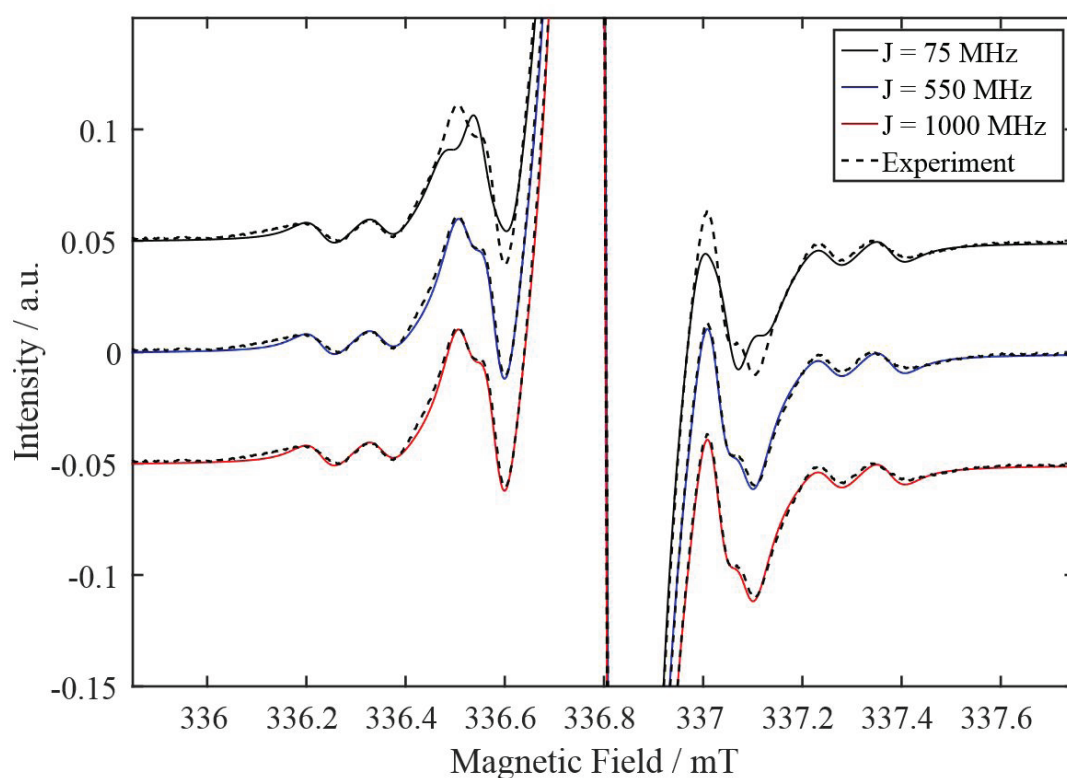


Figure S6: Room temperature *cw*-EPR spectra (X-Band) simulated for $15^{\bullet\bullet}$ assuming different values of J . The experimental spectrum of $15^{\bullet\bullet}$ is overlaid as a dotted line.

4.2 cw-EPR spectroscopy on $15^{••}$ in the frozen state

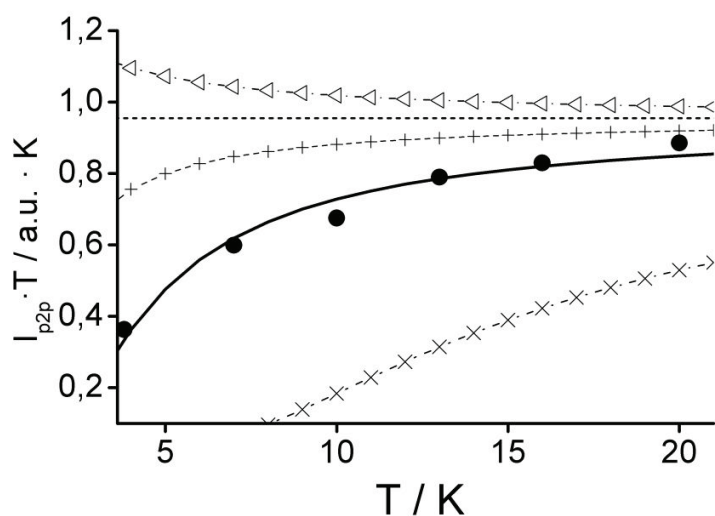


Figure S7: Bleany-Bowers fit of the intensity of the half-field signal I_{p2p} versus the temperature T . The best fit for the experimental data provided $J = -2.81 \text{ cm}^{-1}$. \bullet exp. Data; — $J = -2.81 \text{ cm}^{-1}$; Δ $J = +1.00 \text{ cm}^{-1}$; $+$ $J = -1.00 \text{ cm}^{-1}$; \times $J = -10.0 \text{ cm}^{-1}$.

The frozen-solution *cw*-EPR spectrum of $15^{••}$ was measured as described in the main text. In the main-field region, two transitions occur. One being the $\Delta m_s = 1$ transition and yielding the Pake pattern, the other one is a $\Delta m_s = 2$ double-quantum transition giving the central line. The latter transition requires two coherent photons and therefore its intensity scales differently from the $\Delta m_s = 1$ transition with the microwave power as shown below in figure S78.

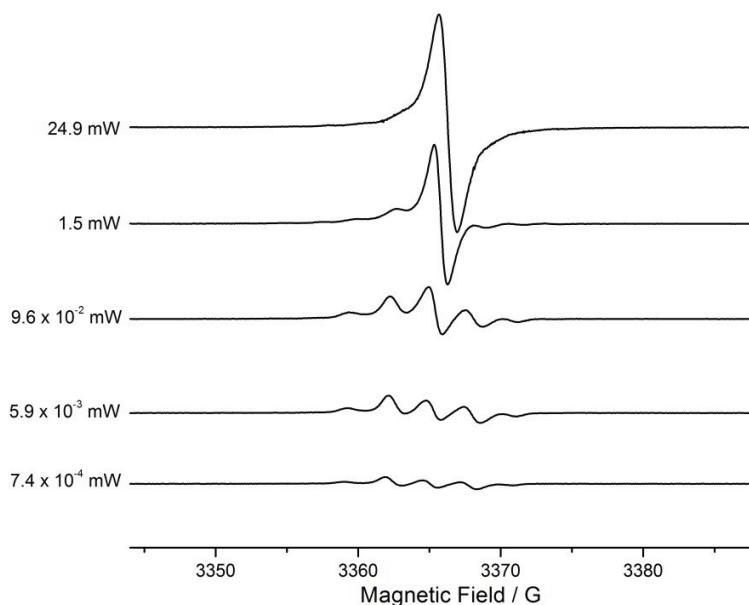


Figure S8: *cw*-EPR spectrum of $15^{••}$ at 100 K at different microwave power.

4.3 cw-EPR spectra of new compounds

In the section below, *continuous wave (cw) X-band* EPR spectra of the radical compounds presented in the main text are shown together with the respective fits. A summary of hyperfine coupling constants, isotropic g-values and linewidths obtained from the fits is provided in Table S2.

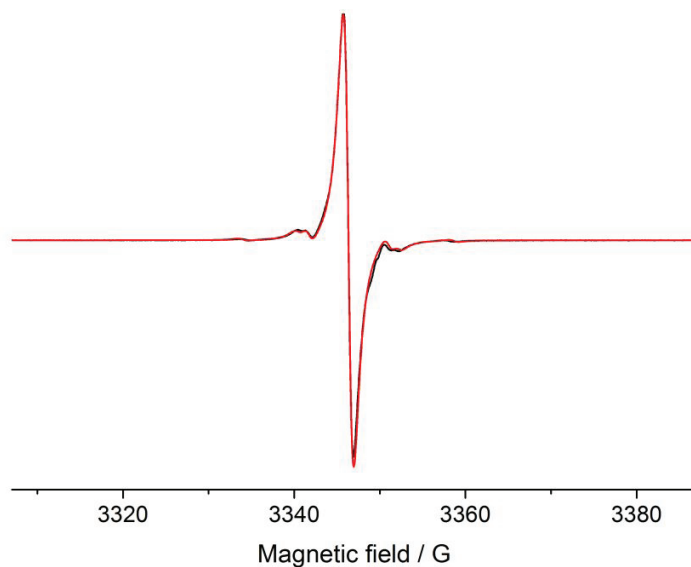


Figure S9: Trityl radical **3•** *cw*-EPR, X-Band, 298K.

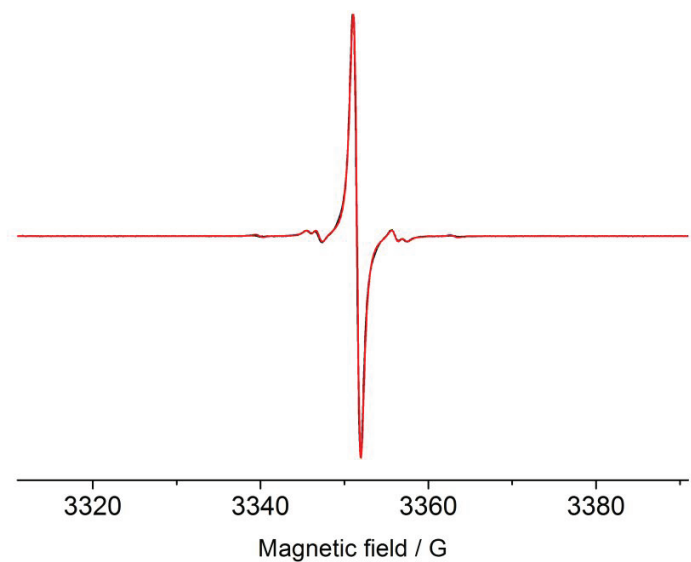


Figure S10: Trityl radical **6•** *cw*-EPR, X-Band, 298K.

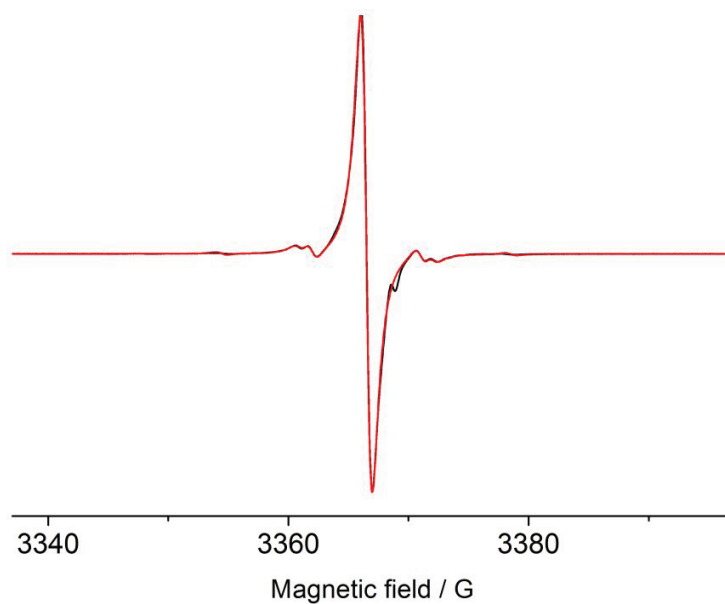


Figure S11: Trityl radical 7^\bullet *cw*-EPR, X-Band, 298K.

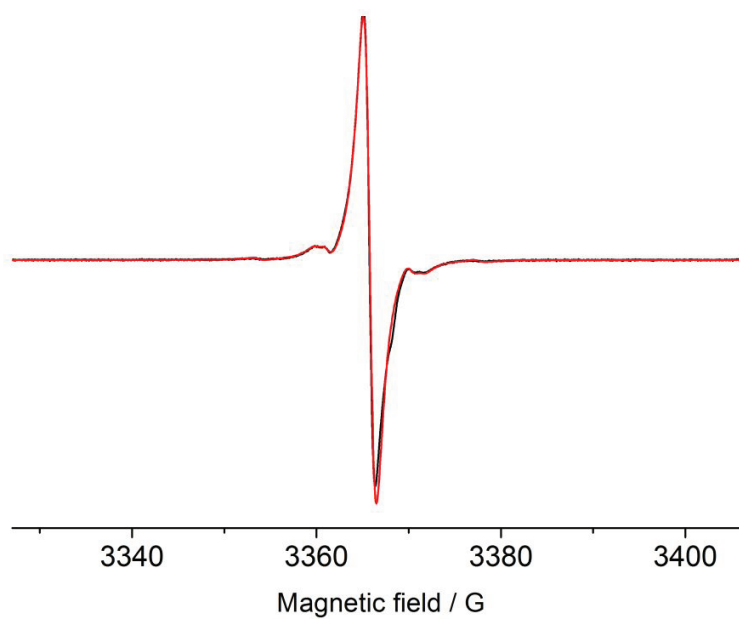


Figure S12: Trityl radical 8^\bullet *cw*-EPR, X-Band, 298K.

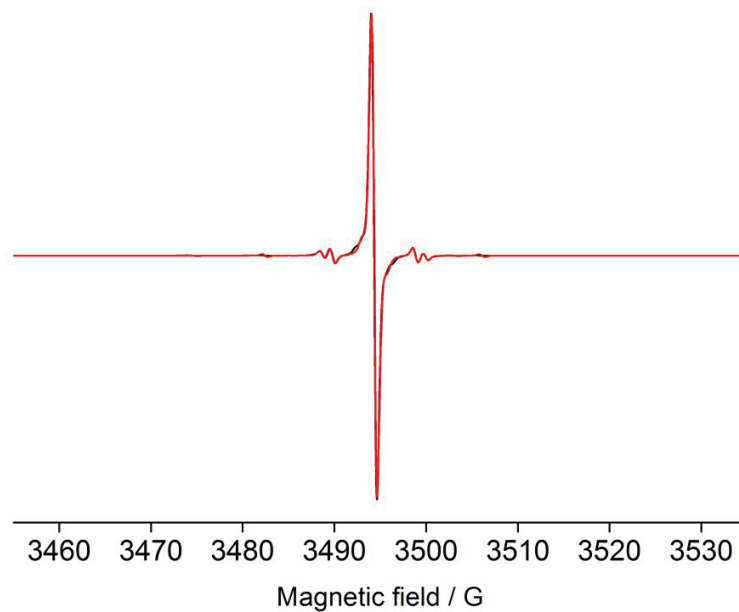


Figure S13: Trityl porphyrin 12• *cw*-EPR, X-Band, 298K.

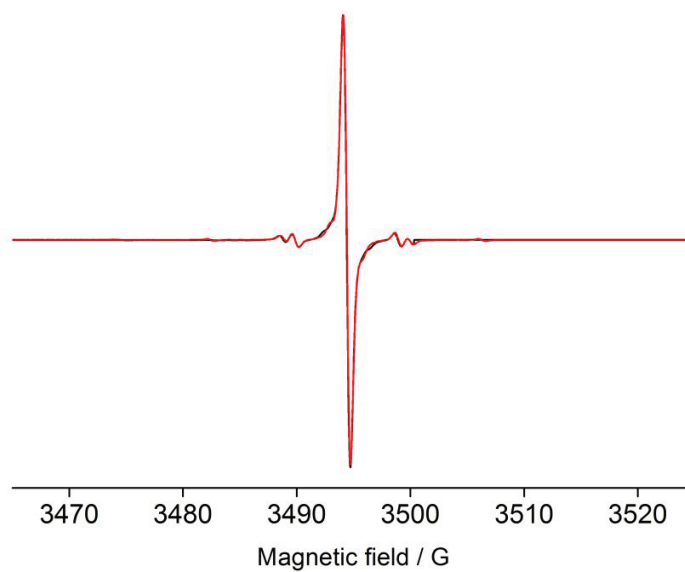


Figure S14: Trityl porphyrin 13• *cw*-EPR, X-Band, 298K.

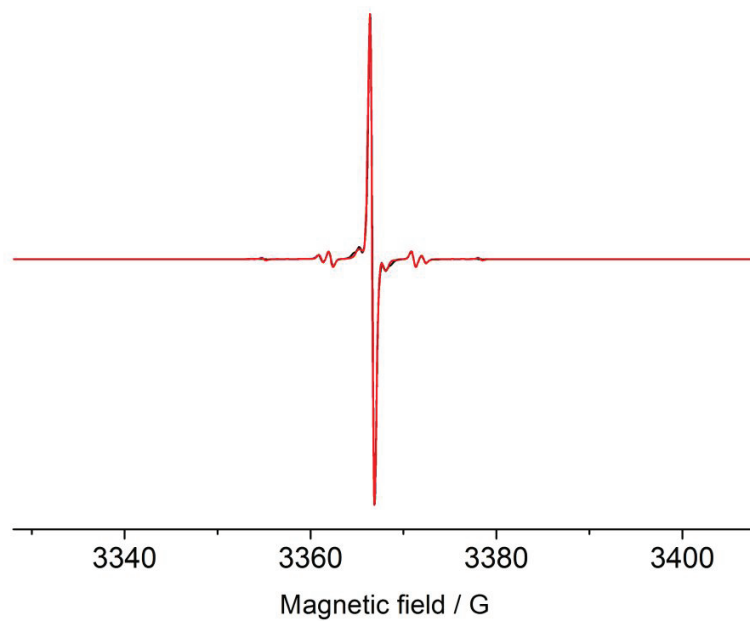


Figure S15: Trityl radical **16**[•] *cw*-EPR, X-Band, 298K.

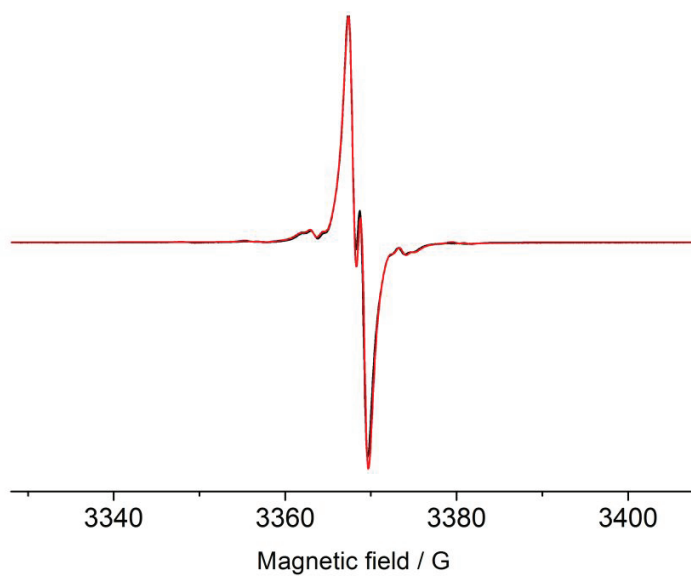
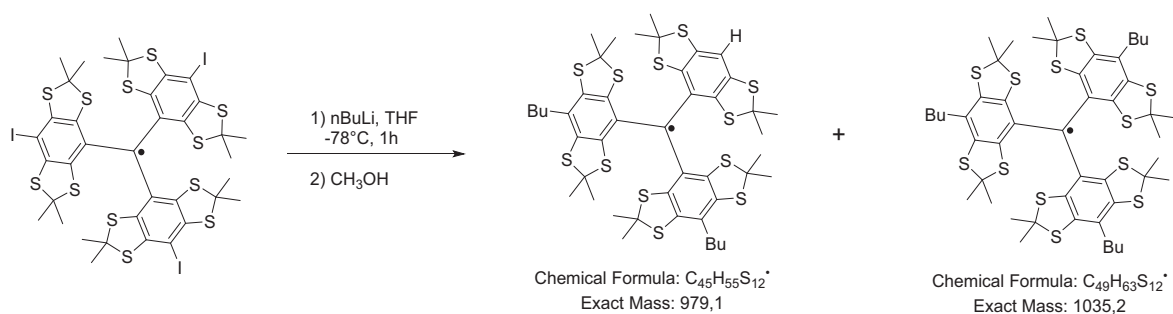


Figure S16: Trityl radical **17**[•] *cw*-EPR, X-Band, 298K.

Table S2: EPR parameters obtained from the fit of the *cw*-EPR spectra.

Compound	Isotropic g-value	A / MHz	lwpp Gaussian / mT	lwpp Lorentzian / mT
3[•]	2.0051	¹³ C _{central} : 68.94 ¹³ C _{ipso} : 32.80 ¹³ C _{ortho} : 26.08	0.0020	0.1224
6[•]	2.0032	¹³ C _{central} : 65.16 ¹³ C _{ipso} : 31.56 ¹³ C _{ortho} : 25.56	0.0502	0.0626
7[•]	2.0038	¹³ C _{central} : 67.67 ¹³ C _{ipso} : 31.56 ¹³ C _{ortho} : 25.56	0	0.0966
8[•]	2.0044	¹³ C _{central} : 67.09 ¹³ C _{ipso} : 31.80 ¹³ C _{ortho} : 25.20	0	0.1415
12[•]	2.0032	¹³ C _{central} : 66.19 ¹³ C _{ipso} : 31.42 ¹³ C _{ortho} : 25.38 ¹³ C _{para} : 6.57 ¹³ C _{meta} : 4.02	0.0482	0.0244
13[•]	2.0031	¹³ C _{central} : 66.75 ¹³ C _{ipso} : 31.09 ¹³ C _{ortho} : 25.32 ¹³ C _{para} : 6.77 ¹³ C _{meta} : 4.50	0.0473	0.0282
15^{••}	2.0036	¹³ C _{ipso} : 31.25 ¹³ C _{ortho} : 25.30	0.0160	0.0551
15^{••} (100K)	$g_{xx} = 2.0036$ $g_{yy} = 2.0036$ $g_{zz} = 2.0034$	¹³ C _{ipso} : 31.25 ¹³ C _{ortho} : 25.30 D _{ee} = 11.17	0.0787 0.0635 (2xΔm _S = 1)	0.0402 0.0731 (2xΔm _S = 1)
16[•]	2.0032	¹³ C _{central} : 66.44 ¹³ C _{ipso} : 31.01 ¹³ C _{ortho} : 24.94 ¹³ C _{para} : 7.87 ¹³ C _{meta} : 5.74	0.0396	0.0172
17[•]	2.0032	¹³ C _{central} : 67.82 ¹³ C _{ipso} : 31.93 ¹³ C _{ortho} : 25.54 ¹ H _{alkyne} : 3.72	0.0135	0.1095

5. Reaction of **3**[•] with *n*-butyl lithium



Trityl radical **3**[•] (100 mg, 79 μmol) was dissolved in 8 mL dry THF and *n*-butyl lithium (98 μL 2.5 M in hexanes, 3.00 eq.) was added at -78 °C. The deep green solution turns deep purple upon the addition of butyl lithium. After 1 h, 0.5 mL methanol was added and the solution was warmed up to room temperature and stirred for 30 min. Then, solvents were removed under reduced pressure and the crude product was subjected to MALDI(+)-MS analysis, which revealed the product composition displayed above. Interestingly, the main products were coupling products with butyl lithium and not the exchange products.

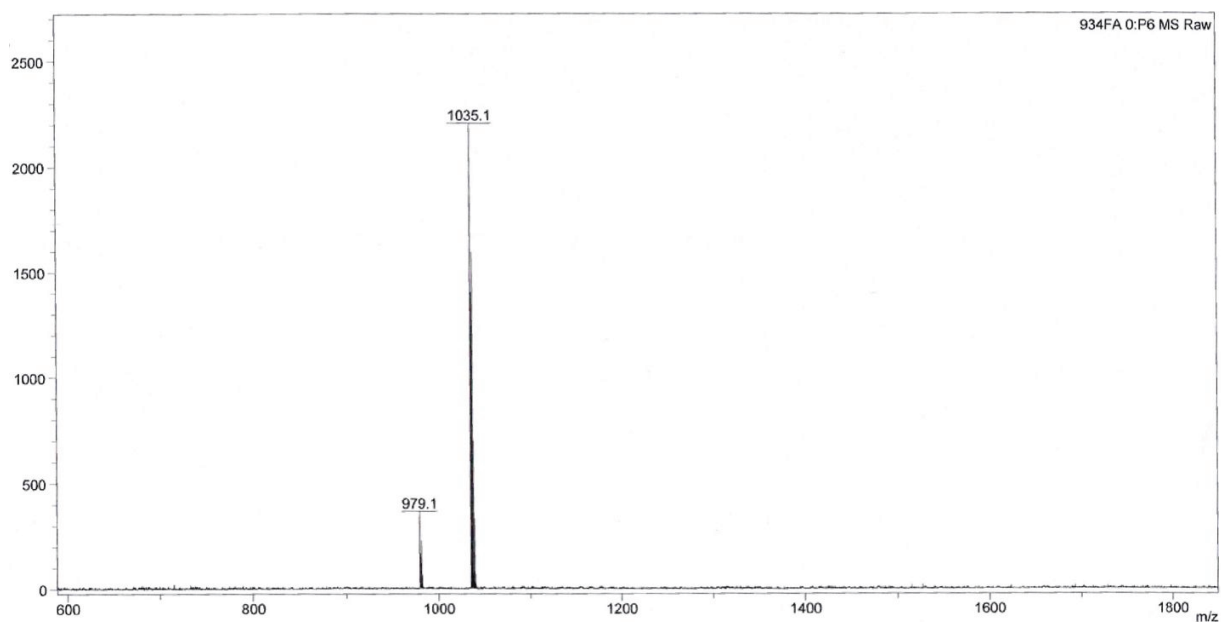


Figure S17: MALDI(+)-spectrum of crude product of the reaction of **3**[•] with *n*BuLi.

6. Catalysts for Suzuki-Coupling

For the reaction of **5** to **6-OH**, the suitability of catalyst $\text{Pd}(\text{OAc})_2 + 2 \text{tBu}_3\text{P}$ was also tested. The aim of this was to test whether the oxidative addition of Pd^0 is inhibited by the steric situation, since the electron-rich tBu_3P would accelerate this step. However, one sees a decrease in the reaction rate, presumably due to the large cone-angle of tBu_3P and the steric demand associated with it. The reaction was carried out under the same conditions as described in the synthesis section. $^1\text{H-NMR}$ allowed to analyze the product mixture, since the signal of the central OH-group is quite sensitive to para-functionalization.

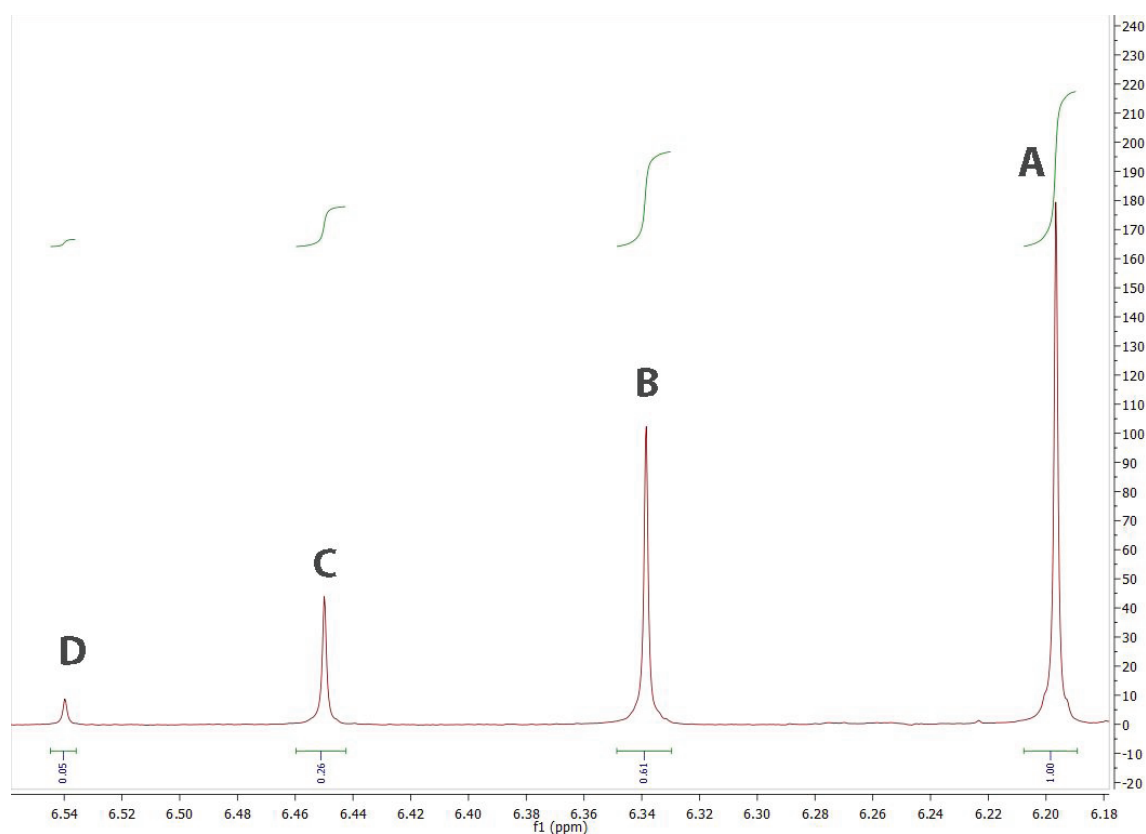


Figure S18: $^1\text{H-NMR}$ -spectrum (500 MHz) of the crude product. Signal A refers to the starting material **5**, signal D to **6-OH**. Signals C and B are originated from the bis- and mono-coupling product, respectively.

7. Oxygen sensitivity of $15^{\bullet\bullet}$

During purification of the trityl biradical $15^{\bullet\bullet}$, a bleaching of the deep green color during column chromatography was observed. This was attributed to an enhanced sensitivity towards oxygen and partial oxidation, which was also observed for a similar trityl biradical before⁷. This behavior might be explained by the triplet state for $15^{\bullet\bullet}$, which is populated by 49.5 % at a J of -2.8 cm^{-1} and at 298 K according to the Boltzmann distribution. Since atmospheric oxygen is also a triplet, the kinetic inhibition of the oxidation could be reduced compared to a doublet trityl radical or a singlet trityl alcohol. Figure S19 shows the ESI(+) mass spectrum of $15^{\bullet\bullet}$ synthesized directly from trityl radical 7^{\bullet} , the intensity of the $[M+17]^+/[M+16]^+$ peak is remarkable here. Note that both peaks overlap and correspond to the trityl alcohol (15-OH^{\bullet}) and the sulfoxide oxidation products. The mass spectrum in figure S20 was recorded from $15^{\bullet\bullet}$ synthesized via the trityl alcohol approach as described in the main text. Here, the peaks assigned to oxidation products exhibit less intensity. The remaining intensity accounts for the monoradical content as seen in the *cw* EPR spectrum.

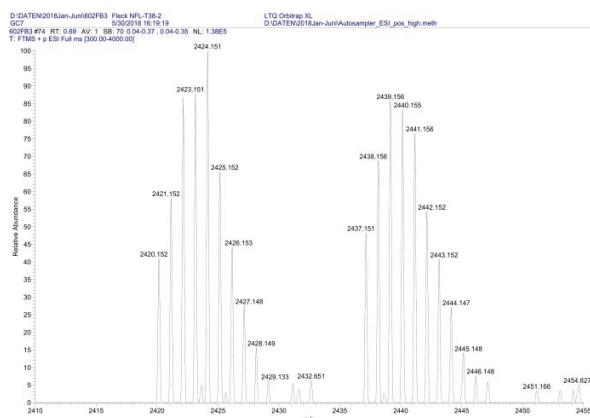


Figure S19: ESI(+)-MS of $15^{\bullet\bullet}$ synthesized from trityl radical 7^{\bullet} after column chromatography.

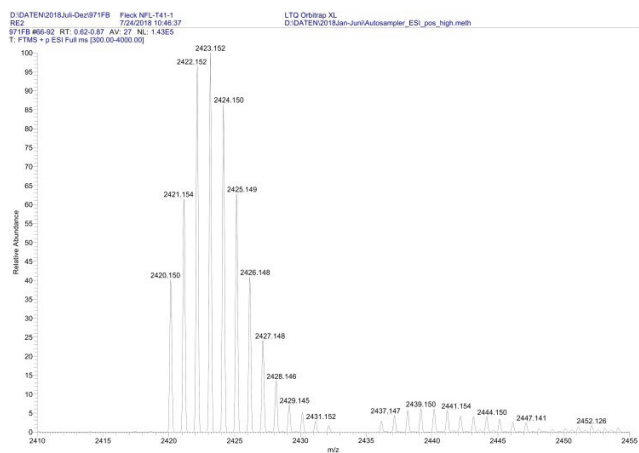


Figure S20: ESI(+)-MS of **15** synthesized from trityl alcohol **9**.

8. Sonogashira reactions

8.1 General procedure for *Sonogashira-Hagihara* reactions

150 mg of **5** (120 μmol), Pd-catalyst (6 μmol , 5 mol%), CuI (12 μmol , 10 mol%) were dissolved in 20 mL of the solvent mixture. Then, the corresponding acetylene (480 μmol , 4 eq.) was added and the reaction mixture was stirred at the corresponding temperature. Solvents were removed under reduced pressure subsequently and the residue was taken up in dichloromethane (30 mL). After washing with 0.1M Na₂EDTA and brine, the organic phase was separated, dried over MgSO₄ and the solvents were removed under reduced pressure.

The crude product was then dried in oil-pump vacuum (10^{-3} mbar) and subjected to analysis without further purification.

8.2 General remarks

The C-C cross coupling under *Sonogashira-coupling* conditions was tested on trityl alcohol **5** with 2-methyl-3-butyn-2-ol, trimethylsilyl acetylene (TMS-acetylene), and triisopropylsilyl acetylene (TIPS-acetylene) as alkynes and using common solvents and catalysts (THF/DIPEA or Et₃N, Pd(Ph₃P)₂Cl₂, CuI, 70°C, 16h). These reaction conditions showed several side products in the MALDI-MS spectra alongside to the coupling products, as shown in figures S21, S36, and S37. The sum formulas of the side products were obtained via APCI-HRMS (S23-30, S38) and revealed an uptake of alkyne equivalents additional to the desired coupling reaction. Therefore, these side-products are called “insertion products”, as they presumably emerge from an insertion of alkyne into the trityl backbone. It is noteworthy, that this unusual reactivity was observed systematically for all alkynes mentioned above. Using only the copper catalyst led to no reaction at all, whereas the sole use of Pd(Ph₃P)₂Cl₂ provided both coupling and insertion products. Other palladium catalysts such as Pd(OAc)₂ + P(^tBu₃P)₃ or Pd(dppf)Cl₂ proved to be inferior both for the coupling and the insertion reaction. Moreover, the choice of either DIPEA or Et₃N as cosolvent did not influence the product composition. Except for the C-I bond, the C-S bonds of the annulated 1,3-dithianes are the only reactive bonds within the molecule. Interestingly, also *Iovine et al.*⁸ observed a competitive carbothiolation process *via* alkyne insertion into the C-S bond of phenylthioacetate under palladium catalysis condition. We thus assume an analogous migratory insertion of alkyne into a C-S bond of the trityl moiety.

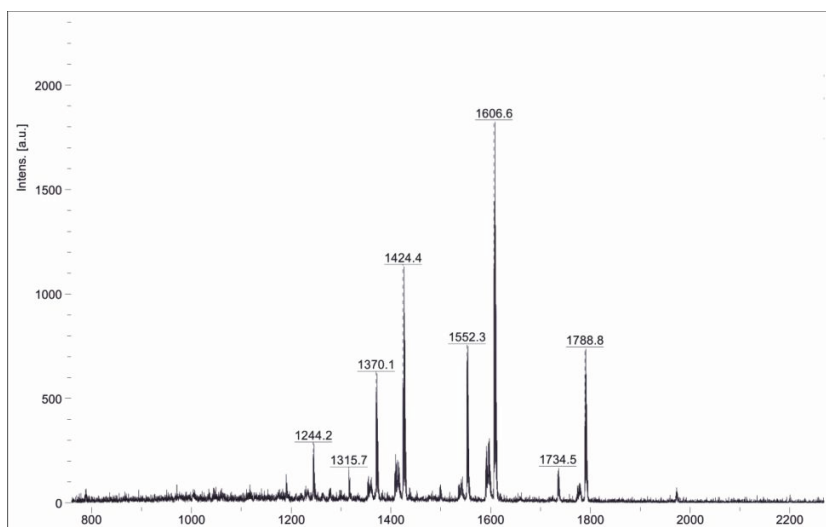


Figure S21: Reaction of **5** with 4 eq. TIPS-acetylene, Pd(Ph₃P)₂Cl₂, and CuI in THF/DIPEA (3:1). The MALDI(+)-spectrum of the product mixture obtained is shown. Notation: C_xI_y = x times coupling (x = 1 – 3) and y times insertion of alkyne. Assignment of peaks [m/z]: 1315.7 (C₁I₀), 1370.1 (C₂I₀), 1424.4 (C₃I₀), 1552.3 (C₂I₁), 1606.6 (C₃I₁), 1734.5 (C₂I₂), 1788.8 (C₃I₂). The peak at 1244.2 corresponds to a C₂-product with a remaining hydrogen instead of iodine.

Whereas the same reactivity was observed for **3**[•] (Figure S31) and **6**, no insertion reactivity was observed for the unsubstituted parent compound, suggesting that the vicinal iodine seems to be crucial for the insertion reaction. According to the mechanism proposed below in Figure S22, the insertion reaction starts with an oxidative addition of palladium(0) into the C_{ar}-I bond analogous to the coupling reaction. Followed by a 1,2-palladium shift, the insertion reaction runs further through a π-coordination of the alkyne to the palladium and a subsequent migratory insertion into the C-S bond. Such a reaction step would be sensitive to steric demands, which is in agreement with our observation, that the insertion reaction becomes disfavored for the bulky TIPS-acetylene compared to 2-methyl-3-butyne-2-ol and TMS-acetylene.

Moreover, the product with presumably one coupled and one inserted 2-methyl-3-butyne-2-ol (C₁I₁) was isolated by column chromatography and in an amount sufficient for ¹H-NMR. As only singlets appeared in the olefin region (Figure S39), a cyclic structure was proposed as given in fig. S22. Surprisingly, the insertion reaction can be suppressed by the use of refluxing CH₂Cl₂/Et₃N as solvent, which is, however, less common for *Sonogashira* couplings. For TIPS-acetylene with Pd(Ph₃P)₂Cl₂, this leads solely to coupling products and no insertion (Figure S32), whereas for the sterically less demanding 2-methyl-3-butyne-2-ol, insertion products are observed, again. However, in that case both the insertion and the coupling reaction seem to be equitable,

since they always occurred side by side throughout the entire reaction progress (fig. S42 – S46). Moreover, the use of Pd(dppf)Cl₂ in CH₂Cl₂/Et₃N caused less insertion compared to Pd(Ph₃P)₂Cl₂ for 2-methyl-3-butyn-2-ol as coupling substrate (fig. S47).

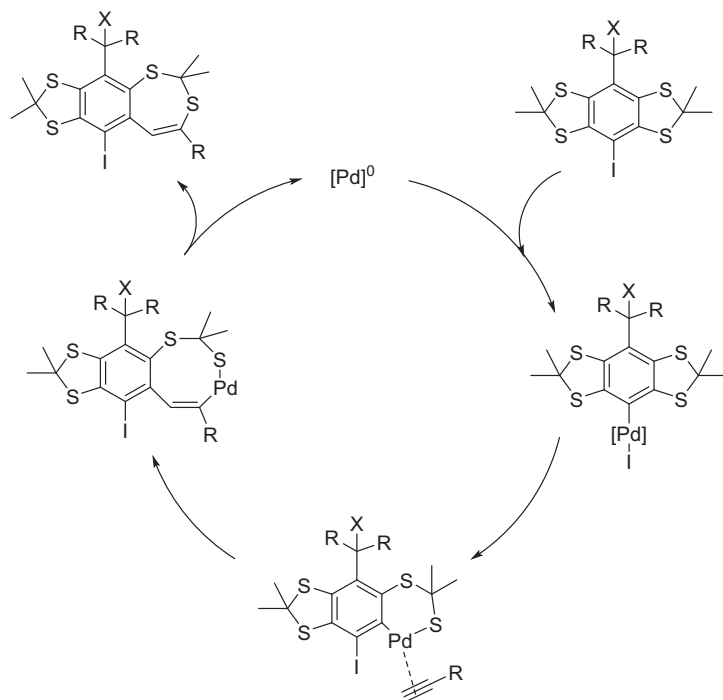


Figure S22: Proposed mechanism of alkyne uptake into the trityl scaffold by a Pd-catalyzed carbothiolation process. Note that X can be either –OH or a radical center and R is a thioaryl-substituent.

All in all, the palladium catalyst is responsible for a presumed migratory insertion of alkyne into the C-S bonds of the thioacetal and which is competing with the *Sonogashira* coupling. By choosing an appropriate solvent, CH₂Cl₂, and a sterically demanding alkyne, TIPS-acetylene, this side reaction can be suppressed. Nonetheless, also the coupling reaction suffers from the steric demand both of the trityl moiety and the TIPS-acetylene, and thus becomes slow. Accordingly, the *Sonogashira-Hagihara* coupling reaction is not versatile with trityl alcohols/radicals and can only be taken into account for bulky acetylenes, such as TIPS-acetylene.

8.3 Reaction with TIPS-acetylene

Following the general procedure, **5** was reacted with triisopropylsilylacetylene in THF/Et₃N 3:1 (v/v) yielding a mixture of insertion and coupling products. An assignment of the peaks to sum formulas and products is presented in table S3. The APCI-spectra are shown below in order of ascending mass as indicated in table S3 (Figures S23-S30).

In the following, products will be denominated with a C_xI_y notation, where *x* indicates the number of coupled alkynes and *y* the number of inserted alkynes according to the sum formula. Note, that APCI-data is presented here. During the ionization process, an α-cleavage at the central carbon is observed leading to an abstraction of the –OH group. Therefore, the [M-17]⁺ peaks are shown here, whereas the MALDI(+)-spectrum shows [M]⁺ peaks. The signal intensities in MALDI(+) spectra do not correspond to the sample composition in a quantitative manner, though a qualitative estimate can be obtained from these.

Table S3: Mass spectrometric data for the product mixture obtained with TIPS-acetylene

MALDI(+)-peak [M] ⁺	APCI-peak [M-17] ⁺	sum formula of the corr. trityl alcohol	product type	HRMS figure
1244.2	1227.2450	C ₅₉ H ₈₀ OS ₁₂ Si ₂	[M-I] C ₂ I ₀	S22
1315.4	1298.9026	C ₄₈ H ₅₈ I ₂ OS ₁₂ Si	C ₁ I ₀	S23
1370.1	1353.1399	C ₅₉ H ₇₉ IOS ₁₂ Si ₂	C ₂ I ₀	S24
1424.4	1407.3796	C ₇₀ H ₁₀₀ OS ₁₂ Si ₃	C ₃ I ₀	S25
1552.3	1535.2886	C ₇₀ H ₁₀₁ IOS ₁₂ Si ₃	C ₂ I ₁	S26
1606.6	1589.5247	C ₈₁ H ₁₂₂ OS ₁₂ Si ₄	C ₃ I ₁	S27
1734.5	1717.4338	C ₈₁ H ₁₂₂ IOS ₁₂ Si ₄	C ₂ I ₂	S28
1788.8	1771.6735	C ₉₂ H ₁₄₄ OS ₁₂ Si ₅	C ₃ I ₂	S29

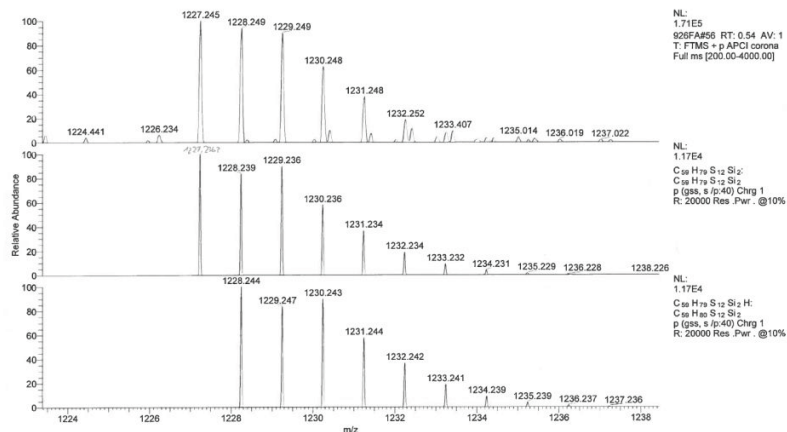


Figure S23: APCI-HRMS of the [M-I] C₂I₀ product.

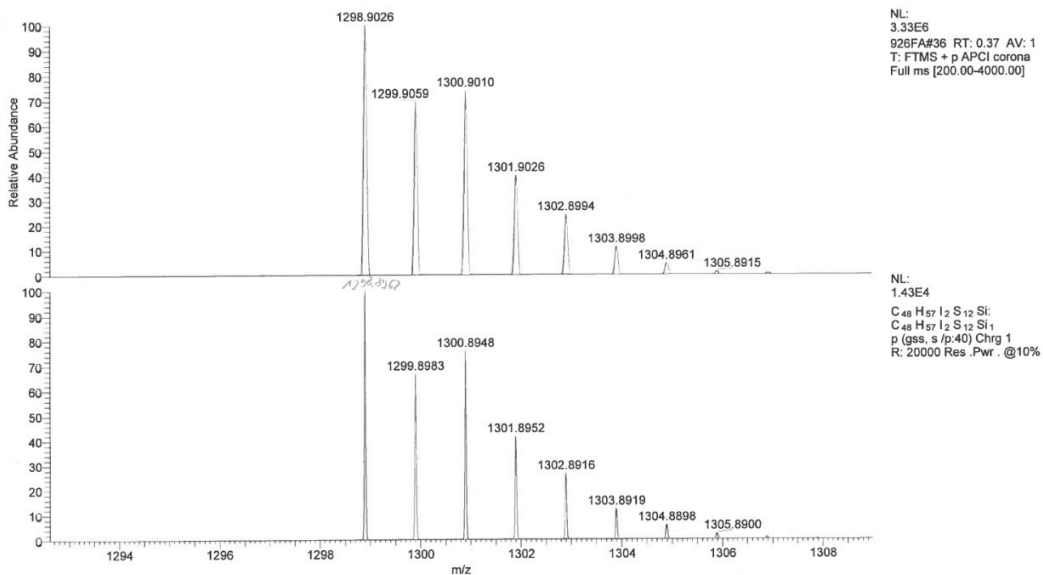


Figure S24: APCI-HRMS of the C₁I₀ product

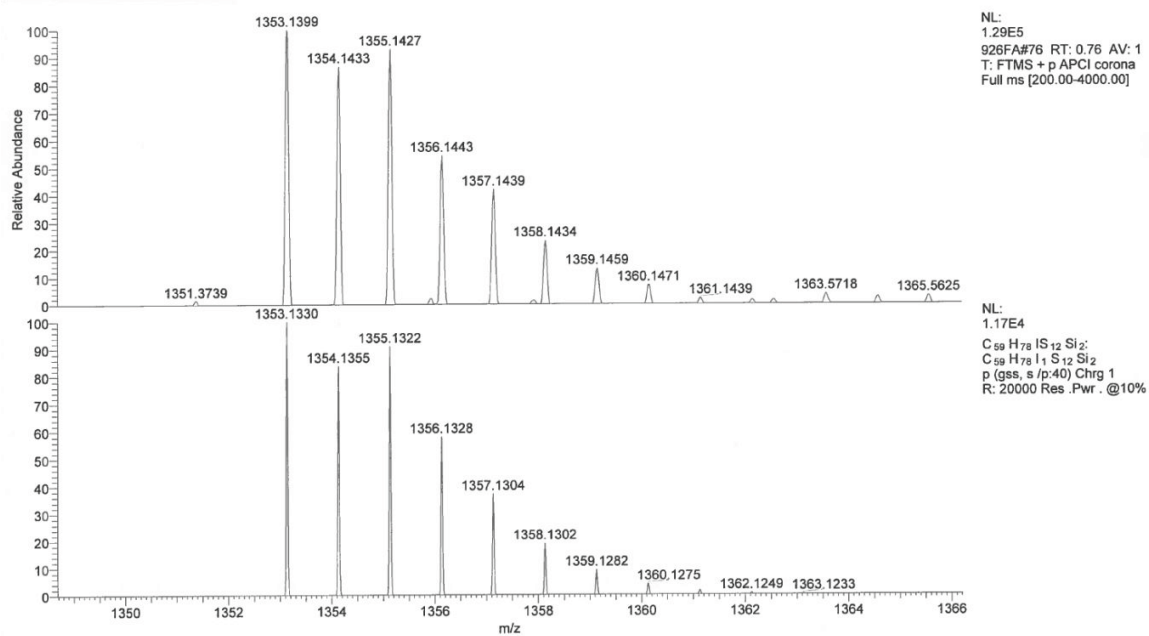


Figure S25: APCI-HRMS of the C₂I₀ product

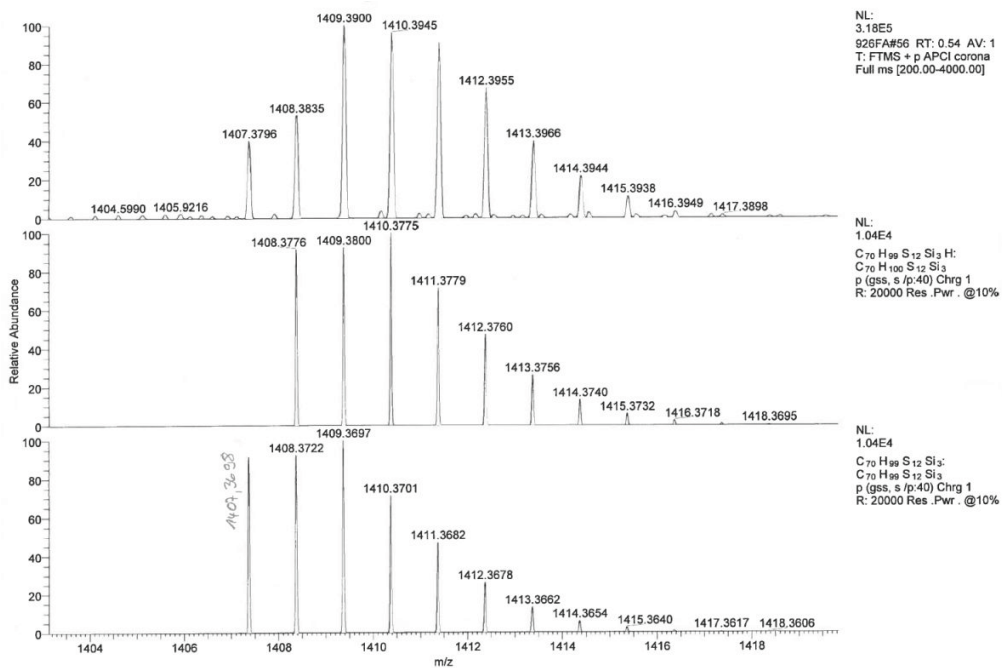


Figure S26: APCI-HRMS of the C₃I₀ product

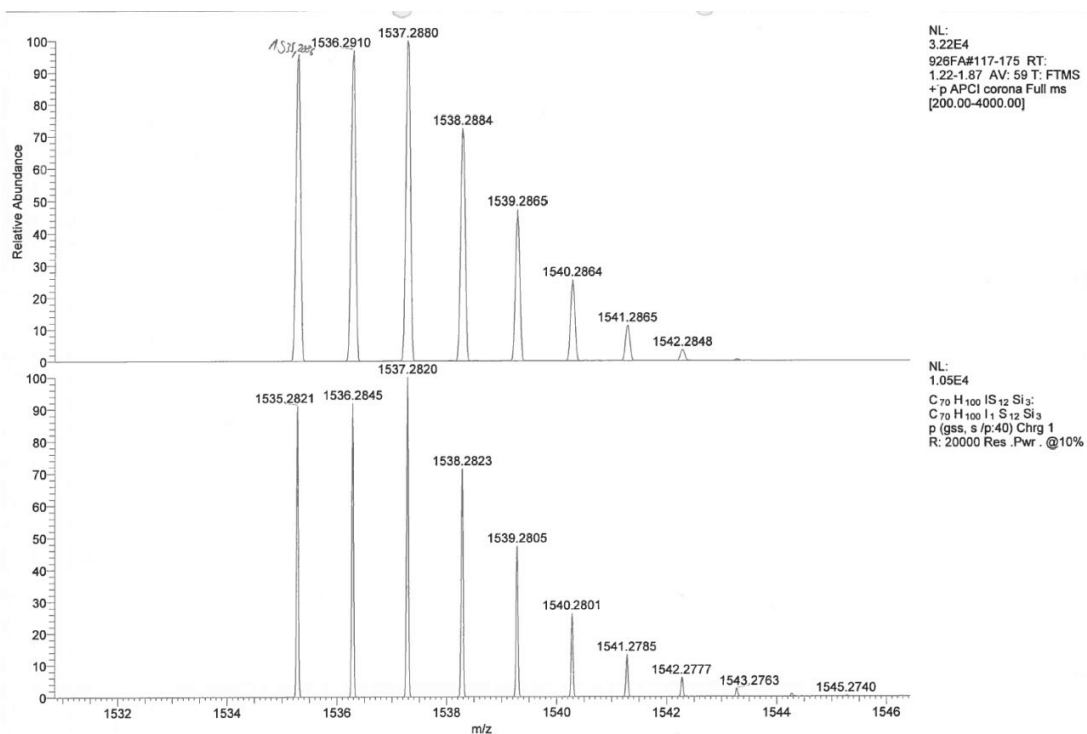


Figure S27: APCI-HRMS of the C_2I_1 product

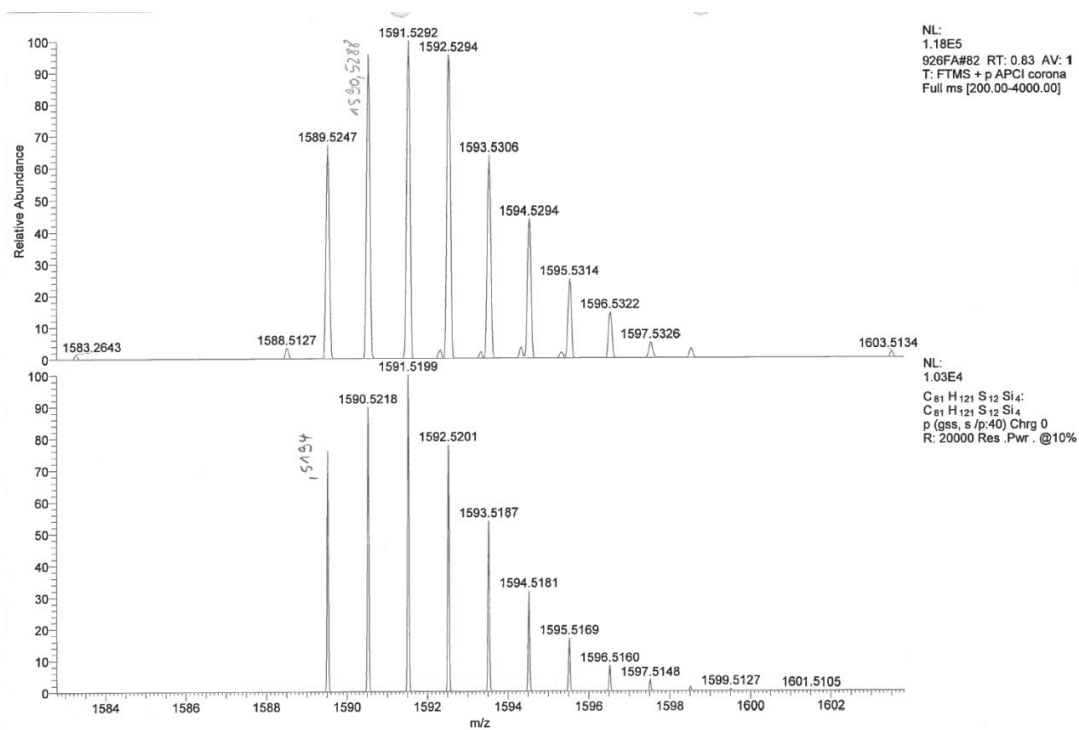


Figure S28: APCI-HRMS of the C_3I_1 product

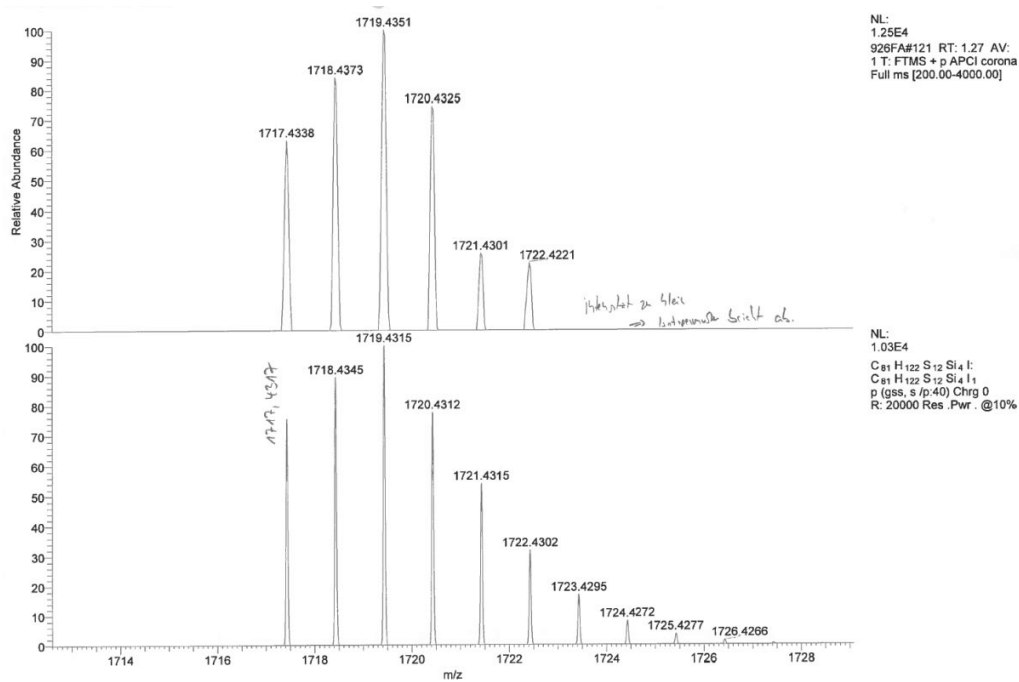


Figure S29: APCI-HRMS of the C₂I₂ product

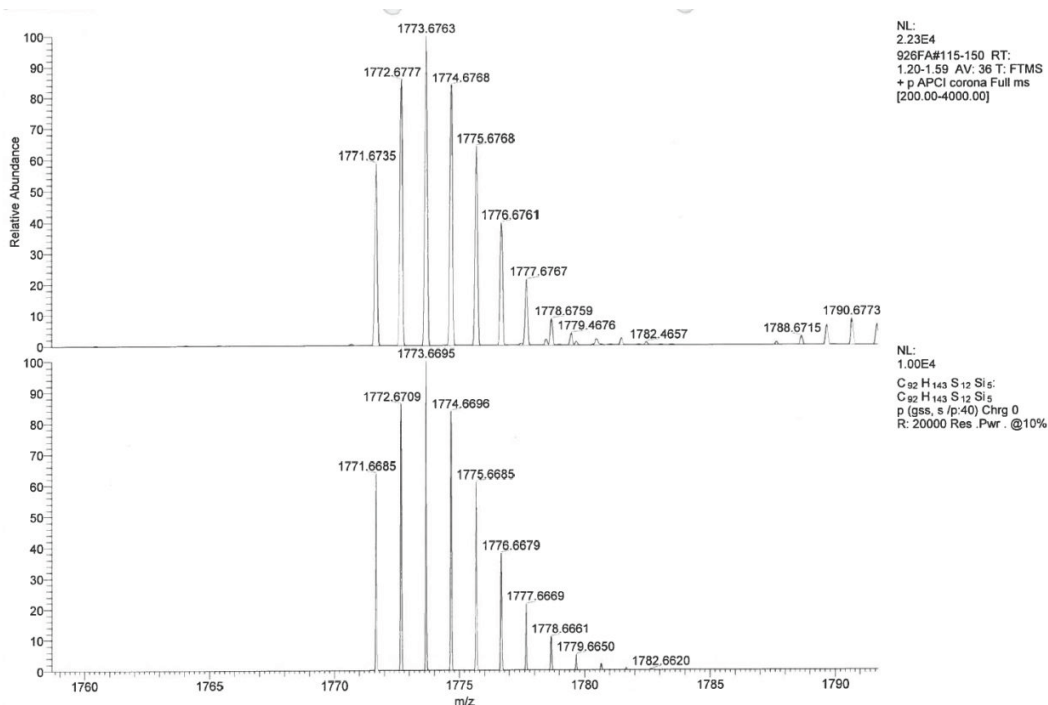


Figure S30: APCI-HRMS of the C₃I₂ product

For radical **3**[•], an analogous reactivity was observed. However, **3**[•] is decently less soluble in THF/Et₃N than **5**, leading to unreacted starting material within the product mixture. Nonetheless, insertion products occur here as well.

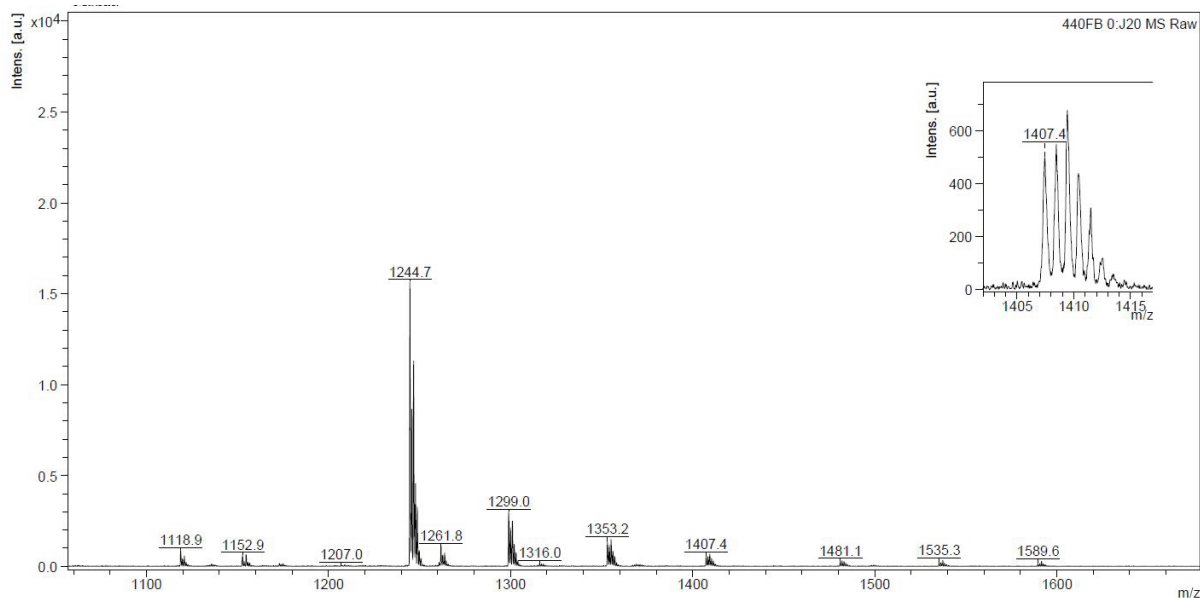


Figure S31: MALDI(+)-spectrum of the product mixture.

Table S4: Mass spectrometric data for the product mixture obtained from the reaction of **3**[•] with TIPS-acetylene.

MALDI(+)-peak [M] ⁺	sum formula of the corr. trityl alcohol	product type
1244.7	C ₃₇ H ₃₆ I ₃ S ₁₂	C ₀ I ₀
1299.0	C ₄₈ H ₅₇ I ₂ S ₁₂ Si	C ₁ I ₀
1353.2	C ₅₉ H ₇₈ I ₁ S ₁₂ Si ₂	C ₂ I ₀
1407.4	C ₇₀ H ₉₉ S ₁₂ Si ₃	C ₃ I ₀
1481.1	C ₅₉ H ₇₉ I ₂ S ₁₂ Si ₂	C ₁ I ₁
1535.3	C ₇₀ H ₁₀₀ I ₁ S ₁₂ Si ₃	C ₂ I ₁
1589.6	C ₈₁ H ₁₂₁ S ₁₂ Si ₄	C ₃ I ₁

In the solvent system $\text{CH}_2\text{Cl}_2/\text{Et}_3\text{N}$ 1:1 (v/v), no insertion products were observed as the MALDI(+)-spectrum below shows (Figure S32), even though no quantitative conversion was achieved. The corresponding HRMS-APCI data is provided below in order of ascending mass and indicated in table S5 (Figures S33-35).

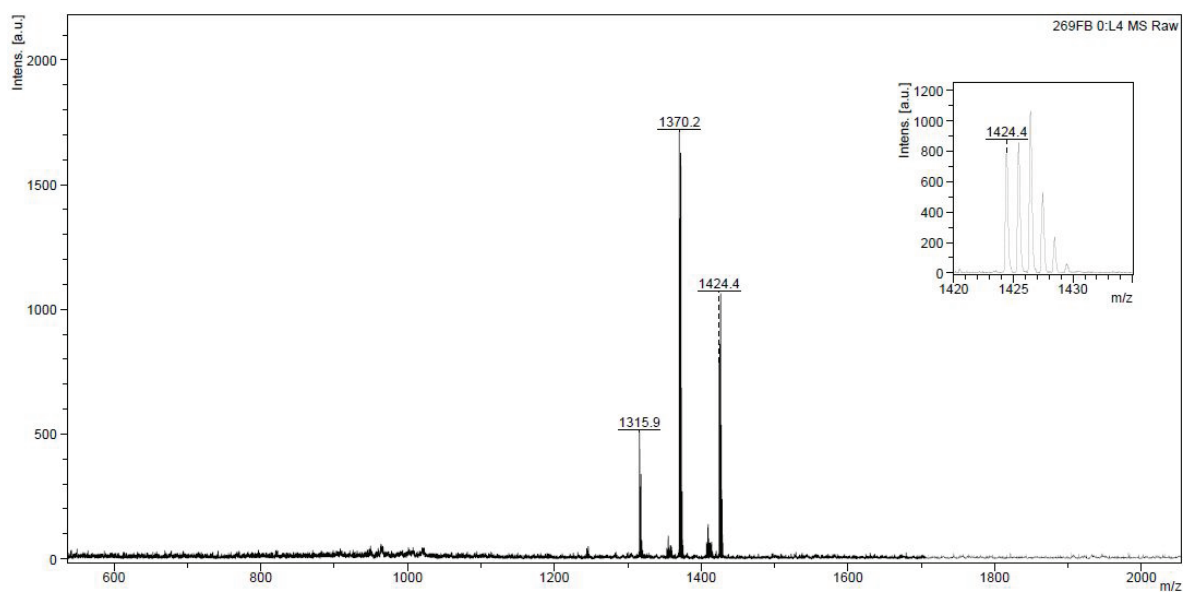


Figure S32: MALDI(+)-spectrum of the product mixture.

Table S5: Mass spectrometric data for the product mixture obtained from the reaction of **5** with TIPS-acetylene in dichloromethane/triethylamine

MALDI(+)-peak [M] ⁺	APCI-peak [M-17] ⁺	sum formula of the corr. trityl alcohol	product type	HRMS figure
1315.9	1298.8998	$\text{C}_{48}\text{H}_{58}\text{I}_2\text{OSi}$	C_1I_0	S32
1370.2	1353.1340	$\text{C}_{59}\text{H}_{79}\text{IOSi}_2$	C_2I_0	S33
1424.4	1407.3715	$\text{C}_{70}\text{H}_{100}\text{OSi}_3$	C_3I_0	S34

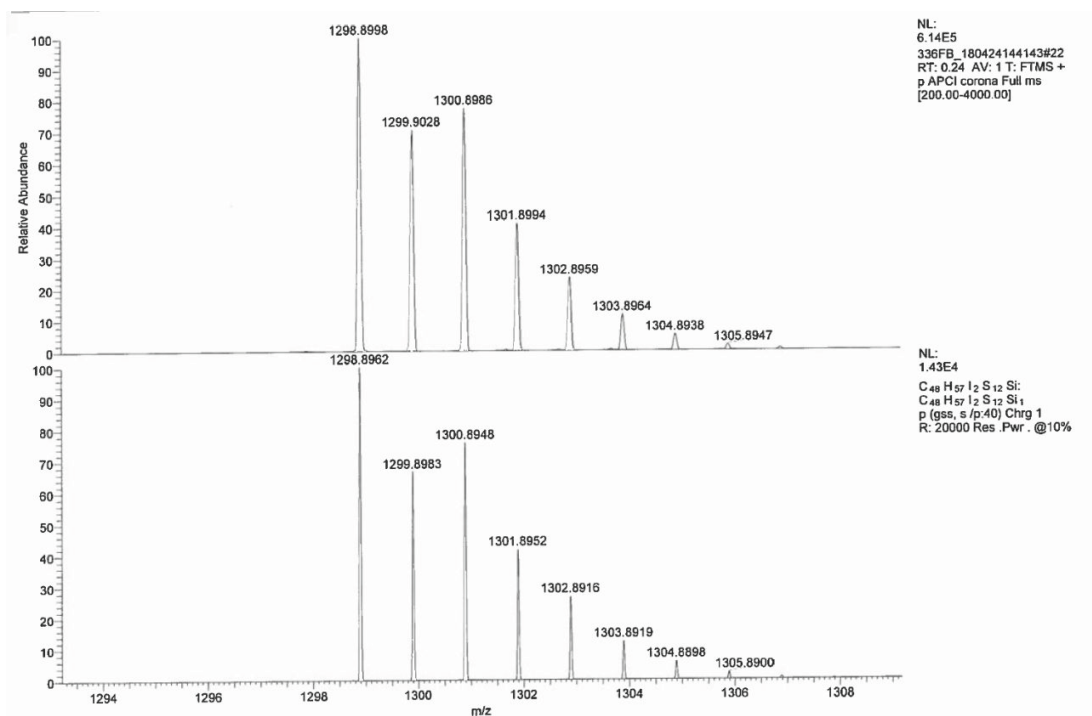


Figure S33: APCI-HRMS of the C₁I₀ product

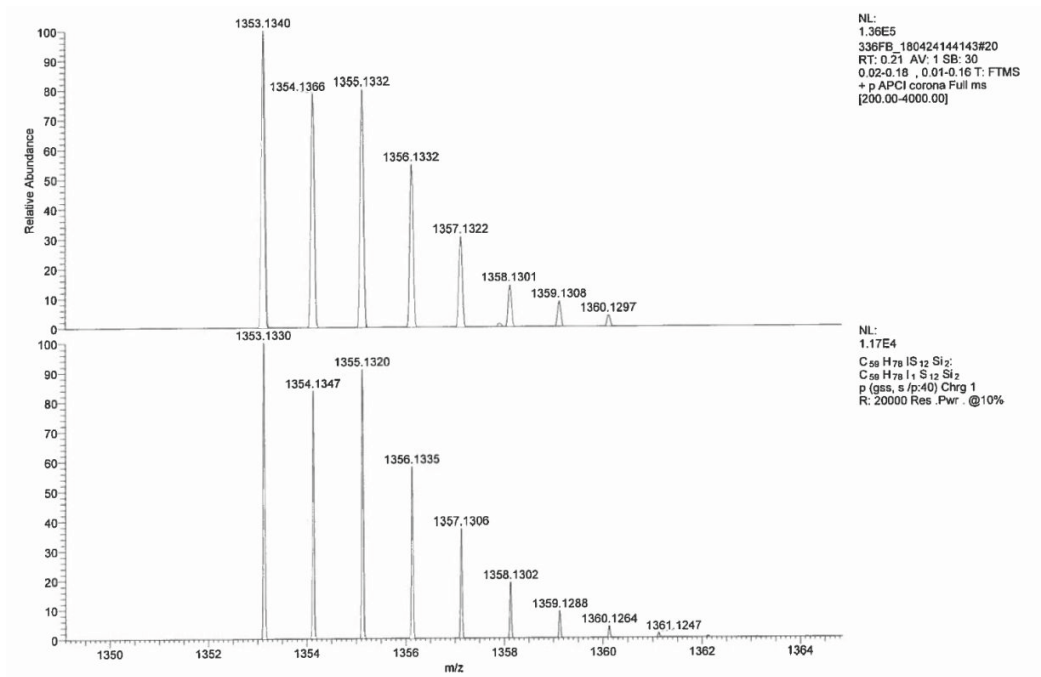


Figure S34: APCI-HRMS of the C₂I₀ product

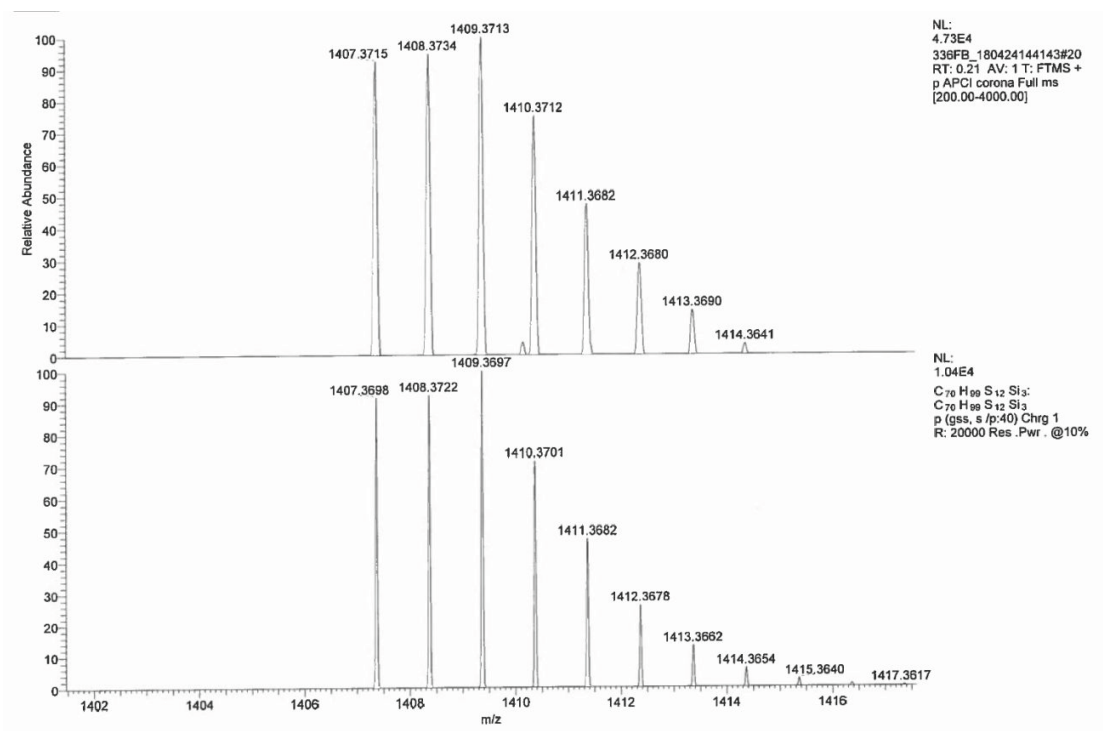


Figure S35: APCI-HRMS of the C₃I₀ product

8.4 Reaction with trimethylsilylacetylene

Following the general procedure, **5** was reacted with trimethylsilylacetylene in THF/Et₃N 3:1 (v/v) yielding a mixture of insertion and coupling products as shown by the MALDI spectrum below.

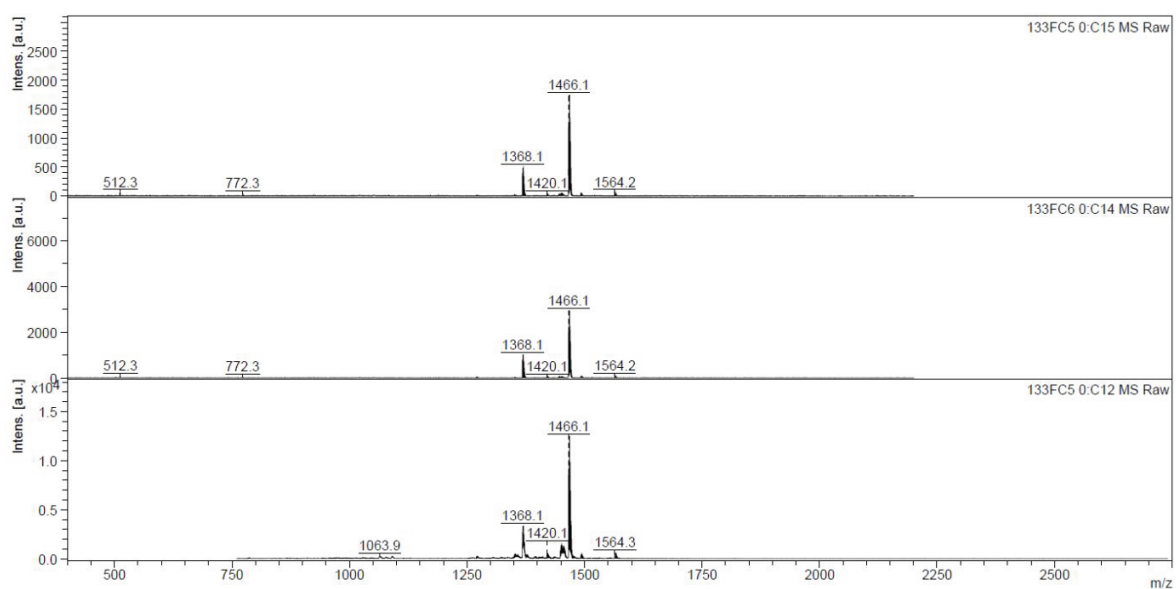


Figure S36: MALDI(+)-spectrum of the product mixture

Table S6: MALDI data for the product mixture from the reaction of **5** with TMS-acetylene.

MALDI(+)-peak [M] ⁺	sum formula of the corr. trityl alcohol	product type
1368.1	C ₆₂ H ₈₄ OS ₁₂ Si ₅	C ₃ I ₂
1466.1	C ₆₇ H ₉₄ OS ₁₂ Si ₆	C ₃ I ₃
1564.2	C ₇₂ H ₁₀₄ OS ₁₂ Si ₇	C ₃ I ₄

8.5 Reaction with 2-Methyl-3-butyn-2-ol

Following the general procedure, **5** was reacted with 2-Methyl-3-butyn-2-ol in THF/Et₃N 3:1 (v/v) yielding a mixture of insertion and coupling products as shown by the MALDI spectrum below.

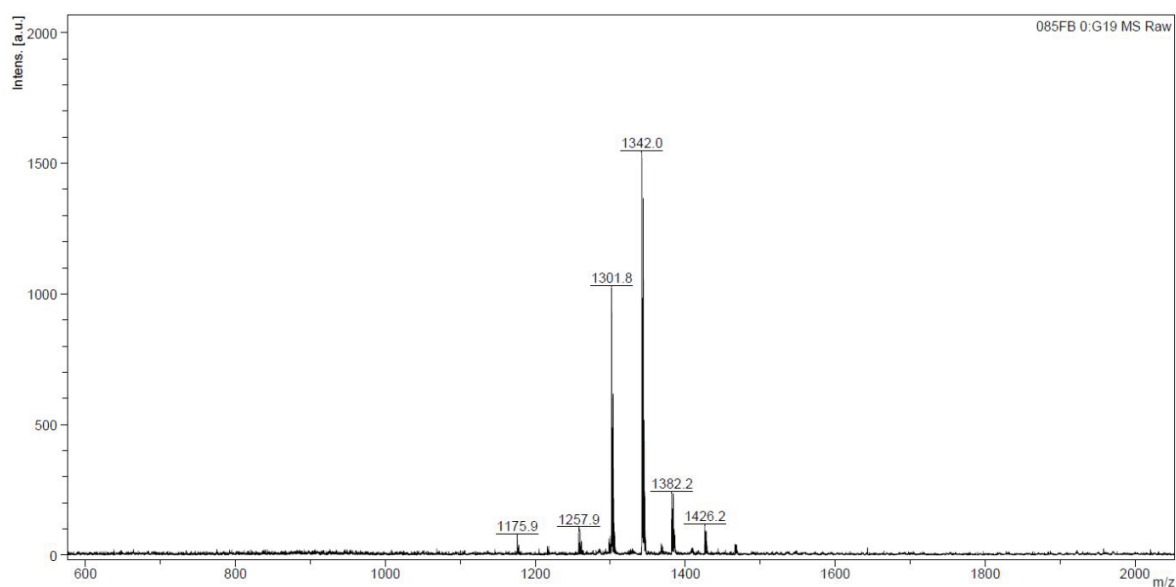


Figure S37: MALDI(+)-spectrum of the product mixture

Table S7: MALDI-data for the product mixture obtained from the reaction of **5** with 2-Methyl-3-butyn-2-ol.

MALDI(+)-peak [M] ⁺	sum formula of the corr. trityl alcohol	product type
1257.9	C ₅₂ H ₅₉ IO ₄ S ₁₂	C ₂ I ₁
1301.8	C ₄₇ H ₅₂ I ₂ O ₃ S ₁₂	C ₁ I ₁
1342.0	C ₅₇ H ₆₇ IO ₅ S ₁₂	C ₂ I ₂
1382.2	C ₆₇ H ₈₂ O ₇ S ₁₂	C ₃ I ₃
1426.2	C ₆₂ H ₇₅ IO ₆ S ₁₂	C ₂ I ₃

The C₁I₁-product of this batch could be isolated by column chromatography on silica eluting with cyclohexane/ethyl acetate 2:1 (v/v). The HRMS-spectrum shown below confirms the assumed sum formula.

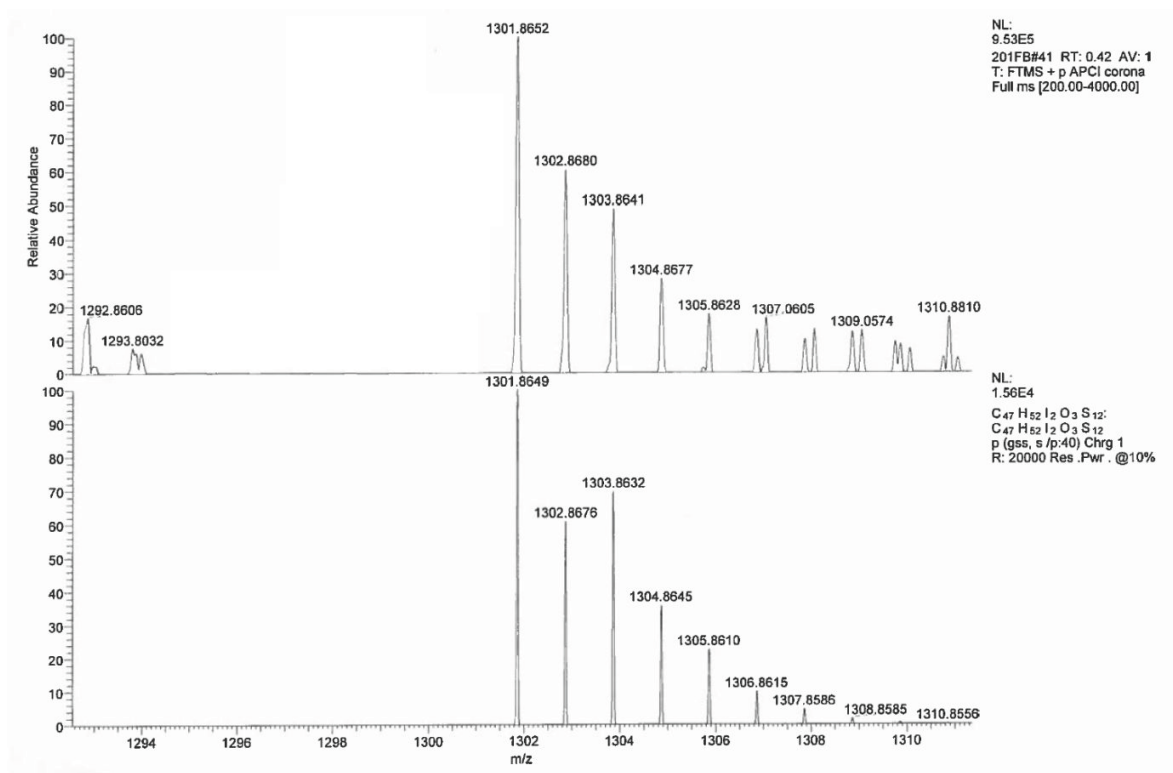


Figure S38: APCI-HRMS of the C₁I₁ product

The structure of this C₁I₁ product was then further studied by ¹H-NMR at 700 MHz, these spectra are shown below.

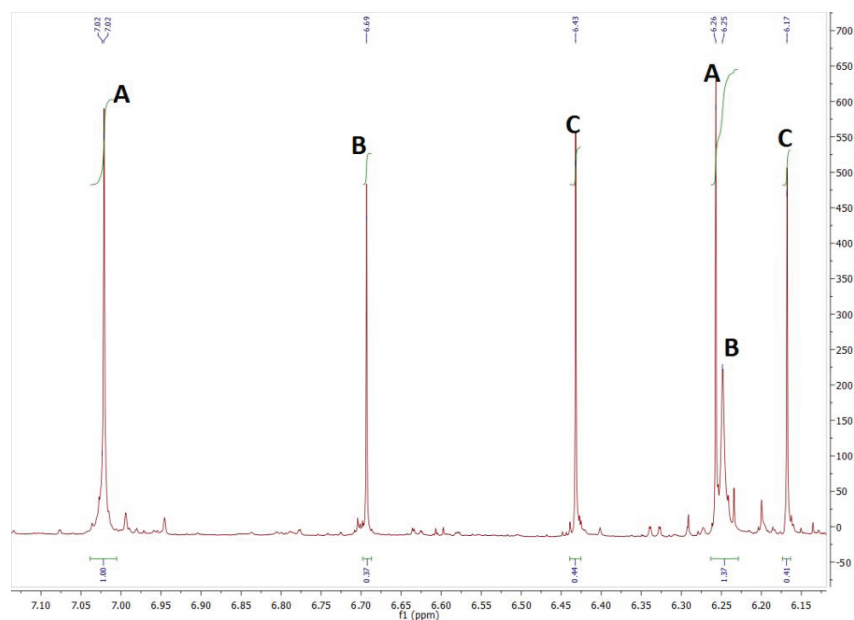


Figure S39: ¹H-NMR (700 MHz, CD₂Cl₂, 298K) of the C₁I₁ product with 2-methyl-3-butyn-2-ol, olefinic region.

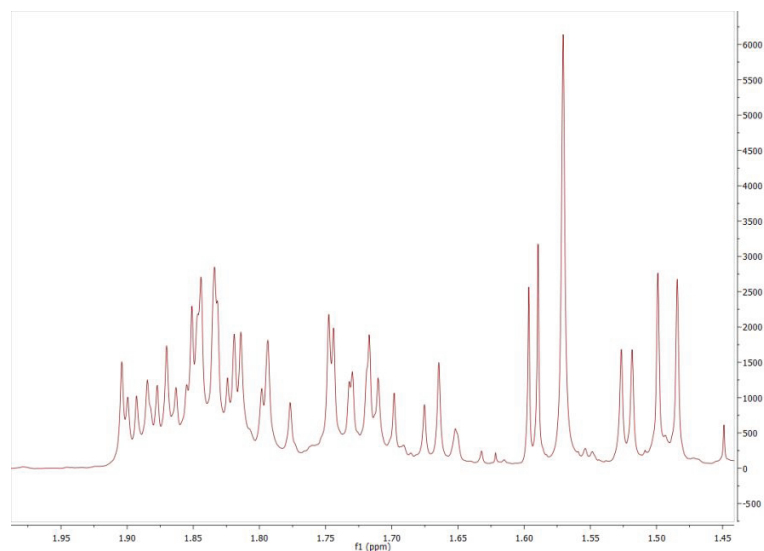


Figure S40: ¹H-NMR (700 MHz, CD₂Cl₂, 298K) of the C₁I₁ product with 2-methyl-3-butyn-2-ol, aliphatic region.

In the aliphatic region between 1.60 and 1.95 ppm, the methyl protons of the thioacetal give resonances. Clearly, more than 12 peaks – as it would be expected for an asymmetric trityl alcohol – are visible, which means that more than one isomer of the C₁I₁ product exists. According to the mechanism proposed in the main text, six isomers plus their enantiomers can exist:

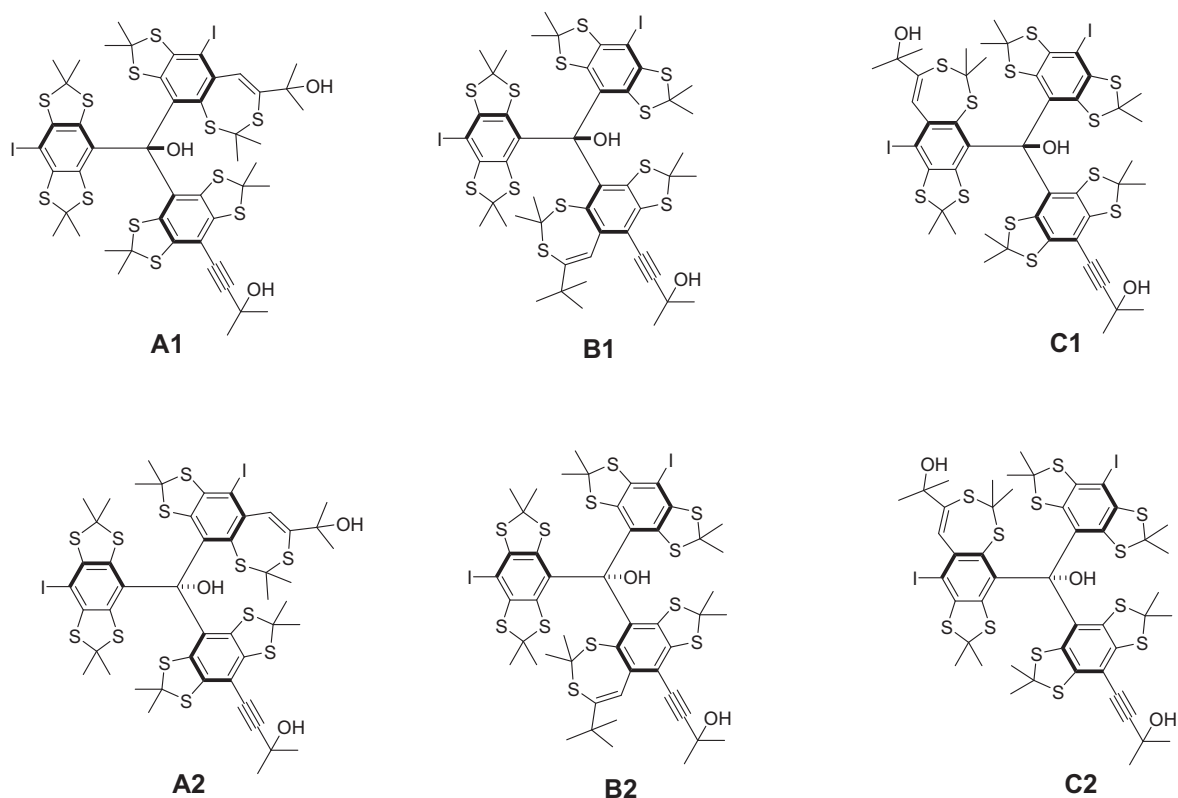


Figure S41: Suggested structures of the insertion products.

For the products **A1**, **B1**, and **C1**, a steric clash of the OH-group with the 7-membered ring can be expected, which disfavors the formation of these products. Regarding the NMR-spectra, the olefinic proton of the 7-membered ring and the central OH-proton are expected to give signals between 6 and 7 ppm, both with an equal integral. As shown in the ¹H-NMR spectrum, three signal pairs (A, B, C) with equal integrals occur between 6 and 7 ppm, presumably originating from **A2**, **B2**, and **C2**.

For this kind of product structure, no scalar coupling is present, so that only singlets are expected corresponding to the experiment. However, the regioselectivity of the alkyne insertion cannot be determined this way and remains unclear.

In a further experiment, **5** was reacted with 2-methyl-3-butyn-2-ol in CH₂Cl₂/Et₃N and samples for MALDI(+)-analysis were extracted after 2 h (fig. S42), 4 h (fig. S43), 6 h (fig. S44), 8 h (fig. S45), and 10 h (fig. S46).

This examination revealed that the coupling- and insertion reaction both occur side by side. At no time, only coupling products without insertion products were observed, meaning that neither of both reaction pathways is kinetically strongly preferred.

The corresponding MALDI(+)-spectra are shown below, the following table presents a peak assignment.

Table S8: MALDI-data for the product mixtures obtained from the reaction of **5** with 2-methyl-3-butyn-2-ol in dichloromethane/triethylamine.

MALDI(+)-peak [M] ⁺	sum formula of the corr. trityl alcohol	product type
1130.0	C ₅₂ H ₅₈ O ₄ S ₁₂	C ₃ I ₀
1173.8	C ₄₇ H ₅₁ IO ₃ S ₁₂	C ₂ I ₀
1217.6	C ₄₂ H ₄₄ I ₂ O ₂ S ₁₂	C ₁ I ₀
1257.9	C ₅₂ H ₅₉ IO ₄ S ₁₂	C ₂ I ₁
1261.5	starting material	
1301.8	C ₄₇ H ₅₂ I ₂ O ₃ S ₁₂	C ₁ I ₁
1342.0	C ₅₇ H ₆₇ IO ₅ S ₁₂	C ₂ I ₂
1382.2	C ₆₇ H ₈₂ O ₇ S ₁₂	C ₃ I ₃
1426.2	C ₆₂ H ₇₅ IO ₆ S ₁₂	C ₂ I ₃

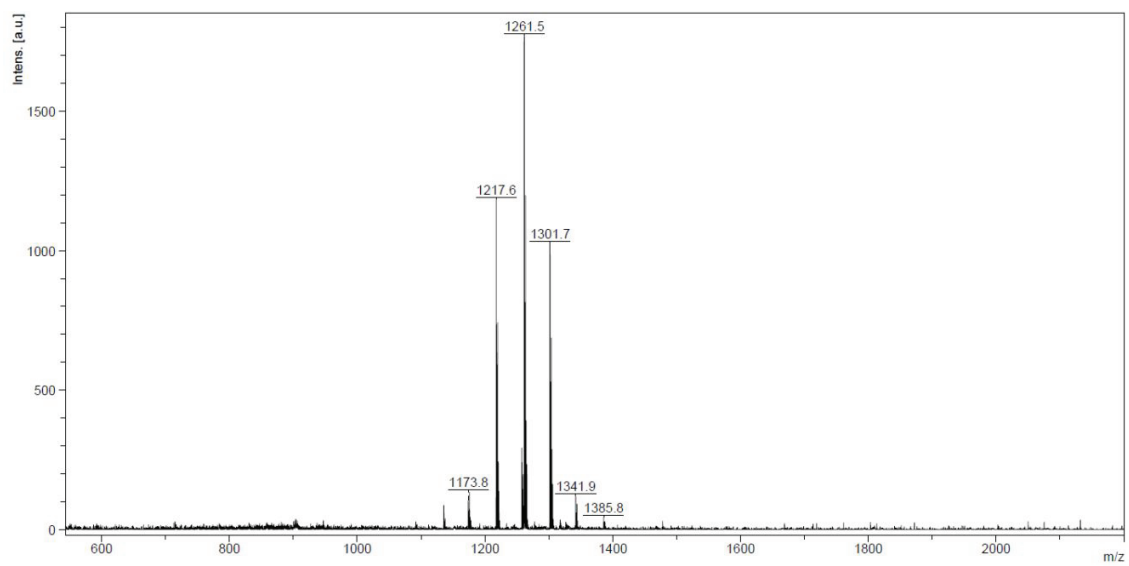


Figure S42: MALDI(+) –spectrum after 2 hours reaction time.

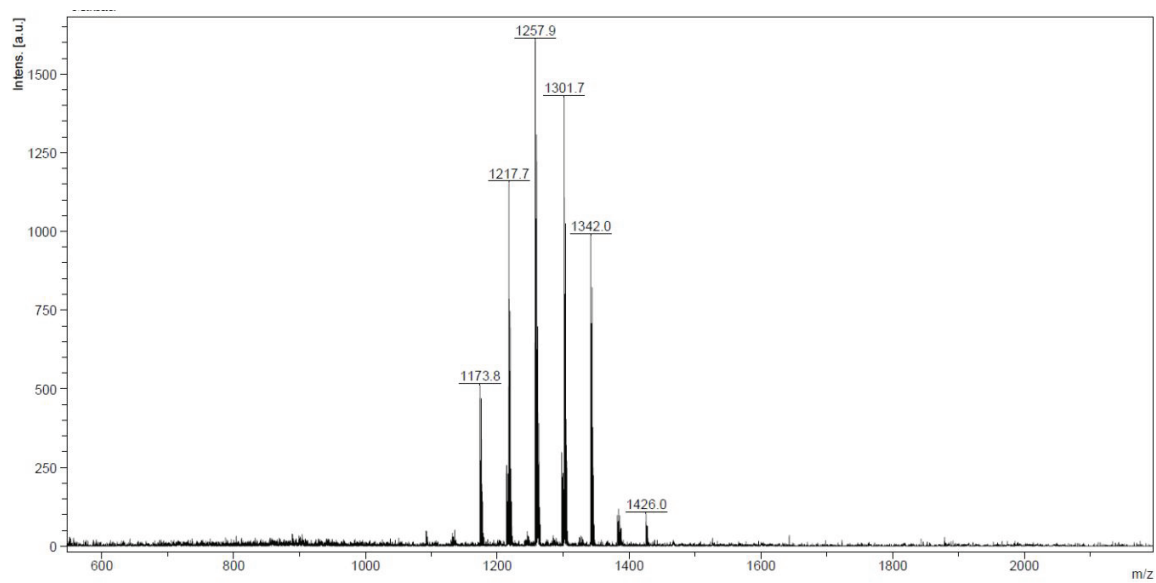


Figure S43: MALDI(+) –spectrum after 4 hours reaction time

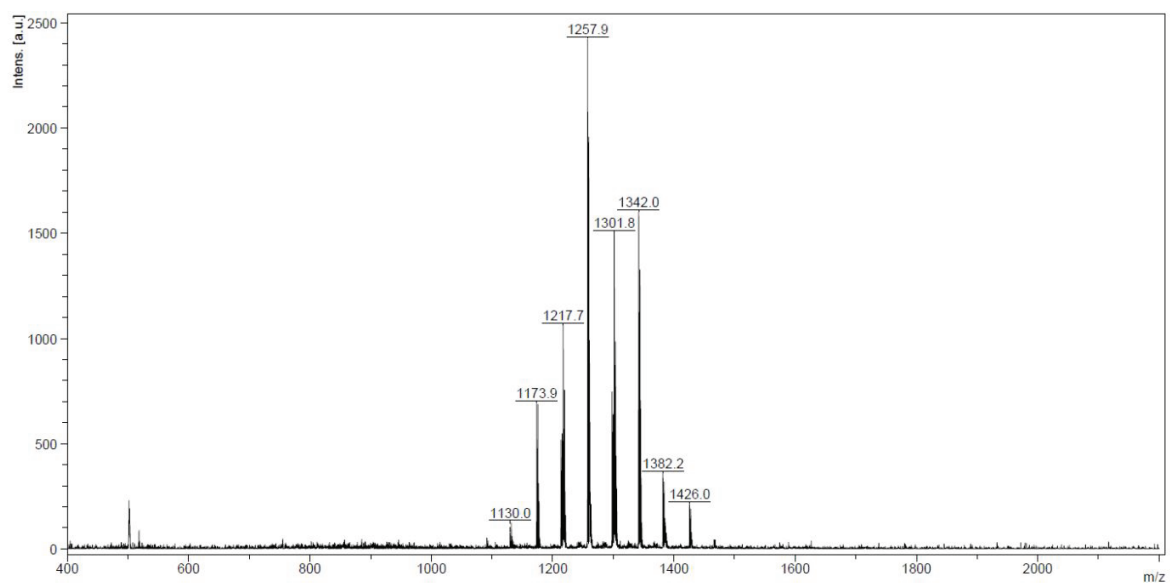


Figure S44: MALDI(+) –spectrum after 6 hours reaction time.

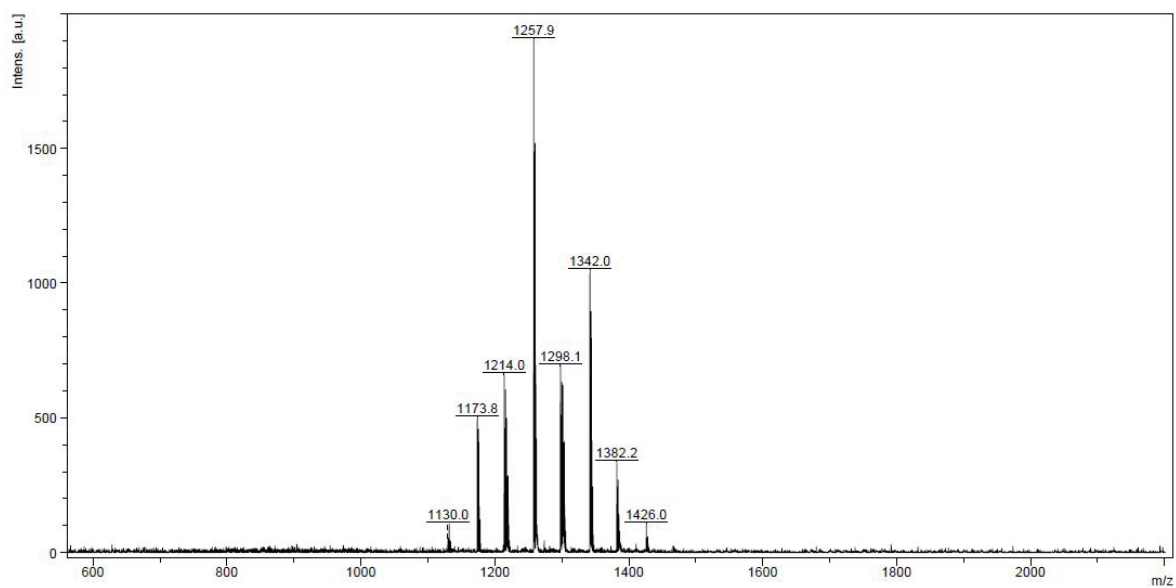


Figure S45: MALDI(+) –spectrum after 8 hours reaction time.

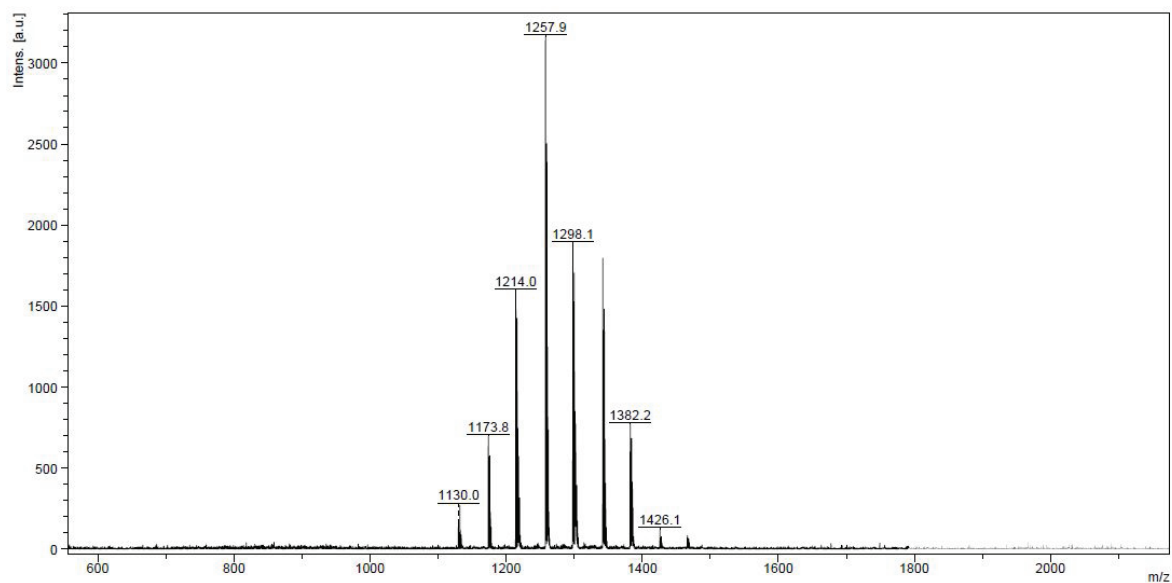


Figure S46: MALDI(+)-spectrum after 10 hours reaction time.

Replacing $\text{Pd}(\text{Ph}_3\text{P})_2\text{Cl}_2$ by $\text{Pd}(\text{dppf})\text{Cl}_2$ in the solvent system $\text{CH}_2\text{Cl}_2/\text{Et}_3\text{N}$ (1:1) led to less insertion. Here, a quantitative coupling alongside insertion occurs, so that the coupling reactions seem to be favored here.

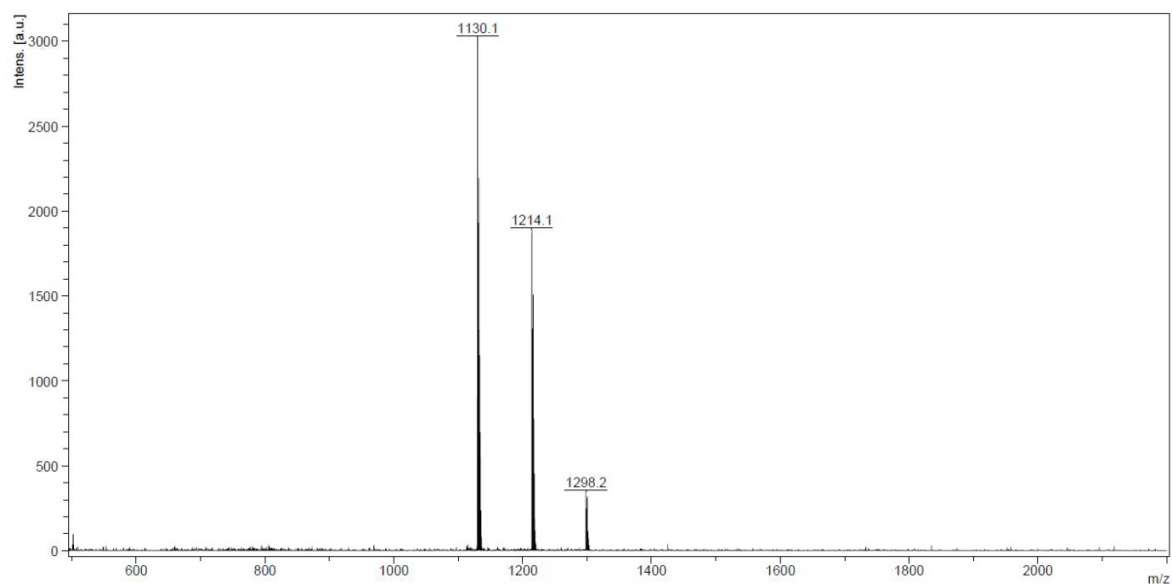


Figure S47: MALDI(+)-spectrum of the product mixture

Table S9: MALDI data for the reaction of **5** with 2-methyl-3-butyn-2-ol catalyzed with Pd(dppf)Cl₂.

MALDI(+)-peak [M] ⁺	sum formula of the corr. trityl alcohol	product type
1130.0	C ₅₂ H ₅₈ O ₄ S ₁₂	C ₃ I ₀
1214.1	C ₅₇ H ₆₆ O ₅ S ₁₂	C ₃ I ₁
1298.2	C ₆₂ H ₇₄ O ₆ S ₁₂	C ₃ I ₂

9. NMR spectra of new compounds

9.1 Trityl alcohol 5

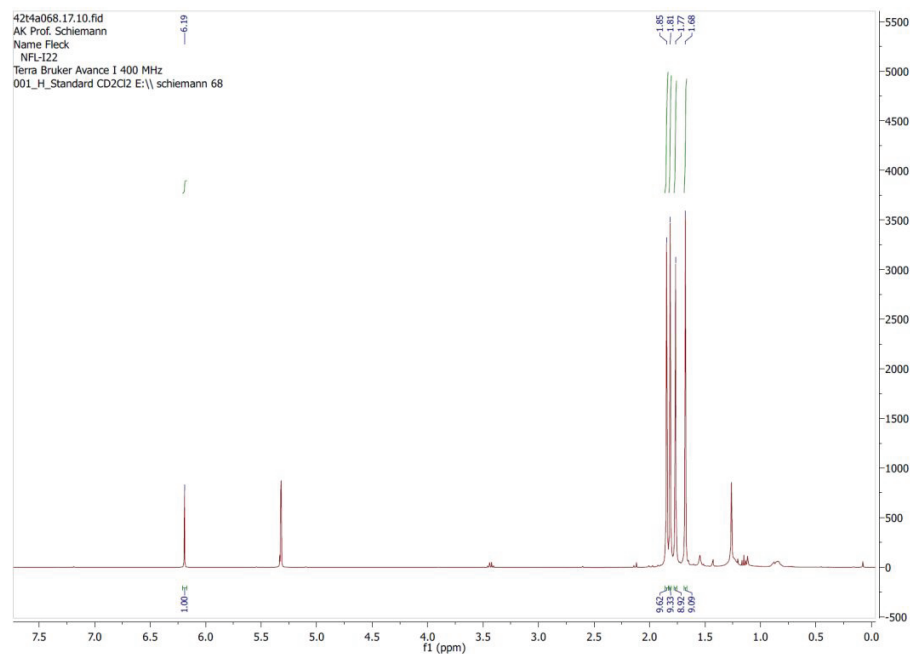


Figure S48: ¹H-NMR, 400 MHz.

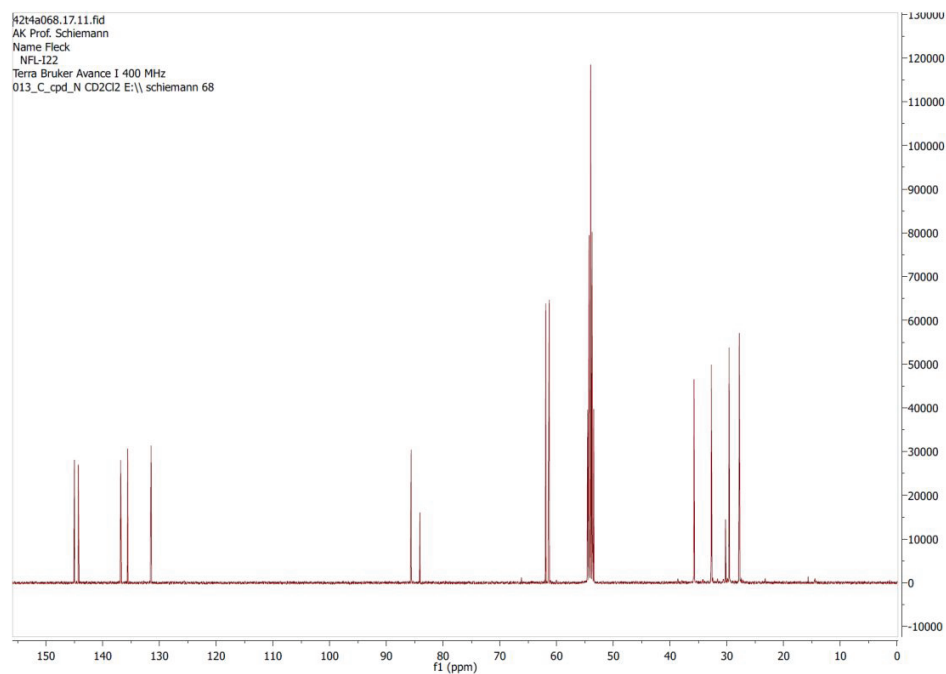


Figure S49: ¹³C{¹H}-NMR, 100 MHz.

9.2 Trityl alcohol 6-OH

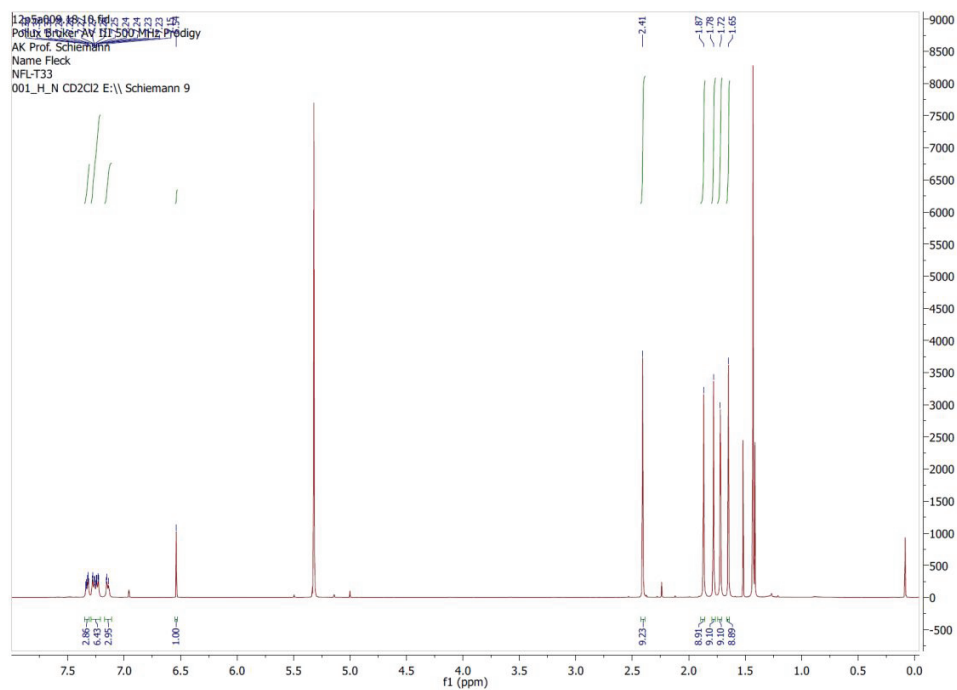


Figure S50: ^1H -NMR, 500 MHz.

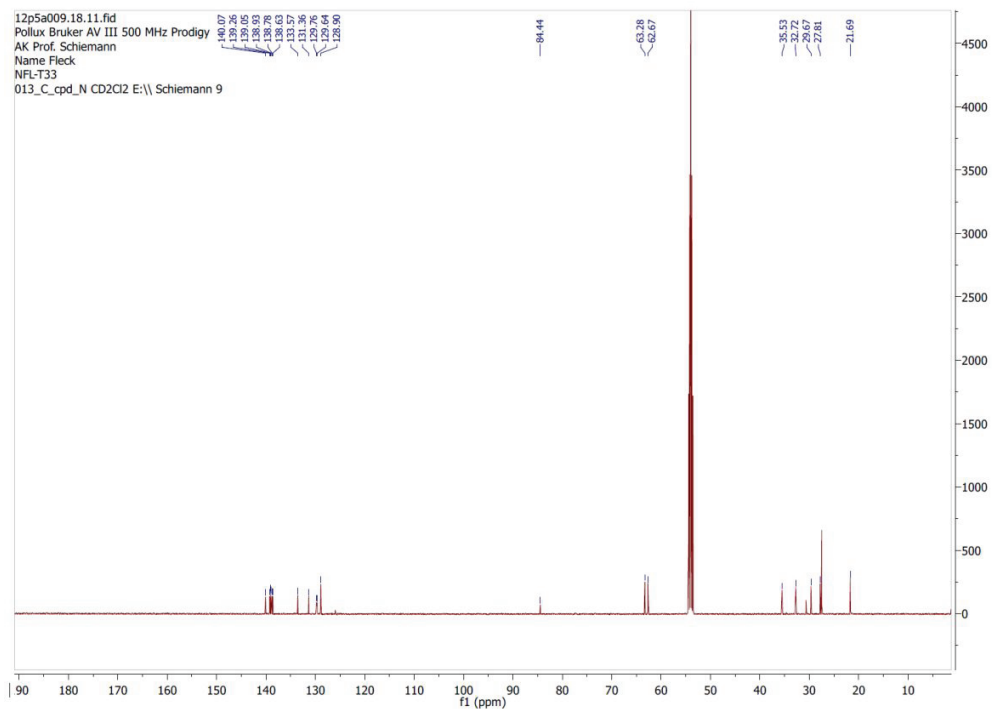


Figure S51: $^{13}\text{C}\{^1\text{H}\}$ -NMR, 125 MHz.

9.3 Trityl alcohol 9

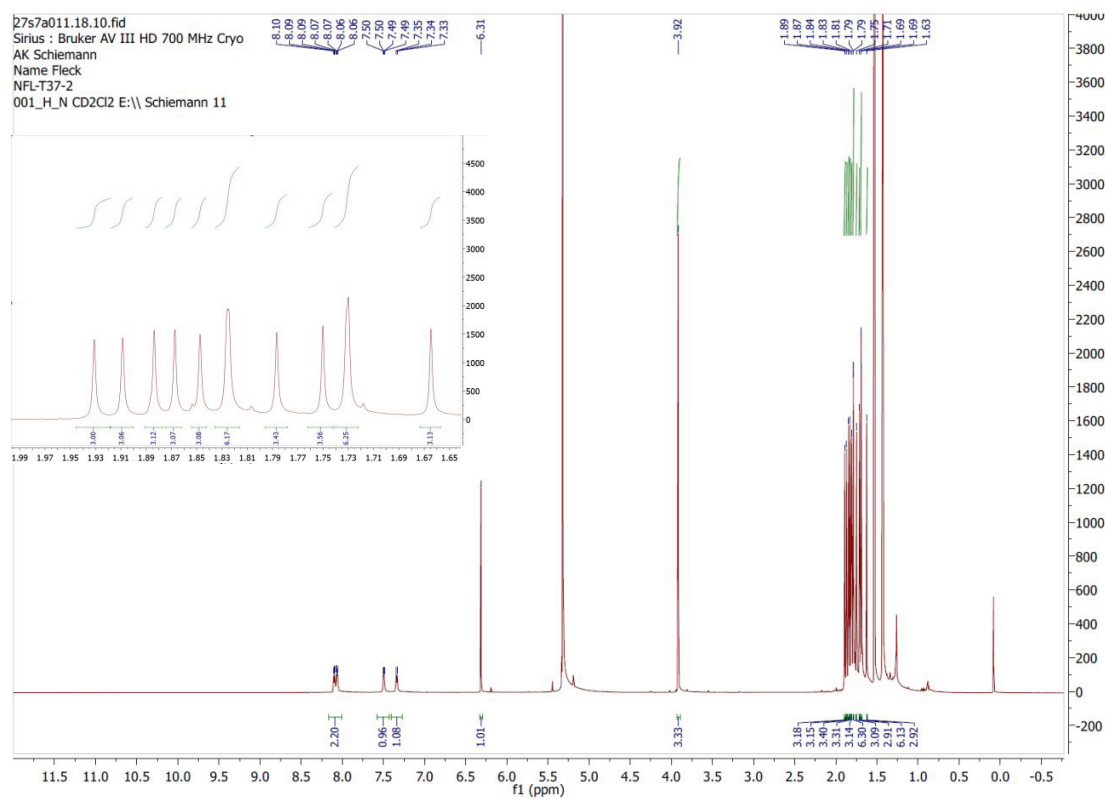


Figure S52: ¹H-NMR, 700 MHz.

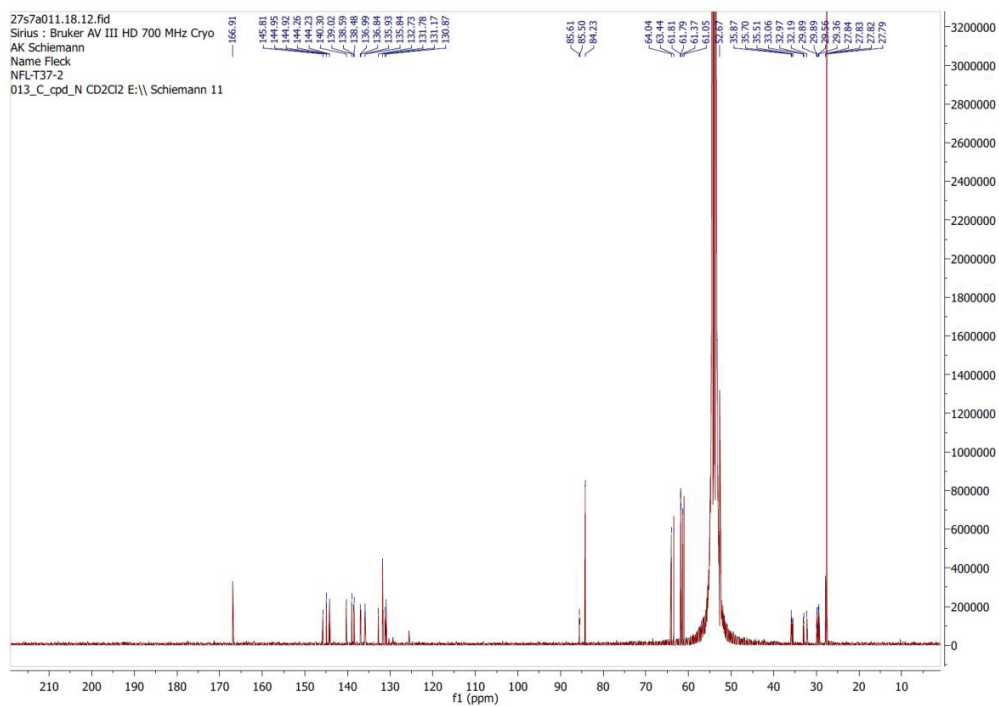


Figure S53: $^{13}\text{C}\{^1\text{H}\}$ -NMR, 175 MHz.

9.4 Trityl alcohol 10

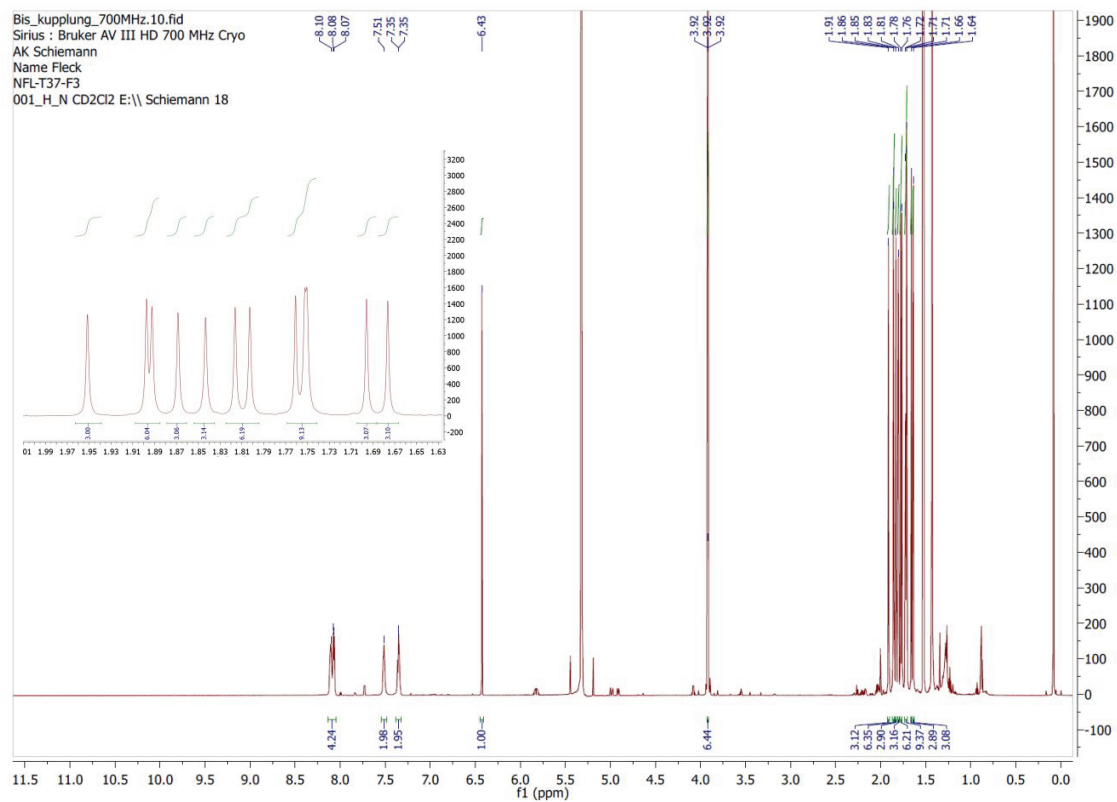


Figure S54: ^1H -NMR, 700 MHz.

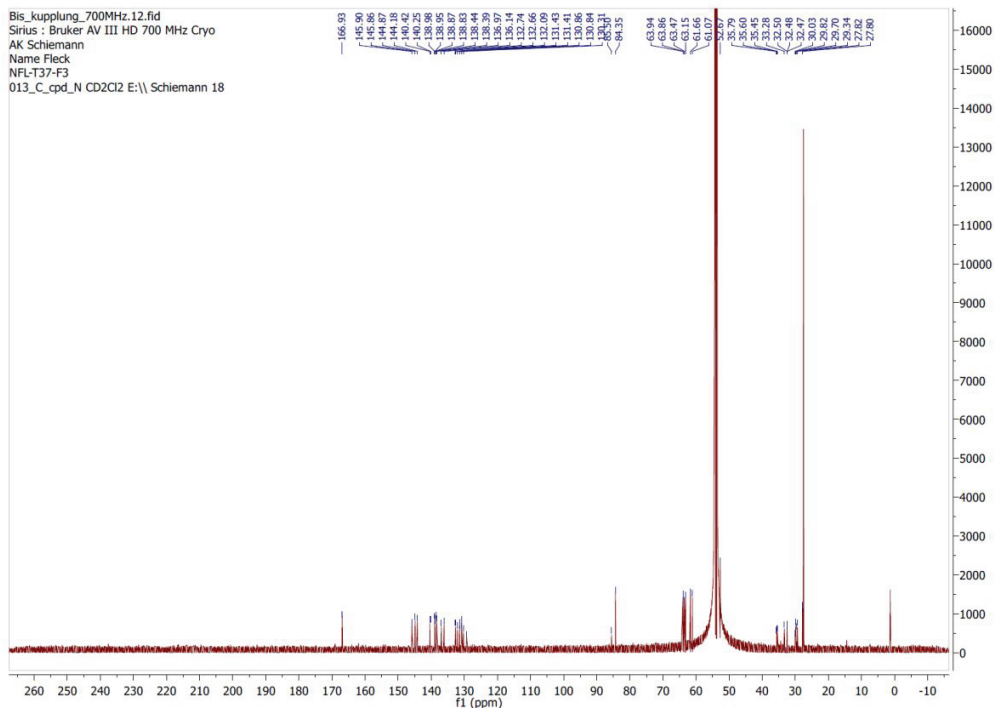


Figure S55: $^{13}\text{C}\{^1\text{H}\}$ -NMR, 175 MHz.

9.5 Trityl alcohol 14

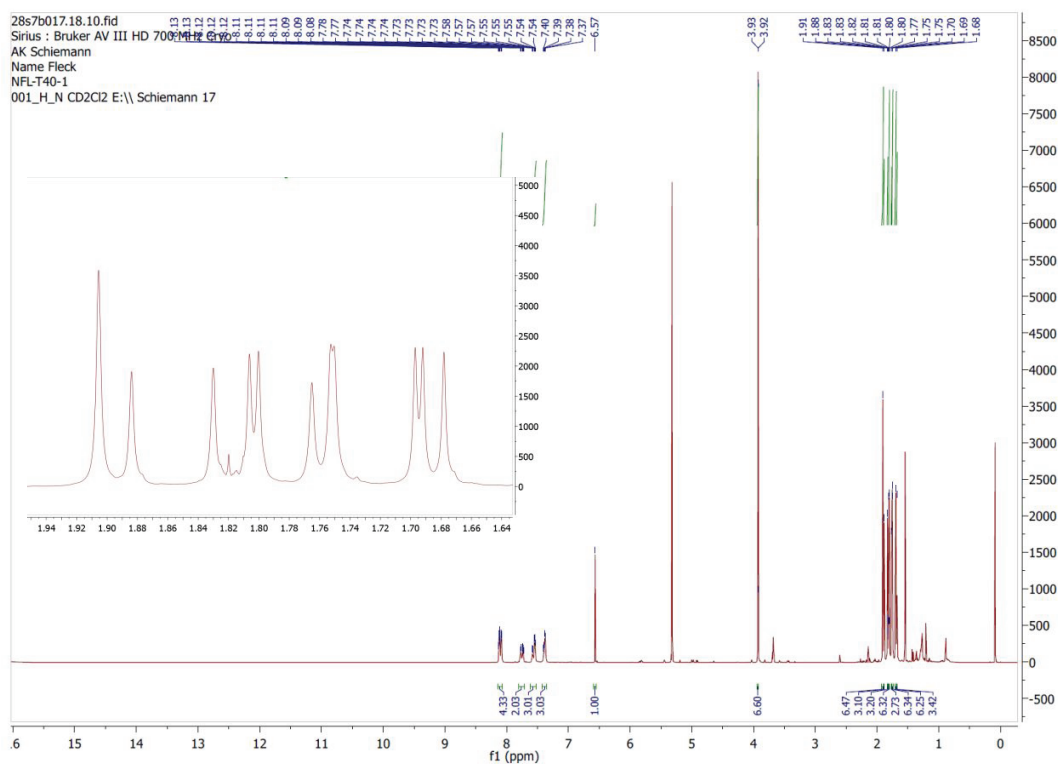


Figure S56: ^1H -NMR, 700 MHz.

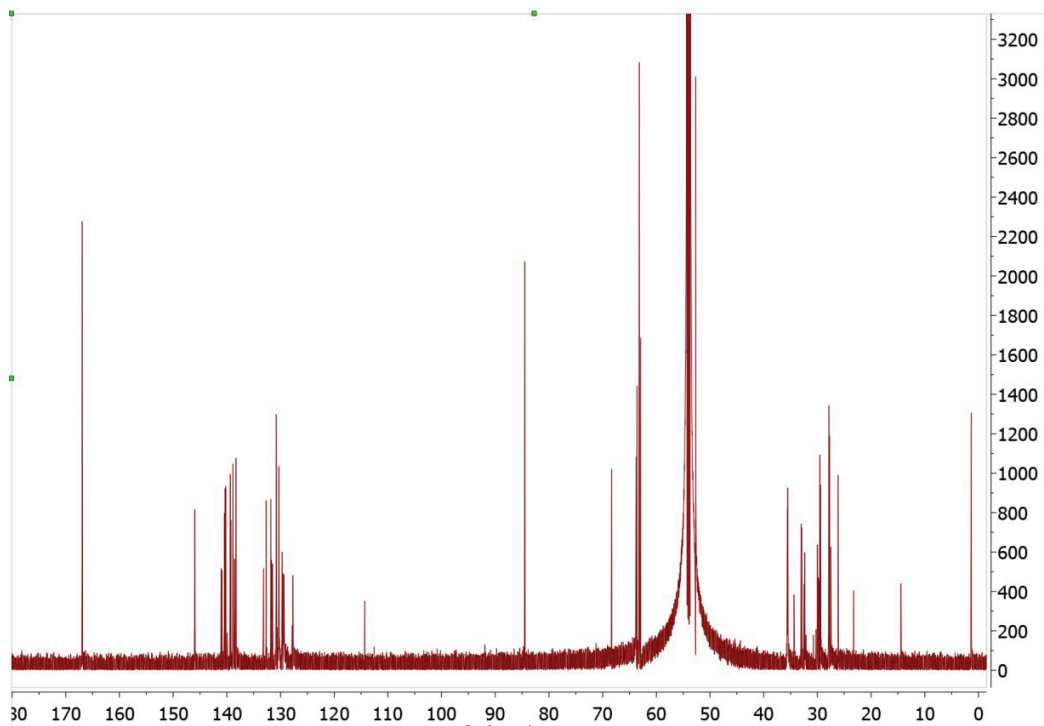


Figure S57a: $^{13}\text{C}\{^1\text{H}\}$ -NMR, 175 MHz.

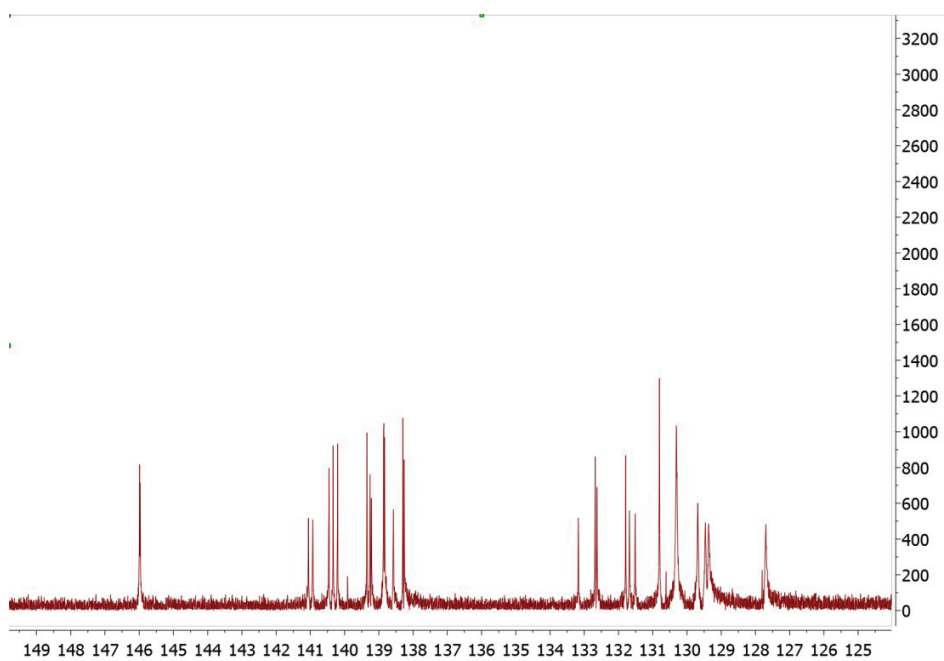


Figure S57b: $^{13}\text{C}\{^1\text{H}\}$ -NMR, 175 MHz.

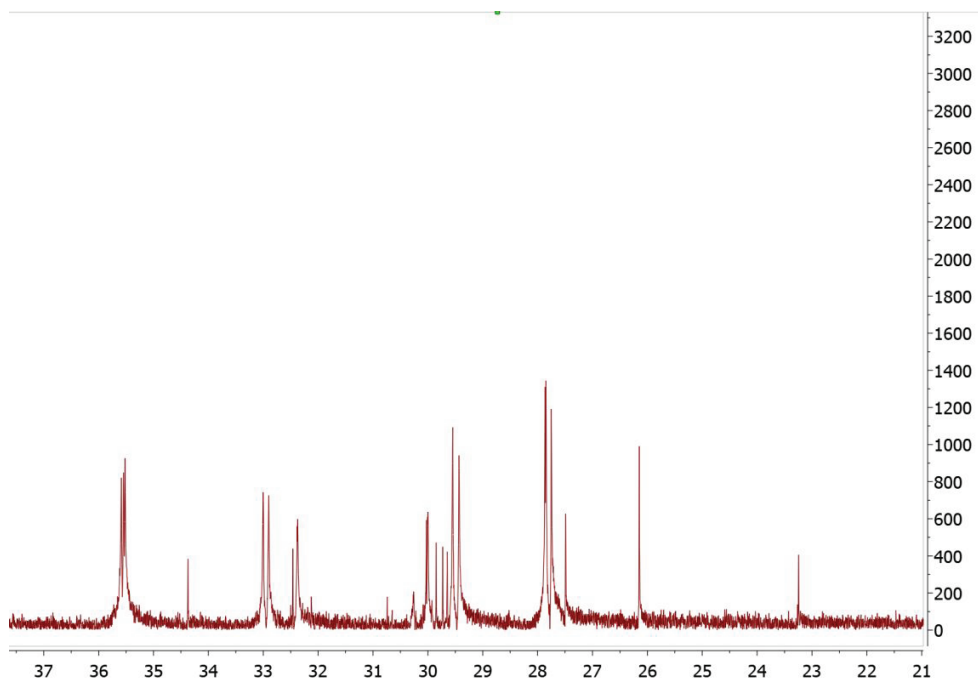


Figure S57c: $^{13}\text{C}\{^1\text{H}\}$ -NMR, 175 MHz.

9.6 Trityl porphyrin 12-OH

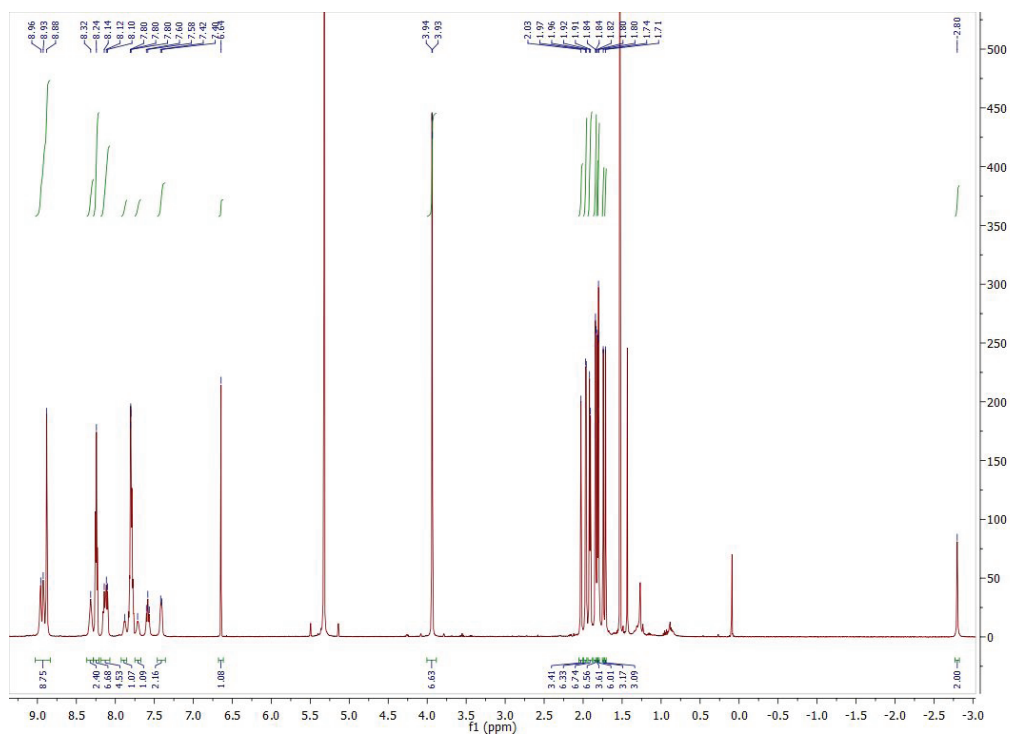


Figure S58: ^1H -NMR, 700 MHz.

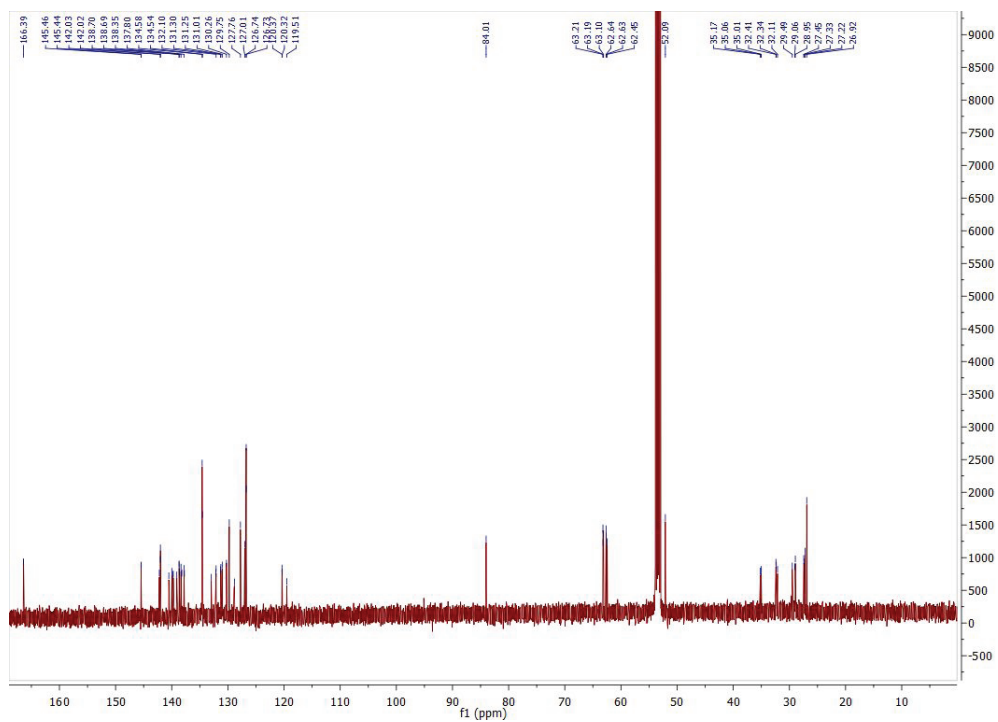


Figure S59: $^{13}\text{C}\{^1\text{H}\}$ -NMR, 175 MHz.

10. High-Resolution Mass Spectra

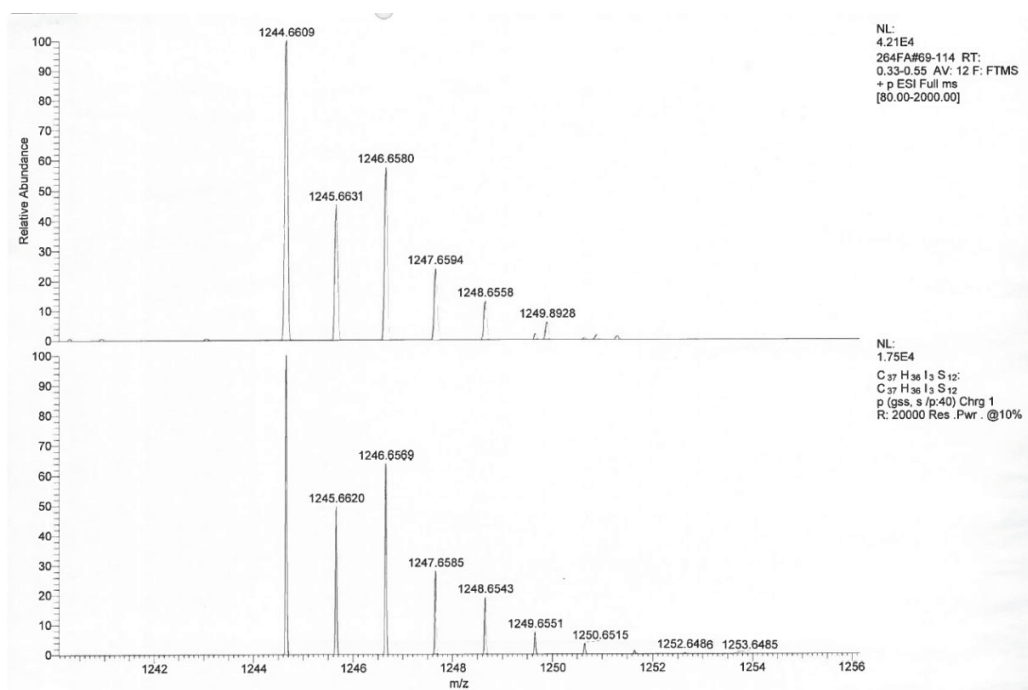


Figure S60: ESI(+)-HRMS of trityl radical 3^\bullet .

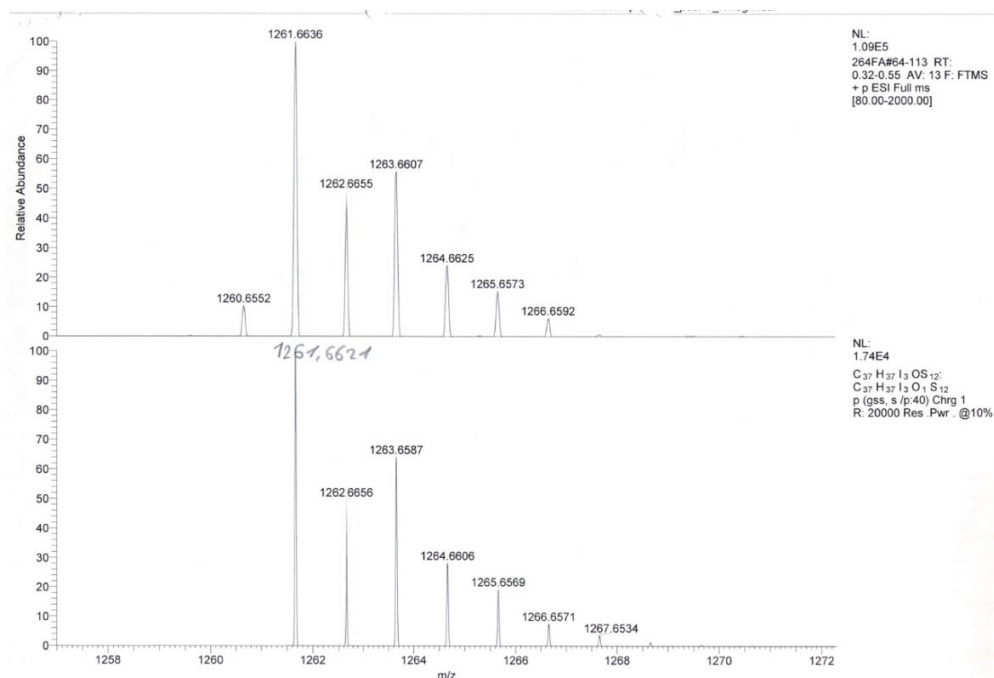


Figure S61: ESI(+)-HRMS of trityl alcohol 5 .

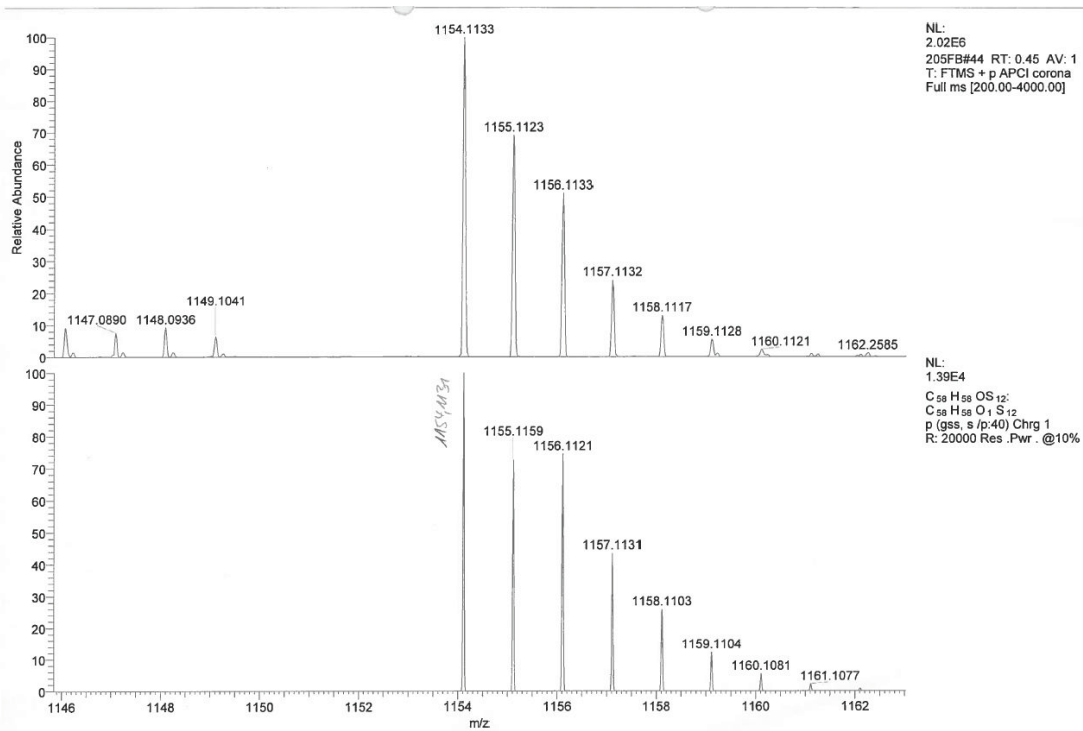


Figure S62: APCIHRMS of trityl alcohol **6-OH**.

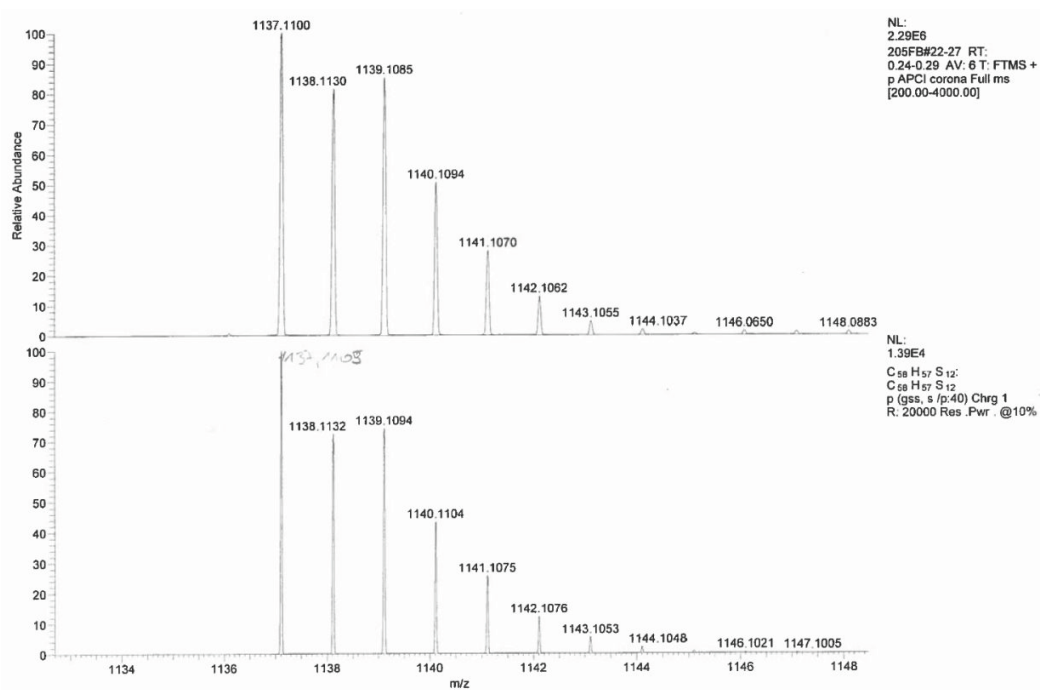


Figure S63: APCI-HRMS of trityl radical **6•**.

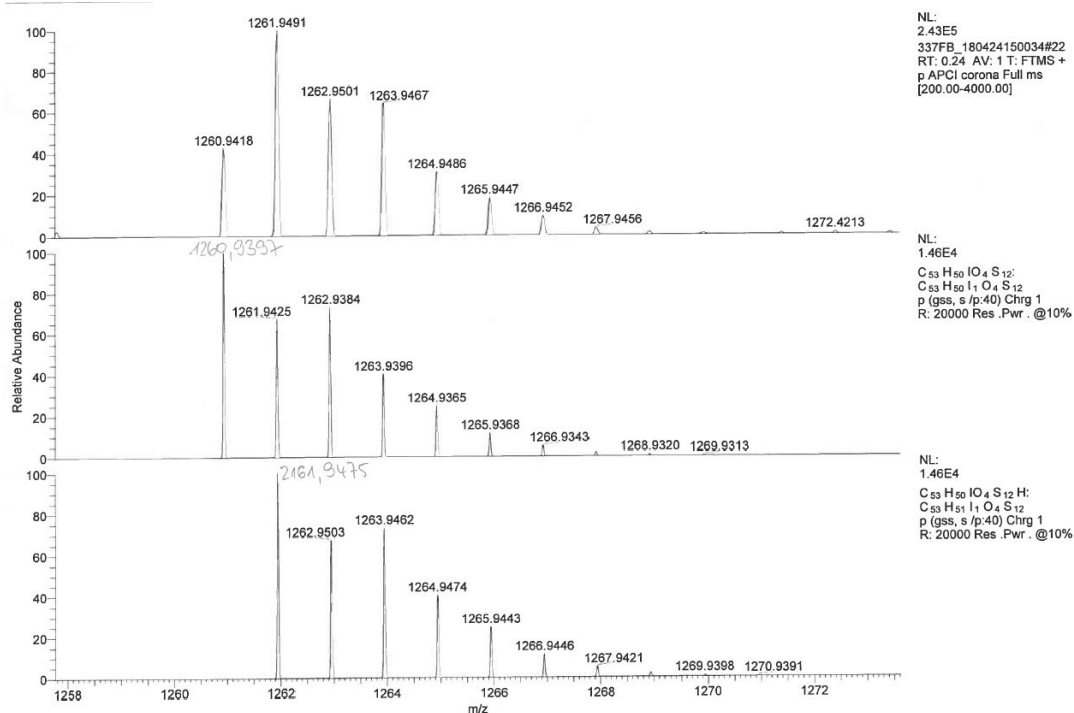


Figure S64: APCI-HRMS of trityl radical 7•.

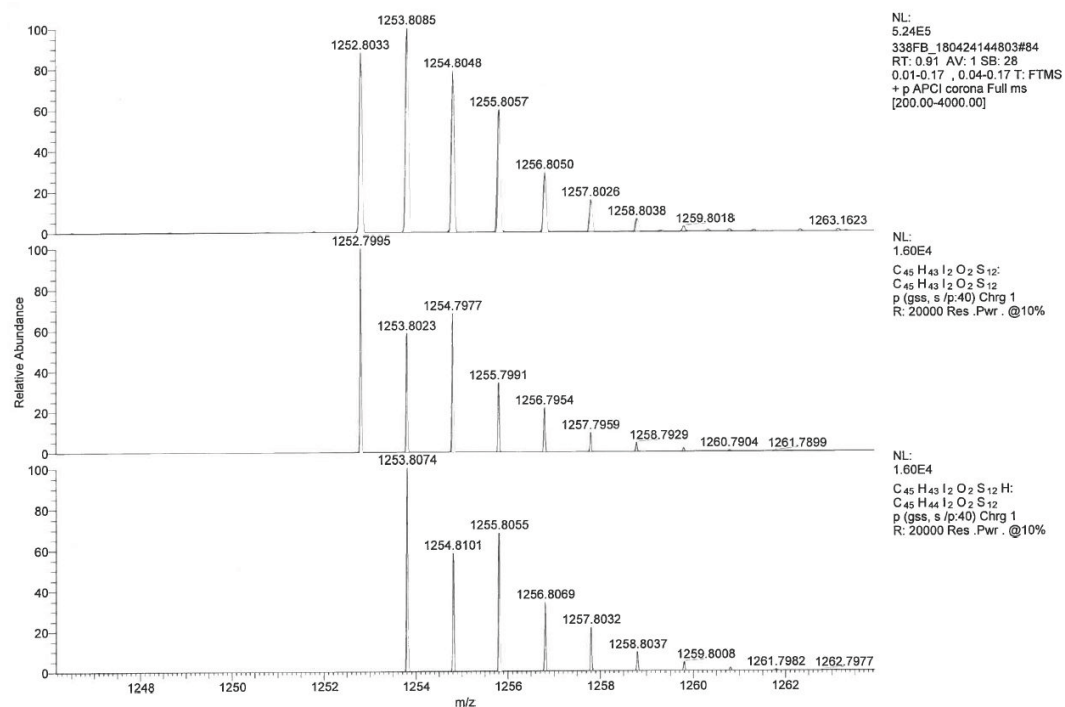


Figure S65: APCI-HRMS of trityl radical 8•.

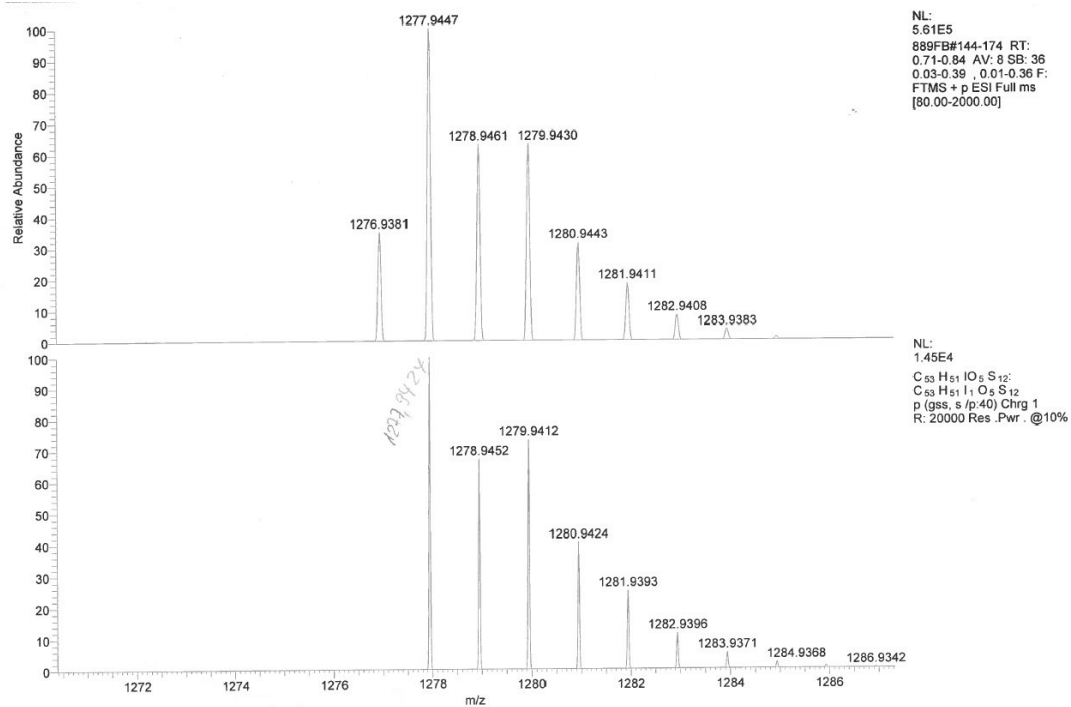


Figure S66: ESI(+)-HRMS of trityl alcohol 9.

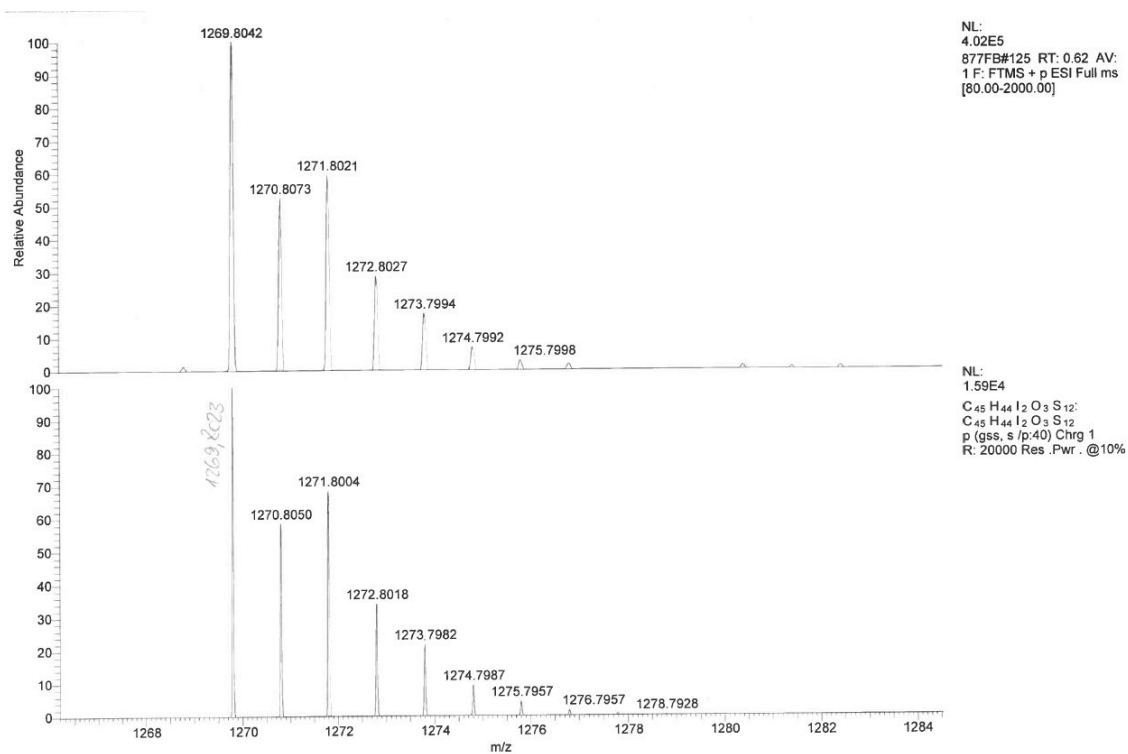


Figure S67: ESI(+)-HRMS of trityl alcohol 10 (Figure S20) .

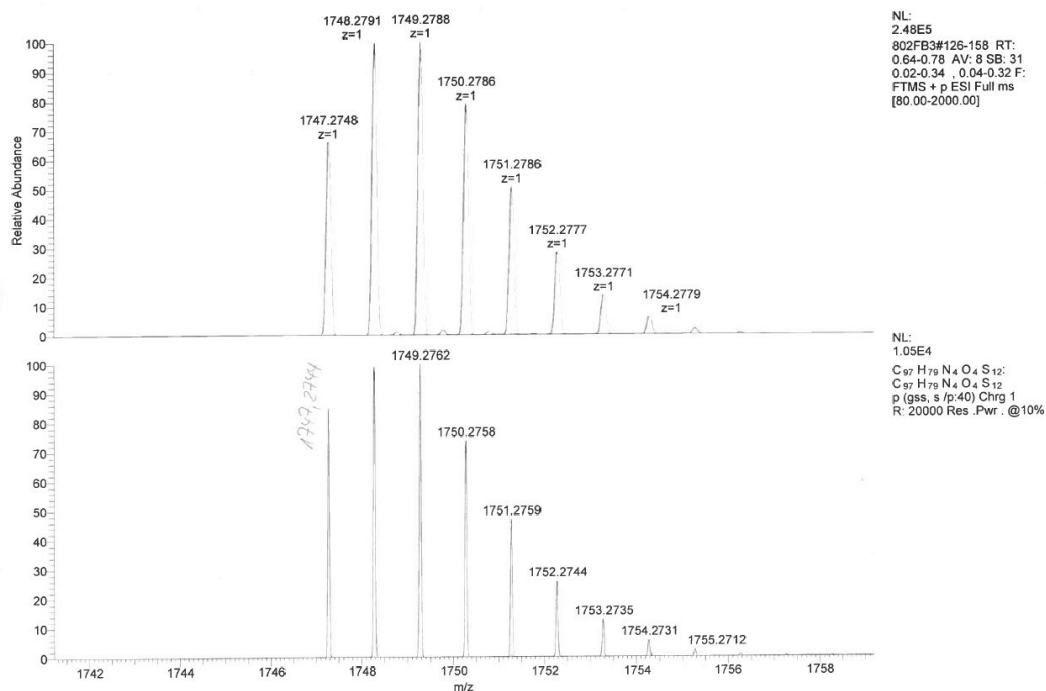


Figure S68: ESI(+)-HRMS of trityl porphyrin 12[•].

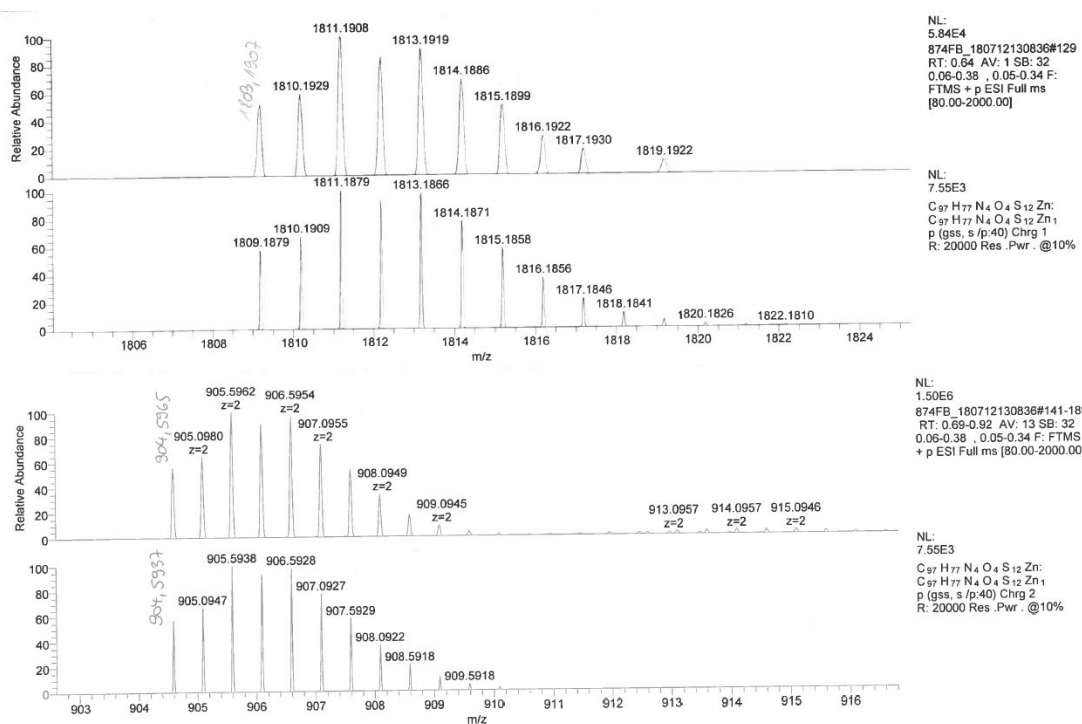


Figure S69: ESI(+)-HRMS of trityl porphyrin 13[•].

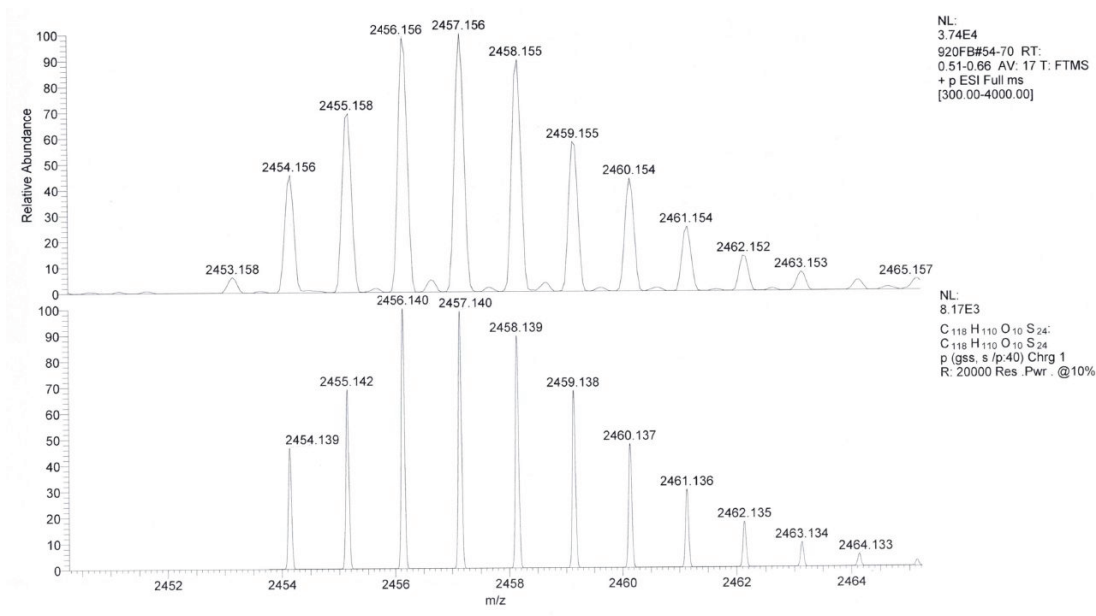


Figure S70: ESI(+)-HRMS of trityl alcohol **14**.

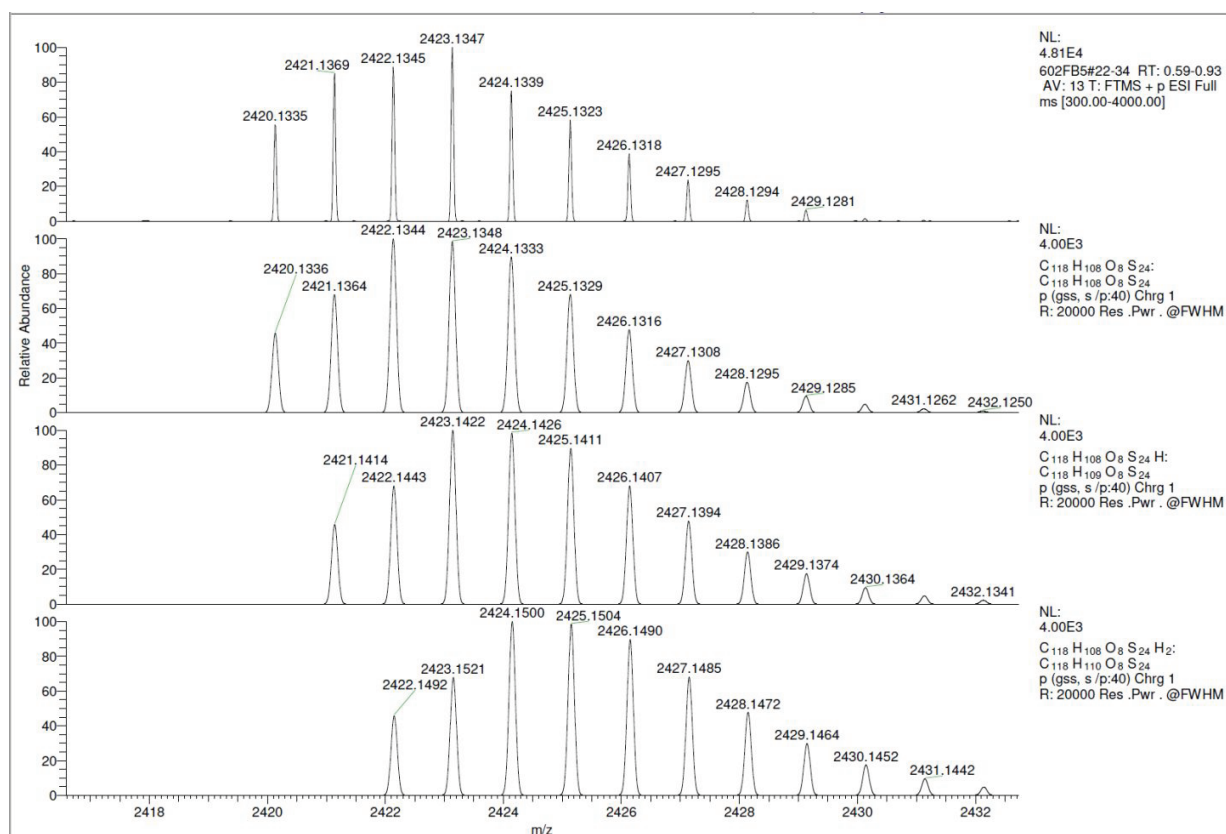


Figure S71: ESI(+)-HRMS of trityl biradical **15••**.

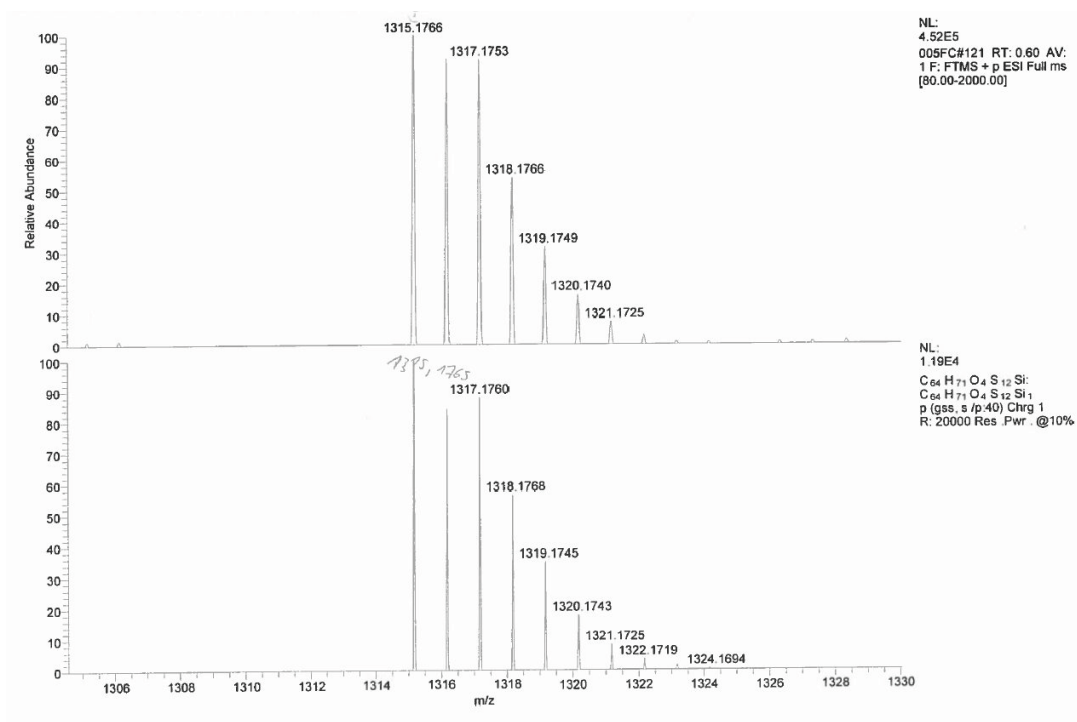


Figure S72: ESI(+)-HRMS of trityl radical **16•**.

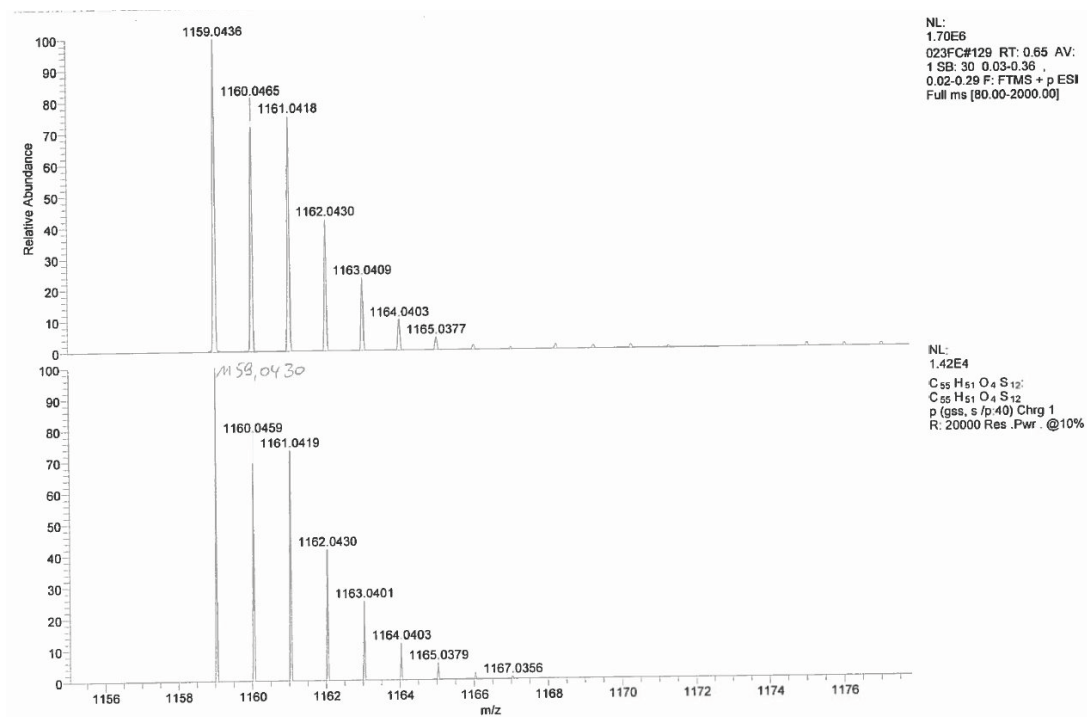


Figure S73: ESI(+)-HRMS of trityl radical **17•**.

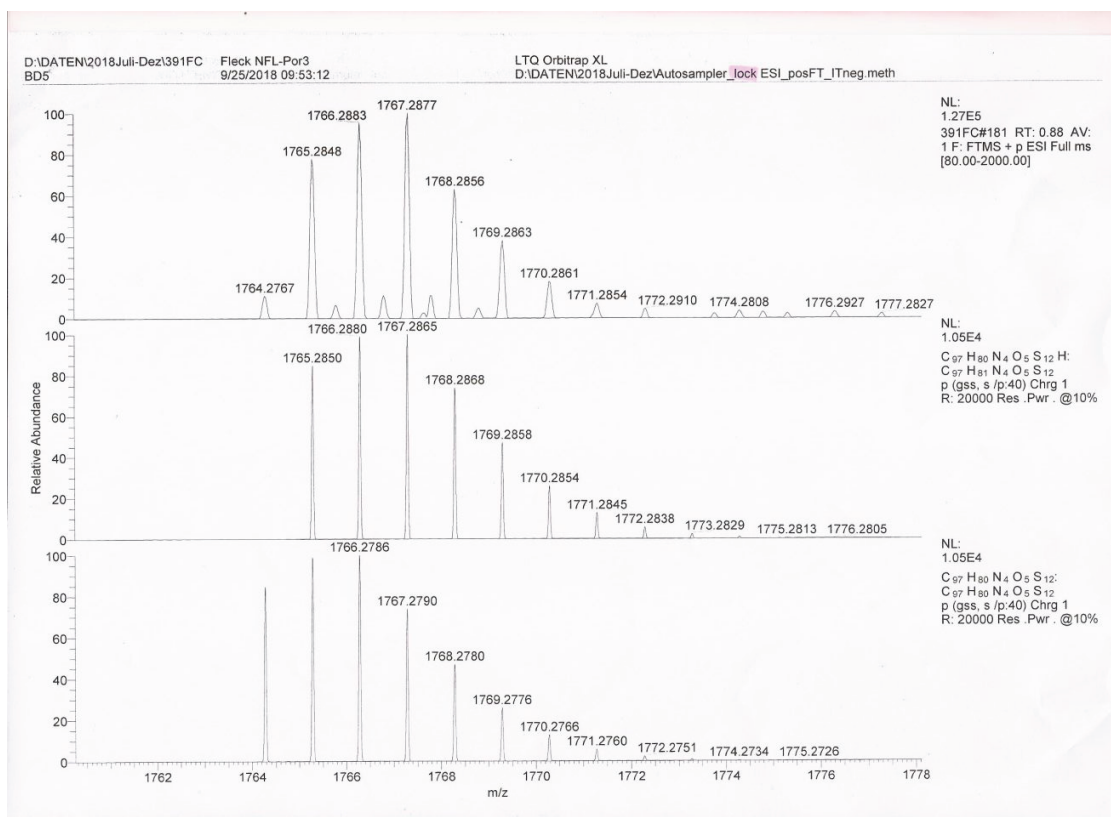


Figure S74: ESI(+)-HRMS of trityl porphyrin 12-OH.

11. MALDI(+) and ESI(+) mass spectra of trityl radicals

In the following, MALDI(+) and ESI(+) mass spectra of all new trityl radicals will be presented serving as an additional purity assessment. Note, that the [M+17]-peak belongs to traces of the corresponding trityl alcohol. Peaks occurring for [M+16] belong to trityl radicals bearing sulfoxide groups due to incorporation of oxygen.

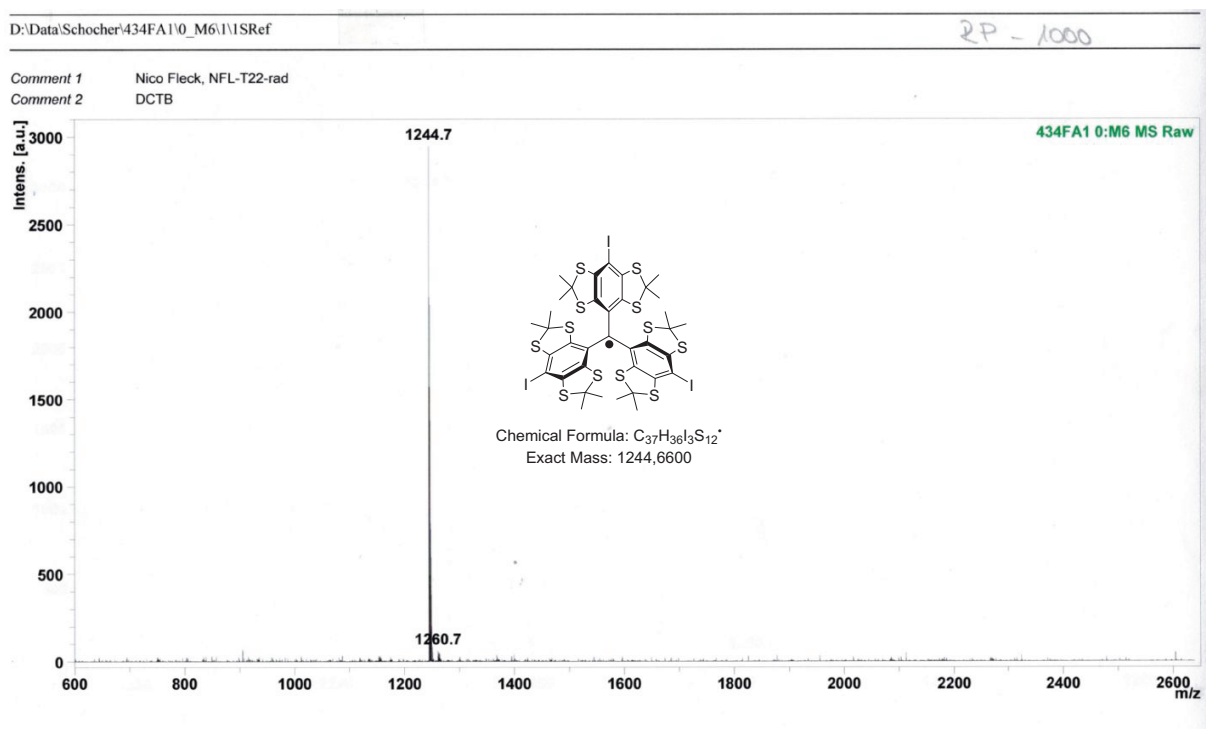


Figure S75: MALDI(+) mass spectrum of radical 3^\bullet .

D:\DATA\Daten\185FB\0_D221

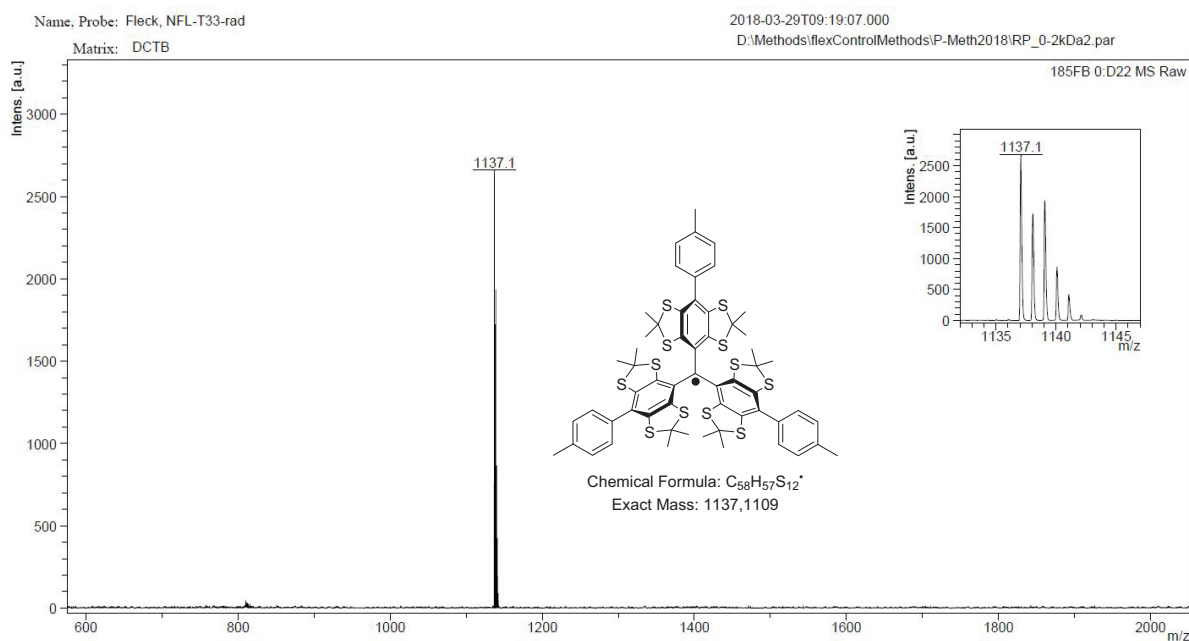


Figure S76: MALDI(+) mass spectrum of radical 6•.

D:\DATA\Daten\287FB\0_A61

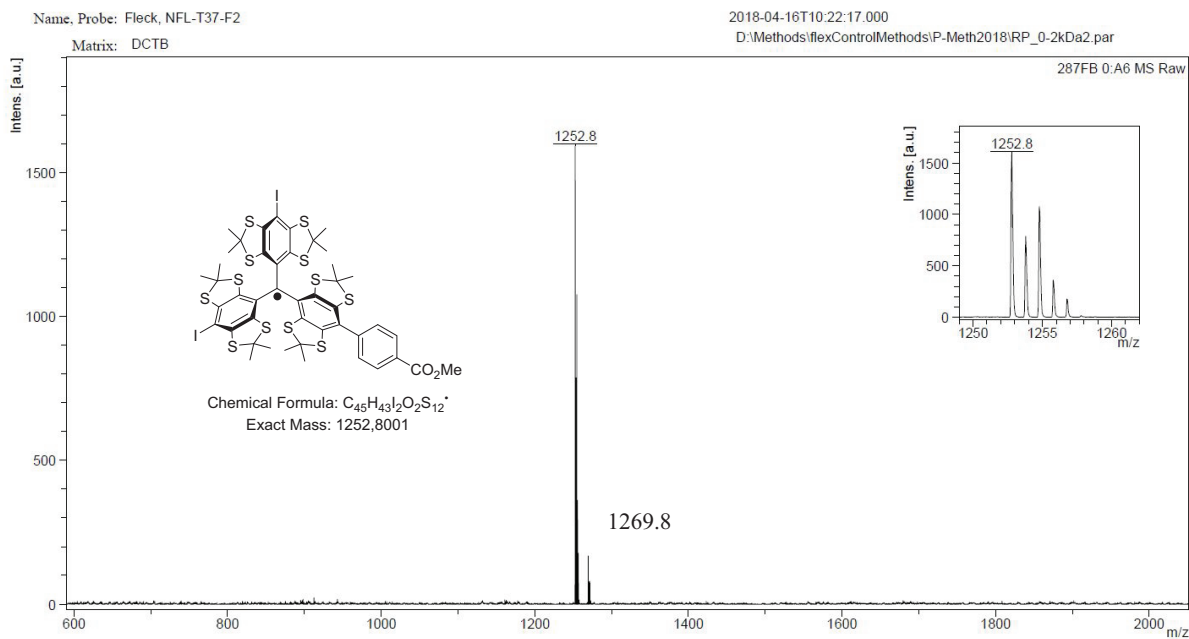
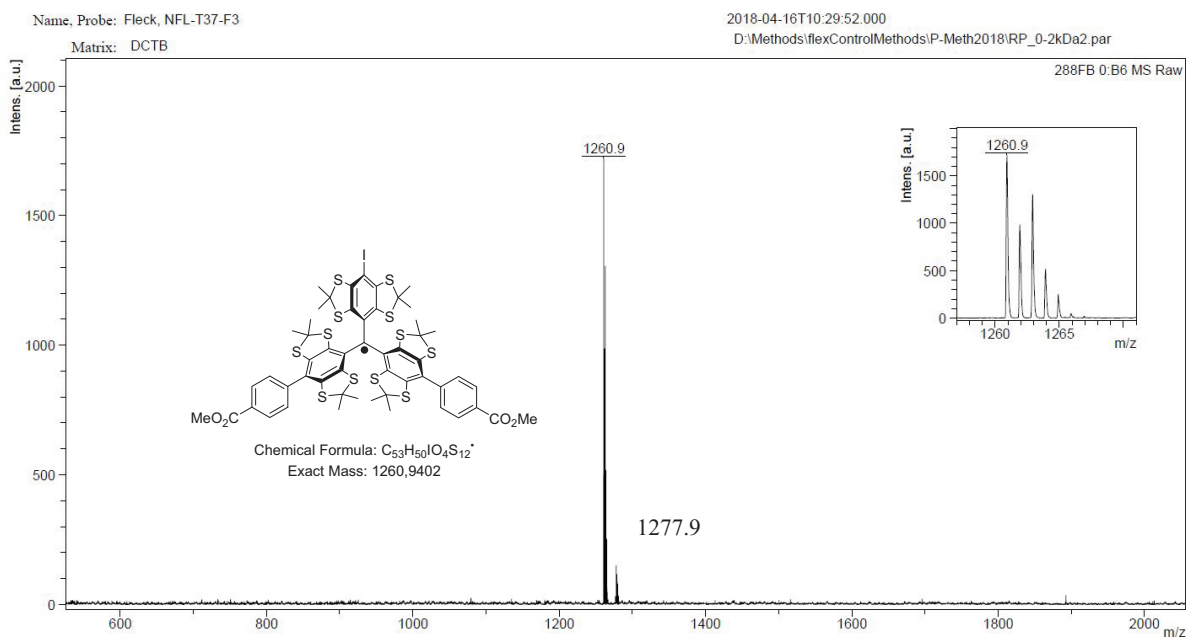
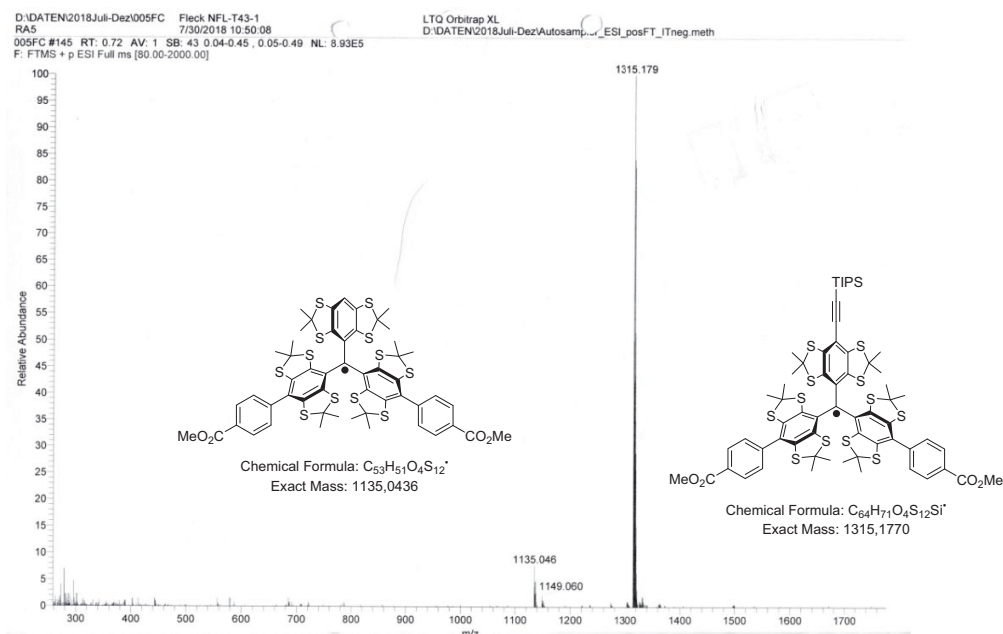


Figure S77: MALDI(+) mass spectrum of radical 7•.

Figure S78: MALDI(+) mass spectrum of radical 8^\bullet .Figure S79: ESI(+) mass spectrum of radical 16^\bullet .

D:\DATEN\2018Juli-Dez\023FC GE4
023FC #133 RT: 0.67 AV: 1 SB: 30 0.03-0.36, 0.02-0.29 NL: 2.35E6
F: FTMS + p ESI Full ms [80.00-2000.00]

LTO Orbitrap XL
D:\DATEN\2018Juli-Dez\Autosamp..._ESI_posFT_ITneg.meth

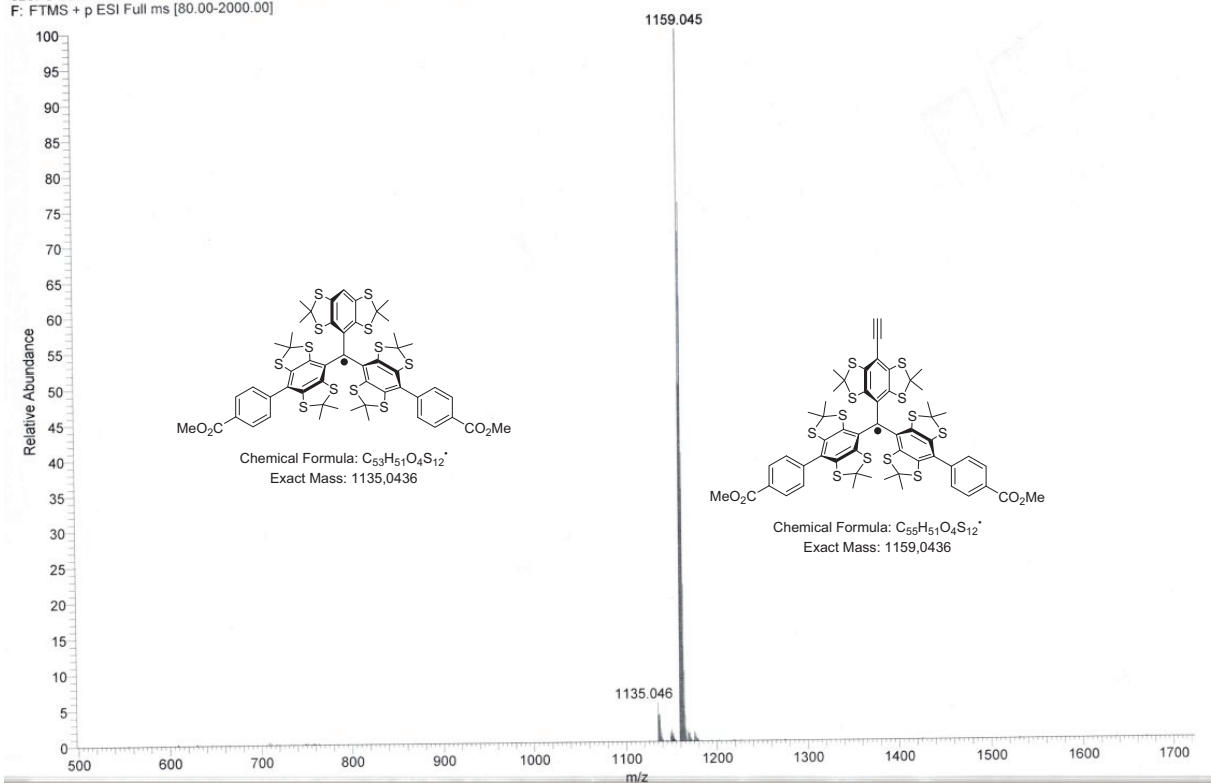


Figure S80: ESI(+) mass spectrum of radical 17•.

12. Medium pressure liquid chromatography

Additionally to mass spectrometry and *cw*-EPR, liquid chromatography (MPLC) was used to examine the purity of all new radical compounds which could not be subjected to NMR analysis. The instrumentation for the MPLC was set up as described in the main text. Besides from this, cyclohexane/ethyl acetate was used as solvent. In the following chromatograms, the green line indicates the ethyl acetate gradient. The initial signal in all chromatograms at a retention time of 00:00 min is artificial and belongs to the automatic zero-adjusting of the detector.

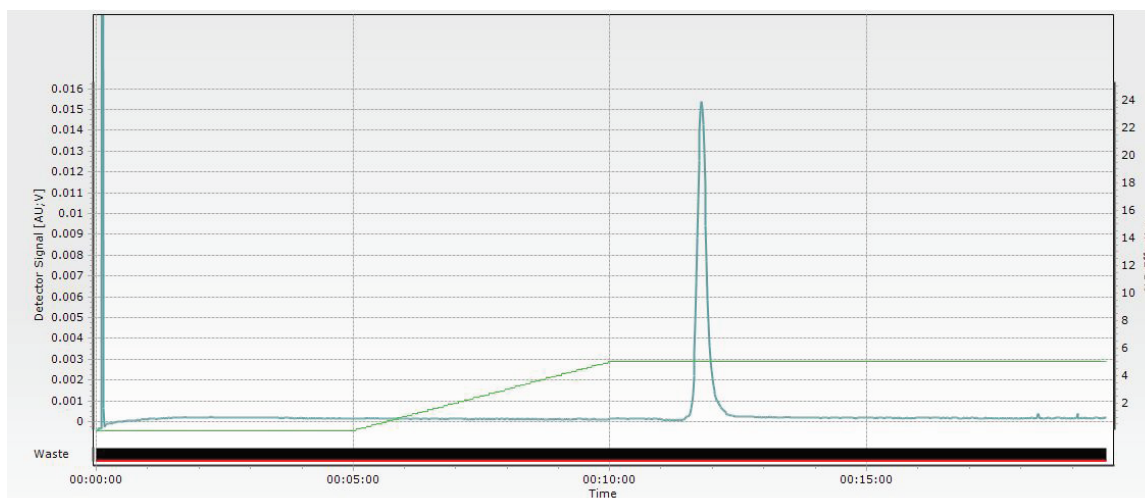


Figure S81: MPLC-chromatogram of radical **3•** ($t = 11:48$ min).

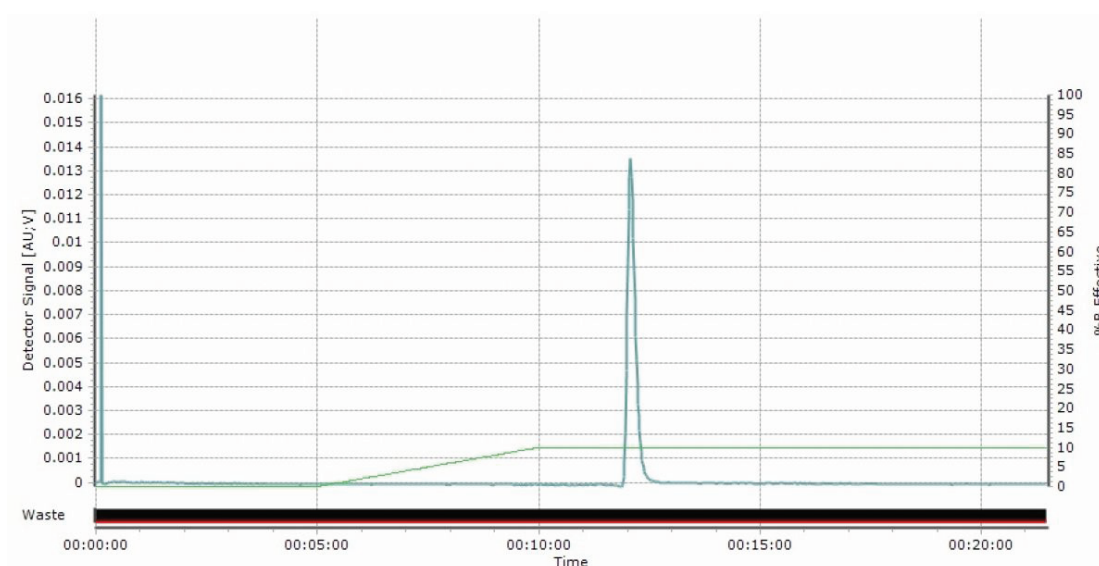


Figure S82: MPLC-chromatogram of radical **6•** ($t = 12:04$ min).

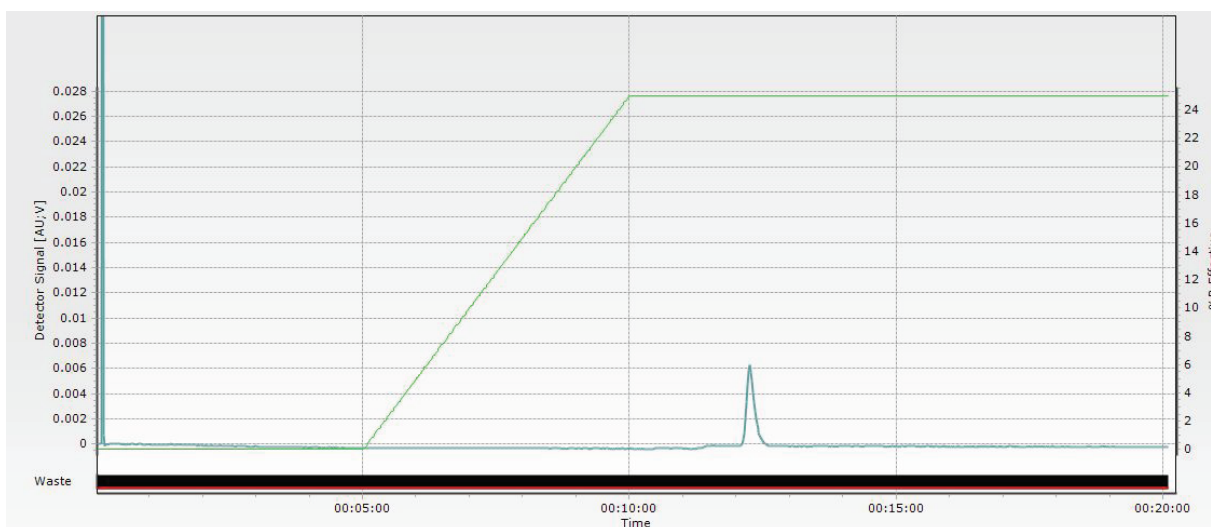


Figure S83: MPLC-chromatogram of radical **7•** (t = 12:14 min).

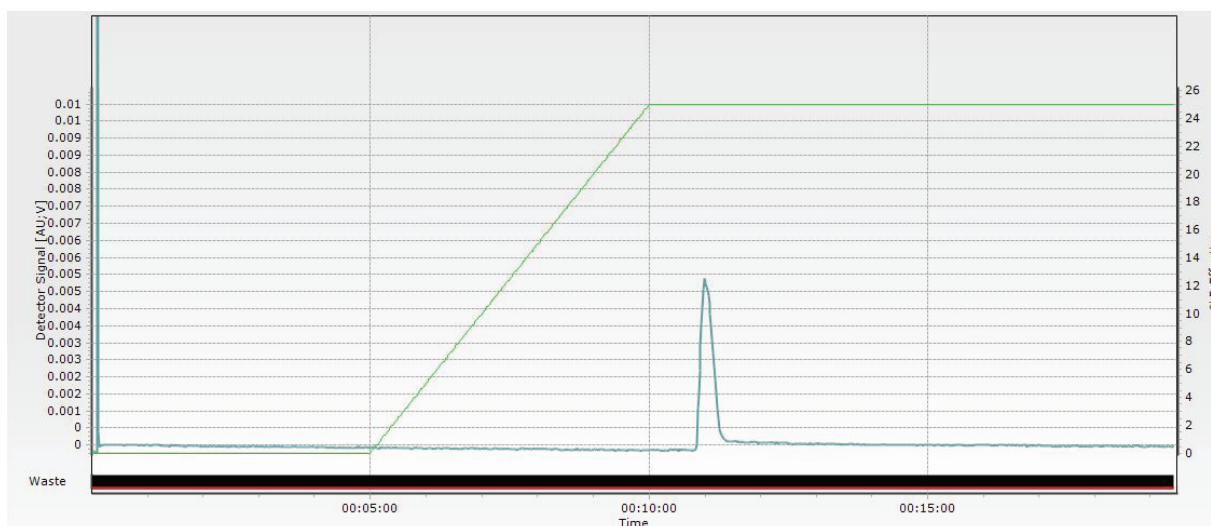


Figure S84: MPLC-chromatogram of radical **8•** (t = 11:00)

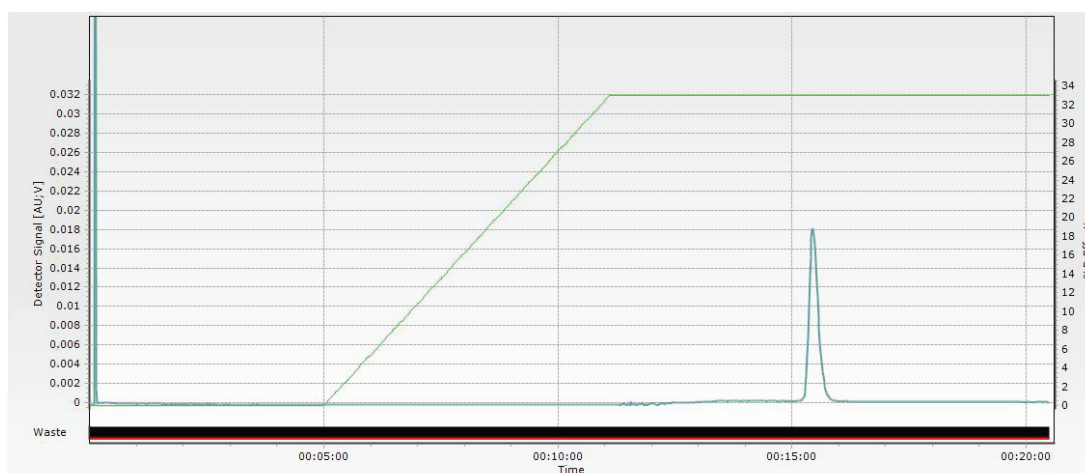


Figure S85: MPLC-chromatogram of biradical $15^{\bullet\bullet}$ ($t = 15:26$).

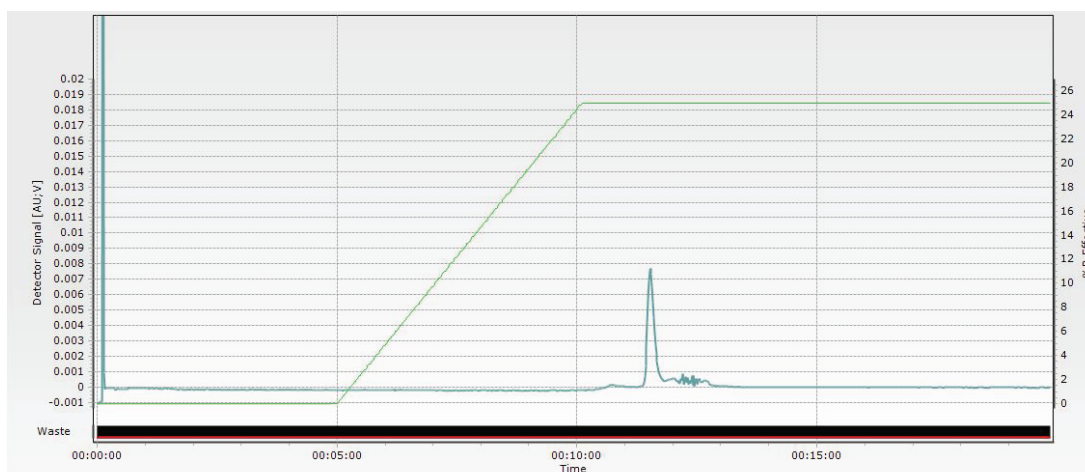


Figure S86: MPLC-chromatogram of radical 16^{\bullet} ($t = 11:31$ min)

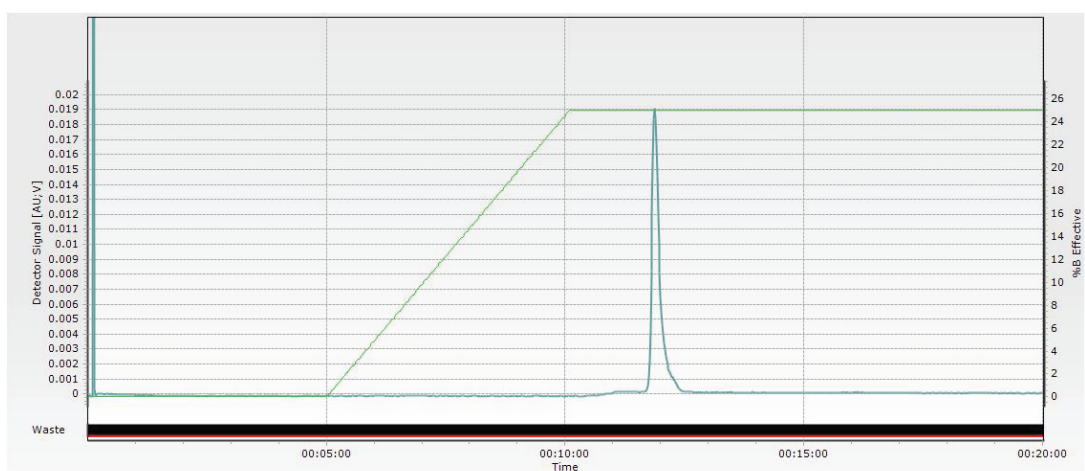


Figure S87: MPLC-chromatogram of radical 17^{\bullet} ($t = 11:52$ min).

13. References

- (1) Elsa, C.; Brecht, M.; Bittl, R. Pulsed Electron – Electron Double Resonance on Multinuclear Metal Clusters : Assignment of Spin Projection Factors Based on the Dipolar Interaction. *J. Am. Chem. Soc.* **2002**, *124*, 12606–12611.
- (2) Grimme, S.; Bannwarth, C.; Shushkov, P. A Robust and Accurate Tight-Binding Quantum Chemical Method for Structures , Vibrational Frequencies , and Noncovalent Interactions of Large Molecular Systems Parametrized for all spd-Block Elements (Z = 1–86). *J. Chem. Theory Comput.* **2017**, *13*, 1989–2009.
- (3) Saxena, S.; Freed, J. H. Theory of Double Quantum Two–Dimensional Electron Spin Resonance with Application to Distance Measurements Theory of Double Quantum Two-Dimensional Electron Spin Resonance with Application to Distance Measurements. *J. Chem. Phys.* **1997**, *107*, 1317–1340.
- (4) Jeschke, G.; Chechik, V.; Ionita, P.; Godt, A.; Zimmermann, H.; Banham, J.; Timmel, C.; Hilger, D.; Jung, H. DeerAnalysis2006 – a Comprehensive Software Package for Analyzing Pulsed ELDOR Data. *Appl. Magn. Reson.* **2006**, *30*, 473–498.
- (5) Edwards, T. H.; Stoll, S. Optimal Tikhonov Regularization for DEER Spectroscopy. *J. Magn. Reson.* **2018**, *288*, 58–68.
- (6) Stoll, S.; Schweiger, A. EasySpin , a Comprehensive Software Package for Spectral Simulation and Analysis in EPR. *J. Magn. Reson.* **2006**, *178*, 42–55.
- (7) Jassoy, J. J.; Meyer, A.; Spicher, S.; Wübber, C.; Schiemann, O. Synthesis of Nanometer Sized Bis- and Tris-Triptyl Model Compounds with Different Extent of Spin – Spin Coupling. *Molecules* **2018**, *23*, 682.
- (8) Iovine, V.; Cruciani, F.; Picini, F.; Varrone, M.; Rossi, E. Competitive Carbothiolation and Sonogashira Cross-Coupling in the Reaction of Trimethylsilylacetylene with Arylthioacetates. *ChemistrySelect* **2016**, *1*, 5201–5205.

[A4]: Excitation Energy Transfer and Exchange-Mediated Quartet State Formation in Porphyrin-Trityl Systems

Reprinted with permission from

Oliver Nolden, Nico Fleck, Emmaline R. Lorenzo, Michael R. Wasielewski, Olav Schiemann, Peter Gilch, Sabine Richer*, *Chem. Eur. J.* **2020**, *27*, 2683 -2691.

Published with Open Access by Wiley-VCH (Weinheim, DE) under CC-BY license, ©**2020** to the authors.

Contributions:

- Experimental Work:
 - Organic synthesis incl. compound characterization
- Writing of the manuscript in parts

Exchange Interactions | Hot Paper |

Oliver Nolden,^{+, [a]} Nico Fleck,^{+, [b]} Emmaline R. Lorenzo,^[c] Michael R. Wasielewski,^[c] Olav Schiemann,^[b] Peter Gilch,^[a] and Sabine Richert^{*, [d]}

Abstract: Photogenerated multi-spin systems hold great promise for a range of technological applications in various fields, including molecular spintronics and artificial photosynthesis. However, the further development of these applications, via targeted design of materials with specific magnetic properties, currently still suffers from a lack of understanding of the factors influencing the underlying excited state dynamics and mechanisms on a molecular level. In particular, systematic studies, making use of different techniques to obtain complementary information, are largely missing. This work investigates the photophysics and magnetic properties of a series of three covalently-linked porphy-

rin-trityl compounds, bridged by a phenyl spacer. By combining the results from femtosecond transient absorption and electron paramagnetic resonance spectroscopies, we determine the efficiencies of the competing excited state reaction pathways and characterise the magnetic properties of the individual spin states, formed by the interaction between the chromophore triplet and the stable radical. The differences observed for the three investigated compounds are rationalised in the context of available theoretical models and the implications of the results of this study for the design of a molecular system with an improved intersystem crossing efficiency are discussed.

Introduction

Due to their versatility, covalently-linked chromophore-radical systems have found a wide range of applications in the fields of information technology, artificial photosynthesis, as well as spin catalysis.^[1–4] In all of these applications, the covalent linkage of a stable radical to the chromophore is used as a means of altering—and thereby controlling—the excited state dynam-

ics of the chromophore, and many of them rely on the ability of the stable radical to act as an efficient triplet sensitizer by enhancing the intersystem crossing rate constant.

An increased triplet yield can for instance serve to improve the efficiency of processes such as triplet-triplet annihilation photon-upconversion,^[5–7] while other applications in organic solar cells or OLEDs make use of the photoluminescence (doublet emission) of a particular class of these π -radical systems.^[3, 8–10]

In the area of molecular spintronics, photogenerated organic multi-spin systems have proven invaluable for exploring the fundamental requirements for spin-information transfer and storage on a molecular level.^[11–14] By photoexcitation, well-defined initial spin states with strong spin polarisation can be generated, which may then be characterised by advanced magnetic resonance techniques with regard to their magnetic properties and spin-spin interactions. Through systematic variations of the molecular design and a careful study of the resulting magnetic properties, it will ultimately be possible to establish design protocols for new magnetic materials exhibiting the desired properties for an efficient transfer and storage of spin information.

Motivated by the large number and potential impact of these applications, a multitude of recent studies have focused on increasing our understanding of the excited state dynamics and deactivation mechanisms in chromophore-radical systems, with the long-term goals of achieving photocontrol of the magnetic properties of materials via spin coupling and exploring the influence of molecular topology on the interaction efficiency.^[1–3, 15–23]

[a] O. Nolden,⁺ Prof. Dr. P. Gilch
Institute of Physical Chemistry
Heinrich Heine University Düsseldorf
Universitätsstraße 1, 40225 Düsseldorf (Germany)

[b] N. Fleck,⁺ Prof. Dr. O. Schiemann
Institute of Physical and Theoretical Chemistry
University of Bonn
Wegelerstraße 12, 53115 Bonn (Germany)

[c] E. R. Lorenzo, Prof. M. R. Wasielewski
Department of Chemistry
Northwestern University
2145 Sheridan Road, Evanston, IL 60208-3113 (USA)

[d] Dr. S. Richert
Institute of Physical Chemistry
University of Freiburg
Albertstraße 21, 79104 Freiburg (Germany)
E-mail: sabine.richert@physchem.uni-freiburg.de

[*] These authors contributed equally to this work.

Supporting information and the ORCID identification number(s) for the author(s) of this article can be found under:
<https://doi.org/10.1002/chem.202002805>.

© 2020 The Authors. Published by Wiley-VCH GmbH. This is an open access article under the terms of the Creative Commons Attribution License, which permits use, distribution and reproduction in any medium, provided the original work is properly cited.

However, despite this effort, the mechanistic behaviour of organic multi-spin systems is up to now only poorly understood and truly systematic studies that could help to elucidate the details of the excited state dynamics, the mechanisms of excited multiplet generation and spin-information transfer, as well as the role of the individual interacting building blocks (i.e. chromophore triplet, bridge, stable radical) remain scarce.

Here, we investigate the spectroscopic properties of a series of covalently-linked chromophore-radical systems using femto-second transient UV-vis absorption (fs-TA) and electron paramagnetic resonance (EPR) techniques. Porphyrins were chosen as the chromophores since they are highly photostable,^[24] exhibit characteristic EPR signatures,^[25] and their central metal can easily be modified, enabling a variation of the excited state energetics while avoiding major changes to the molecular structure. A tetrathiaryl trityl radical, derivatives of which are commonly employed as spin labels,^[26–29] was attached to the porphyrin via a phenyl linker and is used here as the stable radical moiety. Compared to more commonly employed stable radicals, such as nitroxides, trityl radicals are characterised by a very narrow EPR line and slow spin-lattice relaxation,^[30] which might be particularly interesting for spin information storage applications. In addition, the chosen molecular design and synthetic approach allows a systematic modification of the individual building blocks of this photogenerated three-spin system.^[31] The three investigated structures only differ with respect to the central metal bound by the tetraphenylporphyrin (TPP) chromophore as shown in Figure 1 and are henceforth referred to as H₂TPP-trityl, ZnTPP-trityl, and MgTPP-trityl.

Making use of the time-resolution of fs-TA spectroscopy, we explore the mechanism underlying excited multiplet generation in the porphyrin-trityl systems and determine the efficiencies of the various competing excited state reactions. Complementary information is obtained from transient continuous wave EPR experiments, allowing us to identify and characterise the different spin states and spin–spin interactions. It is found that the interaction between the porphyrin triplet and the radi-

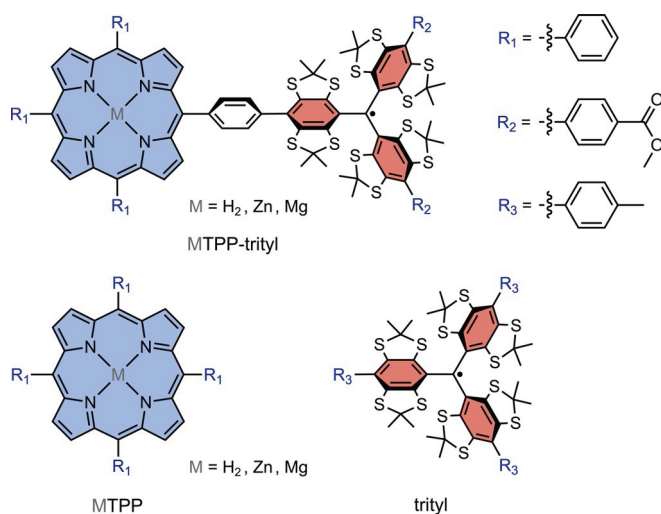


Figure 1. Chemical structures of the investigated chromophore-radical systems and their building blocks.

cal falls within the strong coupling regime, resulting in the formation of (doublet and) quartet states at cryogenic temperatures. Optical spectroscopy reveals that ultrafast energy transfer (~ 10 ps) from the porphyrin to the trityl radical largely dominates the excited state dynamics at room temperature and in frozen solution, implying a very low quartet formation efficiency. However, despite this low yield, transient EPR enabled the determination of the characteristic magnetic parameters and spin polarisation patterns of the formed quartet states and provided further information on the mechanistic details of quartet formation, as well as on the internal dynamics of the spin system. Finally, the differences observed for the three dyads containing different porphyrin central metals are discussed, together with the implications of the results of this study for the design of a molecular system with an improved intersystem crossing efficiency.

In all transient spectroscopic experiments, the porphyrins were excited at a wavelength of 550 nm, corresponding to an absorption maximum within the porphyrin Q-band region (S_1 state). After photoexcitation of the porphyrin chromophore, a number of different excited state reactions can occur, as schematically shown in Figure 2, mediated by the close proximity of the third spin of the stable radical. The possible processes are (i) excited state electron transfer (ET), (ii) enhanced intersystem crossing (EISC), (iii) excitation energy transfer (EET) and (iv) enhanced internal conversion (EIC) back to the ground state.

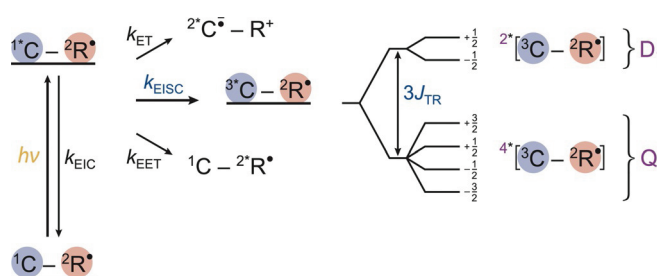


Figure 2. Schematic overview of the photophysical processes expected to occur in covalently-linked chromophore-radical systems assuming a non-negligible exchange interaction J_{TR} . Abbreviations: EIC enhanced internal conversion; ET electron transfer; EET excitation energy transfer; EISC enhanced intersystem crossing.

Results and Discussion

Synthesis and characterisation: H₂TPP-trityl and ZnTPP-trityl were synthesised according to procedures reported previously,^[31] while the synthesis and characterisation of MgTPP-trityl is outlined in the Supporting Information. An NMR characterisation of the compounds and precursor molecules (cf. Figure S1) revealed that MgTPP-trityl is prone to oxidation during the purification process. The batch of MgTPP-trityl thus contained some diamagnetic impurity ($\sim 30\%$), where the radical centre had been transformed into the corresponding triphenylmethanol moiety. Although no such observation was made for ZnTPP-trityl and H₂TPP-trityl, the presence of very small amounts ($\sim 0\text{--}3\%$) of a diamagnetic impurity in the samples

cannot be completely excluded due to the limited sensitivity of ^1H NMR, especially with respect to the radical content of the sample. The presence of such an impurity would be observed as a triplet contribution in the spectroscopic studies, but is by no means expected to influence the photophysical behaviour of the chromophore-radical compounds.

UV-vis absorption spectroscopy: The room temperature UV-vis spectra of the compounds and their porphyrin and trityl building blocks are shown in Figures S4 and S5. As is well-known from the literature,^[24] the spectra of the three tetraphenylporphyrins are qualitatively similar, showing an intense absorption band around 420 nm (porphyrin Soret band, S_2 state) and significantly less intense absorption peaks in the wavelength region of the porphyrin Q-bands from roughly 500 to 620 nm. The individual peak positions, however, differ for the different porphyrins and are also influenced by the solvent polarity. While the spectra of ZnTPP and MgTPP (approximate D_{4h} symmetry) show one prominent absorption peak in the Q-band region, this Q-band peak is shifted to higher wavelengths and split into two major peaks in H_2TPP , due to symmetry breaking induced by the presence of the two protons.

The spectrum of the trityl radical is characterised by a very prominent absorption band in the visible at 460 nm, a strong UV absorption, and a very broad but less intense absorption band extending over the whole visible range into the NIR (~ 900 nm).^[32] The absorption spectra of the porphyrin-trityl compounds are similar to the sum of the UV-vis spectra of their respective building blocks as can be seen from Figures S4 and S5 in the Supporting Information.

Femtosecond transient absorption: In order to get an idea about the efficiencies associated with the individual competing excited state reactions and their temperature dependence, femtosecond transient absorption measurements of the porphyrin-trityl compounds as well as their building blocks were performed in toluene at room temperature and in isotropic frozen 2-methyltetrahydrofuran solution at 85 K. Details on the sample preparation, experimental setup^[33] and data treatment can be found in the Supporting Information. Since the observations for the investigated porphyrin-trityl compounds were qualitatively very similar, only the results obtained for ZnTPP-trityl and its building blocks are presented in the main text, while the corresponding data for the free base analogue are shown in the Supporting Information (Figure S6).

Figure 3 shows the room temperature fs-TA data of the ZnTPP chromophore and trityl radical moieties. The photophysics of ZnTPP is well-known and has already been studied extensively.^[34,35] In agreement with these previous results, we observe a strong ground-state bleach around 420 nm, accompanied by a considerably weaker excited state absorption extending over the entire visible range, with a maximum close to the onset of the ground state bleach at 460 nm. These typical features of the ZnTPP excited singlet state decay with a time constant of about 2.6 ns to form the porphyrin triplet state in high yield.^[36–38] The latter then lives for about 1 μs in solution at room temperature.^[36]

A global kinetic analysis of the data, as presented in detail in the Supporting Information, revealed that the evolution of the

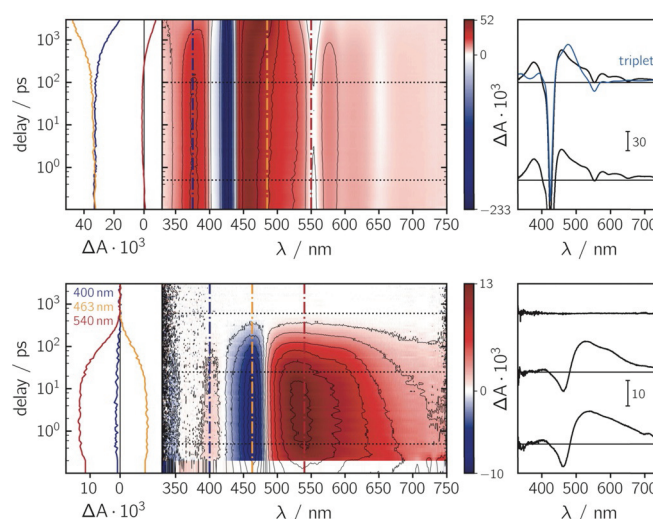


Figure 3. Femtosecond transient absorption data for ZnTPP (top) and the trityl radical (bottom) recorded in toluene solution at room temperature after photoexcitation at 550 nm. The central panel shows a contour plot of the data, where the red and blue colour coding represents positive and negative signals, respectively. The vertical coloured lines in the contour plot indicate the positions corresponding to the kinetic traces shown in the left panel, while the dotted horizontal lines indicate the time delays associated with the spectra shown on the right. The spectrum overlaid in blue corresponds to the spectrum of the ZnTPP excited triplet state, obtained from a global kinetic analysis of the data.

ZnTPP spectra with time can be described satisfactorily with two time constants of 11 ps and 2.6 ns. In addition, we detect an offset which is in line with the $\sim \mu\text{s}$ lifetime of the porphyrin triplet state. The first time constant is likely to be associated with relaxation processes within the S_1 state, while the second time constant can be assigned to the decay of the excited singlet state and simultaneous rise of the T_1 state. As shown in Figure 3, the signatures of the porphyrin excited singlet and triplet states are very similar and may therefore be difficult to distinguish.

The fs-TA spectra obtained for the trityl radical are shown in Figure 3 (bottom). They are characterised by a ground state bleach centred at about 460 nm, and a single, broad, and rather featureless excited state absorption extending from roughly 480 to ~ 800 nm, with a maximum around 540 nm. The excited state absorption features do not change markedly over the course of the excited state lifetime. These features and the ground state bleach decay completely with a time constant of 120 ps, as determined by a global kinetic analysis of the data (cf. SI).

In the proximity of the trityl radical, the excited state dynamics of ZnTPP are considerably altered as evident from Figure 4, showing the spectra of ZnTPP-trityl recorded at room temperature (top) and in frozen solution (bottom). Shortly after photoexcitation of the porphyrin moiety, the typical features of the ZnTPP singlet excited state are observed and found to decay quickly, with a time constant of ~ 10 ps. The decay of the S_1 state is accompanied by the simultaneous rise of a new absorption band in the range from 480 to 800 nm and the formation of a new ground state bleach centred at 460 nm. A

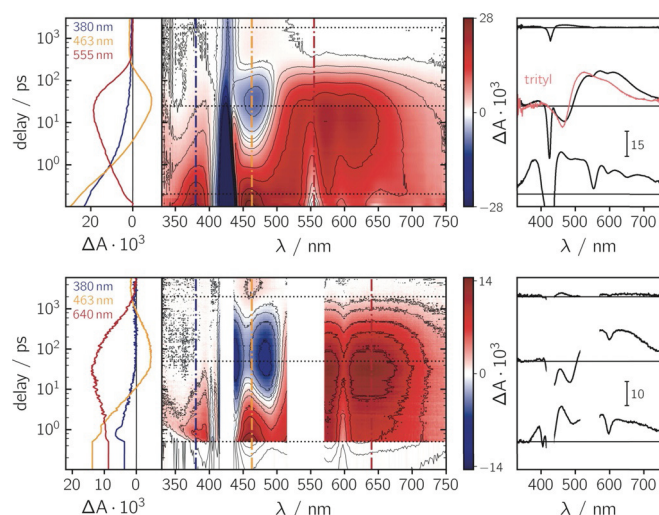


Figure 4. Femtosecond transient absorption data for ZnTPP-trityl recorded in toluene solution at room temperature (top) and frozen 2-methyltetrahydrofuran solution at 85 K (bottom) after photoexcitation at 550 nm. For a comparison of the spectral shape, a representative spectrum of the excited trityl radical is superimposed onto the ZnTPP-trityl data (red line). The wavelength ranges dominated by artefacts from either excitation light scattering or optical saturation were cut out from the spectra recorded at 85 K. In the room temperature data, the ground state bleach extending to $\Delta A = 0.22$ has been truncated for a better comparability of the relative spectral signals.

global kinetic analysis of the room temperature data (cf. SI) revealed that these newly formed excited state features subsequently decay with a time constant of roughly 120 ps. After their complete decay, a small percentage ($\sim 4\text{--}5\%$) of the porphyrin ground state bleach remains, together with some excited state absorption, attributed to the porphyrin triplet state.

In frozen solution, the overall reaction dynamics are qualitatively similar, as shown in Figure 4 (bottom). However, the spectral positions of the individual excited state features appear to be slightly redshifted, due to the different solvent environment (e.g. dielectric constant) and temperature, and the excited state absorption is found to decay with a slower time constant of 650 ps.

The room temperature fs-TA experiments on ZnTPP-trityl were also performed at a different excitation wavelength (i.e. 400 nm) and in 2-methyltetrahydrofuran solution (cf. SI). No marked differences in the spectra were observed, suggesting that the excited state deactivation mechanism in these systems is largely independent of solvent polarity and excitation wavelength (porphyrin Soret vs. Q-band excitation). Even in polar solvents, no spectral features characteristic of ZnTPP ion formation could be observed,^[39] indicating that any contribution of excited state electron transfer to the excited state dynamics can likely be excluded.

When comparing the room temperature fs-TA spectrum obtained for ZnTPP-trityl after the initial decay of the porphyrin S_1 state, e.g. at 25 ps, with that of the excited trityl radical (cf. Figure 4, top), a strong similarity is evident. The spectral features are nearly identical, which is a clear indication for excitation energy transfer (EET) from the porphyrin to the trityl radical taking place in ZnTPP-trityl. A detailed analysis of the rela-

tive spectral amplitudes and time constants (cf. SI) demonstrated that this energy transfer (i) is very efficient with a quantum efficiency of $\Phi_{\text{EET}} \geq 95\%$ and (ii) occurs equally fast at room temperature and in frozen solution, with a time constant of ~ 10 ps (no thermal activation barrier).

For energy transfer from the chromophore to the radical to occur, the radical needs to have low-lying electronic states that are accessible from the chromophore's excited singlet state. In principle, two different energy transfer mechanisms could be invoked to explain the experimental observations: Dexter-type energy transfer requires orbital overlap as it is based on an electron exchange mechanism. The associated transfer rates show an exponential distance dependence and a strong dependence on the bridge structure.^[40,41] On the other hand, Förster resonance energy transfer is based on a dipolar mechanism, requiring spectral overlap of the fluorescence spectrum of the energy donor (ZnTPP) and the absorption spectrum of the energy acceptor (trityl), but no orbital overlap. The transfer rate depends on the distance between donor and acceptor as r_{DA}^{-6} .^[42]

In order to evaluate whether the experimentally observed rate constants could be in agreement with Förster theory, we performed calculations of the expected Förster energy transfer rate for ZnTPP-trityl, as detailed in the Supporting Information. The employed formalism relies on the validity of the point-dipole approximation and is therefore likely not to yield accurate results in the case of the investigated structures, since the centre-to-centre distance between chromophore and radical is not significantly larger than their individual molecular sizes. Nevertheless, a good estimate can be obtained. The calculations were carried out with a centre-to-centre distance of $r_{\text{DA}} = 1.3$ nm and for different values of κ^2 , describing the relative orientation of the transition dipole moments within the porphyrin and trityl moieties with respect to the vector connecting them. The correct value for κ^2 cannot easily be predicted, but given the covalent linkage between donor and acceptor and the known orientation of the transition dipole moments within the porphyrin and trityl moieties, it might be reasonable to assume that κ^2 is larger than one and maybe even close to its maximum value of four. Provided this assumption holds true, energy transfer time constants between 10 and 40 ps should be feasible (cf. SI).

The experimentally observed EET time constant of ~ 10 ps thus seems to be consistent with a Förster-type mechanism, although a contribution from Dexter-type energy transfer cannot be excluded in view of the rather short distance between donor and acceptor and the covalent linkage between the two reaction partners, resulting in non-negligible exchange coupling.^[31]

The high efficiency of excitation energy transfer in these covalently-linked porphyrin-trityl systems naturally imposes severe limitations on the efficiency of the enhanced intersystem crossing (EISC) process and therefore the efficiency of excited multiplet formation. Efficient EISC should result in rapid quenching of the porphyrin S_1 state accompanied by a simultaneous rise of the porphyrin T_1 state. Here, we find that excited state deactivation is dominated by EET, suggesting that the

rate constant of EISC is at least an order of magnitude smaller than that found for EET. From the ratio of the intensities of the initial ground state bleach and the ground state bleach remaining after complete decay of the trityl excited state absorption, we can estimate that the quantum efficiency of EISC can at most reach a value of ~5% in these systems.

In addition, part of this remaining triplet absorption could also result from a contribution of molecules where either (i) the trityl radical has been deactivated (diamagnetic impurity) or (ii) the orbital overlap between the chromophore and trityl moieties is negligibly small (unfavourable molecular conformation). Such molecules would undergo “normal”, i.e. spin-orbit coupling induced, intersystem crossing (ISC) to the porphyrin triplet state.

Since different origins for the triplet state contribution to the fs-TA spectra of ZnTPP-trityl can be envisioned, only an upper limit for the EISC yield of $\Phi_{\text{EISC}} \leq 5\%$ can be given as a result from the analysis of the femtosecond transient absorption data.

Electron paramagnetic resonance: In order to verify whether excited multiplet formation can be observed for the different porphyrin-trityl compounds and to characterise the magnetic properties of the individual spin states formed by the interaction of the porphyrin triplet and the trityl radical, transient continuous wave (cw) EPR measurements were performed in isotropic frozen 2-methyltetrahydrofuran solution at 80 K. Details on the sample preparation and experimental setup are given in the Supporting Information.

Figure 5 (left) shows a comparison of the transient cw EPR spectrum of the ZnTPP triplet state and the spectrum of the trityl radical, recorded in pulse mode. The spectrum of the trityl radical is very narrow, due to the lack of hyperfine coupling interactions to nearby magnetic nuclei, and exhibits an isotropic g value of 2.0028, as determined by a spectral simulation of the corresponding room temperature cw EPR spectrum (cf. Figure S13). Some slight structural broadening is observed in the wings of the spectrum due to ^{13}C satellite-transitions.^[31]

Compared to the spectrum of the trityl radical, the triplet state spectrum of ZnTPP is very broad. As it is typical for the triplet states of organic chromophores,^[43] the spectral shape and width is dominated by the zero-field splitting (ZFS) interaction, described by the following Hamiltonian:

$$\mathcal{H}_{\text{ZFS}} = \text{SDS} = D\left(S_z^2 - \frac{1}{3}S^2\right) + E\left(S_x^2 - S_y^2\right) \quad (1)$$

and parametrised by the two ZFS parameters D and E . In the case of the investigated porphyrins, D is known to be positive as determined from magnetophotoselection experiments,^[44] implying an oblate spin density distribution. Due to differences in the intersystem crossing rates to the individual triplet sublevels, triplet spectra are typically spin-polarised, leading to the observation of absorptive (a) as well as emissive (e) transitions.

To determine the zero-field splitting D values as well as the relative initial populations of the three triplet sublevels, numerical simulations of the triplet state spectra were carried out. In good agreement with previously published results,^[45,46] D_T values of 930 MHz, 1150 MHz and 890 MHz were obtained for ZnTPP, H₂TPP and MgTPP, respectively. While the out-of-plane triplet sublevel (Z) is primarily populated in ZnTPP, resulting in an $aaaae$ spin polarisation pattern, the in-plane levels (X , Y) are overpopulated in H₂TPP and MgTPP as evident from the $eeaaa$ polarisation pattern. The experimental spectra, simulations and further simulation parameters for all three tetraphenylporphyrins are shown in Figure S14 in the Supporting Information.

Compared to the spectra of the two building blocks, significant differences are observed in the transient cw EPR spectra of ZnTPP-trityl as shown in Figure 5 (right). The overall spectral width is considerably reduced compared to that of the ZnTPP triplet state and a strong absorptive feature is found to dominate the central part of the transient spectrum. In addition, the spectral shape is found to change with time: While an overall a/e spin polarisation could be detected shortly after laser excitation, the spectra detected after a few microseconds are found to be entirely in absorption and are largely dominated by the central absorptive feature.^[47]

This central feature with broad, significantly less intense, wings, observed after a few microseconds, is characteristic for a quartet state with Boltzmann population. In addition, a similar time evolution of the spin polarisation (a/e polarisation turning into net absorptive features) has been observed before for a porphyrin-nitroxide system,^[1,16] and could be attributed to thermal equilibration of the populations within the quartet state.^[48] We therefore tentatively assign the spectral features observed here for ZnTPP-trityl to the quartet state.

From a detailed analysis of the characteristic magnetic parameters (i.e. zero-field splitting parameters D_Q , E_Q and the g value g_Q) and spin polarisation patterns of the quartet state, important information on the quartet state formation mechanism can be obtained. However, before we discuss the implications of the present experimental results, the proposed mechanism for quartet state formation,^[3,18,19,49] graphically summarised in Figure 6, shall briefly be outlined here.

According to this model, light absorption leads to π - π^* singlet excitation of the porphyrin moiety. From this so-called excited sing-doublet state (2S_1),^[24] EISC occurs to yield the chromophore triplet state. The triplet state is split into trip-doublet (2T) and trip-quartet (4T) states by the exchange interaction ($\Delta E_{DQ} = 3J_{\text{TR}} \ll k_B T$). Typically, the lowest trip-doublet state (2T_1)

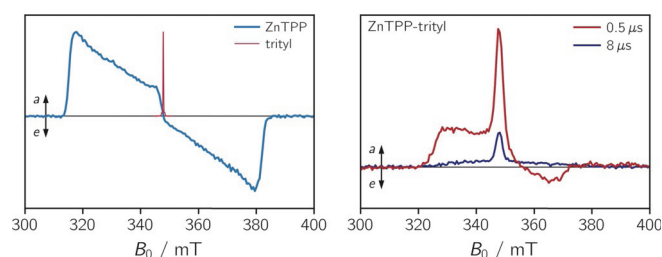


Figure 5. Comparison of the transient cw EPR spectrum of the triplet state of ZnTPP with the field-swept FID-detected spectrum of the trityl radical (left) and transient cw EPR spectra of ZnTPP-trityl at two different time delays after photoexcitation at 550 nm (right). All spectra were recorded at the X-band (9.75 GHz) in frozen 2-methyltetrahydrofuran at 80 K.

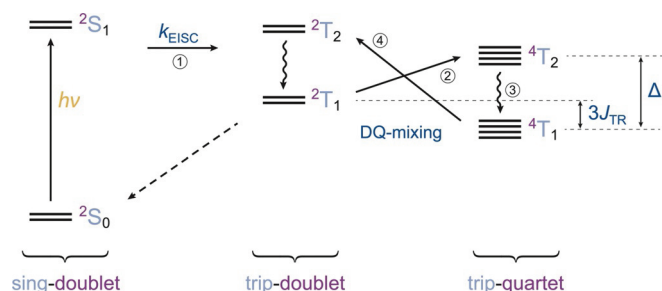


Figure 6. Processes and energetic states involved in quartet state formation. The individual energetic states are labelled with terms of the form jA_i , where the superscript j indicates the overall spin multiplicity, A the spin multiplicity of the chromophore, and the subscript i the energetic ordering (low to high) of the states with identical multiplicities.

is populated first by EISC, since, due to different exchange interactions of the two triplet electrons with the electron of the radical, the trip-doublet state acquires some sing-doublet character, implying that the relaxation from the excited sing-doublet state to the trip-doublet becomes partially allowed.^[24] The following transition from the doublet to the quartet state is spin-forbidden, but can be mediated by spin-orbit coupling (SOC).^[3,18,19] Efficient mixing of quartet-doublet eigenstates by SOC is however only possible when involving a nearby state with different orbital angular momentum. In metal porphyrins, the lowest two triplet states ($E_{u,x}$, $E_{u,y}$; π - π^* excitation) are nearly degenerate and are likely to fulfil this role. The energetic difference between the two states involved in the mixing is referred to as Δ and needs to be (significantly) smaller than the thermal energy.

The mixing of 2T_1 and 4T_2 by SO-ISC is then followed by fast internal conversion from 4T_2 to 4T_1 . Through SOC-mediated mixing, the doublet states acquire some quartet character (and vice versa), which will depend on the energy difference between doublet and quartet states ($3J_{TR}$) and will also be spin sublevel specific. This spin-selectivity leads to spin polarisation of the observed quartet state (4T_1). In the following, back and forth transitions between quartet and doublet states (i.e. thermal repopulation of the trip-doublet through mixing of 4T_1 with 2T_2) will deplete any initially overpopulated sublevels, causing a thermal equilibration of the populations. The decay to the ground state then primarily occurs from the doublet states, since the transition is spin allowed.

By SO-ISC the quartet $|\pm\frac{1}{2}\rangle$ and $|\pm\frac{3}{2}\rangle$ sublevels are always expected to be equally populated. Therefore, the $|\pm\frac{1}{2}\rangle \leftrightarrow |\pm\frac{3}{2}\rangle$ and $|\pm\frac{1}{2}\rangle \leftrightarrow |\pm\frac{3}{2}\rangle$ transitions will have equal and opposite polarisations, the so-called multiplet polarisation. The oppositely polarised multiplet contributions cancel each other in the centre of the spectrum and thus do not contribute to the central quartet feature which results from so-called net polarisation.

Since net and multiplet polarisation have different properties (spectral positions, orientation dependence, magnetic field dependence, time behaviour),^[18,19] the time evolution of the polarisation and the ratio of net to multiplet polarisation in the quartet spectra can provide valuable information on the internal dynamics of the system, especially the relative magnitudes of Δ and $3J_{TR}$.

The disappearance of the a/e multiplet polarisation in less than a few μ s in the spectrum of ZnTPP-trityl (cf. Figure 5) suggests that the doublet-quartet mixing (equilibration of the quartet populations) is rather fast on the EPR time scale, implying that the energy gaps ($3J_{TR}$, Δ) are small compared to the thermal energy ($k_B T \cong 55 \text{ cm}^{-1}$ at 80 K and 205 cm^{-1} at room temperature). Further, from a numerical simulation of the data, as shown in Figure 7, the relative ratios of the net to multiplet polarisation, the quartet zero field splitting parameters, D_Q and E_Q , as well as the g_Q value of the quartet state can be obtained. The D_Q value is of particular interest, since it is related to the dipolar interaction between the triplet and radical D_{TR} as $D_Q = \frac{1}{3}(D_T + D_{TR})$. The obtained g_Q value of 2.001 is well in line with the predictions for a quartet state from calculations based on the magnetic parameters of the chromophore triplet and stable radical.^[50] This and the fact that the spectrum can be fit as a combination of net and multiplet polarisation, using the same magnetic parameters for both contributions, strongly supports our statement that the transient cw EPR spectra observed for ZnTPP-trityl arise from a single species with quartet multiplicity. An overview of the experimental and calculated g and D values of all involved spin states is provided in Table S2.^[S1]

Transient cw EPR spectra were also acquired for H_2 TPP-trityl and MgTPP-trityl as shown in Figure 7. While the spectral widths are found to be similar in all cases, significant differences in the initial spin polarisation patterns are observed. In particular, it is noted that multiplet polarisation is observed for the quartet states of ZnTPP-trityl and MgTPP-trityl, whereas

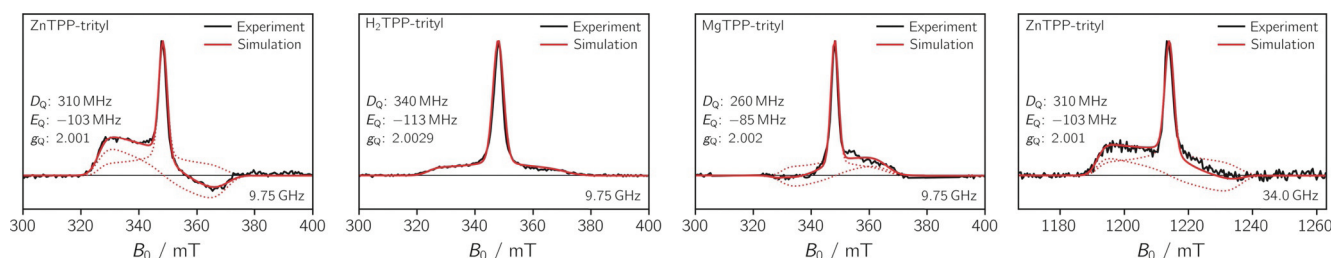


Figure 7. Transient cw EPR spectra of ZnTPP-trityl, H_2 TPP-trityl and MgTPP-trityl (from left to right) at the X-band (9.75 GHz) and ZnTPP-trityl (right) at the Q-band (34.0 GHz) together with the best numeric fit to the experimental data. All spectra were recorded in frozen 2-methyltetrahydrofuran solution at 80 K at about 1 μ s after photoexcitation at 550 nm. The quartet state spectrum was simulated as the sum of net and multiplet components (red dotted lines) with different weights. The simulation parameters are indicated in the figure.

only net polarisation could be detected on the EPR time scale in the case of H₂TPP-trityl. The central quartet peak is found to be positive for all investigated compounds, implying a positive sign of the exchange interaction J_{TR} between chromophore triplet and radical.^[19]

Although the formation of quartet states should go hand in hand with excited doublet state formation,^[23,52–54] no doublet signatures could be detected experimentally. Possible reasons for this could either be (i) fast relaxation or (ii) spectral overlap with the quartet feature: Fast relaxation of the doublet excited state (on the EPR time scale) could be favoured since the transition to the ground state doublet is spin-allowed. Fast relaxation also implies a broad spectral feature, which might be difficult to detect. In addition, since the g values of radical and triplet are very similar, also the g values of the formed quartet and doublet states will differ only little. Therefore, it is also plausible that the (weaker) signature of the doublet state is buried underneath the quartet spectrum and accounts for minor asymmetries observed in the experimental spectra. In addition, assuming the validity of the model for quartet formation outlined above, the doublet state is not expected to be spin polarised, implying a rather weak signal.

The opposite multiplet polarisation pattern observed for ZnTPP-trityl and MgTPP-trityl (a/e vs. e/a) might suggest a strong correlation between the quartet state polarisation and the polarisation of the triplet precursor ($aaaaee$ vs. $eeaaaa$), i.e. a direct influence of the relative initial triplet state populations and the sign of D_{T} in agreement with previous observations.^[55] However, an exception is known in the literature, where the polarisation pattern of the quartet state formed in a free-base porphyrin-verdazyl system was found to differ from that of the corresponding porphyrin triplet state,^[56] implying that the mechanism is likely to be more complex and that other factors, such as the signs of D_{Q} , D_{TR} and J_{TR} or the proximity of vibrational states for mixing, also need to be taken into consideration.^[19,22]

The qualitative similarity of the transient cw EPR spectra recorded for ZnTPP-trityl at X- (9.75 GHz) and Q-band (34.0 GHz) frequencies (cf. Figure 7) indicates that this system clearly falls within the strong coupling regime. Within this regime, the exchange interaction between triplet and radical, J_{TR} , has to be larger than any other relevant magnetic interactions in the system, i.e. (i) all hyperfine couplings, the difference in the Zeeman frequencies between triplet and radical, and (iii) the zero-field splitting in the triplet state. This situation is easily reached in porphyrin-trityl systems, since the hyperfine couplings in the triplet state are no larger than about 4 MHz,^[43,44] and the difference in Zeeman frequencies is proportional to the difference in g values, which is almost negligible here (cf. Table S2). The strong coupling limit is thus reached as soon as J_{TR} exceeds the magnitude of the triplet D value ($\sim 0.033 \text{ cm}^{-1}$).

When having a closer look at the spectra acquired for ZnTPP-trityl at the X- and Q-bands, it further appears that the ratio of net vs. multiplet polarisation is slightly increased at the Q-band (no negative intensities on the high-field side due to cancellation of the signal with the contribution of the absorptive net polarisation). This is in line with the theoretical predic-

tion that the relative contribution of the net polarisation to the spectra should increase linearly with the field strength and thus supports the validity of the proposed mechanism for quartet state formation (cf. Figure 6).

For all compounds it is observed that $|D_{\text{Q}}| \sim |3E_{\text{Q}}|$, which should imply a comparatively large contribution of the net polarisation.^[19] Nonetheless, compared to typical net:multiplet ratios expected based on the above-mentioned mechanism, the contribution of the net polarisation to the quartet spectra of Figure 7 is surprisingly large. In particular, the complete absence of multiplet polarisation in the spectrum of H₂TPP-trityl is intriguing and cannot readily be explained since spin-selective spin-orbit induced intersystem crossing from the doublet to the quartet excited state should always lead to the observation of multiplet spin polarisation.^[17,19,48,49,55]

This apparent inconsistency can be resolved by assuming that doublet-quartet mixing is fast on the EPR time scale: By the time of detection, a significant part (or all) of the multiplet polarisation might already have decayed. However, to explain the experimental observations, these equilibration dynamics would need to be considerably faster in H₂TPP-trityl as compared to ZnTPP-trityl or MgTPP-trityl, implying a smaller Δ and/or J_{TR} in H₂TPP-trityl (cf. Figure 6). Small differences in the molecular geometry or spin delocalisation of the triplet wavefunction could result in marked differences in J_{TR} . Free base porphyrins are non-symmetric and non-planar. The porphyrin core is also likely to be more flexible, resulting in a larger distribution of J_{TR} . Differences in geometry and/or triplet delocalisation are also suggested by the larger experimental D_{T} value of H₂TPP as compared to ZnTPP and MgTPP. On the other hand, no big differences in terms of delocalisation and J_{TR} are expected between ZnTPP and MgTPP, in line with their near identical D_{T} values.

Compared to the variations in J_{TR} , even more significant differences could be imagined between H₂TPP-trityl and ZnTPP-trityl/MgTPP-trityl regarding the excited state energetics (and therefore Δ): In metal porphyrins, the splitting between Q_x and Q_y is typically about 30 cm^{-1} ,^[24,25] implying that the degeneracy of the $^3E_{\text{u}}$ states is only slightly lifted and that these two states could well be involved in quartet-doublet mixing, since the energy gap is reasonably small compared to the thermal energy. In H₂TPP, the D_{4h} symmetry is broken, leading to a much larger splitting between Q_x and Q_y of the order of 2800 cm^{-1} .^[24] The mechanism thus needs to involve a different state in the case of the molecules containing H₂TPP as the chromophore since any mixing processes involving the second triplet state would clearly be too slow.

Conclusions

In the present study we investigated the photophysics and magnetic properties of a series of three porphyrin-trityl compounds, that only differ with respect to the porphyrin central metal. A detailed analysis of the femtosecond transient absorption data recorded at room temperature and in frozen solution enabled us to determine the efficiencies of the individual competing excited state reactions. It was found that excitation

energy transfer largely dominates the excited state dynamics with a temperature-independent time constant of ~ 10 ps and an efficiency of $\geq 95\%$, imposing severe limitations on the yield of enhanced intersystem crossing and therefore the efficiency of excited multiplet formation.

Nonetheless, the sensitivity of transient cw EPR was sufficient to detect the formation of quartet states for all three investigated compounds in frozen solution and numerical simulations of the data allowed the characterisation of the relevant magnetic parameters. No significant differences were observed between the spectra recorded at different microwave frequencies, as expected for a system that clearly falls within the strong coupling regime. Differences in the quartet state characteristics between the different compounds were discussed and could be rationalised in the context of previously invoked theoretical models and predictions,^[3,18,19,22] strongly supporting the validity of the proposed mechanism for this class of compounds. However, in view of the potential applications of such triplet-radical systems, the low EISC yield observed here is, of course, a substantial drawback. Future studies in this direction should thus focus on improving the design of the molecular system to increase the enhanced intersystem crossing efficiency. To this end, it will be necessary to find out how to suppress excitation energy transfer while keeping the exchange interaction between chromophore triplet and radical in a favourable range for EISC:

In the case of the investigated porphyrin-trityl compounds, it is likely that the frozen solution samples are composed of molecules with different conformations (i.e. varying dihedral angles between the porphyrin plane and the phenyl spacer, and therefore different J_{TR}). The EPR signal is thus expected to arise from only a small percentage of molecules in the sample that happen to adopt a conformation favouring EISC over EET. The efficiency of both mechanisms (EET and EISC) depends on the molecular conformation (i.e. orientation of transition dipoles and/or orbital overlap), but if the most favourable conformation for the two excited state deactivation mechanisms were different, one might have a chance to increase the efficiency of EISC by a slight modification of the present molecular design (e.g. by changing the bridge structure: topology, rigidity, extent of conjugation and/or length).

However, it is well possible that a change of the bridge structures is not sufficient to effectively suppress EET. In this case, the excited state energetics of radical and chromophore would need to be modified to eliminate the spectral overlap required for EET, which would most likely imply the choice of a different radical since the UV-vis absorption of the trityl radical extends over the entire visible range. To safely exclude the possibility of energy transfer, the energies of both the S_1 and T_1 states of the chromophore would need to be smaller than the lowest excitation energy of the radical.

Supporting Information

Synthesis and characterisation of the compounds, UV-vis absorption spectra, approximation of the Förster rate, description of the experimental setups for fs-TA and transient EPR, addi-

tional fs-TA data and global kinetic analysis, additional transient EPR data and simulations, as well as DFT calculations of the spin densities.

Acknowledgements

This work was supported by the Deutsche Forschungsgemeinschaft (DFG, German Research Foundation)—Project number 417643975 (S.R.) and GRK 2482 'ModISC', project B2 (P.G.), as well as the University of Freiburg through project number 2100297101 (Innovationsfonds Forschung) and the U.S. National Science Foundation under grant no. CHE-1900422 (M.R.W.). The authors acknowledge support by the state of Baden-Württemberg through bwHPC and the German Research Foundation (DFG) through grant number INST 40/467-1 FUGG (JUSTUS cluster) and thank the SIBW/DFG for financing EPR instrumentation that is operated within the MagRes Center of the University of Freiburg (grant no. INST 39/928-1 FUGG). E.R.L. was supported by a U.S. National Science Foundation Graduate Research Fellowship (DGE-1842165). S.R. would like to express her gratitude to Prof. S. Weber (University of Freiburg, Germany) for providing her access to his EPR instrumentation and equipment, and to Prof. A. van der Est (Brock University, Canada) for fruitful discussions. Open access funding enabled and organized by Projekt DEAL.

Conflict of interest

The authors declare no conflict of interest.

Keywords: enhanced intersystem crossing · excitation energy transfer · excited multi-spin systems · quartet state formation · transient EPR spectroscopy

- [1] S. Yamauchi, *Bull. Chem. Soc. Jpn.* **2004**, *77*, 1255–1268.
- [2] A. Kawai, K. Shibuya, *J. Photochem. Photobiol. C* **2006**, *7*, 89–103.
- [3] Y. Teki, *Chem. Eur. J.* **2020**, *26*, 980–996.
- [4] A. L. Buchachenko, V. L. Berdinsky, *Chem. Rev.* **2002**, *102*, 603–612.
- [5] Z. Wang, J. Zhao, A. Barbon, A. Toffoletti, Y. Liu, Y. An, L. Xu, A. Karatay, H. G. Yaglioglu, E. A. Yildiz, M. Hayvali, *J. Am. Chem. Soc.* **2017**, *139*, 7831–7842.
- [6] J. Han, Y. Jiang, A. Obolda, P. Duan, F. Li, M. Liu, *J. Phys. Chem. Lett.* **2017**, *8*, 5865–5870.
- [7] Z. Wang, Y. Gao, M. Hussain, S. Kundu, V. Rane, M. Hayvali, E. A. Yildiz, J. Zhao, H. G. Yaglioglu, R. Das, L. Luo, J. Li, *Chem. Eur. J.* **2018**, *24*, 18663–18675.
- [8] Y. Hattori, T. Kusamoto, H. Nishihara, *Angew. Chem. Int. Ed.* **2014**, *53*, 11845–11848; *Angew. Chem.* **2014**, *126*, 12039–12042.
- [9] Y. Beldjoudi, M. A. Nascimento, Y. J. Cho, H. Yu, H. Aziz, D. Tonouchi, K. Eguchi, M. M. Matsushita, K. Awaga, I. Osorio-Roman, C. P. Constantinides, J. M. Rawson, *J. Am. Chem. Soc.* **2018**, *140*, 6260–6270.
- [10] X. Ai, E. W. Evans, S. Dong, A. J. Gillett, H. Guo, Y. Chen, T. J. H. Hele, R. H. Friend, F. Li, *Nature* **2018**, *563*, 536–540.
- [11] A. Cornia, P. Seneor, *Nat. Mater.* **2017**, *16*, 505–506.
- [12] B. K. Rugg, M. D. Krzyaniak, B. T. Phelan, M. A. Ratner, R. M. Young, M. R. Wasielewski, *Nat. Chem.* **2019**, *11*, 981–986.
- [13] J. N. Nelson, J. Zhang, J. Zhou, B. K. Rugg, M. D. Krzyaniak, M. R. Wasielewski, *J. Chem. Phys.* **2020**, *152*, 014503.
- [14] J. H. Olshansky, J. Zhang, M. D. Krzyaniak, E. R. Lorenzo, M. R. Wasielewski, *J. Am. Chem. Soc.* **2020**, *142*, 3346–3350.

- [15] C. Corvaja, M. Maggini, M. Prato, G. Scorrano, M. Venzin, *J. Am. Chem. Soc.* **1995**, *117*, 8857–8858.
- [16] K. Ishii, J. Fujisawa, Y. Ohba, S. Yamauchi, *J. Am. Chem. Soc.* **1996**, *118*, 13079–13080.
- [17] K. Ishii, T. Ishizaki, N. Kobayashi, *J. Chem. Soc. Dalton Trans.* **2001**, 3227–3231.
- [18] Y. Kandrashkin, A. van der Est, *Chem. Phys. Lett.* **2003**, *379*, 574–580.
- [19] Y. Kandrashkin, A. van der Est, *J. Chem. Phys.* **2004**, *120*, 4790–4799.
- [20] V. Rozenshtein, A. Berg, E. Stavitski, H. Levanon, L. Franco, C. Corvaja, *J. Phys. Chem. A* **2005**, *109*, 11144–11154.
- [21] E. M. Giacobbe, Q. Mi, M. T. Colvin, B. Cohen, C. Ramanam, A. M. Scott, S. Yeganeh, T. J. Marks, M. A. Ratner, M. R. Wasielewski, *J. Am. Chem. Soc.* **2009**, *131*, 3700–3712.
- [22] V. F. Tarasov, S. S. M. Islam, Y. Ohba, M. D. E. Forbes, S. Yamauchi, *Appl. Magn. Reson.* **2011**, *41*, 175–193.
- [23] M. T. Colvin, A. L. Smeigh, E. M. Giacobbe, S. M. Mickle Conron, A. Butler Ricks, M. R. Wasielewski, *J. Phys. Chem. A* **2011**, *115*, 7538–7549.
- [24] M. Gouterman in *The Porphyrins, Vol. III* (Ed.: D. Dolphin), Academic Press Inc., New York, **1978**.
- [25] J. H. Van der Waals, W. G. Van Dorp, T. J. Schaafsma in *The Porphyrins, Vol. IV* (Ed.: D. Dolphin), Academic Press Inc., New York, **1979**.
- [26] G. W. Reginsson, N. C. Kunjir, S. T. Sigurdsson, O. Schiemann, *Chem. Eur. J.* **2012**, *18*, 13580–13584.
- [27] N. Fleck, C. A. Heubach, T. Hett, F. R. Haege, P. P. Bawol, H. Baltruschat, O. Schiemann, *Angew. Chem. Int. Ed.* **2020**, *59*, 9767–9772; *Angew. Chem.* **2020**, *132*, 9854–9859.
- [28] V. M. Tormyshev, A. S. Chubarov, O. Krumkacheva, D. V. Trukhin, O. Y. Rogozhnikova, A. S. Spitsyna, A. A. Kuzhelev, V. V. Koval, M. V. Fedin, T. S. Godovikova, M. K. Bowman, E. G. Bagryanskaya, *Chem. Eur. J.* **2020**, *26*, 2705–2712.
- [29] Y. Yang, B.-B. Pan, X. Tan, F. Yang, Y. Liu, X.-C. Su, D. Goldfarb, *J. Phys. Chem. Lett.* **2020**, *11*, 1141–1147.
- [30] H. Chen, A. G. Maryasov, O. Y. Rogozhnikova, D. V. Trukhin, V. M. Tormyshev, M. K. Bowman, *Phys. Chem. Chem. Phys.* **2016**, *18*, 24954–24965.
- [31] N. Fleck, T. Hett, J. Brode, A. Meyer, S. Richert, O. Schiemann, *J. Org. Chem.* **2019**, *84*, 3293–3303.
- [32] A. A. Kuzhelev, V. M. Tormyshev, V. F. Plyusnin, O. Y. Rogozhnikova, M. V. Edeleva, S. L. Veber, E. G. Bagryanskaya, *Phys. Chem. Chem. Phys.* **2020**, *22*, 1019–1026.
- [33] A. Reiffers, C. Torres Ziegenbein, L. Schubert, J. Diekmann, K. A. Thom, R. Kühnemuth, A. Griesbeck, O. Weingart, P. Gilch, *Phys. Chem. Chem. Phys.* **2019**, *21*, 4839–4853.
- [34] H.-Z. Yu, J. S. Baskin, A. H. Zewail, *J. Phys. Chem. A* **2002**, *106*, 9845–9854.
- [35] B. Abraham, J. Nieto-Pescador, L. Gundlach, *J. Phys. Chem. Lett.* **2016**, *7*, 3151–3156.
- [36] M. Montalti, A. Credi, L. Prodi, M. T. Gandolfi, *Handbook of photochemistry*, CRC Press, Taylor & Francis Group, Boca Raton, **2006**.
- [37] A. Harriman, *J. Chem. Soc. Faraday Trans. 1* **1980**, *76*, 1978–1985.
- [38] A. Harriman, *J. Chem. Soc. Faraday Trans. 2* **1981**, *77*, 1281–1291.
- [39] D. Villamaina, S. V. Bhosale, S. J. Langford, E. Vauthey, *Phys. Chem. Chem. Phys.* **2013**, *15*, 1177–1187.
- [40] S. S. Skourtis, C. Liu, P. Antoniou, A. M. Virshup, D. N. Beratan, *Proc. Natl. Acad. Sci. USA* **2016**, *113*, 8115–8120.
- [41] S. Bai, P. Zhang, P. Antoniou, S. S. Skourtis, D. N. Beratan, *Faraday Discuss.* **2019**, *216*, 301–318.
- [42] G. D. Scholes, *Annu. Rev. Phys. Chem.* **2003**, *54*, 57–87.
- [43] S. Richert, C. E. Tait, C. R. Timmel, *J. Magn. Reson.* **2017**, *280*, 103–116.
- [44] C. E. Tait, P. Neuhaus, H. L. Anderson, C. R. Timmel, *J. Am. Chem. Soc.* **2015**, *137*, 6670–6679.
- [45] O. Gonen, H. Levanon, *J. Phys. Chem.* **1985**, *89*, 1637–1643.
- [46] C. W. M. Kay, *J. Am. Chem. Soc.* **2003**, *125*, 13861–13867.
- [47] It has to be noted that, in addition to the features shown in Figure 5, also a minor triplet contribution to the EPR spectra was observed and subtracted prior to any further analysis. As mentioned before, this contribution is expected to arise from molecules exhibiting only negligible exchange coupling between the porphyrin and trityl moieties, either because of deactivation of the trityl radical (diamagnetic impurity) or an unfavourable molecular conformation with significantly reduced orbital overlap, i.e. $J_{\text{tr}}=0$. Examples of the original spectra including the triplet contribution are shown in the Supporting Information (Figures S15 and S16) for completeness.
- [48] Y. E. Kandrashkin, M. S. Asano, A. van der Est, *J. Phys. Chem. A* **2006**, *110*, 9607–9616.
- [49] K. Ishii, J. Fujisawa, A. Adachi, S. Yamauchi, N. Kobayashi, *J. Am. Chem. Soc.* **1998**, *120*, 3152–3158.
- [50] A. Bencini, D. Gatteschi, *EPR of exchange coupled systems*, Dover Publications, New York, **2012**.
- [51] In principle, the spin multiplicity could be unambiguously verified by a transient nutation experiment, see for instance: a) N. Mizuoichi, Y. Ohba, S. Yamauchi, *J. Phys. Chem. A* **1997**, *101*, 5966–5968; however, in the present case, no transient signal (apart from some residual porphyrin triplet signal) could be detected in pulse mode, not even at temperatures as low as 5 K. The absence of a transient pulse EPR signal was observed in the literature before, see: b) P. K. Poddutoori, Y. E. Kandrashkin, P. Karr, A. van der Est, *J. Chem. Phys.* **2019**, *151*, 204303; where it was suggested that the T_2 relaxation is too fast for the magnetisation to be refocused. However, in the present case it seems more likely that the quartet state is produced with a very low efficiency and that the EPR sensitivity is simply not high enough to detect it. A low quartet formation yield is consistent with the results from transient absorption presented above and the observation of relatively weak transient cw EPR signals.
- [52] C. Corvaja, L. Franco, A. Toffoletti, *Appl. Magn. Reson.* **1994**, *7*, 257–269.
- [53] J. Fujisawa, K. Ishii, Y. Ohba, S. Yamauchi, M. Fuhs, K. Möbius, *J. Phys. Chem. A* **1999**, *103*, 213–216.
- [54] J. Fujisawa, Y. Iwasaki, Y. Ohba, S. Yamauchi, N. Koga, S. Karasawa, M. Fuhs, K. Möbius, S. Weber, *Appl. Magn. Reson.* **2001**, *21*, 483–493.
- [55] K. Ishii, T. Ishizaki, N. Kobayashi, *J. Phys. Chem. A* **1999**, *103*, 6060–6062.
- [56] P. K. Poddutoori, M. Pilkington, A. Alberola, V. Polo, J. E. Warren, A. van der Est, *Inorg. Chem.* **2010**, *49*, 3516–3524.

Manuscript received: June 10, 2020

Accepted manuscript online: July 18, 2020

Version of record online: December 1, 2020

Chemistry–A European Journal

Supporting Information

Excitation Energy Transfer and Exchange-Mediated Quartet State Formation in Porphyrin-Triptyl Systems

Oliver Nolden^{+, [a]} Nico Fleck^{+, [b]} Emmaline R. Lorenzo,^[c] Michael R. Wasielewski,^[c]
Olav Schiemann,^[b] Peter Gilch,^[a] and Sabine Richert^{*[d]}

Table of Contents

1	Synthesis and characterisation of the porphyrin-trityl compounds	S1
2	UV-vis absorption spectra	S4
3	Approximation of the Förster energy transfer rate	S4
4	Additional fs-TA data and global kinetic analysis	S6
4.1	Room temperature setup and spectra	S6
4.2	Low temperature setup and spectra	S7
4.3	Global kinetic analysis	S9
5	Continuous wave EPR	S11
6	Additional transient EPR data and simulations	S12
6.1	EPR sample preparation and setup	S12
6.2	Triplet state spectra and simulations	S13
6.3	Discussion of the triplet contribution to the transient EPR spectra	S14
6.4	Temperature dependence of the transient EPR spectra	S15
6.5	Additional quartet spectra and simulations	S16
6.6	Discussion of the low signal intensity in transient EPR	S16
7	DFT calculations	S17

List of Figures

S1	$^1\text{H-NMR}$ of the porphyrin-trityl compounds	S1
S2	MALDI(+)-HRMS of MgTPP-trityl	S2
S3	$^1\text{H-NMR}$ of MgTPP-trityl	S3
S4	UV-vis absorption spectra of porphyrin-trityl compounds	S4
S5	UV-vis absorption spectrum of the trityl radical	S5
S6	fs-TA data of H_2TPP and $\text{H}_2\text{TPP-trityl}$	S6
S7	fs-TA data of ZnTPP-trityl in different solvents	S7
S8	fs-TA data of trityl and $\text{H}_2\text{TPP-trityl}$ in frozen solution	S8
S9	Decay associated spectra for ZnTPP and H_2TPP	S9
S10	Decay associated spectra for the trityl radical	S10
S11	Decay associated spectra for ZnTPP-trityl and $\text{H}_2\text{TPP-trityl}$	S10
S12	Decay associated spectra for trityl, ZnTPP-trityl and $\text{H}_2\text{TPP-trityl}$ in frozen solution	S11
S13	cw EPR spectrum of the trityl radical	S12
S14	Simulations of the triplet state EPR spectra of ZnTPP, H_2TPP , and MgTPP	S13
S15	TREPR spectra of $\text{H}_2\text{TPP-trityl}$ and ZnTPP-trityl before and after triplet subtraction	S15
S16	Transient cw EPR spectra of $\text{H}_2\text{TPP-trityl}$ and ZnTPP-trityl at different temperatures	S15
S17	Schematic representation of the energy levels of the quartet state	S16
S18	Comparison of the Q-band transient cw EPR spectra of $\text{H}_2\text{TPP-trityl}$ and ZnTPP-trityl	S16
S19	Comparison of the pulse EPR spectra of $\text{H}_2\text{TPP-trityl}$ with and without photoexcitation	S17
S20	Visualisation of the spin densities predicted by DFT calculations	S17

1 Synthesis and characterisation of the porphyrin-trityl compounds

H₂TPP-trityl, ZnTPP-trityl and the diamagnetic precursor molecule H₂TPP-trityl-OH were synthesised according to the procedures described in an earlier publication [1]. MgTPP-trityl was obtained by treatment of H₂TPP-trityl with MgBr₂(Et₂O) in dichloromethane [2].

Out of these four compounds, MgTPP-trityl was especially prone to oxidation during the purification process. The oxidation transforms the radical center into the corresponding diamagnetic triphenylmethanol moiety (H₂TPP-trityl-OH). As shown in Figure S1, the H_{phenyl} signals of the trityl core are broadened beyond visibility due to paramagnetic relaxation enhancement induced by the trityl radical (highlighted region). In contrast, these signals can be observed for the diamagnetic impurities, enabling the quantification of the radical content. Using this approach, H₂TPP-trityl and ZnTPP-trityl show no clear indication of diamagnetic impurities, whereas MgTPP-trityl exhibits a porphyrin:radical ratio of 1:0.75, determined by integration of the ¹H-NMR spectrum.

It should be noted that this method is likely not sensitive enough to detect an impurity content lower than a few percent, so small amounts of a diamagnetic impurity cannot be completely excluded even for H₂TPP-trityl and ZnTPP-trityl. In addition, it needs to be added that neither MALDI(+) nor ESI(+) mass spectrometry allow a reliable quantification in the present case, since signals belonging to sulfoxide impurities (M+16) can hardly be distinguished from trityl alcohol (M+17) impurities. Moreover, the presence of free-base porphyrin could also be probed by ¹H-NMR through observation of the characteristic signal at approximately -2.8 ppm. As shown in Figure S1, neither the zinc nor the magnesium complex contained any significant amount of free-base porphyrin.

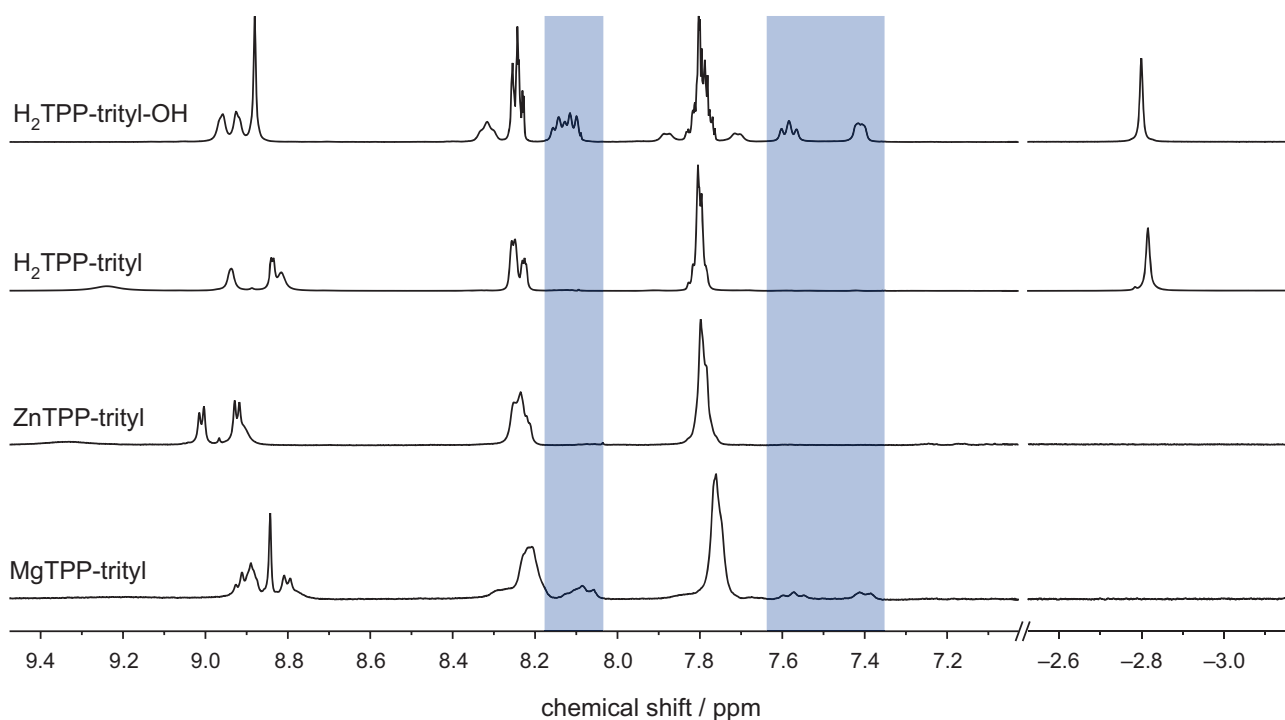


Figure S1: ¹H-NMR (700 MHz, CD₂Cl₂, 298 K) of H₂TPP-trityl-OH, H₂TPP-trityl, ZnTPP-trityl, and MgTPP-trityl. The region affected by paramagnetic broadening is highlighted.

Synthesis of MgTPP-trityl. H₂TPP-trityl (15 mg, 8.6 μmol) was dissolved in 4 mL dry dichloromethane and triethyl amine (69.1 mg, 95 μL, 640 μmol, 80 eq.) and magnesium bromide etherate (88 mg, 342 μmol, 40 eq.) was added. The reaction mixture was stirred at room temperature under argon for 45 minutes, diluted with 10 mL dichloromethane, washed with 5% NaHCO₃ (2×10 mL), and then dried over MgSO₄.

The solvents were evaporated under reduced pressure and the residue was purified by column chromatography on silica eluting with cyclohexane/methanol 90:10 (v/v). This provided the title compound as a purple solid in a yield of 12 mg (78 %, 6.8 μ mol).

$^1\text{H-NMR}$ (700 MHz, CD_2Cl_2 , 298 K, δ in ppm): 8.95–8.75 (m, 8H, H_{pyrrol}), 8.24–8.18 (m, 6H, $\text{H}_{\text{phenyl, por}}$), 7.78–7.72 (m, 9H, $\text{H}_{\text{phenyl, por}}$).

The following signals occur additionally for the corresponding triphenylmethanol contained as an impurity: 8.14–8.04 (m, 4H), 7.62–7.53 (m, 2H), 7.44–7.36 (m, 2H), 3.90 (s, 3H), 3.89 (s, 3H), 2.03 (s, 3H), 1.92 (s, 6H), 1.91 (s, 6H), 1.83–1.78 (s, 15 H), 1.74 (s, 3H), 1.71 (s, 3H).

Since the baseline in the alkyl region is distorted, probably due to an underlying signal of the 36 methyl hydrogen atoms of the thioketal moiety, the porphyrin:radical ratio is determined by integration in the aromatic region.

HRMS (MALDI+, DCTB, m/z): 1771.242 (calcd. for $\text{C}_{97}\text{H}_{77}\text{N}_4\text{O}_4\text{S}_{12}\text{Mg}$: 1771.245).

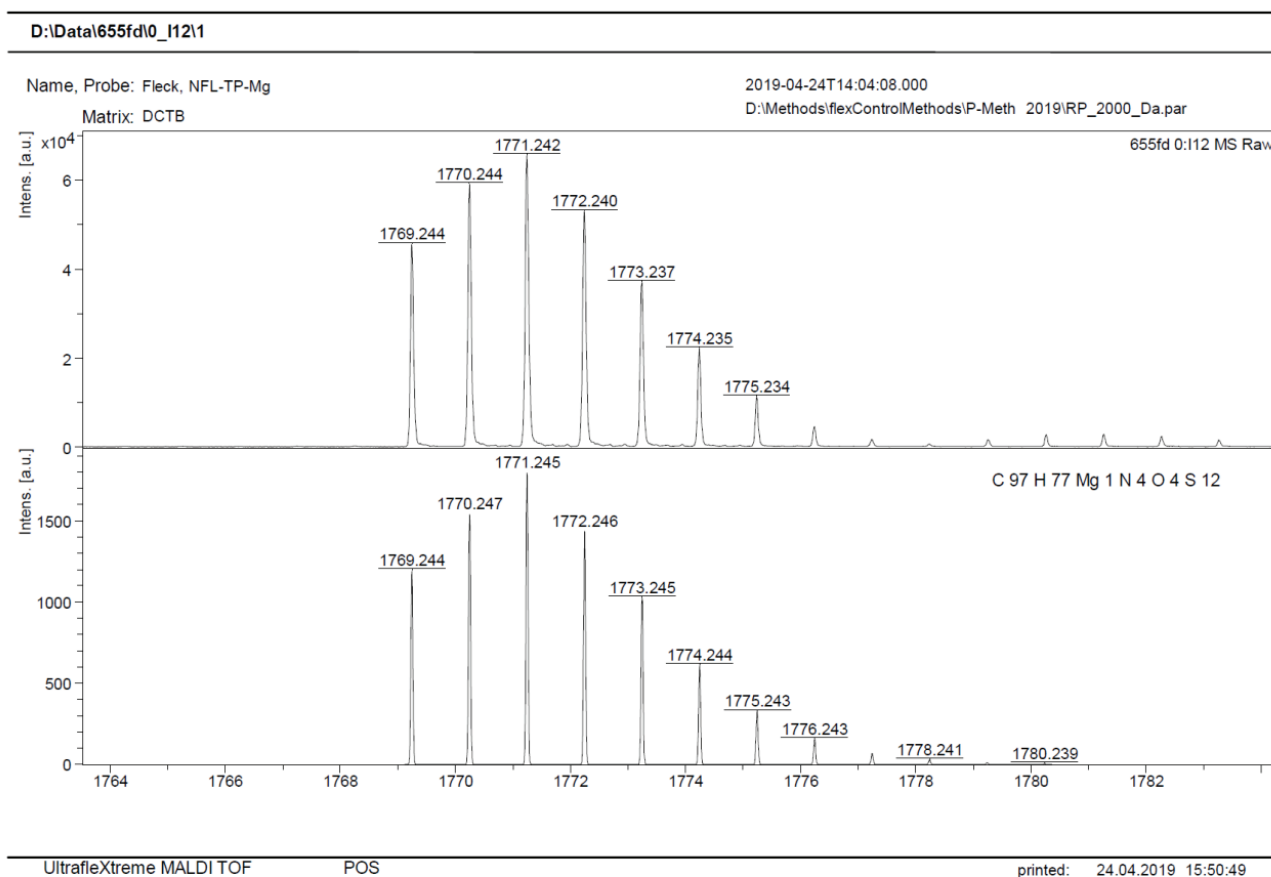


Figure S2: MALDI(+)-HRMS of MgTPP-trityl.

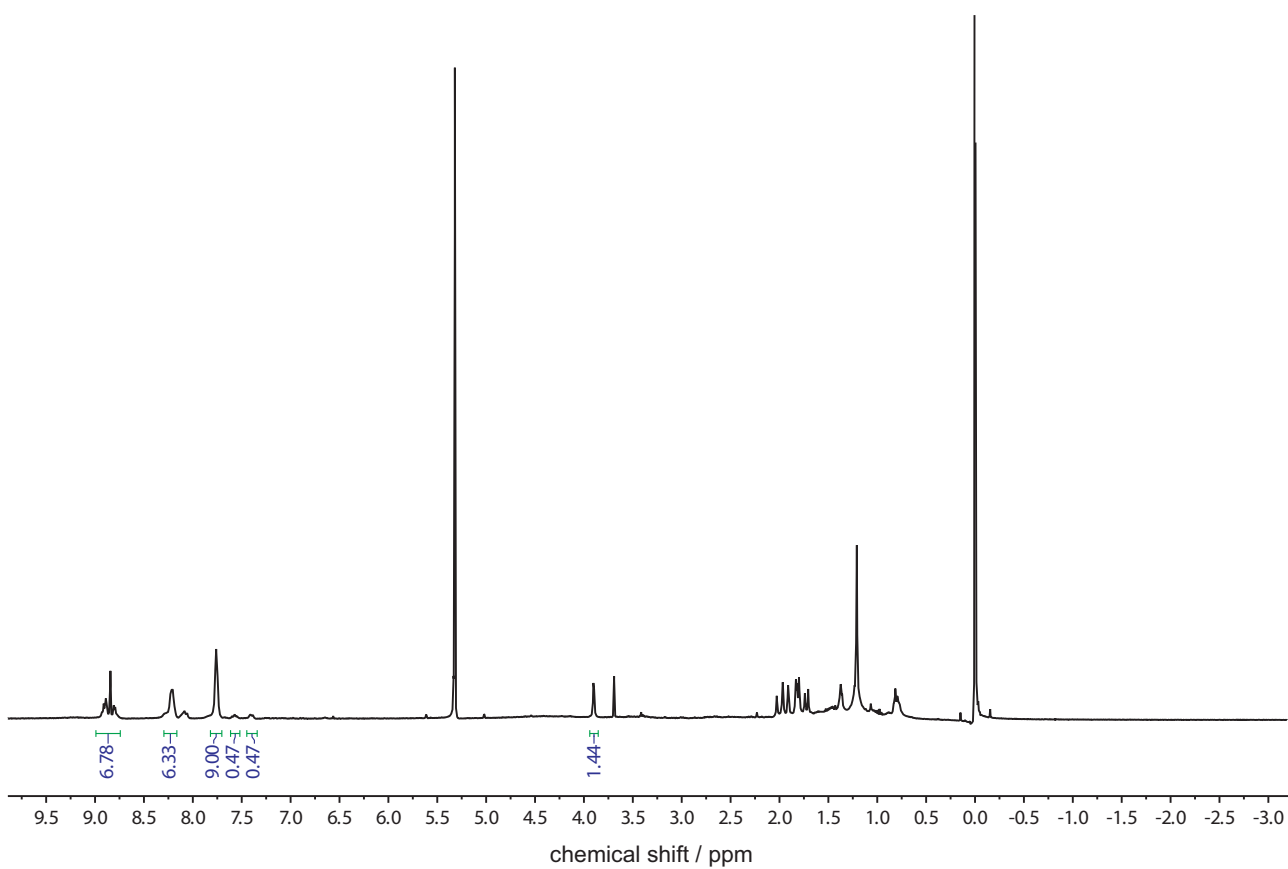


Figure S3: $^1\text{H-NMR}$ (700 MHz, CD_2Cl_2 , 298 K) of MgTPP-trityl.

2 UV-vis absorption spectra

The UV-vis spectra of the three investigated porphyrin building blocks, ZnTPP, H₂TPP and MgTPP, recorded in toluene solution at room temperature are shown in Figure S4. As it is typical for this class of chromophores, the most intense absorption peak in the visible range is observed around 420 nm (Soret band), while the absorption peaks of the much less intense Q-bands cover the region from about 500 to 660 nm.

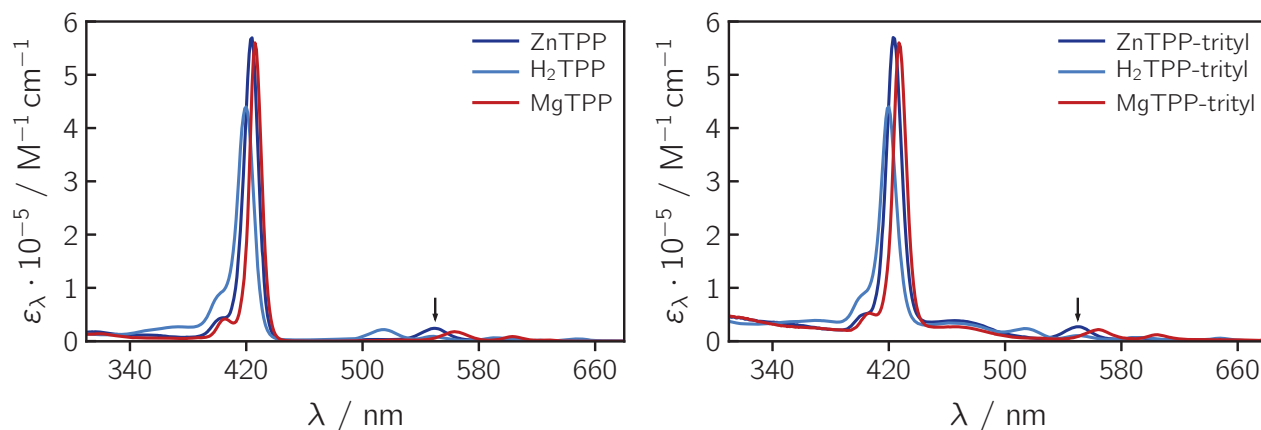


Figure S4: UV-vis absorption spectra of the investigated tetraphenyl-porphyrins (*left*) and the corresponding porphyrin-trityl compounds (*right*) scaled to their known molar absorption coefficients. It is assumed that the molar absorption coefficient of the porphyrin is not influenced by addition of the trityl moiety. The excitation wavelength of 550 nm, chosen for most experiments, is indicated by a black arrow.

The molar absorption coefficients of the three porphyrins at the Soret band maximum amount to $\epsilon(\text{ZnTPP}, 423 \text{ nm}) = 5.74 \cdot 10^5 \text{ M}^{-1} \text{ cm}^{-1}$, $\epsilon(\text{H}_2\text{TPP}, 420 \text{ nm}) = 4.43 \cdot 10^5 \text{ M}^{-1} \text{ cm}^{-1}$ and $\epsilon(\text{MgTPP}, 427 \text{ nm}) = 5.62 \cdot 10^5 \text{ M}^{-1} \text{ cm}^{-1}$ [3]. In the optical experiments, photoexcitation was carried out at 550 nm.

From the characterisation of the porphyrin-trityl compounds it is known that, in a few percent of the sample, the trityl is present in its alcohol rather than its radical form. From the UV-vis and fs-TA spectra of the compounds it can be estimated that this percentage of diamagnetic impurity amounts to roughly $\sim 0\text{--}3\%$ in the case of ZnTPP-trityl and H₂TPP-trityl and to roughly 30% in the case of MgTPP-trityl (for reasons detailed in the synthesis section above). In the transient EPR experiments, these molecules, where the trityl radical has been deactivated, will show up as a triplet ‘impurity’ and contribute to the background signal. Since the triplet signal from porphyrins is quite strong (triplet yields of $>80\%$ [4, 5] and strong spin polarisation), this background can be quite substantial compared to the intensity of the quartet signal.

3 Approximation of the Förster energy transfer rate

The molar absorption coefficient of the trityl radical was estimated from UV-vis data of ZnTPP and ZnTPP-trityl (cf. Figure S4), taking into account the known molar absorption coefficient of ZnTPP at the Soret band maximum of $5.7 \cdot 10^5 \text{ M}^{-1} \text{ cm}^{-1}$ [3, 6]. It was assumed that the molar absorption coefficient at the intensity maximum of the porphyrin Soret band is the same for ZnTPP and ZnTPP-trityl and that the spectrum of ZnTPP-trityl (at least at 460 nm) is equal to the sum of the spectra of ZnTPP and trityl radical with a molar ratio of 1:1. The value for the fluorescence quantum yield of ZnTPP was taken from reference [7] and the center-to-center distance r_{DA} from a DFT model of the ZnTPP-trityl structure.

Table S1: Overview of the results from an approximate calculation of the Förster radius, FRET rates, and efficiencies for ZnTPP-trityl. The following parameters were used: $r_{DA} = 1.3$ nm, $n = 1.496$ (toluene), $\tau_{F,0}^D = 2.6$ ns, $\Phi_{F,0}^D = 0.04$, $\varepsilon^A(460 \text{ nm}) = 3.8 \cdot 10^4 \text{ M}^{-1}\text{cm}^{-1}$.

κ^2	R_0 / nm	τ_{FRET} / ps	Φ_{FRET} / %
$\frac{2}{3}$ (random)	2.42	63	97.6
1 (parallel)	2.59	42	98.4
4 (collinear)	3.26	10	99.6

The Förster radius R_0 (obtained in nm) can be calculated according to [8]

$$R_0^6 = 8.785 \cdot 10^{-11} \frac{\Phi_{F,0}^D \kappa^2}{n^4} \int I_F^D(\lambda) \varepsilon^A(\lambda) \lambda^4 d\lambda \quad (\text{S1})$$

with

$$\int I_F^D(\lambda) d\lambda = 1 \quad (\text{S2})$$

where $\Phi_{F,0}^D$ and I_F^D are the fluorescence quantum yield and fluorescence intensity of the donor, ε^A is the molar absorption coefficient (in $\text{M}^{-1}\text{cm}^{-1}$) of the acceptor and n the refractive index of the medium. The orientation factor κ^2 accounts for the relative orientation of the two transition dipole moment vectors (emission of donor and absorption of acceptor) with respect to the axis connecting the FRET pair.

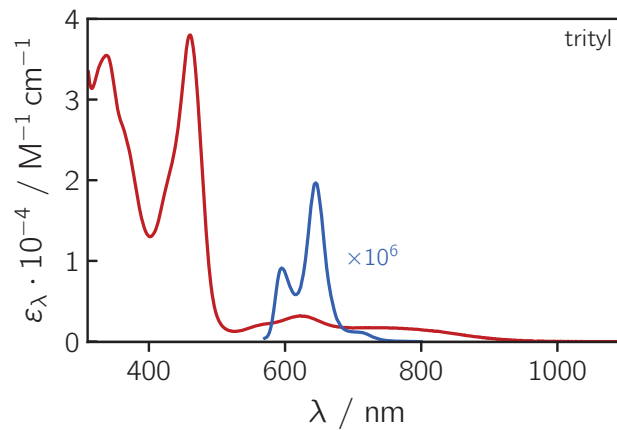


Figure S5: UV-vis absorption spectrum of the trityl radical. The fluorescence spectrum of ZnTPP is superimposed (in blue) for an illustration of the spectral overlap.

The energy transfer rate and FRET efficiency are then given as

$$\tau_{\text{FRET}}^{-1} = k_{\text{FRET}} = \frac{1}{\tau_{F,0}^D} \left(\frac{R_0}{r_{DA}} \right)^6 \quad (\text{S3})$$

and

$$\Phi_{\text{FRET}} = 1 - \frac{\tau_{\text{FRET}}}{\tau_{F,0}^D} \quad (\text{S4})$$

where $\tau_{F,0}^D$ is the fluorescence lifetime of the donor in the absence of any quenchers and r_{DA} is the center-to-

center distance (point dipole) between donor and acceptor. The results obtained for ZnTPP-trityl assuming different values for κ^2 are summarised in Table S1. The spectral overlap of the trityl absorption and ZnTPP fluorescence spectra is illustrated in Figure S5.

4 Additional fs-TA data and global kinetic analysis

4.1 Room temperature setup and spectra

For the room temperature femtosecond TA experiments the samples were prepared in either toluene or 2-methyl-THF solutions. UV-vis spectra were taken before and after the measurements to verify the sample absorbances and confirm the absence of sample degradation during the measurement. Care was taken that the absorbance in the Soret-band region did not exceed a value of about 1.5, to avoid optical saturation of the ground state bleach (GSB) and thus ensure accurate intensity readings in this region. As a consequence, the absorbances at the excitation wavelengths of either 400 nm or 550 nm were fairly low (0.02–0.1).

The setup used for the room temperature measurements was described in detail elsewhere [9–12]. In brief, a Ti:Sapphire amplified laser system (Coherent Libra) with a repetition rate of 1 kHz, a pulse duration of 100 fs and a wavelength of 800 nm was used as the pulse source. Part of its output was used to pump a TOPAS-White non-collinear optical parametric amplifier tuned to deliver pulses peaking at 550 nm. For probing (330–740 nm), a supercontinuum was generated in a CaF₂ plate. The pump beam diameter at the sample was 160 μm (FWHM), while the diameter of the probe beam amounted to 100 μm . The relative polarisation of pump and probe beams was set to the magic angle and the IRF was about 180 fs.

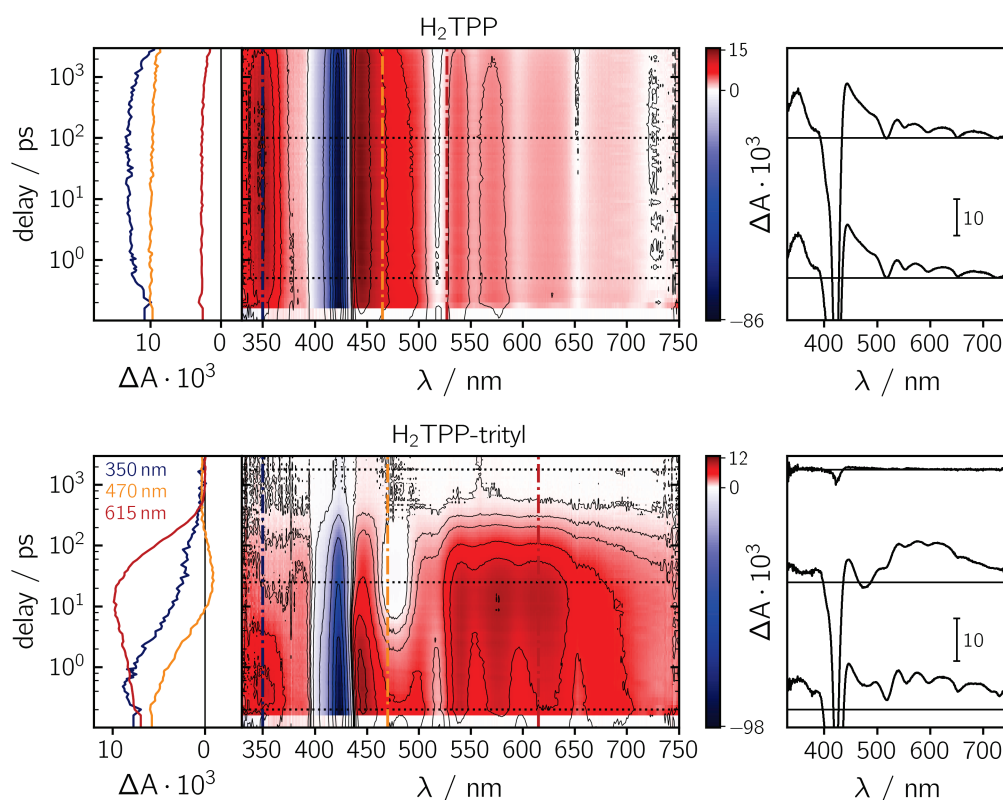


Figure S6: Femtosecond transient absorption data for H₂TPP (*top*) and H₂TPP-trityl (*bottom*) recorded in toluene solution at room temperature after photoexcitation at 550 nm.

During the experiments, the sample solutions (~ 2 mL) were flown continuously. The optical path length of the cuvette was 0.5 mm. The data were acquired with 20 averages per time point and four scans using

a pump power of about 1 mW. A total of 139 spectra were collected, with 50 linear time steps between -1 and 1 ps, followed by logarithmic time steps up to roughly 4 ns. The chopper in the probe beam path was set to a frequency of 500 Hz, while that in the pump path was set to 250 Hz. For every time point, four different sets of data were collected: (i) only the white light (probe) reaches the sample, (ii) pump and probe both blocked, (iii) pump and probe both reach the sample, (iv) only the pump reaches the sample. Signals (i) and (iii) are used for the calculation of ΔA , while signals (ii) and (iv) are needed to account for offsets and pump light scattering. The chirp of the white light was measured in a separate (OKE) experiment and accounted for in the processing of the TA spectra. In addition, solvent spectra were recorded separately under identical conditions as the samples and subtracted from the sample data following the procedure detailed in reference [13].

The TA data were analysed using home-written MATLAB routines. After subtraction of the solvent background, the data were chirp-corrected by interpolation in the time domain using a function of the form $f(x) = p_1 + \frac{p_2}{x^2} + \frac{p_3}{x^4}$ with parameters p_n determined by analysis of the corresponding OKE experiment (i.e. fit of $f(x)$ to the OKE data as a function of wavelength).

The femtosecond TA experiments at room temperature were also carried out at an excitation wavelength of 400 nm and using a solvent with a significantly higher dielectric constant (2-methyltetrahydrofuran vs toluene). No significant differences in either the spectral signatures or kinetics were observed in these two cases as shown below.

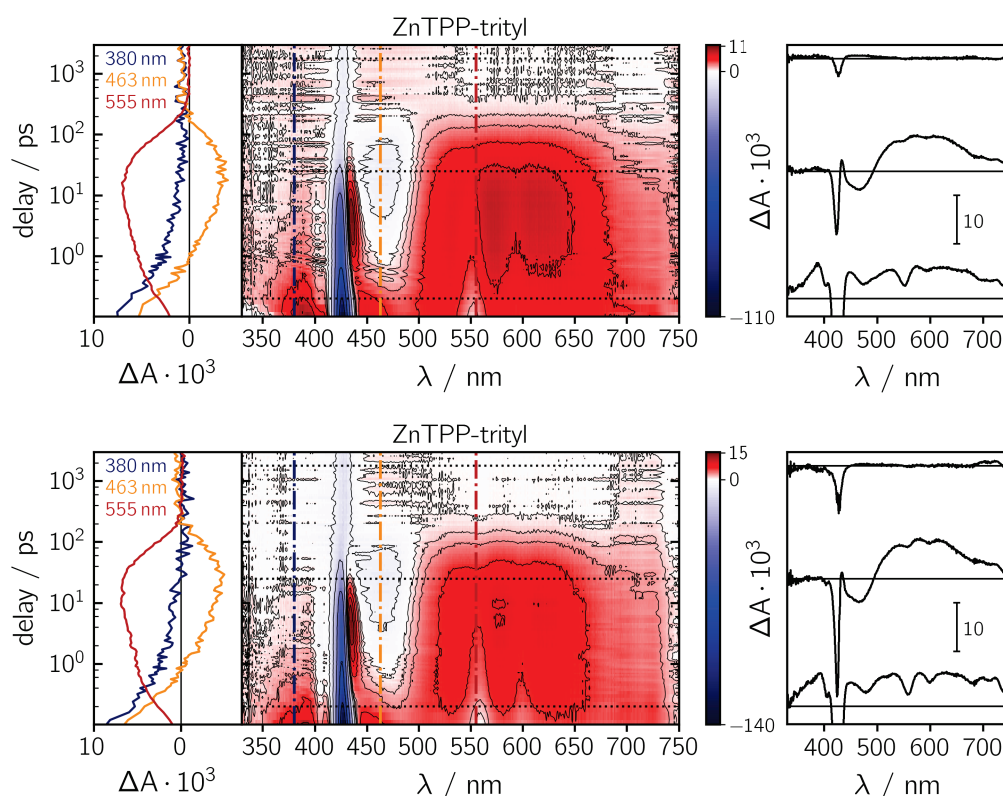


Figure S7: Femtosecond transient absorption data for ZnTPP-trityl recorded in toluene (*top*) and 2-methyltetrahydrofuran (*bottom*) solution at room temperature after photoexcitation at 400 nm.

4.2 Low temperature setup and spectra

To verify whether the efficiencies of the different excited state reactions differ under the conditions applied during the EPR measurements, femtosecond TA experiments were also performed in frozen 2-methyl-THF

solution at 85 K using an optical cryostat. The solvent, 2-methyl-THF, was distilled, deoxygenated and stored in the glove box where the sample solutions were prepared. The sample cell, composed of two quartz windows separated by a teflon spacer (~ 2 mm), was filled with the solution and assembled under oxygen exclusion in the glove box. The sample concentration was adjusted to yield an OD of about 0.3–0.6 at the excitation wavelength in the sample cuvette.

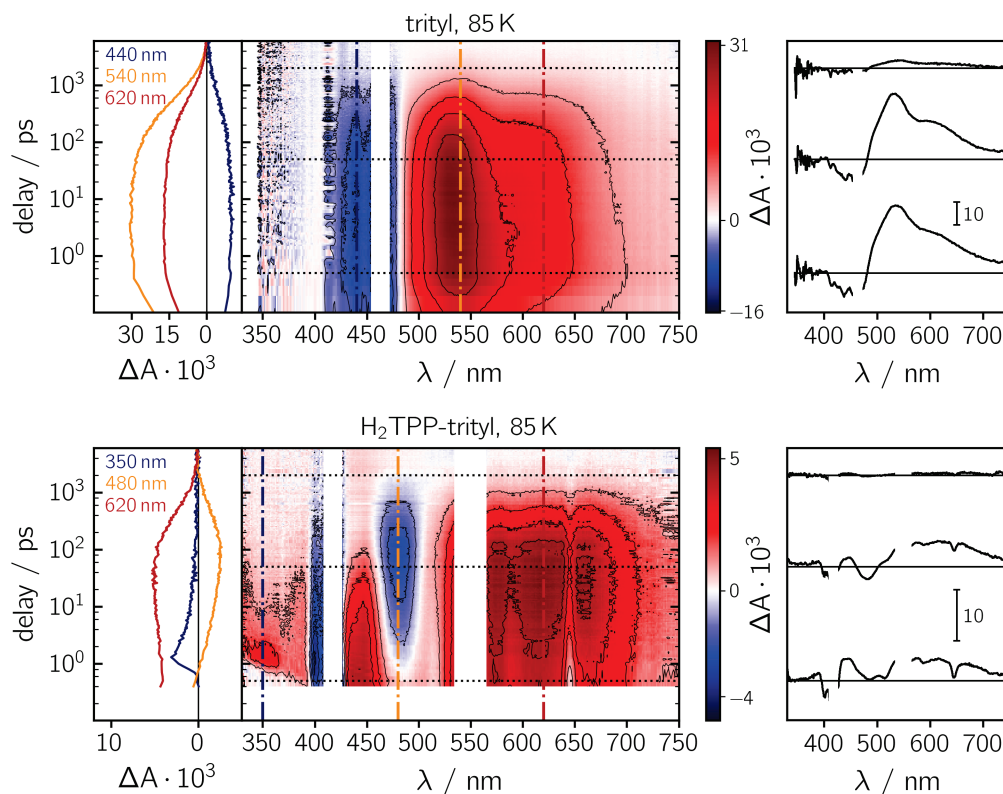


Figure S8: Femtosecond transient absorption data for the trityl radical (*top*) and H_2TPP -trityl (*bottom*) recorded in frozen 2-methyl-THF solution at 85 K after photoexcitation at 414 nm and 550 nm, respectively. The wavelength ranges dominated by artefacts from either excitation light scattering or optical saturation were cut out from the spectra.

The transient absorption measurements were performed with pulses of about 90 fs duration (centred at 827 nm) provided by an amplified Ti:sapphire system (Spitfire, Spectra Physics) at a repetition rate of 1 kHz. The fundamental beam at 827 nm is split into two parts: A small fraction is used for probe white light generation, the other part was guided through an optical parametric amplifier for excitation at 550 nm or frequency doubled for excitation at 414 nm. A commercially available Helios spectrometer (Ultrafast Systems) was used for data acquisition in combination with a slightly modified optical layout. The probe beam is delayed on an optical stage prior to white light generation in a sapphire plate and is then split in a signal and reference beam for signal detection and compensation of intensity fluctuations, respectively. To obtain the transient absorption difference signal, ΔA , the absorption was recorded in the absence and presence of the pump beam using an optical chopper in the pump beam path.

Several scans needed to be averaged until an acceptable signal-to-noise ratio could be obtained. Between individual scans, the cryostat was laterally displaced, whenever necessary, to minimise the effects of sample degradation on the acquired spectra. All TA spectra were acquired using an excitation energy of $\sim 1 \mu\text{J}$. In order to obtain an appreciable signal, a relatively high sample OD of about 0.3–0.6 at the excitation wavelength was required, resulting in optical saturation in certain regions of the spectrum around the intensity maxima of the UV-vis spectra. In addition, artifacts from pump light scatter at the excitation wavelength

could not be avoided when using the cryostat. The wavelength ranges dominated by artefacts from either excitation light scattering or optical saturation were cut out from the spectra. The data were analysed in a similar way as described above for the room temperature experiments.

4.3 Global kinetic analysis

To get a better estimate of the time constants of the excited state reaction processes, a model-free global kinetic analysis of the recorded fs-TA data was carried out [14]. In the case of the porphyrin chromophores and porphyrin-trityl compounds it was found that three and four time constants, respectively, were required in order to accurately reproduce the data recorded at room temperature, while only two time constants were needed for a satisfactory simulation of the trityl radical spectra.

The decay associated spectra (DAS) obtained for ZnTPP and H₂TPP are shown in Figure S9. In the analysis, simultaneous mono-exponential decays are assumed. The DAS are then obtained by plotting the contributions, i.e. amplitudes, of the individual time constants as a function of wavelength.

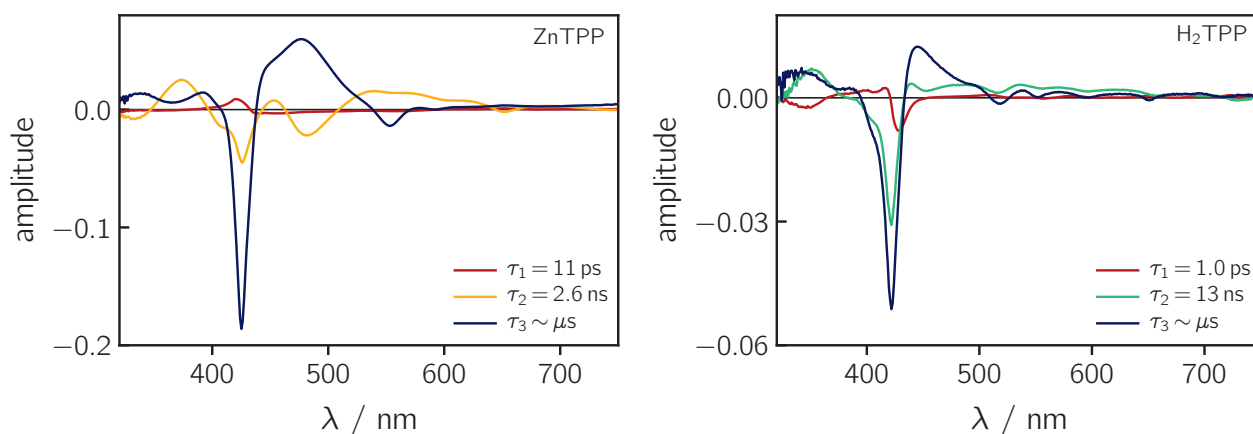


Figure S9: Decay associated spectra and associated time constants obtained from a model-free global kinetic analysis of the femtosecond TA data for ZnTPP (*left*) and H₂TPP (*right*). The lifetimes of the first excited singlet states of ZnTPP and H₂TPP are known from the literature and were kept fixed during the optimisation procedure.

The fs-TA spectra of the porphyrin chromophores, ZnTPP and H₂TPP, are well known and have been extensively analysed in the literature [15–17]. In general, after photoexcitation of the porphyrin, the first excited singlet state decays with a time constant of about 13 ns or 2.6 ns for H₂TPP and ZnTPP, respectively, to form the porphyrin triplet state in high yield [4, 5, 7]. The latter then lives for about 1 μ s in solution at room temperature [7]. The signatures of the porphyrin excited singlet and triplet states are very similar in both cases and may therefore be hard to distinguish.

The first time constants in Figure S9 can be attributed to vibrational relaxation processes occurring in the first excited singlet state of the chromophores, while the second and third time constants represent the decay of the porphyrin singlet and triplet states, respectively.

Figure S10 shows the kinetic analysis of the room temperature fs-TA spectra of the trityl radical. The experimental data could be reproduced with only two time constants, attributed to (i) relaxation within S₁ and (ii) the excited state decay of the trityl radical.

The kinetic analysis of the fs-TA spectra of ZnTPP-trityl and H₂TPP-trityl is shown in Figure S11. Of the four time constants needed to satisfactorily reproduce the experimental data, three were left to vary freely during the analysis, while the fourth time constant was fixed to the known decay constant of the excited triplet state of the porphyrins. This fourth time constant accounts for the residual porphyrin signal left after

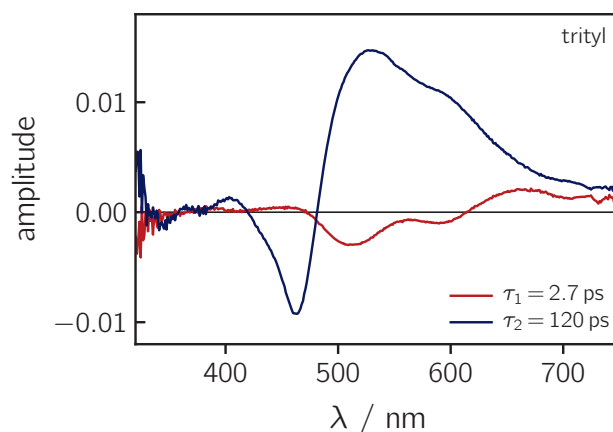


Figure S10: Decay associated spectra and associated time constants obtained from a model-free global kinetic analysis of the femtosecond TA data of the trityl radical.

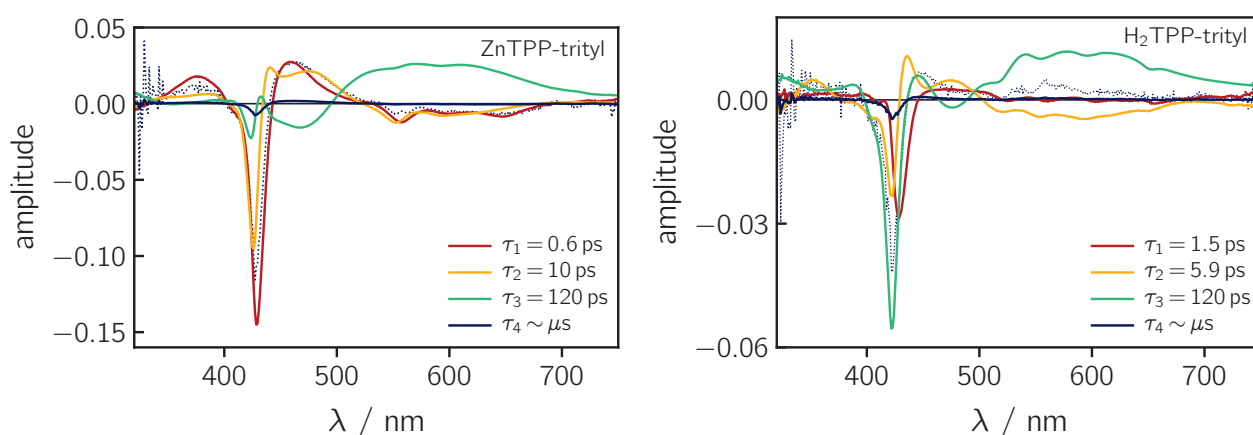


Figure S11: Decay associated spectra and associated time constants obtained from a model-free global kinetic analysis of the femtosecond TA data for ZnTPP-trityl (*left*) and H₂TPP-trityl (*right*). The lifetimes of the first excited singlet states of ZnTPP and H₂TPP are known from the literature and were kept fixed during the optimisation procedure. The blue dotted line represents a scaled version of the component in blue.

complete decay of the trityl radical excited state features (>500 ps). The remaining three time constants can be attributed to the following processes: (i) vibrational relaxation in the first excited singlet state of the porphyrin, (ii) energy transfer from the porphyrin to the trityl, i.e. decay of the porphyrin excited singlet state and simultaneous built-up of the trityl radical features, (iii) decay/lifetime of the trityl radical excited state absorption. In both cases, the energy transfer from the porphyrin to the trityl radical occurs in roughly 10 ps at room temperature.

The analysis of the room temperature fs-TA spectra of ZnTPP-trityl and H₂TPP-trityl was performed twice, either (i) with the third time constant fixed to the determined decay time of the trityl radical species (i.e. 120 ps) or (ii) leaving the third time constant to vary freely. Almost identical decay associated spectra were obtained in both cases and also the variations in the decay times are very minor. For reference, the following τ -values were obtained when leaving the third time constant to vary freely: ZnTPP-trityl – (i) 0.6 ps, (ii) 11 ps, (iii) 94 ps; H₂TPP-trityl – (i) 1.3 ps, (ii) 6.4 ps, (iii) 148 ps.

Although the quality of the data is not perfect, a kinetic analysis was also performed for the fs-TA data recorded in frozen solution. The DAS obtained for the trityl radical, for ZnTPP-trityl and for H₂TPP-trityl in frozen 2-methyl-THF at 85 K are shown in Figure S12. No significant amount of residual porphyrin signal could be detected after complete decay of the trityl excited state absorption, so only three time constants

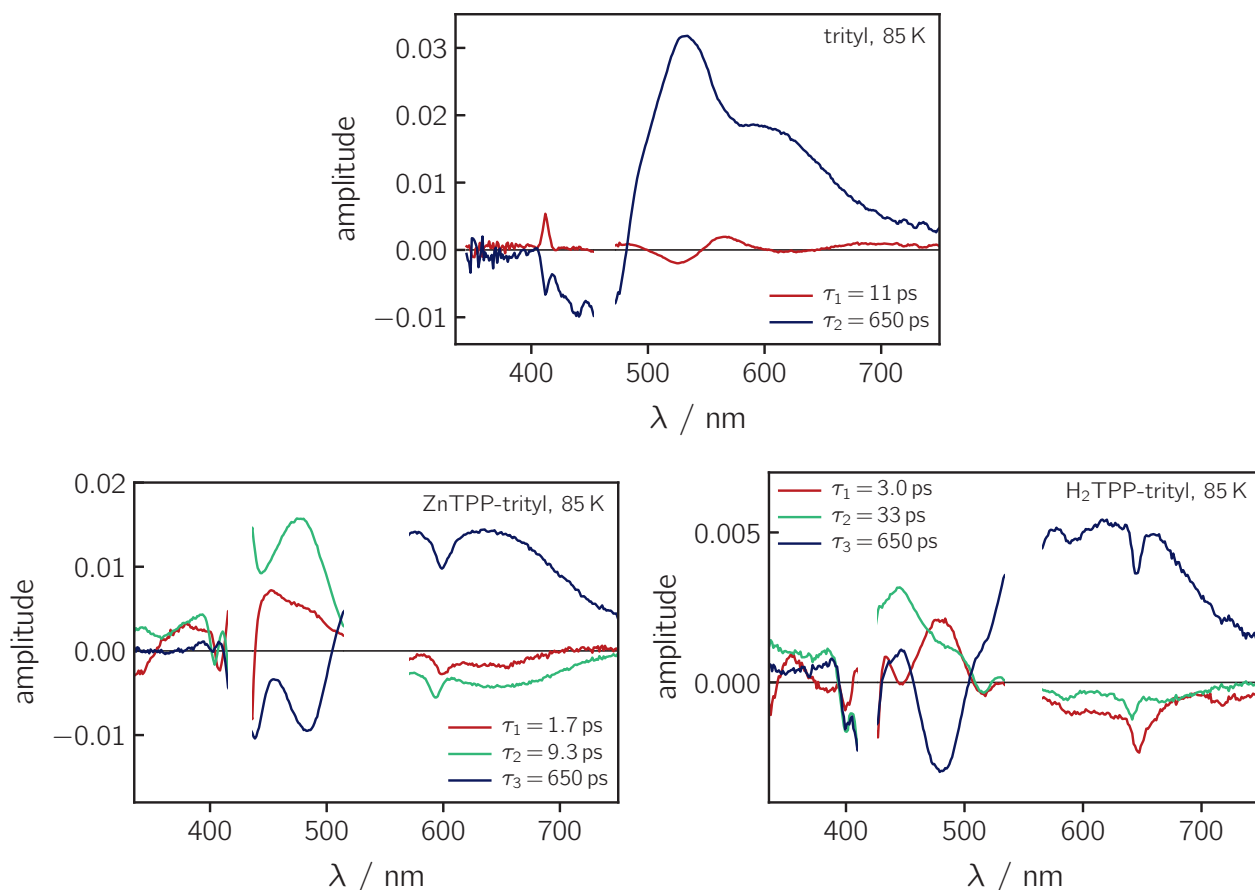


Figure S12: Decay associated spectra and associated time constants obtained from a model-free global kinetic analysis of the femtosecond TA data for trityl (*top*), ZnTPP-trityl (*bottom, left*) and H₂TPP-trityl (*bottom, right*) recorded in frozen 2-methyl-THF solution at 85 K after photoexcitation at 414 nm (*top*) or 550 nm (*bottom*).

were necessary to satisfactorily reproduce the data. It can be seen that the overall kinetics are somewhat slower in frozen solution, but the general trends and spectral features observed at room temperature are conserved: The trityl radical excited state lifetime is increased from about 120 ps to 650 ps. However, the deactivation of the excited porphyrin species in the presence of the stable radical is still almost equally fast (~ 10 ps). Thus, even at 85 K, energy transfer from the porphyrin to the trityl radical seems to dominate the excited state dynamics.

Also for this set of data, the analysis of the fs-TA spectra of ZnTPP-trityl and H₂TPP-trityl was performed twice, either with the third time constant fixed to the determined decay time of the trityl radical species (i.e. 650 ps) or leaving the third time constant to vary freely. As before, almost identical decay associated spectra were obtained in both cases. The variations in the decay times were very minor for ZnTPP-trityl (τ -values of (i) 1.6 ps, (ii) 10 ps, (iii) 560 ps); identical time constants were obtained for H₂TPP-trityl.

5 Continuous wave EPR

To characterise the g -value of the trityl radical, a continuous wave EPR spectrum of H₂TPP-trityl in toluene was recorded in the dark at room temperature. The measurement was carried out at the X-band (9.75 GHz) using a modulation amplitude of 0.1 G and a microwave power of ~ 0.13 mW. The recorded, background-corrected spectrum was frequency-corrected to 9.75 GHz and field-corrected using a carbon fibre standard [18]. A g -value of 2.0028 was obtained for the trityl radical by simulation of the spectrum using EasySpin

[19] as shown below.

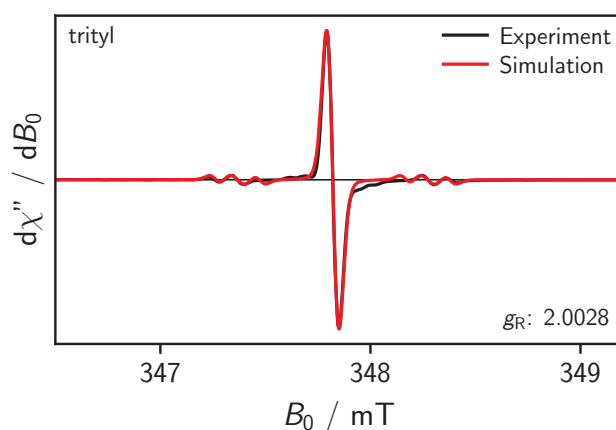


Figure S13: Room temperature continuous wave EPR spectrum of H₂TPP-trityl in toluene recorded in the dark at the X-band (9.75 GHz) using a modulation amplitude of 0.1 G and a microwave power of about 0.13 mW. The *g*-value was extracted from the numerical simulation of the spectrum superimposed in red.

6 Additional transient EPR data and simulations

6.1 EPR sample preparation and setup

For all transient cw EPR measurements, the samples were prepared with an absorbance of roughly 0.3 at the excitation wavelength of 550 nm, measured in a 2 mm cuvette. For measurements at the X-band, the samples in either toluene or 2-methyl-THF were then transferred into quartz EPR tubes with an outer diameter of 3.8 mm (inner diameter \sim 3 mm). The solutions were rapidly frozen in liquid nitrogen before insertion into the EPR resonator for the measurements.

Transient EPR measurements were carried out on a Bruker ELEXSYS E580 spectrometer operated at the X-band (9.75 GHz) and equipped with a Bruker EN 4118X-MD4 resonator. During the measurement, the sample was kept at a constant temperature (80 K, unless stated otherwise) using an Oxford Instruments nitrogen gas-flow cryostat (CF 935). The samples were excited through the top of the sample holder with depolarised light at 550 nm using an excitation energy of 1 mJ at a repetition rate of 20 Hz (pulse duration \sim 5 ns).

The spectra were acquired in direct detection mode with a videoamplifier bandwidth of 20 MHz using the built-in transient recorder (DC-AFC) and a microwave power of 1.5 mW (20 dB). Any positive signal thus corresponds to an absorptive transition (*a*) and any negative signal to an emissive (*e*) one. The time resolution of the experiment is limited by the resonator bandwidth to about 200 ns (\sim 5 MHz). For samples giving only very weak signals, a possibility to enhance the signal-to-noise ratio of the data is to work with the transient recorder in AC-AFC mode and to feed the transient signal through a low-noise voltage preamplifier (Stanford Research Systems SR 560) before it enters the detection circuitry. This configuration was typically used for the acquisition of the data of the porphyrin-trityl compounds, using a bandpass filter of 3 kHz–1 MHz. The time resolution of the spectra is thus somewhat compromised for a better resolution of the spectral shape. Typically, for every magnetic field value, a time trace with 4096 points was recorded using a time base of 4 ns. After data acquisition, the 2D spectra were baseline-corrected in both dimensions using a home-written MATLAB routine.

For the transient cw EPR measurements at Q-band frequencies (34.0 GHz) a Bruker EN 5107D2 resonator was used and the samples were prepared in quartz tubes with an outer diameter of 1.6 mm (inner diameter

of ~ 1 mm). The samples were again excited through the top of the sample holder using an excitation energy of only ~ 0.5 mJ. All other experimental parameters were kept the same.

6.2 Triplet state spectra and simulations

Transient cw EPR spectra of the triplet states of H₂TPP, ZnTPP and MgTPP recorded in frozen toluene at 80 K are shown in Figure S14. The shape of the spectra of these compounds was found not to change significantly over the course of the triplet state lifetime. The spectra shown in the figure were averaged over a time window from 0.2 μ s to 1 μ s after laser excitation. It can be seen that, due to different intersystem crossing mechanisms, the triplet states of H₂TPP and ZnTPP show an opposite spin polarisation [20]. While the spin polarisation pattern in H₂TPP (from low to high field) is eeeaaa, an aaaeee polarisation pattern is obtained for ZnTPP. The triplet state *D*-value of both compounds is known to be positive [21], therefore the observed spin polarisation corresponds to an overpopulation of the in-plane triplet sublevels (*X*, *Y*) in H₂TPP and a predominant population of the out-of-plane triplet sublevel (*Z*) in ZnTPP. Also the triplet state of MgTPP shows an opposite spin polarisation (eeeeaa) as compared to ZnTPP. To determine accurate *g*-values as well as the zero-field splitting *D*-values and relative populations of the excited multiplet states, numerical simulations of the experimental spectra were performed using the MATLAB package EasySpin in combination with home-written fitting routines. The simulation results and parameters can be found in Figure S14.

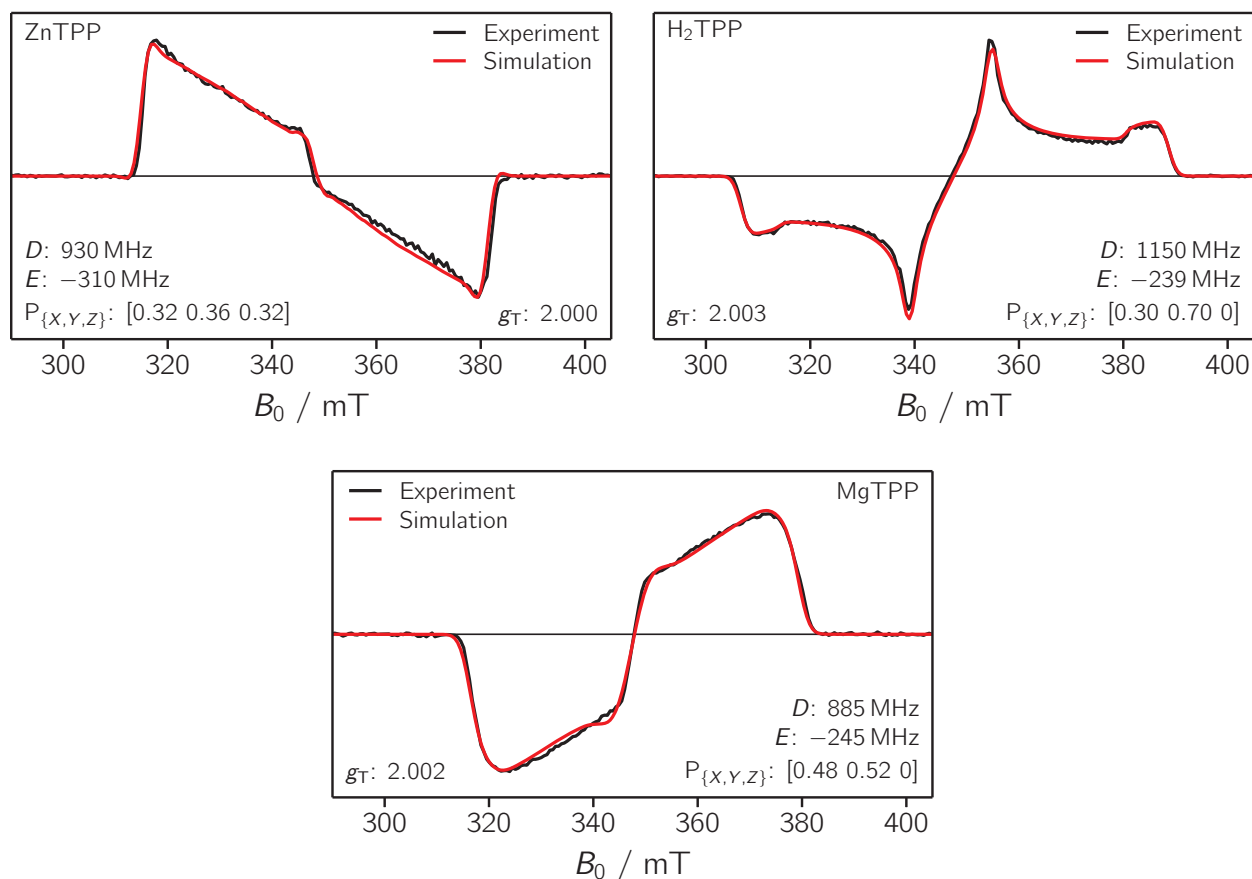


Figure S14: Triplet state transient cw EPR spectra of ZnTPP (left, top) and H₂TPP (right, top) and MgTPP (bottom) recorded about 1 μ s after photoexcitation at the X-band (9.75 GHz) in frozen 2-methyl-THF solution at 80 K together with the best numeric fit to the experimental data. The simulation parameters are indicated in the figure.

Apart from differences in the spin polarisation pattern, it is noted that the triplet state D -value, reflected in the width of the triplet state spectrum, is significantly smaller in ZnTPP as compared to H₂TPP, potentially pointing either towards an increased delocalisation of the triplet state wavefunction in ZnTPP or a different excited state geometry (due to the fact that the porphyrin core is no longer planar in H₂TPP).

In theory, spin-orbit coupling contributions to the ZFS parameter D could be expected in ZnTPP, but previous experiments on Zn-porphyrin triplet states suggest that this is not the case [22]. In addition, in a series of linear Zn-porphyrin oligomers, all experimental observations and trends in D could be consistently explained and reproduced by quantum chemical calculations, taking only the spin-spin contribution to the ZFS into account [20, 23]. Also the fact that the experimental D -value (i.e. spectral width) is almost identical for MgTPP and ZnTPP suggests that only spin-spin contributions to D need to be taken into account.

An overview of the magnetic parameters obtained as a result from the spectral simulations of the triplet and quartet state spectra (cf. also main text) is given in Table S2.

Table S2: Overview of the g - and D -values of the different multiplet states present before and after photoexcitation of H₂TPP-trityl, ZnTPP-trityl and MgTPP-trityl. The g -values of the triplet and radical as well as the D -values of the triplet and quartet state were determined from the experimental data, while the expected g -values of the excited doublet and quartet states were calculated based on g_T and g_R .

Compound	g_T	g_R	g_{D_1}	g_Q	D_T / MHz	D_Q / MHz
H ₂ TPP-trityl	2.0030	2.0028	2.0031	2.0029	1150	340
ZnTPP-trityl	2.000	2.0028	1.999	2.001	930	310
MgTPP-trityl	2.002	2.0028	2.0017	2.0023	890	260

6.3 Discussion of the triplet contribution to the transient EPR spectra

Transient cw EPR spectra of H₂TPP-trityl and ZnTPP-trityl at different time delays after photoexcitation are shown in Figure S15. In all samples, a minor contribution of the corresponding porphyrin triplet state was observed in addition to the quartet state features. Two possible reasons for this could be imagined: (i) As mentioned above, in a small percentage of the molecules, the trityl radical could have been transformed into the corresponding diamagnetic alcohol. Since the second spin centre would be inactive in this case, a triplet background should be observed in both the optical and EPR experiments. (ii) An alternative reason could originate from a relatively large spread of molecular conformations, frozen in at the freezing point of the solvent: Different molecular conformations – with varying dihedral angles of the phenyl linker – should experience different J -couplings between chromophore and radical. For some conformations, the orbital overlap and thus J_{TR} might be too small for quartet state formation to occur. Such molecules, where the triplet state does not feel the presence of the unpaired electron spin of the radical, would also show up as porphyrin triplets in the transient EPR spectra. Since the spin-polarised EPR signals of porphyrin triplets are very strong, already a contribution of only ~1–3% could account for the observed triplet background.

To obtain the pure quartet state spectra as shown in the main text, experimental spectra of ZnTPP and H₂TPP were recorded under the same conditions and multiplied by an appropriate scaling factor before subtraction from the corresponding porphyrin-trityl data. Exemplary spectra for ZnTPP-trityl and H₂TPP-trityl before and after subtraction of the triplet signal are shown in Figure S15.

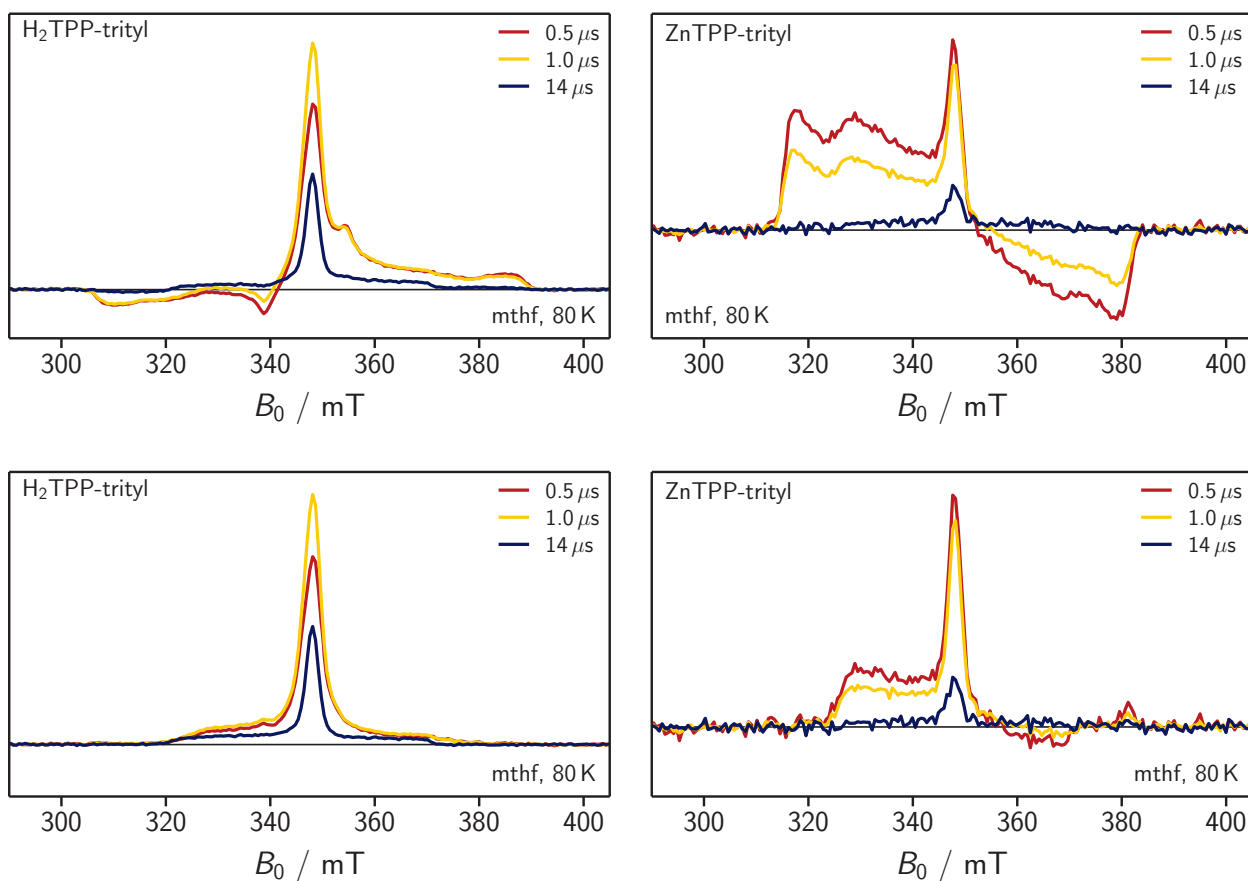


Figure S15: Transient cw EPR spectra of H₂TPP-trityl (*left*) and ZnTPP-trityl (*right*) at different time delays after photoexcitation, before (*top*) and after (*bottom*) subtraction of the triplet background.

6.4 Temperature dependence of the transient EPR spectra

Figure S16 shows transient cw EPR spectra of H₂TPP-trityl and ZnTPP-trityl recorded at different temperatures. It is noted that the spectral shape of the quartet state does not seem to be significantly affected by temperature in the range between 50 and 140 K.

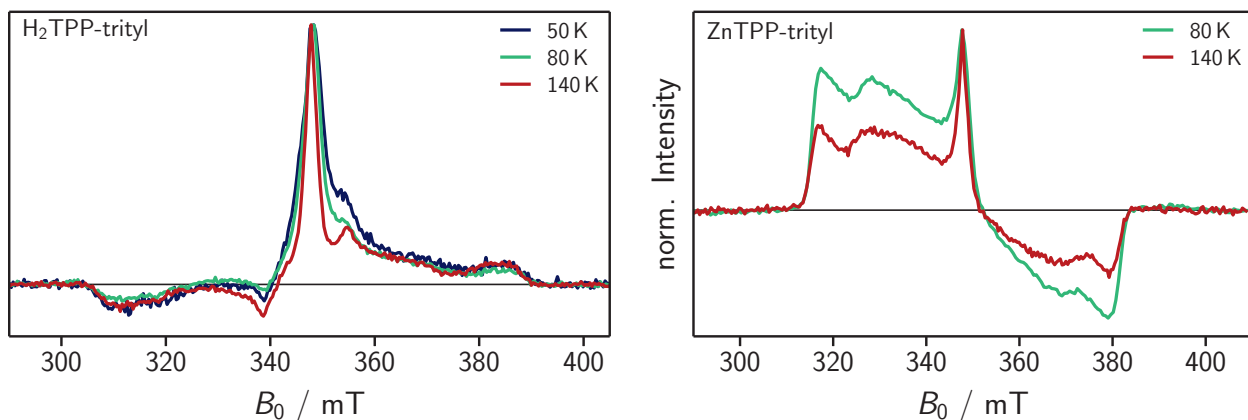


Figure S16: Intensity normalised transient cw EPR spectra of H₂TPP-trityl (*left*) and ZnTPP-trityl (*right*) recorded at different temperatures (as indicated).

6.5 Additional quartet spectra and simulations

Figure S17 shows a schematic energy diagram indicating the allowed EPR transitions of a quartet state. For every orientation of the magnetic field (with respect to the **D**-tensor axes), three transitions are possible, i.e. $|\pm \frac{1}{2}\rangle \leftrightarrow |\pm \frac{3}{2}\rangle$ and $|+\frac{1}{2}\rangle \leftrightarrow |-\frac{1}{2}\rangle$. The maximum spectral separation arises from molecules with their Z-axis parallel to the magnetic field direction and corresponds to $4D_Q$.

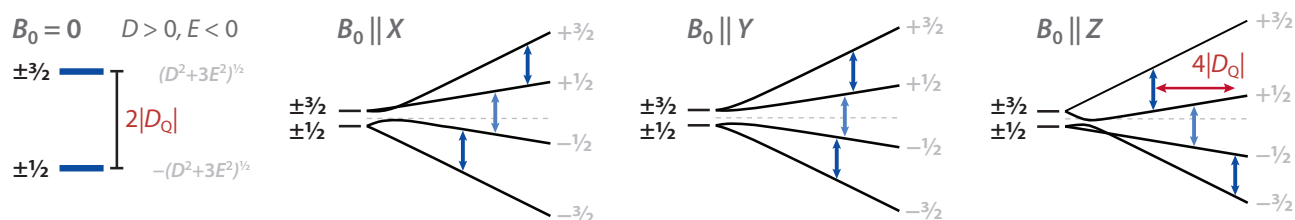


Figure S17: Schematic representation of the energy levels of the quartet state and their Zeeman splitting at different orientations of the external magnetic field with respect to the zero-field-splitting tensor axes. The allowed EPR transitions are indicated by blue arrows.

A comparison of the Q-band transient cw EPR spectra of H₂TPP-trityl and ZnTPP-trityl is shown in Figure S18.

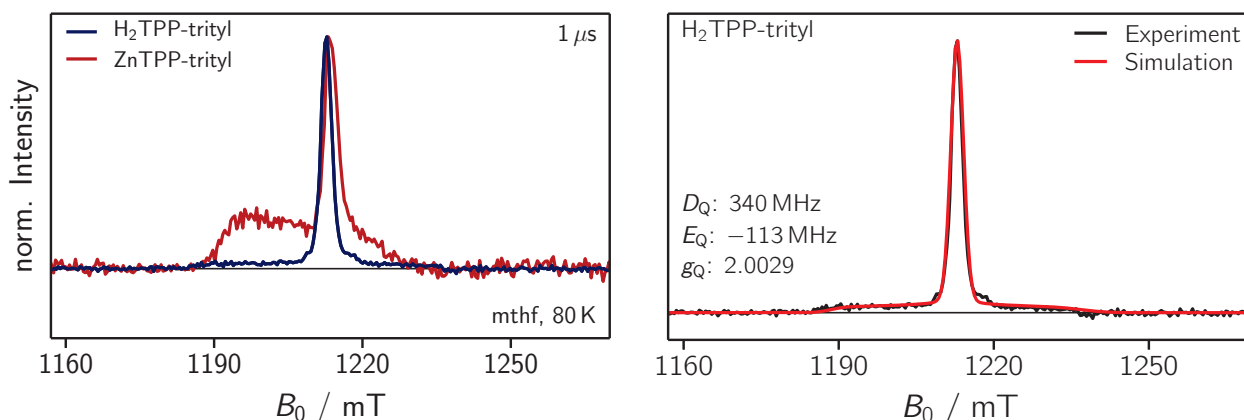


Figure S18: Comparison of the quartet state spectra at $\sim 1\mu\text{s}$ after photoexcitation of H₂TPP-trityl and ZnTPP-trityl recorded at the Q-band (34.0 GHz) in frozen 2-methyl-THF solution at 80 K (*left*) and simulation of the H₂TPP-trityl spectrum (*right*). The simulation parameters (pure net polarisation) are indicated.

6.6 Discussion of the low signal intensity in transient EPR

Unfortunately it is very difficult to make any predictions about the (expected) strength of spin polarised signals, since the mechanism of spin polarisation cannot be predicted easily. Weak spin polarised EPR signals might either arise from an intrinsically weak spin polarisation (i.e. only small population differences), fast spin relaxation, or the fact that the (potentially strongly) spin polarised species is produced only with a low yield.

Regarding the investigated porphyrin-trityl compounds, it is likely that the weak quartet signal observed by transient cw EPR is due to a low quartet formation yield, since no quartet signal could at all be detected in pulse mode (not even at temperatures as low as 5 K). This interpretation is also in agreement with the optical experiments, suggesting rapid and very efficient deactivation of the chromophore's excited state by energy transfer. In addition, no significant changes in the intensity of the radical signal could be observed

in pulse mode upon photoexcitation at 80 K (cf. Figure S19), also implying a rather low quartet formation yield (assuming that the excitation efficiency is high).

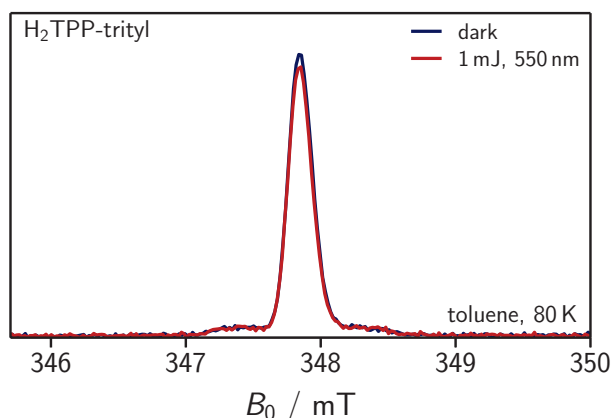


Figure S19: Comparison of the FID-detected field-swept EPR spectra of H₂TPP-trityl recorded with and without photoexcitation in frozen toluene at 80 K.

7 DFT calculations

All DFT calculations were performed using the ORCA program package (version 4.0). For the calculation of the spin density, the structures were first optimised in their (singlet or doublet) ground states using different functionals (CAM-B3LYP, B3LYP, BP86) in combination with the def2-TZVP basis set, RI approximation, and dispersion correction to the energies (D3). Magnetic property calculations (spin densities and hyperfine coupling tensors) in the triplet or quartet states used either the B3LYP or BP86 functionals, in combination with the EPR-II basis set.

For the calculation of the rotational barrier using different functionals (CAM-B3LYP, B3LYP, BP86) in combination with the def2-TZVP basis set, a transition state search and optimisation was first carried out. Frequency calculations confirmed the presence of exactly one imaginary frequency. Starting from the transition state, a series of constraint geometry optimisation steps was performed, scanning the dihedral angle between the porphyrin plane and the plane of the phenyl substituent. Finally, for different thermally accessible dihedral angles, the triplet state spin density was calculated as described above.

A visual representation of some of these results is shown in Figure S20.

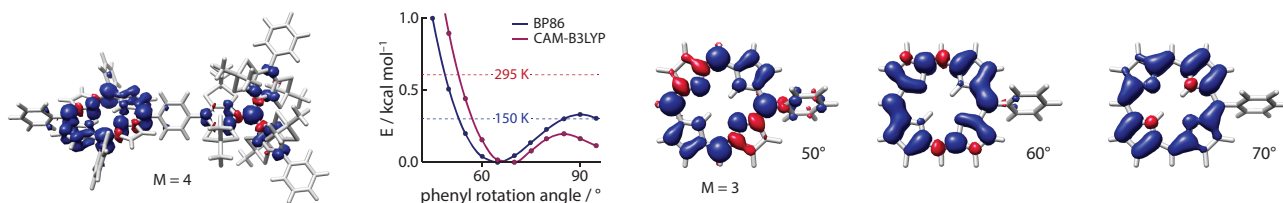


Figure S20: Visualisation of the spin density in the quartet state of H₂TPP-trityl (*left*) and triplet state spin-density distributions on the porphyrin moiety for different thermally accessible dihedral angles between the porphyrin plane and the phenyl linker (*right*).

The different functionals used here predict the energetic minimum for slightly different dihedral angles. However, it can be stated that the energetically preferred dihedral angle is roughly equal to 70°. At room temperature, all dihedral angles between 50 and 130° can be assumed to be significantly populated.

In low temperature measurements, the range of accessible conformations will be governed by the respective situation at the freezing point of the solvent. The freezing point of toluene amounts to roughly 180 K, while that of 2-methyl-THF is ~ 110 K. The exchange interaction between triplet and radical, J_{TR} , will necessarily be different for different molecular conformations since the orbital overlap is affected by rotation of the linker. It is therefore expected that the distribution of exchange interactions is significantly narrower in frozen solution, as compared to room temperature, and shifted towards lower values. The reduced conformational space in frozen solution (restricting the phenyl group rotation to less favourable conformations in terms of orbital overlap) should lead to an overall decrease in J_{TR} , while in fluid solution also conformations with greater $\pi - \pi$ overlap can be accessed.

From the visualisation of the porphyrin triplet state spin density for different dihedral angles of the phenyl linker in Figure S20, it can be seen that already at a dihedral angle of 50° a significant amount of the spin density is spread out onto the phenyl linker.

From the optimised structure of ZnTPP-trityl, a center-to-center distance of 1.3 nm (as used in the calculations of the Förster energy transfer rate) was obtained. However, the effective coupling distance between the two spin centres is predicted to be considerably shorter than the center-to-center distance, due to a significant delocalisation of both the radical and triplet spin densities.

References

- [1] Fleck, N.; Hett, T.; Brode, J.; Meyer, A.; Richert, S.; Schiemann, O. C–C cross coupling reactions of trityl radicals: Spin density delocalization, exchange coupling and a spin label. *J. Org. Chem.* **2019**, *84*, 3293–3303.
- [2] Lindsey, J. S.; Woodford, J. N. A simple method for preparing magnesium porphyrins. *Inorg. Chem.* **1995**, *34*, 1063–1069.
- [3] Taniguchi, M.; Lindsey, J. S. Database of absorption and fluorescence spectra of >300 common compounds for use in PhotochemCAD. *Photochem. Photobiol.* **2018**, *94*, 290–327.
- [4] Harriman, A. Luminescence of porphyrins and metalloporphyrins. Part 1.—zinc(II), nickel(II) and manganese(II) porphyrins. *J. Chem. Soc., Faraday Trans. 1* **1980**, *76*, 1978–1985.
- [5] Harriman, A. Luminescence of porphyrins and metalloporphyrins. Part 3.—heavy atom effects. *J. Chem. Soc., Faraday Trans. 2* **1981**, *77*, 1281–1291.
- [6] Barnett, G. H.; Hudson, M. F.; Smith, K. M. Concerning meso-tetraphenylporphyrin purification. *J. Chem. Soc., Perkin Trans. 1* **1975**, 1401–1403.
- [7] Montalti, M.; Credi, A.; Prodi, L.; Gandolfi, M. T. *Handbook of photochemistry*; CRC Press, Taylor & Francis Group: Boca Raton, 2006.
- [8] Lakowicz, J. R. *Principles of fluorescence spectroscopy*; Springer: New York, 2006.
- [9] Laimgruber, S.; Schachenmayr, H.; Schmidt, B.; Zinth, W.; Gilch, P. A femtosecond stimulated raman spectrograph for the near ultraviolet. *Appl. Phys. B* **2006**, *85*, 557–564.
- [10] Laimgruber, S.; Schmierer, T.; Gilch, P.; Kiewisch, K.; Neugebauer, J. The ketene intermediate in the photochemistry of ortho-nitrobenzaldehyde. *Phys. Chem. Chem. Phys.* **2008**, *10*, 3872–3882.
- [11] Fröbel, S.; Buschhaus, L.; Villnow, T.; Weingart, O.; Gilch, P. The photoformation of a phthalide: a ketene intermediate traced by FSRs. *Phys. Chem. Chem. Phys.* **2015**, *17*, 376–386.
- [12] Reiffers, A.; Torres Ziegenbein, C.; Schubert, L.; Diekmann, J.; Thom, K. A.; Kühnemuth, R.; Griesbeck, A.; Weingart, O.; Gilch, P. On the large apparent Stokes shift of phthalimides. *Phys. Chem. Chem. Phys.* **2019**, *21*, 4839–4853.
- [13] Lorenc, M.; Ziolek, M.; Naskrecki, R.; Karolczak, J.; Kubicki, J.; Maciejewski, A. Artifacts in femtosecond transient absorption spectroscopy. *Appl. Phys. B* **2002**, *74*, 19–27.

- [14] Satzger, H.; Zinth, W. Visualization of transient absorption dynamics – towards a qualitative view of complex reaction kinetics. *Chem. Phys.* **2003**, *295*, 287–295.
- [15] Baskin, J. S.; Yu, H.-Z.; Zewail, A. H. Ultrafast dynamics of porphyrins in the condensed phase: I. Free base tetraphenylporphyrin. *J. Phys. Chem. A* **2002**, *106*, 9837–9844.
- [16] Yu, H.-Z.; Baskin, J. S.; Zewail, A. H. Ultrafast dynamics of porphyrins in the condensed phase: II. Zinc tetraphenylporphyrin. *J. Phys. Chem. A* **2002**, *106*, 9845–9854.
- [17] Abraham, B.; Nieto-Pescador, J.; Gundlach, L. Ultrafast relaxation dynamics of photoexcited zinc-porphyrin: Electronic–vibrational coupling. *J. Phys. Chem. Lett.* **2016**, *7*, 3151–3156.
- [18] Herb, K.; Tschaggelar, R.; Denninger, G.; Jeschke, G. Double resonance calibration of *g* factor standards: Carbon fibers as a high precision standard. *J. Magn. Reson.* **2018**, *289*, 100–106.
- [19] Stoll, S.; Schweiger, A. EasySpin, a comprehensive software package for spectral simulation and analysis in EPR. *J. Magn. Reson.* **2006**, *178*, 42–55.
- [20] Richert, S.; Tait, C. E.; Timmel, C. R. Delocalisation of photoexcited triplet states probed by transient EPR and hyperfine spectroscopy. *J. Magn. Reson.* **2017**, *280*, 103–116.
- [21] Tait, C. E.; Neuhaus, P.; Anderson, H. L.; Timmel, C. R. Triplet state delocalization in a conjugated porphyrin dimer probed by transient electron paramagnetic resonance techniques. *J. Am. Chem. Soc.* **2015**, *137*, 6670–6679.
- [22] Van der Waals, J. H.; Van Dorp, W. G.; Schaafsma, T. J. In *The Porphyrins, Vol IV*; Dolphin, D., Ed.; Academic Press Inc.: New York, 1979.
- [23] Tait, C. E.; Neuhaus, P.; Peeks, M. D.; Anderson, H. L.; Timmel, C. R. Transient EPR reveals triplet state delocalization in a series of cyclic and linear pi-conjugated porphyrin oligomers. *J. Am. Chem. Soc.* **2015**, *137*, 8284–8293.

[A5]: SLIM: A Short-Linked, Highly Redox-Stable Trityl Label for High-Sensitivity In-Cell EPR Distance Measurements

Reprinted with permission from

Nico Fleck, Caspar A. Heubach, Tobias Hett, Florian R. Haege, Pawel P. Bawol, Helmut Batruschat, Olav Schiemann*, *Angew. Chem.* **2020**, *132*, 9854 – 9859.

Nico Fleck, Caspar A. Heubach, Tobias Hett, Florian R. Haege, Pawel P. Bawol, Helmut Batruschat, Olav Schiemann*, *Angew. Chem. Int. Ed.* **2020**, *59*, 9767 - 9772.

Published with Open Access by WILEY-VCH (Weinheim, DE) under CC-BY license ©**2020** to the authors.

Contributions:

- Experimental Work:
 - Organic synthesis incl. compound characterization
 - cw-EPR spectroscopy incl. reduction kinetics
 - Microinjection into oocytes
- Writing of the manuscript



Spin Labeling Hot Paper

How to cite: *Angew. Chem. Int. Ed.* **2020**, *59*, 9767–9772

International Edition: doi.org/10.1002/anie.202004452

German Edition: doi.org/10.1002/ange.202004452

SLIM: A Short-Linked, Highly Redox-Stable Trityl Label for High-Sensitivity In-Cell EPR Distance Measurements

Nico Fleck, Caspar A. Heubach, Tobias Hett, Florian R. Haege, Pawel P. Bawol, Helmut Baltruschat, and Olav Schiemann*

Abstract: The understanding of biomolecular function is coupled to knowledge about the structure and dynamics of these biomolecules, preferably acquired under native conditions. In this regard, pulsed dipolar EPR spectroscopy (PDS) in conjunction with site-directed spin labeling (SDSL) is an important method in the toolbox of biophysical chemistry. However, the currently available spin labels have diverse deficiencies for in-cell applications, for example, low radical stability or long bioconjugation linkers. In this work, a synthesis strategy is introduced for the derivatization of trityl radicals with a maleimide-functionalized methylene group. The resulting trityl spin label, called SLIM, yields narrow distance distributions, enables highly sensitive distance measurements down to concentrations of 90 nM, and shows high stability against reduction. Using this label, the guanine-nucleotide dissociation inhibitor (GDI) domain of *Yersinia outer protein O* (YopO) is shown to change its conformation within eukaryotic cells.

Introduction

Carbon-centered trityl radicals have emerged as important molecules for in-vivo imaging,^[1] oximetry,^[2,3] pH-sensing,^[3] and as polarizing agents in dynamic nuclear polarization (DNP)^[4,5] experiments. Additionally, the so-called Finland trityl **1**^[6] (Figure 1) has been used for synthesizing trityl-based spin labels **2**–**8**^[7–11] out of which **2**^[7] and **3**^[8] paved the way for biomolecular structure determination at physiological temperatures using pulsed dipolar electron-paramagnetic-resonance spectroscopy (PDS).^[12,13] Furthermore, trityl labels **4** and **7** have been shown to be suitable for PDS measurements within cells.^[9,14] Advantages of trityl labels are their long relaxation times T_M at room temperature,^[15] their single-line

EPR spectra yielding large signal-to-noise ratios (SNR),^[16] their spin state of $S = 1/2$, which makes data analysis simple,^[17] and their increased reduction stability compared to *gem*-dimethylnitroxides allowing for in-cell measurements.^[9,14] Although such in-cell measurements are possible, the currently used trityls are still reduced within cells.^[18] In contrast, Gd^{III}-based spin labels are inert to reduction within cells, but, depending on the particular type of the complex, the Gd^{III} ion may be exchanged for metal ions present in the cell.^[19] The relaxation times T_M of Gd^{III} can be shorter or longer than those of trityls, depending on the utilized ligand,^[14,20] and the electron-spin state of $S = 7/2$ imposes challenges on data analysis.^[21,22] Thus, in order to keep the trityl core but to make it more suitable for in-cell measurements, its redox properties have to be tuned, possibly by exchanging the electron-withdrawing carboxy substituents with electron-donating groups. Furthermore, the currently used synthesis strategy for introducing the bioconjugation group via esterification (**4**–**6**, **8**)^[9,11] or amidation (**2**, **3**, **7**)^[7,8,10] of the carboxylic groups (Figure 1) leads to long, flexible linkers that make the PDS-derived distance distributions broad and, in some cases, multimodal.^[11] This, in turn, renders the interpretation of such distance distributions error-prone. Last but not least, the label

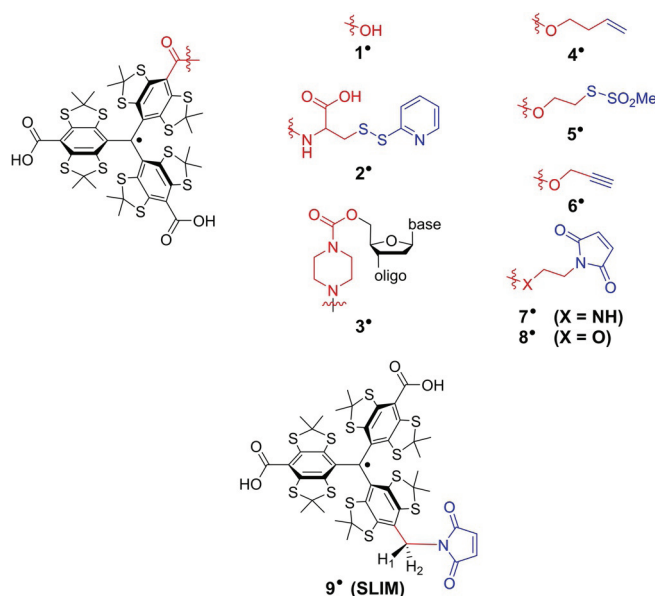


Figure 1. Finland trityl **1**, various trityl labels (**2**–**8**) reported in the literature, and the new trityl label **9**^{*} (SLIM). For the sake of clarity, the radical basis is depicted in black, the linker in red, and the bioconjugation site in blue.

[*] N. Fleck, C. A. Heubach, T. Hett, F. R. Haege, Prof. Dr. O. Schiemann
Institute of Physical and Theoretical Chemistry, University of Bonn
Wegelerstr. 12, 53115 Bonn (Germany)

E-mail: schiemann@pc.uni-bonn.de

P. P. Bawol, Prof. Dr. H. Baltruschat

Institute of Physical and Theoretical Chemistry, University of Bonn
Römerstr. 164, 53117 Bonn (Germany)

Supporting information and the ORCID identification number(s) for the author(s) of this article can be found under:
<https://doi.org/10.1002/anie.202004452>.

© 2020 The Authors. Published by Wiley-VCH Verlag GmbH & Co. KGaA. This is an open access article under the terms of the Creative Commons Attribution License, which permits use, distribution and reproduction in any medium, provided the original work is properly cited.

should not be cleaved from the biomolecule under in-cell conditions, rendering the ester connectivity of the bioconjugation group to the trityl core^[23] and the disulfide bridge forming a methanethiosulfonate group^[24] unsuitable. With respect to the latter, the thioether-forming maleimide group has been confirmed to be advantageous.^[25]

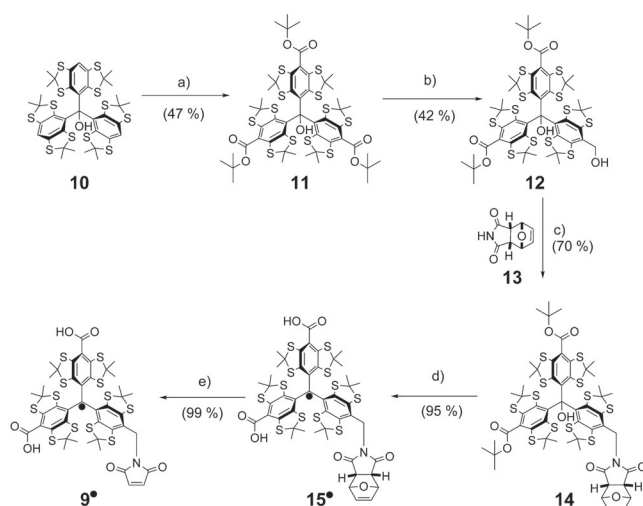
Therefore, the work presented herein introduces a synthesis by which the maleimide group is coupled to the trityl core via just one methylene group leading to the label **9**, called SLIM (short-linked maleimide), which provides narrow distance distributions, increased stability against reduction, high labeling efficiencies, and large signal-to-noise ratios in PDS measurements.

Results and Discussion

Synthesis and Characterization

The synthesis of SLIM **9** is shown in Scheme 1 and starts from trityl alcohol **10**, which can be obtained from 1,2,4,5-tetrachlorobenzene in three steps.^[9] Subsequent deprotonation and treatment with activated Boc-anhydride afforded the threefold ester **11** by adapting a recent protocol of Hintz et al.^[26] Statistical reduction of one ester moiety with LiAlH₄ broke the C₃ symmetry and led to **12** in a yield of 42% (58% based on recovered starting material **11**).

In the next step, the required C–N bond on the way to **9** was formed in a Mitsunobu reaction^[27] between **12** and **13** leading to **14** in a yield of 70%. The excellent Michael-acceptor properties of maleimides required the protection of their C=C bond in form of the Diels–Alder adduct **13** in order to prevent side reactions with Ph₃P,^[28] which is needed as a reagent in the Mitsunobu transformation. The *endo*-isomer of **13**^[29] was chosen over the *exo*-isomer, because it provides sufficient retro-Diels–Alder reactivity already at 60 °C (see



Scheme 1. Synthesis of SLIM **9**: a) 1) *n*-BuLi, TMEDA, Et₂O, rt, 0.5 h; 2) *N*-*tert*-butoxycarbonylpyridinium *tert*-butanolate, Et₂O, 24 h. b) LiAlH₄, THF, rt, 1 h. c) Ph₃P, diethyl azodicarboxylate, THF, 0 °C, 0.5 h. d) 1) CF₃COOH, CH₂Cl₂, rt, 2 h; 2) SnCl₂, THF, 0.3 h. e) CH₃CN, 60 °C, 24 h.

Supporting Information, Section 2.2.4) instead of 150 °C, which is necessary for the cleavage of the *exo*-adduct of **13**.^[30,31] The deprotection at 60 °C is compatible with the thermal stability of the radical center,^[32] which is crucial for the final deprotection to **9**. However, first, the *t*-butyl esters in **14** are cleaved by trifluoroacetic acid concomitant to the abstraction of the hydroxyl group. This leads to tritylium ion **15**⁺, which is then reduced in situ with tin(II) chloride to **15**[•]. Finally, **9** was obtained by simply heating **15**[•] to 60 °C overnight leading to a quantitative deprotection of the maleimide. Relative to starting compound **10**, the overall yield of the five-step synthesis was 13%. The identity and purity of **9** was confirmed by high-resolution mass spectrometry and HPLC (see Supporting Information, Sections 2.3.2–2.3.3). For further characterization, a continuous-wave (cw) X-band EPR spectrum of **9** in a PBS buffer (PBS = phosphate-buffered saline) was recorded at room temperature (Figure 2a). The spectrum displays nine major lines due to hyperfine coupling of the electron spin to the imido nitrogen atom ($A_N = 1.71$ MHz) and the two benzylic hydrogen atoms ($A_{H1} = 6.00$ MHz, $A_{H2} = 2.96$ MHz). The fact that the hyperfine-coupling constants of H1 and H2 (Figure 1) differ from each other is also seen in DFT calculations and can be attributed to the helical chirality of the trityl scaffold (see Supporting Information, Section 8.1). Freezing the sample to 100 K resulted in the EPR spectrum shown in Figure 2b with a splitting between both lines of 7.44 MHz, which is, in large

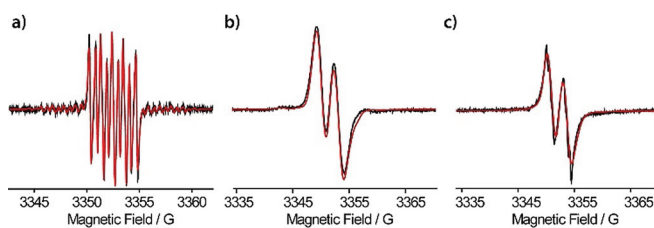


Figure 2. Cw X-band EPR spectra of **9** in a PBS buffer a) at 298 K, b) at 100 K, and c) of **9** bound to the single-cysteine mutant YopO N624C in a PBS buffer at 298 K.

parts, governed by the hyperfine coupling to H1. Thus, and in contrast to the Finland trityl derivatives **2**–**8**, SLIM **9** does not give rise to a single line in the frozen state. However, the spectral width of ≈ 10 G is still, on the one hand, narrow enough to permit full excitation with conventional rectangular pulses and, on the other hand, broad enough to also enable PELDOR experiments.

Redox Stability

With respect to in-cell measurements, the stability of a spin label against reduction is important. As shown in the literature,^[33–35] the *para*-substituents of trityl radicals hold a strong influence on the electrode potentials. Generally, the carbanion T[•] is stabilized by electron withdrawing groups, such as esters or amides, resulting in an increase of the reduction potential. This implies that all spin labels obtained

by esterification or amidation of **1** are more prone to reduction than **1** itself. In contrast, the imidomethylene substituent in **9** rather acts as an electron-donating group, destabilizing the corresponding carbanion and restraining the reduction compared to **1**. Indeed, this behavior is seen in the cyclovoltammograms (Figure S28, Supporting Information). The reduction potential of **9** is lowered by 46 mV compared to **1**, furnishing it with an increased stability towards reduction. Due to the higher reactivity of the corresponding carbanion **9**⁻ towards H⁺, its reduction is less reversible than for **1**, as seen when using slower scan rates (see Supporting Information, Section 4.1). In contrast to the reduction, the oxidation of **9** is slightly promoted by 26 mV compared to **1**. Nonetheless, no oxidative degradation was observed under ambient conditions.

In order to probe the in-cell persistence of **9**, its cw-EPR-signal intensity was monitored over time under several commonly used and in-cell-related conditions.^[18,36,37] In a 4.75 mM ascorbate solution (Figure 3a), **9** does not decay at all, whereas trityl label **8** decays to 62% within 15 h, the *gem*-diethyl label **S5** bound to DNA (see Supporting Information, Section 3.1) is reduced to 18% in the same time and the *gem*-dimethyl label MTSL is completely reduced within 1.5 h.

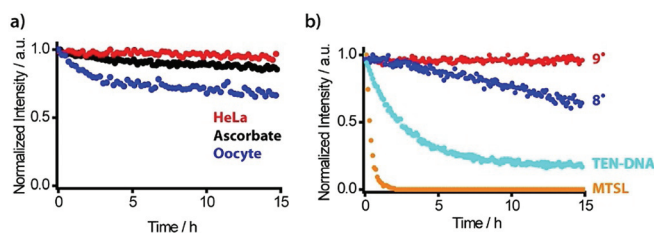


Figure 3. a) Plot of the EPR intensities (double integral) vs. time for 200 μM **9** (red), **8** (blue), tetraethyl nitroxide **S5** (cyan), and MTSL (orange) in a PBS buffer containing 4.75 mM sodium ascorbate, each corresponding to a 24-fold molar excess of ascorbate. b) Plot of the EPR intensities (double integral) against time for **9** conjugated to YopO N624C (50 μM) in HeLa-lysate (red), 4.75 mM ascorbate (black), and *Xenopus laevis* oocyte lysate (blue). The initial intensities were comparable, and the dead time was below 6 min in each case. Label **S5** was conjugated to DNA to provide sufficient water solubility.

In another step, **9** was conjugated to *Yersinia* outer protein O (YopO) mutant N624C and the labeled protein was added to a 4.75 mM solution of ascorbate, HeLa cell lysate, and oocyte lysate. As can be seen in Figure 3b, also under these conditions, **9** is reduced only marginally in the case of ascorbate and HeLa lysate. Even within *Xenopus laevis* oocyte lysate, the most reducing cell lysate tested herein, only a decay to 71% is observed after 15 h. Label **9** is thus considerably more stable than the *gem*-dimethyl nitroxides and at least on par with the best *gem*-diethyl nitroxides according to literature reports.^[36,37]

Spin Labeling

Successful spin labeling requires high site-selectivity and high labeling efficiency. In order to probe for the first aspect, the cysteine-free mutant of YopO^[38,39] was incubated with **9** under typical labeling conditions.^[11] MALDI-MS showed the mass for the unlabeled protein only, indicating that no other amino acid is covalently labeled by **9** (see Supporting Information, Section 3.3.5). Non-covalent labeling and the presence of inseparable aggregates of **9** were tested for by using UV/Vis spectroscopy. The UV/Vis spectrum after labeling shows a weak absorption band at 464 nm (see Supporting Information, Section 3.3.4) indicating that $6.9 \pm 0.6\%$ of non-bound **9** are present in the sample relative to the protein. This behavior of trityls is known^[10,11,40] and, in this case, actually quite effectively diminished by the labeling protocol.

The efficiency of the bioconjugation was subsequently examined using the single-cysteine YopO mutant N624C. ESI-MS (see Supporting Information, Section 3.3.5) confirmed that only one label is bound. The labeling efficiency was estimated to be quantitative based on ESI-MS and $94 \pm 9\%$ based on UV/Vis and EPR spin-counting experiments. Interestingly, **9** covalently bound to YopO yields a room-temperature cw X-band EPR spectrum similar to that of **9** free in the frozen state, which can be simulated by only slightly adjusting the EPR parameters of **9** at 100 K (Figure 2 and Supporting Information, Section 5). Thus, the slow rotation of **9** bound to a protein brings the label into the rigid limit and enables the distinction of bound label from unbound label.

Distance Measurements

In a next step, the effect of the reduced linker length on PDS derived distance distributions was assessed on the double-cysteine mutant YopO Y588C/N624C (see Supporting Information, Section 3.3.1) by labeling it with **9**, **8**, and MTSL. The resulting doubly labeled constructs YopO-**9**, YopO-**8**, and YopO-MTSL were characterized (see Supporting Information, Section 3.3.4) and subjected to double-quantum coherence (DQC)^[41,42] and pulsed electron-electron double-resonance (PELDOR)^[43–45] experiments whose background-corrected time traces are shown in Figure 4 for original time traces, see the Supporting Information, Section 7.5). The PELDOR time trace of YopO-MTSL (Figure 4a) exhibits the typical modulation depth of 32% for Q-band PELDOR and a SNR of $248 \text{ h}^{-1/2}$. The corresponding distance distribution shows a bimodal distribution, which was seen before for other MTSL-YopO mutants involving α -helix 14 in the guanine-nucleotide dissociation inhibitor (GDI) domain.^[11] For YopO-**9**, the narrow spectral width of the trityl signal called for a DQC experiment, which almost tripled the modulation depth to 87% and the SNR to $674 \text{ h}^{-1/2}$ (Figure 4c). This high SNR prompted us to reduce the YopO-**9** concentration to 90 nM, which still gave an SNR of $2 \text{ h}^{-1/2}$ at a time window length of 2.5 μs (see Supporting Information, Section 7.7). Performing PELDOR measurements on YopO-

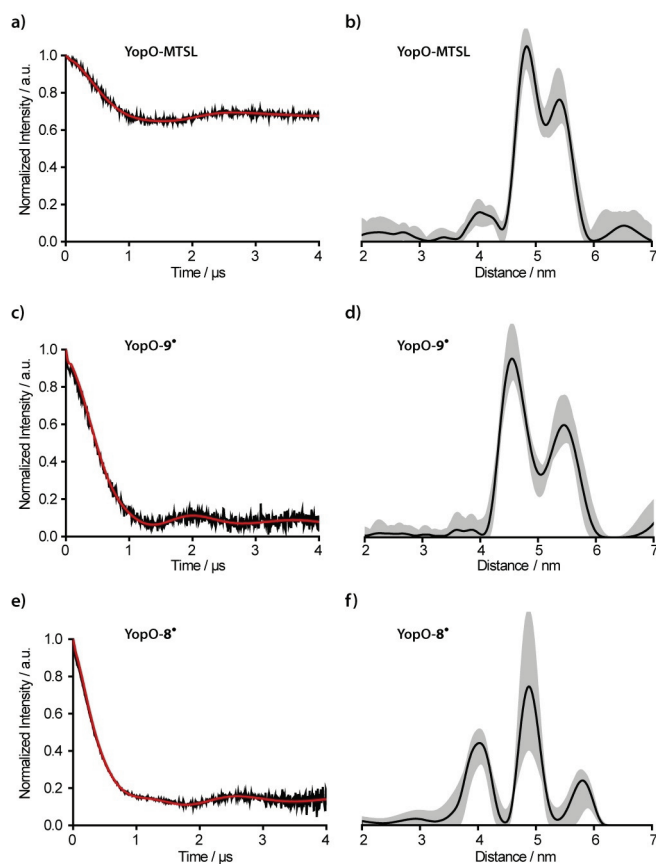


Figure 4. PDS experiments on mutant Y588C/N624C-YopO labeled with a), b) MTSL (PELDOR), c), d) 9^* (DQC), and e), f) 8^* (DQC). Background-corrected time traces (black) are given along with their fits (red) in (a,c,e), and the resulting distance distributions are provided in (b,d,f) in black with the corresponding DeerAnalysis validation shown as grey shaded areas.

9^* provided a SNR of only $155 \text{ h}^{-1/2}$ (see Supporting Information, Section 7.5). This shows that the combination DQC/ 9^* outperforms the PELDOR/MTSL combination.^[11] Notably, the bimodality seen for YopO-MTSL is also resolved for YopO labeled with 9^* , and both the widths and weights of the two modes are very similar in both cases (see Supporting Information, Section 7.5).

Since the bimodality is observed for two different spin labels, MTSL and 9^* , and two PDS techniques, PELDOR and DQC, it can be related to two different conformers of the α -helix, as previously discussed.^[11,39] The peak at 4.5 nm is assigned to the straight form of α -helix 14 (PDB-ID: 2h7o) and the peak at 5.3 nm to its bent form (PDB-ID: 4ci6).^[11,39] In the crystal structures, the bent form is only found when actin is bound, whereas here, in frozen solution, both conformations of α -helix 14 seem to be present even in the absence of the actin ligand. Interestingly, the addition of human platelet actin did not change the obtained distance distribution, strongly indicating that the conformation of α -helix 14 is independent of the actin-binding process (see Supporting Information, Section 7.6).

In contrast, the DQC experiment on YopO- 8^* (SNR of $503 \text{ h}^{-1/2}$) provides a broad trimodal distance distribution

(Figure 4e,f), which is attributed to the longer linker and thus a broader range of label conformers for 8^* , especially with shorter distances (see Supporting Information, Section 8.2.2). The differences in the conformer space of 8^* and 9^* can be quantified in silico^[46] via the accessible volume both labels sample.^[47,48] This yielded 15200 \AA^3 and 6940 \AA^3 for 8^* and 9^* , respectively, and thus, a reduction of the conformer space by 54% upon going from 8^* to 9^* . This example thus nicely highlights the importance of a short linker group as provided by the new SLIM label.

In-Cell Measurements

To test the feasibility of 9^* for in-cell structure elucidation, DQC measurements on the aforementioned Y588C/N624C-YopO mutant were performed within eukaryotic *Xenopus laevis* oocytes. The rationale behind the choice of this type of cells as model system is twofold: first, oocytes exhibit the highest reducing activity of all cell types under study^[36] (Figure 3c) and do, thus, serve as a true in-cell benchmark test for 9^* . Second, although YopO is a prokaryotic protein, its full enzymatic function is only initiated upon translocation into eukaryotic immune cells through the *Yersinia* type-3 secretion system, a needle-like structure that penetrates the outer membrane of the innate immune cells.^[49,50] Here, the oocytes serve as the eukaryotic species and their size enables mimicking this translocation process of YopO- 9^* using a microinjection system (see Supporting Information, Section 6). In this way, samples with a bulk spin concentration of $11 \mu\text{M}$ were obtained and subjected to Q-band DQC experiments.

Due to the presence of Mn^{II} in oocytes and spin-crowding effects, the phase-memory time T_M is shortened compared to in-vitro measurements (see Supporting Information, Section 7.8). However, an incubation of the injected oocytes over 2 h led to a more uniform distribution of the labeled protein within the oocytes enabling a dipolar-evolution-time window of $3.5 \mu\text{s}$ for the in-cell DQC experiment. The obtained time trace (Figure 5a) exhibits a SNR of $23 \text{ h}^{-1/2}$ ($2 \text{ h}^{-1/2} \mu\text{M}^{-1}$), which is considerably higher than previously reported for in-cell measurements with nitroxide-^[36,51,52] and trityl-labeled^[9] biomolecules. Even in comparison to W-band PELDOR/trityl

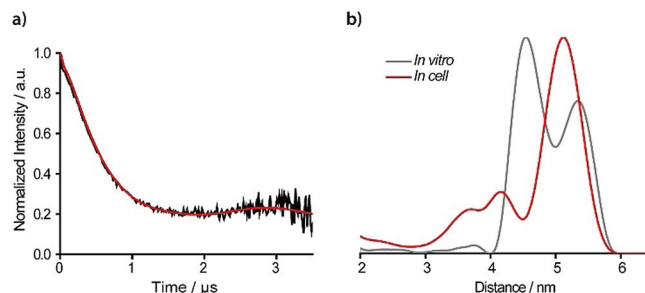


Figure 5. a) Background-corrected in-cell DQC time trace and the corresponding fit of YopO- 9^* after an incubation period of 2 h. b) Distance distribution of the in cell experiment (red) overlaid with the distance distribution obtained in vitro ($3.5 \mu\text{s}$ trace length, grey).

and PELDOR/Gd^{III} measurements, the Q-band DQC/SLIM combination is at least on par.^[14,53–56] Remarkably, the distance distribution from the in-cell measurement differs from the in-vitro-derived ones (Figures 4 d and S38,S39). This can already be seen when comparing the time traces; the in-cell time trace has a considerably longer oscillation period (3 μ s) than the in-vitro counterparts (2 μ s). Accordingly, the long-distance peak at 5.1 nm prevails within oocytes and is now the dominating peak, whereas the peak at 4.5 nm is strongly diminished. This data thus indicates a preferred selection of the bent form of α -helix 14 of the GDI domain of YopO in the eukaryotic cytosol. The straight conformation of α -helix 14 leads to shorter inter-spin distances, which are well pronounced in the in-vitro experiments but are strongly diminished in the in-cell measurement (compare the Supporting Information, Section 7.8). This effect may be related to molecular crowding^[57,58] and/or binding of regulatory proteins such as Rac1^[59] in the eukaryotic cytosol. More in-depth studies on this will follow.

Conclusion

In this work, the trityl spin label SLIM was introduced and probed for its suitability in PDS experiments. Its synthesis involved a Mitsunobu-type transformation using a protected maleimide, which can be deprotected in a mild retro-Diels–Alder reaction. Bioconjugation of SLIM to cysteines proceeds in high yields and site-selectively. Its narrow spectral width enables high-sensitivity distance measurements down to low nanomolar protein concentrations, and the short linker leads to narrow and, thus, more reliable distance distributions. Additionally, SLIM features a high stability towards reduction, making in-cell PDS measurements at high SNRs feasible. In profit of this, it could be shown that the injection of YopO into a eukaryotic cell leads to a change in the conformational ensemble of the GDI domain. Thus, SLIM is a very promising label improving the capability to obtain structural information from biomolecules within their natural cellular environment.

Acknowledgements

Funding of the Deutsche Forschungsgemeinschaft (DFG) via SPP1601 is gratefully acknowledged.

Conflict of interest

The authors declare no conflict of interest.

Keywords: EPR spectroscopy · in-cell measurements · radicals · spin labeling · trityl radical

[1] B. B. Williams, H. J. Halpern, in *Biomedical EPR—Part A: Free Radicals, Metals, Medicine and Physiology* (Eds.: S. R. Eaton,

- G. R. Eaton, L. J. Berliner), Springer US, Boston, **2005**, pp. 283–319.
- [2] B. Epel, C. R. Haney, D. Hleihel, C. Wardrip, *Med. Phys.* **2010**, *37*, 2553–2559.
- [3] A. A. Bobko, I. Dhimitruka, J. L. Zweier, V. V. Khramtsov, *J. Am. Chem. Soc.* **2007**, *129*, 7240–7241.
- [4] G. Mathies, M. A. Caporini, V. K. Michaelis, Y. Liu, K. N. Hu, D. Mance, J. L. Zweier, M. Rosay, M. Baldus, R. G. Griffin, *Angew. Chem. Int. Ed.* **2015**, *54*, 11770–11774; *Angew. Chem.* **2015**, *127*, 11936–11940.
- [5] J. H. Ardenkjær-Larsen, B. Fridlund, A. Gram, G. Hansson, L. Hansson, M. H. Lerche, R. Servin, M. Thaning, K. Golman, *Proc. Natl. Acad. Sci. USA* **2003**, *100*, 10158–10163.
- [6] S. Andersson, A. Rydbeck, R. S. Mahno, US Patent 5728370, **1999**.
- [7] Z. Yang, Y. Liu, P. Borbat, J. L. Zweier, J. H. Freed, W. L. Hubbell, *J. Am. Chem. Soc.* **2012**, *134*, 9950–9952.
- [8] G. Y. Shevelev, O. A. Krumkacheva, A. A. Lomzov, A. A. Kuzhelev, O. Y. Rogozhnikova, D. V. Trukhin, T. I. Troitskaya, V. M. Tormyshev, M. V. Fedin, D. V. Pyshnyi, et al., *J. Am. Chem. Soc.* **2014**, *136*, 9874–9877.
- [9] J. J. Jassoy, A. Berndhäuser, F. Duthie, S. P. Kühn, G. Hagelueken, O. Schiemann, *Angew. Chem. Int. Ed.* **2017**, *56*, 177–181; *Angew. Chem.* **2017**, *129*, 183–187.
- [10] A. Giannoulis, Y. Yang, Y.-J. Gong, X. Tan, A. Feintuch, R. Carmieli, T. Bahrenberg, Y. Liu, X.-C. Su, D. Goldfarb, *Phys. Chem. Chem. Phys.* **2019**, *21*, 10217–10227.
- [11] J. J. Jassoy, C. A. Heubach, T. Hett, F. Bernhard, F. R. Haege, G. Hagelueken, O. Schiemann, *Molecules* **2019**, *24*, 2735.
- [12] G. W. Reginsson, O. Schiemann, *Biochem. Soc. Trans.* **2011**, *39*, 128–139.
- [13] G. Jeschke, *Annu. Rev. Phys. Chem.* **2012**, *63*, 419–446.
- [14] Y. Yang, B. Pan, F. Yang, Y. Liu, X. Su, D. Goldfarb, *J. Phys. Chem. Lett.* **2020**, *11*, 1141–1147.
- [15] A. A. Kuzhelev, D. V. Trukhin, O. A. Krumkacheva, R. K. Strizhakov, O. Y. Rogozhnikova, T. I. Troitskaya, M. V. Fedin, V. M. Tormyshev, E. G. Bagryanskaya, *J. Phys. Chem. B* **2015**, *119*, 13630–13640.
- [16] G. W. Reginsson, N. C. Kunjir, S. T. Sigurdsson, O. Schiemann, *Chem. Eur. J.* **2012**, *18*, 13580–13584.
- [17] N. C. Kunjir, G. W. Reginsson, O. Schiemann, S. T. Sigurdsson, *Phys. Chem. Chem. Phys.* **2013**, *15*, 19673–19685.
- [18] A. P. Jagtap, I. Krstic, N. C. Kunjir, R. Hänsel, T. F. Prisner, S. T. Sigurdsson, *Free Radical Res.* **2015**, *49*, 78–85.
- [19] M. Qi, A. Groß, G. Jeschke, A. Godt, M. Drescher, *J. Am. Chem. Soc.* **2014**, *136*, 15366–15378.
- [20] M. Azarkh, A. Bieber, M. Qi, J. W. A. Fischer, M. Yulikov, A. Godt, M. Drescher, *J. Phys. Chem. Lett.* **2019**, *10*, 1477–1481.
- [21] D. Goldfarb, *Phys. Chem. Chem. Phys.* **2014**, *16*, 9685–9699.
- [22] D. Abdullin, O. Schiemann, *ChemPlusChem* **2020**, <https://doi.org/10.1002/cplu.201900705>.
- [23] Z. Yang, M. D. Bridges, C. J. López, O. Y. Rogozhnikova, D. V. Trukhin, E. K. Brooks, V. Tormyshev, H. J. Halpern, W. L. Hubbell, *J. Magn. Reson.* **2016**, *269*, 50–54.
- [24] R. Igarashi, T. Sakai, H. Hara, T. Tenno, T. Tanaka, H. Tochio, M. Shirakawa, *J. Am. Chem. Soc.* **2010**, *132*, 8228–8229.
- [25] R. Roser, M. J. Schmidt, M. Drescher, D. Summerer, *Org. Biomol. Chem.* **2016**, *14*, 5468–5476.
- [26] H. Hintz, A. Vanas, D. Klose, G. Jeschke, A. Godt, *J. Org. Chem.* **2019**, *84*, 3304–3320.
- [27] K. C. K. Swamy, N. N. B. Kumar, E. Balaraman, K. V. P. P. Kumar, *Chem. Rev.* **2009**, *109*, 2551–2651.
- [28] M. A. Walker, *J. Org. Chem.* **1995**, *60*, 5352–5355.
- [29] E. H. Discekici, A. H. St. Amant, S. N. Nguyen, I. H. Lee, C. J. Hawker, J. Read De Alaniz, *J. Am. Chem. Soc.* **2018**, *140*, 5009–5013.

- [30] O. K. Farha, R. L. Julius, M. F. Hawthorne, *Tetrahedron Lett.* **2006**, *47*, 2619–2622.
- [31] Z. Lu, R. Weber, R. J. Twieg, *Tetrahedron Lett.* **2006**, *47*, 7213–7217.
- [32] N. Fleck, T. Hett, J. Brode, A. Meyer, S. Richert, O. Schiemann, *J. Org. Chem.* **2019**, *84*, 3293–3303.
- [33] X. Tan, L. Chen, Y. Song, A. Rockenbauer, F. A. Villamena, J. L. Zweier, Y. Liu, *Chem. Res. Toxicol.* **2017**, *30*, 1664–1672.
- [34] C. Decroos, V. Bolland, J. L. Boucher, G. Bertho, Y. Xu-Li, D. Mansuy, *Chem. Res. Toxicol.* **2013**, *26*, 1561–1569.
- [35] B. Driesschaert, A. A. Bobko, T. D. Eubank, A. Samouilov, V. V. Khramtsov, J. L. Zweier, *Bioorg. Med. Chem. Lett.* **2016**, *26*, 1742–1744.
- [36] G. Karthikeyan, A. Bonucci, G. Casano, G. Gerbaud, S. Abel, V. Thomé, L. Kodjabachian, A. Magalon, B. Guigliarelli, V. Belle, et al., *Angew. Chem. Int. Ed.* **2018**, *57*, 1366–1370; *Angew. Chem.* **2018**, *130*, 1380–1384.
- [37] T. S. Braun, P. Widder, U. Osswald, L. Groß, L. Williams, M. Schmidt, I. Helmle, D. Summerer, M. Drescher, *ChemBioChem* **2020**, *21*, 958–962.
- [38] E. E. Galyov, S. Håkansson, Å. Forsberg, H. Wolf-Watz, *Nature* **1993**, *361*, 730–732.
- [39] M. F. Peter, A. T. Tuukkanen, C. A. Heubach, A. Selsam, F. G. Duthie, D. I. Svergun, O. Schiemann, G. Hagelueken, *Structure* **2019**, *27*, 1416–1426.
- [40] I. Marin-Montesinos, J. C. Paniagua, A. Peman, M. Vilaseca, F. Luis, S. Van Doorslaer, M. Pons, *Phys. Chem. Chem. Phys.* **2016**, *18*, 3151–3158.
- [41] S. Saxena, J. H. Freed, *Chem. Phys. Lett.* **1996**, *251*, 102–110.
- [42] S. Saxena, J. H. Freed, *J. Chem. Phys.* **1997**, *107*, 1317–1340.
- [43] A. D. Milov, K. M. Salikhov, M. D. Schirov, *Fiz. Tverd. Tela* **1981**, *23*, 975–982.
- [44] A. Milov, A. Ponomarev, Y. Tsvetkov, *Chem. Phys. Lett.* **1984**, *110*, 67–72.
- [45] M. Pannier, S. Veit, A. Godt, G. Jeschke, H. W. Spiess, *J. Magn. Reson.* **2000**, *142*, 331–340.
- [46] G. Hagelueken, R. Ward, J. N. Naismith, O. Schiemann, *Appl. Magn. Reson.* **2012**, *42*, 377–391.
- [47] K. Sale, L. Song, Y. Liu, E. Perozo, P. Fajer, *J. Am. Chem. Soc.* **2005**, *127*, 9334–9335.
- [48] G. Hagelueken, D. Abdullin, O. Schiemann, *Methods Enzymol.* **2015**, *563*, 595–622.
- [49] G. V. Plano, K. Schesser, *Immunol. Res.* **2013**, *57*, 237–245.
- [50] W. L. Lee, J. M. Grimes, R. C. Robinson, *Nat. Struct. Mol. Biol.* **2015**, *22*, 248–255.
- [51] I. Krstić, R. Hänsel, O. Romainczyk, J. W. Engels, V. Dötsch, T. F. Prisner, *Angew. Chem. Int. Ed.* **2011**, *50*, 5070–5074; *Angew. Chem.* **2011**, *123*, 5176–5180.
- [52] P. Widder, J. Schuck, D. Summerer, M. Drescher, *Phys. Chem. Chem. Phys.* **2020**, *22*, 4875–4879.
- [53] A. Martorana, G. Bellapadrona, A. Feintuch, E. Di Gregorio, S. Aime, D. Goldfarb, *J. Am. Chem. Soc.* **2014**, *136*, 13458–13465.
- [54] Y. Yang, F. Yang, Y. Gong, J. Chen, D. Goldfarb, X. Su, *Angew. Chem. Int. Ed.* **2017**, *56*, 2914–2918; *Angew. Chem.* **2017**, *129*, 2960–2964.
- [55] Y. Yang, F. Yang, Y. Gong, T. Bahrenberg, A. Feintuch, X. Su, D. Goldfarb, *J. Phys. Chem. Lett.* **2018**, *9*, 6119–6123.
- [56] F. Wojciechowski, A. Groß, I. T. Holder, L. Knörr, M. Drescher, J. S. Hartig, *Chem. Commun.* **2015**, *51*, 13850–13853.
- [57] H.-X. Zhou, *FEBS Lett.* **2013**, *587*, 1053–1061.
- [58] Y. Wang, M. Sarkar, A. E. Smith, A. S. Krois, G. J. Pielak, *J. Am. Chem. Soc.* **2012**, *134*, 16614–16618.
- [59] G. Prehna, M. I. Ivanov, J. B. Bliska, C. E. Stebbins, *Cell* **2006**, *126*, 869–880.

Manuscript received: March 26, 2020

Version of record online: April 30, 2020

Supporting Information

SLIM: A Short-Linked, Highly Redox-Stable Trityl Label for High-Sensitivity In-Cell EPR Distance Measurements

*Nico Fleck, Caspar A. Heubach, Tobias Hett, Florian R. Haege, Pawel P. Bawol, Helmut Baltruschat, and Olav Schiemann**

anie_202004452_sm_miscellaneous_information.pdf

Author Contributions

N.F. Investigation: Lead; Writing—Original Draft: Lead

T.H. Formal analysis: Lead; Investigation: Supporting; Writing—Original Draft: Supporting

F.H. Investigation: Supporting

P.B. Investigation: Supporting

H.B. Writing—Review & Editing: Supporting.

Table of Contents

1. General Procedures and Instrumentation	3
2. Synthesis	4
2.1 General Procedures Synthesis.....	4
2.2 Synthetic Protocols.....	4
2.2.1 Synthesis of S2	4
2.2.2 Synthesis of S3	5
2.2.3 Synthesis of S4	5
2.2.4 Retro Diels-Alder reaction: Kinetics	5
2.2.5 Synthesis of literature known compound 11	6
2.2.6 Synthesis of 12	7
2.2.7 Synthesis of 14	8
2.2.8 Synthesis of 15 [•]	9
2.2.9 Synthesis of 9 [•]	9
2.3 Analytical Data Synthesis.....	10
2.3.1 NMR Spectra	10
2.3.2 HRMS-Data	15
2.3.3 UHPLC Data.....	18
3. Spin Labeling	19
3.1 Tetraethylnitroxide-DNA Construct	19
3.2 SLIM Dilution Series and Calibration Curve.....	19
3.3 <i>Yersinia</i> outer protein O (YopO)	20
3.3.1 Construct Design	20
3.3.2 YopO Expression	21
3.3.3 YopO Purification.....	21

3.3.4 YopO Spin Labeling	22
3.3.5 YopO Mass Spectrometry.....	24
4. Redox Stability	26
4.1 Cyclic Voltammetry.....	26
4.2 Reduction Stability.....	26
4.2.1 Cell Lysates Preparation	26
4.2.2. Stability Measurements	27
5. Simulation of <i>cw</i> -EPR spectra.....	28
6. <i>In Cell</i> Sample Preparation	30
7. Pulsed EPR.....	31
7.1 EPR Sample Preparation	31
7.2 Relaxation Time Measurements.....	31
7.3 Double Quantum Coherence (DQC) Experiments	32
7.4 Pulsed Electron-Electron Double Resonance (PELDOR) Experiments.....	33
7.5 YopO PDS Results.....	34
7.6 PDS on YopO with human platelet actin	36
7.7 Evaluation of Concentration Limit for SLIM / DQC	36
7.8 <i>In Cell</i> Pulsed EPR Measurements	38
8. Theoretical Results.....	40
8.1 Density Functional Theory Computations.....	40
8.2 <i>In Silico</i> Spin Labeling.....	44
8.2.1 Conformer Cloud Volume	44
8.2.2 YopO 8 [•] Label Conformer Selection.....	45
9. Literature	46

1. General Procedures and Instrumentation

NMR spectra were recorded on Avance I 300, Avance I 400, Avance III HD 500, or Avance III HD 700 spectrometers (Bruker BioSpin, Rheinstetten, Germany). Chemical shifts are reported referenced to hydrogen residual peaks of the NMR solvent.^[5]

MALDI(+)-spectra were recorded in a Bruker Daltonics UltraFlex TOF/TOF spectrometer (Bruker, Rheinstetten, Germany). For organic compounds, DCTB was used as the matrix, whereas DHAP was used for protein samples. For ESI(+), a Synapt G2-Si spectrometer (Waters, Milford, USA) was employed. APCI-spectra were obtained on an Orbitrap XL spectrometer (Thermo Fisher Scientific, Bremen, Germany). Protein samples were subjected to mass spectrometric analysis in 20 mM PO₄ buffer (pH = 6.8, 50 mM NaCl).

For analytical chromatography, an UHPLC system (PLATINblue-series, Knauer GmbH, Berlin, Germany) equipped with a Eurospher II 100-2 C18P, 2 μm, 2 x 100 mm column (Knauer GmbH, Berlin, Germany) and a UV detector working at 265 nm was used.

All continuous wave (*cw*) EPR measurements were performed at X-band frequencies (~9.4 GHz) either on an EMXmicro or EMXnano spectrometer (Bruker BioSpin, Rheinstetten, Germany). Measurements at room temperature were done on the EMXmicro using an ER 4122SHQ resonator. Measurements at 100 K were conducted using a Bruker 4119HS resonator in conjunction with a ER 4141VT temperature control system, which operates with a continuous flow of nitrogen gas. For all samples, X-band EPR-tubes with an outer diameter of 5 mm obtained from Wilmad Labglass (Brand of SP Industries, Warminster, USA) were used. Aqueous samples were, however, filled into 10 μL capillaries (Disposable Capillaries, Hirschmann Laborgeräte, Eberstadt, Germany), which were then transferred into the X-band tubes.

cw-EPR spectra of the pure SLIM label and after bioconjugation were recorded in frozen solution using a modulation amplitude of 0.2 G, a microwave power of 7.4 μW (44 dB attenuation), a time constant of 20.48 ms and a conversion time of 20.59 ms. 2000 data points were recorded, corresponding to a resolution of 25 points per G. Quantitative EPR measurements were conducted employing the on-board spin counting routine of the EMXnano spectrometer. *CW*-EPR measurements at room temperature were performed at an attenuation of 25 dB (603.1 μW) and a modulation amplitude of 0.1 G.

Pulsed EPR measurements were conducted at Q-band frequencies (~33.7 GHz) on a Bruker (Bruker BioSpin, Rheinstetten, Germany) ELEXSYS E580 EPR spectrometer equipped with an ER5106QT-II resonator and a 150 W TWT-amplifier (Applied Systems Engineering, Fort Worth, TX, USA). All data was acquired using quadrature detection. The temperature was adjusted to the appropriate value (between 10 K and 50 K) using a CF935 helium gas-flow cryostat (Oxford Instruments, Abingdon, UK) in conjunction with an Oxford Instruments iTC 503 temperature controller.

2. Synthesis

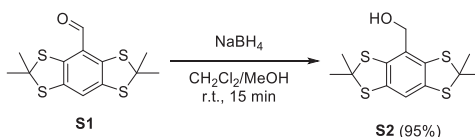
2.1 General Procedures Synthesis

Chemicals were purchased from commercial suppliers and used without further purification. Diethyl ether was dried over 4 Å molecular sieves, and THF was distilled over sodium wire with benzophenone. Where indicated, solvents were degassed by applying three freeze-pump-thaw cycles. Thin layer chromatography was conducted using 250 µm F254 silica plates provided by Merck, and spots were visualized with UV-light at 254 nm. Spots of trityl alcohols can be stained selectively by irradiating the TLC-plate for 5 min with UV-light at 254 nm (5 W). For column chromatography, silica gel (60 Å pore size, 40 – 63 µm particle size) purchased from Merck was used. Solvents were generally removed under reduced pressure by a rotary evaporator, products were further dried in oil-pump vacuum at 10⁻³ mbar. The concentration of *n*-butyl lithium solutions was determined prior to use by titration following the protocol of *Winkle et al.*^[1] Trityl alcohol **10** was obtained following our previously published protocol.^[2] 3aRS,4SR,7RS,7aSR-4,7-epoxy-3,3a,7,7a-tetrahydro-2H-isoindoli-1,3-dione (**13**) was prepared according to the literature.^[3] Compound **S1** was obtained following the procedure of *Hintz et al.*^[4] using DMF instead of *N*-formylpiperidine.

2.2 Synthetic Protocols

2.2.1 Synthesis of **S2**

2,2,6,6-tetramethyl-8-(hydroxymethyl)benzo[1,2-d;4,5-d]bis(1,3-dithiol)



S1 (800 mg, 2.5 mmol) was dissolved in 15 mL dry dichloromethane and 20 mL dry methanol were added. Then, sodium borohydride (300 mg, 3.83 mmol, 1.50 eq.) was added, whereupon the yellow solution lost its color. After 15 minutes of stirring at room temperature, the solvents were removed under reduced pressure and water (30 mL) was added. The aqueous phase was extracted with ethyl acetate (3 x 20 mL) and the unified organic phases were dried over MgSO₄. After removal of the solvents, the crude product is obtained as an off-white solid, which was then purified by column chromatography on silica eluting with CyH/EtOAc (9:1) giving **S2** (*R_f* = 0.18) in a yield of 767 mg (95%).

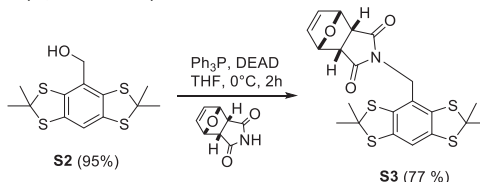
¹H-NMR (400 MHz, CDCl₃, 298 K, δ in ppm): 7.01 (s, 1H), 4.56 (s, 2H), 1.89 (s, 12H).

¹³C{¹H}-NMR (100 MHz, CDCl₃, 298 K, δ in ppm): 136.6, 136.0, 129.5, 116.5, 65.3, 65.2, 31.5.

HRMS (ESI+, *m/z*, [M]⁺): calc. for C₁₃H₁₆OS₄, 316.0078; found 316.0077.

2.2.2 Synthesis of **S3**

2,2,6,6-tetramethyl-8-(1-methyl(3aRS,4SR,7RS,7aSR-4,7-epoxy-3,3a,7,7a-tetrahydro-2H-isoindoli-1,3-dione-2-yl)-benzo[1,2-d;4,5-d]bis(1,3-dithiol)



S2 (300 mg, 0.95 mmol, 1.25 eq.), **13** (125 mg, 0.76 mmol), and Ph_3P (200 mg, 0.76 mmol) were dissolved in 10 mL dry THF. Then, DEAD (132 mg, 120 μL , 0.76 mmol) was added and the reaction mixture was stirred for 1 h at 0°C . Subsequently, the reaction mixture was poured onto water (50 mL) and extracted with CH_2Cl_2 (2 x 30 mL). The unified organic phases were dried over MgSO_4 and solvents were removed under reduced pressure. The product ($R_f = 0.3$) was isolated by column chromatography on silica eluting with CyH/EtOAc (2:1) in a yield of 338 mg (77%).

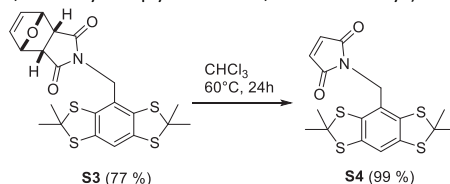
$^1\text{H-NMR}$ (500 MHz, CDCl_3 , 298 K, δ in ppm): 6.99 (s, 1H), 6.44 (bs, 2H), 5.29 (m, 2H), 4.37 (s, 2H), 3.54 (m, 2H), 1.86 (s, 12H).

$^{13}\text{C}\{^1\text{H}\}\text{-NMR}$ (125 MHz, CDCl_3 , 298 K, δ in ppm): 173.9, 136.6, 136.6, 134.9, 124.1, 116.6, 79.4, 65.4, 46.1, 43.1, 31.2.

HRMS (APCI, m/z , $[\text{M}+\text{H}]^+$): calc. for $\text{C}_{21}\text{H}_{22}\text{NO}_3\text{S}_4$, 464.0477; found 464.0474.

2.2.3 Synthesis of **S4**

2,2,6,6-tetramethyl-8-(1-methyl(3,4-dehydropyrididin-1,3-dione-2-yl)benzo[1,2-d;4,5-d]bis(1,3-dithiol)



S3 (100 mg) was dissolved in 20 mL chloroform and stirred at 60°C overnight and under an argon atmosphere. Afterwards, all volatiles were removed and **S4** was obtained in a quantitative yield of 85 mg as a colorless solid.

$^1\text{H-NMR}$ (500 MHz, CDCl_3 , 298 K, δ in ppm): 7.01 (s, 1H), 6.68 (s, 2H), 4.57 (s, 2H), 1.87 (s, 12H).

$^{13}\text{C}\{^1\text{H}\}\text{-NMR}$ (125 MHz, CDCl_3 , 298 K, δ in ppm): 169.73, 136.76, 136.16, 134.15, 124.94, 116.48, 65.62, 42.06, 31.25.

HRMS (ESI+, m/z , $[\text{M}+\text{H}]^+$): calc. for $\text{C}_{21}\text{H}_{22}\text{NO}_3\text{S}_4$, 316.0215; found 316.0213.

2.2.4 Retro Diels-Alder reaction: Kinetics

Since **15** \bullet is paramagnetic and therefore not suitable for NMR-measurements, model compound **S3** was used in order to examine the Retro-Diels-Alder reaction leading to **9** \bullet . For this, 100 mg of **S3** were dissolved in 5 mL CDCl_3 and heated to 60°C under argon. Then, samples of 0.5 mL were drawn out of the reaction mixture with a syringe, cooled, and subjected to $^1\text{H-NMR}$ analysis immediately. Since **S3** and its Retro-Diels-Alder product **S4** can be differentiated by NMR, it was possible to extract the reaction kinetics, which follows a first order rate law as shown in Figure S1. After 1380 min (23 h), complete conversion to the free maleimide was observed.

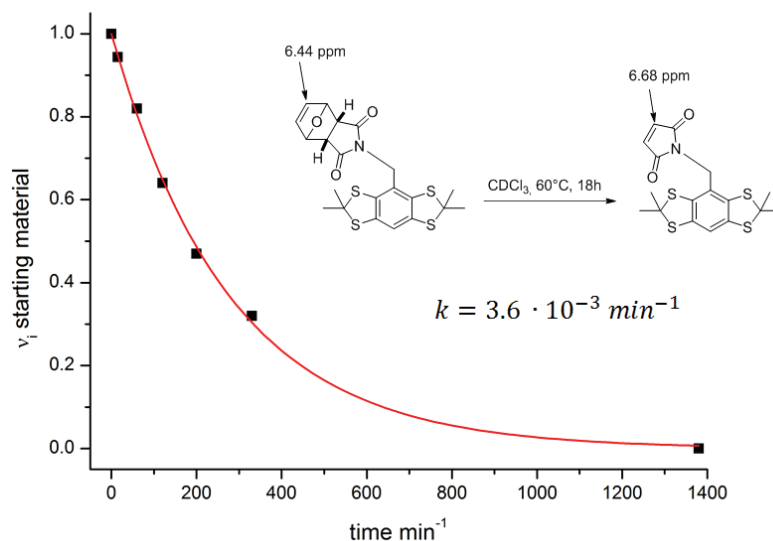
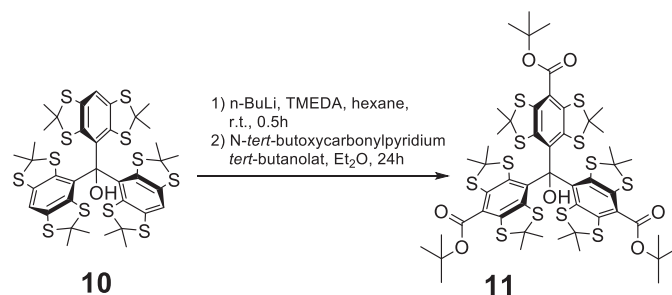


Figure S1: Kinetics for Retro-Diels-Alder reaction based on $^1\text{H-NMR}$. Experimentally determined molar ratio of starting material (black dots) with exponential fit (red line).

Based on a first-order rate law, a rate constant of 0.0036 min^{-1} was found by least-square fitting. This value compared well to rate constants obtained for similar furane-maleimide adducts.^[6] From this, it was concluded that the tetrathioaryl-substituent does not influence the Retro-Diels-Alder reactivity. Therefore, the same conditions were applied in the synthesis of **9**.

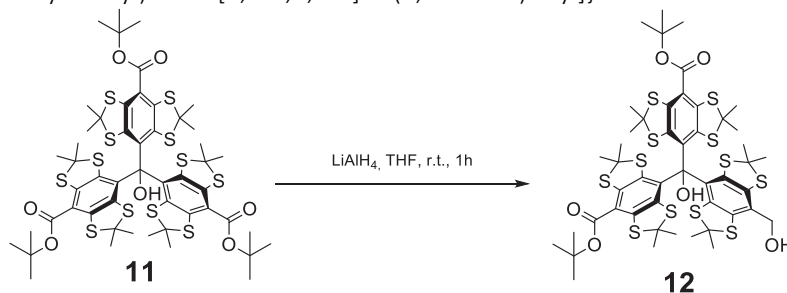
2.2.5 Synthesis of literature known compound **11**



Tris[2,2,6,6-tetramethyl-8-(carboxy-tert-butyl)benzo[1,2-d;4,5-d]bis(1,3-dithiol-4-yl)methanol]trityl alcohol **10** (3.00 g, 3.40 mmol) was dissolved in 100 mL dry Et_2O and N,N,N',N' -tetramethylethylenediamin (5.0 mL, 3.87 g, 34.0 mmol, 10 eq.) were added under argon. Then, the solution was cooled down to 0°C and n -butyl lithium (2.5 M in hexane, 13.6 mL, 34.0 mmol, 10 eq.) was added slowly. The yellowish solution obtained by this was stirred for 2 h at room temperature. In parallel, a solution of N,N -dimethylamino pyridine (12.44 g, 102.0 mmol, 30 eq.) and di- $tert$ -butyl dicarbonate (18.42 g, 18.36 mL, 84.7 mmol, 25 eq.) in 300 mL dry Et_2O was prepared and stirred for 90 min at room temperature. Then, the solution of the lithiated trityl alcohol was transferred to the activated Boc_2O , whereupon the reaction mixture turned greenish and was stirred overnight in order to complete the carbonylation. After quenching with 300 mL water, the organic phase was separated and the aqueous one extracted with 100 mL Et_2O . The unified organic phases were dried over MgSO_4 and the solvent was removed. The yellow-orange crude product was purified by column chromatography on silica eluting with $\text{CyH}/\text{Et}_2\text{O}$ (3:1, v/v) giving **11** as an orange solid ($R_f = 0.38$) in a yield of 1.88 g (16 mmol, 47 %). The analytical data is in accordance with the literature.^[2]

2.2.6 Synthesis of **12**

Bis[[2,2,6,6-tetramethyl-8-(carboxy-tert-butyl)benzo[1,2-d;4,5-d]bis(1,3-dithiol)-4-yl]]-[[2,2,6,6-tetramethyl-8-(hydroxymethyl)benzo[1,2-d;4,5-d]bis(1,3-dithiol)-4-yl]]methanol



Trityl alcohol **11** (345 mg, 0.29 mmol) was dissolved in 15 mL THF, in parallel a solution of lithium aluminum hydride (170 mg, 4.47 mmol in 10 mL THF, 0.45 mmol mL⁻¹) was prepared. Then, the reduction was started by addition of 0.5 mL (0.23 mmol, 0.78 eq.) of the LiAlH₄ solution to the reaction mixture. After stirring for 5 min, the conversion was checked by TLC on SiO₂ eluting with CyH/EtOAc (2:1), where the product appears at R_f = 0.78 below the starting material. It was continued with a repetitive addition of 0.25 mL LiAlH₄-solution and evaluation by TLC after 5 min, until significant amounts of the twofold reduction product occur. Then, the reaction mixture was quenched by slow addition of 30 mL water and extracted with diethyl ether. The organic phase was separated and dried over MgSO₄, after removal of the solvents, an orange crude product was obtained, which was purified by column chromatography on silica eluting with CyH/EtOAc (2:1, v/v). The product **12** was isolated as a yellow solid (R_f = 0.78) in a yield of 136 mg (42 %, 58 % brsm). Note, that the starting material (93 mg, 0.08 mmol, 27 mol%) could be recovered and used again in order to maximize the yield of this statistical transformation.

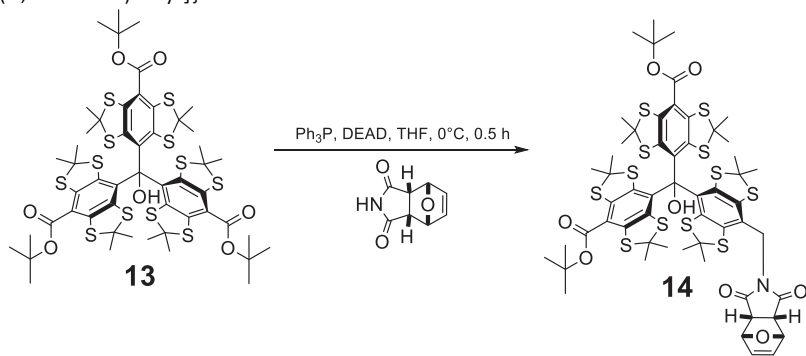
¹H-NMR (700 MHz, CDCl₃, 298 K, δ in ppm): 6.68 (s, 1H), 4.71 (d, ²J_{H,H} = 12.4 Hz, 1H), 4.66 (d, ²J_{H,H} = 12.4 Hz, 1H), 1.79 (s, 6H), 1.78 (s, 3H), 1.77 (s, 3H), 1.77 (s, 3H), 1.73 (s, 3H), 1.72 (s, 3H), 1.71 (s, 3H), 1.66 (s, 3H), 1.65 (s, 9H), 1.65 (s, 9H), 1.63 (s, 3H), 1.62 (s, 3H).

¹³C{¹H}-NMR (176 MHz, CDCl₃, 298 K, δ in ppm): 165.58, 141.48, 141.43, 141.38, 141.05, 140.59, 140.50, 140.42, 140.20, 139.26, 138.53, 137.88, 137.72, 134.53, 134.42, 130.95, 130.56, 123.04, 122.98, 84.48, 84.39, 84.27, 66.04, 63.36, 62.57, 61.99, 61.07, 60.86, 60.83, 35.01, 34.86, 34.04, 33.36, 32.02, 31.17, 30.13, 29.69, 29.33, 28.55, 27.89, 27.86, 27.58.

HRMS (MALDI+, DCTB-matrix, *m/z*, [M]⁺): calc. for C₄₈H₅₈O₆S₁₂, 1114.0876; found 1114.0884.

2.2.7 Synthesis of **14**

Bis[[2,2,6,6-tetramethyl-8-(carboxy-tert-butyl)benzo[1,2-d;4,5-d]bis(1,3-dithiol)-4-yl]]-[[2,2,6,6-tetramethyl-8-(1-methyl(3aRS,4SR,7RS,7aSR-4,7-epoxy-3,3a,7,7a-tetrahydro-2H-isoindoli-1,3-dione-2-yl)-[1[1,2-d;4,5-d]bis(1,3-dithiol)-4-yl]]methanol



Trityl alcohol **12** (34 mg, 30.5 μmol), triphenyl phosphine (15 mg, 57.2 μmol , 1.87 eq.), and 3aRS,4SR,7RS,7aSR-4,7-epoxy-3,3a,7,7a-tetrahydro-2H-isoindoli-1,3-dione (10 mg, 60.6 μmol , 1.98 eq.) were dissolved in 1.5 mL dry THF under argon. Then, the reaction mixture was cooled down to 0 °C and 14 μL diethylazodicarboxylate (DEAD, 14 μL , 15.5 mg, 89.3 μmol , 2.92 eq.) were added, whereupon an immediate color change from orange to dark brown was observed. After stirring for 30 min at 0 °C, TLC (SiO_2 , CyH/EtOAc 2:1, v/v) showed complete consumption of the starting material and water (10 mL) was added. The mixture was extracted with CH_2Cl_2 and the organic phase was separated and dried over MgSO_4 . After removal of the solvents under reduced pressure, column chromatography on silica eluting with CyH/EtOAc (2:1 v/v) was performed in order to isolate the product ($R_f = 0.43$) as a yellow solid in a yield of 27 mg (70 %).

$^1\text{H-NMR}$ (700 MHz, CDCl_3 , 298 K, δ in ppm): 6.66 (s, 1H), 6.46 (dd, $^3J_{\text{H,H}} = 5.8$, $^3J_{\text{H,H}} = 1.6$ Hz, 1H), 6.43 (dd, $^3J_{\text{H,H}} = 5.9$, $^3J_{\text{H,H}} = 1.6$ Hz, 1H), 5.30 – 5.27 (m, 2H), 4.59 (d, $^2J_{\text{H,H}} = 14.6$ Hz, 1H), 4.48 (d, $^2J_{\text{H,H}} = 14.6$ Hz, 1H), 3.54 – 3.46 (m, 2H), 1.78 (s, 3H), 1.77 (s, 3H), 1.76 (s, 9H), 1.73 (s, 3H), 1.72 (s, 3H), 1.69 (s, 3H), 1.67 (s, 3H), 1.65 (s, 15H), 1.64 (s, 9H), 1.62 (s, 3H).

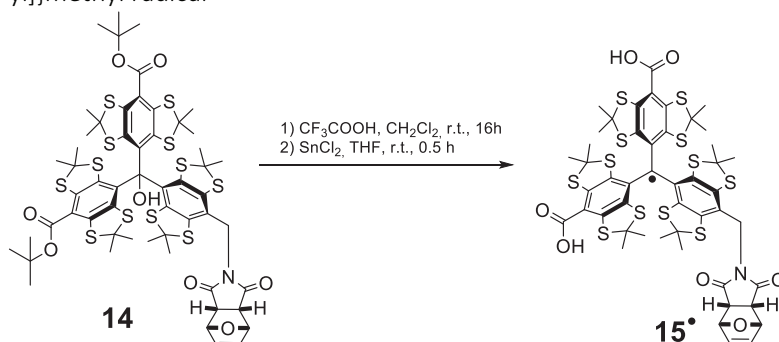
$^{13}\text{C}\{^1\text{H}\}\text{-NMR}$ (176 MHz, CDCl_3 , 298 K, δ in ppm): 173.90, 173.72, 165.60, 165.57, 141.51, 141.44, 141.36, 141.12, 140.72, 140.67, 140.53, 140.29, 139.33, 138.84, 138.57, 137.61, 134.97, 134.84, 134.50, 134.35, 130.65, 125.18, 123.02, 122.97, 84.47, 84.38, 84.28, 79.53, 63.39, 62.58, 62.14, 60.98, 60.88, 60.81, 46.15, 46.13, 44.00, 34.99, 34.92, 34.00, 33.27, 32.17, 31.41, 29.85, 29.81, 29.13, 28.55, 27.66, 27.54, 27.51.

HRMS (MALDI+, DCTB-matrix, m/z , $[\text{M-furane}]^+$): calc. for $\text{C}_{52}\text{H}_{59}\text{NO}_7\text{S}_{12}$, 1193.0935; found 1193.0922.

Note that **14** underwent Retro-Diels-Alder cleavage during mass-spectrometry, so that no M^+ -peak was found neither in MALDI nor in ESI.

2.2.8 Synthesis of **15**[•]

Bis[[2,2,6,6-tetramethyl-8-carboxylbenzo[1,2-d;4,5-d]bis(1,3-dithiol)-4-yl]]-[[2,2,6,6-tetramethyl-8-(1-methyl(3aRS,4SR,7RS,7aSR-4,7-epoxy-3,3a,7,7a-tetrahydro-2H-isoindoli-1,3-dione-2-yl)-benzo[1,2-d;4,5-d]bis(1,3-dithiol)-4-yl]]methyl radical



Trityl alcohol **14** (15 mg, 11.9 μmol) was dissolved in 100 μL dry CH₂Cl₂ under an argon atmosphere. Then, 2.0 mL CF₃COOH were added, whereupon the reaction mixture turned dark green. After stirring overnight, tin(II)-chloride (3.3 mg in 100 μL tetrahydrofuran, 17.8 mmol, 1.5 eq.) was added, whereupon a color change to brown was observable. After additional stirring for 15 min, all liquids were removed through high vacuum and the residue was taken up in 5 mL dichloromethane. The organic phase was washed with water, separated, and dried over MgSO₄. After removal of the solvents, a brown residue was obtained, which was purified by MPLC on RP-C18-silica eluting with CH₃CN/H₂O 4:1 (v/v). The first fraction was isolated and solvents were removed under reduced pressure obtaining **15** as a brown solid in a yield of 14 mg (95 %).

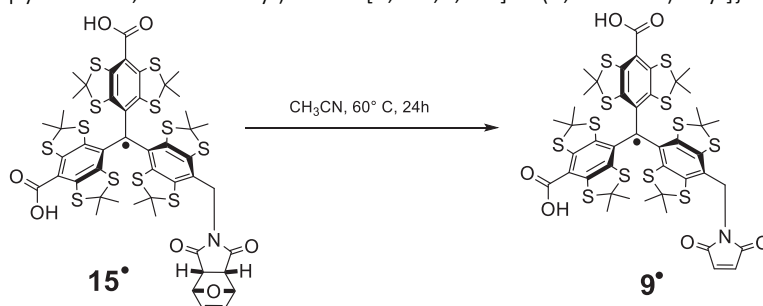
UHPLC (60 % CH₃CN, 40 % H₂O; each with 0.05 % CF₃COOH; t_r): 1.81 min

HRMS (MALDI+, DCTB-matrix, m/z, [M]⁺): calc. for C₄₈H₄₆NO₇S₁₂, 1131.9917; found 1131.9906

cw-EPR (X-Band, DMSO, 200 μM, 298 K): g-value = 2.0034; A_N = 1.51 MHz, A_H = 3.39 MHz, A_H = 5.16 MHz, A_{C,central} = 66.10 MHz, A_{C,ipso} = 31.11 MHz, A_{C,ortho} = 25.43 MHz, A_{C,para} = 6.83 MHz, A_{C,meta} = 3.51 MHz.

2.2.9 Synthesis of **9**[•]

Bis[[2,2,6,6-tetramethyl-8-carboxylbenzo[1,2-d;4,5-d]bis(1,3-dithiol)-4-yl]]-[[2,2,6,6-tetramethyl-8-(1-methyl(3,4-dehydropyrolidin-1,3-dione-2-yl)-benzo[1,2-d;4,5-d]bis(1,3-dithiol)-4-yl]]methyl radical



Trityl radical **15**[•] (10 mg, 8.8 μmol) was suspended in 5 mL dry degassed acetonitrile and stirred at 60 °C for 24 h under argon atmosphere. All volatiles were removed in high vacuum and the product was obtained as a brown solid in quantitative yield of 9 mg.

UHPLC (60% CH₃CN, 40% H₂O; each with 0.05% CF₃COOH; t_r): 2.04 min

HRMS (MALDI+, DCTB-matrix, m/z, [M-furane]⁺): calc. for C₄₄H₄₂NO₆S₁₂, 1063.966; found 1063.968

cw-EPR (X-Band, DMSO, 200 μM, 298 K): g-value = 2.0034; A_N = 1.48 MHz, A_H = 3.48 MHz, A_H = 6.06 MHz, A_{C,central} = 66.16 MHz, A_{C,ipso} = 31.22 MHz, A_{C,ortho} = 25.45 MHz, A_{C,para} = 6.86 MHz, A_{C,meta} = 3.57 MHz.

2.3 Analytical Data Synthesis

2.3.1 NMR Spectra

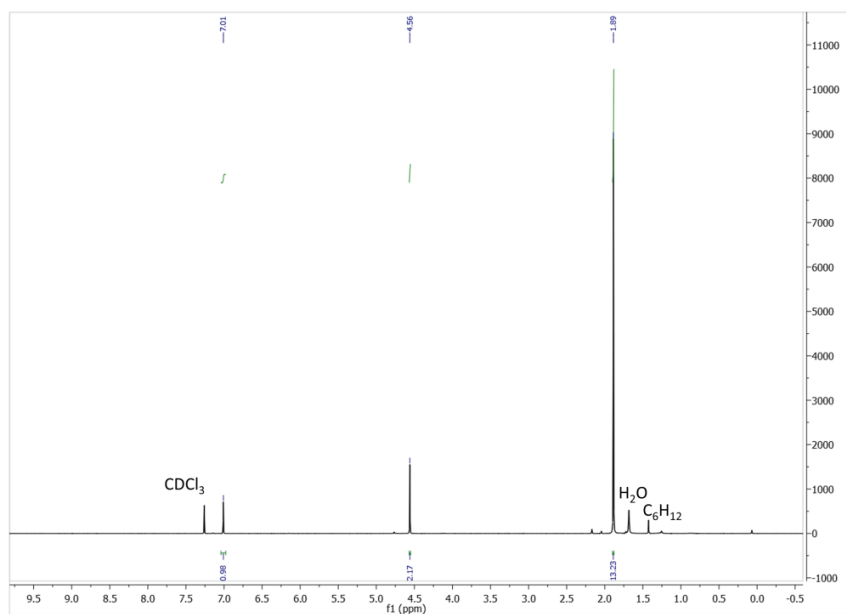


Figure S2: $^1\text{H-NMR}$ (500 MHz, 298 K, CDCl_3) of S2.

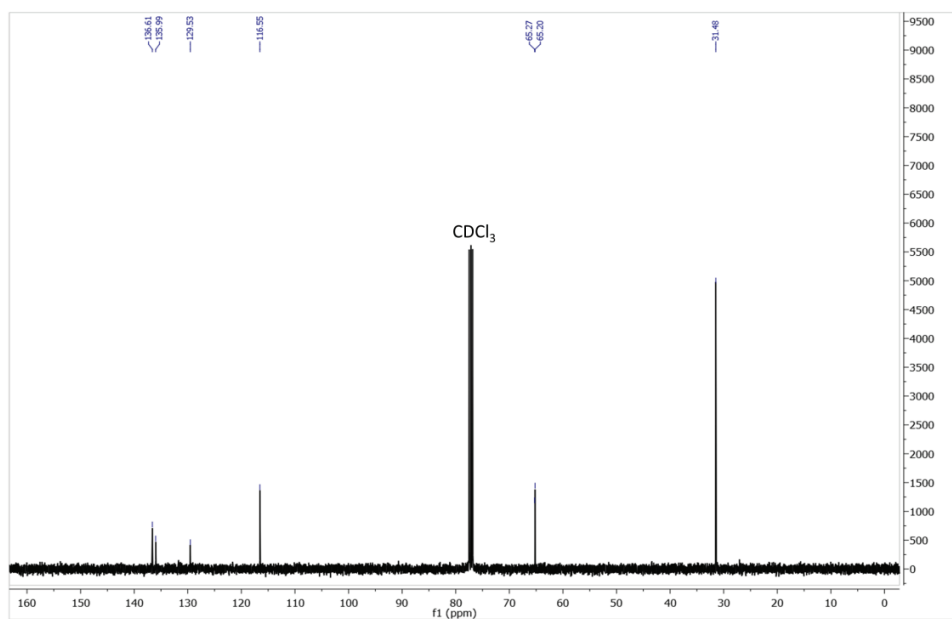


Figure S3: $^{13}\text{C}\{^1\text{H}\}$ -NMR (125 MHz, 298 K, CDCl_3) of S2

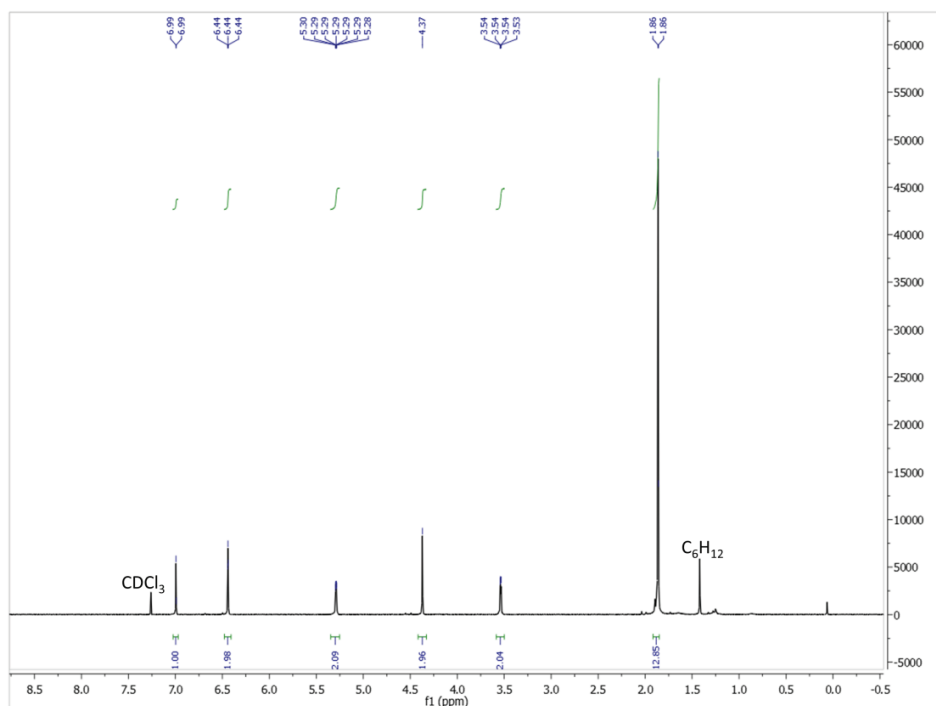


Figure S4: ¹H-NMR (500 MHz, 298 K, CDCl₃) of S3.

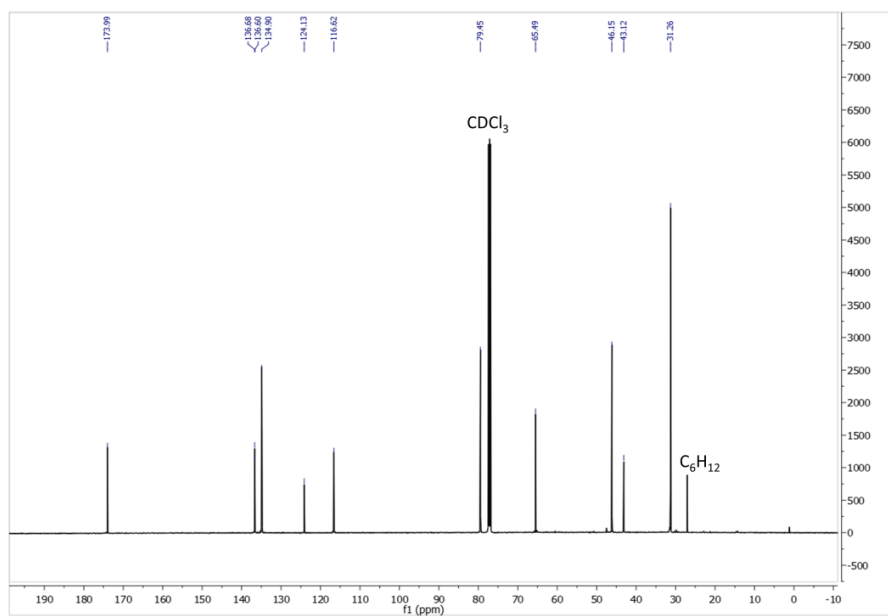


Figure S5: ¹³C{¹H}-NMR (125 MHz, 298 K, CDCl₃) of S3.

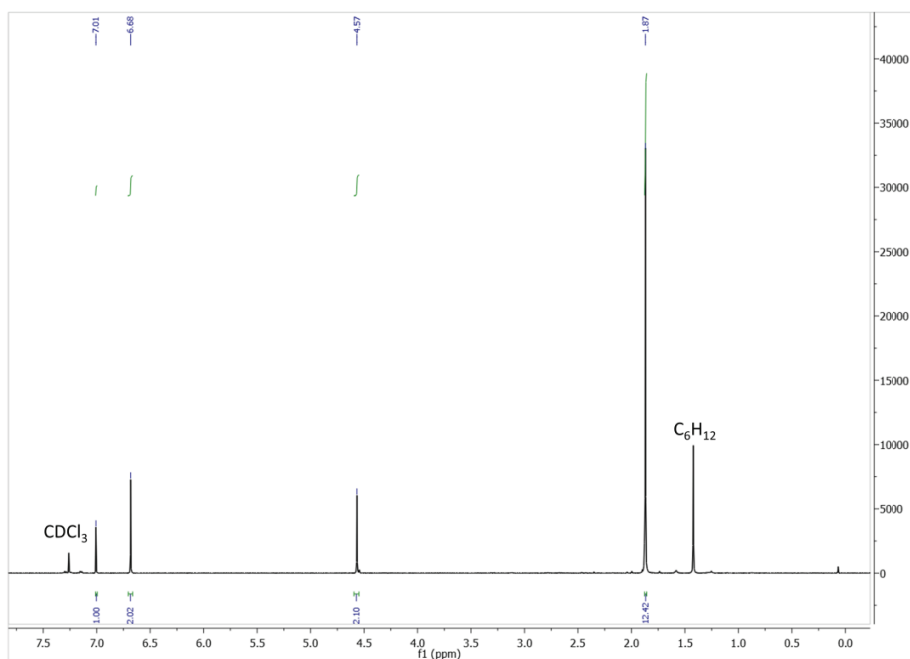


Figure S6: $^1\text{H-NMR}$ (500 MHz, 298 K, CDCl_3) of **S4**.

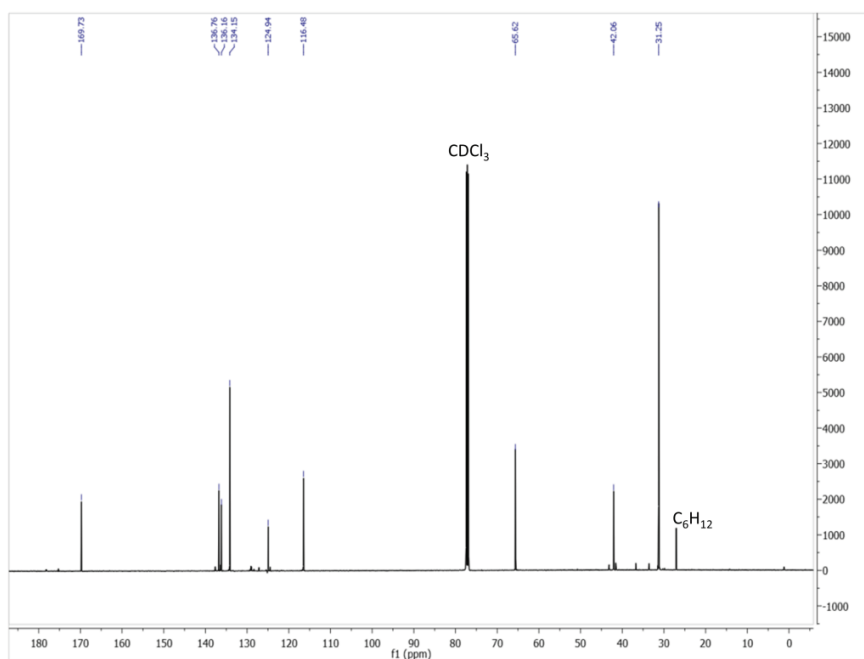


Figure S7: $^{13}\text{C}\{^1\text{H}\}$ -NMR (125 MHz, 298 K, CDCl_3) of **S4**.

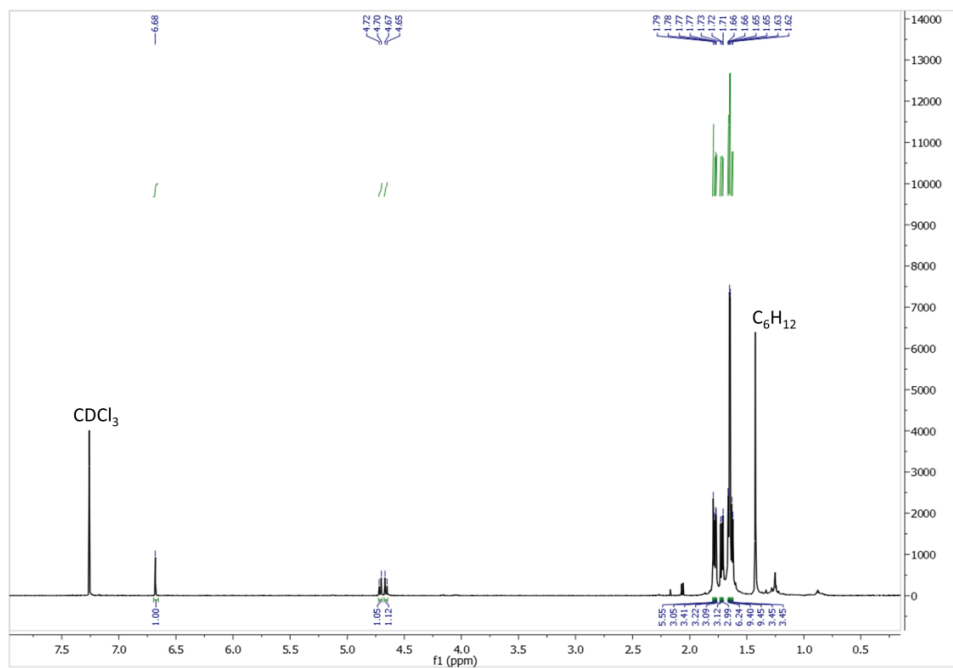


Figure S8: $^1\text{H-NMR}$ (700 MHz, 298 K, CDCl_3) of **12**.

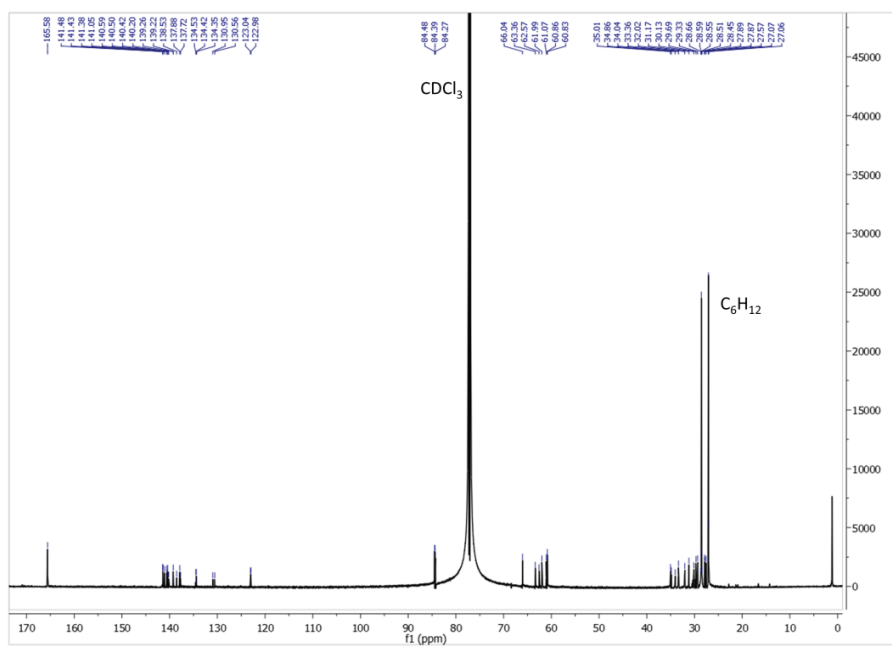


Figure S9: $^{13}\text{C}\{^1\text{H}\}$ -NMR (176 MHz, 298 K, CDCl_3) of **12**.

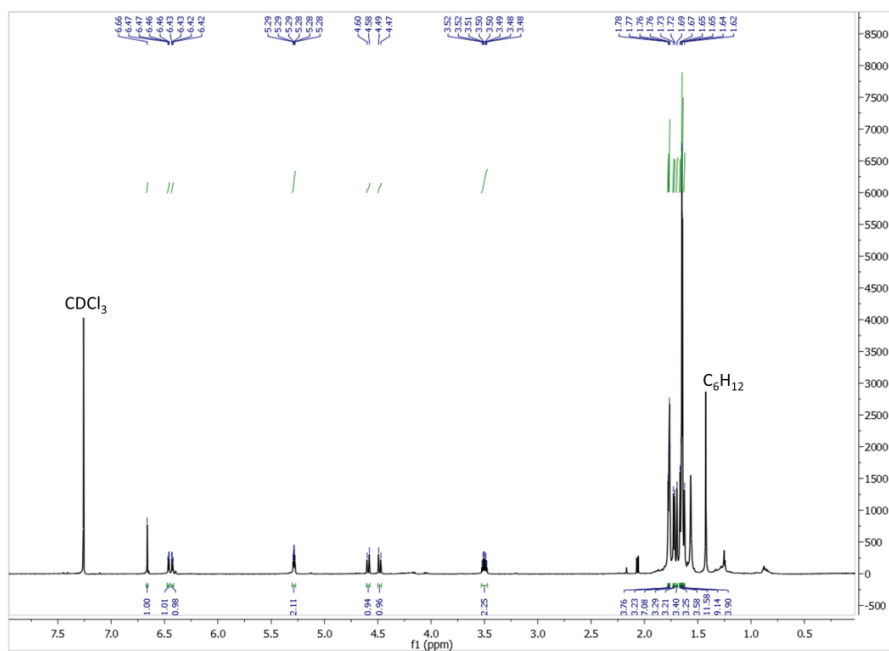


Figure S10: $^1\text{H-NMR}$ (700 MHz, 298 K, CDCl_3) of **14**.

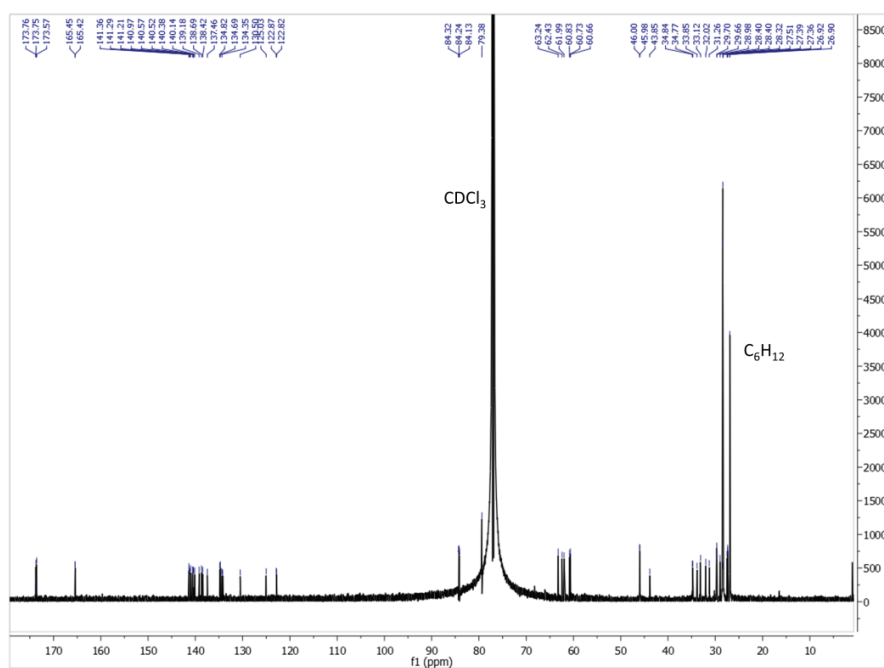


Figure S11: $^{13}\text{C}\{^1\text{H}\}$ -NMR (176 MHz, 298 K, CDCl_3) of **14**.

2.3.2 HRMS-Data

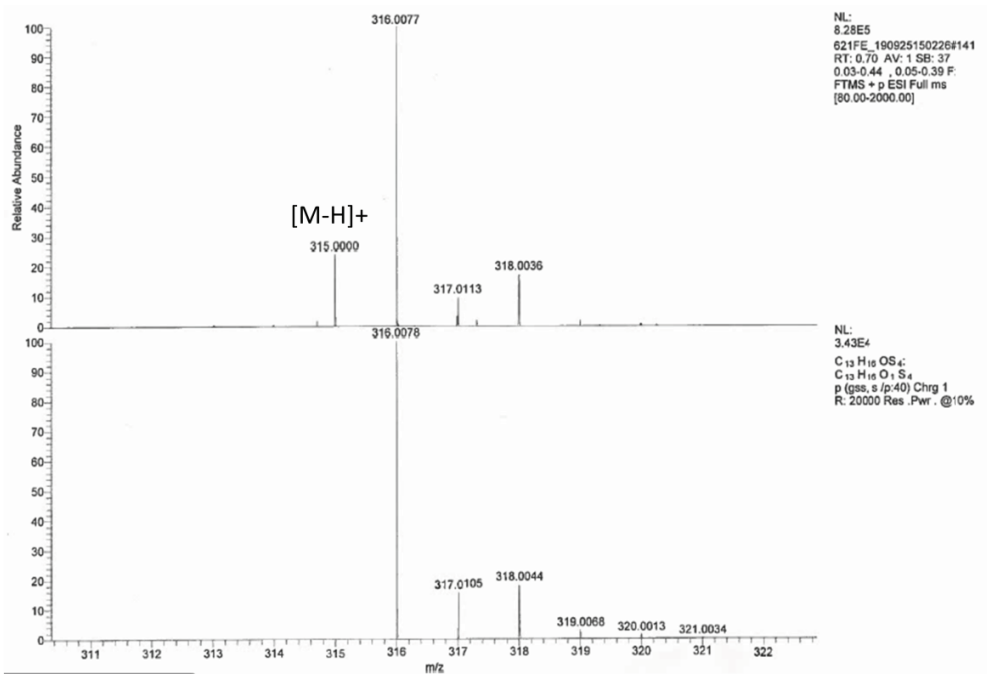


Figure S12: ESI(+)-HRMS (top) of S2 and calculated isotope pattern for M⁺ (bottom).

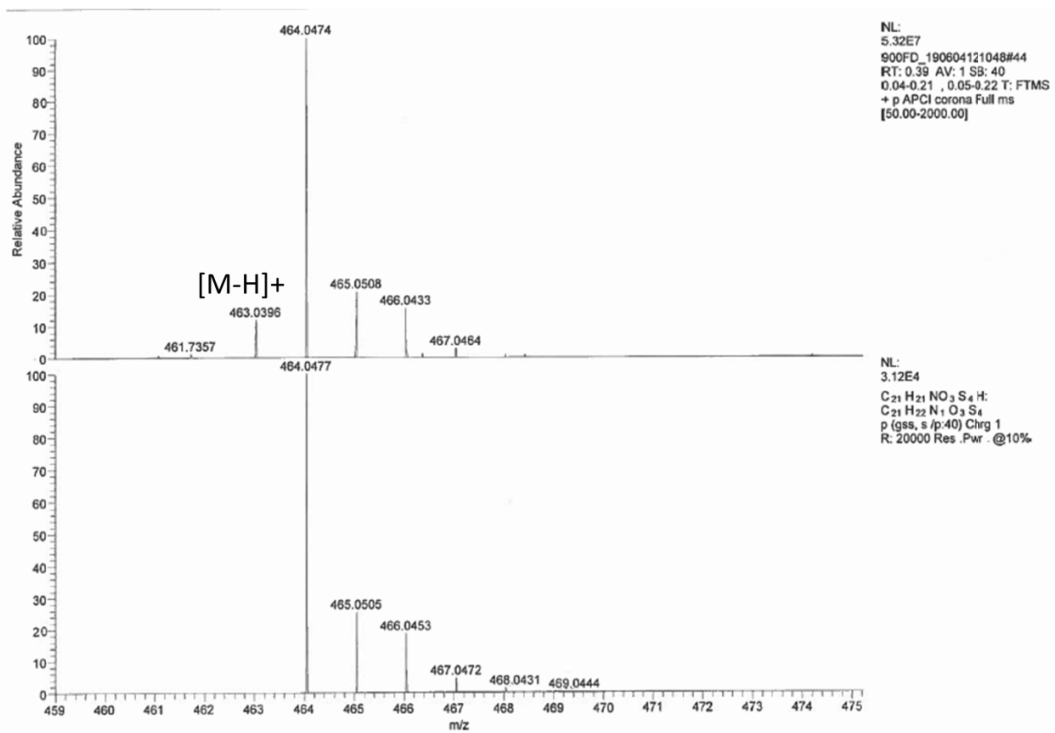


Figure S13: APCI-HRMS (top) of S3 and calculated isotope pattern for [M+H]⁺ (bottom).

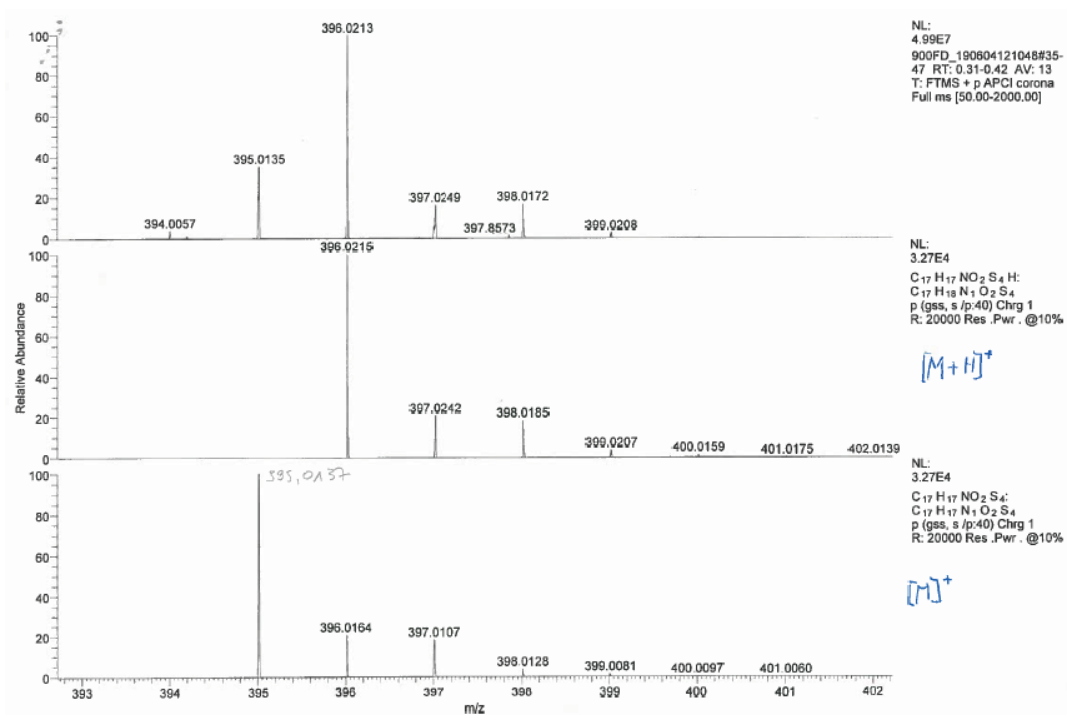


Figure S14: APCI-HRMS (top) of **S4** and calculated isotope patterns (bottom).

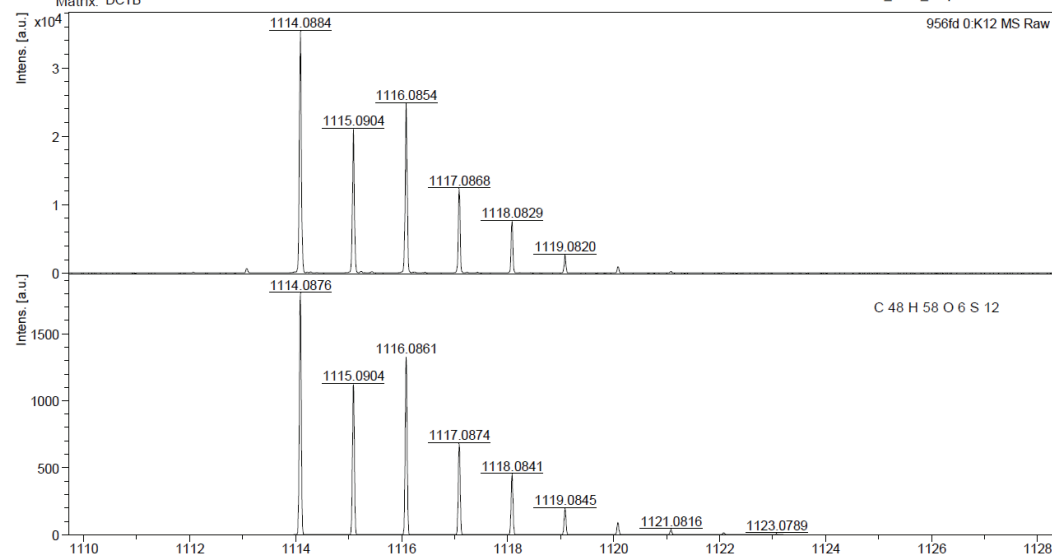
D:\Data\956fd\0_K1211

Name, Probe: Fleck, NFL-FT-04

2019-06-13T13:53:43.000

Matrix: DCTB

D:\Methods\flexControlMethods\IP-Meth_2019\RP_1000_Da.par



UltrafleXtreme MALDI TOF

POS

printed: 13.06.2019 14:14:10

Figure S15: MALDI(+)-HRMS (top) of **12** and calculated isotope pattern for M^+ (bottom).

D:\Data\955fd2\0_J1111

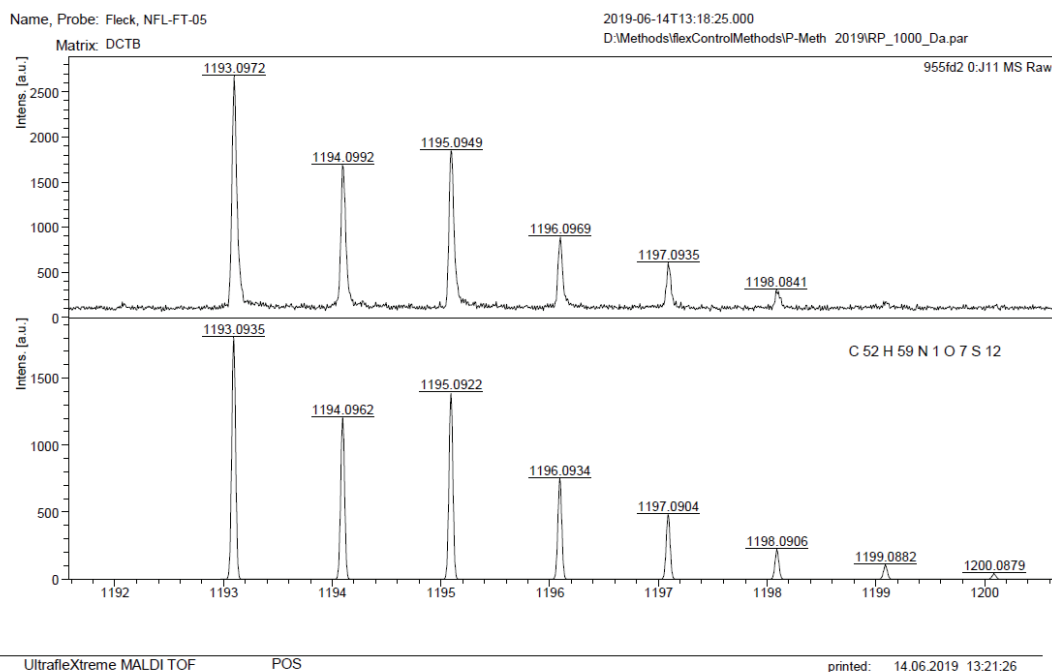


Figure S16: MALDI(+)-HRMS (top) of **14** and calculated isotope pattern for M^+ (bottom).

D:\Data\052fe\0_F911

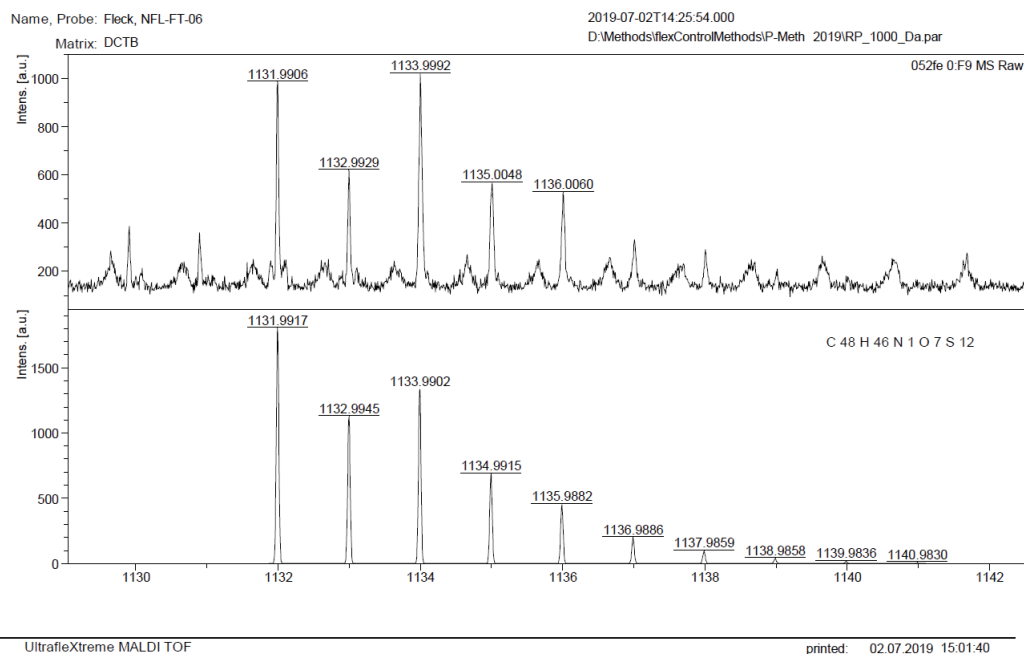


Figure S17: MALDI(+)-HRMS (top) of **15*** and calculated isotope pattern for M^+ (bottom). Note, that the $[M]^+$ -peak shown here is not the base peak due to Retro-Diels-Alder fragmentation in the mass spectrometer and therefore suffers from low intensity. The regularly appearing noisy peaks belong to the spectrometer background.

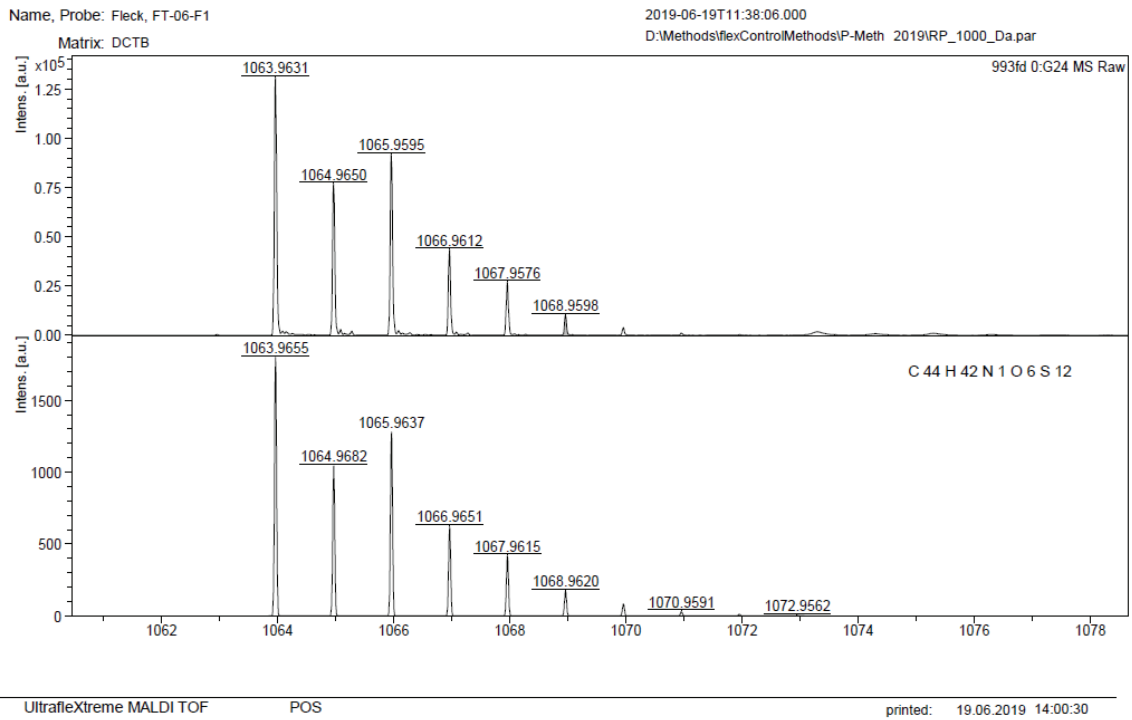


Figure S18: MALDI(+)-HRMS (top) of **9** and calculated isotope pattern for M^+ (bottom).

2.3.3 UHPLC Data

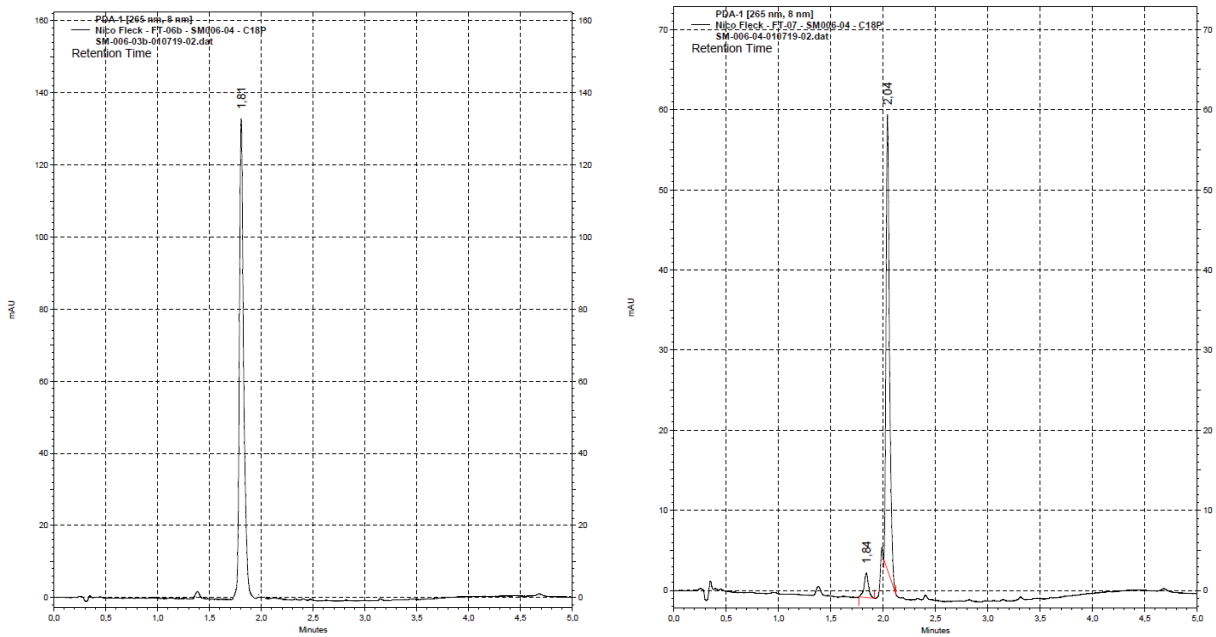
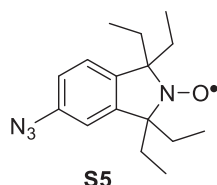


Figure S19: UHPLC chromatogram of **15** (left) and of **9** (right).

3. Spin Labeling

3.1 Tetraethylnitroxide-DNA Construct

Since the isoindoline based tetraethylnitroxide **S5** does not possess sufficient solubility in aqueous environments, it was conjugated to a DNA strand. This yielded a water-soluble construct, which is suitable for stability measurements.



For this, a DNA strand (5' GGG TGX CTG GTA CCC 3', obtained from *Metabion*, X = 5-ethynyl-2'dU) was labeled with **S5**^[7] using our recently published protocol.^[8] Annealing of the labeled strand with the complementary unmodified strand provided the singly labeled DNA duplex used for the stability studies.

3.2 SLIM Dilution Series and Calibration Curve

To create a stock solution of **9**[•] for subsequent protein labeling, the free label **9**[•] was dissolved in DMSO. Since potential weighing errors may have severe impact on the correctness of all following quantification routines, five independent EPR spin count experiments with the DMSO stock diluted 1:100 in POi buffer (20 mM POi pH 6.8, 50 mM NaCl) were performed on an EMXnano EPR spectrometer. The final concentration based on the mean value of these measurements accounted to 2.58 mM of **9**[•].

A dilution series of **9**[•] in POi buffer was set up and measured on a Cary 100 UV-vis spectrometer (Agilent Technologies, Santa Clara, CA, USA) and the molar extinction coefficients of **9**[•] at 271 nm and 459 nm were determined via linearization according to the *Lambert-Beer law*.

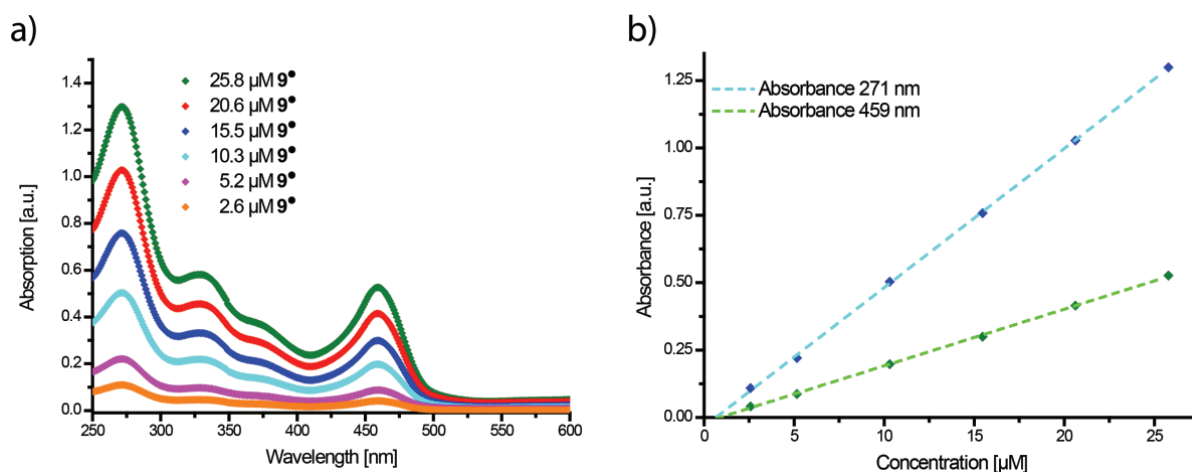


Figure S20: UV-vis dilution series of **9**[•] (a) and the linear fits of the absorbance at 271 nm (cyan) and 459 nm (green) (b).

Table S1: Extinction coefficients of **9[•]** at 271 nm and 471 nm.

Wavelength [nm]	Extinction coefficient ϵ $\left[\frac{L}{\mu\text{mol}\cdot\text{cm}}\right]$
271	0.05152
459	0.02099

The labeling efficiencies of YopO in each labeling experiment using trityls **9[•]** or **8[•]** were determined using the previously implemented technique.^[9] Since the protein itself only absorbs at ~280 nm and both trityl labels show a second absorption maximum at 459 nm (**9[•]**) or 467 nm (**8[•]**), the protein and respective trityl concentrations can be determined as follows:

$$c_{\text{trityl}} = \frac{A_{459/467}}{d \cdot \epsilon_{\text{trityl}}}$$

$$c_{\text{YopO}} = \frac{A_{271} - c_{\text{trityl}} \cdot d \cdot \epsilon_{271, \text{trityl}}}{d \cdot \epsilon_{280, \text{YopO}}}$$

Although slight shifts in the absorption maxima wavelengths are seen for both trityl labels upon bioconjugation, the errors resulting from these shifts are negligible. The extinction coefficient of YopO was calculated using the computing tool ProtParam.^[10] All utilized extinction coefficients are listed in Table S2.

Table S2: Extinction coefficients of YopO, **8[•]** and **9[•]**.

Protein/Trityl	ϵ $\left[\frac{L}{\mu\text{mol}\cdot\text{cm}}\right]$
YopO	$\epsilon_{280} = 0.04939$
9[•]	$\epsilon_{271} = 0.05152$ $\epsilon_{459} = 0.02099$
8[•]	$\epsilon_{280} = 0.01930$ $\epsilon_{467} = 0.00750$

3.3 *Yersinia* outer protein O (YopO)

3.3.1 Construct Design

Truncated YopO₈₉₋₇₂₉ C219A (YopO-WT) from *Yersinia enterocolitica* was cloned in frame into the pGex6p1 vector (GE Healthcare, Chicago, IL, USA), transformed into *E. coli* DH5 α cells and amplified. This construct served as the template for further mutagenesis and cysteine introduction via *QuickChange* mutagenesis^[11] for YopO N624C and YopO Y588C/N624C. The primers are listed in Table S3.

Table S3: YopO primer pairs

	Sequence
Y588C fwd	5'-CAAGGGCAGCCCGTGTCTCTGAAACCTGTAGCTTCC-3'
Y588C rev	5'-GACCTTAGCCTCAGCTAATCGATTCAGGAAGCTACAGGTTTCAG-3'
N624c fwd	5'-GAGAGTGCGAAAAGCGCAACTATCTATTCTGATTTGTCGTTTCAG-3'
N624C rev	5'-GAGCAACATCAGCCCAAGAACCTGAACGACAAATCAGAATAG-3'

After PCR, the new constructs were transformed into *E. coli* DH5 α cells and the successful mutagenesis was confirmed *via* Sanger sequencing.

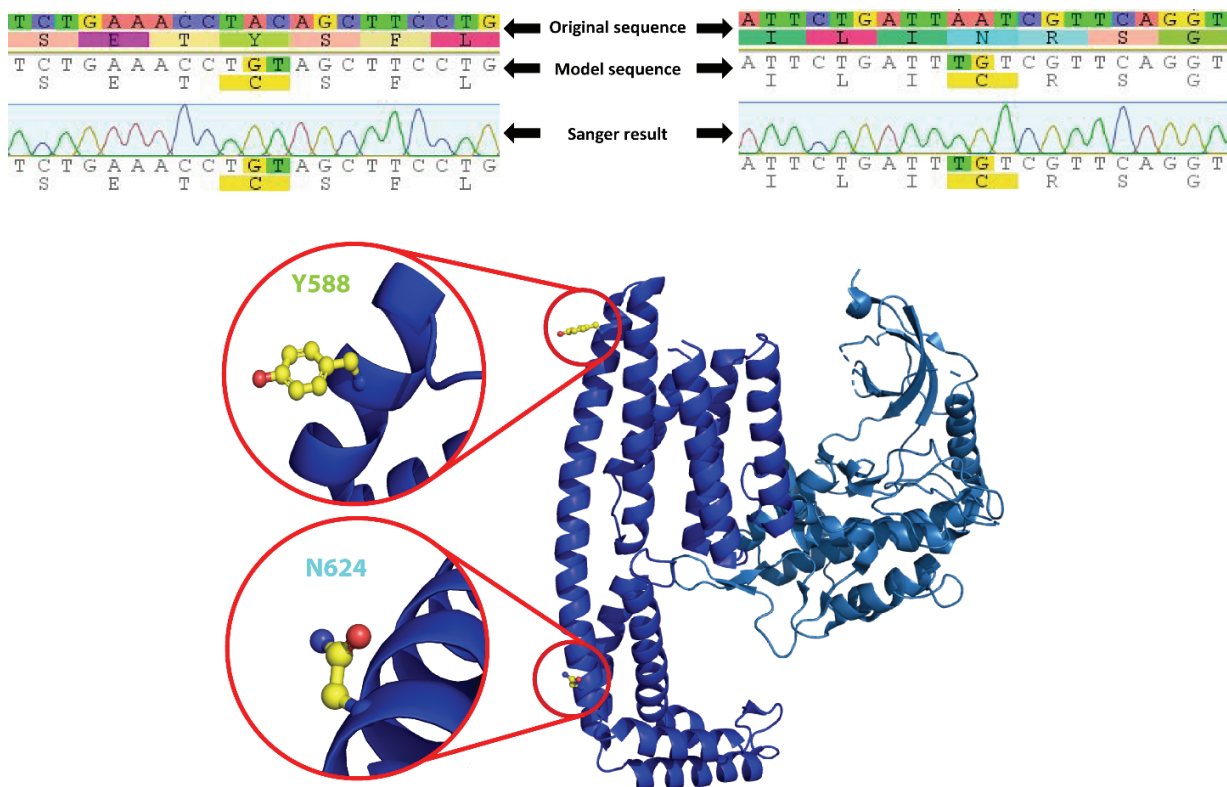


Figure S21: Sequencing results for YopO Y585C/N624C (top, excerpt taken from Geneious (Biomatters Ltd., Auckland, New Zealand)). PyMOL (Schrodinger, New York, NY, USA) representation showing the locations of the unmutated amino acid positions in YopO (PDB-ID: 4ci6) (bottom).

3.3.2 YopO Expression

All YopO constructs were expressed in *E.coli* Rosetta (DE3) cells. From an agar plate, a single colony was picked and grown overnight at 37 °C / 180 rpm in 20 mL LB medium containing 0.3 mM ampicillin and 0.1 mM chloramphenicol. Main-cultures were set up in 1 L LB medium (0.3 mM ampicillin, 0.1 mM chloramphenicol) using 15 mL pre-culture and were incubated at 37 °C / 180 rpm until an OD₆₀₀ of ~0.8 – 1.0 was reached. Protein expression was induced upon the addition of 0.1 mM IPTG (isopropyl β-D-1-thiogalactopyranoside) and the cultures were incubated for ~16 h at 16 °C before being harvested after centrifugal separation (4000 rcf, 20 min, 4 °C).

3.3.3 YopO Purification

The cell pellet was re-suspended in 5 time v/w lysis buffer (50 mM Tris-Cl pH 8.0, 150 mM NaCl, 3 mM DTT), lysed twice in a cell disruptor (Constant Systems Limited, Northampton, UK) and the lysate was spun down to remove the insoluble cell debris (48,500 rcf, 20 min, 4 °C). GST sepharose beads were equilibrated with lysis buffer and incubated with the centrifugal supernatant for 1 h at room temperature under slight agitation. The GST-suspension was ran over a gravity column and the flow-through was passed over the settled beads an additional time to maximize the protein yield. The beads were washed with 50 mL of lysis buffer and then incubated in 20 mL elution buffer (50 mM Tris-Cl pH 8.0, 150 mM NaCl, 1 mM DTT, 100 U PreScission protease) overnight at 4 °C whilst slowly shaking. The suspension was filled back into the gravity column and the protein containing flow-through was diluted with 100 mL no-salt buffer (50 mM Tris-Cl pH 8.0) and 125 μL of a 2 M DTT stock were added. An ion-exchange chromatography on an EnrichQ 10/100

column (Bio-Rad Laboratories GmbH, Feldkirchen, Germany) was performed against a linear gradient of high-salt buffer (50 mM Tris-Cl pH 8.0, 1 M NaCl) and the protein containing fractions were pooled and concentrated down below 3.0 mL. The sample was loaded onto a HiLoad Superdex 200 16/600 (GE Healthcare, Chicago, IL, USA) and size-exclusion chromatography was performed in gel filtration buffer (50 mM Tris pH 8.0, 50 mM NaCl). Pure protein (based on SDS-PAGE) was pooled, flash frozen and stored in 100 μ L aliquots at -80°C .

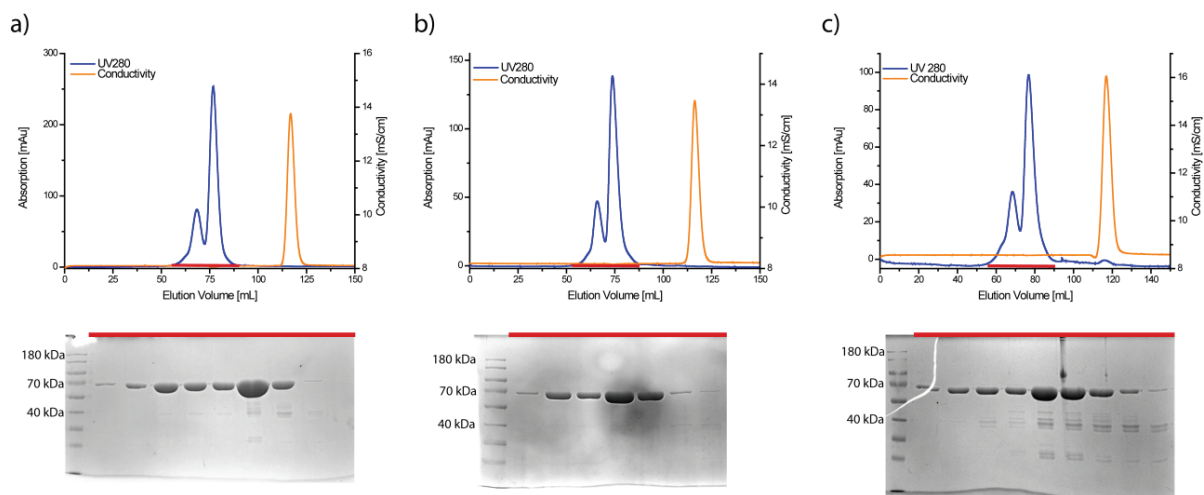


Figure S22: HiLoad Superdex 200 16/600 gel filtration chromatographs of YopO 0-Cys (a), YopO N624C (b) and YopO Y588C/N624C (c) (top) and the corresponding SDS-PAGE gels of the indicated peaks (red) in the elugram. Note that in each gel filtration chromatograph two distinct absorption peaks are seen with the first one corresponding to non-covalent, homomeric YopO dimers (~ 140 kDa) and the latter to monomeric YopO proteins (~ 70 kDa) as also proven by non-reducing SDS-PAGE (not shown here).

3.3.4 YopO Spin Labeling

Prior to each labeling experiment, 20 nmol of YopO were incubated for 1.5 h at 4°C in 2.5 mL phosphate buffer (20 mM POi pH 6.8, 50 mM NaCl) containing a five-fold molar excess of TCEP to cleave any YopO multimers. The reducing agent was removed using a PD-10 desalting column and labeling reactions were set up immediately afterwards.

To the 3.5 mL PD-10 protein eluate, a 5-fold molar excess per cysteine (or 5-fold molar excess per YopO for the YopO-WT C219A construct) of SLIM **9**[•] pre-diluted in 3 mL POi buffer was added resulting in a final concentration of $3.1\ \mu\text{M}$ YopO and $31\ \mu\text{M}$ SLIM trityl respectively. The labeling reaction was incubated for 16 h at 4°C . Next, the incubation solution was split into five equal fractions of 1.3 mL and passed successively over a PD-10 desalting column using the protocol for volumes less than 2.5 mL to remove any unbound free label remnants. All PD-10 eluate fractions were pooled and concentrated using a VivaSpin 6/50k MWCO (Sartorius, Göttingen, Germany) to less than 2.5 mL. For enhanced separation of any aggregation seeds or unbound label, the concentrated fractions were additionally purified using a HiPrep 26/10 desalting column (GE Healthcare, Chicago, IL, USA). Protein containing fractions were pooled, concentrated down to ~ 3.0 mL and a UV-vis spectrum was recorded on a Cary 100 UV-vis spectrometer. The labeling efficiencies were calculated as described in SI section 3.2.

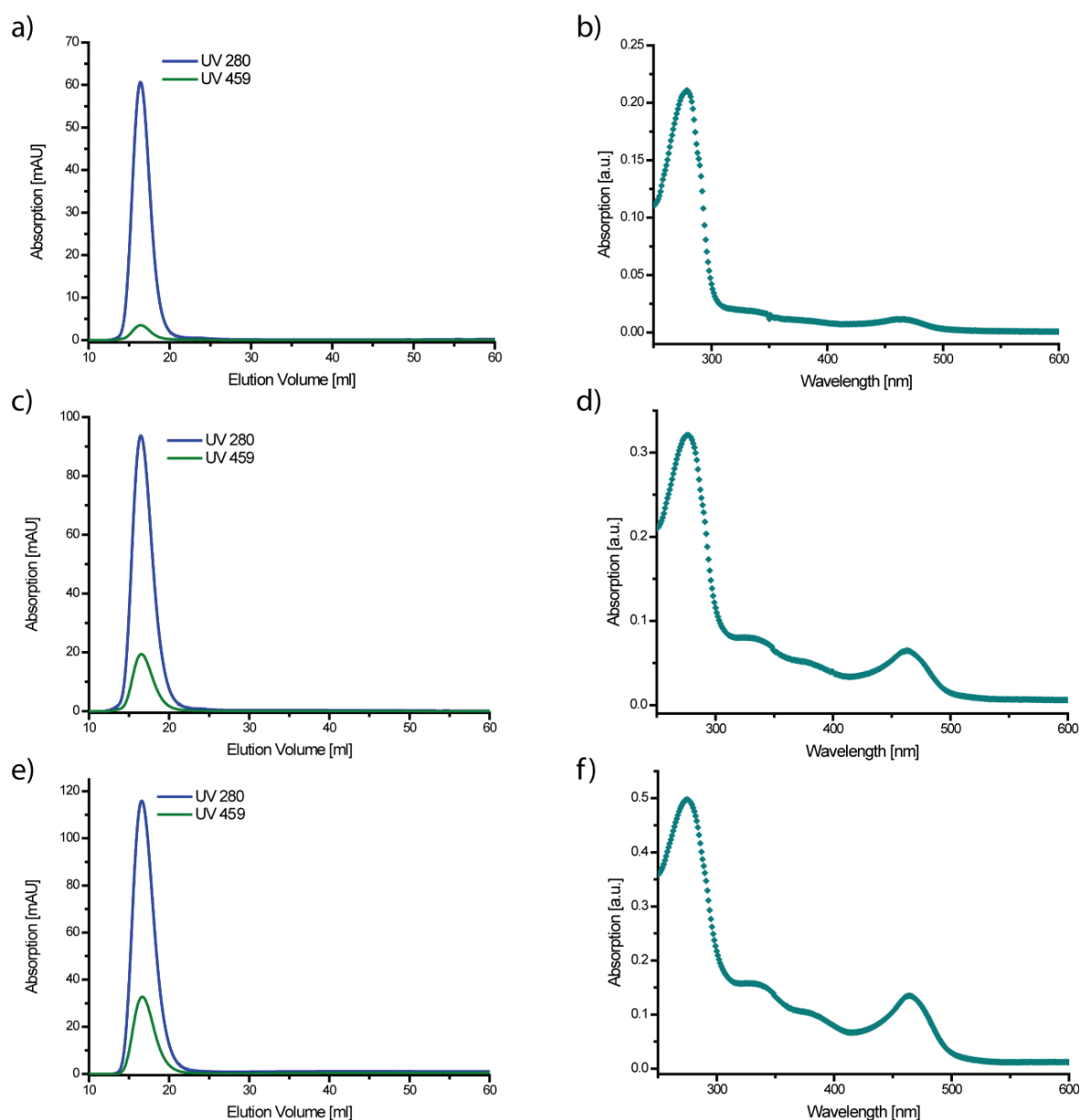


Figure S23: Elution chromatographs of the HiPrep 26/10 runs and UV-vis spectra for YopO 0-Cys (a+b), YopO N624C (c+d) and YopO Y588C/N624C (e+f).

Table S4: Labeling efficiencies for YopO labeled with SLIM.

Construct	Eq. SLIM per protein	Labeling efficiency [%]
YopO-WT	0.071 ± 0.006	7.1 ± 0.6
YopO N624C	0.955 ± 0.088	95.5 ± 8.8
YopO Y588C/N624C	1.916 ± 0.162	95.8 ± 8.8

The YopO Y588C/N624C reference sample labeled with **8**[•] were generated in exactly the same manner as the SLIM trityl samples, only using **8**[•] as the trityl species instead. For the **MTSL** reference sample, 20 nmol YopO were incubated with 3 mM DTT in 2.5 mL gel filtration buffer (50 mM Tris-Cl pH 8.0, 50 mM NaCl) for 2 h before removing the reducing agent via a PD-10 desalting column. Labeling reactions were set up

immediately afterwards by addition of a ten-fold molar excess of **MTSL** per cysteine. The labeling solution was incubated for 16 h at 4 °C. Excess free label was removed via a PD-10 desalting column and the pooled protein fractions were concentrated using a VivaSpin 6/10k MWCO.

All samples that were subjected to *in vitro* pulsed EPR experiments were rebuffed thrice in deuterated PDS buffer (100 mM TES pH 7.4, 100 mM NaCl) using a VivaSpin 6/50k MWCO.

3.3.5 YopO Mass Spectrometry

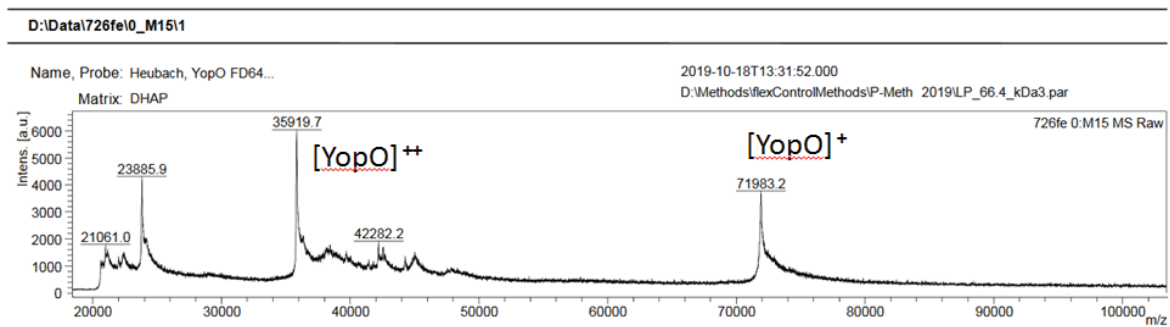


Figure S24: MALDI(+)-spectrum of YopO-WT after incubation with SLIM **9**.

Figure S24 shows the MALDI(+)-spectrum of YopO-WT after incubation with SLIM as described beforehand. While the peak for the unlabeled protein at 71,983 Da (calc. 72,108 for $C_{3176}H_{5085}N_{897}O_{989}S_{14}$) appears very clear, no signal of unspecifically labeled protein occurs, which would be at least 1,063 Da heavier.

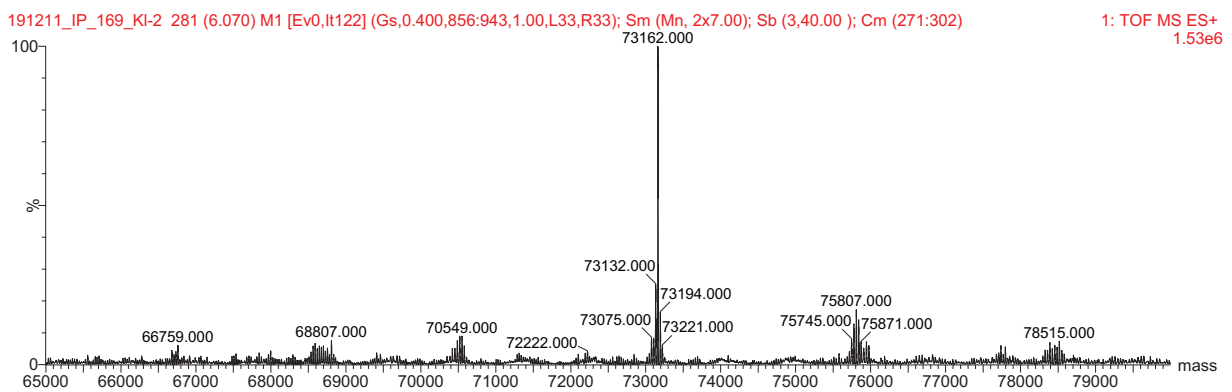


Figure S25: High-resolution ESI(+)-mass spectrum of YopO N624C labeled with SLIM **9**.

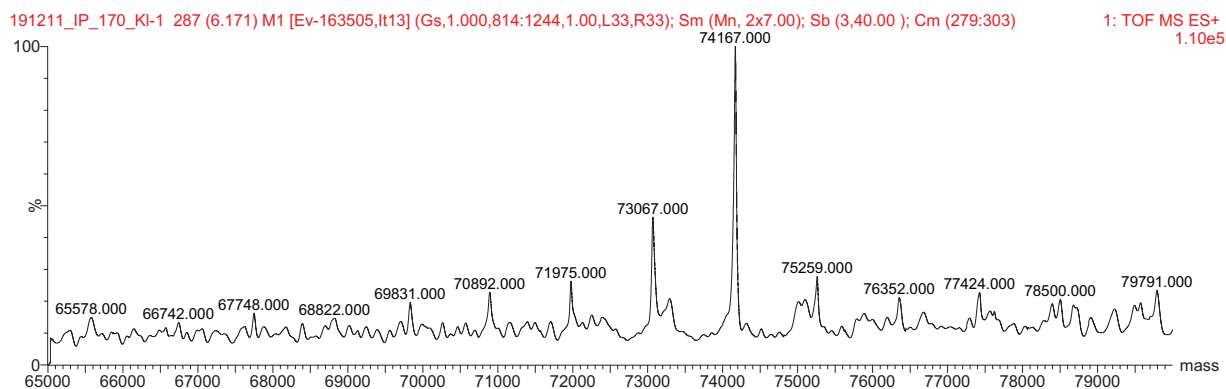


Figure S26: High-resolution ESI(+) of YopO Y588C/N624C labeled with SLIM 9•.

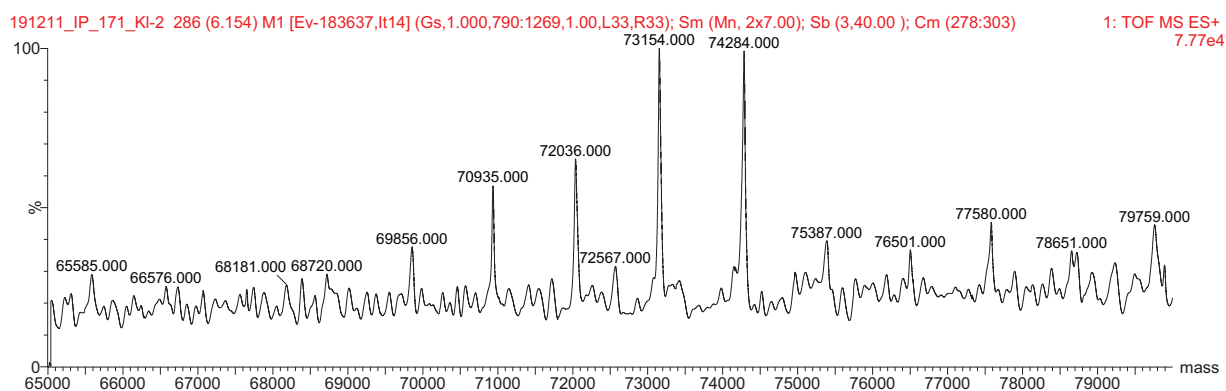


Figure S27: High-resolution ESI(+) of YopO Y588C/N624C labeled with 8•.

The identity of the labeled proteins was confirmed by high-resolution ESI(+) mass spectrometry as shown in Figures S25 – S27. These spectra clearly prove the chemoselective and successful labeling of the YopO mutants within in an accuracy exceeding 15 ppm.

Table S5: Calculated and measured masses for YopO mutants

Mutant	Sum formula	Calc. mass [Da]	Exp. mass [Da]
YopO N624C /w 9•	C ₃₂₁₉ H ₅₁₂₆ N ₈₉₇ O ₉₉₄ S ₂₇	73,162	73,162
YopO Y588C/N624C /w 9•	C ₃₂₅₇ H ₅₁₆₄ N ₈₉₈ O ₉₉₉ S ₄₀	74,167	74,167
YopO Y588C/N624C /w 8•	C ₃₂₆₁ H ₅₁₆₈ N ₈₉₈ O ₁₀₀₃ S ₄₀	74,283	74,284

4. Redox Stability

4.1 Cyclic Voltammetry

Cyclic voltammetry was carried out in a typical three electrode cell equipped with a Luggin capillary and a capacity of 30 mL. The working electrode was a glassy-carbon disc electrode with a surface area of 24.7 mm², and a gold sheet with an area of 50 mm² was used as the counter electrode. As the reference electrode, a reversible hydrogen electrode (RHE) was constructed from a platinum wire in PBS buffer by forming an H₂-bubble at the wire by electrolysis. For the measurement itself, a Bipotentiostat (Model AFCBP1, PINE research, Durham, NC, USA) and an AD converter connected to LabVIEW (National Instruments, Austin, TX, USA) were used. The cyclic voltammogram was also recorded via LabVIEW.

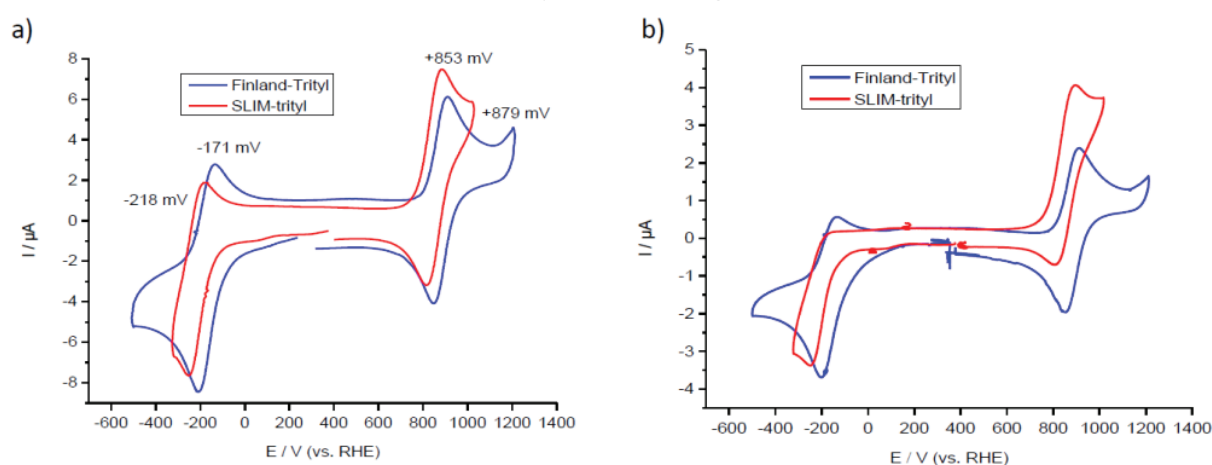


Figure S28: Cyclic voltammogram of SLIM 9• (red) and Finland-Trityl 1• (blue), each 500 μM in PBS buffer at pH 7.4 with a RHE at pH 7.4 as reference. A scan rate of a) 50 mV/s and b) 10 mV/s was applied in clockwise direction. Compared to the Finland-Trityl (blue), the reoxidation of the trityl-anion becomes less reversible, especially at 10 mV/s, for the SLIM-case (red), which means, that the quenching process with H⁺ is faster in that case. The reason for this lies in the increased reactivity of the SLIM-anion, since it is thermodynamically less favored.

4.2 Reduction Stability

4.2.1 Cell Lysates Preparation

Oocytes of the African claw frog *Xenopus laevis* were obtained from EcoCyte Bioscience (Dortmund, Germany) and lysate was prepared following a protocol of *Karthikeyan et al.*^[13]. Within this procedure, the oocytes were mechanically disrupted and solid ingredients as well as the lipid layer was separated off by centrifugation. In total, 70 μL of lysate were obtained from 100 oocytes.

For HeLa cell lysate, HeLa S3 (ATCC® CCL-2.2, human cervical adenocarcinoma) were suspended in PBS buffer (600 μL per 10⁸ cells) and the suspension was frozen in ethanol/CO_{2(s)} for 5 min and subsequently thawed in and 37 °C water bath. This procedure was done three times, whereafter the cells were lysed with rapid oscillation within 5 minutes. Membranes were separated by centrifugation at 15000 rpm at 4 °C and the lysate was collected as the supernatant. It was separated into several aliquots and immediately shock frozen in liquid nitrogen and stored at -80 °C.

4.2.2. Stability Measurements

As outlined in the main text, the stability of SLIM 9^{\bullet} and representatives of other spin label classes were assessed. For this, the respective label was diluted to a concentration of 200 μM in the corresponding medium and filled into a 10 μL capillary, which was then sealed with superglue and transferred into a 3 mm Q-band tube. In analogy to this, the labeled YopO N624C mutant was studied at 50 μM . The tube was then inserted into the spectrometer (EMXmicro) and the spectrometer was tuned properly. After this, a cw-EPR spectrum was recorded every 15 minutes over 15 hours. For reproducible results, it was crucial to warm up the spectrometer in advance to the measurement. Additionally, a home-written bash script was used to monitor the microwave frequency and power throughout the entire measurement. The signal intensities representing the spin concentration are obtained as the double integral over the spectrum for each time point. The dead time, measured from addition of the radical to the respective medium to the beginning of measurement, was kept below 6 minutes.

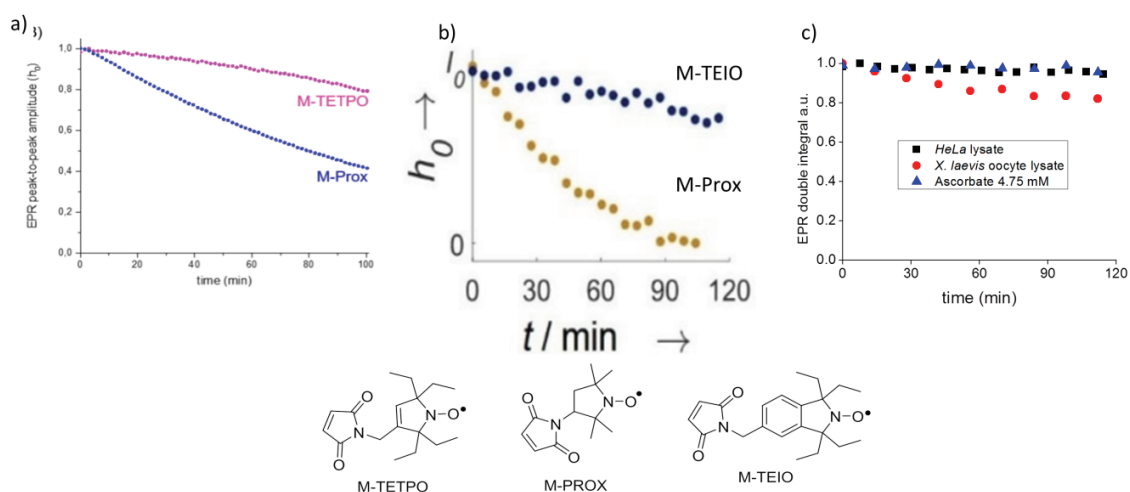


Figure S29: Stability of various spin labels compared to 9^{\bullet} . a) Spin labels M-TETPO and M-PROX in *Xenopus laevis* oocyte lysate. Excerpt from Karthikeyan et al., *Angew. Chem.* **2018**, 57, 1366 – 1370. © 2018 Wiley VCH Verlag GmbH & Co. KGaA, Weinheim, Germany. b) Spin labels M-TEIO and M-PROX in HEK (humane embryonal kidney cells) lysate. Excerpt from T. S. Braun et al., *ChemBioChem* **2019**, accepted manuscript, DOI: 10.1002/cbic.201900537. © to the authors, published by Wiley-VCH Verlag GmbH & Co. KGaA, Weinheim, Germany. c) Stability of 9^{\bullet} in various media.

5. Simulation of cw-EPR spectra

cw-EPR spectra were simulated using the EasySpin^[14] toolbox for MATLAB (MathWorks, Natick, MA, USA). All obtained g-values, hyperfine coupling constants and peak-to-peak linewidths are summarized in Table S6. The spectra of the free (i.e. non-bioconjugated) trityl radicals in liquid solution (SLIM in PBS-buffer, Figure 2a in the main text; SLIM in DMSO, Figure S30a; **15**[•] in DMSO, Figure S30b) have been fitted using the “garlic” routine of EasySpin. Appropriate starting values for the “esfit” routine of EasySpin were taken from the study of *Bowman et al.*^[15]

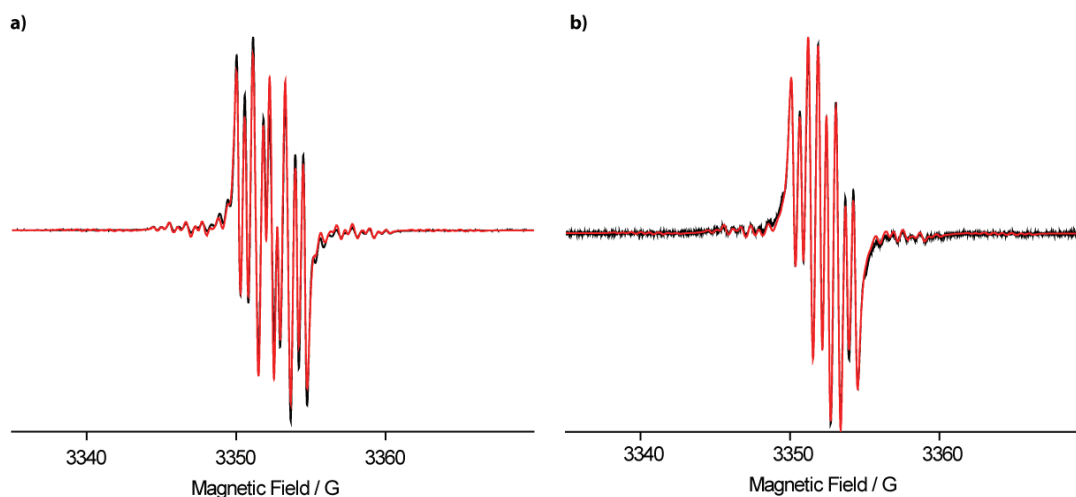


Figure S30: cw-EPR spectra of **9**[•] in DMSO (a) and of **15**[•] in DMSO (b) recorded at 298 K. The EasySpin simulation is overlaid as a red line.

The spectrum of free SLIM in frozen solution at 100 K (Figure 2b in the main text) has been simulated with the “pepper” routine of EasySpin. The starting values of the anisotropic g- and A-tensors have been obtained as described in the following. To start, the percentage contributions pc_{xx} , pc_{yy} , pc_{zz} of g_{xx} , g_{yy} and g_{zz} to the isotropic g-value obtained from a DFT computation (SI, section 8.1) have been determined.

$$pc_{xx} = \frac{g_{xx}^{DFT}}{g_{iso}^{DFT}}; pc_{yy} = \frac{g_{yy}^{DFT}}{g_{iso}^{DFT}}; pc_{zz} = \frac{g_{zz}^{DFT}}{g_{iso}^{DFT}}$$

This procedure was also applied to DFT-derived hyperfine coupling constants A. With these percentages at hand, appropriate starting values (guesses) for the EasySpin fitting could be obtained by multiplying the percentage values with the isotropic g-value and hyperfine coupling constants extracted from the solution spectrum of free SLIM.

$$g_{xx}^{guess} = pc_{xx} \cdot g_{iso}^{fit} \cdot 3$$

The factor 3 in this equation is relevant to finally fulfill the following condition.

$$\frac{g_{xx} + g_{yy} + g_{zz}}{3} = g_{iso}$$

The spectrum of SLIM upon bioconjugation to YopO shown in Figure 2c the main text has been fitted with the “pepper” routine of EasySpin. The results obtained from the simulation of free SLIM in the frozen state were taken as starting values.

Table S6: cw X-band EPR Fitting Parameters

Sample	Fitting Results
(a) 9^\bullet 298 K, DMSO	$g = 2.0034$ $A_N = 1.48$ MHz $A_{H1} = 3.48$ MHz $A_{H2} = 6.06$ MHz LWPP = (0.007, 0.029) mT $A_{C,central} = 66.16$ MHz $A_{C,ipso} = 31.22$ MHz $A_{C,ortho} = 25.45$ MHz $A_{C,para} = 6.86$ MHz $A_{C,meta} = 3.57$ MHz
(b) 9^\bullet 298 K, PBS	$g = 2.0033$ $A_N = 1.71$ MHz $A_{H1} = 2.96$ MHz $A_{H2} = 6.00$ MHz LWPP = (0.006, 0.018) mT $A_{C,central} = 66.91$ MHz $A_{C,ipso} = 31.63$ MHz $A_{C,ortho} = 25.65$ MHz $A_{C,para} = 7.27$ MHz $A_{C,meta} = 3.90$ MHz
(c) 15^\bullet 298 K, DMSO	$g = 2.0034$ $A_N = 1.51$ MHz $A_{H1} = 3.39$ MHz $A_{H2} = 5.16$ MHz LWPP = (0.002, 0.034) mT $A_{C,central} = 66.10$ MHz $A_{C,ipso} = 31.11$ MHz $A_{C,ortho} = 25.43$ MHz $A_{C,para} = 6.83$ MHz $A_{C,meta} = 3.51$ MHz
(d) 9^\bullet 100 K, PBS	$g = (2.0028, 2.0036, 2.0040)$ $A_N = (2.69, 0.64, 1.44)$ MHz $A_{H1} = (4.14, 0.75, 2.86)$ MHz $A_{H2} = (7.28, 7.55, 7.49)$ MHz LWPP = (0.089, 0.025) mT $A_{C,central} = (3.45, 6.24, 185.27)$ MHz $A_{C,ipso} = (37.42, 37.64, 16.24)$ MHz $A_{C,ipso} = (38.11, 35.00, 21.01)$ MHz $A_{C,ipso} = (34.80, 34.87, 23.92)$ MHz
(e) YopO N624C /w 9^\bullet 298 K, PBS	$g = (2.0034, 2.0034, 2.0035)$ $A_N = (2.19, 0.14, 0.94)$ MHz $A_{H1} = (3.64, 1.25, 2.36)$ MHz $A_{H2} = (6.96, 5.05, 7.99)$ MHz LWPP = (0.051, 0.079) mT $A_{C,central} = (3.92, 6.53, 184.78)$ MHz $A_{C,ipso} = (36.92, 37.14, 15.75)$ MHz $A_{C,ipso} = (37.61, 34.50, 21.49)$ MHz $A_{C,ipso} = (34.30, 34.37, 24.42)$ MHz

The observed ^{13}C -hyperfine coupling constants are similar to those reported for the Finland trityl^[15].

6. In Cell Sample Preparation

Stage IV *Xenopus laevis* oocytes were purchased from EcoCyte Bioscience (Dortmund, Germany). All oocytes were visually checked for signs of apoptosis or other cell defects prior to use and only intact oocytes were used for subsequent experiments. Up to 30 oocytes were aligned on a plate with the darker animal hemisphere pointing towards the injection needle and kept moist using MBS buffer (5 mM HEPES pH 7.8, 88 mM NaCl, 1 mM KCl, 1 mM MgSO₄, 2.5 mM NaHCO₃, 0.7 mM CaCl₂). Injection needles were pulled over a Bunsen burner using glass capillaries with an outer diameter of 0.3 mm. Sufficiently thin needles were then filled with light silicone oil, mounted onto a Drummond Nanoject II microinjector (Broomall, PA, USA) and filled with SLIM-labeled YopO Y588C/N624C protein solution (~400 μM protein). For injection, oocytes were placed onto a homemade acryl glass plate with 1.5 mm x 1.5 mm grooves, which was covered with Parafilm (Bemis, Neenah, WI, USA) in advance. Each oocyte was carefully injected with 59.8 nL of protein solution, paying attention to not destroy the outer membrane. The injection itself was carried out into the dark animal hemisphere. If leakage occurred or the oocyte was damaged in other fashion during the injection process, it was discarded using a pipette. After injection of all oocytes, the oocytes were washed off the injection plate into a petri dish using MBS buffer where additional buffer was used to wash the oocyte's surface. Each oocyte was visually checked again for damage and then transferred into a Q-band tube filled to the top with MBS buffer. After up to 20 oocytes were transferred into the tube, excess buffer was removed using a syringe and the oocytes were incubated at 18° C for two hours to allow the protein to equilibrate and homogeneously distribute within the cell. After incubation, the sample was visually checked again and all oocytes appeared with intact spherical shape and the surrounding buffer was clear. Damaged oocytes can be recognized by loss of spherical shape and a nearby turbidity of the surrounding buffer caused by leaking cytosol. Subsequently, the Q-band tube was flash-frozen in liquid nitrogen. Key steps of the preparation and injection procedure are displayed in Figure S31.

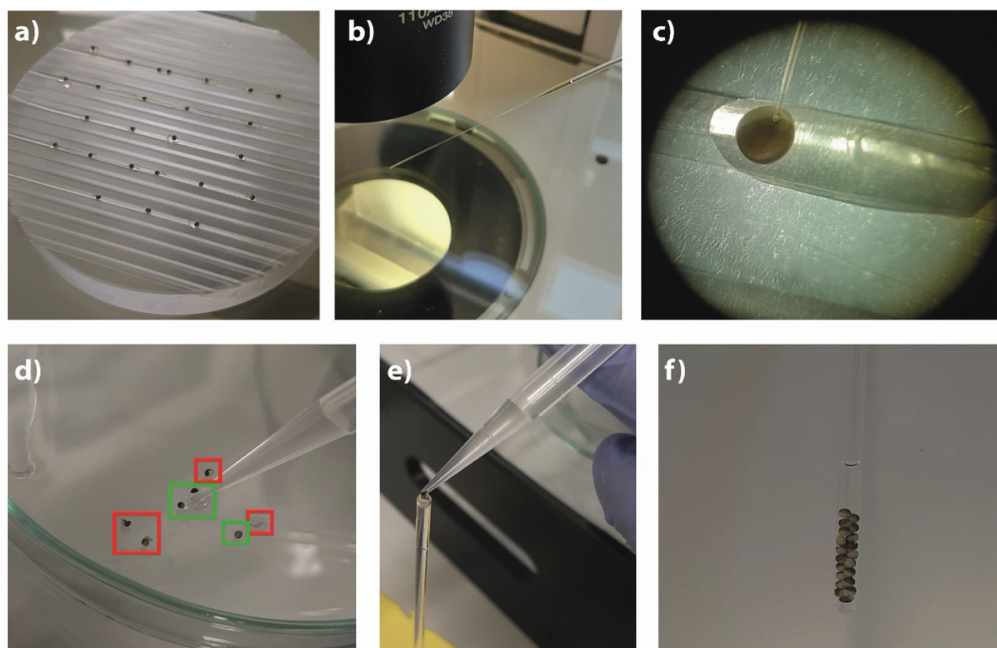


Figure S31: Preparation of *Xenopus laevis* oocytes for in-cell measurement. a) Alignment of the oocytes on the Parafilm-covered acryl glass plate. b) Injection needle with pulled up YopO protein. c) Penetration and injection process of an oocyte, picture taken with a smartphone through the lens of the microscope. d) Visual inspection of the oocytes after washing. Cells in the red square provide the instance of damage and were sorted-out subsequently whereas the ones in the green boxes were considered suitable for further experiments. e) Oocyte transfer into the Q-band tube with an Eppendorf pipette. f) Oocytes filled into the Q-band tube after incubation for 2h.

The maximum bulk concentration limit of spins was estimated using the following equation:

$$c_{\text{spin bulk}} = \frac{N_{\text{oocytes}} * c_{\text{spin}} * 60 \text{ nL}}{V_{\text{Q-band tube}}} = \frac{20 * 800 \mu\text{M} * 60 \text{ nL}}{70 \mu\text{L}} = 13.7 \mu\text{M}$$

Note that this estimation does not account for label degeneration during the two hours of incubation. The final spin concentration is estimated to be approximately 11 μM taking into account the findings of the label stabilities assessed by cw-EPR shown in Figure S29.

7. Pulsed EPR

7.1 EPR Sample Preparation

YopO samples were diluted 1:1 in ethylene glycol- d_6 to a final protein concentration of 25 μM , transferred into a Q-band EPR tube (O.D. 3 mm, Wilmad LabGlass, Vineland, NJ, USA) and flash-frozen in liquid nitrogen.

7.2 Relaxation Time Measurements

For the sake of comparison with other spin labels, the relaxation behavior of 9^\bullet bound to the N624C YopO single cysteine mutant was evaluated with respect to T_1 and T_M obtained by inversion recovery (IR, Figure S32a) and two-pulse electron spin echo envelope modulation (2pESEEM, Figure S32b) experiments. The pulse sequences were applied at the maximum of the echo-detected field swept EPR spectrum and included phase cycling, two steps for 2pESEEM and four steps for IR. Acquisition parameters are given in Table S7.

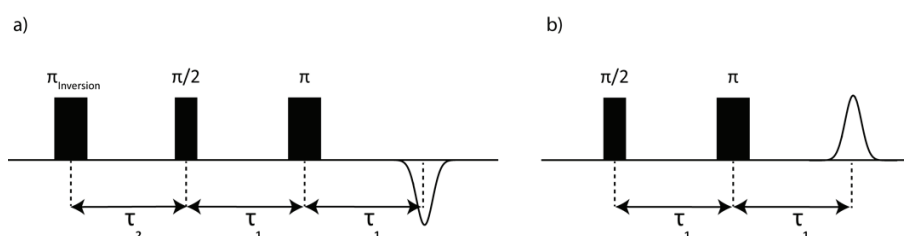


Figure S32: Pulse sequence applied for the inversion recovery (a) and the two-pulse ESEEM (b) experiment.

Table S7: Pulse sequence parameters for relaxation time measurements.

Inversion Recovery		Two-Pulse ESEEM	
Variable	Value	Variable	Value
$\pi/2$	12 ns	$\pi/2$	12 ns
π	24 ns	π	24 ns
$\pi_{\text{Inversion}}$	24 ns	–	–
τ_1	200 ns	τ_1	200 ns
τ_2	400 ns	–	–
τ_2 increment	1 ms	τ_1 increment	8 ns
Shots per Point	1	Shots per Point	1
Shot Repetition Time	1 s (10 K, 30 K) 500 ms (50 K)	Shot Repetition Time	500 ms

The results of the relaxation time measurements are summarized in Figure S33.

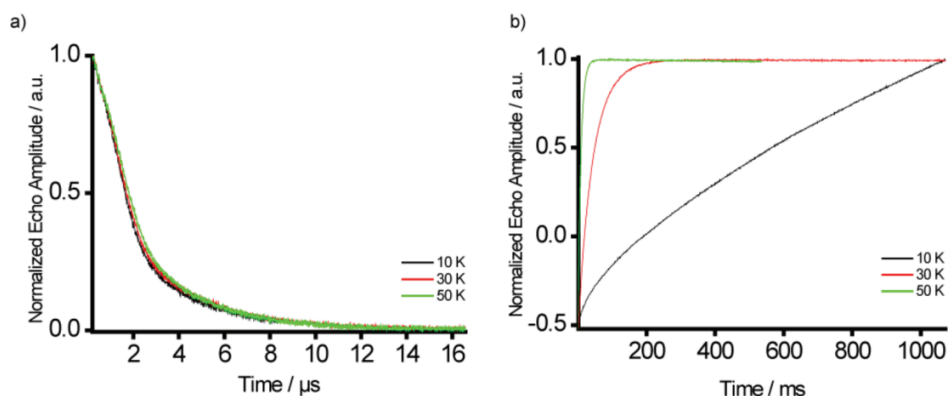


Figure S33: Hahn echo decay curves (a) and inversion recovery traces (b) recorded on **9•** bound to the N624C YopO single cysteine mutant.

7.3 Double Quantum Coherence (DQC) Experiments

The six-pulse Double Quantum Coherence (DQC) sequence (Figure S34) was applied at the magnetic field position corresponding to the maximum of the trityl field-swept EPR spectrum. The phase of the microwave radiation was adjusted on the Hahn echo sequence as to yield a maximally positive amplitude in the real signal channel of the quadrature detector. Proper phase adjustment was checked by summing amplitudes of the Hahn echo obtained from $(\pi/2)_{+x}/(\pi)_{+x}$ and $(\pi/2)_{-x}/(\pi)_{-x}$ pulses which averages out the signal. Pulse lengths and interpulse delays used for the DQC experiment are given in Table S8. The shot repetition time (SRT) was set to 15.3 ms.^[16] A 64-step phase cycle was applied to remove undesired echoes and thus extract the pure double quantum coherence pathway contributions.^[17,18] In order to eliminate deuterium ESEEM from the dipolar traces, a modulation averaging procedure was applied (τ_1 and τ_2 in 8 steps of 16 ns).^[19] DQC measurements on YopO double cysteine mutants labeled with either SLIM or **8•** were performed at 50 K. In order to eliminate the background of the PDS time traces, a background correction^[20] was performed. In the case of DQC (in cell and in vitro), polynomials of third order were used to fit the background contribution. Background correction was done using the DeerAnalysis package, and the “background start” value was chosen such that the corrected time trace was flat at long dipolar evolution times (last quarter of the time trace). In order to obtain an initial guess of the “background start” value, we used the “!” button in DeerAnalysis. The influence of the background on the distance distributions was checked by means of the validation tool in DeerAnalysis. In the present work, only the “background start” parameter was varied, and the variation ranges were set from the first local minimum of the time trace to the point when the oscillations were entirely damped.

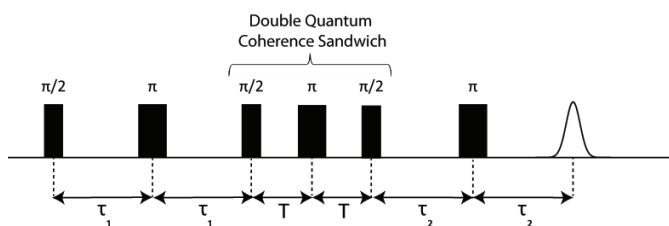


Figure S34: Pulse sequence applied for the DQC experiment.

DQC data were mirrored at the zero-time origin. Next, background correction was performed by DeerAnalysis^[21] using a third order polynomial. Subsequently, the background-corrected dipolar traces were translated into distance distributions via Tikhonov regularization with the optimal regularization parameter α determined according to the L-curve corner criterion. Finally, uncertainty estimations of the distance distributions were computed using the validation routine of DeerAnalysis.^[21]

Table S8: Parameters of the DQC experiment.

Variable	Value
$\pi/2$	12 ns
π	24 ns
τ_1	250 ns
τ_2	4000 ns
T	50 ns
Shots per Point	3
Shot Repetition Time	15.3 ms

7.4 Pulsed Electron-Electron Double Resonance (PELDOR) Experiments

Pulsed Electron-Electron Double Resonance (PELDOR, Figure S35) Spectroscopy was performed both on trityl- and nitroxide-labeled samples of YopO. Pulse lengths and interpulse delays are listed in Table S9. All PELDOR measurements were conducted at 50 K.

For the trityl-labeled YopO samples (**8[•]** and **9[•]**), the pump pulse (π)_B was set to the maximum of the field-swept EPR spectrum and the observer pulses were applied at a frequency offset of -15 MHz relative to the pump frequency. The length of the pump pulse (π)_B was determined by a transient nutation experiment. Regarding the suppression of deuterium ESEEM, an 8-step modulation averaging procedure was applied with a time increment of 16 ns. Additionally, a two-step phase cycle was used in order to remove undesired echoes and to correct for receiver baseline offsets.

For the PELDOR experiment on **R1**-labeled YopO, the pump pulse was applied at the magnetic field position which yields the maximal signal amplitude. The detection sequence was applied at a frequency offset of -100 MHz with respect to the pump frequency. The optimal length of the (π)_B pump pulse was determined by a transient nutation experiment. As mentioned above, a modulation averaging procedure (8 steps with a 16 ns increment) and a two-step phase cycle was used to average out deuterium ESEEM and to remove unwanted echoes as well as baseline offsets. Background correction of the PELDOR time traces was done assuming a 3-dimensional homogeneous distribution. Validation of the background was done in the same way as described above for the DQC data.^[22]

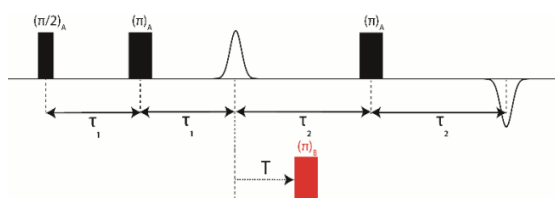


Figure S35: Pulse sequence applied for the PELDOR experiment.

Table S9: Parameters of the PELDOR experiments

Variable	8[•] / 9[•]	MTSL
($\pi/2$) _A	32 ns	12 ns
(π) _A	64 ns	24 ns
(π) _B	60 ns	16 ns
τ_1	260 ns	260 ns
τ_2	4000 ns	4000 ns
Shots per Point	3	3
Shot Repetition Time	15.3 ms	1 ms

7.5 YopO PDS Results

Primary data of the YopO double mutant Y588C/N624C obtained by the different PDS techniques mentioned above are summarized in Figure S36.

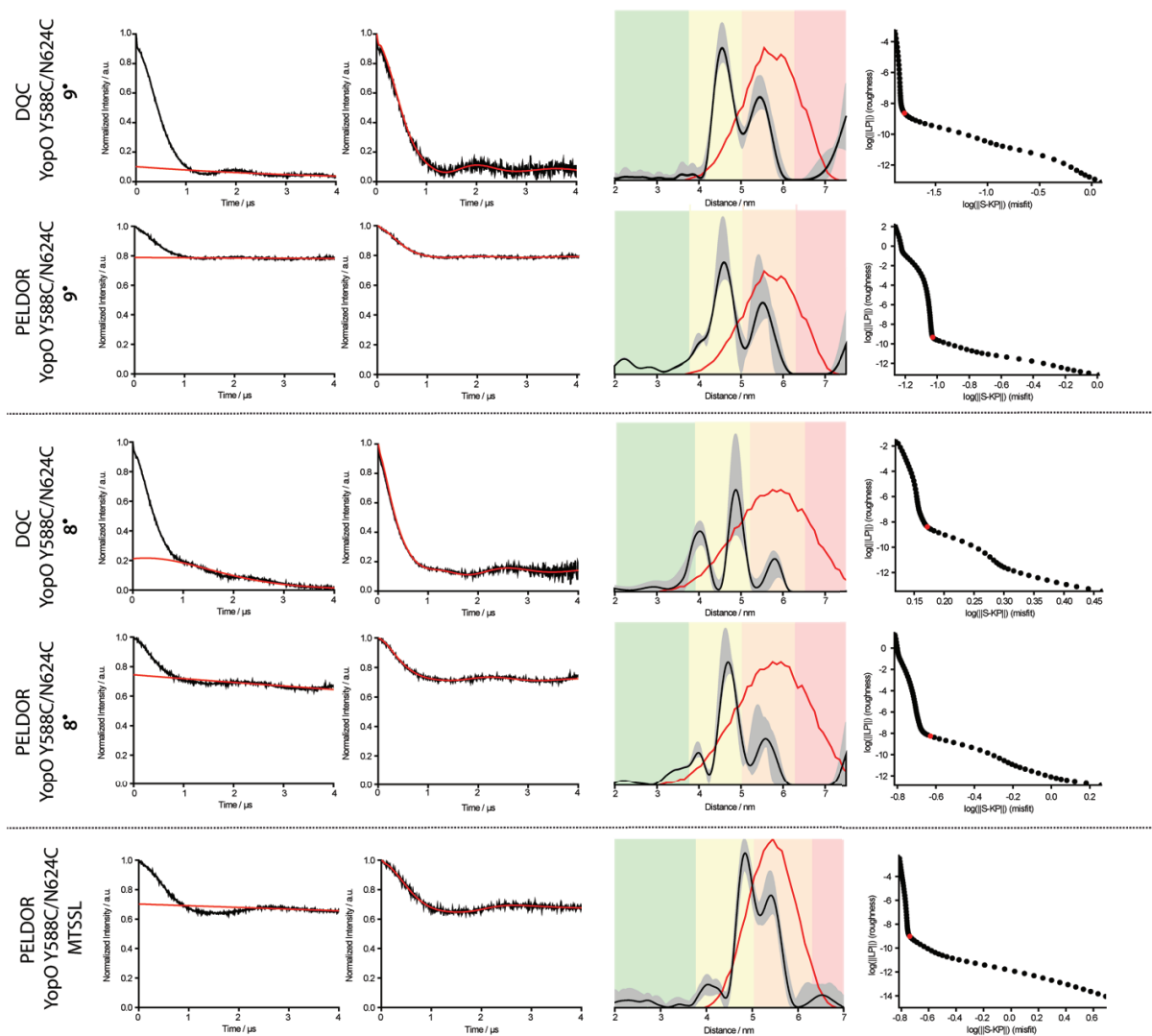


Figure S36: PDS data obtained for YopO Y588C/N624C. The red curves in the third column show the *in silico* predictions of the distance distributions computed by mtsslWizard using the PDB-ID 2h7o.

It should be noted, that the DQC modulation depth should be 100 % according to theory. However, in experiments the modulation depth is usually less (80% - 90%) as in the present case and also as reported for model compounds. This can be attributed to the experimental conditions, where slight imperfections in the phase cycling reduce its efficiency as a double-quantum filter.^[23]

The signal-to-noise ratio (SNR) of the dipolar traces can be defined as

$$SNR = \frac{\lambda}{\sigma_N} \cdot \frac{1}{\sqrt{t}}$$

with modulation depth of the trace λ , the acquisition time of the experiment t and the standard deviation of the noise of the trace σ_N . The noise has been deconvolved from the signal by fitting a polynomial of 8th order to the raw dipolar traces. The pure noise contributions have been obtained by subtracting the fit from the raw data. The SNR has been computed from the primary data prior to background correction by means of the software SnrCalculator.^[24] The SNR values obtained by this method are summarized in Table S10.

Table S10: Signal-to-Noise Ratios obtained for the PDS Experiments on YopO Y588C/N624C.

Experiment	YopO Y588C/N624C 9 [•]	YopO Y588C/N624C 8 [•]	YopO Y588C/N624C R1
DQC	674 h ^{-1/2}	503 h ^{-1/2}	–
PELDOR	155 h ^{-1/2}	131 h ^{-1/2}	248 h ^{-1/2}

In order to quantify the widths of the bimodal distance distributions obtained using SLIM/DQC and MTSL/PELDOR, the distance distributions were fitted as a sum of two Gaussian functions:

$$y = y_0 + \frac{A}{w\sqrt{\pi/2}} \exp\left(-2\left(\frac{x - x_c}{w}\right)^2\right)$$

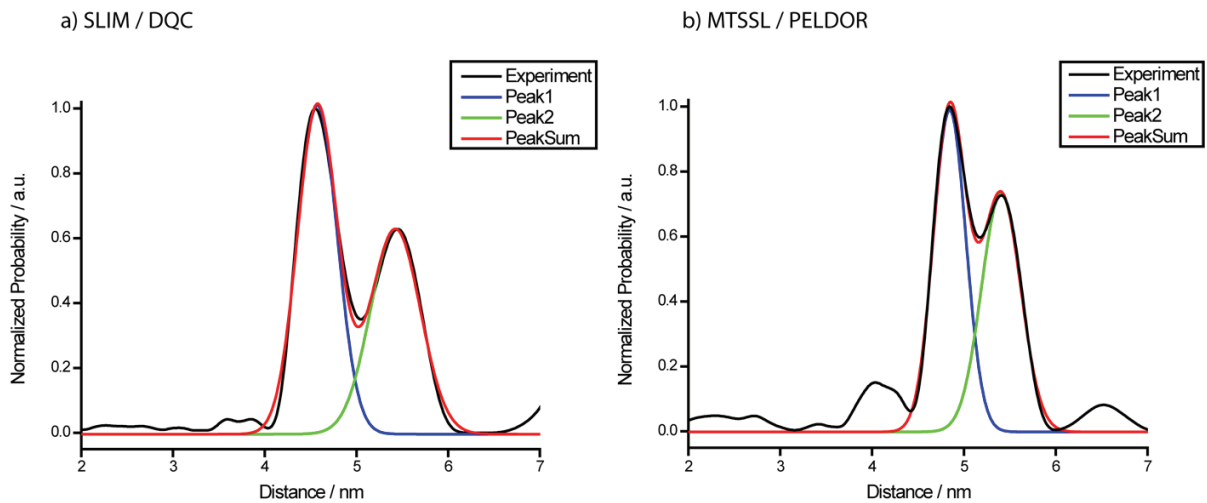


Figure S37: Analysis of the distance distribution bimodality with Gaussian functions.

Table S11: Gaussian function parameters obtained for the fits shown in Figure S46.

	SLIM / DQC	MTSL / PELDOR
Peak 1	Area: A = 0.55 Center: $x_c = 4.57$ nm Width: $w = 0.43$ nm Height: 1.01	Area: A = 0.44 Center: $x_c = 4.84$ nm Width: $w = 0.35$ nm Height: 0.99
Peak 2	Area: A = 0.43 Center: $x_c = 5.42$ nm Width: $w = 0.54$ nm Height: 0.63	Area: A = 0.39 Center: $x_c = 5.41$ nm Width: $w = 0.43$ nm Height: 0.73

7.6 PDS on YopO with human platelet actin

To validate the influence of actin binding to the α -helix 14 conformation, the YopO Y588C/N624C construct labeled with 9^\bullet was incubated with human platelet actin. For this purpose, 1 mg human platelet actin (Cytoskeleton, Inc., Denver, CO, USA) was dissolved in 100 μ L D₂O. Next, 50 μ M YopO- 9^\bullet was incubated with a 2-fold molar excess of actin and a 10-fold molar excess of the actin polymerization inhibitor latrunculin B (Merck KGaA, Darmstadt, Germany) in deuterated YopO-actin Buffer (4 mM TES pH 7.5, 0.4 mM ATP, 0.2 mM CaCl₂, 2 mM NaN₃) for 2 h on ice prior to the addition of 50 % deuterated ethylene glycol and flash freezing. Subsequently, the DQC experiment was performed as described in section 7.3 (Figure S38).

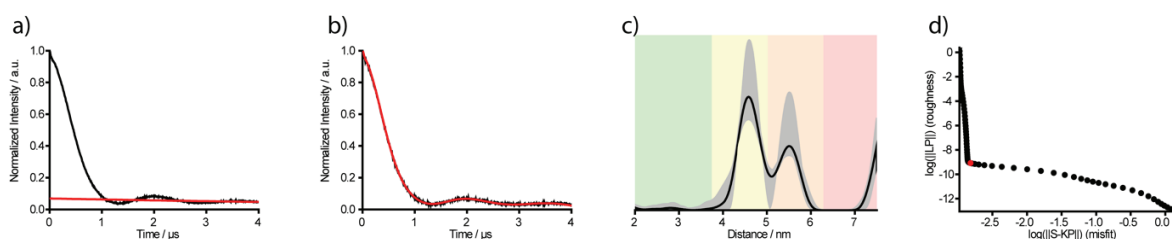


Figure S38: a) Mirrored DQC time trace of YopO Y588C/N624C labeled with 9^\bullet incubated with human platelet actin. The background function is indicated as a red line. b) Background-corrected time trace of (a) with the fit for Tikhonov regularization shown in red. c) Distance distribution obtained via Tikhonov regularization of (b) and the corresponding DeerAnalysis background validation shown in grey. d) L-curve with the chosen regularization parameter α shown in red.

Interestingly, also in complex with human actin a bimodal distance distribution is obtained (Figure S38c). Overlaying both distance distributions obtained for YopO- 9^\bullet in the absence and presence of actin shows that the conformation of α -helix 14 is independent of the actin binding process since both distributions are almost identical (Figure S39a). These data are in contrast to the two deposited crystal structures of YopO in the absence (PDB-ID: 2h7o) and presence (PDB-ID: 4ci6) of actin that show either a straight or bent conformation (Figure S39b+c). Here, we could demonstrate that in solution the α -helix 14 of YopO always resembles both, the straight and bent conformation, statistically and independently of the presence of actin.

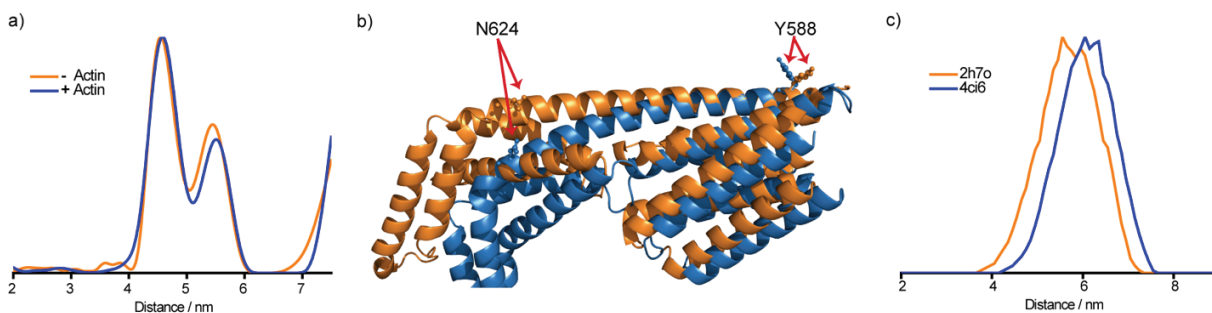


Figure S39: a) Overlaid distance distributions of YopO- 9^\bullet in the absence (orange) and presence (blue) of actin. b) Superposition of the GDI domains of the PDB-IDs 4ci6 (blue) and 2h7o (orange). c) Comparison of the *in silico* distance distributions of Y588C/N624C labeled with 9^\bullet obtained for the different crystal structures of YopO (blue, PDB-ID: 4ci6) and YpkA (orange, PDB-ID: 2h7o).

7.7 Evaluation of Concentration Limit for SLIM / DQC

In order to evaluate the lower concentration limit feasible for DQC experiments in combination with SLIM, YopO Y588C/N624C labeled with 9^\bullet was diluted in PDS buffer. Q-band PDS samples were prepared with the

corresponding final protein concentrations in 30 % glycerol- d_8 . The final spin concentration was verified by comparing the normalized amplitudes of the echo-detected field swept EPR spectra (Figure S40) of the nanomolar samples to the respective values obtained from the doubly labeled 25 μ M YopO Y588C/N624C- 9^\bullet reference sample.

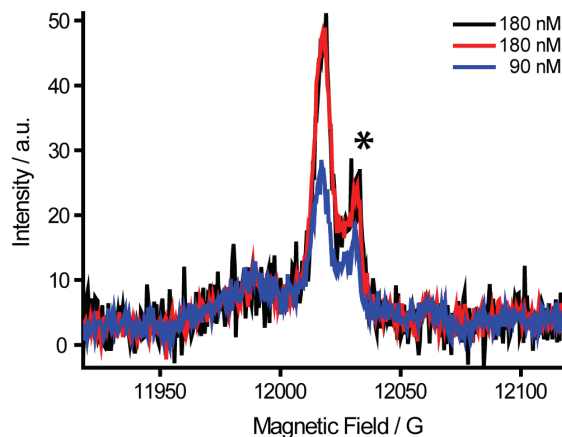


Figure S40: Field swept EPR spectra of nanomolar YopO Y588C/N624C- 9^\bullet samples. The asterisk marks the E' signal stemming from the EPR tube.

As can be seen in Figure S41, even at nanomolar concentration ranges, DQC experiments can be successfully performed, yielding time traces at a SNR of $2\text{ h}^{-1/2}$ in both cases (note that the trace length at 90 nM was set to 2.5 μ s instead of 4 μ s). Both time traces recorded at nanomolar concentrations exhibit the same oscillation period as the 25 μ M reference sample, thus underlining the reliability of the measurements and proving the possibility of DQC at nanomolar concentrations.

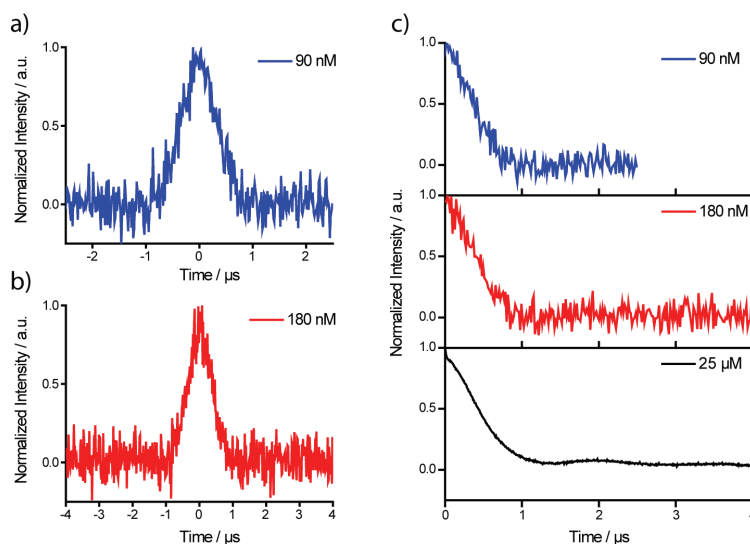


Figure S41: Original DQC time traces of YopO Y588C/N264C labeled with SLIM at a protein concentration of 90 nM (a) and 180 nM (b), respectively. c) Mirrored DQC time traces of the YopO samples at the given protein concentrations with the 25 μ M reference sample (black, bottom) from section 7.5 as benchmark.

7.8 *In Cell* Pulsed EPR Measurements

In order to check for the successful injection and the presence of trityl-labeled YopO within the oocytes, echo-detected field swept EPR spectra were recorded from untreated oocytes and after injection. Field swept spectra obtained from untreated oocytes show signals stemming from Mn(II) and an additional signal at $g = 2.0054$ which may stem from an organic radical endogenously present in oocytes (Figure S42a). After injection of SLIM-labeled protein, the trityl signal at $g = 2.0037$ dominates the spectrum and thus proves successful injection (Figure S42b).

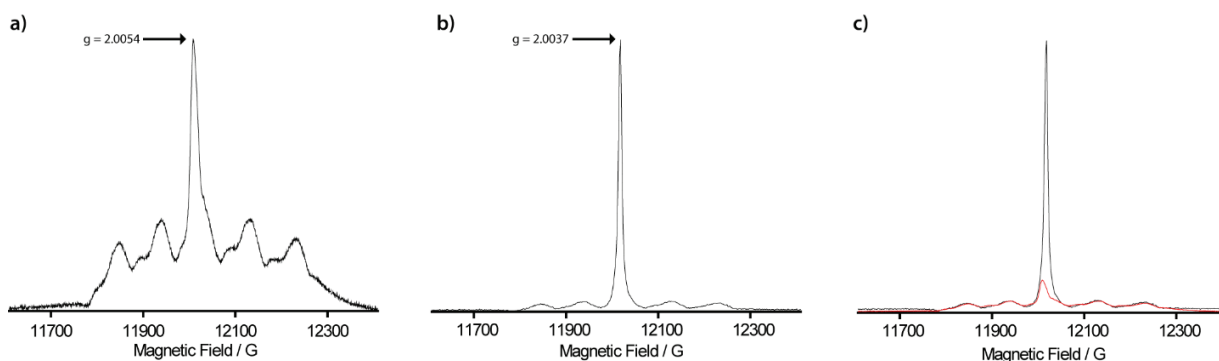


Figure S42: a) Echo-detected field swept EPR Spectrum of pure oocytes prior to injection of spin-labeled protein. The spectrum clearly shows the presence of Mn(II) and of an organic radical giving rise to a signal at $g = 2.0054$. b) Echo-detected field swept EPR spectrum of oocytes after injection of trityl-labeled YopO with the spectrum being dominated by the trityl signal at $g = 2.0037$. c) Overlay of field swept EPR spectra before injection (red) and after injection (black) with the signal amplitude normalized to the Mn(II) signals.

Longitudinal and transverse electron spin relaxation times (T_1 , T_M) were studied for two reasons: Firstly, they provide insight into changes of the environment of the electron spin upon injection of the label into the oocyte cell, e.g. due to the presence of Mn(II) ions.^[25] Secondly, especially the long T_1 relaxation time of trityl species unambiguously proves the presence of spin label within the cell. Therefore, T_1 and T_M were measured in untreated and injected oocytes at the magnetic field positions corresponding to the Mn(II) signal (11937 G), the dominant peak in the untreated oocytes (12009 G) and the trityl signal (12018 G). For details on relaxation measurement techniques, refer to SI section 7.2.

Figure S43 summarizes the results. Subfigures (S43a) and (S43b) contrast the relaxation behavior of SLIM bioconjugated to YopO *in vitro* and *in cell* after 120 minutes of incubation, showing that both longitudinal and transverse relaxation are enhanced in the cellular medium. This may be related to the endogenously present Mn(II) acting as a relaxation enhancer, but could as well be the result of crowding of spin-labeled protein in cell.^[26]

Subfigures (S43c) and (S43d) show the relaxation behavior of the different species contributing to the field sweep spectrum. Comparing especially the longitudinal relaxation times at 12009 G pre- and post-injection shows clear differences related to the presence of trityl spins which are on resonance at this magnetic field. It also clearly points out that T_1 relaxation times can indicate the successful injection of labeled biomolecules into the cells. The fact that both T_1 and T_M are shorter at 12009 G (post injection) than at 12018 G shows the admixture of the fast-relaxing endogenous organic species to the trityl. This emphasizes that a careful inspection of the echo detected field swept EPR spectrum as well as the relaxation times associated with the different species is vital for choosing the correct magnetic field position for subsequent PDS experiments.

Subfigure (S43e) shows the effect of the incubation time of the oocytes after injection before flash-freezing on the transverse relaxation times. The Hahn echo decay curves clearly show that the phase memory time is extended with the incubation time, which is related to a more homogeneous distribution of the labeled biomolecule within the cell and thus reduced intermolecular dipolar coupling between electron spins.^[27] However, when optimizing the incubation time, the optimal tradeoff between the beneficial homogeneous distribution of proteins in cell and the degeneration of the spin label has to be found.

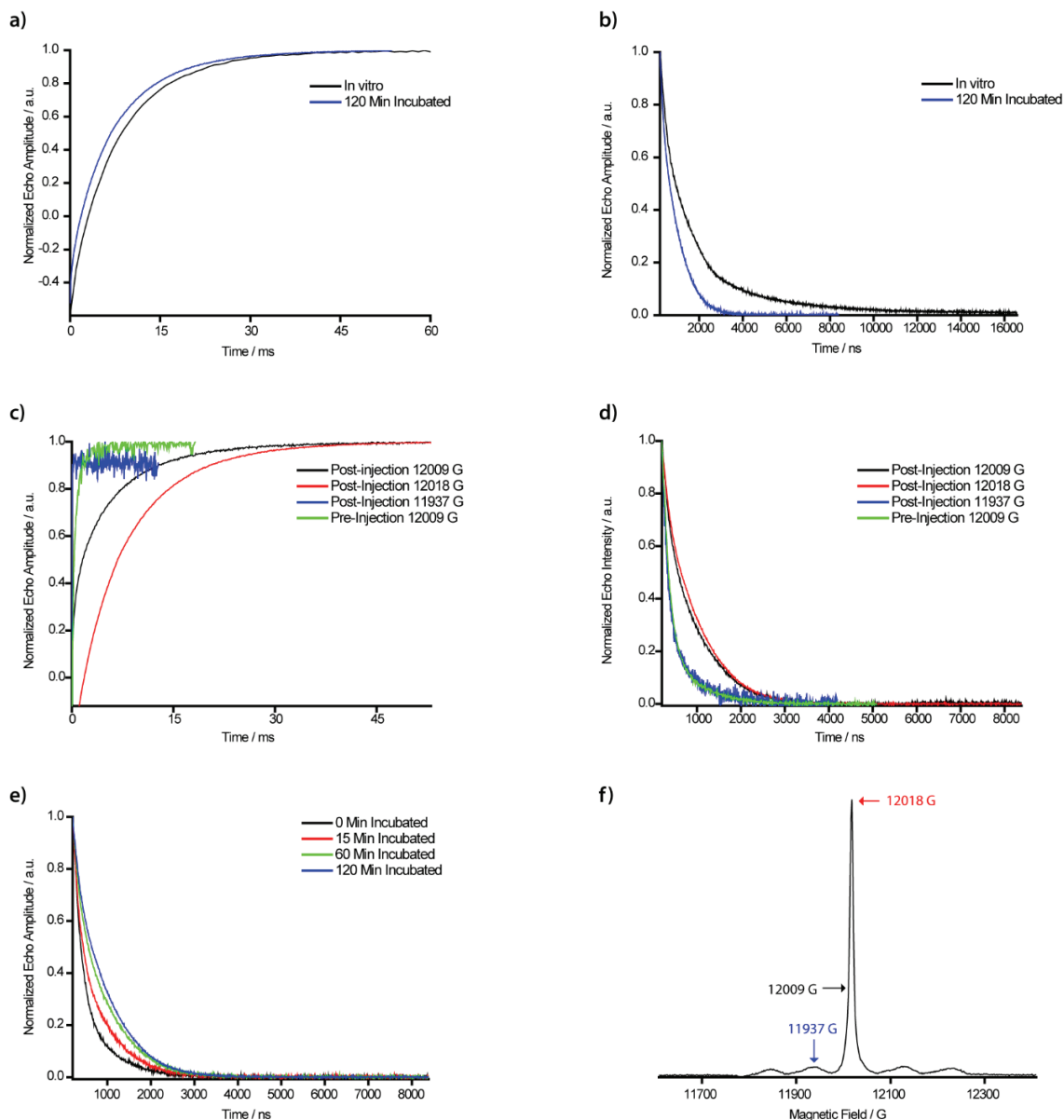


Figure S43: a, b) Comparison of inversion recovery traces (a) and Hahn echo decay curves (b) recorded on the trityl signal (12018 G) in vitro (black) and in oocytes after 120 minutes of incubation time. c, d) Comparison of inversion recovery traces (a) and Hahn echo decay curves at different field positions corresponding to the oocyte signal (12009 G), the trityl signal (12018 G) and the Mn(II) signal (11937 G). e) Hahn echo decay curves recorded on the trityl signal (12018 G) after different incubation times in oocytes. f) Echo-detected field swept EPR spectrum of SLIM-labeled YopO in oocytes with the relevant magnetic field positions marked by arrows.

Due to the cellular environment and the non-deuterated buffer conditions, the acquisition parameter of the DQC experiment were adapted as summarized in Table S12 in order to optimize data acquisition. The thusly obtained *in cell* data are shown in Figure S44.

Table S12: Parameters of the *in cell* DQC experiment.

Variable	Value
$\pi/2$	12 ns
π	24 ns
τ_1	200 ns
τ_2	3500 ns
T	50 ns
Shots per Point	20
Shot Repetition Time	15.3 ms

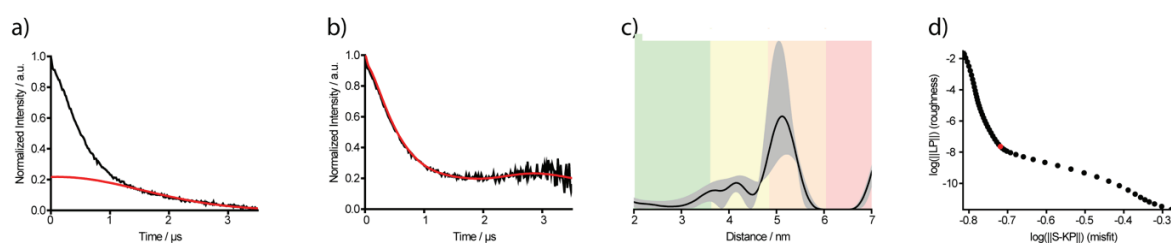


Figure S44: a) Mirrored DQC time trace of YopO Y588C/N624C labeled with 9^\bullet and injected into oocytes with the background function indicated as a red line. b) Background-corrected time trace of (a) with the fit for Tikhonov regularization shown in red. c) Distance distribution obtained via Tikhonov regularization of (b) and the corresponding DeerAnalysis background validation shown in grey. d) L-curve with the chosen regularization parameter α shown in red.

The *in cell* measurement (Figure S44) shows a monomodal distribution peaking at the position corresponding to the longer distance observed in the *in vitro* measurement (5.1 nm) (Figure S36). The marginal distance shift in the *in cell* sample by 0.2 nm as compared to the *in vitro* sample may be related to uncertainties in data analysis.

8. Theoretical Results

8.1 Density Functional Theory Computations

Density Functional Theory computations on the molecules were performed on a 64-core computer cluster using the ORCA quantum chemistry software package.^[28] The structure of the SLIM label has been optimized on the B3LYP/def2-TZVP^[29] level of theory using the RIJCOSX approximation (def2/J as auxiliary basis^[30]) and the D3 dispersion correction.^[31,32] Subsequent computations of the hyperfine coupling constants of the SLIM label 9^\bullet were done using the eprnmr module of ORCA on the B3LYP/def2-TZVP level of theory. Again, the D3 correction was applied to account for dispersion interactions. The molecular coordinates of SLIM after geometry optimization are given in Table S13.

Table S13: Atomic coordinates obtained by the geometry optimization of the SLIM label 9• (B3LYP/def2-TZVP D3).

Atom #	x	y	z				
0C	0.822437	-4.468512	0.846234	45C	-4.304013	2.431863	-2.726321
1C	0.836906	-3.378944	-0.033744	46C	-0.090524	-0.870184	4.771318
2C	-0.277385	-2.513170	-0.122785	47C	2.345594	-0.269754	4.504228
3C	-1.465085	-2.914959	0.518484	48C	-1.651454	3.513353	2.451517
4C	-1.507815	-4.027049	1.359900	49C	-0.182285	-1.167104	-0.679941
5C	-0.345252	-4.788269	1.572933	50N	-1.331366	4.738927	1.735103
6S	2.365651	-5.290236	1.077728	51C	-0.108966	5.031568	1.139118
7S	2.363681	-3.021817	-0.827466	52C	-0.311418	6.319197	0.395878
8S	-3.066299	-4.385054	2.087791	53C	-1.567304	6.720862	0.567024
9S	-2.999576	-2.146905	0.165851	54C	-2.272457	5.728718	1.439150
10C	3.199071	-4.608758	-0.407731	55O	0.898963	4.371152	1.216331
11C	-3.839912	-2.756752	1.672734	56O	-3.410552	5.759731	1.832853
12C	-3.637991	-1.758404	2.807972	57C	-0.433515	-5.909518	2.523218
13C	-5.315318	-2.985467	1.364753	58O	-1.464673	-6.459360	2.838037
14C	3.080261	-5.596215	-1.564262	59O	0.753301	-6.275861	3.058266
15C	4.658581	-4.321717	-0.064033	60C	2.906121	-0.402151	-5.496115
16C	1.052094	-1.455055	-4.241579	61O	2.507925	-0.664279	-6.607399
17C	0.302897	-1.640030	-3.076607	62O	4.175983	0.011064	-5.277491
18C	0.536094	-0.875037	-1.915668	63H	-0.992139	3.324557	-2.195284
19C	1.513713	0.146944	-1.990743	64H	-2.304475	4.314706	-2.852359
20C	2.320287	0.287510	-3.130385	65H	-1.733415	2.885239	-3.739103
21C	2.103083	-0.520609	-4.262503	66H	-5.028164	1.825935	-2.185254
22S	0.563319	-2.412574	-5.634332	67H	-4.196559	2.032594	-3.736678
23S	-1.039701	-2.764592	-3.193954	68H	-4.685154	3.451496	-2.807886
24S	3.615455	1.481568	-3.001868	69H	-1.086391	-0.763576	4.346240
25S	1.925037	1.188523	-0.634814	70H	-0.092883	-0.423299	5.767702
26C	-0.356778	-3.662932	-4.644912	71H	0.135831	-1.935087	4.860390
27C	2.837734	2.418794	-1.633010	72H	3.082504	0.210701	3.864096
28C	1.878102	3.465694	-2.188782	73H	2.626662	-1.315373	4.645177
29C	3.910655	3.054649	-0.757862	74H	2.357191	0.213327	5.483184
30C	0.597941	-4.754896	-4.172463	75H	-1.125465	3.500500	3.403873
31C	-1.498490	-4.226462	-5.481646	76H	-2.719920	3.576766	2.668455
32C	-0.456815	1.303197	2.177858	77H	0.581135	-7.044949	3.623056
33C	-0.179045	0.121516	1.477338	78H	4.593132	0.104008	-6.148042
34C	-0.656535	-0.055615	0.165471	79H	-2.577131	-1.595014	2.990014
35C	-1.534653	0.912754	-0.342675	80H	-4.097248	-2.131301	3.726300
36C	-1.903673	2.029597	0.410410	81H	-4.090710	-0.799500	2.545940
37C	-1.333478	2.263844	1.665453	82H	-5.828978	-3.367062	2.249842
38S	0.509321	1.577533	3.628031	83H	-5.438609	-3.702948	0.555488
39S	0.987282	-0.964955	2.223533	84H	-5.790928	-2.045798	1.076118
40S	-3.174283	3.036474	-0.289618	85H	2.037172	-5.817407	-1.780383
41S	-2.355277	0.696468	-1.876441	86H	3.584867	-6.530087	-1.305844
42C	0.950376	-0.184780	3.892194	87H	3.543547	-5.185410	-2.464058
43C	-2.954208	2.432386	-2.017966	88H	4.734037	-3.606491	0.752264
44C	-1.928818	3.294730	-2.746032	89H	5.176816	-3.914816	-0.935154
				90H	5.163910	-5.244581	0.229331

91H	1.123182	2.997107	-2.818803
92H	2.427607	4.191896	-2.792650
93H	1.384033	3.982716	-1.365307
94H	4.579778	2.300275	-0.346790
95H	3.436322	3.596418	0.062307
96H	4.495029	3.767811	-1.343944
97H	1.028552	-5.275478	-5.030951

98H	0.066827	-5.475829	-3.546476
99H	1.405871	-4.321608	-3.587487
100H	-2.171059	-3.438137	-5.815087
101H	-2.066678	-4.953913	-4.898135
102H	-1.097025	-4.741364	-6.356653
103H	0.486133	6.784077	-0.161815
104H	-2.065948	7.598343	0.186946

For implementing the new SLIM spin label into mtsslWizard, a geometry optimization (PBE/def2-SVP) on the SLIM label attached to a cysteine residue was performed in advance.

The hyperfine coupling constants obtained by DFT on the B3LYP/def-TZVP D3 level of theory are summarized in Table S14. Only hyperfine coupling constants to those nuclei which have also been observed experimentally are listed. For comparison, the isotropic coupling constants obtained by the EasySpin^[14] fit of the cw EPR spectrum recorded in DMSO at 298 K are indicated. The numbering of the atoms within the structure is shown in Figure S45.

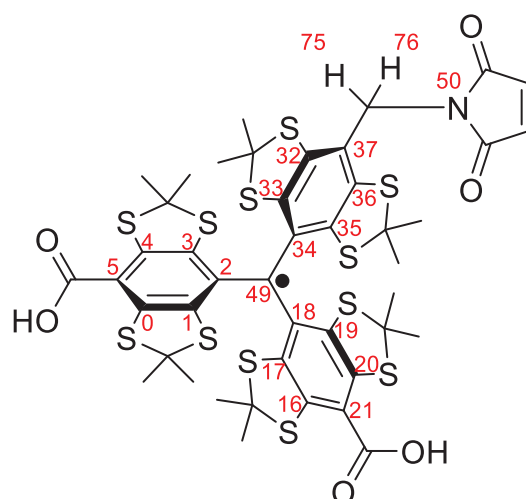


Figure S45: Structure of **9•** with atom enumeration applied for calculation of HFC-tensors.

Table S14: Hyperfine coupling constants obtained by DFT (B3LYP/def-TZVP D3) computations and fitting of the cw-EPR spectrum recorded in DMSO at 298 K.

	Atom #	DFT B3LYP/def-TZVP D3				Experimental
		A _{xx} / MHz	A _{yy} / MHz	A _{zz} / MHz	A _{iso} / MHz	A _{iso} / MHz
	50N	0.8868	0.9107	1.2518	1.0164	1.48
	75H	-0.1694	-0.2959	1.2142	0.2496	3.48
	76H	4.9565	5.1968	6.4721	5.5418	6.06
	49C	4.5936	4.7467	165.4203	58.2535	66.16
ipso	2C	-24.9686	-26.7889	-42.7462	-31.5012	31.22
	18C	-24.5157	-26.3190	-42.0361	-30.9569	31.22
	34C	-24.0005	-25.0611	-34.8107	-27.9575	31.22
ortho	1C	22.6342	24.0242	43.8507	30.1697	25.45
	3C	11.4835	13.2499	33.6639	19.4658	25.45
	17C	14.2218	15.7777	35.8105	21.9367	25.45
	19C	19.5899	20.9609	43.1771	27.9093	25.45
	33C	20.0554	21.6460	34.2153	25.3056	25.45
	35C	15.3674	17.2719	28.6021	20.4138	25.45
para	5C	0.1572	1.0402	20.5164	7.2379	6.86
	21C	0.1456	1.0618	22.5647	7.9240	6.86
	37C	0.2124	0.9007	14.8309	5.3147	6.86
meta	0C	-1.9590	-2.9847	-12.0474	-5.6637	3.57
	4C	-4.8282	-5.7410	-13.6552	-8.0748	3.57
	16C	-4.1915	-5.1499	-14.3902	-7.9105	3.57
	20C	-2.8695	-3.9180	-12.8359	-6.5411	3.57
	32C	0.1930	-0.8838	-6.3693	-2.3534	3.57
	36C	-2.0127	-2.9963	-8.3120	-4.4403	3.57

8.2 *In Silico* Spin Labeling

Distance distributions were computed based on the two crystal structures of YopO deposited in the Protein Data Bank (PDB-IDs: YpkA 2h7o and YopO 4ci6) using the mtsslWizard^[31] plugin for PyMOL. The maximal number of conformers to be found was 200 and the clashscore criteria were set to “loose”, implying that a *van-der-Waals* cutoff of 2.5 Å was set and 5 clashes were allowed.^[32,33]

8.2.1 Conformer Cloud Volume

Conformer ensembles of **8**• and SLIM **9**• were generated on YopO N624C. The size of the conformer clouds was determined as described in the following paragraph and schematically shown in Figure S46. Basis of all computations was the prediction of the conformer cloud provided by mtsslWizard (Figure S46a+b). In order to obtain the ensemble of points in space describing the outer hull of the conformer cloud, the Cartesian coordinates of the atom which is the furthest away from the C_β-atom of the cysteine residue were extracted. Herein, the C_β-atom of cysteine serves as a fixed anchor point (Figure S46c).

Next, the overall point cloud containing the atomic coordinates of the carboxylic carbon atom and those of the hull atoms was collected (Figure S46d) which served as a basis for the computation of a so-called α-shape (Figure S46e). This α-shape obtained by the MATLAB command “alphaShape” encompasses the whole point cloud. The smallest possible alpha radius was determined automatically resulting in a tight fit of the 3D sphere to the data points. Finally, the volume of the α-shape was computed using the “volume” command of MATLAB providing a good approximation to the volume of the label conformer cloud.

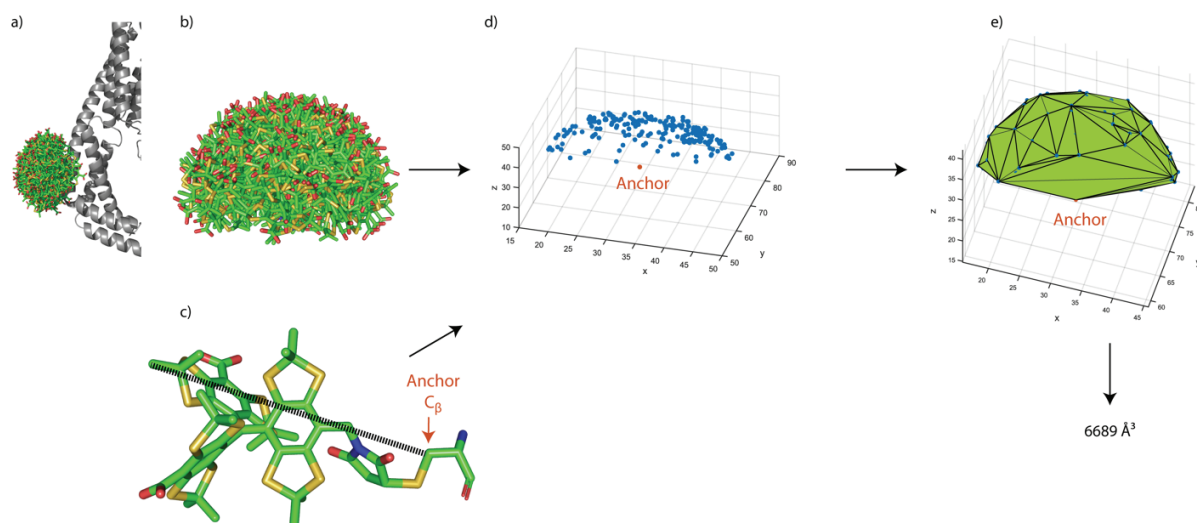
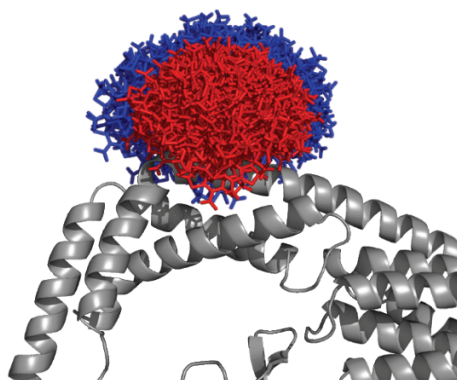


Figure S46: Computation of the volume of an *in silico* generated conformer cloud. a) YopO *in silico* labeled with SLIM at amino acid position N624. b) *In silico* generated conformer ensemble for SLIM. c) Structure of **9**• with the carboxylic carbon atom of cysteine shown as anchor point and the distance to the furthest atom indicated by a dashed line. d) Point cloud symbolizing the positions of the furthest atoms in blue and the anchor point in orange. e) Alpha-shape generated from the ensemble of coordinates shown in (d) with the resulting volume obtained by integration of the alpha-shape. The whole analysis was performed on 10 individually and independently generated conformer clouds of each of the labels SLIM and **8**•. Results are shown in Table S15.

Table S15: Computed volumes of the conformer clouds obtained by *in silico* spin labeling of YopO with 9• and 8•.

YopO N624C-9•		YopO N624C-8•	
Cloud #	Volume / Å ³	Cloud #	Volume / Å ³
1	6589	1	16232
2	6951	2	16637
3	6649	3	15081
4	7512	4	15316
5	7116	5	15986
6	7339	6	12855
7	6684	7	14415
8	7444	8	15539
9	6476	9	14272
10	6642	10	15669
∅	6940	∅	15200



8.2.2 YopO 8• Label Conformer Selection

As outlined in the main text, attractive interactions between the protein's α -helix and the hydrophobic surface of the trityl radical are conspicuous to cause the short-distance artefacts for YopO-8•. Label conformers representative for this are provided in Figure S47 below. It becomes evident that these conformers can only emerge due to the long linker of 8•, which bends over into the propagation direction of the helix.

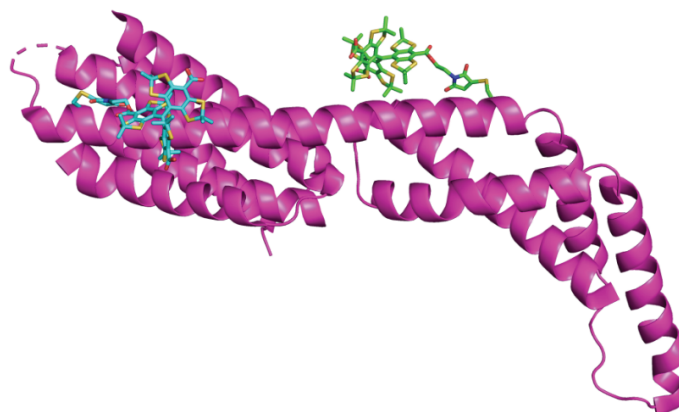


Figure S47: Selected label conformers for YopO-8•.

9. Literature

- [1] M. Winkle, J. Lansinger, R. C. Ronald, *J. Chem. Soc. Chem. Commun.* **1980**, 87–88.
- [2] J. J. Jassoy, A. Berndhäuser, F. Duthie, S. P. Kühn, G. Hagelueken, O. Schiemann, *Angew. Chem. Int. Ed.* **2017**, *56*, 177–181.
- [3] E. H. Discekici, A. H. St. Amant, S. N. Nguyen, I. H. Lee, C. J. Hawker, J. Read De Alaniz, *J. Am. Chem. Soc.* **2018**, *140*, 5009–5013.
- [4] H. Hintz, A. Vanas, D. Klose, G. Jeschke, A. Godt, *J. Org. Chem.* **2019**, *84*, 3304–3320.
- [5] G. R. Fulmer, A. J. M. Miller, N. H. Sherden, H. E. Gottlieb, A. Nudelman, B. M. Stoltz, J. E. Bercaw, K. I. Goldberg, *Organometallics* **2010**, *29*, 2176–2179.
- [6] V. Froidevaux, M. Borne, E. Laborbe, R. Auvergne, A. Gandini, B. Boutevin, *RSC Adv.* **2015**, *5*, 37742–37754.
- [7] M. M. Haugland, A. H. El-Sagheer, R. J. Porter, J. Peña, T. Brown, E. A. Anderson, J. E. Lovett, *J. Am. Chem. Soc.* **2016**, *138*, 9069–9072.
- [8] C. Wuebben, S. Blume, D. Abdullin, D. Brajtenbach, F. Haege, S. Kath-Schorr, O. Schiemann, *Molecules* **2019**, *24*, 4482.
- [9] J. J. Jassoy, C. A. Heubach, T. Hett, F. Bernhard, F. R. Haege, G. Hagelueken, O. Schiemann, *Molecules* **2019**, *24*, 2735.
- [10] <https://web.expasy.org/protparam/>
- [11] H. Liu, J. H. Naismith, *BMC Biotechnol.* **2008**, *8*, 91.
- [12] M. Zehl, G. Allmaier, *Rapid Commun. Mass Spectrom.* **2004**, *18*, 1932–1938.
- [13] G. Karthikeyan, A. Bonucci, G. Casano, G. Gerbaud, S. Abel, V. Thomé, L. Kodjabachian, A. Magalon, B. Guigliarelli, V. Belle, et al., *Angew. Chemie Int. Ed.* **2018**, *57*, 1366–1370.
- [14] S. Stoll, A. Schweiger, *J. Magn. Reson.* **2006**, *178*, 42–55.
- [15] M. K. Bowman, C. Mailer, H. J. Halpern, *J. Magn. Reson.* **2005**, *172*, 254–267.
- [16] U. Stoll, S. (2018) (Goldfarb, D., Stoll, S., Eds.), Chapter 11, Wiley VCH
- [17] P. P. Borbat, J. H. Freed, *Chem. Phys. Lett.* **1999**, *313*, 145–154.
- [18] S. Saxena, J. H. Freed, *J. Chem. Phys.* **1997**, *107*, 1317–1340.
- [19] D. Akhmetzhanov, P. Schöps, A. Marko, N. C. Kunjir, S. T. Sigurdsson, T. F. Prisner, *Phys. Chem. Chem. Phys.* **2015**, *17*, 24446–24451.
- [20] P. P. Borbat, J. H. Freed in: *Methods in Enzymology*, Volume 423: Two-Component Systems, Part B. Eds: M. I. Simon, B. Crane, A. Crane, **2007**, Elsevier.
- [21] G. Jeschke, V. Chechik, P. Ionita, A. Godt, H. Zimmermann, J. Banham, C. Timmel, D. Hilger, H. Jung, *Appl. Magn. Reson.* **2006**, *30*, 473–498.
- [23] A. Meyer, J. J. Jassoy, S. Spicher, A. Berndhäuser, O. Schiemann, *Phys. Chem. Chem. Phys.*, **2018**, *20*, 13858–13869
- [23] <https://github.com/dinarabdullin/SnrCalculator>
- [24] G. Jeschke, Y. Polyhach, *Phys. Chem. Chem. Phys.*, **2007**, *9*, 1895–1910.
- [25] F. Wojciechowski, A. Groß, I. T. Holder, L. Knörr, M. Drescher, J. S. Hartig, *Chem. Commun.* **2015**, *51*, 13850–13853.
- [26] I. Krstic, R. Hänsel, O. Romainczyk, J. W. Engels, V. Dötsch, T. F. Prisner, *Angew. Chem. Int. Ed.* **2011**, *50*, 5070–5074.
- [27] F. Neese, *WIREs Comput. Mol. Sci.* **2012**, *2*, 73–78.
- [28] F. Weigend, R. Ahlrichs, *Phys. Chem. Chem. Phys.* **2005**, *7*, 3297–3305.
- [29] F. Weigend, *Phys. Chem. Chem. Phys.* **2006**, *8*, 1057–1065.
- [30] S. Grimme, S. Ehrlich, L. Goerigk, *J. Comput. Chem.* **2011**, *32*, 1456–1465.
- [31] S. Grimme, J. Antony, S. Ehrlich, H. Krieg, *J. Chem. Phys.* **2010**, *132*, 154104.
- [32] G. Hagelueken, R. Ward, J. H. Naismith, O. Schiemann, *Appl. Magn. Reson.* **2012**, *42*, 377–391.

[A6]: Ox-SLIM: Synthesis of and Site-Specific Labelling with a Highly Hydrophilic Trityl Spin Label

Reprinted with permission from

Nico Fleck, Caspar Heubach, Tobias Hett, Sebastian Spicher, Stefan Grimme, Olav Schiemann*, *Chem. Eur. J.* **2021**, *ahead of print*, chem.202100013

Published with Open Access by Wiley-VCH (Weinheim, DE), ©**2021** to the authors.

The following reprint of the article refers to the typeset manuscript, which is currently available online via the DOI 10.1002/chem.202100013.

Contributions:

- Experimental Work:
 - Organic synthesis incl. compound characterization
 - cw-EPR spectroscopy
 - incl. stability measurements
 - incl. examination of aggregation with proteins
- Writing of the manuscript

Physical Organic Chemistry

Ox-SLIM: Synthesis of and Site-Specific Labelling with a Highly Hydrophilic Trityl Spin Label

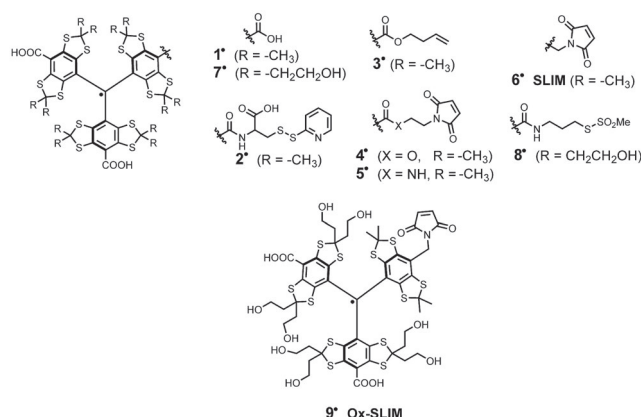
Nico Fleck,^[a] Caspar Heubach,^[a] Tobias Hett,^[a] Sebastian Spicher,^[b] Stefan Grimme,^[b] and Olav Schiemann^{*[a]}

Abstract: The combination of pulsed dipolar electron paramagnetic resonance spectroscopy (PDS) with site-directed spin labelling is a powerful tool in structural biology. Rational design of trityl-based spin labels has enabled studying biomolecular structures at room temperature and within cells. However, most current trityl spin labels suffer either from aggregation with proteins due to their hydrophobicity, or from bioconjugation groups not suitable for in-cell measurements. Therefore, we introduce here the highly hydrophilic trityl spin label Ox-SLIM. Engineered as a short-linked

maleimide, it combines the most recent developments in one single molecule, as it does not aggregate with proteins, exhibits high resistance under in-cell conditions, provides a short linker, and allows for selective and efficient spin labelling via cysteines. Beyond establishing synthetic access to Ox-SLIM, its suitability as a spin label is illustrated and ultimately, highly sensitive PDS measurements are presented down to protein concentrations as low as 45 nM resolving interspin distances of up to 5.5 nm.

Introduction

Since the discovery of the triphenylmethyl radical by Gomberg in 1900,^[1] stable carbon-centred radicals received rising attention. This especially applies to trityl radicals of the tetrathioaryl-type (Scheme 1), derived from the so-called Finland trityl **1**[•].^[2,3] Within the past two decades, **1**[•] and its derivatives found widespread application in in vivo imaging,^[4] oximetry,^[5,6] pH-sensing,^[7] viscosity measurements,^[8] and as polarizing agents in dynamic nuclear polarization (DNP).^[9,10] Moreover, trityl radicals emerged as spin labels^[11–14] for pulsed dipolar electron paramagnetic resonance spectroscopy (PDS)^[15–17] to elucidate structures of biomolecules.^[18,19] Exploiting their long T_M relaxation times,^[20] trityl radicals like **2**^[13] paved the way to PDS measurements at physiological temperatures.^[13,14,21] Recent trends in the development of trityl spin labels focused on their suitability for in-cell measurements, where the reductive intracellular environment presents additional challenges with re-



Scheme 1. Lewis structures of trityl spin labels and their parent compounds.

spect to the stability of the radical centre. Initial studies with **3**^[18] proved the suitability of trityl radicals for this purpose in general, though the bioconjugation proceeded with low efficiency and inseparable aggregates. Trityl spin labels with functional groups for bioconjugation based on maleimides (**4**[•]; **5**[•]; **6**[•])^[22–24] coped with this challenge by providing highly selective and efficient linkage to cysteines. While **2**[•]–**5**[•] are simple esters/amides of **1**[•]; the benzylic CH_2 -linker used to construct the so-called SLIM-trityl **6**[•] was shown to improve the stability towards intracellular reduction by shifting its redox potentials. Concomitantly, a short linker is introduced giving rise to narrow distance distributions.^[24] Another inherent drawback caused by the lipophilic core of these first generation trityl spin labels is aggregation with themselves^[25,26] and hydrophobic interactions with proteins.^[18,19,22,23] This complicates the spin labelling of proteins and can adversely influence the PDS-derived dis-

[a] N. Fleck, C. Heubach, T. Hett, Prof. Dr. O. Schiemann
University of Bonn, Institute of Physical and Theoretical Chemistry
Wegelerstr. 12, 53115 Bonn (Germany)
E-mail: schiemann@pc.uni-bonn.de

[b] S. Spicher, S. Grimme
University of Bonn, Institute of Physical and Theoretical Chemistry
Beringstr. 4, 53115 Bonn (Germany)

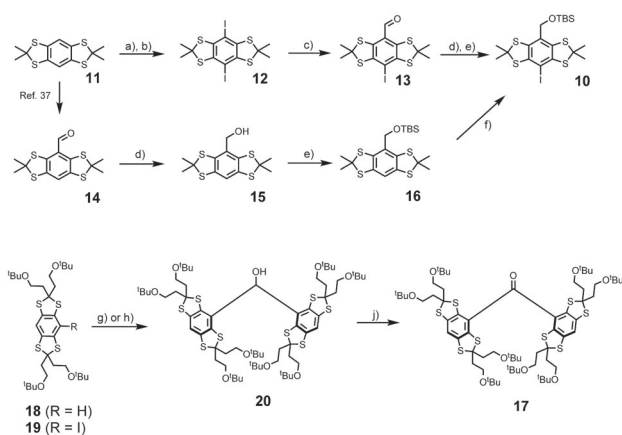
Supporting information and the ORCID identification number(s) for the author(s) of this article can be found under:
<https://doi.org/10.1002/chem.202100013>.

© 2021 The Authors. Chemistry - A European Journal published by Wiley-VCH GmbH. This is an open access article under the terms of the Creative Commons Attribution Non-Commercial License, which permits use, distribution and reproduction in any medium, provided the original work is properly cited and is not used for commercial purposes.

tance distributions. With bovine serum albumin for instance, aggregation of **1**[•] occurred already at protein concentrations above 60 μM .^[27] Therefore, efforts have been undertaken to increase the hydrophilicity of trityl radicals. For imaging and sensing purposes, conjugation of **1**[•] to dendritic PEG-esters,^[28,29] dextrans,^[30] or oligopeptides^[31] addressed this issue. However, the resulting radicals become very large and are therefore not suitable as spin labels. Other approaches aimed for hydrophilic trityl cores by hydroxylation of the thioketal's methyl-substituents.^[32] Accordingly, the Ox063 radical **7**[•] was reported early in patent literature but efficient synthetic access was disclosed only recently.^[33] Based on this core, the hydrophilic spin label **8**[•] has been introduced,^[34] and utilized for distance measurements on outer membranes of *E. coli* just recently.^[35] Despite its high water-solubility, the methanethiosulfonate bioconjugation site is not suitable for in-cell applications^[36] and such long linking groups lead to unnecessarily broad distance distributions.^[22,35] Therefore, we report here the modular synthesis of the hydroxylated short linked maleimide trityl (Ox-SLIM) **9**[•] that combines the reduction resistance and short linkage of **6**[•] with the hydrophilicity of **7**[•]. The hydroxyl-groups on two of the bithioketalaryl moieties provide the hydrophilicity, whereas the third, not hydroxylated bithioketalaryl-unit carries the benzylic maleimide and ensures high accessibility for labelling. Finally, it is shown that Ox-SLIM **9**[•] enables highly sensitive PDS measurements down to protein concentrations as low as 45 nM at a distance of 5.5 nm.

Results and Discussion

The synthesis of Ox-SLIM **9**[•] needs aryl building block **10**, which can be obtained via two alternative routes from bithioketal **11**^[3,37] (Scheme 2). The first route starts with aromatic tri-

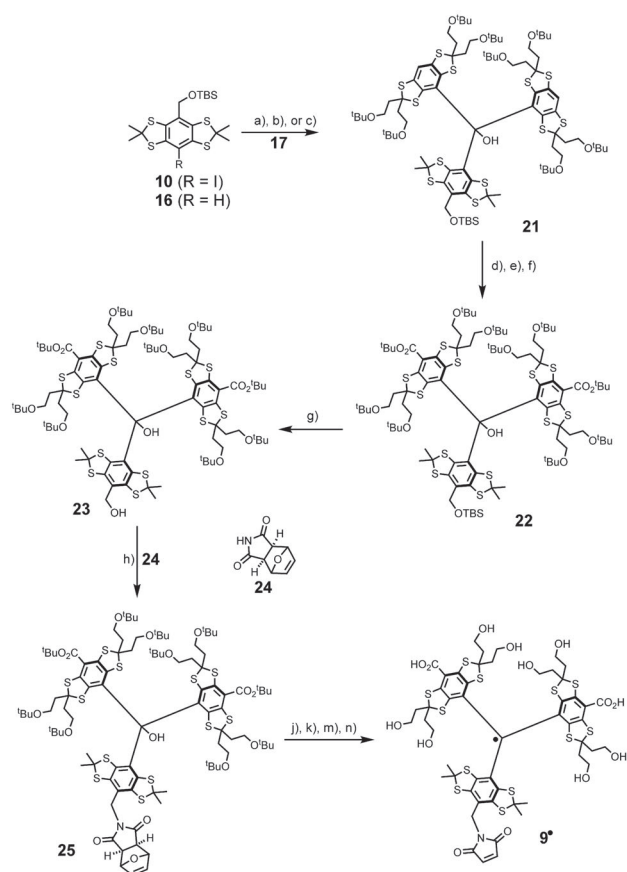


Scheme 2. Synthesis of building blocks **10** and **17**. a) 6.5 equiv. LiTMP, 0.1 equiv. Et_3NCl , 12 equiv. Me_3SiCl , THF, -95°C to r.t., 16 h. b) 3.0 equiv. ICl , CH_2Cl_2 , r.t., 3 h, 86% over two steps. c) 1.1 equiv. $n\text{BuLi}$, THF, -95°C , 45 min, then 15.0 equiv. DMF, to r.t., 16 h, 73% yield. d) 2.0 equiv. NaBH_4 , $\text{CH}_2\text{Cl}_2/\text{MeOH}$ 2:1, r.t., 30 min, 93% from **14**. e) 1.2 equiv. $t\text{BuMe}_2\text{SiCl}$, 2.5 equiv. Imidazole, DMF, r.t., 16 h, 82% over two steps from **13**, 91% from **15**. f) 1. LiTMP, THF, -78°C , 2 h. 2. I_2 , to r.t., 16 h, 56%. g) 0.95 equiv. $n\text{BuLi}$, THF, -95°C , then 0.4 equiv. HCO_2Me , r.t., 16 h, 36%, for **12**. h) 1.95 equiv. $t\text{BuLi}$, 0.48 equiv., THF, -95°C , 45 min, then 0.48 equiv. HCO_2Me , r.t., 16 h, 88%, for **13**. i) 1.25 equiv. Dess–Martin-periodinane, CH_2Cl_2 , r.t., 60 min, 93%.

methylsilylation of **11** by reaction with lithium tetramethylpiperide (LiTMP) and in situ quenching with trimethylsilyl chloride. Noteworthy, the basicity of LiTMP ($\text{p}K_a = 37$)^[38] is not sufficient for quantitative deprotonation of **11**, but it does not react with Me_3SiCl either due to its low nucleophilicity.^[38] This transformation avoids the use of stronger yet more nucleophilic bases such as lithium alkyls, which were shown to cleave the carbon–sulfur bond in **11**.^[32,40] An *ipso*-iododesilylation with ICl then afforded **12** in a yield of 86%. Lithium-halogen exchange with $n\text{BuLi}$ at -95°C runs cleanly without any evidence for thioketal-cleavage, and quenching with DMF gave aldehyde **13** in a yield of 73% after acidic workup. Subsequent carbonyl reduction with NaBH_4 and transformation of the benzylic alcohol to the TBS-ether with TBS-Cl under classical Corey conditions^[41] provided **10** in a yield of 82% over the last two steps, and of 51% with respect to **11**. However, the poor solubility of aldehyde **13** in most organic solvents rendered a scale-up of this route cumbersome. Therefore, alternative access to **10** was sought for, and achieved via aldehyde **14**, the synthesis of which has been described recently.^[40] Reduction of **14** with NaBH_4 gave alcohol **15** and subsequent silylation yielded TBS-ether **16**, both in yields of 93% and 95%, respectively. Next, **16** was iodinated adapting a recent procedure by Poncelet et al.^[33] Though the iodination proceeded with a conversion of only 65% on a 2 gram scale, simple recrystallization from CH_3CN allowed for isolation of pure **10** in a yield of 56%, or 39% with respect to **11**.

In the second branch of the converging synthesis towards **9**[•], ketone **17** was synthesized from thioketals **18** and **19**, which are available in three and four steps, respectively, following a recent protocol.^[33] Deprotonation of **18** with $n\text{BuLi}$ and reaction of the resulting anion with methyl formate provided diarylmethanol **20**, if performing the lithiation at -95°C . However, the yield of 36% was fairly low. This was also the case when using MeLi .^[40] By contrast, generating the lithiumaryl from **19** via lithium–halogen exchange with $t\text{BuLi}$ at -95°C increased the yield to 89%. In the final step of this branch, Dess–Martin-oxidation of **20** led to ketone **17** in a yield of 93%.

Within the further synthesis, the most critical step is the formation of the triarylmethanol scaffold in **21** (Scheme 3). Considering the DFT-optimized structure of ketone **17** (Figures S71 and 72), the Bürgi–Dunitz trajectory appears blocked by the bulky *tert*-butoxy substituents and this steric congestion requires tremendous structural reorganization during the transformation. Ultimately, side-reactions such as thioketal cleavage^[32,40] or decomposition of lithium organyls through reaction with solvent molecules makes this transformation additionally cumbersome. To cope with these issues, the required nucleophile was generated from **10** by lithium-halogen exchange with exactly 2.0 equiv. $t\text{BuLi}$ at -95°C . While other lithium alkyls leave the corresponding alkyl halide behind, no electrophiles remain in the solution using $t\text{BuLi}$, so that the aryl lithium can only react with the ketone. In this way, **21** was obtained in an isolated yield of 83%, while the use of $s\text{BuLi}$ ^[33] resulted in our hands in a yield of only 31%. Moreover, metal–halogen exchange performed superior compared to direct lith-



Scheme 3. Final steps for the synthesis of **9'**. a) *t*BuLi, -95°C , Et_2O , 45 min, then **17**, to r.t., 16 h, 83%; b) *s*BuLi, -95°C , Et_2O , 45 min, then **17**, to r.t., 16 h, 31%; c) MeLi, THF, r.t., 100 min, exchange for Et_2O , then **18**, 16 h, 11%. a, b) for **10**, c) for **16**. d) *s*BuLi, -20°C , TMEDA, 120 min. e) CO_2 , to r.t., 16 h. f) *O*-*tert*-butyl-*N,N'*-diisopropylisourea, PhMe, 60°C , 4 h, 47% over three steps. g) *n*Bu₄NF, THF, 45°C , 3 h, 82%. h) ADDP, *n*Bu₃P, **24**, THF, r.t., 5 h, 71%. i, 1) $\text{CF}_3\text{SO}_3\text{H}$, CH_3CN , r.t., 4 h. 2) SnCl_2 , THF, r.t., 20 min. j) HCO_2H , 45°C , 16 h. l) NaHCO_3 , MeOH, r.t., 16 h. m) DMF, 100°C , 16 h, 60% over four steps.

iation of **16** with conditions proposed by Hintz et al.,^[40] where the yield dropped to 11%. Noteworthy, the choice of solvent seemed important: No conversion was observed within *n*-hexane, presumably related to lacking stabilization of the ionic intermediate of the nucleophilic addition, while diethyl ether proved suitable for this transformation. Advantageous of the benzylic TBS-ether in **10** and **21** is that it paves the way for the late-stage introduction of the concealed maleimide as outlined below. In addition, any functionality compliant with the metal-halogen exchange conditions (e.g. protected alkynes)^[40] can be incorporated at this stage, highlighting the versatility of the approach chosen here for accessing asymmetric trityl radicals with high hydrophilicity.

Next, the carboxylation of trityl alcohol **21** was carried out by deprotonation with *s*BuLi in TMEDA/*n*-hexane using gaseous CO_2 as electrophile. Other frequently applied carboxylation reagents such as Boc_2O ^[16,24,40] more likely contain traces of water, severely diminishing the yield of the dicarboxylated product. The obtained dicarboxylic acid was then converted into the corresponding *tert*-butyl diester **22** using *O*-*tert*-butyl-diisopropylisourea,^[42] since classical Steglich conditions^[43]

(DCC, DMAP) or the combination $\text{Boc}_2\text{O}/\text{DMAP}$ ^[44] yielded only traces of product. Subsequently, the TBS-ether in **22** was cleaved with commercially available *n*Bu₄NF (TBAF) in THF yielding **23**. Here, 10 equiv of TBAF and a slightly elevated temperature of 45°C were required for sufficient reactivity. The C–N bond required for **9'** was introduced via a Mitsunobu reaction in analogy to our previous work, where the maleimide was concealed as a thermally labile tetrahydroisoindolinone.^[24] However, since elevated temperatures are required in the later route, the *exo*-Diels–Alder adduct of furane and maleimide **24** was used, which does not undergo retro-Diels–Alder fragmentation up to 50°C (Supporting Information section 3.3). Carrying out the transformation with the classical reagents Ph_3P and diethylazodicarboxylate (DEAD), **25** was obtained in a yield of only 32% among many unknown by-products (Supporting Information section 3.1). Using instead tri-*n*-butylphosphine and 1,1'-azodicarbonyldi-piperidine (ADDP) increased the yield of the Mitsunobu-type C–N bond formation and afforded **25** in a yield of 71%. Both, the acceleration of the C–N bond formation owing to the higher $\text{p}K_{\text{a}}$ of the intermediate betaine and steric factors avoiding interactions with the central OH-group are assumed to contribute to this improved yield. In the further course towards **9'**, the corresponding trityl radical was generated with $\text{CF}_3\text{SO}_3\text{H}$ and reduction of the generated tritylium cation with SnCl_2 in situ.

The resulting product was immediately treated with neat formic acid at 45°C for 16 h in order to convert the remaining *tert*-butyl ethers to formate esters and ensure the cleavage of the *tert*-butyl esters. The formate esters were then subjected to very mild hydrolysis with NaHCO_3 in methanol at room temperature. It should be noted that other hydrolysing conditions involving LiOH or $\text{Ba}(\text{OH})_2$ endangered the integrity of the concealed maleimide (Supporting Information section 3.4). Finally, the maleimide group was deprotected by means of a retro-Diels–Alder reaction at 100°C in degassed DMF giving the fully characterized (cw-EPR, HRMS, HPLC; cf. Supporting Information) and water-soluble spin label **9'**.

The room temperature continuous wave (cw) X-band EPR spectrum of **9'** is shown in Figure 1a. In analogy to the spectrum of **6'**,^[24] it consists of nine resolved lines which arise from hyperfine coupling to the benzylic nitrogen ($A_{\text{N}} = 1.48 \text{ MHz}$) and the two magnetically inequivalent benzylic hydrogen atoms ($A_{\text{H1}} = 3.02 \text{ MHz}$; $A_{\text{H2}} = 6.09 \text{ MHz}$). Interestingly, record-

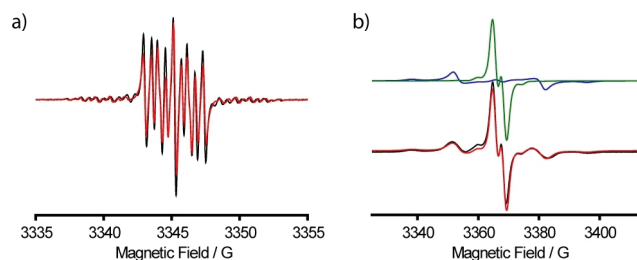


Figure 1. CW X-band EPR spectra of $50 \mu\text{M}$ **9'** in aqueous PBS buffer recorded at a) room temperature and at b) 100 K after addition of 20% glycerol; simulations are overlaid in red. For (b), the experimental spectrum was simulated as a sum of a monomer (green) and a dimer of **9'** (blue).

ing the spectrum in frozen solution does not only reveal the expected apparent doublet of 9^* (in analogy to 6^*), but also exhibits a superimposed Pake pattern (Figure 1 b) in a ratio of 69:31. Analysis of the Pake pattern provides a dipolar coupling constant of 19.4 G corresponding to an interspin distance of 9.9 Å.^[22] The Pake pattern is attributed to a noncovalent dimer (9^*)₂, which was experimentally observed in ESI(–)-MS (Figure S51). Additional evidence for (9^*)₂ was obtained through a computational study involving a conformer search by the CREST^[45] algorithm at the GFN-FF^[46] level of theory. The conformation of lowest energy found by CREST was further optimized by B97-3c^[47] and is shown in Figure 2. Hybrid-DFT

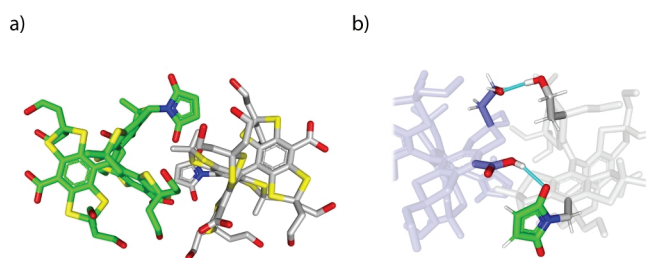


Figure 2. DFT structure of (9^*)₂. a) Complete view, and b) close-up with hydrogen bonds highlighted in light blue.

single-point calculations (PBE0,^[48] def2-TZVPP^[49]) combined with GFN2-xTB^[50] thermostatical contributions and COSMO-RS(H₂O)^[51] solvation free energies revealed that the homodimer is stabilized by $\Delta G = -14.8$ kcal mol⁻¹ due to the formation of hydrogen bonds involving one maleimido substituent (SI section 8.1). For the Ox063-radical 7^* , a similar dimerization was shown to be facilitated by Me₄N⁺ as a template,^[25] a role fulfilled here by the maleimide moiety. Interestingly, high concentrations of glycerol suppressed dimerization to (9^*)₂, presumably due to competitive hydrogen bonding, underpinning the non-covalent nature of the dimer (Supporting Information section 6.4). As mentioned above, the hydrophobicity of the first-generation trityl spin labels 2^* – 6^* leads to their aggregation with biomolecules. The concomitant immobilization triggers extensive line-broadening and consequently peak-to-peak amplitude reduction in the cw EPR spectra. This signal depletion has been implemented as a semi-quantitative measure of non-specific aggregation with proteins.^[27,29,32] In order to test this, a cysteine-free construct (C219A) of yersinia outer protein O (YopO) was expressed, purified,^[24] and added in increasing amounts to solutions of spin labels 4^* , 6^* , and 9^* (Figure 3 a). For both 4^* and 6^* , significant signal depletion occurs, indicating aggregation with the protein. By contrast, virtually no signal depletion was encountered for 9^* , highlighting the hydrophilic nature of 9^* which impedes the aggregation.

Next, the performance of 9^* as a spin label was evaluated. Performing the labelling experiment on the cysteine-free YopO construct with 4 equivalents of 9^* , a minor extent of unspecific labelling (7%, Figure 3 b and Supporting Information section 5.2) was observed. Applying the same labelling conditions to the double-cysteine mutant (Y588C/N624C), YopO could be doubly labelled with 9^* with a labelling efficiency of 85% (Fig-

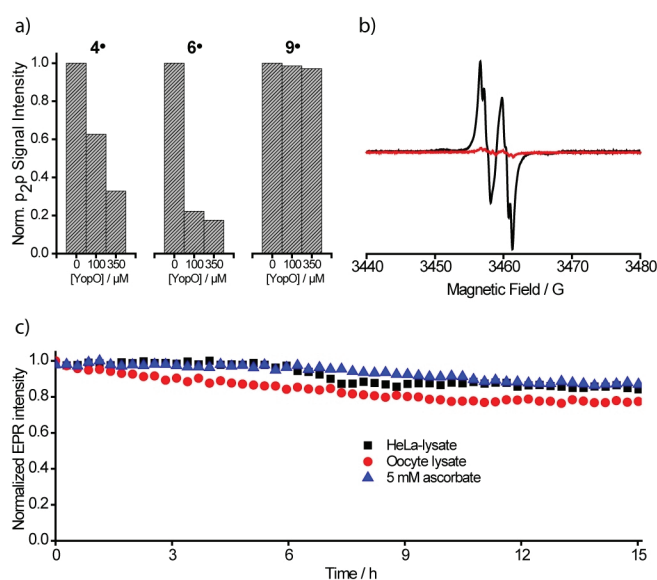


Figure 3. Properties of Ox-SLIM 9^* . a) CW X-band EPR peak-to-peak amplitude of trityl spin labels 4^* , 6^* , and 9^* (50 μ M in PBS-buffer) at increasing concentration of cysteine-free YopO C219A. b) CW X-band EPR spectra of YopO Y588T^{ox}/N624T^{ox} (black) and YopO C219A (red) after labelling and workup. The spectra were recorded at 298 K in PBS-buffer. c) EPR double integral intensity of Y588T^{ox}/N624T^{ox} in HeLa lysate, *X. laevis* oocyte lysate, and 5 mM sodium ascorbate monitored over time.

ure 3 b and Supporting Information section 5.3). Since the dimer (9^*)₂ is only formed in appreciable amounts upon freezing it does not interfere with the labelling reaction, and once bound to a cysteine the maleimide group cannot be involved into the dimer formation anymore. In the following, the side chain generated by binding 9^* to a cysteine residue is called T^{ox}.

In order to pave the way for future in-cell applications, the reduction stability of Y588T^{ox}/N624T^{ox} was assessed within aqueous solutions of 5 mM ascorbate and lysates of HeLa cells and *Xenopus laevis* oocytes. As shown in Figure 3 c, YopO Y588T^{ox}/N624T^{ox} exhibits a high stability in these media, attributed to the imidomethylene-motif of 9^* , which destabilizes the anionic species resulting from reduction.^[24]

Finally, a PDS measurement was performed on YopO Y588T^{ox}/N624T^{ox}. Exploiting the high sensitivity of the double quantum coherence (DQC) experiment,^[24] the time trace shown in Figure 4 a was obtained. It exhibits an SNR^[52] of 133 h^{-1/2}, exceeding the value obtained with 6^* (46 h^{-1/2}) due to a longer T_M-relaxation time (Supporting Information chapter 7). The corresponding distance distribution shows a bimodal shape with most probable distances at 4.60 and 5.48 nm (Figure 4 b), which coincide very well with the results obtained for 6^* on this mutant, and supports the idea that the reason for the bimodality are two different structure of the α -helix, at which the labels are bound.^[24] Slight changes in the intensity distribution of the two peaks is attributed to different time trace lengths and different conformer clouds of the different labels. The high SNR prompted us to perform DQC measurements on a 45 nm sample of YopO Y588T^{ox}/N624T^{ox}, which still yielded an SNR of 1.24 h^{-1/2} at a dipolar evolution time of

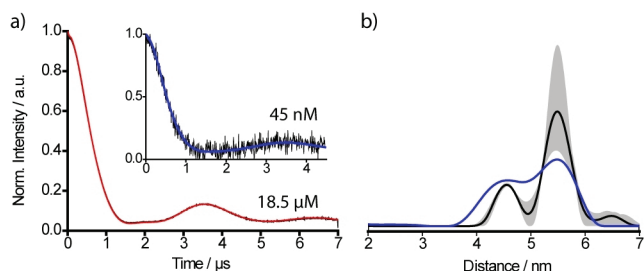


Figure 4. PDS measurements with **9'**. a) Background-corrected DQC time traces obtained for YopO Y588T^{ox}/N624T^{ox} (black), overlaid with their fits by DeerAnalysis (red/blue), shown at both 18.5 μM and 45 nM protein concentrations. b) Distance distribution derived from the time trace of the 18.5 μM sample with the background validation indicated in grey. The distance distribution obtained from the 45 nM samples is overlaid in blue.

4.5 μs (Supporting Information chapter 7). This implies a sensitivity improvement exceeding a factor of 2 compared to our recent publication.^[24]

Conclusions

In this study, the highly hydrophilic trityl spin label Ox-SLIM **9'** was introduced through a streamlined synthesis without a statistical step. The chosen approach is highly versatile and the intermediates presented in this study can be utilized as precursors to various hydrophilic trityl radicals. Additionally, an improved Mitsunobu/retro-Diels–Alder sequence is used for the introduction of the maleimide. Overall, label **9'** combines most recent developments on trityl spin labels in a single molecule, i.e., a short linker, bioresistance, and no aggregation with proteins. Demonstrated for the protein YopO, **9'** allows efficient labelling of cysteines in a selective fashion. Finally, distance measurements with protein concentrations down to 45 nM were viable, thus setting a new benchmark.

Acknowledgements

Funding by the DFG via SPP1601 is gratefully acknowledged. Open access funding enabled and organized by Projekt DEAL.

Conflict of interest

The authors declare no conflict of interest.

Keywords: biophysical chemistry · electron paramagnetic resonance · pulsed dipolar spectroscopy · spin labelling · trityl radicals

- [1] M. Gomberg, *J. Am. Chem. Soc.* **1900**, *22*, 757–771.
- [2] S. Andersson, A. Rydbeck, R. S. Mahno, US Patent 5728370, **1999**.
- [3] T. J. Reddy, T. Iwama, H. J. Halpern, V. H. Rawal, *J. Org. Chem.* **2002**, *67*, 4635–4639.
- [4] B. B. Williams, H. J. Halpern, *Biomed. EPR, Part A: Free Radicals, Metals, Medicine and Physiology* (Eds.: S. R. Eaton, G. R. Eaton, L. J. Berliner), Springer US, Boston, **2005**, pp. 283–319.
- [5] B. Epel, C. R. Haney, D. Hleihel, C. Wardrip, *Med. Phys.* **2010**, *37*, 2553–2559.

- [6] A. A. Bobko, I. Dhimitruka, T. D. Eubank, C. B. Marsh, J. L. Zweier, V. V. Khramtsov, *Free Radic. Biol. Med.* **2009**, *47*, 654–658.
- [7] A. Boš-Liedke, M. Walawender, A. Woźniak, D. Flak, J. Gapiński, S. Jurga, M. Kucińska, A. Plewiński, M. Murias, M. Elewa, L. Lampp, P. Imming, K. Tadzysak, *Cell Biochem. Biophys.* **2018**, *76*, 19–28.
- [8] M. Poncelet, B. Driesschaert, *Angew. Chem. Int. Ed.* **2020**, *59*, 16451–16454; *Angew. Chem.* **2020**, *132*, 16593–16596.
- [9] G. Mathies, M. A. Caporini, V. K. Michaelis, Y. Liu, K. N. Hu, D. Mance, J. L. Zweier, M. Rosay, M. Baldus, R. G. Griffin, *Angew. Chem. Int. Ed.* **2015**, *54*, 11770–11774; *Angew. Chem.* **2015**, *127*, 11936–11940.
- [10] J. H. Ardenkjær-Larsen, B. Fridlund, A. Gram, G. Hansson, L. Hansson, M. H. Lerche, R. Servin, M. Thaning, K. Golman, *Proc. Natl. Acad. Sci. USA* **2003**, *100*, 10158–10163.
- [11] G. W. Reginsson, N. C. Kunjir, S. T. Sigurdsson, O. Schiemann, *Chem. Eur. J.* **2012**, *18*, 13580–13584.
- [12] "Trityl Radicals as Spin Labels": O. Krumkacheva, B. Elena, in *Electron Paramagnetic Resonance*, The Royal Society of Chemistry, Cambridge, **2017**, pp. 35–60.
- [13] Z. Yang, Y. Liu, P. Borbat, J. L. Zweier, J. H. Freed, W. L. Hubbell, *J. Am. Chem. Soc.* **2012**, *134*, 9950–9952.
- [14] G. Y. Shevelev, O. A. Krumkacheva, A. A. Lomzov, A. A. Kuzhelev, O. Y. Rogozhnikova, D. V. Trukhin, T. I. Troitskaya, V. M. Tormyshev, M. V. Fedin, D. V. Pyshnyi, E. G. Bagryanskaya, *J. Am. Chem. Soc.* **2014**, *136*, 9874–9877.
- [15] G. W. Reginsson, O. Schiemann, *Biochem. Soc. Trans.* **2011**, *39*, 128–139.
- [16] G. Jeschke, *Annu. Rev. Phys. Chem.* **2012**, *63*, 419–446.
- [17] P. P. Borbat, J. H. Freed, in *EMagRes*, Wiley, Chichester, **2017**, pp. 465–494.
- [18] J. J. Jassoy, A. Berndhäuser, F. Duthie, S. P. Kühn, G. Hagelueken, O. Schiemann, *Angew. Chem. Int. Ed.* **2017**, *56*, 177–181; *Angew. Chem.* **2017**, *129*, 183–187.
- [19] B. Joseph, V. M. Tormyshev, O. Y. Rogozhnikova, D. Akhmetzyanov, E. G. Bagryanskaya, T. F. Prisner, *Angew. Chem. Int. Ed.* **2016**, *55*, 11538–11542; *Angew. Chem.* **2016**, *128*, 11710–11714.
- [20] A. A. Kuzhelev, D. V. Trukhin, O. A. Krumkacheva, R. K. Strizhakov, O. Y. Rogozhnikova, T. I. Troitskaya, M. V. Fedin, V. M. Tormyshev, E. G. Bagryanskaya, *J. Phys. Chem. B* **2015**, *119*, 13630–13640.
- [21] Z. Yang, G. Jiménez-Osés, C. J. López, M. D. Bridges, K. N. Houk, W. L. Hubbell, *J. Am. Chem. Soc.* **2014**, *136*, 15356–15365.
- [22] J. J. Jassoy, C. A. Heubach, T. Hett, F. Bernhard, F. R. Haege, G. Hagelueken, O. Schiemann, *Molecules* **2019**, *24*, 2735.
- [23] A. Giannoulis, Y. Yang, Y.-J. Gong, X. Tan, A. Feintuch, R. Carmieli, T. Bahrenberg, Y. Liu, X.-C. Su, D. Goldfarb, *Phys. Chem. Chem. Phys.* **2019**, *21*, 10217–10227.
- [24] N. Fleck, C. A. Heubach, T. Hett, F. R. Haege, P. P. Bawol, H. Baltruschat, O. Schiemann, *Angew. Chem. Int. Ed.* **2020**, *59*, 9767–9772; *Angew. Chem.* **2020**, *132*, 9854–9859.
- [25] I. Marin-Montesinos, J. C. Paniagua, M. Vilaseca, A. Urtizberea, F. Luis, M. Feliz, F. Lin, S. Van Doorslaer, M. Pons, *Phys. Chem. Chem. Phys.* **2015**, *17*, 5785–5794.
- [26] I. Marin-Montesinos, J. C. Paniagua, A. Peman, M. Vilaseca, F. Luis, S. Van Doorslaer, M. Pons, *Phys. Chem. Chem. Phys.* **2016**, *18*, 3151–3158.
- [27] Y. Song, Y. Liu, W. Liu, F. A. Villamena, J. L. Zweier, *RSC Adv.* **2014**, *4*, 47649–47656.
- [28] W. Liu, J. Nie, X. Tan, H. Liu, N. Yu, G. Han, Y. Zhu, F. A. Villamena, Y. Song, J. L. Zweier, Y. Liu, *J. Org. Chem.* **2017**, *82*, 588–596.
- [29] Y. Song, Y. Liu, C. Hemann, F. A. Villamena, J. L. Zweier, *J. Org. Chem.* **2013**, *78*, 1371–1376.
- [30] M. Poncelet, B. Driesschaert, O. Tseytlin, M. Tseytlin, T. D. Eubank, V. V. Khramtsov, *Bioorg. Med. Chem. Lett.* **2019**, *29*, 1756–1760.
- [31] B. Driesschaert, P. Leveque, B. Gallez, J. Marchand-Brynaert, *Tetrahedron Lett.* **2013**, *54*, 5924–5926.
- [32] Y. Qu, Y. Li, X. Tan, W. Zhai, G. Han, J. Hou, G. Liu, Y. Song, Y. Liu, *Chem. Eur. J.* **2019**, *25*, 7888–7895.
- [33] M. Poncelet, J. L. Huffman, V. V. Khramtsov, I. Dhimitruka, B. Driesschaert, *RSC Adv.* **2019**, *9*, 35073–35076.
- [34] V. M. Tormyshev, A. S. Chubarov, O. A. Krumkacheva, D. V. Trukhin, O. Y. Rogozhnikova, A. S. Spitsyna, A. A. Kuzhelev, V. V. Koval, M. V. Fedin, T. S. Godovikova, M. K. Bowman, E. G. Bagryanskaya, *Chem. Eur. J.* **2020**, *26*, 2705–2712.

- [35] S. Ketter, A. Gopinath, O. Rogozhnikova, D. Trukhin, V. M. Tormyshev, E. G. Bagryanskaya, B. Joseph, *Chem. Eur. J.* **2021**, *27*, 2299–2304.
- [36] R. Igarashi, T. Sakai, H. Hara, T. Tenno, T. Tanaka, H. Tochio, M. Shirakawa, *J. Am. Chem. Soc.* **2010**, *132*, 8228–8229.
- [37] K. Kopp, O. Schiemann, N. Fleck, *Molecules* **2020**, *25*, 3666.
- [38] M. Campbell, V. Snieckus, E. W. Baxter, in *e-EROS*, Wiley, **2008**, <https://doi.org/10.1002/047084289X.r1143.pub2>.
- [39] T. D. Krizan, J. C. Martin, *J. Am. Chem. Soc.* **1983**, *105*, 6155–6157.
- [40] H. Hintz, A. Vanas, D. Klose, G. Jeschke, A. Godt, *J. Org. Chem.* **2019**, *84*, 3304–3320.
- [41] E. J. Corey, A. Venkateswarlu, *J. Am. Chem. Soc.* **1972**, *94*, 6190–6191.
- [42] R. M. Burk, G. D. Berger, R. L. Bugianesi, N. N. Girotra, W. H. Parsons, M. M. Ponpipom, *Tetrahedron Lett.* **1993**, *34*, 975–978.
- [43] B. Neises, W. Steglich, *Angew. Chem. Int. Ed. Engl.* **1978**, *17*, 522–524; *Angew. Chem.* **1978**, *90*, 556–557.
- [44] K. Takeda, A. Akiyama, H. Nakamura, S. I. Takizawa, Y. Mizuno, H. Takayanagi, Y. Harigaya, *Synthesis* **1994**, *1994*, 1063–1066.
- [45] P. Pracht, F. Bohle, S. Grimme, *Phys. Chem. Chem. Phys.* **2020**, *22*, 7169–7192.
- [46] S. Spicher, S. Grimme, *Angew. Chem. Int. Ed.* **2020**, *59*, 15665–15673; *Angew. Chem.* **2020**, *132*, 15795–15803.
- [47] J. G. Brandenburg, C. Bannwarth, A. Hansen, S. Grimme, *J. Chem. Phys.* **2018**, *148*, 064104.
- [48] J. P. Perdew, M. Ernzerhof, K. Burke, *J. Chem. Phys.* **1996**, *105*, 9982–9985.
- [49] A. Schäfer, C. Huber, R. Ahlrichs, *J. Chem. Phys.* **1994**, *100*, 5829–5835.
- [50] C. Bannwarth, S. Ehlert, S. Grimme, *J. Chem. Theory Comput.* **2019**, *15*, 1652–1671.
- [51] J. Reinisch, M. Diedenhofen, R. Wilcken, A. Udvarhelyi, A. Glöß, *J. Chem. Inf. Model.* **2019**, *59*, 4806–4813.
- [52] D. Abdullin, P. Brehm, N. Fleck, S. Spicher, S. Grimme, O. Schiemann, *Chem. Eur. J.* **2019**, *25*, 14388–14398.

Manuscript received: January 3, 2021

Accepted manuscript online: January 6, 2021

Version of record online:

Supporting Information

Ox-SLIM: Synthesis of and Site-Specific Labelling with a Highly Hydrophilic Trityl Spin Label

Nico Fleck,^a Caspar Heubach,^a Tobias Hett,^a Sebastian Spicher,^b Stefan Grimme,^b and
Olav Schiemann^{*,a}.

Institute of Physical and Theoretical Chemistry, University of Bonn, ^aWegelerstr. 12, 53115 Bonn, Germany

^bBeringstr. 4, 53115 Bonn, Germany. *schiemann@pc.uni-bonn.de

Contents

1. General Procedures and Instrumentation	4
2. Synthetic Procedures	5
2.1 Thioketal 12	5
2.2 Aldehyde 13	5
2.3 Thioketal 10	6
2.4 Alcohol 15	6
2.5 Thioketal 16	7
2.6 Thioketal 10	7
2.7 Diarylmethanol 20	8
2.7.1 Method A	8
2.7.2 Method B	9
2.8 Diarylketone 17	10
2.9 Trityl alcohol 21	10
2.10 Trityl alcohol 22	11
2.11 Trityl alcohol 23	12
2.12 Trityl alcohol 25	13
2.13 Trityl radical 9[•] (Ox-SLIM)	14
3. Reaction Optimization	15
3.1 Mitsunobu Reaction	15
3.2 Formation of t-Butyl Esters for 22	16
3.3 Thermal stability of <i>exo</i> -Tetrahydroisoindolindione	16
3.4 Tests for conversion of 25[•] to 9[•]	18
4. Analytical data	19
4.1 NMR-Spectroscopy	19
4.2 Mass-Spectrometry	37
4.3 Liquid-Chromatography	46
5. Spin Labelling	47
5.1 Preparations	47
5.2 Labeling of YopO ₈₉₋₇₂₉ C219A with 9[•]	47
5.3 Labeling of YopO ₈₉₋₇₂₉ Y588C/N624C with 9[•]	48
5.4 Protein Mass-Spectrometry	49

5.5 Activity Assay	50
6. CW EPR-Spectroscopy	50
6.1 Simulation of CW EPR Spectra.....	50
6.2 Reduction Stability.....	52
6.3 Binding of Spin Labels to Cystein-Free YopO C219A.....	52
7. Pulsed EPR-spectroscopy.....	54
7.1 Sample Preparation	54
7.2 Relaxation Time Measurements.....	54
7.3 Double Quantum Coherence (DQC) Experiments	56
7.4 Determination of the Signal-to-Noise Ratio (SNR).....	57
8. Computational Data.....	58
8.1 Homodimer of 9[•]	58
8.1.1 Coordinates for 9[•] in xyz-format.....	59
8.1.2 Coordinates for (9[•]) ₂ in xyz-format	60
8.2 Ketone 17	64
8.2.1 Coordinates for 17 in xyz-format	65
9. References	67

1. General Procedures and Instrumentation

NMR-Spectroscopy: NMR spectra were recorded on Avance I 300, Avance I 400, Avance III HD 500, or Avance III HD 700 spectrometers (Bruker BioSpin, Rheinstetten, Germany). Chemical shifts are reported referenced to hydrogen residual peaks of the NMR solvent.^[1]

Mass-Spectrometry: MALDI(+)-spectra were recorded in a Bruker Daltonics UltraFlex TOF/TOF spectrometer (Bruker, Rheinstetten, Germany). For organic compounds, DCTB was used as the matrix, whereas DHAP was used for protein samples. For ESI-MS of protein samples, a Synapt G2-Si spectrometer (Waters, Milford, USA) was employed. APCI-spectra and ESI-spectra of organic compounds were obtained on an Orbitrap XL spectrometer (Thermo Fisher Scientific, Bremen, Germany). Protein samples were subjected to mass spectrometric analysis in 20 mM PO_i buffer (pH = 6.8, 50 mM NaCl).

Chromatography: For analytical chromatography, an UHPLC system (PLATINblue-series, Knauer GmbH, Berlin, Germany) equipped with an Eurospher II 100-2 C18P, 2 μm, 2 x 100 mm column (Knauer GmbH, Berlin, Germany) and a UV detector working at 265 nm was used.

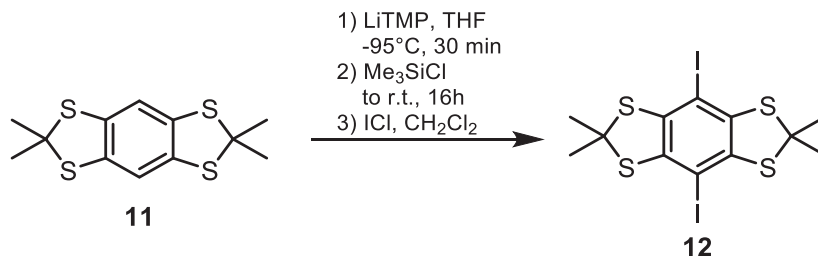
CW EPR: All continuous wave (*cw*) EPR spectra were recorded at X-band frequencies (~9.4 GHz) either on an EMXmicro or EMXnano spectrometer (Bruker BioSpin, Rheinstetten, Germany). On the EMXmicro, room temperature measurements were performed using an ER 4122SHQ (Bruker BioSpin, Rheinstetten, Germany) resonator, while measurements at 100 K were conducted with a 4119HS (Bruker) resonator in conjunction with an ER 4141VT temperature control system (Oxford cryogenics, UK). For all samples, X-band EPR-tubes with an outer diameter of 5 mm obtained from Wilmad Labglass (Brand of SP Industries, Warminster, USA) were used. Liquid aqueous samples were filled into 10 μL capillaries (Disposable Capillaries, Hirschmann Laborgeräte, Eberstadt, Germany) and these were placed in the X-band tubes. CW EPR measurements at room temperature were performed at an attenuation of 25 dB (603.1 μW) and a modulation amplitude of 0.1 G. CW EPR spectra at 100 K were recorded with an attenuation of 44 dB. Quantitative EPR measurements were conducted employing the on-board spin counting routine of the EMXnano spectrometer.

Pulsed EPR: Pulsed EPR measurements were conducted at Q-band frequencies (~33.7 GHz) on a ELEXSYS E580 EPR spectrometer equipped with an ER5106QT-II resonator (Bruker BioSpin, Rheinstetten, Germany) and a 150 W TWT-amplifier (Applied Systems Engineering, Fort Worth, TX, USA). All data was acquired using quadrature detection. The temperature was adjusted to 50 K using a CF935 helium gas-flow cryostat (Oxford Instruments, Abingdon, UK) and an Oxford Instruments iTC 503 temperature controller.

Synthesis: Chemicals purchased from commercial suppliers were used without further purification. Dry solvents were purchased from *Acros Organics* in sealed bottles containing molecular sieves. Where indicated, solvents were degassed by applying three freeze-pump-thaw cycles. Thin layer chromatography was conducted using 250 μm F254 silica plates provided by Merck, spots were visualized with UV-light at 254nm. Spots of trityl alcohols can be stained selectively by irradiating the TLC-plate for 5min with UV-light at 254nm (5W). For column chromatography, silica gel (60Å pore size, 40–63 μm particle size) purchased from Merck was used. Solvents for chromatography were purchased in analytical grade and used as received. The concentration of butyl lithium solutions was determined prior to use by titration against 2,5-dimethoxybenzylalcohol following the protocol of Winkle et al^[2]. Compounds **11**^[3], **14**^[4], **18**^[5], **19**^[5], and **24**^[6] were prepared according to literature protocols.

2. Synthetic Procedures

2.1 Thioketal **12**



Et₃NHCl (96 mg, 0.7 mmol, 10 mol%) and 2,2,6,6-tetramethylpiperidin (6.92 g, 8.27 mL, 49.12 mmol, 7.00 eq.) were dissolved in 200 mL dry THF under argon. After cooling down to -95°C, *n*-butyl lithium (28.6 mL, 1.6 M in hexanes, 45.6 mmol, 6.50 eq.) was slowly added and the reaction mixture was stirred for 30 minutes to ensure complete formation of LiTMP. Then, **9** (2.00 g, 7.01 mmol) was added as a solid in an argon stream and the reaction mixture was stirred for further 45 min at -95°C. Afterwards, trimethylsilyl chloride (9.07 g, 10.60 mL, 84.1 mmol, 12 eq.) was added dropwise. After continuous stirring for 60 min, the mixture was allowed to warm up while stirred overnight.

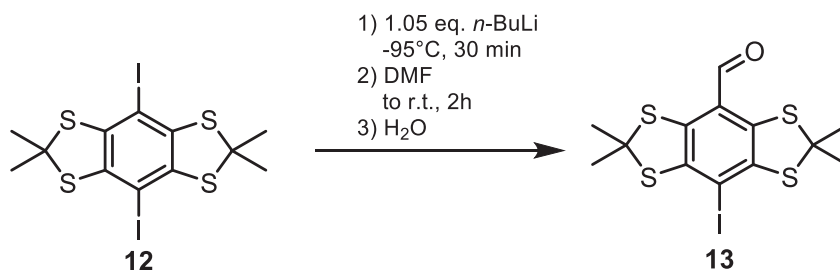
50 mL 2M NaOH were slowly added and the organic phase was separated off. After extraction of the aqueous phase with 100 mL diethyl ether, the organic phases were unified and dried over MgSO₄. After removal of the solvents under reduced pressure, a yellow solid is obtained. To remove silanols and silyl ethers, the crude product was washed with cold acetone (3x15 mL), so that a white crystalline solid is obtained. The intermediate obtained, 2,2,6,6-Tetramethyl-4,8-bis(trimethylsilyl)-benzo[1,2-d;4,5-d]bis(1,3-dithiol) is used in the next step without further purification. For the *ipso*-iododesilylation, the obtained product is dissolved in 60 mL dry dichloromethane and cooled down to 0°C. Then, a solution of iodine monochloride (3.40 g, 1.10 mL, 21.03 mmol, 3.00 eq.) in 10 mL dichloromethane is added dropwise. After stirring for 1h under continuous cooling, the orange precipitate is collected and washed with cold acetone (3 x 20 mL) yielding the title compound as a bright yellow/greenish solid in a yield of 3.29 g (86 %).

¹H-NMR (500 MHz, CDCl₃, 298 K, δ in ppm): 1.91 (s, 12H)

¹³C{¹H}-NMR (125 MHz, CDCl₃, 298 K, δ in ppm): 139.2, 81.3, 59.0, 32.2

HRMS (EI, *m/z*, [M]⁺): calcd for C₁₂H₁₂I₂S₄, 537.7911; found 537.7911.

2.2 Aldehyde **13**



Compound **10** (3.22 g, 5.93 mmol) was dissolved in 250 mL dry THF and cooled down to -95 °C. Thereupon, *n*-butyl lithium (4.07 mL, 1.6 M in hexanes, 6.52 mmol, 1.1 eq.) was added dropwise resulting in a bright yellow color of the reaction mixture. After stirring at -95 °C for 30 min, dry DMF (7 mL, 6.65 g, 91.0 mmol, 15.3 eq.) was added and the reaction mixture was allowed to warm up overnight. Methanol (50

mL) was added carefully, whereupon the reaction mixture turned orange/yellow immediately. Solvents were removed under reduced pressure and the residue was taken up in 300 mL dichloromethane. After washing with water (50 mL) and brine (50 mL), the organic phase was dried over MgSO₄ and solvents were removed under reduced pressure yielding the orange title compound, which was subjected to column chromatography on SiO₂ eluting with cyclohexane/ethylacetate 2:1 (v/v). The title compound is obtained as an orange solid in a yield of 1.73 g (73%).

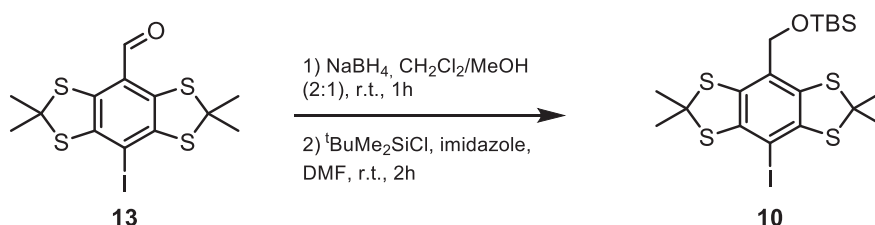
It should be noted, that using less THF results in precipitation of the starting material upon cooling. This leads to an effective excess of butyl lithium yielding the dialdehyde.

¹H-NMR (400 MHz, CDCl₃, 298 K, δ in ppm): 9.95 (s, 1H), 1.95 (s, 12H)

¹³C{¹H}-NMR (100 MHz, CDCl₃, 298 K, δ in ppm): 188.5, 144.2, 136.3, 125.1, 88.9, 63.7, 32.2.

HRMS (APCI, *m/z*, [M+H]⁺): calcd for C₁₃H₁₄IOS₄, 440.8965; found 440.8965.

2.3 Thioketal **10**



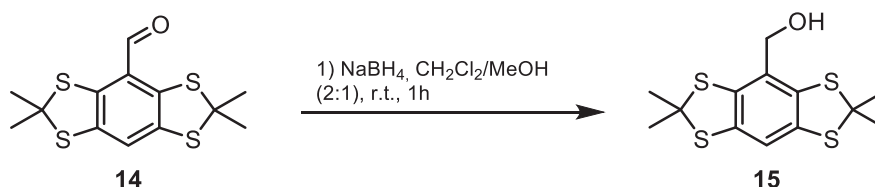
Compound **13** (1.56 g, 3.54 mmol) was dissolved in 80 mL dichloromethane and 40 mL methanol were added. Then, sodium borohydride (269 mg, 7.08 mmol, 2.0 eq.) was added, whereupon the reaction mixture lost its orange color quickly. After stirring for 1h, the solvents were evaporated and the residue was transferred into a Schlenk-flask and dried in high vacuum. Afterwards, imidazole (602 mg, 8.85 mmol, 2.5 eq.) was added and the mixture was dissolved in dry DMF. Upon complete dissolution, *tert*-butyldimethylsilyl chloride (640 mg, 4.25 mmol, 1.2 eq.) was added and the reaction mixture was stirred overnight. After dilution with 100 mL brine, the aqueous phase was extracted twice with dichloromethane and washed with brine several times in order to remove the DMF. The unified organic phases were dried over MgSO₄ and solvents were removed under reduced pressure. The yellow residue was suspended in 15 mL cyclohexane and filtered. Removal of the solvents from the filtrate and purification of the crude product by column chromatography on SiO₂ eluting with cyclohexane/ ethyl acetate 97:3 (v/v) yielded the title compound in a yield of 1.61 g (82 %) over two steps.

¹H-NMR (400 MHz, CDCl₃, 298 K, δ in ppm): 4.46 (s, 2H), 1.88 (s, 12H), 0.91 (s, 9H), 0.08 (s, 6H).

¹³C{¹H}-NMR (100 MHz, CDCl₃, 298 K, δ in ppm): 142.5, 133.0, 129.8, 81.2, 65.1, 62.3, 31.7, 26.1, 18.6, -5.1.

HRMS (ACPCI, *m/z*, [M]⁺): calcd for C₁₉H₂₉IOS₄Si, 555.9910; found 555.9902.

2.4 Alcohol **15**



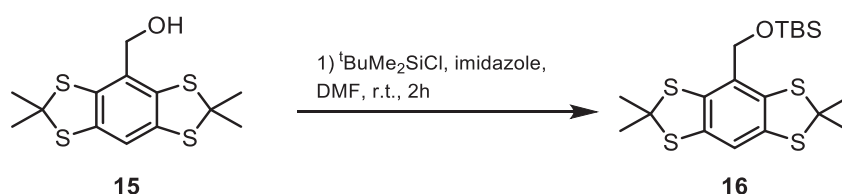
Aldehyde **14** (2.00 g, 6.39 mmol) was dissolved in 100 mL dichloromethane and 50 mL methanol were added. Sodium borohydride (486 mg, 12.78 mmol, 2.00 eq.) was added, whereupon the reaction mixture lost its orange color quickly. After stirring for 1h, the solvents were evaporated and the residue was taken up in 70 mL dichloromethane and the organic phase was washed with water, brine, and dried over MgSO₄. The solvents were removed under reduced pressure to yield the title compound as a colorless solid in a yield of 1.88 g (93 %).

¹H-NMR (500 MHz, CDCl₃, 298 K, δ in ppm): 7.01 (s, 1H), 4.56 (s, 2H), 1.89 (s, 12H)

¹³C{¹H}-NMR (125 MHz, CDCl₃, 298 K, δ in ppm): 136.6, 136.0, 129.5, 116.6, 65.3, 65.2, 31.5.

HRMS (APCI, *m/z*, [M]⁺): calcd for C₁₃H₁₆OS₄, 316.0078; found 316.0077.

2.5 Thioketal **16**



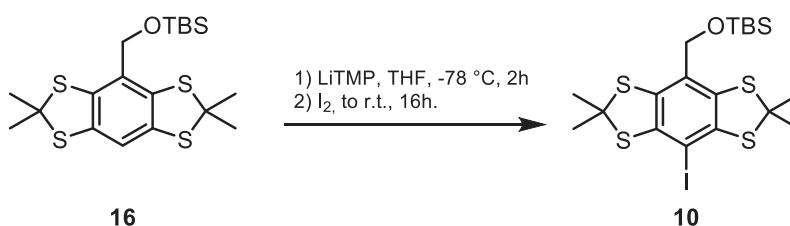
Alcohol **15** (1.71 g, 5.41 mmol) and imidazole (920 mg, 13.52 mmol, 2.50 eq.) were dissolved in 25 mL dry DMF and *tert*-butyldimethylsilyl chloride (974 mg, 6.49 mmol, 1.2 eq.) was added. The reaction mixture was stirred at room temperature over 2 h and quenched by addition of 100 mL water. Extraction was performed with 2 x 50 mL dichloromethane and the unified organic phases were washed with 3 x 100 mL brine. The organic phase was dried over MgSO₄ and solvents were removed under reduced pressure, giving a colorless oil. Purification was performed by column chromatography on silica eluting with cyclohexane/ethyl acetate 97:3 affording the title compound as a slowly crystallizing oil in a yield of 2.12 g (91 %).

¹H-NMR (500 MHz, CDCl₃, 298 K, δ in ppm): 6.99 (s, 1H), 4.55 (s, 2H), 1.87 (s, 12H), 0.91 (s, 9H), 0.08 (s, 6H).

¹³C{¹H}-NMR (125 MHz, CDCl₃, 298 K, δ in ppm): 136.3, 135.6, 130.3, 116.2, 65.3, 64.9, 31.3, 26.1, 18.6, -5.1.

HRMS (APCI, *m/z*, [M]⁺): calcd for C₁₉H₃₀OS₄Si, 430.0943; found 430.0940.

2.6 Thioketal **10**



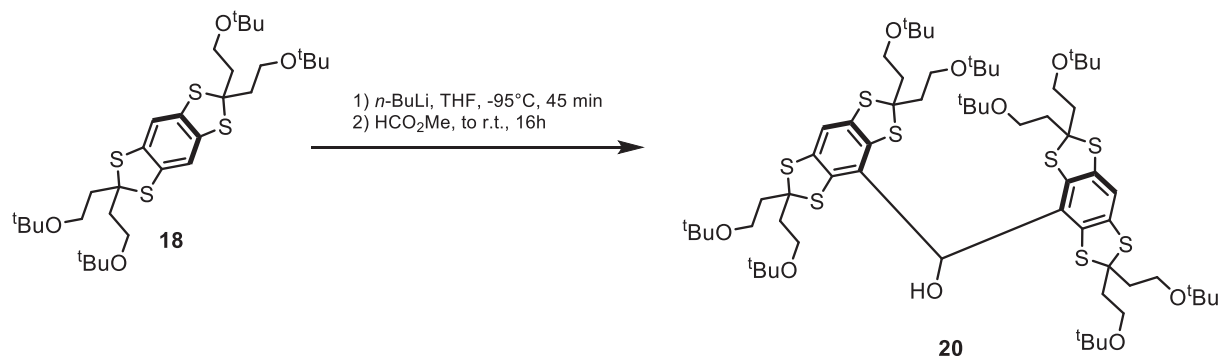
2,2,6,6-Tetramethylpiperidine (1.72 g, 2.07 mL, 12.2 mmol, 2.50 eq.) were dissolved in 50 mL dry THF and cooled to -96 °C. Then, *n*-butyl lithium (1.6 M in hexane, 7.63 mL, 12.2 mmol, 2.50 eq.) was added and the mixture was stirred for 45 min. Meanwhile, a solution of **16** (2.10 g, 4.88 mmol) in 20 mL dry THF is prepared and then added to the LiTMP solution. After stirring for 2 h at -96 °C, iodine (3.09 g, 12.2 mmol, 2.50 eq.) was added and reaction mixture was stirred for 16 h while warming up to room temperature. Then, 50 mL saturated Na₂S₂O₃ solution was added and the mixture was extracted with 3 x 40 mL diethyl ether. The organic phase was washed with water, brine, and dried over MgSO₄. After removal of the sol-

vents under reduced pressure, a yellowish crude product is obtained, which is recrystallized from acetonitrile to yield the pure title compound as a colorless solid in a yield of 1.52 g (56 %).

Analytical data of **10** is provided above.

2.7 Diarylmethanol **20**

2.7.1 Method A



Compound **18** (2.00 g, 3.17 mmol) was dissolved in 50 mL dry THF and cooled to -95°C. Then, *n*-butyl lithium (2.5 M in hexanes, 1.2 mL, 3.00 mmol, 0.95 eq.) was added dropwise resulting in a bright yellow reaction mixture. After stirring for 45 min, methyl formate (76 mg as a solution in 0.95 mL Et₂O, 1.27 mmol, 0.4 eq.) was added and the reaction mixture was allowed to reach room temperature overnight. Subsequently, THF was removed under reduced pressure and the residue was taken-up in 100 mL dichloromethane. After washing with water (50 mL) and brine (50 mL), the organic phase was dried over MgSO₄ and solvents were removed under reduced pressure. The crude product was subjected to column chromatography on silica eluting with cyclohexane/diethyl ether 3:1 (v/v) yielding the title compound as a pale-yellow foam in a yield of 736 mg, 36 % (71 % based on recovered **18** (985 mg)).

¹H-NMR (700 MHz, CD₂Cl₂, 298 K, δ in ppm): 7.03 (s, 2H), 3.49 (m, 16H), 2.28 (m, 16H), 1.15 (2x s, 72H)

¹³C{¹H}-NMR (175 MHz, CD₂Cl₂, 298 K, δ in ppm): 138.2, 135.1, 130.6, 116.8, 73.39, 73.38, 71.5, 59.2, 59.0, 41.4, 40.8, 27.9.

Note that due to the asymmetry of **20** for steric reasons, diastereotopic effects increase the number of ¹³C-signals. As visible from figure S1, this asymmetry is reduced on the NMR-timescale with increasing temperature.

HRMS (ESI+, *m/z*, [M]⁺): calcd for C₆₅H₁₀₈O₉S₈ 1288.5754, found 1288.5753

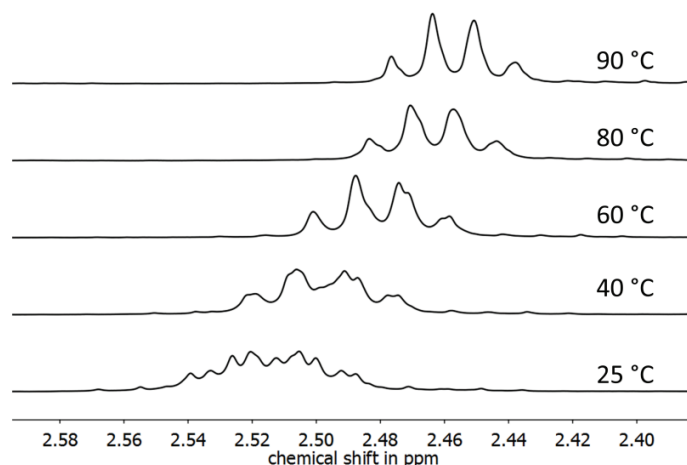
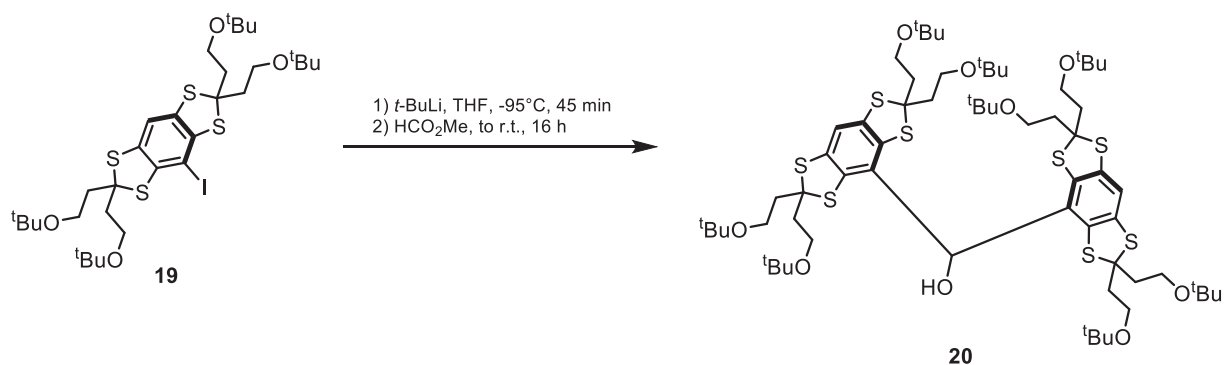


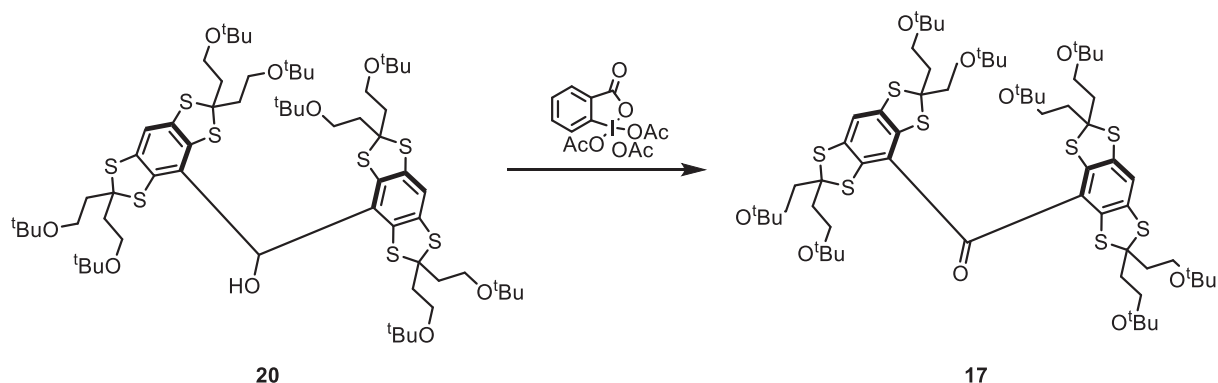
Figure S1: $^1\text{H-NMR}$ spectrum of **20** in toluene- d^8 at variable temperatures.

2.7.2 Method B



19 (2.87 g, 3.79 mmol) was dissolved in 60 mL dry THF and cooled down to -95°C , whereupon *tert*-butyl lithium (1.24 M in cyclohexane, 5.96 mL, 7.39 mol, 1.95 eq.) was added slowly. The reaction mixture was stirred for 45 min at -95°C and methyl formate (109 mg, 111 μL , 1.82 mmol, 0.48 eq.; dissolved in 0.9 mL dry THF) was added. The reaction mixture was stirred overnight while warming up to room temperature. The workup and the subsequent isolation of the title compound is carried out according to the aforementioned procedure involving direct lithiation of **18**. Yield 2.17 g (89%), based on **19**, and 66 % over two steps referring to **18**.

2.8 Diarylketone **17**



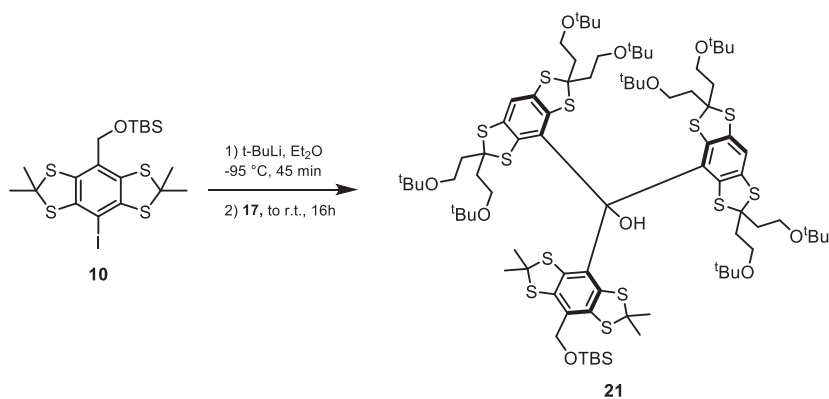
20 (2.96 g, 2.30 mmol) was dissolved in 50 mL dry dichloromethane. Then, *Dess-Martin-periodinane* (1.22 g, 2.87 mmol, 1.25 eq.) was added as a solid, whereupon the reaction mixture turned deep orange within 3 minutes of stirring. After further stirring at room temperature for 60 min, the reaction mixture was poured onto 50 mL ice-water and adjusted to pH 10 with 2M NaOH. The organic phase was separated and the aqueous layer extracted with 30 mL dichloromethane. The unified organic phases were dried over MgSO₄ and solvents were removed under reduced pressure to give the crude product as a dark orange oil. Subjecting it to column chromatography on silica and eluting with cyclohexane/diethyl ether 3:1 (v/v) yielded the title compound as an orange foam in a yield of 2.74 g (93 %).

¹H-NMR (700 MHz, CD₂Cl₂, 298 K, δ in ppm): 7.14 (s, 2H), 3.50 (t, 16, ³J_{H,H} = 6.4 Hz), 2.32 (t, 16H, ³J_{H,H} = 6.4 Hz), 1.14 (s, 72H).

¹³C{¹H}-NMR (175 MHz, CD₂Cl₂, 298 K, δ in ppm): 194.2, 139.0, 136.7, 128.3, 119.3, 73.4, 72.5, 59.0, 41.0, 27.9.

HRMS (MALDI+, *m/z*, [M]⁺): calcd for C₆₅H₁₀₆O₉S₈ 1286.5597, found 1286.5588

2.9 Trityl alcohol **21**



10 (1.173 g, 2.10 mmol) was dissolved in 25 mL dry diethyl ether and cooled down to -95°C. Then, *t*-butyl lithium (1.65 M in pentane, 2.55 mL, 4.21 mmol, 2.00 eq.) was added dropwise to the solution. After stirring for 45 min, **17** (1.68 g, 1.30 mmol, 0.62 eq., dissolved in 20 mL Et₂O) was added slowly and the cooling bath was removed. The reaction mixture was stirred overnight while warming up to room temperature. Afterwards, the reaction was quenched by addition of 50 mL brine, the etheric phase was separated and the aqueous layer was extracted twice with 30 mL Et₂O. The unified organic phases were dried over

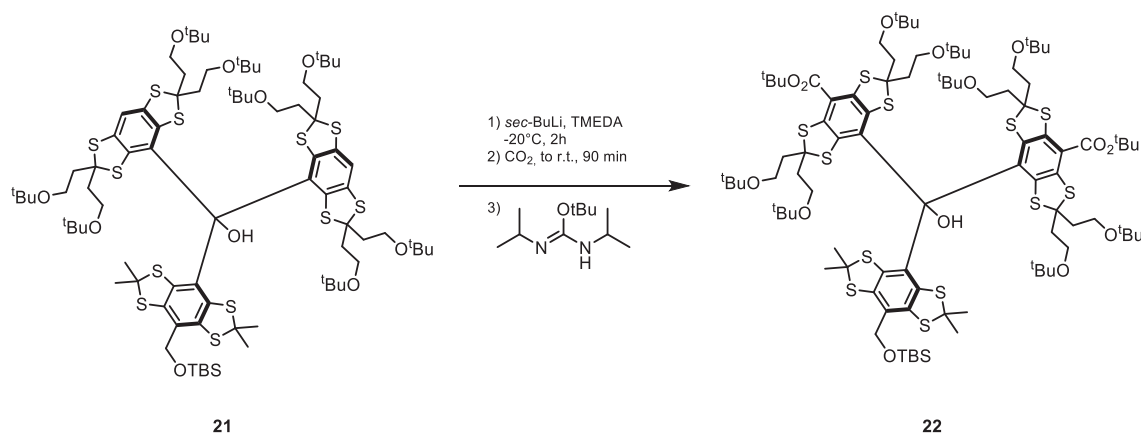
MgSO₄ and subjected to column chromatography on silica eluting with cyclohexane/diethyl ether 9:1 (v/v) to provide the title compound as an off-white foam in a yield of 1.84 g (1.072 mmol, 83 % referred to **17**).

¹H-NMR (700 MHz, CD₂Cl₂, 298 K, δ in ppm): 7.15 (s, 1H), 7.10 (s, 1H), 6.48 (s, 1H), 4.69 (d, 1H, ²J_{H,H} = 11.8 Hz), 4.59 (d, 1H, ²J_{H,H} = 11.8 Hz), 3.59 – 3.16 (m, 16H), 2.50 – 2.00 (m, 16H), 1.82 (s, 3H), 1.80 (s, 3H), 1.77 (s, 3H), 1.70 (s, 3H), 1.18 (s, 9H), 1.15 (s, 18H), 1.13 (s, 9H), 1.11 (s, 9H), 1.11 (s, 9H), 1.06 (s, 9H), 1.03 (s, 9H), 0.94 (s, 9H), 0.13 (s, 3H), 0.10 (s, 3H).

¹³C{¹H}-NMR (175 MHz, CD₂Cl₂, 298 K, δ in ppm): 139.77, 139.67, 139.46, 138.85, 138.77, 138.71, 138.60, 138.47, 138.43, 138.29, 137.50, 137.32, 132.86, 132.49, 131.90, 131.43, 118.43, 118.19, 84.17, 73.67, 73.39, 73.34, 73.32, 73.27, 73.26, 73.17, 73.11, 72.96, 71.10, 70.49, 69.52, 69.36, 66.39, 63.98, 63.05, 60.19, 59.65, 59.34, 59.32, 58.75, 58.71, 58.57, 58.27, 54.43, 54.22, 54.00, 53.78, 53.57, 45.41, 43.47, 40.87, 40.46, 39.77, 39.45, 38.90, 37.70, 34.61, 31.10, 30.78, 27.94, 27.92, 27.90, 27.88, 27.86, 27.81, 26.42, 18.93, -4.48, -4.76.

HRMS (MALDI+, *m/z*, [M]⁺): calcd for C₈₄H₁₃₆O₁₀S₁₂Si 1716.6546, found 1716.6621.

2.10 Trityl alcohol **22**



Trityl alcohol **21** (970 mg, 0.565 mmol) was dissolved in 20 mL dry TMEDA and cooled down to -20 °C. Then, *sec*-butyl lithium (6.83 mL, 1.24 M in cyclohexane, 8.47 mmol, 15.0 eq.) was added slowly. After 90 min, additional *sec*-butyl lithium (2.27 mL, 1.24 M in cyclohexane, 2.83 mmol, 5.0 eq.) was added and stirring at -20 °C was continued for further 30 min. The brown reaction mixture was diluted with 30 mL dry TMEDA and CO₂ (purity 4.5, 40 L gas volume) was bubbled through the solution for 4 hours, while the reaction mixture was warmed to room temperature after 2h. The solvents were removed under reduced pressure and the residue was taken-up in 50 mL diethyl ether. After washing with saturated 50 mL NH₄Cl solution, the organic phase was separated, dried over MgSO₄ and the solvents were removed under reduced pressure. The carboxylic acid product was dissolved in 20 mL dry toluene. In order to obtain the corresponding tert.-butyl ester, *O*-*tert*-butyl-*N,N'*-diisopropylisourea (339 mg, 404 μL, 1.69 mmol, 3.0 eq.) was added and the reaction mixture heated to 60°C under inert atmosphere for 4h. After cooling down to room temperature, water (10 mL) and sat. NH₄Cl (10 mL) was added. The organic phase was separated, the aqueous layer extracted with 10 mL Et₂O, and the unified organic phases dried over MgSO₄. The solvents were removed under reduced pressure. Subjecting the crude product to column chromatography on silica and eluting with cyclohexane/diethyl ether 3:1 (v/v) afforded the title compound as a bright yellow foam in a yield of 508 mg (47.0 %).

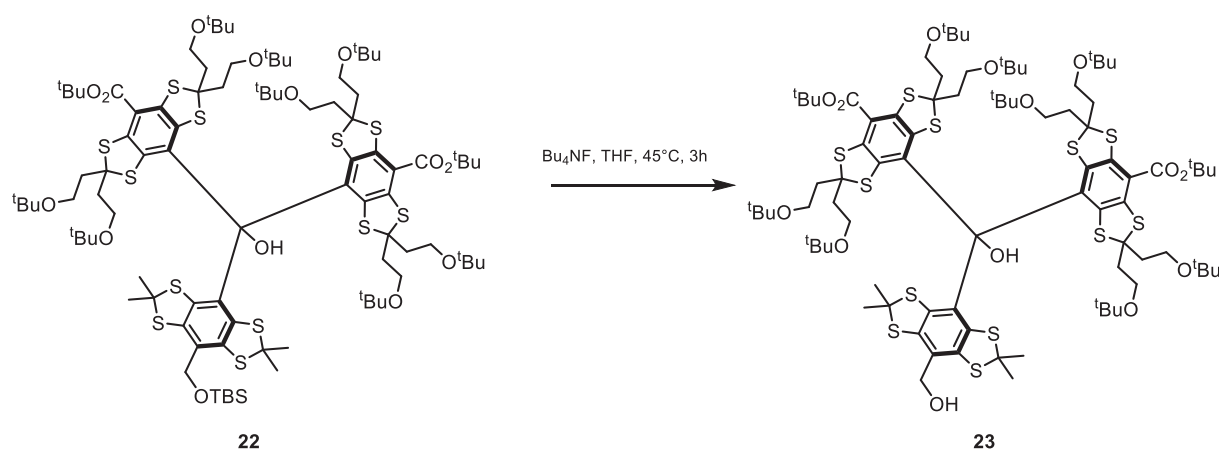
¹H-NMR (500 MHz, CD₂Cl₂, 298 K, δ in ppm): 6.87 (s, 1H), 4.69 (d, 1H, ²J_{H,H} = 11.7 Hz), 4.64 (d, 1H, ²J_{H,H} = 11.7 Hz), 3.60 – 3.23 (m, 16H), 2.38 – 2.00 (m, 16H), 1.79 (s, 3H), 1.79 (s, 3H), 1.77 (s, 3H), 1.72 (s, 3H),

1.62 (s, 9H), 1.60 (s, 9H), 1.15 (s, 9H), 1.15 (s, 9H), 1.14 (s, 9H), 1.11 (s, 27H), 1.08 (s, 9H), 1.06 (s, 9H), 0.94 (s, 9H), 0.12 (s, 3H), 0.12 (s, 3H).

¹³C-NMR (125 MHz, CD₂Cl₂, 298 K, δ in ppm): 165.76, 165.62, 141.39, 141.17, 141.12, 140.55, 140.33, 140.29, 139.89, 139.56, 139.33, 139.31, 138.82, 138.48, 135.46, 134.88, 131.51, 130.59, 123.95, 123.62, 84.66, 84.31, 84.12, 73.44, 73.40, 73.32, 73.31, 73.26, 73.25, 73.17, 73.16, 68.18, 68.16, 67.35, 66.97, 66.79, 63.36, 62.49, 59.84, 59.70, 59.32, 59.22, 58.58, 58.51, 58.41, 58.34, 54.43, 54.22, 54.00, 53.78, 53.57, 44.17, 43.97, 40.62, 40.38, 39.43, 38.90, 38.78, 34.97, 34.16, 28.67, 28.64, 28.03, 27.98, 27.96, 27.94, 27.92, 27.91, 27.90, 26.46, 19.01, -4.71, -4.77.

HRMS (MALDI+, *m/z*, [M]⁺): calcd for C₉₄H₁₅₂O₁₄S₁₂Si 1916.7594, found 1916.7604.

2.11 Trityl alcohol **23**



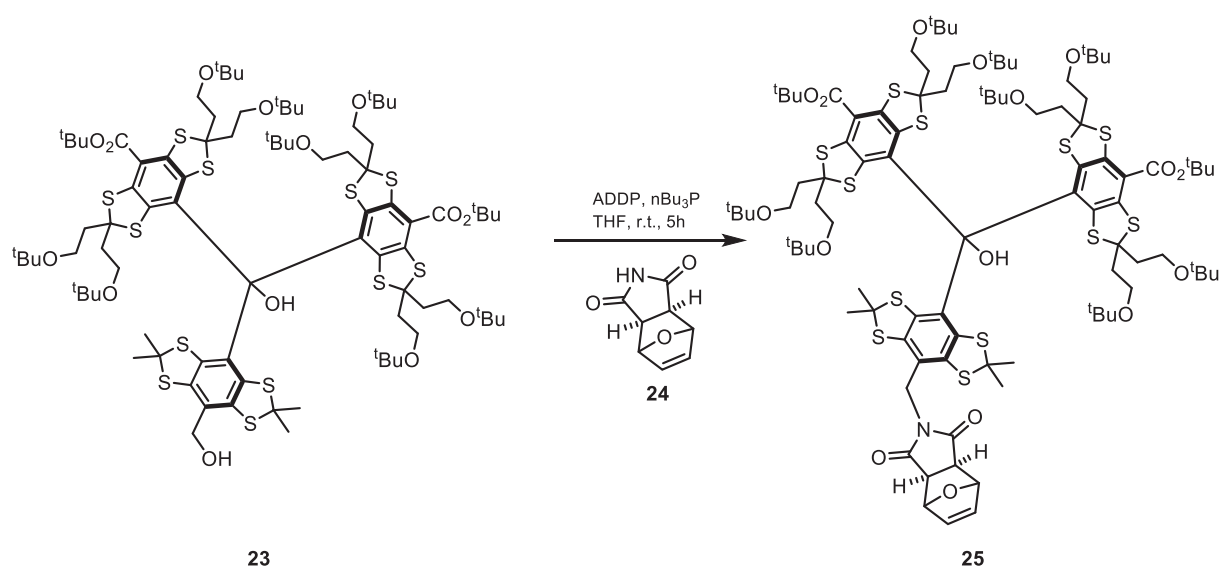
Trityl alcohol **22** (263 mg, 137.8 μmol) were dissolved in 7 mL dry THF and tetra-*n*-butyl ammonium fluoride (1.38 mL, 1M in THF, 1.38 mmol, 10.0 eq.) was added. The reaction mixture was stirred at 45 °C under TLC control (cyclohexane/diethyl ether 1:1, SiO₂), which proved quantitative conversion after 5h. The solvent was removed under reduced pressure and the residue taken-up in 20 mL dichloromethane. Washing with 20 mL brine and removing the solvents after drying over MgSO₄ gave a dark orange oil, which was purified via column chromatography on silica eluting with a cyclohexane/diethyl ether gradient of 3:1 to 1:1 (v/v), providing the title compound as an orange foam in a yield of 203 mg (82%).

¹H-NMR (500 MHz, CDCl₃, 298 K, δ in ppm): 6.75 (s, 1H), 4.63 (d, 1H, ²J_{H,H} = 12.4 Hz), 4.58 (d, 1H, ²J_{H,H} = 12.4 Hz), 3.62 – 3.19 (m, 16H), 2.40 – 1.99 (m, 16H), 1.80 (s, 3H), 1.78 (s, 3H), 1.75 (s, 3H), 1.70 (s, 3H), 1.61 (s, 9H), 1.60 (s, 9H), 1.15 (s, 9H), 1.14 (s, 9H), 1.12 (s, 9H), 1.09 (s, 9H), 1.08 (s, 18H), 1.05 (s, 9H), 1.02 (s, 9H).

¹³C-NMR (125 MHz, CDCl₃, 298 K, δ in ppm): ¹³C NMR (126 MHz, CDCl₃) δ 165.52, 165.27, 141.38, 140.70, 140.63, 140.37, 140.34, 140.04, 139.60, 139.54, 138.64, 138.61, 137.76, 137.69, 135.55, 134.17, 130.36, 129.81, 123.32, 122.72, 84.15, 83.99, 83.84, 73.30, 73.12, 73.10, 72.98, 72.91, 72.84, 72.81, 72.79, 68.39, 67.01, 66.88, 66.29, 65.91, 63.16, 62.26, 59.54, 59.15, 58.95, 58.46, 58.44, 58.19, 57.92, 57.82, 43.54, 42.25, 41.11, 41.05, 39.47, 38.81, 38.10, 37.91, 35.17, 34.35, 28.46, 28.43, 27.77, 27.72, 27.71, 27.68, 27.65, 27.62, 27.60.

HRMS (MALDI+, *m/z*, [M]⁺): calcd for C₈₈H₁₃₈O₁₄S₁₂ 1802.6730, found 1802.6734.

2.12 Trityl alcohol **25**



Trityl alcohol **23** (135 mg, 75 μmol) and compound **24** (34 mg, 210 μmol , 2.8 eq.) were placed in a Schlenk-tube and dissolved in 6 mL dry THF. Then, tri-*n*-butylphosphine (36 μL , 44 mg, 180 μmol , 2.4 eq., dissolved in 0.4 mL THF) and subsequently 1,1'-(azodicarbonyl)dipiperidine (46 mg, 180 μmol , 2.4 eq., dissolved in 1.0 mL THF) were added. The reaction mixture was stirred at room temperature under TLC control (CyH/Et₂O 1:1, SiO₂), until completion was observed after 4h. Then, water (10 mL) was added and the mixture was extracted with Et₂O (10 mL) twice. The organic phases were unified, washed with brine, dried over MgSO₄ and solvents were removed under reduced pressure to yield an orange oil, which was purified via column chromatography on silica eluting with cyclohexane/diethyl ether 1:1 (v/v) to afford the title compound as an orange foam in a yield of 104 mg (71%).

¹H-NMR (500 MHz, CDCl₃, 298 K, δ in ppm): 6.76 (s, 1H), 6.49 (dd, 1H, ³J_{H,H} = 6.0 Hz, ³J_{H,H} = 1.5 Hz), 6.47 (dd, 1H, ³J_{H,H} = 6.0 Hz, ³J_{H,H} = 1.5 Hz), 5.29 (m, 1H), 5.27 (m, 1H), 4.63 (d, 1H, ²J_{H,H} = 12.4 Hz), 4.54 (d, 1H, ²J_{H,H} = 12.4 Hz), 3.59 – 3.26 (m, 16H), 2.91 (d, ³J_{H,H} = 6.7 Hz), 2.85 (d, ³J_{H,H} = 6.7 Hz), 2.42 – 2.02 (m, 16H), 1.79 (s, 6H), 1.77 (s, 3H), 1.69 (s, 3H), 1.62 (s, 18H), 1.17 (s, 9H), 1.14 (s, 9H), 1.13 (s, 9H), 1.11 (s, 9H), 1.10 (s, 9H), 1.10 (s, 9H), 1.05 (s, 9H), 1.04 (s, 9H).

¹³C-NMR (125 MHz, CDCl₃, 298 K, δ in ppm): 2x 174.89*, 2x 165.44*, 141.17, 140.61, 140.55, 140.39, 139.99, 139.96, 139.85, 139.51, 138.88, 138.69, 138.62, 138.31, 136.74, 136.62, 135.00, 133.90, 130.55, 125.64, 124.75, 123.30, 122.85, 84.21, 83.92, 83.88, 80.99, 80.98, 73.11, 73.09, 73.01, 72.96, 72.88, 72.85, 72.75, 67.90, 66.81, 66.51, 66.40, 63.54, 63.48, 59.33, 59.21, 58.69, 58.35, 58.30, 58.20, 58.02, 47.56, 47.17, 43.73, 43.30, 42.27, 41.30, 40.25, 39.48, 39.16, 38.83, 38.30, 34.77, 32.51, 30.46, 29.14, 28.50, 28.46, 27.80, 27.77, 27.76, 27.72, 2x 27.67*.

*Note, that some signal splittings are not fully resolved in the spectrum.

HRMS (MALDI+, m/z , [M]⁺): calcd for C₉₆H₁₄₃NO₁₆S₁₂ 1949.7050, found 1949.7060.

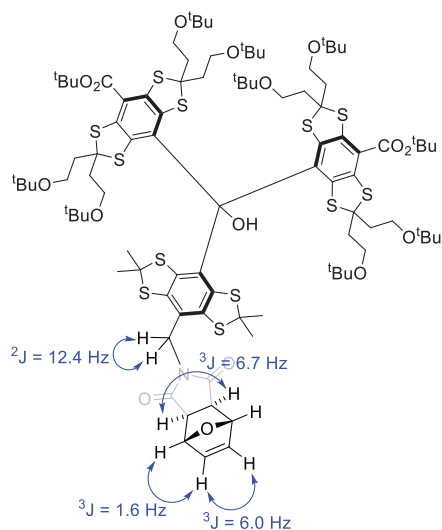
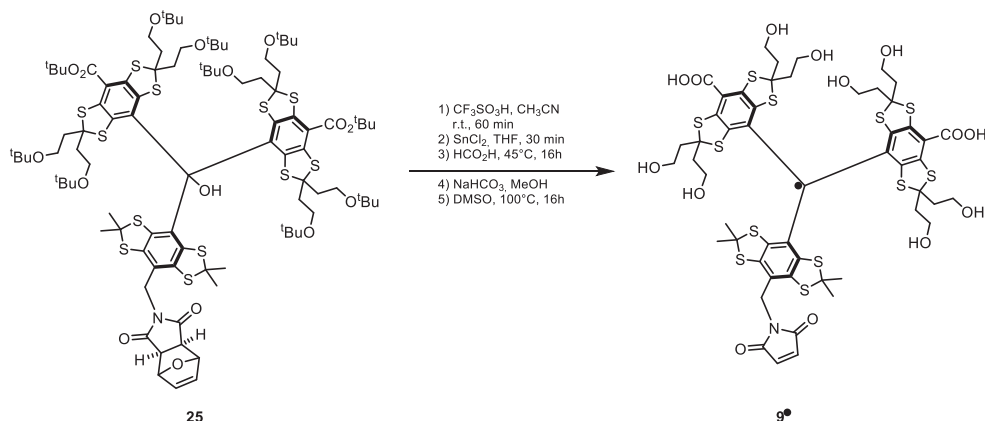


Figure S2: Scalar $J_{H,H}$ coupling in **25** as derived from 2D-NMR experiments.

2.13 Trityl radical **9[•]** (Ox-SLIM)



25 (25 mg, 12.8 μmol) was dissolved in 2 mL dry acetonitrile and triflic acid (77 mg, 45 μL , 512 μmol , 40 eq.) were added whereupon the reaction mixture turned dark green. After stirring for 1h at room temperature, tin(II)-chloride (4.8 mg, 25.6 μmol , 2.0 eq.; dissolved in 200 μL THF) was added and stirring was continued for 30 min. Afterwards, solvents were removed under reduced pressure and 4 mL formic acid were added to the dark green residue. The reaction mixture was stirred at 45°C for 16h and all volatile compounds were removed in high-vacuum subsequently. Then, sodium bicarbonate (172 mg, 2.05 mmol, 160 eq.) and 4 mL methanol were added and the suspension was stirred at room temperature for 16 hours. The dark green suspension was filtered and the filtrate was loaded onto a 20g C18 cartridge (Flash-Pure EcoFlex by Büchi, Germany). Salts were removed by elution with 150 mL methanol/water (80:20 + 0.1 % HCO_2H), while the title compound was eluted by ramping the gradient to pure methanol (+0.1 % formic acid). The dark brown residue was dissolved in 2 mL dry DMF and the resulting brownish green solution was degassed by applying three freeze-pump-thaw cycles and then heated to 100°C for 16 hours. After removal of all volatiles in high vacuum at 45°C, the title compound was isolated via preparative HPLC as a brown solid in a yield of 10 mg (60%).

HRMS (MALDI+, m/z , $[\text{M}]^+$): calcd for $\text{C}_{52}\text{H}_{58}\text{O}_{14}\text{S}_{12}$ 1304.0500, found 1304.0528.

HRMS (ESI-, m/z , $[\text{2M-H}]^-$): calcd for $\text{C}_{104}\text{H}_{115}\text{N}_2\text{O}_{28}\text{S}_{24}$ 2609.094, found 2609.093 (base peak).

Preparative HPLC was performed using a Knauer Eurospher II 100-5 C18 column (250 x 16 mm; pre-column 30 x 16 mm). For each run, 9 mg of the crude product were injected as a solution in 100 μ L methanol. The product was isolated as the fraction with a retention time of 12.69 min.

Gradient (A = CH₃CN + 0.1 % CF₃COOH; B = H₂O + 0.1 % CF₃COOH)

Start: 10% A + 90% B

05,0 min: 10% A + 90% B

20,0 min: 100% A

25,0 min: 100% A

25,5 min: 10% A + 90% B

30,0 min: 10% A + 90% B

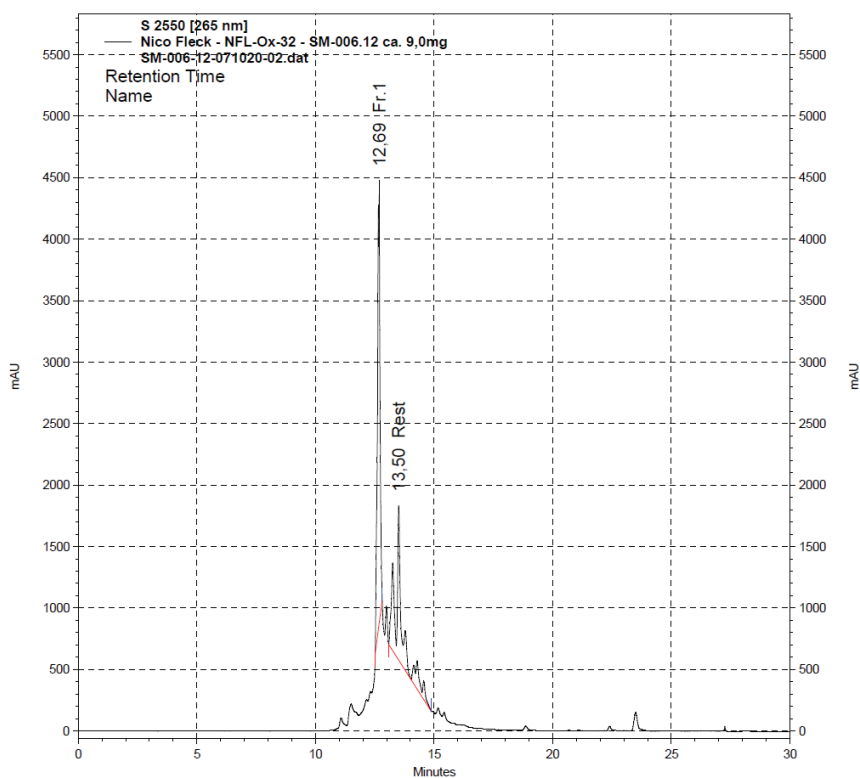


Figure S3: Chromatogram of preparative HPLC @265 nm.

3. Reaction Optimization

3.1 Mitsunobu Reaction

Performing the C-N bond formation from **23** to **25** under classical conditions using DEAD and Ph₃P, the product was obtained in a yield of only 31 %. The formation of several unknown byproduct was evident from TLC (Figure S4).

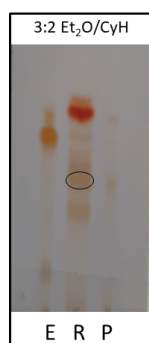
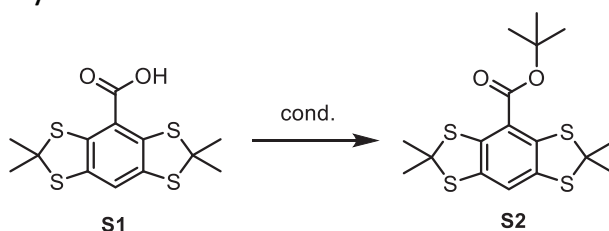


Figure S4: TLC-analysis of the crude reaction mixture of the Mitsunobu-reaction of **23** to **25** using $\text{Ph}_3\text{P}/\text{DEAD}$.
E = starting material, *R* = reaction mixture (product encircled), *P* = product.

3.2 Formation of *t*-Butyl Esters for **22**



Scheme S1: Model reaction for the formation of **22**.

After carboxylation of **21** with CO_2 , the formation of the *t*-butyl esters was required and the model reaction shown in scheme S1 was employed to seek for appropriate conditions. Compound **S1** was obtained by a protocol recently published by *Wessig et al.*^[7] The esterifications were run at a 100 mg scale and 0.1 M with the conditions indicated in table S1 and the product was isolated via column chromatography on silica eluting with *n*-hexane/ethyl acetate 2:1.

Table S1: Condition screening for the synthesis of *tert.*-butyl esters according to Scheme S1.

entry	conditions	yield S2 (isolated)
1	<i>Steglich</i> : 1 eq. DCC, 1 eq. DMAP, 2 eq. <i>t</i> -BuOH, CH_2Cl_2 , r.t. 16h	trace
2	1 eq. DMAP, 3 eq. Boc_2O , r.t., 16h	44 %
3	1.25 eq. <i>O-tert.</i> -butyl- <i>N,N'</i> -diisopropylisourea, toluene, 60°C, 2h.	95 %

Analytical data of **S2**:

$^1\text{H-NMR}$ (400 MHz, CDCl_3 , 298 K, δ in ppm): 7.11 (s, 1H), 1.84 (s, 12H), 1.67 (s, 9H).

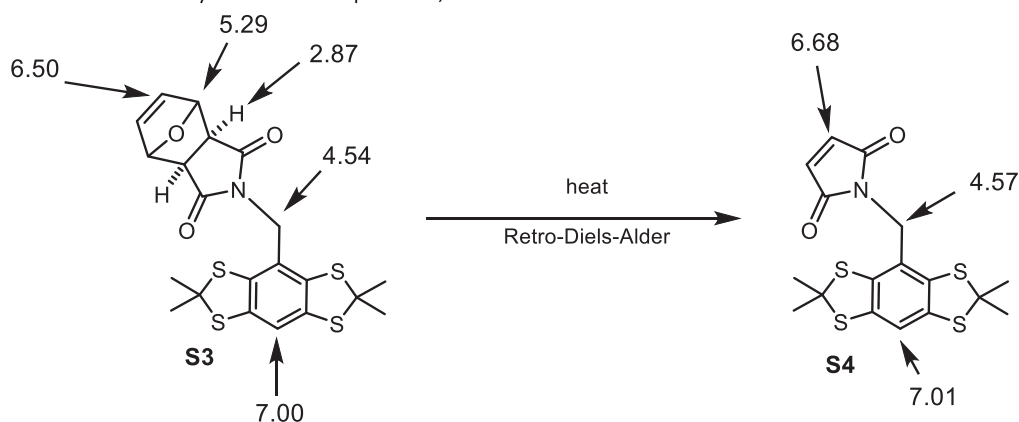
$^{13}\text{C-NMR}$ (100 MHz, CD_2Cl_2 , 298 K, δ in ppm): 164.9, 139.3, 136.6, 122.2, 119.1, 84.4, 63.1, 31.5, 28.5.

MS (EI, *m/z*): 386.1 [24%, M^+], 330.0 [51%, $\text{M}-\text{C}_4\text{H}_8$]⁺, 315.0 [100%, $\text{M}-\text{CH}_3-\text{C}_4\text{H}_8$]⁺.

3.3 Thermal stability of *exo*-Tetrahydroisoindolindione

While the thermal stability of the *endo*-tetrahydroisoindolindione moiety used to conceal the maleimide in our previous study on SLIM^[8] is low, so that an unblocking temperature of 60°C is sufficient, this is not the case for the thermodynamically more favored *exo*-product. Seeking for unblocking conditions, compound **S3** was synthesized in analogy to its *endo*-derivative^[8] and subjected to *Retro-Diels-Alder* reaction

through simple heating in DMF. As shown in Scheme S2 and Figure S5 the chemical shift of the vinylic protons differs remarkably in both compounds, so that the reaction can be tracked via $^1\text{H-NMR}$.



Scheme S2: Retro-Diels-Alder fragmentation of *exo*-tetrahydroisoindolindione **S3** to maleimide **S3**. Chemical shifts in $^1\text{H-NMR}$ (in ppm, CDCl_3) are indicated to the respective proton-bearing positions with arrows.

The analytical data of **S4** is provided in the Supporting Information of the study on SLIM.^[8] The analytical data for **S3** is:

$^1\text{H-NMR}$ (500 MHz, CDCl_3 , 298 K, δ in ppm): 7.00 (s, 1H), 6.50 (m, 2H), 5.29 (s, 2H), 4.54 (s, 2H), 2.87 (s, 2H), 1.87 (s, 12H).

$^{13}\text{C-NMR}$ (125 MHz, CD_2Cl_2 , 298 K, δ in ppm): δ 175.2, 136.73, 136.70, 136.6, 124.3, 116.5, 81.0, 65.6, 47.5, 43.3, 31.3.

HRMS (ESI+, m/z , $[\text{M-furane}]^+$): calcd for $\text{C}_{17}\text{H}_{17}\text{NO}_2\text{S}_4$ 395.0137, found 395.0136.

Note, that compound **S3** undergoes Retro-Diels-Alder fragmentation during MS.

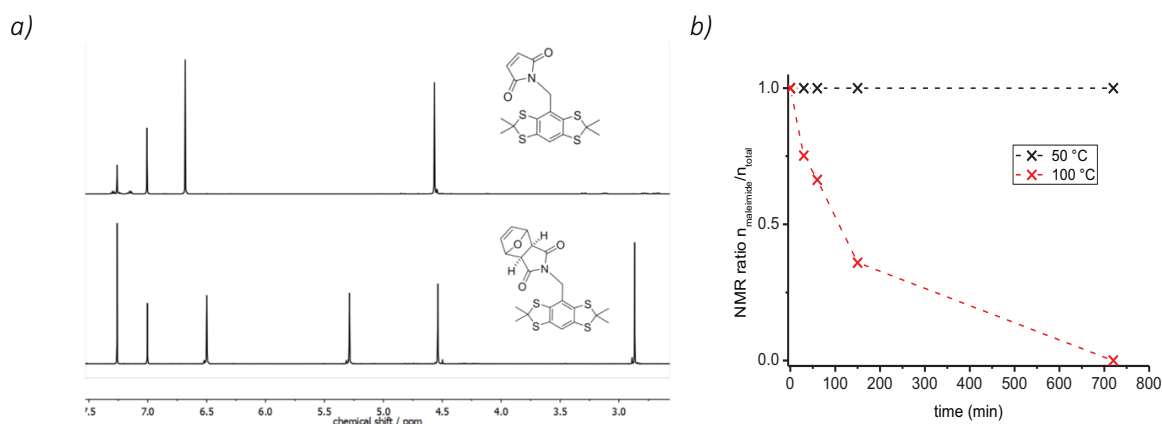
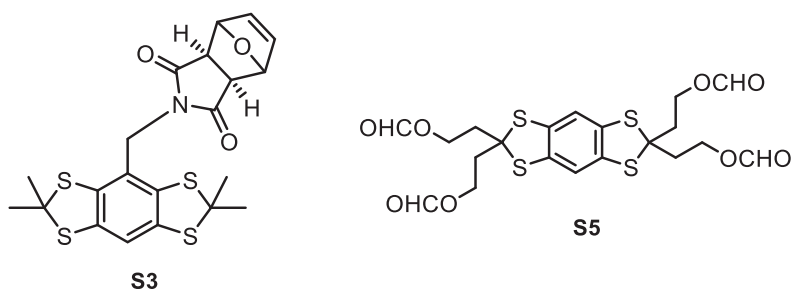


Figure S5: a) $^1\text{H-NMR}$ spectra of **S3** and **S4**. b) Kinetics of the Retro-Diels-Alder cleavage of **S3**.

Through integration of the $^1\text{H-NMR}$ spectra, the molar fraction of the maleimide was determined for several timepoints as shown in figure S5b. Clearly, no conversion is observed at 50°C , while slow unblocking occurs at 100°C yielding the free maleimide quantitatively after 12 hours.

3.4 Tests for conversion of **25** to **9**



Scheme S3: Compounds S3 and S5

Seeking for appropriate conditions to hydrolyze the formate ester intermediate occurring in the synthesis of **9** from **25**, compounds **S3** and **S5** were synthesized (*vide supra* for **S3**) and subjected to various hydrolyzing conditions shown in table S2. The extent of hydrolysis was determined from ¹H-NMR spectra of the crude reaction mixture. As shown in Table S2, it turned out, that conditions typically applied for ester hydrolysis (LiOH/H₂O/THF, entry 1) led to a hydrolysis of the concealed maleimide. Even a milder surrogate, Ba(OH)₂/MeOH (entry 2) led to significant hydrolysis of the latter one. **S5** was obtained by heating **18** in neat formic acid at 45 °C for 2 h.

Table S2: Screening for ester cleavage.

No.	conditions / substrate conversion	Hydrolysis of S5	Hydrolysis of S3
1	10 eq. LiOH, 2h r.t., THF/MeOH/H ₂ O (5:5:1)	100 %	100 %
2	20 eq. Ba(OH) ₂ , MeOH/THF (5:3), 2h, r.t.	100 %	62 %
3	5 eq. KOSiMe ₃ , THF, r.t., 2 h	100 %	20 %
4	40 eq. K ₂ CO ₃ , MeOH, r.t., 16h	100 %	0 %
5	80 eq. NaHCO ₃ , MeOH, r.t., 16h	100 %	0 %

Analytical data for **S5**:

¹H-NMR (500 MHz, CDCl₃, 298 K, δ in ppm): 8.04 (s, 4H), 6.98 (s, 2H), 4.44 (t, 8H, ³J_{H,H} = 7.4 Hz), 2.46 (t, 8H, ³J_{H,H} = 7.4 Hz).

¹³C-NMR (125 MHz, CD₂Cl₂, 298 K, δ in ppm): δ 160.7, 135.1, 116.6, 69.8, 60.8, 39.6.

HRMS (MALDI+, *m/z*): calcd for [M]⁺ C₂₀H₂₂O₈S₄ 518.0192, found 518.0173.

4. Analytical data

4.1 NMR-Spectroscopy

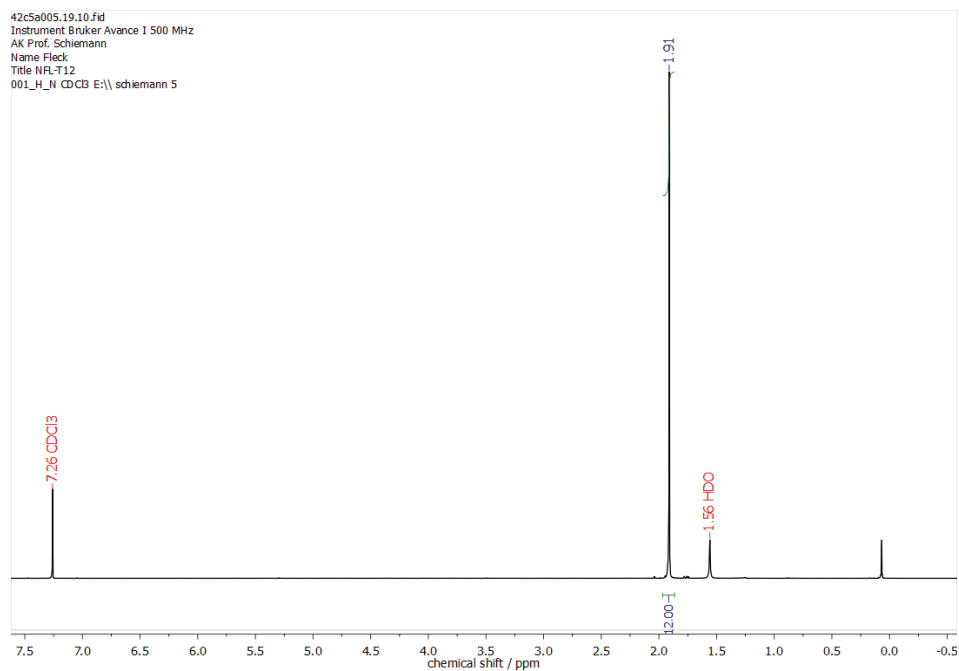


Figure S6: ^1H -NMR spectrum (CDCl_3 , 500 MHz) of Thioketal **12**

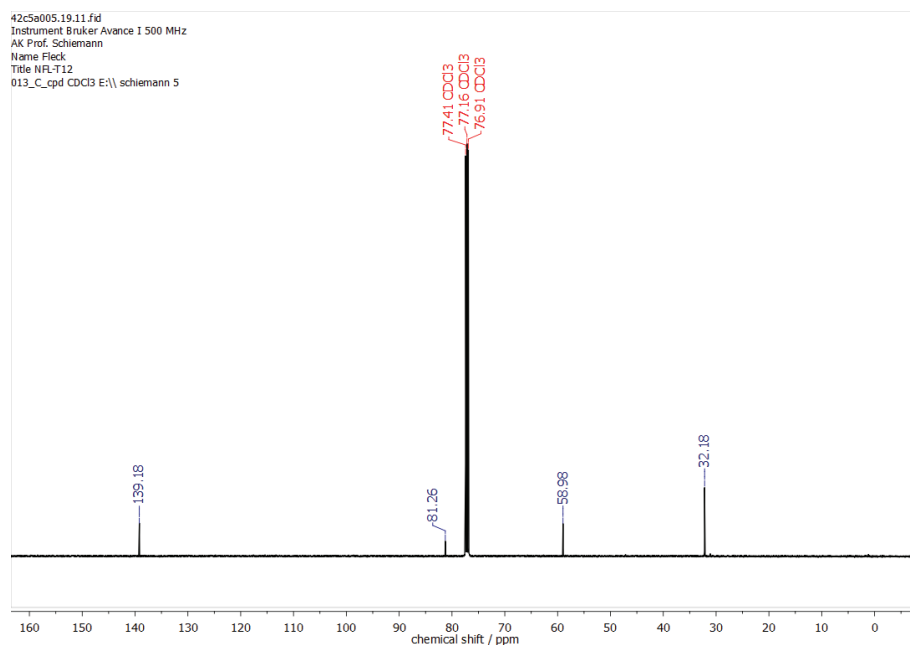


Figure S7: ^{13}C -NMR spectrum (CDCl_3 , 125 MHz) of Thioketal **12**

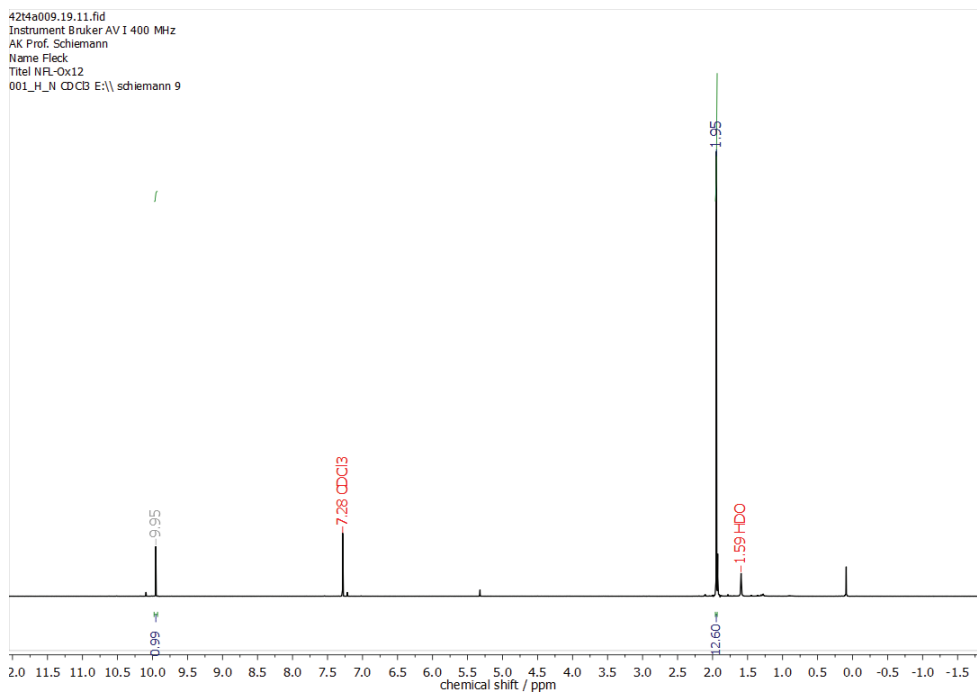


Figure S8: ¹H-NMR spectrum (CDCl₃, 400 MHz) of Aldehyde 13

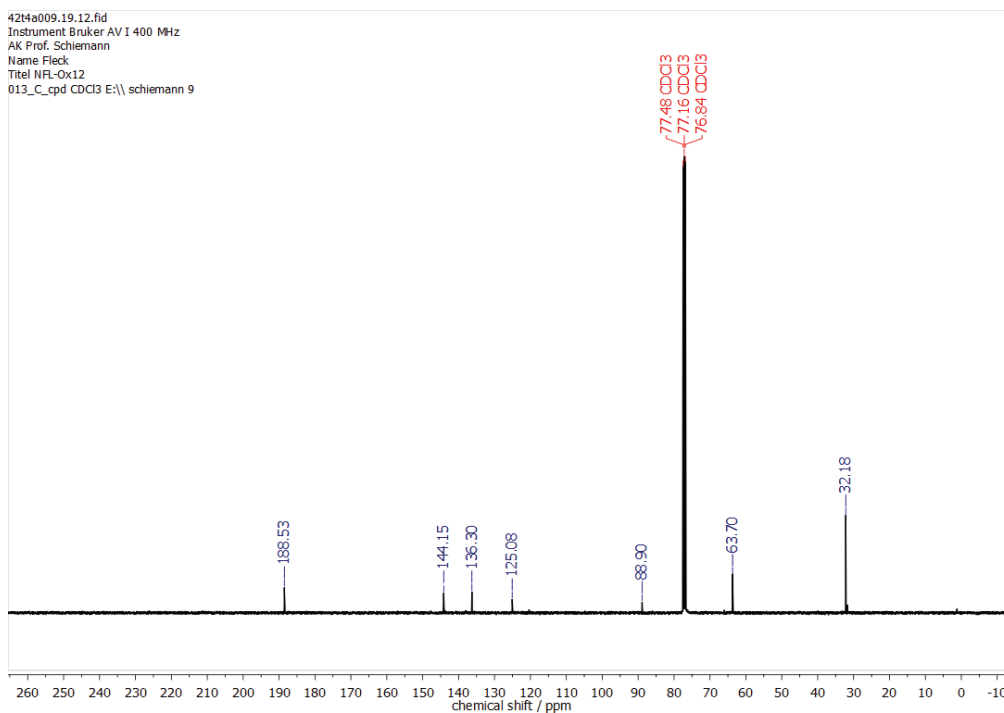


Figure S9: ¹³C-NMR spectrum (CDCl₃, 100 MHz) of Aldehyde 13

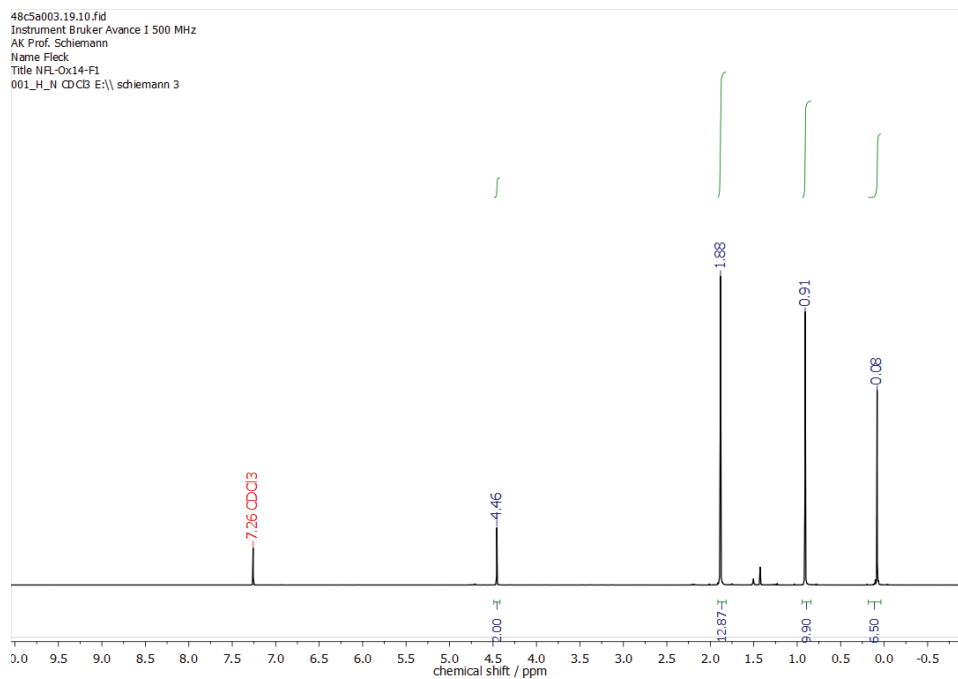


Figure S10: ¹H-NMR spectrum (CDCl₃, 500 MHz) of Thioketal 10

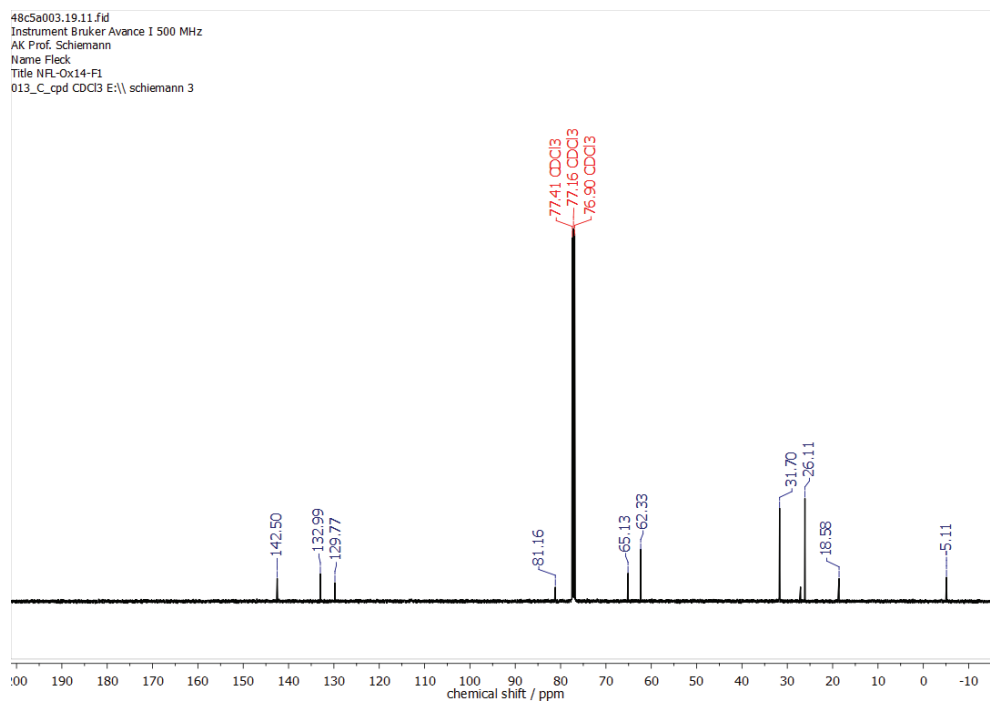


Figure S11: ¹³C-NMR spectrum (CDCl₃, 125 MHz) of Thioketal 10

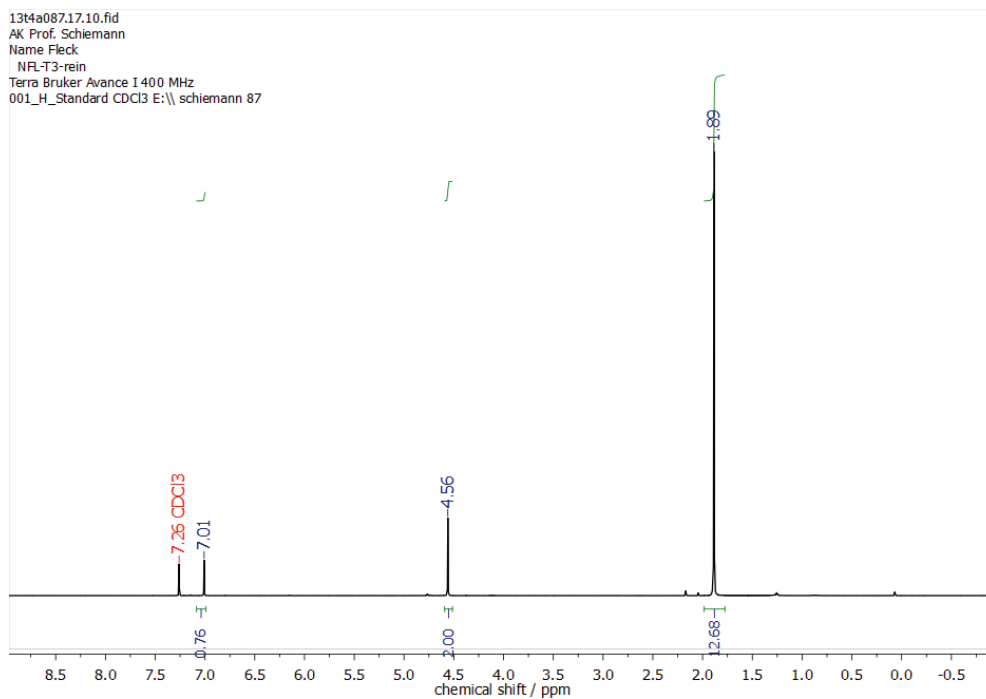


Figure S12: $^1\text{H-NMR}$ spectrum (CDCl_3 , 400 MHz) of Alcohol 15.

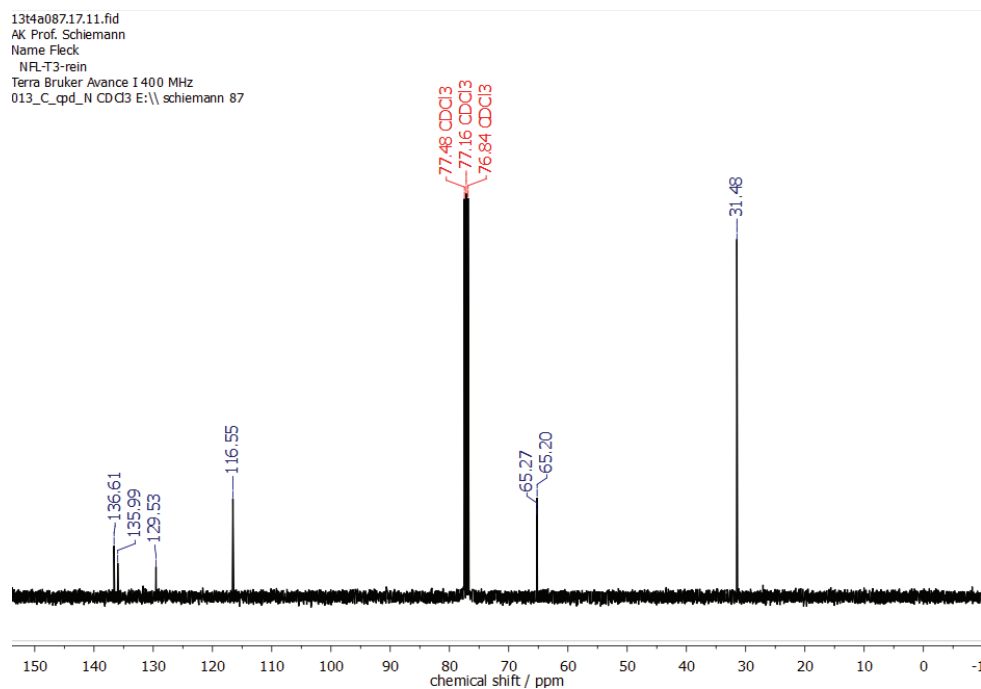


Figure S13: $^{13}\text{C-NMR}$ spectrum (CDCl_3 , 100 MHz) of Alcohol 15.

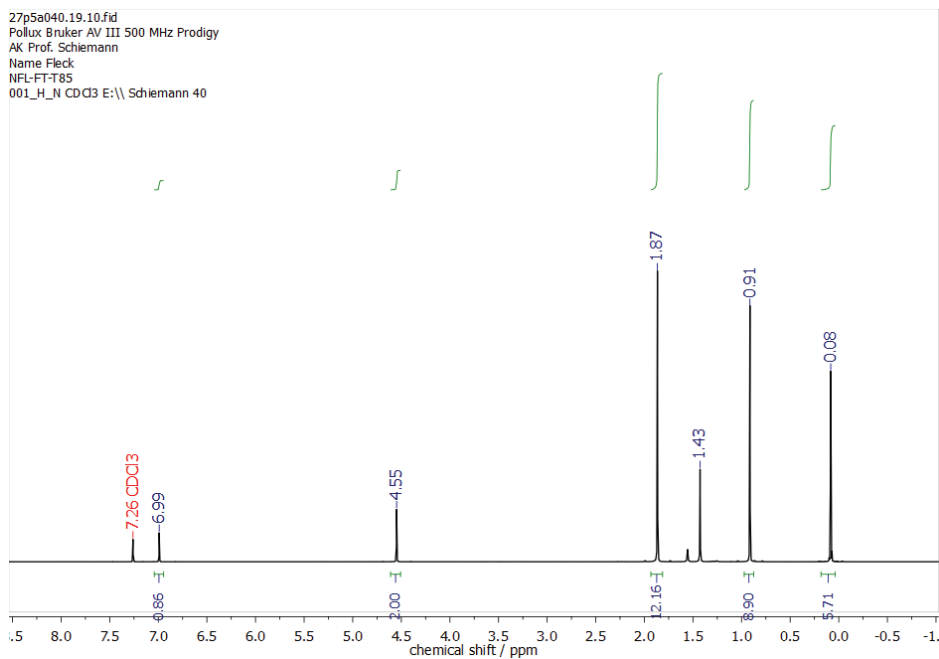


Figure S14: ^1H -NMR spectrum (CDCl_3 , 500 MHz) of Thioketal **16**. The peak at 1.43 ppm is attributed to cyclohexane residues in the sample, present even after thorough drying at 10^{-3} mbar overnight.

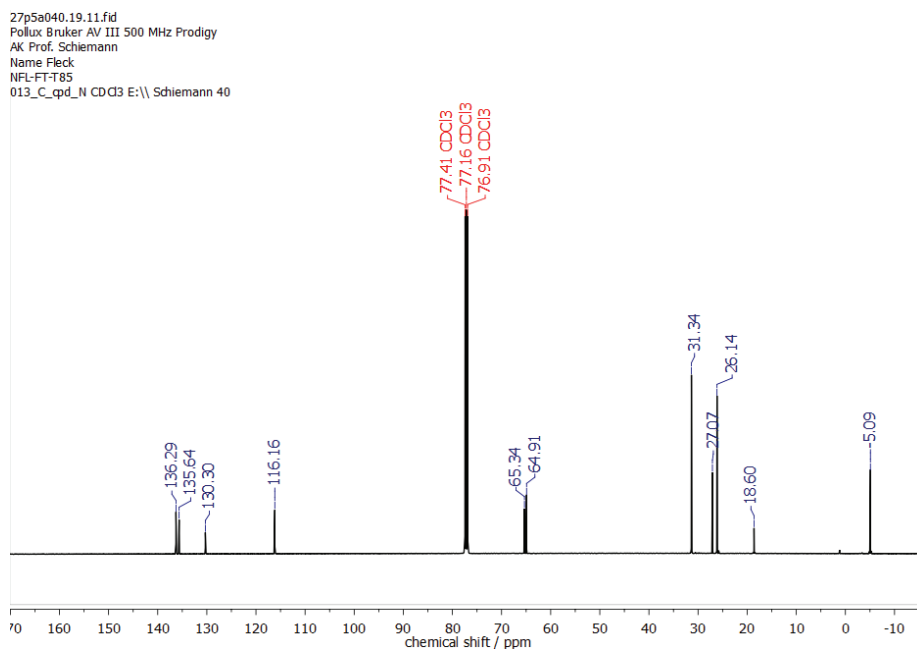


Figure S15: ^{13}C -NMR spectrum (CDCl_3 , 125 MHz) of Thioketal **16**. The peak at 27.07 ppm belongs to cyclohexane (*vide supra*).

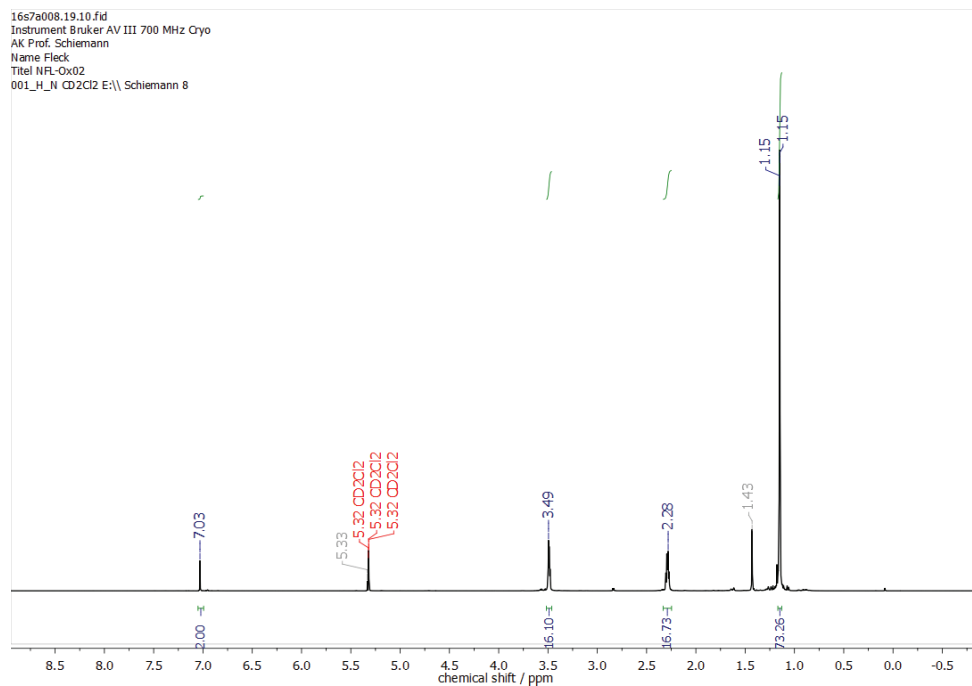


Figure S16: ^1H -NMR spectrum (CD_2Cl_2 , 700 MHz) of Diarylmethanol **20**. The peak at 5.33 ppm belongs to non-deuterated dichloromethane and the one at 1.43 to a small impurity of cyclohexane.

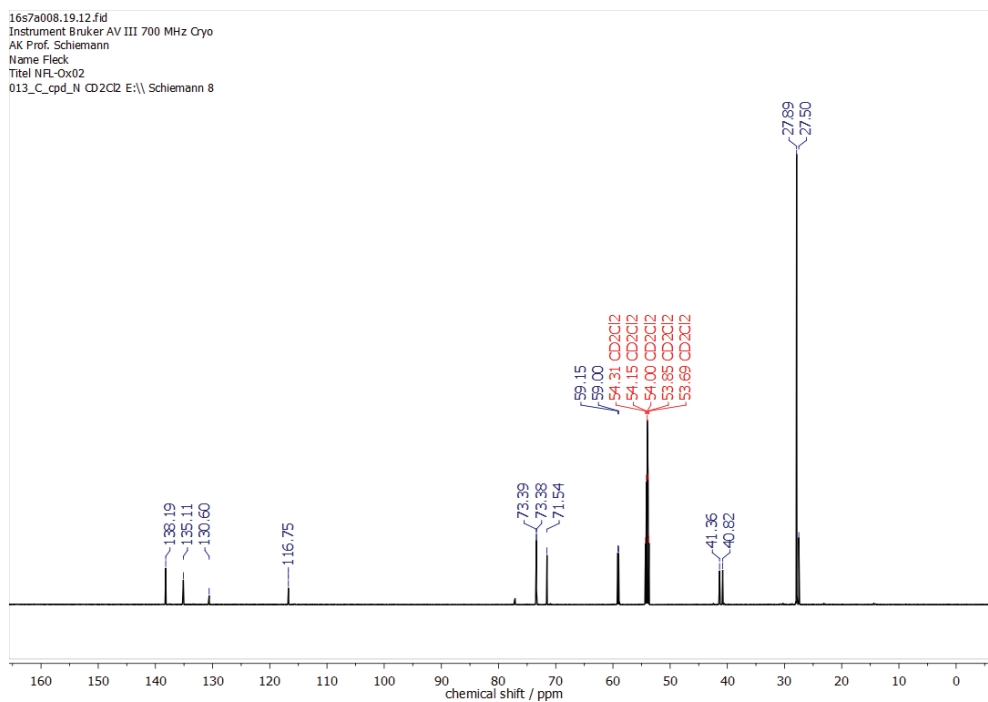


Figure S17: ^{13}C -NMR spectrum (CD_2Cl_2 , 175 MHz) of Diarylmethanol **20**. The peak at 27.50 ppm belongs to a small impurity of cyclohexane.

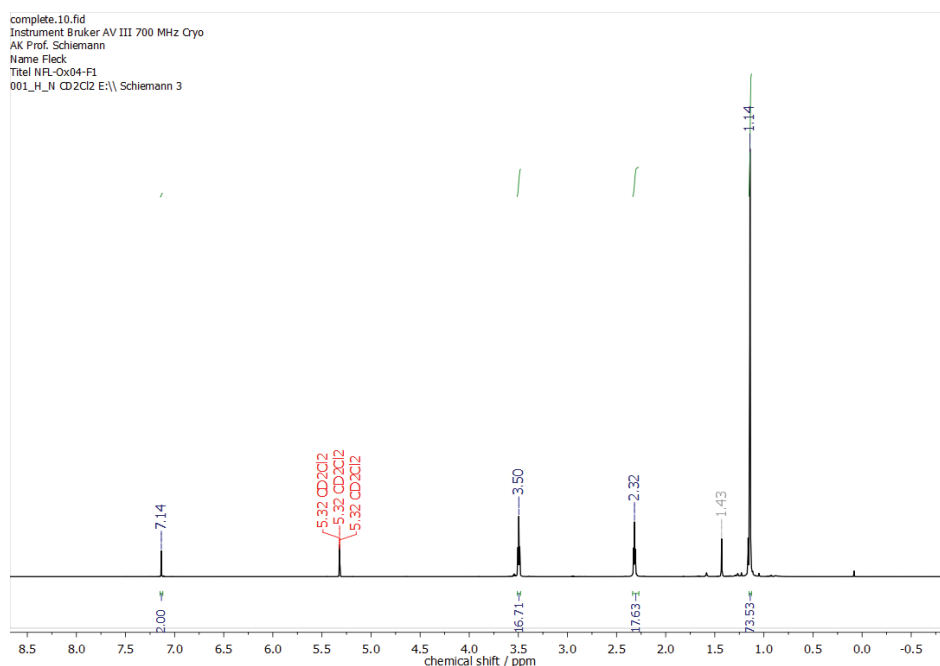


Figure S18: ^1H -NMR spectrum (CD_2Cl_2 , 700 MHz) of Diarylketone **17**. The peak at 1.43 ppm belongs to a small impurity of cyclohexane.

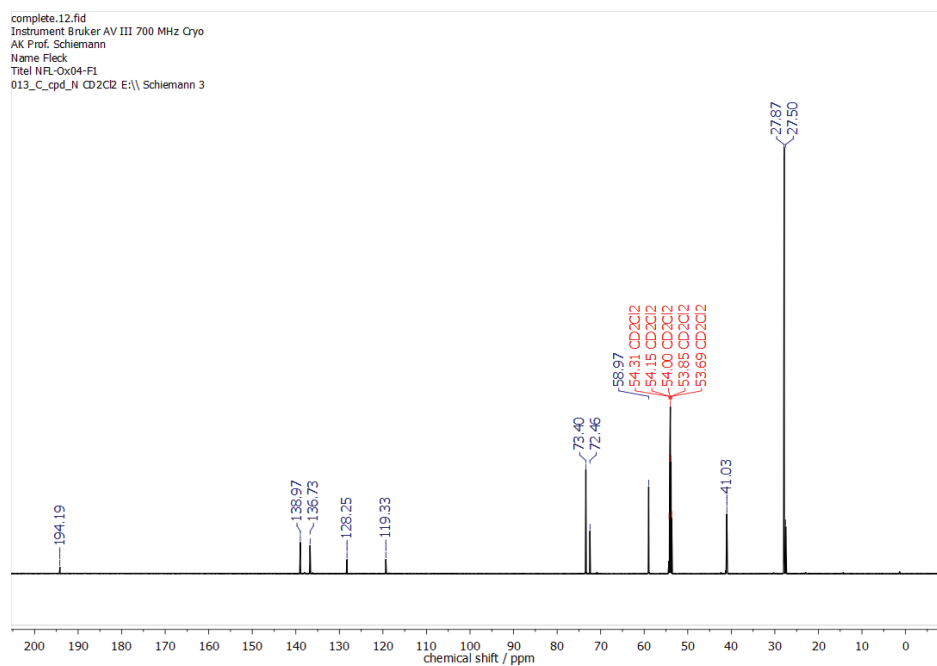
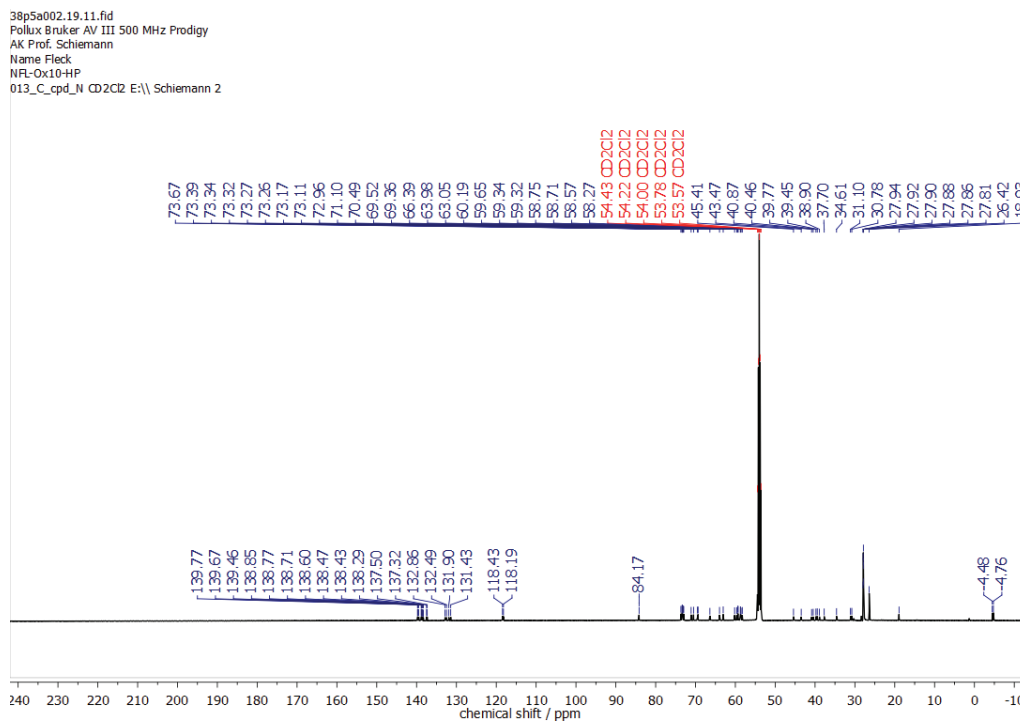
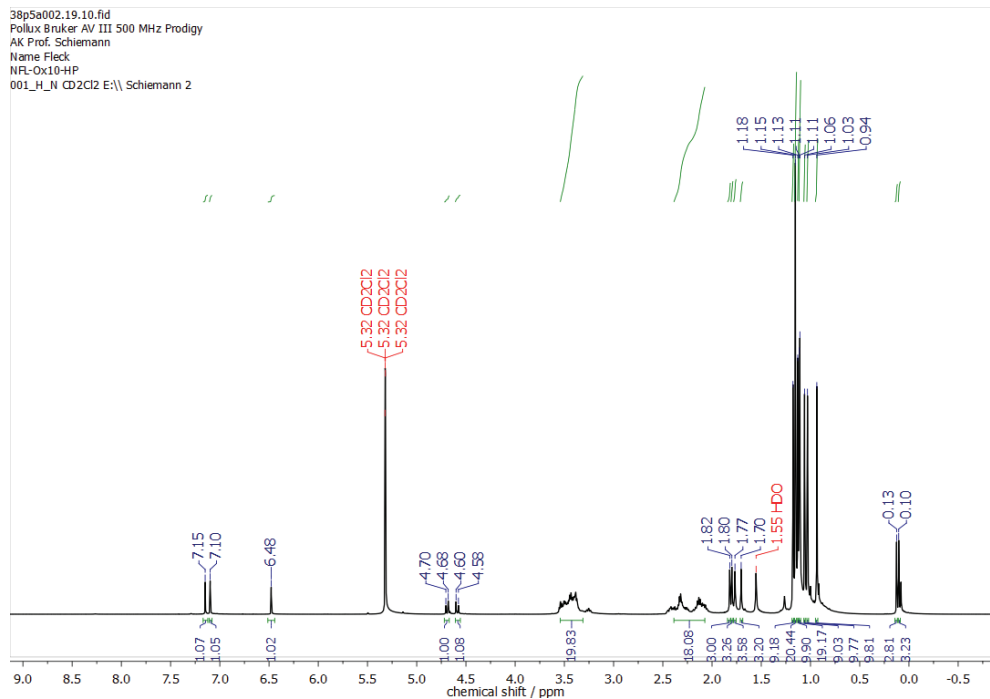


Figure S19: ^{13}C -NMR spectrum (CD_2Cl_2 , 175 MHz) of Diarylketone **17**. The small peak at 27.5 ppm is attributed to an impurity by cyclohexane.



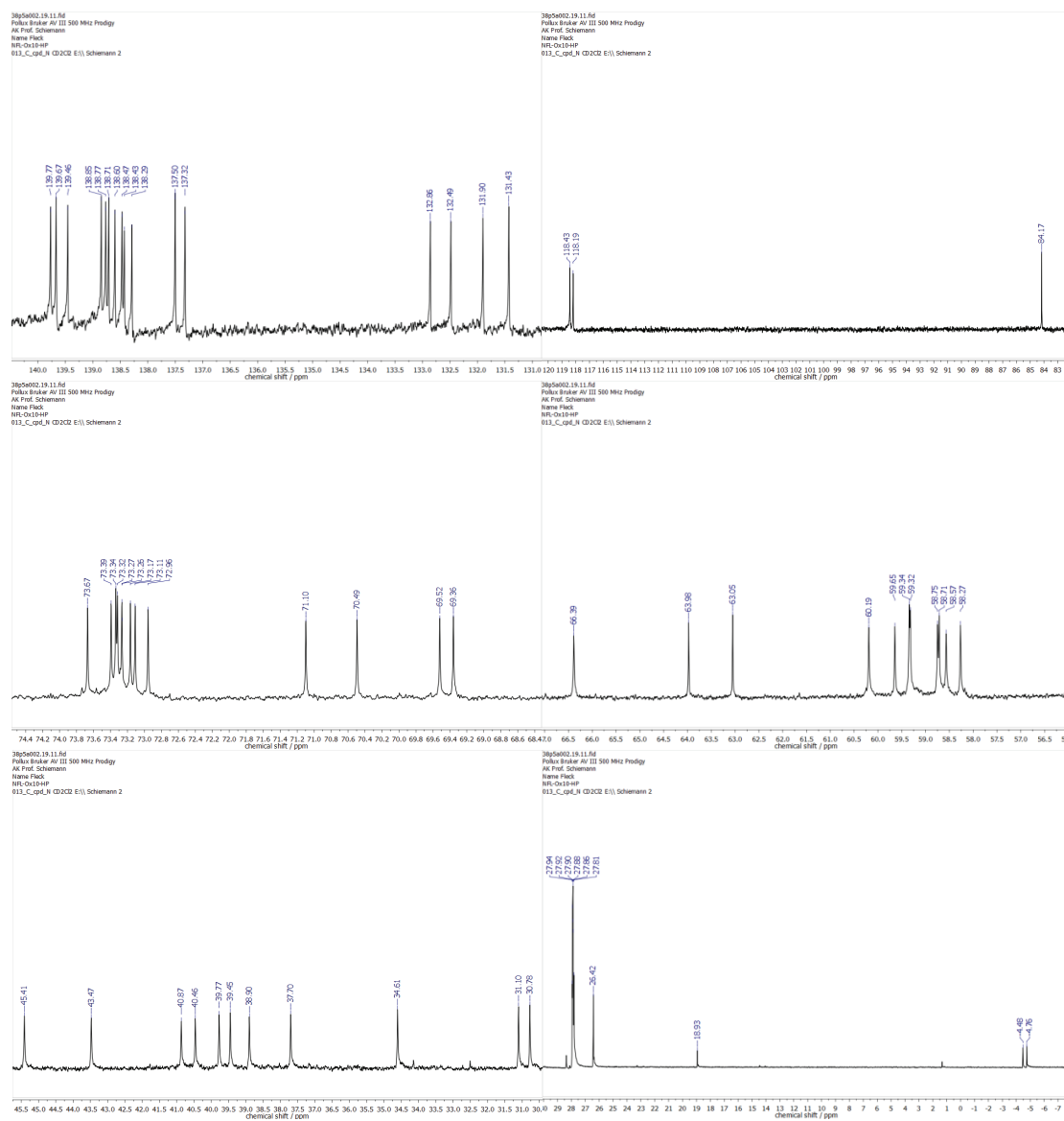


Figure S22: ^{13}C -NMR spectrum (CD $_2$ Cl $_2$, 125 MHz) of Trityl alcohol **21**, close-up views.

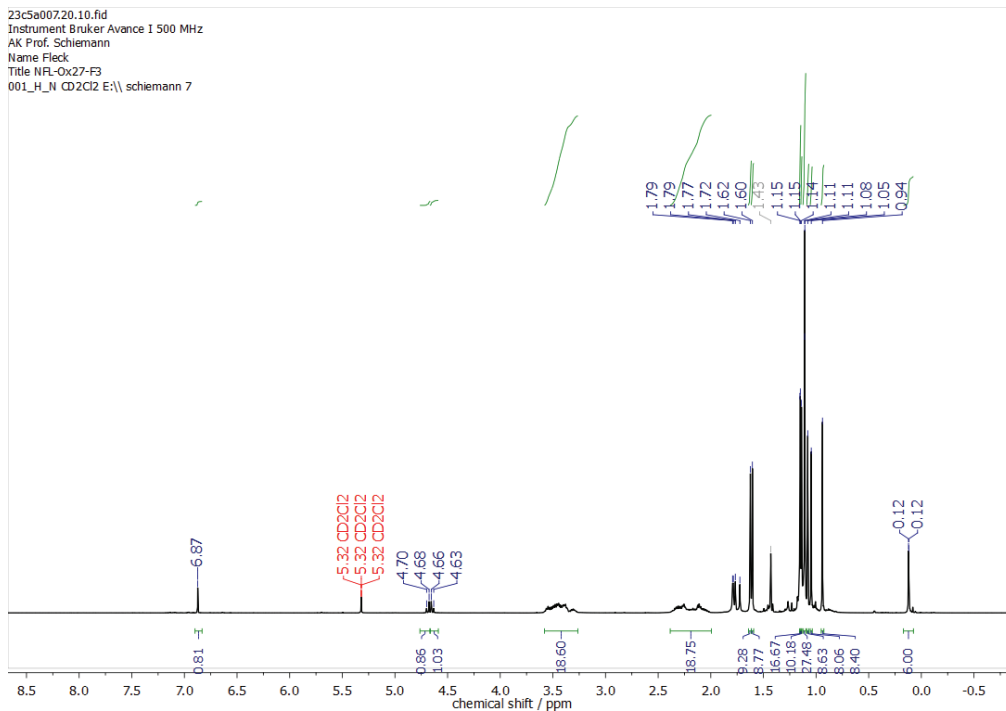


Figure S23: $^1\text{H-NMR}$ spectrum (CD_2Cl_2 , 500 MHz) of Trityl alcohol **22**. The peak at 1.43 ppm belongs to a small impurity of cyclohexane.

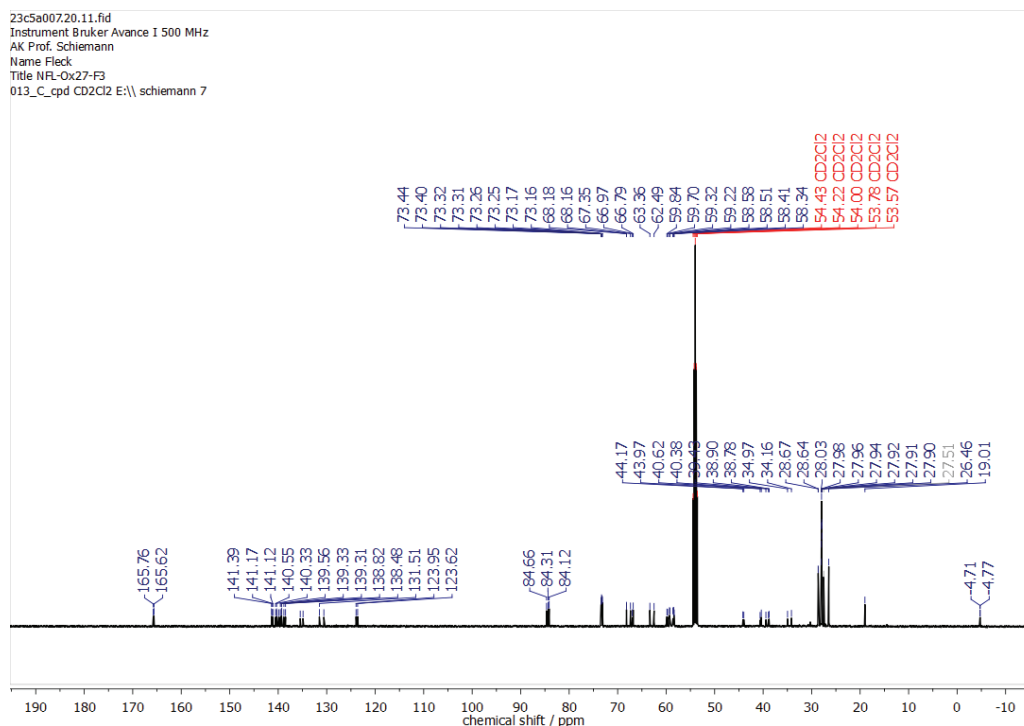


Figure S24: $^{13}\text{C-NMR}$ spectrum (CD_2Cl_2 , 125 MHz) of Trityl alcohol **22**, full view.

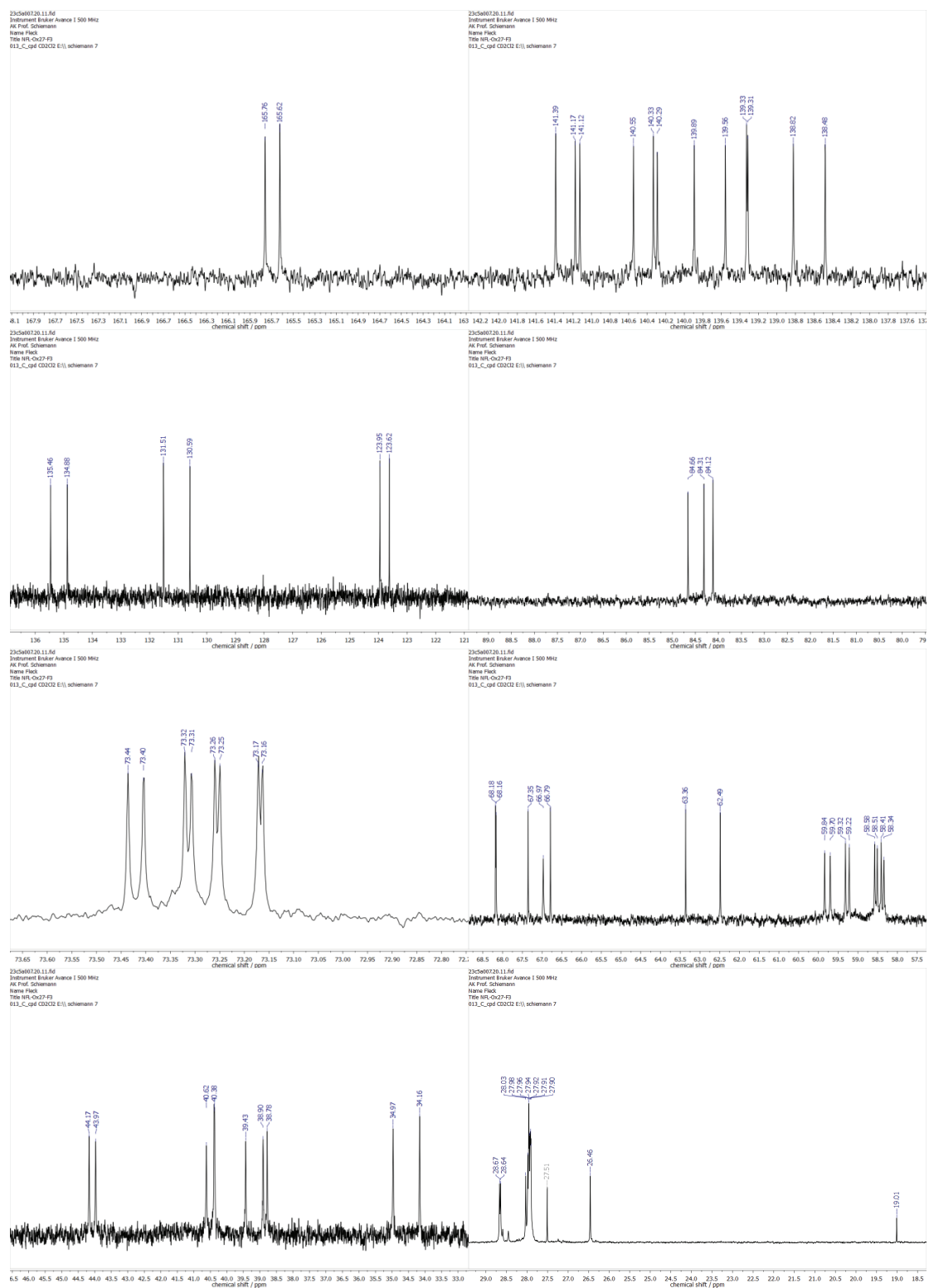
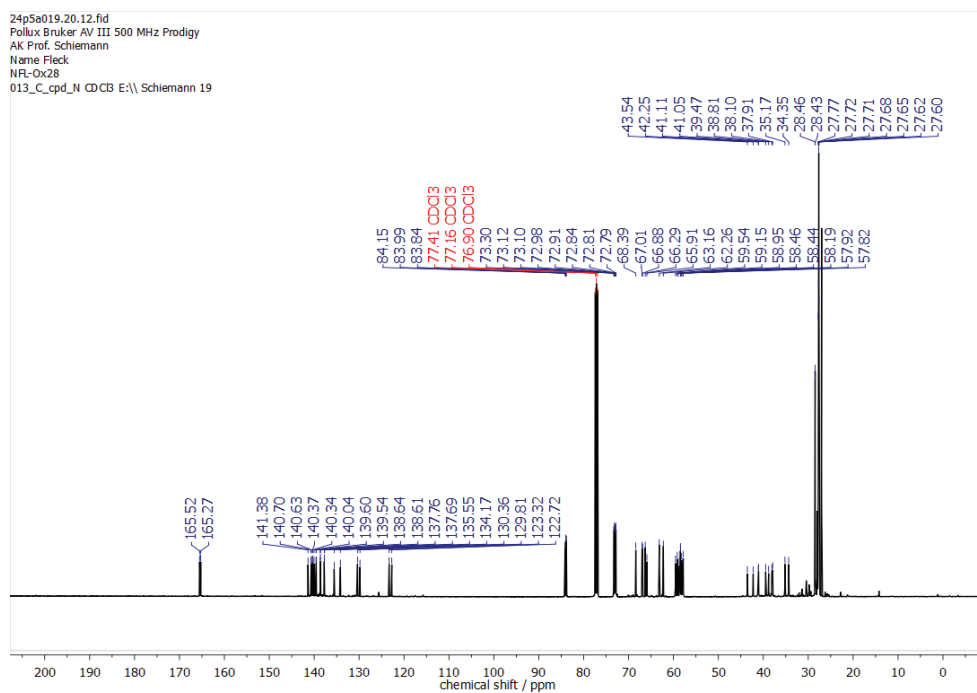
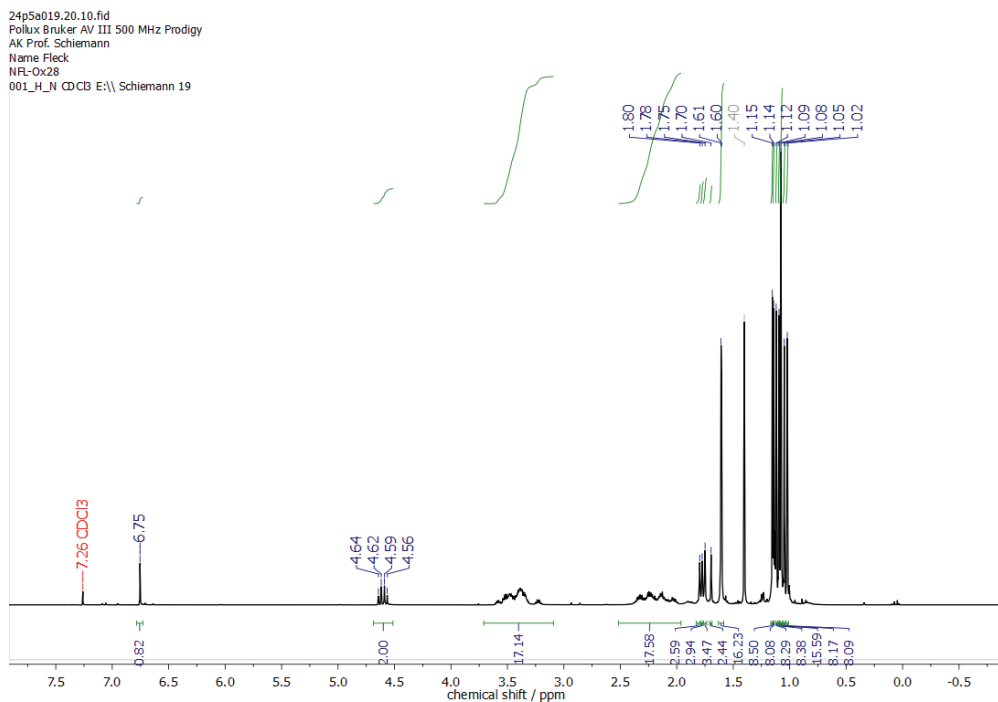


Figure S25: ^{13}C -NMR spectrum (CD_2Cl_2 , 125 MHz) of Trityl alcohol **22**, close-up views.



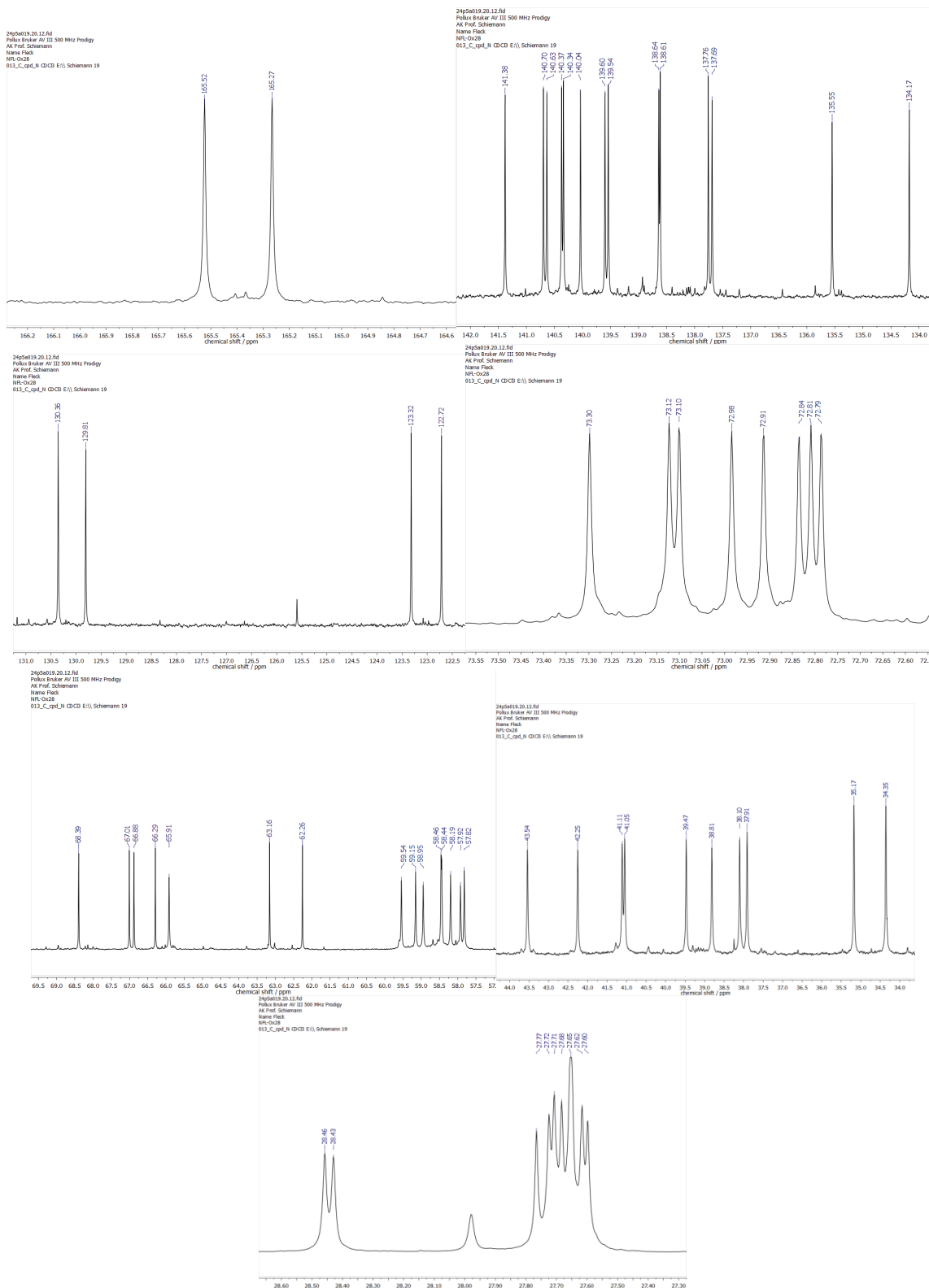


Figure S28: ^{13}C -NMR spectrum (CD $_2$ Cl $_2$, 125 MHz) of Trityl alcohol **23**, close-up views.

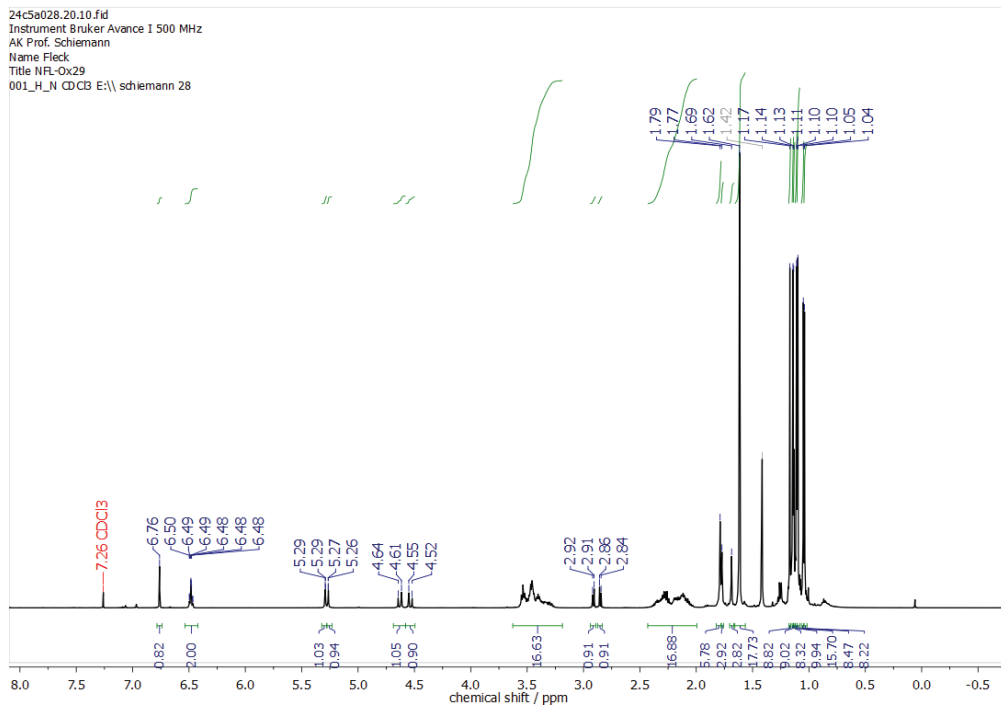


Figure S29: ¹H-NMR spectrum (CDCl₃, 500 MHz) of Trityl alcohol 25.

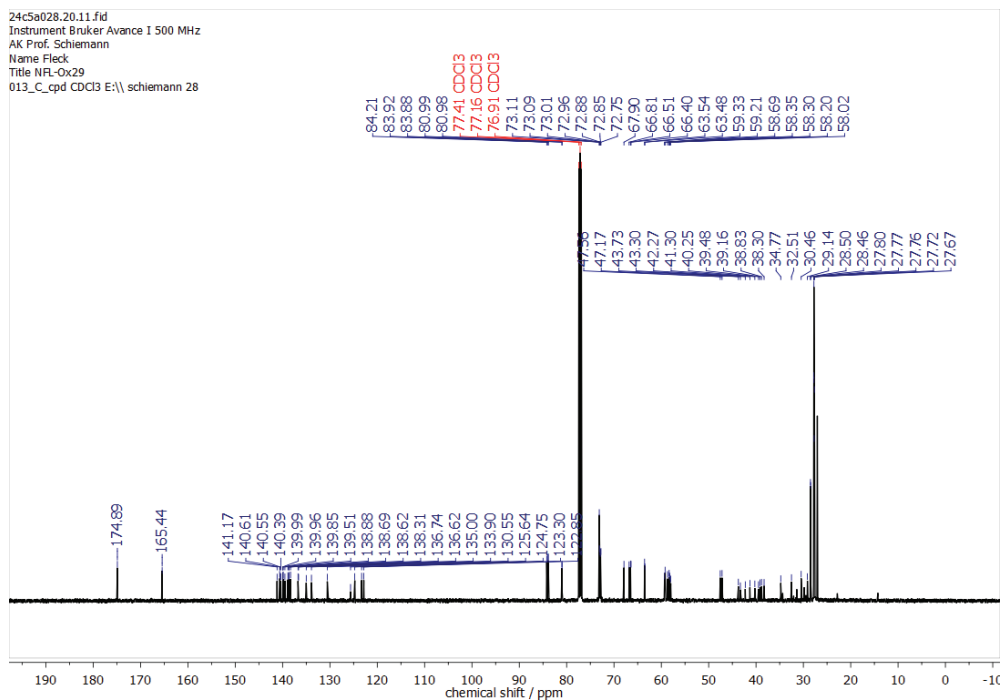


Figure S30: ¹³C-NMR spectrum (CDCl₃, 125 MHz) of Trityl alcohol 25, full view.

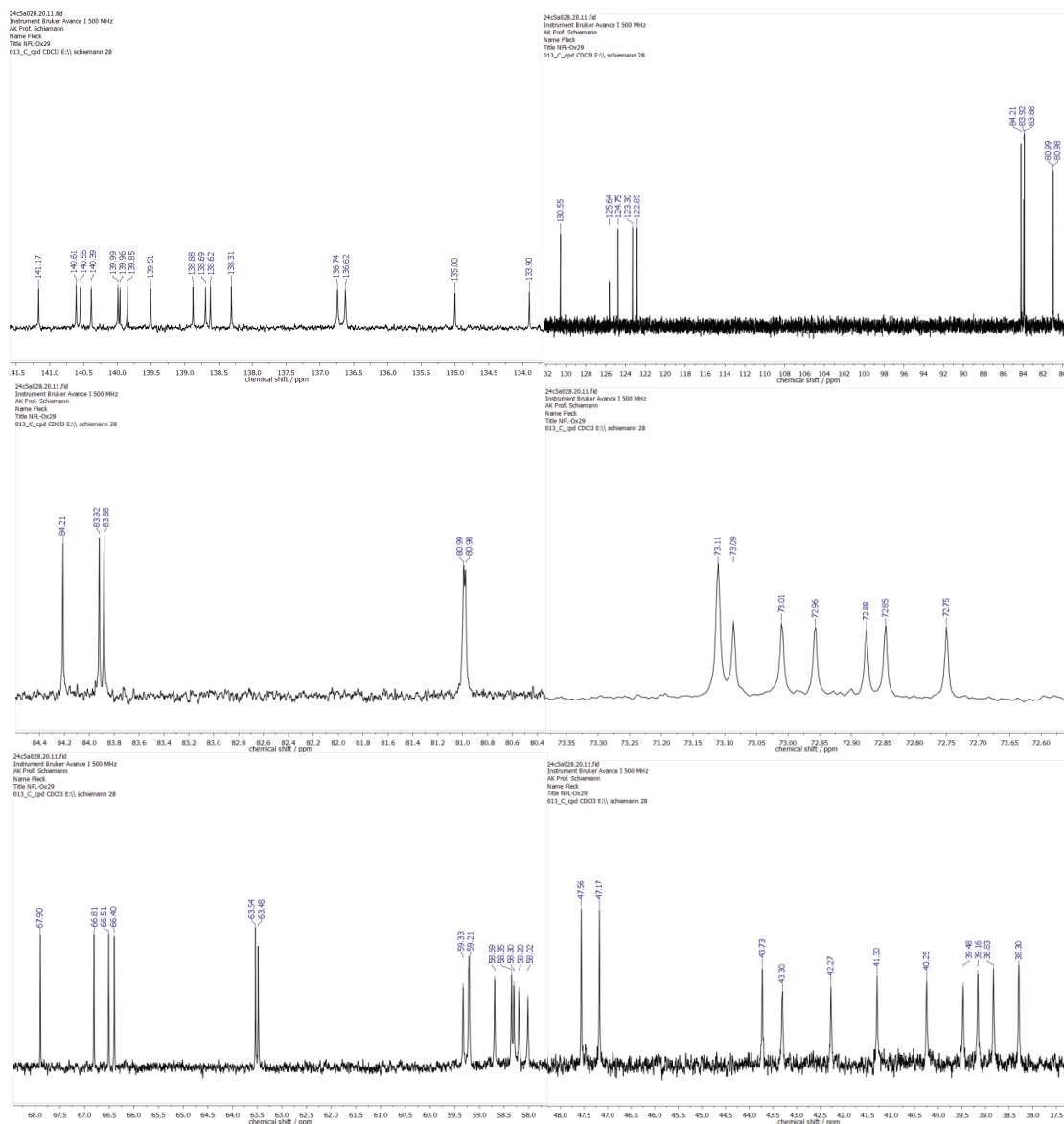


Figure S31: ^{13}C -NMR spectrum (CDCl₃, 125 MHz) of Trityl alcohol **25**, close-up views.

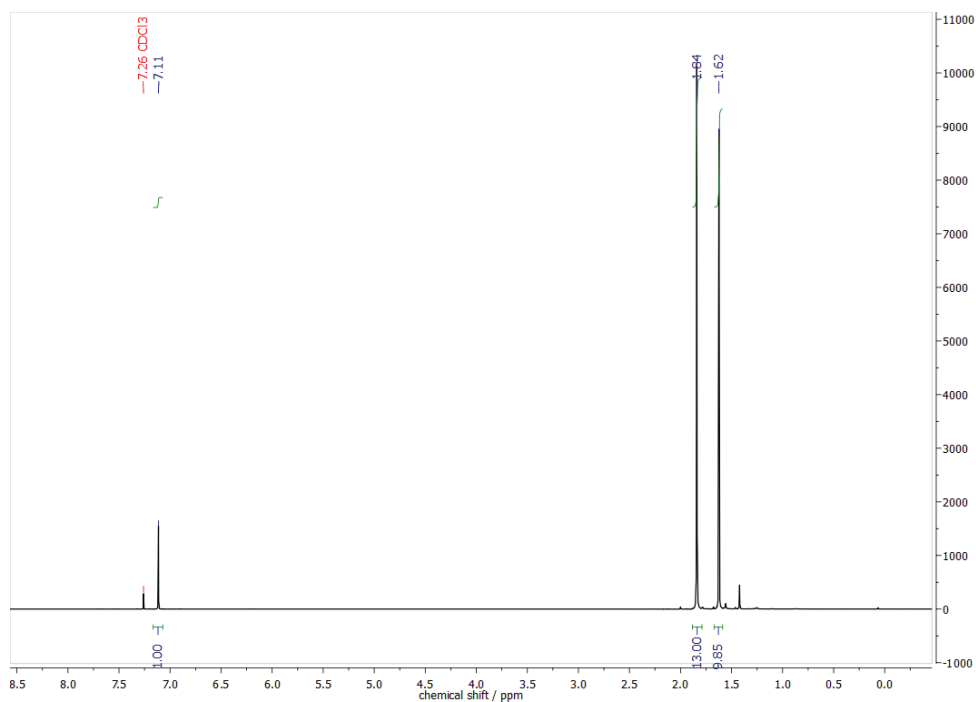


Figure S32: $^1\text{H-NMR}$ spectrum (CDCl_3 , 400 MHz) of Compound S2.

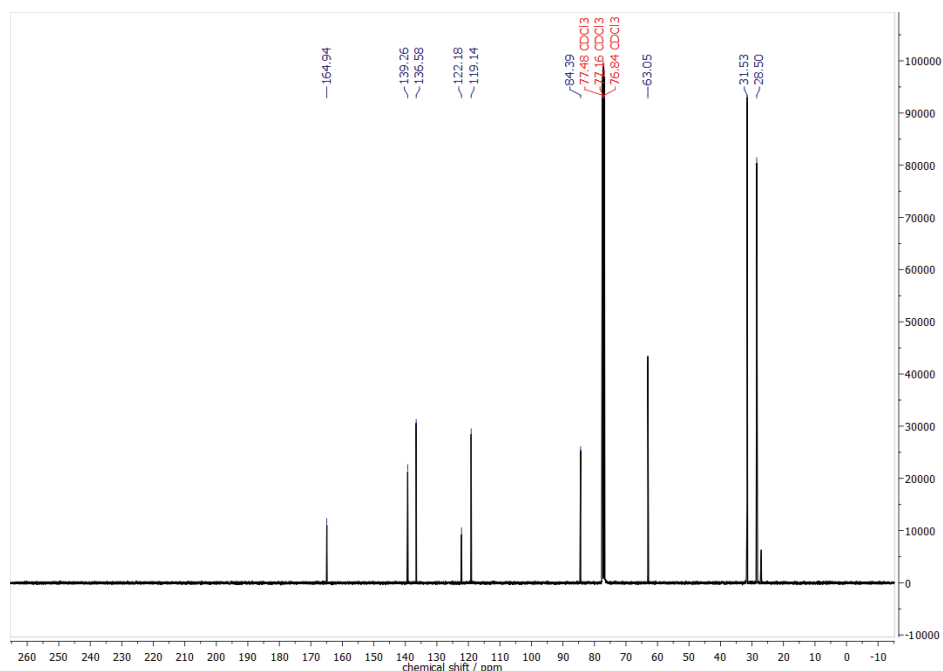


Figure S33: $^{13}\text{C-NMR}$ spectrum (CDCl_3 , 100 MHz) of Compound S2.

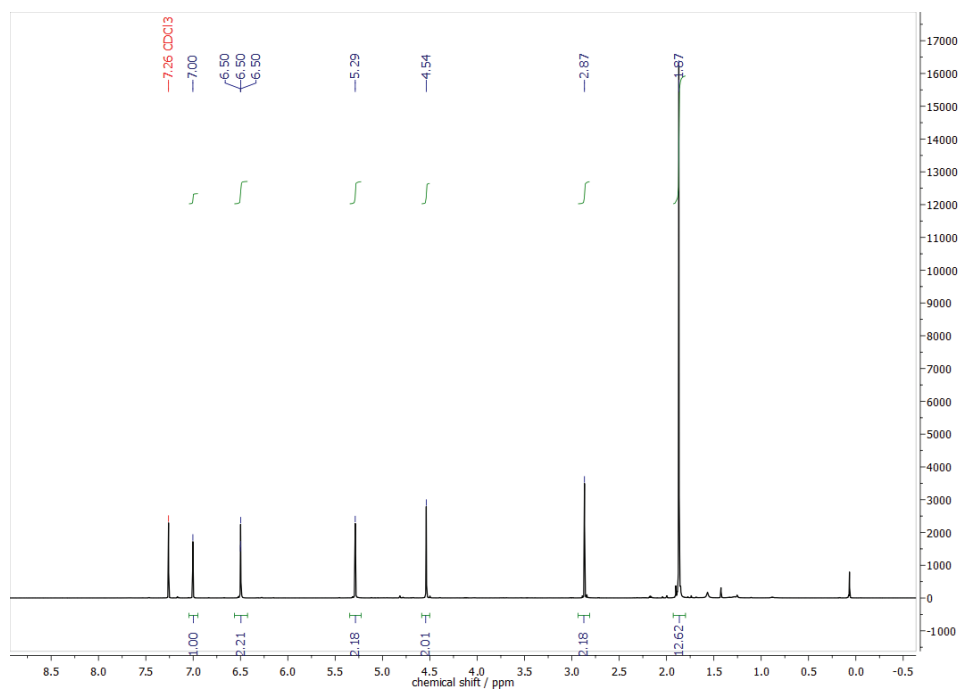


Figure S34: $^1\text{H-NMR}$ spectrum (CDCl_3 , 500 MHz) of Compound S3.

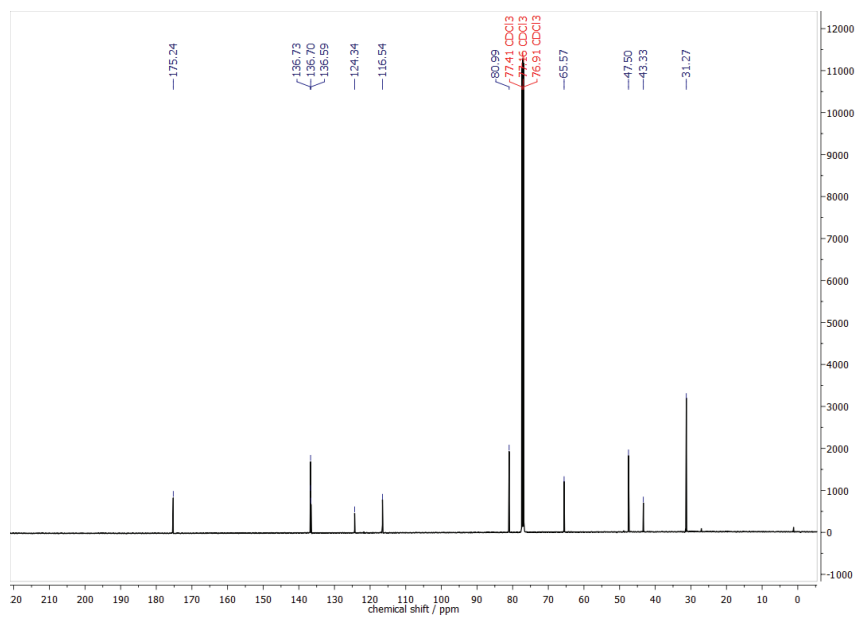


Figure S35: $^{13}\text{C-NMR}$ spectrum (CDCl_3 , 125 MHz) of Compound S3.

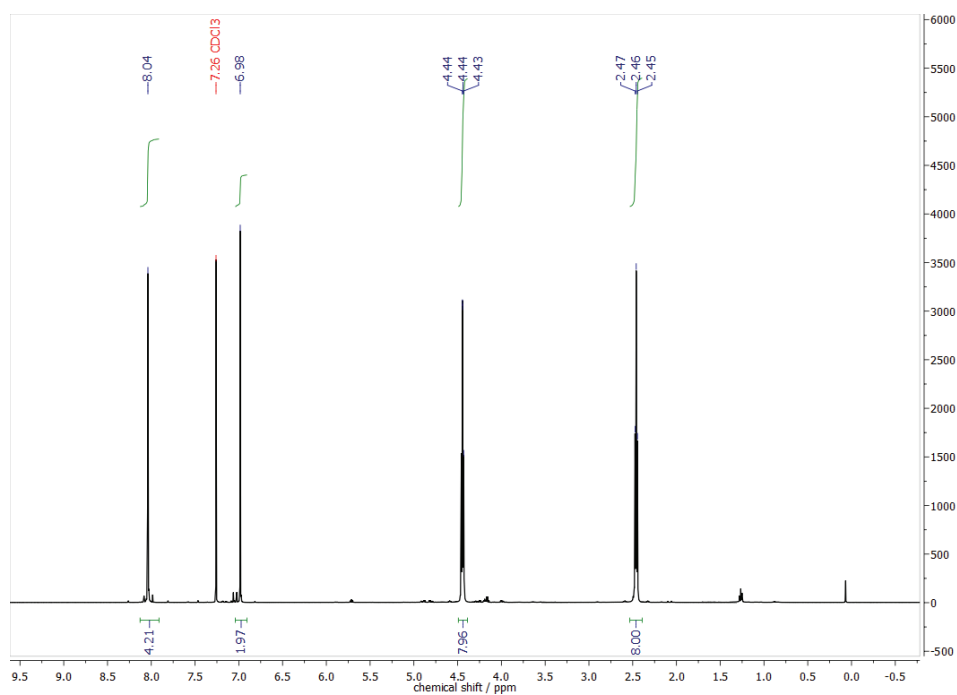


Figure S36: $^1\text{H-NMR}$ spectrum (CDCl_3 , 500 MHz) of Compound S5.

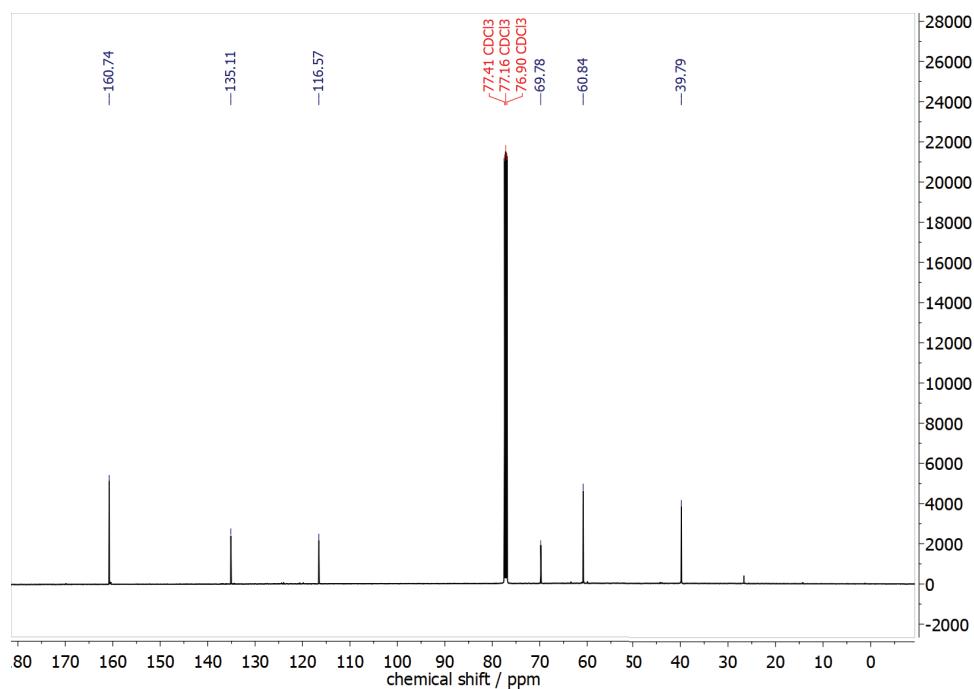


Figure S37: $^{13}\text{C-NMR}$ spectrum (CDCl_3 , 125 MHz) of Compound S5.

4.2 Mass-Spectrometry

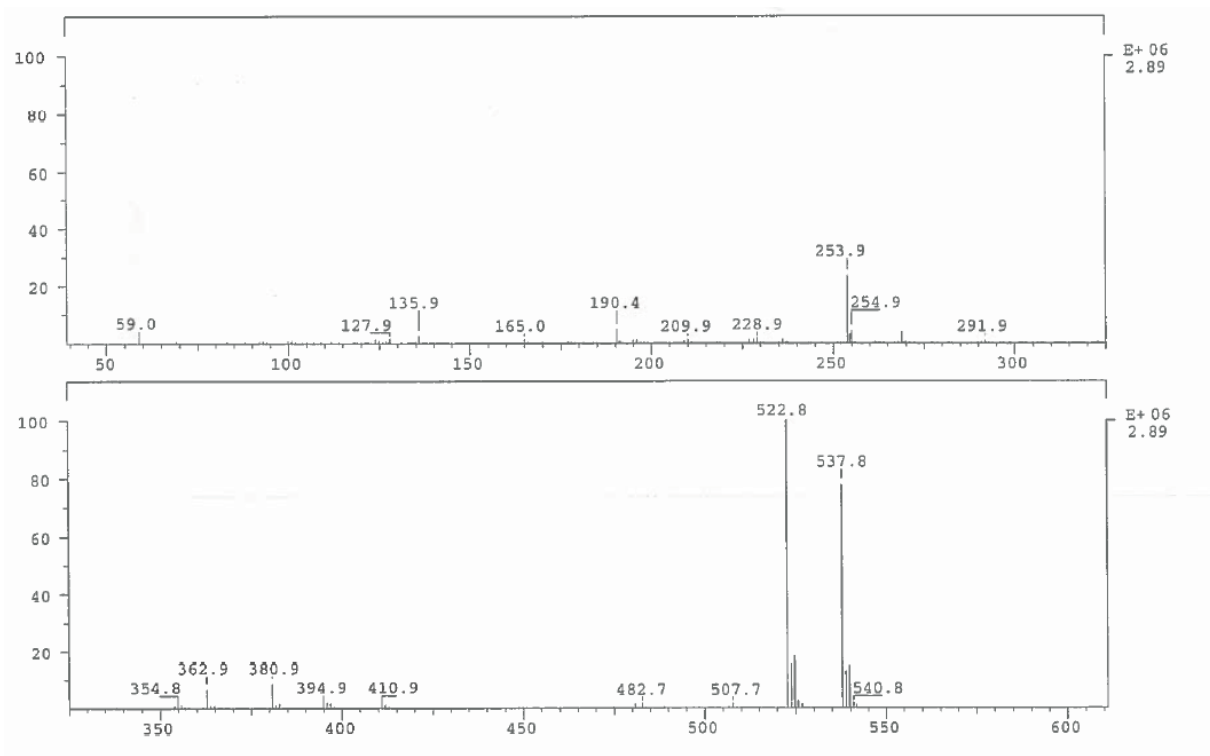


Figure S38: EI(70 eV) mass spectrum of Thioketal 12.

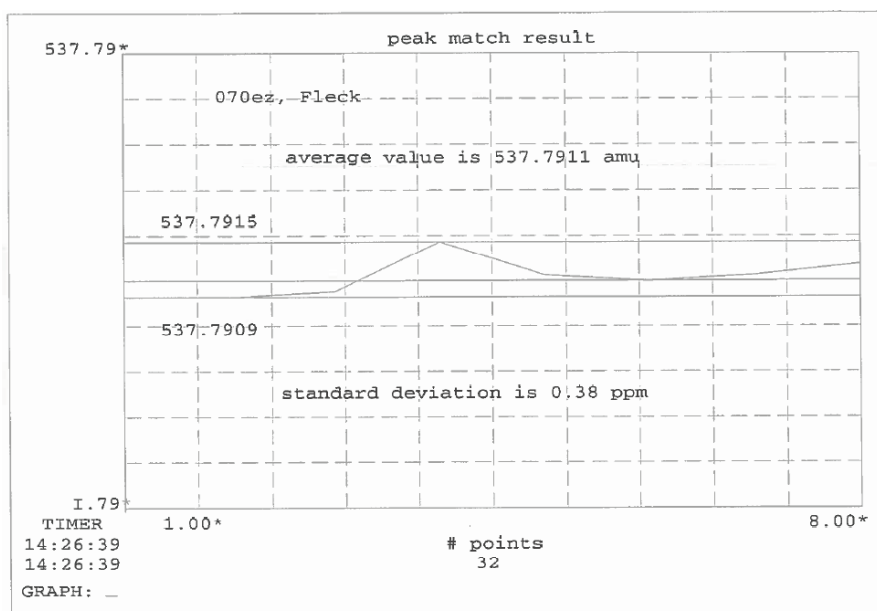


Figure S39: HRMS result of Thioketal 12 (EI, 70 eV).

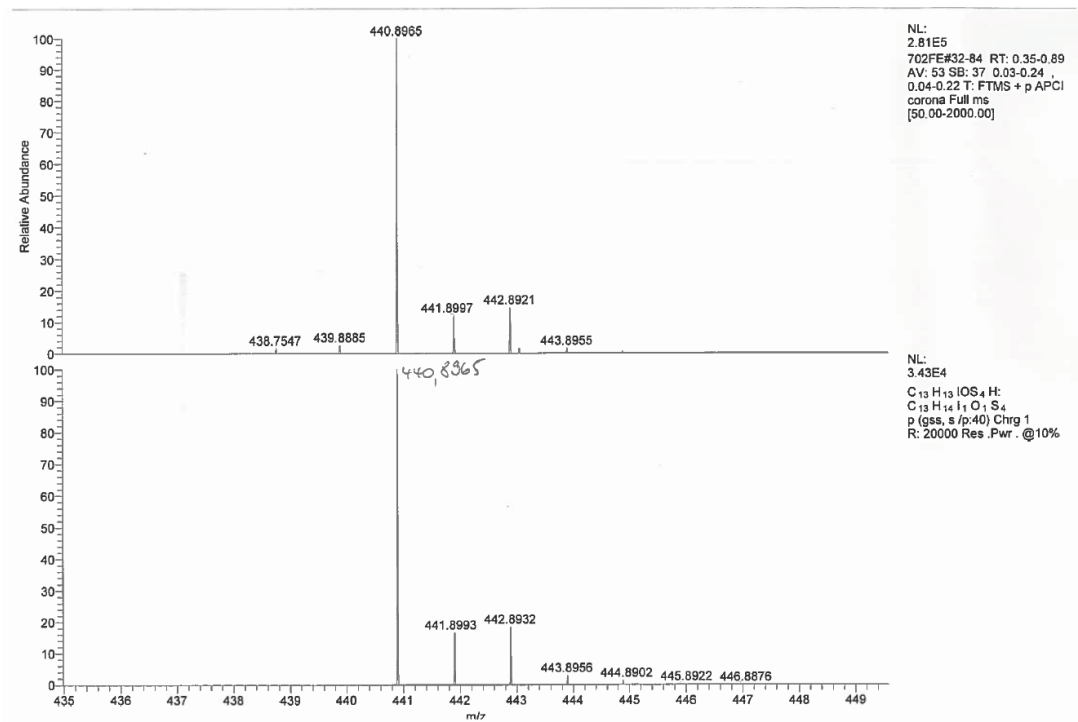


Figure S40: APCI-HRMS of Aldehyde 13.

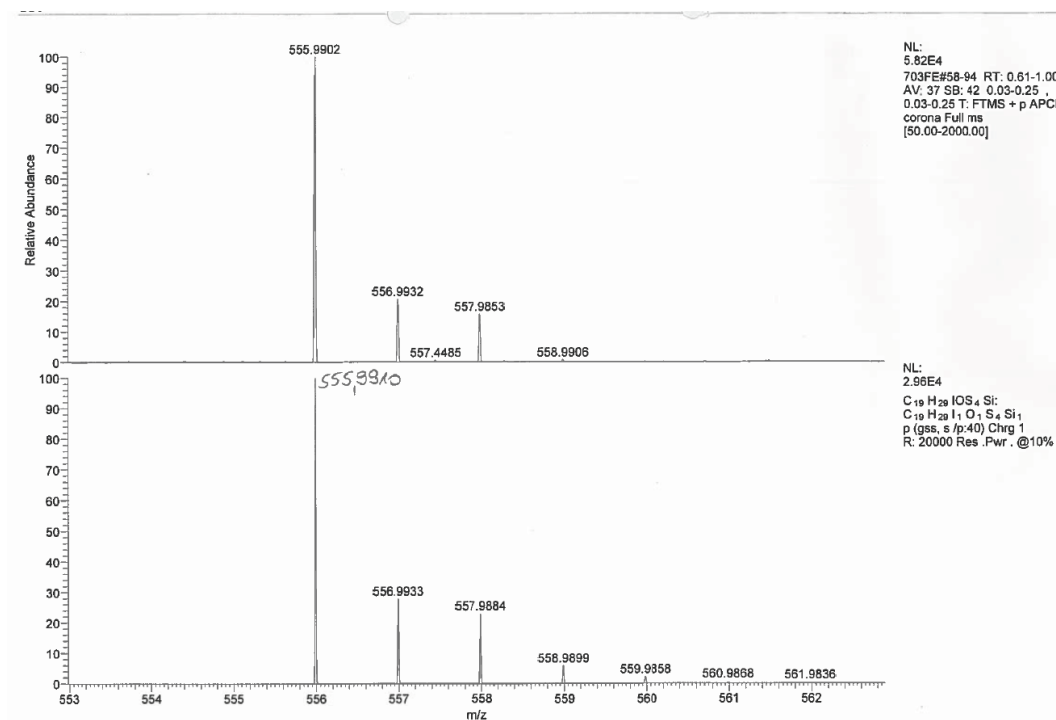


Figure S41: APCI-HRMS of Thioketal 10.

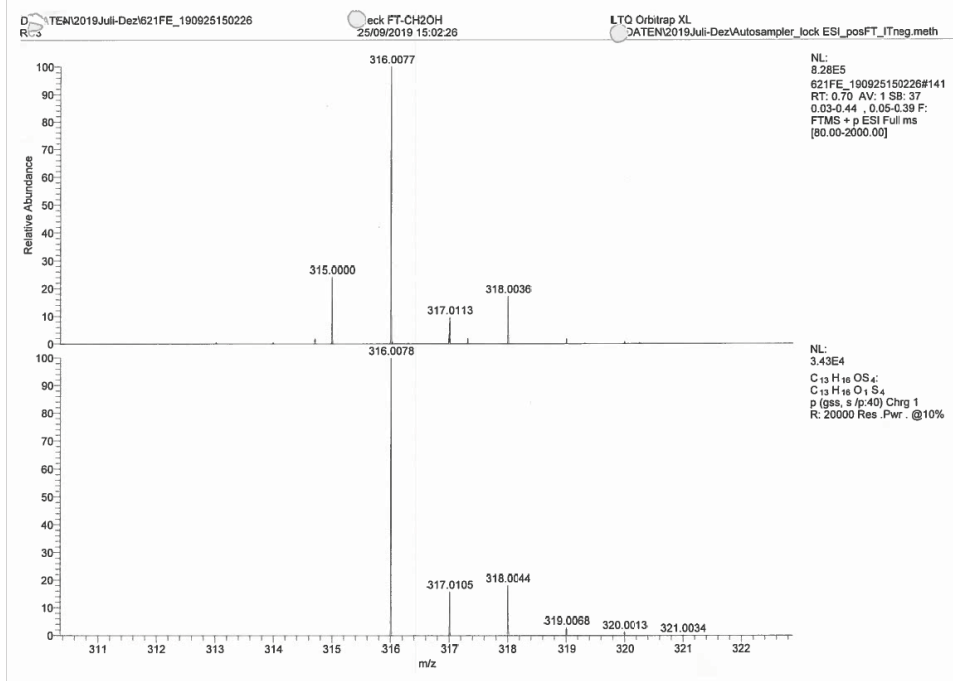


Figure S42: ESI(+)-HRMS of Alcohol 15.

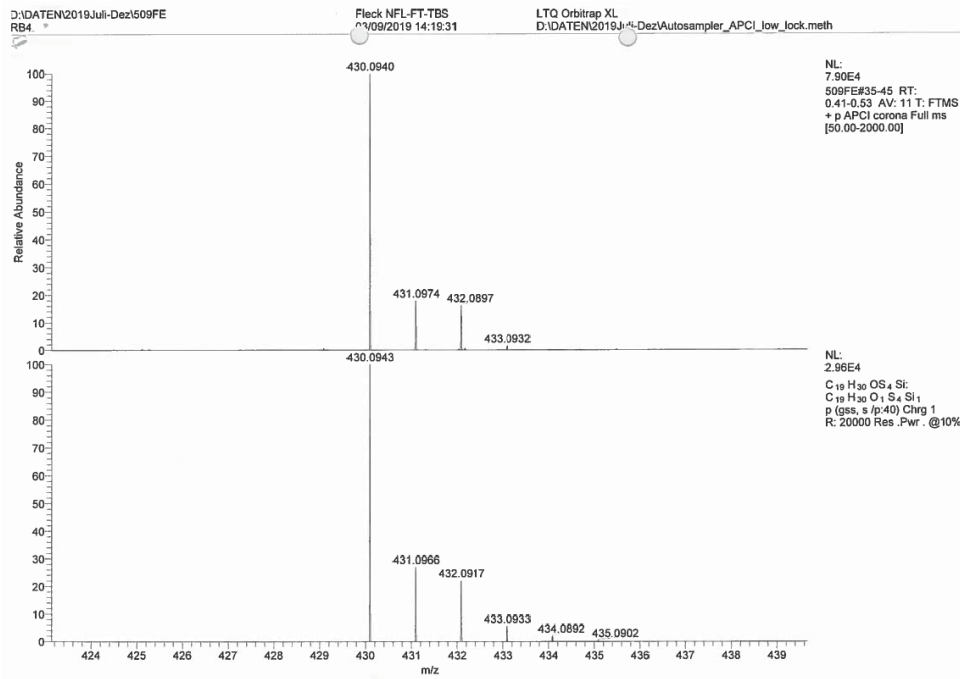


Figure S43: APCI-HRMS of Thioketal 16.

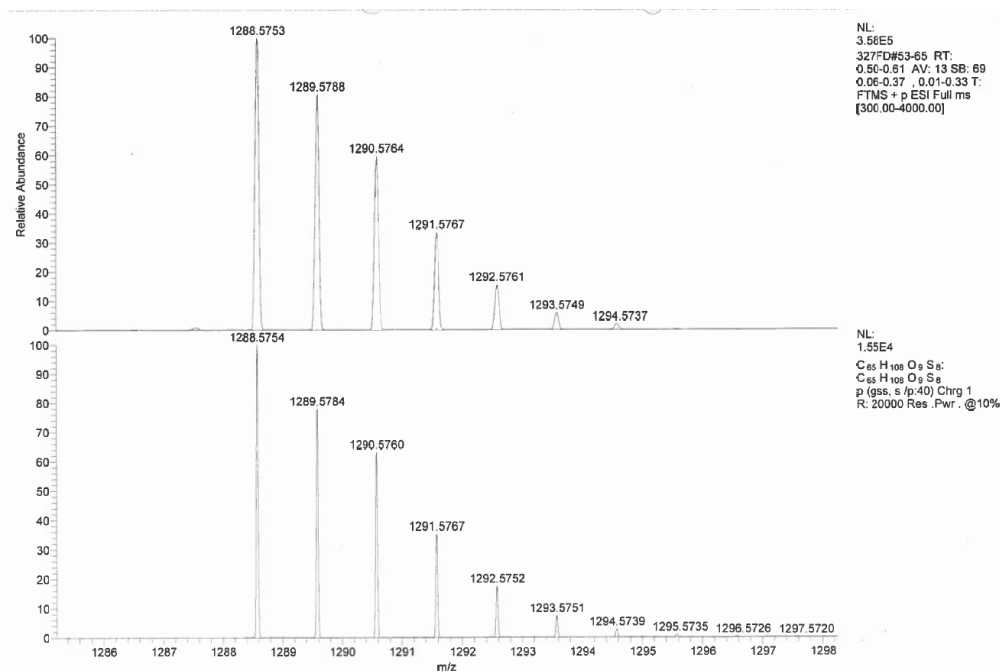


Figure S44: ESI(+)-HRMS of Diarylmethanol 20.

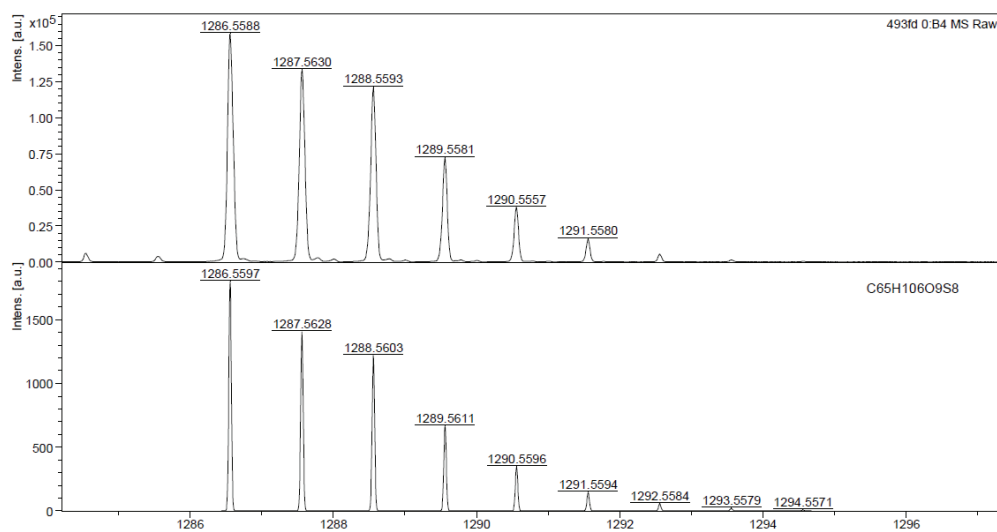


Figure S45: MALDI(+)-HRMS of Diarylketone 17.

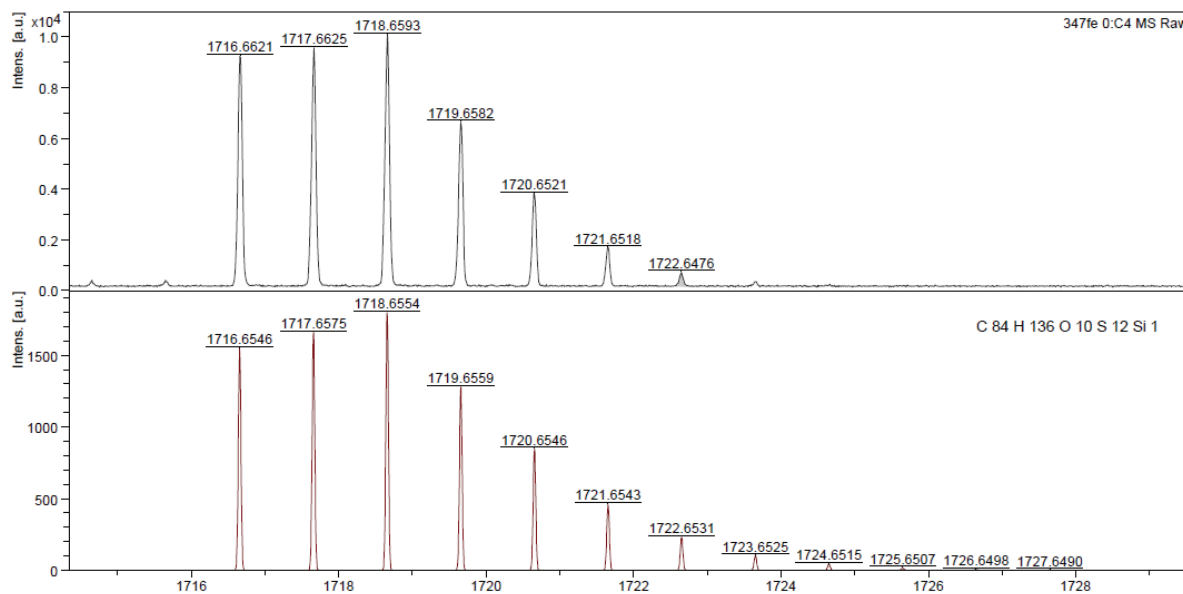


Figure S46: MALDI(+)-HRMS of Trityl alcohol 21.

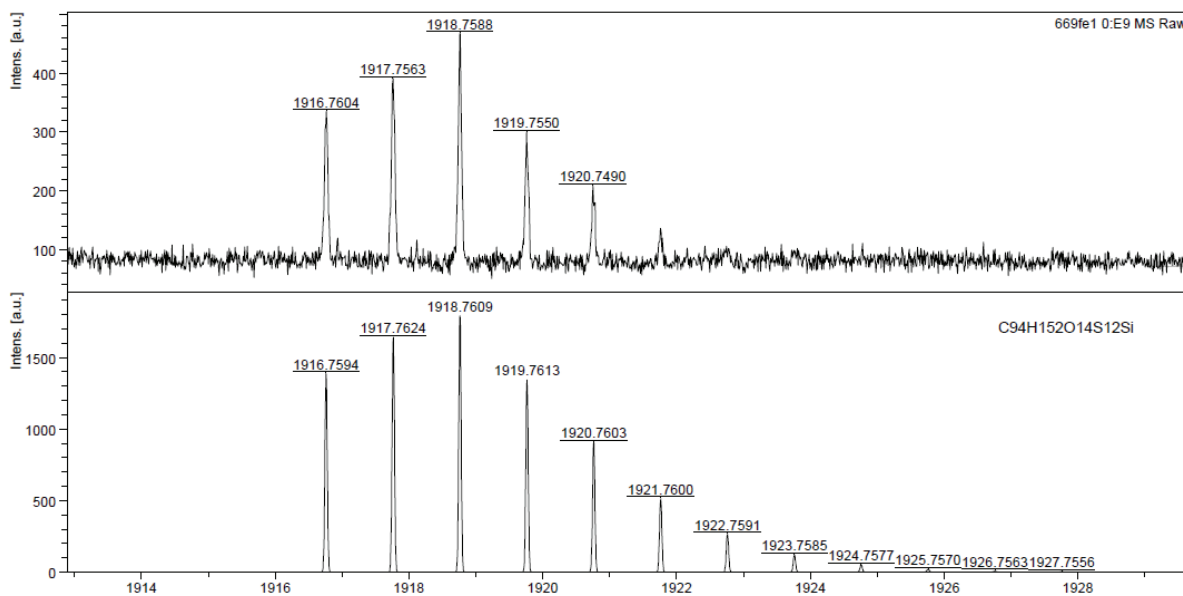


Figure S47: MALDI(+)-HRMS of Trityl alcohol 22.

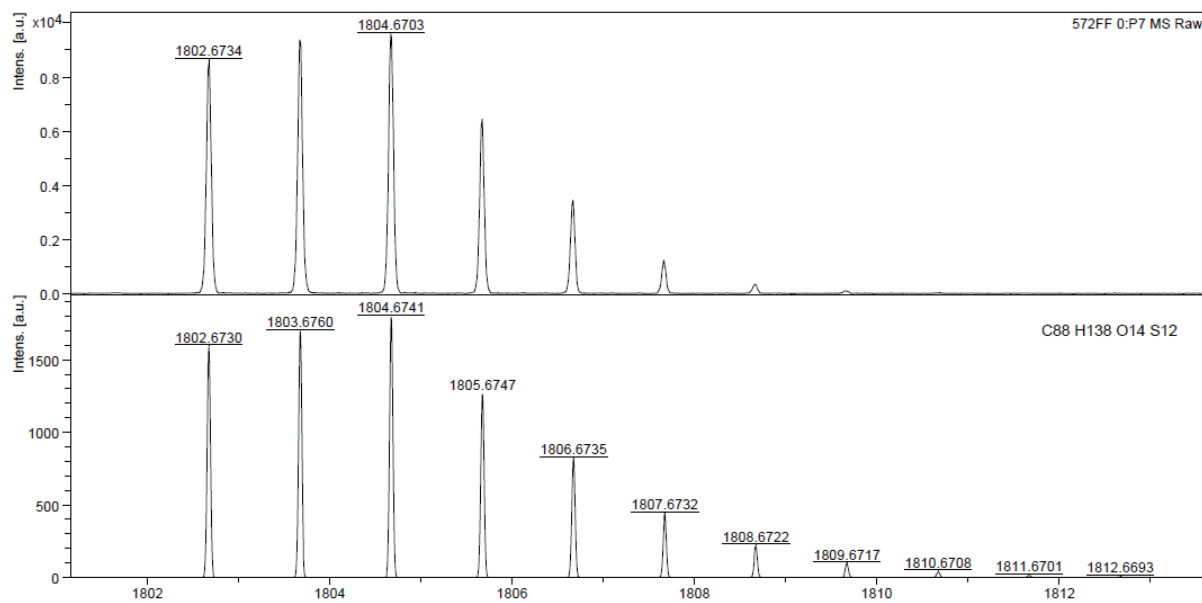


Figure S48: MALDI(+)-HRMS of Trityl alcohol 23.

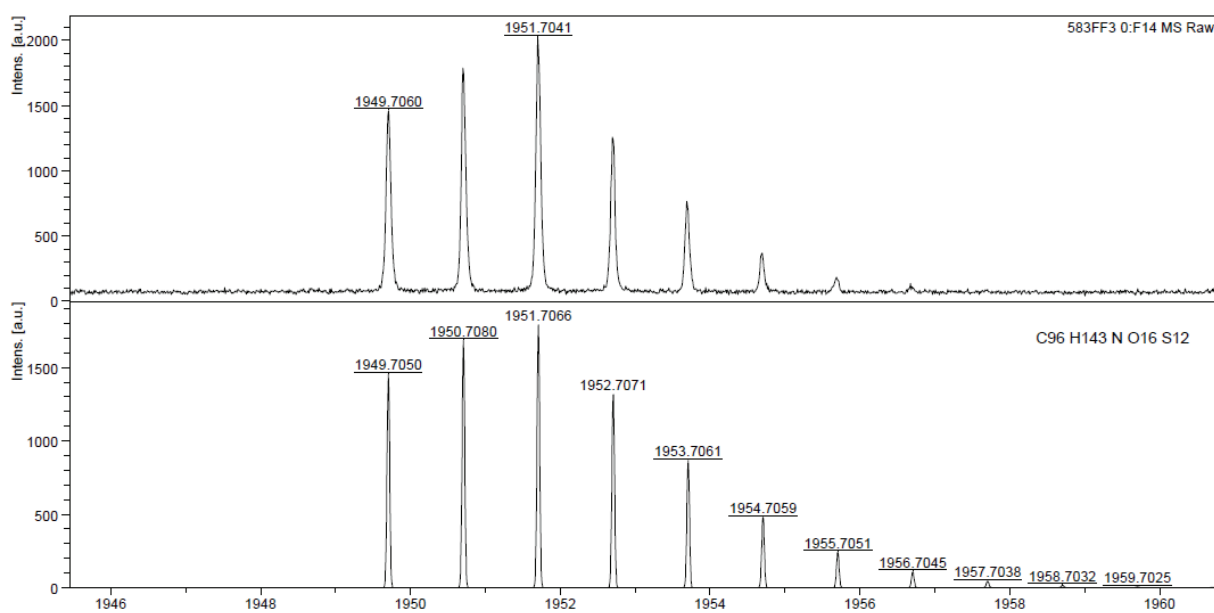


Figure S49: MALDI(+)-HRMS of Trityl alcohol 25.

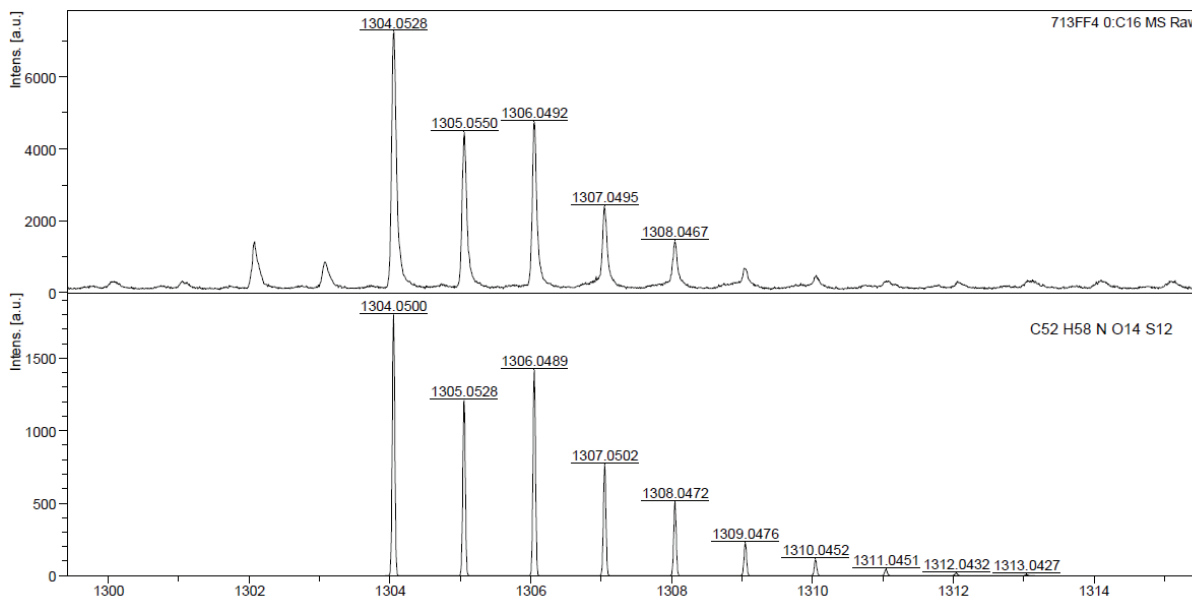


Figure S50: MALDI(+)-HRMS of **9**.

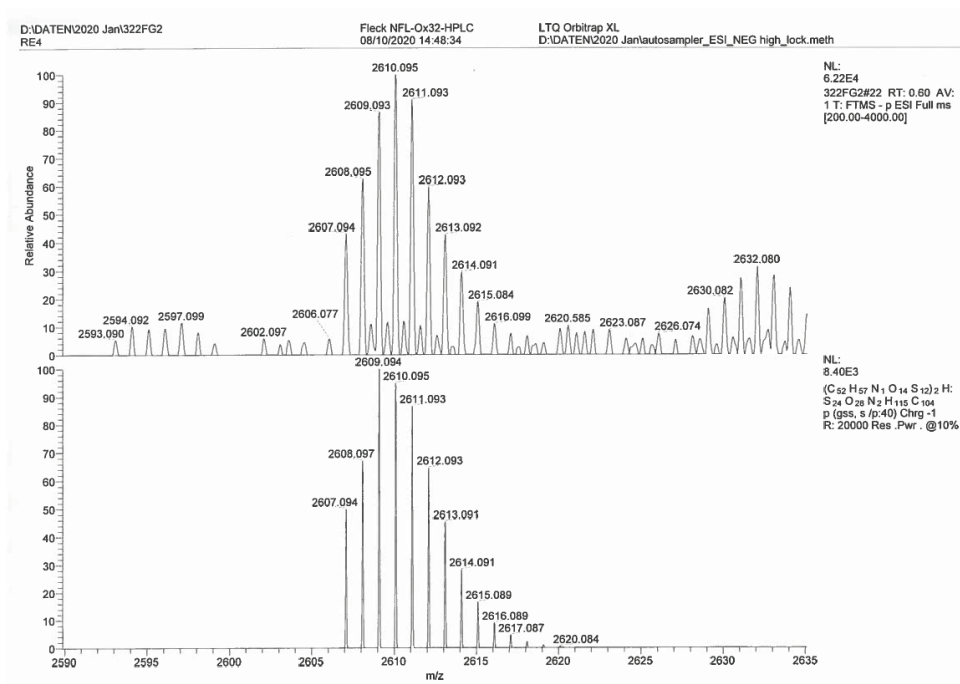


Figure S51: ESI(-)-HRMS of $[(9^-)_2\text{-H}]^-$.

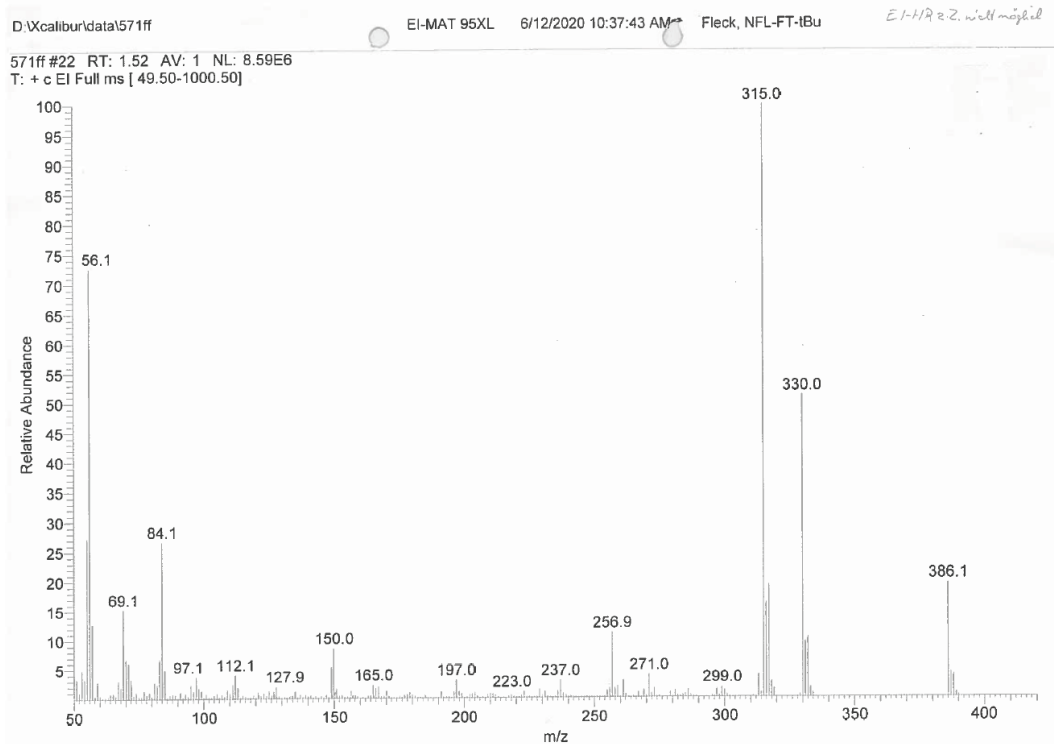


Figure S52: EI-MS of S2.

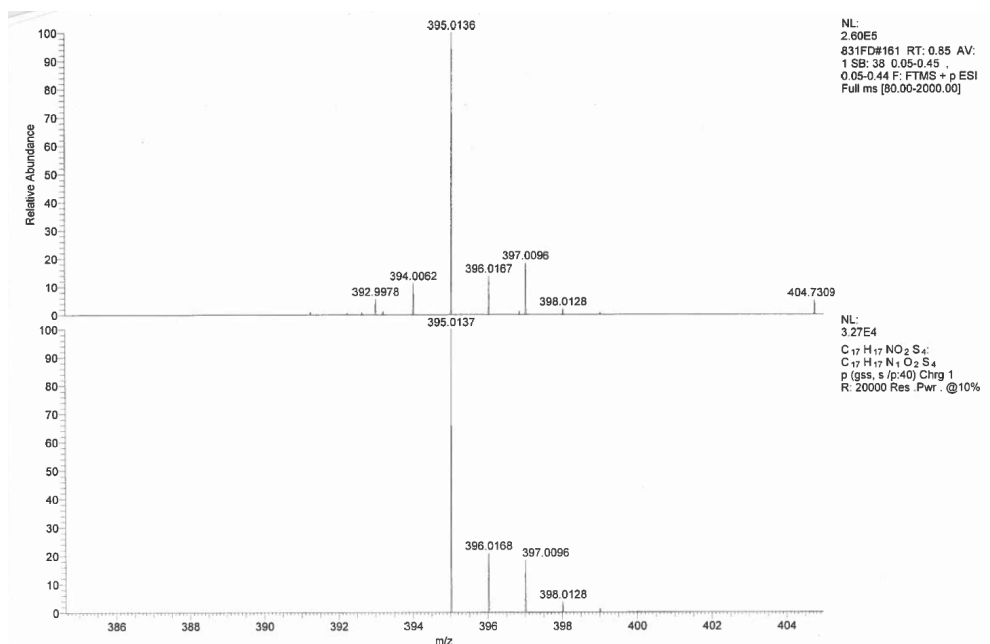


Figure S53: ESI(+) HRMS of S3 [S3-furane]⁺.

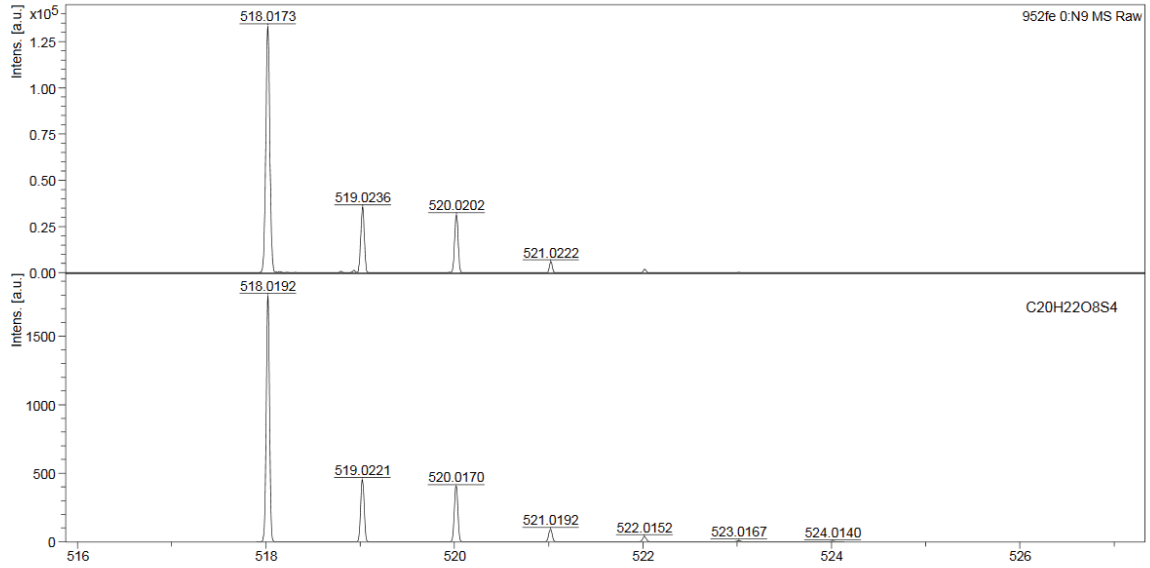


Figure S54: MALDI(+)-HRMS of S5.

4.3 Liquid-Chromatography

Nico Fleck - NFL-Ox32-HPLC - SM-006-13 auf KNAUER Eurospher II 100-3 C18; 3µm; 2,0 x 100mm (19120315187)- 265nm

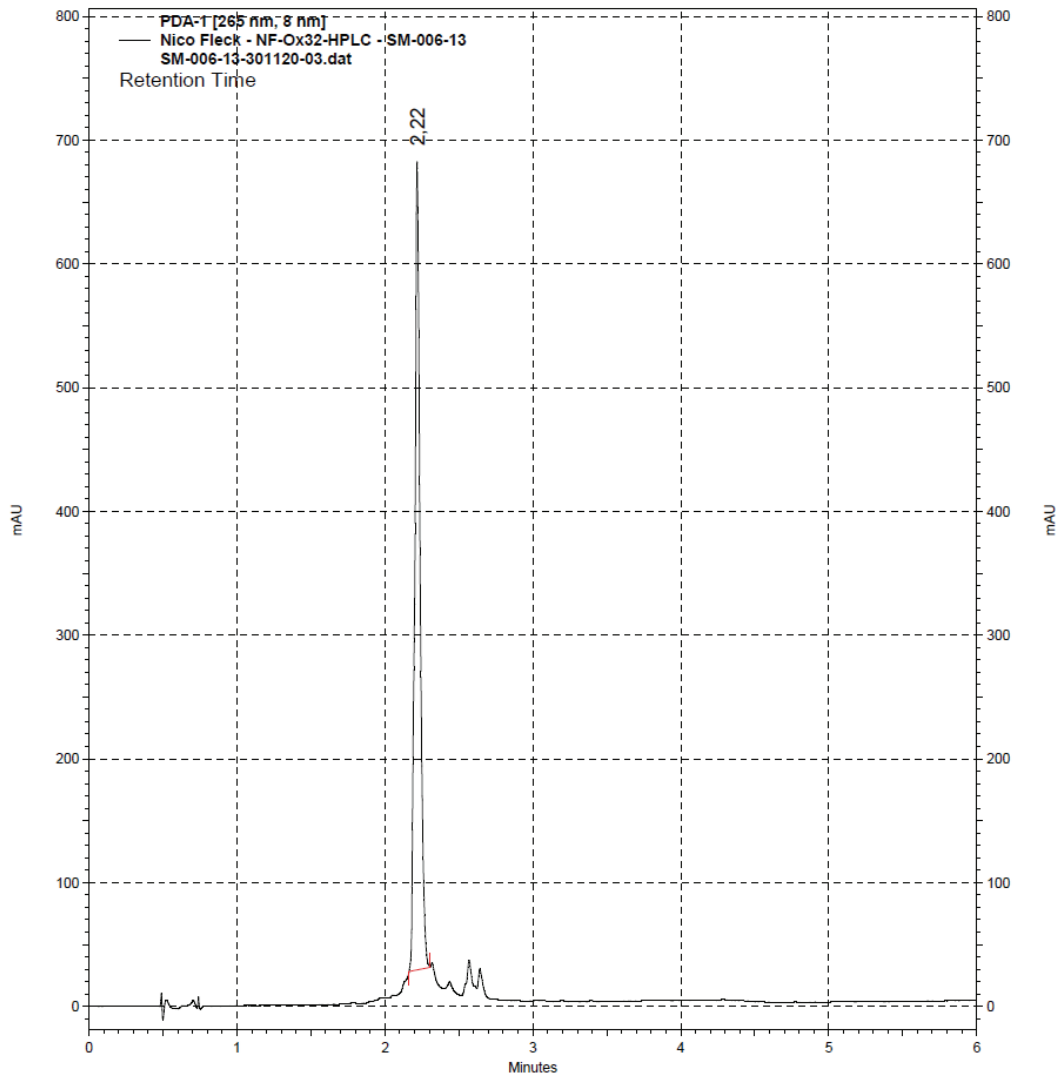


Figure S55: Analytical UHPLC of 9°.

UHPLC

Column: Knauer Eurospher II 100-3, C18, 3.0 µm; 2.0 x 100 mm.

A: Acetonitrile + 0.1 % TFA

B: Water + 0.1% TFA

Gradient:

0:00 min 10% A + 90 % B

4:00 min 70% A + 30% B

5. Spin Labelling

5.1 Preparations

In order to create a stock solution of **9**[•] for labeling, the free label was dissolved in DMSO and three independent dilutions (1:10) in PBS buffer (137 mM NaCl, 2.7 mM KCl, 10 mM Na₂HPO₄, 1.8 mM KH₂PO₄, pH 7.4) were prepared from the DMSO stock solution. CW EPR spectra were recorded of these three samples and the spins counted. Based on the mean value of the EPR spin count experiments, the concentration of the stock solution was determined to be 2.1 mM. Then, the extinction coefficient of **9**[•] was determined. A 10 μM solution of **9**[•] was prepared in labeling buffer (20 mM PO_i, 50 mM NaCl, pH 6.8) and an UV-vis spectrum recorded (Cary 100 UV-vis spectrometer from Agilent Technologies, Santa Clara, CA, USA). Using the *Lambert-Beer* equation below, molar extinction coefficients were calculated for **9**[•] at 457 and 280 nm.

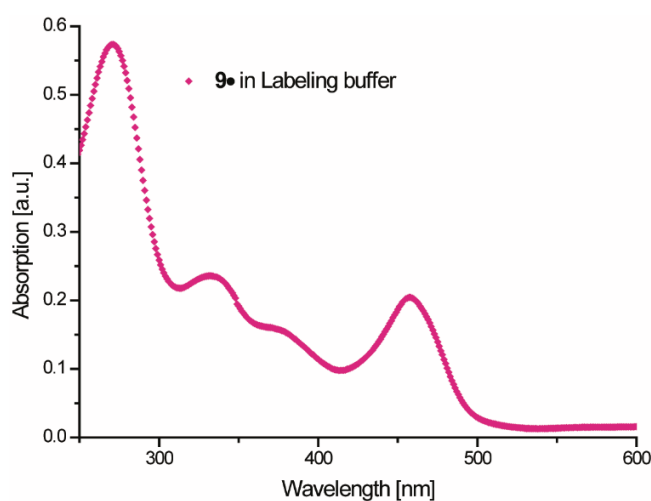


Figure S56: UV-Vis spectrum of **9**[•] in Labeling buffer, recorded at a Cary 100 UV-vis.

$$\epsilon_{457} = \frac{A_{457}}{1 \text{ cm} * 10 \frac{\mu\text{mol}}{\text{L}}} \quad ; \quad \epsilon_{280} = \frac{A_{280}}{1 \text{ cm} * 10 \frac{\mu\text{mol}}{\text{L}}}$$

Table S3: Extinction coefficients of **9**[•].

Wavelength [nm]	Extinction coefficient ϵ [$\frac{\text{L}}{\mu\text{mol} * \text{cm}}$]
457	0.0204
280	0.0574

5.2 Labeling of YopO₈₉₋₇₂₉ C219A with **9**[•]

In order to evaluate the site-specificity of **9**[•] in labeling, the new label was incubated with the cysteine-free mutant YopO₈₉₋₇₂₉ C219A (expressed as described previously^[8]). 20 nmol of YopO₈₉₋₇₂₉ C219A were incubated with 200 nmol TCEP in 1.5 mL Labeling buffer (20 mM PO_i, 50 mM NaCl, pH 6.8) for 2 h at 4°C followed by removing the reducing agent via a benchtop PD-10 desalting column.

A fivefold excess of **9**[•] (100 nmol, 47.5 μL of a 2.1 mM stock of **9**[•] in DMSO) was prediluted in 2.5 mL labeling buffer and then added to the 3.5 mL PD10 eluate containing the protein fraction. The reaction mixture was incubated for 16 h at 4 °C., after which excess label was removed via a PD-10 column (4 times 1.5 mL load) and the protein containing eluate concentrated to approximately 2 mL using a VivaSpin 6/50k MWCO (Sartorius, Göttingen, Germany). Any remaining label remnants were removed using a HiPrep 26/10 Desalting column on an Äkta avant system. The fractions showing an absorbance at 280 nm were

Page S47 of S68

pooled and concentrated to 2.0 mL. A UV-vis spectrum was recorded and the molar ratios of YopO and **9**[•] calculated based on the extinction coefficients of YopO ($0.04939 \text{ L } \mu\text{mol}^{-1} \text{ cm}^{-1}$), **9**[•] (see SXX) and the method previously described^[6]. According to this method, the cysteine-free mutant was labeled to an extent of 7 %. For the PDS measurements, the protein sample was concentrated to 200 μL and rebuffered thrice with deuterated PDS buffer (100 mM TES, 100 mM NaCl, pH 7.4) using a VivaSpin 6/50k MWCO.

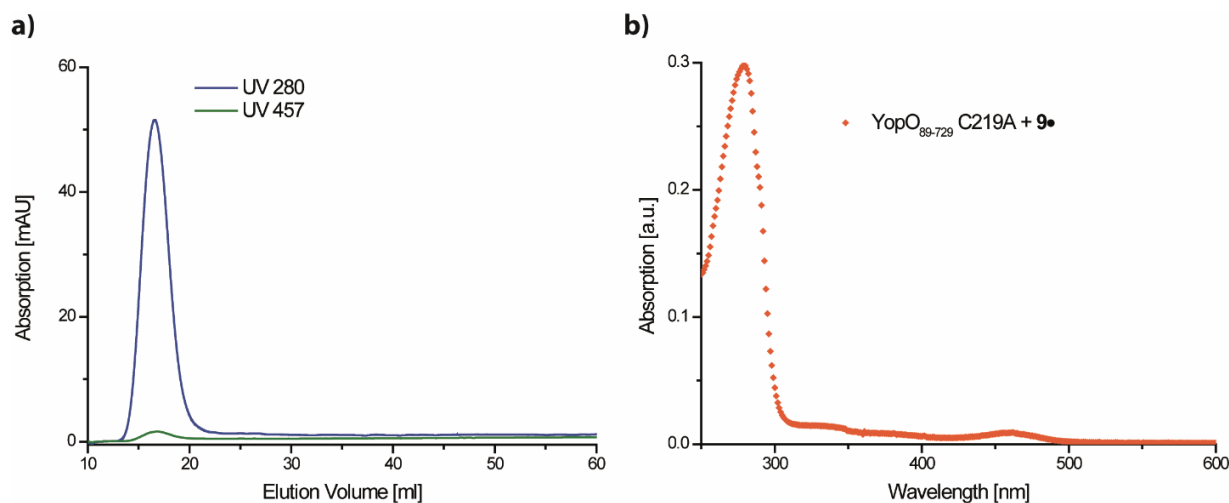


Figure S57: (a) HiPrep 26/10 Desalting chromatograph of YopO₈₉₋₇₂₉ C219A after incubation with **9**[•]. (b) UV-Vis spectrum of cysteine-free YopO after excess label removal recorded at a Cary 100 UV-vis spectrometer.

Table S4: Concentrations and molar ratio of YopO and **9**[•] after incubation and purification.

YopO [μM]	9 [•] [μM]	Molar Ratio YopO : 9 [•]
5.4	0.4	1 : 0.07

5.3 Labeling of YopO₈₉₋₇₂₉ Y588C/N624C with **9**[•]

The double cysteine mutant YopO₈₉₋₇₂₉ Y588C/N624C was obtained from a previous study recently published by us^[8]. 20 nmol of the double cysteine construct YopO₈₉₋₇₂₉ Y588C/N624C were reduced in a total of 1.5 mL labeling buffer (20 mM POi, 50 mM NaCl, pH 6.8) using a tenfold molar excess of TCEP to cleave any intermolecular disulfide bridges. After an incubation period of 2 h at 4 °C, the reducing agent was removed using a benchtop PD-10 desalting column and the labeling reaction was set up immediately afterwards. To the 3.5 mL PD-10 eluate containing the reduced protein, a 4-fold molar excess of **9**[•] per cysteine (160 nmol, 76 μL of a 2.1 mM stock of **9**[•] in DMSO) prediluted in 2.5 mL Labeling buffer was added leading to a final labeling concentrations of 3 μM YopO and 24 μM **9**[•], respectively. The labeling reaction was incubated for 16 h at 4 °C. Then excess label was removed using a PD-10 desalting column (4 times 1.5 mL load). The protein containing fractions were pooled and concentrated to 2 mL using a VivaSpin 6/50k MWCO and loaded onto a HiPrep 26/10 Desalting column to remove any remaining free label. The elution peak showing an absorption at 280 nm was pooled and concentrated down to 2.4 mL before recording a UV-vis absorption spectrum.

The molar ratio of YopO to **9**[•] was calculated as described above for the cysteine-free construct. Based on this, 1.69 equivalents of **9**[•] per YopO were determined (labeling efficiency of 85 %). For further PDS experiments, the protein sample was concentrated to 200 μL and rebuffered thrice with deuterated PDS buffer (100 mM TES, 100 mM NaCl, pH 7.4) using a VivaSpin 6/50k MWCO.

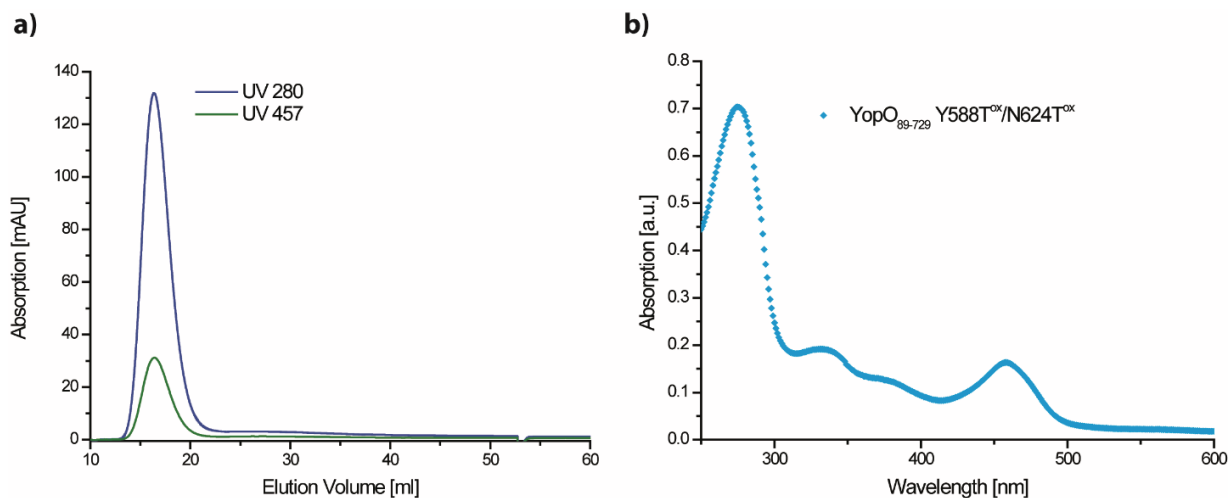


Figure S58: (a) HiPrep 26/10 Desalting chromatograph of $\text{YopO}_{89-729} \text{Y588T}^{\text{ox}}/\text{N624T}^{\text{ox}}$ after incubation with 9^{\bullet} . (b) UV-Vis spectrum of labeled $\text{YopO}_{89-729} \text{Y588T}^{\text{ox}}/\text{N624T}^{\text{ox}}$ after removal of excess free 9^{\bullet} .

Table S5: Concentrations and molar ratio of $\text{YopO}_{89-729} \text{Y588C}/\text{N624C}$ and 9^{\bullet} after labeling and workup.

YopO [μM]	9^{\bullet} [μM]	Molar Ratio YopO : 9^{\bullet}
4.8	8.1	1 : 1.69

5.4 Protein Mass-Spectrometry



Figure S59: ESI(+) mass spectra of protein samples. Top: Cysteine-free $\text{YopO}_{89-729} \text{C219A}$ mutant after incubation with 9^{\bullet} as described in section 5.2, calculated mass: 72108.57 Da ($\text{C}_{3176}\text{H}_{5085}\text{N}_{897}\text{O}_{989}\text{S}_{14}$). Bottom: Doubly-labelled $\text{YopO}_{89-729} \text{Y588T}^{\text{ox}}/\text{N624T}^{\text{ox}}$ mutant (section 5.3), calculated mass: 74645.67 Da ($\text{C}_{3273}\text{H}_{5196}\text{N}_{898}\text{O}_{1015}\text{S}_{40}$).

5.5 Activity Assay

The structural integrity of YopO after labeling with **9**[•] was evaluated based on the autophosphorylation capability of YopO^[9]. Here, 2 μ M of YopO Y588T^{ox}/N624T^{ox} and the cysteine-free wild type were incubated with 6 μ M G-actin (extracted from rabbit muscle acetone powder) in phosphorylation buffer (50 mM Tris, 10 mM MgCl₂, 1 mM ATP, 2 mM MnCl₂, pH 8.0) for 1.5 h at 37 °C. Samples without G-actin served as a negative control. After the incubation time, samples were quenched by addition of 8x SDS sample buffer and boiled for 5 min at 95 °C.

An SDS-PAGE was ran (10% gel, 50 min, 175 V, 300 mA) and the acrylamide gel was fixed in 45% MeOH, 10% AcOH (2 times for 30 min, 100 mL each). The gel was washed with MilliQ water (3 times for 10 min, 100 mL each) and stained in the dark with 100 mL Pro-Q Phosphoprotein Diamond Stain (Thermo Fisher Scientific, Waltham, MA, USA) for 90 min. Subsequently, the gel was washed in 20% Acetonitril, 50 mM NaOAc pH 4.0 (3 times for 30 min, 100 mL each) and MilliQ water (2 times for 5 min, 100 mL each). Phosphorylated proteins were detected using an UV-table equipped with a 590 nm longpass emission filter. Afterwards, the gel was stained in Coomassie Brilliant Blue for total protein visualization. As seen in Figure S60, YopO Y588T^{ox}/N624T^{ox} remained active with only marginally reduced activity compared to the wild type.

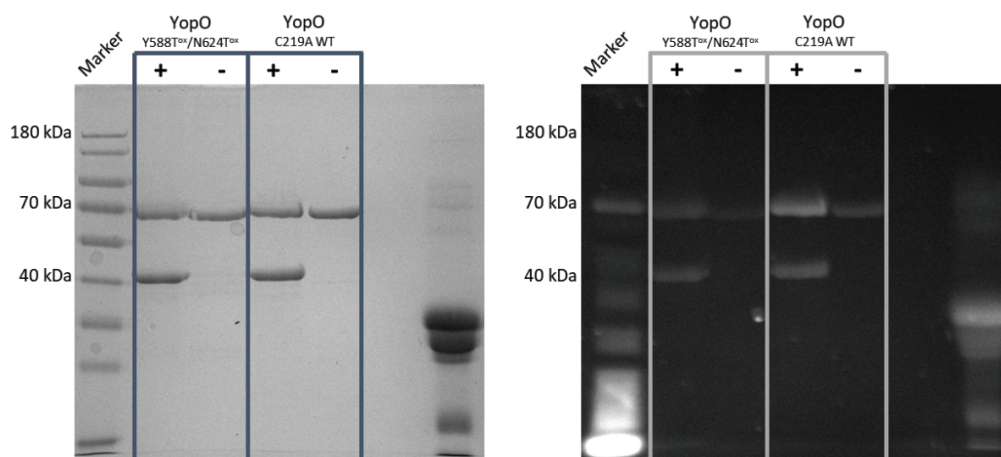


Figure S60: Coomassie stained SDS gel (left) and the corresponding Pro-Q-stained gel (right). Phosphorylated proteins appear significantly brighter than other proteins in the Pro-Q-stained gel.

6. CW EPR-Spectroscopy

6.1 Simulation of CW EPR Spectra

CW EPR spectra were simulated using the EasySpin^[10] toolbox for Matlab (MathWorks, Natick, MA, USA). The spectrum of 50 μ M free (i.e. non-bioconjugated) **9**[•] in PBS buffer at RT was fitted using the “garlic” function of EasySpin (see main text, Figure 1). Appropriate starting values for the “esfit” routine were taken from our study on **6**[•].^[8] All obtained g-values, hyperfine coupling constants A, and peak-to-peak linewidths (lwpp) are summarized in Table S6; hyperfine coupling constants are correlated with the nuclei by the numbering shown in Figure 61.

Table S6: Fitting parameters of the cw EPR spectrum of 9^\bullet recorded in PBS buffer at RT.

Fitting result	Value
g	2.0033
A_{N1}	1.48 MHz
A_{H2}	3.02 MHz
A_{H3}	6.09 MHz
A_{C4}	66.32 MHz
A_{C5}	31.60 MHz
A_{C6}	25.82 MHz
A_{C7}	3.59 MHz
A_{C8}	7.02 MHz
lwpp (Gaussian)	0.0116 mT
lwpp (Lorentzian)	0.0256 mT

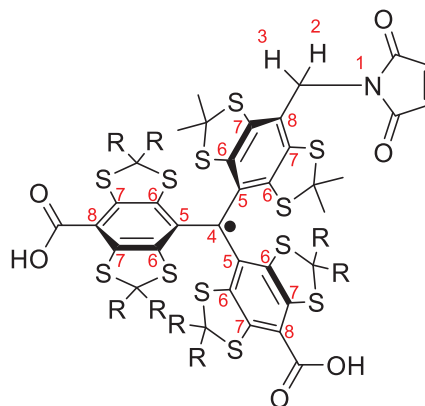


Figure S61: Structure of 9^\bullet with the atoms labelled according to the nuclei given in Table S6.
 $R = \text{CH}_2\text{CH}_2\text{OH}$.

CW EPR spectra of 9^\bullet recorded at 100 K were simulated with the “pepper” function of EasySpin, appropriate starting values for the fit were taken from [8]. As 9^\bullet exists in an equilibrium between a monomeric and a dimeric form, two spin systems were defined for the simulation. The Pake pattern stemming from the dimer (9^\bullet)₂ was fitted using a home-written function in EasySpin. Herein, the interspin distance r was transformed into a dipolar coupling constant via $D = 52.04 \text{ MHz}/r^3$, and r was varied to find the optimal value. The g -values of the monomer and the dimer were assumed to be equal. The parameters of the best fit are collected in Table S7. The weights of the monomer 9^\bullet and the dimer (9^\bullet)₂ were fitted individually for each spectrum, depending on the glycerol content (Fig. S65).

Table S7: Fitting parameters of the cw EPR spectrum of 9^\bullet obtained at 100 K:

Fitting result	Value
Monomer 9^\bullet	
g	2.0034
A_{N1}	1.31 MHz
A_{H2}	2.75 MHz
A_{H3}	7.03 MHz
A_{C4}	66.45 MHz
A_{C5}	32.66 MHz; 30.96 MHz; 31.81 MHz
A_{C6}	25.63 MHz; 24.17 MHz; 27.54 MHz; 26.14 MHz; 25.92 MHz; 28.89 MHz
A_{C8}	7.22 MHz; 7.26 MHz; 7.10 MHz
lwpp (Lorentzian)	0.1112 mT
lwpp (Gaussian)	0.0807 mT
Dimer (9^\bullet)₂	
g	2.0034
r	0.987 nm
lwpp (Lorentzian)	0.0114 mT
lwpp (Gaussian)	0.2664 mT

6.2 Reduction Stability

The reduction stability of **9**[•] was evaluated using the doubly labelled YopO₈₉₋₇₂₉ Y588C/N624C construct. Oocytes of the African claw frog *Xenopus laevis* were obtained from EcoCyte Bioscience (Dortmund, Germany) and the lysate was prepared following a protocol of *Karthikeyan et al.*^[111]

For HeLa cell lysate, HeLa S3 (ATCC[®] CCL-2.2, human cervical adenocarcinoma) cells were suspended in PBS buffer (600 μ L per 10⁸ cells), the suspension was frozen in ethanol/CO_{2(g)} for 5 min, and subsequently thawed in a 37 °C water bath. This procedure was repeated three times, whereupon the cells were lysed with rapid oscillation for 5 minutes. Membranes were separated by centrifugation at 15000 rpm at 4 °C and the lysate was collected as the supernatant. It was separated into several aliquots, immediately shock-frozen in liquid nitrogen, and stored at -80 °C.

Then, YopO₈₉₋₇₂₉ Y588T^{Ox}/N624T^{Ox} was diluted to a concentration of 50 μ M in the corresponding reductive medium and filled into a 10 μ L capillary, which was sealed with superglue and transferred into a 3 mm outer diameter Q-band tube. The EPR-tube was inserted into the spectrometer (EMXmicro) and the spectrometer properly tuned. After this, a cw EPR spectrum was recorded every 15 minutes over 15 hours. A home-written bash script was used to monitor the microwave frequency and power throughout the entire measurement. The signal intensities representing the spin concentration were obtained as the double integral over the spectrum for each time point. The dead time, measured from mixing the radical and the respective medium to the beginning of measurement, was kept below 6 minutes.

6.3 Binding of Spin Labels to Cystein-Free YopO C219A

As described in the main text, the extent of non-specific binding of spin labels **4**[•], **6**[•], and **9**[•] was studied by addition of a cysteine-free YopO₈₉₋₇₂₉ C219A to radical solutions in PBS buffer. The respective protein was obtained from a previous study recently published by us^[8] and used as a stock solution in PBS buffer. The protein was added to a solution of the radical in PBS buffer, so that the indicated final concentrations were achieved and then incubated for 20 min at room temperature. The samples were transferred into 10 μ L capillaries, which were sealed with glue on both ends and fitted into a 4 mm outer diameter X-band EPR tube. The tube position was pre-adjusted through the tubeholder and not changed throughout the experiment for each radical. X-band cw EPR spectra (ModAmp. 0.2G, attenuation 25 dB, 298 K, 10 scans each) were recorded (Figures S62 – S64). In the main text, the respective peak-to-peak intensities are shown (Figure 3a). It is important to note that the double-integral remained constant within a deviation of 10 % for each radical.

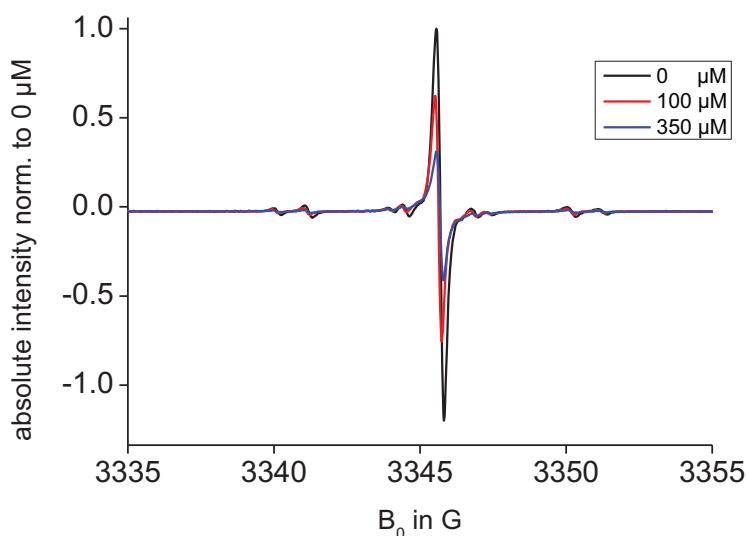


Figure S62: Measurement for radical **4**[•].

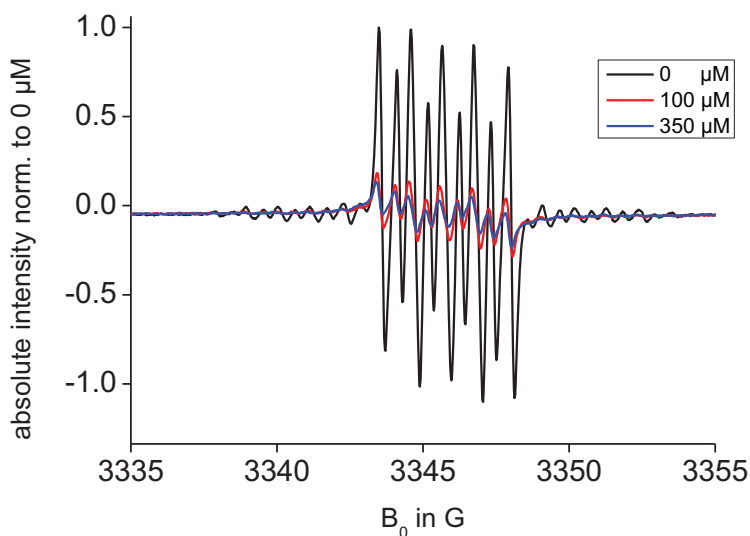


Figure S63: Measurement for radical 6•.

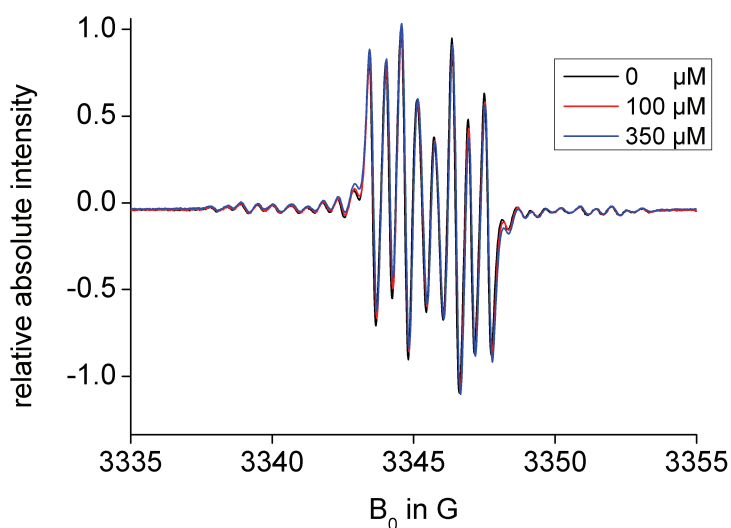


Figure S64: Measurement for radical 9•.

6.4 CW EPR on 9• in Glycerol/Water Mixtures

Dissolving 9• in mixtures of PBS-buffer and glycerol, the cw EPR spectra shown in Figure S65 were recorded at 100 K. A minimum content of 20 % glycerol was required as a cryo-protectant. With rising glycerol content, the features of the Pake pattern arising from homodimerization of 9• decreased. By simulation of the respective EPR spectra, the monomer/dimer fractions provided in Table S8 were found. Simulation of the EPR spectra was done as described in section 6.1.

Table S8: Dimer content of the EPR samples.

Glycerol content [%]	Monomer 9• [%]	Dimer (9•) ₂ [%]
20	72	28
60	85	15
85	99	1

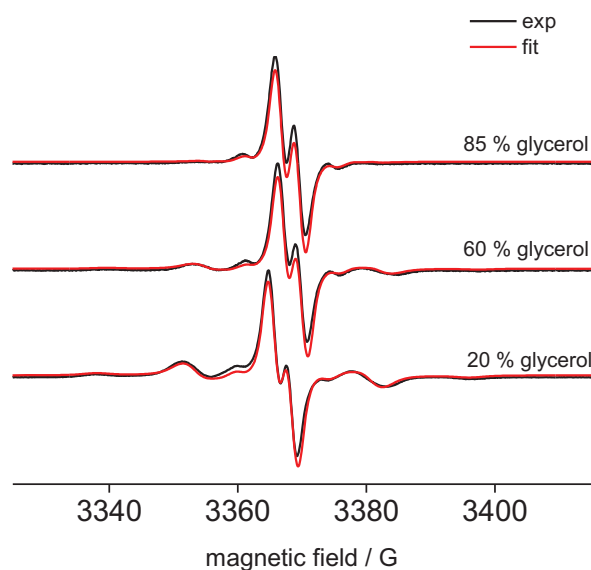


Figure S65: cw EPR spectra of 9^\bullet at 100 K in glycerol/PBS-buffer mixtures.

7. Pulsed EPR-spectroscopy

7.1 Sample Preparation

YopO samples in deuterated buffer were diluted 1:1 in ethylene glycol- d_6 , transferred into a Q-band EPR tube (O.D. 3 mm, Wilmad LabGlass, Vineland, NJ, USA) and flash-frozen in liquid nitrogen.

7.2 Relaxation Time Measurements

In order to compare the electron spin relaxation behavior of Ox-SLIM 9^\bullet and its predecessor SLIM 6^\bullet , T_1 and T_M relaxation times were measured at 50 K by inversion recovery (Figure S66a) and two-pulse electron spin echo envelope modulation (Figure S66b) experiments, respectively. The pulse sequences were applied at the maximum of the echo-detected field swept EPR spectrum and included phase cycling, two steps for 2pESEEM and four steps for IR. Acquisition parameters are given in Table S9. Measurements were carried out on the constructs YopO Y588T^{ox}/N624T^{ox} and Y588T^{SLIM}/N624T^{SLIM}.

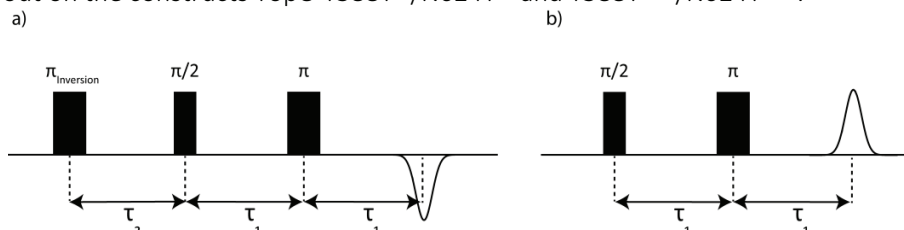


Figure S66: Pulse sequence applied for the inversion recovery (a) and the two-pulse ESEEM (b) experiment.

Table S9: Pulse sequence parameters for relaxation time measurements.

Inversion Recovery		Two-Pulse ESEEM	
Variable	Value	Variable	Value
$\pi/2$	12 ns	$\pi/2$	12 ns
π	24 ns	π	24 ns
$\tau_{\text{Inversion}}$	24 ns	–	–
τ_1	200 ns	τ_1	200 ns
τ_2	400 ns	–	–
τ_2 increment	1 ms	τ_1 increment	8 ns
Shots per Point	1	Shots per Point	10
Shot Repetition Time	500 ms	Shot Repetition Time	15 ms

The results of the relaxation time measurements are shown in Figure S67. Inversion recovery traces were fitted with a single exponential $y = a \cdot \exp\left(-\frac{t}{T_1}\right) + c$, with a being the pre-exponential factor, T_1 the transverse relaxation time, and c an offset. Two-pulse ESEEM traces could be fitted with a stretched exponential decay $y = a \cdot \exp\left(-\left(\frac{2t}{T_M}\right)^b\right) + c$, wherein T_M is the phase-memory time quantifying the Hahn echo decay. All fit parameters are collected in Table S10.

Table S10: Fit parameters of the relaxation curves.

	Inversion Recovery	Two-Pulse ESEEM
	$y = a \cdot \exp\left(-\frac{t}{T_1}\right) + c$	$y = a \cdot \exp\left(-\left(\frac{2t}{T_M}\right)^b\right) + c$
Y588T ^{ox} /N624T ^{ox}	$a = -1.552$ $T_1 = 11 \text{ ms}$ $c = 0.994$	$a = 1.171$ $T_M = 4.00 \mu\text{s}$ $b = 0.783$ $c = -0.016$
Y588T ^{SLIM} /N624T ^{SLIM}	$a = -1.508$ $T_1 = 7.8 \text{ ms}$ $c = 0.992$	$a = 1.574$ $T_M = 1.45 \mu\text{s}$ $b = 0.621$ $c = 0.011$

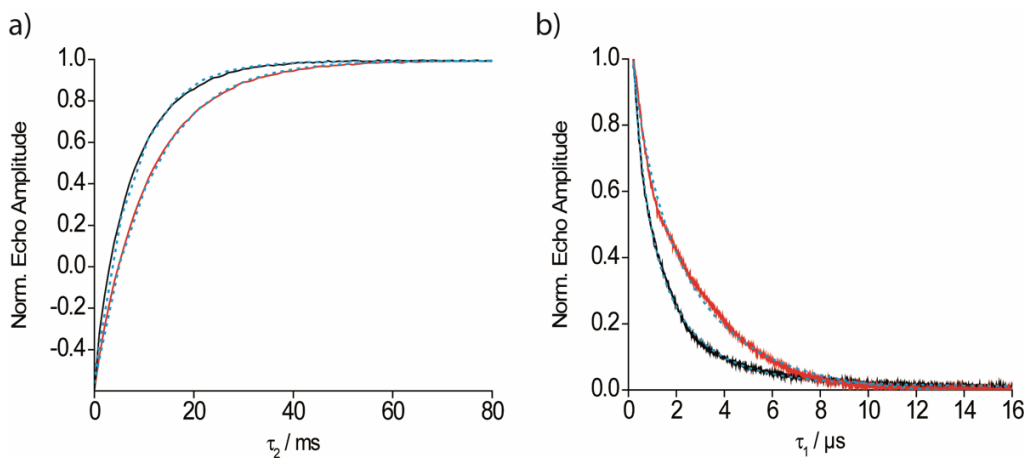


Figure S67: Relaxation experiments on YopO Y588T^{ox}/N624T^{ox} (red) and Y588T^{SLIM}/N624T^{SLIM} (black). Overlay of (a) the Inversion Recovery and (b) the Two-Pulse ESEEM time traces. The blue dashed lines are the fits.

7.3 Double Quantum Coherence (DQC) Experiments

The six-pulse Double Quantum Coherence (DQC) sequence (Figure S68) was applied at the maximum of the trityl field-swept EPR spectrum. In the DQC experiment, the interpulse delays τ_1 and τ_2 are incremented and decremented, respectively, and the integral of the DQC echo is recorded as a function of $\tau_1 - \tau_2$.

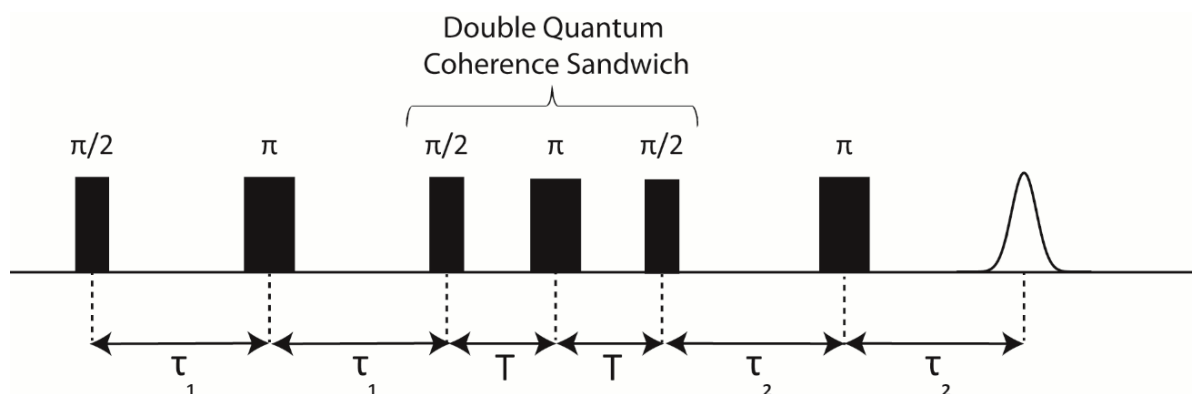


Figure S68: Schematic representation of the 6-pulse Double Quantum Coherence (DQC) experiment.

A 64-step phase cycle was applied to remove undesired echoes and thus extract the pure double quantum coherence pathway.^[12,13] In order to eliminate deuterium ESEEM from the dipolar time trace, a modulation averaging procedure was applied, i.e. τ_1 and τ_2 were incremented by 8 steps of 16 ns and the respective traces were summed up.^[14] All DQC measurements were performed at 50K.

As the pure DQC echo cannot be observed in the transient mode of the spectrometer, the phase of the microwave pulses was adjusted on the Hahn echo sequence to yield a maximally positive amplitude in the real signal channel of the quadrature detector. Proper phase adjustment was checked by summing amplitudes of the Hahn echo obtained from $(\pi/2)_{+x}/(\pi)_{+x}$ and $(\pi/2)_{-x}/(\pi)_{-x}$ pulses, which averages out the signal. The same applies to $(\pi/2)_{+y}/(\pi)_{+y}$ and $(\pi/2)_{-y}/(\pi)_{-y}$ pulses. Pulse lengths and interpulse delays used for the DQC experiment are given in Table S11.

Table S11: Parameters for the DQC experiment

Variable	Value
$\pi/2$	12 ns
π	24 ns
τ_1	200 ns
τ_1 increment	4 ns
τ_2	7000 ns ([YopO] = 18.5 μ M) 4500 ns ([YopO] = 45 nM)
τ_2 decrement	4 ns
T	50 ns
Shots per Point	3
Shot Repetition Time	15 ms

The symmetric DQC time traces were mirrored at the zero-time. Transformation of the mirrored traces into distance distributions was done with the DeerAnalysis toolbox for Matlab^[15]. In order to eliminate the intermolecular background of the primary data, a background correction was performed assuming a homogeneous three-dimensional distribution of background objects. The “background start” value was

chosen such that the background-corrected time trace was flat at long dipolar evolution times (last quarter of the time trace); an initial guess of the “background start” value was obtained using the “!” button in DeerAnalysis. The influence of the background correction on the distance distributions was checked by means of the validation tool in DeerAnalysis. Herein, only the “background start” parameter was varied, and the variation ranges were set from the first local minimum of the time trace to the point when the oscillations were entirely damped.

For the sake of comparison, the construct YopO Y588T^{SLIM}/N624T^{SLIM} shown in our previous study^[8] was measured again with the same parameters applied to Y588T^{ox}/N624T^{ox}. The time traces before and after background correction, the resulting distance distribution, and the L-curves for Tikhonov-regularization are shown in Figure S69.

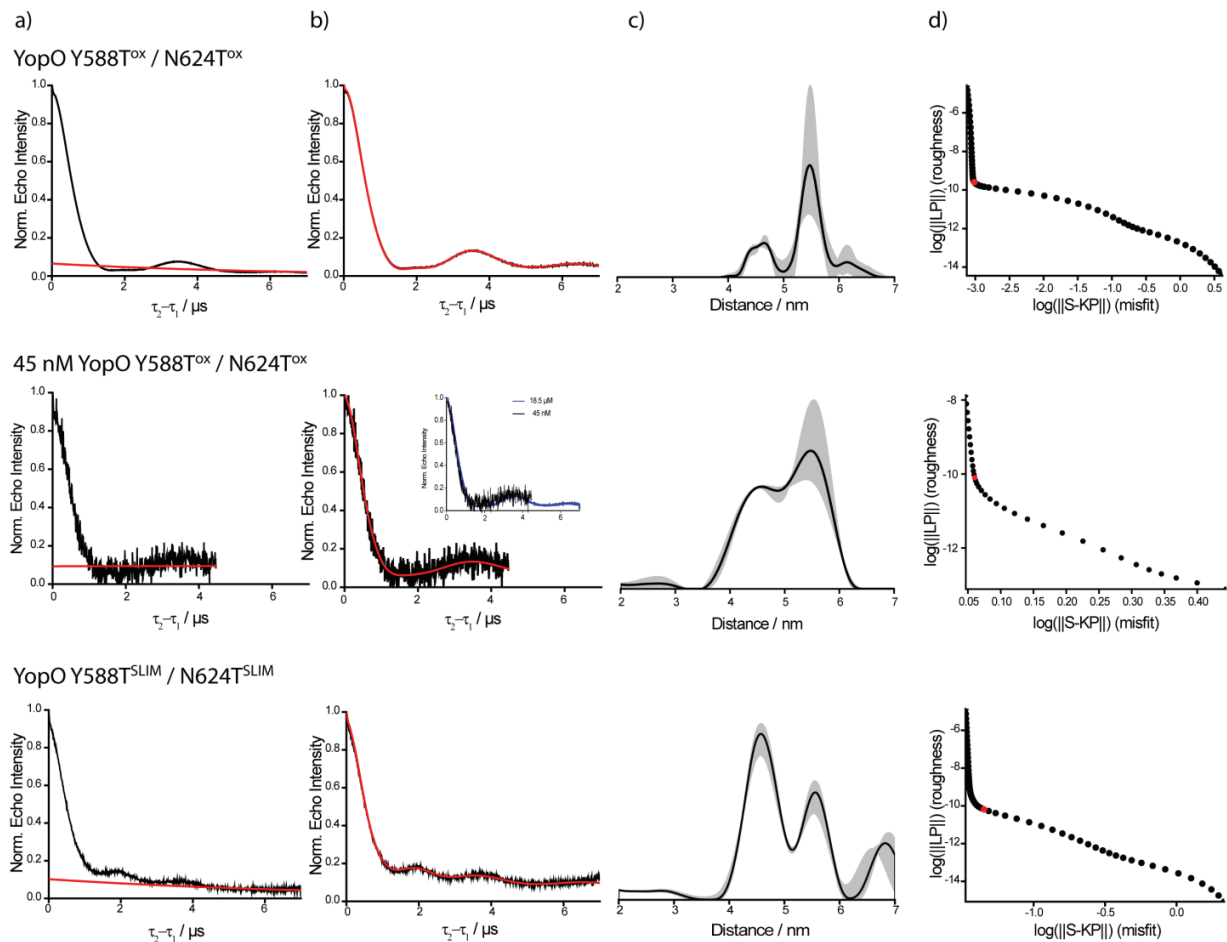


Figure S69: PDS data obtained for YopO Y588C/N624C labelled with Ox-SLIM 9[•] (18.5 μ M in top row, 45 nM in middle row) and SLIM 6[•] (12.5 μ M in bottom row). Raw DQC time traces with the background fits shown in red (a). Background-corrected DQC time traces with fits from Tikhonov-regularization in red (b). Distance distributions with the background validation from DeerAnalysis shown as grey shaded area (c). L-curves with the chosen regularization parameter in red (d). For Ox-SLIM, a comparison of the data acquired at 18.5 μ M and 45 nM is shown as in inset in part c). The shorter dipolar evolution time chosen for the measurement at 45 nM leads to an artificial broadening of the distance distribution.

7.4 Determination of the Signal-to-Noise Ratio (SNR)

The SNR of the DQC-traces was determined using the software “SNRcalculator” developed inhouse^[16] and available free of charge via github.^[17] Table S12 contains the SNR values in reference to the measurement time, and in reference to the measurement time and the spin concentration. As can be seen from the values related to measurement time and concentration, the SNR obtained with Y588T^{ox}/N624T^{ox} exceeds the one obtained with the corresponding SLIM-labelled construct Y588^{SLIM}/N624T^{SLIM} by a factor of 2 (Table S12). With respect to the 45 nM measurement, it should be noted, that the dipolar evolution time was set to 4.5 μ s, coming along with an intrinsic increase in SNR.

Table S12: SNR of the DQC experiments. Note that the given concentrations are protein concentrations.

SNR related to	Y588T ^{SLIM} /N624T ^{SLIM} (12.5 μ M protein, 7.0 μ s trace length)	Y588T ^{ox} /N624T ^{ox} (18.5 μ M protein, 7.0 μ s trace length)	Y588T ^{ox} /N624T ^{ox} (45 nM protein, 4.5 μ s trace length)
measurement time	46 h ^{-1/2}	133 h ^{-1/2}	1.24 h ^{-1/2}
measurement time and spin concentration	1.84 μ M ⁻¹ h ^{-1/2}	3.59 μ M ⁻¹ h ^{-1/2}	13.8 μ M ⁻¹ h ^{-1/2}

8. Computational Data

8.1 Homodimer of 9[•]

For the input structures, a conformer search was performed applying the Conformer-Rotamer Ensemble Sampling Tool (CREST)^[18] at the GFN-FF^[19] level of theory. The energetically lowest conformers found for the trityl dimer and monomer were further optimized using the composite method B97-3c.^[20] On the optimized geometries free energies were calculated using a multilevel approach. High level single-point energies were calculated with the hybrid density functional PBE0^[21] in a large def2-TZVPP^[22] basis set. The D4^[23] London dispersion correction was applied throughout. Solvation contributions to free energy were calculated with COSMO-RS^[24,25] also including the volume work to go from an ideal gas at 1 bar to 1 mol L⁻¹ in solution. For the COSMO-RS free energy, two singlepoint calculations with PBE/TZ (one in gas-phase and one in an ideal conductor) were performed. BP86/TZ single-point calculations did not converge, but the effect of the choice of the GGA is rather small for usage with COSMO-RS.S9 The output of these calculations was then processed by the COSMOtherm program.^[26] Thermostatistical contributions to the free energy were calculated using GFN2-xTB^[26] and the modified RRHO scheme (mRRHO).^[28] The total free energies were then calculated as the sum of the single-point energy, dispersion contribution, thermostaistical and solvation contribution according to

$$\Delta G = \Delta E + \Delta\delta G_{solv} + \Delta G_{mRRHO}$$

where Δ indicates the differences between the dimer and the monomers. The respective values are provided in Table S13 below.

Table S13: Energetic contributions to the dimerization energy for (9[•])₂

ΔE PBE0-D4/def2-TZVPP	ΔG_{mRRHO}^{298} GFN2-xTB	$\Delta\delta G_{solv}(H_2O)$ COSMO-RS(H ₂ O)	ΔG
-42.4 kcal/mol	23.1 kcal/mol	4.4 kcal/mol	-14.8 kcal/mol

All quantum mechanical calculations were performed with the TURBOMOLE 7.2.^[29] (DFT) and xtb 6.3.2 (GFN1-xTB^[30] GFN2-xTB^[27] GFN-FF^[19]) program packages with default convergence criteria 10⁻⁷ E_h for energies and 10⁻⁵ E_h Bohr⁻¹ for gradients. The resolution-of-identity (RI) approximation for the Coulomb inte-

grals was generally used to speed up the DFT calculations using matching default auxiliary basis sets.^[31,32] For the integration of the exchange-correlation contribution, the numerical quadrature grid m4 was employed. All calculations were performed on Intel© Xeon E5-2660 v4 @ 2.00GHz machines.

8.1.1 Coordinates for 9[•] in xyz-format

C	-0.4949901	1.9359712	-3.4976828	O	3.7145243	6.5672039	-1.9674405
C	-0.1477457	0.9793283	-2.5434918	C	1.9029259	3.8994369	1.8081888
C	-0.6799248	0.9976607	-1.2451473	C	2.5277210	4.7599228	2.8880280
C	-1.7164983	1.9077493	-0.9773188	O	1.6736736	4.8005900	4.0431354
C	-2.0654557	2.8705192	-1.9210424	C	-2.8444682	-2.2736285	0.7911791
C	-1.3896629	2.9726475	-3.1541467	C	-2.0830419	-1.3890231	0.0186387
S	0.2924100	1.7729644	-5.0641787	C	-0.9959967	-0.6847147	0.5853994
S	0.9917650	-0.2684588	-3.0201439	C	-0.7691305	-0.8465290	1.9723303
S	-3.4404255	3.8849796	-1.4405032	C	-1.5468739	-1.7215848	2.7278496
S	-2.5508461	1.9567599	0.5721558	C	-2.5679962	-2.4766684	2.1424664
C	0.6983481	-0.0333133	-4.8286172	S	-4.1543532	-3.0984530	-0.0633689
C	-3.1484607	3.7030162	0.3834955	S	-2.5057964	-1.3068409	-1.6880621
C	-4.4607394	3.8687622	1.1389617	S	-1.1317122	-1.8420103	4.4420640
C	-2.0820238	4.7005921	0.8170192	S	0.4899398	0.0172058	2.8596747
C	-1.6910054	4.6557905	2.2847786	C	-3.3363328	-2.9610733	-1.7143625
O	-0.7379061	5.6898132	2.5005016	C	-0.3293579	-0.1801341	4.5030333
C	-5.6605385	3.0855938	0.6216019	C	0.7273471	-0.1761137	5.5874166
O	-6.7886940	3.2417746	1.4746657	C	-1.3742313	0.8985964	4.7054881
C	1.9382341	-0.3886686	-5.6407140	C	-4.3790480	-2.9703974	-2.8099415
C	3.2652961	0.1960032	-5.1890224	C	-2.3041914	-4.0558145	-1.8813270
O	3.8138258	-0.4737529	-4.0460764	C	-3.3333961	-3.4874185	2.9459433
C	-0.5278818	-0.8370843	-5.2612706	C	-0.1306619	0.1325251	-0.2269001
C	-0.3937229	-2.3419412	-5.1523181	N	-2.4658997	-4.4197839	3.6408387
O	-1.7019111	-2.8992838	-5.3331311	C	-1.4535306	-5.1702668	3.0570080
C	3.3538100	1.2837811	0.5603033	C	-0.8079302	-5.9360503	4.1621093
C	2.0812656	1.2896056	-0.0070677	C	-1.4524831	-5.6717214	5.2962060
C	1.2909986	0.1151193	0.0047268	C	-2.5492326	-4.7037690	5.0157694
C	1.9553558	-1.0913528	0.3155291	O	-1.1825680	-5.1926177	1.8700672
C	3.2663892	-1.1081214	0.8064448	O	-3.3644514	-4.2399947	5.7785399
C	3.9307910	0.1055376	1.0750896	C	-1.4599762	4.1288889	-4.0863355
S	4.1745343	2.8614927	0.5284518	O	-0.8790799	4.1150833	-5.1532594
S	1.5207547	2.8298099	-0.6538619	O	-2.1140002	5.2457642	-3.7174118
S	3.9623548	-2.7006122	1.0940016	C	5.1355084	0.0334085	1.9433825
S	1.1851064	-2.6518899	0.1019937	O	5.6198828	-1.0305994	2.2704070
C	2.6031634	3.8345104	0.4606966	O	5.6614924	1.1682803	2.4459212
C	2.7922315	-3.5300111	-0.0975256	H	-4.7138427	4.9287144	1.1676041
C	2.5845905	-4.9941313	0.2565815	H	-4.2801643	3.5777201	2.1752072
C	3.3598777	-3.3197685	-1.5014185	H	-2.4422657	5.7037996	0.5852560
C	2.4913694	-3.7608062	-2.6690930	H	-1.1866847	4.5375103	0.2191855
O	3.0570312	-3.3885899	-3.9181029	H	-1.2749460	3.6732449	2.5209452
C	2.2101777	-5.2805551	1.7112736	H	-2.5640610	4.8108205	2.9255809
O	1.4604658	-6.4835519	1.8419809	H	-0.1555781	5.4319789	3.2312119
C	2.8607247	5.2069336	-0.1408003	H	-5.3999414	2.0344222	0.4833762
C	3.3512062	5.2474051	-1.5825978	H	-5.9716801	3.4666074	-0.3476667

H	-6.6430685	2.7144088	2.2670583	H	2.9084859	7.0693207	-2.1265971
H	1.7475702	-0.0804598	-6.6714343	H	1.7695619	2.8833405	2.1805204
H	2.0465259	-1.4712776	-5.6640142	H	0.9102524	4.2966291	1.6167572
H	3.1728533	1.2647206	-4.9908377	H	2.6120969	5.7947935	2.5688890
H	3.9956366	0.0677013	-5.9845949	H	3.5254971	4.4109075	3.1619147
H	3.3617787	-0.1067087	-3.2728515	H	1.6886137	3.9278666	4.4514126
H	-0.7673866	-0.5656032	-6.2895777	H	1.4699505	-0.9499067	5.4204727
H	-1.3765911	-0.5289254	-4.6530686	H	0.2676872	-0.3328304	6.5614355
H	0.0052846	-2.6128385	-4.1726797	H	1.2317904	0.7886879	5.6163965
H	0.2879539	-2.7324609	-5.9090707	H	-2.1111302	0.8801995	3.9078396
H	-1.5944857	-3.8278931	-5.5610259	H	-0.9012671	1.8804810	4.7089367
H	3.4790737	-5.5519050	-0.0210282	H	-1.8861065	0.7548238	5.6557099
H	1.7866368	-5.3808304	-0.3788417	H	-5.1101329	-2.1797404	-2.6703470
H	4.3252164	-3.8234692	-1.5543511	H	-4.8965949	-3.9281006	-2.8232534
H	3.5647943	-2.2557260	-1.6211869	H	-3.8930990	-2.8402920	-3.7740590
H	1.4880696	-3.3399564	-2.5494870	H	-1.5666116	-4.0263305	-1.0855719
H	2.3915357	-4.8452325	-2.6965481	H	-1.7984396	-3.9310115	-2.8361938
H	3.3396619	-2.4588878	-3.8733827	H	-2.7902791	-5.0302365	-1.8622619
H	1.6572107	-4.4340351	2.1223414	H	-4.0108769	-4.0395712	2.2994792
H	3.1066577	-5.4021780	2.3151966	H	-3.9269235	-3.0058334	3.7224762
H	0.5500188	-6.2581487	1.5959233	H	-2.5022193	5.1572920	-2.8220476
H	3.5953491	5.7272266	0.4730028	H	5.1723055	1.9576961	2.1349345
H	1.9333759	5.7774972	-0.0516458	H	0.0407758	-6.5732437	3.9778256
H	2.6041252	4.8275015	-2.2591898	H	-1.2725522	-6.0507625	6.2875859
H	4.2496636	4.6445562	-1.6893162				

8.1.2 Coordinates for (9[•])₂ in xyz-format

C	-3.8936910	-3.0593819	0.8301341	C	-7.0603958	-5.0944499	-0.4441218
C	-4.7076312	-2.0312016	0.3604217	C	-6.8580236	-6.5944346	-0.5017522
C	-4.2538562	-0.7014106	0.3185761	O	-6.5180191	-7.0027077	-1.8277042
C	-2.9596980	-0.4235122	0.8038267	C	-5.1500816	-4.2855640	-1.9793368
C	-2.1785854	-1.4317538	1.3828504	C	-6.0216348	-4.0719059	-3.2095239
C	-2.6264648	-2.7698175	1.3768260	O	-6.7746510	-2.8660460	-3.2446710
S	-4.5552399	-4.6892109	0.6789993	C	-7.9646900	0.4231058	2.3708455
S	-6.3125681	-2.4878821	-0.1996784	C	-6.6957868	0.2365277	1.8140127
S	-0.6404322	-0.8935977	2.0444910	C	-6.4419892	0.4956083	0.4441687
S	-2.2835887	1.1990422	0.7869996	C	-7.5363028	0.9134116	-0.3466331
C	-5.8217345	-4.2213794	-0.6115940	C	-8.8089988	1.0394997	0.1945435
C	-1.0903949	0.8920567	2.1683750	C	-9.0650843	0.7595071	1.5514775
C	0.2062325	1.6562876	1.9355244	S	-8.1116930	0.1732678	4.1093300
C	-1.8022589	1.2376556	3.4742436	S	-5.4407074	-0.3484951	2.8974896
C	-1.0233866	1.0956550	4.7758208	S	-10.0329311	1.6036524	-0.9732293
O	-0.9406597	-0.2461812	5.2603496	S	-7.4077125	1.1911794	-2.0876534
C	0.1173095	3.1668107	1.9813561	C	-6.2781326	0.1194963	4.4586050
O	-0.7661439	3.7165485	1.0142404	C	-9.1945508	0.7933528	-2.4083570

C	-9.5547687	1.5236936	-3.6960071	O	-11.5131628	0.7424468	1.4049605
C	-9.3702870	-0.7380910	-2.4597885	H	0.6263142	1.3412339	0.9823911
C	-10.5545550	-1.3769322	-1.7762646	H	0.9192754	1.3439572	2.6942462
O	-11.7976133	-0.9943350	-2.3837031	H	-2.7174592	0.6518587	3.5370583
C	-10.9680978	1.3079407	-4.2124298	H	-2.1304577	2.2746795	3.3897703
O	-11.9556352	1.6708882	-3.2631392	H	-1.5006268	1.7299121	5.5273316
C	-6.0438617	-0.9941819	5.4859210	H	-0.0002780	1.4441698	4.6749989
C	-4.6231413	-1.5112826	5.6549221	H	-1.8255664	-0.4931392	5.5744166
O	-3.6706974	-0.5580687	6.1447712	H	1.1266652	3.5696271	1.8609711
C	-5.8016526	1.4799370	4.9628773	H	-0.2379626	3.5154665	2.9480622
C	-5.9321881	2.6346423	3.9888767	H	-0.5526271	3.3492444	0.1440337
O	-5.4073296	3.8500203	4.5286270	H	-7.7959046	-4.8061302	-1.1954299
C	-3.2001373	1.7463765	-3.0295172	H	-7.4960064	-4.8687541	0.5278725
C	-3.9171584	0.8706724	-2.2222854	H	-7.7922255	-7.0700812	-0.1870123
C	-4.6209282	1.3206630	-1.0857907	H	-6.0828943	-6.8977980	0.2090244
C	-4.6935341	2.7163522	-0.8876693	H	-6.4284825	-7.9607908	-1.8273484
C	-3.9151543	3.5821439	-1.6687627	H	-4.7053097	-5.2740933	-2.0851614
C	-3.1128003	3.1051276	-2.7070801	H	-4.3249067	-3.5740230	-1.9770038
S	-2.4476645	1.0307549	-4.4654265	H	-6.7414158	-4.8805435	-3.3012696
S	-3.9706043	-0.8114462	-2.7593157	H	-5.3628919	-4.1391617	-4.0854947
S	-4.0761603	5.3015438	-1.3020658	H	-6.2135505	-2.1498088	-2.9110618
S	-5.6874304	3.4590495	0.3498891	H	-8.8575177	1.1897788	-4.4693050
C	-3.6361673	-0.3897912	-4.5294535	H	-9.3813349	2.5876372	-3.5462196
C	-4.7965253	5.0819101	0.3934112	H	-8.5019199	-1.2016651	-2.0016732
C	-5.8117523	6.1804493	0.6398994	H	-9.3392344	-1.0447564	-3.5047620
C	-3.7126344	5.0550400	1.4448275	H	-10.5567915	-1.1175683	-0.7169204
C	-2.9789377	-1.5676965	-5.2153385	H	-10.4299961	-2.4600952	-1.8536285
C	-4.9198181	0.0314481	-5.2145974	H	-12.5099501	-1.4093497	-1.8865103
C	-2.2222329	4.0358045	-3.4801776	H	-11.1064709	0.2734449	-4.5317999
C	-5.1338506	0.3657471	-0.1276349	H	-11.1057207	1.9382254	-5.0914354
N	-0.9192176	3.4781993	-3.7902256	H	-12.1405033	0.8585652	-2.7656668
C	-0.3397775	3.4958955	-5.0777766	H	-6.6433939	-1.8554817	5.1931185
C	1.0053370	2.8710551	-4.9315140	H	-6.4326432	-0.6619777	6.4518246
C	1.1857610	2.5455828	-3.6524804	H	-4.2255338	-1.8468340	4.6997426
C	-0.0215389	2.9431380	-2.8775562	H	-4.6483261	-2.3834322	6.3125596
O	-0.8653053	3.9466511	-6.0679519	H	-3.8893649	-0.3439335	7.0578694
O	-0.2040430	2.8374267	-1.6790302	H	-4.7574991	1.3934010	5.2558736
C	-1.8194984	-3.8909958	1.8712478	H	-6.3731399	1.7064088	5.8689105
O	-2.2643588	-5.0142263	2.0605191	H	-6.9703311	2.7656168	3.6778621
O	-0.5251972	-3.5882125	2.0520564	H	-5.3456959	2.4405410	3.0966733
C	-10.4120613	0.6881302	2.1752669	H	-5.9735129	4.1194175	5.2597678
O	-10.5470624	0.5237193	3.3734242	H	-6.2658872	6.0447065	1.6197646

H	-6.5923219	6.1827426	-0.1141861	C	4.3530341	2.2401973	0.7248711
H	-5.3181845	7.1508811	0.6407127	C	4.3070131	0.8248577	0.8730936
H	-4.1563996	4.8987470	2.4266007	C	3.7205878	0.3175538	2.0670016
H	-3.1808523	6.0064048	1.4515460	C	3.3989608	1.1747978	3.1258688
H	-2.9889957	4.2721897	1.2558973	C	3.5737324	2.5604308	3.0006448
H	-2.0606082	-1.8623551	-4.7176151	S	4.0892771	4.8207839	1.4227285
H	-2.7485234	-1.3173219	-6.2491146	S	4.8498983	3.0242833	-0.7776855
H	-3.6589578	-2.4173540	-5.2280139	S	2.7165844	0.4470046	4.5815396
H	-5.3752677	0.8737616	-4.7028614	S	3.3777822	-1.3788756	2.3367184
H	-5.6298800	-0.7943684	-5.2134596	C	3.9816966	4.6140909	-0.4211154
H	-4.7154355	0.3208929	-6.2443653	C	3.2098991	-1.2928439	4.1757057
H	-2.0928522	4.9590345	-2.9174692	C	2.0678112	-2.2505876	4.5176133
H	-2.6628968	4.2972251	-4.4423666	C	4.5142408	-1.6764785	4.8598916
H	-0.0142961	-4.4116338	2.1854873	C	5.7397563	-0.8765115	4.4784586
H	-11.2795512	0.8643130	0.4560407	O	6.8725616	-1.4890348	5.0926540
H	1.6762612	2.7413319	-5.7643399	C	1.7212340	-2.3735292	5.9936171
H	2.0366393	2.0859307	-3.1781376	O	1.3878933	-1.1406750	6.5975534
C	8.4096607	1.2813426	-0.7355450	C	4.7463445	5.7557582	-1.0765740
C	7.2196506	0.9817595	-0.0812103	C	4.9847105	5.6306725	-2.5792228
C	6.1289099	0.4259737	-0.7815124	O	3.8259583	5.4819422	-3.3792530
C	6.2594938	0.2943183	-2.1746804	C	2.5158533	4.4816874	-0.8238486
C	7.4582220	0.5739951	-2.8391749	C	1.6378721	5.6937483	-0.6073633
C	8.5741822	1.0390613	-2.1140023	O	1.8536260	6.6427490	-1.6720875
S	9.6515398	2.0046243	0.3138487	C	4.8728553	-3.7673213	-0.4396349
S	7.1764016	1.2802985	1.6532430	C	5.3280460	-2.4648828	-0.2309025
S	7.4475170	0.3685843	-4.5859918	C	4.4580456	-1.3724160	-0.3613357
S	4.8623099	-0.0620310	-3.1638986	C	3.1369448	-1.6393068	-0.7510285
C	9.0150020	1.2294056	1.8802580	C	2.6881551	-2.9496612	-0.9716653
C	5.8154017	-0.5283325	-4.6673324	C	3.5499307	-4.0354656	-0.7989476
C	6.0169036	-2.0407741	-4.7231880	S	6.1043332	-5.0330293	-0.2644313
C	5.0288799	-0.0559576	-5.8907268	S	7.0120084	-2.3005959	0.2608504
C	4.7778536	1.4419291	-6.0028051	S	0.9845002	-3.0854309	-1.4235993
O	3.7009195	1.7336764	-6.8964893	S	1.9741832	-0.3454452	-1.0003537
C	6.6897711	-2.6675606	-3.5224214	C	7.1399793	-4.0315926	0.8989302
O	6.6554897	-4.0843845	-3.6818804	C	0.8476936	-1.3591772	-2.0553879
C	9.3849084	2.1547428	3.0355980	C	-0.5710129	-0.8946320	-1.8673248
C	8.6505326	1.9114135	4.3457558	C	1.2974863	-1.3140635	-3.5012475
O	8.9113815	0.6481699	4.9645717	C	8.5791484	-4.4901915	0.8175745
C	9.4863562	-0.2151784	2.0070341	C	6.5763307	-4.1140432	2.3015741
C	10.9087553	-0.4309997	2.5012745	C	3.1795556	-5.4782234	-1.0310279
O	11.9127172	0.3500719	1.8662487	C	4.9199523	-0.0153320	-0.1037693
C	3.9996554	3.0838026	1.7675573	N	1.7787172	-5.8009797	-0.9780962

C	1.0223181	-6.1886377	-2.1041205	H	4.3718433	-1.5972588	5.9369299
C	-0.3585877	-6.4070182	-1.6014305	H	5.6231068	0.1558075	4.8183280
C	-0.3829657	-6.1858856	-0.2880897	H	5.8610156	-0.8576742	3.3939283
C	0.9851210	-5.7999159	0.1587070	H	7.5752272	-0.8256091	5.1285220
O	1.4587952	-6.3237361	-3.2227759	H	2.5599125	-2.7774954	6.5591177
O	1.3675304	-5.5328594	1.2861701	H	0.9025221	-3.0972768	6.0823824
C	9.8337771	1.2456185	-2.8748130	H	0.5660792	-0.8118957	6.1826069
O	9.8412507	1.3158578	-4.0861545	H	5.7253946	5.8309709	-0.6046741
O	11.0046971	1.3091351	-2.2091810	H	4.2181131	6.6859604	-0.8710425
C	3.2288699	3.4361256	4.1464862	H	5.6078507	4.7595444	-2.7831941
O	2.2560287	3.2774040	4.8445398	H	5.5638297	6.5093735	-2.8879220
O	4.0850610	4.4571185	4.4144014	H	3.1550409	6.0981043	-3.0493950
H	6.5910122	-2.2752624	-5.6216346	H	2.0884833	3.6461252	-0.2767086
H	5.0367741	-2.5069647	-4.8412096	H	2.4875989	4.2093619	-1.8745669
H	4.0595723	-0.5565416	-5.8747801	H	1.8478852	6.1562336	0.3598398
H	5.5424591	-0.4176227	-6.7839957	H	0.5958739	5.3778312	-0.5991280
H	5.6854431	1.9706177	-6.2966299	H	1.2398888	7.3738582	-1.5534721
H	4.4746792	1.8432539	-5.0399190	H	-0.6987601	0.1155019	-2.2400822
H	3.9904673	1.5446720	-7.7949637	H	-0.8575867	-0.9146931	-0.8251755
H	6.1590442	-2.3802053	-2.6180665	H	-1.2526059	-1.5286776	-2.4253098
H	7.7192155	-2.3101228	-3.4339149	H	2.3219829	-1.6591350	-3.6040547
H	6.7902014	-4.4687845	-2.8055669	H	1.2298547	-0.2976914	-3.8834255
H	9.1501880	3.1764664	2.7372779	H	0.6572675	-1.9534880	-4.1070706
H	10.4619674	2.1131250	3.1899039	H	9.1978613	-3.8806454	1.4738354
H	7.5745643	1.9425513	4.1856878	H	8.9660651	-4.4182942	-0.1946391
H	8.8906527	2.7227618	5.0354483	H	8.6644838	-5.5215368	1.1542180
H	9.7251130	0.7117728	5.4730595	H	5.5413132	-3.7865196	2.3218256
H	9.3379694	-0.7002035	1.0433220	H	7.1425474	-3.4755478	2.9773081
H	8.8257671	-0.7276989	2.7048122	H	6.6228806	-5.1396442	2.6648227
H	11.1365891	-1.5001371	2.4268353	H	3.7062296	-6.0883119	-0.2981488
H	10.9748947	-0.1729793	3.5547079	H	3.5216779	-5.7905719	-2.0180235
H	11.8825050	0.1730305	0.9198203	H	10.8552958	1.2797253	-1.2408027
H	2.3379547	-3.2433860	4.1478192	H	4.8555411	4.4129332	3.8296794
H	1.1821422	-1.9409421	3.9692696	H	-1.1612756	-6.7050240	-2.2538034
H	4.7103727	-2.7283807	4.6417264	H	-1.2086577	-6.2445693	0.40046

8.2 Ketone **17**

Using the functional PBE0^[20] in a def2-TZVP^[21]-basis set as implemented in ORCA, structure optimization was carried out for ketone **17** with the results shown in Figures S70 and S71.

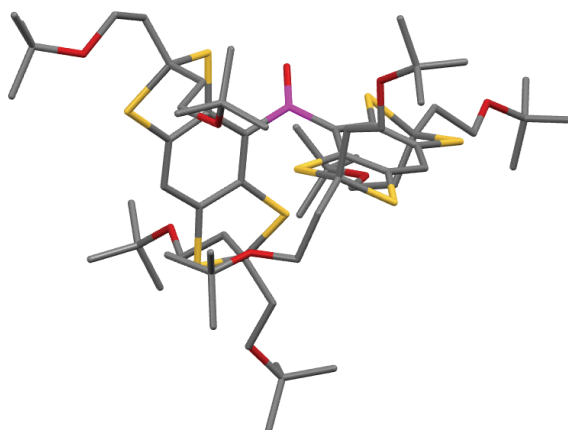


Figure S70: DFT optimized structure of ketone **17** with the carbonyl carbon atom highlighted in purple. View along the Bürgi-Dunitz trajectory. Hydrogen atoms were omitted for the sake of clarity.

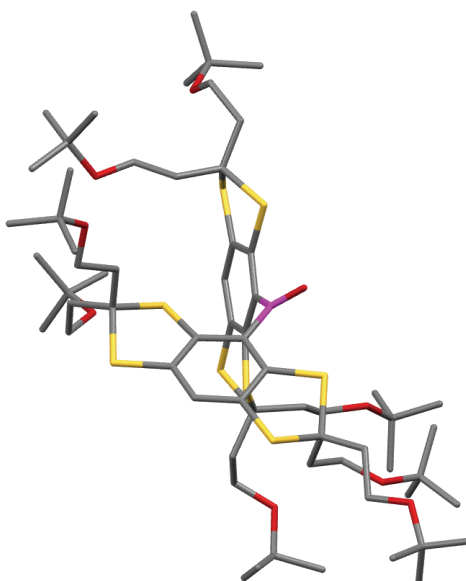


Figure S71: DFT optimized structure of ketone **17** with the carbonyl carbon atom highlighted in purple, sideview. Hydrogen atoms were omitted for the sake of clarity.

8.2.1 Coordinates for 17 in xyz-format

C	-1.5401940	-1.1908634	-1.7527480	C	0.3840497	4.0406194	1.1377207
C	-1.9758575	-2.3983075	-1.2012024	S	-1.8801500	3.2965016	2.5535714
C	-1.2629327	-2.9971456	-0.1718917	C	-3.1061511	2.1556856	1.7559891
C	-0.1602437	-2.3491369	0.3670176	S	-2.0937481	0.9237364	0.8183265
C	0.2001233	-1.0768192	-0.0851606	S	2.3959538	2.6856746	-2.0335005
C	-0.4781491	-0.5003321	-1.1643035	C	3.6867074	3.4703460	-0.9618372
S	-2.4528852	-0.6097434	-3.1394871	S	2.7768266	4.8253809	-0.0646506
C	-4.0146107	-1.4894271	-2.6416766	C	-3.9855575	2.8931957	0.7522793
S	-3.4387005	-3.0961644	-1.9025299	C	-3.9270649	1.4589794	2.8384592
S	0.7840741	-2.9955940	1.7118124	C	-3.2009684	0.4356187	3.6993074
C	2.2389823	-1.8794974	1.4121585	O	-3.0936830	-0.8232059	3.0553177
S	1.4990927	-0.2855722	0.8108895	C	-4.8814010	3.9721188	1.3234705
C	-4.7396625	-0.6071120	-1.6231324	O	-5.7006203	4.4127300	0.2538540
C	-4.7609169	-1.7413885	-3.9498430	C	4.7363803	4.0628306	-1.8860349
C	-6.1648399	-2.3032132	-3.8382592	C	5.8815846	4.7586872	-1.1828512
O	-6.2223815	-3.4451983	-3.0018438	O	6.7488891	5.2229515	-2.2009642
C	-5.8211247	-1.2301508	-0.7524972	C	4.1985821	2.4789000	0.0885317
O	-6.2722298	-0.2617831	0.1958188	C	4.8086702	1.1892763	-0.4172521
C	2.9029525	-1.5258730	2.7397292	O	6.0596496	1.4611094	-1.0196574
C	3.6369563	-2.6292248	3.4919895	C	7.9259183	5.9509209	-1.7960672
O	4.9774599	-2.8091351	3.0568340	C	8.7694615	5.1447903	-0.8145807
C	3.1444735	-2.4012064	0.3024023	C	7.5443398	7.3027196	-1.2020808
C	3.6631985	-3.8219360	0.3904150	C	8.6845303	6.1470123	-3.0990208
O	4.4155953	-4.0142976	-0.8010867	C	6.7014197	0.3903448	-1.7473717
C	6.0422939	-2.3101655	3.9010128	C	7.9919173	1.0276834	-2.2361902
C	7.2981875	-2.5952629	3.0955419	C	7.0044800	-0.7856725	-0.8261195
C	5.9073515	-0.8117092	4.1446736	C	5.8504790	-0.0546035	-2.9307193
C	6.0796329	-3.0752590	5.2189856	C	-3.9305608	-1.9054412	3.5171415
C	-6.4577218	-4.7384809	-3.6080308	C	-3.5305943	-2.3148138	4.9301842
C	-7.8678566	-4.7959195	-4.1829254	C	-3.6149847	-3.0283046	2.5434040
C	-6.3245458	-5.7047686	-2.4430771	C	-5.4113284	-1.5505918	3.4464358
C	-5.4152646	-5.0519478	-4.6735748	C	-6.4348770	5.6422266	0.4350913
C	-7.6268127	0.2213552	0.0666718	C	-7.2501157	5.6198928	1.7220103
C	-7.7591099	1.2518025	1.1765980	C	-5.4841978	6.8336042	0.4136974
C	-8.6224403	-0.9126526	0.2872517	C	-7.3580236	5.6855940	-0.7716640
C	-7.8439416	0.8932976	-1.2839035	C	-0.0836696	0.8357121	-1.6654439
C	-0.6908903	3.1709715	1.2558737	O	0.0933731	1.0425816	-2.8570526
C	-0.8219397	2.0728176	0.3968897	C	5.2684686	-5.1733041	-0.8677069
C	0.0877164	1.9096921	-0.6614368	C	4.4740711	-6.4545275	-0.6452512
C	1.1521200	2.8103501	-0.7944109	C	5.8154865	-5.1302450	-2.2856276
C	1.3227036	3.8408437	0.1345195	C	6.4089191	-5.0593792	0.1386228

H	-1.5790646	-3.9527444	0.2222976	H	-8.8469664	1.3141727	-1.3411429
H	-5.1531380	0.2444063	-2.1660970	H	-7.7407353	0.1904928	-2.1091398
H	-3.9982989	-0.1935594	-0.9437329	H	0.5046475	4.8546241	1.8394255
H	-4.1470745	-2.3927764	-4.5681190	H	-4.6101755	2.1450997	0.2624322
H	-4.8384787	-0.7852321	-4.4757800	H	-3.3580802	3.3335973	-0.0206112
H	-6.5343463	-2.5152100	-4.8423693	H	-4.7698135	0.9749012	2.3493450
H	-6.8382213	-1.5533404	-3.4193445	H	-4.3474102	2.2311782	3.4854893
H	-5.4043360	-2.0688618	-0.1975713	H	-3.7128461	0.3512281	4.6588597
H	-6.6459838	-1.6292393	-1.3318997	H	-2.1878856	0.7815617	3.9092618
H	2.1262359	-1.1181634	3.3859786	H	-4.2727023	4.7808736	1.7345732
H	3.6109187	-0.7192504	2.5528346	H	-5.4990382	3.5779861	2.1358133
H	3.1228440	-3.5849676	3.3677359	H	4.2538074	4.7641377	-2.5641305
H	3.5996932	-2.4028249	4.5571065	H	5.1556995	3.2567197	-2.4835557
H	3.9938059	-1.7230121	0.2341131	H	6.3956107	4.0583739	-0.5247519
H	2.6082991	-2.3173973	-0.6417294	H	5.5029462	5.5868988	-0.5723474
H	4.2859257	-3.9601800	1.2703538	H	3.3577245	2.2045010	0.7239052
H	2.8244556	-4.5205776	0.4407173	H	4.9128121	2.9930952	0.7313839
H	7.2518914	-2.0937692	2.1318144	H	4.1165019	0.7086727	-1.1098038
H	7.4048142	-3.6627126	2.9172806	H	4.9277583	0.5141199	0.4394694
H	8.1812656	-2.2443939	3.6262955	H	8.2958362	5.0602551	0.1617393
H	5.8965034	-0.2692772	3.2009995	H	9.7339891	5.6277907	-0.6656287
H	6.7492224	-0.4489470	4.7323018	H	8.9442662	4.1415262	-1.1989034
H	4.9998074	-0.5671079	4.6940470	H	7.0237963	7.1996619	-0.2517193
H	6.1262463	-4.1461740	5.0307542	H	6.8992646	7.8473469	-1.8892169
H	5.2062915	-2.8731437	5.8368401	H	8.4352017	7.9024188	-1.0200931
H	6.9563638	-2.7908805	5.7992013	H	8.9600227	5.1842080	-3.5251627
H	-8.5976500	-4.5407569	-3.4165634	H	9.5912257	6.7269820	-2.9359340
H	-8.0900513	-5.7977777	-4.5475048	H	8.0627784	6.6723196	-3.8212781
H	-7.9971192	-4.1108685	-5.0196599	H	8.5992490	1.3498750	-1.3919079
H	-7.0421080	-5.4589717	-1.6628213	H	7.7741420	1.9000886	-2.8493449
H	-5.3262624	-5.6488738	-2.0158789	H	8.5705488	0.3219272	-2.8293303
H	-6.5068732	-6.7265785	-2.7710810	H	7.5175822	-0.4388781	0.0698245
H	-5.4949656	-4.3860250	-5.5315219	H	7.6496248	-1.5035248	-1.3305385
H	-5.5502787	-6.0678244	-5.0418389	H	6.1047145	-1.3207843	-0.5309691
H	-4.4120639	-4.9670081	-4.2620789	H	5.5744259	0.8001543	-3.5456235
H	-7.5352782	0.8026823	2.1420359	H	4.9411064	-0.5616935	-2.6171995
H	-8.7729811	1.6470755	1.2093893	H	6.4085633	-0.7546269	-3.5503687
H	-7.0779388	2.0818907	1.0090255	H	-2.4654769	-2.5353802	4.9677233
H	-8.4373694	-1.3944189	1.2458904	H	-4.0790720	-3.2041176	5.2386303
H	-8.5604507	-1.6705333	-0.4914954	H	-3.7455458	-1.5331980	5.6572396
H	-9.6420745	-0.5295624	0.2869781	H	-2.5536995	-3.2643256	2.5805064
H	-7.1285927	1.7010745	-1.4225644	H	-3.8603079	-2.7300436	1.5269045

H	-4.1826911	-3.9240554	2.7902642	H	-6.7773501	5.6466118	-1.6911582
H	-5.6723719	-0.7598426	4.1492877	H	-7.9484123	6.6001376	-0.7742022
H	-6.0163559	-2.4195801	3.7028575	H	3.6237024	-6.4990340	-1.3240694
H	-5.6837948	-1.2269720	2.4445911	H	4.1028300	-6.5289330	0.3753607
H	-6.6158093	5.6454187	2.6063785	H	5.1016119	-7.3256058	-0.8279106
H	-7.8715479	4.7268906	1.7670774	H	5.0035982	-5.1916231	-3.0074644
H	-7.9034740	6.4898818	1.7657773	H	6.5010525	-5.9573298	-2.4624591
H	-4.8163767	6.8384279	1.2732056	H	6.3487712	-4.1966282	-2.4548408
H	-6.0435940	7.7680762	0.4326256	H	6.0528870	-5.1137087	1.1649888
H	-4.8785136	6.8144563	-0.4901023	H	6.9286228	-4.1115901	0.0114546
H	-8.0363472	4.8343663	-0.7617914	H	7.1257641	-5.8669440	-0.0038681

9. References

- (1) Fulmer, G. R.; Miller, A. J. M.; Sherden, N. H.; Gottlieb, H. E.; Nudelman, A.; Stoltz, B. M.; Bercaw, J. E.; Goldberg, K. I.; Gan, R.; Apiezon, H., *Organometallics* **2010**, *29*, 2176–2179.
- (2) Winkle, M.; Lansinger, J.; Ronald, R. C., *J. Chem. Soc. Chem. Commun.* **1980**, 87–88.
- (3) Kopp, K.; Schiemann, O.; Fleck, N., *Molecules* **2020**, *25*, 3666.
- (4) Hintz, H.; Vanas, A.; Klose, D.; Jeschke, G.; Godt, A., *J. Org. Chem.* **2019**, *84*, 3304–3320.
- (5) Poncelet, M.; Huffman, J. L.; Khramtsov, V. V.; Dhimitruka, I.; Driesschaert, B., *RSC Adv.* **2019**, *9*, 35073–35076.
- (6) Graham, B.; Fayter, A. E. R.; Houston, J. E.; Evans, R. C.; Gibson, M. I., *J. Am. Chem. Soc.* **2018**, *140*, 5682–5685.
- (7) Wessig, P.; Freyse, D.; Schuster, D.; Kelling, A., *Eur. J. Org. Chem.* **2020**, *2020*, 1732–1744.
- (8) Fleck, N.; Heubach, C. A.; Hett, T.; Haege, F. R.; Bawol, P. P.; Baltruschat, H.; Schiemann, O., *Angew. Chem. Int. Ed.* **2020**, *59*, 9767–9772.
- (9) Trasak, C.; Zenner, G.; Vogel, A.; Yüksesdag, G.; Rost, R.; Haase, I.; Fischer, M.; Israel, L.; Imhof, A.; Linder, S.; Schleicher, M.; Aepfelbacher, M., *J. Biol. Chem.* **2007**, *282*, 2268–2277.
- (10) Stoll, S.; Schweiger, A., *J. Magn. Reson.* **2006**, *178*, 42–55.
- (11) Karthikeyan, G.; Bonucci, A.; Casano, G.; Gerbaud, G.; Abel, S.; Thomé, V.; Kodjabachian, L.; Magalon, A.; Guigliarelli, B.; Belle, V.; Ouari, O.; Mileo, E., *Angew. Chem. Int. Ed.* **2018**, *57*, 1366–1370.
- (12) Borbat, P. P.; Freed, J. H., *Chem. Phys. Lett.* **1999**, *313*, 145–154.
- (13) Saxena, S.; Freed, J. H., *J. Chem. Phys.* **1997**, *107*, 1317–1340.
- (14) Akhmetzhanov, D.; Schöps, P.; Marko, A.; Kunjir, N. C.; Sigurdsson, S. T.; Prisner, T. F., *Phys. Chem. Chem. Phys.* **2015**, *17*, 24446–24451.
- (15) Jeschke, G.; Chechik, V.; Ionita, P.; Godt, A.; Zimmermann, H.; Banham, J.; Timmel, C.; Hilger, D.; Jung, H., *Appl. Magn. Reson.* **2006**, *30*, 473–498.
- (16) Abdullin, D.; Brehm, P.; Fleck, N.; Spicher, S.; Grimme, S.; Schiemann, O., *Chem. Eur. J.* **2019**, *25*, 14388–14398.
- (17) <https://github.com/dinarabdullin/SnrCalculator>
- (18) Pracht, P.; Bohle, F.; Grimme, S., *Phys. Chem. Chem. Phys.* **2020**, *22*, 7169–7192.
- (19) Spicher, S.; Grimme, S., *Angew. Chem. Int. Ed.* **2020**, *59*, 15665–15673.
- (20) Brandenburg, J. G.; Bannwarth, C.; Hansen, A.; Grimme, S., *J. Chem. Phys.* **2018**, *148*, 64104.
- (21) Perdew, J. P.; Ernzerhof, M.; Burke, K., *J. Chem. Phys.* **1996**, *105*, 9982–9985.
- (22) Schäfer, A.; Huber, C.; Ahlrichs, R., *J. Chem. Phys.* **1994**, *100*, 5829–5835.

- (23) Caldeweyher, E.; Ehlert, S.; Hansen, A.; Neugebauer, H.; Spicher, S.; Bannwarth, C.; Grimme, S., *J. Chem. Phys.* **2019**, *150*, 154122.
- (24) Klamt, A., *J. Phys. Chem.* **1995**, *99*, 2224–2235.
- (25) Klamt, A.; Jonas, V.; Bürger, T.; Lohrenz, J. C. W., *J. Phys. Chem. A* **1998**, *102*, 5074–5085.
- (26) Eckert, F.; Klamt, A., *AIChE J.* **2002**, *48*, 369–385.
- (27) Bannwarth, C.; Ehlert, S.; Grimme, S., *J. Chem. Theory Comput.* **2019**, *15*, 1652–1671.
- (28) Grimme, S., *Chem. - A Eur. J.* **2012**, *18*, 9955–9964.
- (29) Furche, F.; Ahlrichs, R.; Hättig, C.; Klopper, W.; Sierka, M.; Weigend, F., *Wiley Interdiscip. Rev. Comput. Mol. Sci.* **2014**, *4*, 91–100.
- (30) Grimme, S.; Bannwarth, C.; Shushkov, P., *J. Chem. Theory Comput.* **2017**, *13*, 1989–2009.
- (31) Eichkorn, K.; Treutler, O.; Öhm, H.; Häser, M.; Ahlrichs, R., *Chem. Phys. Lett.* **1995**, *240*, 283–290.
- (32) Weigend, F., *Phys. Chem. Chem. Phys.* **2006**, *8*, 1057–1065.

[A7]: Synthesis of μ_2 -Oxo-Bridged Iron(III) Tetraphenylporphyrin–Spacer–Nitroxide Dimers and their Structural and Dynamics Characterization by using EPR and MD Simulations

Reprinted with permission from

Dinar Abdullin, Nico Fleck, Christoph Klein, Philipp Brehm, Sebastian Spicher, Arne Lützen, Stefan Grimme, Olav Schiemann*, *Chem. Eur. J.* **2019**, *25*, 2586 – 2596.

Published by Wiley-VCH (Weinheim, DE), ©**2019** Wiley-VCH Verlag GmbH & Co. KGaA

Contributions:

- Experimental Work:
 - Organic synthesis incl. compound characterization
 - Parts of cw-EPR spectroscopy
- Writing of the manuscript in parts

Step Motors | Hot Paper |

 Synthesis of μ_2 -Oxo-Bridged Iron(III) Tetraphenylporphyrin-Spacer-Nitroxide Dimers and their Structural and Dynamics Characterization by using EPR and MD SimulationsDinar Abdullin,^{+, [a]} Nico Fleck,^{+, [a]} Christoph Klein,^[a, b] Philipp Brehm,^[a] Sebastian Spicher,^[c] Arne Lützen,^[b] Stefan Grimme,^[c] and Olav Schiemann^{*, [a]}

Abstract: Iron(III) porphyrins have the propensity to form μ_2 -oxo-dimers, the structures of which resemble two wheels on an axle. Whereas their crystal structure is known, their solution structure and internal dynamics is not. In the present work, the structure and dynamics of such dimers were studied by means of electron paramagnetic resonance (EPR) spectroscopy and quantum chemistry based molecular dynamics (MD) simulations by using the semiempirical tight-binding method (GFN-xTB). To enable EPR investigation of the dimers, a nitroxide was attached to each of the tetraphenylporphyrin cores through a linear and a bent linker. The inter-nitroxide distance distributions within the dimers were determined by continuous-wave (cw)-EPR and pulsed elec-

tron-electron double resonance (PELDOR or DEER) experiments and, with the help of MD, interpreted in terms of the rotation of the porphyrin planes with respect to each other around the Fe–O–Fe axis. It was found that such rotation is restricted to the four registers defined by the phenyl substituents. Within the registers, the rotation angle swings between 30° and 60° in the proximal and between 125° and 145° in the distal register. With EPR, all four angles were found to be equally populated, whereas the 30° and 145° angles are strongly favored to the expense of the 60° and 125° angles in the MD simulation. In either case, the internal dynamics of these dimers thus resemble the motion of a step motor.

Introduction

Porphyrins are heterocyclic organic compounds that display a large variability of molecular structures and physicochemical properties.^[1,2] The variability of porphyrin structures is achieved in several different ways, for instance, by metalation of the macrocycle core, alteration of peripheral substituents, or linkage of multiple macrocycles together. This provides a large playground for designing new materials with desired properties and, hence, causes tremendous interest for porphyrins in different fields of natural sciences and chemical engineering.^[2] The most common porphyrins include tetraphenylporphyrin (TPP) and octaethylporphyrin (OEP). Both have a singlet ground spin state, but can be photoexcited to a paramagnetic

triplet spin state.^[3] This allows such porphyrins to be studied by time-resolved electron paramagnetic resonance (EPR) techniques^[4] and even to be considered for the role of spin labels for biomolecules.^[5] Furthermore, the porphyrin core can also host a number of different metal ions, such as Mg²⁺, Zn²⁺, Cu²⁺, Mn²⁺/Mn³⁺, Fe²⁺/Fe³⁺, or Co²⁺/Co³⁺.^[2] As several of these ions are paramagnetic, the corresponding metalloporphyrins can be studied by EPR.^[6] For instance, the EPR studies on iron porphyrins and their biological counterparts, known as hemes, has helped a lot in understanding the biological processes taking place in hemoproteins.^[7] Because of the increasing importance of pulsed EPR techniques for distance measurements in structural biology,^[8] metalloporphyrins^[9–14] or other metal complexes^[15–18] are also used as model systems to test such distance measurements to metal centers.



Previous studies on iron porphyrins revealed their interesting tendency to form dimeric species, in which the iron ions in two TPP rings are connected with each other through an oxygen atom.^[14,19–21] This phenomenon is usually called μ_2 -oxo-dimerization. Many previous publications have dealt with the identification and structural characterization of such μ_2 -oxo-bridged Fe³⁺ porphyrins owing to their interesting physicochemical properties, such as their catalytic activity in oxidizing alkanes.^[22,23] In some cases, the dimerization process was found to be reversible: treating the monomeric porphyrins with an aqueous basic solution resulted in formation of μ_2 -oxo-bridged dimers, whereas the analogous treatment of the

[a] Dr. D. Abdullin,⁺ N. Fleck,⁺ C. Klein, P. Brehm, Prof. Dr. O. Schiemann
Institute of Physical and Theoretical Chemistry
University of Bonn, Wegelestr. 12, 53115 Bonn (Germany)
E-mail: schiemann@pc.uni-bonn.de

[b] C. Klein, Prof. Dr. A. Lützen
Kekulé Institute of Organic Chemistry and Biochemistry
Gerhard-Domagk-Str. 1, 53121 Bonn (Germany)

[c] S. Spicher, Prof. Dr. S. Grimme
Mulliken Center for Theoretical Chemistry
University of Bonn, Beringstr. 4, 53115 Bonn (Germany)

[*] These authors contributed equally to this work.

 Supporting information and the ORCID identification number(s) for the author(s) of this article can be found under:
 <https://doi.org/10.1002/chem.201805016>

dimers with an aqueous acidic solution led to the breakup into monomeric species.^[14] The presence of μ_2 -oxo-bridged dimers in solution was proven by several methods, for example, electrospray ionization (ESI) mass spectrometry^[23–25] and ultraviolet-visible (UV/Vis) spectroscopy.^[26] The UV/Vis spectra of Fe^{3+} porphyrins contain a Soret band, which corresponds to electronic transitions within the porphyrin, as well as several Q bands, which originate from charge transfer between the porphyrin and the Fe^{3+} ion. Upon μ_2 -oxo dimerization, a characteristic shift of the Soret band towards lower wavelengths as well as significant changes within the Q bands occur. These changes cause the observable difference in the color of the monomeric (green) and dimeric (red) Fe^{3+} porphyrins dissolved in organic solvents. Crystallographic studies on μ_2 -oxo-bridged FeTPPs revealed that the two TPP cores are almost coplanar, that the dihedral angle between them is only 3.7° , and that they form a staggered configuration with a twist angle of 54.6° .^[27] The two Fe–O bonds are 1.763 Å long and form an almost linear bridge between the porphyrins with an Fe–O–Fe angle of 174° . Although this crystallographic data provides a clear picture of the static molecular structure of μ_2 -oxo-bridged FeTPPs, its structure and dynamics in solution is unclear.

In the present study, the synthesis of two differently bridged Fe^{III} TPP/nitroxide pairs **1-Cl** and **2-Cl** (Figure 1) is described and their μ_2 -oxo-dimerization is confirmed. Different molecular linkers were used for the two porphyrins with the aim of disentangling the effect of these linkers on the dynamics of the μ_2 -oxo-bridged TPP cores. The TPP rotamer dynamics within the dimers in solution is unraveled by using a combination of EPR spectroscopy and molecular dynamics (MD) simulations based

on the semiempirical tight-binding method GFN-xTB.^[28] These data show that such dimers may be regarded as molecular step motors.

Results and Discussion

Synthesis

The linkage of the FeTPPCL to a nitroxide through a connecting bridge was achieved by two alternative synthetic routes depicted in Figure 1. The concept of click chemistry^[29] was used to synthesize compound **1-Cl**, whereas Sonogashira–Hagihara coupling^[9] was adopted to obtain compound **2-Cl**. Both syntheses make use of porphyrin **3** as a precursor, which was obtained in accordance with previous publications.^[30–33] For compound **1-Cl**, zinc porphyrin **4** was generated by treating porphyrin **3** with zinc acetate. This step allows the incorporation of Cu^{2+} into the porphyrin core to be avoided during the click reaction performed later on. Next, the copper(I)-catalyzed azide alkyne cycloaddition (CuAAC)^[34] reaction of **4** with 4-azido-4'-hydroxybiphenyl, obtained from 4-iodo-4'-hydroxybiphenyl by an Ullmann-type reaction,^[35] was carried out to yield porphyrin **5**. Note that it was also possible to perform these two subsequent reactions in one pot starting from 4-iodo-4'-hydroxybiphenyl and generating the azide in situ by using CuI in DMSO as the copper(I) source for the Ullmann step. Subsequently, the zinc ion of **5** was removed by hydrochloric acid, which resulted in porphyrin **6**. The Fe^{3+} -chlorido center was incorporated into **6** by reaction with Fe^{2+} -chloride. This reaction was carried out in THF in the presence of oxygen. Note that these conditions are much milder than the ones proposed by Adler et al.,^[36] who used DMF at 150°C as a solvent. The obtained iron porphyrin **7** was then used for Mukaiyama esterification^[37] with 2,2,5,5-tetramethyl-3-pyrrolin-oxyl-3-carboxylic acid, which provided the final compound **1-Cl**. An overall yield of 9% was achieved for **1-Cl** starting from **3**. For compound **2-Cl**, a more divergent approach was realized. First, Sonogashira–Hagihara coupling of **3** with the nitroxide-labeled biphenyl **8**^[9,10] was carried out to provide porphyrin **9**. Finally, the Fe^{3+} ion was introduced into **9** by the same procedure as described above for compound **7**. This gave an overall yield of 6% for porphyrin **2-Cl**. The μ_2 -oxo-bridged dimers **1₂O** and **2₂O** were obtained upon treatment with aqueous sodium hydroxide (see Experimental Section for details). The reversibility of the dimerization process was tested by treatment of these dimers with aqueous hydrochloric acid, which yielded the monomeric porphyrins **1-Cl** and **2-Cl** again. Both monomers **1-Cl** and **2-Cl** as well as dimers **1₂O** and **2₂O** were analyzed by mass spectrometry, UV/Vis, and EPR spectroscopy.

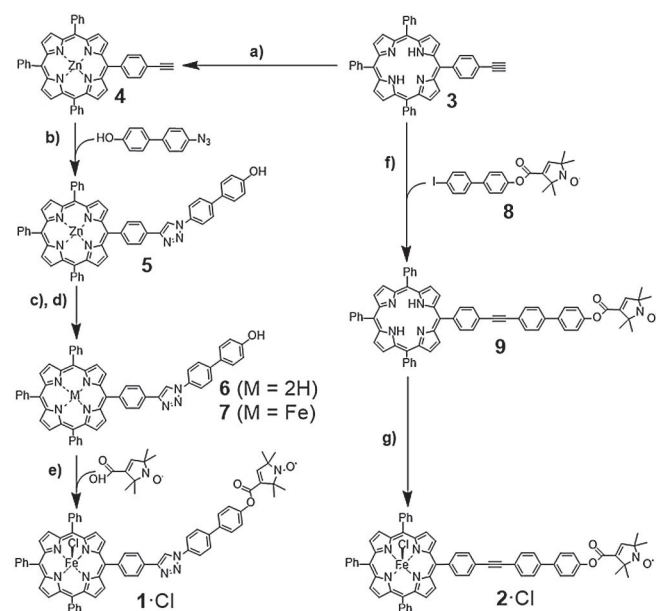


Figure 1. Synthesis of model compounds **1-Cl** and **2-Cl**. a) $\text{Zn}(\text{OAc})_2$, $\text{CH}_2\text{Cl}_2/\text{MeOH}$ (1:1), r.t., 16 h, quant. b) 4-Hydroxy-4'-azidobiphenyl, CuSO_4 , sodium ascorbate, $\text{DMSO}/\text{H}_2\text{O}$ (10:1), 70°C , 72 h, 95%. c) HCl , CH_2Cl_2 , r.t., 5 min, 93%. d) FeCl_2 , THF, 80°C , 2 h, 66%. e) 2,2,5,5-Tetramethyl-3-pyrrolin-1-oxyl-3-carboxylic acid, CMPI (2-chloro-1-methylpyridinium iodide), DMAP, Et_3N , CH_2Cl_2 , r.t., 18 h, 78%. f) $[\text{Pd}(\text{PPh}_3)_4]$, Et_3N , 70°C , 4 h, 59%. g) FeCl_2 , THF, 70°C , 2 h, 91%.

Mass spectrometry

The MALDI mass spectra of compounds **1-Cl** and **2-Cl** revealed that they undergo partial dimerization during or after the synthesis, probably upon exposure to air moisture. However, significant dimerization of **1-Cl** and **2-Cl** could be detected only after base treatment. The MALDI mass spectra of the base-

treated porphyrins are depicted in Figure 2. These spectra display intense peaks at $m/z=2154.6$ for $1_2\cdot\text{O}$ and $m/z=2068.6$ for $2_2\cdot\text{O}$, respectively. The peaks correspond to the dimers of **1-Cl** and **2-Cl** in which the Fe^{3+} ions lost their chloride ligands and are bridged to each other through an oxygen atom. In addition, both spectra contain two minor peaks, which appear at $m/z=1069.3$ and 1104.3 in the case of the sample derived from **1-Cl** and at $m/z=1026.3$ and 1061.3 in that derived from **2-Cl**. These peaks are assigned to the monomeric porphyrins with and without the chloride atom occurring as $[\text{M}]^+$ and $[\text{M}-\text{Cl}]^+$, respectively. Each of the MALDI mass spectra of the acid-treated samples of the dimeric porphyrins shows only the two peaks of the corresponding monomeric porphyrins listed above but no peaks of the μ_2 -oxo-bridged dimers. Although MALDI mass spectra do not provide a quantitative estimate for the relative amount of detected species, it seems that the acid treatment leads to quantitative conversion into monomers, whereas the base treatment forms dimers but monomers can still be detected. An additional peak at $m/z=2133.7$ for $2_2\cdot\text{O}$ can be assigned to a reduced adduct with H_2O and Na^+ , which has the composition $[(2-\text{Cl})_2\cdot\text{O} + 4\text{H}_2\text{O} + \text{Na}]^+$.

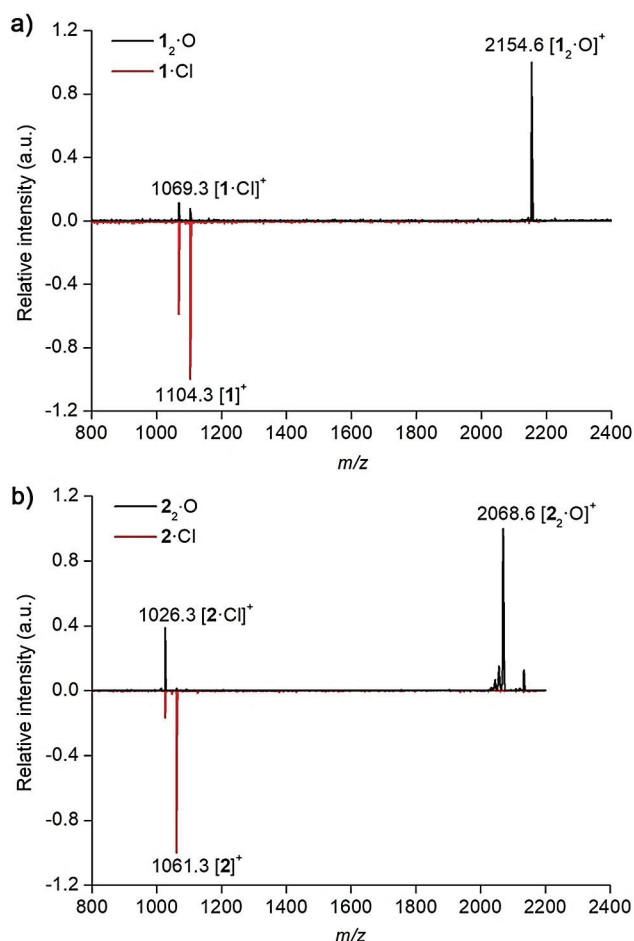


Figure 2. MALDI mass spectra of a) μ_2 -oxo-bridged dimer $1_2\cdot\text{O}$ (black) and monomer **1-Cl** (red) and b) μ_2 -oxo-bridged dimer $2_2\cdot\text{O}$ (black) and monomer **2-Cl** (red). For the sake of comparison, the spectra of **1-Cl** and **2-Cl** are plotted inverted.

UV/Vis spectroscopy

As a means of reference, UV/Vis spectra of the monomers **1-Cl** and **2-Cl** were measured first (Figure 3). Both spectra display a Soret band at 422 nm and Q-bands at 372, 508, 573, and 689 nm. These values are in agreement with those found earlier for the $\text{Fe}(\text{TPP})\text{Cl}$ complex dissolved in toluene.^[38] The UV/Vis spectra of the dimers $1_2\cdot\text{O}$ and $2_2\cdot\text{O}$ show the expected shift of the Soret band to shorter wavelengths, 415 nm for $1_2\cdot\text{O}$ and 413 nm for $2_2\cdot\text{O}$, and the expected change in the Q-bands, showing now only two bands at 571 and 612 nm in the $1_2\cdot\text{O}$ sample and at 573 and 613 nm in the $2_2\cdot\text{O}$ sample. Such differences were previously reported in the literature and were assigned to μ_2 -oxo-dimerization of Fe^{3+} porphyrins.^[26,39] Note that these changes in the Q-bands lead to the noticeable difference of the color of their solutions. The toluene solutions of dimeric porphyrins $1_2\cdot\text{O}$ and $2_2\cdot\text{O}$ feature a greenish color, whereas their monomeric counterparts have a reddish color.

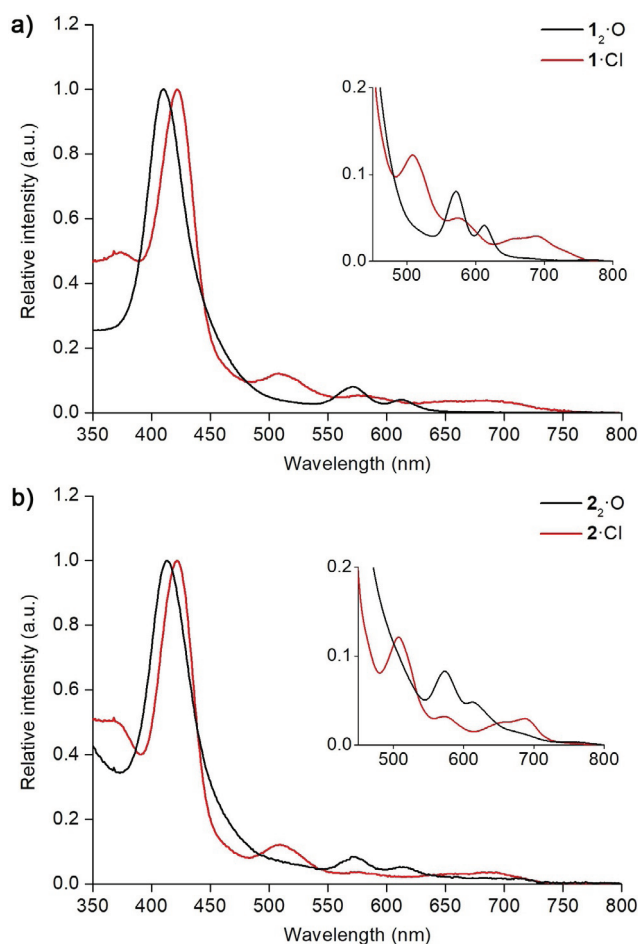


Figure 3. UV/Vis spectra of a) $1_2\cdot\text{O}$ (black) and **1-Cl** (red) and b) $2_2\cdot\text{O}$ (black) and **2-Cl** (red). The insets show the magnified region of the Q-bands.

Continuous-wave (cw)-EPR spectroscopy

Both porphyrins **1-Cl** and **2-Cl** contain paramagnetic centers, the nitroxide and the Fe^{3+} center, and thus can be investigated by means of continuous-wave EPR (cw-EPR) spectroscopy.

As the relaxation rates of both spin centers differ, the cw-EPR experiments on the porphyrin samples were performed at two different temperatures, at 10 K for the Fe^{3+} center (Figure 4) and at 100 K for the nitroxide (Figure 5).

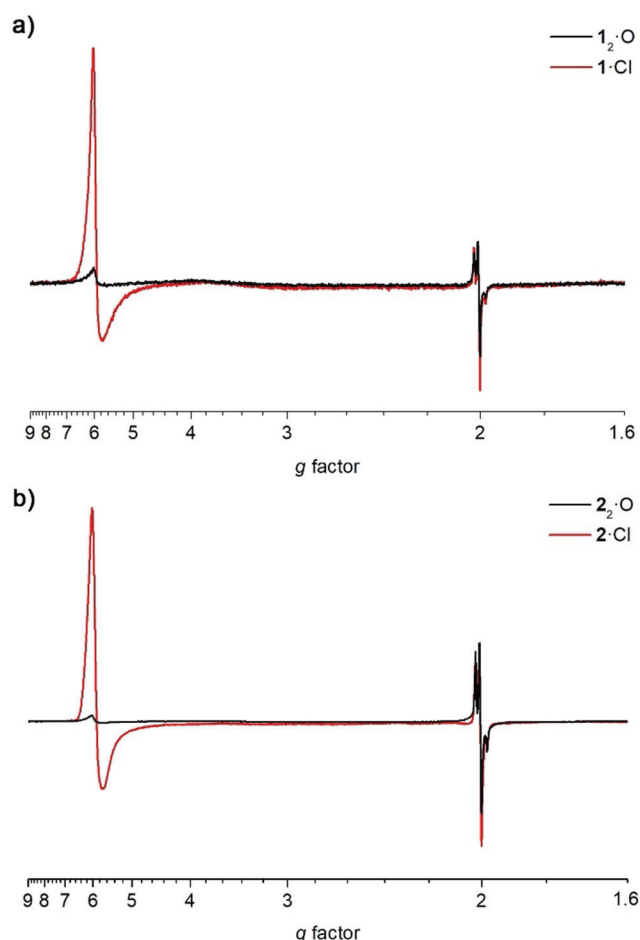


Figure 4. X-band cw-EPR spectra of a) 1_2-O (black) and 1-Cl (red) and b) 2_2-O (black) and 2-Cl (red). All spectra were recorded at 10 K.

Figure 4 depicts the cw-EPR spectra of the monomeric (1-Cl and 2-Cl) and dimeric (1_2-O and 2_2-O) porphyrins recorded at 10 K. Both monomers, 1-Cl and 2-Cl display an intense peak at $g=5.92$, which proves that the Fe^{3+} ions are in the high-spin state.^[40,41] The other component of the axial spectrum of high-spin Fe^{3+} ions usually appears at $g\approx 2$, but is overplayed by the more intense nitroxide spectrum. In the dimer samples 1_2-O and 2_2-O , the line at $g=5.92$ almost disappears, whereas the nitroxide spectrum preserves the intensity observed in the acid-treated samples. The disappearance of the high-spin Fe^{3+} signal in 1_2-O and 2_2-O can be attributed to the strong antiferromagnetic exchange interaction between two μ_2 -oxo-bridged Fe^{3+} ions, which results in a total spin of $S=0$.^[21] By comparing the integral intensities of the high-spin Fe^{3+} signal in 1-Cl and 1_2-O , as well as in 2-Cl and 2_2-O , the amount of the monomeric porphyrins in the samples of 1_2-O and 2_2-O was estimated to be 6% in the case of 1_2-O and 3% in the case of 2_2-O . These values reveal that the base treatment led to efficient formation

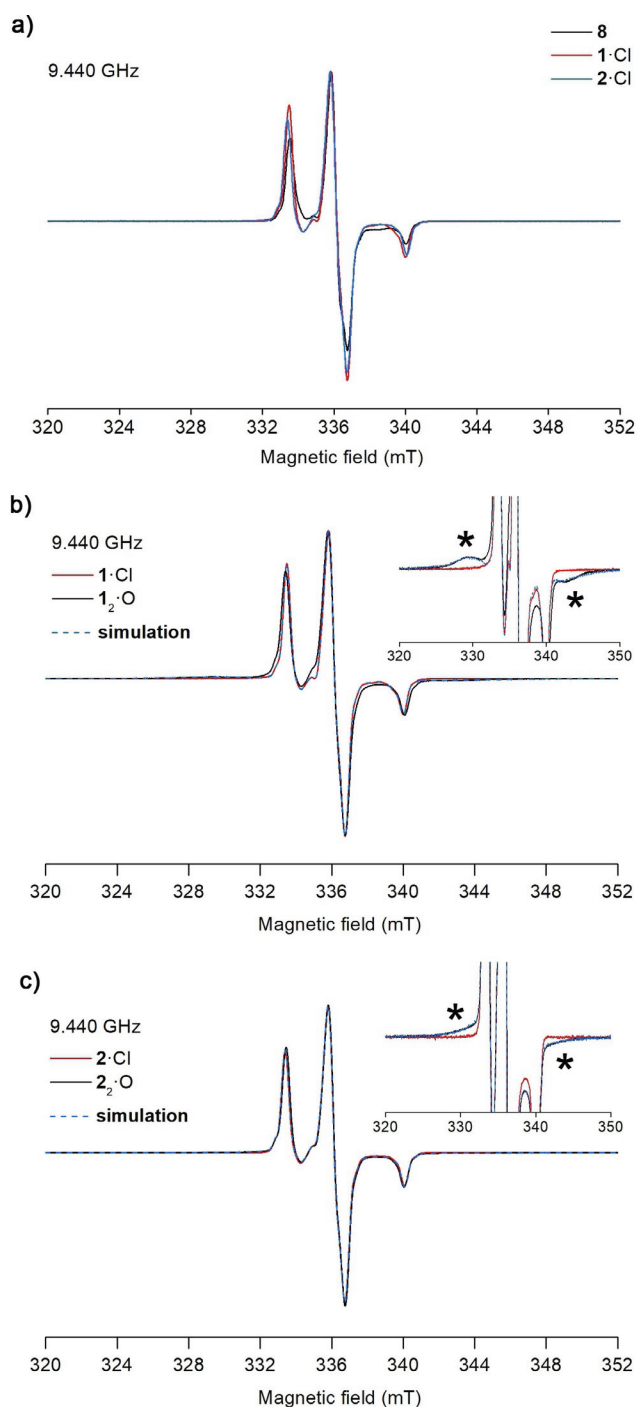


Figure 5. X-band cw-EPR spectra of the nitroxide at 100 K. a) The reference spectrum of nitroxide **8** is overlaid with the spectra of 1-Cl and 2-Cl . b) The spectrum of 1_2-O is overlaid with the spectrum of 1-Cl . The inset shows the magnified part of the spectra, in which the strong dipolar couplings of the nitroxides in 1_2-O manifest themselves (marked by asterisk). The simulation of the 1_2-O spectrum is depicted by a blue dashed line. c) The spectrum of 2_2-O is overlaid with the spectrum of 2-Cl . The inset shows the magnified part of the spectra, in which the strong dipolar couplings of the nitroxides in 2_2-O manifest themselves (marked by asterisk). The simulation of the 2_2-O spectrum is depicted by a blue dashed line.

of the μ_2 -oxo-bridged porphyrins independently of the type of the molecular bridge between the porphyrin core and the nitroxide group.

The 100 K nitroxide spectra of all four porphyrins samples as well as the spectrum of nitroxide **8** are depicted in Figure 5. The nitroxide spectra of the monomeric porphyrins **1-Cl** and **2-Cl** have, at the same concentration and within the same solvent, very similar shapes and linewidths as the spectrum of the uncoupled nitroxide **8** (Figure 5a). This reveals that the high-spin Fe^{3+} in **1-Cl** and **2-Cl**, which is roughly 25 Å apart from the nitroxide center (see computational results below), has a negligible effect on the nitroxide spectrum at the given temperature. The nitroxide spectra of 1_2-O and 2_2-O are similar to **1-Cl** and **2-Cl** in shape and linewidth, but they have additional broad signals on both sides of the nitroxide spectrum (asterisk in the insets in Figures 5b,c). These signals result from the pairs of nitroxides, which experience a strong dipolar coupling between each other owing to their proximity in the structure of some of the μ_2 -oxo-bridged dimers (see below). The strong dipolar coupling between the pairs of nitroxide centers leads to an additional splitting of the corresponding EPR lines. The value of this splitting is determined by the inter-spin distance r in two ways.^[42] First, the dipolar splitting is proportional to r^{-3} . Second, the dipolar splitting is 3/2 times larger for the strong coupling regime, which is realized for $r < 7$ Å, than for the weak coupling regime, which corresponds to $r > 15$ Å. The distances in the range $7 \text{ Å} < r < 15 \text{ Å}$ result in an intermediate dipolar coupling, which is not adequately described neither by the weak coupling nor by the strong coupling model. In the weak coupling regime, the dipolar splitting cannot be resolved in the cw-EPR spectrum but contributes to the EPR linewidth.

To estimate the corresponding inter-nitroxide distance distributions and the percentage of the dimers with such short distances, the spectra of 1_2-O and 2_2-O were simulated. In the

simulations, both spectra were considered as a superposition of unbroadened and dipolar broadened nitroxide spectra. The spectra of **1-Cl** and **2-Cl** were used for the unbroadened part. The dipolar broadened spectrum was calculated by convolution of the unbroadened spectra with a dipolar spectrum corresponding to a normal distribution of the inter-nitroxide distances (see Experimental Section for details).^[42,43] A good fit to the nitroxide spectrum of 1_2-O was obtained with 25% μ_2 -oxo-bridged dimers having a mean inter-nitroxide distance of 6.3 Å with a standard deviation of 0.4 Å (dashed lines in Figure 5b). The other 75% of μ_2 -oxo-bridged dimers in 1_2-O should then have inter-nitroxide distances above 15–20 Å, yielding the almost unbroadened nitroxide spectrum owing to the absence of a strong dipolar coupling between the two nitroxides. In the case of 2_2-O , good agreement with the experimental spectrum was obtained with 15% μ_2 -oxo-bridged dimers having a mean inter-nitroxide distance of 7 Å with a standard deviation of 2 Å (dashed lines in Figure 5c).

PELDOR spectroscopy

To test whether longer nitroxide–nitroxide distances are also present in the dimers, pulsed electron–electron double resonance (PELDOR or DEER)^[44,45] measurements were performed. The results of these measurements are summarized in Figure 6 (see Experimental Section for details). The PELDOR time traces of **1-Cl** and **2-Cl** display only a monotonous decay, which is due to the inter-molecular dipolar interactions, but no dipolar modulation (Figure 6a, dotted curves). This indicates that the acid-treated samples contain only the monomeric porphyrins, as also found by MALDI, and that the used PELDOR settings

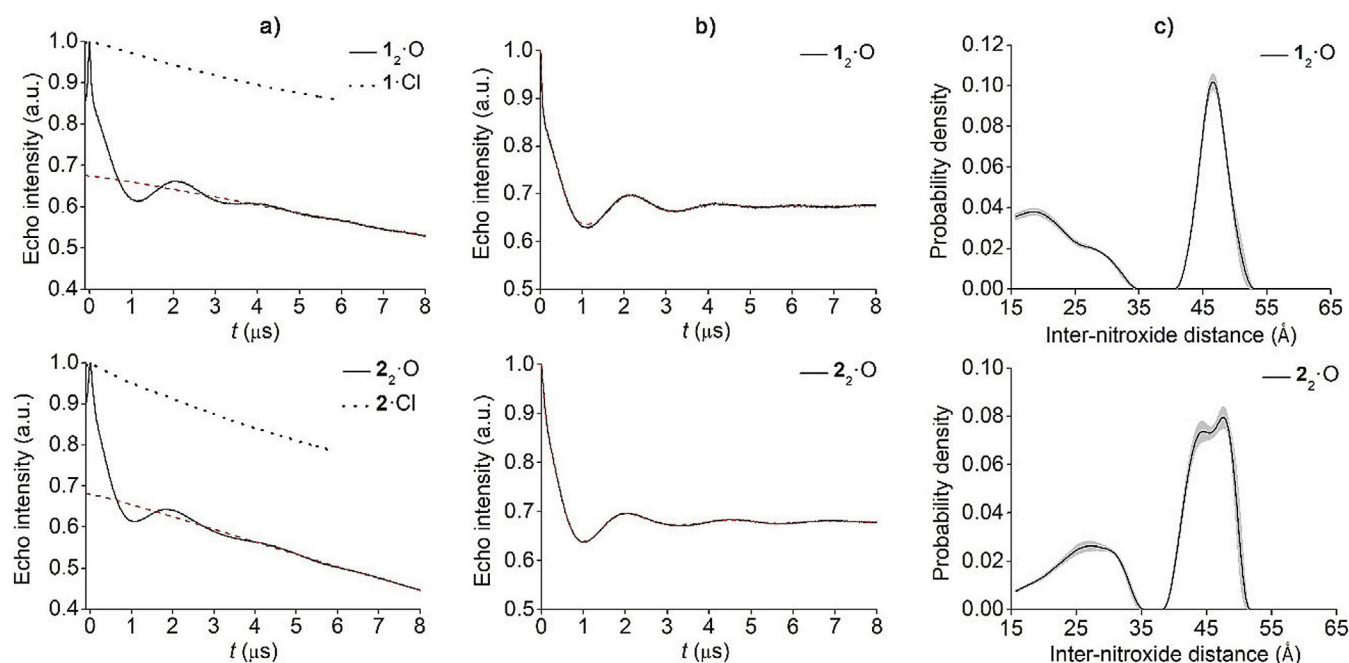


Figure 6. PELDOR measurements of the acid-treated and base-treated samples of **1-Cl** and **2-Cl**. a) Original PELDOR time traces. The background fits for the time traces of 1_2-O and 2_2-O are shown as red dashed lines. b) Background-corrected PELDOR time traces of 1_2-O and 2_2-O and their fits obtained by Tikhonov regularization. c) Inter-nitroxide distance distributions of 1_2-O and 2_2-O . The gray shades depict the estimated errors of the distance distributions, which were obtained by means of the validation toolbox of the DeerAnalysis program.

exclude the measurement of Fe^{3+} /nitroxide distances. In contrast, the PELDOR time traces of 1_2-O and 2_2-O show a prominent dipolar modulation with a modulation depth of 32% (Figure 6a, solid curves). The obtained value of modulation depth is in agreement with the expected value for the used pump pulse lengths of 14 ns (see Figure S1 in the Supporting Information), which provides further evidence for quantitative dimerization of the porphyrin molecules into 1_2-O and 2_2-O . To obtain the inter-nitroxide distance distributions, the PELDOR time traces were analyzed by means of the program DeerAnalysis (see Experimental Section for details).^[46] The optimal fits to the PELDOR time traces and the corresponding inter-nitroxide distance distributions are shown in Figure 6. Interestingly, the inter-nitroxide distance distributions of both μ_2 -oxo-bridged dimers consist of two regions of non-zero probability with zero probability between them. The first region is between 15 and 35 Å, the second between 40 and 55 Å. The short distances around 6–7 Å seen in the cw-EPR experiments are not seen in the PELDOR experiment. This is related to the distance dependence of the modulation depth factor, leading to a lower distance limit for PELDOR of around 15 Å.^[42,46] In more detail, in the case of 1_2-O , the distance distribution displays an asymmetric peak with a maximum at 19.9 Å and a shoulder at about 27 Å, as well as a symmetric peak centered at 46.6 Å. The distance distribution of 2_2-O exhibits an asymmetric peak with a maximum at 27.7 Å and a bi-modal peak with maxima at 44.7 and 47.4 Å. The high signal-to-noise ratio, the length of the PELDOR time traces, and the clearly resolved oscillation periods render the mean values and the shape of the inter-nitroxide distance distributions as being reliable (see the validation results in Figure 6).

A possible explanation for the multiple peaks in the experimental inter-nitroxide distance distributions can be provided in terms of the relative orientation of two porphyrins in the μ_2 -oxo-bridged dimers. If the two porphyrin ring planes could rotate freely around the Fe-O-Fe axis, which would lead to a uniform distribution of the dihedral angle ϕ ($\text{C}_1\text{-Fe}_1\text{-Fe}_2\text{-C}_2$ in Figure 7) between the two porphyrin planes, a smooth nitroxide–nitroxide distance distribution covering a large distance range would have to be expected. This is clearly not the case. In contrast, in a very simple geometric model, steric clashes between the orthogonal phenyl substituents are minimized if ϕ takes values around $(45^\circ + 90^\circ \cdot n)$, where $n = 0, 1, 2, 3$. This defines four registers, of which two are symmetry related in the case of 1_2-O and 2_2-O , leading to two principally different orientations. Interestingly, an available crystal structure^[27] of $[\text{Fe}(\text{TPP})]_2\text{O}$ reveals that the porphyrin planes do indeed adopt a staggered configuration but with a twist angle ϕ of 54.6° (Figure 7). The crystallographic value of ϕ deviates by 10° from 45° , which might be due to attractive interactions between the phenyl rings of two adjacent TPPs. Because of the symmetry within a register, an angle of 35.4° is equivalent to an angle of 54.6° . Thus, the twist angle ϕ can adopt eight possible values in 1_2-O and 2_2-O , $\pm 35.4^\circ$ and $\pm 54.6^\circ$ in the proximal register and $\pm 125.4^\circ$ and $\pm 144.6^\circ$ in the distal register (Figure 7). The proximal and distal register are defined by the two nitroxide arms being close to or far away from each other, respectively.

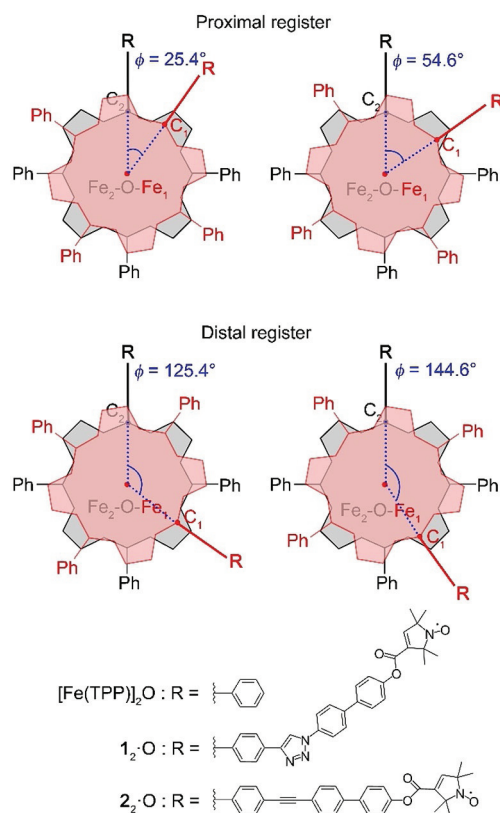


Figure 7. A schematic representation of the μ_2 -oxo-bridged porphyrin conformers. The coplanar mean porphyrin planes of the adjacent porphyrins are drawn as red and gray polygons. The dihedral angle between two porphyrin planes, $\text{C}_1\text{-Fe}_1\text{-C}_2\text{-Fe}_2$, is denoted as ϕ .

If these ϕ values would indeed be occupied, this would lead to a rough distance distribution with relatively short inter-nitroxide distances for the proximal register with $\phi = \pm 35.4^\circ$ and $\pm 54.6^\circ$ and significantly longer inter-nitroxide distances for the distal register with $\phi = \pm 125.4^\circ$ and $\pm 144.6^\circ$. To test this hypothesis and to correlate the predicted inter-nitroxide distances with the experimentally determined values, *in silico* structure simulations were performed for the μ_2 -oxo-bridged dimers 1_2-O and 2_2-O .

Molecular modeling and dynamics simulations

The μ_2 -oxo-bridged porphyrin systems are difficult to describe by *ab initio* electronic structure theory. The bi-radical ground state cannot be properly described in conventional density functional theory (DFT) owing to the partial multireference nature of such states. More importantly, the system's size of about 250 atoms introduces an impractical computational price at the DFT level of theory, as the desired simulation techniques are MD simulations and the calculation of energetic barriers. Owing to the non-trivial electronic structure and the molecular size of the investigated systems, the semiempirical GFN-xTB/GBSA^[47,48] method was applied and solvation effects were only treated implicitly.

First, two initial structures with a dihedral angle ϕ of 54.6° and 144.6° , corresponding to the conformers in the proximal

and the distal registers were generated and optimized at the GFN-xTB/GBSA(toluen) level of theory. Second, a conformer/rotamer ensemble (CRE) was generated for each initial structure by using the MF-MD-GC/GFN-xTB algorithm^[49] and the energetically lowest conformer was determined for each CRE. This procedure yielded two conformers for each of the dimers: $1_2\cdot O_\alpha$ and $1_2\cdot O_\beta$ for the dimer $1_2\cdot O$, and $2_2\cdot O_\alpha$ and $2_2\cdot O_\beta$ for the dimer $2_2\cdot O$. GFN-xTB analysis of the rotation profile around the dihedral angle ϕ was carried out to obtain a qualitative energetic overview. Energies were computed at the GFN-xTB/GBSA(toluen) level of theory as well as the thermostistical contribution for Gibbs free energy within the rigid-rotor-harmonic-oscillator (RRHO) approximation. The rotation profile around ϕ as well as the calculated relative Gibbs free energies of the two conformers for dimers $1_2\cdot O$ and $2_2\cdot O$ are shown in the energy diagram in Figure 8. Our semiempirical model predicts the α -conformer to be more stable than the corresponding β -conformer by approximately 2 kcal mol⁻¹ for both dimers $1_2\cdot O$ and $2_2\cdot O$. The difference in energy is due to attractive dispersion and π - π interactions between the linker, which is only present in the α -conformer of each dimer. Optimization of the rotation path from the α - to β -conformer around the dihedral

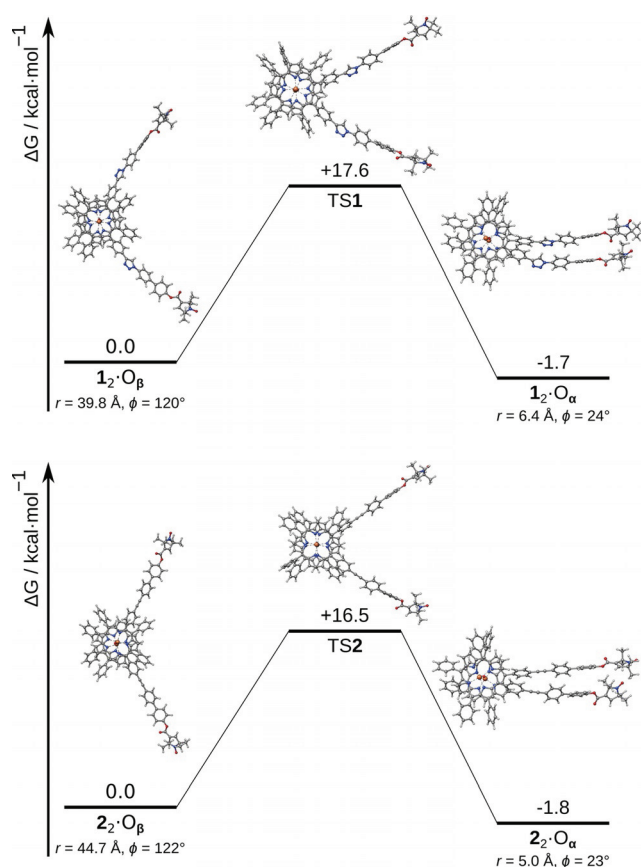


Figure 8. Energy diagram for the rotation along the angle ϕ and the corresponding structures of the μ_2 -oxo-bridged dimers $1_2\cdot O$ and $2_2\cdot O$ calculated at the GFN-xTB level of theory. The molecules are drawn as ball-and-stick models with carbon atoms colored gray, oxygen atoms colored red, nitrogen atoms colored blue, and iron atoms colored orange. The inter-nitroxide distances and the ϕ angles are listed below the names of the corresponding conformers.

angle ϕ produced a low activation barrier profile passing through the transition states TS1 and TS2. The associated computed Gibbs barrier for rotation ΔG^\ddagger at 298.15 K amounts to approximately +19 kcal mol⁻¹ relative to $1_2\cdot O_\alpha$ and $2_2\cdot O_\alpha$ and approximately +17 kcal mol⁻¹ relative to $1_2\cdot O_\beta$ and $2_2\cdot O_\beta$. To get deeper insight into the mechanism of rotation, the rotation path optimization and transition state search was repeated for an artificial porphyrin dimer system where the residues attached to the porphyrin core (see Figure 7) were replaced by methyl groups. GFN-xTB analysis of the rotation path leads to the same energetic barrier of approximately +17 kcal mol⁻¹ as for the untruncated system, revealing the steric hindrance of the phenyl substituents upon rotation as the cause for the high rotation barrier.

For the energetically lowest conformers, MD simulations were carried out for 1 ns at the GFN-xTB/GBSA(toluen) level of theory (see Experimental Section for details) and the inter-nitroxide distances were calculated to determine the corresponding distance distributions. The obtained inter-nitroxide distance distributions are plotted together with the corresponding experimental distributions in Figure 9. Note that two distance distributions were calculated for each dimer, one with the starting structure $1_2\cdot O_\alpha$ or $2_2\cdot O_\alpha$ and the other with the

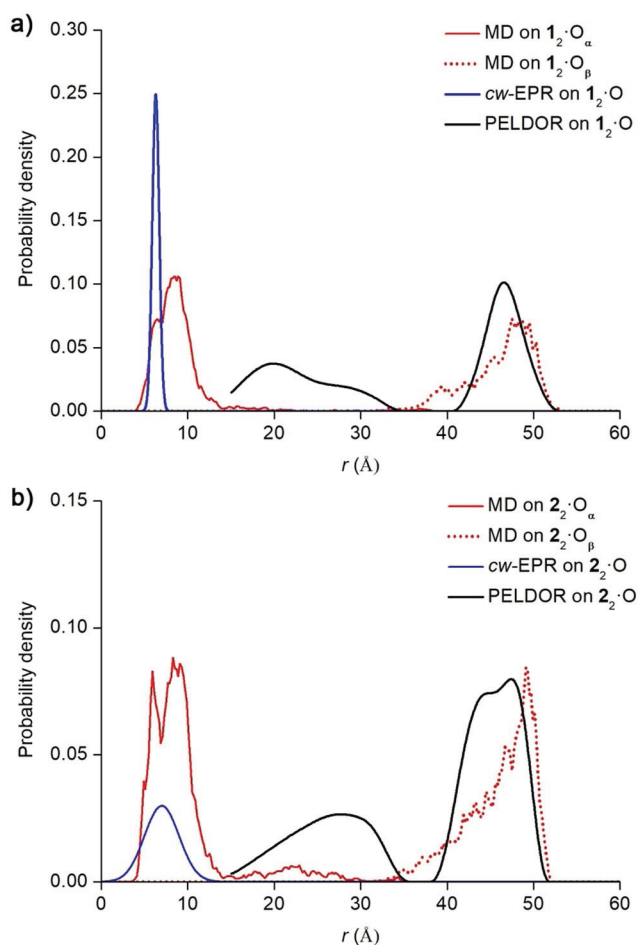


Figure 9. Comparison of the experimental and calculated inter-nitroxide distance distributions in the μ_2 -oxo-bridged dimers a) $1_2\cdot O$ and b) $2_2\cdot O$.

starting structure $1_2\cdot O_\beta$ or $2_2\cdot O_\beta$. This was necessary, because the phenyl substituents pose high-energy barriers that the conformer dynamics cannot overcome. This in turn means that the conformers are confined to their registers at normal temperature. Accordingly, the two MD derived distributions do not overlap with each other: the distributions that correspond to the starting structures $1_2\cdot O_\alpha$ and $2_2\cdot O_\alpha$ display a non-zero probability for the distance in the range 0–30 Å, whereas the distributions that correspond to the starting structures $1_2\cdot O_\beta$ or $2_2\cdot O_\beta$ have a non-zero probability between 30 and 55 Å, showing that the MD simulations exclude the transition between the two starting structures of the dimers. It should be mentioned that the MD-derived distributions calculated with different starting structures are weighted equally in Figure 9, which is justified because the α - and β -conformers of each dimer are similar in energy (Figure 8).

Comparison of EPR and MD results

Comparison of the in silico derived distance distributions with the experimental ones reveals several similarities. First, the MD simulations reproduce the distance peak between 40 and 50 Å of the PELDOR-derived distributions for both dimers, although the shape of the distributions is different. Second, the distance peak below 10 Å, which was found from cw-EPR experiments for both dimers, is also confirmed by the MD simulations. Both methods, MD and EPR, also agree on the width of the short distance peak for $2_2\cdot O$, but in the case of $1_2\cdot O$ the experimental distance peak is significantly narrower than the MD result. The most prominent discrepancy between the in silico and experimental distance distributions is observed in the range 15 to 35 Å. The PELDOR-derived distributions of $1_2\cdot O$ and $2_2\cdot O$ contain an intense distance peak in this range. In contrast, the MD-derived distributions predict almost zero probability for these distances.

To interpret the outlined similarities and differences between the MD- and EPR-derived distance distributions, the correlation between the inter-nitroxide distance and the twist angle ϕ was investigated by using the MD data (Figure 10). Remarkably, only few distinct correlation peaks were obtained for both dimers. The MD simulations on the α -conformers of both dimers (proximal register) yielded an intense correlation peak around $\phi=30^\circ$ and only a very weak correlation peak around $\phi=60^\circ$, which is almost absent for $1_2\cdot O$. The MD simulations on the β -conformers led to an intense correlation peak around $\phi=145^\circ$ and again a weaker correlation peak around $\phi=125^\circ$. All four values of the ϕ angle are in good agreement with the ϕ angles determined from the crystal structure of $[\text{Fe}(\text{TPP})_2\text{O}]$ (see above). The correlation peaks at $\phi\approx 125^\circ$ and 145° (distal register) correspond in the MD simulation to inter-nitroxide distances of 47.7 and 49.5 Å for $1_2\cdot O$, and 42.3 and 49.5 Å for $2_2\cdot O$. These distances are very close to the distance observed by PELDOR (46.6 Å for $1_2\cdot O$, 44.7 and 47.4 Å for $2_2\cdot O$). Moreover, the larger distance difference for the two conformers in the distal register for $2_2\cdot O$ (7.2 Å) compared with $1_2\cdot O$ (1.8 Å) mirrors itself in the bi- (resolved distances) versus uni-modality (unresolved distances) of the long-distance peak in the experi-

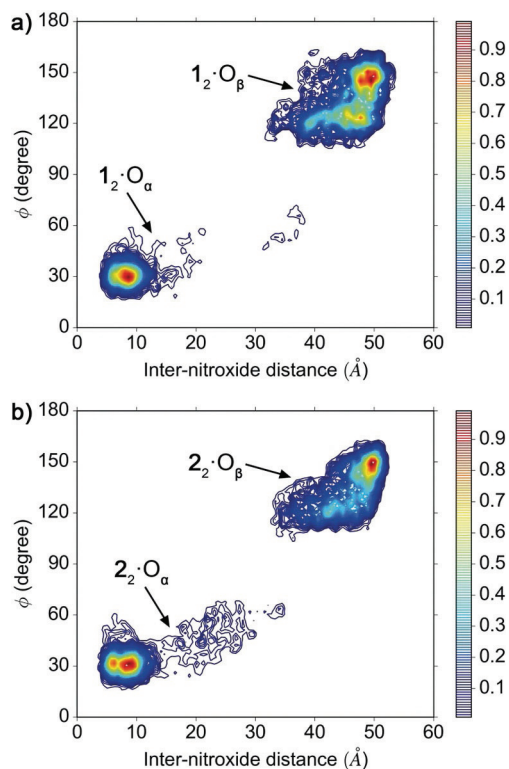


Figure 10. Correlation between the inter-nitroxide distances and the twist angle ϕ as determined from MD simulations on the μ_2 -oxo-bridged dimers a) $1_2\cdot O$ and b) $2_2\cdot O$. The arrows denote the correspondence of the correlation peaks to the starting structures used for the MD simulations.

mental PELDOR data (Figure 9). The similar intensity of the two long-distance maxima in the PELDOR-derived distance distribution of $2_2\cdot O$ reveals that the two conformers with $\phi\approx 125^\circ$ and 145° are equally abundant. In contrast, the conformer with $\phi\approx 145^\circ$ is favored against the conformer with $\phi\approx 125^\circ$ by the MD simulation. This discrepancy causes the difference in the shape of the PELDOR- and MD-derived inter-nitroxide distance distributions in the range 40–50 Å (Figure 9).

Another pair of correlation peaks, around $\phi=30^\circ$ and 60° , is associated with inter-nitroxide distances in the range 5 to 35 Å. The correlation peak at $\phi\approx 30^\circ$ corresponds to an inter-nitroxide distance of 8.5 Å for both dimers. This prediction is close to the distances determined by cw-EPR (6.3 Å for $1_2\cdot O$, 7 Å for $2_2\cdot O$). The correlation peak around $\phi=60^\circ$, corresponding to the distance range of 15 to 30 Å, is almost absent in the MD of $1_2\cdot O$ (Figure 10a) and very weak and smeared for $2_2\cdot O$ (Figure 10b). In contrast to the MD simulations, the PELDOR-derived distance distributions contain a clear peak in this distance region for both $1_2\cdot O$ and $2_2\cdot O$. Thus, it seems that although both methods, EPR and MD, show that both registers are populated, the weight of the conformers within each register differs. This might be attributed to the simulation of the dynamics of $1_2\cdot O$ and $2_2\cdot O$ having been performed in liquid solution, whereas the corresponding EPR results were obtained on glassy frozen solutions. Usage of an implicit solvation model may also introduce a deviation between theory and experiment, as steric effects are not taken into account.

In addition, MD predicts a non-zero probability for the ϕ angles between 125° and 145° , as well as between 30° and 60° (can be seen only for 2_2-O). This shows that the two porphyrin planes can rotate relative to each other within each of the registers in a “scissors-like” motion. For the 2_2-O molecule, in which the linker is linear and fairly rigid, such a “scissors-like” motion should result in two bimodal inter-nitroxide distance peaks, corresponding to proximal and distal registers. Indeed, the bimodal peaks between 0 and 35 \AA as well as between 40 and 50 \AA can be seen in the EPR-derived distance distributions of 2_2-O (Figure 9b). In the case of 1_2-O , the kinked linker makes it difficult to resolve the bimodality of the peaks. Nevertheless, for both dimers, EPR and MD show clearly a zero probability for angles/distances between registers. As shown by GFN-xTB analysis, the conformations with $\phi = 90^\circ \cdot n$, where $n = 0, 1, 2, 3$, have high energetic barriers posed by steric clashes of the phenyl rings, which prevents an exchange between registers. This also means that different registers can only be occupied during dimer assembly. By using the distance distributions of the EPR data, one can estimate the relative occupation of the proximal versus distal register. For 1_2-O , this yields 59% and 41% for the proximal and the distal register, respectively, and for 2_2-O , 44% and 56% for the proximal and distal register, respectively. Thus, both registers are, within experimental error, equally populated.

Conclusions

Two synthetic approaches, one based on click chemistry and the other on Sonogashira–Hagihara coupling, were successfully applied to synthesize two new Fe^{3+} porphyrins, **1-Cl** and **2-Cl**, each linked to a nitroxide group. Treating the monomeric samples with an aqueous basic solution, the monomers were converted almost quantitatively into μ_2 -oxo-bridged dimers 1_2-O and 2_2-O . The structure and dynamics of the μ_2 -oxo dimers was then investigated by means of cw-EPR and PELDOR spectroscopy. The cw-EPR experiments were used to determine the short inter-nitroxide distances below 15 \AA , whereas the PELDOR experiments allowed the determination of long inter-nitroxide distances above 15 \AA . Thus, both methods complement each other nicely. To interpret the obtained distance constraints in terms of structure and dynamics of the dimers, the combined cw-EPR/PELDOR derived inter-nitroxide distance distributions were compared with the results of the MD simulations. This comparison yielded several fruitful results. It was shown that the conformers of the μ_2 -oxo-bridged dimers occupy four registers that are defined by the phenyl substituents. The dimer rotamers cannot exchange their register by rotation owing to the high energetic barrier of $17\text{--}19 \text{ kcal mol}^{-1}$ posed by the phenyl substituents. Within each register, two favorable conformers were identified. They correspond to the twist angle between the two porphyrin cores of 30° and 60° in the case of the proximal register and 125° and 145° in the case of the distal registers. The population of these two conformers in each register was weighted differently by EPR and MD. Additionally, it was proposed based on MD simulations that μ_2 -oxo-bridged porphyrin planes can rotate relative to

each other around the Fe-O-Fe axis within each of the registers. Such a “scissor-like” motion corresponds to an exchange of the favorable conformers within each register. Importantly, both synthesized porphyrin dimers display very similar dynamics of the central TPP core, which hints towards a minor effect of the linker on the intrinsic dynamics of the TPPs and, thus, allows us to extend the derived conclusions to other FeTPP-based μ_2 -oxo dimers. With respect to using such dimers within molecular machines, one might view them as molecular step motors. Furthermore, the present study provides a basis for using these compounds as models for testing pulsed EPR-based distance measurements to high-spin Fe^{3+} ions with large zero-field splitting constants.

Experimental Section

Synthesis

The details of the synthesis of **1-Cl** and **2-Cl** and their precursors, as well as the corresponding analytics (MS, NMR, elemental analysis, etc.), are given in the Supporting Information. The dimerization of **1-Cl** and **2-Cl** to the μ_2 -oxo-bridged dimers 1_2-O and 2_2-O , respectively, was achieved by treatment of the monomers with aqueous sodium hydroxide. In particular, a $200 \mu\text{M}$ solution of **1-Cl** or **2-Cl** in toluene was prepared and mixed with 0.05 M aqueous NaOH in a volume ratio of 1:1. The obtained solution was shaken for 2 min by means of a Vortex Genie 2 (Scientific Industries Inc.) and then incubated for 1 min to achieve separation of water and toluene layers. After this, the toluene layer was extracted and the entire procedure was repeated again to ensure efficient dimer formation. Subsequently, the toluene layer was transfused into a clean tube and the solvent was evaporated from the samples under high vacuum. The reversibility of the dimerization process was tested by treatment of the dimers with aqueous hydrochloric acid. This procedure was done in complete analogy to the treatment with NaOH except for the fact that 0.05 M aqueous HCl was used instead of 0.05 M aqueous NaOH. This procedure again gave rise to the monomers **1-Cl** and **2-Cl**.

Mass spectrometry

Matrix-assisted laser desorption/ionization (MALDI) mass spectra were measured by using an Autoflex II TOF/TOF (Bruker) spectrometer.

UV/Vis spectroscopy

UV/Vis spectra were recorded by using SPECORD 200 (Analytik Jena AG) and Cary 100 UV/Vis (Agilent Technologies) spectrometers. All spectra were taken in the range from 300 nm to 800 nm with a 1 nm step. All UV/Vis samples were prepared with the concentration of $10 \mu\text{M}$ in deuterated toluene.

cw-EPR spectroscopy

cw-EPR experiments were carried out with an X-Band EPR spectrometer EMXmicro (Bruker) equipped with super-high-quality resonator (SHQ). cw-EPR spectra were collected at two different temperatures, 10 K and 100 K . To obtain 100 K , the variable-temperature accessory ER 4131VT (Bruker) was employed. For 10 K , the resonator was mounted inside a continuous-flow helium cryostat ER4112HE (Bruker), the temperature of which was controlled by

the Mercury iTC system (Oxford Instruments). The cw-EPR measurements at 100 K were performed with a microwave power of 0.1927 mW (30 dB), a modulation frequency of 100 kHz, a modulation amplitude of 0.2 mT, and a time constant of 10.24 ms. The 10 K cw-EPR spectra were acquired by using a microwave power of 17.22 mW (10 dB), a modulation frequency of 100 kHz, a modulation amplitude of 0.1 mT, and a time constant of 10.24 ms. All cw-EPR samples were prepared with a nitroxide spin concentration of 200 μM in deuterated toluene. The sample volume was kept constant at 200 μL . Moreover, the cw-EPR measurements at 10 K were performed with the same resonator Q factor (≈ 500) and the same receiver gain (40 dB) for all samples.

Determination of spin–spin distances from cw-EPR spectra

The nitroxide spectra of 2-Cl and 2₂-O were simulated by using the convolution method.^[42,43] Both spectra were considered as a superposition of unbroadened spectra $f_u(B)$ and dipolar broadened nitroxide spectra $f_b(B)$:

$$f(B) = w f_b(B) + (1 - w) f_u(B)$$

where w is the weight of the dipolar broadened part in the total spectra. The nitroxide spectra of 1-Cl and 2-Cl were used for the unbroadened part $f_u(B)$. The dipolar broadened spectrum was calculated by convolution of the unbroadened spectra with a dipolar spectrum $f_{dd}(B)$:

$$f_b(B) = f_u(B) \otimes f_{dd}(B)$$

The dipolar spectrum was calculated in the strong coupling approximation for a normal distribution $P(r)$ of the inter-nitroxide distances with a mean distance $\langle r \rangle$ and a standard deviation σ_r :

$$f_{dd}(B) = \int_0^\infty P(r) dr \int_0^{\pi/2} D(r, \theta) \sin\theta d\theta$$

in which:

$$D(r, \theta) = \frac{3 \mu_0 g \beta}{4 4\pi r^3} (1 - 3 \cos^2 \theta)$$

$$P(r) = \frac{1}{\sqrt{2\pi}\sigma_r} \exp\left(-\frac{(r - \langle r \rangle)^2}{2\sigma_r^2}\right)$$

Here, μ_0 is the vacuum permeability, g is the g -factor of the nitroxide, β is the Bohr magneton, r is the inter-nitroxide distance, and θ is the angle between the distance vector and the direction of the external magnetic field. The integral of $f_{dd}(B)$ was solved by means of Monte-Carlo method using 10^6 samples.

In the present analysis, the values of the mean distance $\langle r \rangle$, its standard deviation σ_r , and the weight w were optimized manually until the convolution of the unbroadened cw-EPR spectra $f_u(B)$ with the dipolar spectrum provided the best fit to the cw-EPR spectra of 2-Cl and 2₂-O. The MATLAB-based source code of the optimization program is available at <https://github.com/dinarabdulin/DipolarBroadeningFitting>.

PELDOR spectroscopy

PELDOR experiments were performed on the same samples as the cw-EPR experiments. All samples had the nitroxide spin concentration of 200 μM in deuterated toluene. The measurements were car-

ried out with an ELEXSYS E580 (Bruker) spectrometer using a Flex-Line probehead with a Q-band resonator ER5106QT-2 (Bruker). All microwave pulses were amplified by a 150 W TWT amplifier (model 187Ka). To achieve the working temperature of 50 K, a continuous-flow helium cryostat CF935 (Oxford Instruments) and a temperature control system iTC 503S (Oxford Instruments) were employed.

The PELDOR experiments were performed with the standard four-pulse sequence $\pi/2(\nu_{\text{det}}) - \tau_1 - \pi(\nu_{\text{det}}) - (\tau_1 + t) - \pi(\nu_{\text{pump}}) - (\tau_2 - t) - \pi(\nu_{\text{det}}) - \tau_2$ -echo. The frequency of the pump pulse and the magnetic field were adjusted to be in resonance with the maximum of the nitroxide spectrum, whereas the frequency of the detection pulse was set 100 MHz lower than the frequency of the pump pulse. All PELDOR measurements were performed with the lengths of detection $\pi/2$ - and π -pulses of 16 and 32 ns, respectively, and the pump pulse was 14 ns long. The π -pulse was phase-cycled to eliminate receiver offsets. The τ_1 interval was set to a starting value of 250 ns and was incremented during each experiment eight times with a step of 16 ns, to suppress the deuterium ESEEM (electron spin echo envelope modulation). The τ_2 interval was set to 10 μs . The position of the pump pulse relative to the primary echo was incremented with a step of 8 ns. All PELDOR spectra were recorded at 50 K with a repetition time of 3 ms. The signal was averaged over 250 runs to achieve a good signal-to-noise ratio.

Determination of spin–spin distances from PELDOR data

The inter-nitroxide distance distributions were determined from the experimental PELDOR time traces by means of the program DeerAnalysis.^[46] First, the time traces were divided by an exponential decay to remove the background resulting from the inter-molecular interactions. Then, Tikhonov regularization was applied to the background-free time traces, yielding the desired distance distributions. The best regularization parameter was determined through the L-curve approach. The validation of the inter-nitroxide distance distributions was done by varying the background starting time from 2 μs to 6 μs with a step of 100 ns and the background dimension from 3.0 to 3.5 with a step 0.1.

Computational details

For all four initial structures, the generation of the conformer/rotamer ensemble (CRE) was performed by using the semiempirical tight-binding method GFN-xTB and the CRE search algorithm.^[49] The MF-MD-GC/GFN-xTB algorithm consists of three steps: normal mode following (MF), molecular dynamics (MD) simulations, and "pseudo-genetic" structure crossing (GC). In all steps, GFN-xTB is used as the underlying electronic structure method. The CRE generation was conducted in toluene as the solvent, simulated by the implicit GBSA solvation model.^[47,48] The energetically lowest conformer found for each initial structure was fully optimized at the GFN-xTB/GBSA(toluene) level of theory and molecular dynamics (MD) simulations were carried out with implicit solvent GBSA (toluene) on each structure at 298 K for 100 ps, 500 ps, and 1 ns with a time step of 4 fs and an equilibration phase of 10 ps. The SHAKE^[50] algorithm was used to constrain all bonds. For geometry optimization and MD simulation, the stand-alone program xtb^[51] was used. Evaluation of the trajectories was performed with the program TRAVIS.^[52]

The calculation of free energies was performed as follows. Single-point energies E were computed at the GFN-xTB level of theory. Harmonic vibrational frequencies were calculated at the same level to obtain the thermostatical corrections G_{RRHO} . The solvation free energy ΔG_{soln} was calculated by GBSA at 298.15 K in the respective

solvent (toluene). The free energy is then the sum of all contributions:

$$G = E + G_{\text{RRHO}}^T + \Delta G_{\text{soln}}^T(X)$$

Reaction paths were calculated for all reactions to get a good guess of the transition state structure. To begin from reasonable geometries, the start and end structures were optimized with GFN-xTB/GBSA. The reaction path was then calculated with the growing string method GSM^[53] by using GFN-xTB/GBSA as the underlying electronic structure method. An additional frequency calculation was performed to check for a true transition state with only one imaginary mode.

Acknowledgments

This work was funded by the German Research Foundation (DFG) within the collaborative research center SFB813 "Chemistry at Spin Centers" (projects A6 and Z2).

Conflict of interest

The authors declare no conflict of interest.

Keywords: complex formation • DEER spectroscopy • metal centers • nitroxide • pulsed dipolar spectroscopy

- [1] L. P. Cook, G. Brewer, W. Wong-Ng, *Crystals* **2017**, *7*, 223.
- [2] *Handbook of Porphyrin Science, Vol. 1–44* (Eds.: W. Kadish, K. M. Smith, R. Guilard), World Scientific, Singapore, **2010**.
- [3] C. W. M. Kay, *J. Am. Chem. Soc.* **2003**, *125*, 13861–13867.
- [4] S. Richert, C. E. Tait, C. R. Timmel, *J. Magn. Reson.* **2017**, *280*, 103–116.
- [5] M. Di Valentin, M. Albertini, M. G. Dal Farra, E. Zurlo, L. Orian, A. Polimeno, M. Gobbo, D. Carbonera, *Chem. Eur. J.* **2016**, *22*, 17204–17214.
- [6] A. Abragam, B. Bleaney, *Electron Paramagnetic Resonance of Transition Ions*, Oxford University Press, Oxford, **1970**.
- [7] A. Messerschmidt, R. Huber, T. Poulos, K. Wieghardt, *Handbook of Metalloproteins, Vol. 1–2*, Wiley, Chichester, **2001**.
- [8] *Structural Information from Spin-Labels and Intrinsic Paramagnetic Centers in the Biosciences, Structure and Bonding, Vol. 152* (Eds.: C. R. Timmel, J. R. Harmer), Springer, Heidelberg, **2013**.
- [9] B. E. Bode, J. Plackmeyer, T. F. Prisner, O. Schiemann, *J. Phys. Chem. A* **2008**, *112*, 5064–5073.
- [10] B. E. Bode, J. Plackmeyer, M. Bolte, T. F. Prisner, O. Schiemann, *J. Organomet. Chem.* **2009**, *694*, 1172–1179.
- [11] J. E. Lovett, A. M. Bowen, C. R. Timmel, M. W. Jones, J. R. Dilworth, D. Caprotti, S. G. Bell, L. L. Wong, J. Harmer, *Phys. Chem. Chem. Phys.* **2009**, *11*, 6840–6848.
- [12] A. M. Bowen, M. W. Jones, J. E. Lovett, T. G. Gaule, M. J. McPherson, J. R. Dilworth, C. R. Timmel, J. R. Harmer, *Phys. Chem. Chem. Phys.* **2016**, *18*, 5981–5994.
- [13] M. H. Rakowsky, K. M. More, A. V. Kulikov, G. R. Eaton, S. S. Eaton, *J. Am. Chem. Soc.* **1995**, *117*, 2049–2057.
- [14] M. H. Rakowsky, A. Zecevic, G. R. Eaton, S. S. Eaton, *J. Magn. Reson.* **1998**, *131*, 97–110.
- [15] D. Akhmetzyanov, P. Schöps, A. Marko, N. C. Kunjir, S. T. Sigurdsson, T. F. Prisner, *Phys. Chem. Chem. Phys.* **2015**, *17*, 24446–24451.
- [16] A. Meyer, O. Schiemann, *J. Phys. Chem. A* **2016**, *120*, 3463–3472.
- [17] A. Potapov, Y. Song, T. J. Meade, D. Goldfarb, A. V. Astashkin, A. Raitsimring, *J. Magn. Reson.* **2010**, *205*, 38–49.
- [18] P. Lueders, G. Jeschke, M. Yulikov, *J. Phys. Chem. Lett.* **2011**, *2*, 604–609.
- [19] E. B. Fleischer, T. S. Srivastava, *J. Am. Chem. Soc.* **1969**, *91*, 2403–2405.
- [20] E. B. Fleischer, J. M. Palmer, T. S. Srivastava, A. Chatterjee, *J. Am. Chem. Soc.* **1971**, *93*, 3162–3167.
- [21] K. S. Murray, *Coord. Chem. Rev.* **1974**, *12*, 1–35.
- [22] E. Tabor, J. Poltowicz, K. Pamin, S. Başğ, W. Kubiak, *Polyhedron* **2016**, *119*, 342–349.
- [23] E. V. Kudrik, P. Afanasiev, L. X. Alvarez, P. Dubourdeaux, M. Clémancey, J. M. Latour, G. Blondin, D. Bouchu, F. Albrieux, S. E. Nefedov, A. B. Sorokin, *Nat. Chem.* **2012**, *4*, 1024–1029.
- [24] T. Gozet, L. Huynh, D. K. Bohme, *J. Mass Spectrom.* **2010**, *45*, 35–42.
- [25] A. M. N. Silva, A. Aguir, S. S. Balula, A. M. G. Silva, M. Rangel, *J. Mass Spectrom.* **2014**, *49*, 763–765.
- [26] S. K. Ghosh, R. Patra, S. P. Rath, *Inorg. Chim. Acta* **2010**, *363*, 2791–2799.
- [27] A. B. Hoffman, D. M. Collins, V. W. Day, E. B. Fleischer, T. S. Srivastava, J. L. Hoard, *J. Am. Chem. Soc.* **1972**, *94*, 3620–3626.
- [28] S. Grimme, C. Bannwarth, P. Shushkov, *J. Chem. Theory Comput.* **2017**, *13*, 1989–2009.
- [29] H. C. Kolb, M. G. Finn, K. B. Sharpless, *Angew. Chem. Int. Ed.* **2001**, *40*, 2004–2021; *Angew. Chem.* **2001**, *113*, 2056–2075.
- [30] R. Luguayo, L. Jaquinod, F. R. Fronczek, M. G. H. Vicente, K. M. Smith, *Tetrahedron* **2004**, *60*, 2757–2763.
- [31] J. Rochford, E. Galoppini, *Langmuir* **2008**, *24*, 5366–5374.
- [32] P. Brodard, S. Matzinger, E. Vauthey, O. Mongin, C. Papamicaël, A. Gossauer, *J. Phys. Chem. A* **1999**, *103*, 5858–5870.
- [33] T. Kengthanomma, P. Thamyongkit, J. Gasiorowski, A. M. Ramil, N. S. Sariciftci, *J. Mater. Chem. A* **2013**, *1*, 10524–10531.
- [34] M. Meldal, C. W. Tomøe, *Chem. Rev.* **2008**, *108*, 2952–3015.
- [35] J. Andersen, U. Madsen, F. Björkling, X. Liang, *Synlett* **2005**, 2209–2213.
- [36] A. D. Adler, F. R. Longo, F. Kampas, J. Kim, *J. Inorg. Nucl. Chem.* **1970**, *32*, 2443–2445.
- [37] T. Mukaiyama, *Angew. Chem. Int. Ed. Engl.* **1979**, *18*, 707–721; *Angew. Chem.* **1979**, *91*, 798–812.
- [38] F. Paulat, N. Lehnert, *Inorg. Chem.* **2008**, *47*, 4963–4976.
- [39] N. Sadasivan, H. I. Eberspaecher, W. H. Fuchsman, W. S. Caughey, *Biochemistry* **1969**, *8*, 534–541.
- [40] H. Aissaoui, R. Bachmann, A. Schweiger, W. D. Woggon, *Angew. Chem. Int. Ed.* **1998**, *37*, 2998–3002; *Angew. Chem.* **1998**, *110*, 3191–3196.
- [41] F. Trandafir, P. Heerdt, M. Fittipaldi, E. Vinck, S. Dewilde, L. Moens, S. Van Doorslaer, *Appl. Magn. Reson.* **2007**, *31*, 553–572.
- [42] J. E. Banham, C. M. Baker, S. Ceola, I. J. Day, G. H. Grant, E. J. J. Groenen, C. T. Rodgers, G. Jeschke, C. R. Timmel, *J. Magn. Reson.* **2008**, *191*, 202–218.
- [43] H. J. Steinhoff, N. Radzwill, W. Thevis, V. Lenz, D. Brandenburg, A. Antson, G. Dodson, A. Wollmer, *Biophys. J.* **1997**, *73*, 3287–3298.
- [44] A. D. Milov, K. M. Salikhov, M. D. Shchirov, *Fiz. Tverd. Tela* **1981**, *23*, 975–982.
- [45] G. Jeschke, M. Pannier, A. Godt, H. W. Spiess, *Chem. Phys. Lett.* **2000**, *331*, 243–252.
- [46] G. Jeschke, V. Chechik, P. Ionita, A. Godt, H. Zimmermann, J. Banham, C. R. Timmel, D. Hilger, H. Jung, *Appl. Magn. Reson.* **2006**, *30*, 473–498.
- [47] W. Clark Still, A. Tempczyk, R. C. Hawley, T. Hendrickson, *J. Am. Chem. Soc.* **1990**, *112*, 6127–6129.
- [48] S. Grimme, P. Shushkov, unpublished results.
- [49] S. Grimme, C. Bannwarth, S. Dohm, A. Hansen, J. Pisarek, P. Pracht, J. Seibert, F. Neese, *Angew. Chem. Int. Ed.* **2017**, *56*, 14763–14769; *Angew. Chem.* **2017**, *129*, 14958–14964.
- [50] J. P. Ryckaert, G. Ciccotti, H. J. C. Berendsen, *J. Comput. Phys.* **1977**, *23*, 327–341.
- [51] Please contact E-mail: xtb@thch.uni-bonn.de to obtain the program.
- [52] M. Brehm, B. Kirchner, *J. Chem. Inf. Model.* **2011**, *51*, 2007–2023.
- [53] P. Zimmerman, *J. Chem. Theory Comput.* **2013**, *9*, 3043–3050.

Manuscript received: October 4, 2018

Revised manuscript received: November 13, 2018

Accepted manuscript online: November 23, 2018

Version of record online: January 21, 2019

CHEMISTRY

A **European** Journal

Supporting Information

Synthesis of μ_2 -Oxo-Bridged Iron(III) Tetraphenylporphyrin–Spacer–Nitroxide Dimers and their Structural and Dynamics Characterization by using EPR and MD Simulations

Dinar Abdullin^{+, [a]} Nico Fleck^{+, [a]} Christoph Klein,^[a, b] Philipp Brehm,^[a] Sebastian Spicher,^[c] Arne Lützen,^[b] Stefan Grimme,^[c] and Olav Schiemann*^[a]

chem_201805016_sm_miscellaneous_information.pdf

Supporting Information

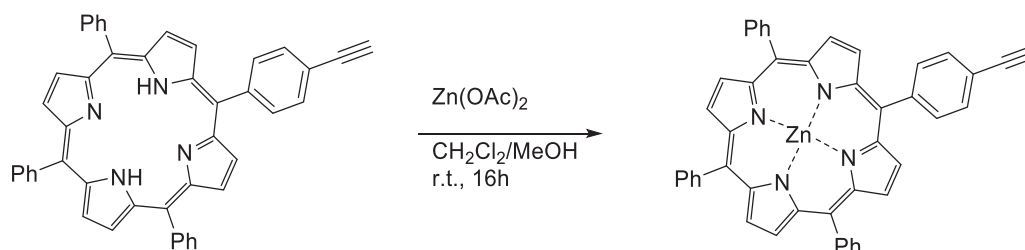
Table of Contents

1	Materials and methods	3
1.1	Synthesis	3
1.2	General procedures for the dimerization/monomerization of iron(III) porphyrins ...	10
1.3	High pressure liquid chromatography	11
1.4	Elemental analysis	11
1.5	NMR	11
1.6	Mass spectrometry	11
2	Analytical data.....	12
2.1	PELDOR measurements on bis-nitroxide reference compound.....	12
2.2	MD simulations for the dimers $\mathbf{1}_2\cdot\mathbf{O}$ and $\mathbf{2}_2\cdot\mathbf{O}$	13
2.3	Mass spectra	15
2.4	The atomic coordinates of the optimized porphyrin structures	21
3	Literature	63

1 Materials and methods

1.1 Synthesis

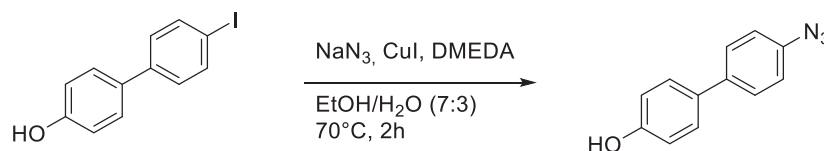
Zinc(II)-5-(4-ethynylphenyl)-10,15,20-triphenylporphyrine (**4**)



5-(4-Ethynylphenyl)-10,15,20-triphenylporphyrin (97 mg, 0.15 mmol) was dissolved in 50 mL of dichloromethane and zinc(II) acetate (150 mg, 0.68 mmol, 4.50 eq.) dissolved in 15 mL of methanol was added. The mixture was stirred overnight at room temperature. After the solvents had been evaporated, the residue was taken up in dichloromethane and washed with water. The organic phase was dried with MgSO_4 and the solvents were removed under reduced pressure. The crude product was purified by column chromatography on silica gel using cyclohexane/ CH_2Cl_2 1:1 (v/v) as the eluent, $R_f = 0.65$. The analytical data were in accordance with the literature.^[1]

Yield: 98 mg (92 %)

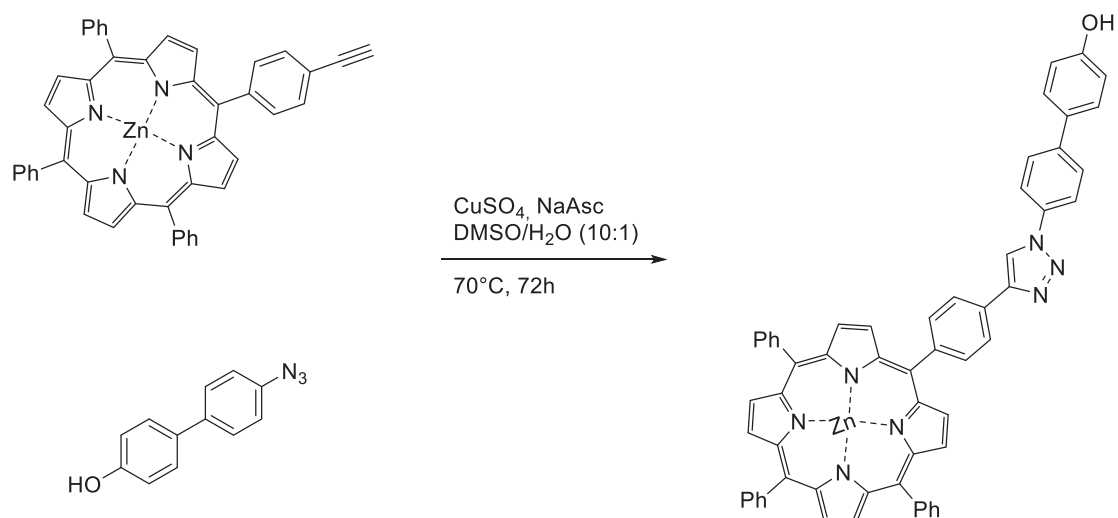
4-Hydroxy-4'-azidobiphenyl



4-Iodo-4'-hydroxybiphenyl (600 mg, 2.00 mmol), sodium azide (270 mg, 4.00 mmol, 2.00 eq.), copper(I) iodide (40 mg, 0.20 mmol, 0.10 eq.) and sodium ascorbate (20 mg, 0.10 mmol, 0.05 eq.) were suspended in a mixture of DMSO/water (5:1, 10 mL) and *N,N'*-dimethylethylenediamine (30 μL , 0.27 mmol, 0.14 eq.) was added. The DMSO/water mixture was purged with argon for 15 min in advance. After heating to 70°C for 2 h, the reaction mixture was poured into 30 mL of brine and extracted with ethyl acetate (3×30 mL). The combined organic phases were dried with MgSO_4 and the solvent was removed under reduced pressure. The title compound was obtained after column chromatography on silica using cyclohexane/ EtOAc 2:1 as the eluent, $R_f = 0.81$. The analytical data were in accordance to the literature.^[2]

Yield: 318 mg (74%)

Zinc(II)-5-(4-(1-(4'-hydroxy-1,1'-biphenyl)-2,3-triazo-4-yl)phenyl)-10,15,20-triphenylporphyrin (**5**)



Zinc(II)-5-(4-ethynylphenyl)-10,15,20-triphenylporphyrine (98 mg, 0.14 mmol) and 4-hydroxy-4'-azidobiphenyl (100 mg, 0.47 mmol, 3.35 eq.) were dissolved in 5.0 mL of DMSO. Aqueous solutions of copper(II) sulfate (0.7 mL, 0.01 M in H_2O , 0.007 mmol, 5 mol%) and sodium ascorbate (0.35 mL, 0.1 M in H_2O , 0.035 mmol, 25 mol%) were added. Note that the sodium ascorbate solution was prepared just before the reaction. The reaction mixture was stirred for 72 h at 70°C . Afterwards, the mixture was diluted with dichloromethane and washed with water and brine. The organic phase was dried with MgSO_4 and the solvents were removed under reduced pressure. Purification by column chromatography on silica using $\text{CH}_2\text{Cl}_2/\text{CH}_3\text{OH}$ 10:1 (v/v) as the eluent gave the title compound, $R_f = 0.52$.

Yield: 123 mg (95%).

$^1\text{H-NMR}$ (500 MHz, CD_2Cl_2 , δ in ppm): 9.03 (d, 2H, $J = 4.6$ Hz), 8.98 (d, 2H, $J = 4.6$ Hz), 8.96 (s, 4H), 8.46 (s, 1H), 8.31 (d, 2H, $J = 8.0$ Hz), 8.25 – 8.21 (m, 6H), 8.20 (d, 2H, $J = 7.9$ Hz), 7.88 (d, 2H, $J = 8.4$ Hz), 7.80 – 7.75 (m, 9H), 7.73 (d, 2H, $J = 8.4$ Hz), 7.53 (d, 2H, $J = 8.2$ Hz), 6.92 (d, 2H, $J = 8.2$ Hz).

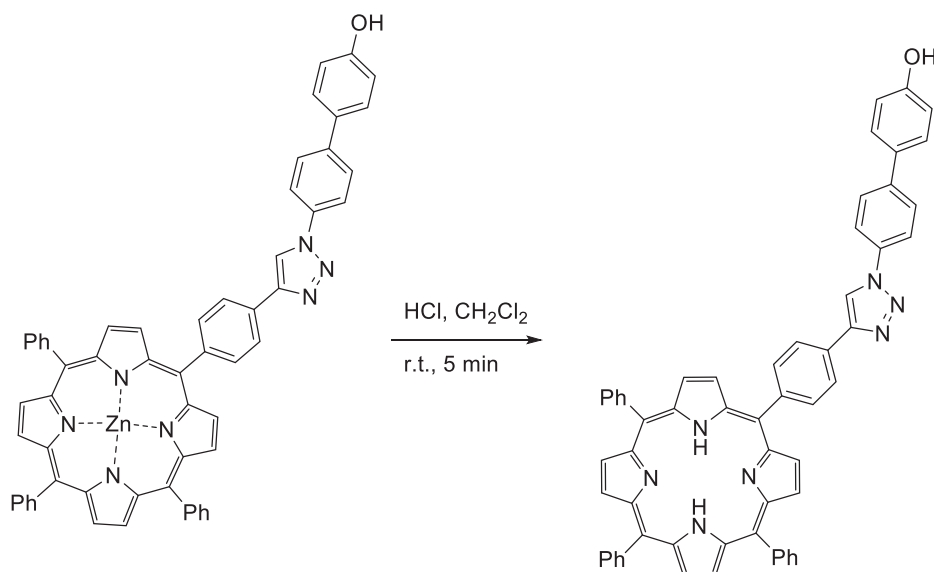
$^{13}\text{C-NMR}$ (125 MHz, CD_2Cl_2 , 298 K, δ in ppm): 155.8, 150.8, 150.8, 150.8, 150.7, 148.7, 143.5, 143.4, 141.8, 136.2, 135.6, 135.0, 135.0, 132.6, 132.6, 132.5, 132.5, 132.4, 130.0, 128.8, 128.3, 128.1, 127.1, 124.5, 121.8, 121.8, 121.3, 121.0, 118.6, 116.4.

ESI(+) (m/z): 912.3 $[\text{M}+\text{H}]^+$, 934.2 $[\text{M}+\text{Na}]^+$

MALDI(+), DCTB^a-matrix (m/z): 911.3 $[\text{M}]^+$

^a *trans*-2-[3-(4-*tert*-Butylphenyl)-2-methyl-2-propenylidene]malononitrile

5-(4-(1-(4'-Hydroxy-1,1'-biphenyl)-2,3-triazo-4-yl)phenyl)-10,15,20-triphenylporphyrin (**6**)



Zinc(II)-5-(4-(1-(4'--(methoxymethoxy)biphenyl),2,3-triazo-4-yl)phenyl),10,15,20-triphenylporphyrin (123 mg, 0.135 mmol) was dissolved in 35 mL of dichloromethane and hydrochloric acid (1.50 mL, 37 % aq., 18.1 mmol, 135 eq.) was added at once. The mixture was stirred for 5 min at room temperature and then poured onto water. After extraction with dichloromethane the combined organic phases were washed with 5 % NaHCO₃ and brine. Then, the organic phase was dried with MgSO₄ and the solvents were removed under reduced pressure. The resulting residue was purified via column chromatography on silica (eluent: CH₂Cl₂ to CH₂Cl₂/CH₃OH 10:1 (v/v), R_f = 0.38).

Yield: 110 mg (93 %)

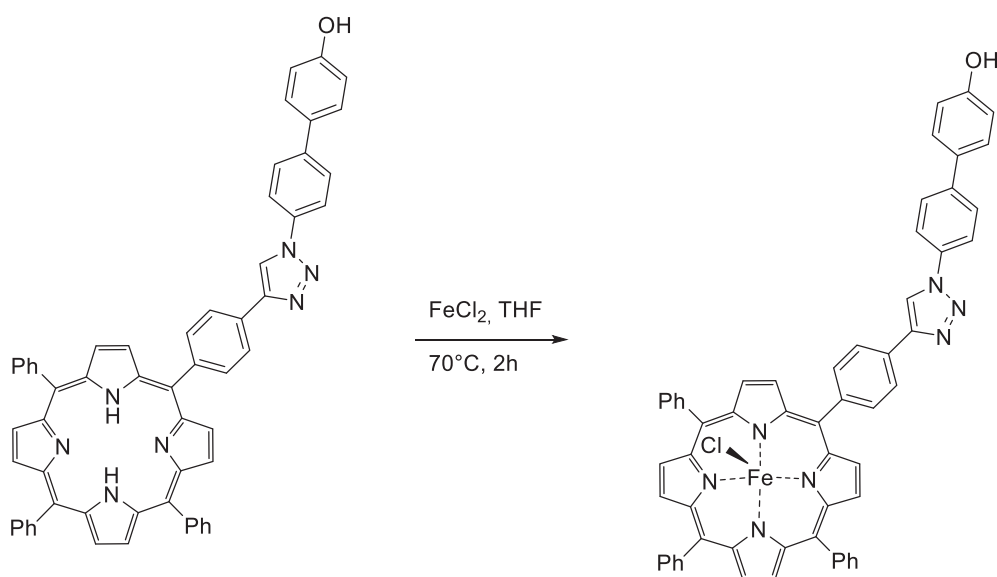
¹H-NMR (500 MHz, CD₂Cl₂, δ in ppm): 8.97 (d, 2H, J = 4.8 Hz), 8.90 (d, 2H, J = 4.8 Hz), 8.88 (s, 4H), 8.53 (s), 8.33 (m, 4H), 8.26 – 8.20 (m, 6H), 7.95 (d, 2H, J = 8.4 Hz), 7.83 – 7.74 (m, 11H), 7.58 (d, J = 8.5Hz), 6.96 (d, J = 8.5Hz), –2.80 (s, 2H).

¹³C-NMR (125 MHz, CD₂Cl₂, δ in ppm): 156.6, 148.7, 142.8, 142.6, 141.9, 136.3, 135.8, 135.1, 132.6, 130.5, 128.9, 128.5, 128.4, 128.3, 127.3, 124.7, 121.4, 120.9, 120.9, 120.1, 118.7, 116.4.

ESI(+) (*m/z*): 850.3289 [M+H]⁺ (calc. 850.3297)

MALDI(+), DCTB-matrix (*m/z*): 849.4 [M]⁺

Iron(III)-chlorido-5-(4-(1-(4'-hydroxy-1,1'-biphenyl)-2,3-triazo-4-yl)phenyl)-10,15,20-triphenylporphyrin (7)



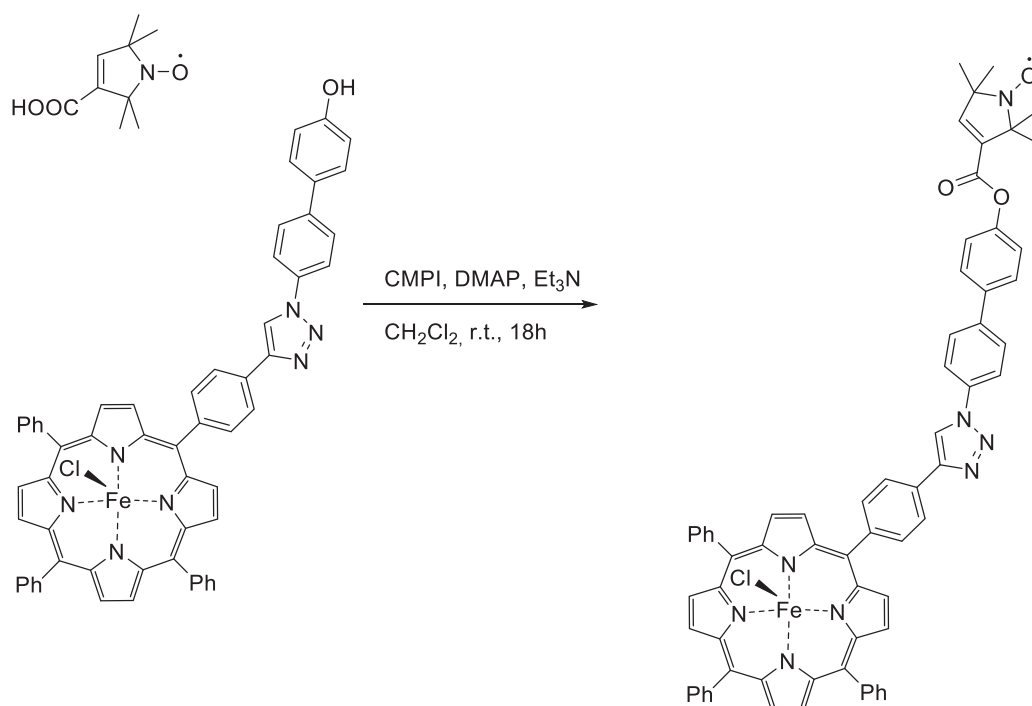
5-(4-(1-(4'-Hydroxybiphenyl)-2,3-triazo-4-yl)phenyl),10,15,20-triphenylporphyrin (110 mg, 0.13 mmol) was dissolved in 40 mL of THF. Afterwards, Fe(II) chloride tetrahydrate (100 mg, 0.52 mmol, 4.00 eq.) was added and the mixture was heated to reflux for 2 h. After cooling down to room temperature, the reaction mixture was poured into 100 mL 0.1 M HCl and extracted with dichloromethane. The organic phase was washed with water and brine and dried with MgSO₄. After removal of the solvents under reduced pressure, the product was purified via column chromatography on silica gel (eluent: CH₂Cl₂/CH₃OH 15:1 (v/v), R_f = 0.63).

Yield: 80 mg (66%)

ESI(+) (*m/z*): 903.2444 [M-Cl]⁺ (calc. 903.2405)

MALDI(+), DCTB-matrix (*m/z*): 903.2 [M-Cl]⁺

Iron(III)-chlorido-5-(4-(1-bipheny-(4''-1-oxyl-2,2,5,5-tetramethyl-2,5-dihydro-1H-pyrrole-3-oxycarbonyl),2,3-triazo-4-yl)phenyl)-10,15,20-triphenylporphyrin (1·Cl)



Iron(III)-chlorido-5-(4-(1-(4''-hydroxybiphenyl),2,3-triazo-4-yl)phenyl),10,15,20-triphenylporphyrine (60 mg, 0.064 mmol), 14 mg 2,2,5,5-tetramethyl-3-pyrrolin-1-oxyl-3-carboxylic acid (14 mg, 0.077 mmol, 1.20 aq.), 2-chloropyridinium iodide (20 mg, 0.077 mmol, 1.20 aq.), 4-dimethylamino pyridine (4 mg, 0.02 mmol, 0.4 aq.) were placed in a round bottom flask which was then evacuated for 30 min. Subsequently, 5 mL of dry dichloromethane and triethyl amine (22 μ L, 0.15 mmol, 2.4 aq.) were added. The reaction mixture was stirred at room temperature overnight and then poured onto ice-water. The product was extracted with dichloromethane. The organic phase was washed with brine and dried over MgSO₄. The pure product was isolated after column chromatography on silica gel (eluent: CH₂Cl₂/CH₃OH 20:1 (v/v), R_f = 0.47).

Yield: 54 mg (77 %)

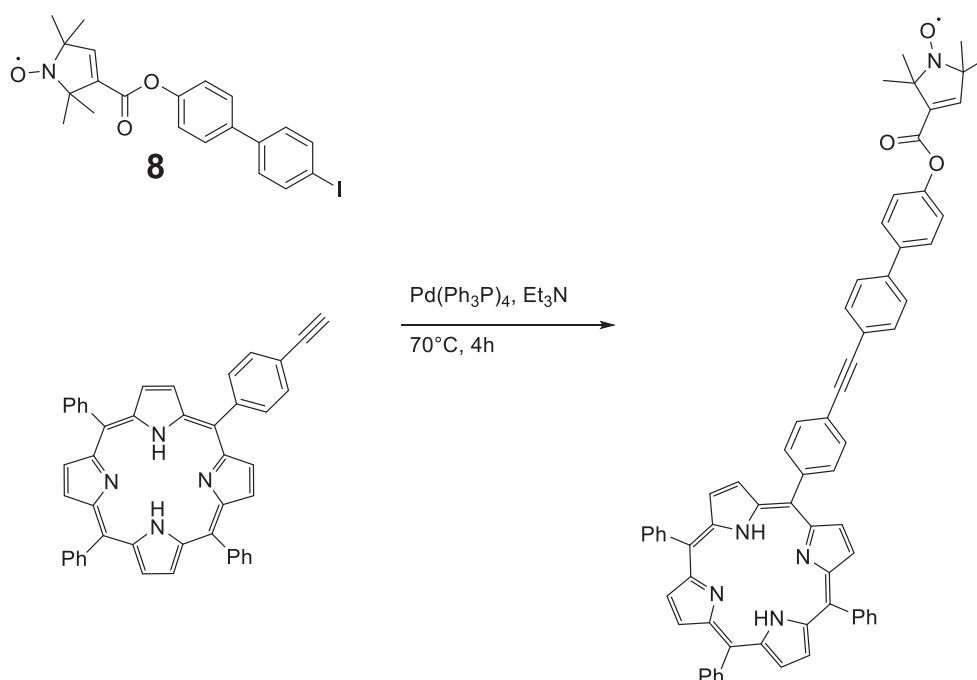
HRMS ESI(+) (m/z): 1069.3278 [M-Cl]⁺ (calc. 1069.3278), 1104.2961 [M]⁺ (calc. 1104.2963)

MALDI(+), DCTB-matrix (m/z): 1069.3 [M-Cl]⁺, 1104.3 [M]⁺, 2154.6 [(M-Cl)₂O]⁺

cw X-band EPR in d₈-toluene (nitroxide moiety): $g_{11} = 1.998$, $g_{22} = 2.006$, $g_{33} = 2.012$; $A_{11} = 12$ MHz, $A_{22} = 13$ MHz, $A_{33} = 90$ MHz

EPR (iron center): see main text

5-[4-(4'-(1-Oxyl-2,2,5,5-tetramethylpyrrolin-3-oxycarbonyl)-1,1'-biphenyl)-ethynyl-phenyl]-10,15,20-triphenylporphyrin (**9**)



Compound **8** was obtained in accordance to the procedure reported by Bode *et al.*^[3]

5-(4-Ethynylphenyl)-10,15,20-triphenylporphyrin (440 mg, 0.69 mmol, 1.00 eq.), **8** (264 mg, 0.57 mmol, 0.83 eq.) and Pd(PPh₃)₄ (119 mg, 0.09 mmol, 15.0 mol-%) were mixed under argon atmosphere. After addition of 5 mL of anhydrous DMF and 15 mL of anhydrous NEt₃ the solution was heated to 70 °C and stirred for 4 h. Then the mixture was cooled to 35 °C and stirred for another 68 h. After the mixture had been cooled to room temperature, the reaction was quenched by addition of 50 mL water. The organic phase was washed three times with 50 mL water. The combined aqueous layers were extracted with CH₂Cl₂ and the extract dried with Na₂SO₄. After removal of the solvents the product could be obtained as purple solid after column chromatography on silica gel (eluent: CH₂Cl₂, R_f = 0.60).

Yield: 326 mg (59 %)

¹H-NMR (700.4 MHz, CD₂Cl₂, δ in ppm): 8.89-8.91 (m, 8H), 8.20-8.26 (m, 8H), 7.97 (d, 2H, J = 7,5 Hz), 7.69-7.87 (m, 16H), 7.29 (br s), 1.43 (s, 12H), -2.79 (s, 2H).

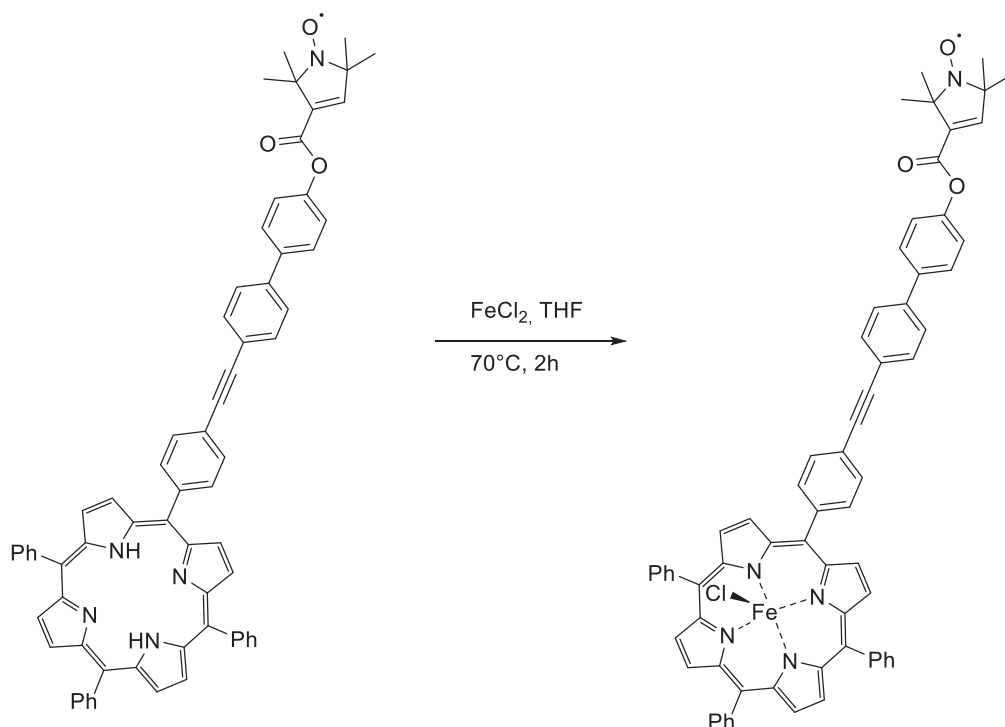
¹³C-NMR (176.1 MHz, CD₂Cl₂, δ in ppm) = 142.6, 142.3, 140.4, 138.5, 135.0, 134.9, 132.5, 130.3, 128.4, 128.1, 127.4, 127.1, 123.0, 122.7, 120.7, 120.6, 119.5, 90.5, 90.5.

ESI(+) (*m/z*): 487.7 [M+2H]²⁺, 973.4 [M+H]⁺

HRMS ESI(+) (*m/z*): 973.3994 [M+H]⁺ (calc. 973.3986)

Elemental analysis (%): C 82.36, H 5.26, N 6.99 (calc. for C₆₇H₅₀N₅O₃: C 82.69, H 5.18, N 7.20)

Iron(III)-chlorido-[5-[4-[(4'-(1-oxyl-2,2,5,5-tetramethyl-pyrrolin-3-carboxylat)-(1,1'-biphenyl)-4-yl)ethynyl]-phenyl]-10,15,20-triphenylporphyrin] (2·Cl)



A solution of **9** (130 mg, 13 μmol , 1.00 eq.) in 15 mL of anhydrous THF was heated to 70 °C. After adding FeCl₂ (36 mg 0.28 mmol, 2.15 eq.), the reaction mixture was stirred for 2 h. After cooling to room temperature, the solvent were removed and the crude product was purified by filtration through a short column (silica gel, eluent: CH₂Cl₂ to CH₂Cl₂ + 4% MeOH). The product was then dissolved in 50 mL of CH₂Cl₂ and washed with 1 M HCl solution and 50 mL water. The organic layer was dried with Na₂SO₄. After removal of the solvents the product was dissolved in as less CH₂Cl₂ as possible and poured into an excess of n-hexane (about 50 mL). The product could be obtained as a red-brown solid after filtration.

Yield: 109 mg (79 %)

MALDI(+), DCTB-matrix (*m/z*): 1026.3 [M-Cl]⁺, 1061.3 [M]⁺

ESI(+) (*m/z*): 513.2 [M-Cl]²⁺, 530.6 [M]²⁺, 1026.3 [M-Cl]⁺, 1061.3 [M]⁺;

HRMS ESI(+) (*m/z*): 1061.2790 [M]⁺ (calc. 1061.2792)

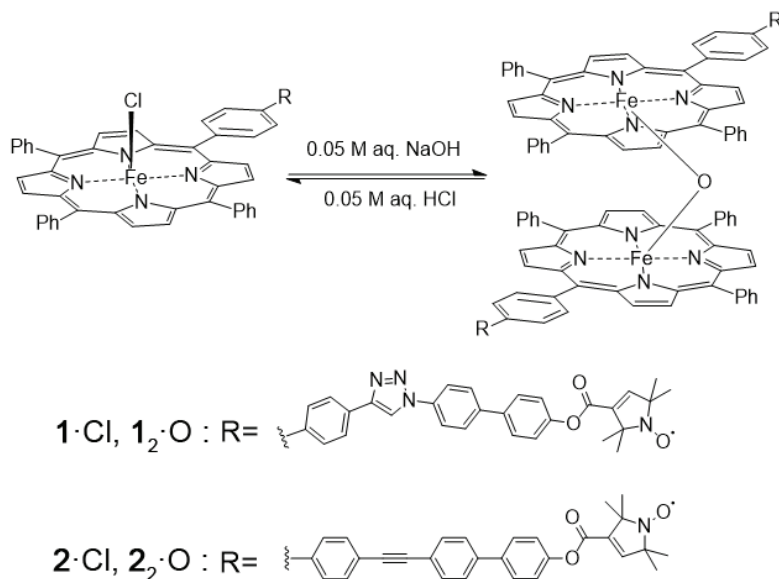
Elemental analysis (%): C 75.48, H 4.66, N 4.48 (calc. for C₆₇H₄₈ClFeN₅O₃: C 75.74, H 4.55, N 6.59).

cw X-band EPR in d₈-toluene (nitroxide moiety): g₁₁ = 2.0021, g₂₂ = 2.0062, g₃₃ = 2.0091; A₁₁ = 7

MHz, A₂₂ = 12 MHz, A₃₃ = 93 MHz

EPR (iron center): see main text

General procedures for the dimerization/monomerization of iron(III) porphyrins



The dimerization of $1 \cdot \text{Cl}$ and $2 \cdot \text{Cl}$ to the μ_2 -oxo-bridged dimers $1_2 \cdot \text{O}$ and $2_2 \cdot \text{O}$, respectively, was achieved by treatment of the monomers with aqueous sodium hydroxide. In particular, a 200 μM solution of $1 \cdot \text{Cl}$ or $2 \cdot \text{Cl}$ in toluene were prepared and mixed with 0.05 M aqueous NaOH in a volume ratio of 1:1. The obtained solution was shaken for 2 min by means of a Vortex Genie 2 (Scientific Industries Inc) and then incubated for 1 min to achieve separation of water and toluene layers. After this, the toluene layer was extracted and the entire procedure was repeated again to ensure efficient dimer formation. Subsequently, the toluene layer was transfused into a clean tube and the solvent was evaporated from the samples under high vacuum.

The reversibility of the dimerization process was tested via treatment of the dimers with aqueous hydrochloric acid. This procedure was done in complete analogy to the treatment with NaOH except for the fact that 0.05 M aqueous HCl was used instead of 0.05 M aqueous NaOH. This procedure again gave rise to the monomers $1 \cdot \text{Cl}$ and $2 \cdot \text{Cl}$.

1.2 *High pressure liquid chromatography*

High pressure liquid chromatography (HPLC) was performed on a Knauer instrument using a Daicel Chiralpak IA column (5 μm , 250 x 20 mm) on a semipreparative scale.

1.3 *Elemental analysis*

Elemental analysis was carried out on an elemental analyzer Vario EL (Heraeus technology group / Elementar Analysensysteme GmbH).

1.4 *NMR*

^1H and ^{13}C NMR spectra were recorded at 298 K using Avance III HD Ascend 700 (Bruker), DMX 500 (Bruker), and AM 400 (Bruker) spectrometers. ^1H NMR chemical shifts are reported relative to residual non-deuterated solvent as internal standard.^[4] ^{13}C NMR chemical shifts are reported relative to deuterated solvent as internal standard.^[4] Signals were assigned on the basis of ^1H , ^{13}C , HMQC, HMBC, DEPT-135, and ^1H , ^1H -COSY NMR experiments.

1.5 *Mass spectrometry*

ESI mass spectra were recorded on a LTQ Orbitrap XL spectrometer (Thermo Fisher). For MALDI mass spectroscopy, an Autoflex II TOF/TOF (Bruker) spectrometer was employed.

2 Analytical data

2.1 PELDOR measurements on bis-nitroxide reference compound

The bis-nitroxide reference compound **10** (Figure S1a) was synthesised in accordance to the procedure described elsewhere.^[3] The PELDOR sample of **10** was dissolved in deuterated toluene to a concentration of 200 μM . The PELDOR time trace of **10** was acquired in accordance to the description given in the Experimental Section of the main text. The analysis of the PELDOR time trace was done by means of the program DeerAnalysis^[5] (Figure S1b-d). The modulation depth λ of 32 % was determined for the background-corrected time trace.

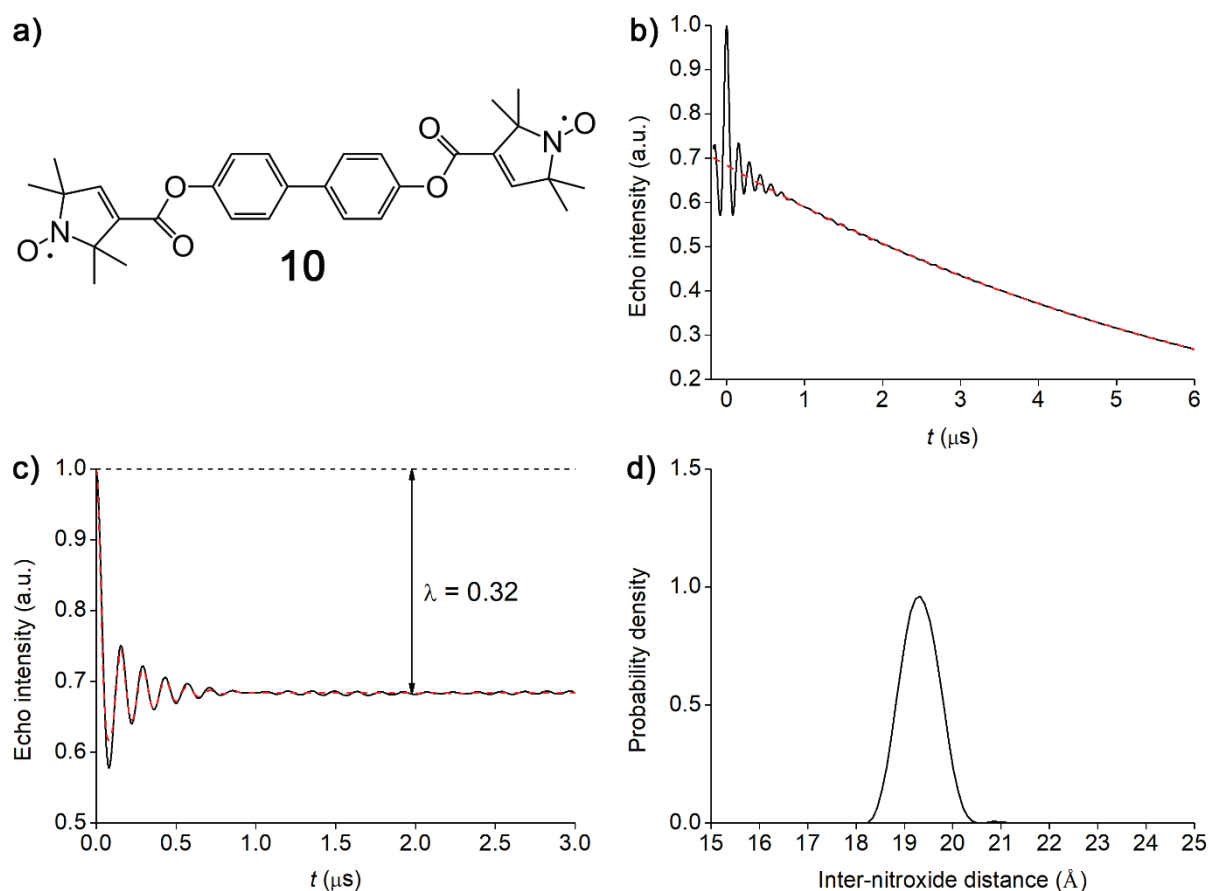


Figure S1: PELDOR measurements on bis-nitroxide reference compound **10**. **a)** The structure of bis-nitroxide reference compound **10**. **b)** The original PELDOR time trace (black line) and its background fit (red dashed line). **c)** The background-corrected PELDOR time trace (black line) and its fit obtained by Tikhonov regularization (red dashed line). **d)** The inter-nitroxide distance distribution in **10**.

2.2 MD simulations for the dimers $1_2 \cdot \text{O}$ and $2_2 \cdot \text{O}$

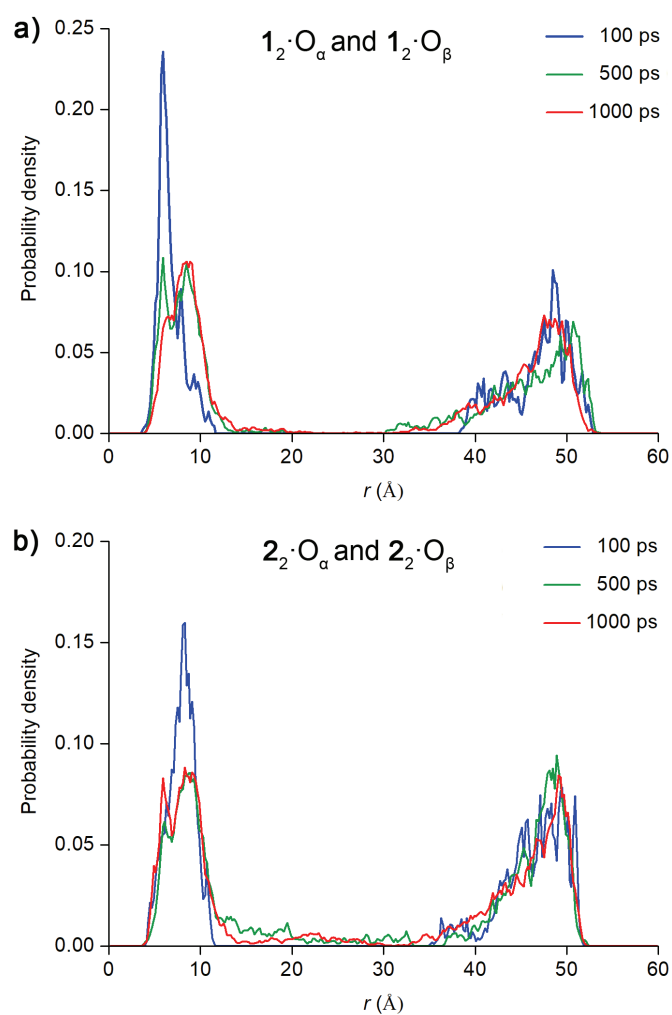


Figure S2: Inter-nitroxide distance distributions obtained from 100, 500, and 1000 ps long MD simulations on **a)** $1_2 \cdot \text{O}_\alpha$ and $1_2 \cdot \text{O}_\beta$, and **b)** $2_2 \cdot \text{O}_\alpha$ and $2_2 \cdot \text{O}_\beta$.

Table S1. Energies for the porphyrin system $\mathbf{1}_2\cdot\text{O}$, α - and β -conformer and transition state TS1.

	$\mathbf{1}_2\cdot\text{O}_\alpha$	$\mathbf{1}_2\cdot\text{O}_\beta$	TS1
\mathbf{E} / a.u.	-418.55072	-418.53628	-418.51412
$\delta\mathbf{G}_{\text{solv}}$ / a.u.	-0.15522	-0.16079	-0.16696
$\mathbf{G}_{\text{RRHO}}^{\text{T}}$ a.u.	1.77309	1.76691	1.77901
$\Delta G(\mathbf{1}_2\cdot\text{O}_\alpha) - \Delta G(\mathbf{1}_2\cdot\text{O}_\beta) = -1.7 \text{ kcal mol}^{-1}$			
$\Delta G(\text{TS1}) - \Delta G(\mathbf{1}_2\cdot\text{O}_\alpha) = 19.3 \text{ kcal mol}^{-1}$			
$\Delta G(\text{TS1}) - \Delta G(\mathbf{1}_2\cdot\text{O}_\beta) = 17.6 \text{ kcal mol}^{-1}$			

Table S2. Energies for the porphyrin system $\mathbf{2}_2\cdot\text{O}$, α - and β -conformer and transition state TS2.

	$\mathbf{2}_2\cdot\text{O}_\alpha$	$\mathbf{2}_2\cdot\text{O}_\beta$	TS2
\mathbf{E} / a.u.	-399.89458	-399.88072	-399.85636
$\delta\mathbf{G}_{\text{solv}}$ / a.u.	-0.15033	-0.15529	-0.16352
$\mathbf{G}_{\text{RRHO}}^{\text{T}}$ / a.u.	1.72068	1.71467	1.72474
$\Delta G(\mathbf{2}_2\cdot\text{O}_\alpha) - \Delta G(\mathbf{2}_2\cdot\text{O}_\beta) = -1.8 \text{ kcal mol}^{-1}$			
$\Delta G(\text{TS2}) - \Delta G(\mathbf{2}_2\cdot\text{O}_\alpha) = 18.3 \text{ kcal mol}^{-1}$			
$\Delta G(\text{TS2}) - \Delta G(\mathbf{2}_2\cdot\text{O}_\beta) = 16.5 \text{ kcal mol}^{-1}$			

Table S3. Energies for the porphyrin system $\mathbf{2}_2\cdot\text{O}$, α - and β -conformer and transition state TS2.

	start	end	TS
\mathbf{E} / a.u.	-257.29157	-257.28543	-257.25523
$\delta\mathbf{G}_{\text{solv}}$ / a.u.	-0.07356	-0.06914	-0.08223
$\mathbf{G}_{\text{RRHO}}^{\text{T}}$ / a.u.	1.10194	1.10401	1.10848
$\Delta G(\text{start}) - \Delta G(\text{end}) = -0.2 \text{ kcal mol}^{-1}$			
$\Delta G(\text{TS}) - \Delta G(\text{start}) = 17.4 \text{ kcal mol}^{-1}$			
$\Delta G(\text{TS}) - \Delta G(\text{end}) = 17.2 \text{ kcal mol}^{-1}$			

2.3 Mass spectra

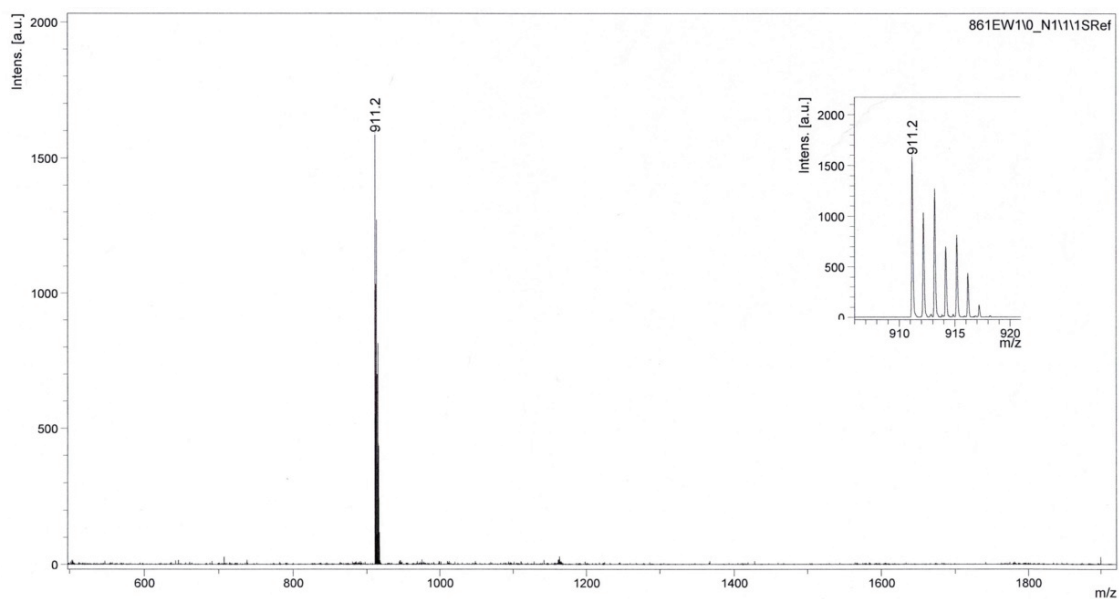


Figure S3: MALDI(+) mass spectrum of **5**.

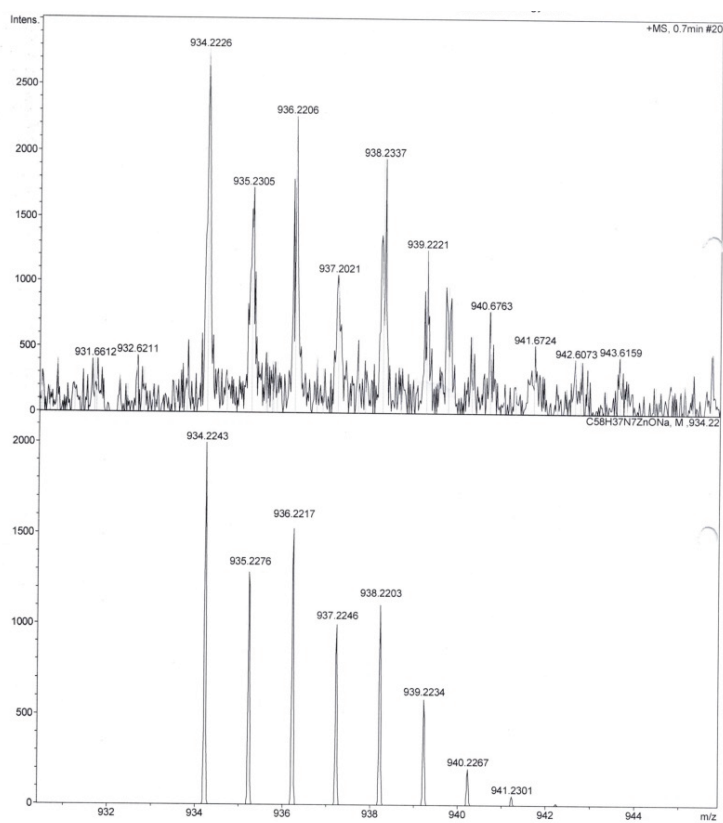


Figure S4: ESI(+) high-resolution mass spectrum of **5**. The upper spectrum is the experimental spectrum and the lower one is its simulation.

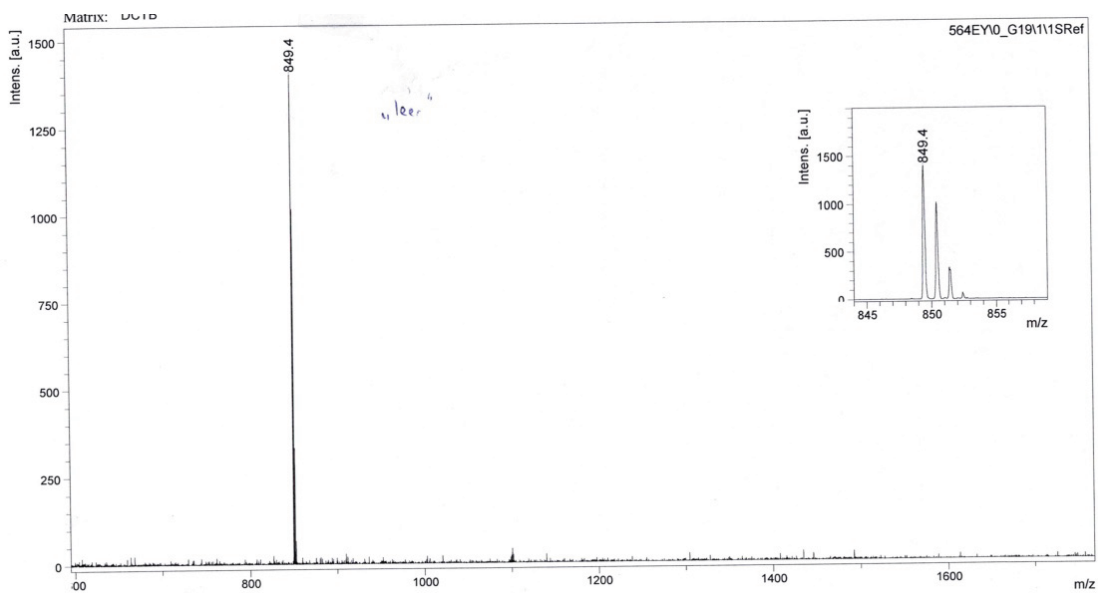


Figure S5: MALDI(+) mass spectrum of **6**.

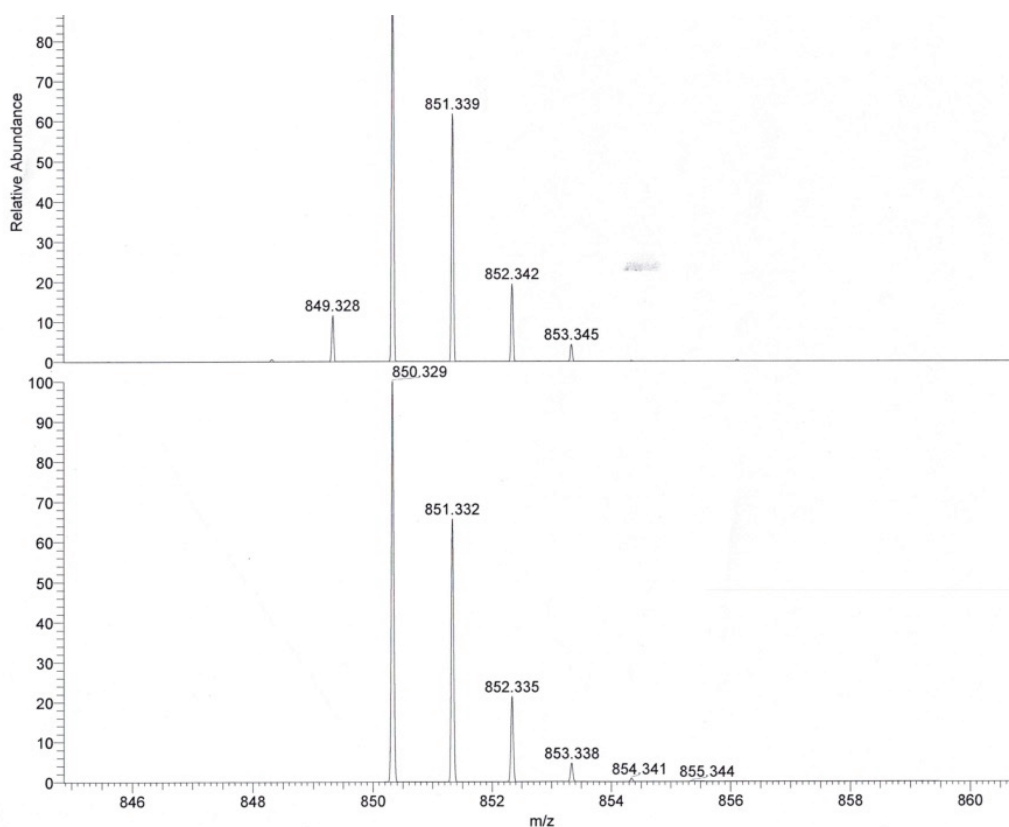


Figure S6: ESI(+) high-resolution mass spectrum of **6**. The upper spectrum is the experimental spectrum and the lower one is its simulation.

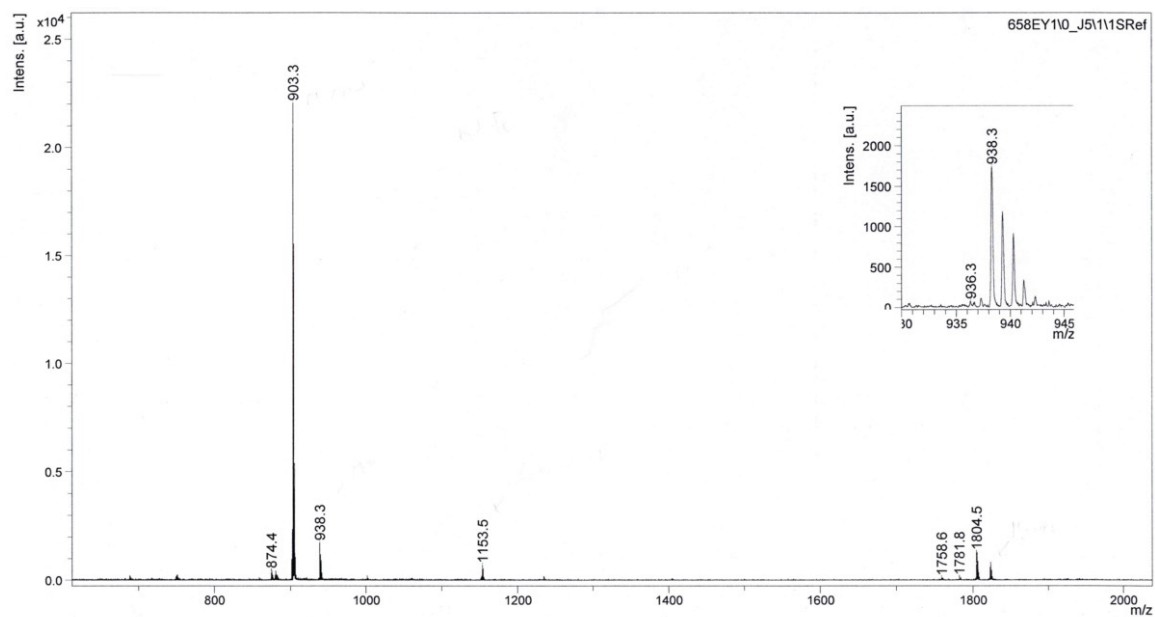


Figure S7: MALDI(+) mass spectrum of **7**.

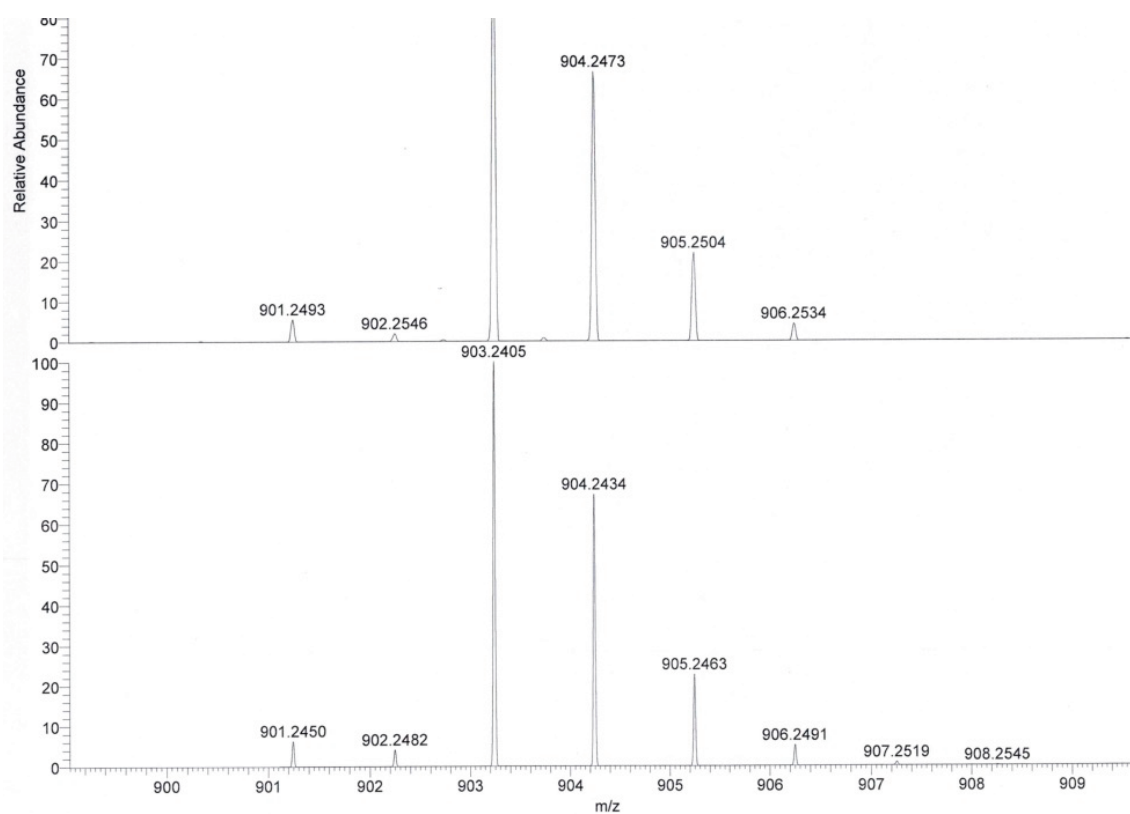


Figure S8: ESI(+) high-resolution mass spectrum of **7**. The upper spectrum is the experimental spectrum and the lower one is its simulation.

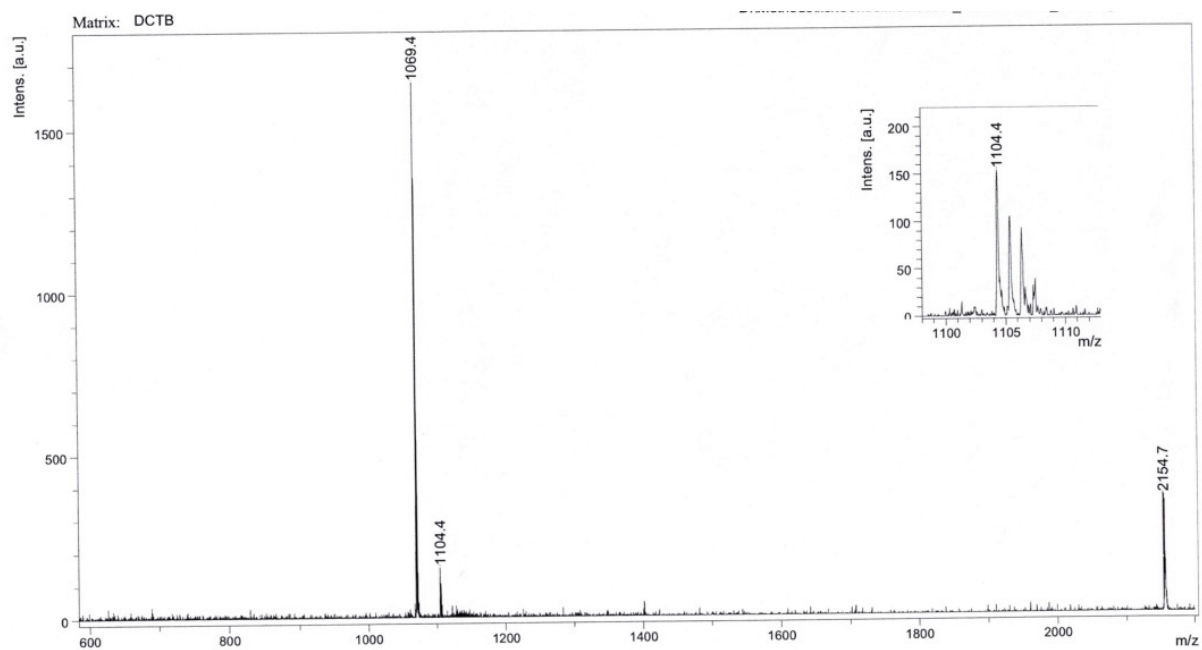


Figure S9: MALDI(+) mass spectrum of **1·Cl**.

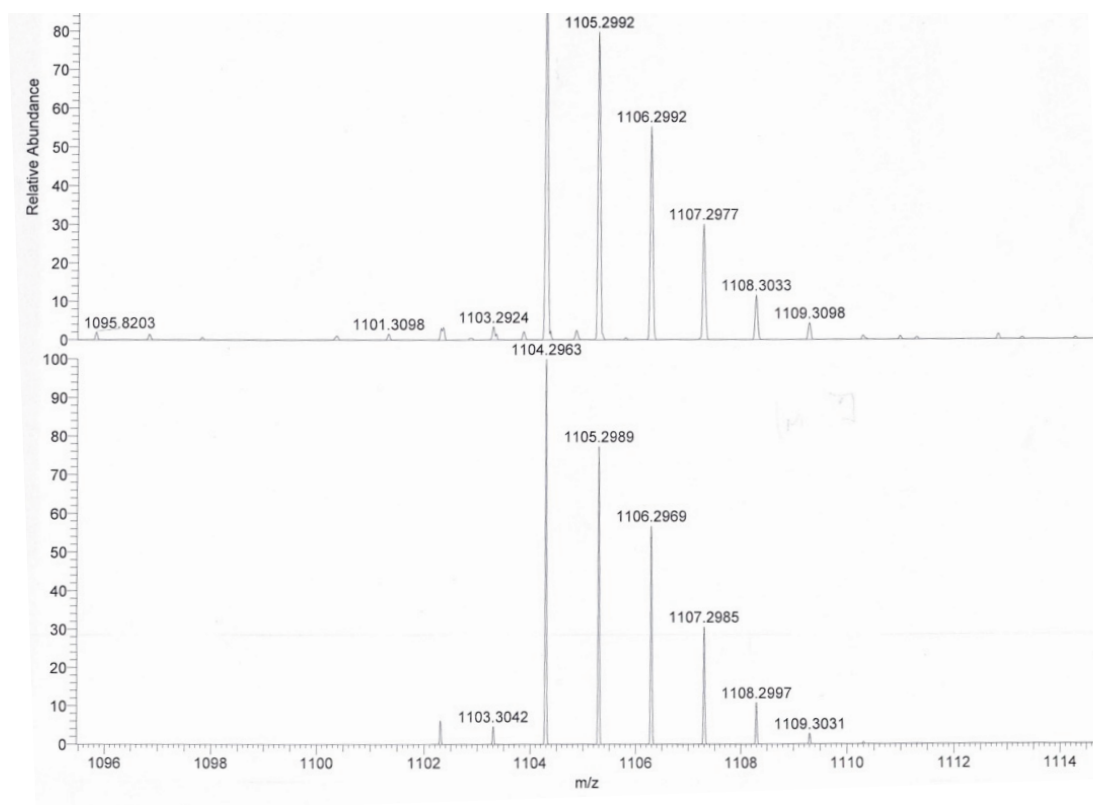


Figure S10: ESI(+) high-resolution mass spectrum of **1·Cl**. The upper spectrum is the experimental spectrum and the lower one is its simulation.

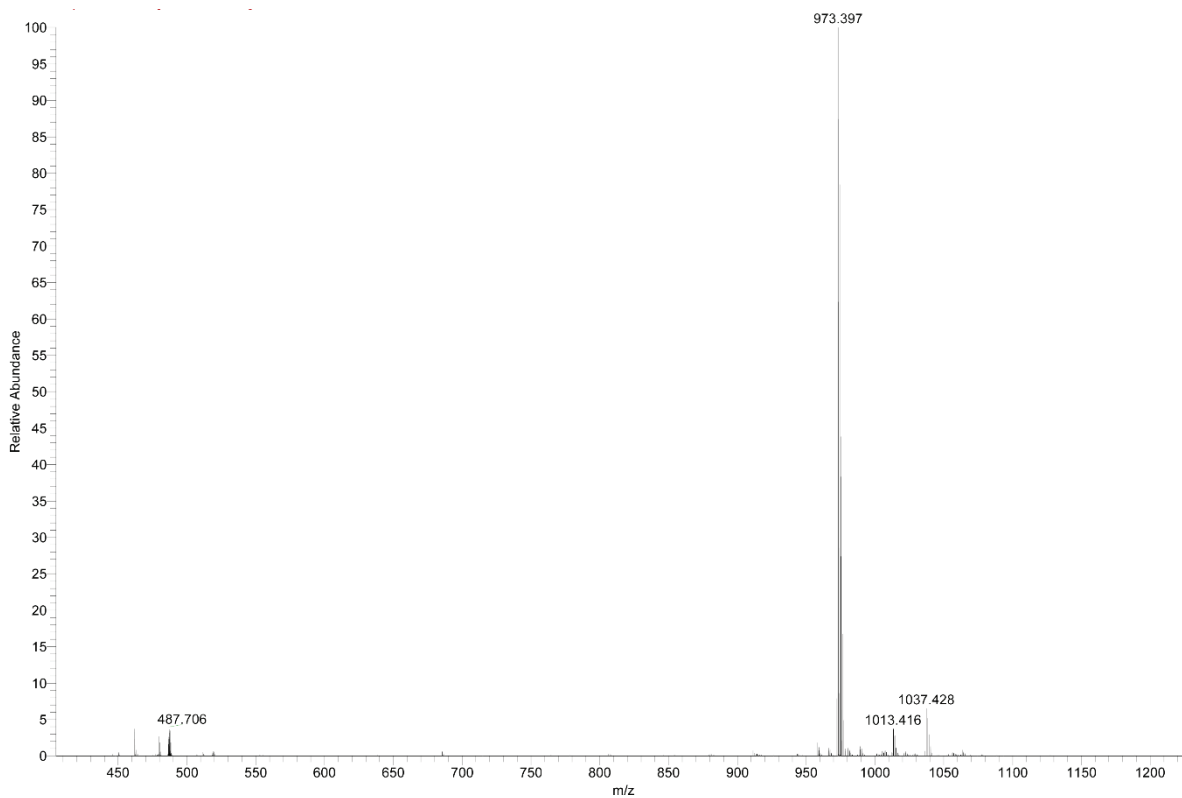


Figure S11: ESI(+) mass spectrum of **9**.

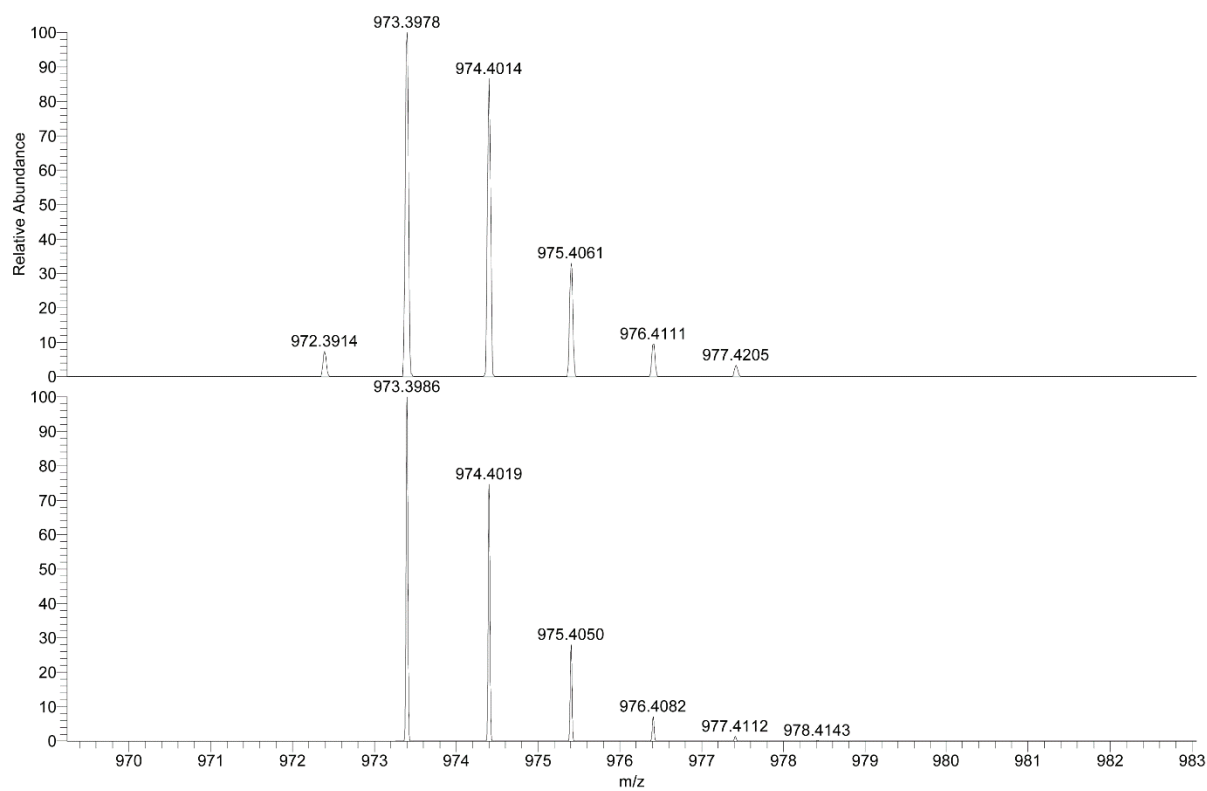


Figure S12: ESI(+) high-resolution mass spectrum of **9**. The upper spectrum is the experimental spectrum and the lower one is its simulation.

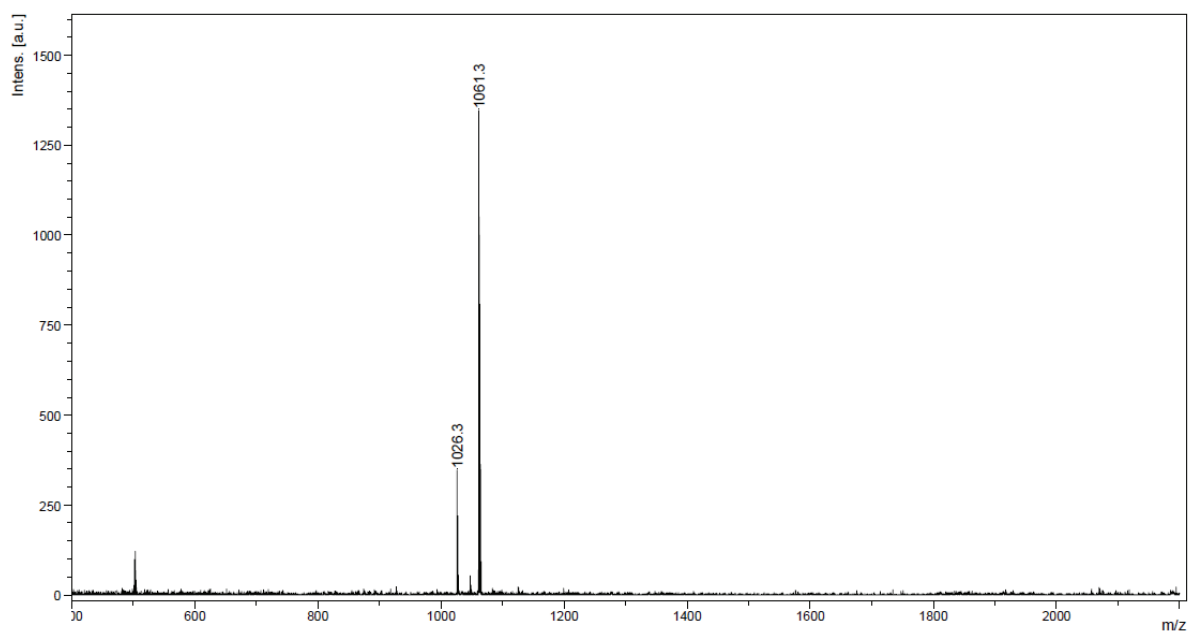


Figure S13: MALDI(+) mass spectrum of **2·Cl**.

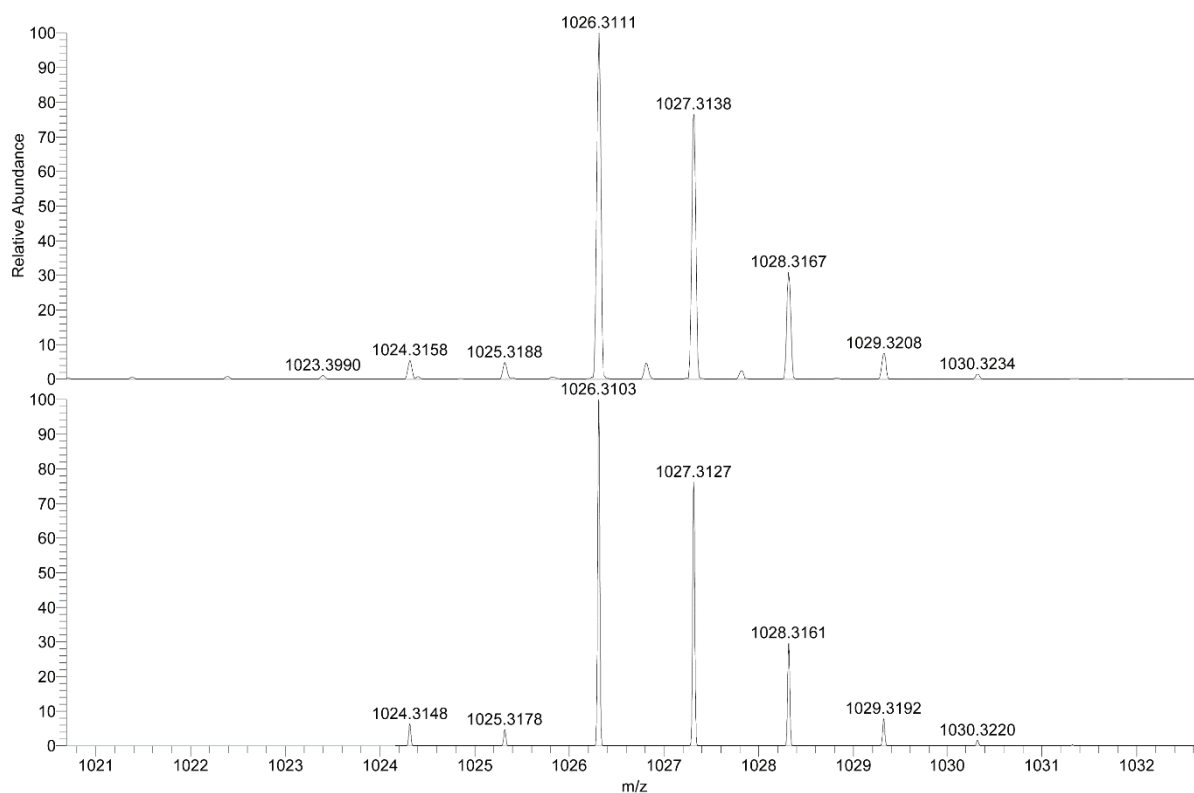


Figure S14: ESI(+) high-resolution mass spectrum of **2·Cl**. The upper spectrum is the experimental spectrum and the lower one is its simulation.

2.4 *The atomic coordinates of the optimized porphyrin structures*

The atomic coordinates of $\mathbf{1}_2 \cdot \mathbf{O}_a$

C	9.4047671	0.7993054	2.3674745
N	8.0947172	1.1318279	2.1354293
C	7.9941966	2.4758026	2.3629647
C	6.8540769	3.2694609	2.2328799
C	5.5814855	2.7340715	2.0858547
N	5.2982297	1.3995303	2.0774417
C	3.9417103	1.2894300	2.0874239
C	3.2406209	0.0901847	2.1508906
C	3.8557038	-1.1538102	2.0375205
N	5.1716647	-1.3960995	1.7340463
C	5.2652050	-2.7390056	1.4865830
C	6.3978439	-3.4334397	1.0728732
C	7.6588993	-2.8524582	1.0417181
N	7.9380587	-1.5788383	1.4508377
C	9.2952446	-1.4989552	1.5566021
C	10.0028925	-0.4231421	2.0830557
C	11.4482421	-0.6039034	2.3532238
C	12.4063197	0.2211853	1.7630466
C	13.7558568	0.0305387	2.0207230
C	14.1674570	-0.9812923	2.8781703
C	13.2212803	-1.8040643	3.4758462
C	11.8718575	-1.6195214	3.2138990
H	11.1351507	-2.2583484	3.6896208
H	13.5357785	-2.5945067	4.1495512
H	15.2230789	-1.1290396	3.0797325
H	14.4913572	0.6734575	1.5490324
H	12.0884540	1.0053937	1.0869458
C	9.8930926	-2.7319540	1.1293813
C	8.8794344	-3.5645561	0.7921456
H	8.9437569	-4.5733613	0.4185241
H	10.9537204	-2.9188510	1.0818507
FE	6.6300904	-0.0574520	1.5134718
O	6.4015642	0.4091160	-0.0885231
FE	6.8273783	0.4594304	-1.7153814
N	4.9766745	1.2598819	-2.1481430
C	3.8068751	0.5581952	-2.0953571
C	3.7084580	-0.8189097	-2.2561528
C	4.8239527	-1.6204489	-2.5128639

N 6.1397680 -1.2761102 -2.3861846
C 6.8642114 -2.3878791 -2.7327850
C 8.2338950 -2.5579028 -2.5625220
C 9.0560965 -1.5630904 -2.0424138
N 8.6949745 -0.2651872 -1.8267191
C 9.8317161 0.3937344 -1.4492251
C 9.9628726 1.7755159 -1.3809458
C 8.9060585 2.6407528 -1.6488075
N 7.5951708 2.2963169 -1.8343802
C 6.9163833 3.4715831 -2.0298341
C 5.5386515 3.6389610 -2.1117268
C 4.6420303 2.5769757 -2.0886966
C 3.2169126 2.7190145 -1.9884805
C 2.7007736 1.4673771 -1.9681889
H 1.6641380 1.1861040 -1.8910773
H 2.6914724 3.6576011 -1.9138163
C 4.9894135 5.0145456 -2.1760432
C 5.2124039 5.9191149 -1.1367592
C 4.6819985 7.1992760 -1.1932583
C 3.9295970 7.5953689 -2.2916041
C 3.7044677 6.7022826 -3.3312655
C 4.2265337 5.4182537 -3.2731892
H 4.0537488 4.7238799 -4.0887169
H 3.1175478 7.0066422 -4.1917561
H 3.5166894 8.5976391 -2.3362486
H 4.8542724 7.8915279 -0.3757279
H 5.7919689 5.6081698 -0.2748517
C 7.8409327 4.5663833 -2.0711411
C 9.0705197 4.0545210 -1.8207288
H 10.0126781 4.5770961 -1.7808056
H 7.5748430 5.5920019 -2.2708179
C 11.2946176 2.3723724 -1.1240449
C 12.3757531 2.1049283 -1.9661380
C 13.6113671 2.6905855 -1.7315346
C 13.7855830 3.5506973 -0.6550571
C 12.7152820 3.8259427 0.1862030
C 11.4779018 3.2448890 -0.0488507
H 10.6448223 3.4560723 0.6114555
H 12.8432375 4.4963636 1.0296457
H 14.7531427 4.0062062 -0.4731350
H 14.4421945 2.4769008 -2.3960781

H 12.2407092 1.4509069 -2.8210522
C 10.9201246 -0.5347821 -1.3400797
C 10.4441695 -1.7429827 -1.7252653
H 10.9721446 -2.6815138 -1.7768173
H 11.9178025 -0.2862220 -1.0171232
C 8.8525394 -3.8513714 -2.9359408
C 8.4257416 -5.0497255 -2.3619368
C 9.0221461 -6.2518087 -2.7128555
C 10.0492620 -6.2753815 -3.6471905
C 10.4772121 -5.0889841 -4.2291275
C 9.8859326 -3.8852156 -3.8752458
H 10.2172082 -2.9621842 -4.3391872
H 11.2772696 -5.1007715 -4.9621520
H 10.5157430 -7.2157514 -3.9209495
H 8.6860335 -7.1752933 -2.2533741
H 7.6318545 -5.0329487 -1.6250603
C 5.9812238 -3.4091394 -3.2117780
C 4.7165297 -2.9474803 -3.0408476
H 3.7881941 -3.4366513 -3.2903469
H 6.2916592 -4.3576319 -3.6196557
C 2.3885699 -1.4698496 -2.1345270
C 1.2608063 -1.0415531 -2.8408216
C 0.0099232 -1.5668221 -2.5619739
C -0.1479399 -2.5470500 -1.5771792
C 0.9932293 -3.0398343 -0.9354906
C 2.2382175 -2.5104646 -1.2119581
H 3.1071196 -2.8661275 -0.6712017
H 0.8840225 -3.8203256 -0.1893367
C -1.4589326 -3.0255222 -1.1696094
C -2.7161285 -2.5372333 -1.4464588
N -3.5518108 -3.3265548 -0.7350435
N -2.8541287 -4.2507610 -0.0613788
N -1.6035718 -4.0764809 -0.3179627
C -4.9402956 -3.2605980 -0.5686337
C -5.5390817 -4.0001109 0.4526780
C -6.9024742 -3.9143905 0.6596339
C -7.7018595 -3.0943472 -0.1441363
C -7.0916798 -2.3828253 -1.1813025
C -5.7258456 -2.4580958 -1.3951721
H -5.2778214 -1.8859008 -2.1977997
H -7.6849564 -1.7331643 -1.8147267

C -9.1431002 -2.9464445 0.1258122
C -9.6167748 -2.9473479 1.4421822
C -10.9597288 -2.7572081 1.7120953
C -11.8540990 -2.5684164 0.6615688
C -11.4091817 -2.5688567 -0.6555237
C -10.0602422 -2.7591922 -0.9115523
H -9.7195830 -2.7659476 -1.9407932
H -12.0973345 -2.4122599 -1.4755805
O -13.1675711 -2.3176929 1.0301736
C -14.2380384 -2.5990226 0.2701077
O -14.2024365 -3.1903192 -0.7858350
C -15.4774223 -2.0954058 0.8908855
C -15.6102983 -1.5604345 2.1073394
C -17.0190624 -1.1186824 2.3751034
N -17.6512778 -1.3672294 1.0643263
O -18.5808259 -0.5974736 0.6230343
C -16.7878936 -2.1252867 0.1399899
C -16.7349946 -1.4445517 -1.2276353
H -16.1182562 -2.0307326 -1.9061055
H -16.3114790 -0.4482607 -1.1283560
H -17.7425378 -1.3644130 -1.6329304
C -17.3206823 -3.5611015 0.0039084
H -18.3155265 -3.5430564 -0.4391078
H -16.6534490 -4.1385521 -0.6346904
H -17.3767971 -4.0375482 0.9814805
C -17.1231667 0.3591654 2.7586621
H -18.1700331 0.6598940 2.7673236
H -16.6953802 0.5128823 3.7475033
H -16.5835053 0.9695088 2.0374559
C -17.6994780 -1.9994743 3.4371348
H -18.7504187 -1.7246435 3.5178236
H -17.2174377 -1.8561671 4.4026770
H -17.6276977 -3.0497622 3.1583184
H -14.8230780 -1.4333668 2.8368822
H -11.3265947 -2.7391650 2.7312106
H -8.9254038 -3.0701119 2.2676968
H -7.3537094 -4.4990257 1.4538693
H -4.9228343 -4.6311764 1.0829048
H -3.0576882 -1.7126568 -2.0460441
H -0.8541130 -1.2001632 -3.1058394
H 1.3633418 -0.2921138 -3.6178693

C	6.2492201	-4.8726233	0.7508285
C	6.9150053	-5.8490508	1.4938427
C	6.7494155	-7.1937768	1.1947685
C	5.9180418	-7.5821725	0.1521714
C	5.2509544	-6.6178061	-0.5921252
C	5.4123604	-5.2731261	-0.2927489
H	4.8978324	-4.5204452	-0.8785996
H	4.6025744	-6.9125848	-1.4106742
H	5.7914245	-8.6341561	-0.0804854
H	7.2704007	-7.9431888	1.7817270
H	7.5509299	-5.5530127	2.3213895
C	4.0025082	-3.3712277	1.7297991
C	3.1316799	-2.3910280	2.0716146
H	2.0846345	-2.4888570	2.3074759
H	3.8169529	-4.4307216	1.6546900
C	1.7616321	0.1291498	2.2560585
C	1.0096727	0.6774971	1.2158278
C	-0.3732389	0.6675842	1.2550681
C	-1.0474301	0.1146522	2.3480510
C	-0.2937680	-0.4110207	3.4031636
C	1.0897794	-0.4055699	3.3579093
H	1.6593927	-0.8125354	4.1872133
H	-0.8094318	-0.8301425	4.2619199
C	-2.5006914	0.0871929	2.4051580
C	-3.4359589	0.5790203	1.5227835
N	-4.6279454	0.2915436	2.0922284
N	-4.4416916	-0.3450428	3.2566068
N	-3.1730588	-0.4681614	3.4494801
C	-5.9293338	0.5748823	1.6612980
C	-7.0155325	0.0774693	2.3832601
C	-8.3059255	0.3515447	1.9695276
C	-8.5491651	1.1237601	0.8284434
C	-7.4501839	1.6208541	0.1206870
C	-6.1542147	1.3531679	0.5258752
H	-5.3249903	1.7556329	-0.0420990
H	-7.6047636	2.2423350	-0.7538704
C	-9.9234087	1.4149170	0.3805030
C	-10.9587633	1.5926754	1.3033958
C	-12.2453837	1.8974355	0.8890794
C	-12.5051382	2.0310700	-0.4694818
C	-11.4974089	1.8457152	-1.4090026

C -10.2175396 1.5361603 -0.9818717
H -9.4414941 1.3760112 -1.7210343
H -11.7216464 1.9480153 -2.4637117
O -13.7554353 2.4187112 -0.9469844
C -14.8950464 1.8941785 -0.4679442
O -14.9402701 0.9999927 0.3464946
C -16.0916979 2.5254208 -1.0592269
C -17.3461051 2.1600551 -0.7686502
C -18.3584485 2.9822979 -1.5016208
N -17.4880693 3.8824762 -2.2597110
O -17.9400346 4.7893283 -3.0329466
C -16.0550404 3.6650325 -2.0517723
C -15.4343110 4.9498736 -1.4869749
H -14.3582386 4.8301146 -1.3820922
H -15.8649667 5.1784496 -0.5127778
H -15.6418864 5.7734020 -2.1699613
C -15.4126786 3.2865155 -3.3935776
H -15.6227806 4.0710880 -4.1202042
H -14.3364441 3.1822023 -3.2765030
H -15.8254047 2.3456434 -3.7559863
C -19.2483243 3.8066607 -0.5596898
H -19.8215880 4.5220344 -1.1487153
H -19.9303690 3.1508622 -0.0217642
H -18.6334908 4.3486822 0.1576366
C -19.2109550 2.1563316 -2.4759348
H -19.8060741 2.8329975 -3.0883984
H -19.8718503 1.4924720 -1.9215988
H -18.5684302 1.5628660 -3.1250175
H -17.6421970 1.3671997 -0.0947465
H -13.0343651 2.0443891 1.6156799
H -10.7548312 1.5192531 2.3656781
H -9.1359983 -0.0631282 2.5303591
H -6.8363171 -0.5293662 3.2633972
H -3.3449456 1.0812255 0.5765894
H -0.9320041 1.0849602 0.4245135
H 1.5206697 1.0936765 0.3562151
C 3.3447226 2.5967237 2.1090895
C 4.3602393 3.4918647 2.0770988
H 4.2984718 4.5680314 2.0558808
H 2.2847848 2.7931177 2.1365567
C 7.0226721 4.7370144 2.3331405

C	6.3775156	5.4771946	3.3254975
C	6.5551422	6.8509882	3.4040579
C	7.3783792	7.5037430	2.4955854
C	8.0291385	6.7746791	1.5085765
C	7.8552560	5.4010345	1.4293752
H	8.3587224	4.8336635	0.6550994
H	8.6743037	7.2775856	0.7957912
H	7.5137364	8.5782895	2.5581545
H	6.0504254	7.4148291	4.1819047
H	5.7509012	4.9701321	4.0515994
C	9.2470004	2.9842113	2.8377207
C	10.1110514	1.9390621	2.8720797
H	11.1373225	1.9371974	3.2023321
H	9.4237678	4.0035851	3.1416765

The atomic coordinates of $\mathbf{1}_2 \cdot \mathbf{O}_\beta$

C	1.5988410	6.5291056	2.4247566
N	0.3725057	6.0209524	2.0826931
C	-0.4747293	7.0917957	1.9997268
C	-1.8128538	7.0643639	1.6185403
C	-2.5153313	5.8800227	1.4331838
N	-2.0125196	4.6282523	1.6526190
C	-3.0760645	3.7742383	1.6108249
C	-3.0386547	2.4180364	1.9198040
C	-1.8482843	1.7274290	2.1240327
N	-0.5832846	2.2361225	1.9846184
C	0.2691686	1.1715855	2.0821783
C	1.6597116	1.1910321	1.9734594
C	2.3950473	2.3678007	1.9943859
N	1.8614562	3.6132684	2.1560854
C	2.9112165	4.4707120	2.2702462
C	2.8079164	5.8424595	2.4711509
C	4.0542142	6.6127495	2.6946787
C	4.8690905	6.3406388	3.7948799
C	6.0422891	7.0542677	3.9931237
C	6.4214116	8.0401496	3.0911302
C	5.6182104	8.3143510	1.9914750
C	4.4401294	7.6093263	1.7966915
H	3.8178635	7.8169321	0.9335295
H	5.9129553	9.0799308	1.2813866
H	7.3421210	8.5931418	3.2445059
H	6.6652772	6.8377367	4.8549079
H	4.5727147	5.5742486	4.5033880
C	4.1502553	3.7502895	2.1614976
C	3.8298360	2.4482636	1.9740185
H	4.4954239	1.6128702	1.8282488
H	5.1308943	4.1976508	2.1989884
FE	-0.0665269	4.1287713	1.6361596
O	0.4022863	4.1292490	0.0204178
FE	0.0832703	4.1183634	-1.6316791
N	-0.4230788	6.0023154	-2.0326716
C	0.4207596	7.0781182	-2.0505521
C	1.7942837	7.0768960	-1.8086926
C	2.5434888	5.9102719	-1.7553045

N	2.0455569	4.6575768	-1.9677052
C	3.1123832	3.8140993	-1.9718441
C	3.0468775	2.4400087	-2.1767519
C	1.8466571	1.7392632	-2.2520843
N	0.5863717	2.2319832	-2.0332541
C	-0.2522229	1.1510264	-2.0372460
C	-1.6210114	1.1598598	-1.7861049
C	-2.3532503	2.3347248	-1.6640495
N	-1.8472951	3.5931604	-1.8302874
C	-2.9206927	4.4339597	-1.8914290
C	-2.8707257	5.7891441	-2.2014126
C	-1.6754757	6.4943917	-2.2941341
C	-1.5933820	7.8909638	-2.6039184
C	-0.3006084	8.2588700	-2.4219012
H	0.1411725	9.2325559	-2.5622904
H	-2.4198705	8.5074381	-2.9187501
C	-4.1451506	6.5027572	-2.4464576
C	-4.4923873	7.6342930	-1.7062312
C	-5.6928858	8.2887367	-1.9385730
C	-6.5614616	7.8274883	-2.9192007
C	-6.2214042	6.7080678	-3.6679186
C	-5.0238607	6.0488783	-3.4331286
H	-4.7570231	5.1825606	-4.0291971
H	-6.8927907	6.3460443	-4.4397862
H	-7.5004558	8.3395819	-3.1005535
H	-5.9538486	9.1620790	-1.3502156
H	-3.8204887	7.9915343	-0.9351248
C	-4.1333657	3.6944922	-1.6856814
C	-3.7809445	2.3957675	-1.5338555
H	-4.4249690	1.5504559	-1.3565902
H	-5.1211578	4.1248480	-1.6505474
C	-2.3250922	-0.1428803	-1.7282863
C	-3.3444615	-0.4500135	-2.6315606
C	-3.9892854	-1.6770445	-2.5729269
C	-3.6254104	-2.6140883	-1.6145057
C	-2.6090424	-2.3196996	-0.7149676
C	-1.9611170	-1.0947059	-0.7732974
H	-1.1745340	-0.8623646	-0.0646571
H	-2.3199059	-3.0459743	0.0373812

H -4.1339588 -3.5710055 -1.5684611
H -4.7800159 -1.9035329 -3.2805923
H -3.6204799 0.2704786 -3.3942448
C 0.4811605 -0.0353821 -2.3683212
C 1.7782256 0.3308339 -2.5117446
H 2.6190083 -0.2908215 -2.7748814
H 0.0484123 -1.0146210 -2.4952682
C 4.3164598 1.6833294 -2.2578632
C 4.5977129 0.6767110 -1.3311225
C 5.7950579 -0.0147357 -1.3773733
C 6.7440938 0.2739263 -2.3631430
C 6.4584556 1.2760566 -3.2967555
C 5.2650288 1.9737365 -3.2419204
H 5.0543052 2.7438469 -3.9767669
H 7.1885881 1.5025263 -4.0677186
C 8.0083866 -0.4411687 -2.4309595
C 8.5104459 -1.4464173 -1.6356030
N 9.7224617 -1.7270060 -2.1634761
N 9.9568041 -0.9422209 -3.2240062
N 8.9362916 -0.1724649 -3.3887631
C 10.6901830 -2.6610599 -1.7725929
C 10.4616959 -3.5267689 -0.7031983
C 11.4357227 -4.4403784 -0.3382031
C 12.6496966 -4.5163175 -1.0265462
C 12.8635105 -3.6419665 -2.0971889
C 11.8994295 -2.7231742 -2.4674078
H 12.0740224 -2.0444175 -3.2942816
H 13.8043335 -3.6662286 -2.6358970
C 13.6792254 -5.4962449 -0.6346296
C 14.4528415 -6.1432732 -1.6020423
C 15.4214512 -7.0688087 -1.2476008
C 15.6207244 -7.3550655 0.0975708
C 14.8705221 -6.7162253 1.0804310
C 13.9047248 -5.7958646 0.7124949
H 13.3339714 -5.2913315 1.4834940
H 15.0540703 -6.9464879 2.1228702
O 16.5958432 -8.2380538 0.5492072
C 16.9480889 -9.3547789 -0.1035668
O 16.4559935 -9.7396539 -1.1387075

C 18.0229545 -10.0746558 0.6119811
C 18.6129417 -9.7141740 1.7559108
C 19.6720134 -10.6913443 2.1720982
N 19.5902269 -11.6694781 1.0865455
O 20.3310120 -12.7093531 1.0403563
C 18.5872093 -11.3648993 0.0664351
C 17.5524000 -12.4970346 0.0129088
H 16.8185972 -12.2884147 -0.7636950
H 17.0434021 -12.5860364 0.9718221
H 18.0611328 -13.4348992 -0.2084083
C 19.2785774 -11.1907211 -1.2927607
H 18.5346498 -10.9875950 -2.0611097
H 19.9851281 -10.3627356 -1.2508639
H 19.8168291 -12.1056371 -1.5390001
C 19.3586956 -11.3842522 3.5063359
H 19.4616906 -10.6776185 4.3274322
H 18.3418379 -11.7746924 3.4963337
H 20.0560937 -12.2096719 3.6483605
C 21.0777714 -10.0723420 2.1939096
H 21.1641210 -9.3714227 3.0218337
H 21.2701662 -9.5467338 1.2593872
H 21.8131015 -10.8677804 2.3136304
H 18.3841995 -8.8334760 2.3386919
H 16.0117092 -7.5569243 -2.0119780
H 14.2876307 -5.9344224 -2.6530912
H 11.2371398 -5.1183146 0.4842123
H 9.5278790 -3.4959672 -0.1562011
H 8.1148000 -1.9523978 -0.7735451
H 5.9969069 -0.7832971 -0.6394638
H 3.8750160 0.4515745 -0.5552226
C 4.3244599 4.5513850 -1.7395101
C 3.9698781 5.8495707 -1.5907159
H 4.6063206 6.6943931 -1.3817810
H 5.3093935 4.1171394 -1.6728878
C 2.4733603 8.3837711 -1.6576359
C 3.5041449 8.7712957 -2.5156301
C 4.1296641 9.9988646 -2.3515067
C 3.7366886 10.8540419 -1.3299492
C 2.7081896 10.4791103 -0.4750347

C 2.0784895 9.2546878 -0.6397788
H 1.2817572 8.9584916 0.0328744
H 2.3960650 11.1415856 0.3255651
H 4.2304225 11.8113874 -1.2011569
H 4.9279569 10.2904799 -3.0263705
H 3.8029006 8.1147948 -3.3261083
C 2.3652197 -0.1078172 1.8882924
C 3.3206503 -0.4817457 2.8350181
C 3.9688461 -1.7042231 2.7331538
C 3.6730670 -2.5690544 1.6873508
C 2.7206737 -2.2075058 0.7432035
C 2.0693560 -0.9874759 0.8442735
H 1.3321036 -0.7024297 0.1024452
H 2.4847075 -2.8773370 -0.0770498
H 4.1840038 -3.5226373 1.6087251
H 4.7079868 -1.9845725 3.4764711
H 3.5416293 0.1804466 3.6655036
C -0.4690914 -0.0191084 2.3813726
C -1.7780810 0.3311911 2.4379617
H -2.6222540 -0.2972544 2.6715400
H -0.0306132 -0.9872890 2.5628199
C -4.3190512 1.6841349 2.0219371
C -4.5606500 0.5519401 1.2403098
C -5.7676736 -0.1198799 1.3166343
C -6.7698731 0.3158224 2.1888317
C -6.5222242 1.4387960 2.9858331
C -5.3177901 2.1137774 2.9011623
H -5.1375325 2.9770822 3.5333806
H -7.2912548 1.7784015 3.6728631
C -8.0492209 -0.3698856 2.2735848
C -8.5329355 -1.4455903 1.5634820
N -9.7763427 -1.6469506 2.0524694
N -10.0465808 -0.7496650 3.0102784
N -9.0189388 0.0164749 3.1458669
C -10.7447073 -2.5979929 1.7064106
C -10.5236929 -3.4990475 0.6650003
C -11.4966412 -4.4295326 0.3426797
C -12.7062313 -4.4809090 1.0407927
C -12.9142818 -3.5689629 2.0805716

C -11.9472559 -2.6390584 2.4141553
H -12.1127769 -1.9388590 3.2248371
H -13.8372466 -3.5987771 2.6490145
C -13.7395993 -5.4716767 0.6871753
C -15.0949580 -5.1287809 0.7135465
C -16.0655763 -6.0566084 0.3787482
C -15.6874440 -7.3469694 0.0198578
C -14.3470469 -7.7108168 -0.0204741
C -13.3850181 -6.7704428 0.3128057
H -12.3403306 -7.0596462 0.2943073
H -14.0523557 -8.7108791 -0.3099950
O -16.7192800 -8.2090231 -0.3373937
C -16.7099661 -9.5253001 -0.0820176
O -15.8263179 -10.1146479 0.4954198
C -17.9370216 -10.1753615 -0.5891660
C -18.9449919 -9.5937070 -1.2467560
C -20.0198132 -10.5758903 -1.6066668
N -19.4704198 -11.8089808 -1.0416986
O -20.0741673 -12.9319907 -1.1240803
C -18.1671544 -11.6554267 -0.3959905
C -17.1314574 -12.5230769 -1.1244706
H -16.1639068 -12.4318673 -0.6339882
H -17.0381835 -12.2043317 -2.1618725
H -17.4570269 -13.5626739 -1.0997182
C -18.2782714 -12.0590354 1.0805445
H -17.3054171 -11.9700454 1.5608474
H -18.9912352 -11.4144932 1.5932362
H -18.6227864 -13.0909365 1.1431141
C -20.1917538 -10.7442257 -3.1237904
H -20.6416900 -9.8497918 -3.5500274
H -19.2244442 -10.9163966 -3.5940699
H -20.8377929 -11.6012464 -3.3134060
C -21.3654979 -10.2632953 -0.9358783
H -21.8062594 -9.3732183 -1.3804645
H -21.2230070 -10.0965162 0.1310904
H -22.0365974 -11.1101815 -1.0780888
H -19.0140193 -8.5472013 -1.5069076
H -17.1164459 -5.7939191 0.3891027
H -15.3945694 -4.1213314 0.9786566

H	-11.3177224	-5.1120117	-0.4804851
H	-9.6000876	-3.4764471	0.1005705
H	-8.1031573	-2.0512069	0.7861970
H	-5.9348749	-0.9895448	0.6909853
H	-3.7968817	0.2084906	0.5532817
C	-4.2722084	4.4982491	1.2868951
C	-3.9228842	5.8011235	1.1664038
H	-4.5566836	6.6383206	0.9243949
H	-5.2460788	4.0551065	1.1556598
C	-2.5248775	8.3575618	1.4897072
C	-3.6216476	8.6577747	2.2997168
C	-4.2690845	9.8791411	2.1813213
C	-3.8317779	10.8164871	1.2543590
C	-2.7403666	10.5274124	0.4454669
C	-2.0891742	9.3086048	0.5648064
H	-1.2422562	9.0803511	-0.0718271
H	-2.3935587	11.2538386	-0.2820015
H	-4.3408892	11.7700040	1.1627835
H	-5.1183770	10.1016896	2.8191134
H	-3.9559362	7.9371360	3.0385635
C	0.2085100	8.2881090	2.3968663
C	1.4888580	7.9374500	2.6707403
H	2.2928920	8.5688230	3.0137897
H	-0.2464033	9.2624592	2.4760949

The atomic coordinates of $\mathbf{1}_2 \cdot \mathbf{O}$ (TS1)

C	-4.3505286	9.1196878	0.9257886
N	-4.6033488	7.8054906	0.6457405
C	-5.5271306	7.8128491	-0.3628058
C	-6.2269522	6.7097918	-0.8316627
C	-5.9909919	5.4138694	-0.3937444
N	-5.0382514	5.0272827	0.5105214
C	-5.0726646	3.6635774	0.5339540
C	-4.2495144	2.8206645	1.2842060
C	-3.3407872	3.2893773	2.2261586
N	-3.1409652	4.5939880	2.5587594
C	-2.2876418	4.5901015	3.6250187
C	-1.9160934	5.7061538	4.3626472
C	-2.2573495	7.0093504	3.9980981
N	-2.9574519	7.3959288	2.8879762
C	-3.0197187	8.7639835	2.9443634
C	-3.6520032	9.5977377	2.0267400
C	-3.7119317	11.0482085	2.3251203
C	-2.5681865	11.8377858	2.3582606
C	-2.6532515	13.1883928	2.6474071
C	-3.8797444	13.7646135	2.9339796
C	-5.0219908	12.9803240	2.9313002
C	-4.9402444	11.6339183	2.6237561
H	-5.8322831	11.0233666	2.6246411
H	-5.9806047	13.4200333	3.1694330
H	-3.9450653	14.8182596	3.1659512
H	-1.7562849	13.7917436	2.6552349
H	-1.6105249	11.3854900	2.1592251
C	-2.3767785	9.2423913	4.1302999
C	-1.8930605	8.1535919	4.7780042
H	-1.3349555	8.1234456	5.6940811
H	-2.3109875	10.2714945	4.4252457
Fe	-3.7157802	6.2138690	1.4431032
O	-2.4711576	5.9833183	0.3719950
Fe	-1.3930961	6.4002057	-0.8201173
N	-0.8408370	4.4281497	-1.0247122
C	0.0411605	3.7573808	-0.2388587
C	0.9685437	4.3358326	0.6233675
C	1.0202007	5.7063579	0.8828428
N	0.1882426	6.6697173	0.3824151
C	0.6011743	7.8518920	0.9359641

C 0.0494987 9.1096351 0.7068376
C -0.9794146 9.3369070 -0.2002143
N -1.5673889 8.3867750 -0.9904123
C -2.3464401 9.0758923 -1.8785086
C -2.9995268 8.5480566 -2.9822606
C -3.0614583 7.1845472 -3.2456547
N -2.4883304 6.1912038 -2.4971221
C -2.8445684 5.0187357 -3.1021254
C -2.4579945 3.7315262 -2.7254307
C -1.5154253 3.4797679 -1.7383623
C -1.0690274 2.1669860 -1.3586335
C -0.0933905 2.3395399 -0.4383909
H 0.4717076 1.5861757 0.0753158
H -1.4580527 1.2440497 -1.7416771
C -3.0538873 2.5863323 -3.4485361
C -4.4246896 2.3516954 -3.3749039
C -4.9875309 1.2688234 -4.0266746
C -4.1918338 0.4132644 -4.7714952
C -2.8289349 0.6468924 -4.8614905
C -2.2621779 1.7236375 -4.2023183
H -1.1993935 1.9061581 -4.2764594
H -2.2041760 -0.0139847 -5.4462577
H -4.6320323 -0.4319654 -5.2815852
H -6.0506991 1.0904463 -3.9490850
H -5.0423944 3.0165052 -2.7893907
C -3.6264694 5.2801917 -4.2723038
C -3.7441403 6.6281617 -4.3736820
H -4.2351109 7.1990314 -5.1386682
H -4.0116173 4.5314968 -4.9373862
C -3.5300863 9.4936820 -3.9964058
C -2.6226676 10.1883434 -4.7929933
C -3.0676822 11.0622028 -5.7685101
C -4.4261729 11.2583634 -5.9591417
C -5.3343207 10.5761197 -5.1668926
C -4.8896611 9.6977254 -4.1936845
H -5.5980889 9.1674744 -3.5789098
H -6.3954355 10.7267629 -5.3079826
H -4.7737964 11.9412442 -6.7214571
H -2.3526655 11.5917836 -6.3827776
H -1.5629324 10.0337816 -4.6447755
C -2.3077785 10.4821896 -1.5934967

C -1.4696461 10.6430616 -0.5454675
H -1.1921321 11.5590773 -0.0638439
H -2.8554248 11.2313116 -2.1315433
C 0.6643151 10.2663418 1.3980838
C 0.6295847 10.3576989 2.7872974
C 1.2011330 11.4380800 3.4361076
C 1.8261250 12.4370644 2.7074871
C 1.8797888 12.3468651 1.3259611
C 1.3025680 11.2706989 0.6745941
H 1.3535742 11.2004929 -0.4026840
H 2.3725123 13.1198828 0.7528001
H 2.2717808 13.2815408 3.2138800
H 1.1546325 11.5010142 4.5140415
H 0.1340909 9.5824530 3.3523465
C 1.7536427 7.6353695 1.7576651
C 2.0151010 6.3064463 1.7226369
H 2.8182510 5.7824968 2.2033591
H 2.2975899 8.4009599 2.2760257
C 1.9757230 3.4509244 1.2424928
C 2.8177687 2.6797354 0.4414682
C 3.7658868 1.8482745 1.0030108
C 3.9012928 1.7648856 2.3889888
C 3.0660262 2.5400823 3.1931867
C 2.1199313 3.3664811 2.6252194
H 1.4639830 3.9512635 3.2497565
H 3.1754620 2.4737557 4.2657206
C 4.8855874 0.8921944 3.0028469
C 5.6887492 -0.0878362 2.4447653
N 6.4025425 -0.5871352 3.4845822
N 6.0543693 0.0555936 4.6069021
N 5.1644755 0.9233995 4.3335737
C 7.3562653 -1.6102499 3.5004242
C 7.9152753 -1.9864523 4.7199328
C 8.8466016 -3.0016512 4.7702903
C 9.2489204 -3.6651382 3.6101452
C 8.6877799 -3.2728039 2.3957233
C 7.7518804 -2.2591122 2.3343434
H 7.3346645 -1.9852132 1.3786417
H 8.9705468 -3.7827321 1.4874079
C 10.2325805 -4.7559702 3.6680161
C 10.2091201 -5.6798367 4.7134104

C 11.1252207 -6.7094224 4.7668265
C 12.0899734 -6.8331614 3.7718444
C 12.1267476 -5.9275579 2.7208778
C 11.2029854 -4.8994133 2.6784752
H 11.2499820 -4.1890948 1.8672135
H 12.8710973 -6.0206373 1.9456426
O 12.9330849 -7.9329222 3.8796081
C 14.2139323 -7.9132373 3.4752680
O 14.7822783 -6.9388208 3.0356616
C 14.8323030 -9.2363523 3.6563723
C 14.2653092 -10.3163506 4.1974334
C 15.1970557 -11.4874163 4.2088311
N 16.3834187 -10.9257089 3.5804016
O 17.4190359 -11.6388730 3.2678830
C 16.2489383 -9.5217615 3.2210325
C 16.4398268 -9.3259866 1.7111628
H 16.3510125 -8.2728458 1.4617758
H 15.6916109 -9.8902573 1.1579082
H 17.4259150 -9.6871812 1.4286294
C 17.2681096 -8.6712009 3.9936919
H 18.2732252 -9.0008892 3.7416804
H 17.1506796 -7.6248455 3.7271458
H 17.1217112 -8.7841820 5.0658170
C 14.6479080 -12.6653038 3.3889872
H 15.4364474 -13.4048897 3.2681417
H 13.8023227 -13.1179484 3.8969473
H 14.3343336 -12.3279432 2.4034794
C 15.5131501 -11.9516063 5.6406203
H 16.2943527 -12.7074046 5.6036372
H 14.6265524 -12.3734291 6.1039595
H 15.8649208 -11.1155785 6.2409975
H 13.2654288 -10.3834586 4.5874999
H 11.1061822 -7.4317943 5.5679718
H 9.4527054 -5.6043755 5.4793103
H 9.2831266 -3.2727869 5.7194010
H 7.6030499 -1.4693392 5.6140118
H 5.7788894 -0.4455663 1.4430657
H 4.4113934 1.2666751 0.3613801
H 2.7312839 2.7458588 -0.6337520
C -1.2335609 5.5095250 5.6641700
C -1.9203373 5.8207294 6.8367258

C -1.3295357 5.6283079 8.0723981
C -0.0419886 5.1226008 8.1579790
C 0.6504675 4.8150660 6.9989985
C 0.0582903 5.0081513 5.7629895
H 0.6080317 4.7811797 4.8634431
H 1.6566615 4.4240602 7.0573286
H 0.4189716 4.9710967 9.1238540
H -1.8757097 5.8731524 8.9728102
H -2.9268996 6.2099082 6.7724368
C -1.9008691 3.2423455 3.9419413
C -2.5361099 2.4371285 3.0603747
H -2.4835240 1.3684429 2.9816901
H -1.2230489 2.9630010 4.7254480
C -4.3926965 1.3633352 1.0884678
C -4.1448383 0.8034388 -0.1627328
C -4.2697735 -0.5546922 -0.3692027
C -4.6590489 -1.3943246 0.6742842
C -4.9235911 -0.8348969 1.9244298
C -4.7916497 0.5241383 2.1278777
H -5.0126873 0.9464875 3.0981536
H -5.2351296 -1.4878075 2.7271399
C -4.7911457 -2.8264164 0.4775251
C -4.6007968 -3.5932038 -0.6595819
N -4.8495503 -4.8666535 -0.2666055
N -5.1736010 -4.8721010 1.0329711
N -5.1431705 -3.6787951 1.4766454
C -4.7936160 -6.0511143 -1.0083038
C -4.9594454 -7.2657466 -0.3460931
C -4.9036928 -8.4500203 -1.0497596
C -4.6768103 -8.4563497 -2.4268783
C -4.5168334 -7.2336463 -3.0772396
C -4.5764925 -6.0415688 -2.3829740
H -4.4587592 -5.1132576 -2.9183833
H -4.3644432 -7.2134711 -4.1454537
C -4.6066830 -9.7214964 -3.1720570
C -5.4668081 -10.7755665 -2.8691523
C -5.4059314 -11.9699469 -3.5615224
C -4.4644875 -12.1271312 -4.5687551
C -3.6011998 -11.0865620 -4.8899767
C -3.6776486 -9.8948209 -4.1980076
H -2.9911263 -9.0986538 -4.4408341

H -2.8771078 -11.2249069 -5.6779540
O -4.3787190 -13.2826803 -5.3402949
C -4.4149875 -14.4980467 -4.7740908
O -4.4566440 -14.6921162 -3.5787807
C -4.3787381 -15.5788554 -5.7723130
C -4.3708610 -16.8741972 -5.4473476
C -4.3455419 -17.7550299 -6.6546469
N -4.3419383 -16.7738983 -7.7280641
O -4.3201478 -17.0979043 -8.9821496
C -4.3612180 -15.3910435 -7.2698640
C -5.6222159 -14.6856331 -7.7904205
H -5.6098933 -13.6353105 -7.5178078
H -6.5152054 -15.1518626 -7.3786590
H -5.6498962 -14.7782447 -8.8740726
C -3.1039857 -14.6619871 -7.7646695
H -3.0485763 -14.7627415 -8.8466099
H -3.1483424 -13.6109874 -7.5011643
H -2.2112617 -15.1047192 -7.3273768
C -5.5934410 -18.6488492 -6.7401020
H -5.6144505 -19.1293127 -7.7157615
H -5.5685051 -19.4079012 -5.9645358
H -6.4957978 -18.0523476 -6.6258192
C -3.0777968 -18.6229402 -6.7071433
H -3.0237719 -19.1069544 -7.6797355
H -3.1051777 -19.3790676 -5.9287630
H -2.1909303 -18.0073181 -6.5743540
H -4.3817342 -17.2680583 -4.4459279
H -6.0828203 -12.7758748 -3.3220475
H -6.2119942 -10.6539800 -2.0977170
H -5.0130369 -9.3852935 -0.5216668
H -5.1269088 -7.2558586 0.7199458
H -4.3154963 -3.3296062 -1.6535771
H -4.0633063 -0.9644318 -1.3462956
H -3.8432261 1.4467526 -0.9741632
C -6.1213064 3.1828543 -0.3176914
C -6.6966235 4.2710534 -0.8877119
H -7.5080050 4.3054324 -1.5897318
H -6.3891166 2.1515159 -0.4435659
C -7.3233809 6.9207171 -1.8116997
C -8.6368579 7.0406572 -1.3690204
C -9.6644719 7.2396080 -2.2746465

C	-9.3912748	7.3222751	-3.6306750
C	-8.0871043	7.1904803	-4.0781284
C	-7.0589294	6.9845461	-3.1741145
H	-6.0439065	6.8578598	-3.5182259
H	-7.8687659	7.2454678	-5.1352738
H	-10.1943338	7.4831527	-4.3360628
H	-10.6823593	7.3302007	-1.9213723
H	-8.8483748	6.9766186	-0.3106912
C	-5.7973554	9.1588187	-0.7806522
C	-5.0562680	9.9700483	0.0076268
H	-4.9931906	11.0404069	-0.0086846
H	-6.4872787	9.4335620	-1.5545320

The atomic coordinates of $2_2 \cdot O_\alpha$

O	-6.0991231	0.3449968	0.0950726
FE	-6.7738330	0.2133397	1.6317075
N	-7.7725691	1.9351060	1.7345056
C	-9.0718158	2.1412642	1.3593995
C	-9.9567907	1.1863196	0.8668813
C	-9.6668203	-0.1727037	0.8716897
N	-8.5297397	-0.7257493	1.3910357
C	-8.7558384	-2.0686433	1.4688124
C	-7.9068104	-3.0023671	2.0548166
C	-6.6104457	-2.6939826	2.4517393
N	-5.9863108	-1.4828185	2.2975974
C	-4.6731255	-1.6853949	2.6141443
C	-3.6432428	-0.7422429	2.5996756
C	-3.8862473	0.6231619	2.5082460
N	-5.1268472	1.1824486	2.4060408
C	-4.9520512	2.5295934	2.4783988
C	-5.9666392	3.4781460	2.4189986
C	-7.2847307	3.1606282	2.1092185
C	-8.3357494	4.1348319	2.0697384
C	-9.4378504	3.5078439	1.5912460
H	-10.4212452	3.9203913	1.4328296
H	-8.2361763	5.1640039	2.3755507
C	-5.6099025	4.8975537	2.6529316
C	-5.8113316	5.8563680	1.6586522
C	-5.4585924	7.1798577	1.8757162
C	-4.9067455	7.5651527	3.0906867
C	-4.7052851	6.6185920	4.0870550
C	-5.0505626	5.2926817	3.8697367
H	-4.8980837	4.5564665	4.6520385
H	-4.2756087	6.9144798	5.0386599
H	-4.6321266	8.6009155	3.2602697
H	-5.6132181	7.9146350	1.0925462
H	-6.2322806	5.5561198	0.7057829
C	-3.5570035	2.8380797	2.6235249
C	-2.8940829	1.6574396	2.6197306
H	-1.8316384	1.4992976	2.7005852
H	-3.1455848	3.8327134	2.6884795
C	-2.2480744	-1.2209494	2.6706558

C -1.3287428 -0.7356530 3.6060781
C 0.0084820 -1.0814173 3.5270624
C 0.4625472 -1.9321279 2.5106563
C -0.4713292 -2.4893281 1.6272713
C -1.8043145 -2.1385124 1.7129648
H -2.5124462 -2.5371669 0.9965137
H -0.1369687 -3.1716210 0.8533904
C 1.8461853 -2.1758060 2.3285677
C 3.0264847 -2.3270880 2.0995908
C 4.4056631 -2.4571346 1.8036490
C 5.3520952 -1.6632532 2.4645257
C 6.6908409 -1.7477639 2.1329480
C 7.1331603 -2.6236330 1.1347437
C 6.1870125 -3.4298681 0.4919676
C 4.8460087 -3.3504609 0.8181203
H 4.1260157 -3.9787781 0.3052015
H 6.5052264 -4.1369400 -0.2667561
C 8.5557774 -2.6629684 0.7538796
C 8.9359889 -2.9030207 -0.5707587
C 10.2675130 -2.8766834 -0.9527158
C 11.2372242 -2.6047131 0.0035493
C 10.8904899 -2.3859831 1.3317607
C 9.5570428 -2.4200808 1.7002891
H 9.2956488 -2.2593244 2.7397772
H 11.6650249 -2.1826565 2.0611120
O 12.5818080 -2.4634865 -0.3313043
C 13.2352331 -3.3479973 -1.1035361
O 12.7520970 -4.3615204 -1.5465603
C 14.6347865 -2.9247942 -1.3345848
C 15.5744500 -3.6951194 -1.8919901
C 16.8933138 -2.9891448 -1.9956377
N 16.5407252 -1.6629029 -1.4809495
O 17.4363457 -0.7806207 -1.2033902
C 15.1656330 -1.5542982 -0.9864362
C 15.1925494 -1.2639013 0.5189826
H 15.7955238 -0.3735042 0.6900567
H 14.1862089 -1.0883186 0.8899736
H 15.6333676 -2.1015214 1.0575458
C 14.4504773 -0.4357783 -1.7555024

H 13.4343969 -0.3190499 -1.3856374
H 14.4200893 -0.6706666 -2.8186899
H 14.9945310 0.4963268 -1.6133163
C 17.9739199 -3.6156905 -1.1016903
H 18.8352155 -2.9488798 -1.0687480
H 18.2770682 -4.5807660 -1.5029357
H 17.5916327 -3.7517219 -0.0908461
C 17.3903569 -2.8557852 -3.4422800
H 18.2550749 -2.1927949 -3.4600198
H 17.6753213 -3.8309629 -3.8326251
H 16.6062547 -2.4342508 -4.0701376
H 15.4379309 -4.7139810 -2.2278295
H 10.5494891 -3.0463513 -1.9843391
H 8.1791869 -3.0778810 -1.3271368
H 7.4001948 -1.1000721 2.6364720
H 5.0265006 -0.9662134 3.2289185
H 0.7163186 -0.6745682 4.2413464
H -1.6656895 -0.0804387 4.4020126
C -4.4818536 -3.0315232 3.0647604
C -5.6902158 -3.6455333 2.9997231
H -5.9383759 -4.6538931 3.2892689
H -3.5481394 -3.4320311 3.4268729
C -8.4135680 -4.3806768 2.2509578
C -9.5621410 -4.5972106 3.0159147
C -10.0503220 -5.8815632 3.2054726
C -9.4026984 -6.9670841 2.6296160
C -8.2600969 -6.7614604 1.8676256
C -7.7663266 -5.4785559 1.6825161
H -6.8802162 -5.3198598 1.0799046
H -7.7523313 -7.6056192 1.4133586
H -9.7878365 -7.9708226 2.7745039
H -10.9415930 -6.0357077 3.8049767
H -10.0655028 -3.7526421 3.4746396
C -10.0445316 -2.3799035 0.9191412
C -10.6008655 -1.2074589 0.5312713
H -11.5584578 -1.0495546 0.0628023
H -10.4524679 -3.3737597 0.8295192
C -11.2930464 1.6487262 0.4244262
C -11.4040236 2.5825158 -0.6084154

C -12.6482498 3.0386043 -1.0176919
C -13.7999178 2.5745744 -0.3953458
C -13.6996721 1.6521245 0.6380578
C -12.4563802 1.1916595 1.0467443
H -12.3837998 0.4878628 1.8690479
H -14.5956686 1.2908570 1.1322321
H -14.7732945 2.9319698 -0.7139177
H -12.7179007 3.7589904 -1.8260043
H -10.5061839 2.9400613 -1.0988956
FE -6.0225320 -0.0162938 -1.5483959
N -7.1234224 -1.6769281 -1.7887104
C -8.4468233 -1.7453283 -2.1107541
C -9.1927624 -0.7204317 -2.6835020
C -8.7148048 0.5802733 -2.7956449
N -7.5101870 1.0418371 -2.3302332
C -7.5451343 2.4018917 -2.4606759
C -6.5500067 3.3092033 -2.0958678
C -5.2594480 2.9137796 -1.7713163
N -4.8150965 1.6239825 -1.7957733
C -3.4709391 1.6716189 -1.5893346
C -2.6230660 0.5697776 -1.6102297
C -3.0854177 -0.7422632 -1.6745080
N -4.3911167 -1.1570748 -1.6036257
C -4.3523612 -2.5172107 -1.4561895
C -5.4392194 -3.3674937 -1.2782181
C -6.7529043 -2.9387109 -1.4179887
C -7.8979662 -3.8035216 -1.4141853
C -8.9439396 -3.0684768 -1.8612792
H -9.9669957 -3.3790502 -1.9993880
H -7.8915421 -4.8396465 -1.1179948
C -5.1652177 -4.8025129 -1.0274023
C -4.4554768 -5.1923466 0.1101610
C -4.1851754 -6.5317434 0.3488290
C -4.6129070 -7.5000438 -0.5502533
C -5.3125361 -7.1212783 -1.6886421
C -5.5875783 -5.7825371 -1.9273928
H -6.1183631 -5.4910790 -2.8274864
H -5.6446078 -7.8727964 -2.3974990
H -4.4012863 -8.5476173 -0.3644714

H	-3.6387890	-6.8195917	1.2409431
H	-4.1275902	-4.4377785	0.8156702
C	-2.9979933	-2.9791532	-1.5276041
C	-2.2149333	-1.8816940	-1.6641500
H	-1.1403030	-1.8414826	-1.7345487
H	-2.6939433	-4.0127306	-1.4880674
C	-1.1622756	0.7861748	-1.4736781
C	-0.2729338	0.4177279	-2.4863152
C	1.0926629	0.5609262	-2.3132043
C	1.6062914	1.0773303	-1.1162722
C	0.7141333	1.4720040	-0.1111845
C	-0.6487743	1.3308781	-0.2946943
H	-1.3322320	1.6188695	0.4950779
H	1.0979880	1.8776622	0.8186498
C	3.0059360	1.1923798	-0.9206639
C	4.2008795	1.2829389	-0.7411066
C	5.6008133	1.3986086	-0.5516678
C	6.4917992	0.8400565	-1.4776828
C	7.8568382	0.9643807	-1.2997326
C	8.3795863	1.6380589	-0.1903975
C	7.4875397	2.1888249	0.7358467
C	6.1206912	2.0758928	0.5593286
H	5.4431995	2.5141134	1.2839339
H	7.8689102	2.7291475	1.5956546
C	9.8365814	1.7688467	-0.0095342
C	10.6748202	1.9602891	-1.1112593
C	12.0468008	2.0862133	-0.9627179
C	12.5984350	2.0153529	0.3114684
C	11.7852771	1.8182945	1.4244282
C	10.4155049	1.7035409	1.2620759
H	9.7931168	1.5350858	2.1333462
H	12.2373567	1.7518085	2.4065948
O	13.9666396	2.0717652	0.5622312
C	14.8458302	2.7477793	-0.1934894
O	14.5644994	3.4068737	-1.1682914
C	16.2249855	2.5905441	0.3128807
C	16.6134759	1.9864637	1.4400469
C	18.1039901	2.0099571	1.6025098
N	18.5077619	2.7241019	0.3891572

O 19.7073640 3.0878216 0.1797632
C 17.3949921 3.1445818 -0.4636897
C 17.3783714 4.6774592 -0.5495250
H 16.5718096 4.9997007 -1.2053573
H 17.2288891 5.1083940 0.4396278
H 18.3320291 5.0232767 -0.9473139
C 17.5485410 2.5183401 -1.8549482
H 18.5012258 2.8263354 -2.2843378
H 16.7358072 2.8503756 -2.4981269
H 17.5245034 1.4324518 -1.7779501
C 18.7259349 0.6063411 1.5969865
H 18.3716611 0.0457845 0.7327510
H 19.8103484 0.6982136 1.5445224
H 18.4511172 0.0745705 2.5055925
C 18.5576653 2.8062231 2.8345583
H 19.6367795 2.9505447 2.7868231
H 18.3049923 2.2616774 3.7420018
H 18.0691606 3.7796079 2.8548281
H 15.9656183 1.5347065 2.1771507
H 12.6701859 2.2365126 -1.8335965
H 10.2498764 2.0285678 -2.1064968
H 8.5286255 0.5110998 -2.0209488
H 6.1042253 0.3052889 -2.3379654
H 1.7734367 0.2653551 -3.1045297
H -0.6585580 0.0183606 -3.4184708
C -3.0471394 3.0364074 -1.4348386
C -4.1599058 3.8035835 -1.5161909
H -4.2379951 4.8747365 -1.4214171
H -2.0289091 3.3547835 -1.2770147
C -6.8858588 4.7507101 -2.1342618
C -7.9307953 5.2386907 -1.3461300
C -8.2614689 6.5853128 -1.3679465
C -7.5570049 7.4628987 -2.1820338
C -6.5231811 6.9852454 -2.9770390
C -6.1886225 5.6388984 -2.9551571
H -5.3947886 5.2679726 -3.5948145
H -5.9753913 7.6650426 -3.6216888
H -7.8147620 8.5164896 -2.1991974
H -9.0712966 6.9505906 -0.7450916

H -8.4774248 4.5559453 -0.7057867
C -8.7603962 2.7981743 -3.1083067
C -9.4696623 1.6665491 -3.3455550
H -10.4214014 1.5717580 -3.8430581
H -9.0129254 3.8109044 -3.3791817
C -10.5442882 -1.0427701 -3.1974956
C -11.6771569 -0.3763116 -2.7289221
C -12.9356476 -0.6963137 -3.2164977
C -13.0800285 -1.6810546 -4.1849195
C -11.9580250 -2.3463939 -4.6622876
C -10.6994959 -2.0324515 -4.1711852
H -9.8246171 -2.5476434 -4.5535989
H -12.0634633 -3.1149182 -5.4211276
H -14.0645764 -1.9303045 -4.5662290
H -13.8091071 -0.1760470 -2.8380362
H -11.5679847 0.3858389 -1.9670900

The atomic coordinates of $2_2 \cdot O_{\beta}$

O	-0.0156740	-3.5159393	0.0002507
FE	-0.0505775	-3.0879225	1.6275440
N	1.8268499	-3.5532274	2.1030934
C	2.9050339	-2.7130305	2.0626261
C	2.8958830	-1.3657648	1.7123046
C	1.7204814	-0.6479892	1.5236810
N	0.4620344	-1.1471867	1.7066696
C	-0.3836451	-0.0761109	1.6830848
C	-1.7438964	-0.1121554	1.9713731
C	-2.4470938	-1.3025355	2.1241565
N	-1.9451330	-2.5662080	1.9503569
C	-3.0178226	-3.4125627	1.9951959
C	-3.0056785	-4.7988797	1.8403366
C	-1.8352973	-5.5435538	1.8688932
N	-0.5908186	-5.0245085	2.0796758
C	0.2557737	-6.0833823	2.1865297
C	1.6226047	-5.9959121	2.4271319
C	2.3180791	-4.7910454	2.4293099
C	3.7206612	-4.6963800	2.7120897
C	4.0867562	-3.4133409	2.4734294
H	5.0619526	-2.9675166	2.5864296
H	4.3383932	-5.5116431	3.0534304
C	2.3786794	-7.2523307	2.6407895
C	3.4076136	-7.6159343	1.7703113
C	4.1042529	-8.7998315	1.9598211
C	3.7880889	-9.6324379	3.0257488
C	2.7679870	-9.2772029	3.8988899
C	2.0638776	-8.0973588	3.7064323
H	1.2723910	-7.8187610	4.3943029
H	2.5183167	-9.9232003	4.7343754
H	4.3350051	-10.5573322	3.1753168
H	4.8966640	-9.0759224	1.2720716
H	3.6479928	-6.9716348	0.9322167
C	-0.4703340	-7.3133552	2.0235058
C	-1.7643683	-6.9777547	1.8091855
H	-2.6005720	-7.6322225	1.6223690
H	-0.0308883	-8.2980540	2.0445539
C	-4.3075988	-5.4903346	1.7016640
C	-5.1541712	-5.1623715	0.6403295
C	-6.3770778	-5.7986290	0.4901000

C -6.7750495 -6.7668310 1.4029719
C -5.9435188 -7.0941609 2.4663488
C -4.7175113 -6.4620555 2.6162924
H -4.0806740 -6.7079535 3.4594474
H -6.2531051 -7.8450588 3.1861087
H -7.7318900 -7.2645306 1.2866155
H -7.0206040 -5.5379651 -0.3436642
H -4.8406907 -4.4120289 -0.0763538
C -4.2093409 -2.6754787 2.2946680
C -3.8500401 -1.3723223 2.4063936
H -4.4764890 -0.5311982 2.6559049
H -5.1846241 -3.1121694 2.4394781
C -2.4664126 1.1724466 2.1200512
C -3.5820434 1.4673743 1.3344047
C -4.2476473 2.6755560 1.4786662
C -3.8137083 3.6044384 2.4153438
C -2.7087809 3.3183713 3.2068926
C -2.0379978 2.1132373 3.0597254
H -1.1826409 1.8897531 3.6886396
H -2.3672415 4.0380330 3.9437903
H -4.3355073 4.5487566 2.5286238
H -5.1089317 2.8950683 0.8566782
H -3.9180194 0.7477416 0.5977232
C 0.3542137 1.1231737 1.4059131
C 1.6560679 0.7669942 1.2940410
H 2.5006778 1.4009558 1.0801721
H -0.0796000 2.1041121 1.2980777
C 4.1955163 -0.6645422 1.6162720
C 4.4897161 0.4303484 2.4337284
C 5.7081532 1.0779554 2.3364464
C 6.6690994 0.6463773 1.4128346
C 6.3810148 -0.4577314 0.6000622
C 5.1628145 -1.1028482 0.7071310
H 4.9417159 -1.9479938 0.0656963
H 7.1167041 -0.8020736 -0.1186186
C 7.9102586 1.3205028 1.2947363
C 8.9670163 1.9021586 1.1805265
C 10.2035018 2.5812449 1.0447852
C 10.4890679 3.7079677 1.8271656
C 11.6952042 4.3694453 1.6890057
C 12.6552342 3.9280842 0.7722497

C	12.3677318	2.8021898	-0.0066242
C	11.1618021	2.1387867	0.1232252
H	10.9512119	1.2710753	-0.4922836
H	13.0899004	2.4538702	-0.7374265
C	13.9434517	4.6310567	0.6343396
C	15.1266334	3.9174693	0.4236178
C	16.3460870	4.5645141	0.3007510
C	16.3844980	5.9511272	0.3827783
C	15.2212694	6.6847172	0.5972874
C	14.0109325	6.0253459	0.7209771
H	13.1061786	6.6035083	0.8701738
H	15.2785356	7.7645298	0.6623326
O	17.5645069	6.6859899	0.3148560
C	18.6131742	6.3481038	-0.4476202
O	18.6604493	5.3887507	-1.1822441
C	19.7218146	7.3133888	-0.2859476
C	19.7402546	8.3966111	0.4968954
C	21.0428481	9.1341387	0.4021979
N	21.7674679	8.2975348	-0.5552288
O	22.9537507	8.5668197	-0.9432130
C	21.0178581	7.1396438	-1.0416602
C	20.8462892	7.2456306	-2.5630844
H	20.3110518	6.3735450	-2.9345765
H	20.2856675	8.1446769	-2.8159942
H	21.8295001	7.2965553	-3.0301160
C	21.7642609	5.8528656	-0.6639366
H	21.2232053	4.9885262	-1.0449999
H	21.8499128	5.7725766	0.4190023
H	22.7630142	5.8786712	-1.0989128
C	20.8883340	10.5492458	-0.1743971
H	20.3872739	11.1930181	0.5457323
H	20.3042452	10.5182478	-1.0933109
H	21.8771969	10.9513513	-0.3939444
C	21.8112318	9.1673044	1.7315172
H	21.3064459	9.8227331	2.4384636
H	21.8731031	8.1653362	2.1543087
H	22.8189539	9.5394941	1.5478337
H	18.9355280	8.7342273	1.1340888
H	17.2525008	3.9924101	0.1527752
H	15.1014775	2.8343648	0.3783884
H	11.9045904	5.2294857	2.3160254

H	9.7576283	4.0591071	2.5466750
H	5.9247905	1.9255546	2.9777943
H	3.7603792	0.7641033	3.1640818
FE	0.0235636	-3.1531433	-1.6425759
N	-1.8553035	-3.6261016	-2.1031465
C	-2.9277611	-2.7777562	-2.1019851
C	-2.9118767	-1.4184111	-1.8019475
C	-1.7330042	-0.7007948	-1.6366483
N	-0.4773225	-1.2140329	-1.7985710
C	0.3744725	-0.1477730	-1.8152745
C	1.7343420	-0.2027102	-2.1022225
C	2.4305816	-1.4021631	-2.2084835
N	1.9213990	-2.6551711	-1.9854615
C	2.9890230	-3.5091108	-1.9995698
C	2.9683710	-4.8879107	-1.7894837
C	1.7932681	-5.6257747	-1.7830892
N	0.5515893	-5.1093245	-2.0148381
C	-0.3013096	-6.1669818	-2.0745778
C	-1.6671518	-6.0817587	-2.3221494
C	-2.3538726	-4.8731163	-2.3801147
C	-3.7539960	-4.7801147	-2.6750418
C	-4.1120968	-3.4857469	-2.4912405
H	-5.0831451	-3.0376749	-2.6286153
H	-4.3758647	-5.6040813	-2.9867111
C	-2.4309018	-7.3413316	-2.4825197
C	-3.4712757	-7.6554596	-1.6062468
C	-4.1744058	-8.8425186	-1.7452498
C	-3.8534506	-9.7284213	-2.7658288
C	-2.8222047	-9.4227979	-3.6446088
C	-2.1119348	-8.2395094	-3.5026140
H	-1.3121033	-7.9997825	-4.1954568
H	-2.5687480	-10.1103213	-4.4450922
H	-4.4053275	-10.6559531	-2.8755200
H	-4.9757356	-9.0794785	-1.0532555
H	-3.7158269	-6.9699692	-0.8027595
C	0.4177856	-7.3926334	-1.8570869
C	1.7141421	-7.0554789	-1.6598939
H	2.5468612	-7.7057640	-1.4451064
H	-0.0272540	-8.3747467	-1.8334784
C	4.2653458	-5.5838128	-1.6289762
C	4.6610575	-6.5950841	-2.5062928

C 5.8809794 -7.2337771 -2.3365751
C 6.7204996 -6.8734899 -1.2902657
C 6.3368656 -5.8656163 -0.4149677
C 5.1200349 -5.2227373 -0.5851756
H 4.8172428 -4.4416725 0.1027481
H 6.9868382 -5.5792429 0.4052503
H 7.6724127 -7.3766377 -1.1580538
H 6.1792394 -8.0160620 -3.0270828
H 4.0175145 -6.8674692 -3.3361238
C 4.1843928 -2.7911684 -2.3287460
C 3.8327610 -1.4909632 -2.4890812
H 4.4636964 -0.6634265 -2.7707266
H 5.1568931 -3.2388331 -2.4579944
C 2.4623250 1.0715345 -2.3043569
C 3.5786267 1.3962516 -1.5316735
C 4.2471133 2.5958133 -1.7264484
C 3.8158633 3.4853961 -2.7017247
C 2.7107629 3.1687433 -3.4813288
C 2.0367975 1.9727515 -3.2833655
H 1.1808865 1.7250833 -3.9023886
H 2.3713742 3.8571817 -4.2484361
H 4.3397485 4.4230012 -2.8543448
H 5.1085051 2.8394650 -1.1136087
H 3.9127504 0.7074777 -0.7652302
C -0.3565765 1.0655873 -1.5851179
C -1.6605419 0.7215183 -1.4608284
H -2.5015741 1.3681864 -1.2724444
H 0.0828454 2.0474490 -1.5149034
C -4.2079420 -0.7080940 -1.7290074
C -4.4996277 0.3613688 -2.5802434
C -5.7138216 1.0192312 -2.4981491
C -6.6725509 0.6236273 -1.5564307
C -6.3873688 -0.4559728 -0.7102922
C -5.1737308 -1.1115813 -0.8023245
H -4.9543907 -1.9367711 -0.1348873
H -7.1214023 -0.7723384 0.0227844
C -7.9088665 1.3083926 -1.4495710
C -8.9629365 1.8958293 -1.3404466
C -10.1970594 2.5782961 -1.1996708
C -11.1292070 2.1655825 -0.2382030
C -12.3305739 2.8338907 -0.0945321

C -12.6410560 3.9345415 -0.9005146
C -11.7085020 4.3440555 -1.8594623
C -10.5062441 3.6780091 -2.0107172
H -9.7963283 4.0054302 -2.7622551
H -11.9361484 5.1829977 -2.5083729
C -13.9225965 4.6449329 -0.7398954
C -15.0956389 3.9423204 -0.4496110
C -16.3063133 4.5970631 -0.2890346
C -16.3464749 5.9802610 -0.4150769
C -15.1952783 6.7024406 -0.7145938
C -13.9932834 6.0351999 -0.8746960
H -13.0965710 6.6055743 -1.0884500
H -15.2539344 7.7794821 -0.8146335
O -17.5225075 6.7174957 -0.3062472
C -18.5117134 6.4121481 0.5446149
O -18.4970913 5.4900664 1.3267658
C -19.6392494 7.3602302 0.4155674
C -19.7242361 8.4057481 -0.4127324
C -21.0272683 9.1336654 -0.2641076
N -21.6736541 8.3372106 0.7798074
O -22.8362388 8.6096823 1.2317682
C -20.8780377 7.2103582 1.2663311
C -20.6024475 7.3899669 2.7654766
H -20.0288966 6.5428823 3.1377551
H -20.0394779 8.3067089 2.9363210
H -21.5511994 7.4506435 3.2979740
C -21.6327229 5.9003431 1.0022580
H -21.0561199 5.0602921 1.3855171
H -21.7915969 5.7673563 -0.0671341
H -22.5994081 5.9379619 1.5036936
C -20.8543554 10.5768041 0.2319462
H -20.4126486 11.1904214 -0.5506599
H -20.2088701 10.5969555 1.1091436
H -21.8317475 10.9780435 0.4994104
C -21.8838645 9.0928756 -1.5381830
H -21.4351850 9.7152560 -2.3098582
H -21.9625560 8.0701701 -1.9048366
H -22.8811907 9.4658347 -1.3057768
H -18.9686574 8.7212231 -1.1178532
H -17.2054601 4.0338989 -0.0764049
H -15.0701389 2.8613889 -0.3681720

H -13.0300232 2.5102251 0.6689361
H -10.9011001 1.3179375 0.3986611
H -5.9282502 1.8474446 -3.1650432
H -3.7718242 0.6673031 -3.3241863

The atomic coordinates of $2_2\cdot\text{O}$ (TS2)

O	0.558362	-1.578105	5.889479
Fe	2.222237	-1.565341	5.991635
N	2.365568	0.338709	6.846557
C	2.402662	0.634708	8.177132
C	2.227497	-0.267730	9.219603
C	2.193592	-1.653475	9.025002
N	2.474917	-2.302644	7.856333
C	2.618274	-3.624345	8.182961
C	3.058574	-4.623068	7.318479
C	3.249008	-4.414813	5.957860
N	2.920094	-3.286927	5.253771
C	3.246636	-3.549350	3.951390
C	3.049165	-2.699291	2.864505
C	2.671360	-1.364524	3.015534
N	2.626400	-0.698071	4.212475
C	2.470604	0.622001	3.904903
C	2.528385	1.689538	4.807085
C	2.549100	1.516139	6.185504
C	2.775847	2.580509	7.127843
C	2.685380	2.033972	8.361388
H	2.821892	2.517198	9.309568
H	2.998759	3.598063	6.869743
C	2.659152	3.063075	4.277362
C	1.736292	4.053188	4.607712
C	1.898049	5.346299	4.142503
C	2.990126	5.672804	3.352725
C	3.914296	4.695200	3.018948
C	3.746923	3.398631	3.471594
H	4.473290	2.638346	3.219343
H	4.772012	4.946040	2.409245
H	3.123163	6.686428	3.001730
H	1.171089	6.103752	4.399854
H	0.888175	3.800617	5.228420
C	2.329464	0.784166	2.490443
C	2.435104	-0.451776	1.939080
H	2.345847	-0.717798	0.903659
H	2.163482	1.717833	1.987500
C	3.300655	-3.216101	1.509416

C 4.105481 -2.521625 0.602960
C 4.265451 -2.968672 -0.692251
C 3.627437 -4.138341 -1.114477
C 2.885588 -4.878229 -0.188691
C 2.725513 -4.419960 1.101018
H 2.126550 -4.980523 1.802469
H 2.419954 -5.801988 -0.501252
C 3.663394 -4.557382 -2.459147
C 3.594269 -4.914545 -3.613184
C 3.407795 -5.346532 -4.941282
C 3.951575 -4.652407 -6.024447
C 3.671356 -5.051727 -7.314871
C 2.840861 -6.145367 -7.563457
C 2.330033 -6.857910 -6.476935
C 2.609098 -6.469681 -5.184508
H 2.202837 -7.019157 -4.347910
H 1.716670 -7.729510 -6.652525
C 2.471916 -6.508624 -8.938429
C 1.161308 -6.879909 -9.234933
C 0.774329 -7.174489 -10.528240
C 1.712319 -7.108543 -11.547816
C 3.027252 -6.753866 -11.272848
C 3.399448 -6.452951 -9.977904
H 4.425083 -6.187869 -9.770648
H 3.742369 -6.712629 -12.079588
O 1.381289 -7.308444 -12.885237
C 0.610546 -8.333119 -13.272897
O 0.194637 -9.197437 -12.532178
C 0.342804 -8.298036 -14.720049
C -0.279218 -9.276851 -15.381402
C -0.419429 -8.966465 -16.837526
N 0.177014 -7.641827 -16.910594
O 0.302618 -6.985701 -18.017695
C 0.715441 -7.163553 -15.643852
C 2.233055 -6.962661 -15.766127
H 2.427780 -6.329130 -16.629255
H 2.626013 -6.488522 -14.873651
H 2.732652 -7.917796 -15.914277
C 0.035807 -5.842391 -15.255972

H 0.474554 -5.442675 -14.347084
H -1.030571 -5.995189 -15.100746
H 0.170718 -5.128675 -16.065892
C 0.357951 -9.961646 -17.714280
H 0.378283 -9.587611 -18.735628
H -0.120827 -10.935687 -17.695826
H 1.381338 -10.060971 -17.359125
C -1.890624 -8.918700 -17.278854
H -1.941471 -8.519809 -18.289688
H -2.322550 -9.914557 -17.262233
H -2.463508 -8.271054 -16.618962
H -0.643150 -10.192904 -14.949736
H -0.247317 -7.445221 -10.746881
H 0.424133 -6.909540 -8.447391
H 4.070641 -4.488507 -8.145680
H 4.577191 -3.789584 -5.844510
H 4.873261 -2.411434 -1.391437
H 4.611309 -1.622874 0.925693
C 3.863505 -4.843190 3.847879
C 3.861159 -5.380486 5.088941
H 4.256977 -6.327530 5.401591
H 4.273751 -5.263769 2.950566
C 3.418345 -5.941927 7.883408
C 4.433536 -6.043855 8.831595
C 4.801108 -7.278832 9.336425
C 4.152072 -8.426751 8.910833
C 3.135085 -8.332949 7.973869
C 2.775892 -7.100844 7.457342
H 1.990140 -7.022587 6.721553
H 2.624560 -9.225160 7.639972
H 4.441187 -9.390486 9.305789
H 5.600662 -7.346055 10.061455
H 4.946011 -5.149864 9.158213
C 2.348804 -3.819769 9.573027
C 2.059069 -2.599160 10.091456
H 1.781598 -2.362342 11.100310
H 2.389575 -4.759343 10.088940
C 2.209765 0.252716 10.601535
C 1.299178 1.233802 10.986023

C	1.291283	1.718691	12.281729
C	2.198638	1.240353	13.212725
C	3.126545	0.283389	12.834472
C	3.133913	-0.204894	11.540842
H	3.871291	-0.937813	11.245717
H	3.850053	-0.083009	13.549791
H	2.188185	1.615223	14.225614
H	0.576474	2.472115	12.566118
H	0.593706	1.608857	10.259799
Fe	-1.010524	-2.088836	5.602393
N	-0.855556	-4.078500	5.368130
C	-0.774894	-5.007024	6.368515
C	-1.158216	-4.809290	7.687374
C	-1.592084	-3.586473	8.186502
N	-1.638867	-2.400757	7.504204
C	-2.127140	-1.477532	8.385293
C	-2.330272	-0.118093	8.137488
C	-2.066292	0.476290	6.906322
N	-1.721315	-0.176618	5.763805
C	-1.674951	0.764911	4.779154
C	-1.571043	0.501164	3.419503
C	-1.431053	-0.783823	2.889558
N	-1.244171	-1.941088	3.590498
C	-1.209257	-2.946518	2.658978
C	-0.989260	-4.297254	2.922416
C	-0.720564	-4.778082	4.201921
C	-0.423208	-6.158074	4.480866
C	-0.462155	-6.299796	5.825469
H	-0.329819	-7.189863	6.410385
H	-0.216128	-6.905242	3.740018
C	-1.200743	-5.292096	1.844990
C	-0.506417	-5.276693	0.639105
C	-0.765492	-6.224283	-0.336357
C	-1.727933	-7.198585	-0.130198
C	-2.436760	-7.215730	1.060948
C	-2.175658	-6.273208	2.037736
H	-2.738551	-6.284752	2.961734
H	-3.197702	-7.965345	1.229572
H	-1.927708	-7.937282	-0.892170

H	-0.213730	-6.198650	-1.265413
H	0.250997	-4.527896	0.469529
C	-1.412279	-2.408425	1.347152
C	-1.510086	-1.064263	1.486502
H	-1.629648	-0.332114	0.712032
H	-1.462826	-2.977208	0.440394
C	-1.749521	1.625120	2.475320
C	-2.882602	1.680409	1.664352
C	-3.070957	2.724764	0.783788
C	-2.121569	3.746015	0.699470
C	-0.986261	3.694832	1.513283
C	-0.807807	2.647221	2.391555
H	0.070309	2.609107	3.016391
H	-0.249279	4.482347	1.444245
C	-2.305641	4.830418	-0.182137
C	-2.455085	5.773877	-0.922390
C	-2.583796	6.893797	-1.768284
C	-3.507260	6.915822	-2.815689
C	-3.592577	8.017781	-3.641208
C	-2.762409	9.123092	-3.450082
C	-1.855408	9.102331	-2.388945
C	-1.764893	8.007334	-1.558427
H	-1.060601	7.998016	-0.738978
H	-1.228677	9.962880	-2.206434
C	-2.819628	10.280149	-4.352707
C	-4.031234	10.752583	-4.851769
C	-4.082324	11.839767	-5.705461
C	-2.903627	12.475280	-6.069139
C	-1.682432	12.012236	-5.588230
C	-1.645056	10.927519	-4.739022
H	-0.691934	10.564680	-4.385622
H	-0.777286	12.512171	-5.895785
O	-2.822586	13.543585	-6.954538
C	-3.794936	14.451565	-7.119220
O	-4.838950	14.473028	-6.506019
C	-3.405954	15.432944	-8.145689
C	-2.230725	15.510910	-8.772306
C	-2.201500	16.634411	-9.760286
N	-3.543586	17.179515	-9.625336

O	-3.962663	18.195449	-10.306189
C	-4.350906	16.510878	-8.615984
C	-4.718592	17.483826	-7.486117
H	-5.320169	16.971360	-6.741293
H	-3.819171	17.871519	-7.012264
H	-5.281345	18.316311	-7.901675
C	-5.624483	15.929669	-9.244698
H	-6.185500	16.732392	-9.717621
H	-6.234387	15.462385	-8.477103
H	-5.371637	15.188485	-10.000367
C	-1.964628	16.127858	-11.192048
H	-2.652413	15.318322	-11.426380
H	-2.138126	16.945437	-11.888254
H	-0.945315	15.771182	-11.301745
C	-1.146855	17.692524	-9.398511
H	-1.286749	18.560763	-10.038779
H	-0.147289	17.295001	-9.543388
H	-1.260616	18.002322	-8.361962
H	-1.382717	14.867739	-8.618877
H	-5.031233	12.191492	-6.078241
H	-4.954654	10.275877	-4.558450
H	-4.293812	8.013886	-4.463290
H	-4.146988	6.060252	-2.978714
H	-3.951326	2.763382	0.157919
H	-3.624573	0.897378	1.738177
C	-1.955472	2.064441	5.328421
C	-2.196692	1.886004	6.647697
H	-2.440061	2.628524	7.384041
H	-1.979721	2.979237	4.767449
C	-2.933491	0.718975	9.198551
C	-2.314920	0.904080	10.431453
C	-2.903747	1.695421	11.402192
C	-4.125333	2.303439	11.163052
C	-4.758881	2.111129	9.945571
C	-4.166775	1.328998	8.970597
H	-4.665911	1.176857	8.022578
H	-5.718818	2.572061	9.754682
H	-4.583670	2.920259	11.921393
H	-2.411115	1.833956	12.350558

H	-1.364230	0.429773	10.622006
C	-2.432123	-2.106274	9.637722
C	-2.092896	-3.413009	9.516618
H	-2.170461	-4.192643	10.250145
H	-2.860008	-1.612519	10.488199
C	-1.286569	-5.999215	8.568184
C	-0.242385	-6.426949	9.378734
C	-0.407890	-7.516251	10.216559
C	-1.615391	-8.194645	10.247100
C	-2.655116	-7.785462	9.426933
C	-2.493479	-6.693375	8.593673
H	-3.306080	-6.370805	7.957539
H	-3.596076	-8.317834	9.439807
H	-1.746960	-9.041010	10.906171
H	0.406390	-7.829288	10.855566
H	0.694532	-5.897046	9.344537

3 Literature

- [1] J. Rochford, E. Galoppini, *Langmuir* **2008**, *24*, 5366–5374.
- [2] M. Novak, S. A. Glover, *J. Am. Chem. Soc.* **2004**, *126*, 7748–7749.
- [3] B. E. Bode, J. Plackmeyer, T. F. Prisner, O. Schiemann, *J. Phys. Chem. A* **2008**, *112*, 5064–5073.
- [4] G. R. Fulmer, A. J. M. Miller, N. H. Sherden, H. E. Gottlieb, A. Nudelman, B. M. Stoltz, J. E. Bercaw, K. I. Goldberg, *Organometallics* **2010**, *29*, 2176–2179.
- [5] G. Jeschke, V. Chechik, P. Ionita, A. Godt, H. Zimmermann, J. Banham, C. R. Timmel, D. Hilger, H. Jung, *Appl. Magn. Reson.* **2006**, *30*, 473–498.

[A8]: Pulsed EPR Dipolar Spectroscopy on Spin Pairs with one Highly Anisotropic Spin Center: The Low-Spin Fe^{III} Case

Reprinted with permission from

Dinar Abdullin, Philipp Brehm, Nico Fleck, Sebastian Spicher, Stefan Grimme, Olav Schiemann*, *Chem. Eur. J.* **2019**, *25*, 14388 - 14398.

Published with Open Access by Wiley-VCH (Weinheim, DE) under CC-BY license, ©**2019** to the authors.

Contributions:

- Experimental Work:
 - Organic synthesis incl. compound characterization
- Writing of the manuscript in parts

Spectroscopy | Hot Paper |

 Pulsed EPR Dipolar Spectroscopy on Spin Pairs with one Highly Anisotropic Spin Center: The Low-Spin Fe^{III} CaseDinar Abdullin,^[a] Philipp Brehm,^[a, b] Nico Fleck,^[a] Sebastian Spicher,^[c] Stefan Grimme,^[c] and Olav Schiemann^{*[a]}

Abstract: Pulsed electron paramagnetic resonance (EPR) dipolar spectroscopy (PDS) offers several methods for measuring dipolar coupling constants and thus the distance between electron spin centers. Up to now, PDS measurements have been mostly applied to spin centers whose *g*-anisotropies are moderate and therefore have a negligible effect on the dipolar coupling constants. In contrast, spin centers with large *g*-anisotropy yield dipolar coupling constants that depend on the *g*-values. In this case, the usual methods of extracting distances from the raw PDS data cannot be applied. Here, the effect of the *g*-anisotropy on PDS data is studied in detail on the example of the low-spin Fe³⁺ ion. First, this effect is described theoretically, using the work of Bedilo and Maryasov (*Appl. Magn. Reson.* **2006**, 30, 683–702)

as a basis. Then, two known Fe³⁺/nitroxide compounds and one new Fe³⁺/trityl compound were synthesized and PDS measurements were carried out on them using a method called relaxation induced dipolar modulation enhancement (RIDME). Based on the theoretical results, a RIDME data analysis procedure was developed, which facilitated the extraction of the inter-spin distance and the orientation of the inter-spin vector relative to the Fe³⁺ *g*-tensor frame from the RIDME data. The accuracy of the determined distances and orientations was confirmed by comparison with MD simulations. This method can thus be applied to the highly relevant class of metalloproteins with, for example, low-spin Fe³⁺ ions.

Introduction

Pulsed EPR dipolar spectroscopy (PDS), which includes techniques such as pulsed electron–electron double resonance (PELDOR or DEER),^[1,2] double quantum coherence EPR (DQC),^[3] single-frequency technique for refocusing dipolar couplings (SIFTER),^[4] and relaxation induced dipolar modulation enhancement (RIDME),^[5,6] is a valuable method for determining biomolecular structures and their conformational changes during function.^[7] The method is based on the measurement of the dipolar coupling between electron spin centers and provides information about the inter-spin distances and, in favorable


cases, the relative orientation of these centers. As the majority of biomolecules are naturally diamagnetic, PDS on such systems typically requires site directed labeling of the biomolecule with spin labels.^[8–12] The most common spin labels are nitroxides,^[9–12] although a number of alternatives based on Gd³⁺,^[13,14] Cu²⁺,^[15,16] trityl^[17–20] and photoexcited porphyrins^[21] have been reported. In addition to the spin labels, there is a keen interest of using naturally occurring paramagnetic cofactors, such as Cu²⁺,^[22–28] low-spin (LS) Fe³⁺,^[6,29–32] high-spin (HS) Fe³⁺,^[33] HS Mn²⁺,^[34–38] Mo⁵⁺,^[30] Co²⁺,^[39,40] iron–sulfur clusters,^[27,41,42] manganese clusters,^[43] tyrosins,^[44,45] semiquinones^[46] or flavins,^[29,47,48] for PDS measurements. The obvious advantage of using intrinsic spin centers is that the number of spin labels required for PDS and, consequently, the number of structural perturbations to the native biomolecular structure can be reduced. Moreover, intrinsic spin centers often have a well-defined, fixed position within the fold of the biomolecule and, thus, can provide more accurate distance constraints as compared to flexible spin labels. In addition, PDS-based distance measurements between an intrinsic spin center and spin labels at different sites of a biomolecule enable the localization of the intrinsic spin centers within the biomolecular fold through trilateration^[49] or the docking of different parts of protein complexes using paramagnetic metal ions as anchor points.^[50]


Low-spin Fe³⁺ ions occur widely in metalloproteins,^[51–53] for example in hemoglobin, myoglobin, or cytochromes, and constitute as such an important spin probe for PDS. As compared

[a] Dr. D. Abdullin, P. Brehm, N. Fleck, Prof. Dr. O. Schiemann
Institute of Physical and Theoretical Chemistry
University of Bonn, 53115 Bonn (Germany)
E-mail: schiemann@pc.uni-bonn.de

[b] P. Brehm
Current address: Institute of Inorganic Chemistry
University of Bonn, 53115 Bonn (Germany)

[c] S. Spicher, Prof. Dr. S. Grimme
Mulliken Center for Theoretical Chemistry
University of Bonn, 53115 Bonn (Germany)

 Supporting information and the ORCID identification number(s) for the author(s) of this article can be found under:
<https://doi.org/10.1002/chem.201902908>.

 © 2019 The Authors. Published by Wiley-VCH Verlag GmbH & Co. KGaA. This is an open access article under the terms of the Creative Commons Attribution License, which permits use, distribution and reproduction in any medium, provided the original work is properly cited.

to organic radicals and other low-spin metal centers like Cu^{2+} , LS Fe^{3+} ions have a large g -tensor anisotropy and shorter relaxation times, which impose significant challenges on PDS measurements and the corresponding data analysis. Due to the significant g -anisotropy, the spectral width of LS Fe^{3+} ions largely exceeds the bandwidth of typical microwave pulses at usual microwave frequencies. Consequently, when the PDS signal is acquired on the LS Fe^{3+} centers, only a small fraction of these centers contributes to the signal. This, together with the short T_m relaxation rate of the LS Fe^{3+} ions, led to a low signal-to-noise ratio (SNR) of the X- and Q-band PELDOR time traces acquired on the LS Fe^{3+} /nitroxide spin pair in neuroglobin.^[54] Later, the value of SNR was improved by a factor of 30 using composite pulses at W-band.^[32] However, even though a reasonable SNR could be achieved, an accurate conversion of the PELDOR time traces into the distance distributions can be obstructed by orientation selectivity effects, due to selective excitation of certain orientations of the LS Fe^{3+} spin. The common way to account for the orientation selectivity is to measure several PELDOR time traces for different orientations of an anisotropic spin and then to analyze all time traces together.^[55–59] However, this procedure is not applicable to the spin pair LS Fe^{3+} /nitroxide, because the difference in resonance frequencies between LS Fe^{3+} ions and nitroxides exceeds the bandwidths of EPR resonators and microwave amplifiers.

The difficulties of PELDOR experiments involving LS Fe^{3+} /organic radical spin pairs can be circumvented by using another PDS technique called RIDME. The key difference of this technique to PELDOR is that one of the dipolar-coupled spins is flipped not by a selective microwave pulse, called pump pulse, but by non-selective spontaneous relaxation events. Since the T_1 relaxation times of organic radicals is typically much longer than the T_1 relaxation times of LS Fe^{3+} ions, the RIDME signal is usually acquired on the organic radicals, whereas the Fe^{3+} spins are flipped by spontaneous relaxation. The experiment done this way has several advantages. First, the detection of the RIDME signal on the organic radical, which has a small g -anisotropy and a long T_m relaxation time, results in a good SNR of the RIDME time trace. Second, an infinite effective bandwidth of the stochastic Fe^{3+} spin flips can provide RIDME modulation depths of up to 50% and ensures the absence of orientation selectivity from LS Fe^{3+} . These advantages were confirmed in previous RIDME studies on LS Fe^{3+} /flavin,^[29] LS Fe^{3+} /nitroxide^[6,31] and LS Fe^{3+} /trityl^[20] spin pairs.

Although acquiring RIDME time traces on LS Fe^{3+} /organic radical spin pairs is fairly straightforward, the conversion of these time traces into the distance distributions is challenging. As was pointed out by Milikisyants et al.^[6] and later by Astashkin et al.,^[29] the deviation of the three principal g -values of LS Fe^{3+} ions from the g -factor of the free electron ($g_e \approx 2.0023$) is large enough that it cannot be neglected in RIDME data analysis. This means that the common methods of PDS data analysis, which assumes both spins to be almost isotropic, cannot be applied in the present case. Instead, the theory of Bedilo and Maryasov^[60] for the dipolar coupling between anisotropic spins centers has to be used in this case. The first application

of this theory for the analysis of RIDME data was reported by Astashkin et al.^[29] There, the RIDME spectrum of the LS Fe^{3+} /flavin spin pair was simulated using a modified equation for the dipolar coupling constant, which provided estimates of the inter-spin distance and two angles that determine the relative orientation of the Fe^{3+} g -tensor with respect to the distance vector. However, this analysis was done only in a semi-quantitative way, because usage of the four-pulse RIDME sequence lead to time traces with significant dead time and the SNR was rather low.

The aim of the study here is therefore to explore the effect of g -anisotropy on the RIDME data of LS Fe^{3+} /organic radical systems and to establish a quantitative analysis for such data. First, the theory of the dipole–dipole interaction between a LS Fe^{3+} ion and an organic radical is given and then the predictions are derived for the shape of the corresponding dipolar spectra. To confirm the predictions experimentally, two known Fe^{3+} /nitroxide compounds, **1** and **2**,^[61] and one new Fe^{3+} /trityl compound, **1T**, were synthesized (Figure 1) and RIDME data was acquired on them. The obtained RIDME time traces were analyzed using the program DipFit, which was originally developed for the high-spin Fe^{3+} /nitroxide pairs^[33] but was extended here to the case of LS Fe^{3+} . At last, the DipFit-based distance and angular distributions were compared to the results of molecular dynamics (MD) simulations and to the distance distributions obtained for the same RIDME data by means of the program DeerAnalysis.^[62]

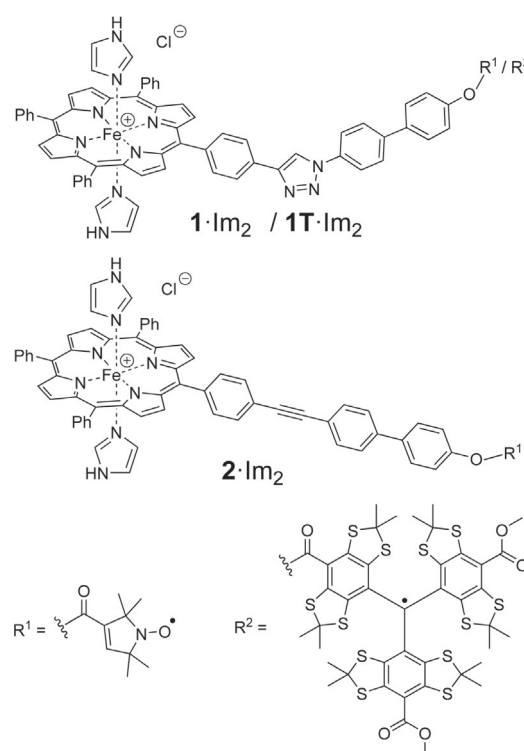


Figure 1. Lewis structures of model compounds **1**·Im₂, **1T**·Im₂ and **2**·Im₂.

Theory

The theory of dipole-dipole interaction between two anisotropic spin- $1/2$ centers was developed by Bedilo and Maryasov^[60] and was later extended to the case of a dipole-dipole interaction between one anisotropic spin- $1/2$ center and one isotropic spin- $1/2$ center.^[29,33] The latter case applies for the spin pairs LS Fe³⁺/organic radical, because the g -anisotropy of organic radical has usually little effect on dipolar spectra and thus can be neglected. Therefore, and as shown previously by us,^[33] the dipolar coupling frequency ν_{dd} of such spin pairs can be described by Equation (1):

$$\nu_{dd} = \frac{\mu_0 \beta_e^2 g_{1\text{eff}} g_e}{4\pi h r^3} \left[1 - 3 \left(\frac{\hat{g}_1 \hat{g}_1^T \mathbf{B}_0}{g_{1\text{eff}}^2 B_0}, \mathbf{n} \right) \left(\frac{\mathbf{B}_0}{B_0}, \mathbf{n} \right) \right] \quad (1)$$

in which μ_0 is the vacuum permeability, h is the Planck constant, \hat{g} and g_{eff} are the g -tensor and the effective g -factor of the LS Fe³⁺ ion, respectively, r is the inter-spin vector with the length r and the unit vector \mathbf{n} , and \mathbf{B}_0 is the vector of applied magnetic field with the length B_0 . Note that the product $(\mathbf{B}_0/B_0, \mathbf{n})$ is usually denoted as $\cos(\theta)$, in which θ is the angle between the inter-spin distance vector and the applied magnetic field. Comparing Equation (1) with the equation for the dipolar coupling between two isotropic spin- $1/2$ centers [Eq. (2)]:

$$\nu_{dd}^{\text{iso}} = \frac{\mu_0 \beta_e^2 g_e^2}{4\pi h r^3} [1 - 3\cos^2(\theta)] \quad (2)$$

reveals that both equations differ by the factor $g_{1\text{eff}}/g_e$ and the angular term in the square brackets. In the case of two isotropic spins, the latter term depends only on the angle θ , whereas when one of the spins is anisotropic, it also depends on the orientation of the distance vector with respect to the g -tensor of the anisotropic spin center. Such orientation can be described by two spherical angles, the polar (ξ) and azimuthal (ϕ)

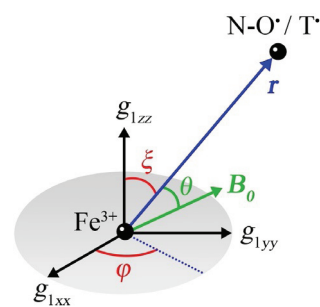


Figure 2. Geometric model of the spin pairs LS Fe³⁺/nitroxide and LS Fe³⁺/trityl in an external magnetic field \mathbf{B}_0 .

angles (Figure 2). Thus, the dipolar coupling frequencies depend not only on r and θ , but also on the g -values of the anisotropic spin center and the angles ξ and ϕ .

To get a deeper insight into how the g -anisotropy of LS Fe³⁺ centers influences the dipolar spectra, spectral simulations were performed on the basis of Equation (1), using $g_{1xx}=1.56$, $g_{1yy}=2.28$, $g_{1zz}=2.91$ for the principal g -values of the low-spin Fe³⁺ center (they correspond to the experimental g -values discussed below). The g -value of the organic radical was set to $g_e=2.0023$ and the inter-spin distance to 2.50 nm. The angles ξ and ϕ were varied in the range $[0^\circ, 90^\circ]$ with steps of 10° and 30° , respectively. Averaging of the dipolar coupling frequency over all possible orientations of the spin pair with respect to \mathbf{B}_0 was done by the Monte-Carlo method using 10^6 random samples. The obtained powder-averaged spectra are shown in Figure 3. The abscissa of the depicted spectra is given in units derived from Equation (3):

$$\nu_0 = \frac{\mu_0 \beta_e^2 g_e^2}{4\pi r^3} \quad (3)$$

which corresponds to the dipolar coupling constant of an isotropic spin pair with the same inter-spin distance as used

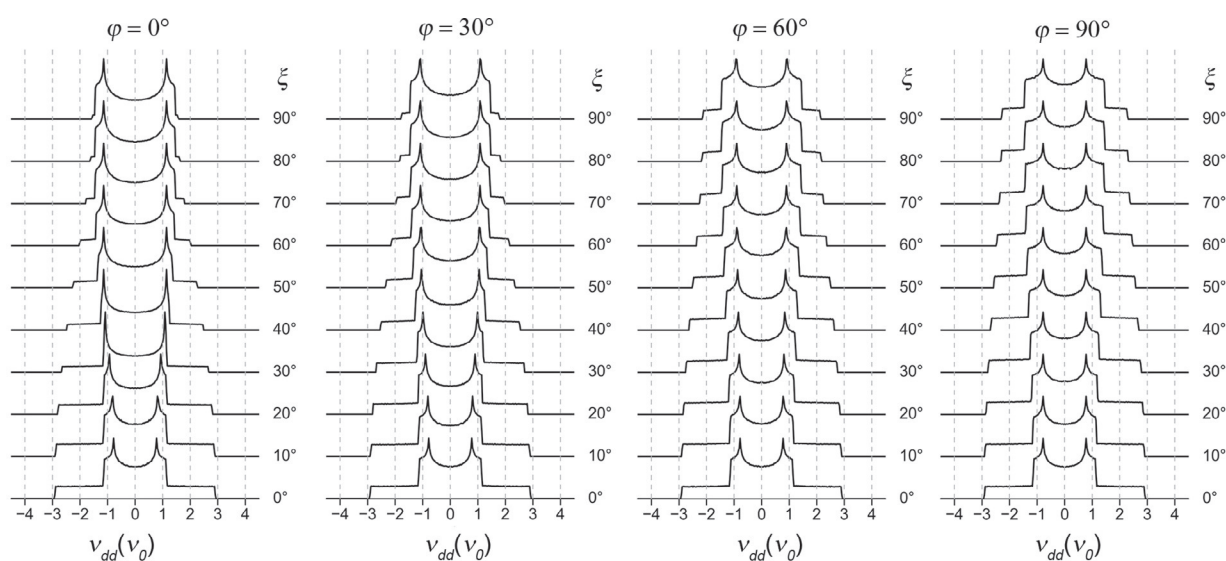


Figure 3. Angular dependence of the dipolar spectrum of a spin pair consisting of an isotropic spin- $1/2$ with $g_{\text{iso}}=g_e$ and an anisotropic spin- $1/2$ with $g_{\text{aniso}}=[1.56, 2.28, 2.91]$.

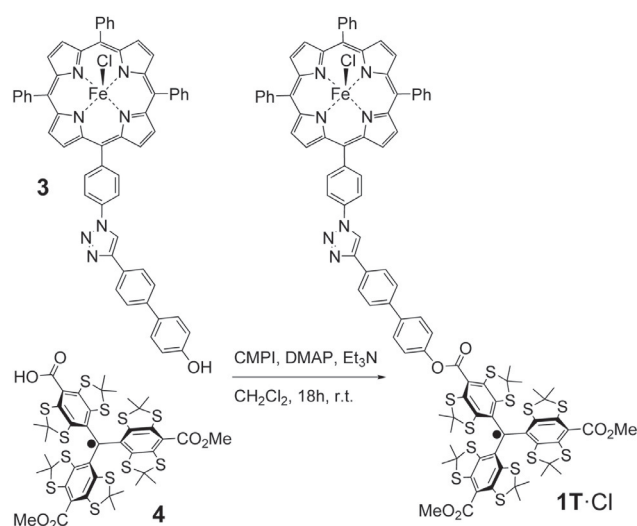
above. Figure 3 reveals a prominent deviation of the calculated spectra from the well-known Pake doublet. Whereas the Pake doublet has two characteristic singularities, often referred to as perpendicular ($\theta=90^\circ$) and parallel ($\theta=0^\circ$) components, all calculated spectra here display three singularities instead. In analogy to the Pake doublet, these singularities can be subdivided into two perpendicular components, which correspond to $\theta=90^\circ$, and one parallel component, which corresponds to $\theta=0^\circ$. Moreover, the frequencies, at which the singularities appear in Figure 3, do not have a fixed ratio, as in the case of the Pake doublet, but depend on the principal g -values of the LS Fe^{3+} center and the angles ξ and ϕ . This dependence can be readily explained on example of four spectra corresponding to the angular combinations $(\xi, \phi)=(0^\circ, 0^\circ)$, $(0^\circ, 90^\circ)$, $(90^\circ, 0^\circ)$ and $(90^\circ, 90^\circ)$. For the angular combination $(0^\circ, 0^\circ)$, r is collinear to the g_{1zz} -axis of the LS Fe^{3+} g -tensor. Consequently, the parallel component of the spectrum is scaled by g_{1zz} yielding a singularity at $2(g_{1zz}/g_e)\nu_0 \approx 2.91 \nu_0$. Then, the other two components of the LS Fe^{3+} g -tensor give rise to two perpendicular components, which appear at $(g_{1xx}/g_e)\nu_0 \approx 0.78 \nu_0$ and $(g_{1yy}/g_e)\nu_0 \approx 1.14 \nu_0$. The same assignment of singularities also holds for the spin pair geometry with $(\xi, \phi)=(0^\circ, 90^\circ)$, because the shape of the dipolar spectrum does not depend on the ϕ angle as soon as the ξ angle equals 0° . For the angular combination $(90^\circ, 0^\circ)$, r is aligned along the g_{1xx} -axis of the LS Fe^{3+} g -tensor. Thus, the parallel component of the spectrum is scaled by g_{1xx} and appears at $2(g_{1xx}/g_e)\nu_0 \approx 1.56 \nu_0$, whereas two perpendicular components are scaled by g_{1yy} and g_{1zz} and appear at $(g_{1yy}/g_e)\nu_0 \approx 1.14 \nu_0$ and $(g_{1zz}/g_e)\nu_0 \approx 1.45 \nu_0$, respectively. Finally, the angular combination $(90^\circ, 90^\circ)$ corresponds to the case where r is collinear to the g_{1yy} -axis of the LS Fe^{3+} g -tensor. In this case, the parallel component of the spectrum is determined by the value of g_{1yy} which yields the singularity at $2(g_{1yy}/g_e)\nu_0 \approx 2.28 \nu_0$, whereas the perpendicular components of the spectrum are scaled by g_{1xx} and g_{1zz} and appear at $(g_{1xx}/g_e)\nu_0 \approx 0.78 \nu_0$ and $(g_{1zz}/g_e)\nu_0 \approx 1.45 \nu_0$.

Note that the dipolar spectra in Figure 3 were simulated for certain values of r , ξ and ϕ . If the molecule, which hosts the spin pair, has some flexibility, the geometric parameters r , ξ and ϕ will have some distributions. Obviously, the distributions $P(r)$, $P(\xi)$ and $P(\phi)$ will affect the shape and the width of the corresponding dipolar spectra. This effect will lead to the averaging of the dipolar frequency given by Equation (1) over these distributions. Moreover, a possible correlation between the values of r , ξ and ϕ might affect the dipolar spectra. Thus, the determination of $P(r)$, $P(\xi)$ and $P(\phi)$ from the dipolar spectra is a complex, ill-posed problem. Nevertheless, a possible algorithm to extract these distributions from the dipolar spectra using several simplifying assumptions is proposed in the Experimental section.

Experimental Section

Synthesis of model compounds

The synthesis and analytics of compounds 1-Cl and 2-Cl have been described previously.^[61] Compound 1T-Cl was obtained according



Scheme 1. Synthesis of model compound 1T-Cl.

to the following protocol (Scheme 1): First, Fe^{3+} -porphyrin **3**^[61] (10 mg, 10.5 μmol), trityl radical **4**^[63] (10.8 mg, 10.5 μmol), 2-chloro-1-methylpyridinium iodide (CMPI; 3.2 mg, 12.6 μmol , 1.2 equiv.), and 4-(*N,N*-dimethylamino)-pyridin (DMAP; 1.0 mg, 4.2 μmol , 0.4 equiv.) were dissolved in 2 mL dry dichloromethane under argon atmosphere. Then, triethyl amine (2.5 μL , 25.2 μmol , 2.5 equiv.) was added and the reaction mixture was stirred for 18 h at room temperature. Afterwards, water (10 mL) and dichloromethane (10 mL) were added and the organic phase was separated. After washing with brine, the solvent of the organic fraction was removed under reduced pressure and the crude product was subjected to column chromatography. Eluting with dichloromethane/methanol (20:1, v/v), the product was isolated as a dark brownish solid in a yield of 12.9 mg (6.6 μmol ; 63%). For analytical data see Figure S1.

All three compounds were converted from the HS- ($S=5/2$) to the LS-state ($S=1/2$) by adding $10^4 e^{\text{equiv.}}$ of imidazole (Im) to 200 μM solutions of the HS compounds in $[\text{D}_8]\text{THF}$, yielding 1-Im₂, 2-Im₂ and 1T-Im₂, respectively. The spin transition was confirmed by means of cw-EPR (see below).

EPR measurements

Details of the experimental setups are described in Chapter 2 of the Supporting Information. The RIDME experiments on the model compounds were performed using the five-pulse sequence $\pi/2-\tau_1-\pi-(\tau_1+t)-\pi/2-T_{\text{mix}}-\pi/2-(\tau_2-t)-\pi-\tau_2\text{-echo}$.^[61] The frequency of the microwave pulses was set in resonance with either the maximum of the nitroxide spectrum, for 1-Im₂ and 2-Im₂, or with the maximum of the trityl spectrum for 1T-Im₂. The lengths of the $\pi/2$ and π pulses were 12 and 24 ns, respectively. τ_1 and τ_2 intervals were set to 300 ns and 3 μs , respectively. The optimal values of T_{mix} and the temperature of RIDME experiments T were determined based on the temperature-dependent inversion recovery measurements on the LS Fe^{3+} center (Chapter 7 in the Supporting Information). This yielded $T_{\text{mix}}=100 \mu\text{s}$ and $T=10 \text{ K}$ for all three model compounds. During the RIDME experiment, t was linearly incremented from -50 ns to 2880 ns in increments of 8 ns, yielding 360 data points in total. The shot repetition time was set to 10 ms. To avoid overlap with unwanted echoes with the detected refocused virtual echo, 16-step phase cycling was employed (Chapter 7 in the Supporting Information). In order to suppress

deuterium ESEEM (Chapter 7 in the Supporting Information), the initial values of τ_1 and τ_2 were incremented stepwise and independently from each other with an increment of 8 ns and 16 steps per inter-pulse interval,^[64] resulting in additional 256 averaging cycles. As a result, the duration of a single RIDME experiment was about 4 hours.

RIDME data analysis

The first step of the RIDME data analysis was the usual removal of the non-oscillating background from the original RIDME time traces. According to the recent publication by Keller et al.,^[65] the shape of the RIDME background is described by an exponential function with an argument having a linear and a quadratic terms with respect to t . In practice, it is often approximated by a stretched exponential function or a third-order polynomial function.^[31,65,66] Here, the background was fitted here by a third order polynomial function using the program DeerAnalysis.^[62] The same program was used to divide the original RIDME time traces by the background function and then to perform fast Fourier transformation (FFT) of the background corrected time traces. This procedure yielded the so-called RIDME spectra.

In the next step, the RIDME time traces were fitted by means of the program DipFit^[33] (free available at <https://github.com/dinarabdullin>). In this program, the distributions $P(r)$, $P(\xi)$ and $P(\phi)$ were approximated by Gaussians and the corresponding mean values $\langle r \rangle$, $\langle \xi \rangle$, $\langle \phi \rangle$ and standard deviations Δr , $\Delta \xi$, $\Delta \phi$ were used as fitting parameters. All six fitting parameters were optimized until the simulated time trace or the simulated spectrum provided the best root-mean-square deviation (RMSD) to the experimental time trace or the experimental spectrum, respectively. The simulation of the dipolar spectrum for certain values of $\langle r \rangle$, $\langle \xi \rangle$, $\langle \phi \rangle$, Δr , $\Delta \xi$, and $\Delta \phi$ was done by averaging Equation (1) over the corresponding distributions $P(r)$, $P(\xi)$ and $P(\phi)$ and, additionally, over the angle θ (powder averaging). The averaging was performed via the Monte-Carlo method with 10^6 random samples. The values of r , ξ and ϕ were assumed to have no correlation with each other. The g -tensor of the LS Fe^{3+} center was set to the experimental values described below. For simplicity, the nitroxide's and trityl's principal g -values were set to g_e . In order to simulate the RIDME time trace, the 10^6 values of the dipolar frequency were used to compute the sum in Equation (4):^[67]

$$\frac{V(t)}{V(0)} = 1 - \frac{\lambda}{N} \sum_{i=1}^N (1 - \cos(2\pi\nu_{dd}^i t)) \quad (4)$$

in which, N is the number of Monte-Carlo samples, and λ is the modulation depth parameter, which was determined from the experimental RIDME time traces.

Molecular modeling

The structure optimization and MD simulations for model compounds **1**·Im₂, **2**·Im₂ and **1T**·Im₂ were done using the stand-alone program xtb.^[68] Evaluation of the MD trajectories was performed with the program TRAVIS.^[69] Owing to the bi-radical electronic structure and the large molecular size of the model compounds, the semi-empirical tight-binding method GFN2-xTB/GBSA^[70] was applied (for details see Chapter 11 in Supporting Information).

To enable the comparison of the MD results with the structural information from RIDME, the distributions $P(r)$, $P(\xi)$ and $P(\phi)$ were calculated based on the MD trajectories. The values of r were determined as the distance between the Fe atom and the center of

the N–O bond of the nitroxide radical or the central C atom of the trityl radical. To determine the angular parameters ξ and ϕ , the orientation of the LS Fe^{3+} g -tensor relative to tetraphenylporphyrin (TPP) had to be defined. Here, this orientation was set to the one reported for $\text{Fe}(\text{TPP})(4\text{-Melm})_2^+$.^[71] Thus, the g_{zz} -axis of LS Fe^{3+} was orthogonal to the TPP plane and aligned with the Fe–N(imidazole) bond. The corresponding g_{xx} - and g_{yy} -axes were aligned with two orthogonal Fe–N(porphyrin) bonds within the TPP plane. Based on this definition of the g -axes, ξ was determined as the angle between the g_{zz} -axis of LS Fe^{3+} and the inter-spin vector r . The angle between the g_{xx} -axis and the projection of r on the TPP plane yielded the value of ϕ . The resulting MD distributions of r , ξ and ϕ are summarized in Figure S10.

Results and Discussion

Preparation of the model compounds

The HS-precursors **1**·Cl, **2**·Cl and **1T**·Cl were synthesized as described in the Experimental part. Adding 10^4 equivalents of imidazole to the three compounds lead to the formation of the bis-imidazole adducts **1**·Im₂, **2**·Im₂ and **1T**·Im₂ and conversion of the Fe^{3+} from the HS- to the LS-state. In order to confirm the LS-state of the Fe^{3+} ions in **1**·Im₂, **2**·Im₂ and **1T**·Im₂, X-band cw-EPR spectra of these compounds were measured at 15 K (Figures 4 and S2). The obtained spectra do show the

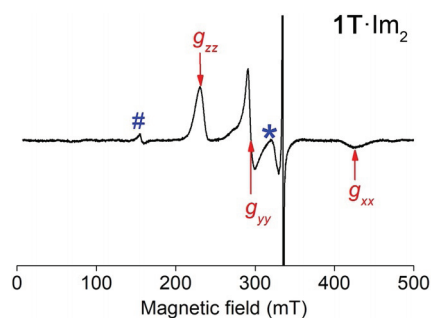


Figure 4. X-band cw-EPR spectrum of **1T**·Im₂⁺. The spectrum have been recorded with a microwave frequency of 9.400 GHz at a temperature of 15 K. The spectral positions, which correspond to the principal g -values of the LS Fe^{3+} ion, are marked by arrows. The unsaturated signal of the trityl radicals is given in Figure S3. The cavity background signal is marked by a star, and the hash symbol shows the position of the signal assigned to free Fe^{3+} ions.

characteristic signal of the LS Fe^{3+} ion, which is overlaid with the sharp saturated signal of the nitroxide or trityl radicals. No HS Fe^{3+} signal, as found for **1**·Cl and **2**·Cl,^[61] was observed in the region of $g \approx 6$. Thus, cw-EPR proofs complete conversion of the HS Fe^{3+} ion into its LS-state, which is in agreement with previous studies.^[72,73] The principal g -values of the LS Fe^{3+} ion were found to be identical for all three compounds, $g_{zz} = 2.91 \pm 0.01$, $g_{yy} = 2.28 \pm 0.01$ and $g_{xx} = 1.56 \pm 0.04$. All three g -values are in agreement with those reported for the LS Fe^{3+} ion in $\text{Fe}(\text{TPP})(\text{Im})_2^+$ ^[73] and $\text{Fe}(\text{TPP})(4\text{-Melm})_2^+$.^[71] The spectrum of **1T**·Im₂⁺ contains an additional weak signal at $g \approx 4.3$, which is assigned to free Fe^{3+} ions that drop out of the porphyrin ring.^[74]

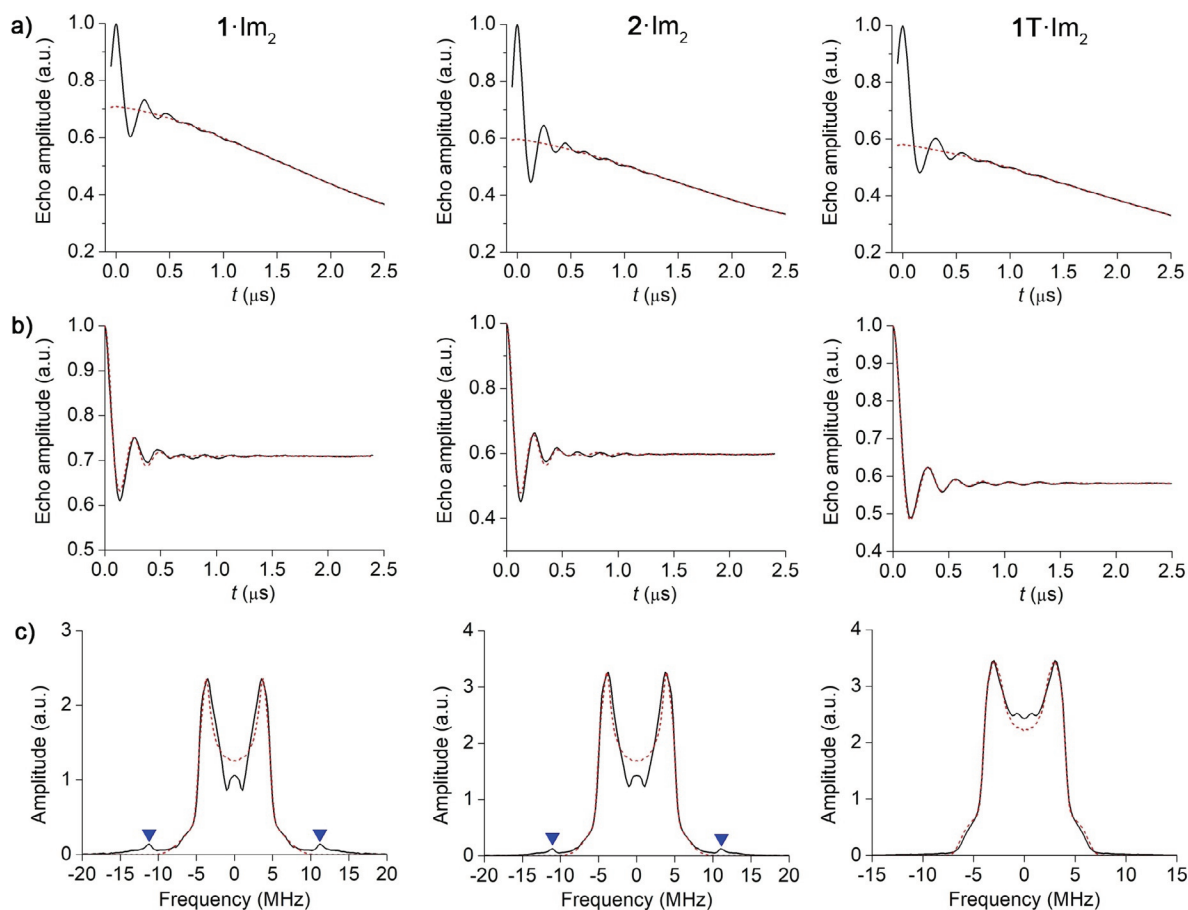


Figure 5. Q-band RIDME data acquired on 1-Im_2 , 2-Im_2 and 1T-Im_2 . a) Original RIDME time traces (black solid lines) overlaid with the corresponding third-order polynomial background fits (red dashed lines). b) Background-corrected RIDME time traces and their fits (red dashed lines) obtained by means of DipFit. c) FFTs of the RIDME time traces are depicted by the black solid lines. The unsuppressed nitrogen ESEEM peak is marked by the triangles. The dipolar spectra simulated for the optimized distributions $P(r)$, $P(\xi)$ and $P(\phi)$ (see Table 1) are depicted by the red dashed lines.

RIDME measurements

The RIDME time traces recorded on 1-Im_2 , 2-Im_2 and 1T-Im_2 are shown in Figure 5a and the corresponding background-corrected time traces are depicted in Figure 5b. All RIDME time traces have a very good SNR (see Chapter 8 in the Supporting Information) and display several clear oscillation periods. The obtained modulation depths equal 30%, 40% and 42% for 1-Im_2 , 2-Im_2 and 1T-Im_2 , respectively. The difference between the modulation depths, as well as the deviation of these depths from the expected value of 50%, is likely due to partial μ_2 -oxo-dimerization of the Fe^{3+} porphyrins, which was already observed earlier for the given model compounds.^[61]

The dipolar spectra corresponding to each of the RIDME time traces are depicted in Figure 5c. In addition to the dipolar spectra, which appear within ± 10 MHz for all three model compounds, the RIDME spectra of 1-Im_2 and 2-Im_2 display a weak peak at about 12 MHz. This peak can be assigned to nitroxide ESEEM (Figure S4) and results from incomplete ^{14}N ESEEM suppression by the modulation averaging Scheme. Since the amplitude of the unsuppressed ESEEM peak is weak, no further attempts were taken to remove it. Note also that

this detrimental ESEEM peak is absent in the RIDME spectrum of the trityl-based model compound 1T-Im_2 .

RIDME data analysis

After the successful acquisition of RIDME data on the model compounds, the next step is the extraction of the distributions $P(r)$, $P(\xi)$ and $P(\phi)$ from this data. This was done by means of the program DipFit, which approximates all three distributions by Gaussians and performs the fitting of the RIDME time traces using the mean values and standard deviations of r , ξ and ϕ as fitting parameters. Figure 5b shows that good fits to the RIDME time traces were obtained for all three model compounds. The parameters of the distributions $P(r)$, $P(\xi)$ and $P(\phi)$, which led to these fits, are listed in Table 1. In order to estimate how defined these parameters are, the six-dimensional parameter space needs to be explored, which is a very time expensive procedure. Instead, the lower bound for parameters' uncertainty was determined here by recording the dependence of the goodness of fit on different pairs of fitting parameters, while setting the four other parameters to their optimized values. As a measure for the goodness of fit, the RMSD be-

Table 1. RIDME- and MD-based parameters of distributions $P(r)$, $P(\xi)$ and $P(\phi)$ in 1-Im₂, 2-Im₂ and 1T-Im₂.

Parameter	1-Im ₂		2-Im ₂		1T-Im ₂	
	RIDME	MD	RIDME	MD	RIDME	MD
$\langle r \rangle$ (nm)	2.48 ± 0.03	2.50	2.44 ± 0.02	2.47	2.64 ± 0.01	2.65
Δr (nm)	0.05 ± 0.05	0.05	0.05 ± 0.04	0.04	0.06 ± 0.02	0.06
$\langle \xi \rangle$ (°) ^[a]	69 ± 21	86	84 ± 23	90	71 ± 19	88
$\Delta \xi$ (°)	24 ± 24	15	23 ± 23	12	3 ± 20	16
$\langle \phi \rangle$ (°) ^[a]	27 ± 27	45	30 ± 30	45	57 ± 7	45
$\Delta \phi$ (°)	20 ± 20	12	13 ± 17	8	30 ± 9	14

[a] These angles were optimized within the range [0°, 90°] but have several symmetry-related values within the range [0°, 360°] (all sets of symmetry-related angles are listed in Chapter 9 of the Supporting Information).

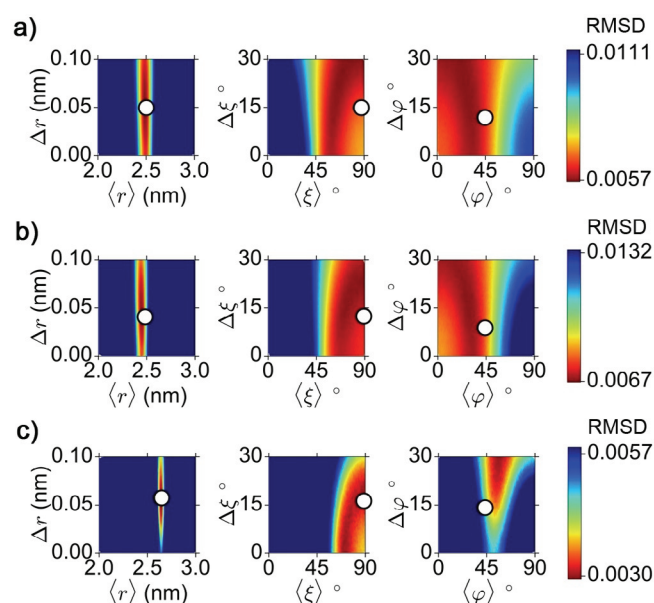


Figure 6. Dependencies of the RMSD between the experimental and simulated RIDME time traces on the mean values and standard deviations of r , ξ and ϕ . The MD-based estimates for the mean values and standard deviations of r , ξ and ϕ are depicted as circles. a) 1-Im₂, b) 2-Im₂, and c) 1T-Im₂.

tween the experimental and simulated time traces was used. The obtained RMSD plots for the mean values and the standard deviations of r , ξ and ϕ are shown in Figure 6, and the RMSD plots for other pairs of fitting parameters are given in Figure S6. Parameter ranges, in which 110% of the minimal RMSD are reached, were used to determine the approximate confidence intervals for the optimized parameters (Table 1). Note that such error-estimation criterion is also used in the program PeldorFit, where it was shown to yield reasonable error estimates of fitting parameters.^[75]

As follows from Table 1, the confidence intervals of the mean inter-spin distance $\langle r \rangle$ and the corresponding standard deviation Δr are well below 1 Å for all three model compounds. Such a precision of the obtained inter-spin distances reveals high sensitivity of the RIDME experiment towards these two parameters. The confidence intervals of the angular parameters $\langle \xi \rangle$ and $\Delta \xi$ are also similar for all three compounds.

They are in the order of $\pm 20^\circ$ for both $\langle \xi \rangle$ and $\Delta \xi$. The confidence intervals for the angular parameters $\langle \phi \rangle$ and $\Delta \phi$ are in average similar to the ones of $\langle \xi \rangle$ and $\Delta \xi$ but display a larger distribution of their values between different model compounds. The precision of the mean value $\langle \phi \rangle$ varies between $\pm 7^\circ$ (1T-Im₂) and $\pm 30^\circ$ (2-Im₂), and the precision of the width $\Delta \phi$ takes values between $\pm 9^\circ$ (1T-Im₂) and $\pm 20^\circ$ (1-Im₂). Such difference in the confidence intervals of $\langle \phi \rangle$ and $\Delta \phi$ correlates with the difference in the best RMSD values obtained for each of the model compounds. Figure 6 reveals that the lowest RMSD value among the three model compounds was obtained for 1T-Im₂, whereas the larger RMSD values were obtained for 1-Im₂ and 2-Im₂.

In addition, the optimized distributions $P(r)$, $P(\xi)$ and $P(\phi)$ were used to simulate the dipolar spectra in Figure 5c. As can be seen, the simulated spectra provide an overall agreement with the experimentally obtained spectra. A slight deviation between the experimental and simulated spectra around the zero frequency for 1-Im₂ and 2-Im₂ can be due to the imperfection introduced by the background correction. This deviation could not be avoided neither by using various different background fitting functions, such as stretched exponential or polynomial, nor by varying the starting point for the background fitting. Recently, Ritsch et al. have reported on a similar effect observed for a Cu²⁺/nitroxide spin system and assigned this distortion of the RIDME spectrum to the background artifact that appears at the beginning of RIDME time traces.^[75] The ongoing work on the description of the RIDME background might help to explain this empirical observation in the future. Another reason for the observed deviation might be a slight orientation selectivity, which is due to the partial excitation of the nitroxide spectrum in the RIDME experiment.

Comparison to MD simulations

In order to relate the obtained distributions $P(r)$, $P(\xi)$ and $P(\phi)$ to the structure and dynamics of the model compounds, MD simulations were carried out for each of them. Based on these simulations, qualitative estimates of all three distributions were derived (Figure S10) and, to allow direct comparison to the RIDME results, the mean values and their standard deviation were calculated for each distribution. The calculated parameters are listed in Table 1 and are depicted in Figure 6 by circles.

Table 1 reveals an excellent agreement between the RIDME and MD distance parameters $\langle r \rangle$ and Δr for all three model compounds. Both methods predict that 1-Im₂ and 2-Im₂ have similar mean Fe³⁺-nitroxide distances of ~ 2.50 nm and ~ 2.47 nm, respectively, whereas the mean Fe³⁺-trityl distance in 1T-Im₂ is ~ 0.15 nm longer than the Fe³⁺-nitroxide distance in the structurally similar compound 1-Im₂. The latter difference is due to the larger size of the trityl radical as compared to the nitroxide radical. The widths of the inter-spin distance distributions Δr are below 0.1 nm and differ between the model compounds by less than 0.02 nm, which reflects a similar flexibility of the linker/nitroxide motifs of 1-Im₂ and 2-Im₂ and the linker/trityl motif of 1T-Im₂.

A good agreement between RIDME and MD was achieved not only for the distance parameters but also for the angular parameters $\langle \xi \rangle$ and $\Delta \xi$. For all three model compounds, MD simulations yielded $\langle \xi \rangle$ and $\Delta \xi$ values of $\sim 90^\circ$ and $\sim 15^\circ$, respectively. Both values are within the confidence intervals of the corresponding parameters determined by RIDME (see

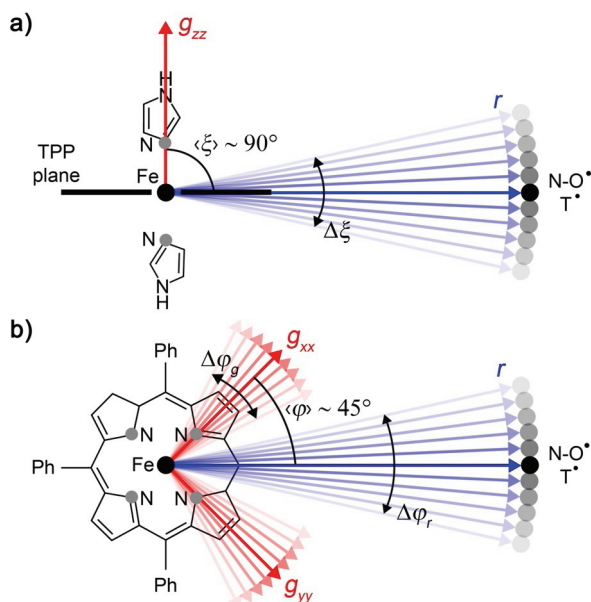


Figure 7. Schematic representation of the geometric parameters $\langle \xi \rangle$ and $\langle \phi \rangle$ and their distributions widths $\Delta \xi$ and $\Delta \phi$ for the model compounds **1-Im₂**, **2-Im₂** and **1T-Im₂**. The Fe^{3+} and nitroxide (or trityl) spin centers are depicted as black spheres. The inter-spin vector is shown by blue vector. The g -axes of the Fe^{3+} ions are depicted as red vectors. a) The view is set parallel to the TPP plane. The TPP core is drawn as a black bar. b) The view is set perpendicular to the TPP plane. $\Delta \phi_r$ denotes the contribution to $\Delta \phi$ which is due to the dynamics of the linker/radical motifs, and $\Delta \phi_g$ denotes the contribution to $\Delta \phi$ which stems from the distribution of g_{xx} - and g_{yy} -orientations within the TPP plane.

Table 1 and Figure 6). Note that $\langle \xi \rangle = 90^\circ$ describes the case where the inter-spin vector is perpendicular to the g_{zz} -axis of the Fe^{3+} ion. As g_{zz} is orthogonal to the TPP plane,^[71] the inter-spin vector has to be in plane with the TPP ring (Figure 7a). In terms of structure, this means that the linker/nitroxide and linker/trityl motifs are in plane with the TPP ring. The distribution of the ξ angles around 90° with a standard deviation $\Delta \xi \sim 15^\circ$ can be attributed to bending dynamics of the linkers, which leads to a slight inclination of the linker/nitroxide and linker/trityl motifs relative to the TPP plane (Figure 7a). This dynamics fits to the observed dynamics of other compounds with similar linker groups.^[25,26,57]

The MD derived value of $\langle \phi \rangle$ is for all three model compounds 45° . This value is within the confidence intervals of the RIDME derived values of $\langle \phi \rangle$ for **1-Im₂** and **2-Im₂** and deviates by 5° from the RIDME derived value of $\langle \phi \rangle$ for **1T-Im₂**. Similarly, the difference between the RIDME and MD estimates of $\Delta \phi$ depends on the model compound. In the case of **1-Im₂** and **2-Im₂**, the RIDME values of $\Delta \phi$ have large confidence intervals (see Figure 6), which include the MD prediction. In the case of

1T-Im₂, the RIDME value of $\Delta \phi$ is well-defined and deviates by at least 7° from the corresponding MD prediction. A possible explanation for this difference can be based on the following: The angle ϕ is determined by the orientations of the g_{xx} - and g_{yy} -axes of the Fe^{3+} ion and the orientation of the inter-spin vector. In the MD simulations, the orientations of the g_{xx} - and g_{yy} -axes were fixed along two orthogonal Fe–N bonds of the TPP ring. Thus, the MD values of $\Delta \phi$ are determined only by the dynamics of the linker/nitroxide or linker/trityl motifs, which changes in the orientation of the inter-spin vector relative to the fixed g -axes. In addition, the distribution of g_{xx} - and g_{yy} -orientations within the TPP plane might also contribute to $\Delta \phi$. According to previous works, such distribution can be caused by rotation of the axial ligands relative to the TPP plane.^[71,76] If one takes this distribution into account, the RIDME width $\Delta \phi$ can be represented as a superposition of a width $\Delta \phi_r$ which is due to the dynamics of the linker/radical motifs, and a width $\Delta \phi_g$ which stems from the distribution of g_{xx} - and g_{yy} -orientations within the TPP plane and which is caused by the rotation of the axial ligands (Figure 7b). If both contributions are approximated by Gaussians with standard deviations $\Delta \phi_r$ and $\Delta \phi_g$, the total width is given by $\Delta \phi^2 = \Delta \phi_r^2 + \Delta \phi_g^2$. Assuming that $\Delta \phi$ and $\Delta \phi_r$ can be associated with the RIDME- and MD-based widths, respectively, $\Delta \phi_g = 26^\circ$ can be determined for **1T-Im₂**. Note that a similar distribution of the g_{xx} - and g_{yy} -orientations around the porphyrin's Fe–N bonds was reported for $\text{Fe}(\text{TPP})(4\text{-Melm})_2^+$; $\pm 25^\circ$ based on proton HYSCORE experiments.^[71]

Comparison with 2-Cl

As the molecular skeleton of **2-Cl** is the same as for **2-Im₂**, both compounds differ only with respect to their spin states, HS for the former and LS for the latter. It is thus of interest to compare the geometric parameters obtained from their RIDME data. The RIDME measurements on HS **2-Cl** were reported in our previous paper.^[33] There, it was not possible to determine the $P(\phi)$ distribution, because the g -tensor of the HS Fe^{3+} ion had axial symmetry. In analogy to the RIDME-based distributions here, the distributions $P(r)$ and $P(\xi)$ of the HS compound were described by the mean values, $\langle r \rangle = 2.52 \pm 0.03$ nm and $\langle \xi \rangle = 89^\circ \pm 4^\circ$, and the standard deviations, $\Delta r = 0.06 \pm 0.05$ nm and $\Delta \xi = 6^\circ \pm 3^\circ$, respectively. These values reveal a good overall agreement with the corresponding values for **2-Im₂** (see Table 1). Thus, these results show the consistency between the distances and angles ξ determined for the LS Fe^{3+} /nitroxide and the HS Fe^{3+} /nitroxide.

Comparison to DeerAnalysis

To reveal the effect of the g -anisotropy on the RIDME data analysis, the RIDME time traces of **1-Im₂**, **2-Im₂** and **1T-Im₂** were additionally analyzed by means of the program DeerAnalysis,^[62] which neglects the anisotropy of the LS Fe^{3+} spin centers. Figure 8 depicts the distance distributions obtained by DeerAnalysis for all three model systems. For the sake of comparison, these distributions are overlaid with the corresponding

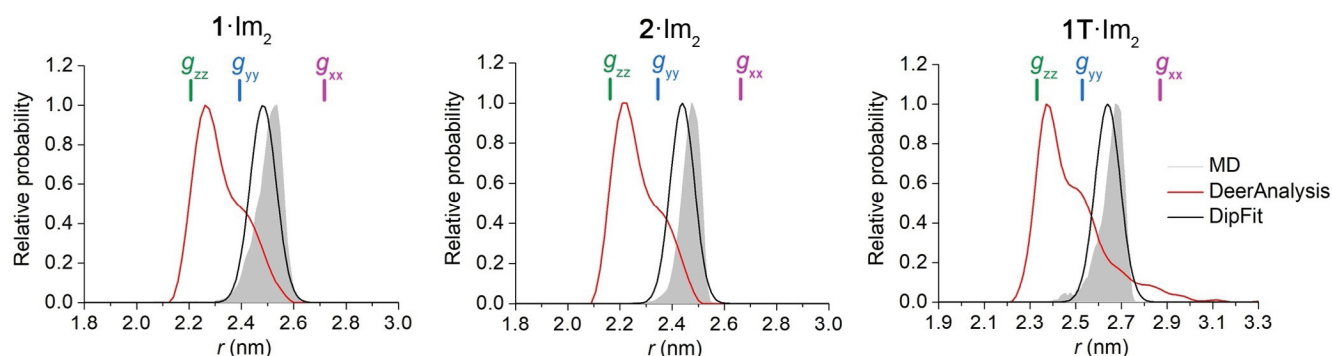


Figure 8. Comparison of DipFit (black lines) and DeerAnalysis (red lines) based inter-spin distance distributions for $1\cdot\text{Im}_2^+$, $2\cdot\text{Im}_2^+$ and $1\text{T}\cdot\text{Im}_2^+$. As a reference, the MD predictions of the distance distributions are depicted as gray shades. Colored bars depict the positions of artificial distances that are obtained for the actual distance (r) and three principal g -values of the LS Fe^{3+} center when the g -anisotropy of the Fe^{3+} center is neglected in the RIDME data analysis.

DipFit and MD distance distributions. As can be seen from Figure 8, the DeerAnalysis distributions have a clear difference to the DipFit and MD distributions. This difference concerns the most probable distances, which are smaller by ~ 0.25 nm for the DeerAnalysis distributions than for the DipFit and MD distributions, as well as the shape of the distance distributions, which are sharp and unimodal in the case of DipFit and MD but are broad and have several prominent shoulders in the case of DeerAnalysis. To interpret the obtained deviation of the DeerAnalysis distance distributions from the corresponding DipFit and MD distributions, it is sufficient to consider Equations (1) and (2). Neglecting their angular parts and putting these two equations equal to each other, then each distance r in Equation (1) will correspond to the distance $r' = r \cdot (g_e/g_{\text{eff}})^{1/3}$ in Equation (2). This result shows that each actual distance r corresponds to a number of artificial distances r' in the DeerAnalysis distribution. Colored bars in Figure 8 depict the positions of these artificial distances calculated for the DipFit parameter $\langle r \rangle$ (Table 1) and the three principal g -values of the LS Fe^{3+} ion (g_{xx} , g_{yy} and g_{zz} in Figure 4). Since g_{zz} ($=2.91$) and g_{yy} ($=2.28$) are larger than g_e , the corresponding artificial distances are smaller than the actual distances. In contrast, g_{xx} ($=1.56$) is smaller than g_e and the corresponding artificial distance is larger than the actual distance. Thus, the g -anisotropy of Fe^{3+} leads to a shift of the DeerAnalysis distances relative to the actual distances, and the different principal g -values of Fe^{3+} give rise to several shoulders in the DeerAnalysis distributions. In order to predict the exact values of the artificial distances and their relative probabilities, the angular terms of Equations (1) and (2) have to be taken into account as well. This will lead to an additional dependence of the artificial distances on angles ξ and ϕ , which are included in the angular term of Equation (1). The dependence of the DeerAnalysis distributions on ξ and ϕ is responsible for the fact that the shoulders in the DeerAnalysis distributions appear at not exactly the calculated artificial distances and that these shoulders have different relative probabilities (see Figure 8).

Thus, the g -anisotropy of the LS Fe^{3+} ion has a significant effect on the RIDME data analysis. Because of this, we revisited the analysis of the RIDME data, reported earlier for the cytochrome P450cam mutant C58R1^[31] (see Chapter 10 in the Sup-

porting Information). Although the g -anisotropy of the LS Fe^{3+} center is smaller for cytochrome P450cam ($g_{xx}=1.91$, $g_{yy}=2.25$, $g_{zz}=2.42$)^[31] then for the model compounds here, a clear difference between the DipFit and DeerAnalysis distance distributions was obtained (Figure 9). This difference concerns mostly

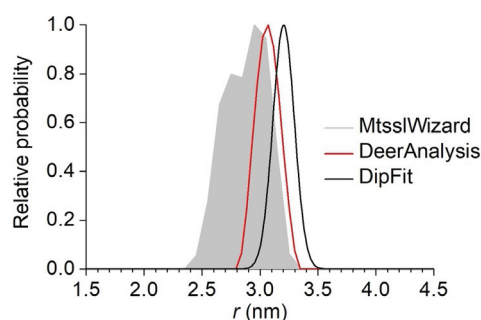


Figure 9. Comparison of DipFit (black lines) and DeerAnalysis (red lines) based inter-spin distance distributions for the cytochrome P450cam mutant C58R1. As a reference, the mtssWizard prediction of the distance distribution is depicted as a gray shade.

the most probable distance, which is smaller by 0.15 nm for the DeerAnalysis distribution as compared to DipFit distribution. The width of the DeerAnalysis distribution is only slightly larger than the width of the DipFit distribution, which is in agreement with the reduced g -anisotropy mentioned above. The DipFit derived distance distribution agrees less well with the MtssWizard^[77,78] prediction than the DeerAnalysis one. However, the difference is close the average error of MtssWizard (~ 0.3 nm) and, thus, can be assigned to the uncertainty of in silico prediction.

Conclusions

The effect of the g -anisotropy of LS Fe^{3+} ions on the RIDME data was described in detail and confirmed experimentally for LS Fe^{3+} /nitroxide and LS Fe^{3+} /trityl spin pairs. The dipolar spectra of such spin pairs were shown to depend not only on the inter-spin distances but also on the principal g -values of LS Fe^{3+} and the relative orientation of the inter-spin vector rela-

tive to the g -frame of Fe^{3+} . The latter orientation was described by two angular parameters, a polar angle ξ and an azimuthal angle ϕ . The distance distribution $P(r)$ and the angular distributions $P(\xi)$ and $P(\phi)$ could be extracted from the experimental RIDME data with the fitting program DipFit. In contrast, the analysis of the same RIDME data using the program DeerAnalysis, which neglects g -anisotropy, led to an error of 0.25 nm in the mean inter-spin distances, compared to 0.01 nm in the case of DipFit, and errors in the distribution width and shape. In addition, to the distance parameters, DipFit yielded the mean values and standard deviations of angular parameters ξ and ϕ with an average uncertainty of 20° . The comparison of the RIDME-derived distributions $P(r)$, $P(\xi)$ and $P(\phi)$ with their MD-based predictions revealed very good consistency for all three model systems considered. This result proves that not only $P(r)$ but also $P(\xi)$ and $P(\phi)$ can be reliably determined from the RIDME data. Thus, this work provides an important guideline for further applications of PDS to the highly relevant class of LS Fe^{3+} containing proteins and extends the arsenal of available programs for the analysis of PDS data from anisotropic spin centers.

Acknowledgements

This work was funded by the German Research Foundation (DFG) within the collaborative research center SFB813 "Chemistry at Spin Centers" (projects A6 and Z2).

Conflict of interest

The authors declare no conflict of interest.

Keywords: EPR spectroscopy · iron(III) · proteins · spin labels · trityl radicals

- [1] A. D. Milov, K. M. Salikhov, M. D. Shchirov, *Fiz. Tverd. Tela* **1981**, *23*, 975–982.
- [2] R. E. Martin, M. Pannier, F. Diederich, V. Gramlich, M. Hubrich, H. W. Spiess, *Angew. Chem. Int. Ed.* **1998**, *37*, 2833–2837; *Angew. Chem.* **1998**, *110*, 2993–2998.
- [3] S. Saxena, J. H. Freed, *Chem. Phys. Lett.* **1996**, *251*, 102–110.
- [4] G. Jeschke, M. Pannier, A. Godt, H. W. Spiess, *Chem. Phys. Lett.* **2000**, *331*, 243–252.
- [5] L. V. Kulik, S. A. Dzuba, I. A. Grigoryev, Y. D. Tsvetkov, *Chem. Phys. Lett.* **2001**, *343*, 315–324.
- [6] S. Milikisyants, F. Scarpelli, M. G. Finiguerra, M. Ubbink, M. Huber, *J. Magn. Reson.* **2009**, *201*, 48–56.
- [7] *Structure and Bonding*, Vol. 152: *Structural Information from Spin-Labels and Intrinsic Paramagnetic Centres in the Biosciences* (Eds.: C. R. Timmel, J. R. Harmer), Springer, Heidelberg, **2013**.
- [8] C. Altenbach, T. Marti, H. G. Khorana, W. L. Hubbell, *Science* **1990**, *248*, 1088–1092.
- [9] W. L. Hubbell, C. J. López, C. Altenbach, Z. Yang, *Curr. Opin. Struct. Biol.* **2013**, *23*, 725–733.
- [10] R. Ward, O. Schiemann, *Struct. Bonding (Berlin)* **2012**, *152*, 249–281.
- [11] E. G. Bagryanskaya, O. A. Krumkacheva, M. V. Fedin, S. R. A. Marque, *Methods Enzymol.* **2015**, *563*, 365–396.
- [12] J. P. Klare, H. J. Steinhoff, *Photosynth. Res.* **2009**, *102*, 377–390.
- [13] A. Potapov, Y. Song, T. J. Meade, D. Goldfarb, A. V. Astashkin, A. Raitsimring, *J. Magn. Reson.* **2010**, *205*, 38–49.
- [14] Y. Yang, F. Yang, Y. J. Gong, T. Bahrenberg, A. Feintuch, X. C. Su, D. Goldfarb, *J. Phys. Chem. Lett.* **2018**, *9*, 6119–6123.
- [15] T. F. Cunningham, M. R. Putterman, A. Desai, W. S. Horne, S. Saxena, *Angew. Chem. Int. Ed.* **2015**, *54*, 6330–6334; *Angew. Chem.* **2015**, *127*, 6428–6432.
- [16] M. J. Lawless, J. L. Sarver, S. Saxena, *Angew. Chem. Int. Ed.* **2017**, *56*, 2115–2117; *Angew. Chem.* **2017**, *129*, 2147–2149.
- [17] G. W. Reginsson, N. C. Kunjir, S. T. Sigurdsson, O. Schiemann, *Chem. Eur. J.* **2012**, *18*, 13580–13584.
- [18] Z. Yang, Y. Liu, P. Borbat, J. L. Zweier, J. H. Freed, W. L. Hubbell, *J. Am. Chem. Soc.* **2012**, *134*, 9950–9952.
- [19] G. Y. Shevelev, O. A. Krumkacheva, A. A. Lomzov, A. A. Kuzhelev, O. Y. Rogozhnikova, D. V. Trukhin, T. I. Troitskaya, V. M. Tormyshev, M. V. Fedin, D. V. Pyshnyi, E. G. Bagryanskaya, *J. Am. Chem. Soc.* **2014**, *136*, 9874–9877.
- [20] J. J. Jasso, A. Berndhäuser, F. Duthie, S. P. Kühn, G. Hagelueken, O. Schiemann, *Angew. Chem. Int. Ed.* **2017**, *56*, 177–181; *Angew. Chem.* **2017**, *129*, 183–187.
- [21] M. Di Valentin, M. Albertini, M. G. Dal Farra, E. Zurlo, L. Orian, A. Polimeno, M. Gobbo, D. Carbonera, *Chem. Eur. J.* **2016**, *22*, 17204–17214.
- [22] E. Narr, A. Godt, G. Jeschke, *Angew. Chem. Int. Ed.* **2002**, *41*, 3907–3910; *Angew. Chem.* **2002**, *114*, 4063–4066.
- [23] I. M. C. Van Amsterdam, M. Ubbink, G. W. Canters, M. Huber, *Angew. Chem. Int. Ed.* **2003**, *42*, 62–64; *Angew. Chem.* **2003**, *115*, 64–67.
- [24] C. W. M. Kay, *J. Am. Chem. Soc.* **2003**, *125*, 13861–13867.
- [25] B. E. Bode, J. Plackmeyer, T. F. Prisner, O. Schiemann, *J. Phys. Chem. A* **2008**, *112*, 5064–5073.
- [26] B. E. Bode, J. Plackmeyer, M. Bolte, T. F. Prisner, O. Schiemann, *J. Organomet. Chem.* **2009**, *694*, 1172–1179.
- [27] J. E. Lovett, A. M. Bowen, C. R. Timmel, M. W. Jones, J. R. Dilworth, D. Caprotti, S. G. Bell, L. L. Wong, J. Harmer, *Phys. Chem. Chem. Phys.* **2009**, *11*, 6840–6848.
- [28] Z. Yang, D. Kise, S. Saxena, *J. Phys. Chem. B* **2010**, *114*, 6165–6174.
- [29] A. V. Astashkin, B. O. Elmore, W. Fan, J. G. Guillemette, C. Feng, *J. Am. Chem. Soc.* **2010**, *132*, 12059–12067.
- [30] A. V. Astashkin, A. Rajapakshe, M. J. Cornelison, K. Johnson-Winters, J. H. Enemark, *J. Phys. Chem. B* **2012**, *116*, 1942–1950.
- [31] D. Abdullin, F. Duthie, A. Meyer, E. S. Müller, G. Hagelueken, O. Schiemann, *J. Phys. Chem. B* **2015**, *119*, 13534–13542.
- [32] C. L. Motion, J. E. Lovett, S. Bell, S. L. Cassidy, P. A. S. Cruickshank, D. R. Bolton, R. I. Hunter, H. El Mkami, S. Van Doorslaer, G. M. Smith, *J. Phys. Chem. Lett.* **2016**, *7*, 1411–1415.
- [33] D. Abdullin, H. Matsuoka, M. Yulikov, N. Fleck, C. Klein, S. Spicher, G. Hagelueken, S. Grimme, A. Luetzen, O. Schiemann, *Chem. Eur. J.* **2019**, *25*, 8820–8828.
- [34] D. Banerjee, H. Yagi, T. Huber, G. Otting, D. Goldfarb, *J. Phys. Chem. Lett.* **2012**, *3*, 157–160.
- [35] D. Akhmetzyanov, J. Plackmeyer, B. Endeward, V. P. Denysenkov, T. F. Prisner, *Phys. Chem. Chem. Phys.* **2015**, *17*, 6760–6766.
- [36] I. Kaminker, M. Bye, N. Mendelman, K. Gislason, S. T. Sigurdsson, D. Goldfarb, *Phys. Chem. Chem. Phys.* **2015**, *17*, 15098–15102.
- [37] A. Martorana, Y. Yan, Y. Zhao, Q.-F. Li, X.-C. Su, D. Goldfarb, *Dalton Trans.* **2015**, *44*, 20812–20816.
- [38] A. Meyer, O. Schiemann, *J. Phys. Chem. A* **2016**, *120*, 3463–3472.
- [39] A. Giannoulis, K. Ackermann, P. E. Spindler, C. Higgins, D. B. Cordes, A. M. Z. Slawin, T. F. Prisner, B. E. Bode, *Phys. Chem. Chem. Phys.* **2018**, *20*, 11196–11205.
- [40] P. E. Spindler, S. J. Glaser, T. E. Skinner, T. F. Prisner, *Angew. Chem. Int. Ed.* **2013**, *52*, 3425–3429; *Angew. Chem.* **2013**, *125*, 3509–3513.
- [41] C. Elsässer, M. Brecht, R. Bittl, *J. Am. Chem. Soc.* **2002**, *124*, 12606–12611.
- [42] M. M. Roessler, M. S. King, A. J. Robinson, F. A. Armstrong, J. Harmer, J. Hirst, *Proc. Natl. Acad. Sci. USA* **2010**, *107*, 1930–1935.
- [43] A. Kawamori, N. Katsuta, H. Mino, A. Ishii, J. Minagawa, T.-A. Ono, *J. Biol. Phys.* **2002**, *28*, 413–426.
- [44] V. P. Denysenkov, D. Biglino, W. Lubitz, T. F. Prisner, M. Bennati, *Angew. Chem. Int. Ed.* **2008**, *47*, 1224–1227; *Angew. Chem.* **2008**, *120*, 1244–1247.
- [45] V. P. Denysenkov, T. F. Prisner, J. Stubbe, M. Bennati, D. Biglino, W. Lubitz, T. F. Prisner, M. Bennati, *Proc. Natl. Acad. Sci. USA* **2006**, *103*, 13386.

- [46] M. A. Swanson, V. Kathirvelu, T. Majtan, F. E. Frerman, G. R. Eaton, S. S. Eaton, *J. Am. Chem. Soc.* **2009**, *131*, 15978–15979.
- [47] C. W. M. Kay, C. Elsässer, R. Bittl, S. R. Farrell, C. Thorpe, *J. Am. Chem. Soc.* **2006**, *128*, 76–77.
- [48] E. F. Yee, R. P. Diensthuber, A. T. Vaidya, P. P. Borbat, C. Engelhard, J. H. Freed, R. Bittl, A. Möglich, B. R. Crane, *Nat. Commun.* **2015**, *6*, 10079.
- [49] D. Abdullin, N. Florin, G. Hagelueken, O. Schiemann, *Angew. Chem. Int. Ed.* **2015**, *54*, 1827–1831; *Angew. Chem.* **2015**, *127*, 1847–1851.
- [50] Z. Yang, M. R. Kurpiewski, M. Ji, J. E. Townsend, P. Mehta, L. Jen-Jacobson, S. Saxena, *Proc. Natl. Acad. Sci. USA* **2012**, *109*, E993–E1000.
- [51] A. Messerschmidt, R. Huber, T. Poulos, K. Wieghardt, *Handbook of Metalloproteins Vol. 1–2*, Wiley, Chichester, **2001**.
- [52] A. Messerschmidt, W. Bode, M. Cygler, *Handbook of Metalloproteins Vol. 3*, Wiley, Chichester, **2004**.
- [53] A. Messerschmidt, *Handbook of Metalloproteins Vol. 4–5*, Wiley, Chichester, **2011**.
- [54] M. Ezhevskaya, E. Bordignon, Y. Polyhach, L. Moens, S. Dewilde, G. Jeschke, S. Van Doorslaer, *Mol. Phys.* **2013**, *111*, 2855–2864.
- [55] C. Abé, D. Klose, F. Dietrich, W. H. Ziegler, Y. Polyhach, G. Jeschke, H.-J. Steinhoff, *J. Magn. Reson.* **2012**, *216*, 53–61.
- [56] B. Endeward, J. A. Butterwick, R. MacKinnon, T. F. Prisner, *J. Am. Chem. Soc.* **2009**, *131*, 15246–15250.
- [57] G. W. Reginsson, R. I. Hunter, P. A. S. Cruickshank, D. R. Bolton, S. T. Sigurdsson, G. M. Smith, O. Schiemann, *J. Magn. Reson.* **2012**, *216*, 175–182.
- [58] G. W. Reginsson, S. A. Shelke, C. Rouillon, M. F. White, S. T. Sigurdsson, O. Schiemann, *Nucleic Acids Res.* **2013**, *41*, e11.
- [59] D. Abdullin, G. Hagelueken, R. I. Hunter, G. M. Smith, O. Schiemann, *Mol. Phys.* **2015**, *113*, 544–560.
- [60] A. F. Bedilo, A. G. Maryasov, *J. Magn. Reson. Ser. A* **1995**, *116*, 87–96.
- [61] D. Abdullin, N. Fleck, C. Klein, P. Brehm, S. Spicher, A. Lützen, S. Grimme, O. Schiemann, *Chem. Eur. J.* **2019**, *25*, 2586–2596.
- [62] G. Jeschke, V. Chechik, P. Ionita, A. Godt, H. Zimmermann, J. Banham, C. R. Timmel, D. Hilger, H. Jung, *Appl. Magn. Reson.* **2006**, *30*, 473–498.
- [63] J. J. Jassoy, A. Meyer, S. Spicher, C. Wuebben, O. Schiemann, *Molecules* **2018**, *23*, 682.
- [64] K. Keller, A. Doll, M. Qi, A. Godt, G. Jeschke, M. Yulikov, *J. Magn. Reson.* **2016**, *272*, 108–113.
- [65] K. Keller, M. Qi, C. Gmeiner, I. Ritsch, A. Godt, G. Jeschke, A. Savitsky, M. Yulikov, *Phys. Chem. Chem. Phys.* **2019**, *21*, 8228–8245.
- [66] S. Razzaghi, M. Qi, A. I. Nalepa, A. Godt, G. Jeschke, M. Yulikov, *J. Phys. Chem. Lett.* **2014**, *5*, 3970.
- [67] D. Margraf, B. E. Bode, A. Marko, O. Schiemann, T. F. Prisner, *Mol. Phys.* **2007**, *105*, 2153–2160.
- [68] Please contact: xtb@thch.uni-bonn.de to obtain the program.
- [69] M. Brehm, B. Kirchner, *J. Chem. Inf. Model.* **2011**, *51*, 2007–2023.
- [70] C. Bannwarth, S. Ehlert, S. Grimme, *J. Chem. Theory Comput.* **2019**, *15*, 1652–1671.
- [71] E. Vinck, S. Van Doorslaer, *Phys. Chem. Chem. Phys.* **2004**, *6*, 5324–5330.
- [72] T. Ikeue, Y. Ohgo, T. Saitoh, T. Yamaguchi, M. Nakamura, *Inorg. Chem.* **2001**, *40*, 3423–3434.
- [73] F. A. Walker, D. Reis, V. L. Balke, *J. Am. Chem. Soc.* **1984**, *106*, 6888–6898.
- [74] S. V. Nistor, E. Goovaerts, S. Van Doorslaer, S. Dewilde, L. Moens, *Chem. Phys. Lett.* **2002**, *361*, 355–361.
- [75] I. Ritsch, H. Hintz, G. Jeschke, A. Godt, M. Yulikov, *Phys. Chem. Chem. Phys.* **2019**, *21*, 9810–9830.
- [76] N. V. Shokhirev, *J. Am. Chem. Soc.* **1998**, *120*, 981–990.
- [77] G. Hagelueken, R. Ward, J. H. Naismith, O. Schiemann, *Appl. Magn. Reson.* **2012**, *42*, 377–391.
- [78] G. Hagelueken, D. Abdullin, O. Schiemann, *Methods Enzymol.* **2015**, *563*, 595–622.

Manuscript received: June 25, 2019

Revised manuscript received: August 5, 2019

Accepted manuscript online: August 6, 2019

Version of record online: October 9, 2019

CHEMISTRY

A **European** Journal

Supporting Information

Pulsed EPR Dipolar Spectroscopy on Spin Pairs with one Highly Anisotropic Spin Center: The Low-Spin Fe^{III} Case

Dinar Abdullin,^[a] Philipp Brehm,^[a, b] Nico Fleck,^[a] Sebastian Spicher,^[c] Stefan Grimme,^[c] and Olav Schiemann^{*[a]}

chem_201902908_sm_miscellaneous_information.pdf

Table on contents

1	Analytics for compound 1T ·Cl.....	3
2	Experimental setup for EPR measurements.....	4
	2.1 cw-EPR measurements.....	4
	2.2 Pulsed EPR measurements.....	4
3	cw-EPR spectra of the ls Fe ³⁺ center in 1 ·Im ₂ , 2 ·Im ₂ and 1T ·Im ₂	5
4	cw-EPR spectra of the organic radicals in 1 ·Im ₂ , 2 ·Im ₂ and 1T ·Im ₂	6
5	ESEEM experiments on nitroxide and trityl centers of 1 ·Im ₂ , 2 ·Im ₂ and 1T ·Im ₂	8
6	Inversion recovery experiments on the ls Fe ³⁺ center of 1 ·Im ₂ , 2 ·Im ₂ and 1T ·Im ₂	10
7	RIDME experiments on 1 ·Im ₂ , 2 ·Im ₂ and 1T ·Im ₂	11
	7.1 Choosing the value of T_{mix}	11
	7.2 ESEEM suppression scheme.....	11
	7.3 Phase cycling.....	12
8	Signal-to-noise ratio of RIDME time traces.....	13
9	DipFit analysis of the RIDME time traces of 1 ·Im ₂ , 2 ·Im ₂ and 1T ·Im ₂	14
10	DipFit analysis of the RIDME time trace of the P450cam mutant C58R1.....	16
11	MD simulations for 1 ·Im ₂ , 2 ·Im ₂ and 1T ·Im ₂	18
12	Optimized structure of 1 ·Im ₂	21
13	Optimized structure of 2 ·Im ₂	25
14	Optimized structure of 1T ·Im ₂	29
	References.....	35

1 Analytics for compound 1T·Cl

Electrospray ionization (ESI+) mass spectra were measured using an OrbitrapXL (Thermo Fisher Scientific) instrument. Gel permeation chromatography (GPC) was conducted on an Agilent 1200 Series analytical GPC system running isocratically with unstabilized THF at a flow rate of 1 ml/min. The system was equipped with polystyrene column (8 mm x 300 mm, four-column set, porosity 10 nm, 100 nm, 10000 nm, and 100000 nm) purchased from PSS Polymer Standard Service GmbH, Germany. The sample was dissolved in unstabilized THF containing 0.1 % trifluoroacetic acid in order to cleave μ_2 -oxo dimers.

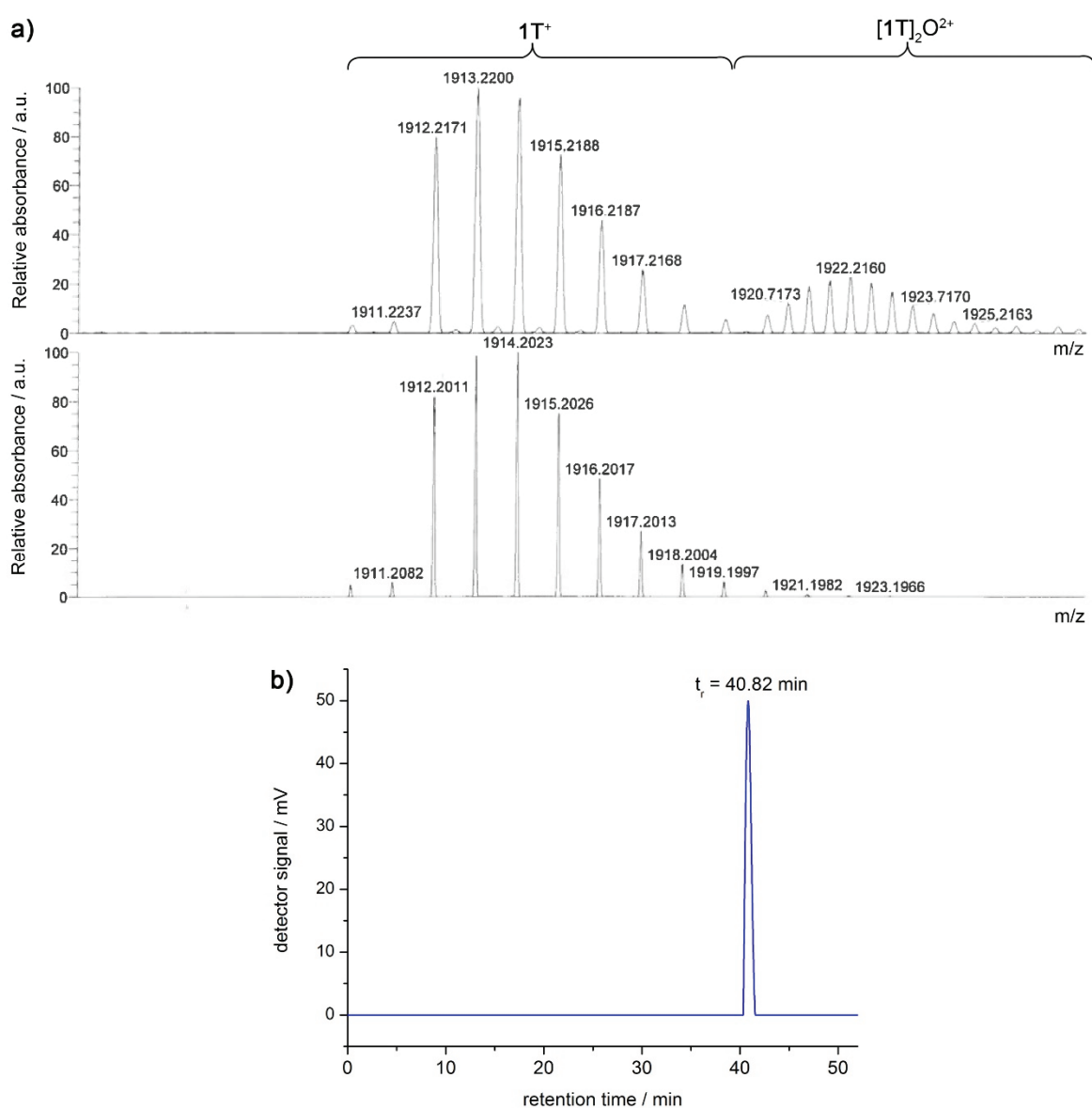


Figure S1. a) The experimental (top) and simulated (bottom) HRMS ESI+ spectrum of $1T \cdot Cl$. Since the spectrum was measured before the HCl-treatment, it reveals the presence of μ_2 -oxo-dimers in the sample. b) GPC-elugram of $1T \cdot Cl$.

2 Experimental setup for EPR measurements

2.1 cw-EPR measurements

Continuous wave EPR (cw-EPR) measurements were carried out using a X-band EPR spectrometer EMXmicro (Bruker) equipped with a super high quality resonator (SHQ). The resonator was mounted onto a continuous flow helium cryostat ER4112HE (Bruker), whose temperature was controlled by a Mercury iTC system (Oxford Instruments). To obtain the temperature of 100 K, a nitrogen-based variable temperature accessory ER 4131VT (Bruker) was employed.

2.2 Pulsed EPR measurements

Pulsed EPR measurements were carried out on a Bruker ELEXSYS E580 spectrometer using a Flexline probe head with a Q-band resonator ER5106QT-2 (Bruker). Microwave pulses were amplified with a 150 W TWT amplifier (model 187Ka). In order to obtain temperatures around 10 K, the resonator was mounted inside a continuous flow helium cryostat CF935 (Oxford Instruments) and the temperature inside the cryostat was adjusted by a temperature control system ITC 503 (Oxford Instruments).

3 cw-EPR spectra of the $1s\text{Fe}^{3+}$ center in $1\cdot\text{Im}_2$, $2\cdot\text{Im}_2$ and $1\text{T}\cdot\text{Im}_2$

The cw-EPR spectra of the $1s\text{Fe}^{3+}$ center in $1\cdot\text{Im}_2$, $2\cdot\text{Im}_2$ and $1\text{T}\cdot\text{Im}_2$ were acquired at 15 K with a microwave power of 5.529 mW (15 dB), a modulation frequency of 100 kHz, a modulation amplitude of 0.4 mT, and a time constant of 10.24 ms. The central field was set to 255.0 mT, the sweep width to 500.0 mT, the field step to 0.1 mT, and the number of averages to 4.

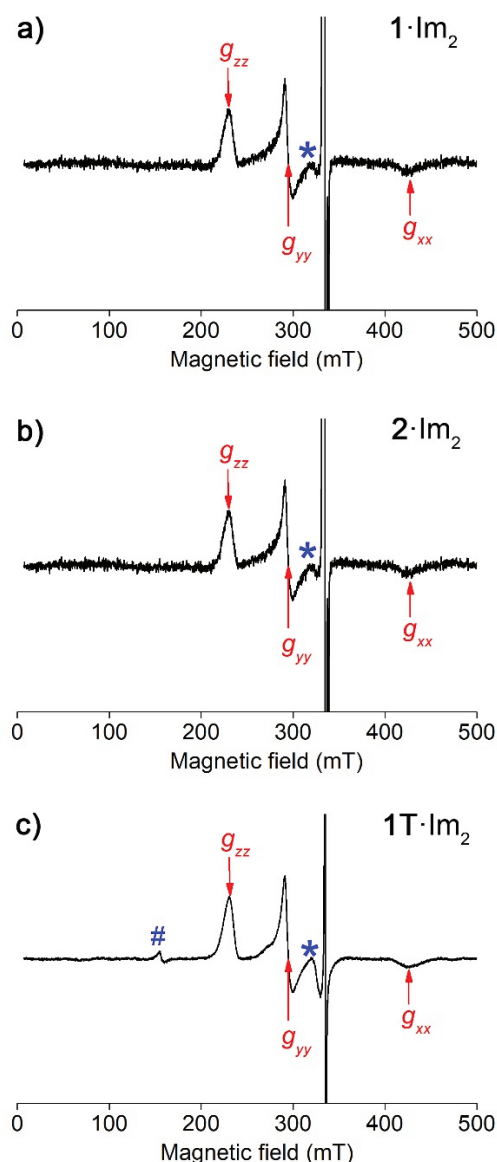


Figure S2. X-band cw-EPR spectra of a) $1\cdot\text{Im}_2^+$, b) $2\cdot\text{Im}_2^+$, and c) $1\text{T}\cdot\text{Im}_2^+$. All spectra have been recorded with a microwave frequency of 9.400 GHz at a temperature of 15 K. The spectral positions, which correspond to the principal g -values of the $1s\text{Fe}^{3+}$ ion, are marked by arrows. The values of g_{zz} and g_{yy} could be readily determined from all three spectra. In contrast, the signal corresponding to g_{xx} is fairly weak and broad. Thus, in order to determine the exact value of g_{xx} , the cw-EPR spectrum of $1\text{T}\cdot\text{Im}_2^+$ was measured with a sample concentration of 500 μM instead of 200 μM . The unsaturated signals of the organic radicals are given in Figure S3. The cavity background signal is marked by a star, and the hash symbol shows the position of the signal assigned to free Fe^{3+} ions.

4 cw-EPR spectra of the organic radicals in $1\cdot\text{Im}_2$, $2\cdot\text{Im}_2$ and $1\text{T}\cdot\text{Im}_2$

The cw-EPR spectra of the nitroxide center in $1\cdot\text{Im}_2$ and $2\cdot\text{Im}_2$ and the trityl center in $1\text{T}\cdot\text{Im}_2$ were acquired at 100 K with a microwave power of 1.937 mW (20 dB), a modulation frequency of 100 kHz, a modulation amplitude of 0.1 mT (nitroxide) or 0.01 mT (trityl), and a time constant of 10.24 ms. The microwave frequency was around 9.450 GHz. The central field was set to 336.6 mT, the sweep width to 20 mT, the field step to 0.1 mT, and the number of averages to 1.

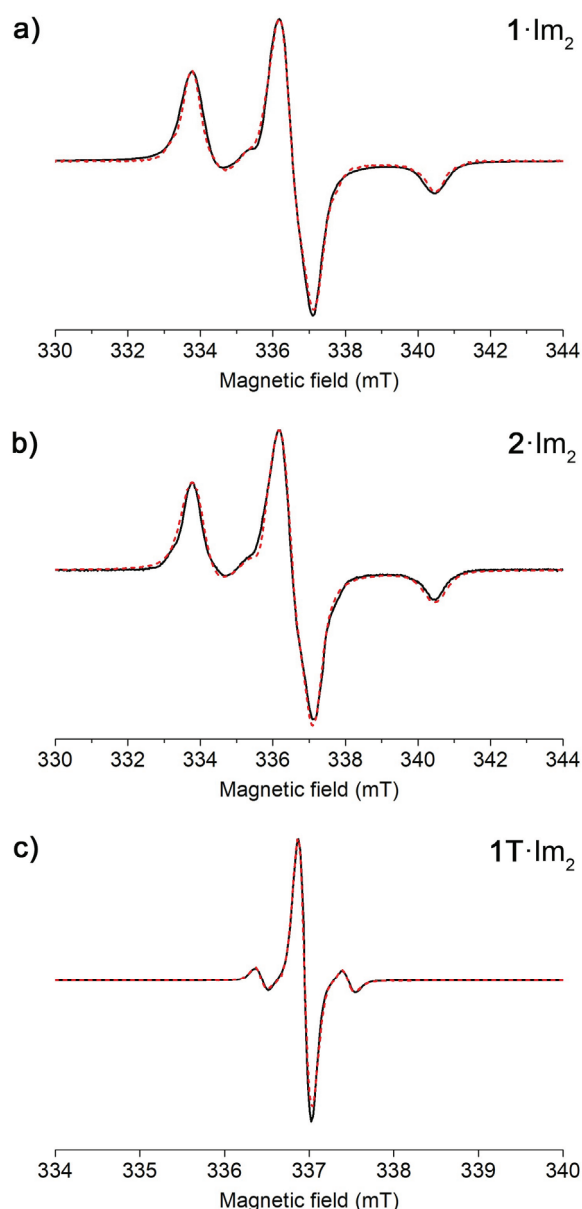


Figure S3. X-band cw-EPR spectra (black solid lines) and their simulations (red dashed lines) for **a)** the nitroxide center of $1\cdot\text{Im}_2$, **b)** the nitroxide center of $2\cdot\text{Im}_2$ and **c)** the trityl center of $1\text{T}\cdot\text{Im}_2$. All spectra have been recorded with a microwave frequency of 9.450 GHz at a temperature of 100 K. The simulations were done by means of the program EasySpin.^[1] The parameters of the simulations are listed in Table S1.

Table S1. EPR parameters of the nitroxide and trityl spin centers in **1**·Im₂, **2**·Im₂ and **1T**·Im₂.

Parameter	1 ·Im ₂	2 ·Im ₂	1T ·Im ₂
<i>g</i>	[2.0096±0.001, 2.0068±0.001, 2.0027±0.001]	[2.0096±0.001, 2.0068±0.001, 2.0027±0.001]	2.0038±0.001
<i>A</i> (¹⁴ N) / MHz	[12±6, 12±6, 94±1]	[12±6, 12±6, 94±1]	-
<i>A</i> (¹³ C) / MHz	-	-	29±1
<i>A</i> -strain ^a / MHz	[0, 0, 12]	[0, 0, 12]	-
ΔH_{pp} ^b / mT	[0.26 0.24]	[0.26 0.24]	[0.14 0.04]

^a For definition see: <http://easyspin.org/documentation/broadenings.html>^b The broadening is described by a Voigt line shape.

5 ESEEM experiments on nitroxide and trityl centers of $1\cdot\text{Im}_2$, $2\cdot\text{Im}_2$ and $1\text{T}\cdot\text{Im}_2$

Electron spin echo envelop modulation (ESEEM) measurements were carried out using the pulse sequence $\pi/2-t-\pi-t\text{-echo}$. The lengths of the $\pi/2$ - and π -pulse were 12 and 24 ns, respectively. The initial value of t was set to 300 ns and, in course of the experiment, was incremented 2048 times with a constant step of 8 ns. The short repetition time was 1 ms. To suppress unwanted echoes, 2-step phase cycling was performed. For the nitroxide-based compounds $1\cdot\text{Im}_2$ and $2\cdot\text{Im}_2$, the ESEEM time traces were recorded at three different field positions, called here as positions A, B, and C (Figure S4a). Position A corresponds to the maximum of the nitroxide spectrum and contains contributions from all three components of the ^{14}N hyperfine tensor. Note that this position was also used for the detection of the RIDME time traces. In contrast, position C is selective for the A_{zz} component of the ^{14}N hyperfine tensor. Position B represents an intermediate case between positions A and C. For the trityl-based compound $1\text{T}\cdot\text{Im}_2$, the ESEEM time traces was recorded only at the maximum of the trityl spectrum, denoted as position D in Figure S4a. For each the samples, the temperature of the ESEEM experiments was set to be the same as the temperature of the corresponding RIDME experiment.

The ESEEM time traces and spectra of all three model compounds are depicted Figure S4b. The corresponding ESEEM spectra are shown in Figure S4c. All spectra in Figure S4c display the distinct peaks at about 7.8 and 15.6 MHz. These peaks can be assigned to the single and double Larmor frequency of deuterium, which is present in a large amount in the deturated solvent. In addition to the deuterium ESEEM, the nitroxide-based model compounds $1\cdot\text{Im}_2$ and $2\cdot\text{Im}_2$ display one more peak whose frequency depends strongly on the detection position. It appears at 10.8 MHz and 9.6 MHz for the positions A and B, respectively, but it is absent in the spectrum for the position C. Such behavior suggest that this peak should originate from the ^{14}N nucleus of the nitroxide center, whose ESEEM frequency is determined by a combination of the ^{14}N Larmor frequency, the ^{14}N hyperfine coupling constant and the ^{14}N quadrupole coupling constant.^[2] Since the value of the ^{14}N hyperfine coupling constant is orientation dependent, it will yield different ESEEM frequencies for different detection positions. For the x - and y -components of the ^{14}N hyperfine tensor, which are in the order of 7-12 MHz, such combination yields an observable peak at around 10.8 MHz (positions A and B). In contrast, the z -component of the ^{14}N hyperfine tensor (~ 93 MHz) is so large that no ESEEM peak can be seen (position C). Note that this nitrogen ESEEM peak was already reported previously for the model compound $2\cdot\text{Cl}$ and also for the reference nitroxide compound.^[3]

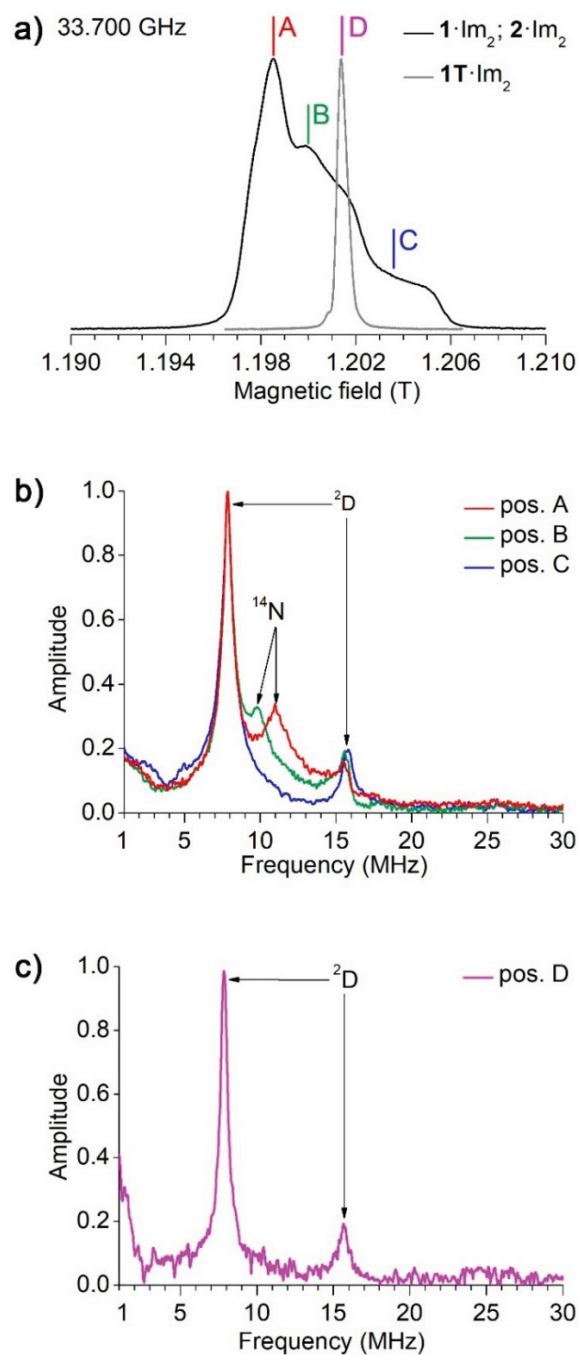


Figure S4. Q-band ESEEM experiments on the nitroxide centers of $1\cdot\text{Im}_2$ and $1\text{T}\cdot\text{Im}_2$ and the trityl center of $2\cdot\text{Im}_2$. **a)** The Q-band echo-detected EPR spectra of nitroxide (black line) and trityl (gray line) spin centers. The detection positions in the ESEEM experiments are depicted by short bars and labeled with letters A-D. **b)** The ESEEM spectra of the nitroxide spin center in $1\cdot\text{Im}_2$ and $2\cdot\text{Im}_2$. **c)** The ESEEM spectra of the trityl spin center in $1\text{T}\cdot\text{Im}_2$. The deuterium and nitrogen ESEEM peaks are marked by arrows.

6 Inversion recovery experiments on the 1s Fe³⁺ center of 1·Im₂, 2·Im₂ and 1T·Im₂

Inversion recovery measurements were carried out using the pulse sequence π - t - $\pi/2$ - τ - π - τ -*echo*. The frequency of the microwave pulses was in resonance with either the g_1 -, g_2 - or g_3 -component of the 1s Fe³⁺ spectrum. The lengths of the $\pi/2$ - and π -pulses were 12 and 24 ns, respectively. Depending on the detection position, τ was set either to 468 ns (for $g_{eff} = 2.91$), 320 ns (for $g_{eff} = 2.28$) or 304 ns (for $g_{eff} = 2.66$). The initial value of t was 500 ns, which was incremented 512 times with a step that depended on the temperature. It ranged from 200 ns at 16 K to 8 μ s at 6 K. The shot repetition time was adjusted in accordance with the t increment and ranged from 120 μ s to 4.1 ms.

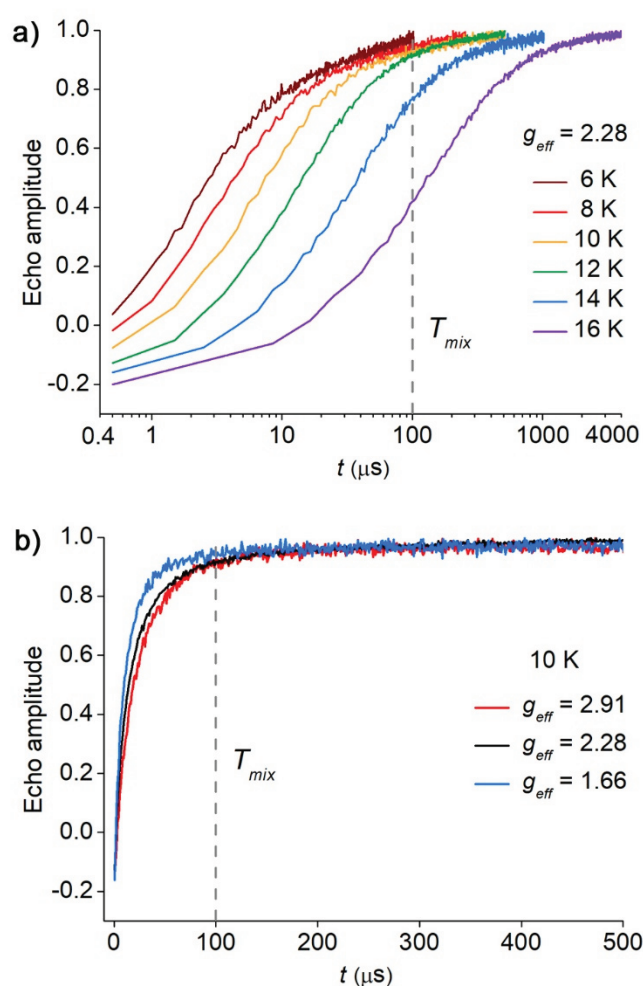


Figure S5. Inversion recovery of the 1s Fe³⁺ magnetization in 1·Im₂, 2·Im₂ and 1T·Im₂ at Q-band. **a)** The temperature dependence of the inversion recovery for the 1s Fe³⁺ centers recorded at an effective g -factor of 2.28. **b)** The dependence of the inversion recovery on the effective g -factor of the 1s Fe³⁺ at which the inversion recovery experiment was performed ($T = 10$ K). The value of T_{mix} is depicted as a dashed line.

7 RIDME experiments on 1·Im₂, 2·Im₂ and 1T·Im₂

7.1 Choosing the value of T_{mix}

The optimal way to perform a RIDME experiment on ls Fe³⁺/nitroxide and ls Fe³⁺/trityl spin pairs implies the detection of the echo signal from the slow-relaxing nitroxide or trityl spins, while the fast-relaxing Fe³⁺ spins are flipped stochastically in the interval T_{mix} . In this case, the length of T_{mix} should to be in agreement with the T_1 relaxation rate of the Fe³⁺ spins. Such an agreement can be readily obtained by performing an inversion recovery experiment on the Fe³⁺ spin centers and setting T_{mix} to a time, at which almost complete recovery of the Fe³⁺ longitudinal magnetization took place. The fact that the relaxation rate of the ls Fe³⁺ spin centers is temperature dependent makes it possible to adjust the optimal value of T_{mix} with temperature. This, in turn, can be employed to ensure that the length of T_{mix} fulfills a few additional criteria. One of such criteria is the need of T_{mix} to be significantly longer than any other inter-pulse time intervals in the RIDME pulse sequence, which helps to avoid unwanted flipping of the Fe³⁺ spins in these intervals. Moreover, T_{mix} has to be much shorter than the spin diffusion rates of the detected nitroxide or trityl spins, so that the spin diffusion does not significantly reduce the SNR of the RIDME signal. For the model compounds 1·Im₂, 2·Im₂ and 1T·Im₂, the latter two criteria are well-fulfilled for $T_{mix} = 100 \mu\text{s}$, which fits to the T_1 relaxation rate of the Fe³⁺ spins for all three model systems at a temperature of 10 K (Figure S5a). It is also worth mentioning that the ls Fe³⁺ centers of all three model compounds showed a rather weak orientation dependence of their transversal relaxation time T_1 (Figure S5b) as compared to the strong orientation dependence found for the corresponding hs Fe³⁺ center.^[3] This fact simplifies the task of choosing the optimal value of T_{mix} and ensures the same modulation depth for different orientations of the ls Fe³⁺ ions with respect to \mathbf{B}_0 .

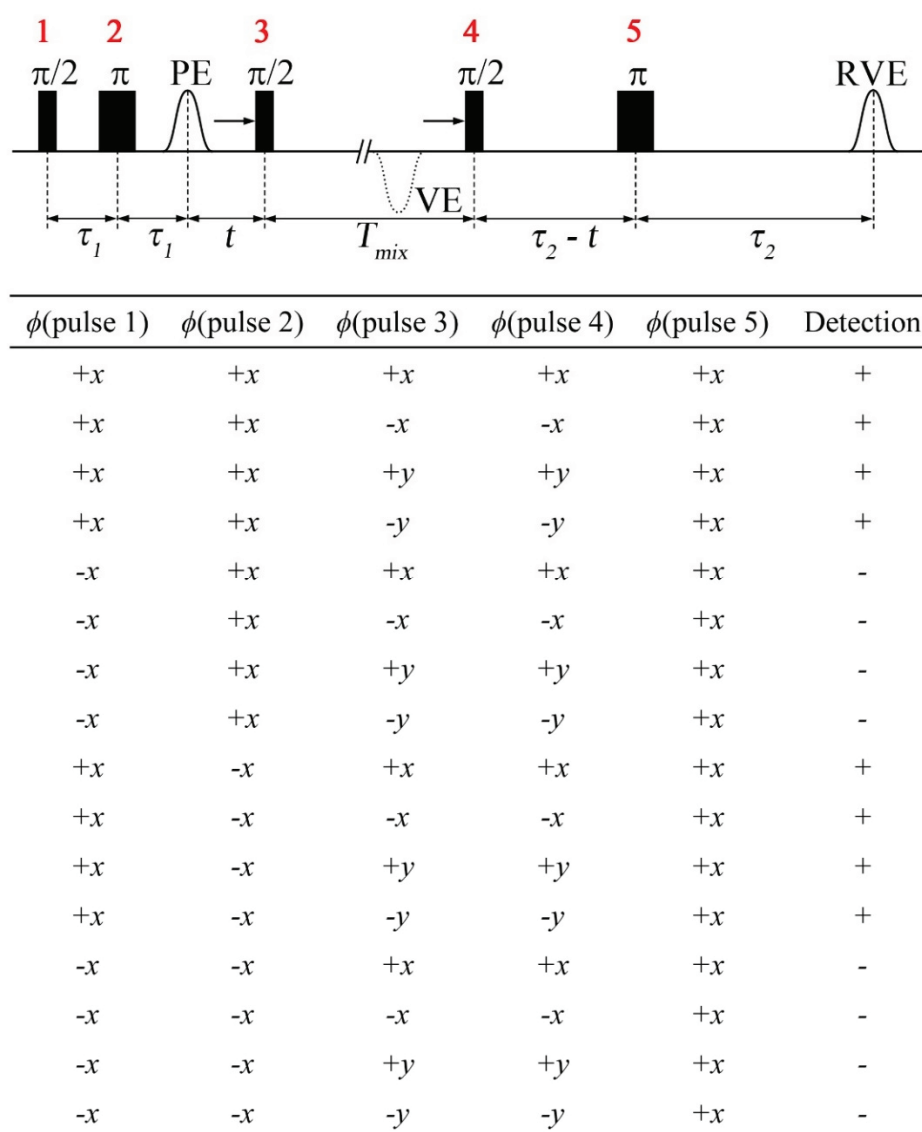
7.2 ESEEM suppression scheme

Since ESEEM penetrates into the RIDME time traces and causes unwanted artifacts in the corresponding spectra, additional steps have to be taken during the RIDME measurements to suppress them. As the deuterium ESEEM peak at 7.8 MHz is the most intense one for all three model compounds (see Figure S4), it was the main target of the ESEEM suppression in the present study. The suppression of this peak was done in accordance to the method proposed by Yulikov and co-workers.^[4] The idea behind this method is to average the RIDME time trace over one period of ESEEM modulation. To do this, the initial values of intervals τ_1 and τ_2 in the RIDME sequence were incremented consecutively 16 times with a step of 8 ns,

resulting in 256 individual RIDME time traces. The sum of these time traces yielded the averaged time trace with the ESEEM artifacts suppressed.

7.3 Phase cycling

In order to avoid an overlap of the detected reversed virtual echo with unwanted echoes, the RIDME time traces were acquired using 16-step phase cycling (Scheme S2). As compared to the usual 8-step phase cycling,^[5] in which the phases of 1st, 3rd and 4th m.w. pulses are varied, the 16-step phase cycling scheme introduces an additional phase cycle [(+x) (-x)] for the 2nd m.w. pulse. This additional phase cycle allowed more efficient suppression of the unwanted reversed virtual echo, which is created by the 1st, 2nd, 4th and 5th m.w. pulses and which interferes with the detected echo at time $t = \tau_1$.



Scheme S2. 16-step phase cycle used for 5-pulse RIDME sequence.

8 Signal-to-noise ratio of RIDME time traces

The signal-to-noise ratio (SNR) of the background-corrected RIDME time traces was determined by means of the program SnrCalculator (free available at <https://github.com/dinarabdullin/SnrCalculator>). In this program, the SNR is determined as a ratio between the modulation depth of the RIDME time trace and the standard deviation of noise.^[6] To extract the noise from the experimental RIDME time traces, first these time traces are interpolated using the Savitzky-Golay filter and then the result of interpolation is subtracted from the time traces.

Table S2. SNR of the RIDME time traces of $1 \cdot \text{Im}_2$, $2 \cdot \text{Im}_2$ and $1\text{T} \cdot \text{Im}_2$.

Parameter	$1 \cdot \text{Im}_2$	$2 \cdot \text{Im}_2$	$1\text{T} \cdot \text{Im}_2$
<i>modulation depth (%)</i>	29	40	42
<i>SNR (unitless)</i>	905	1616	3520
<i>SNR ($1 / h^{1/2}$)</i>	59	64	70
<i>SNR (dB)</i>	447	798	1739
<i>SNR (dB / $h^{1/2}$)</i>	29	31	35

9 DipFit analysis of the RIDME time traces of $1 \cdot \text{Im}_2$, $2 \cdot \text{Im}_2$ and $1\text{T} \cdot \text{Im}_2$

Due to the inversion symmetry of the magnetic tensors (spin Hamiltonian), the 180° rotation of one of the g -tensor principal axes of the $1s \text{Fe}^{3+}$ center does not influence the shape of the RIDME time trace.^[7] This leads to four symmetry-related sets of angular parameters $\langle \zeta \rangle$ and $\langle \varphi \rangle$, which provide identical RIDME time traces and thus can not be distinguished in RIDME data analysis. Tables S3, S4 and S5 list the symmetry-related sets of angular parameters for the model compounds $1 \cdot \text{Im}_2$, $2 \cdot \text{Im}_2$ and $1\text{T} \cdot \text{Im}_2$, respectively.

Table S3. Symmetry-related sets of RIDME-derived parameters of $1 \cdot \text{Im}_2$.

Transformation	Fitting parameter					
	$\langle r \rangle$ (nm)	Δr (nm)	$\langle \zeta \rangle$ ($^\circ$)	$\Delta \zeta$ ($^\circ$)	$\langle \varphi \rangle$ ($^\circ$)	$\Delta \varphi$ ($^\circ$)
Fitting result	2.48 ± 0.03	0.05 ± 0.05	69 ± 21	24 ± 24	27 ± 27	20 ± 20
180° rotation about g_{xx}			111 ± 21		333 ± 6	
180° rotation about g_{yy}			111 ± 21		153 ± 6	
180° rotation about g_{zz}			69 ± 21		207 ± 6	

Table S4. Symmetry-related sets of RIDME-derived parameters of $2 \cdot \text{Im}_2$.

Transformation	Fitting parameter					
	$\langle r \rangle$ (nm)	Δr (nm)	$\langle \zeta \rangle$ ($^\circ$)	$\Delta \zeta$ ($^\circ$)	$\langle \varphi \rangle$ ($^\circ$)	$\Delta \varphi$ ($^\circ$)
Fitting result	2.44 ± 0.02	0.05 ± 0.04	84 ± 23	23 ± 23	30 ± 30	13 ± 17
180° rotation about g_{xx}			96 ± 23		330 ± 30	
180° rotation about g_{yy}			96 ± 23		150 ± 30	
180° rotation about g_{zz}			84 ± 23		210 ± 30	

Table S5. Symmetry-related sets of RIDME-derived parameters of $1\text{T} \cdot \text{Im}_2$.

Transformation	Fitting parameter					
	$\langle r \rangle$ (nm)	Δr (nm)	$\langle \zeta \rangle$ ($^\circ$)	$\Delta \zeta$ ($^\circ$)	$\langle \varphi \rangle$ ($^\circ$)	$\Delta \varphi$ ($^\circ$)
Fitting result	2.64 ± 0.01	0.06 ± 0.02	71 ± 19	3 ± 20	57 ± 7	30 ± 9
180° rotation about g_{xx}			109 ± 19		303 ± 7	
180° rotation about g_{yy}			109 ± 19		123 ± 7	
180° rotation about g_{zz}			71 ± 19		237 ± 7	

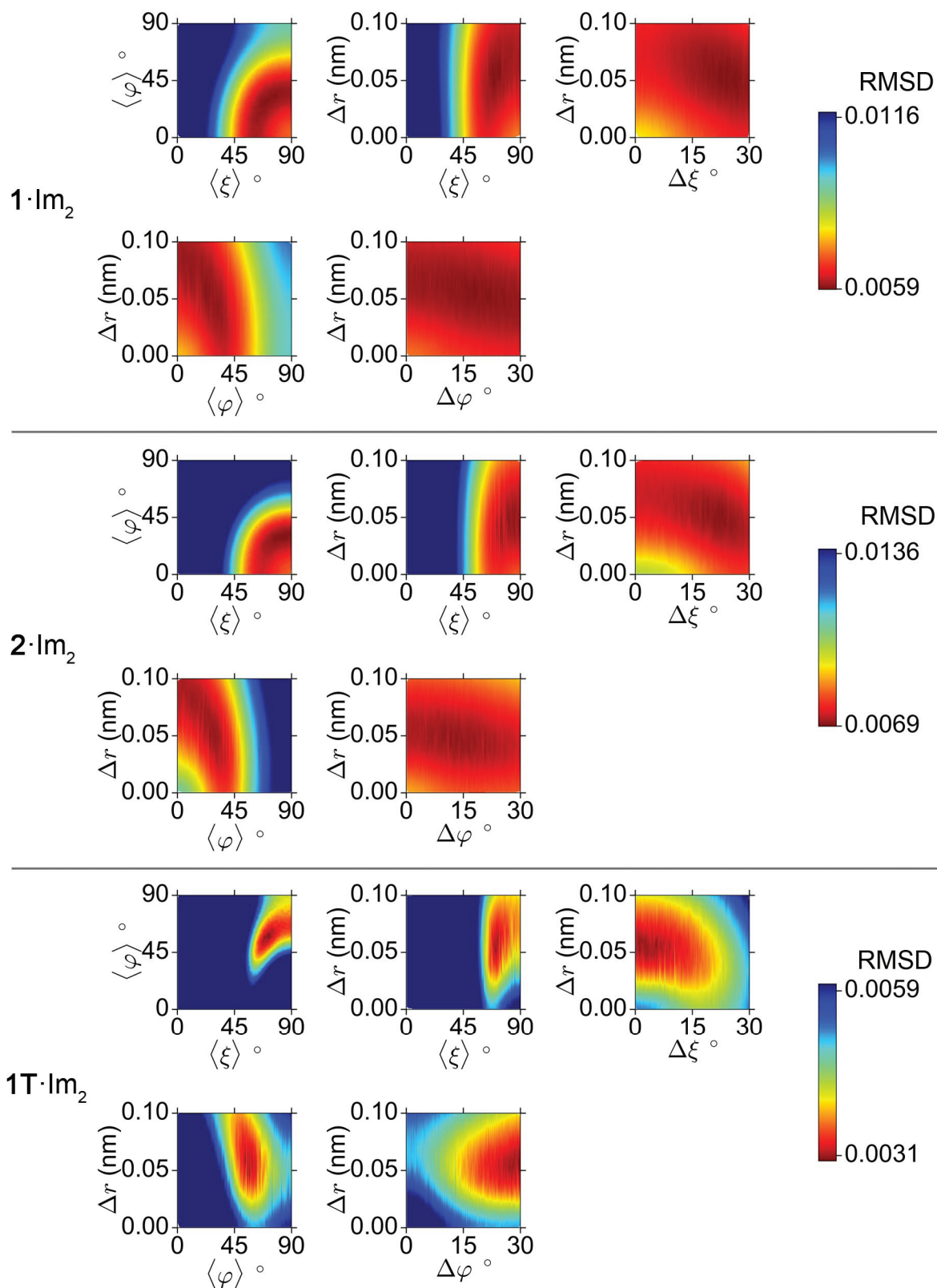


Figure S6. Dependencies of the RMSD between the experimental and simulated RIDME time traces on different pairs of fitting parameters.

10 DipFit analysis of the RIDME time trace of the P450cam mutant C58R1

The RIDME time trace of the cytochrome P450cam mutant C58R1 (Figure S7) was taken from our previous paper.^[8] This time trace was measured at the Q-band frequency on the C58R1 sample with the protonated buffer. The DipFit procedure, which was applied to fit the RIDME time trace of C58R1, was identical to the one described in the Experimental section of the main text. An important difference to the case of the model compounds was the use of other g -values for the 1s Fe^{3+} center: $g_{xx} = 1.91$, $g_{yy} = 2.25$, $g_{zz} = 2.42$.^[8] The results of the DipFit analysis are summarized in Figure S7, Figure S8 and Table S6.

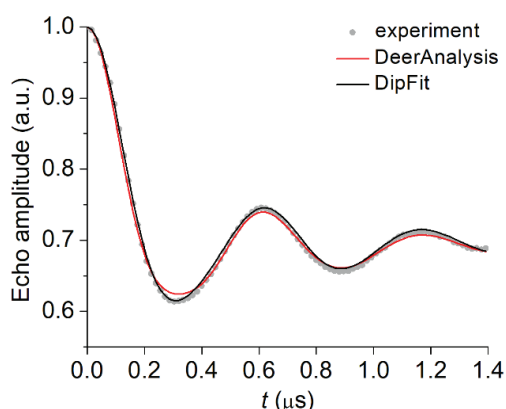


Figure S7. Background-corrected RIDME time trace (gray dots) of the P450cam mutant C58R1 is shown together with its fits obtained by means of DipFit (black line) and DeerAnalysis (red) programs.

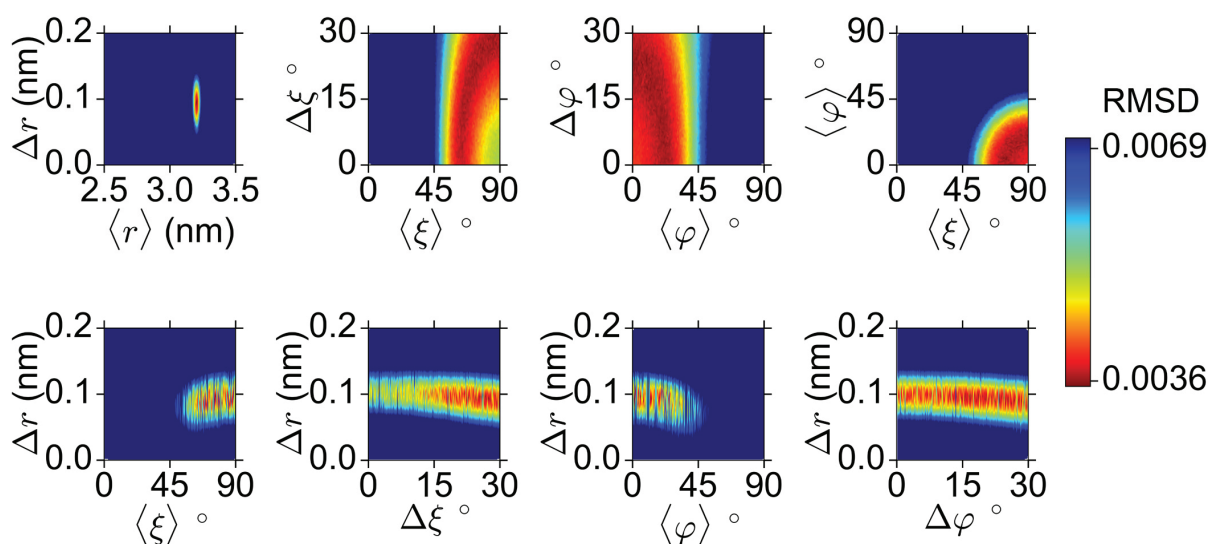


Figure S8. Dependencies of the RMSD between the experimental and simulated RIDME time traces on the mean values and standard deviations of the fitting parameters r , ξ and φ .

Table S6. RIDME-derived parameters of C58R1.

Transformation	Fitting parameter					
	$\langle r \rangle$ (nm)	Δr (nm)	$\langle \xi \rangle$ (°)	$\Delta \xi$ (°)	$\langle \varphi \rangle$ (°)	$\Delta \varphi$ (°)
Fitting result	3.20 ± 0.01	0.09 ± 0.01	77 ± 18	26 ± 26	11 ± 18	20 ± 20
180° rotation about g_{xx}			103 ± 18		349 ± 18	
180° rotation about g_{yy}			103 ± 18		169 ± 18	
180° rotation about g_{zz}			77 ± 18		191 ± 18	

11 MD simulations for 1·Im₂, 2·Im₂ and 1T·Im₂

The structure optimization and MD simulations for model compounds 1·Im₂, 2·Im₂ and 1T·Im₂ were done using the stand-alone program *xtb*.^[9] Evaluation of the MD trajectories was performed with the program TRAVIS.^[10] Owing to the bi-radical electronic structure and the large molecular size of the model compounds, the semi-empirical tight-binding method GFN2-xTB/GBSA^[11–13] was applied. The modeling began with the generation of initial structures for all three compounds, followed by the optimization of these structures at the GFN2-xTB/GBSA(THF) level of theory. Next, a conformer/rotamer ensemble (CRE) was generated for each initial structure using the search algorithm *crest*.^[14] The CRE generation was conducted using THF as a solvent, which was simulated by the implicit GBSA solvation model.^[15] For each CRE, the energetically lowest conformer was determined and later used as a starting point for molecular dynamic (MD) simulations. The MD simulations were carried out using the implicit solvent GBSA (THF) and a temperature of 298 K. The SHAKE^[16] algorithm was used to constrain all bonds. The time window was set to 1 ns, the time step to 4 fs, and the equilibration phase to 10 ps.

To enable the comparison of the MD results with the structural information from RIDME, the distributions $P(r)$, $P(\zeta)$ and $P(\varphi)$ were calculated based on the MD trajectories. The values of r were determined as the distance between the Fe atom and the center of the N-O bond of the nitroxide radical or the central C atom of the trityl radical. To determine the angular parameters ζ and φ , the orientation of the $1s$ Fe³⁺ g -tensor relative to tetraphenylporphyrin (TPP) had to be defined. Here, this orientation was set to the one reported for Fe(TPP)(4-MeIm)₂⁺.^[17] Thus, the g_{zz} -axis of $1s$ Fe³⁺ was orthogonal to the TPP plane and aligned with the Fe-N(imidazole) bond. The corresponding g_{xx} - and g_{yy} -axes were aligned with two orthogonal Fe-N(porphyrin) bonds within the TPP plane. Based on this definition of the g -axes, ζ was determined as the angle between the g_{zz} -axis of $1s$ Fe³⁺ and the inter-spin vector \mathbf{r} . The angle between the g_{xx} -axis and the projection of \mathbf{r} on the TPP plane yielded the value of φ . The resulting MD distributions of r , ζ and φ are summarized in Figure S9. Increasing the MD time window from 500 ps to 1 ns did not lead to any significant change in the predicted distributions (Figure S9), suggesting that the system may be regarded as equilibrated. To allow direct comparison to the RIDME results, the calculated distributions were approximated by Gaussians (Figure S10) and the mean values and their standard deviation were calculated for each distribution (Table 1 in the main text).

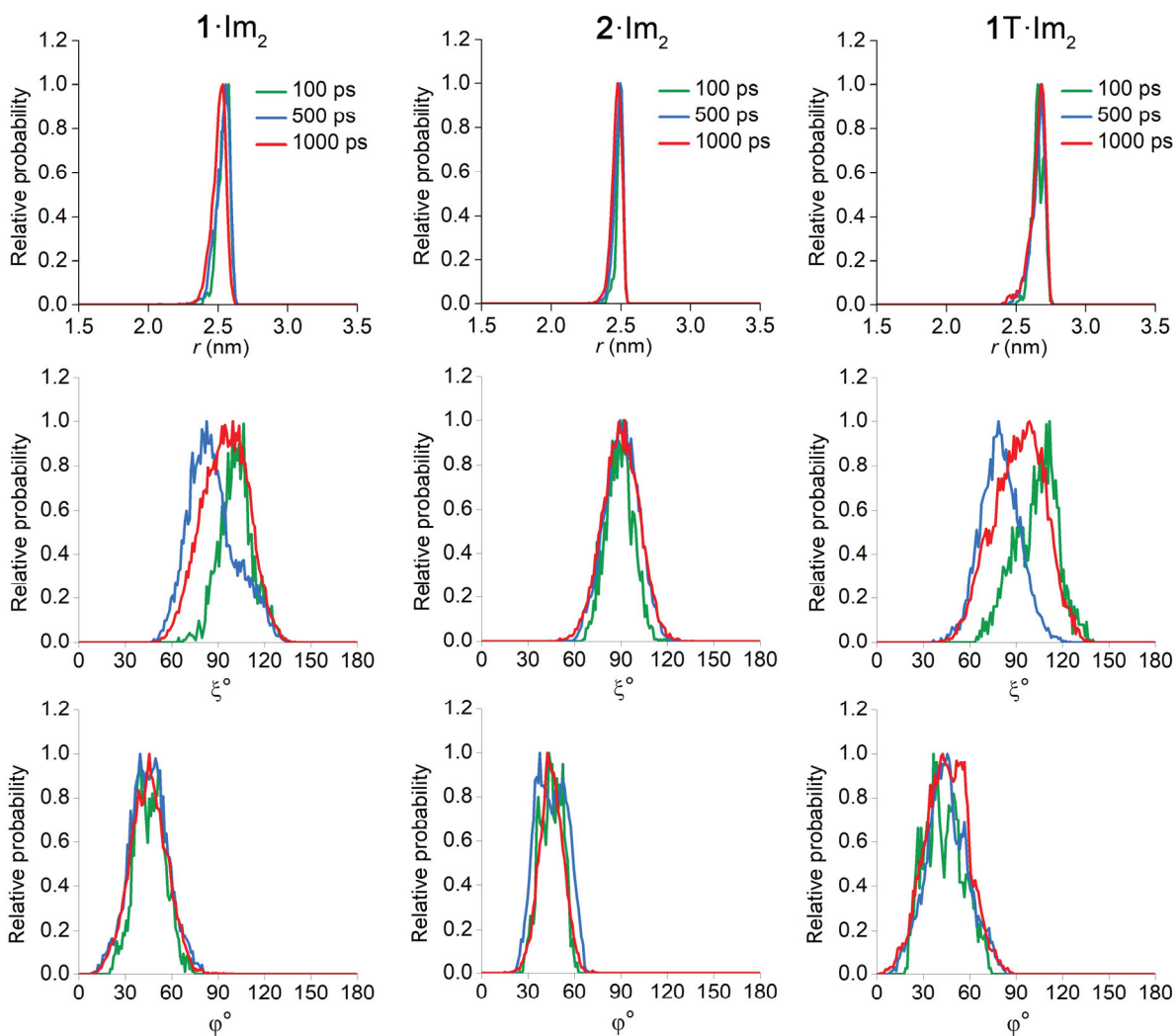


Figure S9. The MD predictions of the distributions $P(r)$, $P(\xi)$ and $P(\varphi)$ for the MD time window of 100 ps (green), 500 ns (blue) and 1 ns (red).

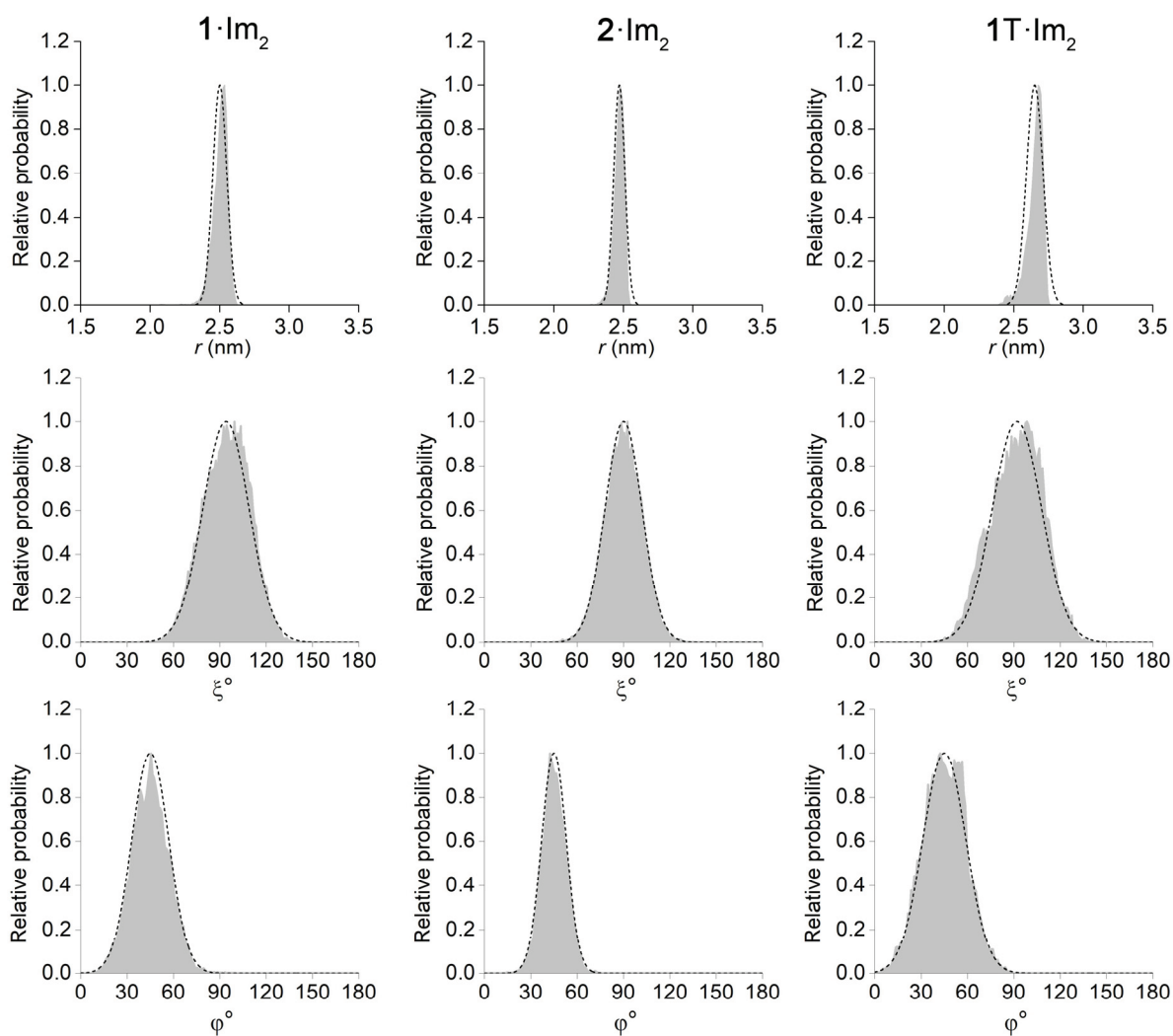


Figure S10. The MD predictions (gray shades) of the distributions $P(r)$, $P(\xi)$ and $P(\varphi)$ in the model compounds $1 \cdot \text{Im}_2$, $2 \cdot \text{Im}_2$ and $1\text{T} \cdot \text{Im}_2$. The fits of all distributions by Gaussians is depicted by black dashed lines. The parameter of the Gaussians are listed in Table 1 of the main text.

12 Optimized structure of 1·Im₂

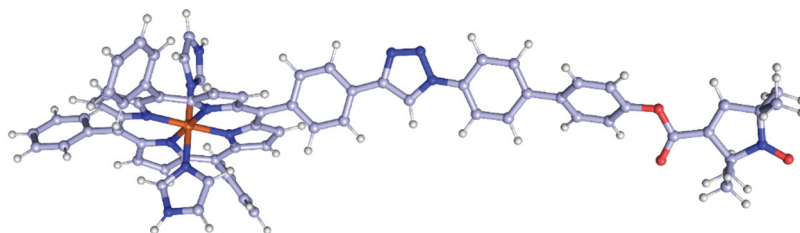


Figure S11. The ball-and-stick model of the optimized structure of 1·Im₂. Atom colors: hydrogen – gray, carbon – light blue, nitrogen – blue, oxygen – red, iron – orange.

Coordinates:

C	9.0412882095	-0.8778968290	-0.1546458267
C	9.5851035568	0.4043541572	-0.1215458661
C	8.8160102991	1.5671492657	-0.1687173700
N	7.4584552954	1.6345565673	-0.0965809828
C	7.1353038864	2.9559563739	-0.1785624841
C	5.8583194149	3.4919363046	-0.0244253908
C	4.7189510263	2.7159933598	0.1868361936
N	4.6481786189	1.3586447814	0.1193023457
C	3.3554995585	1.0275909332	0.3930123602
C	2.8100600854	-0.2526456844	0.3158935406
C	3.5527460983	-1.3851647321	-0.0181322707
N	4.9042196801	-1.4460702394	-0.1587191226
C	5.1986726153	-2.7366666636	-0.4802283406
C	6.4783611164	-3.2769313772	-0.5855594003
C	7.6442758350	-2.5301211683	-0.4182263177
N	7.7188797745	-1.1777177820	-0.2883794346
FE	6.1813507496	0.0907602425	-0.1061408889
N	6.0555490604	0.2497481110	-2.1110751481
C	7.0506345306	0.3891225780	-2.9570363959
N	6.5952643534	0.4810078446	-4.2193391655
C	5.2353953507	0.3947141664	-4.1715213680
C	4.9143818760	0.2511343900	-2.8549997842
H	3.9524146616	0.1477067382	-2.3973846785
H	4.6239844678	0.4397706439	-5.0483561375
H	7.1528999275	0.5949593165	-5.0508237850
H	8.0859565888	0.4285978062	-2.6852103316
N	6.3088035698	-0.0578723290	1.8994952513
C	6.2890590492	0.9263077736	2.7691925393
N	6.3789843632	0.4552210292	4.0258365419
C	6.4608263753	-0.9035530910	3.9491534671
C	6.4162383779	-1.2079930122	2.6217179399

H	6.4559958993	-2.1642526361	2.1427061021
H	6.5421798566	-1.5261114306	4.8154344492
H	6.3827088073	1.0022145193	4.8720642432
H	6.2089281454	1.9647075442	2.5188254410
C	8.9541393097	-3.1084234256	-0.3170686677
C	9.8199268986	-2.0838330344	-0.1381640659
H	10.8818091948	-2.1318155365	0.0008981965
H	9.1688239091	-4.1582755642	-0.3533854100
C	6.6168443564	-4.7270048065	-0.8317650680
C	6.0994988025	-5.6567997579	0.0657408493
C	6.2405682276	-7.0121965250	-0.1703893567
C	6.8947211879	-7.4567434717	-1.3071926747
C	7.4130900367	-6.5386457315	-2.2053574894
C	7.2797712438	-5.1829639512	-1.9678324545
H	7.6804150813	-4.4648643583	-2.6690078327
H	7.9239473859	-6.8803520668	-3.0933429680
H	7.0019805907	-8.5148458643	-1.4916445975
H	5.8395753870	-7.7239399734	0.5358248543
H	5.5974296063	-5.3107296000	0.9578945874
C	3.9893218915	-3.4994418303	-0.6101344041
C	2.9685112164	-2.6643314927	-0.3079402623
H	1.9178542789	-2.8780237938	-0.3024276818
H	3.9371329726	-4.5302816851	-0.8996947247
C	1.3650555261	-0.4256259206	0.5588930039
C	0.4172079654	0.2269830035	-0.2256291849
C	-0.9322894022	0.0507086785	0.0057873642
C	-1.3678151930	-0.7805807239	1.0361553659
C	-0.4198461284	-1.4341601408	1.8238884402
C	0.9263894271	-1.2626735923	1.5837924107
H	1.6562288183	-1.7690805727	2.1987630618
H	-0.7664004164	-2.0745682910	2.6196531211
C	-2.7766851291	-0.9880060210	1.3083620787
C	-3.9065009401	-0.4936656147	0.6812327405
N	-4.9459069043	-1.0319031670	1.3669519753
N	-4.4702399908	-1.8054764061	2.3515884361
N	-3.2031203544	-1.7851231207	2.3249425261
C	-6.3221194888	-0.8830672682	1.1711211875
C	-6.8363470384	-0.0292816803	0.2011424867
C	-8.2035384282	0.0847530995	0.0438719069
C	-9.0824969517	-0.6476343279	0.8389170401
C	-8.5520282251	-1.4989336844	1.8081729000
C	-7.1892824828	-1.6158662373	1.9779327145
H	-6.7709022481	-2.2662865009	2.7290960890
H	-9.2164853029	-2.0582265423	2.4487805101

C	-10.5355326174	-0.5267684622	0.6590203936
C	-11.3545577336	-1.6535826024	0.7207087860
C	-12.7179712832	-1.5444920845	0.5423557261
C	-13.2859462015	-0.2983037019	0.3063369708
C	-12.4909071839	0.8369207579	0.2564850899
C	-11.1247579932	0.7133988792	0.4263027389
H	-10.5104533336	1.6005597263	0.4018808858
H	-12.9302524684	1.8061592157	0.0857112736
O	-14.6722363491	-0.2652942162	0.1861566843
C	-15.2797061980	0.5525331782	-0.6823690670
O	-14.7262271141	1.2948327854	-1.4525973776
C	-16.7489591048	0.4083753088	-0.5868166725
C	-17.4349928519	-0.3588852169	0.2600692532
C	-18.9100997891	-0.2354975186	0.0479248850
N	-18.9750676337	0.7217066880	-1.0512010976
O	-20.0419028528	1.1098774448	-1.5479073532
C	-17.6665712395	1.1745085217	-1.5033604311
C	-17.4790273816	0.8021950949	-2.9770222675
H	-16.5089374216	1.1544341398	-3.3145592737
H	-18.2621355216	1.2687078023	-3.5693907826
H	-17.5301549720	-0.2765295928	-3.1092453610
C	-17.5605615124	2.6910547403	-1.3164033388
H	-16.5897857336	3.0274214492	-1.6676727893
H	-18.3445705136	3.1804902295	-1.8887141602
H	-17.6701437301	2.9564118094	-0.2669298546
C	-19.6411609356	0.3436137597	1.2645571710
H	-19.6480984665	-0.3794371327	2.0747270620
H	-20.6657673013	0.5791182286	0.9869255415
H	-19.1518199631	1.2524131993	1.6074230001
C	-19.5591931565	-1.5527508528	-0.3923789841
H	-19.5699618770	-2.2578256568	0.4334570233
H	-20.5809335847	-1.3587562809	-0.7099039290
H	-19.0097629890	-1.9904036372	-1.2227591887
H	-17.0202963369	-1.0003546802	1.0157887607
H	-13.3551932060	-2.4140763182	0.5800842009
H	-10.9161131763	-2.6260648933	0.8847726388
H	-8.5946537993	0.7359069516	-0.7231187689
H	-6.1816429404	0.5477601781	-0.4327629029
H	-4.0278373783	0.1566732486	-0.1569461666
H	-1.6506931530	0.5603509943	-0.6186720652
H	0.7461386332	0.8643735091	-1.0340512381
C	2.6006985584	2.2082797455	0.7028490158
C	3.4430835989	3.2579056484	0.5589246497
H	3.2362796801	4.2989957665	0.7115688212

H	1.5700186618	2.2233944117	0.9973652210
C	5.7006178092	4.9607351069	-0.0350765175
C	4.8848656559	5.5679343911	-0.9860274526
C	4.7320204696	6.9420774401	-1.0045333961
C	5.3840633512	7.7277957262	-0.0686413310
C	6.1916325504	7.1321024766	0.8856831083
C	6.3514538440	5.7584250152	0.9018637820
H	6.9755468572	5.2941770261	1.6523270399
H	6.6983092675	7.7397399267	1.6207270611
H	5.2622783652	8.8002149312	-0.0820072158
H	4.1017094627	7.4019117536	-1.7512095749
H	4.3803514354	4.9530786080	-1.7175230558
C	8.3212579603	3.7413174674	-0.3683618941
C	9.3658638596	2.8805921372	-0.3470283050
H	10.4085508231	3.1019533494	-0.4636255929
H	8.3433265371	4.8042424684	-0.5063875328
C	11.0548419084	0.5499315636	-0.0869165964
C	11.8492826416	0.0363483653	-1.1081645975
C	13.2238794878	0.1835543748	-1.0692682855
C	13.8238655737	0.8408976654	-0.0082956266
C	13.0415342919	1.3555930188	1.0121727935
C	11.6664920297	1.2156990761	0.9717896904
H	11.0545794919	1.6127560781	1.7689903586
H	13.5046998399	1.8682960327	1.8420898188
H	14.8969650137	0.9527616796	0.0224528860
H	13.8289135127	-0.2154095531	-1.8698808688
H	11.3817516254	-0.4700092709	-1.9408053851

13 Optimized structure of 2·Im₂

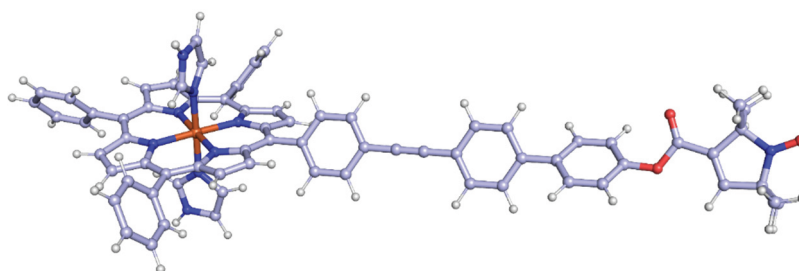


Figure S12. The ball-and-stick model of the optimized structure of 2·Im₂. Atom colors: hydrogen – gray, carbon – light blue, nitrogen – blue, oxygen – red, iron – orange.

Coordinates:

FE	-5.8420560134	0.0182963455	-0.0086127061
N	-7.2095393603	1.4809277763	0.0795054969
C	-6.9708929417	2.8196648127	0.0244272326
C	-5.7485112222	3.4247128430	-0.2649750324
C	-4.5529681224	2.7208069541	-0.3919611763
N	-4.3887857264	1.3841364559	-0.1881513208
C	-3.0534793205	1.1430129179	-0.2869834271
C	-2.4272569549	-0.0926537023	-0.1248091988
C	-3.1210207918	-1.2933846136	0.0176818952
N	-4.4729007999	-1.4449048011	-0.0487316078
C	-4.7119055886	-2.7834819641	0.0144272555
C	-5.9615154321	-3.3992933239	-0.0446817054
C	-7.1661176550	-2.6989800228	-0.0252732861
N	-7.3018652396	-1.3512837034	0.1235161531
C	-8.6384787717	-1.1092021979	0.2148648761
C	-9.2368020680	0.1370406813	0.3989542387
C	-8.5343655593	1.3397601557	0.3640898243
C	-9.1372173159	2.6286319796	0.5544103854
C	-8.1690013216	3.5476369204	0.3327643459
H	-8.2436220658	4.6155866418	0.3918007320
H	-10.1591183212	2.7977131962	0.8308861688
C	-10.6997883818	0.1797742878	0.6003709956
C	-11.5236749429	0.8544952639	-0.2962719782
C	-12.8930138781	0.8846070492	-0.1049768712
C	-13.4574806096	0.2462489481	0.9866465522
C	-12.6456952286	-0.4267382294	1.8846244197
C	-11.2769973311	-0.4639907691	1.6914452181
H	-10.6415295334	-0.9842834444	2.3936443404
H	-13.0809131513	-0.9246204432	2.7383461276
H	-14.5260426391	0.2725926380	1.1365505679

H	-13.5218008602	1.4075434320	-0.8102223314
H	-11.0850186115	1.3475667703	-1.1523300376
C	-9.3722515837	-2.3339173052	0.0699052782
C	-8.4583893767	-3.3195760466	-0.0900980963
H	-8.6344982522	-4.3653658024	-0.2472064321
H	-10.4413545983	-2.4161612962	0.0701427815
C	-6.0041239670	-4.8752231358	-0.0932356014
C	-5.4077910934	-5.5585049138	-1.1495783626
C	-5.4450867001	-6.9397807125	-1.2016053514
C	-6.0705950812	-7.6578475084	-0.1958708087
C	-6.6611941393	-6.9871101733	0.8619959117
C	-6.6310406966	-5.6053660791	0.9126402210
H	-7.0864183901	-5.0833917689	1.7424354390
H	-7.1466731054	-7.5423669498	1.6508245926
H	-6.0970460419	-8.7361663987	-0.2358067243
H	-4.9843511490	-7.4581560919	-2.0293735107
H	-4.9245887164	-4.9960700846	-1.9355556808
C	-3.4775225554	-3.4972217104	0.1780070315
C	-2.4906950130	-2.5710709227	0.1914022981
H	-1.4378438555	-2.7300561190	0.3168003548
H	-3.3894801056	-4.5601607912	0.2886003492
C	-0.9526100963	-0.1278826092	-0.1472967968
C	-0.2180698247	0.5947573375	0.7920087984
C	1.1602398344	0.5712902277	0.7792315994
C	1.8421282113	-0.1723711789	-0.1875978355
C	1.1094509570	-0.8927332226	-1.1342809411
C	-0.2690382491	-0.8710863872	-1.1085046621
H	-0.8304697875	-1.4219934002	-1.8496305963
H	1.6331124825	-1.4639830352	-1.8866245854
C	3.2510553973	-0.1914822416	-0.2084188834
C	4.4592581066	-0.2038895753	-0.2249476001
C	5.8682962351	-0.2148187155	-0.2408118002
C	6.5609143605	-0.9339367030	-1.2179626149
C	7.9392852392	-0.9428335701	-1.2260382168
C	8.6650636243	-0.2322215576	-0.2697068021
C	7.9680882401	0.4870508224	0.7016406563
C	6.5900674548	0.4953350925	0.7219077891
H	6.0575788394	1.0483180427	1.4818070233
H	8.5167558667	1.0244095601	1.4610232734
C	10.1335244374	-0.2399488295	-0.2828862273
C	10.8532092982	0.9239280189	-0.0219524316
C	12.2350551972	0.9286287740	-0.0285940349
C	12.9158929657	-0.2509526323	-0.2888730938
C	12.2180442164	-1.4216533054	-0.5576751751

C	10.8384895702	-1.4114058434	-0.5572937453
H	10.3008694974	-2.3280393551	-0.7471094828
H	12.7677400288	-2.3276932806	-0.7598581767
O	14.3062707189	-0.3262993122	-0.3541219720
C	15.0761967921	0.3279662596	0.5220508189
O	14.6816786667	0.9913725649	1.4467958218
C	16.5082679744	0.1119877362	0.2160249275
C	17.0260200449	-0.5673831459	-0.8069095730
C	18.5211985566	-0.5600572809	-0.7757464804
N	18.7916563155	0.2264932627	0.4228911363
O	19.9363548924	0.4764066837	0.8229899339
C	17.5858069443	0.6868587558	1.0974707253
C	17.5736258779	2.2182184163	1.1279700179
H	18.4557553308	2.5757676012	1.6531403083
H	17.5749663679	2.6218428312	0.1175671973
H	16.6805070567	2.5574904295	1.6439399899
C	17.5506729271	0.1229012135	2.5209442538
H	17.5375925490	-0.9648634977	2.5020139589
H	16.6565404319	0.4786735726	3.0240264592
H	18.4313021251	0.4569550475	3.0637877036
C	19.1200884330	-1.9607082278	-0.6039809037
H	20.1846843623	-1.8719411506	-0.4009875714
H	18.6456407080	-2.4797393596	0.2257563100
H	18.9768807578	-2.5412263818	-1.5104766355
C	19.1393542235	0.1439272141	-1.9892163902
H	18.6791669372	1.1175842175	-2.1414411081
H	18.9950091183	-0.4567883390	-2.8822816455
H	20.2045862285	0.2808640984	-1.8190086473
H	16.4749843999	-1.0709614467	-1.5797337498
H	12.7756358390	1.8403182961	0.1678544092
H	10.3258698732	1.8466892819	0.1666990177
H	8.4649895574	-1.4875044476	-1.9965764239
H	6.0060989160	-1.4800831865	-1.9668082833
H	1.7236322757	1.1273434168	1.5140439883
H	-0.7426637168	1.1675449982	1.5432817194
C	-2.3566017156	2.3547000029	-0.6152492790
C	-3.2889047346	3.3323681415	-0.6902273562
H	-3.1451629006	4.3666204676	-0.9330803846
H	-1.3011054336	2.4335945912	-0.7867819054
C	-5.7190165587	4.8955355978	-0.4005138690
C	-4.9527269074	5.6749756756	0.4615146713
C	-4.9356649225	7.0518912477	0.3332233701
C	-5.6782522365	7.6679269402	-0.6602270021
C	-6.4429563823	6.9002402153	-1.5228728531

C	-6.4673815501	5.5238673796	-1.3919988512
H	-7.0600026210	4.9228402453	-2.0667610613
H	-7.0229477764	7.3759022895	-2.2997749693
H	-5.6623111924	8.7425042292	-0.7609339054
H	-4.3417288252	7.6463427476	1.0115046019
H	-4.3797903951	5.1954576533	1.2423884933
N	-6.0127000091	-0.0446579011	-2.0184277761
C	-7.1235115419	-0.0036368105	-2.7183964952
N	-6.8619837732	-0.0875539763	-4.0350530974
C	-5.5098085050	-0.1869594736	-4.1786988494
C	-4.9953076651	-0.1588534681	-2.9172238044
H	-3.9748218177	-0.2101501333	-2.5988126095
H	-5.0359539029	-0.2663700683	-5.1346493641
H	-7.5383781590	-0.0809625358	-4.7818967981
H	-8.1074023399	0.0811711251	-2.3035119892
N	-5.6820216997	0.0680292967	2.0027418885
C	-5.7007076122	-0.9581986072	2.8224997847
N	-5.5749192797	-0.5525967673	4.0987586556
C	-5.4710671918	0.8068730496	4.0882640315
C	-5.5391034146	1.1784407519	2.7790160956
H	-5.4980831718	2.1572065309	2.3479587361
H	-5.3616817265	1.3836382866	4.9827163098
H	-5.5588620866	-1.1417500836	4.9160467527
H	-5.7986690576	-1.9816800354	2.5220351742

14 Optimized structure of 1T·Im₂

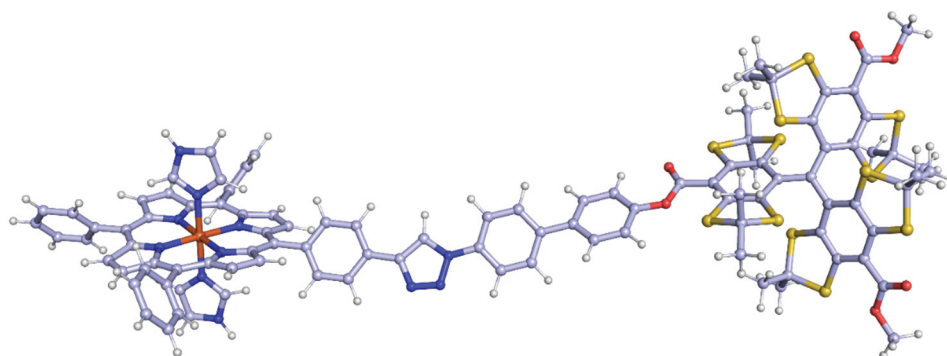


Figure S13. The ball-and-stick model of the optimized structure of 1T·Im₂. Atom colors: hydrogen – gray, carbon – light blue, nitrogen – blue, oxygen – red, sulfur – yellow, iron – orange.

Coordinates:

C	14.3038601483	2.3811080705	1.4740992920
C	15.6033025601	2.7822573594	1.7752286665
C	16.7369179409	2.0584543188	1.4123727564
N	16.7493877655	0.8275802088	0.8318015107
C	18.0591070946	0.4671527543	0.7278975246
C	18.5363959451	-0.7564629708	0.2594286080
C	17.7164418801	-1.7506299888	-0.2742789991
N	16.3810752430	-1.6407060108	-0.5194948503
C	16.0017791608	-2.8110067963	-1.1017966581
C	14.7322682370	-3.1084398974	-1.5916776269
C	13.6338291295	-2.2635400039	-1.4497145144
N	13.5979856420	-1.1088231255	-0.7302930472
C	12.3181477100	-0.6488981776	-0.8079574790
C	11.8113522042	0.4750895926	-0.1551004925
C	12.5966203233	1.3478295301	0.5985878821
N	13.9535845401	1.3105047665	0.7097230946
FE	15.1705590874	-0.1524731694	0.0721126127
N	14.9054617513	-1.1205560458	1.8295562862
C	15.8379238531	-1.6405839284	2.5946712154
N	15.2970944384	-2.2181018073	3.6825562646
C	13.9456564222	-2.0548931678	3.6035426546
C	13.7172496629	-1.3712715526	2.4471874046
H	12.7902048868	-1.0445644972	2.0240049902
H	13.2758817343	-2.4247531628	4.3514153562
H	15.7953323548	-2.6880215379	4.4215579644
H	16.8881931181	-1.6159621640	2.3857464174
N	15.4347073594	0.8122150212	-1.6895622710
C	14.5161464268	1.4229204124	-2.4030124532

N	15.0489163819	1.9466668698	-3.5214818807
C	16.3802764464	1.6524338133	-3.5176214310
C	16.6053247683	0.9474485634	-2.3735253171
H	17.5196103939	0.5359257477	-1.9995532029
H	17.0406372472	1.9579344674	-4.3020014672
H	14.5574564564	2.4613525640	-4.2347985080
H	13.4805566202	1.4953567408	-2.1391712476
C	12.0686744637	2.4417188497	1.3636609741
C	13.1288798257	3.0821184054	1.9084118623
H	13.1242659852	3.9376852831	2.5544567575
H	11.0272522433	2.6700087926	1.4778045504
C	10.3682554564	0.7614870504	-0.2723156292
C	9.4190803622	-0.1643950133	0.1544156732
C	8.0699421045	0.1028529262	0.0389465947
C	7.6345761907	1.3052743382	-0.5153329564
C	8.5829696970	2.2347787687	-0.9421648952
C	9.9292438005	1.9667279970	-0.8181720597
H	10.6569242249	2.6909738780	-1.1560748066
H	8.2370298896	3.1624845390	-1.3702029779
C	6.2257197995	1.6137715310	-0.6622756759
C	5.0972165964	0.8823123952	-0.3367352208
N	4.0569571314	1.6694946125	-0.7071118398
N	4.5294706027	2.8098891957	-1.2255463224
N	5.7972911668	2.7865594051	-1.2017571576
C	2.6817200020	1.4330047657	-0.6179585503
C	2.1714062960	0.3470255102	0.0850703293
C	0.8063319903	0.1472367889	0.1402368646
C	-0.0752754115	1.0228259757	-0.4905123941
C	0.4516495986	2.1138230520	-1.1819504424
C	1.8129508669	2.3183603084	-1.2507570699
H	2.2285173920	3.1552999084	-1.7886725707
H	-0.2136752556	2.7941557393	-1.6910589225
C	-1.5258350292	0.8011986410	-0.4308230629
C	-2.0563359226	-0.4806074927	-0.5438631332
C	-3.4203899778	-0.7049450044	-0.5012509153
C	-4.2784478125	0.3729145026	-0.3356911813
C	-3.7656265502	1.6626786359	-0.2145635951
C	-2.4050059818	1.8718753828	-0.2652184386
H	-2.0158045124	2.8724367673	-0.1535330232
H	-4.4553517570	2.4805999262	-0.0791963861
O	-5.6585266376	0.3000630581	-0.2732730959
C	-6.3859904746	-0.8136717774	-0.3857170573
O	-5.9597248941	-1.9326781378	-0.5961057971
C	-7.8163750055	-0.5543118244	-0.2445851953

C	-8.3618729570	0.6717068235	0.1507204754
C	-9.7402558083	0.8287364014	0.2221421634
C	-10.6128971543	-0.2539058518	-0.0041937953
C	-10.0485523865	-1.4921032107	-0.3616301303
C	-8.6736277477	-1.6257637736	-0.5237945770
S	-8.0483458901	-3.1543527446	-1.0522074634
C	-9.6946391032	-3.8086677612	-1.6244082315
C	-9.7718951592	-5.2948649515	-1.3367243219
H	-9.6436657240	-5.4859914718	-0.2737211958
H	-8.9836468384	-5.8126028871	-1.8787062334
H	-10.7347678986	-5.6931125185	-1.6509818499
C	-9.8634112317	-3.4865685910	-3.0984053434
H	-9.0573858363	-3.9433093707	-3.6690804656
H	-10.8154747012	-3.8694769235	-3.4621215573
H	-9.8385070536	-2.4095358349	-3.2588001694
S	-11.0006707450	-2.9258680643	-0.6706066190
C	-12.0348203265	-0.0917300915	0.1301374966
C	-12.6673544957	1.0831187035	-0.3858082637
C	-13.7188082371	1.7116771091	0.3163736825
C	-14.3345100801	2.8514969840	-0.1946900466
C	-13.8905870797	3.4208501594	-1.3927522791
C	-12.8397241981	2.8206429873	-2.0959570268
C	-12.2548743031	1.6592410707	-1.6091353435
S	-11.1085559521	0.8723823479	-2.6765862653
C	-10.7330358933	2.3774308647	-3.6692201103
C	-9.5775540228	3.1151771725	-3.0166512291
H	-9.8294778574	3.3807508841	-1.9911321149
H	-9.3613316148	4.0266970960	-3.5702324586
H	-8.6886748633	2.4862291110	-3.0054394321
C	-10.4457781149	1.9862871913	-5.1050233101
H	-10.2587285415	2.8780229880	-5.6992620401
H	-9.5688445496	1.3434680686	-5.1495802199
H	-11.2927657809	1.4541393931	-5.5315592481
S	-12.2448456812	3.4509068138	-3.6057002558
C	-14.5749611899	4.6350059433	-1.8245619698
O	-15.4259135597	5.1751993462	-1.1448423174
O	-14.1855728340	5.0806412939	-3.0179199581
C	-14.8151269476	6.2652993475	-3.4855415609
H	-15.8931132553	6.1125371005	-3.5662389738
H	-14.3815758476	6.4709350418	-4.4605155527
H	-14.6263184955	7.0907694952	-2.7963918220
S	-15.6228254479	3.5752916649	0.7070903562
C	-15.7835833674	2.1755135254	1.9280948651
C	-16.0311139075	2.7404451485	3.3124491867

H	-15.2088050083	3.3854685674	3.6127415510
H	-16.9479170756	3.3257233082	3.3087620033
H	-16.1296771823	1.9358634101	4.0385765414
C	-16.8955230228	1.2513871700	1.4626293740
H	-17.8346825415	1.7991580591	1.4233264264
H	-16.6745138681	0.8670247621	0.4682485730
H	-17.0024806539	0.4109660374	2.1466195407
S	-14.2038444509	1.2275756373	1.9173677698
C	-12.8012986078	-1.1313282091	0.7489742480
C	-12.3048388784	-1.8228969445	1.8729763580
C	-13.0189704570	-2.8743628599	2.4398104817
C	-14.2611146809	-3.2474415773	1.9156063084
C	-14.7644750736	-2.5802813628	0.7934662332
C	-14.0578478527	-1.5218647265	0.2363093188
S	-14.8027188245	-0.7367352616	-1.1414976436
C	-15.9186430834	-2.1438877968	-1.5564824582
C	-17.2104270958	-1.6132070418	-2.1446053760
H	-17.0064728816	-1.0627054832	-3.0608282404
H	-17.7070900110	-0.9495979274	-1.4404122721
H	-17.8787063198	-2.4406468265	-2.3727369828
C	-15.1893695776	-3.0914619991	-2.4914891640
H	-15.8139237227	-3.9569730162	-2.7036995387
H	-14.9545619146	-2.5851847358	-3.4262002958
H	-14.2598473199	-3.4335249732	-2.0380285362
S	-16.2711468132	-3.0224998014	0.0369715766
C	-14.9746354775	-4.2995796161	2.6325292501
O	-14.5128618325	-4.8361673306	3.6210704601
O	-16.1704655601	-4.5891513562	2.1230022330
C	-16.9136743146	-5.5991243251	2.7909317532
H	-17.0672103112	-5.3252122090	3.8365646401
H	-17.8632120544	-5.6688780813	2.2671708654
H	-16.3795990245	-6.5504664613	2.7500984866
S	-12.3574885896	-3.6844703805	3.8195847655
C	-10.6856631566	-2.8641533052	3.7101523528
C	-9.7462467496	-3.7855747192	2.9512571892
H	-10.1416238262	-3.9909665436	1.9578704815
H	-9.6452721340	-4.7274353000	3.4862983699
H	-8.7633240114	-3.3285180564	2.8473324025
C	-10.1909249660	-2.5395343770	5.1053691828
H	-10.8797650240	-1.8625038652	5.6050213110
H	-10.1194976053	-3.4550530026	5.6882869662
H	-9.2086497202	-2.0728493255	5.0613650304
S	-10.8805878319	-1.3112911220	2.7414956880
S	-10.3162478178	2.4266087074	0.6603868107

C	-8.7412155132	2.9501934475	1.4612430596
C	-8.5553634646	4.4448777636	1.2948614095
H	-8.5327412791	4.7127729375	0.2407871623
H	-7.6185324549	4.7540853998	1.7535627826
H	-9.3738073814	4.9782428512	1.7740147748
C	-8.7581146437	2.5148967861	2.9148231514
H	-7.8076475125	2.7573140416	3.3866404525
H	-9.5586152523	3.0259642552	3.4465726339
H	-8.9245635464	1.4409352462	2.9917194193
S	-7.3855498078	2.0520861103	0.5763182389
H	-3.8071534800	-1.7053760698	-0.6005346468
H	-1.3951789120	-1.3209396571	-0.6927236419
H	0.4171431892	-0.6887186359	0.7014945767
H	2.8283283798	-0.3382153417	0.5976562821
H	4.9762264931	-0.0879590650	0.0925888654
H	7.3513073279	-0.6265027247	0.3815095616
H	9.7483279433	-1.0963608288	0.5915184487
C	11.5359797060	-1.5084120776	-1.6505014871
C	12.3522106857	-2.5127363959	-2.0458714106
H	12.1222233938	-3.3366725210	-2.6922784960
H	10.5081039426	-1.3494688808	-1.9113087469
C	14.5404141260	-4.3872937252	-2.3058770164
C	13.6419866361	-5.3360095468	-1.8255756554
C	13.4653946661	-6.5349736279	-2.4917707950
C	14.1777614361	-6.7995410242	-3.6496568987
C	15.0706251610	-5.8596702426	-4.1370942775
C	15.2540226068	-4.6628035758	-3.4689225967
H	15.9450429018	-3.9256004827	-3.8518355336
H	15.6261452080	-6.0600332110	-5.0413117323
H	14.0375379306	-7.7347519245	-4.1703189730
H	12.7698462325	-7.2658307963	-2.1063044635
H	13.0918319727	-5.1305658060	-0.9184305793
C	17.1186993329	-3.7097913674	-1.1751440651
C	18.1838684549	-3.0511023434	-0.6627032354
H	19.1877961201	-3.4080157388	-0.5417259658
H	17.0808867993	-4.7115847851	-1.5552287574
C	19.9893614703	-1.0156533629	0.3329087937
C	20.7208581038	-1.2668688077	-0.8246565069
C	22.0810592749	-1.5064366715	-0.7568556028
C	22.7282322095	-1.5049535567	0.4675653547
C	22.0084424326	-1.2590780211	1.6248462128
C	20.6492378160	-1.0130996805	1.5586873682
H	20.0876972676	-0.8249711189	2.4630560594
H	22.5077899233	-1.2588214864	2.5824478473

H	23.7896071422	-1.6942860797	0.5198055814
H	22.6382313423	-1.6945148124	-1.6625768913
H	20.2171715622	-1.2625240110	-1.7807885063
C	18.9018104229	1.5272211766	1.2042068455
C	18.0805634648	2.5142628097	1.6309101850
H	18.3495460937	3.4683615616	2.0393112404
H	19.9739343164	1.5156594494	1.1942446022
C	15.7908628361	4.0471872746	2.5151596207
C	16.4136900561	4.0515188691	3.7600829945
C	16.5865133958	5.2351972449	4.4539748119
C	16.1463780225	6.4309049430	3.9111691059
C	15.5290591329	6.4367523568	2.6714447362
C	15.3489541563	5.2533514817	1.9788923813
H	14.8739509135	5.2575596954	1.0083391860
H	15.1868841676	7.3669674074	2.2425264704
H	16.2842481036	7.3547796170	4.4522176450
H	17.0663191498	5.2250744039	5.4214927202
H	16.7509228266	3.1170142955	4.1852226042

References

- [1] S. Stoll, A. Schweiger, *J. Magn. Reson.* **2006**, *178*, 42–55.
- [2] M. Florent, I. Kaminker, V. Nagarajan, D. Goldfarb, *J. Magn. Reson.* **2011**, *210*, 192–199.
- [3] D. Abdullin, H. Matsuoka, M. Yulikov, N. Fleck, C. Klein, S. Spicher, G. Hagelueken, S. Grimme, A. Luetzen, O. Schiemann, *Chem. - A Eur. J.* **2019**, DOI 10.1002/chem.201900977.
- [4] K. Keller, A. Doll, M. Qi, A. Godt, G. Jeschke, M. Yulikov, *J. Magn. Reson.* **2016**, *272*, 108–113.
- [5] S. Milikisyants, F. Scarpelli, M. G. Finiguerra, M. Ubbink, M. Huber, *J. Magn. Reson.* **2009**, *201*, 48–56.
- [6] T. Bahrenberg, Y. Yang, D. Goldfarb, A. Feintuch, *Magnetochemistry* **2019**, *5*, 20.
- [7] D. Abdullin, G. Hagelueken, R. I. Hunter, G. M. Smith, O. Schiemann, *Mol. Phys.* **2015**, *113*, 544–560.
- [8] D. Abdullin, F. Duthie, A. Meyer, E. S. Müller, G. Hagelueken, O. Schiemann, *J. Phys. Chem. B* **2015**, *119*, 13539–13542.
- [9] Please contact xtb@thch.uni-bonn.de to obtain the program.
- [10] M. Brehm, B. Kirchner, *J. Chem. Inf. Model.* **2011**, *51*, 2007–2023.
- [11] S. Grimme, C. Bannwarth, P. Shushkov, *J. Chem. Theory Comput.* **2017**, *13*, 1989–2009.
- [12] C. Bannwarth, S. Ehlert, S. Grimme, *J. Chem. Theory Comput.* **2019**, *15*, 1652–1671.
- [13] S. Grimme, C. Bannwarth, S. Dohm, A. Hansen, J. Pisarek, P. Pracht, J. Seibert, F. Neese, *Angew. Chemie Int. Ed.* **2017**, *56*, 14763–14769.
- [14] S. Grimme, *J. Chem. Theory Comput.* **2019**, *15*, 2847–2862.
- [15] W. Clark Still, A. Tempczyk, R. C. Hawley, T. Hendrickson, *J. Am. Chem. Soc.* **1990**, *112*, 6127–6129.
- [16] J. P. Ryckaert, G. Ciccotti, H. J. C. Berendsen, *J. Comput. Phys.* **1977**, *23*, 327–341.
- [17] E. Vinck, S. Van Doorslaer, *Phys. Chem. Chem. Phys.* **2004**, *6*, 5224–5330.

[A9]: Pulsed EPR Dipolar Spectroscopy under the Breakdown of the High-Field Approximation: The High-Spin Iron(III) Case

Reprinted with permission from

Dinar Abdullin, Hideto Matsuoka, Maxim Yulikov, Nico Fleck, Christoph Klein, Sebastian Spicher, Gregor Hagelueken, Stefan Grimme, Arne Lützen, Olav Schiemann*,
Chem. Eur. J. **2019**, *25*, 8820 - 8828.

Published by Wiley-VCH (Weinheim, DE), ©**2019** Wiley-VCH Verlag GmbH & Co. KGaA

Contributions:

- Sample preparation for model compounds
- Writing of the manuscript in parts

Physical Chemistry | Hot Paper |

 Pulsed EPR Dipolar Spectroscopy under the Breakdown of the High-Field Approximation: The High-Spin Iron(III) CaseDinar Abdullin,^[a] Hideto Matsuoka,^[a, b] Maxim Yulikov,^[c] Nico Fleck,^[a] Christoph Klein,^[a, d] Sebastian Spicher,^[e] Gregor Hagelueken,^[a] Stefan Grimme,^[e] Arne Lützen,^[d] and Olav Schiemann^{*[a]}

Abstract: Pulsed EPR dipolar spectroscopy (PDS) offers several methods for measuring dipolar coupling and thus the distance between electron-spin centers. To date, PDS measurements to metal centers were limited to ions that adhere to the high-field approximation. Here, the PDS methodology is extended to cases where the high-field approximation breaks down on the example of the high-spin Fe³⁺/nitroxide spin-pair. First, the theory developed by Maryasov et al. (*Appl. Magn. Reson.* **2006**, *30*, 683–702) was adapted to derive equations for the dipolar coupling constant, which revealed that the dipolar spectrum does not only depend on the length and orientation of the interspin distance vector

with respect to the applied magnetic field but also on its orientation to the effective *g*-tensor of the Fe³⁺ ion. Then, it is shown on a model system and a heme protein that a PDS method called relaxation-induced dipolar modulation enhancement (RIDME) is well-suited to measuring such spectra and that the experimentally obtained dipolar spectra are in full agreement with the derived equations. Finally, a RIDME data analysis procedure was developed, which facilitates the determination of distance and angular distributions from the RIDME data. Thus, this study enables the application of PDS to for example, the highly relevant class of high-spin Fe³⁺ heme proteins.

Introduction

Pulsed EPR dipolar spectroscopy (PDS), which includes techniques such as pulsed electron–electron double resonance (PELDOR or DEER),^[1,2] double quantum coherence EPR (DQC),^[3] single-frequency technique for refocusing dipolar couplings (SIFTER),^[4] and relaxation-induced dipolar modulation enhancement (RIDME),^[5,6] is a valuable method for acquiring nanometer distance constraints for the characterization of biomolecular structures and their conformational changes during function.^[7] In the case of diamagnetic biomolecules, PDS measurements require the site-specific labeling of a biomolecule with two

spin labels, which are most commonly two nitroxide labels.^[7] When a biomolecule contains an intrinsic paramagnetic metal center, PDS can be applied to determine the distance between such a metal center and a single spin label. The latter case has several advantages and applications: 1) the use of metal centers for PDS allows to reduce the number of spin labels and, consequently, the number of protein mutations, 2) it enables orthogonal spin labeling^[8] as the metal center has different spectroscopic properties than the majority of spin labels, 3) the distance constraints obtained from such PDS measurements enable the localization of metal ions within the protein fold by trilateration^[9,10] and the docking of different parts of protein complexes using metal ions as anchor points.^[11]

To date, PDS measurements have been applied to a variety of different intrinsic metal centers, such as Cu²⁺,^[12–20] Mn²⁺,^[21–25] Co²⁺,^[26,27] and low-spin Fe³⁺,^[6,28–31] as well as iron-sulfur^[17,32–34] and manganese^[35,36] clusters. In all these cases, the protocols for PSD measurements are well-established and the extraction of distance constraints from the corresponding PDS data can be readily achieved under the high-field approximation.^[37,38] Yet, there is a long-standing challenge in applying PDS to high-spin ions, for which the zero-field splitting (ZFS) is so large that the high-field approximation breaks down. A highly relevant example for such a case is the high-spin Fe³⁺ ions in heme proteins. So far, only Rakowsky et al. reported on continuous-wave EPR based distance measurements between a high-spin Fe³⁺ and a nitroxide in a model system using saturation recovery experiments.^[39] However, the extraction of distances from saturation recovery data is complicated and prone


[a] Dr. D. Abdullin, Dr. H. Matsuoka, N. Fleck, Dr. C. Klein, Dr. G. Hagelueken, Prof. Dr. O. Schiemann
Institute of Physical and Theoretical Chemistry
University of Bonn, Bonn (Germany)
E-mail: schiemann@pc.uni-bonn.de

[b] Dr. H. Matsuoka
Current address: Graduate School of Science
Osaka City University, Osaka (Japan)

[c] Dr. M. Yulikov
Laboratory of Physical Chemistry, ETH Zurich, Zurich (Switzerland)

[d] Dr. C. Klein, Prof. Dr. A. Lützen
Kekulé Institute of Organic Chemistry and Biochemistry
University of Bonn, Bonn (Germany)

[e] Dr. S. Spicher, Prof. Dr. S. Grimme
Mulliken Center for Theoretical Chemistry
University of Bonn, Bonn (Germany)

 Supporting information and the ORCID identification number(s) for the <-author(s) of this article can be found under:
<https://doi.org/10.1002/chem.201900977>.

to errors, because: 1) the dipolar coupling leads only to an additional exponential decay of the time trace and not to an oscillation, which makes it difficult to separate the dipolar contribution from relaxation, 2) several empirical parameters need to be adjusted in the analysis, and 3) a reference measurement on the same sample with the ion in a diamagnetic state is required. That other EPR methods based on PDS have not been applied to high-spin Fe^{3+} ions is likely due to the magnetic properties of these ions. One being the ZFS,^[43,44] which is typically so large that it leads to the violation of the high-field approximation at most of the available microwave frequencies. To date, all PDS studies have been exclusively based on such high-field approximation, which excludes the application of available PDS data analyses for high-spin Fe^{3+} ions. Moreover, the large ZFS of the high-spin Fe^{3+} ions leads to very broad EPR spectra, which span over effective g values of roughly 2 to 6.^[43,44] Consequently, the spectral width of Fe^{3+} exceeds significantly the bandwidth of typical microwave pulses, making most of PDS experiments unfeasible because a too small fraction of Fe^{3+} centers would contribute to the signal. Furthermore, a large difference in resonance frequencies between the Fe^{3+} ions and nitroxides prevents the application of double-frequency PELDOR technique to the high-spin Fe^{3+} /nitroxide pairs, due to the limited bandwidths of EPR resonators and microwave amplifiers. Another important property of high-spin Fe^{3+} ions is their short relaxation times^[39,45–48] and their orientation dependence,^[48] which sets high requirements for the experimental set-up and might introduce unwanted orientation selectivity to the PDS experiments.

The most promising technique for circumventing these difficulties is RIDME. Recently, RIDME has gained a significant interest in the community^[30,49,50] because it is especially well-suited for spin pairs that consist of a slow relaxing spin label and a fast relaxing metal center. For such spin pairs, the RIDME time trace is acquired on the slow relaxing spin label, whereas the fast relaxing metal center is flipped by spontaneous relaxation. An infinite effective bandwidth of the stochastic spin flips implies that the RIDME experiment has low requirements on the resonator and amplifier bandwidth. Recent RIDME studies on metal ion/spin label and metal ion/metal ion pairs, such as low-spin Fe^{3+} /nitroxide,^[6,30] low-spin Fe^{3+} /trityl,^[51] Cu^{2+} /nitroxide,^[20] Mn^{2+} /nitroxide,^[25] and Gd^{3+} / Gd^{3+} ,^[49,52–54] confirmed these advantages and showed better signal-to-noise ratios and less orientation selectivity as compared to PELDOR. However, the RIDME time traces have typically a more complicated background and more pronounced ESEEM artifacts as compared to PELDOR,^[30,52] and for the high-spin Mn^{2+} and Gd^{3+} centers with small ZFS, also contained contributions from overtones of the dipolar frequency.^[25,53]

The aim of the work presented here is to establish the PDS-based approach for distance measurements between a high-spin Fe^{3+} ion and a nitroxide. To achieve this goal, several steps were accomplished: 1) the theoretical background of the dipole–dipole interaction between a high-spin Fe^{3+} ion and a nitroxide was developed; 2) two model systems, the high-spin heme-bridge-nitroxide compound **1** and the nitroxide-labeled mutant of the heme protein met-myoglobin **Q8R1** (Figure 1),

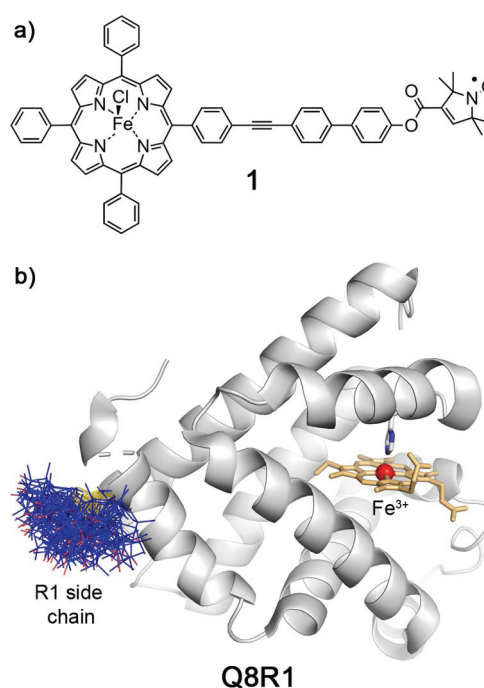


Figure 1. Model systems used for the RIDME-based distance measurements on high-spin Fe^{3+} /nitroxide spin pairs. a) The Lewis structure of model compounds **1**. b) The structural model of the met-myoglobin mutant **Q8R1**. This model is based on the crystal structure of met-myoglobin (PDB ID: 1WLA^[40]) shown in gray. The heme group and the Fe^{3+} ion are depicted as orange sticks and red sphere, respectively. The MtsIWizard^[41,42] generated conformers of the R1 side chain at site Q8 are depicted as blue/red sticks.

were synthesized and used for RIDME measurements; 3) the obtained RIDME data were analyzed using the theory established in step 1; 4) the accuracy of the RIDME measurement and analysis was verified by comparing the distance and angular distributions with corresponding *in silico* predictions.

Theoretical Section

The spin system considered in the following consists of a high-spin Fe^{3+} with $S_1=5/2$ and a nitroxide with $S_2=1/2$. Both spin centers are assumed to be separated by several nanometers and the exchange interaction to be negligible. The spin Hamiltonian of this spin system in an applied constant magnetic field \mathbf{B}_0 can be written as [Eq. (1)]:

$$\hat{H} = \hat{H}_1 + \hat{H}_2 + \hat{H}_{DD} \quad (1)$$

where \hat{H}_1 and \hat{H}_2 are the spin Hamiltonians of the Fe^{3+} and nitroxide spins, respectively, and \hat{H}_{DD} is the Hamiltonian of the dipole–dipole interaction between both spins. For the sake of simplicity, the hyperfine interaction of both spin centers is omitted. Thus, the spin Hamiltonian of the nitroxide spin is determined by its Zeeman interaction with \mathbf{B}_0 only [Eq. (2)]:

$$\hat{H}_2 = \beta_e \mathbf{B}_0^T \hat{g}_2 \mathbf{S}_2 \quad (2)$$

Here, β_e is the Bohr magneton, \hat{g}_2 is the g -tensor of the nitroxide, and \mathbf{S}_2 is the spin vector of $S_2=1/2$. The symbol “ T ” denotes transposition. The spin Hamiltonian of the Fe^{3+} spin is given by the sum of the ZFS and the Zeeman interaction terms [Eq. (3)]:

$$\hat{H}_1 = D \left[\hat{S}_{1z}^2 - \frac{S_1(S_1 + 1)}{3} \right] + E \left[\hat{S}_{1x}^2 - \hat{S}_{1y}^2 \right] + \beta_e \mathbf{B}_0^T \hat{g}_1 \mathbf{S}_1 \quad (3)$$

where D and E are the axial and rhombic parameters of the ZFS tensor, \hat{g}_1 is the g -tensor of the high-spin Fe^{3+} , and \mathbf{S}_1 is the spin vector of $S_1=5/2$ with the Cartesian coordinates $(\hat{S}_{1x}, \hat{S}_{1y}, \hat{S}_{1z})$. The energy levels (eigenvalues) and the wave functions (eigenvectors) of the Hamiltonian given by Equation (3) can be readily found in many textbooks.^[43,44] In the case of positive axial ZFS ($D > 0$ and $E = 0$), the spin energy levels of the high-spin Fe^{3+} in the absence of external magnetic field consist of three degenerate doublets with the spin projections on the ZFS z -axis $m_s = \pm 1/2, \pm 3/2$, and $\pm 5/2$. The doublet with $m_s = \pm 1/2$ has the lowest energy, whereas the doublets with $m_s = \pm 3/2$ and $m_s = \pm 5/2$ lay $2D$ and $6D$ above it, respectively. When the external magnetic field is applied, the Zeeman interaction leads to the splitting of each of the doublets. If the ZFS is much larger than the Zeeman interaction, the Fe^{3+} spins are still quantized along the ZFS z -axis and m_s remains to be a good quantum number. Furthermore, if the ZFS is also much larger than the thermal energy of the system, only the lowest doublet with $m_s = \pm 1/2$ is populated. In this case, the energy levels of the high-spin Fe^{3+} can be described by an effective spin $S'_1 = 1/2$ and, consequently, \hat{H}_1 can be substituted by a simplified Hamiltonian [Eq. (4)]:

$$\hat{H}'_1 = \beta_e \mathbf{B}_0^T \hat{g}'_1 \mathbf{S}'_1 \quad (4)$$

Here, \hat{g}'_1 is the effective g -tensor of high-spin Fe^{3+} . In the case of $D > 0$ and $E = 0$, \hat{g}'_1 is also axial and has the principle values $g'_{1xx} = g'_{1yy} = 6.0$ (also denoted as $g'_{1\perp}$) and $g'_{1zz} = 2.0$ (also denoted as $g'_{1\parallel}$). When E is nonzero, all three principle values of \hat{g}'_1 differ.^[55] Considering the high-spin Fe^{3+} ion as an effective spin-1/2 system and using the point-dipole approximation, the dipole-dipole interaction term can be written as [Eq. (5)]:

$$\hat{H}_{DD} = \frac{\mu_0 \beta_e^2}{4\pi r^3} \left[(\hat{g}'_1 \mathbf{S}'_1, \hat{g}_2 \mathbf{S}_2) - 3(\hat{g}'_1 \mathbf{S}'_1, \mathbf{n})(\hat{g}_2 \mathbf{S}_2, \mathbf{n}) \right] \quad (5)$$

where μ_0 is the vacuum permeability, r is the distance vector which connects the Fe^{3+} and nitroxide spin centers, r and \mathbf{n} are the length and the unit vector of r , respectively. The round brackets denote the scalar product of two vectors. Using perturbation theory, Bedilo and Maryasov have derived a more convenient form of Equation (5) for the case of two anisotropic spin-1/2 centers,^[56] which was later used for the case of low-spin Fe^{3+} .^[6,28] Since high-spin Fe^{3+} can be described as an anisotropic spin-1/2 center under the specified conditions, the equations of Bedilo and Maryasov can be adapted for the present study. According to their work, Equation (5) can be transformed into [Eq. (6)]:

$$\hat{H}_{DD} = \frac{\mu_0 \beta_e^2}{4\pi r^3} \left[\hat{A} + \hat{B} + \hat{C} + \hat{D} + \hat{E} + \hat{F} + \hat{G} + \hat{H} + \hat{I} \right] \quad (6)$$

The expressions for all alphabetic operators can be found in the original publication.^[56] Here, it is assumed that only the secular part \hat{A} of Equation (6) provides a significant contribution to the Hamiltonian, because the dipolar interaction between an high-spin Fe^{3+} and a nitroxide is typically much smaller than the difference of their Larmor frequencies. The term \hat{A} is given by [Eq. (7)]:

$$\hat{A} = \hat{S}'_{1k_1} \hat{S}_{2k_2} \left[(\hat{g}'_1 \mathbf{k}_1, \hat{g}_2 \mathbf{k}_2) - 3(\hat{g}'_1 \mathbf{k}_1, \mathbf{n})(\hat{g}_2 \mathbf{k}_2, \mathbf{n}) \right] \quad (7)$$

Here, \mathbf{k}_1 and \mathbf{k}_2 determine the quantization axes of each of the spins [Eq. (8)]:

$$\mathbf{k}_1 = \frac{\hat{g}'_1 \mathbf{B}_0}{(\hat{g}'_1 \mathbf{B}_0, \hat{g}'_1 \mathbf{B}_0)^{1/2}}, \quad \mathbf{k}_2 = \frac{\hat{g}_2 \mathbf{B}_0}{(\hat{g}_2 \mathbf{B}_0, \hat{g}_2 \mathbf{B}_0)^{1/2}} \quad (8)$$

The operators \hat{S}'_{1k_1} and \hat{S}_{2k_2} denote the projections of the spin vectors \mathbf{S}'_1 and \mathbf{S}_2 onto the corresponding quantization axes \mathbf{k}_1 and \mathbf{k}_2 , respectively. When the secular approximation is applied not only to \hat{H}_{DD} but also to \hat{H}'_1 [Eq. (4)] and \hat{H}_2 [Eq. (2)], the total spin Hamiltonian takes the form [Eq. (9)]:

$$\hat{H} = \beta_e g'_{1\text{eff}} B_0 \hat{S}'_{1k_1} + \beta_e g_{2\text{eff}} B_0 \hat{S}_{2k_2} + h \nu_{dd} \hat{S}'_{1k_1} \hat{S}_{2k_2} \quad (9)$$

Here, $g'_{1\text{eff}}$ and $g_{2\text{eff}}$ are the effective g factors of the Fe^{3+} and nitroxide spin centers for a particular orientation of the magnetic field, h is the Planck constant, and ν_{dd} is the dipolar coupling frequency [Eq. (10)]:

$$\nu_{dd} = \frac{\mu_0 \beta_e^2}{4\pi h r^3} \left[(\hat{g}'_1 \mathbf{k}_1, \hat{g}_2 \mathbf{k}_2) - 3(\hat{g}'_1 \mathbf{k}_1, \mathbf{n})(\hat{g}_2 \mathbf{k}_2, \mathbf{n}) \right] \quad (10)$$

If the anisotropy of the nitroxide g -tensor (\hat{g}_2) is neglected, the nitroxide spin will be quantized along the direction of the applied magnetic field, $\mathbf{k}_2 = \mathbf{B}_0/B_0$, where B_0 is the magnitude of \mathbf{B}_0 . In this case, Equation (10) can be further simplified to [Eq. (11)]:

$$\nu_{dd} = \frac{\mu_0 \beta_e^2 g'_{1\text{eff}} g_{2\text{eff}}}{4\pi h r^3} \left[1 - 3 \left(\frac{\hat{g}'_1 \mathbf{B}_0}{\hat{g}'_1 \mathbf{B}_0}, \mathbf{n} \right) \left(\frac{\mathbf{B}_0}{B_0}, \mathbf{n} \right) \right] \quad (11)$$

Note that the product $(\mathbf{B}_0/B_0, \mathbf{n})$ is usually denoted as $\cos(\theta)$, where θ is the angle between the inter-spin distance vector and the applied magnetic field. Comparing Equation (11) with the equation for the dipolar coupling between two isotropic spin-1/2 centers [Eq. (12)]:

$$\nu_{dd}^{\text{iso}} = \frac{\mu_0 \beta_e^2 g_{1\text{eff}} g_{2\text{eff}}}{4\pi h r^3} [1 - 3\cos^2(\theta)] \quad (12)$$

reveals that both equations differ by the first term in round brackets in Equation (11). In the case of two isotropic spins, this term equals $\cos(\theta)$, whereas in the case of the high-spin Fe^{3+} /nitroxide pair it also depends on the orientation of the distance vector with respect to iron's effective g -tensor. Such orientation can be described by two spherical angles, the polar (ξ) and azimuthal (φ) angles (Figure 2). Thus, for the high-spin Fe^{3+} /nitroxide pair, the dipolar coupling frequency depends not only on θ but also on ξ and

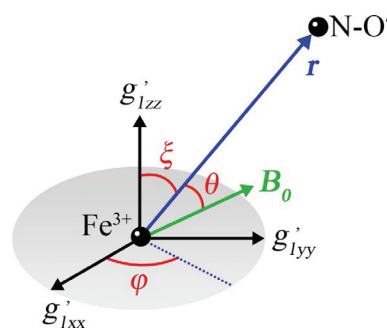


Figure 2. Geometric model of a high-spin Fe^{3+} /nitroxide spin pair in an external magnetic field \mathbf{B}_0 .

φ . In the case when $E=0$, g'_{1xx} and g'_{1yy} are indistinguishable, the dipolar coupling frequency will be dependent on the angles θ and ξ but not on φ .

So far, the equation of the dipolar coupling frequency [Eq. (11)] was derived only for a single orientation of a spin system with respect to the external magnetic field. In order to obtain the spectrum of the dipole–dipole interaction for an ensemble of randomly oriented molecules, the dipolar coupling frequency has to be averaged over all possible orientations of the spin pair with respect to the applied magnetic field. Such powder averaging was done numerically by using 10^6 random samples. For the test calculations, the Fe^{3+} /nitroxide distance was set to 2.50 nm.

The g -factor of the nitroxide was assumed to be isotropic and equal to $g_e = 2.0023$. The ZFS tensor of the high-spin Fe^{3+} was assumed to be axial with $D = 10 \text{ cm}^{-1}$, which yielded an axial g -tensor for Fe^{3+} with $g'_{1x} = g'_{1y} = 6.00$ and $g'_{1z} = 2.00$. The angle ξ between g'_{1z} of Fe^{3+} and the inter-spin distance vector was varied in the range 0° to 90° . The obtained powder-averaged spectra are shown in Figure 3a. The abscissa of the depicted spectra is given in the units of [Eq. (13)]:

$$\nu_0 = \frac{\mu_0 \beta_e^2 g_e^2}{4\pi r^3} \quad (13)$$

For the sake of comparison, the same powder averaging was also applied to Equation (12) with $g_{1\text{eff}} = g_{2\text{eff}} = g_e$, yielding the dipolar spectrum for two isotropic spin-1/2 centers (Figure 3b). The latter spectrum is known as a Pake doublet. Importantly, the spectra in

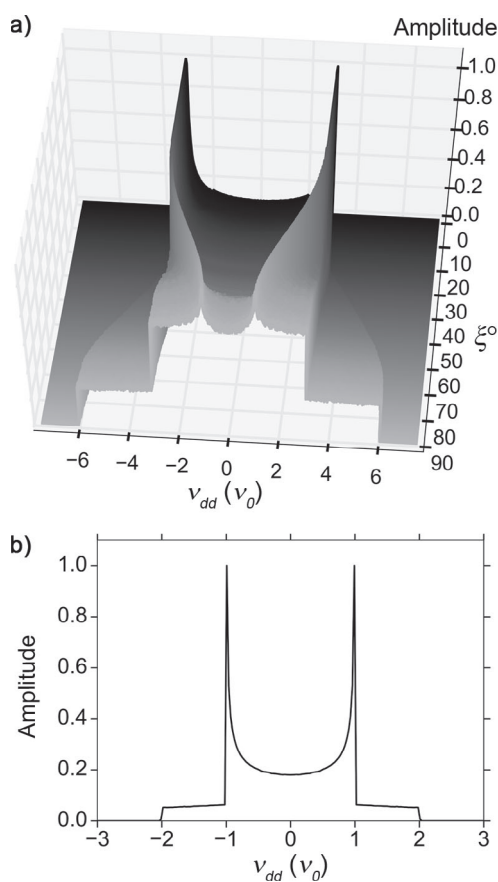


Figure 3. The dipolar spectra of: a) the Fe^{3+} /nitroxide spin pair plotted against the angle ξ and, b) two isotropic spin-1/2 centers (Pake doublet).

Figure 3a reveal prominent differences to the Pake doublet in Figure 3b. First, the dipolar spectra of the high-spin Fe^{3+} /nitroxide pair are significantly broader than the Pake doublet. This stems from the fact that ν_{dd} is proportional to the effective g -factor of the high-spin Fe^{3+} , which is three-times larger than g_e for two out of three canonical orientations. Second, the shape of the dipolar spectrum of a high-spin Fe^{3+} /nitroxide pair differs from the shape of the usual Pake doublet and, as predicted above, depends strongly on the angle ξ . The reason for this is the large anisotropy of the g -values of high-spin Fe^{3+} , which leads to the additional dependence of ν_{dd} on ξ .

To gain deeper insight into the shapes of the obtained spectra in Figure 3a, ν_{dd} is plotted as a function of θ in Figure 4 for two particular cases, $\xi = 90^\circ$ and $\xi = 0^\circ$. In the case of $\xi = 90^\circ$ (Figure 4a),

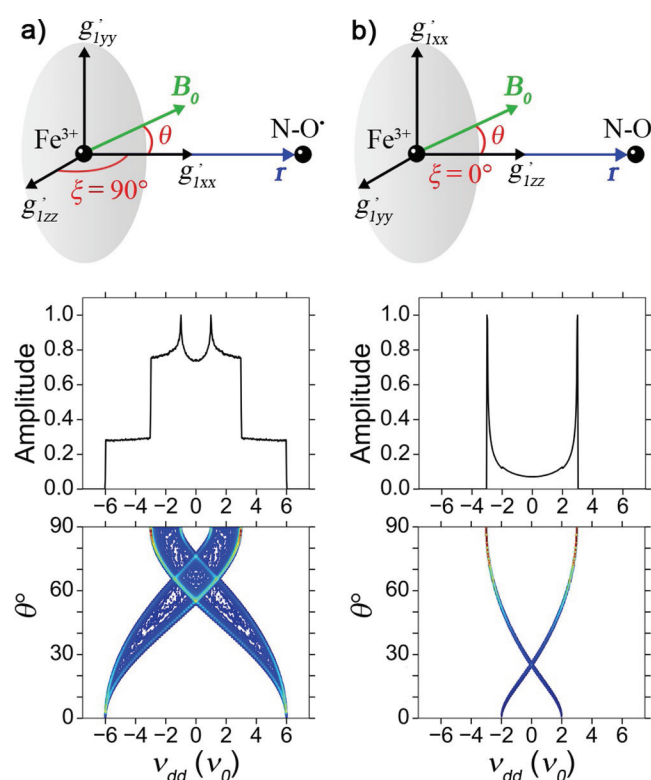


Figure 4. Simulation of the dipolar spectra for the Fe^{3+} /nitroxide spin pair with a) $\xi = 90^\circ$ and b) $\xi = 0^\circ$. Top: The geometric model of a high-spin Fe^{3+} /nitroxide spin pair with fixed ξ angle. Middle: The corresponding dipolar spectrum. Bottom: The corresponding dipolar spectrum plotted for different values of θ .

the parallel component ($\theta = 90^\circ$) of the spectrum scales with g'_{1y} of Fe^{3+} , which is about three-times larger than g_e . Consequently, the parallel component appears in the spectrum at $\pm 6\nu_0$ and not at $\pm 2\nu_0$ as for the Pake doublet. The perpendicular component ($\theta = 0^\circ$) of the spectrum scales with the g -values of Fe^{3+} ranging from $g'_{1z} \sim 1g_e$ to $g'_{1x} \sim 3g_e$. This gives rise to two features in the spectrum at $\pm\nu_0$ and $\pm 3\nu_0$. In the case of $\xi = 0^\circ$ (Figure 4b), the perpendicular component ($\theta = 90^\circ$) of the spectrum corresponds to g'_{1x} or g'_{1y} of Fe^{3+} . Since $g'_{1x} = g'_{1y} \sim 3g_e$, the perpendicular component of the spectrum can be observed at $\pm 3\nu_0$. The parallel component ($\theta = 0^\circ$) of this spectrum scales with g'_{1z} and, thus, should appear at $\pm 2\nu_0$. Since the parallel component has a smaller probability and appears at lower frequencies than the per-

pendicular component, it does not yield any prominent features in the spectrum.

Note that all dipolar spectra of the high-spin Fe^{3+} /nitroxide pair in Figure 3a and Figure 4 were simulated for certain values of r and ξ . However, if the molecule would have some flexibility, r and ξ would have some distributions. Clearly, the distributions of r and ξ will affect both the shape and the width of the corresponding dipolar spectra. Vice versa, the shape and the width of the corresponding dipolar spectrum should allow the determination of the distributions of r and ξ .

If the ZFS of the high-spin Fe^{3+} would be rhombic, Equation (11) will be still valid for the high-spin Fe^{3+} /nitroxide spin pair, but the dipolar spectrum will depend also on the E/D ratio and the φ angle (Chapter 1 in the Supporting Information). In the following, we limit our consideration to the high-spin Fe^{3+} ions with axial ZFS. Note that this case covers a large number of heme proteins. The case of highly rhombic high-spin Fe^{3+} ions will be investigated in detail in future studies.

Experimental Section

Synthesis of compound 1

The synthesis of model compound **1** and the corresponding analytics have been described previously.^[57] For the RIDME measurements, **1** was dissolved in deuterated THF to yield a concentration of 200 μM .

Synthesis of met-myoglobin mutant Q8R1

The amino acid Q8 of the wild-type met-myoglobin was mutated to a cysteine and the mutant was expressed, purified and spin labeled with the methanethiosulfonate nitroxide spin label (MTSL, abbreviated as R1 side chain when attached to a cysteine), yielding **Q8R1** (Chapter 1 in the Supporting Information). The high-spin state of the heme Fe^{3+} ion, the absence of low-spin heme, the absence of the free label, and the high labeling efficiency (> 90%) were confirmed by means of continuous-wave X-band EPR experiments on **Q8R1** (Chapter 2 in the Supporting Information). For the RIDME measurements, **Q8R1** was prepared in deuterated phosphate buffer containing 20% deuterated glycerol at a protein concentration of 100 μM .

RIDME measurements

Pulsed EPR measurements were carried out on a Bruker ELEXSYS E580 spectrometer using a Flexline probe head with a Q-band resonator ER5106QT-2 (Bruker). Microwave pulses were amplified with a 150 W TWT amplifier (model 187Ka). To obtain liquid helium temperatures, a continuous flow helium cryostat CF935 (Oxford Instruments), a temperature control system ITC 503 (Oxford Instruments), and a vacuum pump EPS40 (Oxford Instruments) were employed. RIDME experiments were performed using the five-pulse sequence $\pi/2-\tau_1-\pi-(\tau_1+t)-\pi/2-T_{\text{mix}}-\pi/2-(\tau_2-t)-\pi-\tau_2-\text{echo}$ ^[6] (Figure 5). The frequency of the microwave pulses was set in resonance with the

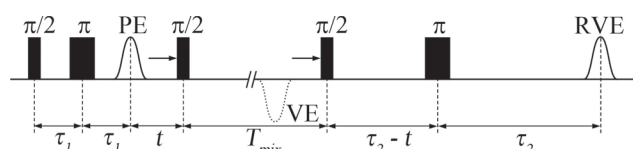


Figure 5. Dead-time free five-pulse RIDME sequence.

maximum of the nitroxide signal. The lengths of the $\pi/2$ and π pulses were 10 and 20 ns, respectively. τ_1 and τ_2 intervals were set to 250 ns and 2 μs , respectively. The length of T_{mix} was optimized to fit the T_1 relaxation rate of the high-spin Fe^{3+} ions (see Results and Discussion). At the temperature of 3 K, T_{mix} was set to 1 ms for both samples, **1** and **Q8R1**. During the RIDME experiment, t was linearly incremented from -32 ns to 1768 ns in increments of 4 ns, yielding 450 data points in total. The shot repetition time was set to 100 ms. To avoid overlap with unwanted echoes with the detected reversed virtual echo, 8-step phase cycling was employed. In order to suppress deuterium ESEEM in the RIDME time traces, the initial values of τ_1 and τ_2 were incremented consecutively eight times with an increment of 16 ns, resulting in 64 averages for each RIDME time trace.^[52] The total duration of a single RIDME experiment was about 6.4 h.

RIDME data analysis

As the dipolar spectra of the high-spin Fe^{3+} /nitroxide spin pairs deviates significantly from the Pake doublet, the existing algorithms for the analysis of the dipolar time traces of two isotropic spin-1/2 centers cannot be applied to the present case. Instead, a new analysis routine was developed, which uses Equation (11) as a basis for the fitting of the experimental dipolar spectra.

The analysis begins with the usual removal of the non-oscillating background from the original RIDME time trace. This background stems from the loss of coherence by detected spins due to spin diffusion. The exact expression of the RIDME background is still missing in the literature but, as was shown in earlier reports,^[30,49] a stretched exponential function or a polynomial function can yield a good approximation of this background. Here, the background was fitted by a third order polynomial function using the program DeerAnalysis.^[38] The same program was also used to divide the original RIDME time trace by the background function and then to perform fast Fourier transformation (FFT) of the background-free time trace. The outcome of the FFT is the dipolar spectrum. In case of the high-spin Fe^{3+} /nitroxide spin pair, the dipolar spectrum encodes information about the distribution of the interspin distance r , $P(r)$, and the distribution of the angle ξ , $P(\xi)$. The determination of $P(r)$ and $P(\xi)$ from the experimental dipolar spectrum is an ill-posed problem. The most common way to solve such problems is to use regularization methods, for example, Tikhonov regularization.^[38] Implementation of the Tikhonov regularization for the case when the dipolar time trace/spectrum encodes unknown distributions of two variables is complicated and will be the topic of future studies. Here, a simpler approach was employed by assuming that both distributions $P(r)$ and $P(\xi)$ can be approximated by normal distributions. Thus, the problem is reduced to finding the optimal values of two mean values ($\langle r \rangle$ and $\langle \xi \rangle$) and two standard deviations (σ_r and σ_ξ), for which the simulated dipolar spectrum will fit best to the experimental dipolar spectrum. This optimization problem was solved using a genetic algorithm^[58] that was implemented in a home-written program DipFit (Chapter 5 in the Supporting Information). The simulation of the dipolar spectrum for certain values of $\langle r \rangle$, σ_r , $\langle \xi \rangle$, and σ_ξ was carried out by averaging ν_{dd} in Equation (11) over the corresponding distributions of r and ξ , and additionally, over the angle θ (powder averaging). The averaging was performed with the Monte-Carlo method with 10^6 random samples. The values of r , ξ , and θ were assumed to have no correlation with each other. The spectral simulations based on Equation (11) required also the principal g -values of both spins. For simplicity, the nitroxide's principal g -values were set to g_e . For the high-spin Fe^{3+} , the effective principal g -values were calculated from the actual g -factors and the ZFS parameters. In the

case of **1**, the actual g -factor and the ZFS parameters were assumed to be the same as of FeTPPCI ($D=6.465\text{ cm}^{-1}$, $E=0.02\text{ cm}^{-1}$),^[59] yielding $g'_{1x}=5.91$, $g'_{1y}=6.02$, and $g'_{1z}=1.95$. In the case of **Q8R1**, the g factor and ZFS parameters of the Fe^{3+} ion in wild-type myoglobin ($D=9.26\text{ cm}^{-1}$, $E=0.0023\text{ cm}^{-1}$)^[48] were used to obtain $g'_{1x}=5.93$, $g'_{1y}=5.94$, and $g'_{1z}=2.00$.

Importantly, the RIDME experiment assigns weights to different components of the high-spin Fe^{3+} /nitroxide dipolar spectra. Before the origin of these weights is explained, it has to be emphasized that the RIDME signals were measured on the slow relaxing nitroxide spins, while the fast relaxing Fe^{3+} spins experienced stochastic flips in the time interval T_{mix} (Figure 5). The probability that a spin-1/2 experiences an odd number of stochastic flips in the time interval T_{mix} is given by^[5] [Eq. (14)]:

$$p = \frac{1}{2} \left[1 - \exp\left(-\frac{T_{\text{mix}}}{T_1}\right) \right] \quad (14)$$

where T_1 is the spin-lattice relaxation time. Note that T_1 of the high-spin Fe^{3+} ions is usually anisotropic. It is significantly shorter for the g'_{1x} and g'_{1y} components as compared to the g'_{1z} component of the iron's g -tensor.^[47,48] Therefore, different flip probabilities p are obtained for the different spectral components of the high-spin Fe^{3+} ion. To minimize the difference of the flip probabilities, T_{mix} was set to be larger than the longest T_1 .

In addition, Equation (14) does not accurately describe the probability of the stochastic flips of the high-spin Fe^{3+} ions at very low temperatures, at which the Zeeman energy becomes comparable to the thermal energy. At these conditions, the Boltzmann populations of the two lowest energy levels of the high-spin Fe^{3+} ions, corresponding to $m_s = \pm 1/2$, depend strongly on the effective g -factor of these ions. This dependence translates also on p , because the probability that the stochastic flips of the Fe^{3+} spins in the time interval T_{mix} will change the m_s state from $+1/2$ to $-1/2$ or vice versa is proportional to the product of both Boltzmann populations. When this dependence is taken into account, Equation (14) can be replaced by [Eq. (15)]:

$$p = \frac{2 \exp(-g'_{\text{eff}} \beta_e B_0 / k_B T)}{(1 + \exp(-g'_{\text{eff}} \beta_e B_0 / k_B T))^2} \left[1 - \exp\left(-\frac{T_{\text{mix}}}{T_1}\right) \right] \quad (15)$$

Here, k_B is the Boltzmann constant, and T is the temperature. The factor 2 in front of the Boltzmann term takes into account the transitions "up" and "down". Figure 6 depicts the dependence $p(g'_{\text{eff}})$ for two temperatures, 300 K and 3 K. Both curves were calculated for g'_{eff} in the range from 2.0 to 6.0, $T_{\text{mix}} \gg T_1$, and $B_0 = 1.1980\text{ T}$. As can be seen, the flip probability at 300 K is almost constant for all g'_{eff} and equals to about 0.5. In contrast, the flip probability at

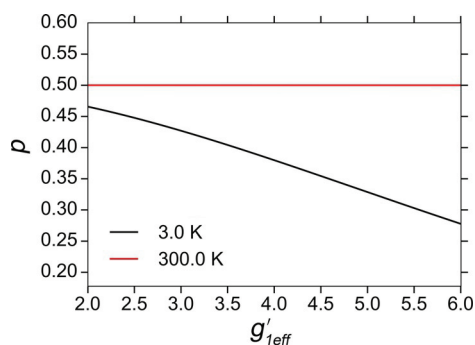


Figure 6. The function $p(g'_{\text{eff}})$ at 300 and 3 K.

3 K decreases monotonously from $g'_{\text{eff}} = 2.0$ to $g'_{\text{eff}} = 6.0$. Moreover, all values of the flip probability at 3 K are significantly below 0.5. These results have two consequences for the RIDME signals recorded at 3 K. First, the modulation depth of the RIDME time traces will decrease from 50% down to 33%. Second, the components of the RIDME spectra that correspond to different g'_{eff} will have different weights. To account for this, the weights given by Equation (15) were included in DipFit and the temperature of the RIDME experiment was used as an additional optimization parameter (Chapter 5 in the Supporting Information).

Molecular modeling

In order to estimate the distributions of $P(r)$ and $P(\xi)$ for **1** and **Q8R1**, the structure and dynamics of these molecules were determined in silico. In the case of **1**, molecular dynamics (MD) simulations were carried out for 1 ns on the GFN-xTB/GBSA(THF)^[60] quantum chemistry level of theory (Chapter 7 in the Supporting Information). For each 4 fs time step of these simulations, the values of r and ξ were determined as the Fe–NO' distance and the angle between the Fe–Cl bond and the Fe–NO' distance vector, respectively. The structure modeling for **Q8R1** was carried out using the crystal structure of wild-type myoglobin (PDB ID: 1WLA^[40]) and the possible conformers of the R1 side chain were modeled into this structure at site Q8 using the program MtssiWizard.^[41,42] This yielded an ensemble of different conformers of the R1-labeled protein (Figure 1 b). For each conformer, the Fe–NO' distance and the angle $N_\delta(\text{H93})\text{--Fe--NO}$ were determined as the estimates for r and ξ , respectively. The histograms of these parameters were used as their distributions.

Results and Discussion

RIDME measurements on **1** and **Q8R1**

The optimal way to perform the RIDME experiment on Fe^{3+} /nitroxide spin pairs implies the detection of the echo signal from the nitroxide spins, while the Fe^{3+} spins are flipped stochastically in the interval T_{mix} . To maximize the modulation depth of the corresponding RIDME time trace, the value of T_{mix} should be adjusted such that the majority of the Fe^{3+} spins are flipped. Moreover, T_{mix} should be significantly longer than any other interpulse time interval in the RIDME pulse sequence, which avoids unwanted flipping of the Fe^{3+} spins in these intervals. While fulfilling this condition, T_{mix} still has to be kept as short as possible to minimize spin diffusion of the detected nitroxide spins. A series of inversion recovery experiments on the Fe^{3+} center of **1** and **Q8R1** revealed that all these requirements are fulfilled best for $T_{\text{mix}}=1\text{ ms}$ at the temperature of 3 K. Despite the difference in the T_1 relaxation rates of the Fe^{3+} centers with different effective g -factors (Figure 7 and Chapter 3 in the Supporting Information), the chosen value of T_{mix} ensures the highest probability of stochastic flips for all Fe^{3+} centers. The chosen temperature, in turn, satisfies the requirement that the T_1 relaxation of all Fe^{3+} centers is significantly slower than the time intervals τ_1 and τ_2 .

For both, **1** and **Q8R1**, the RIDME signal was acquired at the maximum of the nitroxide Q-band spectrum, because this maximizes the signal-to-noise ratio of the signals and minimizes the orientation selection effects due to partial excitation of the

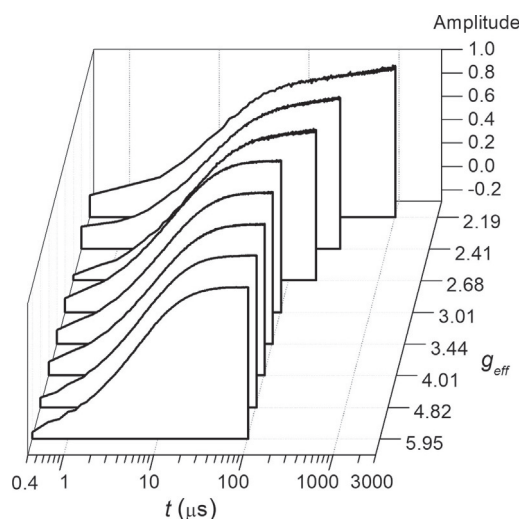


Figure 7. The inversion recovery time traces of **1** at 3 K are plotted against g_{eff} values of high-spin Fe^{3+} .

nitroxide centers by microwave pulses. In order to minimize nitroxide ESEEM artifacts (Chapter 4 in the Supporting Information), the RIDME experiment was performed at Q-band and modulation averaging was employed as described in the Experimental Section.

The RIDME time traces recorded on **1** and **Q8R1** are shown in Figure 8a. The corresponding background-corrected time traces and their FFTs are depicted in Figure 8b and c, respectively. As can be seen, both RIDME time traces are well modulated with modulation depths of 28% and 33% for **1** and **Q8R1**, respectively. Thus, the predicted reduction of the modulation depth from 50% down to 33% due to the reduced probability of the Fe^{3+} spin flips at a temperature of 3 K (Figure 6) is experimentally confirmed. Even more important, the FFTs of both time traces yield the dipolar spectra, the shapes of which are in excellent agreement with the theoretical spectra derived above (Figure 3). Indeed, both spectra have a much larger width than $\pm 2\nu_0$ and three turning points instead of two on either side of the zero. These turning points appear at ± 3.5 MHz, ± 9.2 MHz, and ± 19.0 MHz for **1** and at ± 2.7 MHz, ± 6.1 MHz, and ± 12.1 MHz for **Q8R1**. In addition, Figure 8c reveals two weak and sharp peaks on top of the dipolar spectrum of **1**. These peaks appear at 7.8 and 10.7 MHz and are due to incomplete suppression of deuterium and nitrogen ESEEM frequencies. Since both ESEEM peaks are fairly weak, no further attempts were taken here to remove these artifacts. Note that such ESEEM artifacts are not seen for **Q8R1**, which reveals that the suppression of deuterium ESEEM worked more efficiently for this sample.

Next, the distance distributions $P(r)$ and the distributions of the ξ angle $P(\xi)$ were extracted from the obtained dipolar spectra of **1** and **Q8R1** using the home-written program DipFit, which is based on the equations derived above and uses a genetic algorithm for the fitting of the experimental dipolar spectra. During this analysis, it turned out that good fits to the experimental spectra can be obtained only if the spectral weights given by Equation (15) are taken into account.

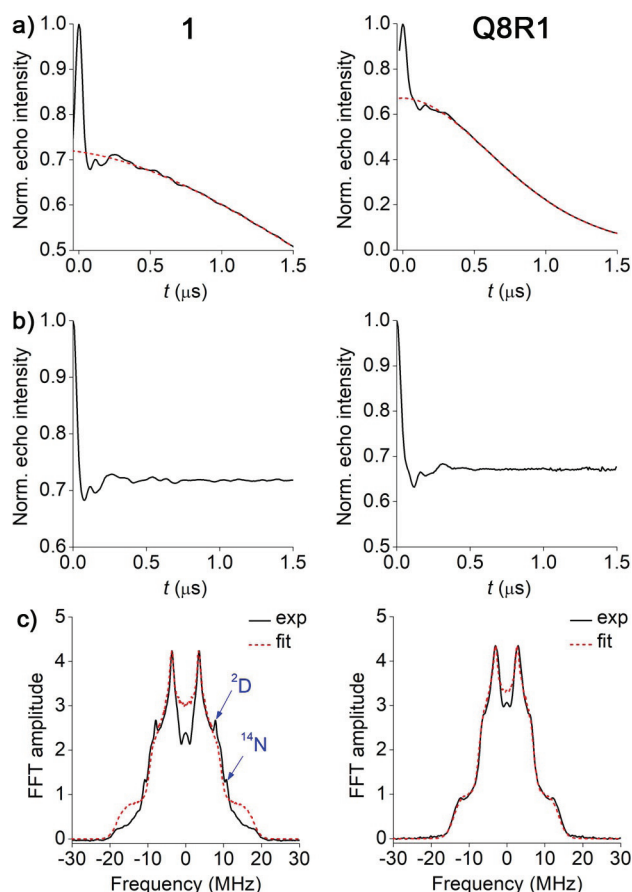


Figure 8. RIDME on **1** and **Q8R1**. a) The original RIDME time traces (black) and their background fits (red). b) The background-corrected RIDME time traces, and c) their FFTs (black) together with the fits (red) obtained by means of the program DipFit. The ESEEM artifacts are marked by arrows.

Moreover, these weights were found to be dependent on the temperature, so that even 0.5 K deviation at a temperature from 3 K lead to a prominent change in the calculated fits (Figure S10 and S11).

Since the precision of the experimentally measured temperature was above 1 K, the temperature was also optimized by DipFit. As can be seen from Figure 8c, DipFit provided good fits to both RIDME spectra. The optimized parameters of $P(r)$ and $P(\xi)$ are listed in Table 1, and the corresponding distributions are depicted in Figure 9. The optimized values of the temperature deviate from 3 K by not more than 1.4 K, which is within the experimental error of the temperature measurement.

Comparison to in silico structures

To check whether the RIDME-derived distributions $P(r)$ and $P(\xi)$ are in agreement with the structure and dynamics of the model systems, MD and MtsslWizard simulations were carried out for **1** and **Q8R1**, respectively. These simulations yielded the shaded distributions in Figure 9 and the mean values and standard deviations given in Table 1.

Comparing the RIDME- and MD-derived parameters for **1** reveals that they agree very nicely with each other. The mean

Table 1. RIDME-derived distance and angular parameters of **1** and **Q8R1** and their in silico predictions.

Molecule	RIDME data analysis ^[a]					MD/MtsslWizard simulations ^[c]			
	$\langle r \rangle$ (nm)	σ_r (nm)	$\langle \xi \rangle$ (°)	σ_ξ (°)	T (K) ^[b]	$\langle r \rangle$ (nm)	σ_r (nm)	$\langle \xi \rangle$ (°)	σ_ξ (°)
1	2.52 ± 0.03	0.06 ± 0.05	89 ± 4	6 ± 3	1.6 ± 0.2	2.46	0.06	90	15
Q8R1	2.77 ± 0.01	0.08 ± 0.02	85 ± 3	6 ± 1	2.1 ± 0.1	3.19	0.23	80	5

[a] The error estimation procedure is described in detail in Chapter 5 of the Supporting Information. [b] The temperature was optimized in the range 3(±2) K, given by the precision of the temperature measurement. [c] MD simulations were done on **1** and MtsslWizard simulation on **Q8R1**.

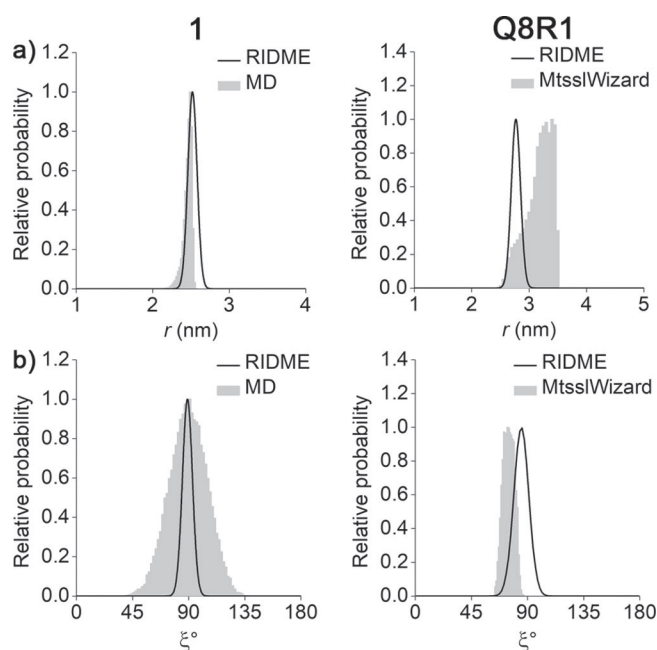


Figure 9. Comparison of the RIDME-derived distributions with the corresponding in silico predictions for **1** (left column) and **Q8R1** (right column). a) $P(r)$, and b) $P(\xi)$.

distances deviate by less than 1 Å and also the distance distribution widths agree (Table 1). Their shapes are slightly different (Figure 9a), because the distance distribution in DipFit was assumed to have a Gaussian shape. The mean ξ angles are also consistent for both MD and RIDME (Table 1). The only parameter of **1** that differ between the two methods is the width of the $P(\xi)$ distribution. The RIDME-derived width suggests that the ξ angle has a well-defined value in **1**, whereas MD predicts a much broader distribution of this angle (Figure 9b). One possible explanation for this difference might be that the MD simulation overestimates the conformational flexibility as a result of using an implicit solvation model, which neglects properties of the solvent such as the viscosity.

A good agreement between the RIDME-derived distributions and their in silico predictions was also achieved for **Q8R1**. Although the overall MtsslWizard-derived distance distribution is broader than the RIDME-derived distribution, the shoulder matches perfectly with the distance peak determined by RIDME (Figure 9a). Note that in silico methods like MtsslWizard are prone to overestimating the conformational ensemble of the R1 side chain (Figure S12), especially, when the spin label

has energetically favorable conformation.^[61] Also both $P(\xi)$ distributions of **Q8R1** agree well with each other. The mean ξ angle differ by 10° only and the corresponding distribution widths by 1° only (Table 1). Note that the small difference between the mean ξ angles may be caused by a slight noncollinearity of the g_{zz} axis of the high-spin Fe^{3+} and the $\text{Fe}-\text{N}_\epsilon(\text{H93})$ bond, which is neglected in the simulations.

Conclusions

The methodology of RIDME measurements on high-spin Fe^{3+} /nitroxide spin pairs was developed and successfully tested on two model systems. The large ZFS of the high-spin Fe^{3+} ion was explicitly taken into account in the calculation of the dipolar spectrum of this spin pair, revealing a significant deviation of the predicted spectrum from the Pake doublet and its dependence on the relative orientation of the distance vector with respect to the effective g -tensor of the high-spin Fe^{3+} . The comparison of the RIDME-derived distributions $P(r)$ and $P(\xi)$ with their in silico predictions revealed very good consistency, proving that not only $P(r)$ but also $P(\xi)$ can be reliably determined. Thus, a solid proof for applicability and high fidelity of RIDME for the distance and ξ angle measurements on Fe^{3+} /nitroxide spin pairs is provided. This result lays the foundation for further applications of PDS to the highly relevant class of heme containing proteins, enabling for example, the localization of high-spin Fe^{3+} ions within the fold of protein structures by trilateration.

Acknowledgements

This work was funded by the German Research Foundation (DFG) within the collaborative research center SFB813 "Chemistry at Spin Centres" (projects A6 and Z2).

Conflict of interest

The authors declare no conflict of interest.

Keywords: biophysics • DEER spectroscopy • EPR spectroscopy • nitroxide • pulsed dipolar spectroscopy

[1] A. D. Milov, K. M. Salikhov, M. D. Shchirov, *Fiz. Tverd. Tela* **1981**, *23*, 975–982.

- [2] R. E. Martin, M. Pannier, F. Diederich, V. Gramlich, M. Hubrich, H. W. Spiess, *Angew. Chem. Int. Ed.* **1998**, *37*, 2833–2837; *Angew. Chem.* **1998**, *110*, 2993–2998.
- [3] S. Saxena, J. H. Freed, *Chem. Phys. Lett.* **1996**, *251*, 102–110.
- [4] G. Jeschke, M. Pannier, A. Godt, H. W. Spiess, *Chem. Phys. Lett.* **2000**, *331*, 243–252.
- [5] L. V. Kulik, S. A. Dzuba, I. A. Grigoryev, Y. D. Tsvetkov, *Chem. Phys. Lett.* **2001**, *343*, 315–324.
- [6] S. Milikisyants, F. Scarpelli, M. G. Finiguerra, M. Ubbink, M. Huber, *J. Magn. Reson.* **2009**, *201*, 48–56.
- [7] *Structure and Bonding, Vol. 152* (Eds.: C. R. Timmel, J. R. Harmer), *Structural Information from Spin-Labels and Intrinsic Paramagnetic Centres in the Biosciences*, Springer, Heidelberg, **2013**.
- [8] L. Garbuio, E. Bordignon, E. K. Brooks, W. L. Hubbell, G. Jeschke, M. Yulikov, *J. Phys. Chem. B* **2013**, *117*, 3145–3153.
- [9] D. Abdullin, N. Florin, G. Hagelueken, O. Schiemann, *Angew. Chem. Int. Ed.* **2015**, *54*, 1827–1831; *Angew. Chem.* **2015**, *127*, 1847–1851.
- [10] E. G. B. Evans, M. J. Pushie, K. A. Markham, H.-W. Lee, G. L. Millhauser, *Structure* **2016**, *24*, 1057–1067.
- [11] Z. Yang, M. R. Kurpiewski, M. Ji, J. E. Townsend, P. Mehta, L. Jen-Jacobson, S. Saxena, *Proc. Natl. Acad. Sci. USA* **2012**, *109*, E993–E1000.
- [12] E. Narr, A. Godt, G. Jeschke, *Angew. Chem. Int. Ed.* **2002**, *41*, 3907–3910; *Angew. Chem.* **2002**, *114*, 4063–4066.
- [13] I. M. C. Van Amsterdam, M. Ubbink, G. W. Canters, M. Huber, *Angew. Chem. Int. Ed.* **2003**, *42*, 62–64; *Angew. Chem.* **2003**, *115*, 64–67.
- [14] C. W. M. Kay, H. El Mkami, R. Cammack, R. W. Evans, *J. Am. Chem. Soc.* **2007**, *129*, 4868–4869.
- [15] B. E. Bode, J. Plackmeyer, T. F. Prisner, O. Schiemann, *J. Phys. Chem. A* **2008**, *112*, 5064–5073.
- [16] B. E. Bode, J. Plackmeyer, M. Bolte, T. F. Prisner, O. Schiemann, *J. Organomet. Chem.* **2009**, *694*, 1172–1179.
- [17] J. E. Lovett, A. M. Bowen, C. R. Timmel, M. W. Jones, J. R. Dilworth, D. Caprotti, S. G. Bell, L. L. Wong, J. Harmer, *Phys. Chem. Chem. Phys.* **2009**, *11*, 6840–6848.
- [18] Z. Yang, D. Kise, S. Saxena, *J. Phys. Chem. B* **2010**, *114*, 6165–6174.
- [19] A. M. Bowen, M. W. Jones, J. E. Lovett, T. G. Gaule, M. J. McPherson, J. R. Dilworth, C. R. Timmel, J. R. Harmer, *Phys. Chem. Chem. Phys.* **2016**, *18*, 5981–5994.
- [20] A. Meyer, D. Abdullin, G. Schnakenburg, O. Schiemann, *Phys. Chem. Chem. Phys.* **2016**, *18*, 9262–9271.
- [21] D. Banerjee, H. Yagi, T. Huber, G. Otting, D. Goldfarb, *J. Phys. Chem. Lett.* **2012**, *3*, 157–160.
- [22] D. Akhmetzyanov, J. Plackmeyer, B. Endeward, V. P. Denysenko, T. F. Prisner, *Phys. Chem. Chem. Phys.* **2015**, *17*, 6760–6766.
- [23] I. Kaminker, M. Bye, N. Mendelman, K. Gislason, S. T. Sigurdsson, D. Goldfarb, *Phys. Chem. Chem. Phys.* **2015**, *17*, 15098–15102.
- [24] A. Martorana, Y. Yan, Y. Zhao, Q.-F. Li, X.-C. Su, D. Goldfarb, *Dalton Trans.* **2015**, *44*, 20812–20816.
- [25] A. Meyer, O. Schiemann, *J. Phys. Chem. A* **2016**, *120*, 3463–3472.
- [26] A. Giannoulis, K. Ackermann, P. E. Spindler, C. Higgins, D. B. Cordes, A. M. Z. Slawin, T. F. Prisner, B. E. Bode, *Phys. Chem. Chem. Phys.* **2018**, *20*, 11196–11205.
- [27] P. E. Spindler, S. J. Glaser, T. E. Skinner, T. F. Prisner, *Angew. Chem. Int. Ed.* **2013**, *52*, 3425–3429; *Angew. Chem.* **2013**, *125*, 3509–3513.
- [28] A. V. Astashkin, B. O. Elmore, W. Fan, J. G. Guillemette, C. Feng, *J. Am. Chem. Soc.* **2010**, *132*, 12059–12067.
- [29] A. V. Astashkin, A. Rajapakshe, M. J. Cornelison, K. Johnson-Winters, J. H. Enemark, *J. Phys. Chem. B* **2012**, *116*, 1942–1950.
- [30] D. Abdullin, F. Duthie, A. Meyer, E. S. Müller, G. Hagelueken, O. Schiemann, *J. Phys. Chem. B* **2015**, *119*, 13534–13542.
- [31] C. L. Motion, J. E. Lovett, S. Bell, S. L. Cassidy, P. A. S. Cruickshank, D. R. Bolton, R. I. Hunter, H. El Mkami, S. Van Doorslaer, G. M. Smith, *J. Phys. Chem. Lett.* **2016**, *7*, 1411–1415.
- [32] C. Elsässer, M. Brecht, R. Bittl, *J. Am. Chem. Soc.* **2002**, *124*, 12606–12611.
- [33] M. M. Roessler, M. S. King, A. J. Robinson, F. A. Armstrong, J. Harmer, J. Hirst, *Proc. Natl. Acad. Sci. USA* **2010**, *107*, 1930–1935.
- [34] A. M. Bowen, E. O. D. Johnson, F. Mercuri, N. J. Hoskins, R. Qiao, J. S. O. McCullagh, J. E. Lovett, S. G. Bell, W. Zhou, C. R. Timmel, L. Lok Wong, J. R. Harmer, *J. Am. Chem. Soc.* **2018**, *140*, 2514–2527.
- [35] A. Kawamori, N. Katsuta, H. Mino, A. Ishii, J. Minagawa, T.-A. Ono, *J. Biol. Phys.* **2002**, *28*, 413–426.
- [36] H. Nagashima, M. Asada, H. Mino, *Biophys. Physicobiol.* **2018**, *15*, 45–50.
- [37] D. Goldfarb, *Struct. Bonding (Berlin)* **2012**, *152*, 163–204.
- [38] G. Jeschke, V. Chechik, P. Ionita, A. Godt, H. Zimmermann, J. Banham, C. R. Timmel, D. Hilger, H. Jung, *Appl. Magn. Reson.* **2006**, *30*, 473–498.
- [39] M. H. Rakowsky, A. Zecevic, G. R. Eaton, S. S. Eaton, *J. Magn. Reson.* **1998**, *131*, 97–110.
- [40] R. Maurus, C. M. Overall, R. Bogumil, Y. Luo, A. G. Mauk, M. Smith, G. D. Brayer, *Biochim. Biophys. Acta Protein Struct. Mol. Enzymol.* **1997**, *1341*, 1–13.
- [41] G. Hagelueken, R. Ward, J. H. Naismith, O. Schiemann, *Appl. Magn. Reson.* **2012**, *42*, 377–391.
- [42] G. Hagelueken, D. Abdullin, R. Ward, O. Schiemann, *Mol. Phys.* **2013**, *111*, 2757–2766.
- [43] A. Abragam, B. Bleaney, *Electron Paramagnetic Resonance of Transition Ions*, Oxford University Press, Oxford, **1970**.
- [44] J. R. Pilbrow, *Transition Ion Electron Paramagnetic Resonance*, Oxford University Press, New York, **1990**.
- [45] B. J. Gaffney, G. R. Eaton, S. S. Eaton, *J. Phys. Chem. B* **1998**, *102*, 5536–5541.
- [46] Y. Zhou, B. E. Bowler, G. R. Eaton, S. S. Eaton, *J. Magn. Reson.* **2000**, *144*, 115–122.
- [47] F. Trandafir, P. Heerdt, M. Fittipaldi, E. Vinck, S. Dewilde, L. Moens, S. Van Doorslaer, *Appl. Magn. Reson.* **2007**, *31*, 553–572.
- [48] M. Fittipaldi, I. García-Rubio, F. Trandafir, I. Gromov, A. Schweiger, A. Bouwen, S. Van Doorslaer, *J. Phys. Chem. B* **2008**, *112*, 3859–3870.
- [49] S. Razzaghi, M. Qi, A. I. Nalepa, A. Godt, G. Jeschke, M. Yulikov, *J. Phys. Chem. Lett.* **2014**, *5*, 3970.
- [50] A. V. Astashkin, *Methods Enzymol.* **2015**, *563*, 251–284.
- [51] J. J. Jassoy, A. Berndhäuser, F. Duthie, S. P. Kühn, G. Hagelueken, O. Schiemann, *Angew. Chem. Int. Ed.* **2017**, *56*, 177–181; *Angew. Chem.* **2017**, *129*, 183–187.
- [52] K. Keller, A. Doll, M. Qi, A. Godt, G. Jeschke, M. Yulikov, *J. Magn. Reson.* **2016**, *272*, 108–113.
- [53] K. Keller, V. Mertens, M. Qi, A. I. Nalepa, A. Godt, A. Savitsky, G. Jeschke, M. Yulikov, *Phys. Chem. Chem. Phys.* **2017**, *19*, 17856–17876.
- [54] A. Collauto, V. Frydman, M. D. Lee, E. H. Abdelkader, A. Feintuch, J. D. Swarbrick, B. Graham, G. Otting, D. Goldfarb, *Phys. Chem. Chem. Phys.* **2016**, *18*, 19037–19049.
- [55] C. Scholes, *J. Chem. Phys.* **1970**, *52*, 4890–4895.
- [56] A. F. Bedilo, A. G. Maryasov, *J. Magn. Reson. Ser. A* **1995**, *116*, 87–96.
- [57] D. Abdullin, N. Fleck, C. Klein, P. Brehm, S. Spicher, A. Lützen, S. Grimme, O. Schiemann, *Chem. Eur. J.* **2019**, *25*, 2586–2596.
- [58] D. Abdullin, G. Hagelueken, R. I. Hunter, G. M. Smith, O. Schiemann, *Mol. Phys.* **2015**, *113*, 544–560.
- [59] J. Nehrkor, J. Telsler, K. Holdack, S. Stoll, A. Schnegg, *J. Phys. Chem. B* **2015**, *119*, 13816–13824.
- [60] S. Grimme, C. Bannwarth, P. Shushkov, *J. Chem. Theory Comput.* **2017**, *13*, 1989–2009.
- [61] D. Abdullin, G. Hagelueken, O. Schiemann, *Phys. Chem. Chem. Phys.* **2016**, *18*, 10428–10437.

Manuscript received: March 2, 2019

Accepted manuscript online: April 24, 2019

Version of record online: June 6, 2019

CHEMISTRY

A **European** Journal

Supporting Information

Pulsed EPR Dipolar Spectroscopy under the Breakdown of the High-Field Approximation: The High-Spin Iron(III) Case

Dinar Abdullin,^[a] Hideto Matsuoka,^[a, b] Maxim Yulikov,^[c] Nico Fleck,^[a] Christoph Klein,^[a, d] Sebastian Spicher,^[e] Gregor Hagelueken,^[a] Stefan Grimme,^[e] Arne Lützen,^[d] and Olav Schiemann^{*[a]}

chem_201900977_sm_miscellaneous_information.pdf

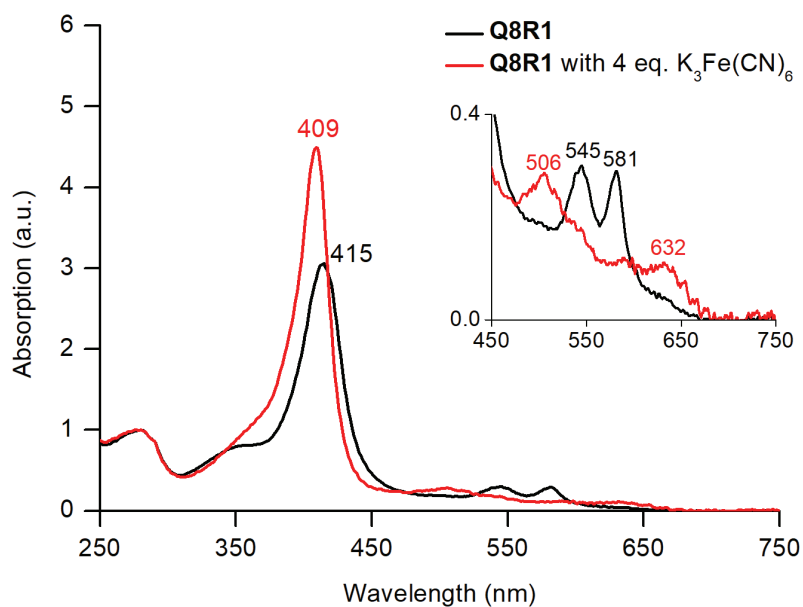
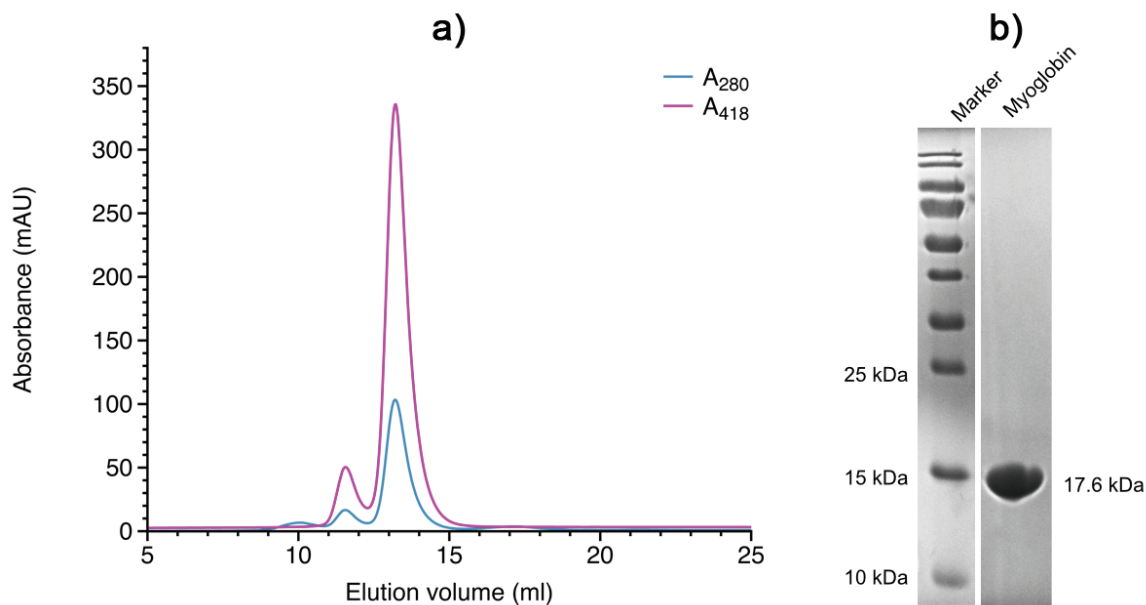
Table of Contents

1 Cloning, protein expression, purification and spin labelling of the met-myoglobin mutant Q8R1	3
2 Characterization of the met-myoglobin mutant Q8R1 by continuous-wave EPR	5
3 Inversion recovery of the Fe ³⁺ spin center in 1 and Q8R1	7
4 Nitroxide ESEEM measurements on 1 and Q8R1	9
5 Analysis of the RIDME data by means of the program DipFit.....	12
6 MtsslWizard and MMM simulations on the met-myoglobin mutant Q8R1	15
7 MD simulations on the model compound 1	16
8 The atomic coordinates of 1	17
References	21

1 Cloning, protein expression, purification and spin labelling of the met-myoglobin mutant Q8R1

The DNA sequence for myoglobin from equine heart muscle and its Q8C mutant for spin labelling purposes were synthesized. The gene was cloned into the pBADHisTEV vector (Huanting Liu, University of St Andrews) and transformed into *E. coli* C43 cells. A single colony was picked and grown overnight in 15 ml LB-medium supplemented with 50 µg/ml ampicillin (LB_{amp}). On the next day, 1 l LB_{amp} medium was inoculated with 10 ml of the o/n culture and grown at 37°C with shaking (180 rpm) until an OD₆₀₀ of 0.5-1.0 was reached. Protein production was then induced by adding 0.2% L-arabinose. 2 mM 5-aminolevulinic acid were additionally added to increase the amount of bound heme in myoglobin. The culture was grown for 4 h at 37°C with shaking (180 rpm). Cells were harvested by centrifugation at 4.000xg and the pellets re-suspended in buffer A (50 mM Tris-Cl pH 8.0, 50 mM NaCl). The suspension was lysed in a cell disruptor (Constant Systems). The lysate was centrifuged for 20 min at 48.000xg at 4°C and the supernatant was bound to ~1.5 ml NiNTA resin equilibrated with buffer A. After incubation for 1 h at room temperature, the beads were successively washed with 100 ml buffer A, 50 ml buffer A with 1 mM TCEP, 50 ml buffer A and then labelled with 15 ml buffer A including 0.16 mM MTSSL. To elute the labelled protein, 4 ml of TEV protease were added and the beads were incubated for 3 h at room temperature with slow rolling and then overnight at 4°C. The cleaved His-tag and TEV protease were removed by running a second Ni column on the next day. The flow through was diluted with an equal volume of 50 mM Tris-Cl pH 8.0 and applied to a MonoQ 5/50 column. The myoglobin was in the flow-through of this column and was concentrated to 5 ml. The sample was then loaded onto a Superdex HiLoad 75 16/600 gelfiltration column equilibrated with gelfiltration buffer (50 mM Tris pH 8.0 and 150 mM NaCl). Protein containing fractions of the eluate were combined and concentrated. The protein concentration was measured and a 4-fold excess of K₃[Fe(CN₆)] was added.¹ The color of the solution changed from red to brown, indicating the formation of met-myoglobin. The conversion of myoglobin into the met-form was also confirmed by means of UV-Vis measurements, which revealed the typical bands²⁻⁴ of met-myoglobin after the treatment with K₃[Fe(CN₆)] (Figure S2). Finally, the sample was loaded onto a G25 column, equilibrated with 100 mM NaPi in D₂O, pH 7.5. For EPR

measurements, the sample was concentrated to a final concentration of 100 μM and supplemented with 20% glycerol- d_8 .



2 Characterization of the met-myoglobin mutant Q8R1 by continuous-wave EPR

To characterize both spin centers of **Q8R1**, continuous-wave EPR (cw-EPR) were recorded at two different temperatures, 10 K and 300 K. All cw-EPR experiments were done on an X-Band EPR spectrometer EMXmicro (Bruker) equipped with the super-high-quality resonator (SHQ) using a microwave power of 16.75 mW (10 dB), a modulation frequency of 100 kHz, a modulation amplitude of 0.1 mT, and a time constant of 20.48 ms. For 10 K, the resonator was mounted inside a continuous flow helium cryostat ER4112HE (Bruker), whose temperature was controlled by a Mercury iTC system (Oxford Instruments).

The cw-EPR spectrum of **Q8R1** at 10 K is depicted in Figure S3 together with the cw-EPR spectrum of the wild-type met-myoglobin (equine skeletal muscle, Sigma Aldrich). Both spectra show a typical high-spin Fe^{3+} signal and no traces of low-spin Fe^{3+} . The spectrum of **Q8R1** contains additionally the nitroxide signal at g -values around 2, which overlaps with the g_{zz} -component of the high-spin Fe^{3+} signal. The high-spin Fe^{3+} signal of both wild-type met-myoglobin and Q8R1 were simulated by means of the program EasySpin,⁵ yielding the EPR parameters (Table S1) that are in agreement with the parameters reported earlier.⁶

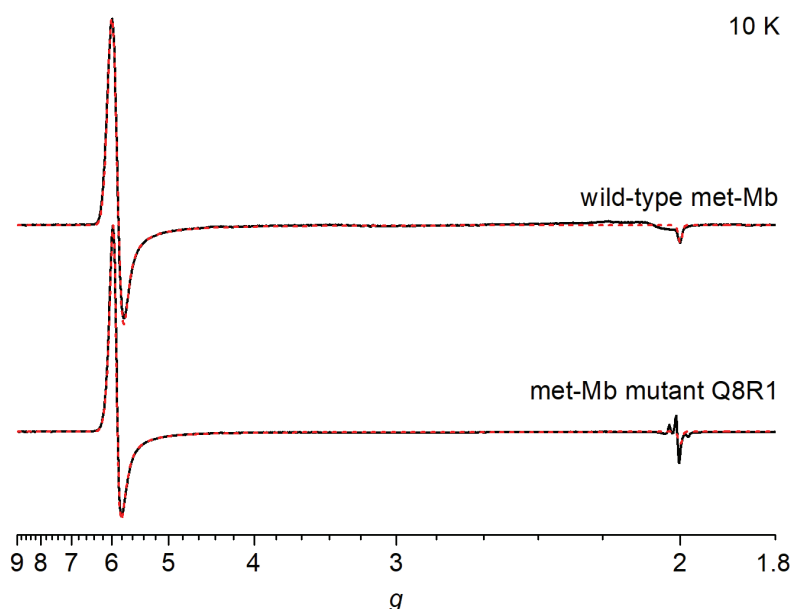


Figure S3. X-band cw-EPR spectra of wild-type met-myoglobin (top) and its mutant **Q8R1** (bottom). Both spectra were measured at 10 K. The high-spin Fe^{3+} signal in both spectra was simulated by means of the program EasySpin, which yielded the fits that are depicted by red dashed lines. The parameters of the simulations are listed in Table S1.

Table S1. EPR parameters of the high-spin Fe³⁺ ion in wild-type met-myoglobin and its mutant **Q8R1**.

Parameter	Wild-type of met-myoglobin	Met-myoglobin mutant Q8R1
<i>g</i>	[1.98, 1.98, 2.00]	[1.98, 1.98, 2.00]
<i>D, E</i> / cm ⁻¹	9.26, 0.0023	9.26, 0.0023
<i>H</i> -strain ^a / MHz	[400, 400, 50]	[200, 450, 50]

^a For definition see: <http://easyspin.org/documentation/broadenings.html>

The cw-EPR spectrum of **Q8R1** at 300 K (Figure S4) reveals the nitroxide signal, which is typical for the MTSL spin label bound to the protein. The corresponding EPR parameters of the nitroxide center were determined by means of the program EasySpin⁵ and listed in Table S2. In addition, the intensity of the nitroxide spectrum was compared to the intensity of a reference sample, which contained 100 μM MTSL in the same buffer as **Q8R1**. This comparison revealed that the sample of metmyoglobin **Q8R1** is quantitatively labelled.

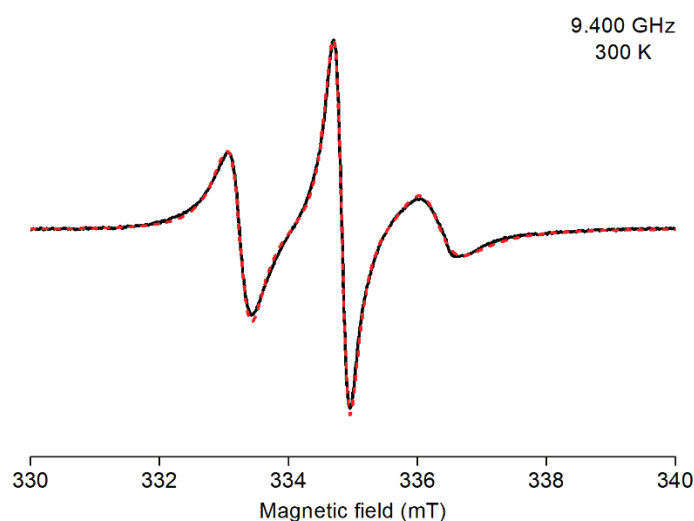


Figure S4. X-band cw-EPR spectrum of met-myoglobin **Q8R1** (black) at 300 K. The nitroxide signal was simulated by means of the program EasySpin, which yielded the fits that are depicted by red dashed lines. The parameters of the simulations are listed in Table S2.

Table S2. EPR parameters of the nitroxide center in the met-myoglobin mutant **Q8R1**.

Parameter	Value
<i>g</i>	[2.0088, 2.0047, 2.0037]
<i>A</i> (¹⁴ N) / MHz	[17.5 21.5 96.9]
<i>τ_c</i> / ns	2.44
ΔH_{pp} (inhomogeneous) / MHz	0.7

3 Inversion recovery of the Fe³⁺ spin center in **1** and Q8R1

The inversion recovery measurements were carried out on an ELEXSYS E580 (Bruker) spectrometer with a Q-band resonator ER5106QT-2 (Bruker). All microwave pulses were amplified via a 150 W TWT amplifier (model 187Ka). To obtain the temperature of about 3 K, a continuous flow helium cryostat CF935 (Oxford Instruments), a temperature control system ITC 503 (Oxford Instruments), and a vacuum pump EPS40 (Oxford Instruments) were employed. The inversion recovery experiments were done using the pulse sequence π - t - $\pi/2$ - τ - π - τ - $echo$. The length of the $\pi/2$ - and π -pulses was set to 10 and 20 ns, respectively, and τ was set to 300 ns. The initial value of t was set to 400 ns and, in the course of the experiment, was incremented 512 times with a constant step ranging from 500 ns to 20 μ s. The shot repetition time was adjusted in accordance to the increment of t and ranged from 500 μ s to 20 ms. To suppress unwanted echoes, 4-step phase cycling was employed.

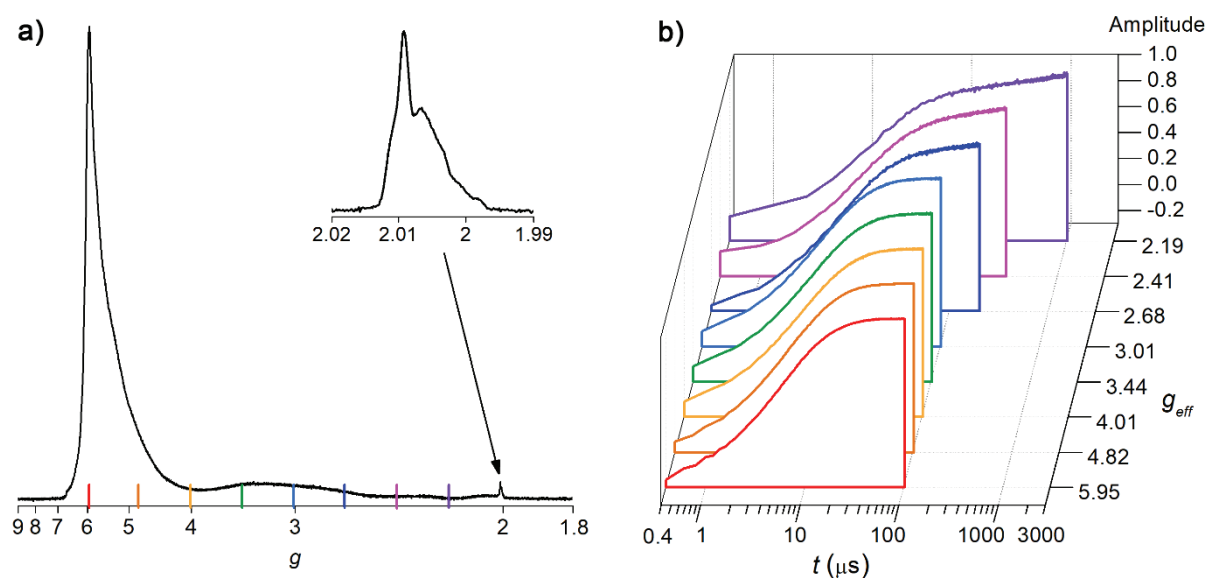


Figure S5. Inversion recovery measurements on the high-spin Fe³⁺ center in **1** at Q-band at 3 K. **a)** The detection positions are depicted as colored bars. The magnified nitroxide spectrum of **1** is shown in the offset. **b)** The obtained inversion recovery time traces are plotted against the effective g value of high-spin Fe³⁺. The color code corresponds to the color code of the detection position **a)**.

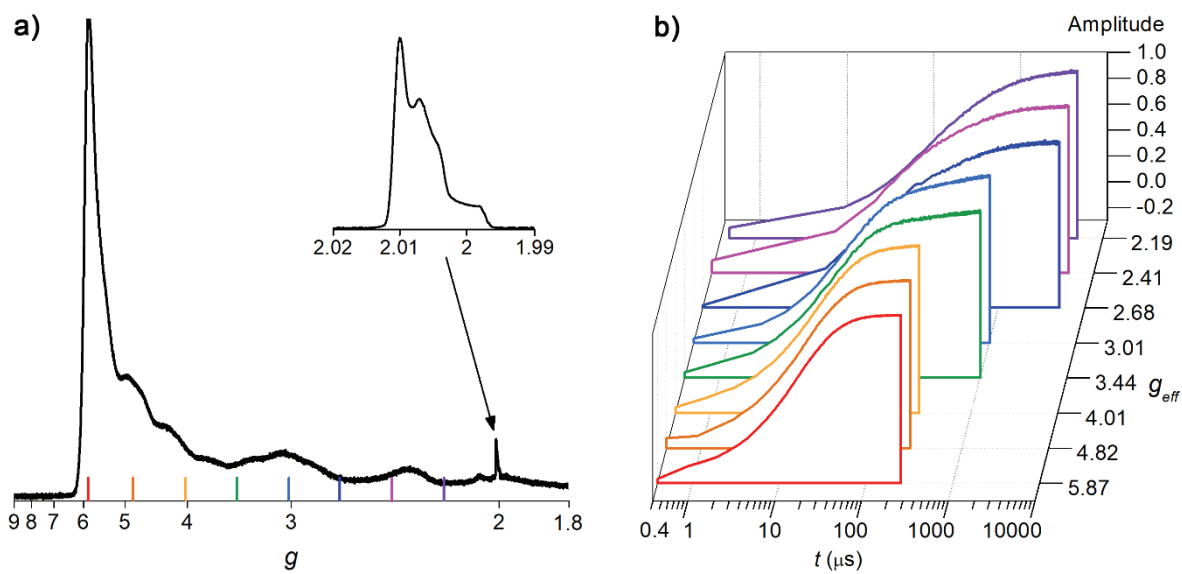


Figure S6. Inversion recovery measurements on the high-spin Fe^{3+} center in **Q8R1** at Q-band at 3 K. **a)** The detection positions are depicted as colored bars. The magnified nitroxide spectrum of **Q8R1** is shown in the offset. **b)** The obtained inversion recovery time traces are plotted against the effective g value of high-spin Fe^{3+} . The color code corresponds to the color code of the detection position **a)**.

4 Nitroxide ESEEM measurements on **1** and **Q8R1**

The electron spin echo envelop modulation (ESEEM) measurements were carried out on an ELEXSYS E580 (Bruker) spectrometer with a Q-band resonator ER5106QT-2 (Bruker). All microwave pulses were amplified via a 150 W TWT amplifier (model 187Ka). To obtain the temperature of about 3 K, a continuous flow helium cryostat CF935 (Oxford Instruments), a temperature control system ITC 503 (Oxford Instruments), and a vacuum pump EPS40 (Oxford Instruments) were employed. The ESEEM experiments were done using the two-pulse sequence $\pi/2$ - t - π - t -echo. The length of the $\pi/2$ - and π -pulse was set to 10 and 20 ns, respectively. The initial value of t was set to 200 ns and, in course of the experiment, was incremented 2048 times with a constant step of 8 ns. The short repetition time was set to 100 ms. To suppress unwanted echoes, 2-step phase cycling was employed. For both systems, **1** and **Q8R1**, two-pulse ESEEM time traces were acquired at three different field positions on the nitroxide, called here positions A, B, and C (Figure S7a). Position A corresponds to the maximum of the nitroxide spectrum and contains contributions from all three components of the ^{14}N hyperfine tensor (A_{xx} , A_{yy} , A_{zz}). Note that this position was also used for detection of the RIDME time traces. Position C is selective for the A_{zz} component of the ^{14}N hyperfine tensor. Position B represents an intermediate case between positions A and C. All ESEEM time traces are depicted in Figure S7b and the corresponding FFT spectra are shown in Figure S7c.

The ESEEM spectra of **1** reveal three distinct peaks. Two of them are almost independent on the chosen detection position and appear at about 7.8 and 15.6 MHz. These peaks can be assigned to the single and double Larmor frequency of deuterium (at 1.1984 T), which is present in a large amount in the solvent of **1** (THF- d_8). The third ESEEM peak depends strongly on the detection position. It appears at 10.8 MHz and 9.6 MHz for the positions A and B, respectively, but it is absent in the spectrum for the position C. Such behavior suggest that this peak should originate from the ^{14}N nucleus of the nitroxide center, whose ESEEM frequency is determined by a combination of the ^{14}N Larmor frequency and the hyperfine coupling constant $A(^{14}\text{N})$.⁷ Since the value of hyperfine coupling constant is orientation dependent, it will yield different ESEEM frequencies for different detection positions. For the x - and y -components of the ^{14}N hyperfine tensor, which are in the order of 7-12 MHz, such combination yields an observable peak at around 10.8 MHz

(positions A and B). In contrast, the z-component of the ^{14}N hyperfine tensor (~ 93 MHz) is so large that no ESEEM peak can be seen (position C).

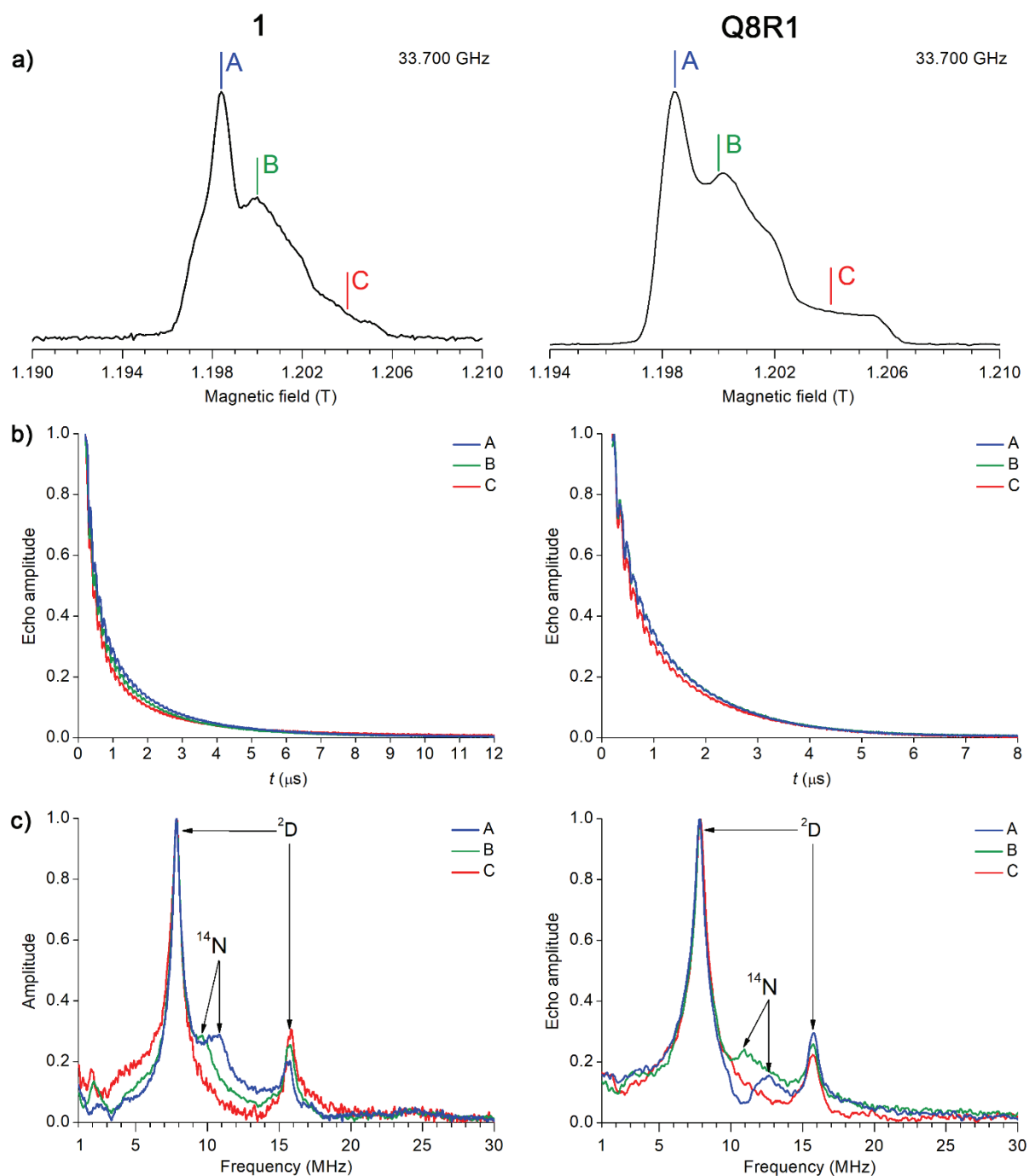


Figure S7. Two-pulse ESEEM measurements on the nitroxide center of **1** (left column) and **Q8R1** (right column) at Q-band at 3 K. **a)** The detection positions in the ESEEM experiments are depicted as colored bars. **b)** The ESEEM time traces and **c)** the corresponding ESEEM spectra plotted for the three different detection positions. The ESEEM peaks are marked by arrows.

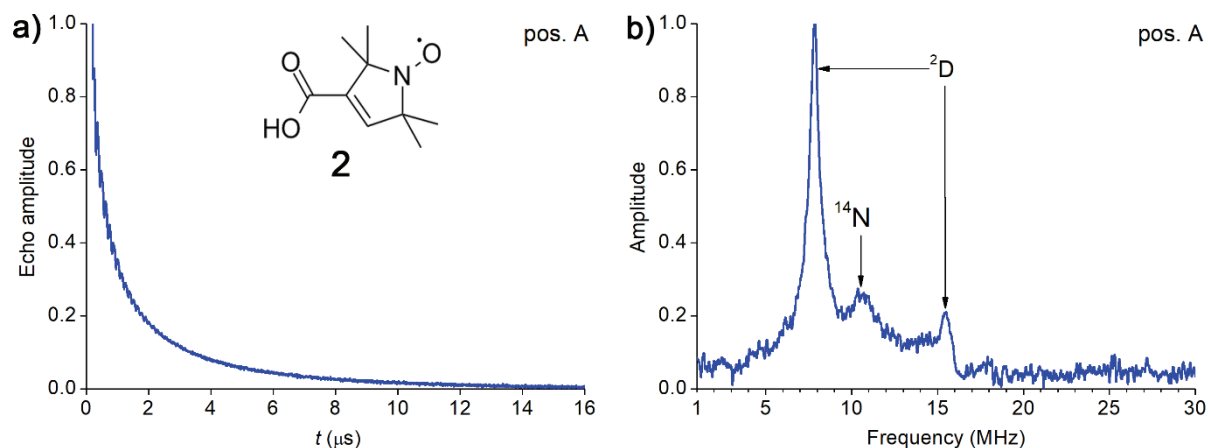


Figure S8. Two-pulse ESEEM measurements on nitroxide **2** at Q-band at 3 K. **a)** The ESEEM time traces and **b)** the corresponding ESEEM spectra are shown for the position A (see Figure S7a). The ESEEM peaks are marked by arrows.

In addition, to check that the ^{14}N ESEEM peak originates from the nitroxide center and not from the nitrogen nuclei of the porphyrin, ESEEM experiments were performed on the porphyrin-free derivative of **1**, the nitroxide **2** (Figure S8a). These experiments revealed that the ESEEM spectrum of **2** indeed contains the peak at 10.8 MHz for the position A (Figure S8b). Similar to the model compound **1**, the ESEEM spectra of **Q8R1** contains three peaks, with two of them assigned to deuterium and the other one to the ^{14}N nucleus of the nitroxide center. The only difference to the spectra of **1** is that the ^{14}N ESEEM peaks of **Q8R1** appear at slightly higher frequencies, at 12.7 MHz and 10.9 MHz for the positions A and B, respectively. Such discrepancy maybe due to a slight difference in the hyperfine coupling constants $A(^{14}\text{N})$ between both molecules.

Since the nitroxide ESEEM penetrates into the RIDME time traces of **1** and **Q8R1** and causes unwanted artifacts in the corresponding RIDME spectra, additional steps have to be taken during the RIDME measurements to suppress them. Because the deuterium ESEEM peak at 7.8 MHz is more intense than the other two ESEEM peaks, it was the main target of the ESEEM suppression in the present study. The suppression of this peak was done in accordance to the method proposed by Yulikov and co-workers.⁸ The idea behind this method is to average the RIDME time trace over one period of ESEEM modulation. To do this, the initial values of intervals τ_1 and τ_2 in the RIDME sequence were incremented consecutively 8 times with a step of 16 ns, resulting in 64 individual RIDME time traces. The sum of these time traces yielded the averaged time trace with the ESEEM artifacts suppressed.

5 Analysis of the RIDME data by means of the program DipFit

The program DipFit was developed to enable the determination of distance and angular constraints from the RIDME spectra acquired on the spin pairs consisting of a high-spin Fe^{3+} and a nitroxide. The idea behind this program is essentially the fitting of RIDME spectra using a distance distribution, $P(r)$, and the angular distributions, $P(\xi)$ and $P(\varphi)$, as fitting parameters (for definitions of r , ξ , and φ see Figure 3 in the main text). The present study considers only the case when the ZFS tensor of a high-spin Fe^{3+} ion is axial ($E = 0$) and, therefore, only $P(r)$ and $P(\xi)$ are required for the fitting. To reduce the number of fitting parameters, both distributions were parameterized. Such parameterization was done by assuming that $P(r)$ and $P(\xi)$ have Gaussian shapes and, consequently, can be described by two parameters – a mean value ($\langle r \rangle$ and $\langle \xi \rangle$) and a standard deviation (σ_r and σ_ξ). The values of r and ξ were supposed to have no correlation between each other. In addition to these parameters, the temperature of the RIDME experiment, T , was considered as a fitting parameter. As a result, the fitting of the RIDME spectra was done using five parameters: $\langle r \rangle$, σ_r , $\langle \xi \rangle$, σ_ξ , and T . The calculation of the fit was performed based on Equation 11 (see the main text). Averaging of the dipolar frequency (ν_{dd}) over all possible orientations of a spin pair with respect to the applied magnetic field and over the distributions $P(r)$ and $P(\xi)$ was done by means of the Monte-Carlo method with 10^6 random samples. The components of the calculated spectrum that correspond to different effective g -values of the high-spin Fe^{3+} ion were weighted in accordance to Equation 15 (see the main text). After the calculation, the goodness of the fit was evaluated by computing the root-mean-square deviation (RMSD) between the experimental RIDME spectrum and its fit. In order to find the optimal values of the fitting parameters, which would deliver the lowest RMSD, a genetic algorithm was included into the DipFit program. The genetic algorithm was used a number of times in the EPR literature,^{5,9-11} which revealed its efficiency in finding the global minimum of optimization problems with many fitting parameters. The detailed description of the genetic algorithm can be found in our previous publication.¹¹ It should be noted here that the genetic algorithm has several intrinsic settings.¹¹ In the present study, the genetic algorithm was used with a generation size of 128, a mutation rate of 0.01, a crossover rate of 0.50, and a total number of populations (optimization steps) of 400. These settings ensured the convergence of the fitting algorithm to its global minimum for both systems, **1** and **Q8R1**. As can be seen from Figure S9, the RMSD value

reached its minimum after the first 50-100 optimization steps and later did not change significantly, revealing that the global minimum was found.

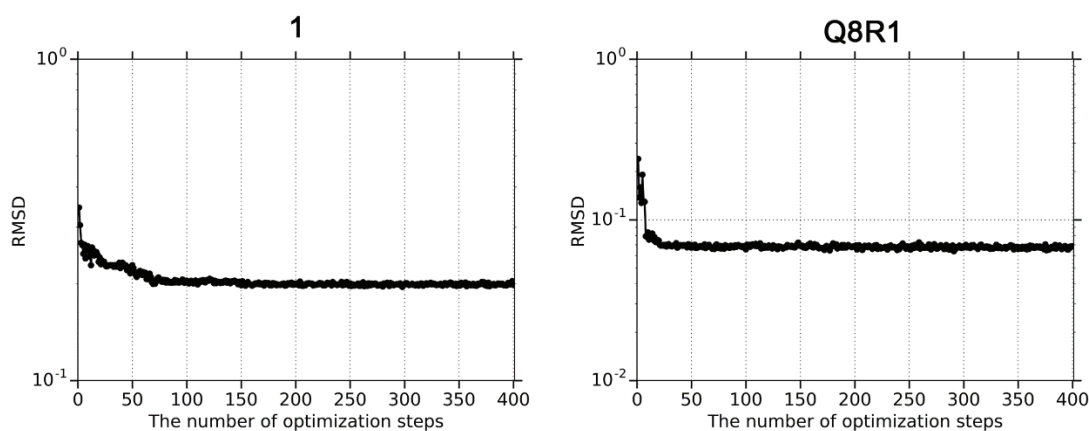


Figure S9. RMSD between the experimental RIDME spectra and their fits plotted against the optimization step of the genetic algorithm.

The fitting described above yields two important results, namely, the best fit to the experimental RIDME spectrum (Figure 8c in the main text) and the optimized values of the fitting parameters (Table 1 in the main text), that is the optimized values of $\langle n \rangle$, σ_r , $\langle \xi \rangle$, and σ_ξ (Figure 9 in the main text).

In order to access the error on these parameters, the RMSD values were evaluated here within one- or two-dimensional sub-spaces of fitting parameters by varying only a single fitting parameter or a pair of fitting parameters and setting the other fitting parameters to their optimized values. Thus, RMSD values were consecutively recorded in dependence of $\langle n \rangle$ and σ_r , then in dependence of $\langle \xi \rangle$ and σ_ξ , and finally in dependence of T . For test systems **1** and **Q8R1**, these three dependences are depicted in Figure S10. Remarkably, all RMSD plots reveal a single and well-defined minimum around the optimized values of the fitting parameters. This proves that all fitting parameters can be unambiguously determined from the present RIDME data.

In order to obtain a quantitative error estimate for each fitting parameter from the corresponding RMSD plot, a threshold for the maximal acceptable RMSD value was set to 110 % of the lowest RMSD value in that plot. Thus, the parameter ranges, in which the RMSD value was below this threshold, determined the error bars of the corresponding parameter. The result of such error estimation is summarized in Table 1 of the main text.

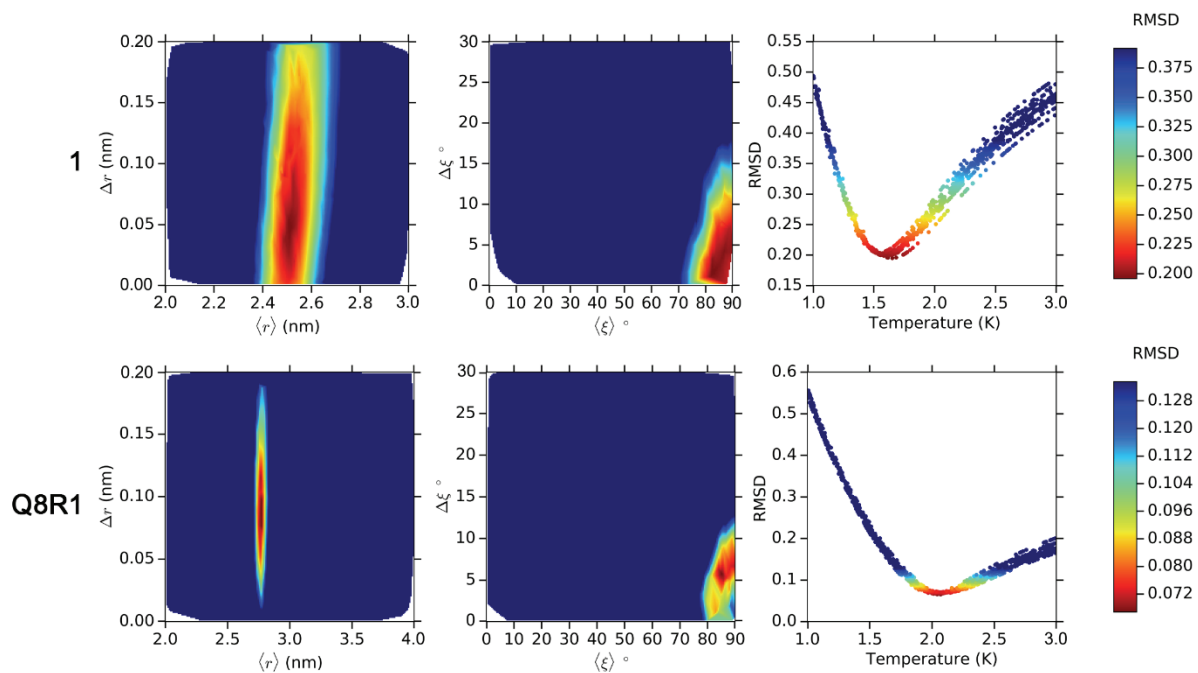


Figure S10. RMSD between the experimental RIDME spectra and their fits plotted against individual fitting parameters.

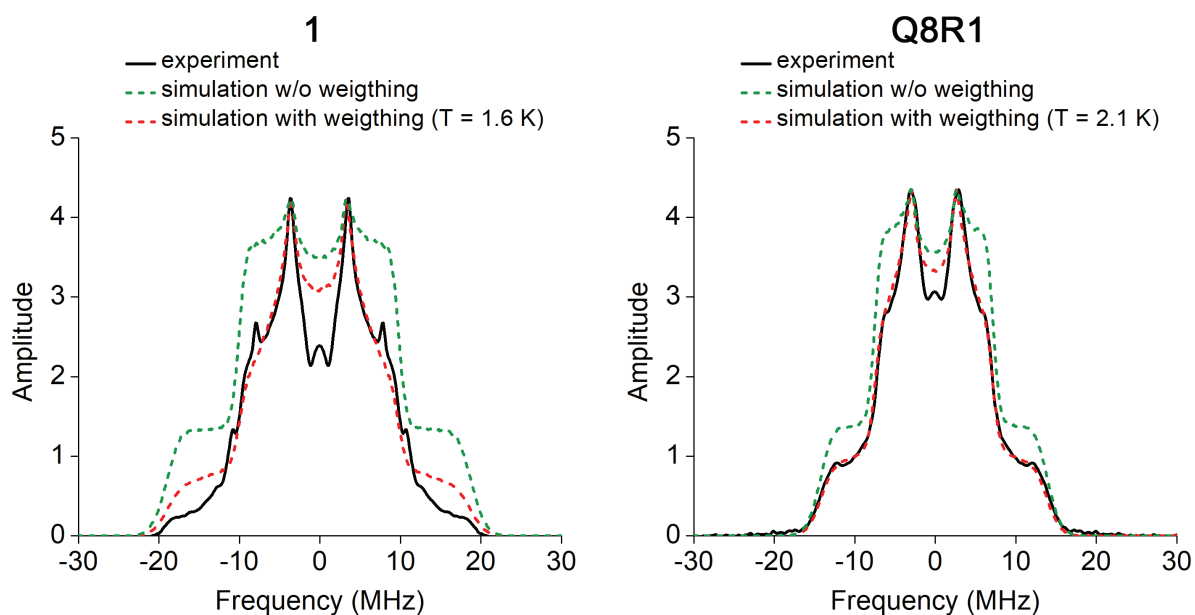


Figure S11. The fits (dashed line) to the RIDME spectra of **1** and **Q8R1** (black solid line) were calculated with and without weighting based on by Equation 15 (see the main text). The fits were calculated with the parameters of $P(r)$ and $P(\xi)$ that are listed in Table 1 of the main text.

6 MtssIWizard and MMM simulations on the met-myoglobin mutant Q8R1

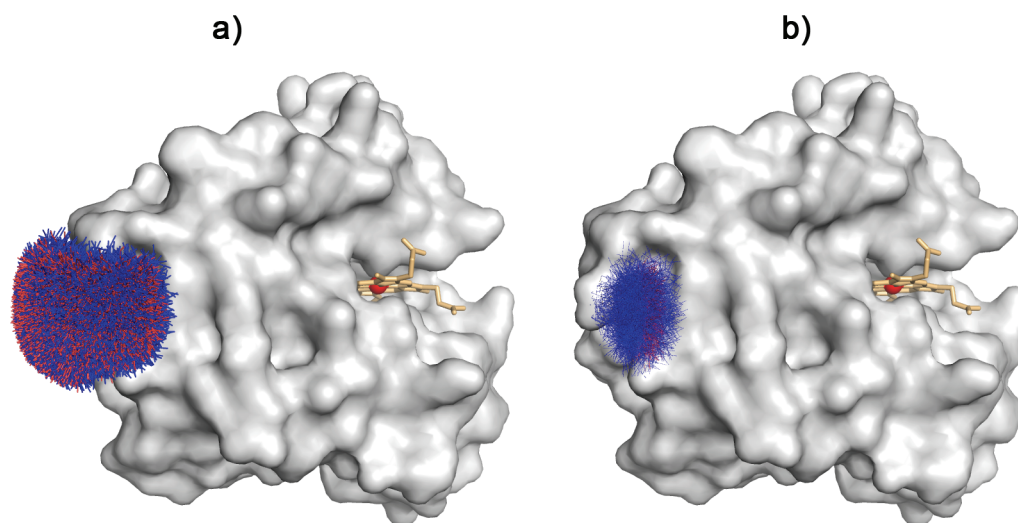


Figure S12. The structural models of the met-myoglobin mutant **Q8R1**. The models are based on the crystal structure of met-myoglobin (PDB-ID 1wla¹²) shown as gray surface. The heme group and the Fe^{3+} ion are depicted as orange sticks and red sphere, respectively. **a)** The conformers of the R1 side chain at the site Q8 were generated by means of the program MtssIWizard^{13,14} using the “painstaking” mode. All conformers are depicted as blue sticks with the read tops that correspond to the N-O[•] radical. **b)** The Fe^{3+} /nitroxide distance was determined for all MtssIWizard-generated conformers of the R1 side chain shown in **a)** (see Figure 9a of the main text) and only those conformers that provide a distance within the 1σ range (± 0.08 nm) around the experimentally determined distance of 2.77 nm were plotted (blue/red sticks).

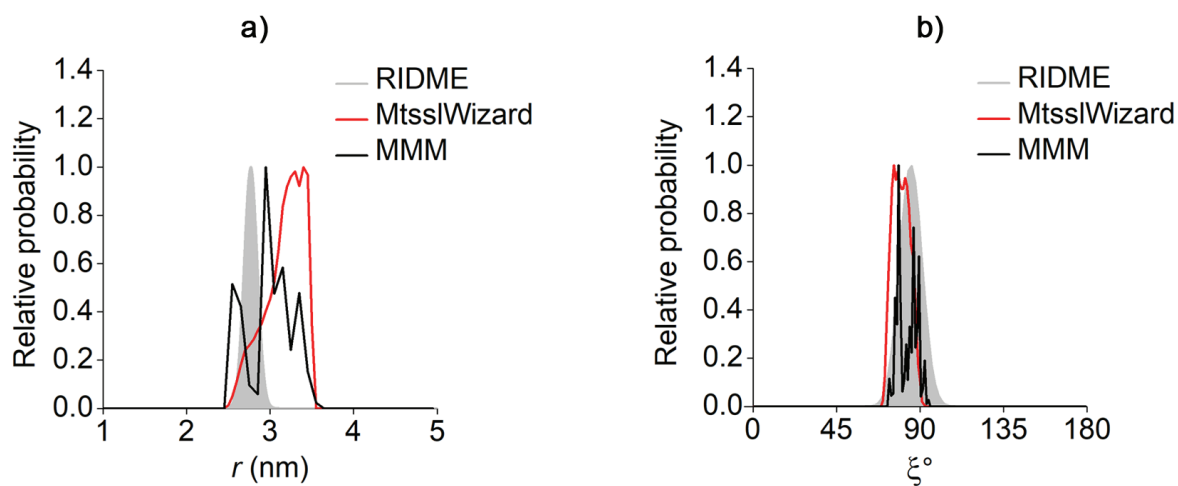


Figure S13. The experimental distributions $P(r)$ and $P(\xi)$ distributions of Q8R1 are compared with the corresponding predictions obtained by means of the programs MtssIWizard^{13,14} and MMM¹⁵.

7 MD simulations on the model compound 1

For the initial structure of **1**, the generation of the conformer/rotamer ensemble (CRE) was performed using the semi-empirical tight-binding method GFN-xTB and the CRE search algorithm.¹⁶ The MF-MD-GC/GFN-xTB algorithm consists of three steps: normal mode following (MF), molecular dynamics (MD) simulations, and 'pseudo-genetic' structure crossing (GC). In all steps, GFN-xTB is used as the underlying electronic structure method. The CRE generation was conducted in THF as the solvent, simulated by the implicit GBSA solvation model.^{17,18} The energetically lowest conformer found for the initial structure was fully optimized at the GFN-xTB/GBSA(THF) level of theory and molecular dynamics (MD) simulations were carried out with implicit solvent GBSA(THF) at two different temperatures, 298 K and 165 K (the freezing point of THF). The MD simulations were done for 100 ps, 500 ps, and 1 ns with a time step of 4 fs and an equilibration phase of 10 ps. Increasing the simulation time from 100 ps to 1 ns did not lead to any significant change in the $P(r)$ and $P(\xi)$ distributions (Figure S13), suggesting that the system may be regarded as equilibrated. The SHAKE¹⁹ algorithm was used to constrain all bonds. For geometry optimization and MD simulation the stand-alone program xtb²⁰ was used. Evaluation of the trajectories was performed with the program TRAVIS.²¹

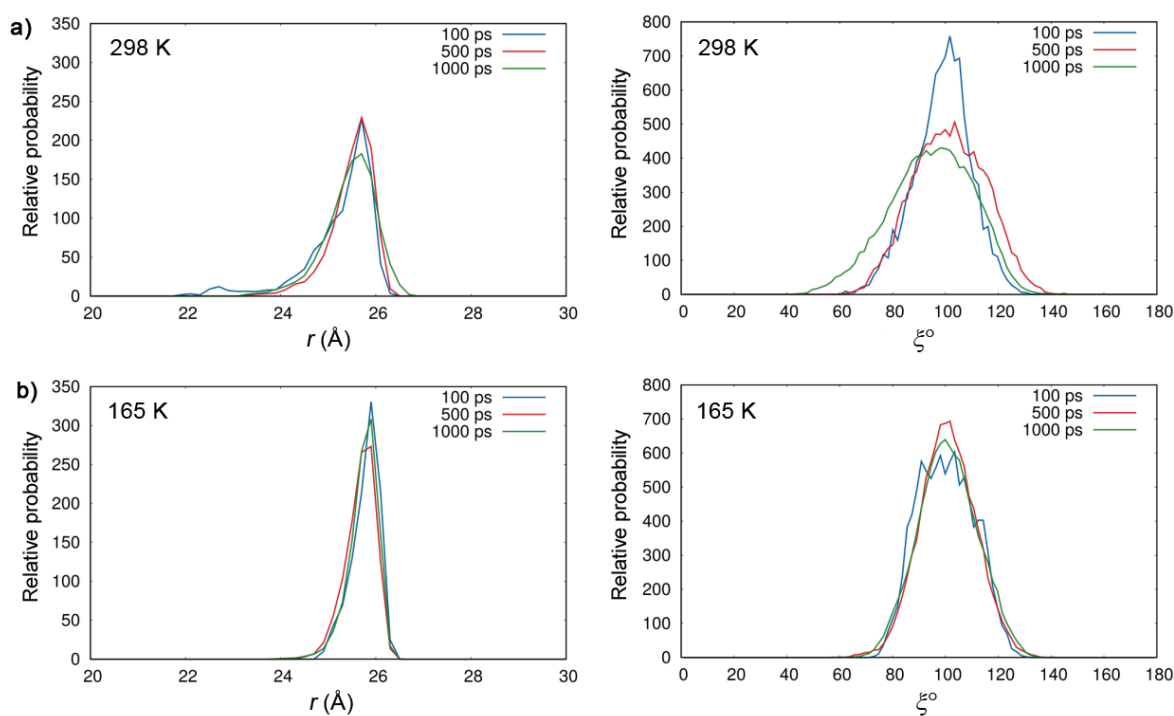


Figure S14. $P(r)$ and $P(\xi)$ distributions obtained from MD simulations on **1** at **a)** room temperature (298 K) and **b)** the freezing point of the solvent THF (165 K). Each distribution was determined from the MD simulations with the time frames of 100 ps, 500 ps, and 1 ns.

8 The atomic coordinates of 1

CL	6.3835495	0.0093357	2.2475824
FE	6.4223112	-0.0073422	0.0490312
N	5.0262256	-1.3730336	-0.2871562
C	3.6761012	-1.1611994	-0.3920664
C	3.0126610	0.0411528	-0.1524108
C	3.6829623	1.2444236	0.0457689
N	5.0285095	1.4251496	-0.1201052
C	5.2466030	2.7702160	-0.0137465
C	6.4635414	3.4031644	-0.2484836
C	7.6551544	2.7039130	-0.4226237
N	7.8288223	1.3533529	-0.2549847
C	9.1820931	1.1399937	-0.3042702
C	9.8354327	-0.0583896	-0.0238795
C	9.1585314	-1.2585392	0.1655770
N	7.8195985	-1.4419564	-0.0466847
C	7.5979408	-2.7855472	0.0680655
C	6.3904189	-3.4218405	-0.2038203
C	5.2066326	-2.7253522	-0.4325378
C	3.9625477	-3.3512612	-0.7727866
C	3.0134475	-2.3833094	-0.7418454
H	1.9597668	-2.4783558	-0.9481063
H	3.8396115	-4.3962440	-1.0065299
C	6.3642047	-4.9022761	-0.2367152
C	5.5388677	-5.6200241	0.6311151
C	5.5245022	-7.0068060	0.5994631
C	6.3290042	-7.6935999	-0.3004696
C	7.1508150	-6.9872414	-1.1690225
C	7.1718702	-5.6006709	-1.1365241
H	7.8057704	-5.0511914	-1.8241372
H	7.7783102	-7.5186962	-1.8762774
H	6.3154361	-8.7775699	-0.3253479
H	4.8825745	-7.5541926	1.2812645
H	4.9179209	-5.0871899	1.3433823
C	8.8167986	-3.4589691	0.4189695
C	9.7830796	-2.5114922	0.4857776

H	10.8249714	-2.6392865	0.7309487
H	8.9084123	-4.5179360	0.5987426
C	11.3137110	-0.0521719	0.0640578
C	11.9622287	0.7560084	0.9999533
C	13.3466575	0.7580530	1.0861388
C	14.1005973	-0.0410365	0.2364958
C	13.4635902	-0.8447732	-0.6999467
C	12.0791082	-0.8531506	-0.7856357
H	11.5854701	-1.4712383	-1.5277976
H	14.0478290	-1.4675042	-1.3687707
H	15.1828257	-0.0369001	0.3033929
H	13.8394999	1.3864349	1.8202111
H	11.3757124	1.3735306	1.6719299
C	9.8589604	2.3583827	-0.6395666
C	8.9123602	3.3258567	-0.7196971
H	9.0452381	4.3682057	-0.9597201
H	10.9206300	2.4507979	-0.8017877
C	6.4909959	4.8831860	-0.2981234
C	7.2826782	5.6118732	0.5916213
C	7.2995916	6.9981184	0.5426763
C	6.5311980	7.6737371	-0.3964568
C	5.7417361	6.9564829	-1.2859147
C	5.7180118	5.5704630	-1.2362453
H	5.1089036	5.0128749	-1.9396479
H	5.1414863	7.4788233	-2.0230325
H	6.5472712	8.7572798	-0.4350260
H	7.9153457	7.5538241	1.2417372
H	7.8751078	5.0884611	1.3345569
C	4.0167054	3.4475948	0.2865024
C	3.0483985	2.5008405	0.3309877
H	1.9992314	2.6319794	0.5404561
H	3.9193045	4.5084422	0.4514204
C	1.5341466	0.0370483	-0.1196008
C	0.8000098	0.8527742	-0.9854472
C	-0.5824892	0.8553867	-0.9517578
C	-1.2704788	0.0404916	-0.0432238

C	-0.5364206	-0.7796771	0.8235038
C	0.8459624	-0.7810764	0.7812710
H	1.4050039	-1.4103340	1.4656932
H	-1.0588238	-1.4135883	1.5313939
C	-2.6874087	0.0496804	-0.0040534
C	-3.8986409	0.0645662	0.0242948
C	-5.3153481	0.0902979	0.0554387
C	-6.0273173	-0.7516746	0.9197702
C	-7.4094602	-0.7222855	0.9445015
C	-8.1233850	0.1493929	0.1157867
C	-7.4098816	0.9906514	-0.7442060
C	-6.0281189	0.9615963	-0.7789435
H	-5.4892166	1.6154349	-1.4556894
H	-7.9449151	1.6612666	-1.4078310
C	-9.5969021	0.1827066	0.1482474
C	-10.3359941	-0.9957502	0.2818679
C	-11.7219042	-0.9781266	0.3075408
C	-12.3809102	0.2400970	0.1996063
C	-11.6680515	1.4294380	0.0797029
C	-10.2850570	1.3962459	0.0494680
H	-9.7344629	2.3264255	-0.0322848
H	-12.2067776	2.3666971	0.0122848
O	-13.7676432	0.3683879	0.2507720
C	-14.6234470	-0.5400185	-0.2248511
O	-14.3204427	-1.5811023	-0.7580927
C	-16.0263216	-0.1034799	-0.0275887
C	-16.4494217	1.0272953	0.5445932
C	-17.9460186	1.1218194	0.5622211
N	-18.3143826	-0.1397961	-0.0888380
O	-19.5052223	-0.4781835	-0.2844946
C	-17.1740662	-0.9667141	-0.4938423
C	-17.2505584	-2.3160275	0.2319744
H	-18.1894358	-2.8072033	-0.0213534
H	-16.4158794	-2.9421682	-0.0784064
H	-17.2052425	-2.1662156	1.3097736
C	-17.2089305	-1.1560816	-2.0158492

H	-17.1322442	-0.1917395	-2.5162342
H	-18.1481755	-1.6309498	-2.2972140
H	-16.3753224	-1.7859630	-2.3215369
C	-18.5345257	1.1414140	1.9797336
H	-18.3030563	2.0894265	2.4609619
H	-18.1168512	0.3281200	2.5716425
H	-19.6157164	1.0205115	1.9179418
C	-18.4869337	2.2891808	-0.2752412
H	-18.2580901	3.2322722	0.2167949
H	-18.0335833	2.2830334	-1.2655510
H	-19.5670187	2.1848826	-0.3752003
H	-15.8229087	1.8055569	0.9555654
H	-12.2745525	-1.9021934	0.4129693
H	-9.8229851	-1.9485063	0.3516007
H	-7.9432526	-1.3697473	1.6317532
H	-5.4879779	-1.4275550	1.5741701
H	-1.1406647	1.4890560	-1.6318886
H	1.3215301	1.4763942	-1.7034365

References

- 1 S. A. Bylka and L. A. Andersson, *J. Chem. Educ.*, 1997, **74**, 426–430.
- 2 E. Lloyd and A. G. Mauk, *FEBS Lett.*, 1994, **340**, 281–286.
- 3 B. A. Springer and S. G. Sligar, *Biochemistry*, 1987, **84**, 8961–8965.
- 4 J. G. Guillemette, Y. Matsushima-Hibiya, T. Atkinson and M. Smith, *Protein Eng. Des. Sel.*, 1991, **4**, 585–592.
- 5 S. Stoll and A. Schweiger, *J. Magn. Reson.*, 2006, **178**, 42–55.
- 6 M. Fittipaldi, I. García-Rubio, F. Trandafir, I. Gromov, A. Schweiger, A. Bouwen and S. Van Doorslaer, *J. Phys. Chem. B*, 2008, **112**, 3859–3870.
- 7 M. Florent, I. Kaminker, V. Nagarajan and D. Goldfarb, *J. Magn. Reson.*, 2011, **210**, 192–199.
- 8 K. Keller, A. Doll, M. Qi, A. Godt, G. Jeschke and M. Yulikov, *J. Magn. Reson.*, 2016, **272**, 108–113.
- 9 B. Filipič and J. Štrancar, *Appl. Soft Comput.*, 2001, **1**, 83–90.
- 10 T. Spalek, P. Pietrzyk and Z. Sojka, *J. Chem. Inf. Model.*, 2005, **45**, 18–29.
- 11 D. Abdullin, G. Hagelueken, R. I. Hunter, G. M. Smith and O. Schiemann, *Mol. Phys.*, 2015, **113**, 544–560.
- 12 R. Maurus, C. M. Overall, R. Bogumil, Y. Luo, A. G. Mauk, M. Smith and G. D. Brayer, *Biochim. Biophys. Acta - Protein Struct. Mol. Enzymol.*, 1997, **1341**, 1–13.
- 13 G. Hagelueken, R. Ward, J. H. Naismith and O. Schiemann, *Appl. Magn. Reson.*, 2012, **42**, 377–391.
- 14 G. Hagelueken, D. Abdullin, R. Ward and O. Schiemann, *Mol. Phys.*, 2013, **111**, 2757–2766.
- 15 Y. Polyhach, E. Bordignon and G. Jeschke, *Phys. Chem. Chem. Phys.*, 2011, **13**, 2356–2366.
- 16 S. Grimme, C. Bannwarth, S. Dohm, A. Hansen, J. Pisarek, P. Pracht, J. Seibert and F. Neese, *Angew. Chemie Int. Ed.*, 2017, **56**, 14763–14769.
- 17 W. Clark Still, A. Tempczyk, R. C. Hawley and T. Hendrickson, *J. Am. Chem. Soc.*, 1990, **112**, 6127–6129.
- 18 S. Grimme, F. März and P. Shushkov, .
- 19 J. P. Ryckaert, G. Ciccotti and H. J. C. Berendsen, *J. Comput. Phys.*, 1977, **23**, 327–341.
- 20 Please contact xtb@thch.uni-bonn.de to obtain the program.
- 21 M. Brehm and B. Kirchner, *J. Chem. Inf. Model.*, 2011, **51**, 2007–2023.